BESSY - Annual Report

2005

Berliner Elektronenspeicherring-Gesellschaft für Synchrotronstrahlung m.b.H.

Published by:
Berliner Elektronenspeicherring-Gesellschaft
für Synchrotronstrahlung m.b.H. (BESSY)

Albert-Einstein-Str.15
12489 Berlin
Tel. +49 30 6392 2999
Fax +49 30 6392 2990
info@bessy.de
www.bessy.de

Edited by:
Dr. Kai Godehusen

BESSY GmbH
Albert-Einstein-Straße 15
12489 Berlin . Germany
Fon +49-30 / 63 92 - 29 99
Fax +49-30 / 63 92 - 29 90

Geschäftsführung:
Prof. Dr. Dr. h.c. Wolfgang Eberhardt
Prof. Dr. Eberhard Jaeschke
Aufsichtsratvorsitzender:
Prof. Dr. Dr. h.c. mult. Joachim Treusch

Sitz der Gesellschaft:
Berlin
Handelsregister:
Amtsgericht Charlottenburg
HRB 14 635

Bankverbindung:
Deutsche Bank AG
Berlin
Kto 417 300 101
BLZ 100 700 00

Leibniz
Gemeinschaft

BESSY Inside

‘Physics is not one of the favorite subjects of German school children!’ titled a newspaper recently. This is not a surprise. It probably never was during the last decades – but it became more apparent that physics education in schools and pre-schools is lacking time, interest and enthusiasm. This is a dramatic issue also for a scientific institution such as BESSY, since science needs well educated students. For the realization of our future plans, like our soft X-ray Free Electron Laser, we also need clever new scientists ready to eagerly venture into new fields and address entirely new scientific questions.

In order to involve the public especially young people more in science and what scientists do, several initiatives have been started in recent years reaching back to the Year of Physics in 2000 and finding another climax celebrating the centennial of Einstein’s ‘magic five papers’ in 1905. During this ‘Einstein Year’, BESSY was involved in manifold activities. We demonstrated the photoelectric effect with hands-on experiments on the exhibition ship MS Einstein. The exhibition ‘Highlights der Physik’ and likewise the events ‘Lange Nacht der Wissenschaften’ and ‘Physik zum Frühstück’ had a focus on Einstein’s work. The television science programme – ***‘nano’-*** visited Adlershof with their ‘nanoCamper’, a group of twelve selected high school students who were introduced to the daily work of scientists. At their day at BESSY they took control of the machine, injecting electrons in the storage ring and kicking them out afterwards. They crystallized proteins and built a 3d protein model from scratch, and they learned about non-destructive material analysis using X-rays. Every event has been very successful and we feel encouraged to keep on introducing children and students of all age into the fascinating world of physics, chemistry and biology.

That even ‘good old’ school and textbook science can be exciting, especially when this science is revamped by the use of new experimental evidence has been shown by Uwe Becker’s group from Fritz-Haber-Institute. They downsized the classical double slit experiment onto atomic scale leaving electrons ‘in doubt’ of their state of origin (see Highlights). This is only one of the exciting research results obtained by our steadily increasing user community.

There is good news for our current and future users. The construction of the Willy-Wien-Labor is proceeding with the new Metrology Light Source of the PTB which will start operations in 2007. BESSY itself passed the stringent evaluation of the Leibniz Association with flying colors in the year 2005 and we are very pleased that following the positive evaluation report we received funding to hire more desperately needed beamline scientists to improve our user support.

Finally, we would like to thank all our users and staff members who through their efforts and dedication made 2005 yet another successful year. Enjoy browsing through the Annual Report and the Highlights 2005.

Content

First measurements at the BAM 7 T wavelength shifter for its use as a primary source standard

R. Klein, G. Brandt, L. Cibik, M. Gerlach, M. Hoffmann, M. Krumrey, G. Ulm
Physikalisch-Technische Bundesanstalt, Abbestraße 2 – 12, 10587 Berlin, Germany

M. Scheer
BESSY GmbH, Albert-Einsteinstraße 15, 12489 Berlin, Germany

For more than 20 years PTB has been using the calculable radiation of bending magnets from the BESSY I and BESSY II electron storage rings in the visible, UV, VUV and X-ray spectral range for radiometry [1], especially for the calibration of radiation sources [2] and energy-dispersive detectors [3].

The calculation of the spectral photon flux ϕ for a given photon energy E requires the measurement of all parameters that enter the Schwinger equation [4] with high accuracy [5]. These parameters are the electron beam current I, the electron energy W, the magnetic induction at the radiation source point B, the vertical electron beam size and divergence and the geometric parameters defining the angular acceptance.

Nevertheless, the usable spectral range is limited on the high energy side to about the 10 to 20 fold of the characteristic energy. This is on the one hand due to the low photon flux because of the exponentially decreasing flux at these energies and on the other hand due to the increasing relative uncertainty in the calculation of the spectral photon flux. For photon energies E that are large compared to the characteristic energy E_c the uncertainty in the calculation of ϕ is dominated by the relative uncertainty in the measurement of B and W, which are in the order of 10^{-4}. For a small angular acceptance in the forward direction of the synchrotron radiation emission the relative uncertainty $\Delta\phi/\phi$ scales roughly as

$$\Delta\phi/\phi \approx (E/E_c - 1) \cdot \Delta B/B \text{ and } \Delta\phi/\phi \approx 2 \cdot E/E_c \cdot \Delta W/W, \qquad (1)$$

respectively.

To extend the radiometry based on calculable synchrotron radiation sources to higher photon energies, a source with a higher characteristic photon energy as compared to a bending magnet is needed. Already at BESSY I, PTB had used a 6 T superconducting wavelength shifter (WLS) [6] for that purpose. At BESSY II, PTB has access to the BAM 7 T WLS, which has a more than five-fold higher characteristic energy as the BESSY II bending magnets. The WLS was procured according to the PTB and BAM specifications and is operated by the BESSY GmbH.

Unfortunately, the magnetic field map of a WLS is more complicated than in the case of a bending magnet. The bending magnet has a large area of homogeneous magnetic field, whereas a wavelength shifter shows a magnetic field map as illustrated in fig. 1 with large field gradients in the direction of the orbit. So the determination of the magnetic induction at the radiation source point is difficult, not only because the field map must be determined, but also because it strongly depends on the exact location of the source point in the device. The magnetic field in the center of the WLS along the orbit s can be approximated by

$$B(s) = B_0 \cdot \cos(2\pi s/\lambda_s). \qquad (2)$$

For small variations of the observation angle in the horizontal plane by $\Delta\alpha_h$, the shift Δs of the source point along the orbit is

$$\Delta s \approx R \cdot \Delta\alpha_h, \tag{3}$$

with R being the bending radius, which is approximately 1 m for the 7 T WLS. At the specification of the WLS emphasis was put on a rather flat top of the main pole field (λ_s = 0.45 m), so that for a source point located at $s_0 = 0$, the relative change of the magnetic induction $\Delta B/B$ will stay below $1 \cdot 10^{-4}$ for $|\Delta s| < 1$ mm.
The field of the wavelength shifter was characterized before installation and with NMR probes which are mounted in the joke, the exact value of the maximum of the main pole field B_0 can be monitored.

Unfortunately, these NMR probes are not working right now for what ever reason, so a precise determination of B_0 is not possible at the moment. Moreover, as can be seen in fig. 1, the upstream steering magnet was moved closer to the WLS by BESSY as was originally designed in order to gain space for the installation of a Landau cavity. This had the side effect, that the trajectory in the WLS is not symmetric with respect to the middle of the WLS anymore. Calculations of the trajectory for this setting predict, that the source point is shifted to $s_0 \approx -4$ mm [7], i.e. upstream away from the flat top into a region with larger field gradients. This has little influence on the performance of the WLS monochromator beamline, but has a major disadvantages for the radiometric use of the undispersed radiation of the device: Even if the NMR probes would work properly,

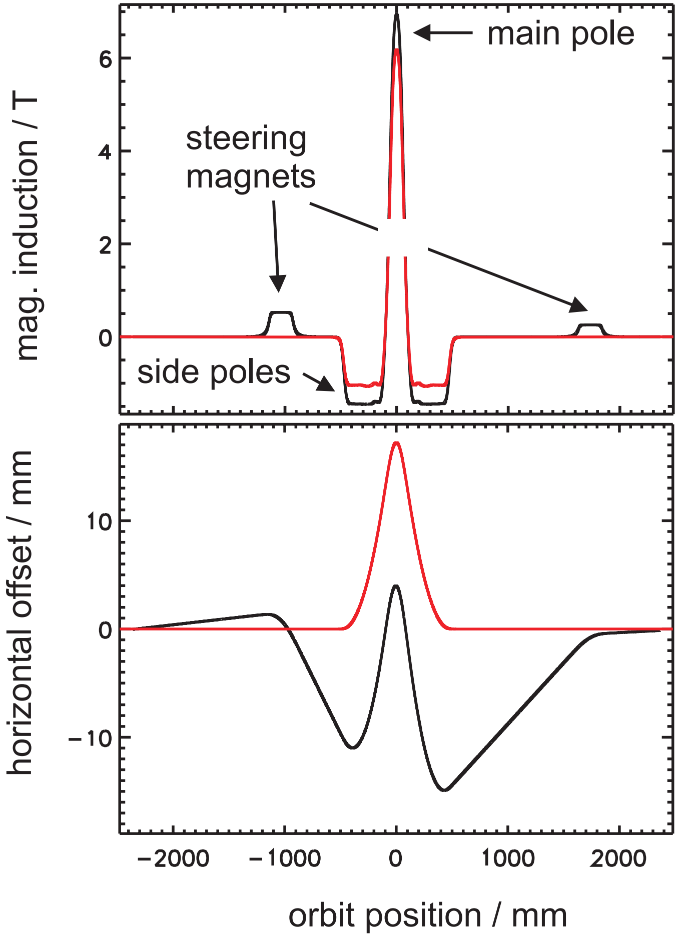

Fig. 1: Top: magnetic induction of the WLS along the electron orbit. In black color the standard setting of the 7T WLS with its asymmetrically placed steering magnets is shown. In red color, a special setting during a PTB shift is shown. The steering magnets were switched off, resulting in a symmetric field map. At this setting, the maximum field could only be set to 6 T in order to avoid to large deviations of the electron trajectory in the horizontal plane; Bottom: the electron trajectory in the WLS for the different field settings.

the magnetic induction could not be precisely determined anymore because it is more sensitive to the exact location of s_0, which can not be determined precise enough.To experimentally detect a possible shift of the source point from the center position, the undispersed radiation of the WLS was measured by a HPGe-detector at different horizontal positions within the beamline acceptance during a special PTB shift with reduced electron beam current. The slightly different observation angles $\Delta\alpha_h$ mean slight shifts of the radiation source point along the orbit and therefore slightly different magnetic inductions at the source points (see eq. 3). The result will be a variation in the photon flux according to (1), which is largest for high values of E/E_C. In fig. 2 the relative change of the photon flux in the photon energy interval from 90 keV to 140 keV is shown. A clear indication for a position depended variation of the flux is seen. The observed relative change in the photon flux is in accordance with the calculated shift of the radiation source point of -4 mm.

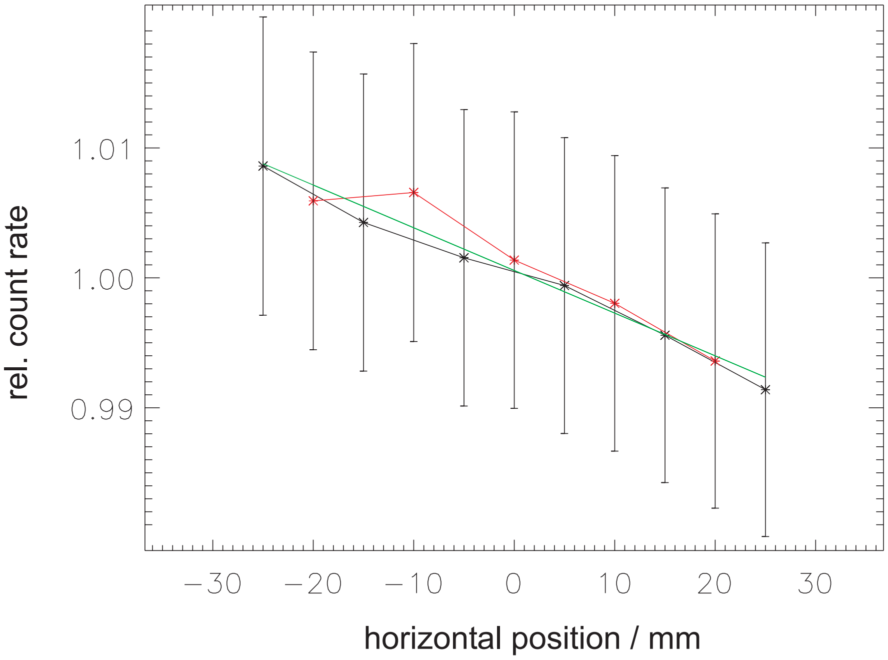

Fig. 2: Relative count rate for photon energies summed from 90 keV to 140 keV, measured with a HPGe-detector with a 4 mm Cu-filter. The detectors aperture of 1 mm diameter was placed approx. 36 m from the radiation source point. The error bars are given by the counting statistics and by the possible variation of the angular acceptance of the aperture during the horizontal movement. The electron beam current was 108 nA.

In another PTB shift, the asymmetrically placed WLS steering magnets were switched off in order to obtain a symmetric field map. In this setting the WLS main pole field could only be set to 6 T maximum magnetic induction due to the large horizontal deviation of the electron beam trajectory. With this setting the trajectory in the WLS (fig. 1 bottom, red curve) is symmetric again and the source point is expected to be at the maximum of the main pole field, thus showing a much smaller field gradient for a variation of the horizontal observation angle. Fig. 3 shows a similar measurement as described above. There no significant inhomogenity is observed. With this symmetric setting, the WLS behaves as expected and - given, the NMR probes are repaired - the use of the WLS as a calculable source of radiation in the hard X-ray spectral range can be further pursued.

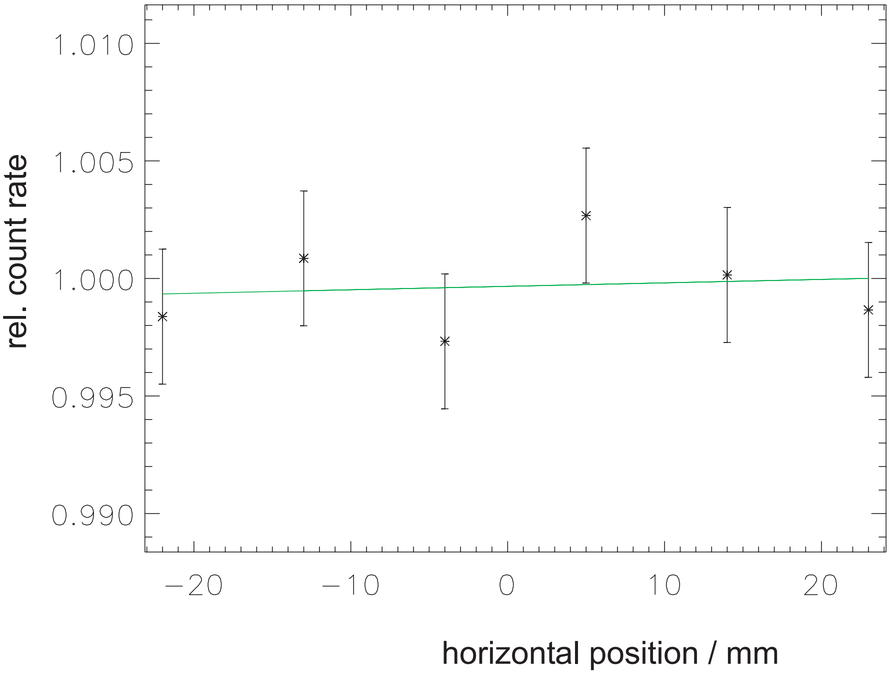

Fig. 3: Relative count rate for photon energies summed from 90 keV to 140 keV, measured with a HPGe-detector with a 4 mm Cu-filter for the special operation mode of the WLS. The detectors aperture of 3 mm diameter was placed approx. 36 m from the radiation source point. The error bars are given by the counting statistics and by the possible variation of the angular acceptance of the aperture during the horizontal movement. The electron beam current was 5.1 nA.

[1] G. Ulm, Metrologia **40** (2003) S101 – S106
[2] M. Richter et al., Nucl. Instrum. Methods **A467/468** (2001) 605 - 608
[3] F. Scholze et al., Metrologia **38** (2001) 391 - 395
[4] J. Schwinger, Phys. Rev. **75** (1949) 1912
[5] R. Klein et al., Proc. of EPAC 2004 (2004) 273 – 275
[6] R. Thornagel et al., Rev. Sci. Instrum. **67** (1996) 653 – 657
[7] M. Scheer, PhD thesis, BESSY 2006, in preparation

Comparison of spectral responsivity scale realizations at 157 nm

A. Gottwald, S. Kück[1], F. Brandt[1], M. Richter

Physikalisch-Technische Bundesanstalt, Abbestr. 2-12, 10587 Berlin
[1]Physikalisch-Technische Bundesanstalt, Bundesallee 100, 38116 Braunschweig

Excimer lasers are nowadays widely used for industrial applications such as photolithography of semiconductor devices. For production control, standardization and safety regulations during testing and production, calibrated radiometers with uncertainties of a few percent in the measurement of pulse energies are needed. At the Physikalisch-Technische Bundesanstalt (PTB), high precision measurement and calibration services are provided for the main excimer laser wavelengths in the UV and DUV spectral regions. Recently, at PTB's laser radiometry facility in the Optics Division a vacuum compatible setup and a calibration chain for the measurement of the average power for F_2-laser radiation at 157 nm was established (Fig. 1) [1]. On the other hand, to maintain a scale of spectral responsivity based on semiconductor photodiodes at wavelengths below 400 nm, PTB uses monochromatized synchrotron radiation of the electron storage ring BESSY II in combination with cryogenic electrical substitution radiometers as primary detector standards [2, 3]. This allows determination of radiant power with relative uncertainties well below 1 % also at 157 nm, however, limited to a few µW cw power as available at the Normal-Incidence-Monochromator (NIM) beamline for detector calibration [4]. To extend the calibration facilities, a F_2-laser system was installed, with the possibility of being alternatively coupled into the beamline behind the NIM. This allows the direct measurement of the average laser power emitted by the pulsed excimer laser using the primary detector standard SYRES II, and for the calibration of suitable transfer detector devices, since the SYRES II radiometer had been shown to be insensitive to the radiation pulse structure [5].

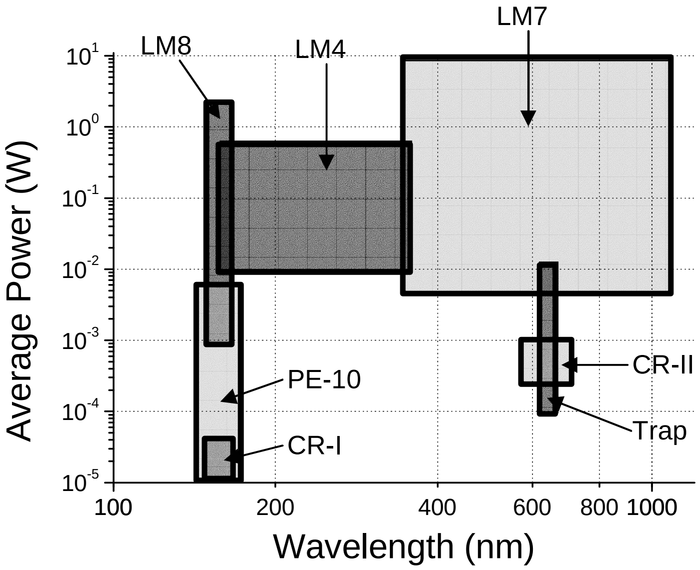

Figure 1.
Schematic calibration chains:
CR-I: SYRES II cryogenic radiometer at the PTB laboratory at BESSY II.
CR-II: cryogenic radiometer at the PTB laser radiometry facility;
LM4, LM7, LM8: Standard detectors at the PTB laser radiometry facility.
Trap: Si-trap detector at the PTB laser radiometry facility.
PE-10: pyroelectric detector as transfer standard in this comparison

The two realizations of the spectral responsivity scale at 157 nm have been compared – worldwide for the first time – using an OPHIR PE-10 pyroelectric detector, which is able to span over the gap in intensities between laser-based and synchrotron radiation-based instrumentation (for details, see [6]). At the two facilities, this detector was calibrated regarding its pulse energy responsivity, i. e. the detector output voltage per laser pulse energy.

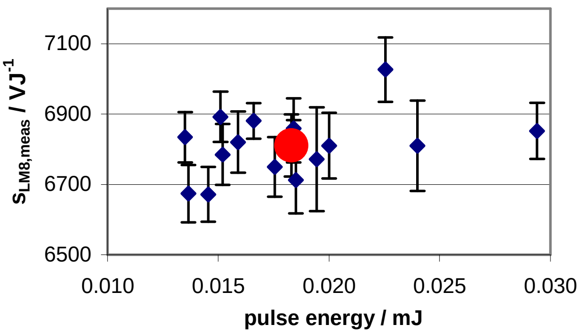

Figure 2. Results of the calibration run for the PE-10 detector in vacuum at PTB laser radiometry facility: Responsivity (200 µJ-range, not corrected for the switching factor) as a function of the applied pulse energy. The diamonds correspond to single measurements, the large circle corresponds to the mean value.

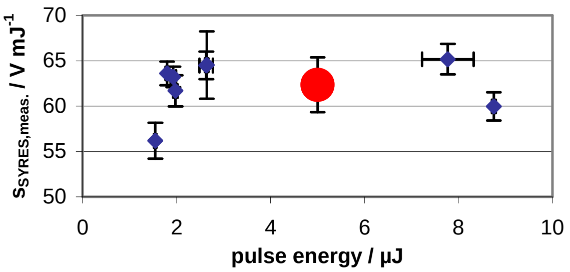

Figure 3. Results of the PE-10 powermeter calibration with the SYRES II primary standard in the PTB laboratory at BESSY II. The responsivity (20 µJ-range, without correction for plasma contribution) is shown for different pulse energies (diamonds); the large circle indicates the mean value.

At the PTB laser radiometry facility, a total set of 16 measurements at 157 nm in vacuum atmosphere (about 1×10^{-6} mbar) were performed (Fig. 2). No significant dependence of the responsivity on the applied average power, repetition rate, or pulse energy was observed. Thus, we determined the responsivity of the OPHIR PE-10 at 157 nm in the 200-µJ measurement range. The responsivity in the 20-µJ-range is obtained by taking into account the switching factor between the two ranges. Finally, we obtain for the responsivity of PE-10 at 157 nm in vacuum atmosphere in the 20-µJ range s_{LM8} = (66700 ± 1090) V/J (standard uncertainty, $k = 1$).

With the SYRES II radiometer at BESSY II, a total of eight measurements at different pulse energies were performed in the lowest pulse energy range of the PE-10, i.e. 20 µJ (Fig. 2). For all measurements, a contribution of (29 $\pm$ 2) % non-VUV plasma glow in the radiant power was determined by using an UV-blocking glass filter, which has to be taken into account for a correction of the measured values. This relatively high contribution is specific for the laser system used at BESSY II. The average responsivity (corrected for the non-157 nm contributions) was determined from all measurements to be s_{SYRES} = (69890 ± 5510) V/J (standard uncertainty, $k = 1$).

In conclusion, the agreement between the responsivities determined is about 4.8 % and, therefore, within the combined standard uncertainties. Hence, this result validates both physical scale realizations. The uncertainty at the PTB laser radiometry group arises mainly from the measurement itself, caused by the requirement to measure at low average powers. The uncertainty at the PTB laboratory at BESSY II is mainly caused by the determination of the fraction of non-VUV radiation from the laser source.

---

[1] S. Kück, F. Brandt, M. Taddeo, Appl. Opt. **44**, 2258 – 2265 (2005).

[2] A. Gottwald, U. Kroth, M. Krumrey, M. Richter, F. Scholze, G. Ulm, *accepted for* Metrologia (2006),

[3] H. Rabus, V. Persch, G. Ulm, Appl. Opt. **36**, 5421 – 5440 (1997).

[4] M. Richter, J. Hollandt, U. Kroth, W. Paustian, R. Thornagel, G. Ulm, Nucl. Instr. and Meth. A **467-468**, 605 – 608 (2001).

[5] M. Richter, U. Kroth, A. Gottwald. Ch. Gerth, K. Tiedtke, T. Saito, I. Tassy, K. Vogler, Appl. Opt. **41**, 7167 – 7172 (2002).

[6] S. Kück, F. Brandt, H.-A. Kremling, A. Gottwald, A. Hoehl, M. Richter, *accepted for* Appl. Opt. (2006)

Polarization dependence of multilayer reflectance in the EUV spectral range

Frank Scholze, Christian Laubis, Christian Buchholz, Andreas Fischer, Sven Plöger, Frank Scholz, and Gerhard Ulm

Physikalisch-Technische Bundesanstalt, Abbestraße 2-12, 10587 Berlin, Germany

The Physikalisch-Technische Bundesanstalt (PTB) with its laboratory at the electron storage ring BESSY II[1] is the European centre of EUV radiometry and supports the national and European industry by carrying out high-accuracy at-wavelength measurements in the EUV spectral region, particularly to support the development of Extreme Ultraviolet Lithography (EUVL), which holds the key to the next generation of computer technology. EUVL imaging requires multilayer optics which have been manufactured with extreme accuracy, in order to ensure a uniform illumination of the wafer plane and an optimized throughput. PTB's EUV reflectometer allows the measurement of mirrors having diameters up to 550 mm, a height of 230 mm, and a weight of up to 50 kg[2]. In response to the increasing demands of the industry,, substantial improvements in the total measurement uncertainty and repeatability at PTB have been demonstrated[3,4]. The measurements at PTB are carried out using highly polarized synchrotron radiation[5]; whereas EUVL uses EUV pulsed plasma sources emitting unpolarized radiation. For a full understanding and specification of the optics it is therefore essential to know the polarization properties of the optical components. We will demonstrate here that taking advantage of all possible movements of detector and sample in the EUV reflectometer enables sound measurements of polarization properties up to angles of incidence of 20° to the normal.

The polarization vector of the incident radiation is parallel to the X-axis. This results in pure S-polarization in our normal mode of operation, i.e. using the Θ and 2Θ axis for the setting of the incidence and exit angle of the radiation. There is, however, also the possibility of using the X-movement of the detector and the tilt-motion of the sample to obtain a P-polarization geometry. This is shown schematically in Fig. 1.

As the tilt-axis was only designed to compensate for the curvature of mirrors, its range is restricted to ±10°. If a wedge is used to offset the angle of the sample, it allows measurements of angles of incidence between 0° and 20°. The detector manipulator allows the distance of the detector to the Θ-axis to be set to 150 mm and the detector to be moved 125 mm horizontally out of the plane. This corresponds to an angle of 39.8° with respect to the incoming beam and thus matches very well the possible range of the tilt-movement. A further option is to use both axis of rotation and set, e.g. equal angles for Θ and tilt, resulting in a plane of deflection at an orientation of 45° to the electrical field vector. This would be equivalent to a measurement with unpolarized radiation.

The radiation is measured with normal incidence at the detector for the incoming direct beam and also for the reflected beam if we use Θ and 2Θ to position sample and detector in the S-polarization geometry[2]. For the P-polarization geometry shown in Fig. 1, however, the reflected radiation is incident at non-normal direction on the detector diode. Therefore, the signal for the reflected beam must be corrected for the influence of different angles of incidence. This correction is determined experimentally. The diodes used in our measurements are Hamamatsu G1127 GaAsP/Au Schottky diodes. Here, the absorbing front layers are the top Au layer and a thin layer of GaAsP to account for recombination losses at the interface[6]. To interpolate the measurements for different angles of incidence, we assumed that the change in responsivity is only due to the change in the top-layer transmittance:

$$\frac{s(\Theta)}{s(0°)} = \prod_{i=1}^{2} \exp\left(\mu_i d_i \left[1 - \cos\left\{\sin^{-1}\left[\sin(\Theta / n_i)\right]\right\}^{-1}\right]\right), \qquad (1)$$

where s is the responsivity, Θ the angle of incidence (in vacuum), μ the absorption coefficient, d the thickness, and n the refractive index of the respective layer; i=1,2 stands for Au and GaAsP with d(gold)=5.7 nm and d(GaAsP)=3 nm. With this equation an excellent fit of the measured dependence is achieved for the range of incidence angles used.

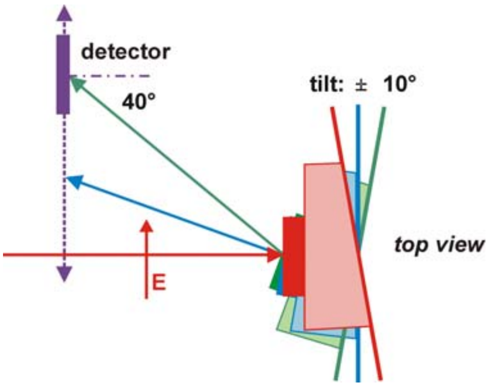

Fig. 1 Scheme of the P-polarization geometry in the EUV-reflectometer. Using a wedge of 10°, the tilt range of ± 10° is transferred to 0° to 20° for the angle of incidence. The direction of the E-vector for the incoming radiation is indicated. The detector movement is linear in this direction.

Using the method as described above, we measured the reflectance as a function of the wavelength for a Mo/Si multilayer mirror with 60 bi-layers with diffusion barriers[7]. We performed measurements for angles of incidence ranging from 2° to the normal up to 20° with S-, P- and a 45° polarization orientation.

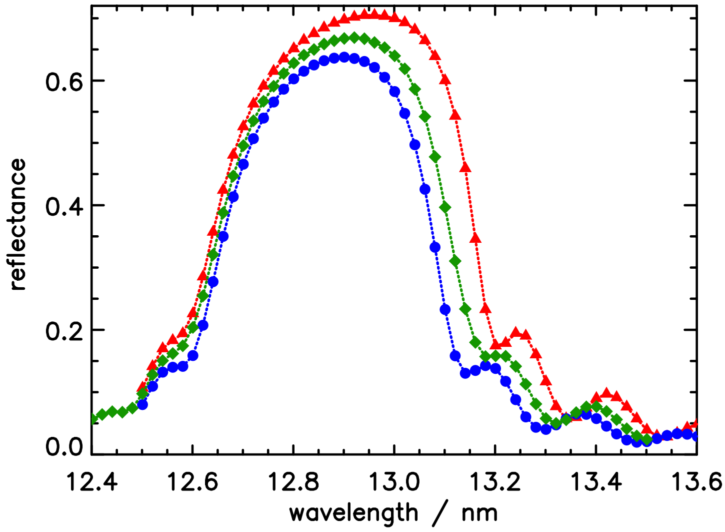

Fig. 2 Reflectance measured at an angle of incidence of 17.5° for S-polarized radiation (▲), P-polarized radiation (●) and with a 45° polarization angle (♦), i.e. equivalent to unpolarized radiation.

Fig. 2 shows results of measurements at an angle of incidence of 17.5° for all 3 polarization orientations. The measurement uncertainties are 0.1 % for absolute reflectance and 2 pm in wavelength. The results clearly show the behaviour which had been expected: the reflectance is lower for P- than for S-polarization and also the bandwidth of the reflectance curve decreases. The measurement at 45° polarization as a representation for unpolarized radiation falls in-between both curves. A comprehensive presentation of the trends of peak wavelength and reflectance is given in Fig. 3. Here, the peak reflectance is plotted as a function of the peak wavelength. By doing so, the cos-dependence of the peak wavelength on the angle of incidence disappears and the curves are linear within our experimental uncertainty of 0.1 %

for the reflectance which is approximated by the height of the plot symbols. The linear dependence allows a reliable interpolation of the measurements at 45° polarization and thus a more detailed comparison of the average values for S- and P-polarization. It turns out that the measured values are slightly but significantly lower than the average value. It must, however, be noted, that the peak reflectance values of each scan were averaged. These appear at slightly different wavelengths for S- and P-polarization, as can be seen in Fig. 2. Averaging the values for each wavelength in the scan therefore results in a slightly lower peak reflectance. This is basically what was measured for the 45° orientation.

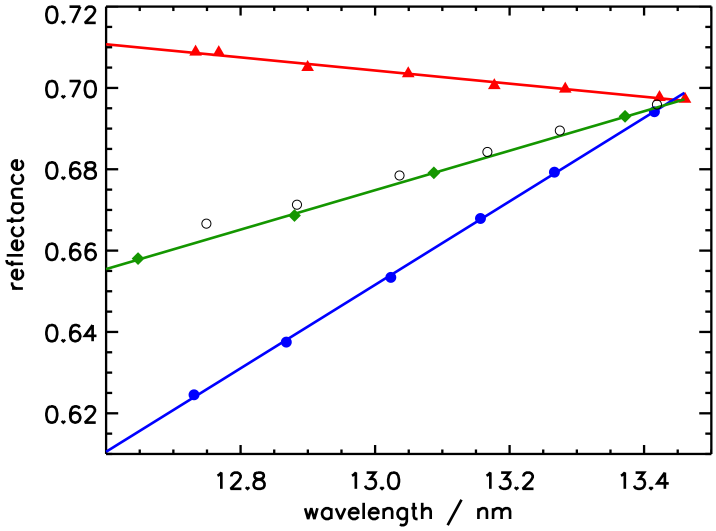

Fig. 3 Peak reflectance versus peak wavelength for S-polarized radiation (▲), P-polarized radiation (●) and with a 45° polarization angle (♦). The average of the S- und P-polarization (○) is shown for comparison. The lines are linear fits of the respective data.

All in all, taking advantage of all possible movements of detector and sample in the EUV reflectometer, we demonstrated the ability to measure detailed polarization properties of EUV optics up to angles of incidence of 20° to the normal. By moving the detector out of plane and tilting the sample we can model any degree of linear polarization by properly balancing the tilt and Θ rotation angles. The results shown here reveal significant differences between reflections in S- and P-polarization geometry already for rather small angles of incidence, such as 5°.

References

1 G. Ulm, B. Beckhoff, R. Klein, M. Krumrey, H. Rabus, and R. Thornagel, "The PTB radiometry laboratory at the BESSY II electron storage ring," Proc. SPIE **3444**, 610-621 (1998)

2 J. Tümmler, G. Brandt, J. Eden, H. Scherr, F. Scholze, G. Ulm, "Characterization of the PTB EUV reflectometry facility for large EUVL optical components," Proc. SPIE **5037**, 265-273 (2003)

3 F. Scholze, C. Laubis, C. Buchholz, A. Fischer, S. Plöger, F. Scholz, H. Wagner, and G. Ulm, "Status of EUV Reflectometry at PTB," Proc. SPIE **5751**, 749-758 (2005)

4 F. Scholze, J. Tümmler, G. Ulm, "High-accuracy radiometry in the EUV range at the PTB soft X-ray radiometry beamline," Metrologia **40**, S224-S228 (2003)

5 F. Scholze, B. Beckhoff, G. Brandt, R. Fliegauf, R. Klein, B. Meyer, D. Rost, D. Schmitz, M. Veldkamp, J. Weser, G. Ulm, E. Louis, A. Yakshin, P. Goerts, S. Oestreich, F. Bijkerk, "The new PTB-beamlines for high-accuracy EUV reflectometry at BESSY II," Proc. SPIE **4146**, 72–82 (2000)

6 F. Scholze, H. Henneken, P. Kuschnerus, H. Rabus, M. Richter, and G. Ulm, "Determination of the electron-hole pair creation energy for semiconductors from the spectral responsivity of photodiodes," Nucl. Instrum. Meth A**439**, 208 - 215 (2000)

7 S. Braun, H. Mai, M. Moss, R. Scholz, and A. Leson, "Mo/Si Multilayers with Different Barrier Layers for Applications as Extreme Ultraviolet Mirrors," Jpn. J. Appl. Phys. **41,** 4074–4081 (2002)

Planned infrared beamlines at the Metrology Light Source of PTB

Ralph Müller[1], Arne Hoehl[1], Roman Klein[1], Gerhard Ulm[1],
Ulrich Schade[2], Karsten Holldack[2], Godehard Wüstefeld[2]

[1] *Physikalisch-Technische Bundesanstalt, Abbestraße 2-12, 10587 Berlin, Germany*
[2] *Berliner Elektronenspeicherring-Gesellschaft für Synchrotronstrahlung m.b.H., Albert-Einstein-Str. 15, 12489 Berlin, Germany*

Electron storage rings have proven to be brilliant radiation sources in the VUV, the soft and the hard X-ray regions of the spectrum. In recent years, their strength as a unique source of IR radiation has also become apparent and is increasingly being exploited at synchrotron radiation facilities around the world. A rapidly growing number of IR beamlines at several synchrotron storage rings have been realized taking advantage of these unique IR light sources [1-3]. In particular, IR radiation in the mid infrared wavelength region is increasingly used in research by means of Fourier transform spectroscopy on biological tissues down to single cells, high-pressure and micro-sample measurements and in investigations on surfaces and thin films applying IR ellipsometry with a high lateral resolution. Applications of IR synchrotron radiation are multidisciplinary, and the number continues to increase as IR beamlines become accessible to an increasing number of users.

Here we present concepts for obtaining infrared synchrotron radiation at the Metrology Light Source (MLS), the new low-energy electron storage ring of the Physikalisch-Technische Bundesanstalt (PTB).

The MLS is designed in close cooperation with BESSY and will be located adjacent to the BESSY II facility in Berlin [4]. Its electron energy can be adjusted between 200 MeV and 600 MeV, maximum stored current will be 200 mA. The building which is going to accommodate the MLS is presently almost completed. First electrons will be stored in 2007, user operation is scheduled to begin in 2008.

PTB will use the MLS as a dedicated facility for radiometry and photon metrology in the UV and VUV range, especially also as a calculable radiation source, a primary source standard in the VIS, UV and VUV. Furthermore, synchrotron radiation in the IR range will be used. At the MLS three beamlines dedicated to the use of IR synchrotron radiation are planned [5] (see Fig. 1): (1) The long period undulator U180 provides radiation with high flux in the MIR spectral range (up to 20 µm), (2) a special THz beamline optimized for the FIR/THz spectral range, and (3) an IR beamline optimized for the MIR to FIR.

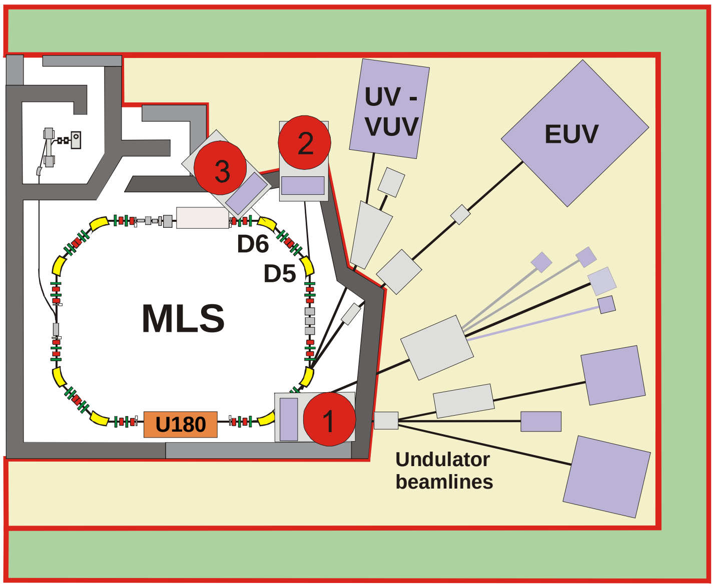

Figure 1: Planned beamlines at the MLS dedicated to the use in the infrared spectral range: (1) Undulator IR, (2) THz beamline, and (3) IR beamline.

The front ends of all IR beamlines are on the roof of the tunnel of the MLS, so there is more space for other beamlines dedicated to the use in the UV, extreme UV and VUV spectral range left in the experimental hall. In the following we will describe the optical design concept of the IR beamline. The scheme of the optical design concept of the IR beamline is shown in Fig. 2. The aim is to develop an IR experimental station at the MLS for the near, mid and far IR wavelength region and to make it accessible to the PTB and to an interested scientific community for a broad field of applications.

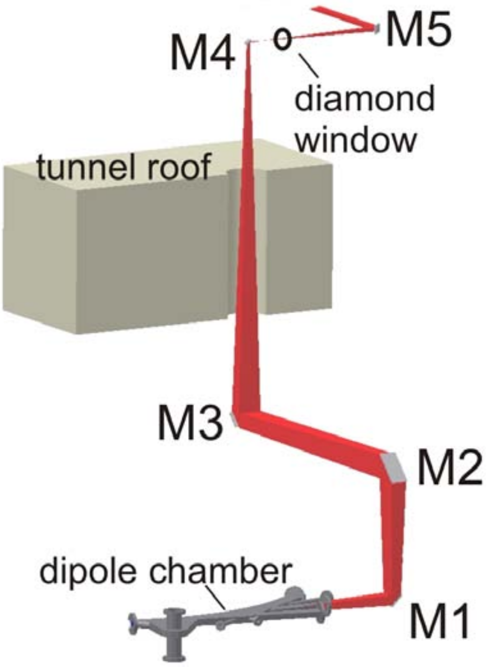

Figure 2: Optical design of the IR beamline (number 3 in Fig. 1) at the MLS.

The IR beamline will be located at the bending magnet D6 at the MLS (Fig. 1). The plane extraction mirror allows - in combination with a special port of the dipole chamber - a horizontal and vertical collecting angle of 64 mrad (h) × 43 mrad (v). At the maximal ring operation conditions of 600 MeV and 200 mA a mirror heat load of about 16 W is expected. Due to this relatively low heat load and with an additional cooling system we expect to have no deformation or destruction effects at the first mirror. So there is no need to split the mirror as, for example, at the IRIS beamline at BESSY II [3]. The first optical component M1 will be placed at a distance of 1550 mm from the source, the first position possible outside the vacuum chamber of the dipole magnet. M1 deflects the photon beam upwards by 90° to a combination of mirrors which focus the beam outside the radiation shielding wall near the plane of a CVD diamond window. The second mirror M2 and the third mirror M3 focus the IR radiation vertically and horizontally, respectively. Both mirrors are cylindrical and deflect the beam by 90° towards the storage ring (M2) and upwards (M3). The beam passes the tunnel roof at a distance of 700 mm after M3. The fourth optical element M4 is a planar mirror and transports the beam to the parabolical mirror M5. M5 collimates the beam and sends it to the remaining optical system. The IR photon beam has an intermediate focus between M4 and M5 at a distance of 4900 mm from the center of M1. After all these reflections the polarization is horizontally oriented. Ray tracing calculations for an energy of 500 cm^{-1} indicate a focal spot size of 2.5 mm (h) × 1.0 mm (v) which should easily pass through the diamond window (30 mm clear aperture). This focus serves as a new source point for the remaining optical system. The diamond window separates the UHV of the storage ring from the remainder of the beamline. The subsequent optical elements should direct the light to the different experiments. By mounting the optics and experiments on the massive storage ring tunnel itself the mechanical stability required for vibration sensitive IR experiments can be achieved.

Fig. 3 shows the expected brilliance at the MLS compared with other IR beamlines. In an optimal beamline design this brilliance is transferred to the experiment with minimal losses. The brilliance is calculated here using the far-field approach taking into account the intrinsic beam size in the center of the bending magnet as well as the source size due to projection and diffraction. The kink in the brilliance curves together with a steeper slope at lower wavelength results when the vertical collecting angle falls short of the natural vertical opening angle of the radiation. The 2 cm^{-1} bandwidth provides suitable resolution in typical spectra of condensed matter.

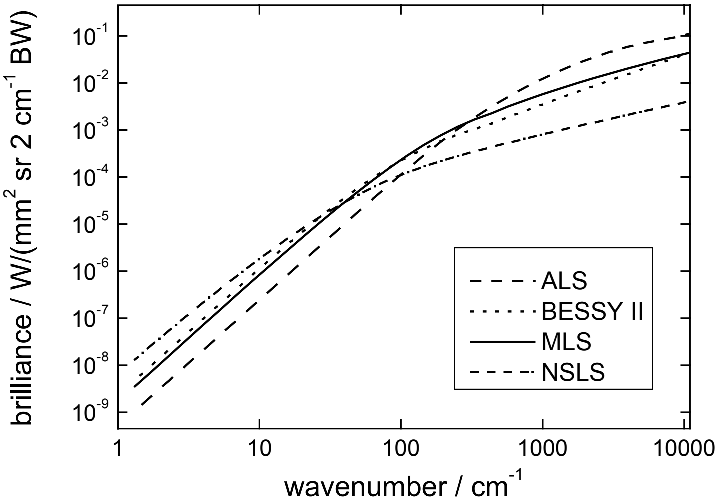

Figure 3: Calculated brilliance of the MLS IR beamline compared to the IR beamlines IRIS at BESSY II [3], U4IR at the NSLS [1], and the IR beamline 1.4 at the ALS [2]. The brilliance is quoted per 1 A ring current.

Intense coherent synchrotron radiation (CSR) can be generated if electron bunches are compressed to 1 mm rms length at the BESSY II storage ring [6]. This option is also envisaged for the MLS by tuning the quadrupoles in an appropriate way. The emitted spectral range of the bunches compressed to 1 mm will be the same as for BESSY II. Recent calculations have shown that the bunch length at the MLS operated in the low-alpha mode is smallest in the straight sections and largest in the section between the bending magnets. Therefore, a higher intensity and broader spectrum of the CSR is expected at the bending magnet ports that are located most closely to a straight section, as is the case for the dedicated THz beamline at bending magnet D5 (Fig. 1) [5]. The optical design is comparable with the new THz beamline at BESSY II [7]. The plane extraction mirror will be placed at about 1550 mm from the source, and deflects the beam upwards to a combination of mirrors which focus the beam outside the radiation shielding wall to the experiment located at the roof of the tunnel. A quartz window after the first mirror separates the UHV of the storage ring from the rest of the beamline.

The production of stable, high power CSR opens a new region in the electromagnetic spectrum which can be applied for imaging, spectroscopic and microscopic methods in solid state physics, biology, chemistry and medicine. Additionally, we plan the use of CSR and incoherent radiation for the characterization and calibration of THz detectors and optical components.

Construction of the IR, the THz, and the undulator IR beamline should be finished by the end of 2006. Commissioning of the MLS and of the beamlines will start in 2007. Special emphasis has to be placed on the commissioning of the low-alpha mode necessary for the use of the THz beamline. The MLS complements the measurement potential available for the PTB at BESSY II [8] in the lower photon energy range and thus enables PTB to use synchrotron radiation from the THz up to the hard X-ray region for high accuracy photon metrology.

[1] W.R. McKinney et al., LBNL, LSBL-414 (1997)
[2] G.L. Carr et al., Il Nuevo Cimento D **20**, 375 (1998)
[3] U. Schade et al., Rev. Sci. Instrum. **73**, 1568 (2001)
[4] R. Klein, G. Ulm, M. Abo-Bakr, P. Budz, K. Bürkmann-Gehrlein, D. Krämer, J. Rahn, G. Wüstefeld, Proceedings of EPAC 2004, Lucerne, Switzerland, 2290 (2004)
[5] R. Müller, A. Hoehl, R. Klein, U. Schade, G. Ulm, U. Schade, K. Holldack, G. Wüstefeld, Infrared Physics & Technology (2006), in press
[6] M. Abo-Bakr, J. Feikes, K. Holldack, G. Wüstefeld, H.-W. Hübers, Phys. Rev. Lett. **88**, 254801 (2002)
[7] K. Holldack, S. Khan, R. Mitzner, T. Quast, G. Wüstefeld, Proc. of the EPAC 2004, Lucerne, Switzerland, 2284 (2004)
[8] G. Ulm, Metrologia **40**, S101 (2003)

CD characterization of EUV masks by EUV scatterometry

Frank Scholze, Bernd Bodermann, Christian Laubis, Gerhard Ulm, Matthias Wurm

Physikalisch-Technische Bundesanstalt, Braunschweig and Berlin, Germany

Uwe Dersch and Christian Holfeld

AMTC GmbH&CoKG, Dresden, Germany

Extreme Ultraviolet Lithography (EUVL) holds the key to the next generation of computer technology. When exposing an EUV mask with EUV radiation of 13.5 nm, the radiation is reflected by a Mo/Si multilayer stack which is about 300 nm thick. In comparison to visible and UV light, where the radiation is reflected at the top interface of the mask, for EUV all layers in the stack contribute to the reflection. Therefore, only EUV radiation provides direct information on the mask performance relevant for an EUVL tool. Scatterometry, the analysis of light diffracted from a periodic structure, is a versatile metrology for characterizing periodic structures, regarding critical dimension (CD) and other profile properties. With respect to the small feature dimensions on EUV masks, the short wavelength of EUV is also advantageous since it minimizes diffraction phenomena. The Physikalisch-Technische Bundesanstalt (PTB) with its laboratory at the electron storage ring BESSY II[1] is the European centre of EUV metrology and supports the national and European industry by carrying out high-accuracy at-wavelength measurements in the EUV spectral region. PTB's EUV reflectometer allows the measurement of mirrors having diameters up to 550 mm, a height of 230 mm, and a weight of up to 50 kg[2]. Iz allows mask surface scanning in Cartesian coordinates at 10 µm positioning reproducibility[3,4]. The probed area (photon beam size) is about 1 mm². The detector can be moved in 3 dimensions (rotation around the sample, radial movement to adjust the distance to the sample and a linear movement out of the reflection plane).

In this contribution we present measurements on prototype EUV masks.

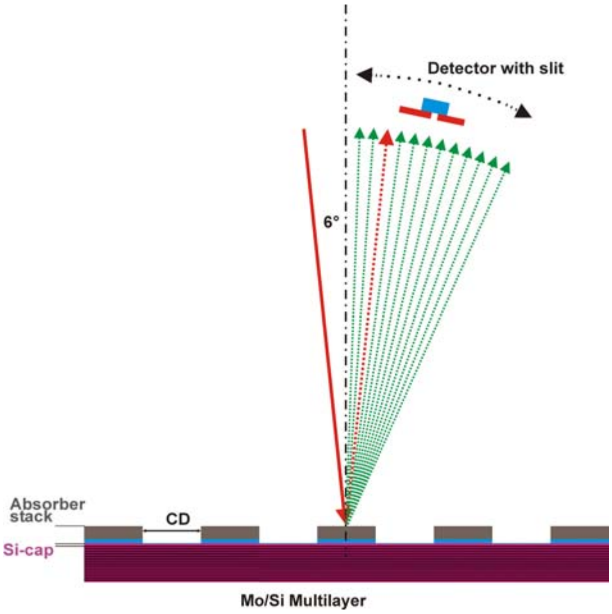

Fig. 1 Sketch of the experimental setup. The illumination angle of the incident synchrotron beam is 6° with respect to the surface normal. The diffraction angle is varied by moving the detector. The investigated line pattern is oriented perpendicular to the scattering plane.

The scheme of a scatterometry measurement is shown in Fig. 1. For homogeneous regions and with equal angles of incidence and exit, it is a reflectometry measurement. Already such measurements at open multilayer (ML) or absorber areas can be used to obtain detailed information on layer thicknesses (see Fig. 2 and 3). By comparison of the reflectance in ML and absorber areas, information can be obtained on the absorber thickness and the thinning of the capping layer due to oxidation in the open ML regions after buffer etch.

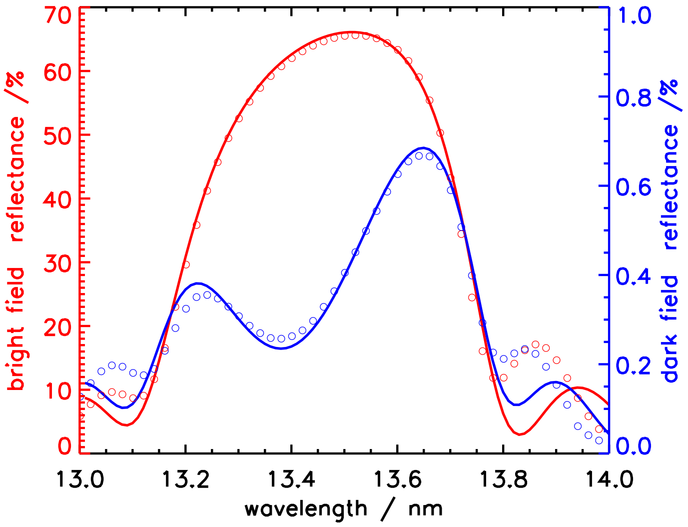

Fig. 2 Spectral reflectance measured in a bright field region (○, red, left scale) and at the absorber layer (○, blue, right scale). The respective lines are model calculations using IMD[5].The parameters are given in Fig. 3.

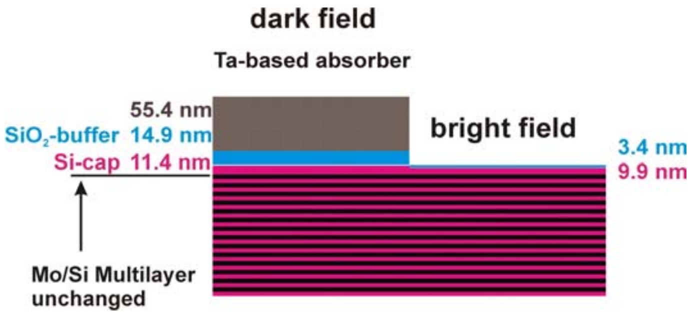

Fig. 3 Scheme of the EUV mask coating layers. The substrate is coated with a Mo/Si multilayer stack with a Si-capping layer. The absorber stack consists of a SiO_2 buffer layer and a Ta-based absorber.

Results of a scatterometry measurement are shown in Fig. 4 with the corresponding scheme of the geometry in Fig. 5. A structure of lines&spaces was illuminated at an angle of 6° to the normal and perpendicular to the orientation of the lines, see Fig. 1. The pitch of the structure was 840 nm and the designed duty cycle 5:1 (dark:bright). It was already known from the process development that the bright areas are smaller than designed. Fig. 4 shows the measured diffraction orders at the angular positions corresponding to the pitch of the structure and the wavelength. It should be noted that this correlation is valid for any geometry. The position of the diffraction orders is only defined by the lateral period (pitch) of the structure. For planar structures, the Fraunhofer-approximation can be used to calculate the so-called form factor. It depends for a given pitch only on the width of the lines. The structures at EUV-masks, however, are 3-dimensional. Due to the oblique angle of incidence, the bright ML-regions are partially shadowed by the absorber lines. In a first approximation, the dark lines are broadened by this shadowing and the dark:bright ratio changes. Although this is a rather crude approximation, it works quite well as illustrated in Fig. 4. Here we measured the diffracted intensity for positive as well as negative diffraction orders. The form factor envelope as given by the Fraunhofer approximation can only be fitted to match either positive or negative orders. The difference in effective line width of 13 nm obtained using the Fraunhofer approximation is indeed very close to the direct geometrical shadowing effect of 14 nm, as shown in Fig. 5. It is therefore obvious that information on the absorber line height and – using more sophisticated electromagnetic field based calculations – also on the line profile can be obtained from scatterometric measurements.

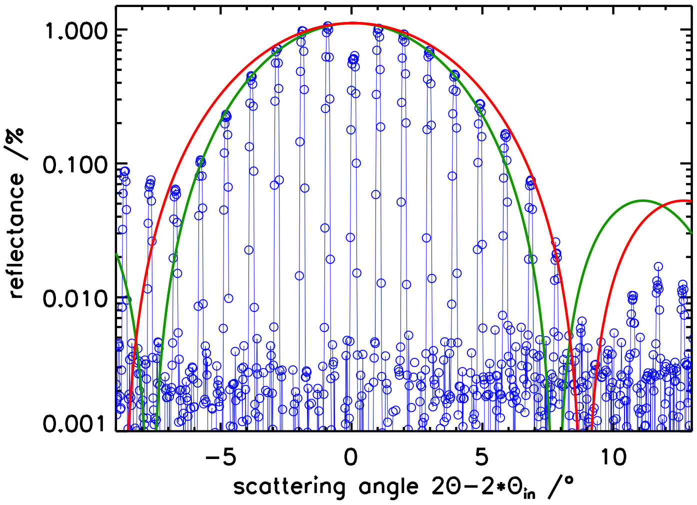

Fig. 4 Diffraction measured at lines&spaces with 840 nm pitch. The 0th order is suppressed by top-to-bottom interference effects. The envelopes shown are calculated using the Fraunhofer approximation for an open width of 92 nm (red) and 105 nm (green). For geometry see Fig. 5.

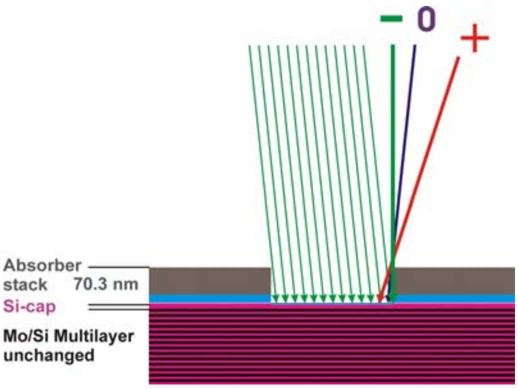

Fig. 5 Scheme of the EUV mask lines&spaces. Due to the finite height of the absorber stack and the oblique angle of incidence, the bright area is partly shadowed. The geometrical difference in apparent width for scattering anlges of ±6° is 14 nm.

The investigations shown here are part of the “ABBILD” project, supported by the Bundesministerum für Bildung und Forschung.

References

1 G. Ulm, B. Beckhoff, R. Klein, M. Krumrey, H. Rabus, and R. Thornagel, "The PTB radiometry laboratory at the BESSY II electron storage ring," Proc. SPIE **3444**, 610-621 (1998)

2 J. Tümmler, G. Brandt, J. Eden, H. Scherr, F. Scholze, G. Ulm, "Characterization of the PTB EUV reflectometry facility for large EUVL optical components," Proc. SPIE **5037**, 265-273 (2003)

3 F. Scholze, C. Laubis, C. Buchholz, A. Fischer, S. Plöger, F. Scholz, H. Wagner, and G. Ulm, "Status of EUV Reflectometry at PTB," Proc. SPIE **5751**, 749-758 (2005)

4 F. Scholze, J. Tümmler, G. Ulm, "High-accuracy radiometry in the EUV range at the PTB soft X-ray radiometry beamline," Metrologia **40**, S224-S228 (2003)

5 D. Windt, "IMD—Software for modeling the optical properties of multilayer films," Computers in Physics **12**, 360-370 (1998)

Alignment of large off-axis EUV mirrors in the EUV reflectometer of PTB

Christian Laubis, Christian Buchholz, Andreas Fischer, Sven Plöger, Frank Scholz, Heike Wagner, Frank Scholze, and Gerhard Ulm

Physikalisch-Technische Bundesanstalt, Abbestraße 2-12, 10587 Berlin, Germany

Extreme Ultraviolet Lithography (EUVL) is the key to the next generation of computer technology. EUVL imaging requires multilayer mirror optics being manufactured with extreme accuracy to ensure uniform illumination at the wafer plane and optimized throughput[1]. The wavelength for the peak mirror reflectivity should be matched to better than 2.5 pm and the uniformity of reflectance should be better than 0.08 %[2]. In response to this demand, substantial improvements in the total measurement uncertainty and repeatability at the Physikalisch-Technische Bundesanstalt (PTB) have been achieved and reported[3,4]. The EUV reflectometer allows the measurement of large mirrors with a diameter as large as 550 mm, a height of 230 mm, and a weight of up to 50 kg[5]. We present here work on the alignment of aspheric off-axis mirrors which is crucial to achieve accurate measurement results for wavelength and reflectivity needed for the validation of the coating development for EUV optics[6,7].

The SX700 soft X-ray bending magnet beamline was designed first of all for a parallel beam with a reasonably low spot size. To use this high quality beam for accurate measurements[3,8], the mirror under test has to be properly aligned. The centre wavelength λ is related to the double-layer thickness d of the coating by the Bragg equation:

$$\lambda \;=\; 2 n_\lambda \, d \cos\Theta_{ML} \;=\; \lambda_0 \cos\Theta_{ML} \,, \tag{1}$$

with n_λ the (average) index of refraction at wavelength λ, and Θ_{ML} the propagation angle in the multilayer coating. Assuming constant n_λ and $\Theta_{ML} = \Theta$ we get a cos-dependence for approximation. To keep the shift in measured wavelength below 2 pm, the angular scales have to be adjusted to better than 0.3° for measurements close to normal incidence (Θ=1.5°) and better than 0.02° for Θ=20°. Thus, for higher angles of incidence (AOI), the alignment requires accurate scales in Θ and 2Θ (see Fig. 3) and the surface of the sample to coincide with the main axis of the goniometer within a few tenth of a millimeter.

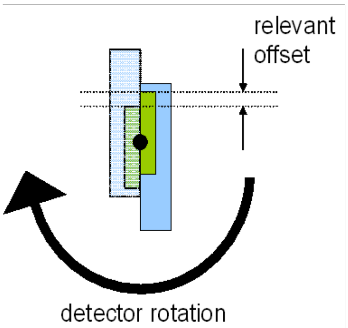

Fig. 1 Determination of zero reflection angle: A 180° rotation around a pivot point (indicated by the black dot) enables the measurement of direct beam (orientation with bright colors) and reflected beam (transparent).
The pivot is designed to be in the center of the surface of the detector, and the offset is measured and corrected.

Our method of measurement involves turning the detector (Ψ-axis) between direct-beam and reflected-beam measurements[5]. Particularly for the alignment, this approach has strong advantages. We rotate the detector (Ψ-axis) to look into the direct beam at 2Θ=0°, see Fig. 1, and define the zero angle to be at the position of the incoming beam. A possible offset of the detector switching axis is accounted for.

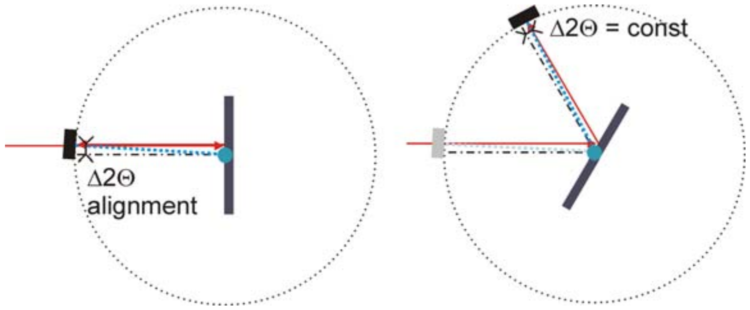

Fig. 2 Scheme of the alignment for the reflection angle. The detector is aligned in the direct beam to define “zero” angle of incidence, left. Due to the symmetry of the reflection geometry, any offset of the beam with respect to the axis of rotation (solid circle in the centre) causes only a fixed offset in detector angle, right.

After defining zero for the detector axis, we define the angle of incidence for the mirror, typically at 1.5° off normal. The detector is moved to 3° and the angle of the sample is scanned to position the beam in the centre of the detector. The main advantage of this approach is illustrated in Fig. 2. Even if the beam is not incident at the correct height, i.e. it does not go through the axis of rotation, the alignment between detector and sample rotation is not disturbed due to the symmetry of the reflection. The angular offset for the reflected beam at the detector is the same for any angle of incidence as well as for the direct beam.

In contrast to the height of the incoming beam which does not affect the determination of the angle of incidence if the axes are properly aligned, as just shown, the surface height of the mirror does. It must coincide with the central axis of the goniometer to assure proper definition of angle of incidence (AOI). The influence of an offset in height (Δz) on the AOI is shown in Fig. 3. Especially AOI scans are susceptible to this misalignment. Equation (2) gives the correlation between the angular offset of the detector axis and the offset in the height of the mirror. The designations are taken from Fig. 3.

$$\sin(\Delta 2\Theta) = \frac{\Delta z}{R_{\mathrm{Det}}} \frac{\sin(2 * \mathrm{AOI})}{\cos(\mathrm{AOI})} = \frac{2\Delta z}{R_{\mathrm{Det}}} \sin(\mathrm{AOI}) \qquad (2)$$

It is seen that the shift in detector angle, respectively misalignment in AOI, is proportional to sin(AOI). In order to minimize this misalignment, we align the AOI at a small angle (1.5°) and use the Θ-axis (which has been qualified with an auto collimation set-up[9]) to go to the desired AOI. Here, the detector-angle is measured to verify the sample height. Any mismatch in detector angle can be converted to a misalignment in sample height. It should be mentioned that any possible offset in incoming photon beam height with respect to the axis of rotation does not compromise this procedure as shown before, see Fig. 2.

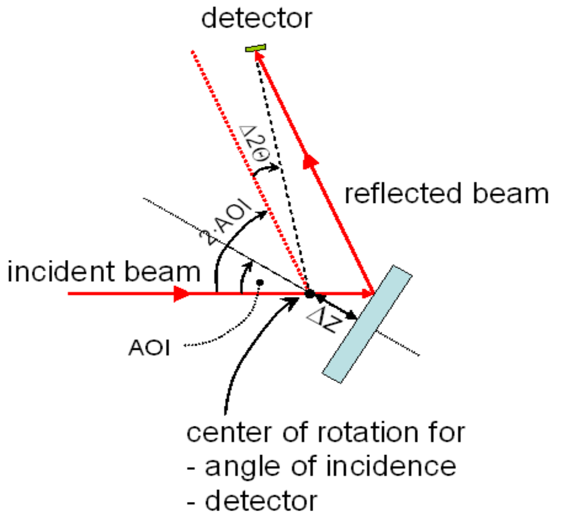

Fig. 3 Visualization of the height adjustment. The mirror surface is not in the center of rotation of the goniometer leading to an inaccurate AOI.
Red arrows symbolize the beam path, the black circle is the main axis (Θ) of the goniometer. The dashed black line from the main axis to the detector symbolizes the detector-arm, the dotted red line shows the direction of the reflected beam. The difference between the direction of the reflected beam path and the angle of the detector-arm is indicated as Δ2Θ.
Δz is the distance from the mirror surface to the center of rotation.

To align a large off-axis EUV mirror, we use alignment mirrors, see Fig. 4. First, Φ (rotation around the optical axis) is adjusted using a pair of alignment mirrors mounted against one edge of the sample at the same position in y (and different positions in x). Using the x-drive of the goniometer to place these alignment mirrors in the beam, their positions are measured with respect to the R–coordinate of the reflectometer. From this measurement, we obtain the angle between R and the y-axis of the mirror. Φ is then set to orientate R parallel to y. In this orientation, Φ_0, the known position of the alignment mirrors is used to correlate the y-coordinates of the sample to the goniometer R-values. Now, at $\Phi = \Phi_0+90°$ where R is parallel to the mirror x-coordinate, we use the third alignment mirror to correlate the x-coordinates of the mirror under test to the goniometer R-values for this value of Φ. Then, we align the angle of incidence in the centre of the mirror under test. Last, we check the height of the mirror. Now, given the shape of the mirror surface, every point on the mirror is known in lateral and angular position of the goniometer coordinates.

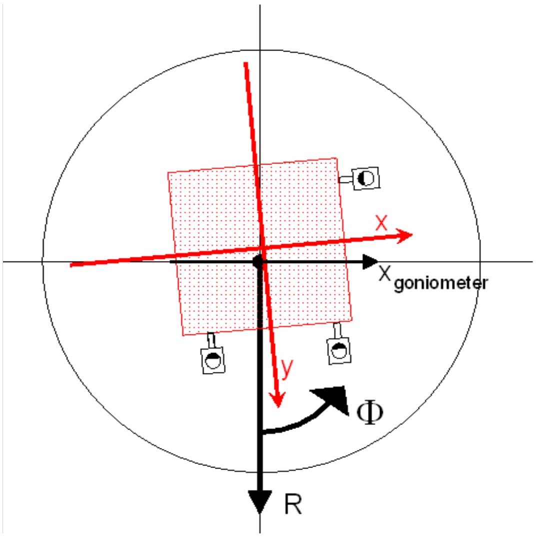

Fig. 4 The different coordinate systems:
Mirror sample: x and y (in red)
Goniometer: R, x, and Φ (black)
Three alignment mirrors are shown touching the mirror side.

References

1 H. Meiling, V. Banine, N. Harned, B. Blumb, P. Kürz, and H. Meijer, "Development of the ASML EUV alpha demo tool," Proc. SPIE **5751**, 90-101 (2005)

2 E. Gullikson, S. Mrowka, and B. Kaufmann, "Recent developments in EUV reflectometry at the Advanced Light Source," Proc. SPIE **4343**, 363 – 373 (2001)

3 F. Scholze, C. Laubis, C. Buchholz, A. Fischer, S. Plöger, F. Scholz, H. Wagner and G. Ulm, "Status of EUV Reflectometry at PTB", Proc. SPIE **5751**, 749-758 (2005)

4 F. Scholze, B. Beckhoff, G. Brandt, R. Fliegauf, A. Gottwald, R. Klein, B. Meyer, U. Schwarz, R. Thornagel, J. Tümmler, K. Vogel, J. Weser, and G. Ulm, "High-accuracy EUV metrology of PTB using synchrotron radiation," Proc. SPIE **4344**, 402-413 (2001)

5 J. Tümmler, G. Brandt, J. Eden, H. Scherr, F. Scholze, G. Ulm, "Characterization of the PTB EUV reflectometry facility for large EUVL optical components," Proc. SPIE **5037**, 265-273 (2003)

6 E. Louis, A. Yakshin, E. Zoethout, R. van de Kruijs, I. Nedelcu, S. van der Westen, T. Tsarfati, F. Bijkerk, H. Enkisch, S. Müllender, B. Wolschrijn, B. Mertens, "Enhanced performance of EUV multilayer coatings," Proc SPIE **5900,** 1-4 (2005)

7 E. Louis, E. Zoethout, R. van de Kruijs, I. Nedelcu, A. Yakshin, S. van der Westen, T. Tsarfati, F. Bijkerk, H. Enkisch, S. Müllender, "Multilayer coatings for the EUVL process development tool," Proc SPIE **5751,** 1170-1177 (2005)

8 F. Scholze, J. Tümmler, G. Ulm, "High-accuracy radiometry in the EUV range at the PTB soft X-ray radiometry beamline," Metrologia **40**, S224-S228 (2003)

9 C. Buchholz, A. Fischer, S. Plöger, F. Scholz, F. Scholze, H. Wagner, "High-accuracy measurement of the angular sample positioning in the PTB EUV-reflectometer," BESSY Annual Report, 11-13 (2003)

Characterization of large off-axis EUV mirrors with high accuracy reflectometry at PTB

Christian Laubis, Christian Buchholz, Andreas Fischer, Sven Plöger, Frank Scholz, Heike Wagner, Frank Scholze, and Gerhard Ulm

Physikalisch-Technische Bundesanstalt, Abbestraße 2-12, 10587 Berlin, Germany

Hartmut Enkisch, Stephan Müllender, Marco Wedowski

Carl Zeiss SMT AG, Carl Zeiss Straße 22, 73446 Oberkochen, Germany

Eric Louis, Erwin Zoethout

FOM-Institute for Plasma Physics, Edisonbaan 14, NL-3439 MN Nieuwegein,
The Netherlands

Extreme Ultraviolet Lithography (EUVL) is the key to the next generation of computer technology. EUVL imaging requires multilayer mirror optics being manufactured with extreme accuracy to ensure uniform illumination at the wafer plane and optimized throughput. As EUVL matures[1,2], the requirements for the accuracy of reflectivity and wavelength measurements become tighter. Especially the wavelength for the peak mirror reflectivity should be matched to better than 2.5 pm and the uniformity of reflectance should be better than 0.08 %[3]. In response to this demand, substantial improvements in the total measurement uncertainty and repeatability at the Physikalisch-Technische Bundesanstalt (PTB), Germany's national metrology institute, have been achieved and reported[4,5,6]. PTB’s EUV reflectometer allows the measurement of large mirrors[7] with a diameter as large as 550 mm, a height of 230 mm, and a weight of up to 50 kg[8]. We present here work on the alignment of aspheric off-axis mirrors which is crucial to achieve accurate measurement results for wavelength and reflectivity needed for the validation of the coating development for EUV optics[9,10].

Carl Zeiss SMT AG produced large off-axis EUV mirrors as they are used e.g. in ASML's alpha demo tools, the predecessor for EUVL production tools by ASML. The coating development and a large part of the actual coatings were done in collaboration with the FOM-Institute. Critical issues for EUVL mirrors are the high reflectivity close to the theoretical limit, the matching of the period to the operating wavelength of the stepper (13.5 nm) and the imaging properties of the EUV optics. The full multilayer stack needs to be controlled laterally to such extend that the initial sub-nanometre surface figure of the substrate is preserved. The so-called added figure error should not exceed 100 pm in order to ensure faultless imaging at 13.5 nm wavelength. For large off-axis EUV mirrors, measurements have to be done at angles significantly off normal, which dramatically increases the influence of angular alignment errors of the sample on the measured peak wavelength. Furthermore, according to the optical design, these optics have gradients of the coating thickness which require exact knowledge of the measurement position in the mirror coordinates.

Extensive studies were done to develop alignment procedures of the sample with respect to the polar coordinates of PTB’s EUV reflectometer. The range of the reflectometer sample R-axis from -10 mm to 290 mm allows the centre area of the mirror to be positioned redundantly, i.e. using the setting $\Phi=\Phi_1$ and R=x as well as $\Phi=\Phi_1 + 180°$ and R=-x, for $|x| < 10$. If everything is well aligned, this is physically the same spot on the sample. Thus for mirrors with a graded coating, a test of the alignment can be done by measuring several points on the mirror surface (sufficiently close the centre) twice. If the mirror was misaligned, the curves measured would not coincide. Particularly for mirrors with a strongly graded coating, this is a sensitive test of the alignment.

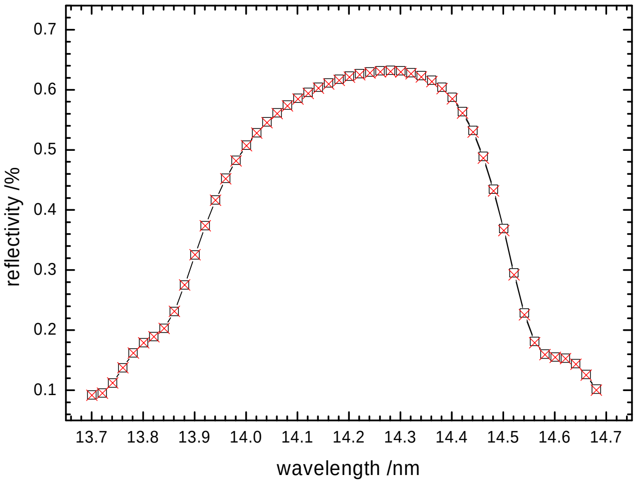

Figure 1 Alignment test of a mirror with graded coating. The figure shows the measured reflectance on the center spot of the mirror, measured at Φ_0 (□), and with the mirror turned by 180° around its optical axis (x).

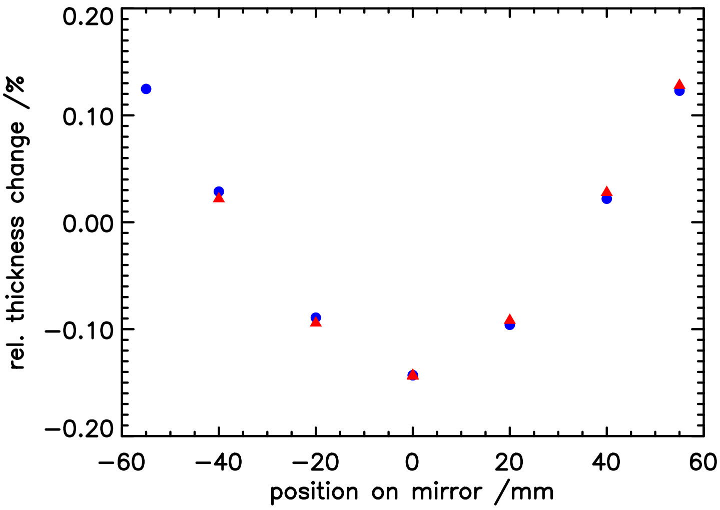

Figure 2 Relative thickness profile of the coating on a projection optics element, measured in two perpendicular directions.

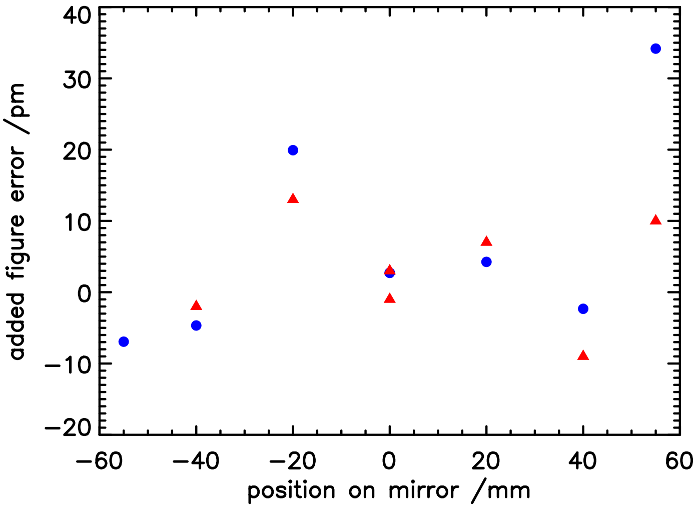

Figure 3 Non correctable added figure error determined in two perpendicular directions. The rms value amounts to 15 pm.

To validate the lateral alignment uncertainty, we used a large off-axis EUV test mirror with a large gradient in its multilayer coating thickness. Figure 1 gives the data for the test. After alignment (Φ_0, R=x) and (Φ_0+180°, R=-x) were measured. The value for center-wavelength of these measurements differs by only 0.6 pm which is, however, well beyond our short term repeatability of 0.06 pm[4]. Given the local gradient of the multilayer of about 3 pm/mm, the positional offset between the two measurements shown is 0.2 mm. This is twice the offset in y-alignment due to the rotation by 180°. This result verifies the uncertainty of 0.1 mm for the lateral alignment of mirrors.

The most critical issue for the multilayer system on the projection optics is the non-correctable added figure error. The wavelength of the mirrors can also be used to determine the multilayer period $\Lambda(r)$ and thus the total film thickness. As an example of an optical element, which is representative for the projection optics, we present results for a concave mirror. The active optical surface has a diameter of 120 mm and the optical design requires a slightly parabolic profile. Figure 2 shows the relative thickness profile obtained, determined in two perpendicular directions where both curves nicely coincide, demonstrating the required rotational symmetry of the coating profile. The design profile can be corrected through lower order Zernike polynomial corrections to determine the alignment-adjusted design period Λ_a. Taking the difference between the measured period $\Lambda(r)$ and the alignment-adjusted design period $\Lambda_a(r)$, the non-correctable added figure error is calculated. The distribution of this figure error is shown in Figure 3 and amounts to an rms value of 15 pm only, which is seven times better than specified.

Our results clearly show that it is possible to meet and verify the tight specifications for the lateral coating profiles of EUV multilayer mirrors. The non-correctable added figure error is significantly better than required and the overall reflectance of the coatings with a special protective capping layer is 65%.

References

1 H. Meiling, V. Banine, P. Kürz, N. Harned, "Progress in the ASML EUV program," Proc. SPIE **5374**, 31 - 42 (2004)

2 H. Meiling, V. Banine, N. Harned, B. Blumb, P. Kürz, and H. Meijer, "Development of the ASML EUV alpha demo tool," Proc. SPIE **5751**, 90-101 (2005)

3 E. Gullikson, S. Mrowka, and B. Kaufmann, "Recent developments in EUV reflectometry at the Advanced Light Source," Proc. SPIE **4343**, 363 – 373 (2001)

4 F. Scholze, C. Laubis, C. Buchholz, A. Fischer, S. Plöger, F. Scholz, H. Wagner and G. Ulm, "Status of EUV Reflectometry at PTB", Proc. SPIE **5751**, 749-758 (2005)

5 R. Klein, A. Gottwald, F. Scholze, R. Thornagel, J. Tümmler, G. Ulm, M. Wedowski, F. Stietz, B. Mertens, N. Koster, and J. Elp, "Lifetime testing of EUV optics using intense sychrotron radiation at the PTB radiometry laboratory," Proc. SPIE **4506**, 105-112 (2001)

6 F. Scholze, B. Beckhoff, G. Brandt, R. Fliegauf, A. Gottwald, R. Klein, B. Meyer, U. Schwarz, R. Thornagel, J. Tümmler, K. Vogel, J. Weser, and G. Ulm, "High-accuracy EUV metrology of PTB using synchrotron radiation," Proc. SPIE **4344**, 402-413 (2001)

7 U. Dinger, G. Seitz, S. Schulte, F. Eisert, C. Münster, S. Burkart, S. Stacklies, C. Bustaus, H. Höfer, M. Mayer, B. Fellner, O. Hocky, M. Rupp, K. Riedelsheimer, P. Kürz, "Fabrication and metrology of diffraction limited soft x-ray optics for the EUV microlithography," Proc SPIE **5193** 18-28 (2004)

8 J. Tümmler, G. Brandt, J. Eden, H. Scherr, F. Scholze, G. Ulm, "Characterization of the PTB EUV reflectometry facility for large EUVL optical components," Proc. SPIE **5037**, 265-273 (2003)

9 E. Louis, A. Yakshin, E. Zoethout, R. van de Kruijs, I. Nedelcu, S. van der Westen, T. Tsarfati, F. Bijkerk, H. Enkisch, S. Müllender, B. Wolschrijn, B. Mertens, "Enhanced performance of EUV multilayer coatings," Proc SPIE **5900,** 1-4 (2005)

10 E. Louis, E. Zoethout, R. van de Kruijs, I. Nedelcu, A. Yakshin, S. van der Westen, T. Tsarfati, F. Bijkerk, H. Enkisch, S. Müllender, "Multilayer coatings for the EUVL process development tool," Proc SPIE **5751,** 1170-1177 (2005)

Re-calibration of the SUMER calibration source

M. Richter, W. Paustian, R. Thornagel
Physikalisch-Technische Bundesanstalt, Berlin, Germany

Characterization of space instrumentation is one of the major activities in the PTB laboratory at BESSY [1,2]. In many cases, calibration of devices is based on operating the storage ring as a primary source standard of calculable synchrotron radiation [3]. In the spectral range of vacuum-UV (VUV) radiation, e. g., the use of transfer source standards calibrated by comparison with BESSY has been established, for many years, as a powerful tool for absolute characterization of solar telescopes at the respective home laboratories under cleanroom conditions or within large vacuum tanks. Outstanding examples are the calibration of the SUMER and CDS telescopes of the *Solar and Heliospheric Observatory* (SOHO), more than ten years ago, within the framework of scientific cooperations with the *Max Planck Institute for Solar System Research* (MPS) and the *Rutherford Appleton Laboratory* (RAL). For this purpose, two hollow cathode rare gas discharge plasma sources with different collimating optics were developed as transfer standards [4,5]. Both standards have widely been used also for the characterization of further instruments (SOL-ACES, SERTS, EIS, MOSES) at different laboratories during the last years.

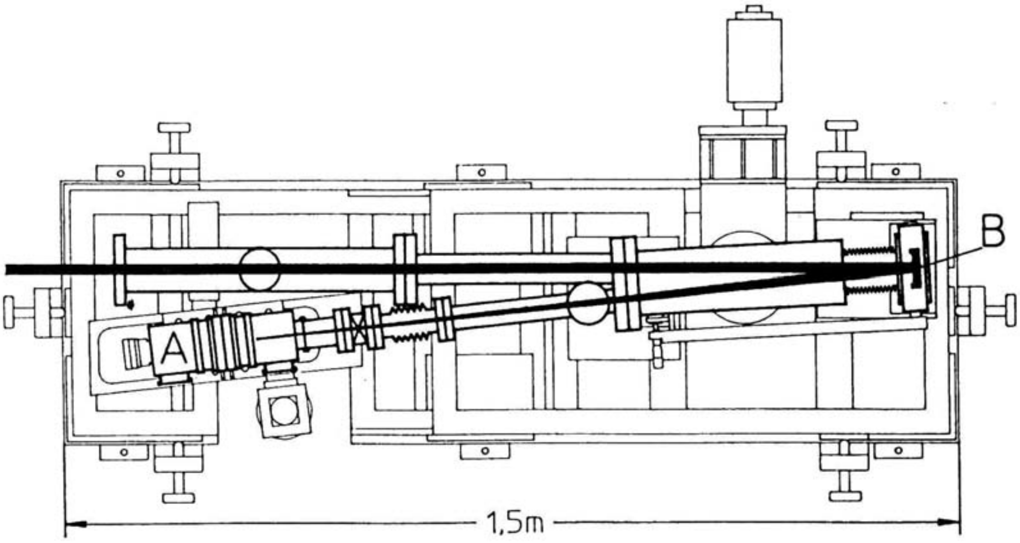

Fig. 1. Scheme of the SUMER calibration source consisting of a hollow cathode plasma source (A) with collimating normal-incidence optics (B).

Fig. 1 shows a scheme of the SUMER calibration setup together with the SUMER calibration source which has recently been re-calibrated in the PTB laboratory at BESSY after more than ten years of operation. The top part of Fig. 2 displays the re-calibration results, i.e.

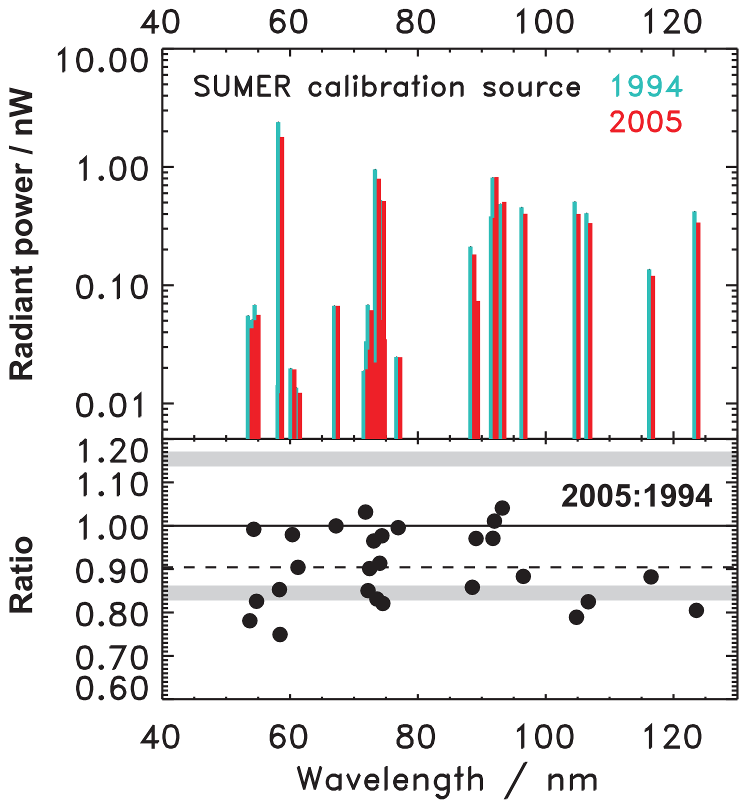

Fig. 2. Top: Radiant power of the SUMER calibration source for various atomic and ionic emission lines of He, Ne, Ar, and Kr as obtained in 1994 and 2005. Bottom: Ratio between the 2005 and 1994 data. The dashed line indicates the mean of the ratio values. The grey areas display the combined relative standard measurement uncertainty (k=1) varying from 14 % to 17 %.

the radiant power for various atomic and ionic emission lines in the wavelength range from 50 nm to 130 nm when operating the source with different rare gases (He, Ne, Ar, Kr). The data are compared to those obtained in 1994. At the bottom of Fig. 2, both datasets have been normalized to the mean value for each emission line, respectively. In summary, the source seems to be slightly degraded by about 10 %, but within the combined relative standard measurement uncertainty only, which varies from 14 % to 17 % depending on the strength of the respective emission line.

As a consequence, the SUMER calibration source has been proven to be a stable VUV radiation source standard over a long period of time. Similar investigations are scheduled for 2006 on the CDS calibration source which currently is part of the VUV calibration facility for space instrumentation at RAL. Its grazing-incidence optics is expected to be even more stable than the normal-incidence optics of the SUMER calibration source. Next instrument, scheduled for characterization with the help of the CDS calibration source at RAL, is the *Extreme Ultraviolet Normal Incidence Spectrometer* (EUNIS) of NASA.

[1] M. Richter et al., Advances in Space Research, in press

[2] M. Richter et al., PTB Mitteilungen **115** (3), 218-221 (2005)

[3] R. Thornagel, R. Klein, G. Ulm, Metrologia **38**, 385-389 (2001)

[4] J. Hollandt, M.C.E. Huber, M. Kühne, Metrologia **30**, 381-388 (1993)

[5] J. Hollandt, M. Kühne, B. Wende, Appl. Opt. **33**, 68 - 74 (1994)

Environmental Analyses by TXRF - NEXAFS and IR-Spectroscopy: Speciation of Br in Organics and Characterization of the Organic Matrix

B. Beckhoff[1], O. Hahn[2], J. Weser[1], M. Wilke[3], G. Ulm[1], O. Jann[2]

[1]Physikalisch-Technische Bundesanstalt (PTB), Abbestraße 2-12, 10587 Berlin, Germany
[2]Bundesanstalt für Materialforschung und –prüfung, (BAM) Unter den Eichen 87, 12205 Berlin
[3]Universität Potsdam, Institut für Geowissenschaften, Karl-Liebknecht-Str. 24, 14476 Golm

Introduction: Many polymers in building materials and consumer products contain flame retardants (FR). The most common organic FR are brominated organic compounds. Due to their worldwide output several FR are now ubiquitous and can be found in sediments, biota, and – moreover - in fine dusts. The major task of FR, reduction of risk of fire, is contrary to possible risks from the toxicity and eco-toxicity of FR [1].

The aim of former studies was the characterization of the emission of certain polybrominated FRs from selected products to determine their contribution to the contamination of the indoor environment. On the basis of these results it was not possible to answer convincingly the question if the distribution of polybrominated FR in the environment is really caused by emission into air. So the aim of this present study is the analysis of trace constituents (e.g. polybrominated FR in polymer matrices) in fine dusts.

Experimental: Due to detection limits of conventional methods the analysis of trace constituents in fine dusts is complicated. In order to simulate prospective experiments based on cascade impactors for sample collecting, some polymers containing brominated flame retardants were abraded mechanically on an ultra-clean silicon wafer surface. The chemical speciation of bromine is obtained by use of Total-Reflection X-ray Fluorescence Analysis (TXRF) in combination with Near-Edge X-ray Absorption Fine Structure (NEXAFS) analysis [2-4]. Synchrotron radiation based infrared spectroscopy (SR-FTIR) in reflection mode is used for the characterization of the polymer matrix. Analysis of the X-ray Absorption Near Edge Structure at K and L absorption edges in the hard x-ray range are employed frequently in the characterisation of element speciation. Due to the small penetration and information depth of only a few nanometers in total reflection beam geometry, self absorption effects are largely negligible even for the analysis of L edges in the soft x-ray range. In addition, the TXRF method offers drastically reduced scattering contributions and thus lowest detection limits.

In the present investigation monochromatized undulator radiation available at the PTB PGM-U49 beamline was employed to probe the Br-L3 and Br-L2 absorption edges of some samples deposited on a silicon wafer surface. For the excitation of the present specimens the PGM-U49 beamline provides an energy resolution of about 300 meV and permits the photon energy to be varied in steps of 250 meV. The PTB employes a reference-free TXRF arrangement providing knowledge of the incident radiant power, of the solid angle of detection and of both the detection efficiency and response. The latter allows for a very reliable spectra deconvolution.

The SR-FTIR measurements were performed at the synchrotron infrared beamline IRIS at BESSY II. A FTIR spectrometer (Bruker 66/v) and an IR microscope (Thermo Nicolet Continuum and Nexus) were used. Due to the fact that synchrotron infrared light is much brighter than a conventional infrared source (e.g. globar) it is possible to carry out FTIR measurements in reflectance with high lateral resolution. A gold sputtered silicon wafer was measured for background correction.

Results and discussion: SR-FTIR spectroscopy in reflection mode provides the classification of different polymers within reasonable measurement times. Figure 1 shows the corrected FTIR spectrum of an artificial "dust" sample in comparison with a polystyrene reference spectrum. It is obvious that the identification of the polymer is possible but there is no reliable indication of the existence of a polybrominated FR.

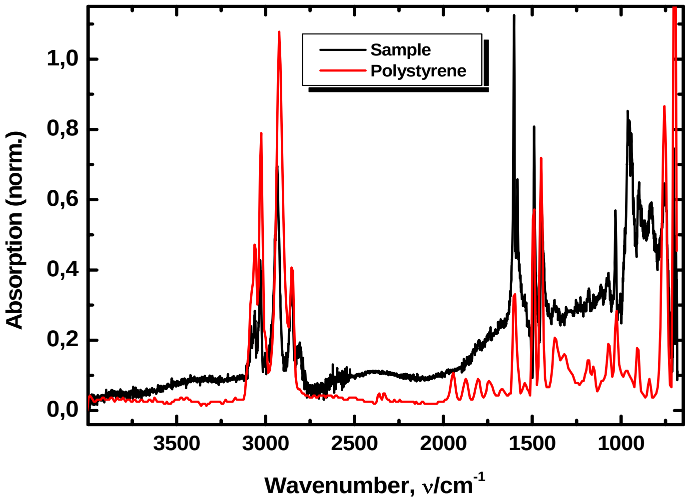

Fig.1: Corrected FTIR spectrum of an artificial "dust" sample in comparison with a polystyrene reference spectrum. The identification of the polymer polystyrene is possible. Due to the fact that characteristic bands for brominated compounds (e.g. ν *= 1050-1040 cm*$^{-1}$ *for aromatic compounds) are not clearly visible there is no reliable indication for the existence of PBFR.*

The initial results demonstrate the potential of the TXRF-NEXAFS method to successfully contribute to the elemental speciation, even of trace elements. The shape of the various TXRF-NEXAFS structures reflects the chemical environment of the element bromine in the different organic matrices (Fig. 2, 3). It is possible to distinguish between an aliphatic polybrominated compound and an aliphatic polybrominated compound: the chemical shift of the L-edge (as well as the K-edge) is caused by different hybridisation of the neighbour atom carbon (sp^2 and sp^3). Due to the fact that sp^2 hybridisation is more electrophilic the electron density at an „aromatic" bromine is a little bit diminished as a consequence the binding energy of the electron which has to be excited is increased.

The combination of TXRF-NEXAFS with SR-FTIR offers the option for reference measurements without need for any chemical sample preparation, thus reducing undesired modifications (e.g. such as in the case of GC/MS).

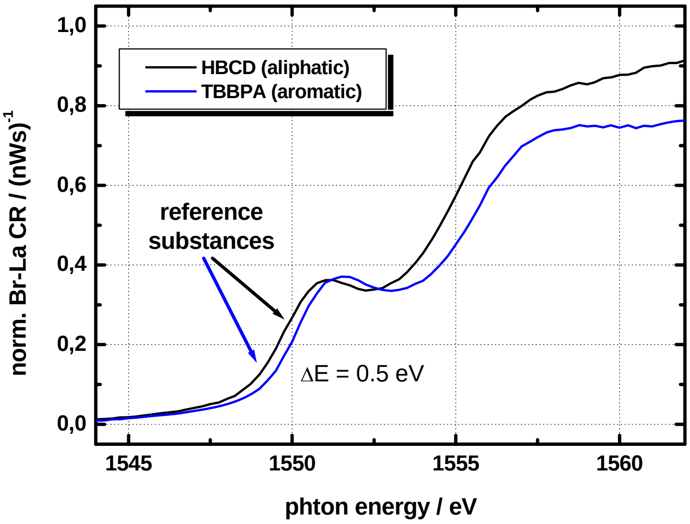

Fig. 2: TXRF-NEXAFS spectra of two different polybrominated flame retardants

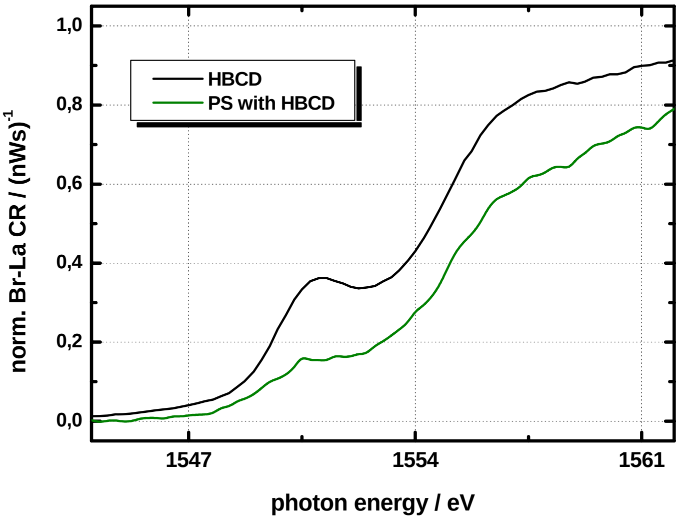

Fig.3: TXRF-NEXAFS spectra of pure HBCD in comparison with PS containing < 2 % HBCD

References

[1] S.Kemmlein, O.Hahn, and O.Jann, Emissions of organophosphate and brominated flame retardants from consumer products and building materials, Atmos. Environ. **39-40** (2003) 5485-5493.

[2] G.Pepponi, B.Beckhoff, T.Ehmann, G.Ulm, C.Streli, L.Fabry, S.Pahlke and P.Wobrauschek, Analysis of organic contaminants on Si wafers with TXRF-NEXAFS, Spectrochim. Acta B **58** (2003) 2245-2253.

[3] B.Beckhoff, R.Fliegauf, G.Ulm, J.Weser, G.Pepponi, C.Streli, P.Wobrauschek, T.Ehmann, L.Fabry, C.Mantler, S.Pahlke, B.Kanngießer, W.Malzer, Ultra-trace analysis of light elements and speciation of minute organic contaminants on silicon wafer surfaces by means of TXRF in combination with NEXAFS, Electrochemical Society Proceedings 'Analytical and Diagnostic Techniques for Semiconductor Materials, Devices, and Processes', 2003-03, (2003) 120-128.

[4] S.Török, J.Osan, B.Beckhoff, G.Ulm, Ultra-trace speciation of nitrogen compounds in aerosols collected on silicon wafer surfaces by means of TXRF-NEXAFS, Powder Diffraction Journal **19** (2004) 81-86.

X-Ray Resonant Raman Scattering (RRS) on Ni

M. Müller[a] , Ch. Zarkadas[b] , B. Beckhoff[a], A. G. Karydas[b]

[a] Physikalisch-Technische Bundesanstalt, Abbestraße 2-12, 10587, Berlin, Germany
[b] Institute of Nuclear Physics, N.C.S.R Demokritos, Aghia Paraskevi 15310, Athens, Greece

The X-ray resonant Raman scattering (RRS) effect on nickel was studied by means of monochromatic polarized exciting radiation. Experiments were carried out at the four crystal monochromator beamline [1] of the Physikalisch-Technische Bundesanstalt (PTB) for synchrotron radiation from 4 to 10 keV at the electron storage ring BESSY II. Resonant Raman spectra of thin Ni foils were recorded at the Cu-Kα (8041 eV) exciting beam energy.
For a pure monoatomic target, and assuming an isotropic emission, the theoretical intensity of the KL-RRS photons in the energy interval E_S, E_S+dE_S, can be expressed in terms of experimental and fundamental parameters by the following formula [2]:

$$\frac{dN_{the}^{RRS}(E_o,E_s)}{dE_s} = N_0(E_0)\cdot\Delta\Omega_d\cdot\frac{N_{AV}}{A_W}\cdot\frac{d^2\sigma_{RRS}}{d\Omega\cdot dE_s}\cdot M_\xi(E_0,\mathrm{E}_s)\cdot\varepsilon_d(E_s)\cdot\frac{1}{\sin\varphi_1} \qquad (1)$$

where $N_0(E_0)$ is the number of the incident monoenergetic photons on the sample surface, having energy E_0, $\Delta\Omega_d$ is the detection solid angle defined by an aperture placed in front of the detector entrance window, N_{AV} is the Avogadro number, A_W is the atomic weight of the target, $\varepsilon_d(E_S)$ the detector efficiency [3,4] at the scattered energy E_S, φ_1 is the angle between the target surface and the incoming exciting beam, and $M_\xi(E_0,E_S)$ is the self absorption factor expressed as follows:

$$M_\xi(E_0,\mathrm{E}_s) = \frac{1-\exp\left[-\mu_{tot}(E_o,E_s)\cdot\xi\right]}{\mu_{tot}(E_o,E_s)} \qquad (2)$$

In Equation (2), ξ denotes the sample thickness and $\mu_{tot}(E_0,E_S)$ the total mass absorption coefficient of the target.

The study of the RRS effect under different combinations of the incident X-ray energy – target elements can contribute significantly to several areas of X-ray spectrometry. From a fundamental aspect, the knowledge of the RRS cross sections can improve the accuracy of the tabulated theoretical attenuation coefficients for energies below the absorption edge of an element and provide possible explanations regarding the discrepancies (up to 5-6 %) observed between experimental and theoretical mass absorption coefficients [5].

The results obtained are compared to existing literature values, whereas the uncertainties associated with the different experimental and analytical approaches are critically evaluated.
For the RRS studies on Ni, a thin Ni foil (purity of 99.99% for the initial bulk material) of 2 µm nominal thickness was measured at exciting beam energy of 8041 eV. During these measurements, transmission scans were also performed for the experimental determination of the absorption correction required for the calculation of the RRS cross sections [2].

The Ni KL-RRS spectrum obtained at the energy of Cu-Kα (8041 eV) is shown in Fig. 4. The spectrum is composed clearly from the pronounced Ni KL-RRS structure, by the bremstrahlung radiation induced by Ni L-shell photo-electrons and also from small interfering fluorescent peaks arising from trace impurities in the thin Ni target. The contribution of the scattered Cu-Kα exciting radiation is minimized, due to the positioning of the detector in the polarization plane and at an angle of 90° with respect to the incident beam axis. The tailing of the Cu-Kα scattered peak is produced mostly by the coexisting Ni KM-RRS structure.

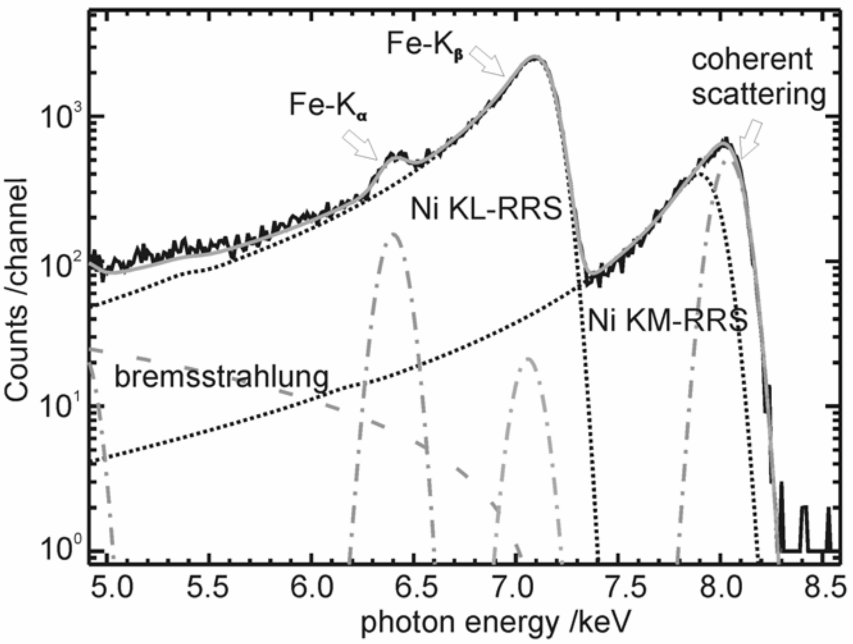

Fig. 1: RRS spectrum and associated components obtained as a result of the fitting procedure

For the extraction of the corresponding Ni KL-RRS cross-sections Eq. (1) was convoluted with the known detector's energy response function and then fitted to the actual experimental data to obtain the net RRS distributions, as follows:

$$\frac{dN_{\exp}^{RRS}(E_o,E_s)}{dE_s}=\int_0^{E_S^{\max}}\frac{dN_{the}^{RRS}(E_o,E_s)}{dE_s}\cdot R_d(E_s,E')\cdot dE' \qquad (3)$$

The height of the RRS distribution was treated as one fitting parameter, whereas in order to generalize the analytical procedure, the onset energy of Eq. (3) was introduced as a second fitting parameter. The onset energy is expected to be equal to, if the Ni target atoms do not participate into any chemical bonding [6]. The small contribution of the Ni L-shell photo-electrons in the spectrum was also taken into account by introducing a simple functional dependence of the electron bremstrahlung cross section on the electron's kinetic energy and the emitted photon's energy [7]. The absorption correction factors used were experimentally determined from transmissions measurements covering an energy region of 4 keV to the highest possible incident photon energy just below the Ni-K absorption edge. The total number of the incident exciting photons was determined from the photodiode measurements, whereas the solid angle subtended by the detector was calculated using the distance and diameter of the detector's calibrated diaphragm. The KL-RRS cross section (*dσ/dΩ*) was next deduced by integrating the double differential KL-RRS cross section to the maximum energy of the scattered RRS photons.

Our results are presented in Table 1 in comparison with the Ni KL-RRS cross sections already reported in the literature. Evidently, there is an excellent agreement between the cross sections determined for polarized and unpolarized radiation, verifying the theoretical predictions regarding the polarization state of the exciting beam. In principle, the results deduced in this work are also in good agreement with previously published values [8-9, 10], within the overall uncertainties achieved.

Referring to our work, the total relative uncertainties of the cross sections, presented in Table 1, are defined by the uncertainty of the first fitting parameter. For the polarized radiation, the constant term, after the end of the fitting procedure with the experimental detector response function, was found to have a relative uncertainty of about 5%. The number N(E_0) of the inci-

Table 1. *Ni KL-RRS cross sections obtained in this work compared to the literature values.*

Reference	Methodology adopted for the extraction of the KL-RRS cross sections	$(d\sigma/d\Omega)_{KL-RRS}$
		r_o^2 /sr
This work, polarized radiation	Integration of the double differential cross sections from 5.0 keV upwards	7.6 ± 0.5
complementary study with unpolarized radiation	Integration of the double differential cross sections from 5 keV upwards	7.7 ± 0.9
Ref. [10]	Integration of the net RRS spectral data from 4.8 keV upwards	7.0 ± 0.2
Ref. [8]	Integration of the net RRS spectral data from 4.8 keV upwards	7.3 ± 0.2
Ref. [9]	Not reported	6.8 ± 0.3

dent exciting photons was measured with a relative uncertainty of 1%, the efficiency $\varepsilon_d(E)$ of the detector used has been determined with a relative uncertainty of 1.5%, and the solid angle of detection $\Delta\Omega_d$ was calculated to have a relative uncertainty of 0.7%. Furthermore, the relative uncertainty in the determination of the sample's thickness ξ, is estimated to about 4%, attributed mostly to the uncertainties of the theoretical mass absorption coefficients employed. Therefore, a total relative uncertainty of 7% was calculated for the Ni KL-RRS cross section $d\sigma(E_0)/d\Omega$ obtained for polarized radiation.

Acknowledgments

This work is partially supported by the Greek State Scholarships Foundation IKY and the German Academic Exchange Service DAAD within the IKYDA program (project 314-ikyda-dr), which is gratefully acknowledged. Furthermore the authors would like to thank their colleagues R. Fliegauf, M. Kolbe, G. Ulm, J. Weser and N. Divis for supporting the present work.

---

[1] M. Krumrey, G. Ulm, High-accuracy detector calibration at the PTB four-crystal monochromator beamline, Nucl. Instr. Meth. A 467-468 (2001) 1175-1178

[2] B. Beckhoff and G.Ulm, Determination of fluorescence yields using monochromatized undulator radiation of high spectral purity and well-known flux, Adv. X-Ray Anal. 44 (2001) 349-354

[3] F. Scholze, M. Procop, Measurement of detection efficiency and response functions for an Si(Li) x-ray spectrometer in the range 0.1-5 keV, X-Ray Spectrom. 30 (2001) 69-76

[4] B. Beckhoff, R. Klein, M. Krumrey, F. Scholze, R. Thornagel, G. Ulm, X-ray detector calibration in the PTB radiometry laboratory at the electron storage ring BESSY II, Nucl. Instr. Meth. A 444 (2000) 480-483

[5] L. Unonius and P. Suortti, Mass Attenuation Coefficients of the Elements Ti, V, Fe, Co, Ni, Cu and Zn for the K Emission Lines between 4.51 and 10.98 keV, J. Appl. Cryst. 22 (1989) 46-52

[6] A.G Karydas, S. Galanopoulos, Ch. Zarkadas, T. Paradellis and N. Kallithrakas-Kontos, Chemical State speciation by resonant Raman scattering, J. Phys.: Condens. Matter 14 (2002) 12367-12381

[7] H. Ebel, X-ray Tube Spectra, X-Ray Spectrom. 28 (1999) 255 - 266

[8] Y. B. Bannett, D.C. Rapaport and I. Freund, Resonant X-Ray Raman Scattering and the infrared divergence of the Compton effect, Phys. Rev. A 16 (1977) 2011-2021

[9] P. Suortti, Scattering of X-Rays near the K Absorption Edge, Phys. Status. Solidi (b). 91 (1979) 657-666

[10] A.F. Kodre and S.M. Shafroth, Resonant Raman scattering of X-rays: Evidence for K-M scattering, Phys. Rev. A 19 (1979) 675-677

Determination of the mechanical properties of electroplated metals

NICOLAS BEISSER, DANIEL SCHONDELMAIER, IVO RUDOLPH, JOSEF KOUBA, BERND LOECHEL

BESSY GmbH, Anwenderzentrum Mikrotechnik, Albert-Einstein-Strasse 15, 12489 Berlin, Germany
E-mail: Nicolas.Beisser@bessy.de, Tel.: +49-30-6392-4681, Fax: +49-30-6392-4682

The characteristics of materials and alloys used in LIGA technology differ considerably from conventionally produced metals with regard to Young's modulus and tensile strength.

Furthermore, alloy compositions are used which are not commonly applied in macro mechanics. For constructing and determining micro components, it is essential to be familiar with their properties.

When using FEM analyses for the construction of a micro-module it is crucial to know about the mechanical characteristics of a material like Young's modulus, tensile strength, yield stress and hardness. Due to the low dimensions of the micro components, the defects resulting from the production process are of particular importance. Likewise, the structure created during an electrodeposition process, is different with respect to material of same composition but fabricated with conventional processes.

To determine the mechanical characteristics of materials used in MEMS it is necessary to employ specially adapted measuring tools with a resolution appropriate for determining the measured values. For this purpose, at BESSY two measurement tools were constructed and realized. The first tool is a tensile-stress testing machine which allows a resolution of 0.1 N for the tensile force and 70 nm for the tensile path [1]. Special tensile samples have to be developed for the new measurement tool with a cross-section of 0.015 mm^2 in the tensile area. The second measurement tool is a bending-stress machine with a resolution of 0.01N for the bending-stress and 70 nm for the bending path. Likewise special bending samples had been developed with a cross-section of 0.09 mm^2 in their bending area. The samples were produced on substrate surfaces by means of a LIGA process.

In order to compare the mechanical properties of both kinds of samples, they were placed on the same area on the substrate.

Presently the determination of the mechanical data for all electrodeposited materials used at BESSY (Ni, NiFe, Cu and Au) is under work.

During the deposition process of the tensile samples (Fig. 1), crucial parameters like current density and temperature were varied in order to determine their influence on tensile strength, Young's modulus, yield strength and hardness.

The crystalline structure of the electroplated metal varies based on deposition conditions and can be observed by means of a micrograph. These experiments were done to understand the correlation between the crystalline structure and measured material properties.

Likewise, the process related non homogenous current density distribution on the substrate surface is taken into account. By this means, the influence of current density distribution on the material properties within a single fabrication batch can be determined.

Resulting from non homogeneous growth, mechanical properties of electrodeposited materials vary in the growth and substrate plane direction. In order to characterize this effect for different materials, using the bending test, strain is applied on micro-beams both in and perpendicular to the growth direction [2, 3]. Force-flexion diagrams are created using employed force and measured flexion.

Based on the accomplished analyses, stress-strain diagrams (Fig. 2) for electrodeposited Ni, NiFe (90/10), Cu and Au are extracted in order to determine tensile strength, yield strength, Young's modulus and elongation limit. Furthermore, the Vickers hardness of the materials was measured and the influence of the deposition parameters (current density and temperature) on the mechanical properties was determined. As in the case of steel, comparison tables for electrodeposited Ni, NiFe, Cu and Au are created illustrating the connection between hardness and tensile strength. The mechanical properties in different directions of electrodeposited Ni, NiFe (90/10), Cu and Au were determined by means of bending test.

For applications like mold inserts or other mechanical parts, determined date will be used for the design development.

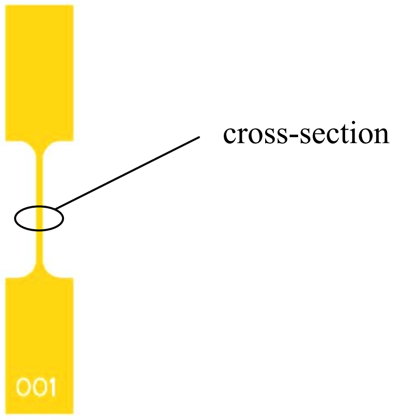

FIGURE 1: sample setup for tensile strength measurement

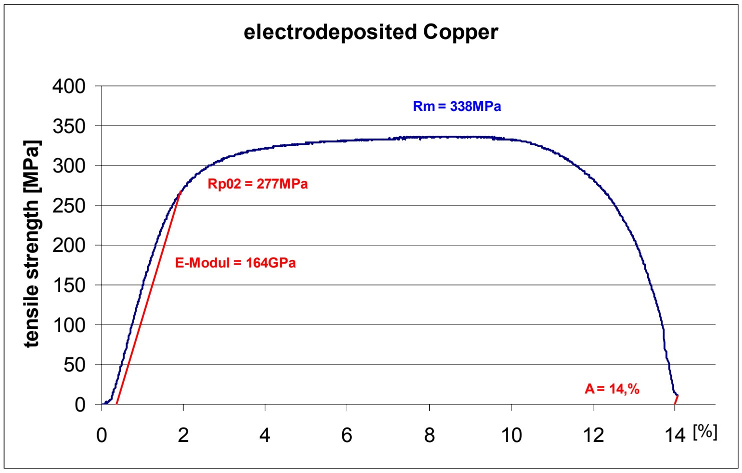

FIGURE 2: force flexion diagram for electrodeposited copper

FIGURE 3: sample setup for bending strength measurement

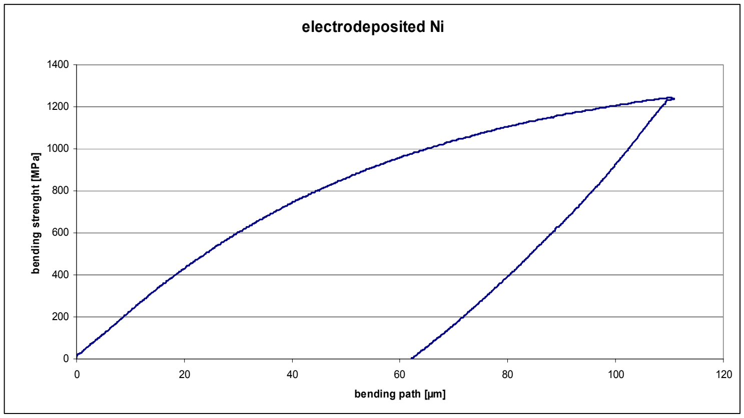

FIGURE 4: force bending diagram for electrodeposited Nickel

References

1. M. Hoffmann, “Ermittlung materialspezifischer Eigenschaften von galvanisch abgeschiedenen Schichten”, Diploma thesis 2004, TFH Berlin
2. S. Timoshenk, Theory of Plates and Shells, McGraw-Hill Education, ISBN 0070858209
3. N. Beisser, “Entwicklung, Konstruktion und Fertigung einer Justiervorrichtung für eine Gradientenlinse in der Mikrotechnik”, Diploma thesis 2003, TFH-Berlin

Photonische Kristalle für das sichtbare Spektrum

KOUBA, J.

BESSY GmbH, Anwenderzentrum für Mikrotechnik; Albert-Einstein-Str. 15, 12489 Berlin

E-Mail: josef.kouba@bessy.de
Tel.: +49 30 6392 3125
Fax: +49 30 6392 4709

Abstrakt: Photonische Kristalle bilden Grundelemente vieler zukünftiger photonischen Komponenten. Bei BESSY werden im Rahmen einer Doktorarbeit photonische Kristalle für das sichtbare Spektrum untersucht. In diesem Beitrag werden erste Ergebnisse der theoretischen Untersuchungen, der Herstellung und der experimentellen Untersuchungen vorgestellt.

Einleitung

Photonische Kristalle sind komplexe Strukturen mit örtlich periodischer Dielektrizitätsfunktion. Diese ermöglichen in Bezug auf Licht die gleichen Funktionalitäten, wie sie Halbleiter für elektrische Ströme zur Verfügung stellen. Man bezeichnet photonische Kristalle daher auch als photonische Bandlückenmaterialien. Sie bestehen aus strukturierten Halbleitern, Gläsern oder Polymeren und zwingen das Licht mittels ihrer spezifischen Brechungsindexstruktur dazu, sich in der für die Bauteilfunktion notwendigen Art und Weise im Medium auszubreiten. Ein wesentliches Merkmal dieser Technik ist die Möglichkeit, Licht auf kleinste Abmessungen unterhalb der Lichtwellenlänge zu führen um lokal hohe Feldintensitäten zu erzeugen und somit eine starke Wechselwirkung zwischen der Materie und Licht zu gewährleisten. Von den dabei auftretenden, z.T. quantenelektrodynamischen Effekten werden neuartige Anwendungen erwartet.

Damit rückt ein entscheidender Durchbruch auf dem Gebiet der optischen Miniaturisierung, die mit konventionellen optischen Techniken eine prinzipbedingte Grenze nicht unterschreiten kann, in greifbare Nähe. Die erfolgreiche Nutzung photonischer Bandlückenmaterialien eröffnet die Möglichkeit einer weiteren Steigerung der Datenübertragungen bei gleichzeitiger Verkleinerung der Geräte und Reduzierung der Kosten. Generell wird die Zielrichtung verfolgt, eine vollständig optische Kommunikationstechnologie zu verwirklichen, da sich gegenwärtig die Elektronik als hauptsächlicher Engpass hinsichtlich der Geschwindigkeit und Übertragungskapazität der Nachrichtenübertragung darstellt. Es existieren bereits Konzepte für rein optische Schaltelemente, die eines Tages als optische Hochgeschwindigkeits-Transistoren genutzt werden könnten. In diesen Schaltelementen werden photonische Kristalle eine zentrale Rolle spielen.

Eine Vielzahl von Arbeiten befasste sich bereits mit photonischen Kristallen und Resonatoren im nahen Infrarot. Diesen Arbeiten stehen bisher jedoch nur sehr wenige Untersuchungen im sichtbaren Spektralbereich gegenüber. Gründe hierfür liegen vor allem in der Technologie der Herstellung der Resonatoren. Zum einen muss das verwendete Material im sichtbaren Spektralbereich transparent sein und gleichzeitig einen möglichst hohen Brechungsindex aufweisen, zum anderen liegen die Strukturgrößen der Resonatoren teilweise unter 100 nm. Dabei wären optische Resonatoren im Sichtbaren insbesondere in Verbindung mit gängigen Fluoreszenzmarkern und Laserfarbstoffen mit Emissionswellenlängen im sichtbaren Spektralbereich äußerst interessante Kandidaten, um an ihnen Effekte der Wechselwirkung zwischen Licht und Materie zu studieren.

Im Rahmen einer Doktorarbeit werden bei BESSY zweidimensionale photonische Kristalle für sichtbares Licht entwickelt, hergestellt und untersucht. Zentraler Punkt der Untersuchung sind die mit Hilfe photonischer Kristalle erzeugten optischen Resonatoren. Diese zeichnen sich durch eine charakteristische optische Modenfrequenz aus, nämlich die des im Resonator erlaubten Modes. Solche Resonatoren können dann als Grundelemente in verschiedenen Anwendungen eingesetzt werden. Die möglichen Anwendungen reichen dabei von selektiven Wellenlängenfiltern über hocheffiziente Leuchtdioden oder Mikrolaser bis hin zu Einzelphotonenquellen für die Quanteninformationsverarbeitung in den zukünftigen Quantenrechnern.

Ergebnisse der Untersuchungen

Die Arbeit befasst sich mit theoretischen Untersuchungen, der Herstellung der Resonatoren und deren Charakterisierung.

Abb. 1 zeigt die Bandstruktur eines photonischen Kristalls für sichtbare Wellenlängen. Die der Berechnung zugrunde liegenden Materialdaten entsprechen den von in der Mikroelektronik standardmäßig verwendetem Siliziumnitrid. Bei der Struktur handelt es sich um eine periodisch perforierte Membrane wie in Abb. 1 dargestellt. Die Periode der Struktur beträgt 280 nm und der Lochradius 112 nm. Die Bandstruktur für das in der Kristallebene linear polarisierte Licht zeigt eine Bandlücke mit etwa 10 % Breite. Die Bandlücke wird auch in dem Transmissionsspektrum im Bereich von 560 bis etwa 700 nm deutlich sichtbar, siehe Abb. 2.

Am einfachsten kann ein optischer Resonator durch Verzicht auf eine oder mehrere Löcher in dem Kristallgitter realisiert werden. Solch eine Verletzung der Periodizität wird in Analogie zu Kristallgittern als Punktdefekt bezeichnet. Bei geeignet konzipierten Punkdefekten ergibt sich eine Eigenfrequenz die innerhalb der Bandlücke des umgebenden Kristalls liegt. Die Bandstruktur einer solchen Struktur ist in der Abb. 3 zu sehen und der zugehörige Eigenmod in der Abb. 4. Die Kavität zeichnet sich durch ein sehr flaches Band über die ganze Brillone-Zone aus, was auf die geringe Frequenzbreite hinweist. Die Resonanzfrequenz der Kavität liegt bei 630 nm. Wie in der Abb. 4 deutlich, wird das Licht sehr stark in der Kavität lokalisiert.

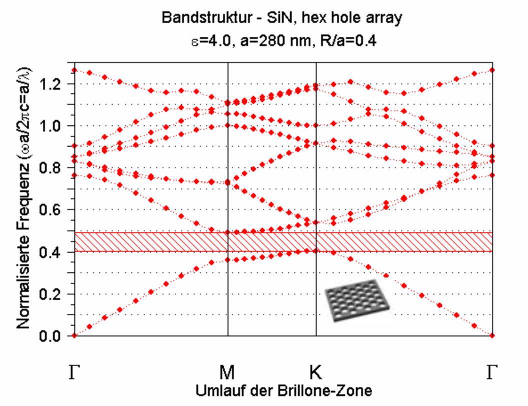

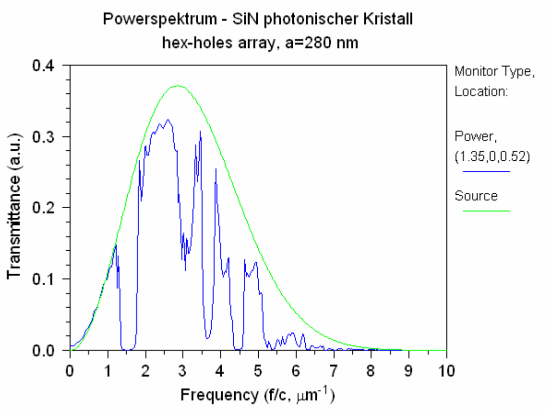

Abb. 1 – Bandstruktur von einem hexagonal angeordneten Lochmuster im SiN; x-Abszisse – Ränder der Brillone-Zone, y-Abszisse – normalisierte Wellenlänge; Bandlücke mit 10 % Breite sichtbar

Abb. 2 – Berechnetes Spektrum des photonischen Kristalls mit 5 Perioden; gleiche Abmessungen wie in Abb.1; Bandlücke aus Abb. 1 ist vom 700 nm bis 560 nm deutlich zu erkennen

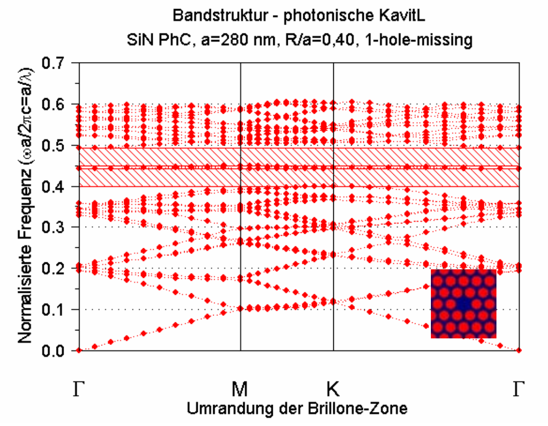

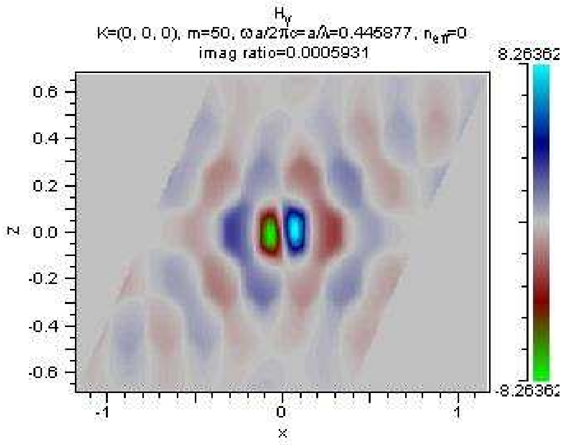

Abb. 3 – Bandstruktur einer Kavität; Strukturabmessungen siehe Abb. 1; 1 Loch ausgelassen; flaches Band korrespondierend zu dem Kavitätsmod bei 630 nm

Abb. 4 – Kavitätsmod des Punktdefekts aus Abb. 3 Resonanzfrequenz bei 630 nm; starke Lokalisierung vom Licht sichtbar

Eine der einfachsten Anwendungen solcher optischen Resonatoren ist ein Wellenlängenfilter. Der Resonator wirkt dabei als eine Art Schaltelement und lässt nur Licht mit der Frequenz durch die der Eigenfrequenz des Resonators entspricht wie in Abb. 7 und Abb. 8 dargestellt.

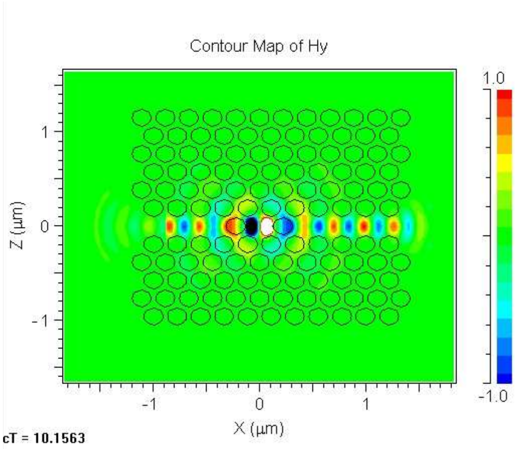

Abb. 5 – Photonische Kavität kombiniert mit Wellenleiterstruktur angeregt mit der Resonanzfrequenz;

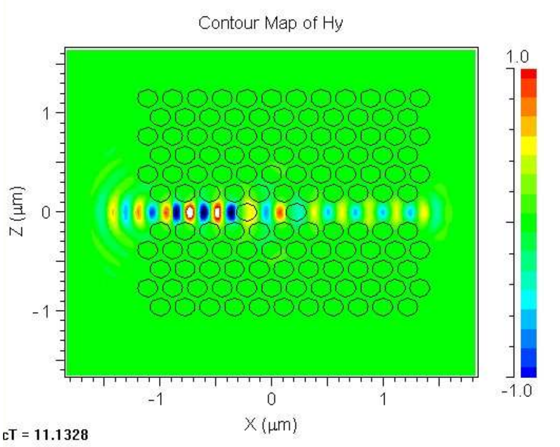

Abb. 6 – Analoge Struktur wie aus Abb. 5 angeregt mit 0.95xResonanzfrequenz

Die Herstellung der photonischen Kristalle für das sichtbare Spektrum stellt mit Perioden kleiner als 200 nm und einzelnen Strukturdetails unterhalb von 30 nm eine technologische Herausforderung dar. Hochauflösende Elektronenstrahllithographie und besondere Trockenätzprozesse mussten entwickelt und optimiert werden, um die Strukturen in geeigneten Materialien herstellen zu können. Beispiele der bereits realisierten Strukturen sind in den Abb. 7 und 8 zu sehen.

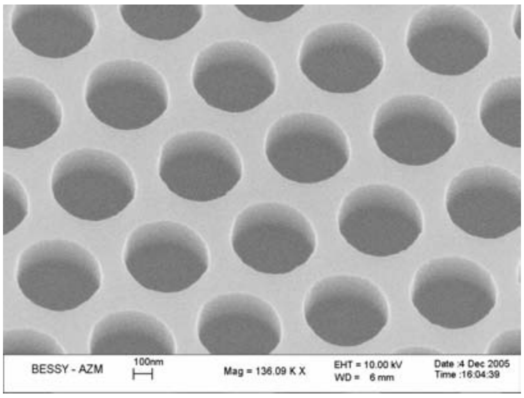

Abb. 7 – Photonischer Kristall aus perforiertem SiN für sichtbare Wellenlängen; Freigeätzte Membranstruktur; Membrandicke 300 nm, Periode 400 nm, Radius der Löcher 150 nm

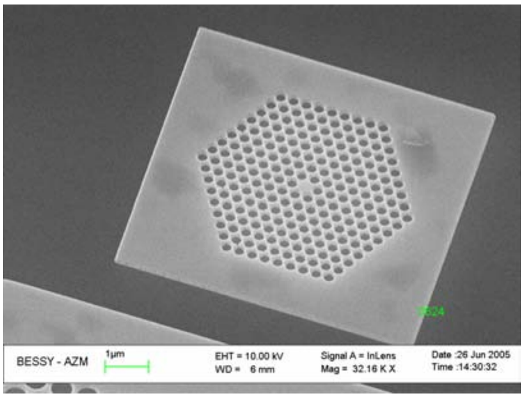

Abb. 8 – Kavitätsstruktur aus perforiertem Silizium für IR optische Wellenlängen; Teststruktur; Membrandicke 500 nm, Periode 500 nm, Radius der Löcher 420 nm

Die Überprüfung der vorhergesagten optischen Eigenschaften erfolgt mir Hilfe von Transmissionsmessungen. Dabei wird in die Kristallstruktur Licht mit passender Wellenlänge eingekoppelt und das Transmissionsspektrum aufgenommen, aus in dem die optischen Eigenschaften nachweisbar sind. Das Einkoppeln des Lichts in die Struktur stellt erneut eine Herausforderung dar, denn die Schichtdicken der photonischen Kristalle betragen nur wenige Hundert Nanometern. Um die Einkopplung zu ermöglichen, ist ein präziser mechanischer Aufbau notwendig. Die ersten Ergebnisse der Untersuchungen werden in kürze erwartet. Zusätzlich zu den Transmissionsmessungen sind in Zusammenarbeit mit der Humboldt Universität zu Berlin und dem Max Born Institut Nahfeldmessungen geplant, um die lokalen Feldintensitäten abbilden zu können.

Zusammenfassung

Im Rahmen einer Doktorarbeit werden bei BESSY photonische Kristalle für den sichtbaren Spektralbereich untersucht. Dabei stehen vor allem optische Resonatoren im Vordergrund, die es ermöglichen starke Lichtintensitäten auf lokal sehr engem Raum zu realisieren und dadurch die Wechselwirkung des Lichts mit der Materie zu studieren. Eine weitere Anwendung der Resonatoren liegt in deren Verwendung als Wellenlängenfilter. Insgesamt zielt die Untersuchung auf die Erprobung der optischen Eigenschaften neuartiger photonischen Komponenten, die mit Hinblick auf die Entwicklung in der Optoelektronik in naher Zukunft breite Anwendung finden werden. Die Arbeiten beinhalten theoretische Untersuchungen, Herstellung der Proben und deren optische Charakterisierung.

Durch die Berechnungen wurden mehrere Resonatortypen vorcharakterisiert. Dabei wurden Daten von Siliziumnitrid verwendet, welches ein branchenübliches Material ist. Durch Optimierung der Herstellungsprozesse wurden erfolgreich Prototypen der optischen Resonatoren im Siliziumnitrid realisiert. Die Herstellung erwies sich als extrem herausfordernd, denn die Strukturgrößen liegen im unteren sub-100 nm Bereich. Durch einen experimentellen Aufbau basierend auf Messung der Transmission sollen in der kommenden Phase die optischen Eigenschaften bestätigt werden. Durch Zusammenarbeit mit weiteren Institutionen sind auch Nahfeldmessungen an den Resonatorstrukturen geplant.

SU-8 – Promising Resist for Advanced Direct LIGA Applications

Kouba, J. [a], Engelke R. [b], Bednarzik M. [a], Ahrens G. [b], Heinz-Ulrich Scheunemann [a],
Gruetzner G. [b], Loechel B. [a], Miller, H. [c], Haase D. [d]

[a] *BESSY GmbH, Albert-Einstein-Str. 15, 12489 Berlin, Germany*
[b] *micro resist technology Koepenicker Str. 32,D-12555 Berlin, Germany*
[c] *MicroChem Corp., 1254 Chestnut Street, Newton, MA 02464, USA*
[d] *Jenoptik Mikrotechnik GmbH, Goeschwitzerstr. 40, 07745 Jena, Germany*

Email: josef.kouba@bessy.de
Phone: +49 30 6392 3125
Fax: +49 30 6392 4709

This work widely uses the contents of the presentation “Comparative study of the Sidewall Profile of PMMA and SU-8 Moulds Made by UDXRL and of Electroformed Metallic Counterpart” to the High Aspect Ratio Micro Structure Technology workshop HARMST 2005 held in Gyeongyu (Republic of Korea), June 10-13, 2005.

Abstract: A case study of use of negative type SU-8 X-ray sensitive resist for fabrication of advanced, highly precise, ultra tall Direct LIGA mechanical micro parts is presented in this paper. Using Direct LIGA technique, ~1 mm tall highly precise metallic gear wheels are being fabricated, previously using PMMA based process. Starting from a non-optimized non satisfying SU-8 process, significant process parameters for process optimization were identified using statistical design of experiment. By varying the significant process parameters, SU-8 process was further optimized with respect to critical aspect of sidewall bow and tilt of metallic structures. After the optimization, metallic parts fabricated using SU-8 process showed comparable quality as those fabricated using PMMA based process.

Introduction

Currently, conventional precision engineering technologies are reaching their limits concerning the feature size and precision demands, so that alternative technologies such as LIGA gain on importance [1]. An excellent example is the fabrication of metallic micro gear wheels, which are used in precision, zero backlash micro harmonic drives [2]. In order to reach their performance, metallic components of the these complex and small gear systems require the highest level of geometrical and dimensional precision, which can only be reached by means of LIGA technology. An assembled micro harmonic drive is depicted in

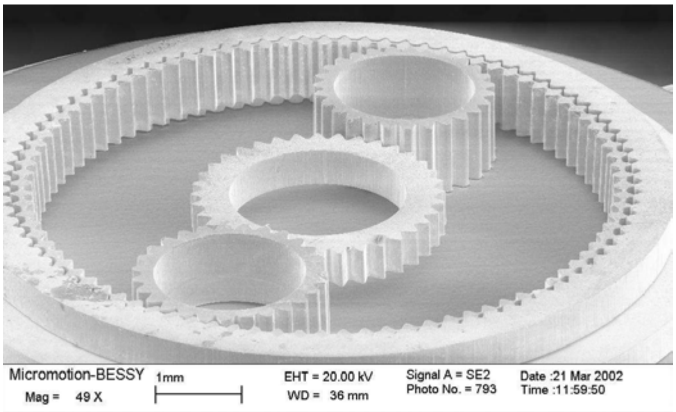

Fig. 1[1].

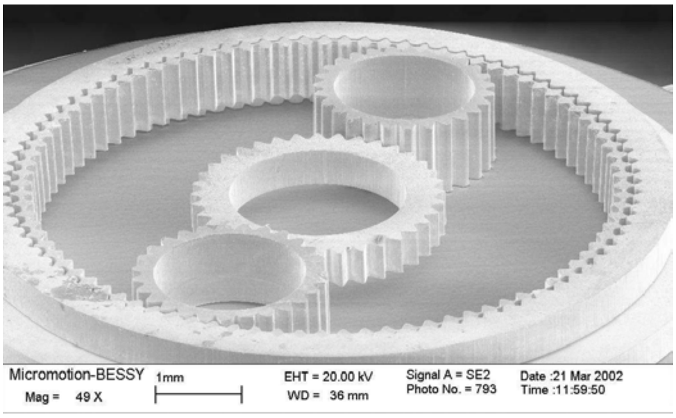

Fig. 1 - Assembled micro harmonic drive with the driven wheel in the middle, two planet wheels and the flexible element called 'flex-spline'

The customer-given specifications including precision requirements are given in

Substrate	4 " Si wafer, 90 % patterned
Resist/metall height	1100/1000 µm
Smallest feature size	25 µm (flex-spline)
Largest aspect ratio	40 (in metall)
Linewidth error	±1 µm
Vertical tolerances per sidewall	±1 µm
Allowed roughness (R_a/R_z)	100 nm

Tab. 1 and clearly illustrate the need of use of LIGA.

Substrate	4 " Si wafer, 90 % patterned
Resist/metall height	1100/1000 µm
Smallest feature size	25 µm (flex-spline)
Largest aspect ratio	40 (in metall)
Linewidth error	±1 µm
Vertical tolerances per sidewall	±1 µm
Allowed roughness (R_a/R_z)	100 nm

Tab. 1 – Dimensional parameters for critical parts of harmonic drive units

As shown in

Substrate	4 " Si wafer, 90 % patterned
Resist/metall height	1100/1000 µm
Smallest feature size	25 µm (flex-spline)
Largest aspect ratio	40 (in metall)
Linewidth error	±1 µm
Vertical tolerances per sidewall	±1 µm
Allowed roughness (Ra/Rz)	100 nm

---

[1] With courtesy of Micromotion GmbH, Mainz, Germany; www.micromotion.de

Tab. 1, fabrication of the most critical parts of the gear assembly – the flex spline – poses the largest challenge, especially regarding the sidewall tolerances.
The fabrication of all the components occurs by the means of Direct LIGA [3]. This reduces the LIGA process on X-ray Lithography and first electroforming step only thus posing high requirements on process stability, repeatability and cost effectiveness.

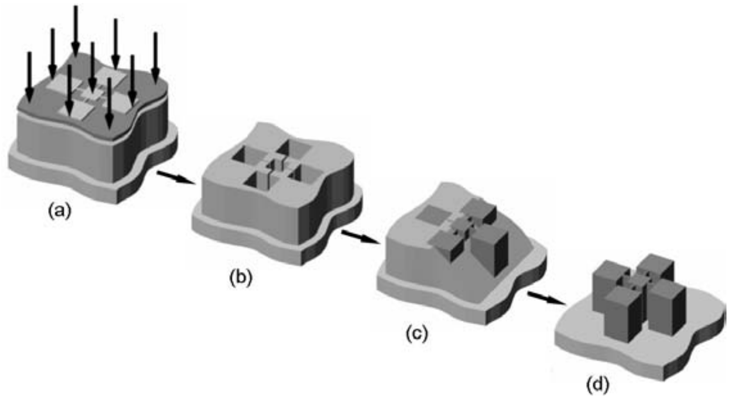

Fig. 2 – Scheme of Direct LIGA process; (a) exposure of the resist via X-Ray mask; (b) development of the exposed resist; (c) electroplating of the metallic micro parts; (d) removal of the resist

Up to recently, the gear wheels such as the ~1 mm tall flex-splines were fabricated using PMMA-based process with overall sufficient quality and yield. But due to the requirements to cut the processing costs, switching to SU-8 process would be preferable since the process costs are smaller as illustrated in In Fehler! **Ungültiger Eigenverweis auf Textmarke.** the costs for X-ray exposure are the bottle neck of the whole process such that cutting the costs of X-ray exposure together with parallelizing of the pre- and post processing steps would reduce the single-part costs significantly.
But using the initial SU-8 resist process failed and the precision requirements couldn't be fulfilled, giving so an impulse for this study. The aim of the work was to optimize the SU-8 process in order to reach the quality of final micro gear wheels similar to those of made using PMMA process.

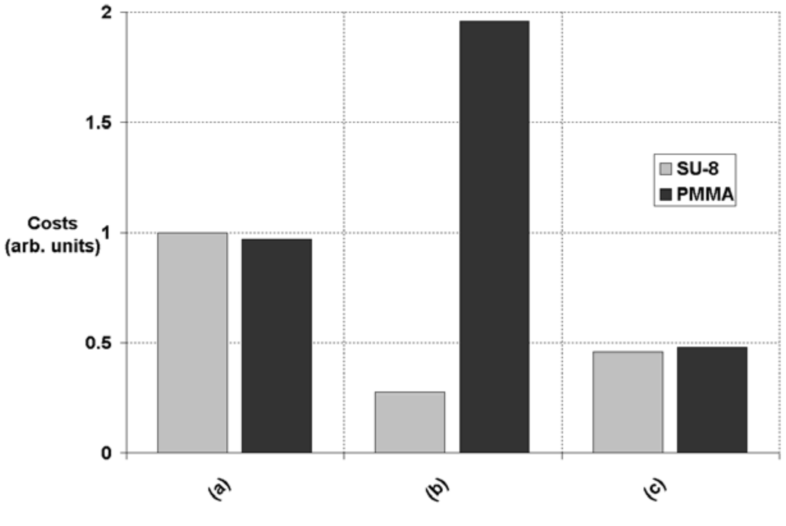

Fig. 3.

In **Fehler! Ungültiger Eigenverweis auf Textmarke.** the costs for X-ray exposure are the bottle neck of the whole process such that cutting the costs of X-ray exposure together with parallelizing of the pre- and post processing steps would reduce the single-part costs significantly.

But using the initial SU-8 resist process failed and the precision requirements couldn't be fulfilled, giving so an impulse for this study. The aim of the work was to optimize the SU-8 process in order to reach the quality of final micro gear wheels similar to those of made using PMMA process.

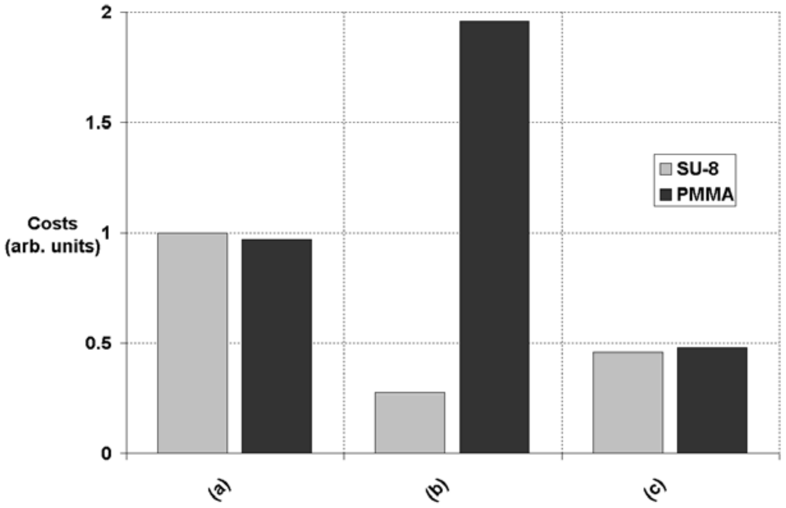

Fig. 3 – Comparison of process costs for PMMA and SU-8 process; (a) – preprocessing costs, (b) – X-Ray exposure related costs, (c) – post processing costs; 4 " Si substrate, 1 mm thick resist; electroforming and inspection not included; all costs related to the preprocessing costs of one SU-8 substrate

SU-8 versus PMMA

SU-8 is nowadays a well known X-ray resist and compared to PMMA, it shows some advantages as well as disadvantages as illustrated in

SU-8	PMMA
Liquid system, spinning or casting easy	Solid system, casting difficult, gluing necessary
Chemically amlipfied, highly sensitive	Non amplified, low sensitivity
Narrow process window	Robust process
Excellent thermal stability	Limited thermal stability
Difficult to remove	Easy to remove
Lithographical performance unclear	Excellent lithographical performance

Tab. 2.

SU-8	PMMA
Liquid system, spinning or casting easy	Solid system, casting difficult, gluing necessary
Chemically amlipfied, highly sensitive	Non amplified, low sensitivity
Narrow process window	Robust process
Excellent thermal stability	Limited thermal stability
Difficult to remove	Easy to remove
Lithographical performance unclear	Excellent lithographical performance

Tab. 2 – Comparison of SU-8 and PMMA with respect to the Direct LIGA process.

One of the main problems of SU-8 resist is its high sensitivity, which at the same time is its main advantage over PMMA. As ilustrated in A summarizing overview gives the

	SU-8	PMMA
Threshold dose	< 0.75 J/cm3	< 250 J/cm3
Contrast	1.4	1.2
Exposure dose - 1100 µm	80 mAmin/cm	1600 mAmin/cm
Exposure time – 4 “ wafer	10 min.	3,5 hrs

Tab. 3. As can be seen, the exposure time is about 20 times shorter in case of SU-8.

	SU-8	PMMA
Threshold dose	< 0.75 J/cm3	< 250 J/cm3
Contrast	1.4	1.2
Exposure dose - 1100 µm	80 mAmin/cm	1600 mAmin/cm
Exposure time – 4 “ wafer	10 min.	3,5 hrs

Tab. 3 – Comparison of SU-8 and PMMA with regards to sensitivity and exposure time (calculated for BESSY synchrotron and with respect to typical process conditions)

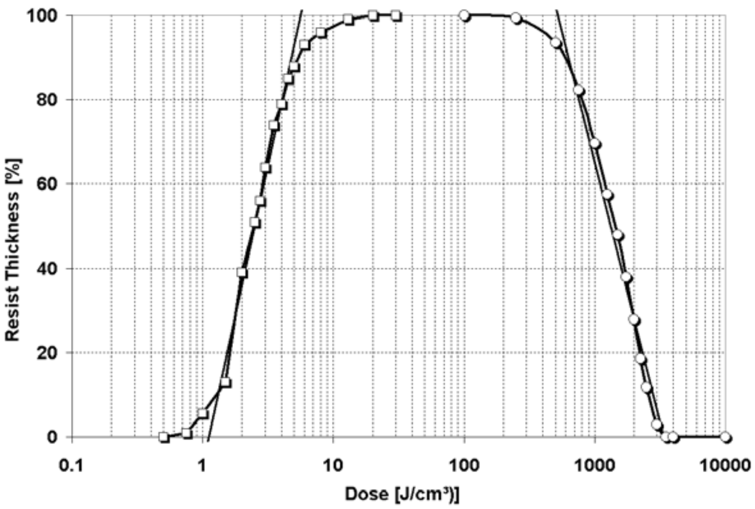

Fig. 4, the threshold dose of SU-8 is in the order of 300 times smaller than that of PMMA, making the resist much more sensitive but at the same time making the process window in case of SU-8 much narrower than that of PMMA. Further, by comparing the slope of the curves, one can see that both resists show about the same contrast.

A summarizing overview gives the

	SU-8	PMMA
Threshold dose	< 0.75 J/cm3	< 250 J/cm3
Contrast	1.4	1.2
Exposure dose - 1100 µm	80 mAmin/cm	1600 mAmin/cm
Exposure time – 4 “ wafer	10 min.	3,5 hrs

Tab. 3. As can be seen, the exposure time is about 20 times shorter in case of SU-8.

	SU-8	PMMA
Threshold dose	< 0.75 J/cm3	< 250 J/cm3
Contrast	1.4	1.2
Exposure dose - 1100 µm	80 mAmin/cm	1600 mAmin/cm
Exposure time – 4 " wafer	10 min.	3,5 hrs

Tab. 3 – Comparison of SU-8 and PMMA with regards to sensitivity and exposure time (calculated for BESSY synchrotron and with respect to typical process conditions)

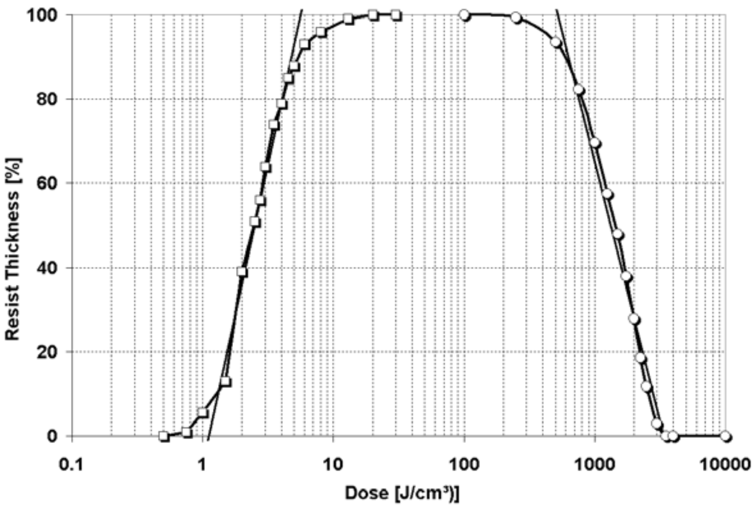

Fig. 4 – Gradation curves for SU-8 (left) and PMMA (right); 1 mm resist thickness, standard processing conditions

Experimental

The study consisted of several steps. Starting with the insufficient structure quality produced using 'standard' SU-8 process, identifying the most significant SU-8 process parameters was the first task in order to be able to start the optimization of the SU8 process. Inspection of fabricated gear wheels and comparison to their PMMA-based counterparts followed.

For SU-8 process, 4 " Si wafers with Ti/Au plating base were used as a substrate.

Standard, commercially available SU-8 resist as well as modified SU-8 resist were used in this study. Commercially available resist was SU-8 100 obtained from *micro resist technology,* chemically modified resist consisted of standard SU-8 epoxy with varying amount of photo active component (PAC). The content of PAC varied from 2 to 6%.

The SU-8 resist layers was prepared by casting of well defined amount of liquid resist on the substrate and baking it on leveled hot plate. By precise control of the process, resist layers of 1100 µm thickness with variation of less than 0.25 % in thickness could be repeatable prepared [4].

By varying the softbake temperature and time between 105 ºC and 130 ºC and 8 to 40 hrs respectively, residual solvent content as an amount of remaining solvent in the resist film after softbake was varied between 2% and 10%. By adjusting the softbake regimes, some variation in the solvent content distribution was also achieved [5].

X-ray exposures were realized at BESSY dipole lithographic beamline DIP 06.1a, featuring an Jenoptik DEX02 scanner. BESSY ring is operated at 1.7 GeV, the radius of the dipole magnet of 4.359 m and magnetic field of 1.35 T result in critical energy of 2.5 keV or critical wavelength of 0.5 nm respectively. 200 µm thick Be window is used to separate the high vacuum region from the scanner. Typically, the ring is operated with 150-250 mA. During the experimental study, exposures of SU-8 were performed using bottom dose ranging from 10 to 40 J/cm^3 using various kinds of filtration of spectra. A special testing mask for the process optimization was fabricated at BESSY. The mask consisted of 180 µm thick graphite substrate carrying 60 µm gold absorber structures. The mask carried 10 identical fields allowing multiple exposures with different conditions on single wafer. For the fabrication of metallic gears, X-ray masks fabricated at CAMD [6] consisting of 550 µm thick Be substrate and 50 µm thick gold absorber were used.

Post exposure bake was realized on the hot plate using temperatures from 60 ºC – 95 ºC and times from 20 min to 60 min.

In case of PMMA process, 4 " Si substrates with oxidized Ti as a plating base were used.

High molecular, 2 mm thick PMMA sheets obtained from Goodfellow were glued to the substrate, using a method as described in [7] and fly-cut to the final thickness of 1050 µm. X-ray exposures were realized at BESSY wavelength shifter lithographic beamline ID06, featuring an Jenoptik DEX01 scanner. Critical energy of the spectra is 7.69 keV corresponding to 0.16 nm critical wavelength. A 200 µm thick Be window is used to separate the high vacuum region from the scanner. X-ray masks fabricated at CAMD consisting of 550 µm thick Be substrate and 50 µm thick gold absorber were used. Bottom dose of 4.0 kJ/cm^3 was used. In order to adjust the spectra, 160 µm thick graphite filter was used.

Electroforming was in both cases performed by Micromotiong GmbH using commercially available Kissler plating bench and sulphite based Ni-Fe plating solution.

Since the line width control and surface roughness could be well controlled as a result of a long lasting and intensive work concentrating on the fabrication of highly precise, high contrast Be based X-ray masks, the inspection concentrated on the remaining aspects which have significant impact on the quality of fabricated gear wheels. These are as our experience show the sidewall bow and the sidewall tilt.

In order to evaluate the sidewall bow, white light interferometery using Wyko NT 1000 was used at group of professor Neyer, University of Dortmund [8].

In order to evaluate the tilt of the gear wheel sidewalls, video based contact angle measurement method as proposed in [9] was used.

In order to evaluate the occurrence of top scum, resist residue or structure collapse during the DoE study (see results), LEO 1560 scanning electron microscope was used.

Results

The unacceptably large deviation as shown in **Fehler! Ungültiger Eigenverweis auf Textmarke.** was the starting point of the SU-8 process optimization. Because of large number of processing parameters in case of SU-8, statistical design of experiment was used at first in order to limit the optimization to the most significant parameters only.

As described above, amount of PAC, remaining solvent content, post exposure bake temperature, post exposure time and bottom dose were varied. As responses, the top scum, also called skin effect, amount of observable residue after development of resist, collapse of the structures and sidewall bow were considered as responses of the variation of process conditions. Since it would take too long time to perform electroplating on each of substrates in order to evaluate shows the typical sidewall bow of gear wheel fabricated using initial SU-8 and PMMA fabrication process respectively. As can be seen, the amplitude of the bow in case of SU-8 approaches 5 µm, which is an unacceptably large dimensional deviation and at the end would even disable the assembly of the gears.

The unacceptably large deviation as shown in **Fehler! Ungültiger Eigenverweis auf Textmarke.** was the starting point of the SU-8 process optimization. Because of large number of processing parameters in case of SU-8, statistical design of experiment was used at first in order to limit the optimization to the most significant parameters only.

As described above, amount of PAC, remaining solvent content, post exposure bake temperature, post exposure time and bottom dose were varied. As responses, the top scum, also called skin effect, amount of observable residue after development of resist, collapse of the structures and sidewall bow were considered as responses of the variation of process conditions. Since it would take too long time to perform electroplating on each of substrates in order to evaluate the metallic structures, the evaluation was limited to resist forms only. As a result of the study, most significant parameters were identified.

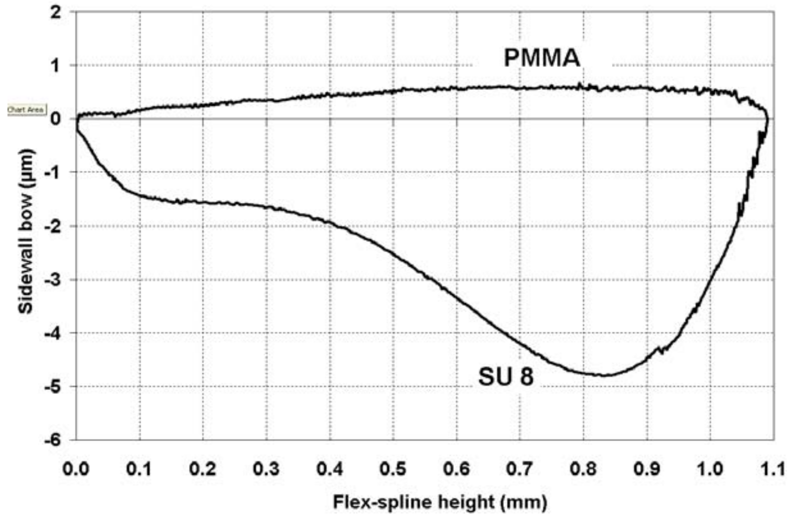

Fig. 5 – Sidewall bow on flex-splines fabricated using SU-8 and PMMA fabrication process.

	Top Scum	Residue	Structure Collapse	Sidewall profile
Correlation Coefficient	0.85	0.95	0.5	0.69
PAC content	**	*	*	NS
Solvent content	***	***	***	***
PEB Temperature	***	**	***	***
PEB Time	***	**	NS	NS
Bottom dose	***	***	NS	**
Solvent content x Bottom dose	***	***	*	NS
Solvent content x PEB Temp.	NS	**	**	**
PAC content x Solvent content	***	*	NS	**

Tab. 4 shows a brief summary of each independent factor and several interactions.

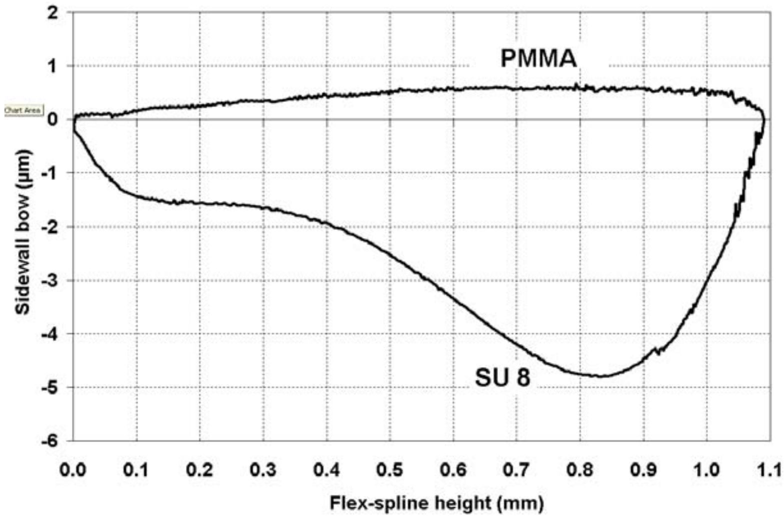

Fig. 5 – Sidewall bow on flex-splines fabricated using SU-8 and PMMA fabrication process.

	Top Scum	Residue	Structure Collapse	Sidewall profile
Correlation Coefficient	0.85	0.95	0.5	0.69
PAC content	**	*	*	NS
Solvent content	***	***	***	***
PEB Temperature	***	**	***	***
PEB Time	***	**	NS	NS
Bottom dose	***	***	NS	**
Solvent content x Bottom dose	***	***	*	NS
Solvent content x PEB Temp.	NS	**	**	**
PAC content x Solvent content	***	*	NS	**

Tab. 4 – Significance factors for various processing parameters; * ~ 90 % confidence interval for significance, ** ~ 95 % confidence interval for significance, *** ~ 99 % confidence interval for significance, NS – not significant

Although the predictive model correlation for structural collapse and sidewall bow were low, two independent variables were found to be highly significant, namely the solvent content, PEB temperature and bottom dose. As indicated from the results, solvent content of 6 % and PEB temperature of 60 ºC should produce the least structure collapse and lowest sidewall bow.

Using the results of the previous study, by further varying the significant parameters, SU-8 process was optimized with respect to the sidewall bow.

Each point of the graph represents the average value of the amplitude of all the measurements at metallic flex-splines produced with the same conditions. The error bars represent the maximum and minimum of all measured values.

The left part of the chart in **Fehler! Ungültiger Eigenverweis auf Textmarke.** shows the best and the worst corresponding values found on metallic flex-splines fabricated using PMMA process as described above. In both of these two cases, the assembled gear wheels were fully functional and exceeded their required life time, so that for this study, these two cases represented the working range considering the sidewall bow.

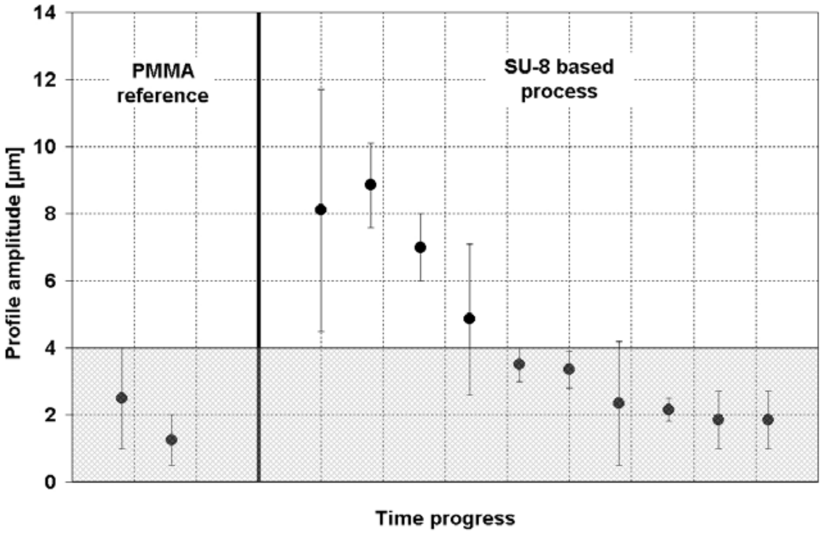

Fig. 6 shows the evolution of the sidewall profile along the time scale of SU-8 process optimization.

Each point of the graph represents the average value of the amplitude of all the measurements at metallic flex-splines produced with the same conditions. The error bars represent the maximum and minimum of all measured values.

The left part of the chart in **Fehler! Ungültiger Eigenverweis auf Textmarke.** shows the best and the worst corresponding values found on metallic flex-splines fabricated using PMMA process as described above. In both of these two cases, the assembled gear wheels were fully functional and exceeded their required life time, so that for this study, these two cases represented the working range considering the sidewall bow.

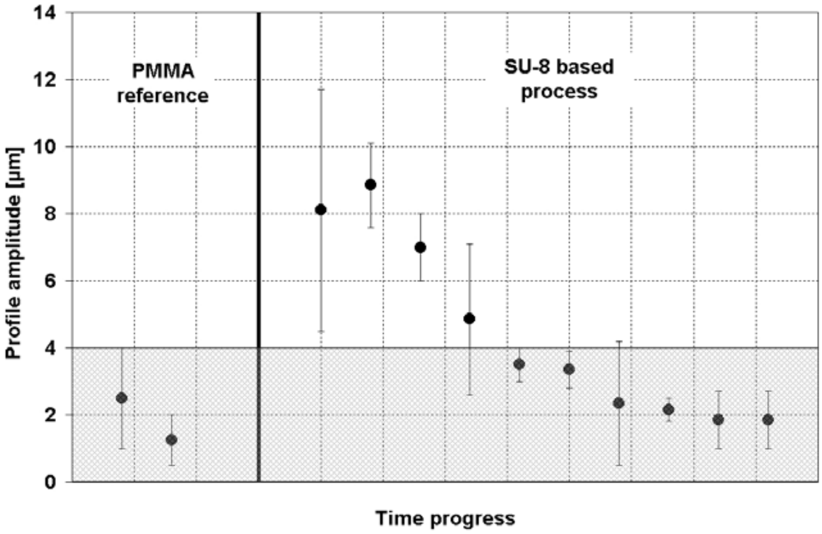

Fig. 6 – Progress of sidewall bow along the process of optimization (right); PMMA reference measurements (left); working range highlighted

As can be seen, the initial results in case of SU-8 process were fully non-satisfying with amplitudes of sidewall bow approaching 12 µm! As the process of SU-8 optimization was carried forward, both the average values and the variation decreased, so that at the end, the amplitudes of bow of SU-8 based fabricated flex-splines reached those of flex-splines fabricated using PMMA process.

As predicted before, the most significant parameter was the solvent content together with the post exposure bake temperature and the bottom dose. It was also found, that the distribution of solvent content in the resist film plays an important role and some specific softbake procedures yielded better results.

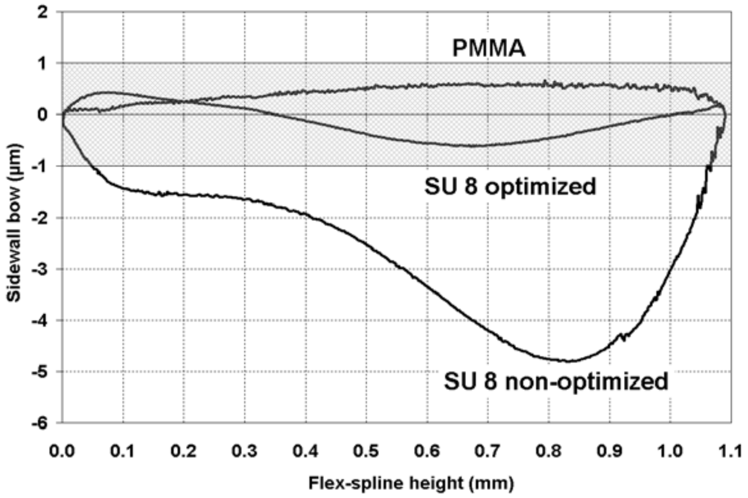

Fig. 7 – Sidewall bow on flex-splines fabricated using optimized SU-8 and PMMA fabrication process; significant improvement in comparison with initial non-optimized SU-8 process; tolerance range of ±1 µm highlighted;

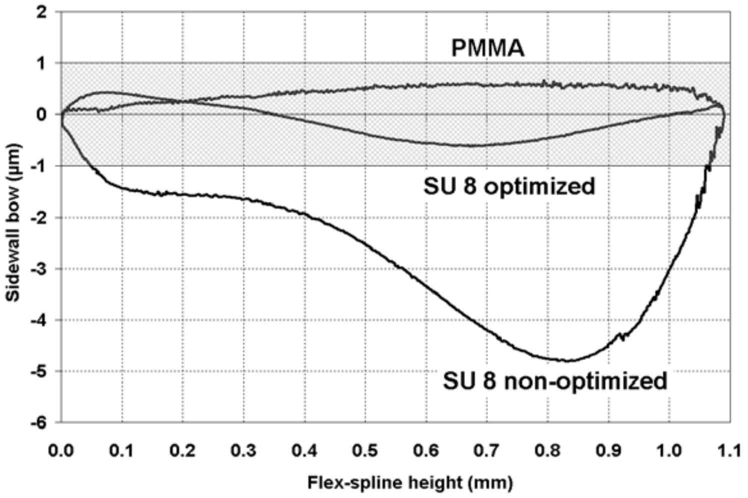

Fig. 7 depicts the typical sidewall bow of a metallic flex-spline fabricated using an optimized SU-8 process in comparison to the corresponding sidewall bow in case of non-optimized SU-8 process and the PMMA process respectively.

The significant improvement in case of optimized SU-8 process can be clearly observed.

The overall sidewall profile consists both of the sidewall bow and the sidewall tilt. Using white light interferometer, only the bow can be measured. Using the contact angle measurement method, sidewall tilt was estimated by several flex-splines fabricated using the optimized SU-8 process and compared to sidewall tilt of flex-splines fabricated using PMMA process. The results of this measurement are shown in

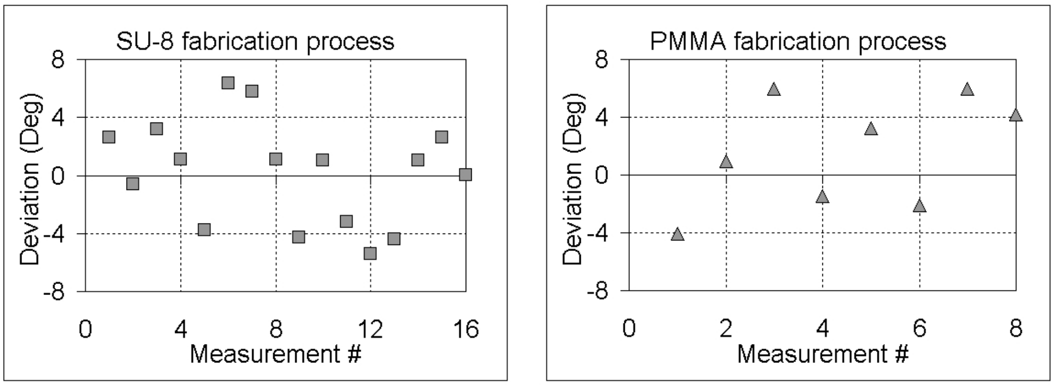

Fig. 8. Square mean deviation of the sidewall tilt was estimated to 3.5 Deg in case of the optimized SU-8 process and 3.9 Deg in case of PMMA process.

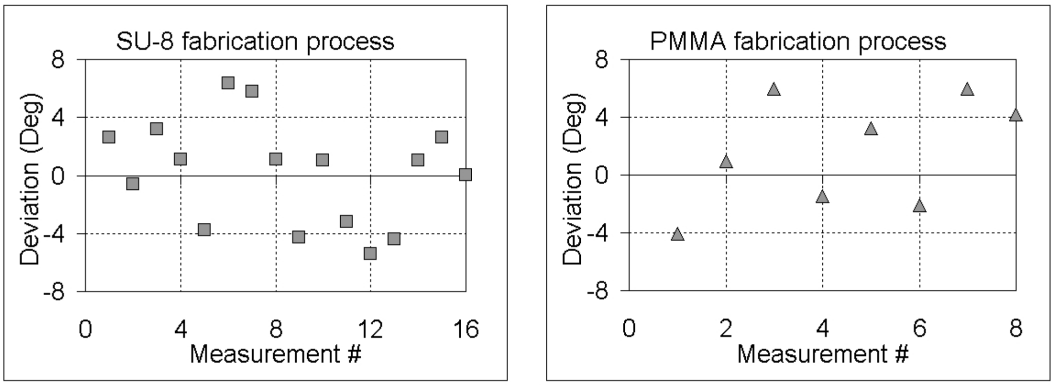

Fig. 8 – Sidewall tilt measured on metallic flex-splines fabricated using optimized SU-8 process (left) and using standard PMMA process (right)

Comparing the square mean values, one can see that the sidewall tilt is comparable. The overall large value of the tilt of approximately 4 Deg is believed to result from the electroforming process and is currently under investigation. Is to be said though, that same as in the case of sidewall bow, the investigated flex-splines fabricated using PMMA process were all well working and acceptable parts, so that these high values of tilt obviously do not disturb the application.

Summary

SU-8 process for fabrication of precise metallic gear wheels with heights of 1 mm, smallest feature size of 25 μm, aspect ratios exceeding 40 and overall very tight tolerances was established. Starting from a non-optimized SU-8 process, by careful design of the experiment, significant process parameters for process optimization were identified. Remaining solvent concentration, post exposure bake temperature and bottom dose were identified among the most significant parameters. By varying significant parameters, SU-8 process was optimized with respect to the sidewall bow. Among optimal conditions, 6 % of remaining solvent content and post bake temperature of 60 ºC were found. Using the optimized SU-8 process, the sidewall bow of the electroplated gear wheels was found comparable to the one of electroplated gear wheels fabricated using PMMA process. Further, the sidewall tilt of metallic gear wheels fabricated using optimized SU-8 process was found comparable to the one of gear wheels fabricated using PMMA process. The results are summarized in

	PMMA process (Reference)	Optimized SU-8 process
Critical Dimensions	1100 µm high, 25 µm wide, aspect ratio 44	
Sidewall bow on metallic parts	< 4 µm	< 4 µm
Sidewall tilt of metallic parts	< 4 Deg	< 3.5 Deg

Tab. 5.

	PMMA process (Reference)	Optimized SU-8 process
Critical Dimensions	1100 µm high, 25 µm wide, aspect ratio 44	
Sidewall bow on metallic parts	< 4 µm	< 4 µm
Sidewall tilt of metallic parts	< 4 Deg	< 3.5 Deg

Tab. 5 – Table summarizing the main results of the study

Concluding, the main task of the study was achieved and SU-8 was proven to be well suitable for presented application.

The authors of this study see further potential in the optimization of the whole fabrication process, both on the resist processing side as well as on the electroplating side, so that further studies and optimization processes are ongoing.

Acknowledgements

Authors would like to thank to all participants and contributors to this work, especially to co-workers from BESSY GmbH, micro resist technology GmbH, Micromotion GmbH, CAMD and University of Dortmund. This research was partially supported by the initiative of the Federal Ministry of Education (BMBF), Berlin.

References

1. **W. Menz, J.Mohr (1997)** Mikrosystemtechnik fuer Ingenieure, VCH Verlaggesselschaft mbH, Weinheim
2. **R. Degen, R. Slatter** (2004) Zero Backlash Micro-Gears and Actuators for Microassembly Applications, www.harmonicdrive.de/de/pdf/fachauf_18.pdf
3. **H.-U. Scheunemann, B. Loechel, L. Jian, D. Schondelmaier, J. Goettert, Y. M. Desta, Z.-G. Ling, T. Morris, J. Joonyoung, V. Singh, R. Degen, U. Kirsch, G. Gruetzner, R. Ruhmann, G. Ahrens,** Providing a Direct-LIGA Service – A Status Report, Book of Abstracts HARMST 2005, Monterey, CA, pp. 281-282
4. **G. Grützner, R. Ruhmann, G. Ahrens, M. Bednarzik, B. Loechel, P. Limbecker, J. Goettert, Y. Desta, V. Singh** (2003), Improved process parameters and impact on structure quality of high aspect ratio SU-8 micro-strustructures, Book of Abstracts HARMST 2005, Monterey, CA, pp. 11-12
5. **R. Ruhmann, G. Ahrens, G. Grützner, N. A.-Staufenbiel, H. Schoeder** (2005), Residual solvent content distribution in ultra-thick SU-8 films and its influence on the imagin quality, HARMST 2005, in press
6. http//www.camd.lsu.edu
7. **S. Achenbach** (2000), Optimierung zur Herstellung von Mikrostrukturen durch Ultratiefe Röntgenlithographie (UDXRL), PhD Thesis, University Karlsruhe
8. http://www-mst.e-technik.uni-dortmund.de/

9. **R. Engelke, G. Ahrens, R. Ruhmann, S. Kopetz, J. Kastner, K. Wiesauer, D. Stifter, B. Loechel, A. Neyer, G. Gruetzner** (2005), Possibilities of Inline Process Inspection of High Aspect ratio LIGA Micro Structures, HARMST 2005, in press

THE PHOTOABSORPTION AND PHOTOIONIZATION OF HALOGENATED ETHYLENES: BROMINATED DERIVATIVES.

R. Locht[1], B. Leyh[1], H.W. Jochims[2], H. Baumgärtel[2].
[1] Molecular Dynamics Laboratory, Department of Chemistry, Institute of Chemistry,
University of Liège, Sart-Tilman par B-4000 Liège 1, Belgium.
[2]Institut für Physikalische und Theoretische Chemie, Freie Universität Berlin,
Takustrasse 3, D-14195 Berlin, Germany.

In our program on the dynamics of highly excited states of the halogenated derivatives of ethylene, particular attention has been paid to the brominated derivatives [1]. The main motivation is not only their importance in chemical and technological applications but also the scarcity, or even the lack of spectroscopic data related to these compounds.

In 2000, a thorough investigation of C_2H_3Br has been presented. The vacuum UV photoabsorption spectrum [2] as well as the threshold and He(I)-photoelectron spectrum [3] have been published. The CIS-spectra of the first six electronic states were measured [3]. The unimolecular photodissociation dynamics of $C_2H_3Br^+$ in the $C_2H_3^+$+Br channel has been studied by the maximum entropy (MEM) method [4]. Finally, the ion-pair formation and dissociative photoionization of this molecule have been investigated by mass spectrometry and TPEPICO techniques [5]: the $C_2H_3^+$+Br^-, $C_2H_3^+$+Br, $C_2H_2^+$+[H,Br] and Br^++[C_2, H_2] channels were considered.

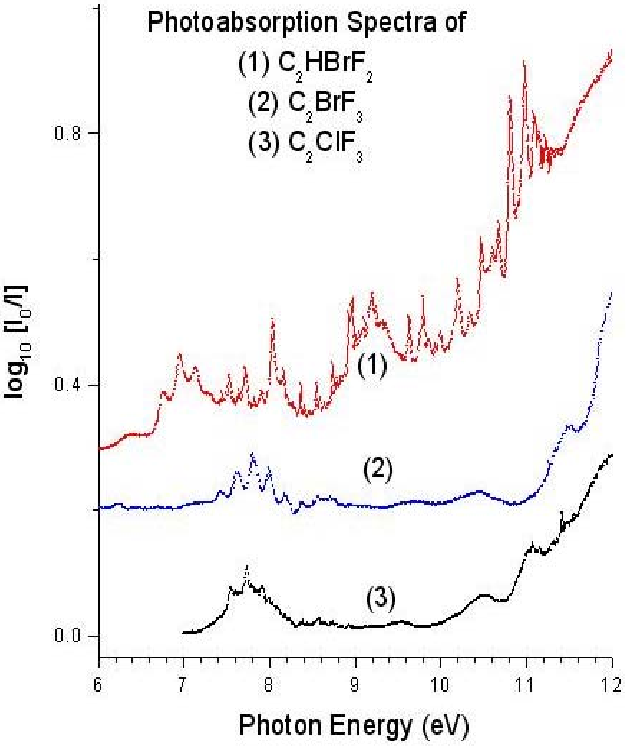

Figure 1.

This research program has been continued by recording the photoabsorption spectrum and the dissociative photoionization mass spectrometry of brominated derivatives of ethylene, e.g. C_2HBrF_2 and C_2BrF_3 in the 5-20 eV photon energy range. The present work has been performed on the 3m-NIM-2 beamline equipped with a 600 ℓ/mm Al grating and entrance and exit slits of 30 μm and 50 μm widths respectively. In addition, the photoelectron spectrum and the kinetic energy distributions of the fragment ions observed at the energy of the HeI (21.2 eV), NeI (16.67-16.85 eV) and ArII (13.47 eV) resonance lines have been recorded in the laboratory.

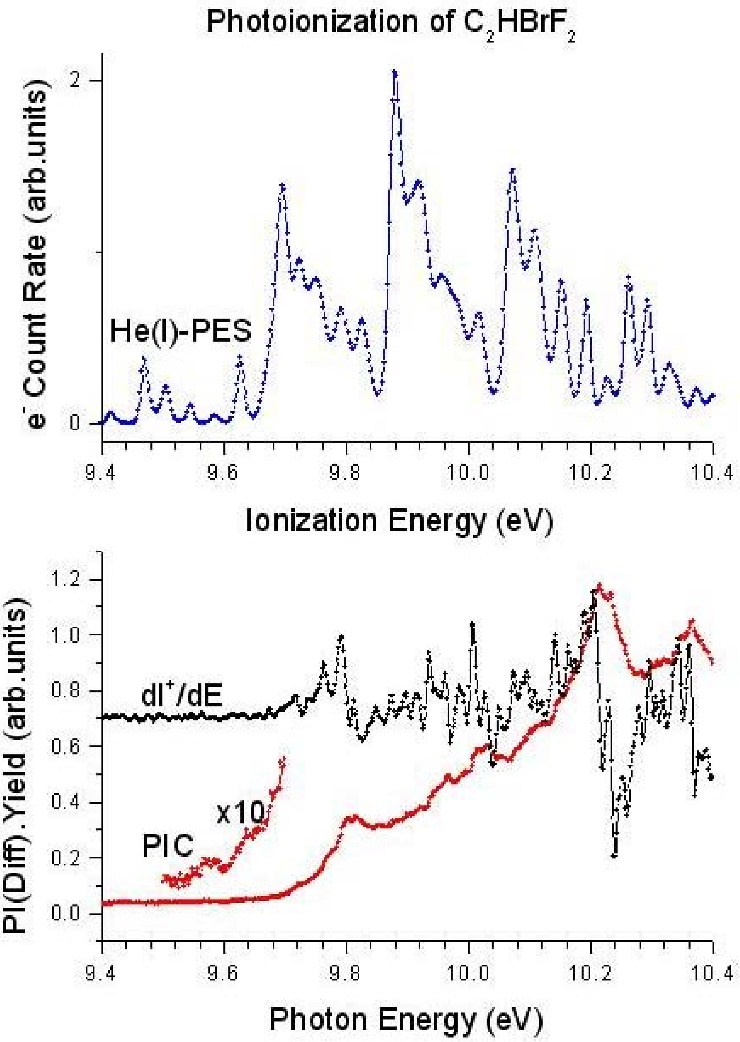

Figure 2.

Fig. 1 shows an example of photoabsorption spectra obtained respectively for (1) C_2HBrF_2, (2) C_2BrF_3 and (3) C_2ClF_3 in the 6-12 eV photon energy range. The spectra related to the latter two compounds clearly differ from the former by the $\pi \rightarrow \pi^*$ transition. This transition, located at about 6.8 eV for C_2HBrF_2, is blue-shifted by about 0.8 eV when the H atom is substituted by F. By contrast, the substitution of the Br atom by Cl has no significant influence on either the shape or the energy position of the spectral features. Furthermore, the H-substitution leads to a severe quenching of the Br (or Cl) lone pair excitation (9-11 eV photon energy range). A deeper analysis of these spectra, combined with all our previous results on about more than ten halogenated ethylene derivatives, is in progress.

The dissociative photoionization of C_2HBrF_2 and C_2BrF_3 has been recorded by mass spectrometry at variable wavelength. Almost all fragment ions present in the 20 eV photon energy mass spectrum have been considered.

Fig. 2 shows a typical example of results obtained by HeI photoelectron spectroscopy and mass spectrometric photoionization. The photoionization efficiency curve (PIC) of the molecular ion $C_2HBrF_2^+$ and its first derivative (dI^+/dE) as observed in the threshold region are displayed in fig. 2 (bottom). This figure clearly shows the complex pattern of autoionization and direct ionization. The best way to disentangle these data is to record both the HeI photoelectron spectrum (PES) and the photoabsorption spectrum (PAS) shown in fig. 1. The latter clearly shows that the ionization threshold region is dominated by Br-lone pair Rydberg transitions. Fig. 2 (upper part) shows the structure for the first HeI PES-band. Several features present in this spectrum correlate with those observed in the PIC by resonant photoionization and are ascribed to direct ionizing transitions. A systematic study is in progress.

Acknowledgments.

The authors gratefully acknowledge the Freie Universität Berlin. R.L. and B.L. are indebted to the Belgian "Fonds National de la Recherche Scientifique" (FNRS) for financial support. The authors wish to thank the BESSY staff, and particularly Dr. G. Reichardt and Dr. W. Braun, for their essential collaboration.

References.

[1]. R. Locht, B. Leyh, H.W. Jochims, H. Baumgärtel, Jahresbericht (**2003**), 48.

[2]. A. Hoxha, R. Locht, B. Leyh, D. Dehareng, K. Hottmann, H.W. Jochims, H. Baumgärtel, Chem.Phys. 260 (**2000**) 237.

[3]. A. Hoxha, R. Locht, B. Leyh, D. Dehareng, K. Hottmann, H. Baumgärtel, Chem.Phys. 256 (**2000**) 239.

[4]. A. Hoxha, R.Locht, A.J. Lorquet, J.C. Lorquet, B. Leyh, J.Chem.Phys. 111 (**1999**) 9256.

[5]. A. Hoxha, B. Leyh, R. Locht, H.W. Jochims, M. Malow, K.-M. Weitzel, H. Baumgärtel, to be published.

Photophysical characteristics of a series of donor-acceptor-polyenes of different length

Hani El-Gezawy, Wolfgang Rettig

Institut für Chemie, Humboldt-Universtät zu Berlin,
Brook-Taylor-Str. 2, D-12489 Berlin, Germany

Abstract:

The photophysical behaviour of a series of donor-acceptor-polyenes of different length has been investigated: 4-dimethylamino-4`-cyanostilbene (DCS), 4-dimethylamino-4`-cyano-1,4-diphenylbutadiene (DCB), 4-dimethylamino-4`-cyano-1,4-diphenylhexatriene (DCH). These compounds show a maximum of the fluorescence yield in the most polar solvents. The three dyes show a pronounced solvatochromic behaviour only for the emission spectra whereas the absorption spectra show a very weak solvatochromic shift which correlates better with the polarizability of the solvents. The nonradiative decay decreases sizeably in the order DCS>DCB>DCH.

Introduction:

For several decades, the photophysical, photochemical and also solvatochromic properties of donor-acceptor-stilbenes have attracted interest. The excited state behavior of trans-stilbene is one of the best-known examples of an adiabatic photoreaction: it reacts to a twisted conformation, which is often referred to as the "phantom-singlet state". This conformation corresponds to a maximum on the ground state surface to which it is strongly coupled, and this pathway thus provides an effective deactivation funnel [1]. The main focus of this project is to study the photophysical properties of a structurally related series of molecules in which the donor (dimethylamino) and acceptor (cyano) substituents are separated by trans-stilbene (DCS), all-trans-diphenyl-butadiene (DCB) and all-trans-diphenyl-hexatriene (DCH). The experimental of UV absorption, steady state emission, time-resolved fluorescence and low temperature techniques are employed here in conjunction with quantum chemical calculation.

The Investigated Compounds:

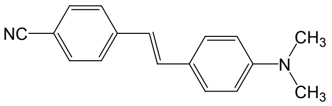

DCS

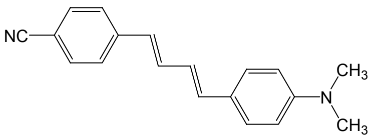

DCB

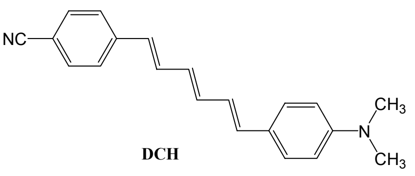

DCH

Temperature dependence of the fluorescence spectra and nonradiative losses:

Fig. 1 shows the temperature dependent emission spectra and the room temperature absorption spectrum of DCS, DCB and DCH in diethyl ether. All compounds show a similar behaviour. As can be seen in Fig. 1, with decreasing temperature the fluorescence intensity increases, and a weak red shift of the fluorescence maximum is observed, explainable by the increasing dielectric constant ε of the solvent at low temperatures.

Table 1 contains the fluorescence decay times and the derived temperature dependent nonradiative decay rates k_{nr} as extracted from the fluorescence intensities. It can be seen that k_{nr} decreases with decreasing temperature but also with a lengthening of the π-electronic system. The former is indicative of an activation barrier leading to the phantom singlet state, the latter indicates that this activation barrier increases for longer diphenylpolyenes.

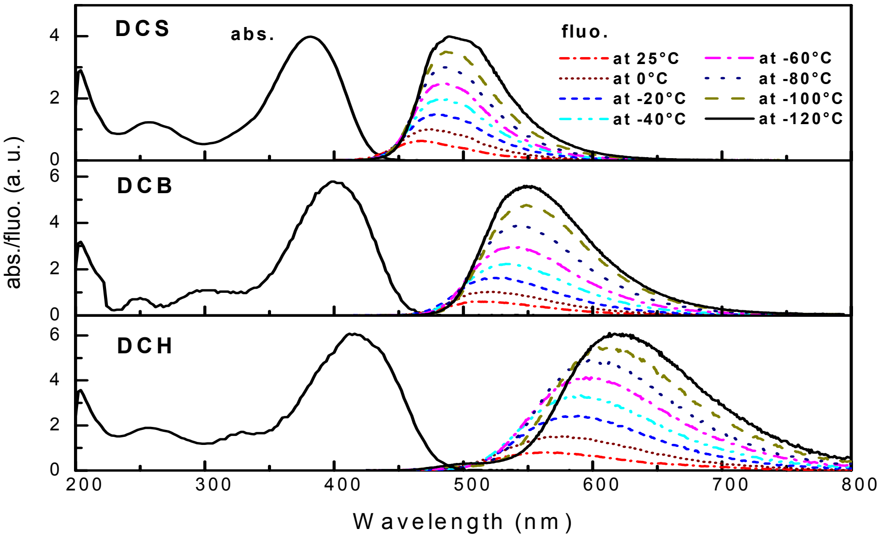

Fig. 1 *Absorption spectrum at room temperature and fluorescence emission spectra of DCS, DCB and DCH at different temperatures in diethyl ether.*

Table 1. Photophysical parameters of DCS, DCB and DCH in diethyl ether at low temperatures

Compound	**T (K)**	**λ_f (nm)**	**Φ_f**	**τ_f (ns)**	**k_f (s^{-1})**	**k_{nr} (s^{-1})**
DCS	298	475	0.032	0.10	$3.20x10^{8}$	$9.68x10^{9}$
	253	482	0.098			$2.95x10^{9}$
	213	487	0.42			$4.42x10^{8}$
	173	490	0.68			$1.51x10^{8}$
	153	492	0.84			$6.09x10^{7}$
	77			1.7		
DCB	298	509	0.085	0.32	$2.62x10^{8}$	$2.82x10^{9}$
	253	525	0.26			$7.38x10^{8}$
	213	538	0.51			$2.56x10^{8}$
	173	548	0.79			$6.88x10^{7}$
	153	550	0.92			$2.19x10^{7}$
	77			1.65		
DCH	298	567	0.091	0.47	$1.94x10^{8}$	$1.94x10^{9}$
	253	589	0.28			$4.99x10^{8}$
	213	595	0.54			$1.65x10^{8}$
	173	613	0.81			$4.55x10^{7}$
	153	617	0.95			$1.02x10^{7}$
	77			1.7		

References:

[1] D.H. Waldeck, Chem. Rev. 91 (1991) 415; J. Saltiel and Y.-P. Sun, in: Photochromism - molecules and systems, Eds. H. Dürr and H. Bouas-Laurent, Elsevier, Amsterdam, 1990, p. 64.

Investigation of photoionization processes in the 3d-transition metal (TM) compounds $FeCl_2$, $FeBr_2$ and $CoCl_2$

Mohamed Al-Hada, Tobias Richter and Peter Zimmermann
Institut für Atomare Physik und Fachdidaktik, Technische Universität Berlin

Michael Martins
Institut für Experimentalphysik, Universität Hamburg

Ömer Görgülüer and Ali Tutay
Science Faculty, Istanbul University

TM compounds $FeCl_2$, $FeBr_2$ and $CoCl_2$ are the systems that have been selected for this investigation. They are important in many different areas of technology, for examples, the magnetic properties of the thin films that have lead to significant improvement in the storage capability of the magnetic devices during the last decade. To understand the physics of such complex systems, deep analysis of the electronic and magnetic structure is needed. The key of the magnetic and electronic properties of these compound system are the $3d$ electrons. Analysis of these systems can be accomplished by exciting $3p$ electrons into the $3d$ shell or by a direct excitation of the 3p electrons.

Photoion and photoelectron spectra of the 3d- TM compounds $FeCl_2$, $FeBr_2$ and $CoCl_2$ were studied by photoionization spectroscopy using molecular beam technique by thermal evaporation of the metal compounds at a temperature of approx. 700 K and monochromatized synchrotron radiation at the BESSY II beamline U125/2-SGM. A time-of-flight spectrometer in pulsed voltage mode has been used to detect partial ion yield spectra of the produced ions in the excitation energy range (50-80) eV. The photoelectrons are created by photons of 100 eV and analyzed using a hemispherical electron spectrometer (Scienta SES-2002).

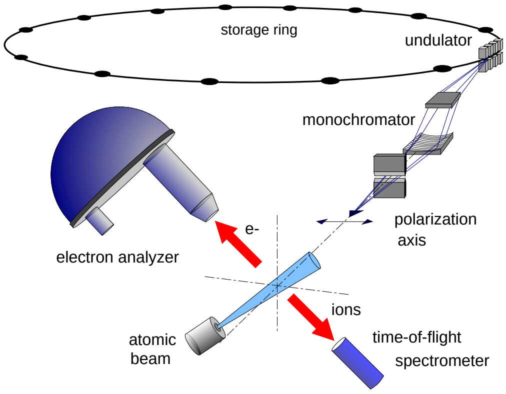

Figure 1: *Experimental Setup*

Experimental results of in singly charged ions of Fe, $FeCl_2$, $FeBr_2$ in the 3p (Fe) excitation region and Co, $CoCl_2$ in the 3p (Co) excitation region are shown in the Fig 2.

3p photoion spectra of $FeCl_2$, $FeBr_2$ and $CoCl_2$ show a close similarity when compared to the corresponding atomic spectra of Fe and Co. The atomic spectra are dominated by strong resonances. These are due to discrete transitions $3p^6 3d^N \rightarrow 3p^5 3d^{N+1}$ with a subsequent emission of a 3d electron $3p^5 3d^{N+1} \rightarrow 3p^6 3d^{N-1}\ \epsilon\iota$. This is caused by the large overlap of the 3p and 3d wavefunction.

For the photoelectron spectra of $FeCl_2$, $FeBr_2$ and $CoCl_2$ the validity of the central field at least for the 3d valence electrons is not existing as a reason of the molecular binding. A charge transfer (CT) model has been applied successfully to the 2p photoelectron spectrum of the $FeCl_2$ [2] Fig

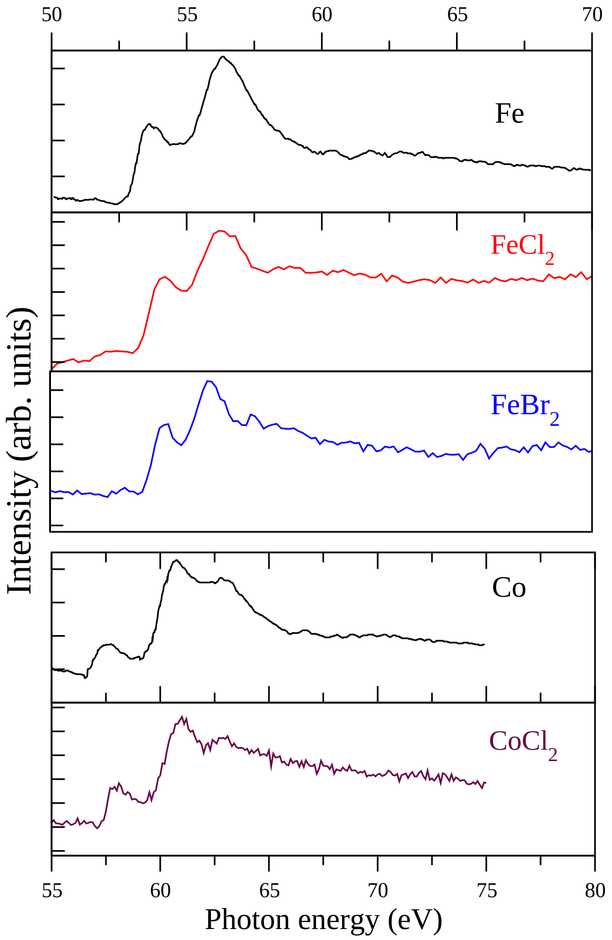

Figure 2: *Partial ion yield spectra of atomic Fe [1] with corresponding molecular $FeCl_2$, $FeBr_2$ and the atomic Co [1] with the corresponding molecular $CoCl_2$ in the region of the 3p (Fe) and (Co) respectively*

3 (left panel). This also results in good agreement with the corresponding solid spectrum. The 3p photoelectron spectrum shows a similarity with the solid 3p $FeCl_2$, thus the interpretation with the charge transfer model by introducing an additional $3d^{N+1}$ configuration will be the key of analyzing the 3p photoelectron spectrum.

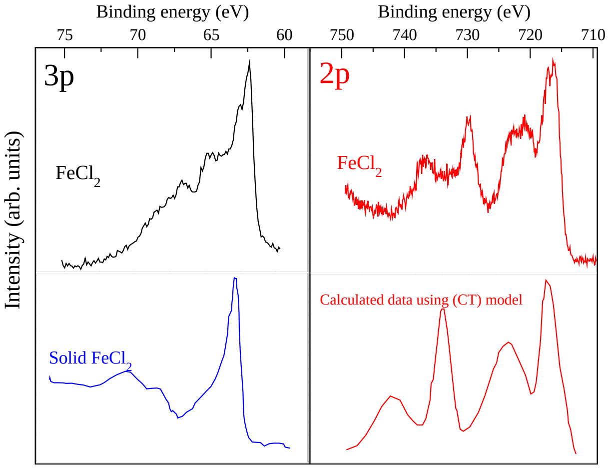

Figure 3: *Experimental 3p $FeCl_2$ taken at a photon energy of 100 eV with the corresponding solid spectrum [3](right panel) and 2p photoelectron spectrum taken at photon energy of 800 eV with calculated data using a CT model.*

[1] H. Feist, M. Feldt, Ch. Gerth, M. Martins, P. Zimmermann Phys. Rev. A 53 760 (1995)
[2] T. Richter, K. Godehusen, T. Wolf, M. Martins, P. Zimmermann Phys. Rev. Lett. 93 023002 (2004)
[3] M. Okusawa. Phys. stat. sol. (b) 124 673 (1984)

Predissociation of the $N_2^+\left(C\ ^2\Sigma_u^+\right)$ state observed via $C\ ^2\Sigma_u^+ \rightarrow X\ ^2\Sigma_g^+$ fluorescence after resonant $1s^{-1}\pi^*$ excitation of N_2

L Werner[1], S Klumpp[1], A Ehresmann[1], Ph V Demekhin[2,4], M P Lemeshko[2], V L Sukhorukov[2,4], K-H Schartner[3] and H Schmoranzer[4]

[1] Institut für Physik, Universität Kassel D-34132 Kassel, Germany
[2] Rostov State University of Transport Communications, 344038 Rostov-on-Don, Russia
[3] I Physikalisches Institut, Justus-Liebig-Universität, D-35392 Giessen, Germany
[4] Fachbereich Physik, Technische Universität Kaiserslautern, D-67653 Kaiserslautern, Germany

E-mail: `ehresmann@physik.uni-kassel.de`

In our recent studies we investigated the vibrationally selective inner-shell photoexcitation of the $N_2(1s^{-1}\pi_g^*)(v)$-resonances and its subsequent autoionization into different levels of the N_2^+ C $^2\Sigma_u^+$ electronic state via the photon-induced dispersed fluorescence spectroscopy (PIFS) (Ehresmann *et al* 2006). One peculiarity of the $C(v') \rightarrow X(v'')$ emission bands with $v' \geq 3$ is that they are very weak compared to bands with $v' = 0, 1, 2$. This behaviour was first observed by (Carroll 1959). A first explanation was given by (Carroll 1959) with the assumption of (Douglas 1952) that a weak predissociation occurs for the vibrational levels of the $C(v')$ state with $v' \geq 3$. The pathway of this indirect predissociation was clarified by (Lorquet and Lorquet 1974) and supported by computing the respective potential curves (Langhoff *et al* 1988). Extended calculations performed in (Ehresmann *et al* 2006) predicted the maximum of the fluorescence intensity for the vibrational sequence with $\Delta v = -5$ if this indirect predissociation is taken into account and for $\Delta v = -6$ if the indirect predissociation is neglected delivering, therefore, an experimental means to unequivocally decide whether the indirect predissocation works here or not. Unfortunately, the vibrational sequence with $\Delta v = -6$ was outside the sensitivity range of the detector used in (Ehresmann *et al* 2006). The main goal of the present work was therefore to cover the fluorescence wavelength range of vibrational sequences between at least $\Delta v \leq -2, \ldots, -8$. The experimental setup in the present work is essentially the same as in (Ehresmann *et al* 2006). The gold coated 600 lines/mm grating of the undulator beamline U49/2 PGM 1 at BESSY II was used to monochromatize the synchrotron radiation which was then focused into a differentially pumped target cell filled with molecular nitrogen at room temperature and at a pressure of 27.6 μbar. The exciting-photon energy was varied from 400 eV to 403 eV in steps of 20 meV with a bandwidth of about 70 meV FWHM at 400 eV, determined mainly by a reasonable signal-to-noise ratio for the observed fluorescence intensities. The fluorescence was dispersed by a 1 m-normal-incidence monochromator (McPherson 225) equipped with a 1200 lines/mm grating (blaze wavelength 150nm; coating Al) and recorded in the fluorescence range between 165 nm and 208 nm by a position-sensitive CsTe microchannel-plate detector (manufactored by Quantar Technology Inc.). The exciting photon energy was calibrated to known (Chen *et al* 1989) energy positions of the $1s^{-1}\pi_g^*(v_r)$ levels. The resolution of this 'monochromator-detector' combination was about

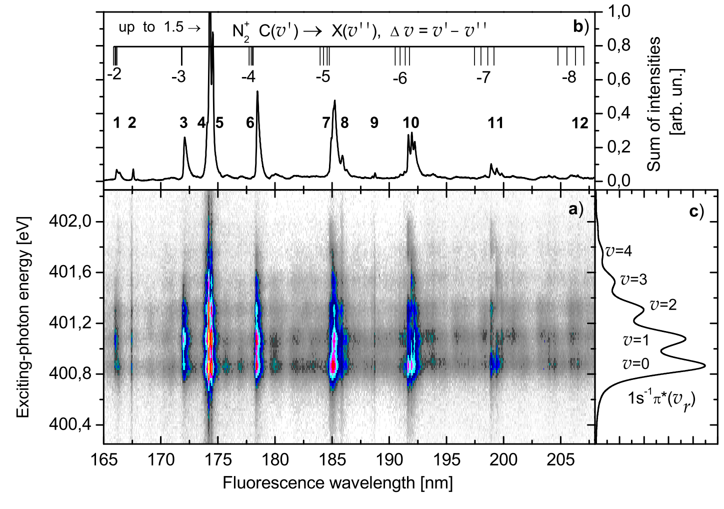

Figure 1. a) Dispersed fluorescence yield as a function of the exciting-photon energy. b) Fluorescence intensities integrated over the exciting-photon energies between 400 and 403 eV. Computed positions of the N_2^+ $(C - X)$ vibronic bands are shown by vertical bars. Numbering of lines and their assignments as listed in table 1. c) Fluorescence intensities integrated over all recorded fluorescence wavelengths.

Table 1. Assignment of the observed fluorescence lines after resonant $1\mathrm{s}^{-1}\pi^*$ excitation of N_2. The line numbering is the same as in figure 1b.

No	$\Delta\lambda_{exp}^{a)}$ [nm]	$\Delta\lambda_{calc}^{b)}$ [nm]	Parts	Transition	$v' - v''$
1	165.98−116.86	165.9−166.2	N_2^+	$C\ ^2\Sigma_u^+, v' \rightarrow X\ ^2\Sigma_g^+, v''$	−2
2	167.57−167.59		NII	$2\mathrm{s}^2 2\mathrm{p}^1(^2\mathrm{P})3\mathrm{p}\ ^3\mathrm{S}_{J'} \rightarrow 2\mathrm{s}^1 2\mathrm{p}^3\ ^3\mathrm{P}_{J''}$	
3	171.59−172.97	171.8−171.9	N_2^+	$C\ ^2\Sigma_u^+, v' \rightarrow X\ ^2\Sigma_g^+, v''$	−3
4	174.03−174.32		NII	$2\mathrm{s}^2 2\mathrm{p}^1(^2\mathrm{P})3\mathrm{p}\ ^3\mathrm{D}_{J'} \rightarrow 2\mathrm{s}^1 2\mathrm{p}^3\ ^3\mathrm{P}_{J''}$	
5	174.27−174.53		NI	$2\mathrm{s}^2 2\mathrm{p}^2(^3\mathrm{P})3\mathrm{s}\ ^2\mathrm{P}_{J'} \rightarrow 2\mathrm{s}^2 2\mathrm{p}^3\ ^2\mathrm{P}_{J''}$	
6	177.82−179.49	177.7−178.1	N_2^+	$C\ ^2\Sigma_u^+, v' \rightarrow X\ ^2\Sigma_g^+, v''$	−4
7	184.23−186.69	184.0−184.8	N_2^+	$C\ ^2\Sigma_u^+, v' \rightarrow X\ ^2\Sigma_g^+, v''$	−5
8	185.79−186.26		NII	$2\mathrm{s}^2 2\mathrm{p}^1(^2\mathrm{P})4\mathrm{p}\ ^3\mathrm{D}_{J'} \rightarrow 2\mathrm{s}^2 2\mathrm{p}^1(^2\mathrm{P})3\mathrm{s}\ ^3\mathrm{P}_{J''}$	
9	188.50−188.52		NIII	$2\mathrm{s}^2(^1\mathrm{S})4\mathrm{f}\ ^2\mathrm{F}_{J'} \rightarrow 2\mathrm{s}^2(^1\mathrm{S})3\mathrm{d}\ ^2\mathrm{D}_{J''}$	
	188.74		NII	$2\mathrm{s}^2 2\mathrm{p}^1(^2\mathrm{P})4\mathrm{p}\ ^1\mathrm{P}_{J'} \rightarrow 2\mathrm{s}^2 2\mathrm{p}^1(^2\mathrm{P})3\mathrm{s}\ ^1\mathrm{P}_{J''}$	
10	190.51−192.98	190.5−191.8	N_2^+	$C\ ^2\Sigma_u^+, v' \rightarrow X\ ^2\Sigma_g^+, v''$	−6
11	197.78−200.31	197.5−199.2	N_2^+	$C\ ^2\Sigma_u^+, v' \rightarrow X\ ^2\Sigma_g^+, v''$	−7
12		204.8−207.0	N_2^+	$C\ ^2\Sigma_u^+, v' \rightarrow X\ ^2\Sigma_g^+, v''$	−8

$^{a)}$ Wavelengths for the transitions in N_2^+ - present measurement (see figure 1); the NI, NII and NIII fluorescence wavelength intervals represent the fine structure components (Kelly 1987) not resolved in present measurement;

$^{b)}$ Present calculations (only $v' = 0\ldots3$ vibrational levels are taken into account due to the indirect predissociation);

$\Delta\lambda_{fl} = 0.1$ nm which is 3 times better than in (Ehresmann *et al* 2006). A two-dimensional fluorescence yield spectrum in the exciting-photon energy range around the $1\mathrm{s}^{-1}\pi^*$ resonance and the fluorescence wavelength range between 165 and 208 nm is displayed in figure 1. Figure 1a shows the 2D- plot recorded by the CsTe detector normalized for the exciting-photon flux. Assignments of the observed fluorescence lines are listed in table 1 where the numbering of the lines corresponds to figure 1b. Wavelengths for the NI, NII and NIII transitions have been assigned by comparing the experimentally determined wavelengths to known spectroscopic data (Kelly 1987). The $C\,(v') \rightarrow X\,(v'')$ fluorescence bands observed in the present fluorescence wavelength range are strongly overlapping with a weak fluorescence emission which starts at approximately 165 nm and can be seen as a background in figure 1. Since this emission was not resolved it was tentatively connected with the $\mathrm{N}_2^+ \left(D\ ^2\Pi_g \rightarrow A\ ^2\Pi_u\right)$ Janin-d'Incan bands when first observed by (Holland and Maier 1971). An exploratory calculation performed in the present work showed that it stems from strongly overlapped ro-vibronic lines of weak $D\ ^2\Pi_g \rightarrow A\ ^2\Pi_u$ transitions and more intense (2) $^2\Pi_g \rightarrow A\ ^2\Pi_u$ transitions in N_2^+. In the present work we corrected the observed fluorescence intensities by a constant background and by the quantum efficiency of the CsTe detector when extracting information on the $C \rightarrow X$ emission from figure 1. Relative doubly integrated emission cross sections for the $C\,(v') \rightarrow X\,(v'')$ fluorescence sequences ($\Delta v = v' - v'' = const$), $\bar{\sigma}_C^X\,(\Delta v)$, have been determined similar to (Ehresmann *et al* 2006) by integrating the fluorescence intensities over the fluorescence wavelength interval $\Delta\lambda_{exp}$ (listed in table 1) and over the present exciting-photon energy range.

Table 2. Doubly integrated cross sections, $\bar{\sigma}_C^X\,(\Delta v)$, for band sequences (relative to $\Delta v = -5$ in percent) observed in the $C\,(v') \rightarrow X\,(v'')$ fluorescence of N_2^+ after $\mathrm{N}_2(1\mathrm{s}^{-1}\pi^*)$ resonant Auger decay and calculated in different approximations.

	N_2^+ ($\mathrm{C}\ ^2\Sigma_u^+,\ v' \rightarrow \mathrm{X}\ ^2\Sigma_g^+,\ v''$), $\Delta v = v' - v''$											
Approximation	3	2	1	0	−1	−2	−3	−4	−5	−6	−7	−8
Exper. ^{a}		6		17	24	48	59	69	100			
Exper. Present ^{b}						16(9)	52(7)	69(6)	100	64(5)	19(2)	
Theory ^{c}	5	7	10	15	22	33	47	65	100	159	85	4
Theory ^{d}	3	5	9	15	20	35	47	70	100	74	22	1
Theory Present ^{e}	1	5	10	14	25	38	53	83	100	66	19	1

$^{\mathrm{a})}$ Data corrected for the quantum efficiency of the CsI detector, Paper I;

$^{\mathrm{b})}$ Data corrected for the quantum efficiency of the CsTe detector;

$^{\mathrm{c})}$ The fluorescence from all v' vibrational levels is taken into account neglecting the indirect predissociation of the $v' \geq 3$ ones; data from table 5 of Paper I;

$^{\mathrm{d})}$ The fluorescence from $v' = 0, 1, 2, 3$ vibrational levels only is taken into account due to the indirect predissociation of the $v' \geq 3$, data from table 5 of Paper I;

$^{\mathrm{e})}$ The indirect predissociation of the $v' \geq 3$ levels is taken into account.

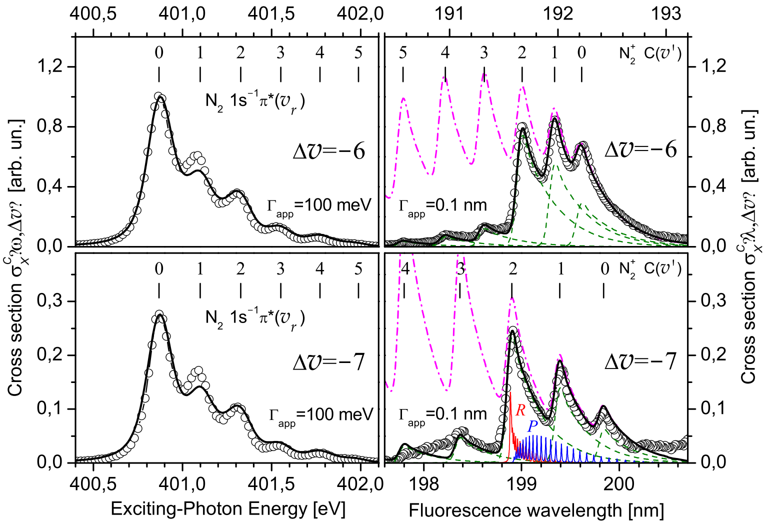

Figure 2. Measured (open circles) and calculated (solid lines) cross sections $\sigma_C^X(\omega,\Delta v)$ (*left panels*) and $\sigma_C^X(\lambda,\Delta v)$ (*right panels*) for band sequences with $\Delta v = -6$ and -7. Partial cross sections for individual $C(v') \to X(v'')$ bands (dashed lines) calculated with accounting for the APD and total $\sigma_C^X(\lambda,\Delta v)$ calculated neglecting indirect predissociation (dash-dot lines) are also shown in the right panels. Typical rotational structure (represented by R and P branches) calculated in the present work for the $C \to X$ band is also shown. Experimental positions of $1\mathrm{s}^{-1}\pi_g^*(v_r)$ vibrational levels (Chen *et al* 1989) are marked in the left panels. Computed $\sigma_C^X(\omega,\Delta v)$ are convolved with a Gaussian of 100 meV FWHM, and $\sigma_C^X(\lambda,\Delta v)$ - of 0.1 nm FWHM.

The $\bar{\sigma}_C^X(\Delta v)$ values normalized to the $\bar{\sigma}_C^X(\Delta v = -5)$ value are listed in the upper part of table 2 together with our previous experimental data from (Ehresmann *et al* 2006). The cross section $\bar{\sigma}_C^X(\Delta v = -8)$ can not be determined since the weak fluorescence from $\Delta v = -8$ sequence is blended by unresolved emission stemming from $(D,(2))\ {}^2\Pi_g \to A\ {}^2\Pi_u$ band systems of N_2^+. One can see that cross sections $\bar{\sigma}_C^X(\Delta v = -3,-4,-5)$ obtained in the present work agree with the previous measurement within the error bars. The difference between 'old' and 'new' values of $\bar{\sigma}_C^X(\Delta v = -2)$ is, possibly, connected with a sharp drop of the quantum efficiency of the CsTe detector at the edge of its sensitivity range. Measured cross sections $\bar{\sigma}_C^X(\Delta v)$ exhibit a maximum at $\Delta v = -5$ that agrees with the prediction of (Ehresmann *et al* 2006) based on the calculation accounting for the predissocation (see line 'Theory^d'). As one can see from figure 1b the improved resolution allows us to observe the individual $C(v') \to X(v'')$ bands for $\Delta v = -6$ and -7 sequences. In large scale the observed cross sections for fluorescence, $\sigma_C^X(\lambda,\Delta v)$, are depicted in figure 2 for sequences $\Delta v = -6$ and -7 (right panels, open circles). In the same figure the cross sections $\sigma_C^X(\omega,\Delta v)$ are also shown (left panels, open circles). Experimental positions of the $1\mathrm{s}^{-1}\pi_g^*(v_r)$ vibrational levels (Chen *et al* 1989) are marked in the left panels. In order to illustrate the influence of the indirect predissociation on the cross sections $\sigma_C^X(\lambda,\Delta v)$ we performed calculations neglecting the predissociation of $v' \geq 3$. The resulting 'model' cross sections are shown in figure 2 by dash-dot lines, in contrast to the solid lines accounting for predissociation. This work was supported by the Deutsche Forschungsgemeinschaft (DFG) and by the Bundesministerium für Bildung und Forschung (BMBF) (Förderkennzeichen 05 ES3XBA/5 and IB/DLR RUS 02/037)

References

Baltzer P, Larsson M, Karlsson L, Wannberg B and Carlsson Göthe M 1992 *Phys. Rev. A* **46**, 5545-5553.

Carroll P K 1959 *Can. J. Phys.* **37**, 880-889.

Chen C T, Ma Y and Sette F 1989 *Phys. Rev. A* **40**, 6737-6740.

Douglas A E 1952 *Can. J. Phys.* **30**, 302-313.

Ehresmann A, Werner L, Klumpp S, Lucht S, Schmoranzer H, Mickat S, Schill R, Schartner K-H, Demekhin P V, Lemeshko M P and Sukhorukov V L 2006 *J. Phys. B: At. Mol. Phys.* **39**, 283-304.

Holland R F and Maier II W B 1971 *J. Chem. Phys.* **55**(3), 1299-1314.

Huber K P and Herzberg G 1979 *Molecular Spectra and Molecular Structure. IV Constants of Diatomic Molecules* Van Nostrand Reinhold Comp. New York.

Kelly R L 1987 *J. Phys. Chem. Ref. Data* **16 (Suppl.1)**, 1-649.

Langhoff S R, Bauschlicher C W and Jr. 1988 *J. Chem. Phys.* **88**(1), 329-336.

Lorquet A J and Lorquet J C 1974 *Chem. Phys. Let.* **26**(1), 138-143.

Schmoranzer H, Liebel H, Vollweiler F, Müller-Albrecht R, Ehresmann A, Schartner K H and Zimmermann B 2001 *Nucl. Instrum. Methods in Phys. Res. A* **467-468**, 1526-1528.

Photoemission in the Molecular Frame induced by soft X ray Elliptically Polarized Light

W.B. Li[1], A. Haouas[2], J.C. Houver[1], L. Journel[2], M. Simon[2] and D. Dowek[1]

[1] Laboratoire des Collisions Atomiques et Moléculaires (UMR 8625 UPS-CNRS), Bat 351, Université Paris-Sud, 91405 Orsay, France
[2] Laboratoire de Chimie Physique-Matière et Rayonnement (UMR 7614 UPMC-CNRS), 11 rue Pierre et Marie Curie, 75231 Paris Cedex 05 France

Work supported by the European Community-Research Institute Action (E.U. RII 3 CT-2004-506008).

Angular distributions from fixed in space molecules like CO and N_2 have been reported in recent years for photoelectrons [1] as well as for fast Auger electrons [2] emitted after K shell photoionization.

In this project we have used the vector correlation method [3] and the linearly or elliptically polarized light delivered by the UE56-1 PGM beamline at BESSY in the soft X ray range. The energy and angular properties of photoelectron emission and multiple Auger decay following non-resonant (e.g. eq.1 or 2) and resonant (e.g. eq.3) dissociative photoionization (DPI) of the NO, CO, N_2 and N_2O molecules have been investigated in the neighborhood of the N 1s and O 1s ionization thresholds:

$$\mathrm{NO} + h\nu(\hat{\mathbf{e}}) \rightarrow \mathrm{NO}^{+}(1s_{\mathrm{N\,or\,O}})^{-1} + e_{\mathrm{ph}} \rightarrow \mathrm{N}^{+} + \mathrm{O}^{+} + e_{\mathrm{ph}} + e_{\mathrm{Au}} \quad \text{(eq.1)}$$

$$\rightarrow \mathrm{N}^{++} + \mathrm{O}^{+} + e_{\mathrm{ph}} + e^{s}_{\mathrm{Au}} + e^{f}_{\mathrm{Au}} \quad \text{(eq.2)}$$

$$\mathrm{NO} + h\nu(\hat{\mathbf{e}}) \rightarrow \mathrm{NO}^{*}(1s_{\mathrm{N\,or\,O}} \rightarrow \pi^{*}) \rightarrow \mathrm{N}^{+} + \mathrm{O}^{+} + e^{s}_{\mathrm{Au}} + e^{f}_{\mathrm{Au}} \quad \text{(eq.3)}$$

e^{s}_{Au} and e^{f}_{Au} refer to the situation where a slow and a fast Auger electrons are produced in double Auger decay, as observed e.g. for Ar 2p and Ne 1s inner-shell photoionization [4].

The experimental approach consisted of measuring the velocity vectors of the two ionic fragments and one of the slow electrons e_{ph} or e^{s}_{Au} collected in a 4π solid angle [5], leading to e.g. the ($\mathbf{V}_N$, $\mathbf{V}_O$, $\mathbf{V}_e$, $\hat{\mathbf{e}}$) quadruplet, where $\hat{\mathbf{e}}$ represents the **k** propagation axis of elliptically polarized light or the **P** polarization axis of linearly polarized light. The spatial analysis of the ($\mathbf{V}_N$, $\mathbf{V}_O$, $\mathbf{V}_e$, $\hat{\mathbf{e}}$) vector correlation provides in particular the molecular frame photoelectron (or slow Auger electron) angular distributions (MFPADs) for each selected process, an observable which is the most sensitive probe of the molecular photoionization dynamics.

The multidimensional data analysis is in progress and several papers are in preparation. Here we report as an example the results of the vector correlation analysis for the DPI reaction according to (eq.4) [6] at the $h\nu = 418$ eV photon excitation energy.

$$\mathrm{NO} + h\nu(\hat{\mathbf{e}}) \rightarrow \mathrm{NO}^{+}({}^{1}\Pi, {}^{3}\Pi, 1s_{\mathrm{N}}^{-1}) + e_{\mathrm{ph}} \rightarrow \mathrm{NO}^{++} + e_{\mathrm{ph}} + e_{\mathrm{Au}} \rightarrow \mathrm{N}^{+} + \mathrm{O}^{+} + e_{\mathrm{ph}} + e_{\mathrm{Au}} \quad \text{(eq.4)}$$

Figure 1 displays the electron-ion kinetic-energy correlation diagram (KECD) (a) which represents a bidimensional (2D) histogram of the (e_{ph}, N^+, O^+) coincident events as a function of the electron energy and the kinetic energy release (KER) of the reaction, as well as the one-dimensional (1D) histograms namely the photoelectron (b) and KER (c) energy spectra, corresponding to the projections of the 2D histogram on the E_e and KER axes, respectively. The two $NO^+(^1\Pi)$ and $NO^+(^3\Pi)$ are partially resolved here, and the KER distribution indicates the contribution of several NO^{++} electronic states [7].

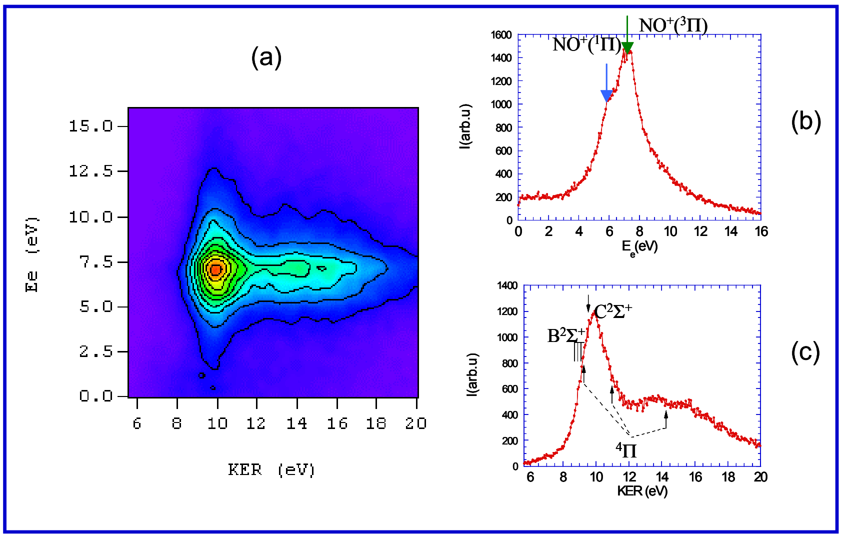

Figure 1 : (a) Electron-ion kinetic-energy correlation diagram (KECD) for the (e_{ph},N^+,O^+) coincident events produced at a photon energy hν ≈ 418 eV, and the 1D projections of the KECD corresponding to the photoelectron and KER energy spectra (see text).

When the light is elliptically polarized, the theory of measurement leading to the molecular frame photoelectron angular distributions (MFPADs) previously developed for linear [3] or circular [8] polarization involves additional terms. If the polarization is described by the three (S_1, S_2, S_3) Stokes parameters, the general analytical form of the complete angular distribution describing a DPI reaction $I(\chi,\gamma,\theta_e,\varphi_e)$ [8] is a function of four angles: (χ,γ) characterize the fragment ion ejection direction in the laboratory frame and (θ_e,φ_e) the photoelectron ejection direction in the molecular frame, defined by the molecular axis and the polarization axis. The reference axis in the laboratory frame is the propagation axis of the light **k**.

Integrating the $I(\chi,\gamma,\theta_e,\varphi_e)$ distribution over the ion azimuthal angle γ leads to an expression identical to the one used for circularly polarized light, except for the $F_{11}(\theta_e)$ term which is multiplied by the Stokes parameter S_3.

$$I_{S3}\,(\chi,\,\theta_e,\,\phi_e) = F_{00}(\theta_e) - 1/2\,F_{20}(\theta_e)\,P_2^{\,0}(\cos\chi) - 1/2\,F_{21}(\theta_e)\,P_2^{\,1}(\cos\chi)\,\cos\,(\phi_e)$$
$$-\,S_3 \times F_{11}(\theta_e)\,P_1^{\,1}(\cos\chi)\,\sin\,(\phi_e) - 1/2\,F_{22}(\theta_e)\,P_2^{\,2}(\cos\chi)\,\cos\,(2\phi_e) \qquad \text{(eq.5)}$$

Here the Stokes parameter S_3 is defined as $S_3 = -1$ for circularly polarized of helicity +1. This demonstrates that the four $F_{LN}(\theta_e)$ functions which provide the MFPADs for any orientation of the molecular axis with respect to the polarization axis of linearly polarized light [3], as well as the product of the Stokes parameter S_3 by the fifth $F_{11}(\theta_e)$ function characterizing the circular dichroism for electron emission in the molecular frame [8], can be derived from a single experiment performed with undefined elliptically polarized light [9].

The S_1 and S_2 Stokes parameters of the light are also determined in such an analysis, by fitting the ion polar and azimuthal angle dependence of the $I(\chi,\gamma,\theta_e,\varphi_e)$ distribution, after integration over the electron angles [9]. S_3 is subsequently determined if the degree of polarization is close to 1.

Figure 2 displays three specific MFPADs derived from the measured $I(\chi,\gamma,\theta_e,\varphi_e)$ distribution for eq.4 at $h\nu = 418$ eV: they correspond to a molecular axis orientation parallel and perpendicular to the polarization axis **P** of linearly polarized light as shown, and to a molecular axis perpendicular to the propagation axis **k** of elliptically polarized light.

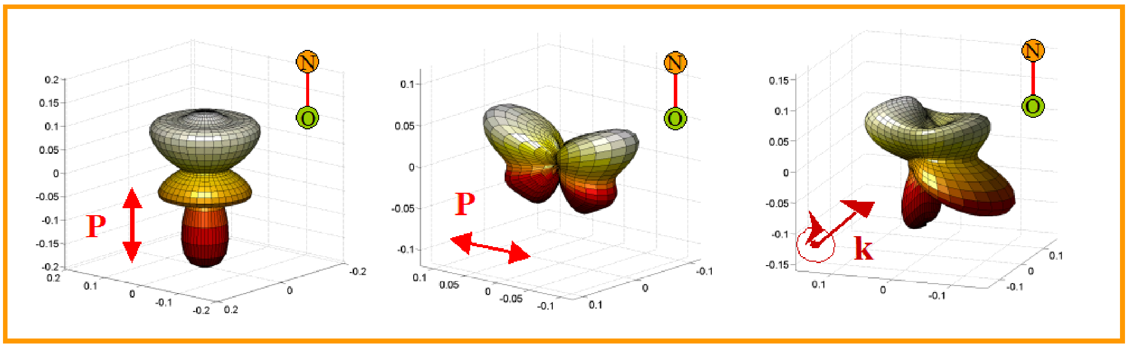

Figure 2 : Measured $I(\theta_e,\varphi_e)$ MFPADs for a molecular axis parallel and perpendicular to linearly polarized light, and for a molecular axis perpendicular to the propagation axis of elliptically polarized light, derived from a single experiment performed with elliptically polarized light..

The MFPADs display strong electron emission anisotropies, with a clear contribution of up to l=3 ($f\sigma$) partial waves. A significant circular dichroism is found, revealed by the left-right asymmetry maximum in the plane perpendicular to the propagation axis **k**. For a molecule parallel to the linear polarization of the light, the results are in good agreement with those obtained previously [10] and multi-channel Schwinger configuration interaction calculations (MCSCI) [10]. The MFPADs measured for a comparable photoelectron energy in the region of the O 1s ionization threshold display a strikingly mirror like shape with respect to those measured at the N 1s edge. These results compare well with recent MCSCI calculations performed in the group of R.R. Lucchese (Texas A&M University, USA) [6].

An example of Stokes parameter set found in this photon energy range is $S_1 \approx -0.4$, and $S_2 \approx 0$, leading to $S_3 \approx 0.92$ in the assumption of a negligible component of unpolarized light.

References

1. e.g. E. Shigemasa et al, Phys. Rev. Lett. **80** 1622 (1998); S. Motoki et al, J. Phys.B **33** 4193 (2000); T. Weber et al, J. Phys.B **34** 3669 (2001).
2. R. Guillemin et al, Phys. Rev. Lett. **87** 203001 (2001); T. Weber et al, Phys. Rev. Lett. **90** 153003 (2003).
3. A. Lafosse et al, Phys. Rev. Lett. **84** 5987 (2000); R.R. Lucchese et al, Phys. Rev. A **65**, 020702 (2002).
4. J. Viefhaus et al, J. Electron Spectrosc. Relat. Phenom. **141** 121 (2004); Phys. Rev. Lett. **92** 083001 (2004).
5. M. Lebech et al, Rev. Sci. Instrum. **73** 1866 (2002).
6. W.B. Li et al, in preparation
7. D. Edvardsson et al, Chem. Phys. Lett. **256** 341 (1996).
8. M. Lebech et al, J. Chem. Phys. **118** 9653 (2003).
9. W.B. Li et al, in preparation
10. K. Hosaka et al, J. Phys.B **37** L49 (2004).

AUGER RELAXATION PROCESSES IN KRYPTON STUDIED WITH A MAGNETIC BOTTLE

J.Palaudoux[1], L.Andric[1], P.Lablanquie[1], F.Penent[1],
U. Becker[2], M. Braune[2], J.Viefhaus[2], J.H.D.Eland[3]

[1] LCPMR, Université Pierre et Marie Curie, 75252 Paris 5, France,
[2] Fritz-Haber-Institut, Faradayweg 4-6, 14195 Berlin, Germany
[3] Physical and Theoretical Chemistry Laboratory, Oxford, OX1 3DW, U.K.

Inner shell ionization leads to the creation of a short lived hole that can often decay non radiatively by emission of Auger electron(s). Photoelectron spectroscopy (PES) and Auger Spectroscopy are powerful analysis tools that reveal many details of such processes. However open questions remain. Are more than one Auger electron released? If this occurs, are they released simultaneously or sequentially? What multiply charged final states are populated by this process? What happens when the two-step approximation, according to which photoelectron and Auger electron emissions are subsequent and independent events, fails? In particular, a detailed description of the *Post Collision Interaction* (PCI) process is needed, when Auger electrons and photoelectron interact and exchange energy with mediation of the ionic core. The proper way to study such processes is to perform a coincidence detection of all released electrons. However, conventional coincidence experiments are often limited to the detection of only two electrons with low efficiencies due to a low angular acceptance and consequently a complete picture of the process is difficult to obtain. Our approach is to use a high efficiency time of flight apparatus having full solid angle (4π) collection efficiency which enables us to detect in coincidence (and resolving in energy) all electrons created in a multiple ionization event.

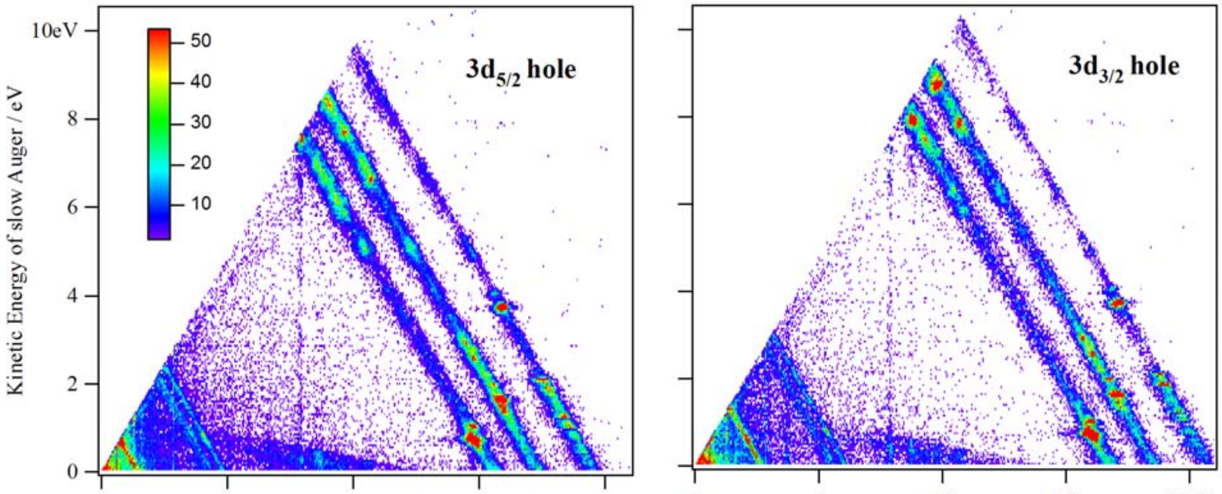

Figure: Decay of krypton 3*d* holes by emission of two Auger electrons. All three electrons of the process are detected in coincidence. The two-dimensional plot of the Auger double continua are filtered according to the associated photoelectron. Intensity colour scale was selected to enhance structures. Maximum count is 321 ($3d_{3/2}$ case) or 534 ($3d_{5/2}$). Random coincidences are not subtracted.

Our experiment uses a 2.4 m long time of flight magnetic bottle electron spectrometer that was initially developed for pulsed VUV laboratory sources by J.H.D.Eland in Oxford [1]. We adapted this technique to synchrotron radiation and made the first experiments at the end of 2003 during the last days of operation of Super ACO [2]. The setup allows the coincident detection of the photoelectrons with **all** (1, 2, 3…) subsequently released Auger electrons. An essential point is the time structure of the light pulses, which has to have sufficiently long time window in order to avoid overlapping time-of-flights of photoelectrons emitted by the different primary processes. Single bunch at BESSY having a pulse period of 800 ns is ideally suited for this purpose. Therefore 2 weeks in the single bunch mode were used on beamline U56/2-PGM-1 for this project, in June and December 2005

The figure reveals the energy map of the Double Auger decay of the Kr 3d hole. It displays events in which 3 electrons (the 3d photoelectron and the two Auger electrons) have been detected in coincidence. Thus Auger spectra are automatically filtered according to which hole ($3d_{5/2}$ or $3d_{3/2}$) is involved. The diagonal lines correspond to a constant sum of the energies of the two Auger electrons and are associated with well defined Kr^{3+} final states. The spectroscopy of the triply charged ion is then readily obtained by this method. The analysis reveals that the Kr triple ionization potential is by 1 eV lower than the value retained in the literature, in agreement with a recent investigation [3]. Intensity along the lines reveals weak continua due to direct Double Auger process and peaks associated with a dominant process of cascade decays. Analysis is underway to characterize the intermediate Kr^{2+} states.

The previous result was obtained at 140eV photon energy, when PCI effects can be neglected. In addition a series of measurements were performed in the immediate vicinity of the 3d thresholds, to study the influence of the energy excess on the PCI process. Coincidence detection of the photoelectron and the Auger electron allow us to study the final state dependence of this phenomenon. Using the same method it has already been shown that in Xenon the PCI profile depends on the Auger kinetic energy [4]. Preliminary analysis gives clear indication that we will be able to reveal the details of the recapture process of the photoelectron in autoionizing states.

Finally this method was extended to study the 3p hole decay in Kr 3p, the 2p hole decay in Argon, and first tests on molecular targets were employed: the Carbon 1s hole decay in CO and the Iodine 3d hole decay in CH_3I were chosen as examples.

References

[1] Eland, J. H. D et al, Phys. Rev. Lett. **90**, 053003 (2003).
[2] Penent, F et al, Phys. Rev. Lett. **95**, 083002 (2005)
[3] J.Viefhaus et al, J. Phys. B, **38**, 3885 (2005)
[4] S.Sheinerman et al, J. Phys. B, **39**, 1017 (2006)

High-resolution photoelectron spectroscopy on laser-excited potassium atoms

M. Meyer[1], D. Cubaynes[1], F. Wuilleumier[1], E. Heinecke[2], T. Richter[2], P. Zimmermann[2],
S.I. Strakhova[3], and A. N. Grum-Grzhimailo[3]

[1] LIXAM, Université Paris-Sud, Bâtiment 350, F-91405 Orsay cedex, France
[2] Institut für Atomare Physik und Fachdidaktik, TU Berlin, 10623 Berlin, Germany
[3] Institute of Nuclear Physics, Moscow State University, Moscow 119992, Russia

The combination of laser and synchrotron radiation (SR) has been used to study electron correlations in atomic potassium. In particular, the photoionization in the 3p-shell from the K $3s^23p^64s$ ground state as well as from the K* $3s^23p^64p$ $^2P_{1/2}$ and $^2P_{3/2}$ laser-excited states has been investigated [1]. Photoelectron spectroscopy on laser-excited alkaline atoms has already a long history and first experiments on Na date back to the year 1982 [2], but the advent of third generation SR sources and high-resolution electron analyzers has given new impetus to these studies allowing now to explore in detail fine-structures in the photoelectron spectrum. In two recent experiments on laser-excited Na [3] and Rb [4], it was shown that it is possible to completely resolve the individual components belonging to different total angular momenta of the $np^5(n+1)p$ electronic configuration of the photoion. Both experimental results, especially the strong intensity variation observed after respective excitation of the $^2P_{1/2}$ and $^2P_{1/2}$ state by the laser, were well described by theory, but by using different coupling schemes. The aim of the present study was therefore to understand these differences and to fill the gap between Na and Rb for a systematic analysis of the electronic interactions.

The experiments have been performed at the UE125/2-SGM beamline of BESSY II using monochromatized synchrotron radiation in the photon energy region between 35 and 70 eV. The potassium vapor produced by a radiatively heated oven was crossed in the source volume of a high-resolution electron analyzer (Scienta SES2002) by the counter-propagating laser and synchrotron radiation. The pumping of the K* $3s^23p^64p$ $^2P_{1/2}$ and $^2P_{3/2}$ excited states was obtained with a continuous wave single-mode Ti:Sa ring laser, which was delivering typically about 800 mW at the wavelengths of interest (765.70 and 770.11 nm). Only electrons emitted under the magic angle (54°44’) with respect to the polarization vector of the SR have been analyzed. Since SR and laser are linearly polarized, this geometry enables us to measure directly the photoionization cross sections for the $^2P_{1/2}$ state, but for the $^2P_{3/2}$ state the alignment of the target has to be taken into account in the final analysis. A complementary series of measurements has therefore been undertaken measuring the photoelectron spectra for different values of the relative angle between both polarization vectors.

One of our main results is displayed in figure 1 showing the photoelectron spectra of laser-excited potassium in the region of the $3p^5$ 4p states after initial excitation to the 4p $^2P_{1/2}$ and 4p $^2P_{3/2}$ state, respectively. Strong variations of the relative intensities of the different multiplet components are observed. The most pronounced changes are found for the $4p[5/2]_3$ line, which is completely missing in the $^2P_{1/2}$ spectrum, and for the $4p[3/2]_2$ line, which shows opposite behavior and is only present in the $^2P_{3/2}$ spectrum. As for the case of laser-excited Na [2], the former can be attributed to a quasi-forbidden, the later to a dynamically forbidden transition. This interpretation is corroborated by theoretical results using the general geometrical model (GGM) [1], which are reproducing perfectly the experimental data.

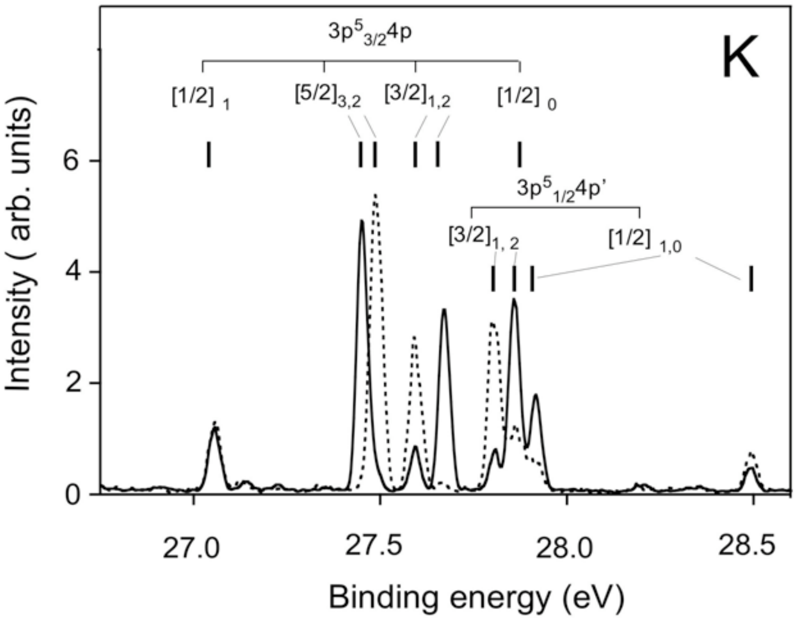

Figure 1: Photoelectron spectrum of laser-excited K in the region of the $3p^5 4p$ states recorded at a photon energy of 42 eV after laser excitation to the 4p $^2P_{3/2}$ (solid line) and 4p $^2P_{1/2}$ (dotted line).

Strong variations of the relative line intensities have also been observed for the $3p^5 5p$ shake-up satellites, in close similarity to the situation in Na. In general, our analysis demonstrates that the $3p^5 4p$ electron spectrum of potassium is closer to the case of sodium than to rubidium, since it cannot be well described by any pure coupling scheme. For the $4p^5 5p$ spectrum of Rubidium the jK coupling model has successfully been applied [4].

References

[1] M. Meyer, D. Cubaynes, F. J. Wuilleumier, E. Heinecke, T. Richter, P. Zimmmermann, S. I. Strakhova, and A. N. Grum-Grzhimailo, J. Phys. B (2006), submitted.

[2] J.M. Bizau, F.J. Wuilleumier, P. Dhez, D. Ederer, J.L. Picqué, J.L. Le Gouët, and P. Koch, in "Laser Techniques for Extreme Ultraviolet Spectroscopy", AIP **90**, 331982 (1982).

[3] D. Cubaynes, M. Meyer, A. N. Grum-Grzhimailo, J.-M. Bizau, E. T. Kennedy, J. Bozek, M. Martins, S. Canton, B. Rude, N. Berrah, and F. J. Wuilleumier, PRL **92**, 233002 (2004).

[4] J. Schulz, M. Tchaplyguine, T. Rander, H. Bergersen, A. Lindblad, G. Öhrwall, S. Svensson, S. Heinäsmäki, R. Sankari, S. Osmekhin, S. Aksela and H. Aksela, Phys. Rev. A **72**, 032718 (2005).

Angular-resolved partial cross sections of doubly excited helium

Y. H. Jiang,[1] R. Püttner,[1] M. Braune,[2] J. Viefhaus,[2]
M. Poiguine,[1] R. Hentges,[2] U. Becker,[2] and G. Kaindl[1]
[1] *Institut für Experimentalphysik, Freie Universität Berlin,*
Arnimallee 14, D-14195 Berlin-Dahlem, Germany
[2] *Fritz-Haber-Institut Berlin, Faradayweg 4-6, D-14195 Berlin-Dahlem, Germany*

Double-excitation states in helium have been considered to be prototypical for two-electron systems with strong electron correlation since their first observation in the 60's of last century. So far, total photoionization cross sections (TCS) and partial cross sections (PCS) have been studied intensively [1, 2]. The angular distribution parameters (ADP), β, provide additional information on the coupling of the outgoing channels in comparison to the TCS and the PCS. Therefore, the resonances show a different behavior in the ADPs as compared to the PCSs and additional resonances are expected to be observable in the ADP. These information can provide additional tests for the quality of theoretical methods that are employed to study quantum chaos in the region close to double ionization threshold of helium [3]. Menzel *at al.* were the first group who reported on the measurements of the ADPs up to the SIT I_5 [4]. Czasch *et al.* [5] studied the ADPs in the photon energy region from the single ionization thresholds (SIT) I_9 to I_{16}. The SIT I_N describes singly ionized helium with the remaining electron possessing the principal quantum number N. In this report, we completed experimental studies for the ADPs from the SITs I_5 to I_7, which fill the gap between Menzel's measurements and the experimental results by Czasch *et al.*.

The experiments were performed at the undulator beamline U125/2-SGM (BUS-beamline) of the Berliner Elektronenspeicherring für Synchrotronstrahlung (BESSY) using a photon energy resolution of $\Omega \cong 6$ meV (FWHM). A number of time-of-flight (TOF) spectrometers were mounted to detect photoelectrons at various angles in the dipole plane, which is oriented perpendicular to the propergation direction of the light. A needle (10 cm long, less than 500 μm inner diameter) directs an effusive jet of gas to the interaction region; the background pressure in the chamber was $\cong 10^{-4}$ mbar. TOF spectra were taken for different photon energies using a step-width of 3 meV and converted into photoemission spectra by the well-known time-to-energy conversion procedure.

The double-excitation ${}^1P^0$ resonances in helium can be assigned by a simplified classification scheme $N, K_{n'}$, with N and n' being ionization threshold of the channel and the running

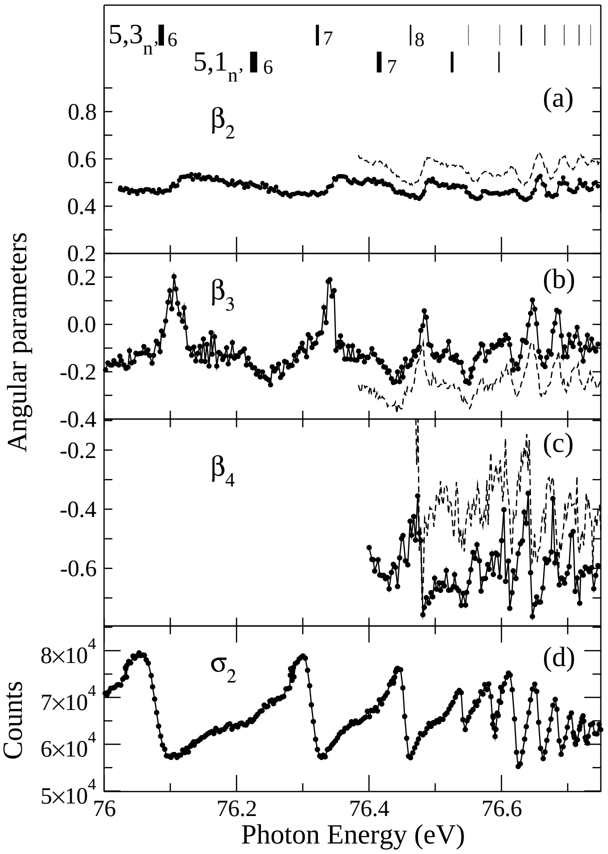

FIG. 1: Angular distribution parameters β_n^5 with (a) $n = 2$, (b) $n = 3$, and (c) $n = 4$, respectively, together with (d) the PCS σ_2^5 below the SIT I_5; the measurements of Menzel *et al.* were displayed by dash lines. The two vertical-bar diagrams in the upper part of the figure give the assignments of the double-excitation resonances specified by n'; with the widths of bars being proportional to the linewidths of the corresponding resonances.

index of Rydberg series, respectively; K represents the angular-correlation quantum number. Preliminary measurements of the β-parameters below the SITs I_5 to I_6 are given in Figs. 1 and 2, respectively. For a better identification of the resonances, the PCSs σ_2^N are also plotted in these figures. Note that the PCSs and ADPs are labeled by σ_n^N and β_n^N, respectively, with n being the principal quantum number for the remaining electron in $\mathrm{He}^+(n)$. Our measurements below the SIT I_5 agree well with experimental results of Menzel *et al.* [4]. The first two members $5,3_6$ and $5,3_7$ of the principal series below the SIT I_5 were observed for the first time in the β_2^5 and β_3^5. These resonances could not be observed in β_4^5 due to the low cross section in combination with a low transmission rate for slow electrons, which are related to this decay channel. For the results presented in Figs. 1 and 2, up to four TOFs are employed and the error bars on absolute value of β are estimated to be less than 15%. Considering these error bars, the present absolute values of β^5 are in agreement with previous measurements and calculations published in Ref. [4]. Interestingly, the resonance $6,2_8$ was clearly observed for the first time by variations in β_2^6 and β_3^6. In contrast to the variations in β, this resonance is strongly suppressed in σ_2 given in Fig. 2(d) as well as in the experimental and theoretical σ_n presented in Ref. [2]. This can be understood by the different dependences of β and σ on the matrix elements for the excitation and decay of the autoionization states and on the phase

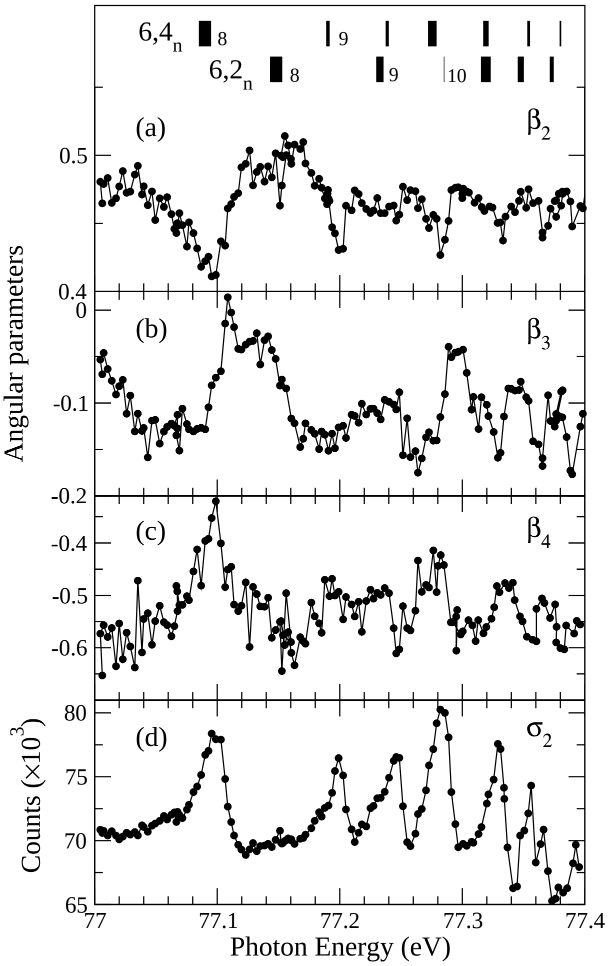

FIG. 2: Angular distribution parameters β_n^6 with (a) $n = 2$, (b) $n = 3$, and (c) $n = 4$, respectively, together with (d) the PCS σ_2^5 below the SIT I_6. For details see Fig. 1.

shifts of the various outgoing channels [6].

In oder to improve the signal-to-noise ratio, in the last beamtime the measurement in regions below the SITs I_6 to I_7 were repeated with 12 TOFs mounted at various angles in the dipole plane. These data are, however, not yet fully analyzed.

This work was supported by the Bundesministerium für Bildung und Forschung, project no. 05 KS1EB1/2, and the Deutsche Forschnungsgemeinschaft, project no. PU 180/1-2.

---

[1] M. Domke *et al.*, Phys. Rev. A **53**, 1424 (1996).
[2] Y. H. Jiang *et al.*, Phys. Rev. A **69**, 042706 (2004).
[3] R. Püttner *et al.*, Phys. Rev. Lett. **86**, 3747 (2001).
[4] A. Menzel *et al.*, Phys. Rev. Lett. **75**, 1479 (1995).
[5] A Czasch *et al.*, Phys. Rev. Lett. **95** 243003 (2005).
[6] Y. H. Jiang *et al.*, J. Phys. B **39**, L9 (2006).

New Vibrational Satellites in Highly Resolved Spectra of Xe/CF_4 Mixtures

V.A. Alekseev
Institute of Physics, St.Petersburg State University, Peterhof, 198504 Russia
N. Schwentner
Institute für Experimental Physik, Freie Universität Berlin, Arnimallee 14, D-14195, Germany

Motivation.

Perfluoromethane is one of the very few molecular gases which are transparent in the range of Xe resonance transitions in the Vac UV region. Studies of pressure broadened contours of these lines provide information on Xe* - CF_4 interaction potentials. In the present work we explored opportunities offered by a recently commissioned 10m normal incidence monochromator[1] at the synchrotron radiation facility BESSY II to record high resolution transmission and fluorescence excitation spectra of Xe/CF_4 mixtures in the Vac UV region. Here we report on observation and assignment of satellites of dipole forbidden transitions in Xe atom.

Experimental.

Intensity of Vac UV radiation in transmission was recorded by a GaAs_photodiode and picoampermeter (Keithley Instruments). Fluorescence was observed at 90 degree via Mg_2F side-on window with use of a solar blind photomultiplier. The optical pathway of SR radiation in the gas cell prior to the fluorescence observation zone was reduced with a special adapter. Perfluoromethane does not deactivate excited Xe atom. The major collision-induced energy transfer process is relaxation to the lowest resonance Xe $6s[3/2]_1$ and metastable Xe $6s[3/2]_2$ states. Typically mixture consisted of ~1-10 mbar of Xe and ~ 0.5-1 bar of CF_4. Spectra of Xe/He mixtures were recorded for comparison. Because of fast relaxation in these high pressure mixtures, Vac UV fluorescence excitation spectra closely followed in shape the absorption spectra, with nearly constant quantum yield over the spectral range 115-150 nm. Most likely emitters are the Xe $6s[3/2]_1$ atoms and Xe_2* dimers formed in the three body recombination process. CF_4 absorbs radiation in the $\lambda < 115$ nm region and the cell passes no light at a CF_4 pressure ~ 1 bar. However, all broadened Xe bands up to LiF cutoff at 104 nm are easily observed in the excitation spectra of Vac UV emission.

Results and discussion.

Figure 1a shows fluorescence excitation spectrum of Xe/He mixture on the red wing of the Xe $6d[3/2]_1$ resonance transition. This region covers dipole-forbidden transitions to numerous states from Xe $6p$'-, $7p$- and $6d$-manifolds. Their energies are indicated by the lower set of sticks in Figure 1a. Most of these transitions are not visible in the spectrum of pure Xe at low pressure. Addition of ~ 1 bar of He weakens the optical selection rules and a sequence of bands appears in the spectrum. These bands in mixture with CF_4 (Fig.1b) are much less intense, most of them are hardly seen on the background of Xe $6d[3/2]_1$ pressure broadened band. More striking, however, is the appearance of several new bands in spectral regions which are not overlapped with any dipole forbidden transitions. In particular, three bands appear on the blue wing of Xe $6d[3/2]_1$ resonance band (Fig.1c and Fig. 1d). The band closest to the resonance transition is so intense that at P_{Xe}=5 mbar (Fig.1d) it transforms to a spectral dip due to complete absorption of SR radiation prior fluorescence observation zone.

The upper sticks in Figures 1 indicate positions of Xe atom levels displaced by the energy of CF_4 ν_3 vibrational quanta. Each extra band in experimental spectra has its counterpart in the group of these displaced energy levels. We conclude that these bands are
$Xe (G)..CF_4 (\nu_3=0) + h\nu \rightarrow Xe(F)..CF_4 (\nu_3=1)$
satellite transitions where Xe (G) states for the ground state and Xe(F) for a dipole forbidden state. In particular, the strongest band on the blue wing of the $6d[3/2]_1$ resonance corresponds to the $7p[1/2]_0$ satellite. This and other intense satellites are located on the wing of pressure broadened resonance bands, implying an intensity borrowing mechanism. Some dipole forbidden transitions are also close in energy to resonance transitions, but they are much less intense than their satellites or absent at all and it seems that the major intensity enhancing factor is excitation of CF_4 vibrations. The CF_4 $\nu_3=0 \rightarrow \nu_3=1$ is a very strong infra red transition, an order of magnitude stronger than in CH_4 molecule.[3] Considering that the satellites are spectrally narrow bands in close proximity to the Xe(F) + CF_4 ($\nu_3=1$) asymptotic energies, the observed effect may be viewed as coupling between the resonance and dipole forbidden atomic states in the electric field of a transient molecular dipole. The selection rules are the same as for the optical coupling. A qualitative explanation of the relative intensities of some satellites may be given in terms of perturbation theory. In particular, coupling of the $6d[3/2]_1$ resonance state with the $7p[1/2]_0$ forbidden state is allowed in the first order and yields the most intense satellite (Fig.1c,d). Coupling with the $6d[7/2]_3$ state is allowed in the second order, while coupling with the $6d[7/2]_4$ state is a higher order effect. It presents a tentative explanation for the high intensity of the remote $6d[7/2]_3$ satellite (Fig.1c,d).
The spectrum in Figure 1d also displays a satellite of the $6d[3/2]_1$ resonance transition. Although this transition is optically allowed, the band is relatively weak. Satellites on the far blue wings of pressure broadened Xe $6s[3/2]_1$, Xe $6s'[1/2]_1$ and Xe $7s[3/2]_1$ resonance bands have been reported earlier.[2] No satellites due to excitation of anyone of the three other vibrational modes of CF_4 molecule, ν_1= 909 cm^{-1}, ν_2 = 435 cm^{-1} , ν_4=632 cm^{-1}, were found in the present study.

The appearance of very strong satellites of dipole forbidden transitions is a striking manifestation of the vibronic coupling phenomena. A large variety of new experiments should be explored to characterize it in detail.

Acknowledgement.

The authors are grateful to the BESSY staff, especially to Dr. G. Reichardt for help with running 10m NIM

References.

1. G. Reichardt *et al*, NIM A 467-468 (2001) 462-465
2. V. A. Alekseev , Opt. Spectrosc. **96** (2004) 492 and references therein
3. D.A. Dixon, J.Phys.Chem. **92** (1988)86.

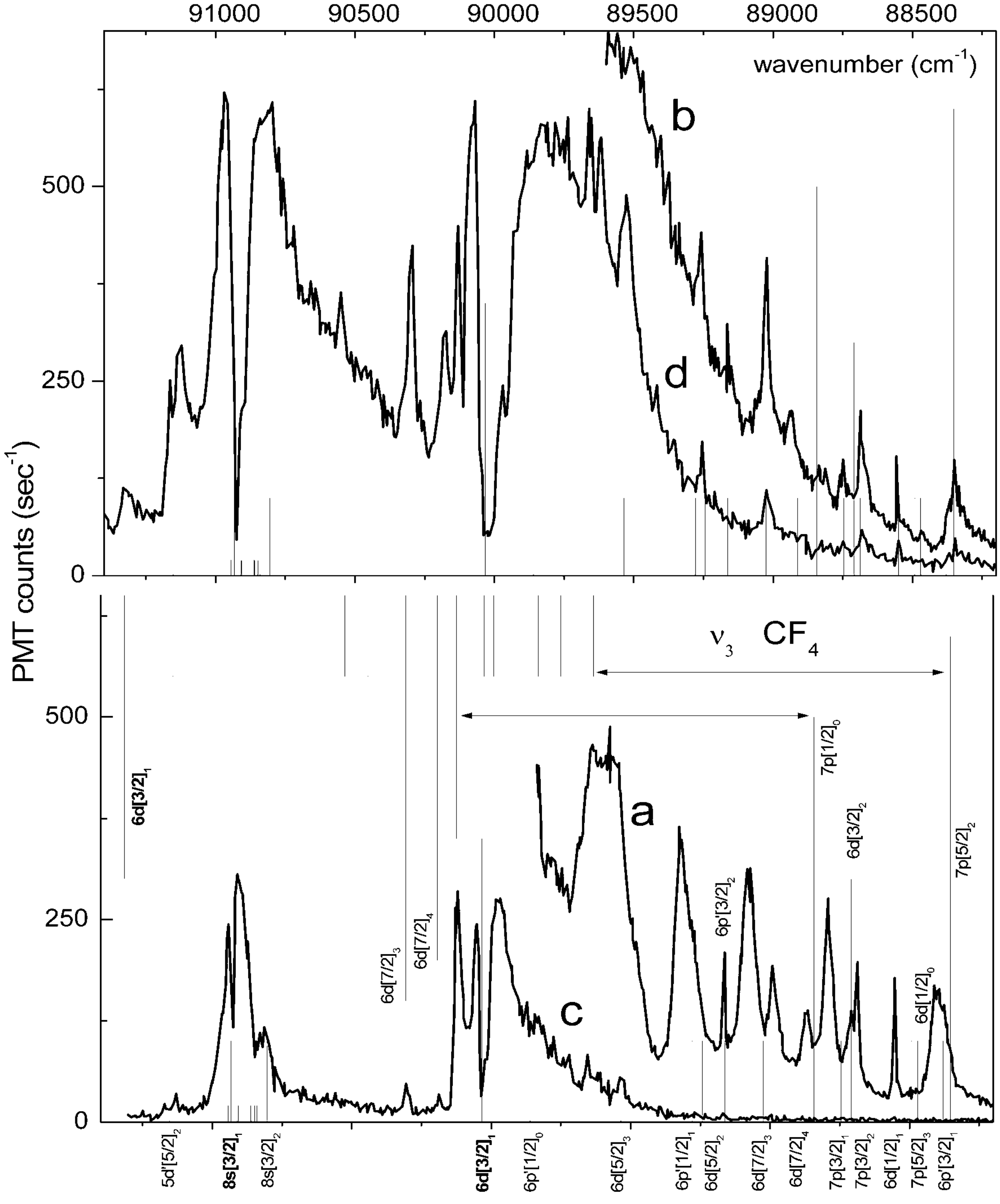

Figure 1 Vac VU fluorescence excitation spectra:
a - Xe (35 mbar) / He(770 mbar) (intensity decreased by a factor of 3),
b - Xe(14 mbar) / CF$_4$ (920 mbar) (intensity decreased by a factor of 2),
c - Xe(0.4 mbar) / CF$_4$ (980 mbar),
d - Xe(5 mbar) / CF$_4$ (860 mbar).
The lower sticks indicates positions of Xe atom levels. The upper sticks shown in the bottom panel are the same set of levels displaced by the energy of CF$_4$ ν_3-quanta (1281 cm^{-1}).
The intensity dips around resonance transitions to Xe 8*s*[3/2]$_1$ and Xe 6*d*[3/2]$_1$ are due to complete absorption of SR radiation prior fluorescence observation zone.

Photoionization of Free Chiral Molecules

ID.05.1.212: Weeks 4/5 2005 UE56/2 PGM2
EU R II 3-CT-2004-506008

Chris Harding, Elisabeth Mikajlo, Ivan Powis,
University of Nottingham, UK
Silko Barth, Uwe Hergenhahn,
IPP Garching

Introduction

It was predicted in 1976 that an un-oriented sample of a chiral molecule could have an angular distribution $I_p(q) = 1 + b_1^p P_1(\cos q) + b_2^p P_2(\cos q)$ with an 'additional' $\cos q$ term when ionized with circularly polarized light (helicity, $p = \pm 1$). Only recently has this been experimentally verified. A new chiral asymmetry results, seen as a difference in the forward-backward photoemission yield for a given enantiomer and polarization and expressed by the chiral parameter $b_1^{\pm 1}$. This should reverse on changing either enantiomer or circular polarization. Alternatively, for a given enantiomer and a fixed detection direction, θ, one can see a new form of circular dichroism *i.e.* the difference between photoelectron yield for the two polarizations. These asymmetries are expected to be of the order 0.1, exceeding by several orders of magnitude previous natural dichroism effects since they arise in the pure electric dipole approximation. Our programme at BESSY II aims to examine these predictions and the general phenomenon in the core ionization region. C 1*s* core ionization is particularly appropriate for initial investigations since the initial orbital is localized and achiral (spherical), so any observed dichroism and chiral asymmetery can be interpreted as a purely final state effect.

Using the rapid switching, two-beam mode of the UE56/2 twin undulators, and methodology developed in 2004, two molecular studies of carvone and fenchone, were undertaken, examining in each case both the molecular enantiomers. Polarimetry scans were made at the photon energies used for these measurements to confirm the degree of circular polarization.

Carvone

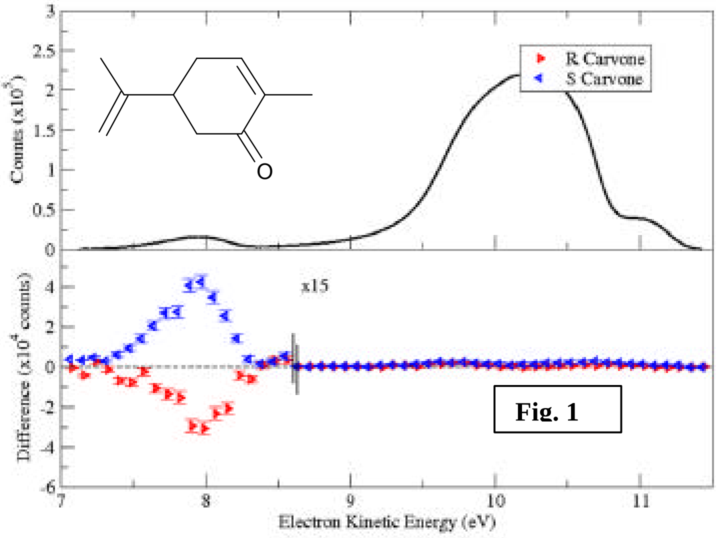

Fig. 1

Fig 1 shows a typical carvone C 1*s* XPS with, beneath, the difference spectrum, $\sigma^{(+)} - \sigma^{(-)}$. Results for both enantiomers are included, and show the anticipated opposite dichroism under the small carbonyl C=O peak.[1]

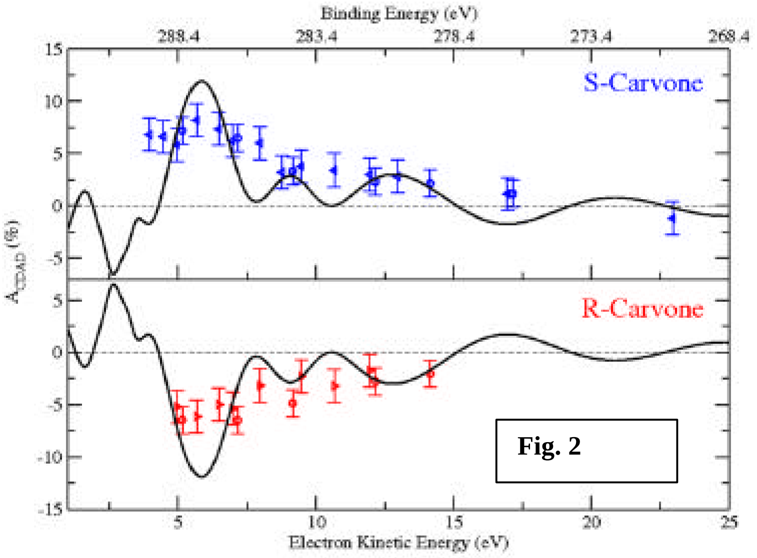

Fig. 2

The variation of the **C**=O dichroism, expressed as a % asymmetry, with photon energy is shown in Fig.2. The solid curves in this Figure are CMS-Xα theoretical calculations of the expected dichroism, assuming only the lowest energy conformers of the flexible carvone molecule are populated. However, better agreement with experiments is obtained when contributions from higher energy conformations are included, although in previous studies these have been discounted.[2] A surprising feature is the sensitivity of the measured **C**=O dichroism to the orientation of the removed isopropenyl tail in the carvone molecule; not only is the dichroism a final state scattering effect, but evidently it operates over a long range.

Fenchone

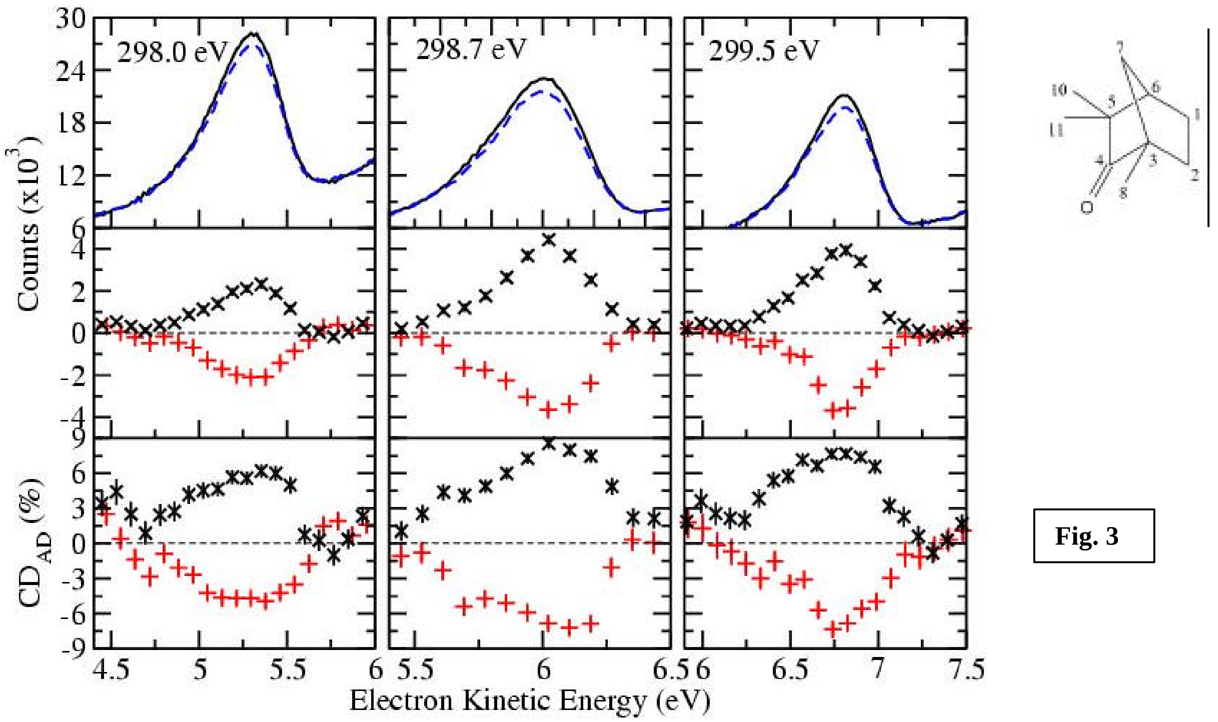

Fig. 3

A similarly extensive set of data were obtained for fenchone. Figure 3, shows (top row) the **C**=O XPS band recorded with different helicity radiation, for each of three example photon energies.

Beneath are the difference spectra for R- (x) and S- (+) enantiomers, with the normalized % asymmetry in the bottom row.

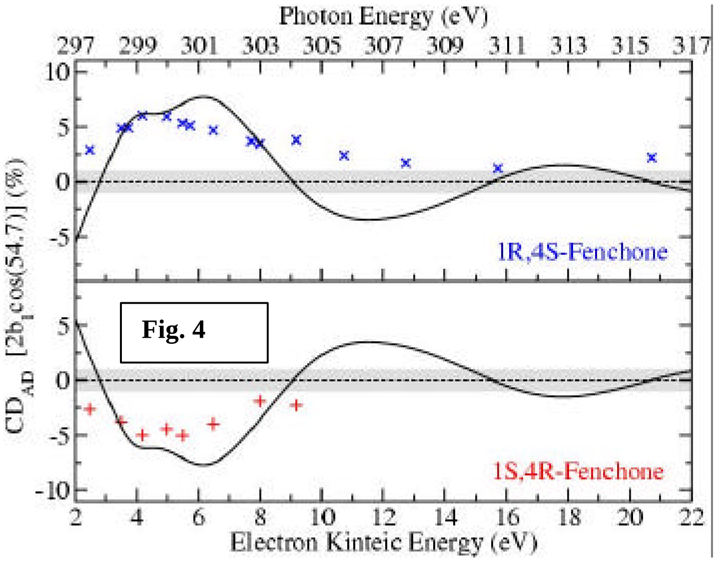

Fig. 4

Figure 4 shows the photon energy dependence of the dichroism. It is interesting to compare these observations with earlier measurements made for the closely related camphor molecule.[3] These species differ only in the removal of two methyl; group s from the bridging C atom (7) in camphor to the C_5 position in fenchone (above). Yet the energy dependence of the dichroism is quite different. Again this shows that the final state electron scattering sensitively probes centers that are not immediately adjacent to the initial site.

References

[1] C. J. Harding, E. A. Mikajlo, I. Powis, S. Barth, and U. Hergenhahn, J. Chem. Phys. **123**, 234310 (2005).

[2] C. J. Harding and I. Powis, J. Chem. Phys. (submitted to J. Chem. Phys.).

[3] U. Hergenhahn, E. E. Rennie, O. Kugeler, S. Marburger, T. Lischke, I. Powis, and G. Garcia, J. Chem. Phys. **120**, 4553 (2004).

Experimental Observation of Spin-orbit Activated Interchannel Coupling Effects in Cesium

T. Richter, P. Zimmermann
Institut für Atomare Physik und Fachdidaktik, Technische Universität Berlin
K. Godehusen
Berliner Elektronenspeicherring-Gesellschaft für Synchrotronstrahlung mbH
M. Yalcinkaya
Department of Physics, Istanbul University

Stimulated by an experimental investigation on the Xenon 3d photoionization ([1]) a new type of configuration interaction of continuum states was predicted [2, 3]. This interchannel coupling is a supposedly general effect fed by the spin orbit interaction. The calculations use a modified version of the spin-polarized random phase approximation with exchange (SPRPAE) methodology. While it was possible to quantitatively describe the Xe photoionization cross section with that new theory, its major impact on other atomic photoionization processes was not noticed before.

We now report on experimental data for the Cesium $3d$ photoionization, that strongly supports predictions based on the spin orbit activated intra channel coupling. Both the partial cross section of the Cs $3d_{5/2}$ photoelectrons and their angular distribution parameter (β) show a pronounced second maximum in the vicinity of the $3d_{3/2}$ threshold. In dipole approximation the β parameter governs the differential cross section from linearly polarized light impinging on unpolarized atoms via the following formula:

$$\frac{d\sigma}{d\Omega}(\theta) = \frac{\sigma}{4\pi}[1 + \frac{1}{2}\beta(3 \cdot \cos^2\theta - 1)]$$

The extra features are not reproduced by uncorrelated numerical calculations (e.g. Hartree-Fock).

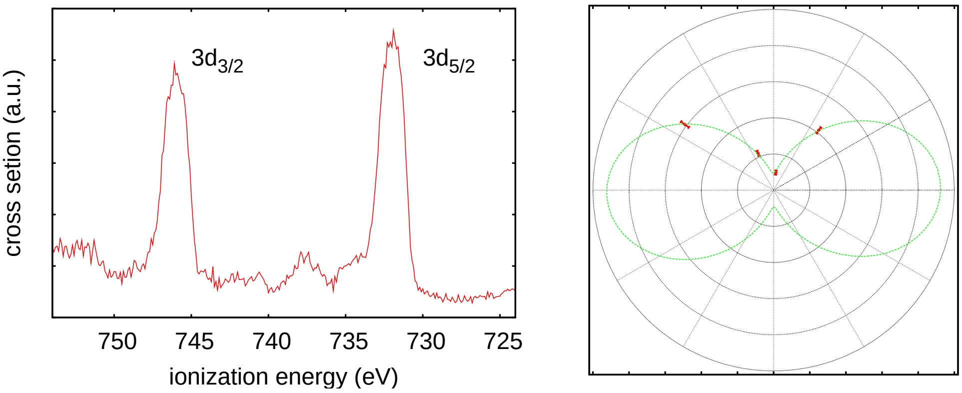

Figure 1: Cs 3d photoelectron spectrum and angular distribution fitted to the experimental data for $3d_{5/2}$

Individual photoelectron spectra are recorded for four different angles of linear polarization using a fixed-in-space electron analyzer. The derived $\frac{d\sigma}{d\Omega}(\theta)$ is fitted with a angular distribution function using β, σ and the instrumental angle as free parameters to acquire β. See [4] for more details.

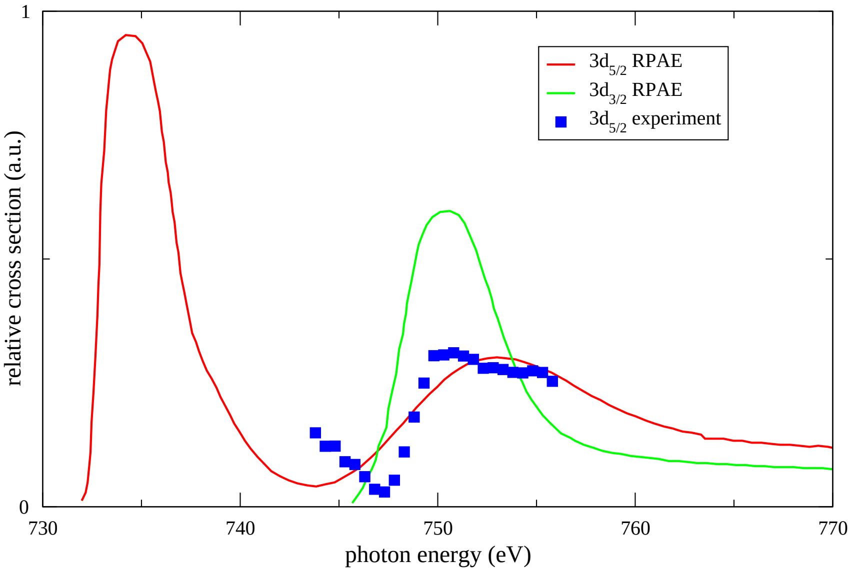

Figure 2: Photoelectron yield measured for Cs $3d_{5/2}$*, calculated for both spin-orbit doublets*

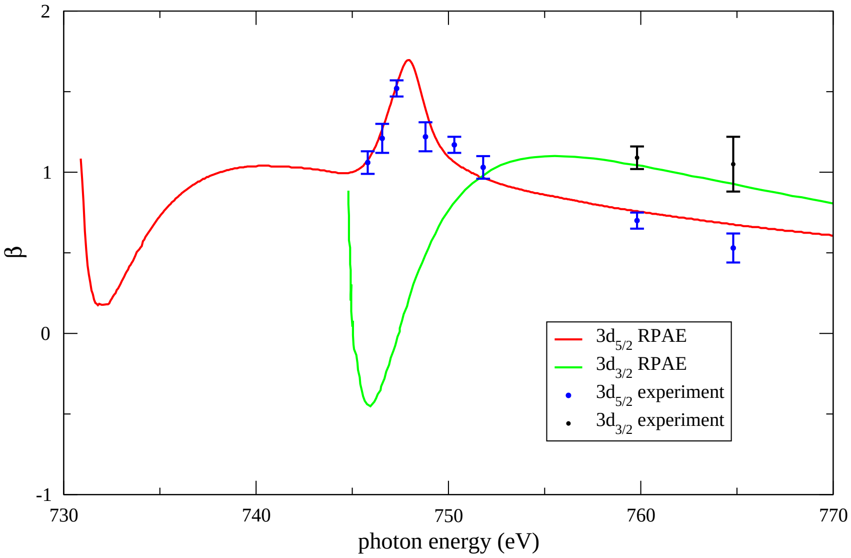

Figure 3: Experimental and predicted β *data*

The interchannel coupling effects are clearly confirmed, while the predicted energy position of the features diverges from the experimental data. Also the deviation is different for the photoelectron yield and the β parameter. This is remarkable as the interference effect should be quite sensitive to even small variations in any channel.

We are thankful for the support of the BESSY staff. This work was in part funded by the Deutsche Forschungsgemeinschaft.

[1] A. Kivimäki, U. Hergenhahn, B. Kempgens, R. Hentges, et al. Phys. Rev. A, **63** 012716 (2000).

[2] M. Y. Amusia, L. V. Chernysheva, S. T. Manson, A. Z. Msezane, et al. Phys. Rev. Lett., **88** 093002 (2002).

[3] M. Y. Amusia, A. S. Baltenkov, L. V. Chernysheva, Z. Felfli, et al. J. Phys. B, **37** 937 (2004).

[4] K. Godehusen, H.-C. Mertins, T. Richter, P. Zimmermann, et al. Phys. Rev. A, **68** 012711 (2003).

Mass-filtered cobalt clusters on non-magnetic surfaces

J. Bansmann, P. Imperia[1], A. Kleibert, F. Bulut[2], M. Getzlaff[2], C. Boeglin[3], A. Barla[3],
K.H. Meiwes-Broer

Institute of Physics, University of Rostock, D-18051 Rostock
[1] Hahn-Meitner-Institut, D-14109 Berlin
[2] Institute of Applied Physics, University of Düsseldorf, D-40225 Düsseldorf
[3] IPCMS Strasbourg, 23 rue du Loess, F-67033 Strasbourg, France

supported by DFG via BA 1612/3-1 (in the DFG priority call 1153).

It is well-known that small clusters deposited on surfaces exhibit magnetic properties that strongly differ from those for thin films and bulk systems [1,2]. Analogously, even large clusters with about several thousands of atoms have enhanced orbital moments although only the outer two layers of the clusters are influenced [3-5]. Moreover, the electronic structure of the interface also has an influence on the magnetic properties of the clusters that cannot be neglected. Large mass-filtered Fe and Co clusters deposited on Ni(111) films show different magnetic properties when compared to deposition on iron and cobalt films [6]. Hybridization effects of the electronic states between clusters and underlying substrate / film can modify these cluster-specific properties significantly. Up to now we have deposited Fe and Co clusters on ferromagnetic films in order to magnetize the clusters remanently by exchange interaction with magnetic film. For the investigations presented here, we have chosen an Au(111) single crystal as a substrate. Cobalt films on Au(111) show spin-reorientation transitions both as a function of film thickness and temperature [7,8]. Mass-filtered cobalt clusters with a size of about 9 nm have been deposited in-situ onto the clean surface and afterwards investigated with XMCD using the superconducting magnet systems of the Strasbourg group. For this purpose the small and transportable arc cluster ion source (briefly described in [9]) has been adapted to the preparation chamber of the magnet system. The source was developed for producing mass-filtered metal clusters in the size range from 5 nm to 15 nm that can be deposited in-situ on surfaces without fragmentation. The mass filtering process is carried out in an electrostatic quadrupole deflector, cf. fig. 1. The measurements

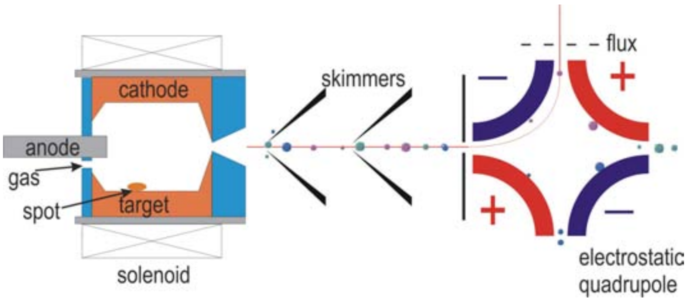

Figure 1: Schematic drawing of the arc cluster ion source ACIS and the mass-filtering unit.

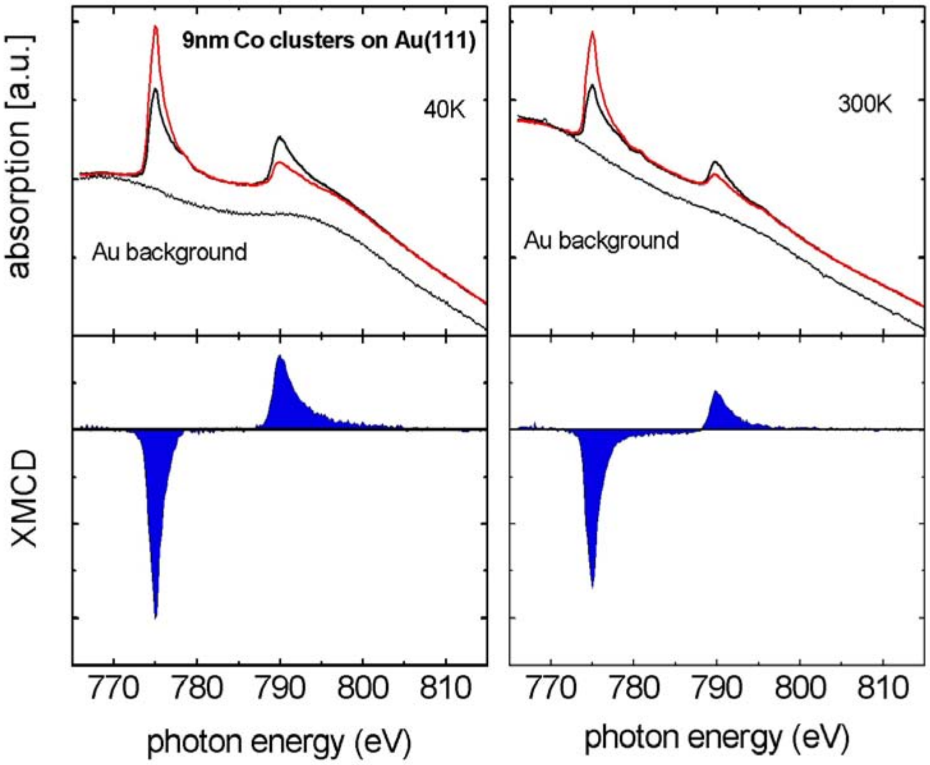

Figure 2: Photoabsorption (upper part) and XMCD spectra (lower part) from an 9 nm clusters Co deposited on clean Au(111).

have been carried out at the UE46-beamline at different temperatures (40 K and 300 K). An external magnetic field of 4 T has always been applied along the direction of the incoming photon beam. For the individual measurements, the photon polarisation has been reversed. The XMCD data taken in total electron yield clearly show the typical absorption features at the Co 2p edge with different intensities in the two peaks when switching the circular polarisation from σ^+ to σ^- , cf. fig. 2. The upper panels show the spectra recorded at 40 K (left) and 300 K (right) at an angle of 40° taken for opposite photon helicities together with the background from the clean Au(111) sample. Please note the strong feature in the clean gold spectrum at low temperature which is located directly at the Co 2p absorption edge. The lower panels display the corresponding XMCD intensity difference. Clearly, the area of the Co $2p_{1/2}$ peak is smaller at 300 K indicating a reduced spin moment when compared to 40 K. By integrating the XMCD curve, one has access to the ratio of orbital to spin moment which is being dicussed in the following. The ratio of orbital (m_L) to spin moment (m_S) presented in fig. 3 significantly depends on the angle of incidence (and thus the magneization direction), the values are different in normal emission and 40° off-normal. The lower data set (40 K) indicates a preferential magnetization orientation in perpendicular magnetization direction whereas the increasing value for 300 K is a clear hint for an in-plane magnetization direction. The spin moment of the cobalt clusters, however, is independent of the direction of

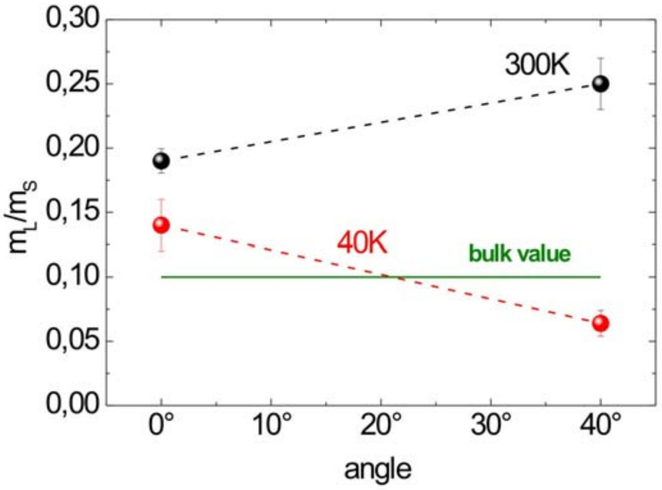

Figure 3: Ratio of orbital (m_L) to spin moment (m_S) for 9 nm Co nanoparticles on Au(111) at 300 K and 40 K for different angles of the magnetization direction with respect to the surface normal. The solid green line denotes the hcp bulk cobalt value.

magnetization after correcting for the dipole term. Thus, it does alter this ratio. Of course, the spin moments are dependent on the temperatures, they vary from $m_S \approx 1.65\,\mu_B$ at 40 K to $1.4\,\mu_B$ at 300 K. The easy magnetization direction is usually oriented along the maximum value of the orbital moment. These results clearly underline the importance of the electronic structure of the substrate on the magnetic properties of deposited clusters. It is not only the size of the clusters that determines the spin and orbital moments, one has also to take into account the interaction with the surface. Further investigations on different surfaces are planned in order to get a better understanding of the interaction between deposited clusters and the surface of the substrate.

References:

[1] K.W. Edmonds et al., J. Magn. Magn. Mat. **220**, (2000).
[2] J.T. Lau et al., Phys. Rev. Lett. **89**, 057201 (2002).
[3] J. Bansmann and A. Kleibert, Appl. Phys. A **80**, in press (2005).
[4] J. Bansmann et al., Surface Science Reports **56**, 189 (2005).
[5] A. Kleibert, Disseration, Univ. Rostock (2006).
[6] J. Bansmann et al., Appl. Phys. A **82**, 73 (2006).
[7] R. Sellmann et al., Phys. Rev. B **64**, 054418 (2001).
[8] Weller et al., Phys. Rev. Lett. **75**, 3752 (1995).
[9] R.P. Methling et al., Europ. Phys. J. D **16**, 173 (2001).

High-Resolution Spectroscopy of Core-Excited Organic Van der Waals-Clusters

R. Flesch, I.L. Bradeanu, J. Plenge, T. Arion, and E. Rühl

Institut für Physikalische Chemie, Universität Würzburg, Am Hubland, 97074 Würzburg

Molecular van der Waals clusters reveal in many cases well-resolved core-to-valence transitions in the regime of inner-shell excitation. Spectral changes occur as a result of cluster formation. These are investigated by using high-resolution near-edge spectrsocopy. It has been earlier shown that spectral shifts, homogenous and inhomogeneous line broadening, as well as variations of the Franck-Condon structure occur as a result of cluster formation [1].

We have studied the C 1s excitation regime in homogenous clusters of pyridine (C_5H_5N) and fluorobenzene (C_6H_5F). These serve as model systems of aromatic molecules. The experiments have been carried out at the UE-52-SGM beamline at BESSY. Clusters are produced by utilizing an adiabatic seeded beam expansion through a nozzle (d=50 μm), where argon is bubbled through the liquid samples. The skimmed jet is tranferred into the ionization region of a time-of-flight mass spectrometer where it is crossed by dispersed undulator radiation. Cations are separated and detected in a time-of-flight mass spectrometer. Photoion yields of fragment ions reflecting properties of the bare molecule and clusters are recorded simulateneously as a function of the photon energy. As a result, spectral shifts and changes in spectral line shapes are accurately determined (cf. [1]). Fig. 1 shows the photoion yield of molecular pyridine (solid line corresponding to the $C_4H_4^+$-yield) and pyridine clusters (dashed line corresponding to the $(C_5H_5N)_2^+$-yield) in the C 1s → π*-regime. The transition of the bare molecule is split due to a chemical shift induced by nitrogen in the heterocyclic system. Ortho (o) carbon sites absorb at higher energy than the meta (m) and para (p) carbon sites (see Fig. 2). It is inferred from Fig. 1 that the overall shape of the band is similar in molecules and clusters and there is excellent agreement with earlier work on

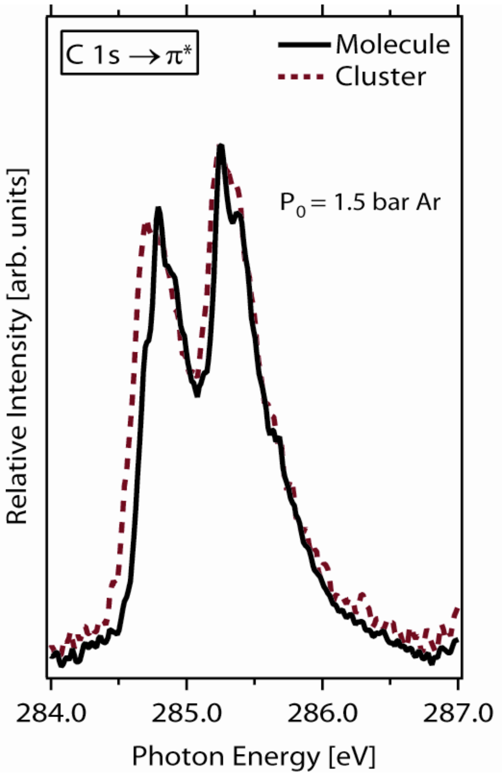

Fig. 1: Comparison of the C 1s → π* transition in pyridine (solid line) and homogenous pyridine clusters (dashed line); seed gas Ar, stagnation pressure: 1.5 bar.

molecular pyridine (cf. [2]). However, there are significant changes between molecular and the cluster spectra: (i) The onset of the C 1s → π*- transition near 284.3 eV is redshifted by 105 meV in clusters relative to isolated molecules; (ii) the o-C 1s → π* transition is significantly broadened in clusters, but not shifted in energy; (iii) a broadening of all spectral features is found in clusters; (iv) the vibrational fine structure at the high-energy side of the band is somewhat less distinct in the case of clusters. We note that similar results are obtained for fluorobenzene, furan, and pyrrole.

Spectral redshifts of core-to-valence transitions in clusters have been observed before, but these are significantly smaller in clusters containing small molecules [1] or homoaromatic species, such as benzene [4]. Detailed investigations have been performed using *ab initio* calculations, similar to related work on benzene clusters [4], where the GSCF3-program is used [5]. We have assumed that a reasonable model structure of the dimer is the antiparallel isomer, which is calculated to be the most stable one. The results are shown in Fig. 2, where a comparison is made between the calculated molecular and dimer v=0-transition. The calculated transition energies are boradened by Voigt-profiles in order to compare the results to the experimental spectra in Fig. 1. Clearly, the sites next to the nitrogen site (o-carbon) show a negligible redshift, whereas that of the m- and p-carbon sites is substantially enhanced. This is in full agreement with the experimental results and underlines the previously observed site-specific energy shifts in clusters containing aromatic molecules [4].

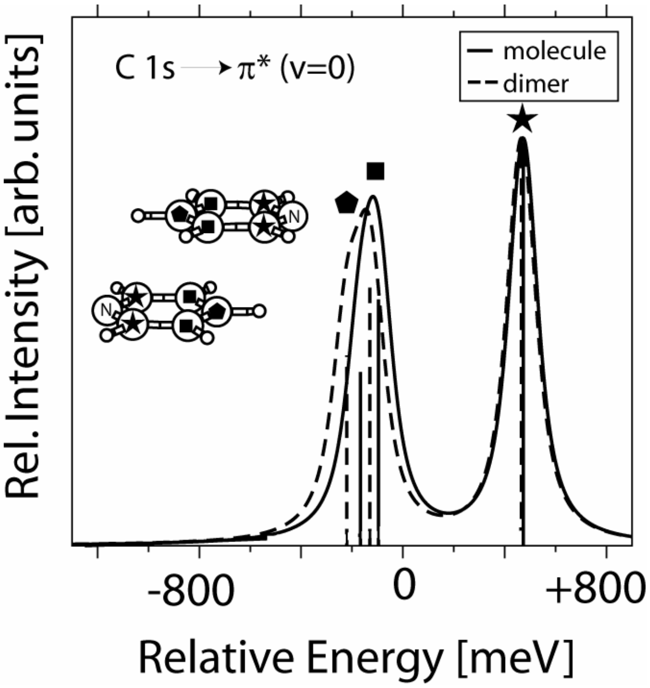

Fig. 2: Comparison of the calculated C 1s → π* (v=0)-transition in pyridine (solid line) and the pyridine dimer (dashed line). The calculated energy shifts (vertical lines correspond to calculated oscillator strengths) are broadened by Voigt profiles (Gaussian width: 40 meV, Lorentzian width: 110 meV).

References

1 A. A. Pavlychev, R. Flesch, and E. Rühl, Phys. Rev. A **70**, 015201 (2004).
2 C. Kolczewski, R. Püttner, O. Plashkevych, H. Ågren, V. Staemmler, M. Martins, G. Snell, A. S. Schlachter, M. Sant'Anna, G. Kaindl, and L. G. M. Petterson, J. Chem. Phys. **115**, 6426 (2001).
3 I.L. Bradeanu, R. Flesch, N. Kosugi, A.A. Pavlychev, E. Rühl, manuscript in preparation (2006).
4 I.L. Bradeanu, R. Flesch, N. Kosugi, A.A. Pavlychev, E. Rühl, Phys. Chem. Chem. Phys., submitted for publication (2005).
5 N. Kosugi, Theoret. Chim. Acta **72**, 149 (1987).

Electronic Ni 3d surface states in NiO/HOPG nanostructures

L. Soriano,[1] M. Abbate,[2] I. Preda,[1] S. Palacín,[1] A. Gutiérrez,[1] J.F. Trigo,[3] A. Vollmer[4] and P.R. Bressler [4]

[1]Departamento de Física Aplicada C-XII, Universidad Autónoma de Madrid, Cantoblanco
E-28049 Madrid, Spain
[2]Departamento de Física, Universidade Federal do Paraná, Caixa Postal 19091, 81531-990
Curitiba PR, Brazil
[3]Departamento de Energía, CIEMAT, Avda. Complutense 22, E-28040 Madrid, Spain
[4]BESSY, Albert Einstein Strasse15, D-12489 Berlin, Germany

This work deals with the study of the electronic structure of the NiO nanostructures formed at the early stages of growth of NiO on highly oriented pyrolytic graphite (HOPG). Our main aim is the study of nanostructured NiO systems where possible surface effects are enhanced by the large surface to volume ratio of the nanostructures. In fact, early studies [1] on 3 nm NiO nanoparticles with unique catalytic properties revealed a splitting of the unoccupied Ni e_g states, as shown by the O 1s XAS spectra. This splitting was interpreted as the result of the lack of the apical oxygen at the NiO surface and the large surface to volume ratio of the nanoparticles. On the other hand, the early stages of growth of NiO/HOPG are known to produce planar NiO islands along the graphite steps as shown by Atomic Force Microscopy (AFM) images.[2] Such a particular arrangement of NiO nanostructures is expected to exhibit similar surface effects as in the NiO nanoparticles. Therefore, the study of this system seems to be well justified.

NiO was deposited on HOPG by reactive evaporation from a pure Ni filament in the preparation chamber. The HOPG substrate was cleaved in air just before being introduced in the preparation chamber. Then, it was thermally annealed in UHV at 300^{o}C to remove any possible surface contamination. Reactive evaporation was performed in an oxygen atmosphere (5×10^{-5} Torr), with the substrate kept at room temperature. The oxygen gas was aimed directly to the sample using a narrow pipe to enhance the oxidation efficiency. The evaporation rate was maintained low enough to study the early stages of NiO growth in more detail. After each XAS analysis, the substrate was introduced in the preparation chamber for the successive evaporations.

XAS measurements were performed at the PM4 plane grating monochromator in the BESSY II storage ring (Berlin). This experiment requires a high photon flux in order to detect an acceptable signal from the small amount of NiO. The optical arrangement of this monochromator was set to optimize both, high photon flux and resolution. The estimated overall resolution was better than 100 meV at 530 eV. The spectra were collected in the total electron yield detection mode. In order to observe possible dichroism effects, the spectra were measured at normal and grazing angles with respect to the incident light. The spectra were normalized to the I_0 current, measured from a clean gold sample, to correct for the beam current. The NiO coverage was calculated from the O 1s XAS intensities following conventional methods. Since the growth of NiO on HOPG is not in a layer-by-layer mode, the estimated coverages should be understood as the equivalent material to form a monolayer.

Fig. 1 shows the O 1s XAS spectra of the NiO overlayers for (a) low and (b) large coverages. For large coverages, the spectrum is in very good agreement with previous spectra published for bulk NiO. This shows that a thin film of stoichiometric NiO can be grown on HOPG at room temperature using this growth method. The unoccupied density of electronic states (UDOS) of O *p* character obtained by *ab-initio* band- structure calculations for antiferromagnetic NiO, are also shown in Fig. 1(c). The spectrum for low coverages (0.5 ML) presents significant differences with respect to that of large coverages, i.e., bulk NiO. The most relevant change in the spectra concerns the e_g region, which is shown in more detail in the inset of Fig. 1. The well defined e_g peak in bulk NiO is split in two broad and unresolved peaks for 0.5 ML of NiO/HOPG. The Ni 3d states in NiO are split by the octahedral crystal field produced by the O into the t_{2g} and e_g sub-bands. However, the lack of the apical O at the surface of NiO breaks the symmetry and results in a pyramidal crystal field. This effect produces the additional splitting of the e_g sub-bands observed for low coverages, where the relative weight of the surface states is much larger than for bulk NiO.

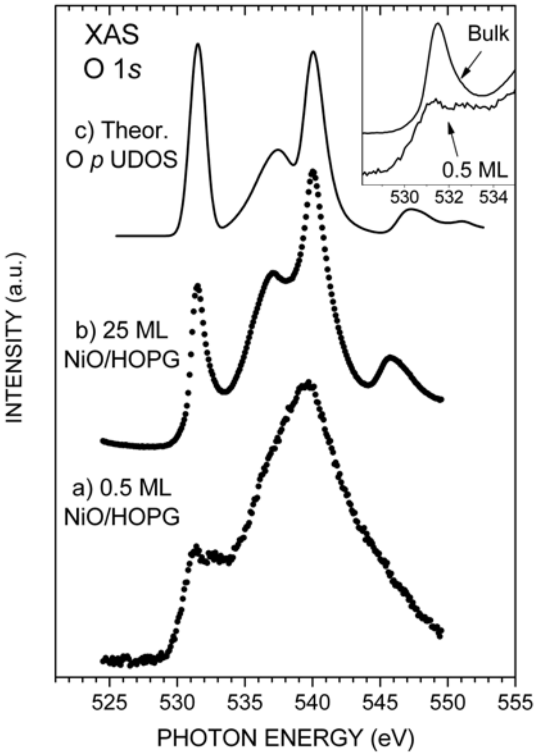

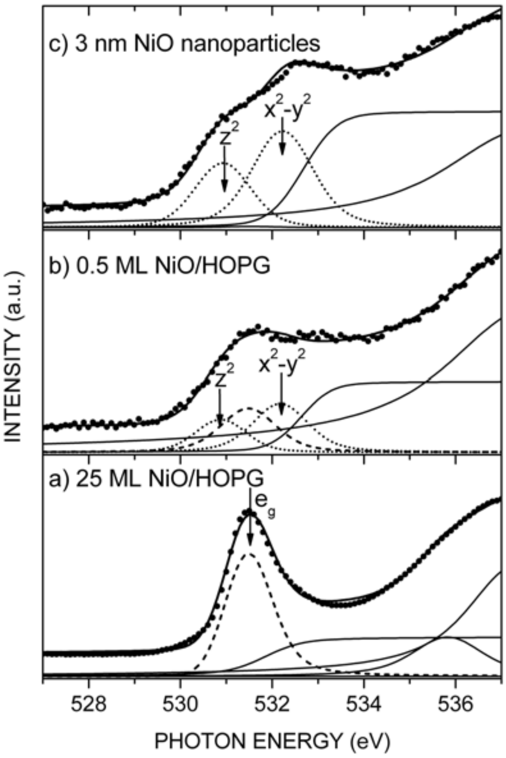

Fig. 1: O 1s XAS spectra for low (a) and large (b) coverages of NiO on HOPG

Fig. 2: Near edge region of the O 1s XAS spectra for (a) low, (b) large coverages of NiO on HOPG and 3 nm NiO anoparticles.

To corroborate this theory, we have calculated the O 1s XAS spectra using cluster model calculations in octahedral and pyramidal symmetries. Fig. 2 shows the near-edge region of the experimental spectra of: (a) large and (b) low coverages of NiO/HOPG. The spectra have been fitted using Lorentzian curves at the positions given by the calculations together with other typical functions in the fittings of XAS spectra to simulate the background and the tails of the higher energy structures. The octahedral calculation for bulk NiO shows a single line (short dash) corresponding to transitions to e_g states. The pyramidal calculation for surface NiO presents two lines (short dots) corresponding to the x^2-y^2 and z^2 final states. As shown in Fig 3(a) the agreement with the spectrum of bulk NiO is excellent. To fit the spectrum of the NiO sub-monolayer, shown in Fig. 2(b), not only the two surface components have been used but also a small contribution of the bulk component has been included.

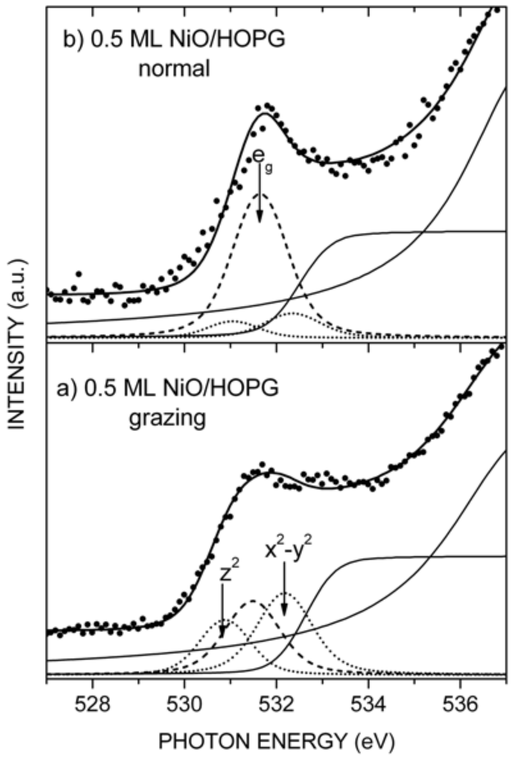

Fig. 3: Near edge region of the O 1s XAS spectra of 0.5 Ml of NiO/HOPG taken at: a) grazing and b) normal incidences.

Fig. 2(c) shows the near edge region of the O 1s XAS spectrum of 3 nm NiO nanoparticles fitted with the surface components. The excellent agreement with the calculations confirm the interpretation of the O 1s XAS spectrum of NiO nanoparticles made in Ref. 1, and strongly suggests that the same splitting mechanism is operating in the case of (0.5 ML) NiO/HOPG.

Fig. 3 shows the O 1s XAS spectra of 0.5 ML NiO/HOPG taken at (a) grazing and (b) normal photon incidence. The spectra exhibit a clear dependence (dichroism) with the relative polarization of the incident light. The normal incidence spectrum, with the electric field **E** parallel to the surface, resembles that of bulk NiO with a relatively broader single e_g peak (short dash). In particular, the distinct splitting due to surface effects (short dots) is very week in this spectrum. On the other hand, in the grazing incidence spectrum, with the electric field **E** perpendicular to the surface, the double peak (x^2-y^2 and z^2) structure (short dots) is clearly observed. The dichroism effect shows that the splitting affects mostly the states perpendicular to the surface, and supports the idea that the splitting is related to the absence of the apical oxygen at the surface. It is worth noting that, in this case, the z^2 orbital forms a dangling bond perpendicular to the surface. This might be related to the enhanced catalytic activity of the larger surface/bulk ratio NiO nanostructures.

In summary, in this work, we have studied the electronic structure of the NiO nanostructures formed at the early stages of growth (0.5 ML) of NiO on HOPG. The results have been compared to those of and 3 nm NiO nano-particles. The Ni 2p XAS spectra of the NiO planar islands confirm that Ni atoms are present in the high spin Ni^{2+} form. On the other hand, the O 1s XAS spectra show exactly, as in the NiO nanoparticles, a splitting of the e_g band which is explained as due to the lack of the apical O atoms at the surface.

Acknowledgments: We want to thank the support of the CICYT of Spain under contract BFM2003-03277 and the European Union through the R II 3.CT-2004-506008 contract. We also thank the staff of BESSY by technical support.

References:

---

[1] L.Soriano, M.Abbate, J. Vogel, J.C. Fuggle, A. Fernández, A.R. González-Elipe, M. Sacchi and J.M. Sanz, Chem. Phys. Lett. **208**, 460 (1993).
[2] C. Morant, L. Soriano, J.F. Trigo and J.M. Sanz, Thin Solid Films, **317**, 59 (1998).

Inner-Shell Excitation of Free Nanoparticles

H. Bresch,[1] B. Langer,[1,2] R. Lewinski, [1] P. Brenner,[1] R. Flesch,[1] C. Graf,[1] T. Martchenko,[3]
O. Ghafur,[3] M.J.J. Vrakking,[3] T. Leisner,[4] B. Österreicher,[4] and E. Rühl[1]

[1]Institut für Physikalische Chemie, Universität Würzburg, Am Hubland, 97074 Würzburg
[2]Max-Born-Institut, Max-Born-Str. 1A, 12489 Berlin
[3] FOM Institute AMOLF, Amsterdam, The Netherlands
[4] Fakultät für Mathematik und Naturwissenschaften, Fachgebiet Experimentalphysik II, TU Ilmenau

Electronic properties of free nanoparticles are investigated in a continuous particle beam using monochromatic synchrotron radiation in the soft x-ray regime. This approach of sample preparation delivers continuously fresh nanoparticles for core level excitation experiments, where any contact of the particles to a substrate is avoided. This approach goes beyond related work, where elastic light scattering has been studied in the vacuum ultraviolet regime [1,2]. It is also complimentary to single, trapped nanoparticles that have been studied by synchrotron radiation in the soft x-ray regime [3,4]. The specific advantage of the present approach is, that properties of the isolated nanoscopic matter cannot be modified as a result of charging or radiation damage. The experimental setup is schematically shown in Fig. 1. It consists of a particle source (atomizer), where either solutions or suspension of pre-made particles are sprayed into a controlled gas phase at normal pressure. The solvent is evaporated in a diffusion dryer. Subsequently, the sample can be mass-selected in a differential mobility analyzer (DMA), so that monodisperse particles are introduced into the experimental chamber, where synchrotron radiation interacts with the particle beam. Alternatively, preferably in the case of pre-made particles from chemical syntheses of well defined size, the entire particle beam is used without primary mass selection. The particle beam is efficiently focussed by an aerodynamic lens, where the beam size is ~0.5 mm in the ionization region. The lens also works as a first differential pumping stage, which is followed by two other differential pumping stages. As a result, the particles are excited and ionized in a high vacuum surroundings, as shown in Fig. 1. Note that this is a widely applicable approach for sample preparation of free nanoscopic matter of diameters larger than 50 nm in the gas phase, where the sample is typically transferred within ca. 5 - 10 s from the solution into the ionization region, which includes size-selection.

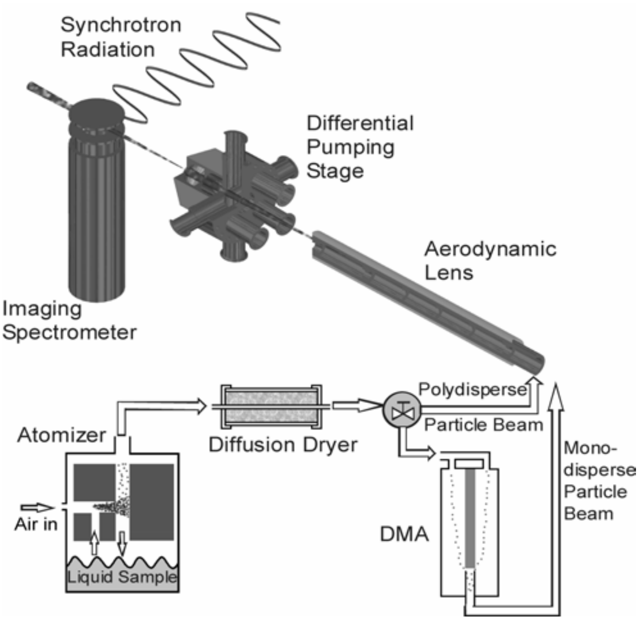

Fig. 1: Schematic diagram of the experimental setup.

We used for first experiments a total electron detector, which is part of a photoelectron imaging spectrometer. This detector also allows us to measure the kinetic energy of photoelectrons emerging from nanoparticles after core level excitation. We have performed the following experiments: (i) total electron yield spectra of mass-selected nanoparticles in the regime of inner-shell absorption edges; (ii) total electron yields of pre-made nanoparticles without primary mass-selection. The occurrence of aggregates of nanoparticles is avoided, as monitored by a condensation nuclei counter; (iii) photoelectron spectra of nanoparticles at selected excitation energies using the imaging spectrometer. Fig. 2 shows as one typical example the near-edge spectrum of sodium sulfate ($Na_2SO_4 \cdot 10\ H_2O$) nanoparticles in the O 1s-regime. These particles were not size-selected and the particle size distribution peaks at ~170 nm. We observe in the total electron yield distinct resonances, which come from the oxygen sites that are bound in the sulfate moiety as well as water moieties that are bound as crystal water. We have modelled the O 1s absorption using the GSCF3 *ab initio* approach [5] along with the known crystal structure of this salt [6]. It becomes evident that the features in the 533-535 eV regime are due sulfate, whereas the maximum near 537 eV is assigned to crystal water. Additional experiments have been performed on NaCl-nanoparticles. These indicate near-edge features at the Cl 2p- and Na 1s-edges, which are comparable to crystalline NaCl. Size-selection indicates that there are no size effects in electronic structure in the regime >50 nm. Experiments at the O 1s-edge indicate that no water is kept in NaCl-crystals, which are prepared *in situ* by primary aerosol formation and subsequent drying. This is unlike the results on sodium sulfate, where the water is bound in the crystal lattice. Furthermore, we have performed first experiments on semiconductor nanoparticles.

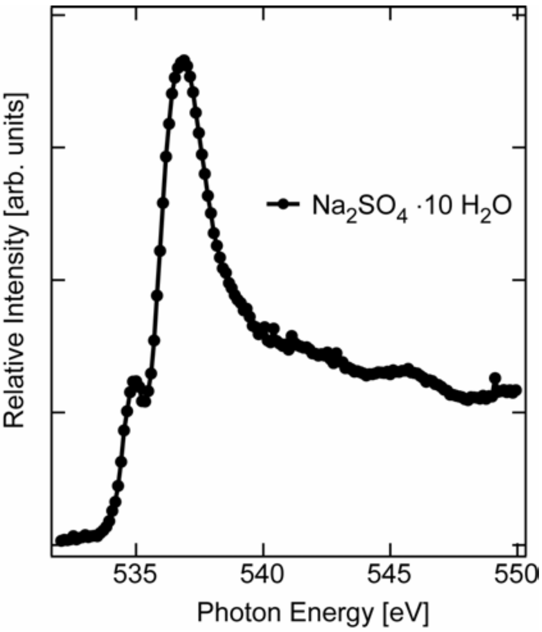

Fig. 2: O 1s-excitation regime of sodium sulfate nanoparticles as recorded by the total electron yield.

This work is supported by the Bundesministerium für Bildung und Forschung (BMBF) grant no.: 05 KS4WW1/7 and the Deutsche Forschungsgemeinschaft (SFB 410-TP C8).

References

1 J.N. Shu, K.R.Wilson, M. Ahmed, S.R. Leone, C. Graf, E. Rühl, J. Chem. Phys. **124**, 034707 (2006).
2 J.N. Shu, K.R.Wilson, A.N. Arrowsmith, M. Ahmed, S.R. Leone, Nano Lett. **5**, 1009 (2005).
3 M. Grimm, B. Langer, S. Schlemmer, T. Lischke, W. Widdra, D. Gerlich, U. Becker, E. Rühl, AIP Conf. Proc. **705**, 1062 (2004).
4 M. Grimm, B. Langer, S. Schlemmer, T. Lischke, W. Widdra, D. Gerlich, U. Becker, R. Flesch, E. Rühl, Phys. Rev. Lett., in print (2006).
5 N. Kosugi, Theor. Chimica Acta **72**, 149 (1987).
6 H.A. Levy, G.C. Lisensky, Acta Cryst. B **34**, 3502 (1978).

Investigation of Trapped Liquid Microdroplets containing Nanoparticles by Soft X-Rays

C. Graf,[a] B. Langer,[a,b] S. Dembski,[a] and E. Rühl[a]

[a] Institut für Physikalische Chemie, Universität Würzburg, Am Hubland, 97074 Würzburg
[b] Max-Born-Institut, Max-Born-Str. 2a, 12489 Berlin

The approach of confining simple model particles in an electrodynamic trap has been demonstrated to be suitable to investigate nanoscopic particulate matter without any contact to a substrate [1]. This requires the use of slightly charged particles, where the particle injection process facilitates electrical charging. More recent work has shown that the charging mechanisms of differently charged, trapped nanoparticles can be derived from such experiments [2]. These works were limited to SiO_2-model particles and served as proof of principle experiments. The results presented in this work are motivated by the progress of colloidal chemistry that allows us to prepare structured nanoparticles in the condensed phase. We have prepared numerous structured core-shell nanoparticle systems containing II-VI-semiconductors of variable size as well as multi-core particles, which are embedded in different environments, such as silica [3] or polymers. We report here first results that build on earlier work, where liquid microparticles were successfully stored in an electrodynamic trap, where the liquid dispersions were injected into the trap via a Piezo nozzle [4]. The required charging is accomplished by the injector nozzle, similar to recent work [5]. The volatile solvent H_2O is readily evaporated, so that finally the trapped liquid particle consist of a liquid polymer droplet (dimethyl siloxane - (60% propylene oxide, 40% ethylene oxide) - block/graft-copolymer (polyalkylene oxide modified silicone oil) obtained from ABCR) with quantum-size semiconductor nanoparticles. This microdroplet is trapped in a high vacuum surroundings. This allows experiments using monochromatic synchrotron radiation in the soft x-ray regime for element-selective excitation, probing the local electronic structure of the absorbing elements. The present experiments were carried out on nanoparticles containing a CdSe core (2.8 nm in diameter) that is surrounded by a thin ZnS shell (thickness: ~0.5 nm), where cysteine is used for stabilization and dispersion in the polymer droplet (see Fig. 1(a)). The investigated particles contain a larger number of such core-shell systems (10^{-3} mol/ℓ), so that element-selective charging experiments can be carried out.

The aim of the present work is to detect via particle charging element-selectively electronic properties of the particle core. This was not easy to accomplish, because of the small size of the cores. The element-selective charging current is derived from changes in particle charge as a function of the excitation energy near the Cd 3d-absorption edge, where the first derivative of the charging curves is used. Note that this quantity is fairly easy to derive for solid nanoparticles, where the constituents represent the major composition of the particles, as evidenced in the case of SiO_2 particles [1,2]. In the case of small core-shell systems this is more difficult to accomplish, since (i) the absorbing cadmium sites are located in the center of the particles and (ii) the semiconductor nanoparticles are located not only on the surface of the polymer droplet that is trapped.

We show as one example recent results from energy scans recorded near the Cd 3d-edge, where the charging current yields distinct maxima that are ascribed to the near-edge structure of these trapped, polymer oil embedded core-shell nanoparticles. The near-edge structures are clearly split as a result of spin-orbit splitting. Earlier work on deposited CdSe nanocrystals indicates that there are size effects in near-edge structure [6]. The present results indicate that the features shown in Fig. 1(b) occur in the same energy regime as in ref. [6]. The present results require further analysis and theoretical modelling in order to derive the extent of changes in electronic structure, which is induced by the local surrounding in polymer embedded core-shell systems.

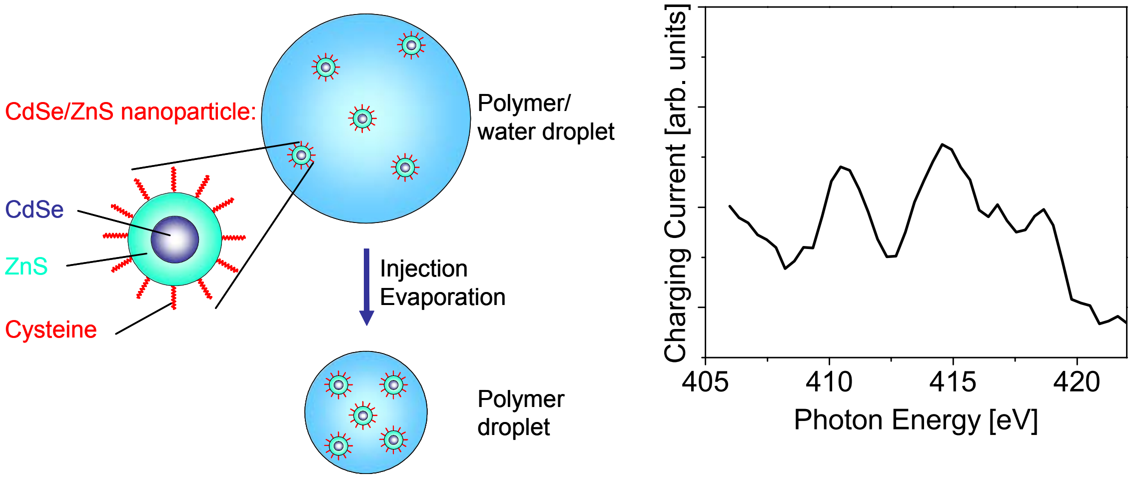

(a) (b)

Fig. 1: (a) Schematic diagram of the CdSe/ZnS nanoparticles and the evaporation of the primarily formed solution droplet; (b) Charging current of a trapped polymer droplet containing CdSe/ZnS nanoparticles in the Cd 3d-excitation regime.

Financial support by the DFG (Sonderforschungsbereich 410 (TP C8)) is gratefully acknowledged.

References

1 M. Grimm, B. Langer, S. Schlemmer, T. Lischke, W. Widdra, D. Gerlich, U. Becker, R. Flesch, and E. Rühl, AIP Conf. Proc. **705**, 1062 (2004).

2 M. Grimm, B. Langer, S. Schlemmer, T. Lischke, W. Widdra, D. Gerlich, U. Becker, R. Flesch, and E. Rühl, Phys. Rev. Lett., in print (2006).

3 C. Graf, S. Dembski, A. Hofmann and E. Rühl, Langmuir, submitted for publication (2006).

4 C. Graf, B. Langer, S. Dembski, R. Lewinski, and E. Rühl, BESSY Annual Report 2004, p. 67.

5 M.A. Hamza, B. Berge, W. Mikosch and E. Rühl, Phys. Chem. Chem. Phys. **6**, 3484 (2004).

6 K. S. Hamad, R. Roth, J. Rockenberger, T. van Buuren, and A. P. Alivisatos, Phys. Rev. Lett. **83**, 3474 (1999).

Gold nanoparticles deposited on sulphide minerals: A combined SR-XPS and STM/STS study

Yu. Mikhlin[a], A. Romanchenko[a], L. Makhova[b], and R. Szargan[b]

[a] *Institute of Chemistry and Chemical Technology SB RAS, Krasnoyarsk,660049, Russia*
[b] *Wilhelm-Ostwald-Institut fur Physikalische und Theoretische Chemie, Universitat Leipzig, D-04103 Leipzig, Germany*

The chemical state and properties of noble metals deposited on metal sulphides is important for several fields. Particularly, so-called "invisible" gold in sulphide minerals forms mainly nanometer-scale metallic particles [1], which are expected to exhibit still poorly studied specific characteristics due to size and surface effects. The reduction of aqueous precious metal complexes is of interest also for concentrating these elements from hydrometallurgical solutions and for preparation of composite nanomaterials. Here, we applied synchrotron radiation XPS together with scanning tunneling microscopy and spectroscopy (STM/STS) to characterize gold species spontaneously deposited on natural metal sulphides under uniform conditions. An unusually strong suppression of electronic tunneling on gold nanoparticles was found both in XPS and STS.

Single crystals (pyrite, FeS_2, galena, PbS) or research grade polycrystalline mineral samples (arsenopyrite, FeAsS, chalcopyrite, $CuFeS_2$, pyrrhotite, Fe_7S_8, sphalerite, (Zn,Fe)S) were polished at silicon carbide paper and then were cleaned by wet filter paper. Some specimens were fractured in air just before microscopic studies or conditioning in aqueous solutions. In etching experiments, the samples were treated in 1 M HCl, 0.5 M H_2SO_4, 1 M HCl + 0.4 M $FeCl_3$, or 0.5 M H_2SO_4 + 0.2 M $Fe_2(SO_4)_3$ solutions without stirring at 50±2 °C, rinsed quickly with a respective cold dilute acid and then with distilled water. Gold was deposited on the minerals from unstirred solutions of $HAuCl_4$ (pH 1.5 or 3) at room temperature; the 10^{-4} M solution and 10 min exposure were used unless otherwise stated. The reacted samples were rinsed with water and allowed to desiccate in air before examination. Photoelectron spectra were measured at the Russian-German beamline equipped with a VG-CLAM 4 analyzer. The photon energy was usually 1000 eV, and the pass energy was 20 eV. Binding energies were corrected for electrostatic charging using the C 1s peak (285.0 eV). The spectra were fitted by convolution of Lorentzian and Gaussian functions using a Unifit program [2]. AFM, STM and STS investigations were performed using a Solver P47 device (NT-MDT, Russia) under ambient conditions in dry air. The tips used in STM/STS measurements were mechanically cut 90% Pt - 10% Ir wires; positive bias was defined as a positive voltage on the sample with respect to the tip.

The uptake of gold was semi-quantitatively characterized by S/Au ratios obtained from the broad XPS scans along with AFM and STM data. The quantities of gold deposited during 10 min contact of a mineral with $HAuCl_4$ media depend strongly on the preliminary treatment of a mineral, being lower for fracture surfaces. The quantities increase if the surfaces were moderately oxidized, in particular, as a result of polishing or exposure of minerals to atmosphere for several days. However, the oxidative etching in Fe^{3+}-bearing media retards the cementation of gold in many times. Figure 1 shows a series of Au 4f spectra from various samples. The peaks of dispersed metal are usually shifted to higher binding energies in comparison with that of a polycrystalline gold plate taken as a standard (83.6 eV). The lines have diverse widths and shapes due to contributions from a few gold species. The spectra are better fitted with three line. The component with binding energy of 83.6 eV can be assigned to bulk gold, and that shifted by 0.5-1 eV to a higher BE is associated with ultrasmall metal particles. A share of Au^+-S species (BE of 85 eV or higher) is minor in all the cases; it somewhat increases with decreasing the total amount of precipitated gold. The very broad Au 4f line observed in the case of sphalerite could be well fitted with similar three components.

Alternatively, the large band width can be explained in terms of non-uniform electrostatic charging of the surface of the wide gap semiconductor. In contrast, the Au 4f band for gold on galena is rather narrow and shifted by almost 1 eV. The uptake of gold onto pyrite surfaces is roughly proportional to the exposure duration; the Au $4f_{7/2}$ binding energy decreases with the growth of the surface concentration of gold, approaching the BE of bulk Au^0.

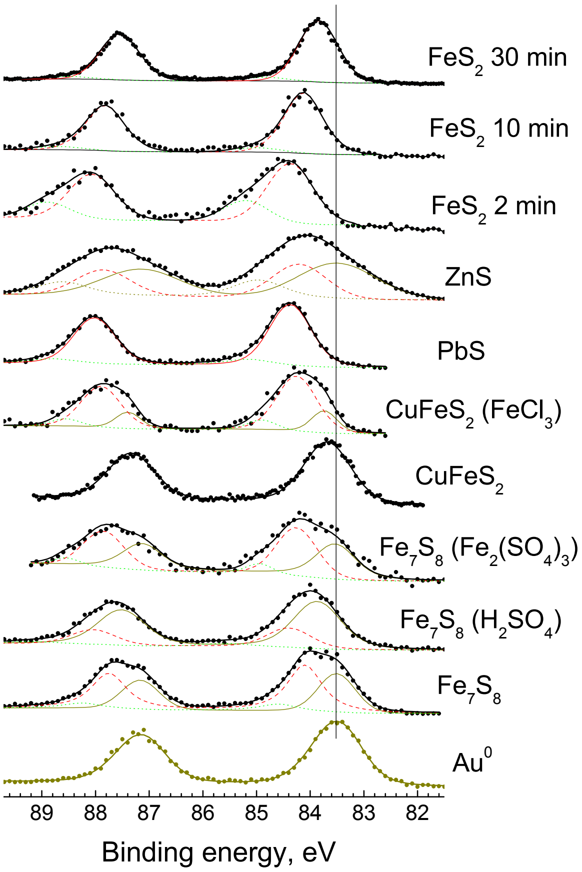

Fig. 1. Au 4f spectra from polycrystalline gold (Au^0) and polished minerals reacted with 10^{-4} M $HAuCl_4$ solution for 10 min; for pyrite the reaction times are shown near the spectra. Some specimens were treated before the gold deposition in solutions marked in brackets.

S 2p spectra from minerals after the deposition of gold demonstrate increased intensities at binding energies of about 163.5 eV, suggesting the formation of polysulfide anions within the reacted surface layers enriched in sulfur due to oxidation by Au(III) species. Only small amounts of sulfur-oxygen species are present. Unfortunately, it was difficult to distinguish a weak contribution from sulphur bonded to Au atoms. The changes of corresponding XPS spectra of metals were not rather informative, and X-ray absorption Fe L-, Cu L-, S L-edge spectra recorded in the TEY mode agreed in general with the above conclusions.

STM examination found that a considerable part of the surface of galena after 10 min conditioning in the 10^{-4} M $HAuCl_4$ solution is bespread with rather uniform gold particles of about 5 nm in diameter (Fig. 2a). A number of particles are placed above fairly loose first particle layer, while uncovered PbS spots up to several hundred nm in size still remain. Gold on the surfaces of pyrrhotite (Fig. 2b) and chalcopyrite represent nanoparticles from 3-5 nm to 30 nm in size, either isolated or arranged in submicrometer composite islands. STM images from pyrite show that gold islands grow both in the number and size from 5 nm to about 50 nm with increase in the deposition time. The majority of the islands are composed of nearly 10 nm clusters (Fig. 2c), which become harder packed over the reaction. The nanoscale inhomogeneity of the mineral surfaces arisen as a result of their oxidation and disordering was also observed.

Tunneling spectra measured above bare metal sulphide surfaces (Fig. 3) commonly display a conductance gap that is typical for semiconducting minerals, while the plots acquired above gold nanoparticles revealed a positive correlation between the current magnitude and the diameter of Au NPs. The tunneling currents increase as the nanoparticles associate to form composite islands and it disappears for dense gold films and sponges, approaching the curves from bulk metal.

The suppressed electronic tunneling seems to cause both the increase in Au 4f binding energies in XPS and the decline of currents in STS as compared with the bulk metal. These phenomena are attributable to Coulomb blockade effects, which take place if the electrostatic energy, $E = e^2/2C$, is larger than the thermal energy, with an insulating layer existing between a nanoparticle and substrate [3,4]. The temporal charging of a nanoparticle over the photoionization process in XPS decreases kinetic energies of the photoelectrons by their interaction with the photoholes formed at core levels in final state [5,6]. The diameter *d* of a gold nanoparticle should be less than 20 nm to be under the $E > kT$ requirement at room temperature and the effect scale obeys to $1/d$ law [6]. The effects have been found on gold nanoparticles less than 5 nm due to leakage currents and electron trapping in a majority of previous studies. In this study, the suppression of electronic tunneling was detected for clusters as large as 20-30 nm, implying special properties of the gold - metal sulphide systems, in particular, a dielectric coating on the oxidized metal sulphides or/and Au^0 NPs. Moreover, a submonolayer of adsorbed sulphur may retard the tunneling by modifying the surface electronic structure. The interaction between metal nanoparticles and supporting materials is known to influence the XPS binding energies too [5,6]. The linkage between the STS and XPS results give more credibility to the Coulomb blockade hypothesis, although it is possible that several factors have simultaneous effect.

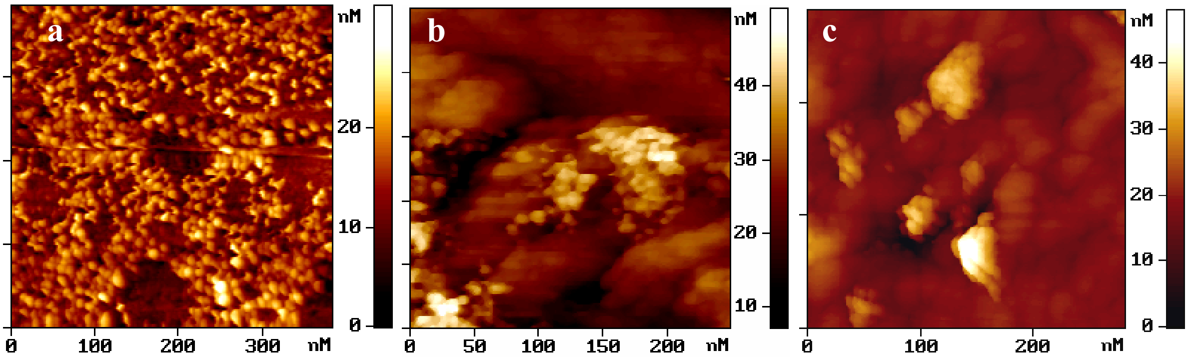

Fig. 2. STM images from the surfaces of (a) PbS (100) (I_{SP}=0.1 nA, V_B=-0.1 V), (b) monoclinic pyrrhotite (I_{SP}=0.2 nA, V_B= -0.4 V), and (c) pyrite (I_{SP}=0.6 nA, V_B=0.1 V) after interaction with 10^{-4} M $HAuCl_4$ solution for 10 min.

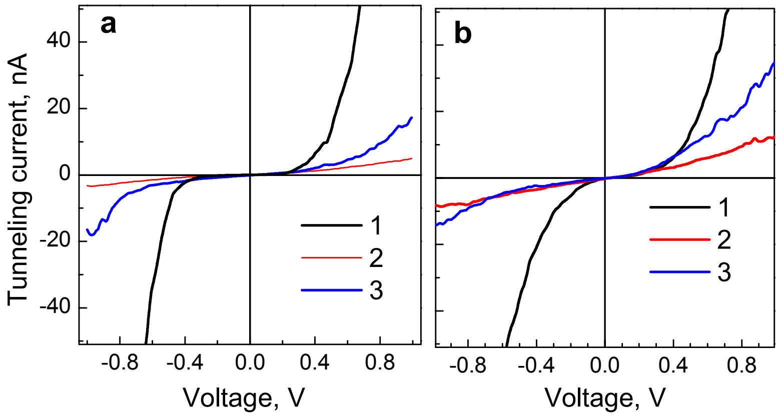

Fig. 3. Tunneling spectra from PbS (a) and FeS_2 (b) samples reacted in 10^{-4} M $HAuCl_4$ for 10 min measured above: (a) bare PbS surface (1), a separated ~5 nm Au^0 particle (2), and a composite formed by Au NPs (3), I_{SP}=0.1 nA, V_B=-0.1 V; (b) bare FeS_2 surface (1), ~12 nm Au^0 particle (2), associated Au NPs (3). I_{SP}=0.6 nA, V_B=-0.1 V.

This work was supported by the bilateral program “Russian-German Laboratory at BESSY”. We thank the staff of BESSY and the Russian-German Laboratory for technical assistance.

1. C. S. Palenik, S. Utsunomiya, M. Reich, S. E. Kesler, L. Wang, and R. C. Ewing, *Am. Mineral.*, **89,** 1359 (2004).
2. R. Hesse, T. Chassé, and R. Szargan, *Fresenius' J. Anal. Chem.*, **365**, 48 (1999).
3. M.-C. Daniel and D. Astruc, *Chem. Rev.*, **104**, 293 (2004).
4. T. Ohgi and D. Fujita, *Surf. Sci.*, **532–535**, 294 (2003).
5. J. Radnik, C. Mohr, and P. Claus, *Phys. Chem. Chem. Phys.*, **5**, 172 (2003).
6. H.-G. Boyen, A. Ethirajan, G. Kästle, F. Weigl, P. Ziemann, G. Schmid, M. G. Garnier, M. Büttner, and P. Oelhafen, *Phys. Rev. B*, **94**, 016804 (2005).

MAGNETIC DOMAINS STRUCTURES IN ULTRA-THIN $NiO/Fe_3O_4(100)$.

C. Boeglin[1], M. Pilard[1], O. Ersen[1], S. Cherifi[2], B. Carvello[2], F. Scheurer[1], P. Imperia[3],
B. Muller[1]
[1] IPCMS, Groupe Surfaces-Interfaces, 23, rue du Loess, Strasbourg CNRS-UMR7504,
[2] Laboratoire Louis Néel, Grenoble
[3]HMI - Berlin

Oxide nanostructures show fascinating new electronic and magnetic properties that suggest successful implementation in many devices of technological interest. In magnetic spin-valves the pinning of a ferromagnetic (FM) transition metal layer is provided by an antiferromagnet (AFM) such as NiO. The insertion of AFM NiO thin films in such complex spin-valve structures makes the characterization of their magnetic properties much more difficult.
Realistic models for the magnetic exchange coupling at the FM / AFM interfaces suggest an atomic-level description of these interfaces.

The way we decided to study this interfaces is to perform epitaxial growth of NiO on ferrimagnetic Fe_3O_4 (100) in the ultra-thin film and small cluster limit. The NiO AFM material is still a challenging by itself because of the complexity of epitaxial growth process and the non-trivial behaviour of the size dependent antiferromagnetic order. A complete work has been performed in our group in order to optimize the growth of NiO films and clusters on metals [1-3]. Since the magnetic properties of these AFM/FM bilayers are strongly related to the interface properties (interdiffusion, oxido-reduction in the metallic FM/AFM oxide layers respectively…) [1-4] we decided to stabilize the FM/AFM interface using a controlled oxidation of the metallic layer at the interface. The Fe_3O_4 template prevents the reduction of NiO and allows a direct measurement of the induced coupling into the Fe layer at the interface.
The measurements were performed at the UE 46 beam line at the Bessy synchrotron storage ring using polarized X-rays and the superconducting 7 Tesla magnet belonging to the IPCMS Strasbourg. The experimental environment of the sample in the superconducting 7 Tesla magnet (fig.1) allows us to prepare in-situ layers in UHV and to apply a magnetic field up to 7 Tesla at a temperature between 4 K and 300 K. The sample can be rotated in the field and with respect to the incident photon beam using two angular rotations, the incidence angle θ and the azimuth angle φ. This allows us to align a specific crystalline axis of the sample along the incident polarized photon beam, usually set parallel to the applied magnetic field. The complex sample rotation (θ, φ) reduces the possibility to work in the very low temperatures ranges of the cryostat (1 – 4 K).
In the framework of size dependent magnetic structures as well as magnetic coupling of AFM/FM spin valve systems we used X-ray magnetic circular and linear dichroïsm XMC(L)D in order to correlate the size dependent magnetism with the structure and topography obtained by LEED-STM. The main goal of our project is to study the magnetic coupling at the interface between a thin antiferromagnetic (AFM) NiO oxide layer and a ferrimagnetic (FM) Fe_3O_4 (100) layer using chemical and magnetic sensitivity of XMC(L)D. Moreover, magnetic field-dependent XMCD measurements at the FeL_3 edge allows to measure the chemical resolved magnetic hysteresis loops in order to probe the presence of exchange bias field and the NiO thickness dependence.
Starting from an ex-situ Fe_3O_4 (100) prepared and fully characterized template, an in-situ annealing procedure has been performed in order to obtain a clean and ordered Fe_3O_4 (100) surface. Comparing the XAS spectra recorded at the $FeL_{2,3}$ edges to XAS spectroscopic fingerprints of different iron oxides, we could define the chemical state of our sample before

performing the NiO growth. A complete angular dependent magnetic characterization of this ferrimagnetic template layer was performed previously to any deposit leading to reference data (Fig2). The measurements were performed along two azimutal orientations of the sample, the in-plane easy axis [100] and the in-plane hard axis [110]. A full set of incidence angles was considered along each direction in order to define the orientations of the hard and easy axis and the magnetocrystalline anisotropy before any magnetic coupling with the ultra-thin NiO layer (fig.3).

Our quantitative data show that the magnetic moment in Fe_3O_4 films is similar to bulk whereas its magnetic exchange coupling with ultra-thin NiO (1Å – 50Å) top-layer brings up new properties induced by the structural anisotropy of the interface. The relatively short sampling depth (about 2 nm) of the XMC(L)D technique, combined with the small thicknesses of the NiO enables sensitivity to the magnetic order in both materials in the vicinity of the interface. Thus we can explore the in-plane spin orientation with respect to crystallographic directions as a function of NiO thickness. We reveal the influence of the structural anisotropy in the NiO films on the magnetic properties at the interface with the Fe_3O_4 film. We show that the strength of the step-induced magnetic anisotropy at the NiO / Fe_3O_4 interface leads to a progressive and thickness dependent reduction of the spin and orbital magnetic moment in the Fe_3O_4 (100) near interface. XMCD quantitative data shows strong modifications of the spin and orbital magnetic moments in the Fe_3O_4 film as well as strong magnetic anisotropies induced by the structural anisotropy of the grown NiO layer.

The magnetic coupling between antiferromagnetic (AFM) NiO and ferrimagnetic (FM) Fe_3O_4 layers has been studied in the ultra-thin film limit. Performing circular and linear magnetic dichroïsm we describe the size dependent magnetic coupling at the NiO/ Fe_3O_4 interface. The strength of the step-induced magnetic anisotropy at the NiO / Fe_3O_4 interface leads to a progressive reduction of the spin and orbital magnetic moment in the Fe_3O_4 (100) near interface. We reveal the influence of the crystallogrophic and structural anisotropy in the NiO films leading to exchange induced specific magnetic properties in the Fe_3O_4 (100) layer.

[1] S. Stanescu, C. Boeglin, A. Barbier, J.P. Deville, Phys. Rev. B 67 (2003) 035419,
[2] S. Stanescu, C. Boeglin, A. Barbier, J.P. Deville, Surface Science 549 (2004) 172-182.
[3] PhD Thesis S. Stanescu – Univ. Strasbourg 2002
[4] H. Ohldag et al. PRL 86 (2001) 2878, H. Ohldag et al. Phys. Rev. Lett. 87 (2001) 247201

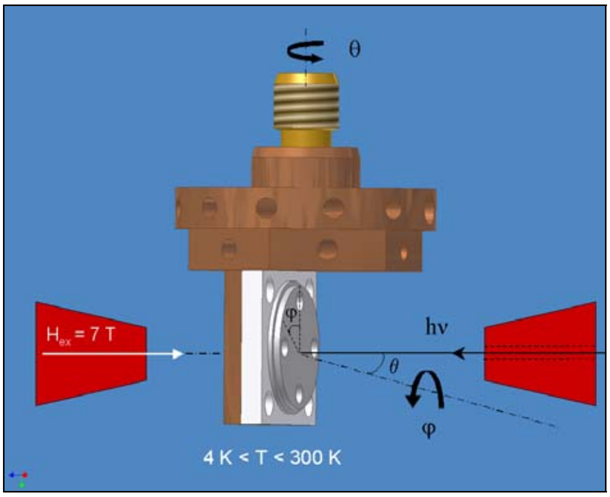

Fig. 1 : Sample holder with two rotation axis (incidence angle θ and azimuth angle φ) and temperature ranging from 4 K to 300 K. The applied magnetic field can be set to a maximum value of 7 Tesla.

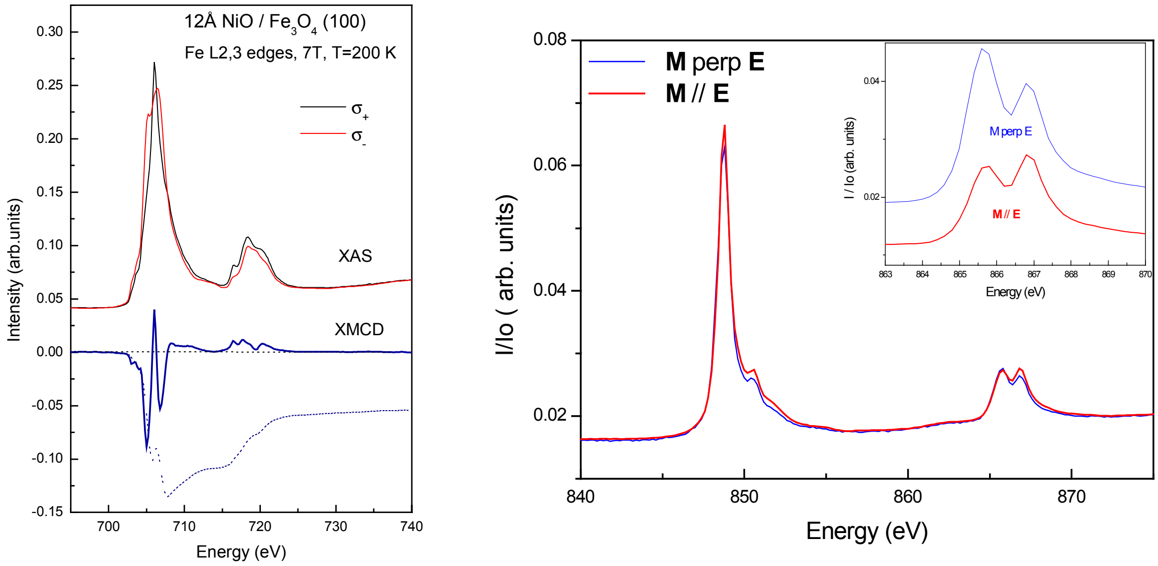

Fig. 2 : (a) X-ray absorption spectra (XAS) taken at the Fe $L_{2,3}$ edges with two oppositely circularly polarized light and the dichroism signal (XMCD) obtained at 200 K in an applied field of 6.5 Tesla. (b) XAS taken at the Ni $L_{2,3}$ edges with vertical and horizontal polarized light in normal incidence in the remanent state and at 200 K .

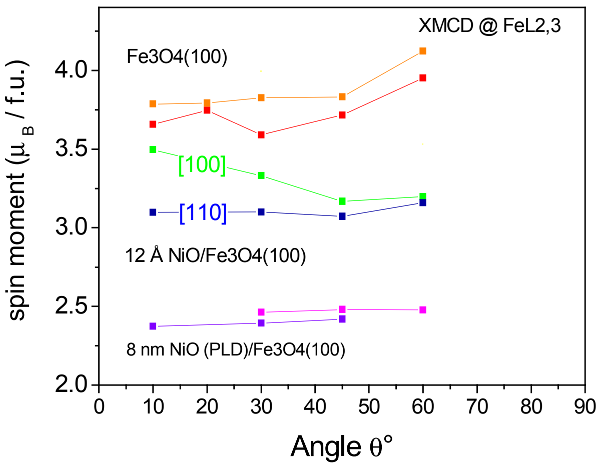

Fig. 3 : Angular evolution of the spin magnetic moment for clean $Fe_3O_4(100)$ before and after NiO growth.

Ion spectroscopy on a free water cluster jet

Silko Barth,[1] Volker Ulrich,[1] Sanjeev Joshi,[1] Axel Reinköster,[2] and Uwe Hergenhahn[1a]

1 Max-Planck-Institut für Plasmaphysik, Boltzmannstr. 2, 85748 Garching
2 Fritz-Haber-Institut der Max-Planck-Gesellschaft, Faradayweg 4-6, 14195 Berlin

The investigation of water clusters can help to understand the properties of the hydrogen network in liquid water, which still challenges theoretical and experimental physical chemists. We have constructed a molecular beam source for water clusters to carry out experiments at BESSY. For this project, in 2005 two weeks of beamtime at a dipole beamline and two weeks of single bunch beamtime at an undulator were alloted.
Experimental: Water clusters can be formed by expanding a jet of water vapour from a heated reservoir into vacuum. Our device is based on this principle, resembling work of other research groups [1]. The reservoir has a volume of 12 ml and it was heated up to 94°C. The hole nozzle with a diameter of 50 µm was operated at a slightly higher temperature of 102°C. Our vacuum setup consists of an expansion chamber (p = 1.6e-3 mbars) extending into the main vacuum chamber (p = 3e-6 mbars). The two volumes are separated from each other by a conical skimmer. The vacuum in the expansion chamber was maintained by two turbomolecular pumps with a total pumping speed of 390 l/s, while in the main chamber two turbomolecular pumps (1200 l/s) and a cryopump (900 l/s) evacuated the system. Clusters were ionized by synchrotron radiation of the TGM4 and the UE52/SGM beamlines. Ions were detected by a linear time-of-flight mass spectrometer with an acceleration region of 6 mm and a drift tube of 80 mm length (see also [2]). The extraction field was pulsed with a fixed frequency of 12.5 kHz for experiments in the multi-bunch mode. In single-bunch mode, alternatively it was possible to operate the instrument with static extraction fields and to measure the ion time-of-flight relative to the synchrotron radiation pulse.

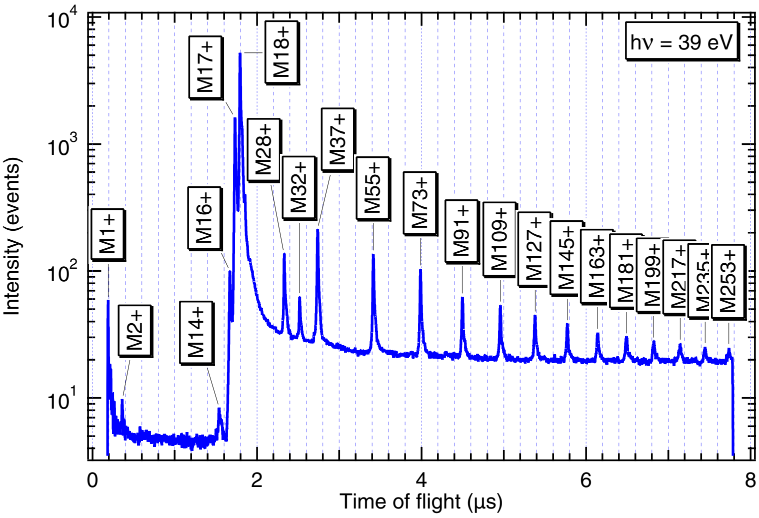

Figure 1: Mass spectrum of our water cluster jet. The largest observed fragment, 253 amu, pertains to the parent cluster $(H_2O)_{15}$.

Results: A typical mass spectrum obtained in multi-bunch mode is shown in Fig. 1. Only protonated water cluster ions can be detected, which is the behaviour observed in experiments with multi-photon laser ionization and electron impact ionization [3]. Due to the large

---

[a] Mailing address: IPP, c/o BESSY, Albert-Einstein-Str. 15, 12489 Berlin, E-Mail: uwe.hergenhahn@ipp.mpg.de

geometry change between the neutral and the ionized cluster, after ionization the clusters stabilize by emission of a neutral OH group.

Near-edge X-Ray Absorption (NEXAFS) spectra were recorded along the O 1*s* ionization edge. The partial yield for selected fragments is shown in Fig. 2. The yield curves for the molecular fragments agree with published data [4]. The first two pre edge excitations have been assigned to 1*s* excitations into the $4a_1$ and $2b_2$ antibonding orbitals. All features at higher energy have Rydberg character.

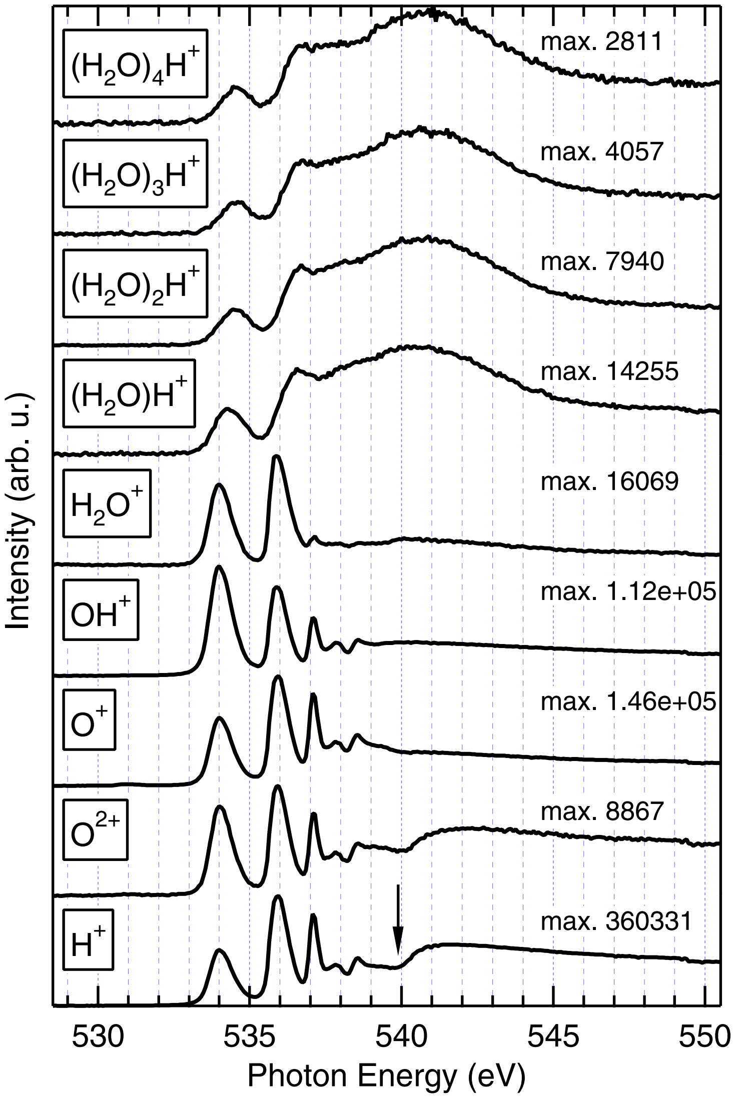

Figure 2: Partial ion yield curves of a free water cluster jet. Measurements were made with a time-of-flight analyser using a static extraction field in single bunch mode. The ionization threshold is 539.9 eV for molecular water (arrow) and about 1.4 eV below that for water clusters [1].

The yield curves for the cluster fragments show a marked dissimilarity with the molecular ones. Indeed, qualitatively they agree much better with published X-Ray absorption data for ice [5]. Comparing with the curves published in [5], we can say that the yield curves from the protonated cluster fragments we observe are in-between the data for surface and bulk ice. A feature typical for the NEXAFS curve of bulk ice is the shape-resonance like enhancement around 541 eV, a typical feature for NEXAFS of surface ice – and for liquid water – is the pronounced pre edge peak around 534.5 eV. Similar ion yield scans for the lightest two cluster fragments have been performed by Björneholm *et al.* [6].

We can obtain additional insight on the nature of these signals by comparing partial yield curves recorded with static and pulsed extraction fields. Due to the fixed, rather low frequency of the pulsed field, in this case only fragments with a low or vanishing kinetic energy release are sampled. This comparison is shown in Fig. 3. While the curves coincide over most of the data range, the shape resonance-like amplification appears to be less pronounced for pulsed extraction fields.

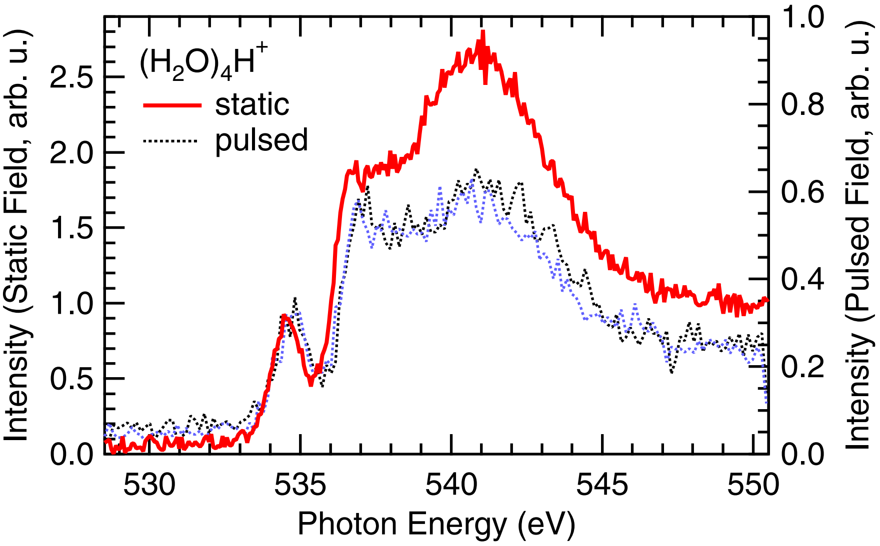

Figure 3: Comparison of the yield curve for the fragment with mass 73 amu measured with a static and a pulsed extraction field. Pulsed extraction fields with two different voltages were used in the experiment (black: 1240 V, blue 310 V).

More experimental work is needed to clarify the parentage of the fragments shown in Fig.s 2, 3 however. Preliminary ion-ion coincidence data recorded as part of this work show that above the O 1*s* ionization edge massive fragmentation of the clusters sets in as can be expected.

We have demonstrated that experimental ion spectroscopy on a water cluster beam can contribute to the understanding of this fascinating and most important substance.

Partial funding by DFG project He 3060/3-1,2 is gratefully acknowledged.

References

[1] C. Bobbert and C. P. Schulz, Eur. Phys. J. D **16**, 95 (2001); G. Öhrwall, R. F. Fink, M. Tchaplyguine, L. Ojamäe, M. Lundwall, R. R. T. Marinho, A. N. d. Brito, S. L. Sorensen, M. Gisselbrecht, R. Feifel, T. Rander, A. Lindblad, J. Schulz, L. J. Saethre, N. Martensson, S. Svensson, and O. Björneholm, J. Chem. Phys. **123**, 054310 (2005).
[2] A. Reinköster, S. Korica, G. Prümper, J. Viefhaus, K. Godehusen, O. Schwarzkopf, M. Mast, and U. Becker, J. Phys. B **37**, 2135 (2004).
[3] P. P. Radi, P. Beaud, D. Franzke, H.-M. Frey, T. Gerber, B. Mischler, and A.-P. Tzannis, J. Chem. Phys. **111**, 512 (1999).
[4] M. N. Piancastelli, A. Hempelmann, F. Heiser, O. Gessner, A. Rüdel, and U. Becker, Phys. Rev. A **59**, 300 (1999).
[5] P. Wernet, D. Nordlund, U. Bergmann, M. Cavalleri, M. Odelius, H. Ogasawara, L. A. Näslund, T. K. Hirsch, L. Ojamäe, P. Glatzel, L. G. M. Pettersson, and A. Nilsson, Science **304**, 995 (2004).
[6] O. Björneholm, F. Federmann, S. Kakar, and T. Möller, J. Chem. Phys. **111**, 546 (1999).

Multiplet splitting in X-ray Absorption Spectroscopy of Small, Size-selected Transition Metal Clusters on Alkali Metal Surfaces

J.T. Lau[1], L. Glaser[2], S. Hankemeyer[2], M. Martins[2], T. Möller[1], and W. Wurth[2]

[1] Technische Universität Berlin, IAPF, PN3-1, Hardenbergstraße 36, 10623 Berlin
[2] Universität Hamburg, Institut für Experimentalphysik, Luruper Chaussee 149 22761 Hamburg

e-mail: tobias.lau@tu-berlin.de

Electron localization and correlation are important factors determining the electronic structure of 3*d* transition metals [1], which retain some of their atomic properties even as itinerant bulk metals [2]. In free 3*d* transition metal atoms, Coulomb interaction of the 2*p* core hole with the localized 3*d* electrons leads to multiplet splitting of the $L_{2,3}$ absorption lines [3]. In bulk transition metals, valence electrons are partially delocalized. In addition, multiplet splitting might be masked by line broadening. The issue of electron localization/delocalization and correlation in the transition from single atoms to bulk metals can ideally be addressed in the investigation of size-selected transition metal clusters. So far, however, the 3d multiplet structure in $L_{2,3}$ X-ray absorption of deposited small metals clusters has not been observed neither on metal nor on HOPG substrates [4–7]. We report here on the first study of the multiplet structure of small chromium clusters deposited on thin potassium films on Cu(100). Potassium films were chosen as substrates, since 3*d* transition metal impurity atoms on alkali metal films show highly localized atomic configurations, as was conclusively shown in XAS for iron, cobalt, and nickel atoms [8].

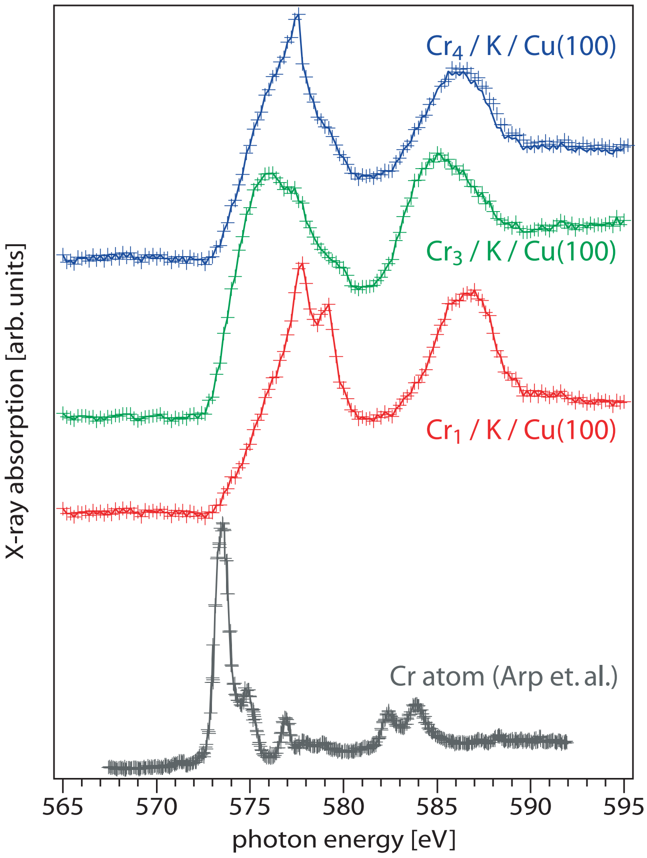

Figure 1: Chromium $L_{2,3}$ X-ray absorption spectra of small chromium clusters on thin K/Cu(100) films measured at 30 K.

For sample preparation, a Cu(100) single crystal was cleaned by repeated sputter and anneal cycles. Thin potassium films were prepared in UHV by evaporation of potassium from alkali metal dispensers (SAES getters). To obtain high quality thin films, these samples were annealed to the onset of potassium desorption [9]. From thermal desorption spectroscopy, we estimate the potassium film thickness to be about 10–15 monolayers. Chromium clusters were produced in a sputtering source [10] and deposited onto the potassium films by a soft-landing technique, using krypton as a buffer layer. For krypton desorption after cluster deposition, the sample was heated to 100 K. All sample preparation was carried out in UHV with a base pressure of less than 1×10^{-10} mbar. X-ray absorption (XA) spectra were taken in total electron yield mode. All spectra shown here were normalized to incoming photon flux. For the chromium spectra, a linear background has been fitted to the pre-edge region and was subtracted to account for a substrate absorption signal.

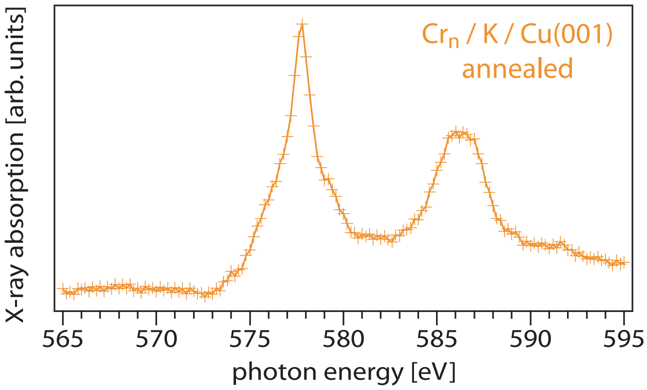

Figure 2: Chromium $L_{2,3}$ X-ray absorption spectra of small chromium clusters on thin potassium films after annealing to 320 K. The spectra are qualitatively similar for Cr_1, Cr_3, and Cr_4.

The $L_{2,3}$ X-ray absorption spectra of Cr_1, Cr_2, and Cr_4 on K/Cu(100), depicted in figure 1 clearly show a multiplet structure at the L_3 edge, proving that atomic-like line shapes can indeed be observed for small metal clusters on suitable metal substrates. Three different components can be distinguished at the L_3 edge of these clusters. In the corresponding spectrum of free chromium atoms [11], also shown in figure 1, three intense lines at the L_3 edge and two intense lines at the L_2 edge carry the main intensity. Although a detailed analysis of the experimental data is still in progress, comparison of the spectra in figure 1 suggests that the same components might also be visible in small clusters. However, they are not resolved at the L_2 edge of the clusters. The intensity at the L_2 edge is much higher for the clusters than for the atom. For the clusters, the branching ratio seems to be rather bulk like, as can be seen by comparison with electron energy loss spectra [12].

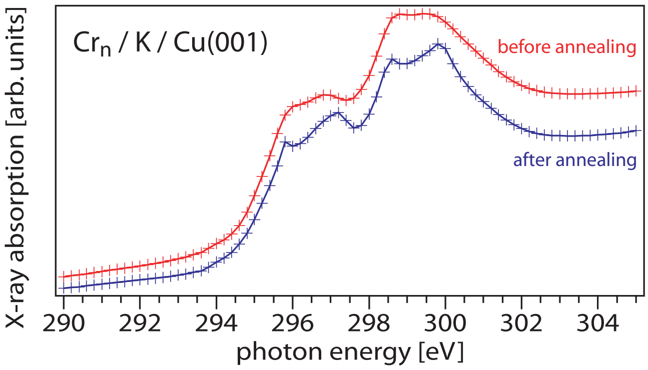

Figure 3: Potassium $L_{2,3}$ X-ray absorption spectra of Cr_n / K / Cu(100) before and after annealing to 320 K. The spectra are qualitatively similar for Cr_1, Cr_3, and Cr_4. No baseline has been subtracted.

Annealing the cluster samples to 320 K, just below the onset of potassium desorption, leads to visible changes in the XA spectra. After annealing, the spectra for all three cluster sizes studied are qualitatively very similar. An averaged spectrum is shown in figure 2. A preliminary analysis suggests that peak intensities change upon annealing, while peak positions seem to remain fixed. The main intensity at the L_3 edge is now concentrated in the medium energy line. Since all clusters yield the same spectra, annealing most likely results in cluster disintegration and chromium atom diffusion into the potassium film. This might be the result of high atomic mobilities in the potassium film close to the desorption temperature.

The effect of annealing on the potassium underlayer can be seen in figure 3. Here, potassium $L_{2,3}$ absorption spectra of the potassium films before and after annealing to 320 K are compared. Again, all spectra are qualitatively similar for all clusters studied. Before annealing, the spectra show a slight double peak structure in the spin-orbit split absorption lines. After annealing, the spectral features are narrower, as was also observed for CO/K/Ni(100) [13]. Here, the splitting of the lines was explained by crystal field splitting and loss of metallic character of the potassium film. A thorough analysis of the Cr/K/Cu(100) spectra is currently in progress. A slight decrease in intensity of the potassium $L_{2,3}$ XA spectra probably indicates potassium desorption upon annealing. The slight double peak structure visible in potassium $L_{2,3}$ XA might result from the krypton desorption procedure, where the sample is temporarily heated to 100 K and adcluster diffusion might already occur.

In summary, we could observe for the first time atomic-like absorption lines of small transition metal clusters on metal substrates. Further investigations will yield a more detailed understanding of the evolution of electronic properties in small metal clusters.

We gratefully acknowledge technical support by BESSY staff members as well as stimulating discussions with P. Gambardella, P. Zimmermann and A. Föhlisch.

References

[1] G. van der Laan, J. Electron Spectrosc. Relat. Phenom. **117–118**, 89 (2001).

[2] M. Magnuson, N. Wassdahl, A. Nilsson, A. Föhlisch, J. Nordgren, and N. Mårtensson, Phys. Rev. B **58**, 3677 (1998).

[3] M. Martins, K. Godehusen, T. Richter, P. Wernet, and P. Zimmermann, J. Phys. B: At. Mol. Opt. Phys. **39**, R79 (2006).

[4] J. T. Lau, A. Achleitner, and W. Wurth, Surf. Sci. **467**, 834 (2000).

[5] J. T. Lau, A. Föhlisch, R. Nietubyč, M. Reif, and W. Wurth, Phys. Rev. Lett. **89**, 057201 (2002).

[6] K. Fauth, S. Gold, M. Heßler, N. Schneider, and G. Schütz, Chem. Phys. Lett. **392**, 498 (2004).

[7] M. Reif, L. Glaser, M. Martins, and W. Wurth, Phys. Rev. B **72**, 155405 (2005).

[8] P. Gambardella, S. S. Dhesi, S. Gardonio, C. Grazioli, and C. Carbone, Phys. Rev. Lett. **88**, 047202 (2002).

[9] W. Frieß, Ph.D. thesis, Technische Universität München, 1995.

[10] J. T. Lau, A. Achleitner, H.-U. Ehrke, U. Langenbuch, M. Reif, and W. Wurth, Rev. Sci. Instrum. **76**, 063902 (2005).

[11] U. Arp, K. Iemura, G. Kutluk, T. Nagata, S. Yagi, and A. Yagishita, J. Phys. B: At. Mol. Opt. Phys. **28**, 225 (1995).

[12] J. Fink, T. Müller-Heinzerling, B. Scheerer, W. Speier, F. U. Hillebrecht, J. C. Fuggle, J. Zaanen, and G. A. Sawatzky, Phys. Rev. B **32**, 4899 (1985).

[13] J. Hasselström, A. Föhlisch, R. Denecke, and A. Nilsson, Phys. Rev. B **62**, 11192 (2000).

Study of chemically synthesized bimetallic nanoparticles by XMCD

O. Margeat[a], D. Ciuculescu[a], C. Amiens[a], B. Chaudret[a], P. Lecante[b], K. Fauth[c], M. Kawwam[c], G. Schütz[c]

a: LCC-CNRS, 205, route de Narbonne, F-31077 Toulouse
b: CEMES-CNRS, 29, rue Jeanne Marvig BP 4347 F-31055 Toulouse
c: Max-Planck-Institut für Metallforschung Heisenbergstr. 3 D-70569 Stuttgart

Soft ferromagnets are of interest for many applications; especially in the nanosized regime they could be relevant to reduce the size of inductors for on chip electronic devices. Size control of NiFe nanoparticles has recently been achieved in our group via the combined use of organometallic precursors and organic ligands (such as long chain carboxylic acid and amine mixtures) during a liquid phase synthesis process[1]. The particles have been characterized by transmission Electron Microscopy (TEM-Figure 1), Wide Angle X-Ray Scattering (WAXS-Figure 2) and Extended X-Ray Absorption Fine Structure (EXAFS) measurements, and magnetic measurements by SQuID (Figure 3). A typical TEM image is displayed Figure 1, showing particles of mean size 2.4nm, well sprayed on the carbon foil of the TEM grid. Interestingly, the structure of these particles is different from that determined for the bulk phase of identical composition as evidenced by WAXS (Figure 2). This structure is surprisingly close to one adopted by Mn in the bulk (β-Mn), which means a larger distribution of metal-metal distances and a globally more compact arrangement. This effect can be related either to surface stress arising from the high surface/core ratio of atoms or to a strong effect of the chemical environment used to control the synthesis as already observed for Fe[2], Co[3] or CoRh[4] systems. Given this exotic structure and the well known sensitivity of the iron magnetic moment on structural details, one can expect that the magnetization in the nanoparticles might deviate considerably from bulk material properties. Furthermore a fit of the ZFC/FC curve leads to an anisotropy value of 3.10^5 J/m^3, i.e. almost 200 times more than in the bulk. Accordingly we can expect a large increase of the orbital moment. This can be related to both size effect and structural changes and raises the question of the atomic distribution in the particle.
We have thus studied the magnetic properties with element sensitivity by XMCD at the $L_{2,3}$-edges of both nickel and iron atoms to determine their spin and orbital contributions to the magnetic properties of the NiFe nanoparticles.

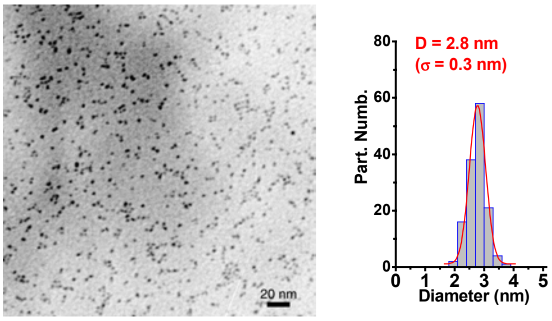

Figure 1 :
TEM image of NiFe particles and related size histogram

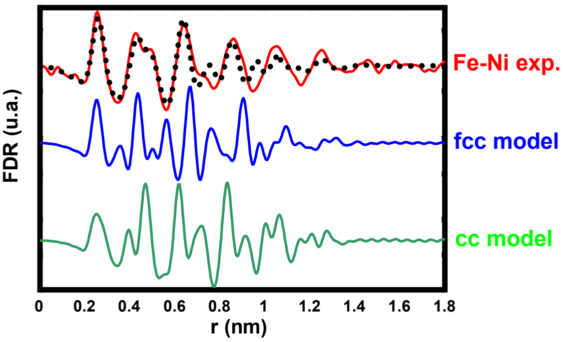

Figure 2 :
Experimental (red) Radial Distribution Function (RDF) obtained by WAXS investigation and comparison to RDF computed from fcc (blue) or cc (green) models, and from a polydetrahedral arrangement such as in β-Mn (doted black line)

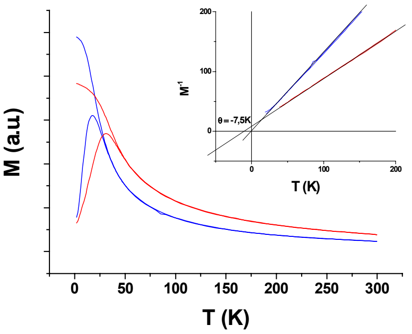

Figure 3 :
ZFC/FC curves on diluted NiFe particles (blue) and interacting NiFe particles (red).

Experiments were carried out on line PM-3. The nanoparticles were deposited as dense layers on silicon substrate in a glove box and transferred into the measurement chamber via a transfer container kept under high vacuum. XAFS spectra were first recorded at both edges (Figure 4), first on as prepared samples, and after voluntary exposure of the samples to air. First, typical absorptions are observed, characteristic of non oxidized nickel and iron atoms. It is noteworthy that in the presence of traces of oxygen, oxidation is observed at iron edge, while nickel XAFS spectrum remains unchanged. After further exposure of the sample to air, nickel atoms start to oxidize. At this stage, the iron content of the nanoparticles if fully oxidized. However, some nickel atoms remain in the metallic state. These results are indicative of a partial chemical segregation in the particles, their surface being enriched in iron while nickel atoms are mainly buried in the core of the particles. This has been further confirmed by Mössbauer studies (Figure 5). Indeed the best fit of the Mössbauer spectra evidence as major contributions: iron atoms (C4: 20%), with high IS and hyperfine field, corresponding to segregated iron atoms at the nanoparticles surface, a NiFe mixed phase (C2 and C3 : 63%) and iron atoms in a nickel rich environment (C1: 15%). These results are once again consistent with a nickel rich core surrounded by an iron rich surface, with a progressive enrichment in iron atoms from the core to the surface of the nanoparticles.

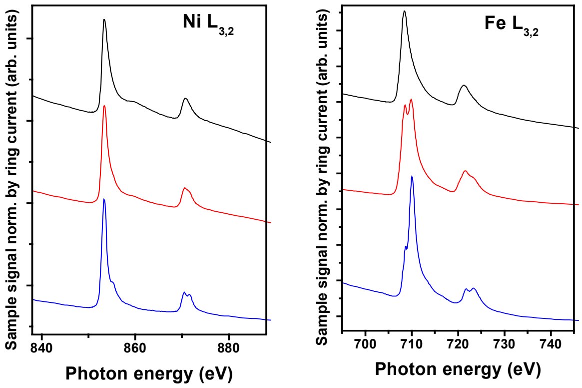

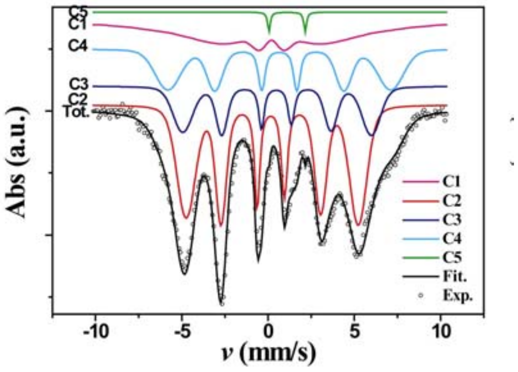

Figure 4: Effect of progressive oxidation on XAFS spectra at Ni and Fe $L_{2,3}$ edges

Figure 5: Mössbauer spectrum recorded at 4K and the 5 contributions to the fit.

Magnetisation loops recorded both at low temperature and close to room temperature at both Fe and Ni edges show that iron and nickel are strongly coupled despite the core-shell structure of the nanoparticles.[5]
XMCD signals were then recorded at various temperatures (Figure 5, T=85K, B = 2.5T) and the magnetic spin and orbital contributions were calculated [6]. Results are reported Table 1. At 14K the value of the magnetic moment per atom is 1.52 μ_B, which allows to estimate the value at saturation: μ =1.58 μ_B, in excellent agreement with the value determined previously from SQUID measurements (1.69 +/- 0.05 μ_B at 2K, 5T).[1]

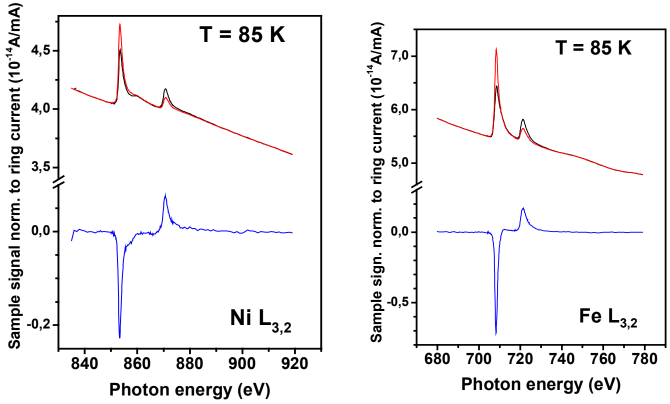

Figure 6:
XMCD signal recorded at 85K at both edges

	Fe			Ni		
	µS	µL	µL/µS	µS	µL	µL/µS
14K	1.8	0.11	0.06	1.0	0.13	0.13
85K	1.8	0.14	0.08	0.95	0.09	0.09
268K	1.6	0.08	0.05	0.93	0.02	0.02

Table 1: Ni and Fe spin and orbital magnetic moments as deduced from XMCD measurements (14K, 2.5T)

These results evidence a strong polarisation of nickel atoms and large orbital contributions as compared to the bulk metal. However, whereas this is the direct consequence of size reduction or chemical segregation inside the particles, is an open question.

Acknowledgements:
We thank C.-H. Fischer and I. Lauermann (both HMI) for access to the CISSY glove-box system, and the permission to adapt it for our transfer purposes. Thanks also to A. Vollmer and M. Neeb (BESSY) for the vacuum transfer chamber. This project was supported by the EU. Contract number : RII 3 CT-2004-506008.

[1] (a) O. Margeat et al. *Synthèse et propriétés de nanoparticules de FeNi obtenues par voie organométallique.* Oral presentation Journée Grand Sud-Ouest, SFC, Oct**. 2004**, Toulouse. (b) *Synthesis of NiFe Nanoparticles : a new structure, new physical properties.* O. Margeat, C. Amiens, B. Chaudret, M. Respaud, P. Lecante, in preparation

[2] (a) C. Amiens et al. *Magnetic Properties of Iron Nanoparticles of New Crystal Structure.* Oral presentation, MRS, Boston Nov; **2004**.

[3] F. Dassenoy, M.-J. Casanove, P. Lecante, M. Verelst, E. Snoeck, A. Mosset, T. Ould Ely, C. Amiens, B. Chaudret, *Experimental Evidence of Structural Evolution in Ultra Fine Cobalt Particles Stabilized in Different Polymers. From a Polytetrahedral Arrangement to the Hexagonal Structure.* J. Chem. Phys. **2000**, 112, 8137-8145.

[4] D. Zitoun, M. Respaud, C. Amiens, B. Chaudret, A. Serres, M.-J. Casanove, M.-C. Fromen, P. Lecante, *Magnetic Enhancement in Nanoscale CoRh Particles*, Phys. Rev. Lett., **2002**, 89(3), 37203.

[5] O. Margeat, D. Ciuculescu, C. Amiens, B. Chaudret, P. Lecante, K. Fauth, M. Kawwam, G. Schütz**,** *XMCD Studies of FeNi Nanoparticles Synthesized by an Organometallic Approach,* Poster, User meeting, Bessy 2005

[6] O. Margeat, D. Ciuculescu, C. Amiens, B. Chaudret, P. Lecante, K. Fauth, M. Kawwam, G. Schütz, manuscript in preparation.

Electron correlation in Rare Earth Phosphate Nano-particles studied by NEXAFS and Resonant inelastic X-ray scattering

E. Suljoti, A. Pietzsch, M. Nagasono, A. Föhlisch and W. Wurth
Institut für Experimentalphysik, Universität Hamburg,
Luruper Chaussee 149, 22761 Hamburg

Lanthanide phosphate nanocrystals ($LaPO_4$ – $YbPO_4$), capped by organic ligands were chemically prepared in liquid-phase synthesis [1]. These nanocrystals have a mean-size of 5-6 nm, high crystallinity and a good solubility in different organic solutions as well as a high luminescence quantum yield, which makes them useful in a variety of applications. As a consequence, it is interesting to study their electronic structure, as a function of lanthanide-ion, cluster size and interface between cluster and ligands. In order to investigate the unoccupied density of states of these clusters we have recently performed near edge x-ray absorption fine structure spectroscopy (NEXAFS).

The Lanthanide nanocrystals were dissolved in 1% solutions of Methanol, and spin-coated on p-type (100) silicon wafers. The Si surfaces were hydrogen-passivated by HF etching to remove the surface oxide. Scanning electron micrographs (SEM) of the spin coated layers showed an uniform size distribution of the nanocrystals in a densely packed layer on the Si surface.

Using the example of $ErPO_4$ nanocrystals, we observe significant differences in the Er $N_{4,5}$ –edge (4d) NEXAFS depending on the detection mode we employ (Figure 1). In Total Electron Yield (TEY) we measure different spectral weights in comparison to the Partial Fluorescence Yield (PFY) (0-30eV energy loss), where only a subset of decay channels is monitored.

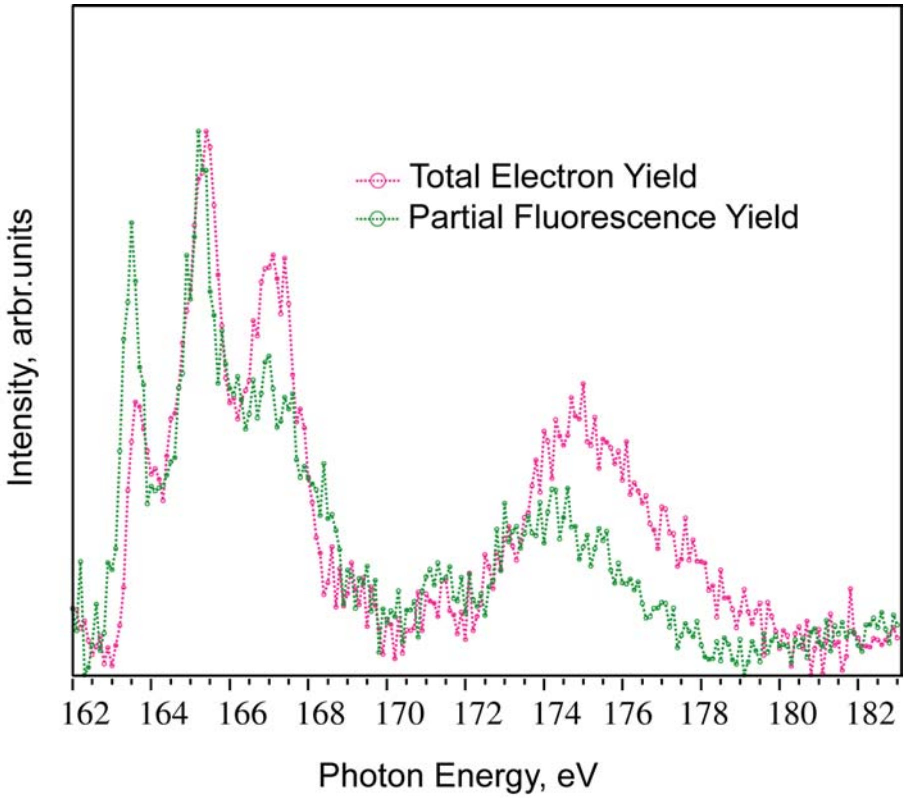

Figure1. NEXAFS of a monolayer $ErPO_4$ colloidal nanocrystals spin coated on a Si (100) wafer. Significant differences in Total Electron Yield and Partial Fluorescence Yield occur.

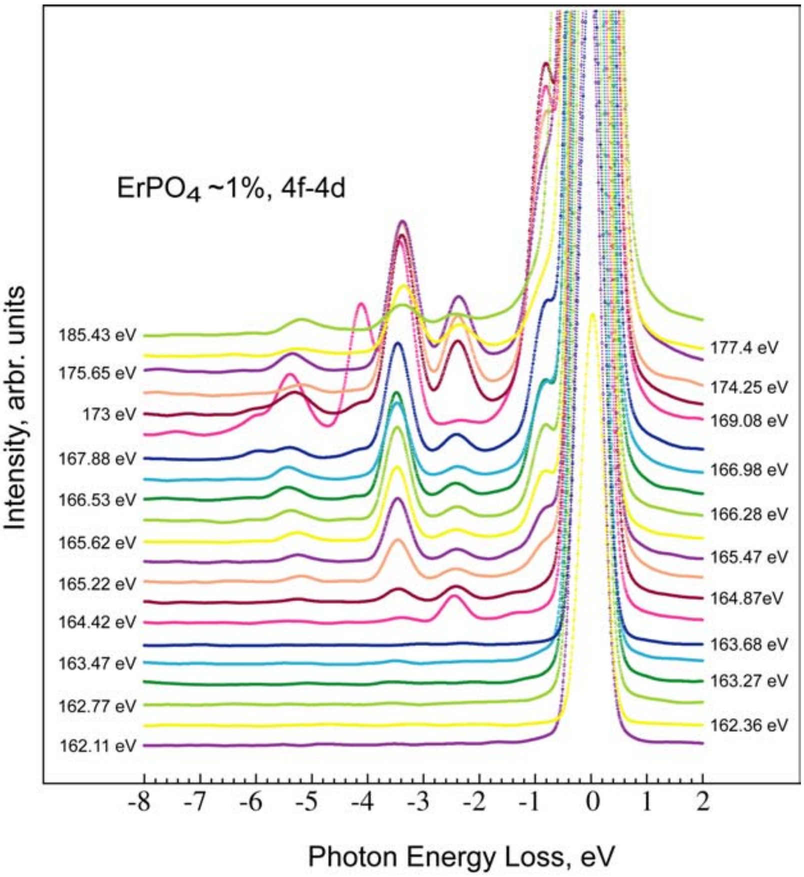

Figure 2. Resonant inelastic X-ray scattering in $ErPO_4$ nanocrystals for different excitation energies according to Fig. 1. Different valence electron-hole final states depending on the excitation energy are created

In the previous part of our investigation, we have established that all the lanthanide-ions in the rare earth phosphate nanocrystals, including Er are in a ‘3^+’ configuration.
To investigate the electron correlation, indicated by the NEXAFS spectra (Fig. 1), we have performed resonant inelastic X-ray scattering (RIXS), with highly selective resonant and detuned excitation.
In Figure 2 the $ErPO_4$ RIXS are summarized. As the inelastic scattering process leads to a valence excited final state (1h,1e), different excitation energies emphasis different electron/hole final states. The focus of our investigation is now to determine deviations between nano-scale crystals and macroscopic crystals, which differ in terms of the surface contributions and eventually in their intrinsic geometric structure.

We are thankful for the nanocrystals by Prof. M. Haase und K. Rücker. We acknowledge support by the DFG Graduiertenkolleg ‘Spektroskopie an lokalisierten atomaren Systemen, Felder und lokalisierte Atome – Atome und lokalisierte Felder’ and the SFB 508 ‘Quantenmaterialien – laterale Strukturen, hybride Systeme und Cluster –‘ .

[1] O. Lehmann, H. Meyssamy, K. Kömpe, H. Schnablegger and M. Haase,
J. Phys. Chem. B **107** (2003) 7449.

Magnetic properties of CoPt clusters and nano particles

L. Glaser*, M. Martins*, M. Wellhöfer*, W. Wurth*, V. Alesandrovic†, H. Weller†, C. Boeglin‡

*Universität Hamburg, Institut für Experimentalphysik, Luruper Chaussee 149, D-22761 Hamburg
†Universität Hamburg, Institut für Physikalische Chemie, Grindelallee 117, D-20146 Hamburg
‡Institut de Physique et Chimie des Materiaux de Strasbourg, 23 rue du Loess BP43, 67034 Strasbourg

Small metal clusters show a strong size dependence of their physical properties. Element specificity and the ability to investigate low target densities makes x-ray magnetic circular dichroism (XMCD) an ideal tool for the exploration of the magnetic structure of low coverage cluster systems [1–4]. In the context of possible applications in magnetic storage media, alloys of 3d metal atoms as Co or Fe with heavy elements like Pd or Pt are promising candidates. Therefore we have started to investigate the magnetic properties of CoPt systems in the size range from very small, mass selected clusters made of several atoms up to nano particles with a diameter of a few nm.

The experiments on the mass selected clusters have been performed using our UHV cluster source, which is described in detail in [5]. The small clusters are generated by high energy ion bombardment (Xe^+) of a cobalt/platinum target. After mass separation using a magnetic dipole field, the clusters are decelerated and deposited onto a thin, out of plane magnetized Fe/Cu(100) surface utilizing krypton as buffer gas in a soft landing scheme. XMCD measurements have been performed under UHV conditions at a base pressure below $3 \cdot 10^{-10}$mbar. The samples have been prepared in situ under UHV conditions and the dichroism spectra have been recorded using the total electron yield (TEY), i.e. the sample current. The measurements have been performed at beamline UE52/1-SGM in a normal incidence geometry.

The nano particles have been prepared chemically [6] and are deposited on a Si wafer as a substrate. Different methods, as spin and dip coating have been applied to create nano particle thin films with a coverage up to one monolayer. The XMCD measurements on the nano particles have been performed in a strong magnetic field up to 7 T using a super conducting magnet at the beamlines UE46-PGM and UE56/2-PGM/1 also in a normal incidence geometry.

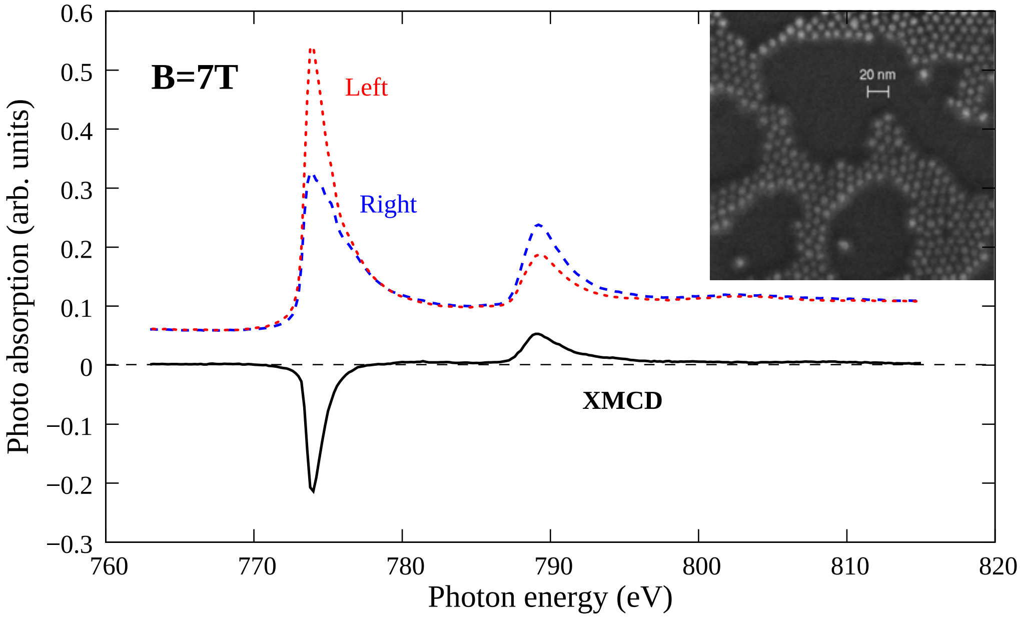

Figure 1: Typical XMCD spectrum of a $CoPt_3$ nano particles sample taken with a magnetic field B=7 T at the Co $L_{2,3}$ edges. The inset shows an SEM image of the sample.

Figure 1 shows a typical XMCD spectrum of a $CoPt_3$ sample at the Co $L_{2,3}$ edges. The inset shows a SEM image of the sample. For possible future applications the chemical stability and the aging of the nano particles is highly important. Figure 2 shows the spectra of two different $CoPt_3$ samples of different age and size. In this case the 7.6 nm sample has been measured approx. 6 month after the synthesis of the nano particles, whereas the 5.0 nm sample is only 2 weeks old.

Clearly in the older 7.6 nm sample a fine structure can be observed, due to oxidation of the Co. Also the newer sample shows some fine structure, however, to a much lower extend. The observed fine structure has no influence on the dichroism spectrum, which has also the shape as in figure 1.

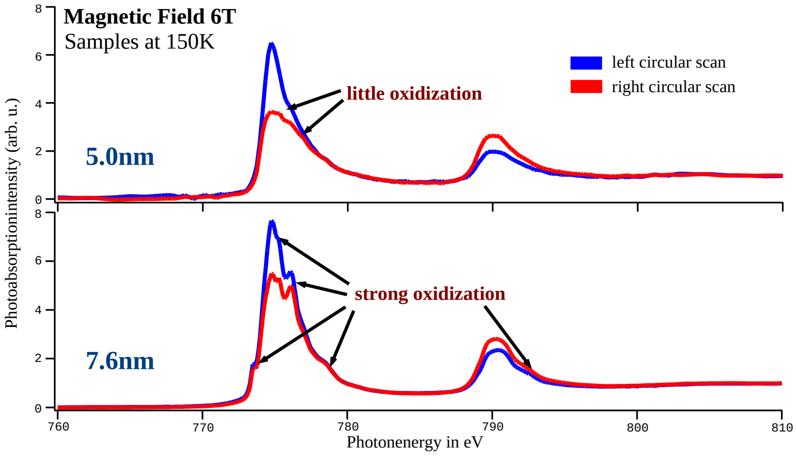

Figure 2: Absorption spectra taken from two samples (5.0 nm, new and 7.6 nm, old) with circular polarized light. The “old” sample shows a strong oxidation.

In figure 3 the spin and orbital moments of different samples, which have been calculated using the XMCD sum rules [7], are depicted. Whereas the orbital moment is not affected by the aging (oxidation) the spin moment drops by 30% from $\approx 2.3\mu_B$ for the new samples down to $\approx 1.6\mu_B$ for the older samples.

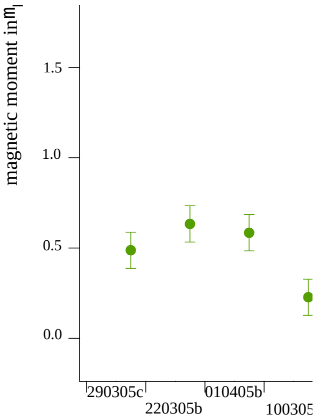

Figure 3: Magnetic spin and orbital moments of different $CoPt_3$ nano particles.

To study the influence of the Pt atoms on the Co atoms in detail we have measured the XMCD spectra of mass selected Co_nPt_m clusters; a typical mass spectrum using a 25% Co/75% Pt alloy target is shown in figure 4.

In the right part of figure 4 a typical absorption and XMCD spectrum is shown for deposited $CoPt_2$ clusters. Due to the low coverage of only 3% of a monolayer, the photoabsoprtion and the XMCD signal a very weak. This makes the ongoing analysis of the spectra complicated, due to the strong EXFAS oszillation from the thin Fe film.

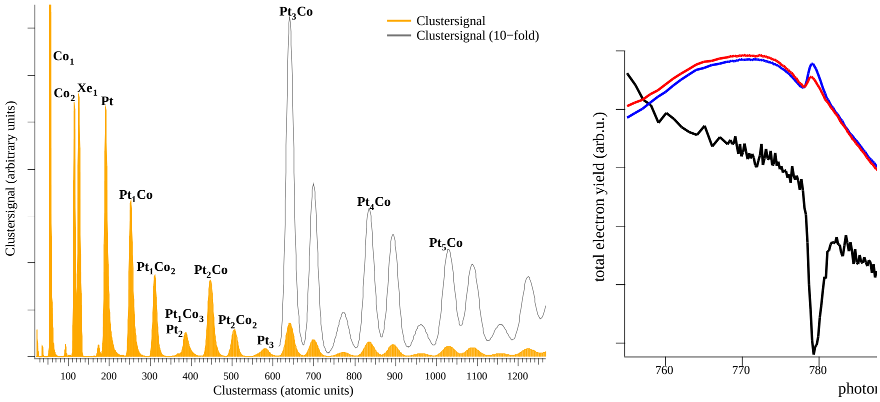

Figure 4: Left: Mass spectrum obtained by our cluster source using a 25% Co, 75% Pt alloy target. Right: X-ray absorption and XMCD spectrum measured for deposited CoPt$_2$ clusters.

The authors would like to thank the BMBF for financial support through grant 05KS4GUB/6 and the BESSY staff for their support during the beamtimes.

References

[1] F. Gambardella, A. Dallmeyer, K. Maiti, M. Malagoli, W. Eberhardt, K. Kern, and C. Carbone, Nature **416**, 301 (2002).

[2] F. Gambardella, S. Dhesi, S. Gardonio, C. Grazioli, P. Ohresser, and C. Carbone, Phys. Rev. Lett. **88**, 047202 (2002).

[3] P. Gambardella, S. Rusponi, M. Veronese, S. S. Dhesi, S. Rusponi, M. Veronese, S. S. Dhesi, P. H. Dederichs, K. Kern, C. Carbone, et al., Science **300**, 1130 (2003).

[4] J. T. Lau, A. Föhlisch, R. Nietubyc, M. Reif, and W. Wurth, Phys. Rev. Lett. **89**, 057201 (2002).

[5] J. Lau, A. Achleitner, H.-U. E. amd U. Langenbuch amd M. Reif, and W. Wurth, Rev. Sci. Instr. **76**, 063902 (2005).

[6] E. Shevchenko, D. Talapin, A. Rogach, A. Kornowski, M. Haase, and H. Weller, J. Am. Chem. Soc. **124**, 11480 (2002).

[7] G. van der Laan, J. Electron Spectrosc. Relat. Phenom. **101-103**, 859 (1999).

ASAXS investigation of gold nanoparticles in glass

[1]A. Hoell, [1]I. Zizak, [2]D. Tatchev, [1]S. Haas, [3]M. Eichelbaum, [3]K. Rademann, [1]J. Banhart
[1]Hahn-Meitner-Institut, Department of structural research, D-14109 Berlin
[2]Institute of Physical Chemistry, Bulgarian Academy of Science, BG-1113 Sofia
[3]Humboldt-Universität zu Berlin, Institut für Chemie, D-12489 Berlin

Colorless glasses doped with very few Au atoms become characteristically ruby-colored after annealing because of the formation of gold colloids. The absorption of light is caused by an exitation of collective oscillations of gold valence electrons, called surface Plasmon resonance. The wavelength of the Plasmon depends on size, shape, topology and the dielectric environment of the metal clusters [1, 2]. Some years ago the nonlinear optical properties of gold nanoparticles became accessible. Therefore it is a challenge to control locally the size, and shape of gold clusters in glasses. The nucleation process of gold clusters can be activated by using synchrotron radiation [3].

Nanosized gold clusters were obtained in glasses of composition 70SiO$_2$-20Na$_2$O-10CaO (mol %) which contains 0.01 mol% of dispersed Au. The gold nanoparticles were grown during annealing at 550^{o}C up to 30 min in regions previously irradiated by 32 keV X-rays. These glasses exhibit interesting nonlinear optical properties that depend on the size and the size distribution of the nanoparticles. Therefore, the aim is to estimate the particle size distributions and their homogeneity by ASAXS.

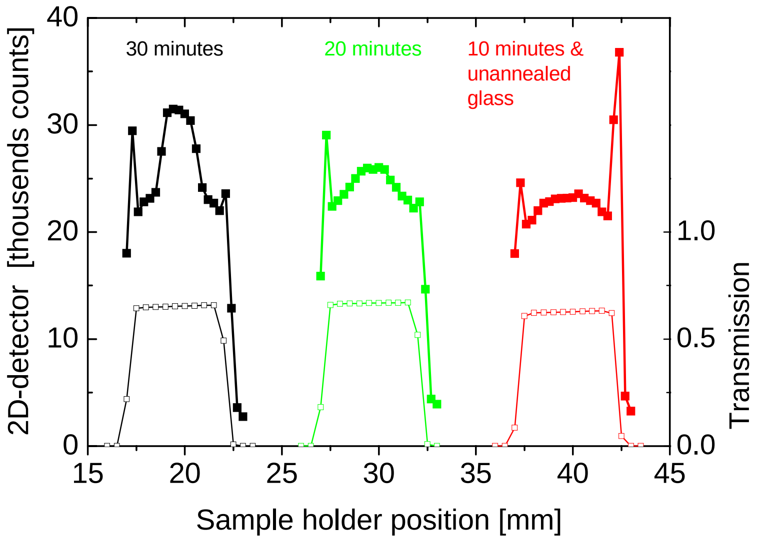

Figure 1: After annealing for 30 minutes the irradiated area scatters significantly stronger than the non-irradiated and also stronger than the shorter annealed samples. In comparison the transmissions in the graphs below show no effect.

In Fig. 1 the integral detector intensities of three different annealed samples are shown as the function of the sample positions. Do to the small amount of gold the transmissions of the irradiated and non irradiated regions are the same showing that the compositions are unchanged. The differences of the intensities from the irradiated and non irradiated area collected by the 2D detector suggest that the growth behavior of gold nanoparticles is faster in irradiated regions.

As shown in Figure 2 the intensity of the scattering at small angles increases with the annealing time, from 10 to 30 min, due to the process of nucleation and growth of gold nanoparticles. The strong anomalous effect near the Au absorption edge, L$_{III}$, is presented in Figure 2.

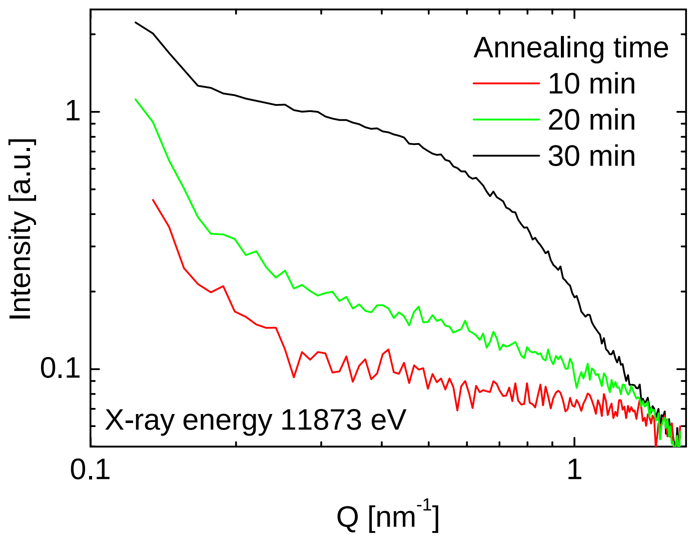

Figure 2: Scattering curves for samples annealed for different time periods at 550°C, measured in the pre-irradiated regions.

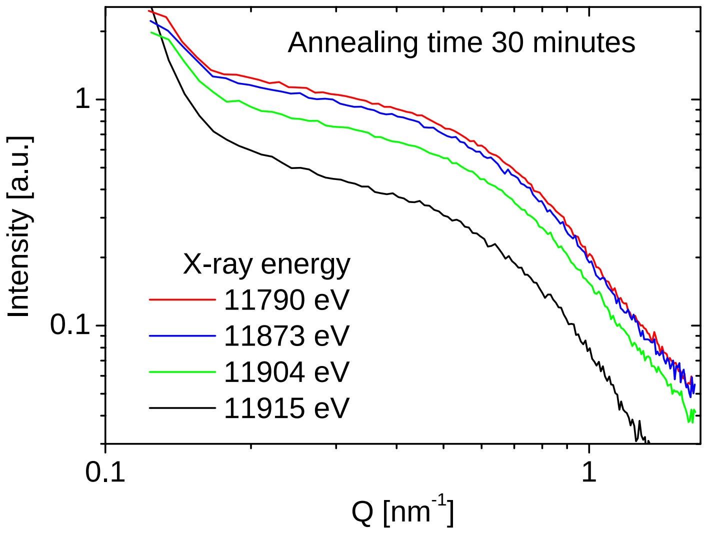

Figure 3: The scattering curves measured at different energies show very clear anomalous scattering effect. $E_k(L_{III})$=11919 eV

A nice outcome is depicted in Figure 3. The Guinier radius of the particles is independent of the x-ray energy. This proves that the particles are homogeneous.

After background subtraction, the scattering curves were fit with spherical particle model by the maximum entropy method. Figure 4 shows the differential volume fraction size distributions for two annealing times. It is seen that the particle size and volume fraction grow with the annealing time.

These results represent the first anomalous small angle x-ray scattering experiment performed with the new ASAXS device installed on the 7T-WLS beamline at BESSY.

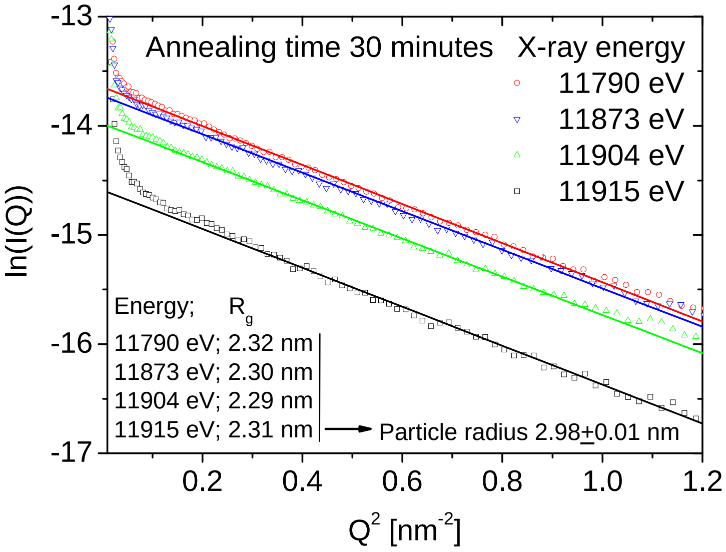

Figure 3 The Guinier radius is independent on the x-ray energy. This means that the particles are homogeneous.

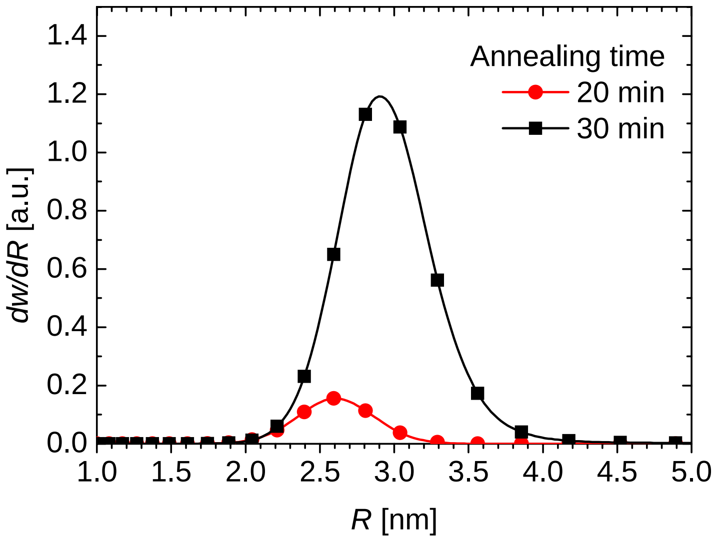

Figure 4 Differential volume fraction size distributions obtained from the scattering curves by the maximum entropy method.

[1] U. Kreibig, M. Vollmer, Optical properties of Metal Clusters, Springer, Berlin, 1995, p.13.
[2] R.H. Doremus, A.M. Turkalo, J. Mat. Science 11 (1976) 903-907.
[3] M. Eichelbaum, K. Rademann, R. Müller, M. Radke, H. Riesemeier, W. Görner, Angew. Chem. Int. Ed. 44 (2005) 7905.

Photoelectron spectroscopy on size-selected Cu-clusters on Si

N. Ferretti, B. Balkaya, A. Vollmer, M. Sperling, M. Neeb, and W. Eberhardt
BESSY mbH, Albert-Einstein Str. 15, D-12489 Berlin-Adlershof

XPS and NEXAFS spectra of deposited mass-selected Cu-clusters of up to 10 atoms have been measured at the Optics-BL PM4 and compared with the respective bulk spectra. The cluster were produced by a magnetron sputter cluster source and mass-selected prior to deposition by a magnetic sector field. A typical Cu-mass spectrum, as measured behind the exit slit of the magnetic mass filter, is shown in the adjoining figure. After passing the mass filter an individual cluster mass was softly landed (~1 eV/atom) onto a biased Si-substrate (1x1cm^2). A cluster coverage of 1-3x10^{12} cluster (~100pA) was reached within 30 minutes for each sample. During deposition the cluster current was recorded on the sample by an electrometer. Afterwards the deposited samples were transfered from the cluster machine to the photoemission chamber SURICAT at PM4 by a battery driven mobile UHV suitcase. A pressure of $< 5x10^{-9}$ mbar was maintained during deposition and transfer.

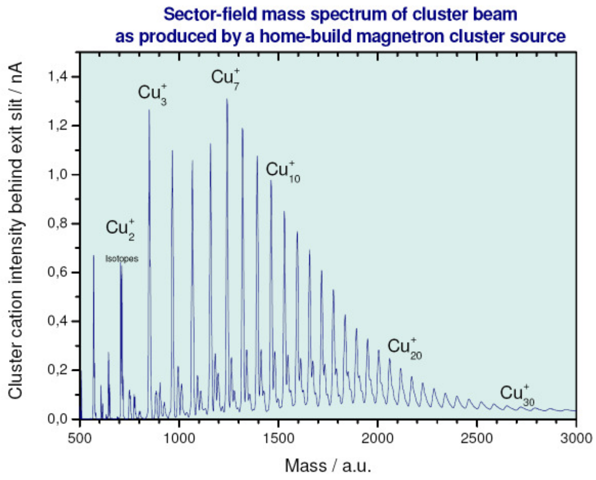

NEXAFS (Cu L_3-edge) and XPS (Cu $2p_{3/2,1/2}$) spectra are shown in the adjoining figures. The absorption spectra have been recorded by measuring the photocurrent on the sample via an amperemeter. The typical signal-to-background signal was 1-10 pA (monochromator exit slit setting=13.5 µm). For a better statistics 5-10 scans have been accumulated for each cluster sample; 20-30 scans for each XPS spectrum (E_{pass}=50eV). The L_3-edge is clearly shifted to higher absorption energy for all cluster by 1-1.5 eV. Similarly, the XPS threshold, as taken from the maximum of the Cu-peak $2p_{3/2}$, shifts to

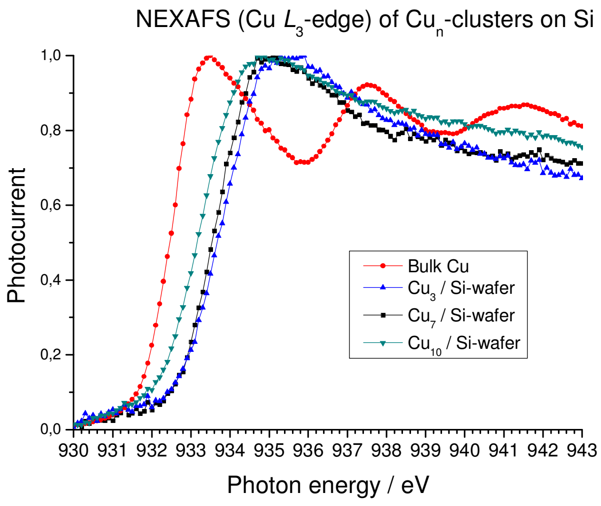

higher binding energy by 0.5-0.9 eV as compared to the bulk. The positive shift results from a reduced final-state screening due to the smaller number of atoms in the clusters and the missing metallicity. Another distinct difference between the bulk and cluster NEXAFS spectra is the missing fine structure beyond the L_3 edge for energies >936 eV (and beyond L_2 absorption feature, not shown here) as these are usually explained by van Hove singularities of a fcc-crystal structure [1] which are absent in the cluster.

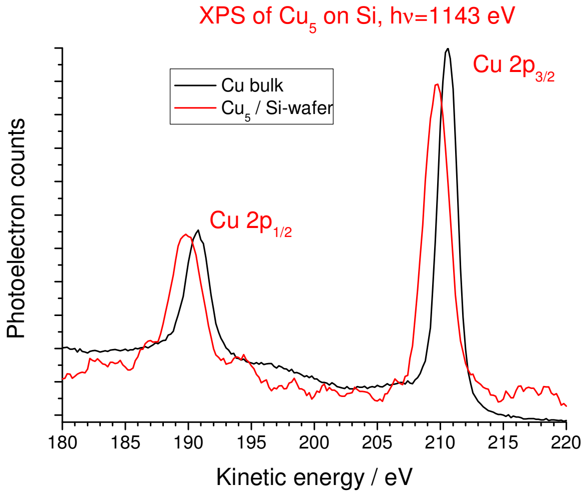

A close inspection of all cluster spectra shows that the absorption edge slightly oscillates as function of the cluster size. The absorption energy for clusters with an odd number of atoms is 0.1-0.2 eV higher than this of the even numbered clusters. This can be explained by an alternating open/closed shell structure as also shown by laser photodetachment of free Cu-cluster anions [2]. Each time a new valence shell is excited from the 2*p* core-level an increase in energy is observed. Each additional Cu-atom contributes with a single *s*-electron to a shell which, in case of non-degeneracy, is filled by two electrons. This leads to an up and down of the absorption energy by each additional atom. Furthermore a closed *d*-shell is not only indicated by the shell structure but also by the energy of the L_3-absorption edge which is located in the continuum, e.g. above the 2*p* XPS threshold, similar to the bulk. Upon oxidation, as experimentally shown for an oxidized Cu_{10}-sample, the first absorption maximum moves below the XPS threshold due to hybridisation of the oxygen with the *d*-shell. From this an open *d*-shell results which is located below the XPS threshold as in bulk CuO. At a cluster size of 10 atoms the XPS and *L*-edge absorption threshold start to converge towards the respective bulk value which has to be further examined for larger clusters in the future (>10 atoms). The difference between the absorption maximum and the XPS threshold is distinctly enhanced by ~1 eV as compared to the bulk which is a clear indication of a semiconductivity of small Cu-cluster on Si. Furthermore the individual character of the cluster spectra verifies that the Cu-cluster are softly landed on the substrate without fracturing and that the clusters do not agglomerate into islands.

[1] H. Ebert, J. Stöhr, S. Parkin, M. Samant, A. Nilsson, Phys. Rev. B **53**, 16067 (1996).
[2] C. Y. Cha, G. Ganteför, W. Eberhardt, J. Chem. Phys. **99**, 6308 (1993).

Wave-Vector Conservation upon Hybridization of 4*f* and Valence-Band States Observed in Photoemission Spectra of Ce Monolayer on W(110)

D. V. Vyalikh[1], Yu. Kucherenko[1, 2], S. Danzenbacher[1], Yu. S. Dedkov[1], C. Laubschat[1], and S. L. Molodtsov[1],

[1]*Institut fur Festkorperphysik, Technische Universitat Dresden, D-01062 Dresden, Germany*
[2]*Institute of Metal Physics, National Academy of Sciences of Ukraine, UA-03142 Kiev, Ukraine*

Angle-resolved resonant photoemission data for a hexagonally ordered monolayer of Ce on W(110) are presented. The spectra reveal a splitting of the $4f^{0}$ ionization peak around a point in **k** space where a degeneracy with a valence-band state is expected. The phenomenon is described within a simple approach to the periodic Anderson model. It is found that the Ce 4*f* state forms a band and hybridization predominantly occurs between the 4*f* and the valence-band states at the same wave vector.

The interaction of localized 4*f* states with itinerant conduction-band states leads to a series of correlation phenomena that have attracted considerable interest in the last few decades. The hybridization may lead to such intriguing phenomena as noninteger *f* occupation, heavy fermion behavior, or even a breakdown of Fermi-liquid properties [1].

A typical and well studied system is Ce metal where hybridization of the trivalent $4f^{1}(5d6s)^{3}$ with $4f^{0}(5d6s)^{4}$ and $4f^{2}(5d6s)^{2}$ configuration is responsible for the isostructural α-γ phase transition related to a volume collapse of 15% [2]. This hybridization is reflected in photoemission (PE) by a characteristic double-peaked structure of the 4*f* spectral function, where in addition to the ionization peak at around 2 eV binding energy (BE) expected for an unhybridized $4f^{1}$ ground state ("$4f^{0}$" peak), a second feature appears at the Fermi energy (E_F) reflecting the Kondo-Suhl resonance with a final-state *f* occupancy close to 1. For the α phase the relative intensity of the latter with respect to the ionization peak is much larger as for the γ phase reflecting the increased hybridization of the ground state [3].

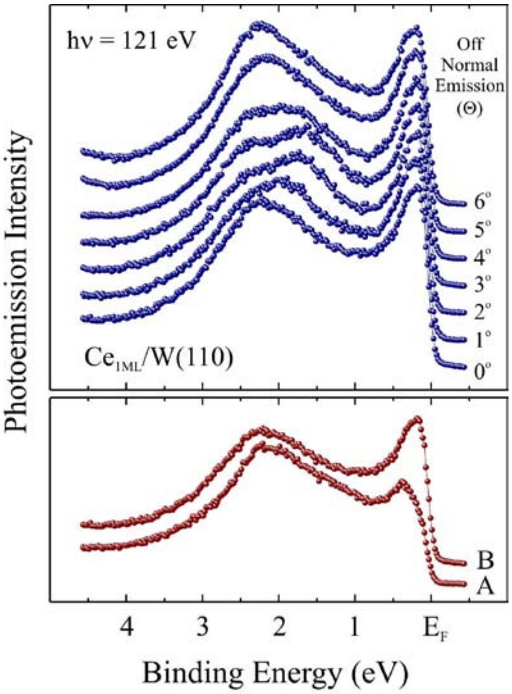

Figure 1. Resonance PE spectra of a Ce monolayer on the W(110) taken at the Ce 4*d* → 4*f* threshold. Lower panel: normal emission PE spectra for different coverages, γ-like Ce (A) and α-like Ce (B). Upper panel: Angle-resolved PE spectra for α-like Ce taken along Γ-K direction of the surface Brillouin zone.

This effect may quantitatively be described in light of the Gunnarsson-Schonhammer approach [4] to the single-impurity Anderson model [5] (SIAM) that considers the interaction of an isolated $4f^{1}$ impurity at energy ε_f with surrounding valence-band (VB) states via hopping processes. A natural weakness of SIAM is, however, that it ignores completely the effects of translation symmetry of structurally ordered solids. Consideration of the latter leads to the periodic Anderson model (PAM).

In PE hybridization effect should be reflected by changes of the *f* signal as a function of a wave-vector (**k** vector), and, in fact, weak dispersion [6]. A possibility to check it is to study the behavior of the spectral function at points in **k** space where the unhybridized *f* state is energetically degenerate with a VB state. Here, the PAM predicts a splitting of the ionization peak into two components corresponding to symmetric and antisymmetric linear combinations of the electron states. An ideal candidate for such an experiment, however, is a Ce monolayer on W(110): As was shown by Gu *et al*. [7], Ce atoms form an ordered hexagonal overlayer on W(110) with interatomic distances shrinking continuously as Ce is added from 9% larger than that in γ-Ce to 3% smaller than that in the α phase. PE spectra reveal a respective increase of the Kondo-peak intensity with decreasing interatomic distances as expected for γ-α transition. The important point here is that since the overstructure (Ce monolayer) is incommensurate and reveals a different symmetry as compared to the substrate surface, only weak electron interactions with the substrate without a pronounced **k** dependence are expected, and the spectra will be governed by the intrinsic properties of the two-dimensional Ce layer.

In the present contribution we show by means of angle-resolved resonant PE experiments at the Ce $4d \rightarrow 4f$ excitation threshold that the $4f$ – derived spectral function reveals a splitting of the ionization peak just around a point in **k** space where a band of *sd* character crosses the BE position, ε_f, of the unhybridized $4f^{\,1}$ state. The data are analyzed within the approach to PAM [8] and excellent agreement between the theory and the experiment is obtained.

The experiments were performed at BESSY using radiation from U125/1-PGM-1 undulator. PE spectra were acquired with a VG CLAM-4 analyzer. The overall energy resolution accounting for thermal broadening was set to 150 meV and angular resolution better than 1^o was used. A structural Ce monolayer was grown on clean W(110) substrate kept at room temperature. All spectra were taken at hν=121 eV, corresponding to the Ce $4d \rightarrow 4f$ resonance, were the electron emission from Ce $4f$ states considerably dominates over that from $5d$ states of tungsten that are close to a Cooper minimum of the photoionization cross section at this photon energy.

The lower panel of figure 1 shows PE spectra taken in normal emission geometry for two different surface densities of Ce atoms on the W(110) substrate. In both cases the corresponding LEED patterns indicate a hexagonal structure of the Ce layer. The spectrum denoted as ***A*** corresponds to the lowest Ce coverage where a hexagonal overstructure in the LEED pattern related to a respective arrangement of Ce atoms is still observed. The shape of this spectrum is typical for γ-like Ce. Further Ce deposition leads to decreasing spacing between Ce atoms, and the shape of the spectrum is changed to that of α-like Ce, with strongly enhanced intensity of the peak near E_F. The spectrum denoted as ***B*** corresponds to a Ce monolayer with interatomic spacing close to that of bulk α-Ce.

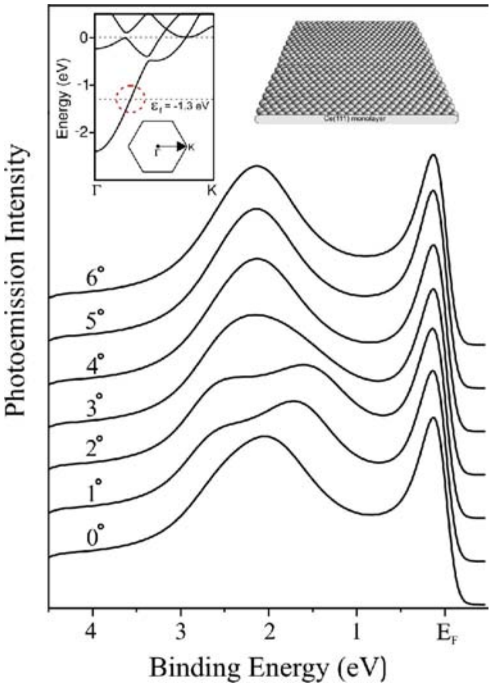

Figure 2. Calculated PE spectra of an α-like Ce(111) monolayer for different emission angles (given in the figure). Inset: the energy-band structure for the Γ-K direction.

The upper panel of figure 1 displays a set of angle-resolved PE spectra recorded along the Γ-K direction of the surface Brillouin zone for the hexagonal α-Ce monolayer. One can see that the peak at E_F, remains practically unchanged in both intensity and line shape. However, the same is not true for the ionization peak. When going away from normal emission, it splits in, at least, two components. This energy splitting is maximal for polar emission angles between 2^o and 3^o. For polar angles larger than 5^o this splitting disappears and the shape of the PE spectra shows no significant differences to the one of normal emission.

For interpretation of the obtained data we consider first the valence-band structure of the hexagonal α-Ce(111) monolayer. Assuming that the incommensurate hexagonal Ce overlayer undergoes only weak interactions with the W(110), we have calculated by LMTO method [9] the electronic structure of a free atomic monolayer with interatomic distances of 3.42 A that are equal to those in bulk α-Ce. The results of the calculations for the Γ-K direction are shown in the inset in figure 2. As follows from geometry of our experiment, for an excitation energy of 121 eV the K – point is reached at a polar emission angle 12.6^o. Thus the **k** points in the given symmetry direction could be characterized by respective polar angles. The bottom of VB is found at the Γ point at a BE of 2.4 eV. When going away from Γ point the valence band shows a parabolic dispersion, and its angular momentum character becomes smoothly changed. The energy position of the unhybridized 4*f* level in Ce metal is about 1.5 eV [10]. Therefore, assuming the 4*f* states to create a dispersionless band at this energy, this *f* band should cross the parabolic VB close to a **k** point corresponding to 3^o. Thus, in the region of this point hybridization effects between 4*f* and VB states are expected. Our following analysis concerning, how these effects influence the 4*f* emission, is the approach based on a simplified PAM applied recently to $CePd_3$ [8]. The calculated PE spectra are shown in the figure 2. In inspection of the spectra one can conclude, that their shape is changed with an increase of the emission angle. The ionization peak split into two maxima that diverge from each other by up to about 1 eV, This behavior is in excellent agreement with that observed in the experimental PE spectra. Thus, the splitting of the peak at 2 eV BE in the angle-resolved spectra of the Ce monolayer on W(110) may be ascribed to the interaction of the 4*f* states with the parabolic VB that leads to the typical picture of two hybridized energy bands.

This work was supported by the Deutsche Forschungsgemeinschaft, SFB 463, Projects TP B4 and TP B16 and BMBF Project N° 05-SF8OD1/4. We are grateful to R. Follath for the expert operation of the U125/1-PGM-1 undulator beamline.

[1]. P. Fulde, *Electron Correlations in Molecules and Solids* (Springer, Heidelberg, 1995).

[2]. D. C. Koskenmaki and K. A. Gschneider, in *Handbook on the Physics and Chemistry of Rare Earths*, edited by K. A. Gschneider and L. Eyring (Elsevier Science, Amsterdam, 1978), Vol. 1, p. 337.

[3]. D. Wieliczka, J. H. Weaver, D. W. Lynch, and C. G. Olson, Phys. Rev. B 26, R7056 (1982).

[4]. O. Gunnarsson and K. Schonhammer, Phys. Rev, Lett. 50, 604 (1983); Phys. Rev. B 28, 4315 (1983).

[5]. P. W. Anderson, Phys. Rev. 124, 41 (1961).

[6]. A. B. Andrews, J. J. Joyce, A. J. Arko, Z. Fisk, and P. S. Riseborough, Phys. Rev. B 53, 3317 (1996); S. L. Molodtsov, J. Boysen, M. Richter, P. Segovia, C. Laubschat, S. A. Gorovikov, A. M. Ionov, G. V. Prudnikova, and V. K. Adamchuk, Phys. Rev. B 57, 033104 (2005).

[7]. C. Gu, X. Wu, C. G. Olson, and D. W. Lynch, Phys. Rev. Lett. 67, 1622 (1991).

[8]. S. Danzenbacher, Yu. Kucherenko, M. Heber, D. V. Vyalikh, S. L. Molodtsov, V. D. P. Servedio, and C. Laubschat, Phys. Rev. B 72, 033104 (2005).

[9]. O. K. Andersen, Phys. Rev. B 12, 3060 (1975).

[10]. Yu. Kucherenko, S. L. Molodtsov, M. Heber, and C. Laubschat, Phys. Rev. B 66, 155116 (2002).

OPTICAL SPECTRA OF TRIGLYCINE SULFATE CRYSTALS IN THE RANGE OF 4-10 EV

B. Andriyevsky [a)], N. Esser [b)], A. Patryn [a)], C. Cobet [b)], W. Ciepluch-Trojanek [a)],
M. Romanyuk [c)]

a) Faculty of Electronics and Computer Sciences, Technical University of Koszalin, Śniadeckich Str. 2, PL-75-453, Koszalin, Poland
b) ISAS – Institute for Analytical Sciences, Department Berlin, Albert-Einstein-Str. 9, 12489 Berlin, Germany
c) The Ivan Franko National University of L'viv, Kyryla i Mefodiya Str. 8, UA-790005, L'viv, Ukraine

The funding source and grant number: EU, R II 3.CT-2004-506008

Theoretical and experimental studies of the electron energy characteristics and optical spectra for triglycine sulphate crystal (TGS), $(NH_2CH_2COOH)_3{\cdot}H_2SO_4$, in the ferroelectric phase have been presented in this paper.

Triglycine sulphate crystal (TGS), $(NH_2CH_2COOH)_3{\cdot}H_2SO_4$, is ferroelectric below 322 K belonging to the monoclinic space group $P2_1$, and above the transition temperature it becomes paraelectric with the center symmetry monoclinic space group $P2_1/m$ [1-3]. Different kinds of chemical bonds are characteristic for the crystal: strong covalent-and-ion bonds in the ions $NH_3^+CH_2COO^-$, $NH_3^+CH_2COOH$, and SO_4^{2-}, and more weaker ion and hydrogen bonds between these quasi-molecular complexes. Because of low symmetry of TGS crystal the essential anisotropy of the optical functions in the fundamental absorption range $h\nu > 5,1$ eV is expected.

Calculations of the band energy dispersion $E(k)$, density of electron states (DOS), and dielectric functions $\varepsilon(\omega)$ of the TGS crystal have been performed for the first time using the CASTEP (CAmbridge Serial Total Energy Package) first principal code based on the density functional theory [4]. Measurements of the dielectric properties of TGS crystals have been done by spectroscopic ellipsometry using the synchrotron-ellipsometer [5] attached to the 3m-NIM-1 off-Rowland circle normal incidence monochromator of the Berlin electron storage ring (BESSY II). The magnitude of the monochromator exit slit gave the possibility to resolve spectral changes of approximately 0.02 eV in the range of 7.3 eV. The complex reflectance ration ρ of the TGS samples was measured with an incidence angle of about 68° from 4.0 to 9.9 eV and converted to the pseudodielectric function $\langle\varepsilon\rangle = \langle\varepsilon_1\rangle + i\langle\varepsilon_2\rangle$ via the two-phase (substrate ambient) model [6]. Measurements were done for two types of sample's: (1) the samples with a cleaved surface perpendicularly to the Y-direction of TGS crystal, and (2) the samples with a mechanically polished surfaces perpendicularly to the Y- and Z-direction. The finish polishing of TGS samples was done with a paste of 1 - 3 μ diamond grains.

Most of the energy states of TGS crystal are of low dispersion in $E(k)$. The dispersion of $E(k)$ is generally greater for the conduction band states than that for the valence states. One of the peculiarities of the TGS band structure is flatness of the bottom states of the conducting bands. The energy band gap of the TGS crystal is indirect and corresponds to optical transitions between Γ [0 0 0] and D [-½ 0 ½] points of the Brillouin zone. The magnitude of this value $E_{gi} = 4.65$ eV is close to the experimental one $E_{gi}^{(e)} = 4.97$ eV obtained from the optical absorption study [7].

The results on DOS for the crystal studied are presented in Fig. 1, 2. The upper part of the valence band (-3.0 ÷ 0.5 eV) is mainly (95%) of *p*-character. In the valence band energy range, 10.0 ÷ -3.0 eV, the part of *p*-states is equal to about 70%, whereas the part of *p*-states is about 20% in the range -23.0 ÷ -11.0 eV (Fig. 2).

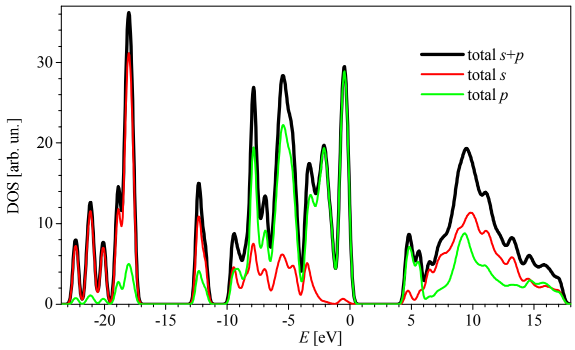

Fig. 1. Densities of electron states (total, *s*, and *p*) of TGS crystal at ferroelectric phase.

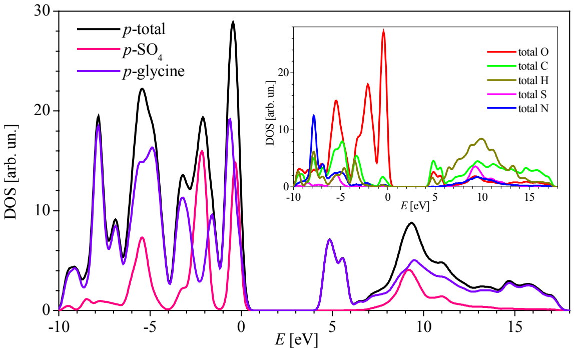

Fig. 2. Densities of electron *p*-states (total, SO_4, and glycine) of TGS crystal at ferroelectric phase. In the insertion, densities of electron states (total, *s*, and *p*) for atoms O, C, H, S, and N of the crystal.

The lower part of the conducting band ($4.0 \div 6.0$ eV) is also mainly of *p*-character (80%). An analysis of DOS in Fig. 2 reveals that both glycine and SO_4 groups give input to the density of *p*-states in the upper part of the valence band ($-3.0 \div 0.5$ eV), whereas the lower part of the conducting band ($4.0 \div 6.0$ eV) is formed predominantly (98%) by the states of three glycine groups. Additional analysis has revealed that the DOS energy dependencies in this region for three different glycine groups are relatively shifted. This testifies the antibonding character of the corresponding electron states.

An analysis of the DOS with regard to local bonding has revealed that the predominant part of DOS in the range of $-3.0 \div 0.5$ eV (92%) is associated with the *p*-states of oxygen (Fig. 2). In particular, the highest valence energy states at $E = -0.2$ eV are formed by the oxygen of SO_4-groups and glycine II group without “short hydrogen” near oxygen. The lower part of the conducting band ($4.0 \div 6.0$ eV) is formed by carbon (53%), oxygen (30%), and hydrogen (16%). In the range of $6.0 \div 11.0$ eV, the part of the hydrogen electron states is equal to about 45%. One of the clear peculiarities of the conduction band DOS is also its mixed character related to the character (*s*-, and *p*-type) and origin (chemical elements) of electron states.

The pseudo-dielectric functions $<\varepsilon> = <\varepsilon_1> + i<\varepsilon_2>$ of the TGS crystal experimentally obtained for different geometries of the relative orientation “light - sample” are presented in Fig. 3. The dielectric functions $\varepsilon_2(\omega)$ calculated using the CASTEP code and experimentally measured using a synchrotron radiation are presented in Fig. 4.

The experimentally obtained $\varepsilon_2(\omega)$ are characterized by a clear spectral band in the range of $6.6 \div 8.2$ eV and a increase in the range of $9.0 \div 10.0$ eV (Fig. 3,4). The spectra of $\varepsilon_2(\omega)$ depend significantly on the orientation of the sample surface. The most pronounced peak of $\varepsilon_2(\omega)$ is observed at the photon energy $\omega = 7.3$ eV for geometry 1, whereas this band is absent for geometry 3 (Fig. 3). The magnitudes of $\varepsilon_1(\omega)$ at $\omega = 4$ eV (Fig. 3) agree satisfactorily with the square of the refractive indices of TGS crystals [9] mentioned in the introduction.

The pseudo-dielectric functions obtained from cleaved and polished TGS crystal surfaces with the same orientation are equal within 15%. This means that the roughness degree of the polished surface does not substantially influence the pseudo-dielectric functions of the crystal in the investigated spectral range.

Comparative analysis of the experimental and theoretical line shape of $\varepsilon_2(\omega)$ of the TGS crystal gives best agreement assuming a scissor factor of 0.9 eV (Fig. 4).

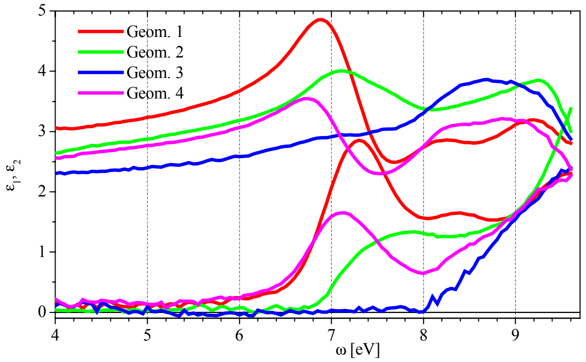

Fig. 3. Optical spectra of real $\varepsilon_1(\omega)$ and imaginary $\varepsilon_2(\omega)$ parts of pseudo dielectric permittivity of TGS crystals for different characteristic geometries and state of reflecting surface: Geom. 1 – Y-cut cleaved, **E** || **X** mainly; Geom. 2 – Y-cut cleaved, **E** || **Z** mainly; Geom. 3 – Z-cut polished, **E** || **Y** mainly; Geom. 4 – Z-cut polished, **E** || **X** mainly.

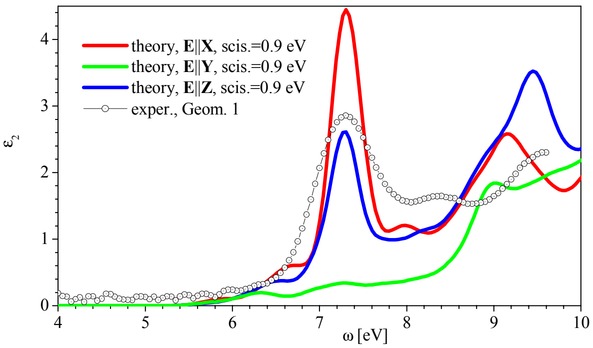

Fig. 4. Theoretical spectra of the imaginary part $\varepsilon_2(\omega)$ of dielectric permittivity of TGS crystals for the cartesian directions **X**, **Y**, **Z** and scissor factor 0.9 eV, and experimental spectrum of pseudo dielectric permittivity $\varepsilon_2(E)$ for the characteristic geometry 1 (Y-cut cleaved, **E** || **X** mainly).

Taking this into account, one can state that the strong spectral band of $\varepsilon_2(\omega)$ with a maximum at $\omega = 7.3$ eV corresponds to direct optical transitions at the Γ-, Y-, B, and E-points between the highest valence band (-1.07 ÷ -0.25 eV), and conduction bands between 5.4 and 6.5 eV. These transitions are associated with the valence *p*-states of oxygen and, predominantly, with the conducting states of hydrogen and carbon (Fig. 2). Whilst these valence *p*-states of oxygen are flat and therefore are of localized type, the corresponding conducting states of hydrogen and carbon are of more delocalized character. The large anisotropy of $\varepsilon_2(\omega)$ in the region of $\omega = 7.3$ eV and peculiarities of the placement of crystal's fragments in the unit cell support the suggestion that the mentioned valence *p*-states of oxygen are associated with SO_4 groups, whereas the conducting states of hydrogen and carbon are mainly belong to the glycine I.

A similar analysis of the experimental and theoretical dielectric functions $\varepsilon_2(\omega)$, band dispersion $E(k)$, and densities of states of TGS crystal evidences an assignment of the experimental maxima in $\varepsilon_2(\omega)$ at 8.35 eV and 9.55 eV to the transitions between the oxygen valence *p*-states, probably partially delocalized, and lower lying delocalized states of the conducting band.

Small maxima in the theoretical dielectric functions of $\varepsilon_2(\omega)$ in the range of 5.4 ÷ 7.0 eV (Fig. 4) correspond to weak optical transitions probably between the electronic states of the glycine groups being of the localized antibonding type in the range of 4.4 ÷ 5.4 eV. These transitions are in good agreement with a position of the long-wave edge of optical absorption of TGS crystals at $\omega \geq 5.2$ eV [7-9].

[1] S. Hoshino, I. Okaya, R. Pepinsky, *Phys. Rev.* **115** (1959) 323.
[2] M. I. Kay, R. Kleinberg, *Ferroelectrics* **5** (1973) 45.
[3] S. R. Fletcher, E. T. Keve, A. C. Skapski, *Ferroelectrics* **14** (1976) 775.
[4] V. Milman, B. Winkler, J. A. White, C. J. Pickard, M. C. Payne, E. V. Akhmatskaya, R. H. Nobes, *Int. J. Quant. Chem.* **77** (2000) 895.
[5] T. Wethkamp, K. Wilmers, N. Esser, W. Richter, O. Ambacher, H. Angerer, G. Jungk, R.L. Johnson, M. Cardona, *Thin Solid Films* **313-314** (1998) 745.
[6] R. M. A. Azzam, and N. B. Bashara, *Ellipsometry and Polarized Light*: North-Holland Personal Library, Amsterdam, 1987, paperback ed.
[7] A. Abu El-Fadl, *Physica B: Physics of Condensed Matter* **269** (1999) 60.
[8] N. A. Romanyuk, B. V. Andriyevsky, I. S. Zheludev, *Ferroelectrics* **21** (1978) 333.
[9] N. A. Romanyuk, A. M. Kostetsky, B. V. Andriyevsky, *Physics of Solid State* **19** (1977) 3095.

Molecular orientation of substituted phthalocyanines: influence of the substrate roughness

H. Peisert[1], I. Biswas[1], L. Zhang[1], M. Knupfer[2], M. Hanack[3], D. Dini[3], D. Batchelor,[4] T. Chassé[1]

[1]*University of Tübingen, IPC, Auf der Morgenstelle 8, 72076 Tübingen, Germany*

[2]*Leibniz Institute for Solid State Research Dresden, P.O. Box 270116, D-01171 Dresden*

[3]*University of Tübingen, Inst. Organ. Chem., Auf der Morgenstelle 18, D-72076 Tübingen*

[4] *Universität Würzburg, Am Hubland, D-97074 Würzburg, Germany*

Recently it was shown that the orientation of organic molecules directly at metal interfaces cannot be deduced from the orientation of the same molecule in thin film systems [1]. In this report we study the influence of the substrate roughness on the growth – we compare the orientation of several alkyl-substituted Phthalocyanine (Pc) molecules on relatively ill defined, technically relevant polycrystalline substrates and on single crystalline model substrates. We focus on the relation between the molecular orientation in the first layers and in thin films using polarization dependent X-ray absorption spectroscopy. The measurements were performed at the UE 52-PGM beamline. The energy resolution was set to 80 meV at photon energy of 400 eV. The absorption was monitored indirectly by measuring the partial electron yield using a channeltron with an applied bias voltage of 360 V (N 1s edge). The raw data are corrected by the energy dependent photon flux and by an additional linear background due to energy dependent cross sections for the absorption. The spectra were normalized to have the same absorption edge step height well above threshold.

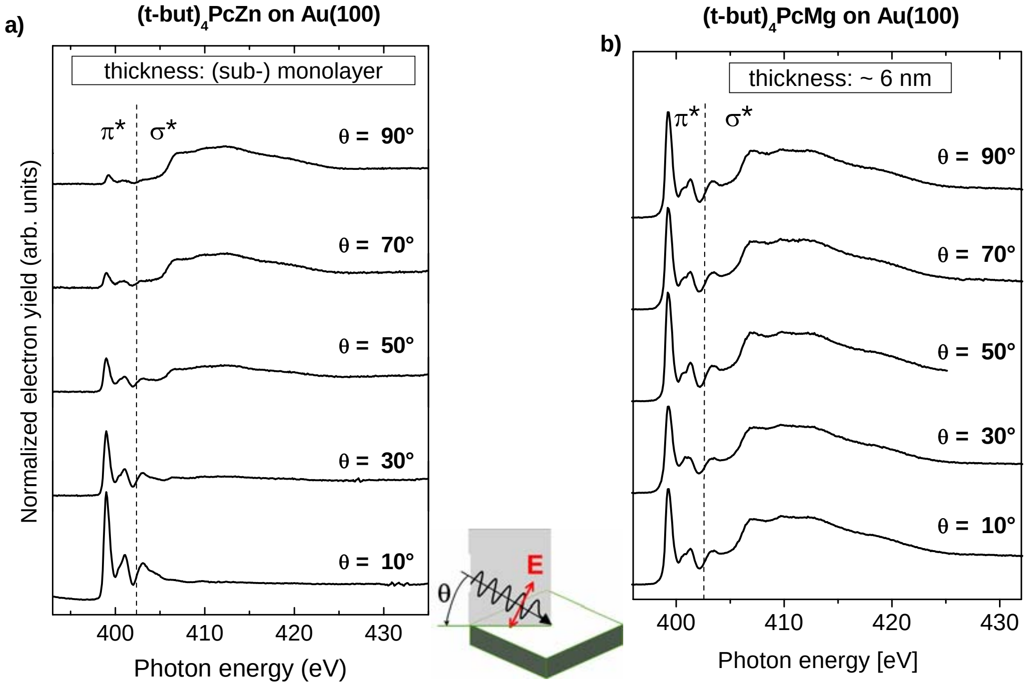

Fig. 1 N1s excitation spectra of (t-But)$_4$PcMg grown Au(100): Different angular dependences are observed for a 10 nm thick film (a) and for a film thickness of 1-2 nm (b). The lower energy features (E < 402 eV) represent the π* resonances, whereas those features above 402 eV are related to the σ* resonances. The sketch illustrates the experimental geometry for p-polarized light.

As an example, in Fig. 1 we compare N1s excitation spectra for different coverages of (t-But)$_4$PcMg on Au(100) as a function of the incidence angle θ of the linearly polarized synchrotron radiation. The geometry of the measurement is depicted in the inset of Fig. 1, normal incidence corresponds to θ = 90° and grazing incidence to θ = 10°. At grazing beam incidence of p-polarized light (i.e. the electric field vector is parallel to the beam – sample normal plane) for flat lying sp^2-hybridised carbon systems, such as phthalocyanines, a maximum intensity is expected for dipolar transitions into groups of individual π* states and the opposite behavior is expected for the $1s \rightarrow \sigma^*$ resonances. For the (sub)-monolayer coverage in Fig. 1a we observe a very clear angular dependence of the π* resonances ($E < 402$ eV). This means, that (t-But)$_4$PcMg forms well defined layers, with the molecules lying flat on the Au(100) substrate surface. In contrast, for the 6 nm thick film of (t-But)$_4$PcMg on Au(100) in Fig. 1b no clear angle dependence can be detected, therefore we suppose that the molecules are almost disordered.

A similar behavior was observed for the other substituted Pc’s, a quantitative analysis of the angle-dependence of the N1s-π* resonance intensity for different coverages of 1,4-(Dec)$_8$PcZn, 2(3)-(t-But)$_4$PcMg and PcH$_2$ on single crystalline gold is presented in Fig. 2. The data points for the ultrathin films and for the thicker film of the unsubstituted PcH$_2$ follow the expected curve for lying molecules, whereas almost no intensity changes are observed for thicker films of substituted Pcs. The exception of PcH$_2$ is not surprisingly, similar to other unsubstituted Pc’s on single crystalline substrates [3] the initial lying adsorption geometry may be locked in and is also observed in thicker films.

In both cases, for substituted and unsubstituted Pc’s, it seems that the molecule-substrate interaction causes an ordered growth within the first layers. For substituted Pc’s however, the relatively weak molecule-molecule interaction cannot enable an ordered growth on single crystalline substrates in thicker films. On the other hand, even on relatively ill-defined surfaces an ordered growth for Pc molecules (partly with small substituents) was observed – the orientation in the thin films was “standing” on the substrate surface [1]. Therefore the question arises whether or not an ordered molecular growth (with a possible change of the orientation) can be obtained for thicker coverages on well defined single crystalline substrates.

For this experiment we have chosen octasubstituted 1,4-(But)$_8$PcZn with a relatively small substituent as organic, and GeS(001) as a very flat substrate with a weakly interacting (van-der-Waals) surface. Compared to PcH$_2$ in (But)$_8$PcZn the separation between the aromatic cores is larger and thus the molecule-molecule interaction is decreased. In this case, not the polar angle of the sample, but the direction of the ***E*** vector of the synchrotron radiation

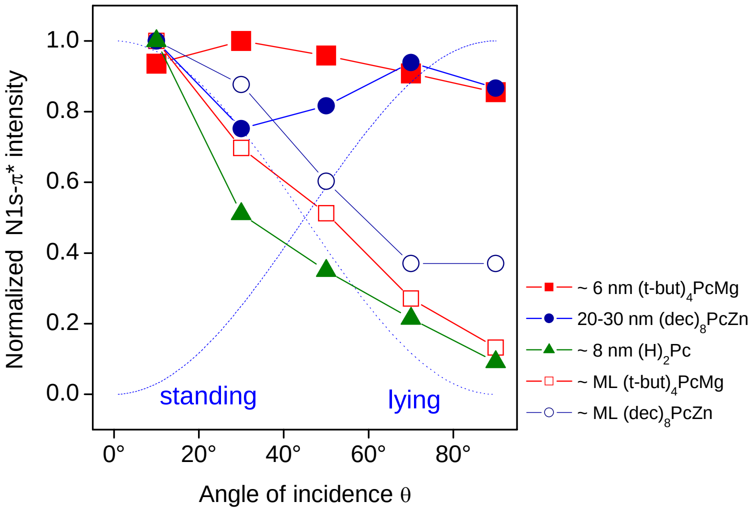

Fig. 2 Angle dependence of the intensity of the π* resonances of (t-But)$_4$PcMg, (Dec)$_8$PcZn and PcH$_2$ on Au(100). The integrated intensity of the structures < 402 eV was used for the analysis. The expected intensity profiles for standing and lying molecules are indicated by dotted and dashed lines, respectively. A preferred orientation (lying molecules) can be only observed within the first organic layers and for thicker films of the unsubstituted PcH$_2$.

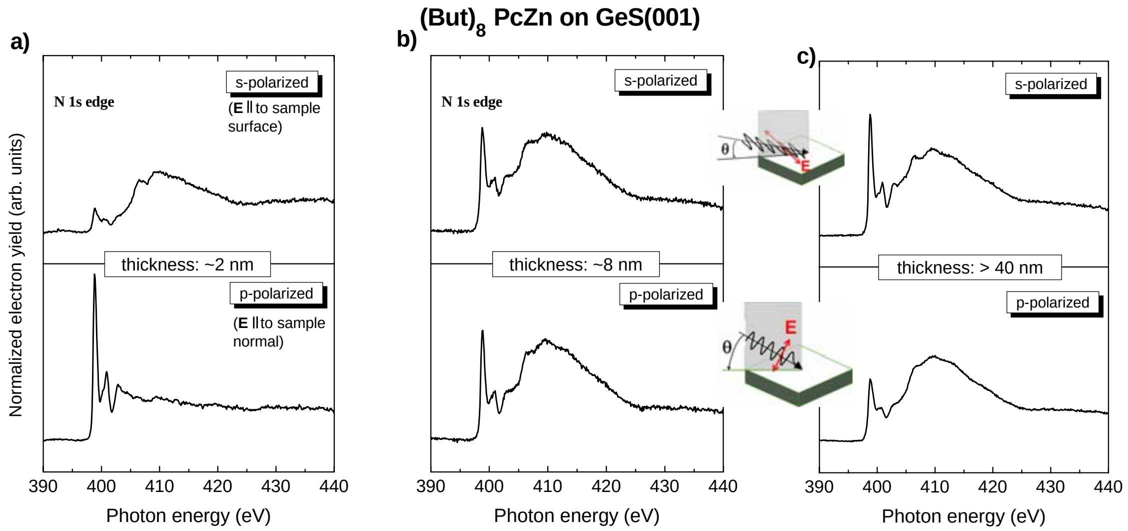

Fig. 3 Comparison of N1s excitation spectra for 1-2 nm (a), of 8 nm (b) and of more than 40 nm (c) thick films of 1,4-(But)$_8$PcZn grown on GeS(001) at grazing incidence using differently polarized light. Whereas an orientation of the molecules parallel to the substrate surface is observed for the first layers, the spectra indicate an almost disordered growth for higher coverages and finally standing molecules in thick films.

was changed at grazing beam incidence, as illustrated in the insets of Fig. 3.

For a ~2 nm coverage of 1,4-(But)$_8$PcZn on GeS(001) we observe for p-polarized light in Fig. 3a (lower panel) a high intensity of N 1s → π* transitions and a low intensity of N 1s → σ* transitions, the opposite behavior is observed for s-polarized light (lying molecules). In contrast, the spectra for 8 nm thick film for p- and s-polarized light (Fig. 3b) show only weak differences, which agree well with the result above on substituted Pc/Au(100) interfaces. Therefore, one could conclude that also 1,4-(But)$_8$PcZn grows almost disordered on GeS(001) at room temperature, except of the first 1-3 layer(s). However, for a very thick film of about 40 nm the corresponding XAS spectra (Fig. 3c) show an opposite intensity variation compared to Fig. 3a. Thus, the geometry changes from lying for the first layer(s) via disordered to standing for thicker films. The change from an ordered growth to a disordered growth after a few layers can be understood assuming a favored maximal interaction at the interface. In this case the aromatic cores of the substituted Pc molecule are lying directly on the interface and the (sterically demanding) substituents disable a strong interaction between aromatic cores in subsequent layers. Possible adsorption sites on the already covered single crystalline surface are energetically similar and a disordered growth occurs. A condition for an ordered growth of standing molecules seems to be a certain degree of roughness, at least on the scale of the size of the molecule, otherwise an initial lying adsorption geometry may be locked in – as observed above for the unsubstituted PcH$_2$ on Au(100). The roughness may originate from the substrate surface itself or from disordered intermediate layers on flat substrates. The favored growth of standing molecules over lying molecules can be discussed on a microscopic scale as well as phenomenologically in terms of different surface energies [4].

For valuable discussions and technical assistance we thank H. Kuhlenbeck, M. J. Cook, I. Chambrier, S. Pohl, Ch. Jung, W. Neu and R. Hübel. Financial support by BESSY is gratefully acknowledged.

[1] H. Peisert, I. Biswas, L. Zhang, M. Knupfer, M. Hanack, D. Dini, M.J. Cook, I. Chambrier, T. Schmid, D. Batchelor, T. Chassé, Chem. Phys. Lett. **403** (2005) 1.

[2] Y. Karzazi, X. Crispin, O. Kwon, J.L. Bredas, J. Cornil, Chem. Phys. Lett. **387** (2004) 502.

[3] H. Peisert, T. Schwieger, J. M. Auerhammer, M. Knupfer, M. S. Golden, J. Fink, P. R. Bressler, and M. Mast, J. Appl. Phys. **90** (2001) 466.

[4] H. Peisert, I. Biswas, L. Zhang, M. Knupfer, M. Hanack, D. Dini, M. J. Cook, I. Chambrier, T. Schmid, D. Batchelor, T. Chassé, Surf. Sci. (accepted).

Optical Properties of UN and UPtGe Single Crystals between 1 and 32 eV

M. Marutzky, U. Pelzer, H. Schröter, S. Weber, and J. Schoenes

Institut für Physik der Kondensierten Materie, Technische Universität Braunschweig,
Mendelssohnstr. 3, 38106 Braunschweig, www.ipkm.tu-bs.de

BMBF 05ES3XBA/5

The uranium monopnictides have been intensively studied since the 1980ies [1]. One topic which have been discussed was the degree of localization of the 5f-states in the monopnictides. In fact, the 5f-states are localized in the heavier uranium monopnictides like USb, and when the pnictide is getting lighter, the 5f-states are becoming more and more delocalized. In consequence, the 5f-states in uranium mononitride are claimed to be relatively itinerant. UN is an antiferromagnet with $T_N = 50$ K and crystallizes in the rocksalt structure like the other uranium monopnictides. While the optical and magneto-optical properties of most of the uranium pnictides are known [2], studies on single crystalline UN have been lacking until now. We have continued the systematic study of the uranium pnictides with the investigation of the optical and magnetooptical properties of UN [3].
In contrast to UN, the antiferromagnet UPtGe has a complicated orthorhombic crystal structure which is discussed for a long time. Nowadays, a noncentrosymmetric EuAuGe structure with two different uranium sites with different magnetic moments is favoured [4]. The magnetic structure of UPtGe is also interesting because UPtGe orders in an incommensurable cycloidal spin structure at $T_N = 50$ K. It was found that the magnetic and electrical properties are anisotropic [5]. We have investigated the optical and magneto-optical anisotropy [6] and related them to UPtGe's electronic structure. This study can test a crystal-orientation dependent calculation of the band structure of UPtGe.

The determination of the optical functions were done mainly by ellipsometric spectroscopy. Ellipsometric spectroscopy provides the full complex optical functions without requiring a Kramers-Kronig transformation, and surface features do affect less the results than other forms of optical spectroscopy. Therefore, ellipsometric spectroscopy is a powerful, non-destructive tool to analyze the electronic structure of materials. The measurements between 1 at 4.5 eV were performed at our home ellipsometer and for higher photon energies at the VUV-ellipsometer at BESSY II.

We had deduced a scheme of the electronic structure of UN (Fig. 1) from magneto-optical measurements in the energy range from 1 to 5 eV and optical measurements from 1 to 10 eV, partially done at the 3m-NIM monochromator at BESSY II [3, 7]. The scheme in Fig 1 predicts a transition $2p(N) \rightarrow 6d_{eg}(U)$ with a transition energy of 11.1 eV which is beyond the energy range of our previous measurements. In order to prove this expected transitions, the optical studies were expanded with the VUV ellipsometer at the TGM4 monochromator. The results are shown in Fig. 2. Unfortunately, it was not possible to get reliable results between 10 and 15 eV because of the low intensity at the TGM4 monochromator. Between 15 and 32 eV this was possible, and the measured slope of the optical conductivity is in accordance with studies on UN polycrystals [8]. In the high energy range a broad peak is visible which is probably a superposition of two absorptions of the transitions $6p(U) \rightarrow 6d_{t2g}(U)$ and $6p(U) \rightarrow 6d_{eg}(U)$.

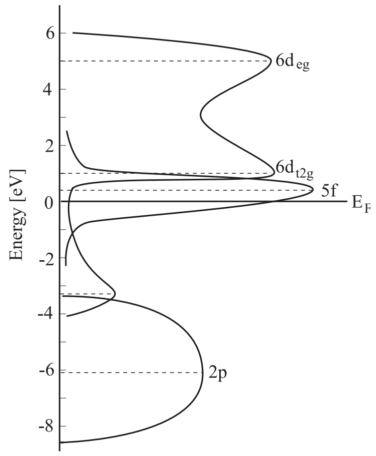

Fig 1: Scheme of the DOS of UN [3].

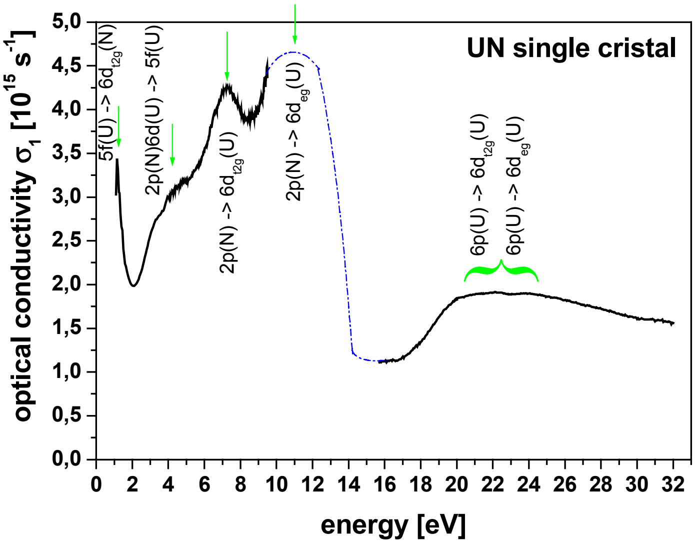

Fig 2: Real part of the optical conductivity of single cristalline UN. The structures in the spectrum are assigned to electronic transitions. The measurements between 1 and 10 eV were performed at the 3m-NIM, those between 15 and 32 eV at the TGM 4-monochromator. The blue line is the expected slope of the optical conductivity.

In order to investigate the optical anisotropy of UPtGe single crystals, we had made measurements on this material with the polarization vector orientated in respect to the crystal direction. This is depicted in Fig 3. The data between 1 and 10 eV once again were collected at the 3m-Nim monochromator, the data at higher energies at the TGM 4. In the energy range between 10 and 15 eV, the same problem with low intensity occurred. Obviously, the optical conductivity of UPtGe shows large anisotropic behaviour. The peaks at 1 eV and at 4 eV arise under participation of f-states, as we know from the Kerr-spectra [6]. Recent calculations [9] let suggest that the structure at 4 eV exists due to 5d(Pt) → 5f(U) transitions and those at 19 and 25 eV are due to 6p(U) →5d(Pt) transitions.

The measurements of the optical properties between 15 and 32 eV at the VUV ellipsometer have expanded our studies on the electronic structure of UN and UPtGe single crystals. Of course, in order to get a full determination of the electronic structure, efforts must be made to close the gap between 10 and 15 eV and to proceed this studies to even higher energies than 32 eV.

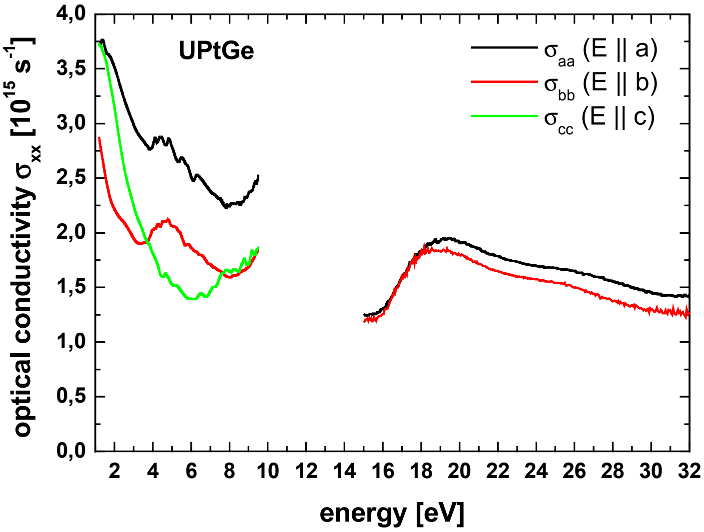

Fig 3: Real part of the optical conductivity of UPtGe with polarization vector parallel to the a, b, and c-axis.

We are indepted to the group of N. Esser, especially C. Cobet and M. Rakel for the opportunity to make measurements at the VUV ellipsometer, the staff at BESSY II, and the BMBF for financial support.

[1] J. Schoenes, in *Handbook Physics and Chemistry of the Actinides* (1984)
[2] J. Schoenes, Phys. Rep. 66 (1980), 187-212
[3] M. Marutzky, U. Barkow, J. Schoenes, and R. Troć, J. Magn. Magn. Mat. 299 (2006), 225-230
[4] D. Mannix, S. Coad, G.H. Lander, and J. Rebizant, Phys. Rev. B 62 (2000), 3801-3810
[5] R. Troć, J. Stępień-Damm, C. Sułkowski, A.M. Strydom, Phys. Rev. B 69 (2004), 094422
[6] M. Marutzky, U. Barkow, S. Weber, J. Schoenes, and R. Troć, in preparation
[7] U. Barkow, M. Marutzky, A.-M. Cârsteanu, D. Menzel, A. Navratil, H. Schröter, S. Weber, J. Schoenes, C. Cobet, and R. Troć, BESSY annual report (2003), 155-157
[8] E.T. Arakawa, and M.W. Williams, J. Nucl. Mat. 41 (1971), 91-95
[9] M. Samsel-Czekała, and R. Troć, unpublished

Low-energy electrodynamics of superconducting diamond

S. Lupi[1], M. Ortolani[1,2], L. Baldassarre[1], U. Schade[2], P. Calvani[1], Y. Takano[3], M. Nagao[3], T. Takenouchi[4], and H. Kawarada[4]

[1]Coherentia-INFM and Dipartimento di Fisica, Università La Sapienza, Rome, Italy
[2]Berliner Elektronenspeicherring-Gesellshaft für Synchrotronstrahlung, Berlin, Germany
[3]National Institute for Materials Science, Tsukuba, Japan
[4]School of Science and Engineering, Waseda University, Tokyo, Japan.

Diamond, with its extraordinary mechanical properties, excellent thermal conductivity, and large insulating gap between the valence and the conduction band, is in principle much more attractive than silicon as a semiconductor. Therefore the electric properties of artificial diamond films, doped by the inclusion of acceptors or donors, are being extensively explored in view of a possible, future diamond-based electronics. In this framework, it has been discovered recently that boron-doped diamond can also become a superconductor [1] below critical temperatures T_c well above the liquid helium temperature [2]. The strongly covalent bonds, the high concentration of impurities, and the high energy of its optical phonon in comparison with the Fermi energy [3], make diamond much different from elemental superconductors where the BCS theory of superconductivity holds.

In September 2005 we measured the reflectivity $R(\omega)$ of a superconducting diamond film down to sub-Terahertz frequencies by use of Coherent Synchrotron Radiation (CSR) produced at BESSY in the low-alpha multibunch mode (stored current 10-20 mA). The CSR beam was extracted at the infrared beamline IRIS and sent to a Michelson interferometer for Fourier-Transform Infrared Spectroscopy (FT-IR). The intensity of this unique CSR source in the sub-THz range (0.1-1 THz corresponding to $3 < \omega < 30$ cm^{-1}) is three orders of magnitude higher than conventional broadband sources. It becomes therefore possible to analyze in detail the low-energy electrodynamics of superconductors, being $\omega < 50$ cm^{-1} ($\hbar\omega < 5$ meV) the typical relevant energy range for the opening of the gap in the density of states at Fermi level. The energy gap manifests itself in the sub-THz response as total reflection ($R(\omega)=1$) with an edge at $\hbar\omega = 2\Delta$ (see Fig. 1-a).

The diamond film was grown by Chemical Vapour Deposition technique. Boron-doping up to around 3% was achieved by exposition to a Boron-rich atmosphere as described in Ref. 2.The superconducting T_c of the film was 6 K. We measured the reflectivity change trough the superconducting transition from 15 K to 2.6 K (Fig. 1-a). We then extracted the value of the superconducting gap $2\Delta(T)$ by means of a fitting procedure based on the BCS theory. We find $2\Delta(T)/\hbar \sim 12$ cm^{-1} which gives $2\Delta/k_BT_c \sim 3$, making the BCS assumption consistent wit the data. The full reflectivity spectrum from the THz to the visible range was then measured at 10 K, and combined with the sub-THz data to obtain the optical conductivity $\sigma_1(\omega)$ at all measured T´s. The inspection of this latter quantity in the sub-THz range the energy range where the infrared conductivity is depleted to build up the zero-frequency collective mode (Fig. 1-b). At the lowest T, the zero-absorption ($\sigma_1(\omega) = 0$) range corresponds again to $\hbar\omega < 2\Delta$ The difference in the frequency-integrated $\sigma_1(\omega)$ between the normal and the superconducting state allows one to calculate the field penetration depth $\lambda(T)$, reported in Fig. 1-c. Furthermore, the spectrum of the charge-lattice interaction $\alpha^2F(\omega)$ (not shown) indicates a coupling between the charge carriers and the optical phonon branch around 120 meV, in agreement with recent theoretical calculations [4]. Our results consistently indicate that diamond, in spite of the above cited peculiarities, behaves as a BCS superconductor in the "dirty" regime (Γ>>Δ).

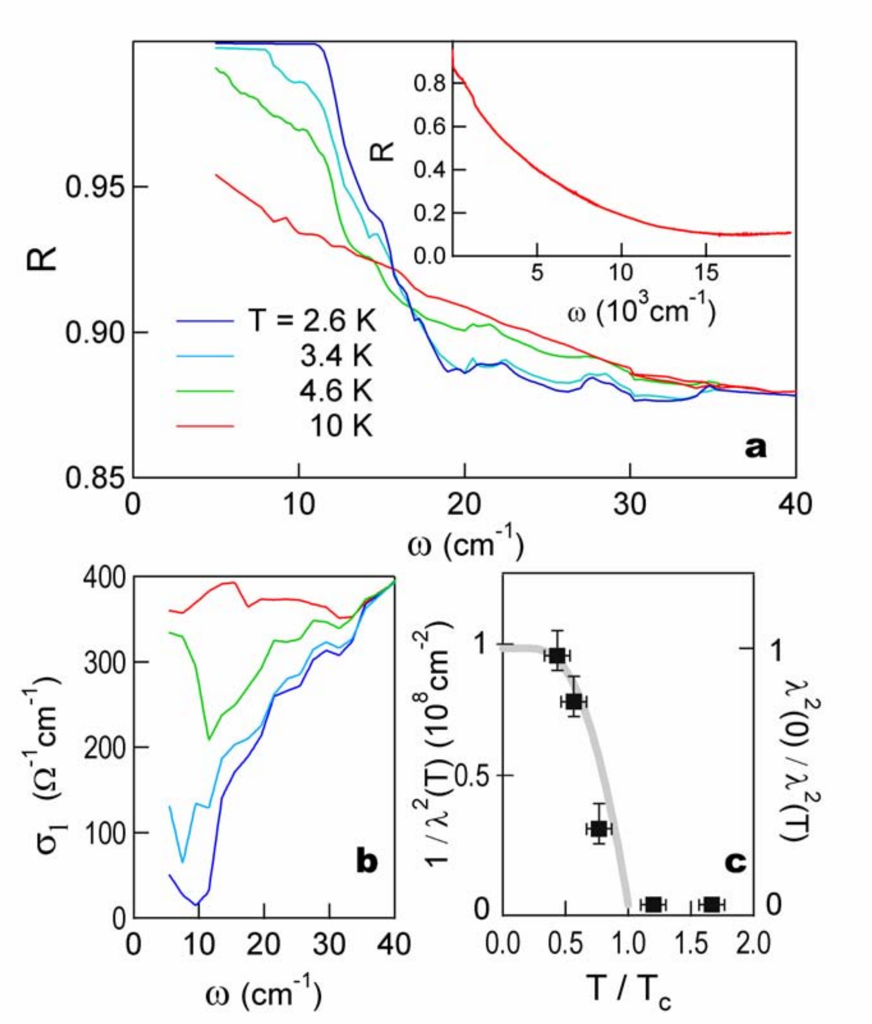

Figure 1. Reflectivity (a), optical conductivity (b), and field penetration depth (c) of a heavily boron-doped, superconducting, diamond film 3-μm thick, with T_c = 6 K. In c), the inverse square of the penetration depth, obtained from missing area in b**)** (experimental points)**,** is reported vs. T/T_c and compared with its behavior for a BCS superconductor in the dirty limit [5], normalized to zero temperature (grey line).

[1] E. A. Ekimov et al., *Nature* **428,** 542-545 (2004).
[2] Y.Takano et al., *Appl. Phys. Lett.* **85,** 2851-2853 (2004).
[3] K.-W. Lee and W.E. Pickett, *Phys. Rev. Lett*. **93**, 237003 (2004).
[4**]** H.J. Xiang et al., *Phys. Rev. B* **70**, 212504 (2004).
[5] M. Dressel and G. Grüner, *Electrodynamics of Solids* Ch. 5, 7, 14 (Cambridge University Press, Cambridge, UK, 2002).

Two-gap superconductivity in MgB_2 probed in the infrared

D. Di Castro[1], M. Ortolani[1,2], P. Calvani[1], N. Zhigadlo[3], S. Kazakov[3], J. Karpinski[3], U. Schade[2], H. Keller[4].

[1]Coherentia - INFM and Dipartimento di Fisica, Universitá La Sapienza, Rome, Italy
[2]Berliner Elektronenspeicherring Gesellschaft für Synchrotronstrahlung, Berlin, Germany
[3]Eidgenössische Technische Hochschule, Zürich, Switzerland
[4]University of Zürich, Switzerland

Since when MgB_2 was found to be a superconductor with a remarkable T_c of 40 K, its electronic properties have been intensively studied. The metallic conduction of MgB_2 takes place in two distinct electronic bands: the quasi-2D σ-band, formed by the hybridized sp_xp_y B orbitals, and the 3D π-band, made of p_z orbitals [1]. The different parity between the π– and σ-bands suppresses the impurity interband scattering, giving rise to the most intriguing feature of the MgB_2 superconductor: multi-gap superconductivity. Indeed, the strong electron-phonon coupling in the σ-band is responsible for a value of the energy gap Δ_σ, which opens below T_c at the Fermi level, much larger than the π-band gap Δ_π (about 7 and 2 meV respectively).

In a standard BCS superconductor, the far-infrared reflectivity $R(\omega)$ in the superconducting state is close to 100% for $\hbar\omega < 2\Delta$, because of total radiation screening from the supercurrent flowing in a surface sheet, whose thickness is determined by the field penetration depth Λ. The normal state $R(\omega) < 100\%$ is then recovered even at $T << T_c$ for $\hbar\omega > 2\Delta$, since the radiation with energy $\hbar\omega$ larger than the Cooper pair energy 2Δ cannot be screened. The latter property makes $R(\omega)$ a useful quantity to determine the gap value, since below T_c it will increase for $\hbar\omega < 2\Delta$. If one now turns to the two-gap case, which is relevant for our work, one may ask whether the radiation with $2\Delta_\pi < \hbar\omega < 2\Delta_\sigma$ would be screened or not, since normal electrons, which are unpaired due to radiation-induced Cooper-pair breaking in the π-band, will coexist with the surface supercurrent generated by the pairs in the σ-band. This question has not yet been addressed theoretically to our knowledge.

Information on the gap value of MgB_2 from Fourier-Transform Infrared Spectroscopy (FT-IR) measurements has been obtained up to now on films, single crystal mosaics and pellets. [2,3,4]. However, we decided to measure the intensity reflected by a single crystal, not a mosaic or a film, in order to be able to compare the data with quantitative models of the electrodynamic in-plane response, based on the Bardeen-Cooper-Schrieffer (BCS) theory. MgB_2 single crystal have a typical size of 300 μm. Few reports of far-infrared ($\omega < 100$ cm^{-1}) FT-IR experiments exist on such small crystals, since the available surface area for the reflection (300x300 μm^2) is 50 to 1000 times smaller than that of a film. The loss of signal intensity can be recovered by the use of infrared synchrotron radiation. Thanks to the high photon flux at the infrared beamline IRIS at BESSY, we could obtain reliable data for the reflectivity ratio $R(\omega, T = 4.2\ \mathrm{K})/R(\omega, T = 45\mathrm{K})$ (hereafter R_s/R_n) in the frequency range $30 < \omega < 100$ cm^{-1} with a spectral resolution of 2 cm^{-1} and a remarkable uncertainty of ±0.5%.

We studied two single crystals of $Mg(B_{1-y}C_y)_2$, one with $y = 0$ (pure, $T_c = 38$ K) and one with $y = 0.083$ (C-doped, $T_c = 32$ K). The effect of C-doping is a moderate decrease of T_c, Δ_σ and Δ_π, together with a strong increase in the carrier scattering rates Γ_σ, Γ_π, which leads to a higher critical field [5], a quantity of interest for applications. The R_s/R_n of the two crystals is reported in Fig. 1-a. In the R_s/R_n of the C-doped sample one finds a cut-off around 60 cm^{-1}, higher than that of the pure sample (40 cm^{-1}). The data can be compared with the prediction of two different BCS-based models for the infrared conductivity of a two-gap superconductor (Fig. 1-b,c). In case 1, we assume that the radiation is screened for any $\hbar\omega < 2\Delta_\sigma$; we have input $2\Delta_\pi = 34$ and 28 cm^{-1} $2\Delta_\sigma = 104$ and 68 cm^{-1} for the pure and C-doped sample respectively, in good agreement with the photoemission data of Ref. 6. In case 2 we assume instead that the screening from the σ-band supercurrent takes place only for $\hbar\omega < 2\Delta_\pi$, and not for $2\Delta_\pi < \hbar\omega < 2\Delta_\sigma$. This is done by using a single effective gap value $\Delta = \Delta_\pi = 34$ and 28 cm^{-1} for the pure and C-doped sample respectively.

The result of the analysis of Fig.1 is the following: case 1 can account for the data from the C-doped sample but not for those from the pure sample. On the other hand, case 2 may explain the data from the pure sample. The increase of Γ_σ due to substitutional impurities drives the superconductor to the dirty limit ($\Gamma_\sigma >> \Delta_\sigma$) [4]. In the dirty limit condition, the field penetration depth Λ is much larger than in the clean-limit condition ($\Gamma_\sigma < \Delta_\sigma$), which is verified in the pure sample. Further infrared studies on high-quality MgB_2 films are needed to clarify the role of the σ-band carriers in the increase of the critical field by C-doping [5,6]. In conclusion, the far-infrared data in Fig. 1 confirm the clean-limit for the pure MgB_2 sample and the dirty-limit for the C-doped sample with $y = 0.083$, and provide new insights in the understanding of two-gap superconductivity.

A paper with the results described here has been submitted to Physical review B.

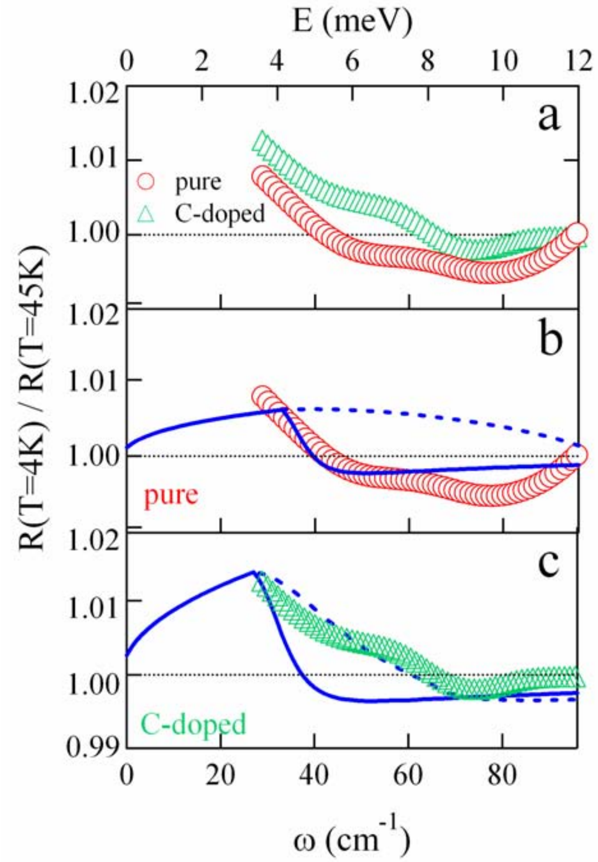

Figure 1. (a). Reflectivity change across the superconducting transition in one pure (red circles) and one C-doped (green triangles). The data in (a) are then shown separately for the pure (b) and C-doped (c) crystals and compared to two BCS-model curves (blue lines, see text). Thick line: case 1, dashed line: case 2 gap values (single effective gap).

[1] A.Y. Liu, I.I. Mazin, and J. Kortus, Phys. Rev. Lett. **87**, 087005 (2001).
[2] J. J. Tu et al., Phys. Rev. Lett **87**, 277001 (2001).
[3] A. Perucchi et al., Phys. Rev. Lett. **89**, 097001 (2002).
[4] M. Ortolani et al., Phys. Rev. B **71**, 172508 (2005).
[5] S. M. Kazakov et al., Phys. Rev. B **71**, 024533 (2005).
[6] S. Tsuda et al., Phys. Rev. B **72**, 064527 (2005).

L-edge x-ray magnetic circular dichroism in transmission and total electron yield of $Co_2Cr_{1-x}Fe_xAl$ Heusler alloy films

M. Kallmayer,[1] H. Schneider,[1] G. Jakob,[1] K. Kroth,[2] H. Kandhpal,[2] U. Stumm,[2] S. Cramm,[3] and H. J. Elmers[1]

[1] *Institut für Physik, Johannes Gutenberg-Universität Mainz,*
Staudingerweg 7, D-55099 Mainz, Germany
[2] *Institut für Anorganische Chemie und Analytische Chemie,*
Johannes Gutenberg-Universität Mainz, Duesbergweg 10-14, D-55099 Mainz, Germany
[3] *Institut für Festkörperforschung, Forschungszentrum Jülich GmbH, D-52425 Jülich, Germany*

Invaluable fundamental quantities for the understanding of electronic properties of matter are the spin and orbital magnetic moment. Using X-ray magnetic circular dichroism (XMCD) in the X-ray absorption spectroscopy (XAS) element-specific moments can be derived from two magnetooptical sum rules [1]. A transmission experiment provides straightforward determination of the X-ray absorption coefficient. The transmission signal is free of artifacts [2], e.g. self-adsorption of the X-ray intensity in the sample, complicating a quantitative evaluation of magnetic moments, or surface properties being different from bulk properties. However, for transmission experiments the samples must not be thicker than a few hundred nanometer. Therefore, the frequently applied experimental methods include a measurement of the total electron yield (TEY) and total fluorescence yield (TFY), which can be applied to thick samples, too and provide a signal proportional to the X-ray absorption. TEY measures the x-ray absorption indirectly via the photoemitted electrons originally stemming from the Auger relaxation of the 2p-core hole [3]. Saturation effects can be accounted for if the X-ray penetration depth is known [4]. TEY is surface sensitive to the limited escape depth of the low-energy electrons (about 25 Å). TFY measures the X-ray photons stemming also from the core-hole relaxation. Since the penetration depth of the outgoing photons is similar to the incident photons self-absorption changes the measured spectra more significantly for TFY than for TEY.

The information depth of TEY is about 2 nm and it would be very helpful to have in addition information on the bulk properties of the sample. Here, we report on an experimental method allowing the measurement of XMCD in transmission [5]. The method can be applied to epitaxial films and allows to determine the X-ray penetration depth of the incoming photons needed for the self absorption correction. We measured XMCD simultaneously with TEY and in transmission for epitaxial $Co_2Cr_{1-x}Fe_xAl$ films, which are interesting for their potential half-metallic ferromagnetic properties [6]. Upon comparing both signals, any uncertainties on the degree of magnetic saturation of the sample or the polarization of the X-ray beam could be avoided. We show that the magnetic moments calculated from the surface sensitive TEY are 17% smaller than the corresponding moments determined from the transmission signal. In both cases the magnetic moment of Cr is much smaller than the expected value as already found for bulk samples [7].

We prepared thin films of the Heusler compound $Co_2Cr_{1-x}Fe_xAl$ with a $B2$ structure on a-plane $(11\bar{2}0)Al_2O_3$ by magnetron sputtering [8]. The films were capped in-situ by 6 nm Al in order to prevent oxidation. The XAS experiments were performed at the UE56/1 - SGM beamline. The incident photon flux was monitored by a Au net. TEY was measured via the sample current (see Fig. 1). The sample was shielded by a conducting tube on a positive bias voltage (100 V) in order to collect all electrons. For the X-ray absorption in the transmission geometry the photon flux transmitted through the thin Heusler films was detected via X-ray luminiscence in the Al_2O_3 substrate [9, 10]. The light intensity in the visible wavelength range (VIS) escaping at the substrate edge was measured by a GaAs - photodiode. Using a reference sample with an ultrathin Co layer on a 250 nm thick Mo seed layer that is not penetrated by X-rays we verified that no X-ray fluorescence light from the sample surface was detected by the photodiode. An external magnetic field of 1.6 Tesla, that is sufficiently large to saturate the sample magnetization was applied perpendicular to the film surface.

Fig. 2 shows the incident-photon-flux-normalized transmission XAS spectra of a 110 nm thick Heusler alloy film taken with the magnetic field applied parallel (I^+_{PD}, solid curve) and antiparallel (I^-_{PD}, dashed curve) to the circular polarization of the incident photons. The reference spectra I_{ref} was assumed to increase linearly with the photon energy, normalized at the pre-edge region of the corresponding element (equivalent to an infinitely large penetration depth) [2]. This reference spectra is needed in order to calculate the relative absorption cross sections from the transmission spectra using the equation

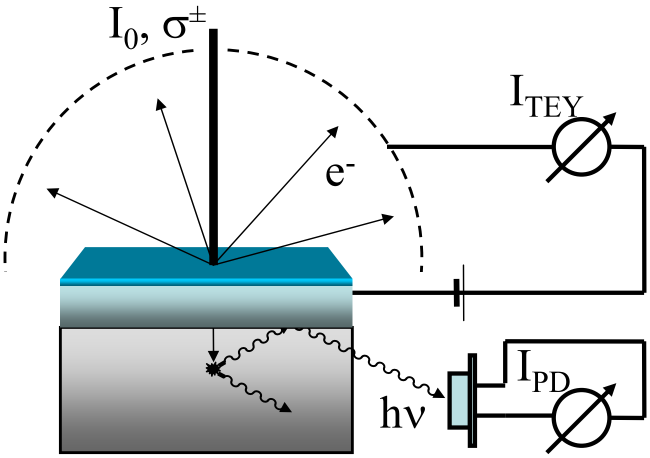

FIG. 1: Cartoon of the experimental setup used for the x-ray absorption experiment in transmission and TEY.

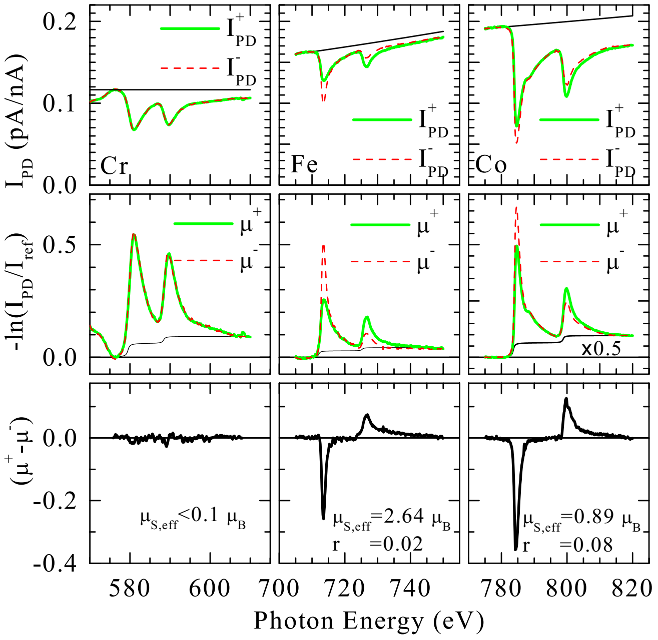

FIG. 2: Absorption spectra obtained by transmission measurements of a 110 nm thick $Co_2Cr_{1-x}Fe_xAl$ Heusler alloy films grown on a-Al_2O_3 and capped by 6 nm Al. The top row shows the photodiode current normalized to the Au-net reference current and the assumed linear increasing reference signal I_{ref} of the sample. In the center row we plot the absorption μ and the step function. The bottom row shows the XMCD spectra.

$\mu^{\pm}(h\nu) = -ln[I_{\pm}(h\nu)/I_{\mathrm{ref}}(h\nu)]/d$, where d is the thickness of the film.

The simultaneously measured TEY spectra normalized to the incident photon flux are shown in Fig. 3. After subtracting the background signal the XAS spectra were multiplied by a constant factor in order to achieve $(I^{+}_{\mathrm{TEY}} + I^{-}_{\mathrm{TEY}}) = \mu^{+} + \mu^{-}$ at the L_3 maximum. A quick inspection shows that the dichroism signal in the TEY $(I^{+}_{\mathrm{TEY}} - I^{-}_{\mathrm{TEY}})$ (Fig. 3) is smaller than in the case of the transmission signal (Fig. 2). As observed for all three elements the step jump between pre- and post-edge intensity is larger for the case of TEY compared to the transmission XAS, indicating a reduction of the number of d-holes at the interface.

The observed reduction can partly be attributed to a temperature effect, i.e. spin wave excitations with anti-nodes at the surface. Low-temperature experiments (100 K) indicate an increase of the Co XMCD - signal by 8 % compared to the value obtained at 300 K. Previous experiments on interface magnetism of pure elements indicate that significant reduction of magnetization occurs only in the topmost 1-2

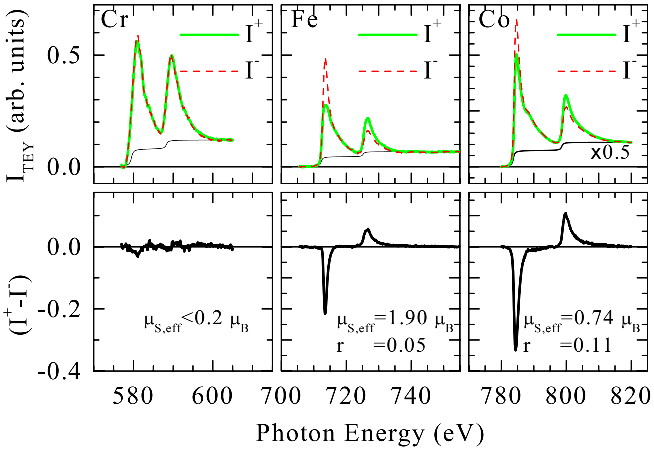

FIG. 3: Absorption spectra obtained by TEY simultaneously measured as the data in Fig. 2.

atomic layers [11]. In view of the limited surface sensitivity of TEY our observation can be explained only by an unrealistic complete quenching of magnetization in the topmost 2 layers. The most probable explanation is therefore a disturbed atomic structure of the Heusler alloy at an extended interface region. It cannot be excluded that an interdiffusion of the Al capping layer with the Heusler alloy took place. This interpretation is supported by the observation of a decrease of the number of *d*-holes at the interface.

The authors would like to thank for financial support from the Deutsche Forschungsgemeinschaft (EL-172/12-1).

[1] B.T. Thole, P. Carra, F. Sette, and G. van der Laan, Phys. Rev. Lett. 68, 1943 (1992).
[2] C.T. Chen, Y.U. Idzerda, H.-J. Lin, N.V. Smith, G. Meigs, E. Chaban, G.H. Ho, E. Pellegrin, and F. Sette, Phys. Rev. Lett. 75, 152 (1995).
[3] J. Stöhr, J. Magn. Magn. Mater. 200, 470 (1999).
[4] R. Nakajima, J. Stöhr, Y. U. Idzerda, Phys. Rev. B 59, 6421 (1999).
[5] M. Kallmayer, H. Schneider, G. Jakob, K. Kroth, H. Kandpal, U. Stumm, S. Cramm, H. J. Elmers, will appear in Appl. Phys. Lett. (2006).
[6] C. Felser, B. Heitkamp , F. Kronast , D. Schmitz , S. Cramm , H. A. Dürr , H.-J. Elmers , G. H. Fecher , S. Wurmehl , T. Block , D. Valdaitsev , S. A. Nepijko , A. Gloskovskii , G. Jakob , G. Schönhense, and W. Eberhardt, J. Phys.: Condens. Matter 15, 7019 (2003).
[7] H. J. Elmers, G. H. Fecher, D. Valdaitsev, S. A. Nepijko, A. Gloskovskii, G. Jakob, G. Schönhense, S. Wurmehl, T. Block, C. Felser, P.-C. Hsu, W.-L. Tsai, Phys. Rev. B 67, 104412 (2003).
[8] G. Jakob, F. Casper, V. Beaumont, S. Falk, H. J. Elmers, C. Felser, H. Adrian, J. Magn. Magn. Mater. 290-291, 1104 (2005).
[9] M. Kirm, G. Zimmerer, E. Feldbach, A. Lushchik, Ch. Lushchik, and F. Savkhin, Phys. Rev. B 60, 502 (1999).
[10] D. J. Huang, C. F. Chang, J. Chen, H.-J. Lin, S. C. Chung, H.-T. Jeng, G. Y Guo, W. B. Wu, S. G. Shyu, C. T. Chen, J. Electrr. Spectr. Rel. Phenomen. 137, 633 (2004).
[11] U. Gradmann, in Handbook of Magnetic Materials, **7** ed. by K. H. J. Buschow, Elsevier, Amsterdam (1993).

Free-Layer Dynamics of a Synthetic Spin Valve With Antiparallel Pinning

F. Wegelin, A. Krasyuk, D. Valdaitsev, S. A. Nepijko, H. J. Elmers, and G. Schönhense
Johannes Gutenberg-Universität Mainz, Institut für Physik, D-55128 Mainz, Germany
I. Krug, C. M. Schneider
Institut für Festkörperforschung IFF-6, Forschungszentrum Jülich GmbH, D-52425 Jülich, Germany

Applying a biasing magnetic field on a thin micron-sized permalloy layer leads to suppression of domain wall creation and thus to the suppression of Landau-Liftschitz flux-closure pattern formation. The magnetization's dynamical behavior of such a magnetically pinned and uniformly magnetized platelet differs from an unbiased particle because the pinning field acts as an additional local bias field.

Such an intrinsic biasing field generating a uniform magnetic ground state can be realized in a spin valve by depositing a multilayer stack of an antiferromagnetic layer (AF) and several ferromagnetic layers (FM) with varying coercitivity which are separated by non-magnetic spacers (NM) such as Cu or Ru. An advanced spin valve structure, designed to maximally exploit the GMR (giant magnetoresistive) effect [1], is depicted in Fig. 1a. The in-plane resistance and $\Delta R/R$ in dependence of an applied field is shown in Fig. 1b. At the interface between the bottommost CoFe (FM) and the PtMn layer (AF) a unidirectional exchange anisotropy is established by cooling down the stack from above Neél temperature while simultaneously applying a field of 1 Tesla. A second CoFe layer of equal thickness is separated from the first by a Ru layer, whose thickness has been adjusted to evoke a strong antiferromagnetic coupling between the two CoFe layers. This way, their magnetic moments cancel out. Due to the strong antiferromagnetic coupling the CoFe/Ru/CoFe sub-stack is magnetically inert against the field magnitudes applied in this experiment. The magnetically soft CoFe/NiFe free layer is separated from the CoFe/Ru/CoFe sub-stack by a Cu layer providing a weak antiferromagnetic coupling (in its first anti-parallel maximum).

The experiment has been performed in a pump-probe setup [2] at BESSY II, Berlin. The pumping is realized by generating an Oerstedt field of several mT in the coplanar waveguide on which the magnetic platelets have been deposited. Ultra-short soft X-ray pulses achieved from synchrotron at the Ni L_3 absorption edge are used for probing stroboscopically while imaging the x-ray magnetic circular dichroism (XMCD) with photoemission electron microscopy (PEEM) with sub-100 nm lateral resolution. A digital electronic delay allows stepwise shifting of the time between pump and probe pulse. The time resolution of 15 ps is not limited by the x-ray pulse length (3 ps) but by the electronic jitter of the trigger pulse (12 ps).

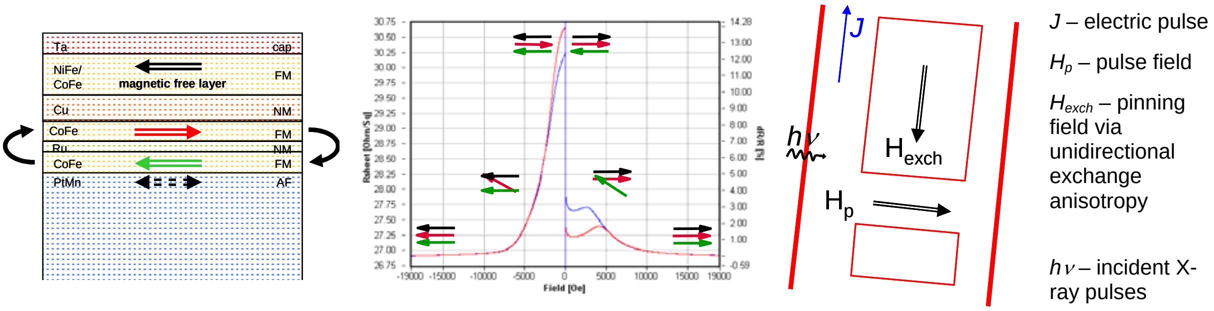

Fig. 1a: GMR spin valve multilayer stack

b: Measurement of the MR-effect. $\Delta R/R = 14\%$.

c: Schematic view of experimental setup.

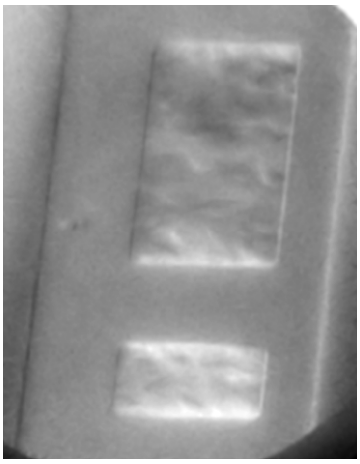

Fig. 2a: Buckling domain structure within anti-parallel pinned spin valve

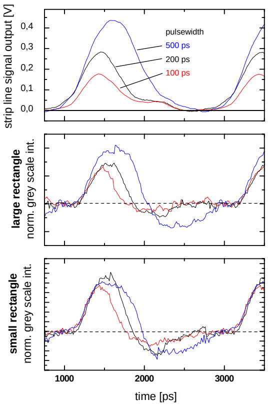

From the magnetic response a critical damping can be concluded.

b: Magnetic response of the two rectangular platelets (upper two plots) on the magnetic field (lower) estimated by the output signal of the strip line. Pulse widths: 100 ps, 200 ps and 500 ps (red, black, blue, respectively).

The magnetic platelets investigated, are 15 µm x 10 µm (upper feature in Fig. 2a) and 10 µm x 5 µm (lower feature in Fig. 2a) in dimension. The microstripline measures 20 µm in width and has been periodically pumped with electric pulses of several 100 ps pulse width. Both rectangular platelets exhibit an almost uniform magnetization state which cannot be observed in unbiased permalloy platelets [3]. A densely packed system of interacting low-angle Neél walls becomes visible which stabilizes itself and forms a buckling state (Fig. 2a).

The pulse field H_p causes an in plane rotation of the magnetization whose ground state orientation is initially parallel to the strip line due to the exchange anisotropy field H_{exch} (Fig. 1c). This becomes clear by analyzing the grey scale values within the regions of the spin valve platelets. As the magnetic field pulse propagates through the stripline, the magnetization rotates coherently out of its initial ground state orientation and falls back into it after the pulse has passed (Fig. 3). Since this critically damped oscillation takes place in absence of magnetic ringing as has been observed in permalloy monolayer platelets, fast magnetic switching is possible [4]. The investigated multilayer stack has already been implemented successfully as read elements for fast magnetic bits' stray field readout in hard disc drives.

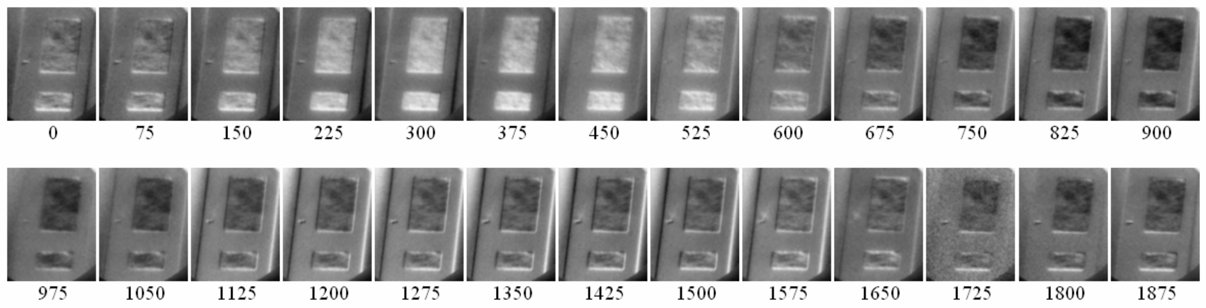

Fig. 3: Selected images (time in ps) of a sequence of one period of 2 ns measured with time increment of 15 ps.

Funded by BMBF (03 N 6500 „Nanocentre"). We thank the staff of BESSY for excellent cooperation.

[1] *Giant Magnetoresistance in soft ferromagnetic Multilayers.* B. Dieny, V.S. Speriosu, S.S.P. Parkin, B.A. Gurney, D.R.Wilhoit, D. Mauri, Phys. Rev. B 43, 1297 (1991).

[2] *Time-resolved Photoemission Electron Microscopy of magnetic Field and Magnetisation Changes.* A. Krasyuk, A. Oelsner, S. A. Nepijko, A. Kuksov, C. M. Schneider, G. Schönhense, Appl. Phys. A 76: 863-868, 2003.

[3] *Self trapping of Magnetic Oscillation Modes in Landau Flux-Closure Structures.* A. Krasyuk, F. Wegelin, S.A. Nepijko, H.J. Elmers, G. Schönhense, M. Bolte, C.M. Schneider, Phys. Rev. Lett. 95, 207201 (2005).

X-ray photoconductivity due to trap-sensitive relaxation of hot carriers

I. Konovalov, L. Makhova, D. Wett, K.-H. Hallmeier, R. Szargan
Wilhelm Ostwald Institute for Physical and Theoretical Chemistry, Universität Leipzig, Linnéstr. 2, D-04103 Leipzig, Germany
R. Mitdank
Department of Physics, Humboldt University of Berlin, Newtonstr. 15, D-12489 Berlin, Germany

Until recently, there was no possibility to directly relate the structural and the electrical manifestations of defects in semiconductors. This relation was usually concluded indirectly by comparing a first-principles calculation of the density of electronic states of the defect structures with the measured density of states.[1] An unambiguous identification of their origin requires a direct experimental method. Recently, a new direct experimental method was proposed which can support the identification of defects in multinary semiconductors.[2] This method has been successfully applied to (MDS) structures, and it requires either an structure or a diode for measurements of the capacitance. Unfortunately, the utilization of metal-dielectric-semiconductor structures multiplies the possibilities of the defect formation, unless a simple p-n homojunction is used, because of the utilization of several different materials in contact. We were able to observe a similar temperature dependent influence of the soft X-ray illumination on the ac photoconductivity of a thin ZnO film without any special barrier structure.

If the photon energy is not enough for photons to be transferred from the core level into another level above the Fermi level, there is no change of the conductivity because the possible final states are normally filled. If the photon energy is large enough for a transition into the conduction band, the conductivity changes immediately after the light pulse. In the intermediate energy region, the ionized donors become filled, and they contribute to the conductivity in the band only after their thermal activation. The latter is a slow and temperature-dependent process, so that the change of the electrical conductivity *lags* with respect to the excitation. The change of the phase of the photoconductivity signal should be especially pronounced at a temperature at which the electron emission rate is equal to the synchrotron frequency of 1.25 MHz. At lower temperatures, the signal magnitude due to emission of carriers from defect states decreases, whereas at higher temperatures the phase lag gets smaller according to a faster emission rate. An obvious “spectral” measurement records the amplitude and phase of the photoconductivity signal at a given (optimal) temperature versus the photon energy in the vicinity of the correspondent X-ray absorption edge. Another “DLTS-like” mode is a measurement of the amplitude and phase versus the temperature at a suitable photon energy. It turned out that only the DLTS-like measurement mode is useful, because the signal in the spectral mode suffers from a significant energy-dependent interference originating from the temperature-independent photoelectron emission current. This fundamental problem is related to the fact that much of the excitation energy is wasted in photoelectron emission processes, which are also capable of causing electrical currents in the sample. Unfortunately, all the measurements of the photoconductivity in the spectral mode performed so far, were dominated by the energy dependent photoelectron signal to such an extent, that no possibility to separate both contributions from each other is in view at the moment.

The samples were ZnO films deposited onto 1x1 cm^2 sapphire substrates using pulsed laser deposition. Sample 1 was an undoped ZnO film, deposited at 16 Pa O_2 at 615 °C, while Sample 2 was a MgO doped (~ 0.05 % MgO according to X-ray fluorescence analysis) ZnO film, deposited at the same temperature, but at 0.03 Pa O_2. A sapphire substrate is necessary for cooling during the measurement. The 0.8x0.8 mm^2 area of interest was separated by scribing four isolating scratches from the middle of the sample area to its sides. The contacting of the samples has been performed at the corners using evaporated Au contacts. The electrical resistance of the samples was in the range 5-15 kOhm at room temperature. During the lock-in photoconductivity measurement, a synchrotron light source (BESSY) in the single bunch mode supplied also a 1.25 MHz bunch synchronous electrical reference signal. A liquid nitrogen cooler and a resistive heater were used for controlling the temperature of the sample in the range of 75…430 K. The temperature of the sample holder was measured using a PT100 sensor, a DT400 sensor was used for comparison. The sample was dc biased by 9 V, so that the current in the sample was proportional to its electrical conductivity and changed periodically with the bunch repetition frequency. After amplification and filtering, the signal was lock-in detected using a quadrature multiplying detector (Gilbert cell type). Two phase components of the signal were digitized and presented in form of amplitude and phase. Unfortunately, the phase information was not useful so far because of a relatively large temperature-dependent phase shift introduced by the stray capacitance in combination with the large resistance of the sample. The dark resistance of the sample represents a compromise between the background conductivity and the cutoff frequency of the input circuit. An optimal signal magnitude can be achieved, if most of the applied voltage drops over the illuminated volume of the sample.

The ac current measurements in the spectral mode (not shown here) could be performed not only at the sample area, but also at an arbitrary conductor connected to the input of the amplifier. In the last case, the signal used to be identical with the total electron yield measured simultaneously by a channeltron detector. However, an additional ac signal of a comparable amplitude, which we relate to photoconductivity, emerged as soon as the illumination spot was located within the narrow current path of the ZnO film. During the measurements versus temperature, the signal to noise ratio could be improved at the expense of the spectral resolution. Similarly to the synchrotron DLTS measurements, we performed excitation around two energies, 15 eV below and 15 eV above the absorption edge. The exit slit of the beamline monochromator (U41PGM) was set to 3 mm, resulting in an estimated spectral linewidth of about 30 eV. In order to estimate the temperature dependence of the photoelectron current, we measured the temperature dependence of the sample current with the beam directed at a solid ZnO contact, while the beam did not illuminate the narrow current path of the film, but one of the contact areas of the film. We recorded rather small continuous variations of the photoelectron (PE) signal with temperature, probably related to a drift of the equipment (Fig. 1, solid line). Typical measurements of the ac photoconductivity versus temperature on both samples are also shown in Figure 1. A constant background was subtracted from the curves at energies above each absorption edge to account for the additional photoelectron current. The measurements were performed going from the cold state to the hot one (both graphs above) and vice versa (below). The features appear shifted by 50 K with respect to each other along the temperature axis at lower temperatures, obviously due to a 25 K delay related to the limited thermal conductivity of the sample, its holder and the contact between them, in spite of a long measurement time of about two hours per curve. The excitation energy was 15 eV below the O *1s* and Zn *2p3* absorption edges (solid squares), as well as 15 eV above it (open circles). The shape of the curves is generally similar, but it differs significantly from that with a misaligned beam. Two specific temperature regions can be distinguished: shallow traps visible between 100 and 200 K, having at least two components, and deeper traps at temperatures above 300 K. This finding is in good agreement with known properties of intrinsic traps in ZnO. Using the literature data,[3,4] we calculated the temperatures at which an emission rate of 1.25×10^{6} s^{-1} (light pulse repetition frequency) was expected for various impurities. E1 trap is expected to manifest itself at a temperature of 93 K, E2 at 193 K, E3 at 302 K and E4 at 339 K. These temperatures match both regions where changes of the conductivity were observed. Extrinsic traps related to Al diffusion are possible, but were not considered here. Traps of the lower temperature region (E1, E2) were significantly less sensitive to the variation of the excitation energy around the Zn L edge than around the O K one. The trap of the higher temperature region (E3 or E4) is sensitive mostly to the variation around the Zn L edge rather than O K one. This trap is present in sample 2, but it was not detected in sample 1, deposited at a higher oxygen pressure. It shows a reverse behavior with less signal while being excited above both absorption edges, and a larger signal magnitude while excited below the edges.

In order to interpret the acquired data it has to be clarified, why the change of the carrier concentration in the bands, which is being induced directly by a core-specific excitation, is related to the trap levels. This question is in focus of the current investigation, but it also arises when

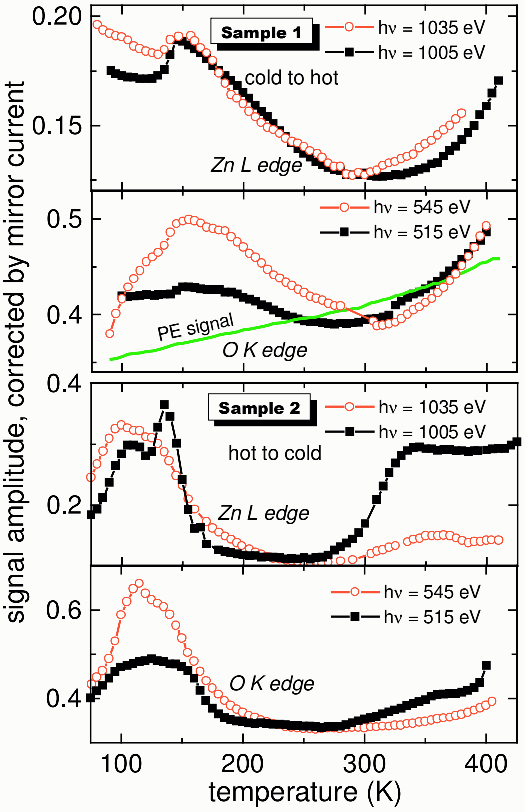

Figure 1. Amplitude of x-ray photoconductivity variation versus temperature.

considering synchrotron DLTS.[2] Indeed, when using an excitation spectrum of 30 eV width, the excitation of electrons from core levels is hardly done into the defect states directly, but mainly into the conduction band, or even in vacuum, depending on whether the excitation energy is slightly or much larger than the x-ray absorption edge. Nevertheless, investigations by Fujioka[2] as well as our own ones show that the carrier concentration in the band, influenced in such a way, is very defect sensitive. In the following, we propose a tentative explanation of this phenomenon.

The inner shell electrons which are being excited are strongly localized near the core. The band states, however, are of delocalized nature and they are also located in the space between the atom frames. Each state in the (conduction) band represents a standing electron wave in the *whole* crystal. However, the electron cloud is distributed non-uniformly, so that nodes and antinodes are located periodically in space. According to Bloch's theorem, the electron wavelength in a crystal is equal or a multiple of the lattice constant. The locations of the antinodes of a plain electron wave, where the electron is most likely to be found, are therefore the same within each of that lattice cells, where the antinodes are present. Consequently, the probability of electron transitions from the localized core levels of an atom to the delocalized band states of the crystal is larger for that band states which antinodes are in the next vicinity of the atoms in question. The electronic states in a band of a multinary compound can be sorted according to their localization at various atoms in the unit cells resulting in the local partial density of states distribution. If we consider trap states, they are more or less localized around their defects, and the deep states are particularly strongly localized. The local nature of the excitation of core electrons makes clear, why the relaxation of hot carriers through the defect states is so probable: the excited electron at one atom (e. g. at a lattice node) arises at the equivalent locations of the corresponding electron wave in many other unit cells (at equivalent lattice nodes), where the defect density of states is likely to be localized. The usual relaxation of a hot carrier through delocalized random band states is less probable in the case of excitation of a core electron, so that relaxation through the defect states with the same localization becomes more probable. Such a transition does not require a significant change of the electron localization within the unit cell. In addition, intraband transitions are often symmetry-forbidden. Therefore, the relaxation of a localized core electron, which was excited into the depth of the conduction band at an atom, is more likely to happen again into a localized (atomic, defect) state at one of the equivalent lattice sites, being not necessarily the same site and being even not necessarily occupied by the same atom sort, if substitutional defects are present. Although all the conduction band states are spread throughout the crystal, the electron which was just excited into the state, tends to conserve its former localization and prefers to transit into a similar locality again. In ZnO, the density of E1 and/or E2 trap states, if identified correctly, is therefore localized in the vicinity of oxygen sites, whereas that of E3 and/or E4 in the vicinity of Zn sites. An oxygen vacancy consists of Zn frames, so that localization of its electrons is at Zn atoms. Sample 2 was deposited at a low oxygen pressure and it is likely to contain more oxygen vacancies than Sample 1. It shows a distinct E3/E4 feature, as related to Zn sites, whereas Sample 1 deposited at high oxygen pressure does not show this feature at all. Moreover, from this point of view we were even able to satisfactorily explain the reverse excitation behavior above 300 K, which was described in the beginning. Since transitions from Zn *2p3* to *4p* conduction band states are symmetry-forbidden, transitions at higher energies are possible into Zn *s* and *d* states above. Both E3 and E4 traps are donors and are filled in ground state. If related to Zn, they are Zn *4s* states. Transitions from *s* and *d* states of the conduction band are symmetry-forbidden. Only transitions from Zn *2p3* directly into *4s* donor traps at lower excitation energies are allowed and observed.

In conclusion, the influence of trap-sensitive relaxation of hot carriers on the ac x-ray photoconductivity in semiconductors were discovered. We were able to separate the defect-induced x-ray resonant photoconductivity signal of thin ZnO films from artifacts. All the results could be qualitatively explained using symmetry selection rules and local transition probabilities. BMBF supportort 05 ES3XBA/5 is acknowledged. We thank Dr. R. Pickenhain, Holger von Wenckstern, and Prof. M. Grundmann for a discussion.

[1] S. B. Zhang, Su-Huai Wei, A. Zunger, and H. Katayama-Yoshida, Phys. Rev. B **57**, 9642 (1998).

[2] H. Fujioka, T. Sekiya, Y. Kuzuoka, M. Oshima, H. Usuda, N. Hirashita, and M. Niwa, Appl. Phys. Lett. **85**, 413 (2004).

[3] F. D. Auret, S. A. Goodman, M. Hayes, M. J. Legodi, H. A. van Laarhoven, and D. C. Look, Appl. Phys. Lett. **79**, 3074 (2001).

[4] F. D. Auret, S. A. Goodman, M. J. Legodi, W. E. Meyer, and D. C. Look, Appl. Phys. Lett. **80**, 1340 (2002).

Mapping the electron correlation in two-electron photoemission

F.O. Schumann, C. Winkler, G. Kerherve and J. Kirschner
Max-Planck Institut für Mikrostrukturphysik, Weinberg 2, 06120 Halle, Germany

1. Experiments at CP-NIM

Introduction

Due to the Coulomb interaction it is energetically unfavorable for electrons to be close to each other. Additionally, the Pauli principle demands that electrons with parallel spin can not be at the same location. Averaging over both spin directions still gives a reduced probability of finding two electrons at the same location.

A more elaborate theoretical treatment defines a pair correlation function $g(\mathbf{r},\mathbf{r}')$.[1] This describes the probability to find an electron at coordinates $\mathbf{r}$ when a second is located at $\mathbf{r}'$. The key result is that g is essentially constant except for small distances $\mathbf{r}$-$\mathbf{r}'$< a few Å where g adopts smaller values. The spatial extent of this region is called exchange-correlation (xc) hole and describes the length scale over which the correlation between electrons is relevant. A recent theoretical publication suggests that k mapping of the double photoelectron emission (DPE) intensity opens an avenue of imaging the xc-hole.[2] We will discuss our results obtained by DPE on a NaCl(100) surface. The experiments were conducted under UHV conditions featuring a novel time-of-flight spectrometer at beamline CP-NIM during single bunch time.[3] A central collector accepts electrons only within a solid angle of ~0.02 sr, the detected electron we may term as "fixed electron". A resistive anode serves as the second detector which allows for a spatial resolution of the impact position. Electrons within a solid angle of ~1 sr are registered which we term as "free electron". A coincidence circuit allows the determination of the individual flight times.

Results

In fig.1 we plotted the 2D energy distribution of coincidence electron pairs upon excitation with 34 eV photons. The energy of the "fixed electron" is labelled with E_1 whereas the "free electron" has the energy E_2. We observe the onset of DPE when the sum energy E_1+E_2 equals ~14.6 eV where DPE becomes energetically possible. More insight can be obtained if we take advantage of the lateral resolution of the set-up. In a first step we select only those coincidences for which the energies E_1 and E_2 are fixed. In other words, we pick a point in the 2D energy distribution shown in fig.1. In order to obtain sufficient statistics we actually select an energy window ~ 0.8 eV around the respective energies. This has been indicated by the square boxes in fig.2 labelled a) and b). We can now proceed and plot the coincidence

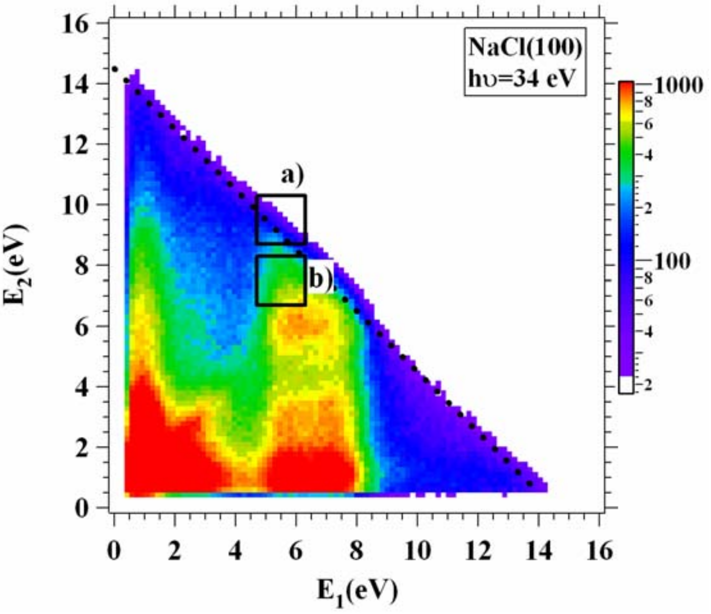

Fig.1 : The 2D energy distribution of coincidence electron pairs from a NaCl(100) surface is plotted. The photon energy was 34 eV. The energy E_1 (E_2) refers to the "fixed electron" ("free electron") The dashed diagonal line marks the onset of pair emission, which occurs for a sum energy of ~14.6 eV. The square boxes labelled a) and b) indicate the events used to generate the 2D momentum plots displayed in fig.2.

intensity as a function of the in-plane momentum $k_{||}$ of the "free electron". We have selected two different regimes within the 2D energy distribution highlighted in fig.1 by the black squares. In the case a) we are right at the onset of pair emission. Case b) describes the situation if emission below the highest occupied level is possible. In fig.2 we display the resulting momentum distributions. In fig.2 a) the energies are E_1=5.5 eV and E_1=9.5 eV (region a) in fig.2). We clearly observe that the region $k_{||}$=0 (outside the "blind spot") is surrounded by a region of diminished intensity. The intensity increases for larger $k_{||}$ values and reaches a maximum for $k_{||}$ ~0.55 Å^{-1} and then falls off rapidly towards the edge of the channelplate. A dramatically different situation is depicted in fig. 3b) where we select E_1=5.5 eV and E_1=7.5 eV. Now the ring of enhanced intensity is essentially gone. Energetically the sum energy E_1+E_2 has been reduced from 15 eV to 13 eV. This energy difference allows for emission of a deeper laying valence band electron or inelastic scattering losses if the electrons originate from the top of the valence band. Our results demonstrate the importance of inelastic scattering which is very effective in destroying the hole shown in fig.2 a).

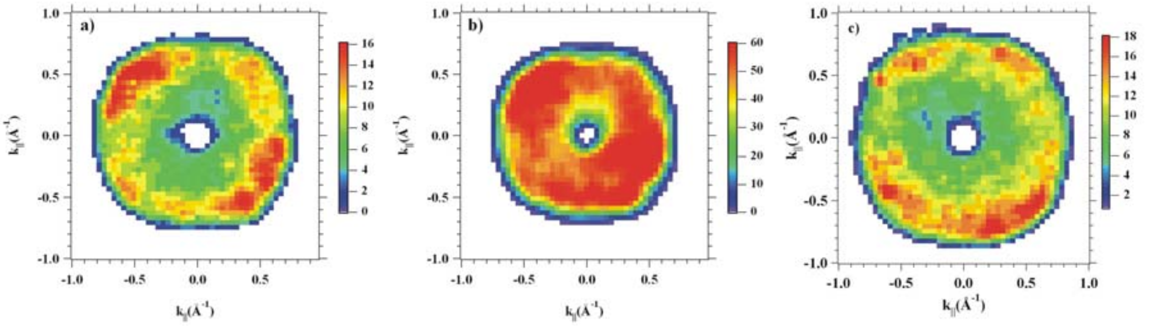

Fig.2: The 2D $k_{||}$ distribution for two different energy pairs from a NaCl(100). In panel a) we have selected E_1=5.5 eV and E_2=9.5 eV. Whereas in panel we have chosen E_1=5.5 eV and E_2=7.5 eV,. In c) we show the result from a LiF(100) surface exited with 30.7 primary electrons. The energies are E_1=7.5 eV and E_2=9.5 eV}

Discussion

It can be shown within the dipole approximation that a product of single particle wave functions yields a zero DPE intensity. However, due to the correlation/interaction such a product of wave functions is not correct and a nonzero DPE intensity results when going beyond the single particle picture.[5] Therefore we can explain the momentum distribution in fig.3 a) as a consequence of the xc-hole. Such a notion is corroborated by a more thorough calculation by Fominykh et al. on the double photoemission of Cu(100).[2] They computed the in-plane momentum distribution (of the "free electron") similar to the plots shown in fig.2 for a photon energy of 42 eV and found that it exhibits a reduced intensity until $k_{||}$ adopts a value of 1.4 Å^{-1}. At this point the intensity rises sharply by roughly an order of magnitude. Shortly thereafter the intensity returns quickly to a small value. The ring of enhanced intensity has a diameter of 2.8 Å^{-1} and a width of ~ 0.2 Å^{-1} The important outcome of the theoretical work is that the reduced intensity is a manifestation of the xc hole. Furthermore it was found that the DPE intensity also displayed the crystallographic symmetry of the surface. For NaCl we find the diameter of the reduced intensity region to be ~1.1 Å^{-1} if the energy of the "free electron" is 9.5 eV, this diameter is significantly smaller than the theoretical value for Cu. Whether this difference is due a comparison between different materials (noble metal versus insulator) is not clear. In that case we may take this as a hint of a material dependence. We emphasize that the size of the xc-hole has been determined from the diameter of the maximum intensity ring, which is near the edge of the detector, hence it is possible that the ring is even larger. This view is supported by the observation that the diameter increases with increasing energy E_2 of the "free electron" (from 0.9 to 1.3 Å^{-1} for 7.5 to 13 eV), because the covered momentum space of the detector becomes larger. According to theory the xc-hole shrinks if

E_2 is increased.[2] Nevertheless, our key observation of a region of reduced intensity due to the xc-hole remains valid and we quote the value for E_2=9.5 eV. In this context we would like to point out that we have performed a similar series of experiments on a LiF(100) surface albeit excited by a primary electron gun.[3] As an example of the resulting momentum distributions we display in fig.3c) the situation for a primary energy of 30.7 eV. The energies E_1 and E_2 are 7.5 eV and 9.5 eV, respectively. With this selection the sum energy has the highest possible value and only pair emission without any inelastic scattering of the pair is possible. Furthermore we have chosen the same value of E_2 as used in fig.2 a) in order to facilitate direct comparison. We immediately notice that there is no qualitative difference between fig. 2a) and b). The study on LiF also showed that inelastic scattering destroys the region of reduced intensity similar to the plot in fig.2 b). Although two different materials have been studied (NaCl versus LiF) their electronic properties are very similar. Hence we conclude that DPE and (e,2e) experiments give qualitatively similar results despite the fact that the underlying mechanisms bear some significant differences.

2. Experiments at TGM 4

Additionally to the spectrometer employed at CP-NIM we started to study the xc hole at metal surfaces at the beamline TGM 4. Since the work function of a metal (typically ~5eV) is smaller than the bandgap of NaCl we expected the energy resolution to be a limiting factor. An obvious solution is an increase of the flight path, while maintaining the angular acceptance angle. This has been achieved by using an elliptical mirror together with the proven detectors also in use with the spectrometers in operating at CP-NIM.

With the elliptical mirror set-up we investigated the momentum distribution of the coincidence intensity from a Cu(100) surface. Despite the fact that the spectrometer was working properly we encountered a too low count rate. Our recent results on the momentum distribution of LiF and NaCl have shown that the size of the xc-hole was just within the acceptance range of the detector. This fact suggested that the size of the xc hole of Cu could be larger than expected. This hypothesis was confirmed in a second experimental run, where a spectrometer with an acceptance angle of 2π in one dimension was employed.

1. P. Fulde, Electron Correlations in Molecules and Solids, Springer Series in Solid State Sciences, Vol. 100 (Springer, Berlin, 1993).
2. N. Fominykh, J. Berakdar, J. Henk, and P. Bruno, Phys. Rev. Lett. **89**, 086402 (2002).
3 F.O. Schumann, J. Kirschner, and J. Berakdar, Phys. Rev. Lett. **95**, 117601 (2005).
4 F.O. Schumann, C. Winkler, G. Keherve, and J. Kirschner, Phys. Rev. B **73**, 041404(R) (2006).
5 J. Berakdar, Phys. Rev. B 58, 9808 (1998).

Momentum dependence of the mass renormalisation in lightly underdoped $Bi_2Sr_2CaCu_2O_8$

I. Santoso[1], A. Mans[1], W. K. Siu[1], S. de Jong[1], Y. Huang[1], R. Follath[2], P. Bressler[2]
M. S. Golden[1]

[1]Van der Waals-Zeeman Institute, Universiteit van Amsterdam, Valckenierstraat 65, 1018 XE Amsterdam,
The Netherlands
[2]BESSY GmbH , Albert Einsteinstrasse 15, 12489 Berlin, Germany

---

The understanding of the mechanism of high temperature cuprate superconductors (HTSC) remains probably *the* fundamental challenge for solid state science. Much progress has been booked but there is still disagreement as to the nature of the bosonic mode mediating pairing in the HTSC. The two main contenders are currently spin fluctuations and phonons. Angle-resolved photoemission offers a very direct handle on the effects of coupling of the electronic system to a bosonic mode in terms of the observation of renormalisation effects in the band structure.

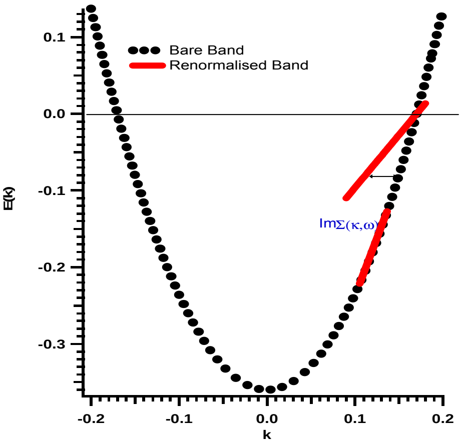

Figure 1: Cartoon of mass renormalisation

In the case of coupling, there is a deviation of the energy position of the many-body, interacting band from the position of the bare (non-interacting) band close to the Fermi level in ARPES spectra. This leads to two branches in the dispersion relation, as illustrated in Fig. 1.

Through characterising the energy, momentum, doping and temperature dependence of these renormalisation effects, we can hope to be able to pin down the identity of the bosonic mode involved.

Most ARPES data have dealt with the investigation of the renormalisation effects along the nodal (zone diagonal) direction [1,2], there are fewer studies of the antinodal ([π,0]) region of k-space [3,4]. The latter region is technically more tricky, as in Bi2212-based systems one needs to explicitly resolve the c-axis bilayer splitting, as well as studying modulation-free crystals (usually achieved by doping Pb for Bi during crystal growth).

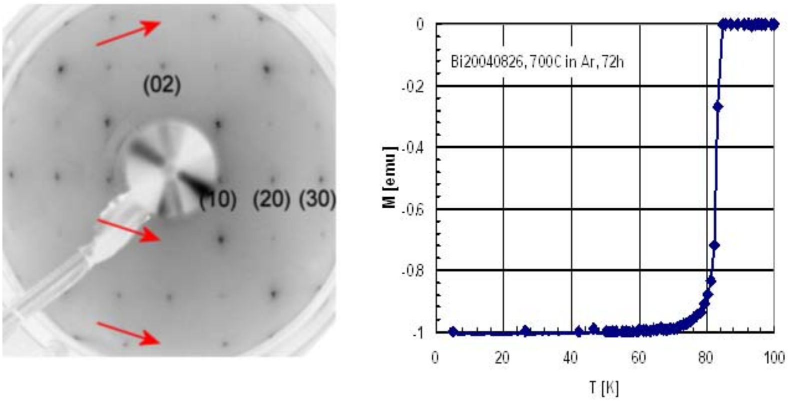

Figure 2: Left: LEED image of the sample showing the systematic absences (indexed in an orthorhombic cell) and a lack of modulation-induced reflections. Left: the sharp superconducting transition at 84 K from SQUID data

Here we report studies of the mass renormalisation of the Fermi surface states in modulation-free, untwinned underdoped $(Pb,Bi)_2Sr_2CaCu_2O_8$ (T_C=84K). The crystals were grown in Amsterdam using the travelling solvent floating zone technique and show excellent cleavage surfaces, as can be seen from the LEED image shown in the left panel of Fig. 2. The systematic absences highlighted with the red arrows point to the fact that there is a glide mirror plane parallel to the real-space *bc* plane. This arises from distortions of the atomic positions away from the ideal tetragonal structure and gives rise to the infamous shadow Fermi surface [5].

The focus of our study is on the investigation as a function of Fermi surface angle (Φ), where 0º means the antinodal (AN) direction and 45º the nodal (see also Fig. 3C).

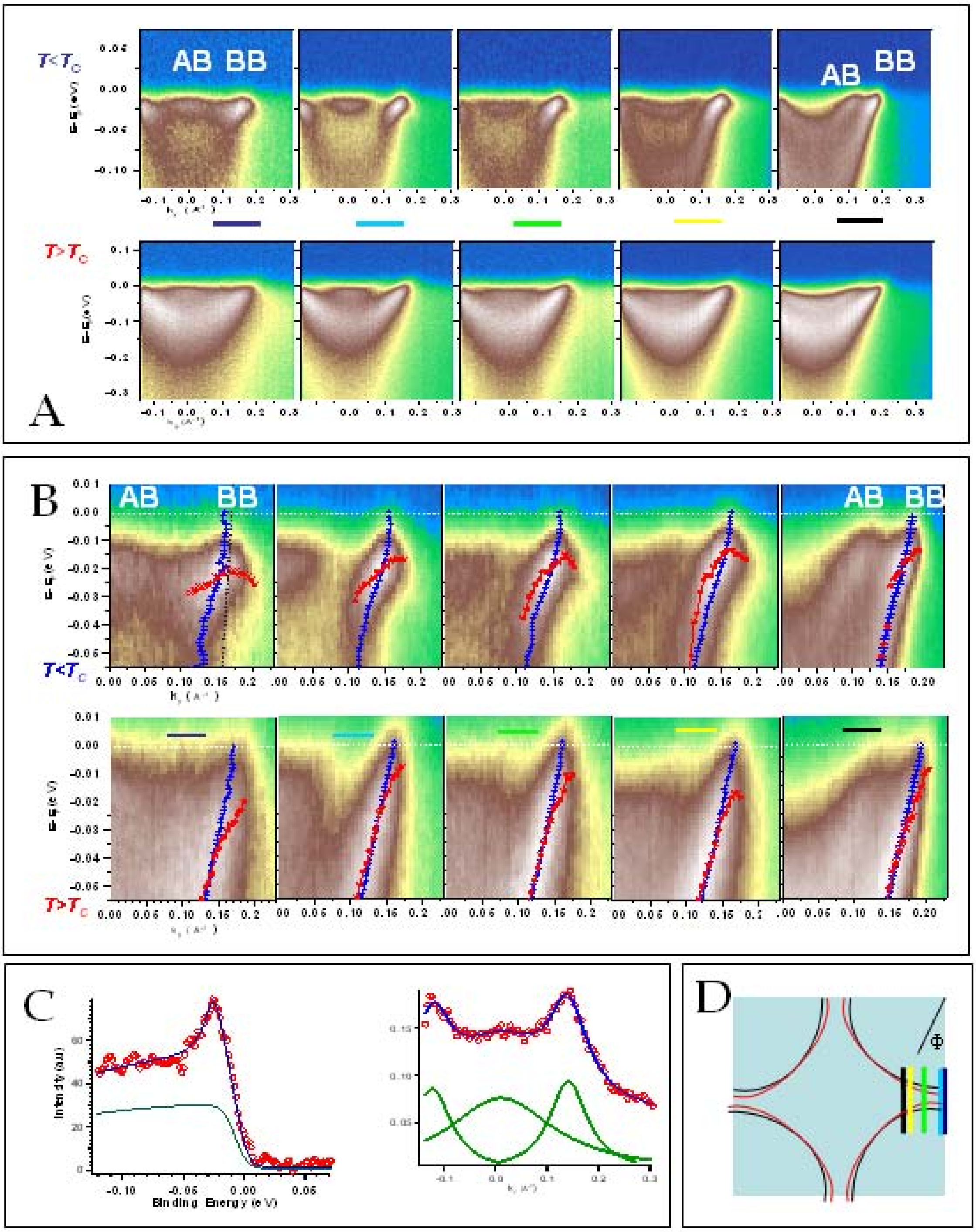

*Figure 3***:** ***(A)*** *ARPES intensity plots as a function of energy and wave vector for each Fermi surface angle at T =28 K (upper panel) and T = 120 K (lower panel). Left to right = AN towards N.* ***(B)*** *Zoom of same data.* ***(C)*** *Typical EDC fit (left) and MDC fit (right) at* k_F *, used for extracting the band dispersion.* ***(D)*** *Fermi surface cartoon, indicating location of the cuts in k-space.*

The ARPES experiments were carried out at the U125/1-PGM beamline using the IFW-Dresden group's SCIENTA SES100-based end station. Spectra were taken using a photon energy of 38 eV in order to give maximal contrast between the two c-axis split bilayer bands. The analyser slit is aligned parallel to the (π,π) – $(\pi,-\pi)$ direction. In order to minimise the impact of photon-induced changes on the spectra, we took a different spot on the crystals for each Fermi surface angle measurement.

In Fig. 3A, we show the collection of data from AN towards the nodal recorded in the superconducting state at T = 28 K (upper panel) and T =120 K (lower panel). One can clearly distinguish the two bilayer-split bands both in the low and high temperature data. To follow the band dispersion, we plot the peak position by fitting the EDC and MDC cuts through the 2D datasets. The EDC dispersion (overlaid in red) is more sensitive to the presence of the gap compared to the MDC dispersion (overlaid in blue). The MDC's are fitted using a simple Lorentzian, while the EDC is fitted using a Lorentzian multiplied by the Fermi-Dirac distribution, including a scaled background taken from $k < k_F$.

In the superconducting state (T = 28 K), the data show clearly a momentum dependence of mass renormalisation. The bonding bilayer split band is strongly renormalised at the antinode (leftmost data panel in Fig. 3A and B). This can be seen by the dramatic flattening of the dispersion (increase in mass) close to E_F compared to the steeper dispersion at higher binding energies. For a Fermi surface angle of ca. 25° (rightmost data panels), the change in velocity at low energies is significantly less.

There is also a clear temperature dependence of the renormalisation effects. For $T > T_C$, and particularly away from the antinode above T_C, the renormalisation effects become quite weak (see for example the rightmost panel of Fig. 3B). This focus of the strongest renormalisation effects in the region of the (p,0) point and their clear reduction in magnitude for $T > T_C$ would speak in favour of the magnetic fluctuation scenario and against the phonon scenario discussed in the introduction.

The next step, of course, is a quantitative evaluation of the renormalisation effects (for example of the bonding band) as a function of FS location and temperature. For 'classical' superconductors, the $T < T_C$ dispersion can be evaluated using the Bogolubov quasiparticle dispersion relation [3], however in high T_C superconductors the gap energy is too similar to the mode energy to be able to do this, and more complex expressions are required [6]. A detailed analysis of the data following these principles is currently underway.

Acknowledgments
We would like to acknowledge financial support from FOM (ILP, SICM[34]), and the EU (R-II-3 CT-2004_506008). Special thanks to the IFW-Dresden group for lending us their SES100 end station, and to the BESSY staff for expert and friendly assistance, both technical and logistic.

References :

[1] T.Valla, A.V. Fedorov, P.D. Johnsom, Q.Li, G.D. Gu and N.Koshizuka, *Phys. Rev. Lett.***85**, 828 (2000)
[2] P.V. Bogdanov, A. Lanzara. S.A. Kellar, X.J. Zhou, E.D. Lu, W.J. Zheng, G. Gu, J.I. Shimoyama, K. Kishio, H. Ikeda. R. Yoshizaki, Z. Hussain, and Z.X. Shen, *Phys. Rev. Lett.* **85**, 2581 (2000)
[3] T.K. Kim, A.A. Kordyuk, S.V. Borisenko, A. Koitzsch, M. Knupfer, H. Berger, and J. Fink, *Phys. Rev. Lett.* **91**, 167002 (2003)
[4] A.D. Gromko, A.V. Fedorov, Y.D. Chuang, J.D. Koralek, Y. Aiura, Y. Yamaguchi, K. Oka, Yoichi Ando and D. Dessau, *Phys. Rev.* **B68,** 174520 (2003)
[5] A. Mans, *et al.*, cond-mat/0508127, *Phys. Rev. Lett.*, in press.
[6] J. Fink, *et al.*, cond-mat/0512307

Transition energies and bowing parameters for In-rich InGaN and InAlN alloys

R. Goldhahn[1], P. Schley[1], A.T. Winzer[1], M. Rakel[2], C. Cobet[2], N. Esser[3], H. Lu[4]
and W.J. Schaff[4]

[1]Institut f. Physik und Inst. f. Mikro- und Nanotechnologien, TU Ilmenau, PF 100565, 98684 Ilmenau, Germany
[2]Institut für Festkörperphysik der TU Berlin, Hardenbergstraße 36, 10623 Berlin, Germany
[3]Institute of Spectrochemistry and Applied Spectroscopy Berlin, Albert-Einstein-Str. 9, 12489 Berlin, Germany
[4]Dept. of Electrical and Computer Engineering, Cornell University, Ithaca, New York 14853, USA

Growth and characterization of In-rich InGaN alloys has attracted much interest recently. It arises from the band gap correction for InN from the long time accepted value of 1.9 eV down to only about 0.7 eV. Due to the reduced band gap a renewed evaluation of many material parameters of InN and their compositional dependence for (In,Ga)N and (In,Al)N alloys is mandatory. For this aim, determination of the dielectric function (DF) by spectroscopic ellipsometry (SE) has become one of the most powerful methods for studying absorption related properties of In-compounds both around the band gap as well as in the range of the high-energy critical points (CP) of the band structure [1-3]. For example, the experimentally determined shape of the DF and the optical anisotropy of InN [1] has been theoretically reproduced recently [4]. Here, we report ordinary DF's up to 9.5 eV for In-rich InGaN and InAlN alloys and their analysis, i.e. transition energies for the CP's and their compositional dependences (bowing parameter). The latter data were determined by fitting the third derivatives of the DF.

The DF's of three $In_xGa_{1-x}N$ films (x=0.67, x=0.69, x=0.77) with ~300 nm thickness and three $In_xAl_{1-x}N$ films (x=0.91, x=0.83, x=0.71) with ~400 nm thickness were determined. Samples were grown on (0001) sapphire by plasma-induced molecular beam epitaxy (MBE) using either GaN or AlN buffer layer. Further growth details as well as results of the structural, electrical and optical characterisation has been published elsewhere [2,5].

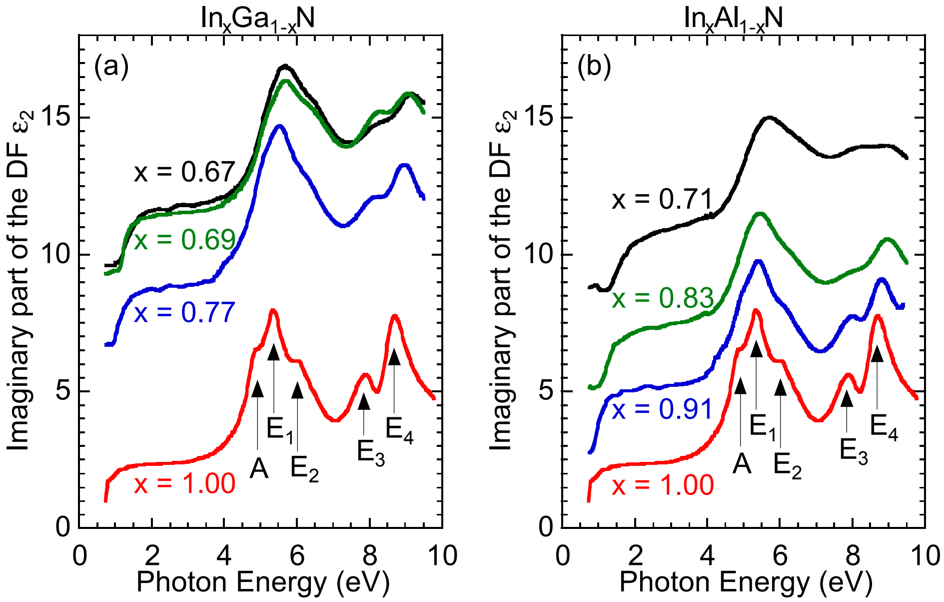

Fig. 1: Imaginary parts of the DF of $In_xGa_{1-x}N$ (a) and $In_xAl_{1-x}N$ (b) alloys obtained from fitting ellipsometric data Y and D. The alloy data are vertically shifted for sake of clarity according to the Indium content.

Figure 1 shows the imaginary part of the DF's for the InGaN (a) and InAlN (b) alloys and in comparison to the data of InN over the whole investigated range from 0.74 eV up to 9.5 eV. Due to the c-axis orientation normal to the surface, these data correspond to the ordinary dielectric tensor component [3]. The data above 4 eV were obtained from the BESSY ellipsometer at the 3m-NIM-monochromator, the excellent matching to the data recorded with a commercial ellipsometer (J.A. Wollam Co., Inc.) in the energy range from 0.74 up to 4.5 eV should be noted. Beside the gap structure in the low-energy range, the shape of the ordinary tensor component is strongly influenced by contributions arising from at least five critical points of the band structure in the energy range above 4.5 eV. All of them are clearly resolved for the alloys despite a larger broadening compared to InN. It confirms the good crystalline quality of the InGaN and InAlN films. As expected for an alloy system, they undergo a continuous shift to higher energies with increasing Ga(Al)-content.

For a high-resolution determination of the transition energies of the critical points following accurate approach was used. One calculate the third derivative of the point-by-point obtained DF (after surface roughness correction) multiplied by the square of the photon energy *E*. The resulting spectra can be fitted [6] via

$$\frac{d^3}{dE^3}\left(E^2\bar{\varepsilon}\right) = \sum_{j=1}^{5} e^{i\cdot f_j} \cdot \frac{C_j}{\left(E + i\cdot\Gamma_j - E_j\right)^{n/2}} , \qquad (1)$$

where f_j, C_j, G_j, and E_j denote the phase angle, the magnitude, the broadening energy, and the transition energy of the j-th CP, respectively. With n=6 corresponding to a two-dimensional critical point, we obtain excellent agreement to the experimental data which is exemplarily demonstrated for $In_{0.77}Ga_{0.23}N$ and $In_{0.91}Al_{0.09}N$ in Fig. 2(a) and (b), respectively.

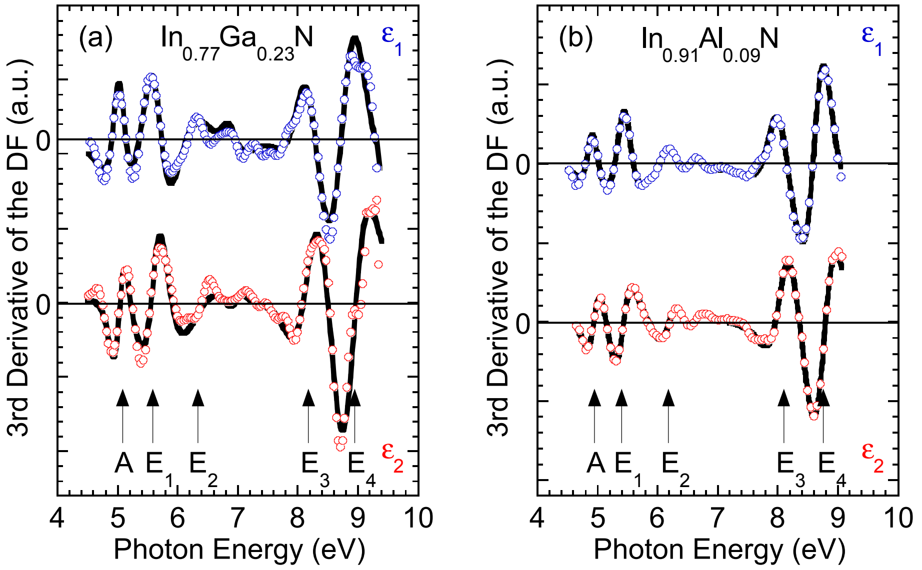

Fig. 2: Fit of the third derivative of the DF for the $In_{0.77}Ga_{0.23}N$ (a) and the $In_{0.91}Al_{0.09}N$ (b) sample. The circles represent the experimental data, and solid lines are the best fit. The transition energies of the critical points are marked by arrows.

Figure 3(a) displays all fitted critical point energies for InGaN alloys. They amount for InN: 4.86 eV (A), 5.44 eV (E_1), 6.06 eV (E_2), 7.99 eV (E_3), and 8.59 eV (E_4). With the values for GaN of 7.00 eV (E_1), 7.96 eV (E_2), 9.25 eV (E_3) bowing parameters of *b*=0.44 eV (E_1), 1.33 eV (E_2), and 0.83 eV (E_3) are obtained. For the determination of the band gap values, carrier induced band gap renormalization and Burstein-Moss shift was taken into account [2]. Taking the values for InN of E_0=0.68 eV [2] and for GaN of E_0=3.45 eV the fit yields *b*=1.77 eV for the fundamental band gap bowing, which is in good agreement with the previously published value of 1.43 eV [7]. Figure 3(b) evinces the results for InAlN alloys. With the values for AlN of 6,30 eV (E_0), 7.97 eV (E_1) and 8.95 eV (E_2) bowing parameters of b=4.0 eV (E_0), 1.8 eV (E_1) and 2.7 eV (E_2) are obtained. No estimations can be made for the other critical points due to the lack of corresponding data for AlN.

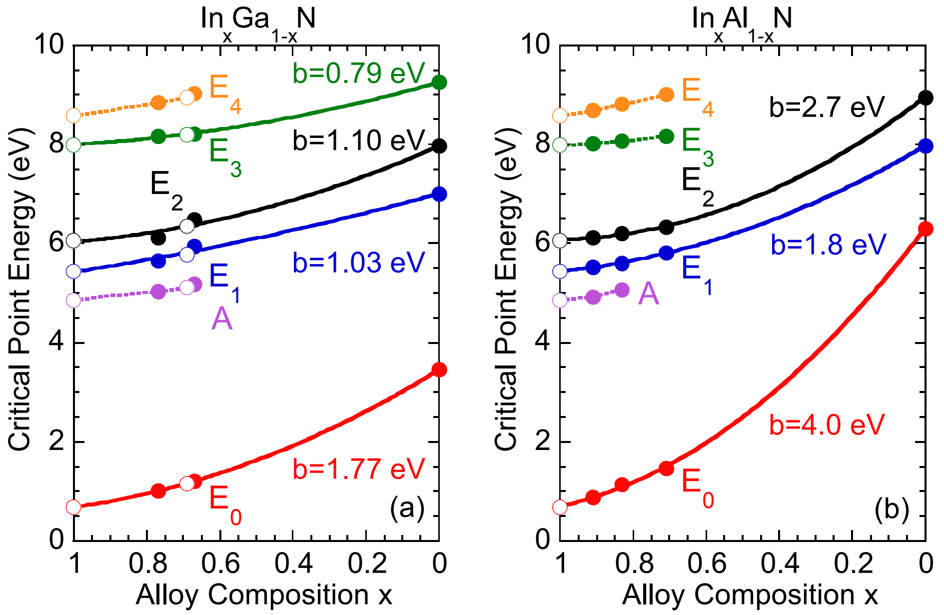

Fig. 3: Resulting critical point energies of InGaN (a) and InAlN (b) alloys as a function of composition. The open and full circles refer to the samples grown on GaN buffer and on AlN buffer, respectively. The solid lines represent the fit results.

In summary, we have determined the DF's of InGaN and InAlN alloys in the energy range from 0.74 eV up to 9.5 eV. Applying a third derivative based DF line shape fitting procedure yields the transition energies in the range of the critical points of the band structure with highest resolution. From the transition energies the bowing parameters for the compositional dependence of four and three critical points for InGaN and InAlN alloys, respectively, are derived.

The work at BESSY was supported by the BMBF grants 05KS4KTB/3 and 05ES3XBA/5. R.G. and the Ilmenau group acknowledge support by the DFG (GO 1378/2,3) and by Thüringer Ministerium für Wirtschaft, Technologie und Arbeit (B509-04011). respectively. The Cornell group is supported by ONR(N000149910936).

References

[1] R. Goldhahn, A.T. Winzer, V. Cimalla, O. Ambacher, C. Cobet, W. Richter, N. Esser, J. Furthmüller, F. Bechstedt, H. Lu, and W.J. Schaff, Superl.&Microstruc. **36**, 591 (2004).

[2] R. Goldhahn, P. Schley, A.T. Winzer, G. Gobsch, V. Cimalla, O. Ambacher, M. Rakel, C. Cobet, N. Esser, H. Lu, and W.J. Schaff, phys. stat. sol. (a) **203**, 42 (2006).

[3] R. Goldhahn, P. Schley, A.T. Winzer, M. Rakel, C. Cobet, N. Esser, H. Lu, and W.J. Schaff, J. Cryst. Growth **288**, 273 (2006)

[4] J. Furthmüller, P.H. Hahn, F. Fuchs, and F. Bechstedt, Phys. Rev B **72**, 205106 (2005).

[5] P. Schley, R. Goldhahn, A.T. Winzer, G. Gobsch, V. Cimalla, O. Ambacher, M. Rakel, C. Cobet, N. Esser, H. Lu, and W.J. Schaff, phys. stat. sol. (a) (in press).

[6] D.E. Aspnes, Phys. Rev. Lett. **28**, 168 (1972); D.E. Aspnes and J.E. Rowe, Phys. Rev. B **5**, 4022 (1972).

[7] J. Wu, W. Walukiewicz, K.M. Yu, J.W. Ager III, E.E. Haller, H. Lu, and W.J. Schaff, Appl. Phys. Lett. **80**, 4741 (2002).

Metal-organic semiconductor interfaces:
In and Sn on CuPc

V.Yu. Aristov [1,2], O.V. Molodtsova[1], V.M. Zhilin[2], D.V. Vyalikh[3], M. Knupfer[1]

[1]Leibniz Institute for Solid State and Materials Research, D-01069 Dresden, Germany
[2]Institute of Solid State Physics, Russian Academy of Sciences, Chernogolovka,
Moscow Distr., 142432, Russia
[3]Institute of Solid State Physics, TU Dresden, D-01069 Dresden, Germany

Organic molecular thin films (OMTF's) have received considerable attention over the past two decades because of their potential applications in the development of OMTF's-based various devices like light-emitting diodes, field effect transistors and photovoltaic cells. The metal-OMTF interface formation carried out in UHV becomes a principal base for organic micro- and nano-device technologies [1]. In spite of the importance of metal-OMTF contacts in general, there is no complete microscopic understanding of this class of interfaces. This is particularly true for contacts that are prepared by deposition of a metal onto an organic film, while in the opposite case, a deposition of organic semiconductors onto metals, there have been quite a large number of experimental and theoretical studies and some progress recently has been achieved as regards basic interfacial properties [1, 2]. The former case (metal deposition onto organic films) is comparatively much less studied [1, 3-5].

The family of the phthalocyanines (Pc's) (which are archetypal organic molecular semiconductors) plays an important role among other OMTF's. Their biological significance, catalytic properties and potential technological applications [6] are the good reason for researcher to pay remarkable attention to these materials. Moreover, Pc's demonstrate good compatibility with UHV and can be successfully grown as thin, ultra-clean, well ordered films on various substrates in standard UHV spectrometers. These films then possess excellent and well defined electronic properties [6]. In the present investigation we have focused on the evolution of the electronic structure of copper phthalocyanine films during metal deposition and on interactions during this process. Indium and tin has been chosen as an example of the metals with a relatively low work function.

The UHV electron spectrometer on the Russian-German high energy resolution dipole beam line of the Berliner Speicherring für Synchrotronstrahlung (BESSY) was used for the preparation of the CuPc film, the metal (In and Sn) deposition and the soft x-ray photoemission spectroscopy measurements. The VB and CL photoemission spectra were acquired with a VG-CLAM4 electron-energy analyzer. The CuPc film preparation as well as other experimental details could be found elsewhere [7].

The bottom spectra in Figures 1(a) -1(c) show C 1*s* core level, extended VB, and the top of the VB recorded from a CuPc film as grown on the Au(100) substrate. The C 1*s* core-level of pristine CuPc is comprised of two components: C-1 which corresponds to the aromatic carbon of the benzene rings of CuPc, and C-2 which is attributed to the carbon linked to nitrogen (pyrolle carbon). In addition each C 1*s* component has an additional satellite contribution, S_{C-1} and S_{C-2} respectively [8]. The onset of the CuPc valence band (peak A) indicates that the initial E_F position is located near the middle of the transport gap. According to [9] the spectral features B and C of the valence band can be attributed to: (i) peak B - the benzene C 2*p*, the bridging aza and pyrolle N 2*p*; (ii) peak C - the benzene C 2*p*, the bridging aza and the pyrolle N 2*p*, and H 1*s*.

Figs 1(a) – 1(d) also present the CuPc C 1*s* core level, the extended valence band, the top of the valence band and the In 4d core level as a function of In coverage on a 70 Å CuPc film. The shape of the C 1*s* core level spectra practically shows no observable changes with increasing In coverage which could indicate that neither pyrolle nor benzene ring carbon atoms show remarkable chemical interaction with the deposited metal. Nevertheless a chemical reaction between In and CuPc becomes evident already upon deposition of smallest amount of the metal – 1-2 Å. In the Figs 1(b) and 1 (c) one clearly observes for such small In coverages a VB shift of about 0.26 eV to higher binding energy.

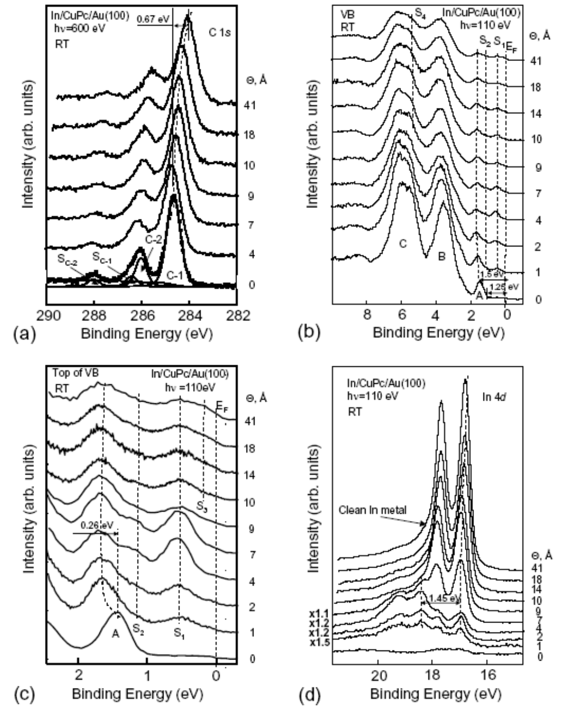

Figura 1. (a) C 1*s* core level, (b) extended valence band, (c) top of the valence band, and (d) In 4*d* core level measured using photoemission spectroscopy, as a function of In deposition on CuPc films at RT.

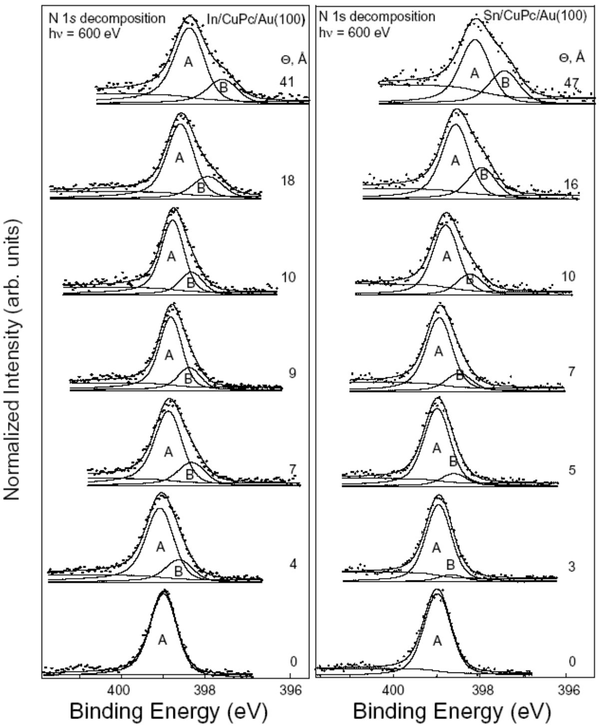

Figura 2. (a) The results of decomposition of the N 1s core level for the spectra recorded from the CuPc films as a function of In (left panel) and Sn (right panel) deposition

At the same time, peaks S_1 and S_2 appear in the gap of CuPc. A third (S_3) feature in the gap and another (S_4) feature which is seen as a shoulder of the peak C appear at a nominal In coverage of ≥□10 Å. Thus after initial deposition In atoms diffuse into the CuPc film and a strong chemical reaction between In the CuPc molecule takes place. This conclusion is further supported by the evolution of the In core levels (Fig. 1(d)). At the smallest In deposition a relatively strong component of the In 4*d* core level appears in the spectra being shifted by 1.45 eV to higher BE with respect to metallic In. In addition one can clearly see that the In 4*d* core level width of the reacted In is very similar to that of the metallic In, which indicates that In atoms being incorporated into the CuPc film are not randomly distributed in the film, but occupy certain, well defined equivalent positions.

Summarizing the discussion presented so far we conclude that indium atoms diffuse into the CuPc film, give up charge to the CuPc molecules and most probably occupy equivalent positions. We now consider Fig. 2 (left panel), where the variations of the N 1*s* core level spectra upon In deposition are shown. From decomposition of N 1*s* it is evident, that with deposition of about 4 Å of In, the component A shows a shift and simultaneously an additional component B appears. This B component leads to the overall N 1*s* asymmetric peak broadening. The B component of the N 1*s* core level must be attributed to those N atoms, which are linked to pyrolle carbon and are involved in a chemical interaction with In atoms. The detailed analysis of A and B component behavior (see Fig. 3 (left panel)) gives us arguments for the conclusions, that the In deposition onto CuPc films is characterized by two stages of the In/CuPc interface formation. The first stage takes place until a nominal In coverage of 5 - 6 Å and is characterized by strong diffusion of the In atoms into the organic film. In atoms occupy sites close to the pyrolle nitrogens (Fig. 4), strongly interact and transfer negative charge to CuPc. This stage comes to the end when a stoichiometry of In_2CuPc is reached. The second stage begins just after the first is completed, at $\Theta \geq 7$ Å: on top of the In_2CuPc compound a metallic indium film is formed (Fig. 5).

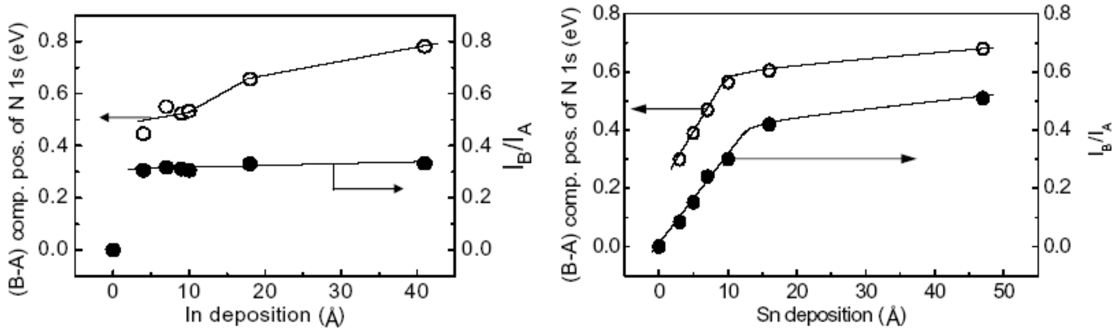

Figura 3. The A-B distance (open circles) and the B/A intensity ratio (closed circles) between A and B components of the N 1s core level from the decomposition presented in Fig.4 with increasing coverage of In.

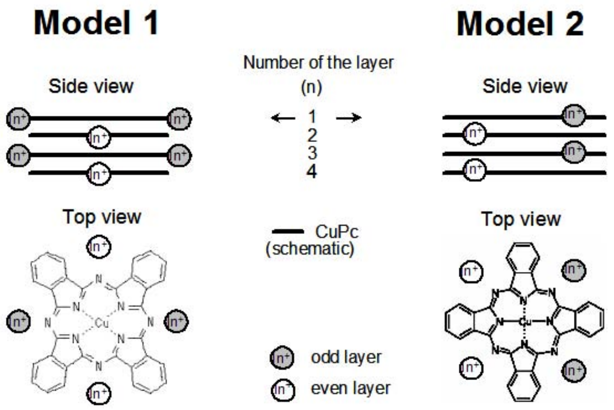

Figure 4. Schematic diagrams of the derived site positions of In ions diffused into the CuPc film. (left panel) In – In direction between two metallic ions belonging to the same CuPc molecule alternately changes by 90 degree viewing the normal to the molecular plane (along the stacking axis). (right panel) Other possible arrangement of In ions in CuPc films.

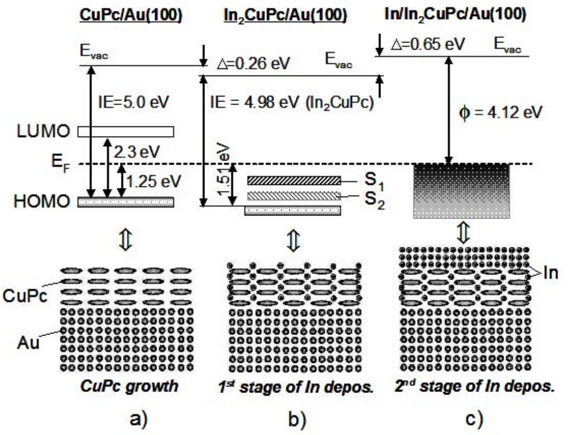

Figure 5. Schematic representation of the energy levels derived from our experiment during indium deposition onto a CuPc film grown on Au(100). The different stages are indicated.

The equivalent results of Sn/CuPc interface formation are presented in Fig. 2 (right panel) and Fig. 3 (right panel). Even simple comparing of the data for In/CuPc and Sn/CuPc interface formation presented in Figs. 2 and Fig. 3 shows evident difference for both systems studied. The detailed discussion will be presented in a forthcoming publication.

References

[1] A. Kahn, N. Koch, W. Gao, J. Polymer Science: Part B: Polymer Physics **41** (2003) 2529.
[2] M. Knupfer and H. Peisert, Phys. Stat. Sol. (a) **201** (2004) 1055.
[3] Y. Hirose, A. Kahn, V. Aristov, P. Soukiassian, Appl. Phys. Lett. **68** (1996) 217.
[4] N.J. Watkins, L. Yan, and Y. Gao, Appl. Phys. Lett. **80** (2002) 4384.
[5] C. Shen, A. Kahn, and J. Schwartz, J. Appl. Phys. **90** (2001) 6236.
[6] S.R. Forrest, Chem. Rev. **97** (1997) 1793, and references therein.
[7] V.Yu. Aristov, O.V. Molodtsova, V.M. Zhilin, D.V. Vyalikh, M. Knupfer, Phys. Rev. B. **72** (2005) 165318.
[8] T. Schwieger, H. Peisert, M. S. Golden, M. Knupfer, J. Fink, Phys. Rev. B **66** (2002) 155207.
[9] N. Papageorgiu et al., Phys. Rev. B **68** (2003) 235105.

ZnO based solid solutions – X-ray spectroscopy studies with ROSA at U41-PGM

D. Wett, A. Demund, D. Schulze, K.-H. Hallmeier, R. Szargan

Wilhelm-Ostwald-Institut, Universität Leipzig, Linnéstr. 2, 04106 Leipzig

Zinc oxide (ZnO) has become an interesting material because of its excellent optical, electronic and dielectric properties and, last but not least, because of its low price. ZnO can be used as transparent, conductive material for solar cell caps, short wavelength lasers, vacuum fluorescent or field-emission displays and light-emitting diodes.$Zn_{1-x}Mg_xO$ alloys from wurtzite-type ZnO (E_{gap} = 3.37 eV) and rock-salt-type MgO (E_{gap} = 7.5 eV) allow the tuning of the direct band-gap [1].

X-ray emission (XES) and absorption (XANES) are suitable methods to gain information on the chemical state of atoms and the electronic structure of materials. Polarisation dependent XANES is used to reveal the geometrical orientation of anisotropic crystals or films, as it is the case in wurtzite type ZnO because of its polarity in c direction [2]. For $Zn_{1-x}Mg_xO$, variations in the OKα spectra depending on x are compared with density functional theory (DFT) calculations of the Zn3d+4s and O2p density of states.

All the meaurements have been carried out using the ROSA (rotatable spectroscopy apparatus) at beamline U41-PGM. This endstation is equipped with a SCIENTA XES 300 spectrometer for XES measurements and an electron analyser. The XANES were taken using a channeltron operated in total electron yield (TEY) mode in order to avoid surface sensitivity. The ZnO crystals were obtained from CrysTec (Berlin). The $Zn_{1-x}Mg_xO$ films on Si were prepared by pulsed laser deposition (PLD).

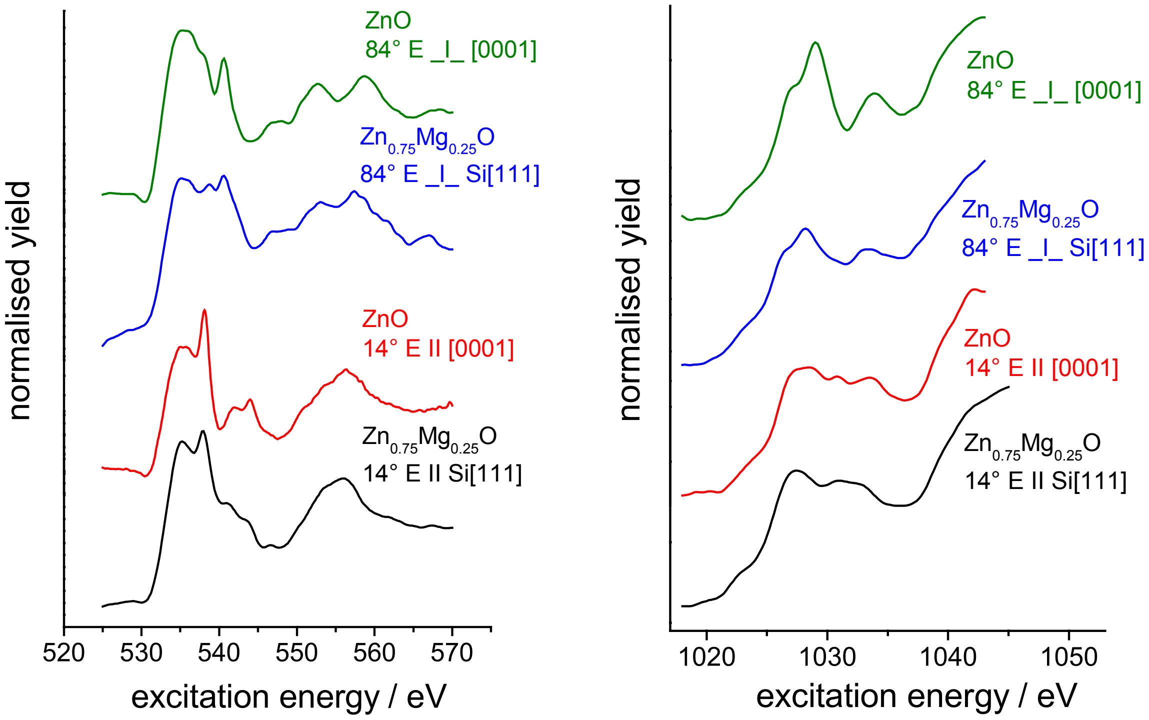

Fig. 1: Polarisation dependence of the OK (left) and ZnL_3 XAS (right) of ZnO and PL deposited $Zn_{0.75}Mg_{0.25}O$/Si(111)

Figure 1 shows the OK (1s→2p) and ZnL3 (2p→3d,4s) XANES of a ZnO single crystalline sample as well as a $Zn_{0.75}Mg_{0.25}O$ film pulsed laser deposited on a Si(111) substrate. Both the OK and ZnL_3 XANES of ZnO have a strong dependence on the polarisation direction of the synchrotron light relative to the sample c-axis indicating an anisotropy of both the Zn3d+4s and O2p empty orbitals in the [0001] direction. An angle of 90° means that the incidence of the horizontal polarised light was normal to the surface. Furthermore, the shapes of the spectra corresponding to the $Zn_{0.75}Mg_{0.25}O$/Si(111) sample point out a c-orientated film growth. The experimental XANES are in good agreement to theoretical data [2].

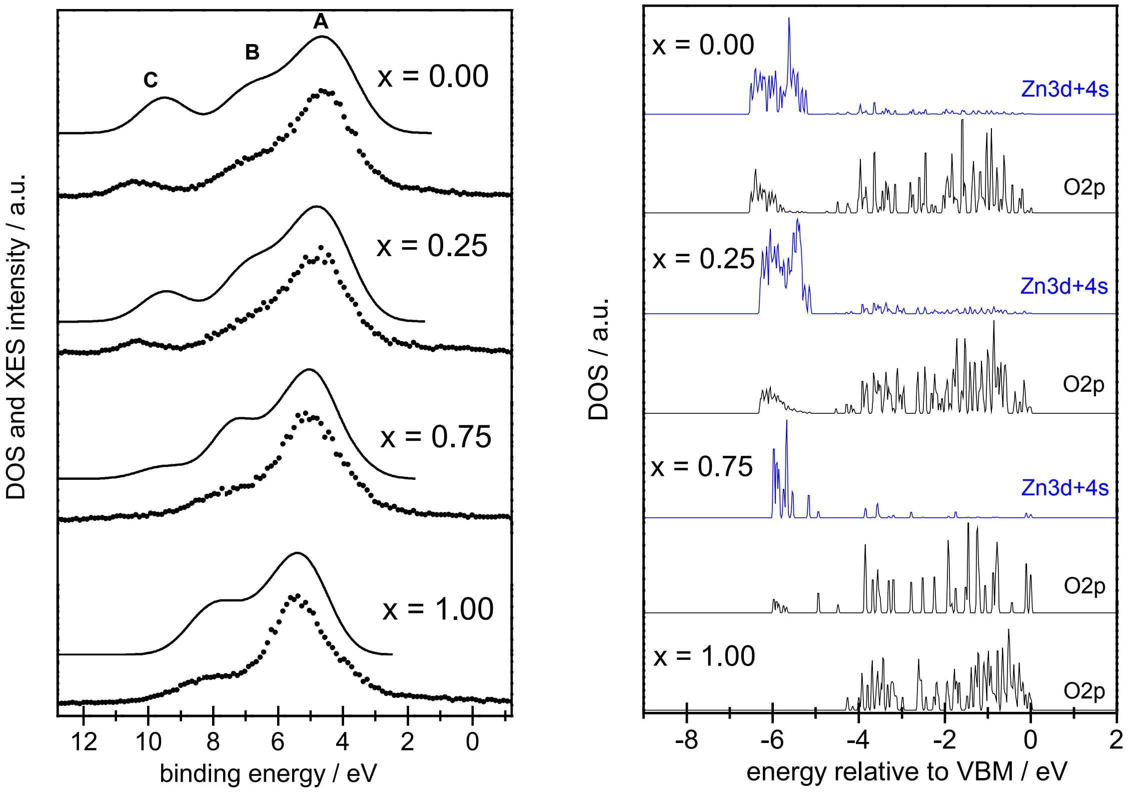

Fig. 2: OKα XES (•••) and O2p DOS (—), Gaussian-broadened by 0.7 eV (left); Zn3d+4s and O2p DOS (right) for different x in $Zn_{1-x}Mg_xO$

The OKα X-ray emission spectra of two different $Zn_{1-x}Mg_xO$ compounds and pure ZnO as well as MgO are shown in figure 2. With respect to our experimental resolution the O2p valence band is formed by 3 subbands A,B,C at energies around 5.0, 7.5 and 10.5 eV, respectively. The intensity of band C is obviously linked to the sample's Zn amount and dissappears in case of pure MgO. By ZnLα XES as well as valence band XPS measurements (not shown here) we found the Zn3d states positioned at the same energy like band C. Therefore, we attributed this feature to O2p-Zn3d mixed valence states. A DFT-GGA calculation of $Zn_{1-x}Mg_xO$ with x = 0, 0.25, 0.75 and 1 does support this finding. The calculated partial densities of states are, after an 0.7 eV Gaussian broadening, in good agreement with the experimental data. The valence band of ZnO is dominated by Zn3d-O2p-mixed states. Taking into account that $Zn_{1-x}Mg_xO$ with x = 0 and 0.25 is of wurtzite type and with x = 0.75 and 1 it is of rocksalt type, the different coordination geometry obviously has no influence on the appearance of feature C.

Acknowledgements:

This work was financed by DFG FOR 404-SZ58/15. We are grateful to M. Lorenz and H. Hochmuth for preparing the $Zn_{1-x}Mg_xO$ films and for the technical support by C. Jung and M. Mast at the U41-PGM beamline, BESSY.

References:

[1] M. Lorenz, E.M. Kaidashev, H. von Wenckstern, V. Riede, C. Bundesmann, D. Spemann, G. Benndorf, H. Hochmuth, A. Rahm, H.-C. Semmelhack, M. Grundmann: Optical and electrical properties of epitaxial $(Mg,Cd)_xZn_{1-x}O$, ZnO, and ZnO:(Ga,Al) thin films on c-plane sapphire grown by pulsed laser deposition
Solid-State Electronics, Volume 47, Issue 12, December 2003, Pages 2205-2209

[2] Teruyasu Mizoguchi, Isao Tanaka, Satoru Yoshioka, Masahiro Kunisu, Tomoyuki Yamamoto, and W. Y. Ching:
First-principles calculations of ELNES and XANES of selected wide-gap materials: Dependence on crystal structure and orientation
Physical Review B 70, 045103 (2004)

Optical transitions through the fundamental direct band gap in $CuInO_2$

Igor Konovalov, Liudmila Makhova, Daniel Wett, Rüdiger Szargan
Wilhelm-Ostwald-Institut für Physikalische und Theoretische Chemie,
Universität Leipzig, Linnéstr. 2, D-04103 Leipzig
Tel.: (0341) 9736490; Fax: (0341) 9736399; E-Mail: ikono@chemie.uni-leipzig.de

Recently, a new class of ternary conductive transparent oxides of p-type having delafossite structure is emerged [1-5]. Electrical and optical properties of these compounds demonstrate interesting and practically important anomalies [6], obviously related to their band structure. Although thin films of e. g. $CuInO_2$ material are transparent, having an apparent band gap of about 3,9 eV (according to measurements of the optical absorption), the material can be doped both p- and n-type, meaning an enormousy large dopability range. However, no successful optical p-n emission device, made of delafossite only, has been reported so far. Further anomaly of the apparent band gap variation vs. ion size appears when comparing properties of various Cu-III-O_2 oxides [6]. Nie et al. have simulated from the first principles the band structure of several delafossite Cu-III-O_2 oxides and found that the band structure is indirect with a narrow band gap ($CuInO_2$: 0.41 eV) between Γ minimum and F maximum (see Fig. 1), thus explaining the wide dopability range [6]. The fundamental direct transitions at Γ point ($CuInO_2$: 0.73 eV) are parity-forbidden. Thus, the apparent optical band gap is even significantly larger. The aim of this work is to clarify experimentally the local partial density of states at Γ point applying the selection rules.

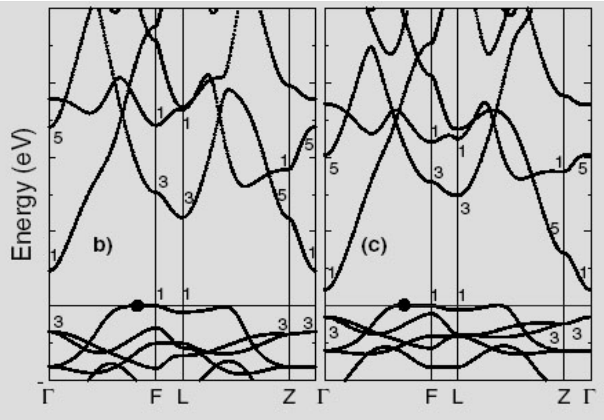

Fig. 1 Simulated band structure of $CuGaO_2$ (left side) and $CuInO_2$ (right side) [6].

We studied the local partial density of states in the valence band using x-ray emission spectroscopy(XES), and in the conduction band using x-ray absorption spectroscopy(XAS) by electron yield. Using the binding energy of the corresponding core lines (as determined by x-ray photoelectron spectroscopy XPS), the spectra were shifted towards the Fermi edge. According to the approximation of LCAO (linear combination of the atomic orbitals) theory, the density of states in the bands can be considered as a sum of the local partial density of states of the contributing atoms. Although the precise energy of the X-ray absorption edge may be influenced by the formation of an exciton with the core hole, the shift is typically small enough for a qualitative consideration. Fig. 2 shows the resulting approximation of the local partial density of electronic states for $CuInO_2$ and $CuGaO_2$ together with an XPS scan of the valence band region.

As it follows from the graphs, both conduction and valence band edges are predominantly Cu s and/or d states (red lines). The transition between these states is a forbidden one, because of the symmetry selection rules. This finding explains the low absorption coefficient in the visible, in spite of a narrow fundamental direct band gaps of both the compounds. The spacing between the copper occupated and unoccupated states in two materials follows the trend shown in Fig. 1. Besides of these expected findings, there are some unexpected observations: the shape of the Cu XAS lines is similar to that in compounds with Cu^{2+}. We repeated the measurements of the XAS using the x-ray photon yield detector in order to increase the information depth of the absorption measurements and minimize the influence of the surface oxidation. The result of the photon yield measurement remained qualitatively identical with that shown in Fig. 2. Further, the position of the copper XAS peak seems to be below the Fermi level. Although this observation can be explained by a possible different doping of the samples in XPS and XES measurements, this finding correlates with the spectra of Cu^{2+}, known from the literature [7]. In this case, the formation of the core level exciton was observed, resulting in a significant decrease of the energy of the Cu 2p absorption edge.

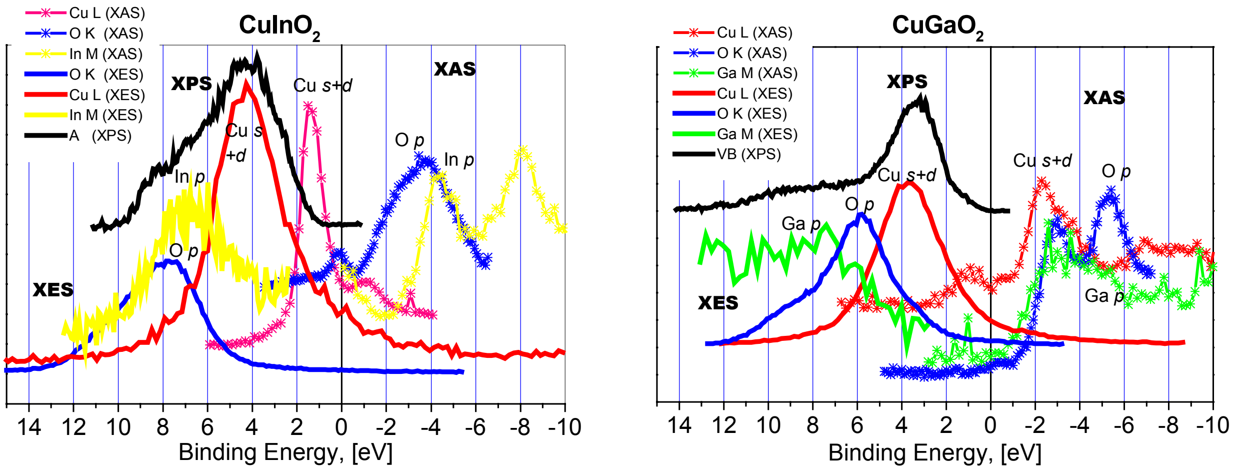

Figure 2. XES and XAS spectra of $CuInO_2$ and $CuGaO_2$ aligned with respect to the binding energy scale from XPS.

[1] H. Kawazoe, M. Yasukawa, H. Hyodo, M. Kurita, H. Yanagi, H. Hosono, „P-type electrical conduction in transparent thin films of $CuAlO_2$“ Lett. to Nature 389 (1997) 939.

[2] M. Shimode, M. Sasaki, K. Mukaida „Synthesis of the Delafossite-Type $CulnO_2$“

[3] H. Yanagi, T. Hase, S. Ibuki, K. Ueda, H. Hosono „Bipolarity in electrical conduction of transparent oxide semiconductor $CuInO_2$ with delafossite structure“ Appl. Phys. Lett. 78 (2001) 1583

[4] J. Robertson, P.W. Peacock , M.D. Towler , R. Needs „Electronic structure of p-type conducting transparent oxides Thin Solid Films 411 (2002) 96

[5] M. Sasaki, M. Shimode „Fabrication of bipolar $CuInO_2$ with delafossite structure“ J. of Phys. and Chem. of Solids 64 (2003) 1675

[6] X. Nie, S.-H. Wei, S. B. Zhang „Bipolar Doping and Band-Gap Anomalies in Delafossite Transparent Conductive Oxides“ Phys. Rev. Lett. 88 (2002) 066405-1

[7] M. Grioni, J. B. Goedkoop, R. Schoorl, F. M. F. de Groot, J. C. Fuggle, F. Schäfers, E. E. Koch, G. Rossi, J. – M. Esteva, R. C. Karnatak „Studies of copper valence states with Cu L_3 x-ray absorption spectroscopy“ Physical Review B 39 (1989) 1541

Quasi-molecular effects in Cr 2*p* absorption spectra of the chromium compounds

M.A. Nesterov[1], A.S. Vinogradov [1], S.A. Krasnikov [1,2], A.B. Preobrajenski [1,3],
M.M. Brzhezinskaya [1], Yu.S. Dedkov [4], S.L. Molodtsov [1,4], R. Puettner [5] and G. Kaindl [5]

[1)] *Institute of Physics, St. Petersburg State University, St. Petersburg, 198504 Russia*
[2)] *School of Physical Sciences, Dublin City University, Dublin 9, Ireland*
[3)] *MAX-lab, Lund University, Lund, Sweden*
[4)] *Institut für Festkörperphysik, Technische Universität Dresden, Dresden, Germany*
[5)] *Institut für Experimentalphysik, Freie Universität Berlin, Berlin, Germany*

Properties of 3*d* transition metal (TM) compounds are usually analyzed taking into account the number of strongly localized 3*d* electrons of TM atoms and the correlation between these electrons. However, the presence of covalent chemical bonding between the 3*d* atom and its environment leads to a decrease of the 3*d* electrons localization and, consequently, to a weakening of the 3*d* electron correlations. Characteristics of the chemical bonding and electron correlations are revealed in parameters of the energy distribution of empty and filled 3*d* electron states. Thus, detailed information on the unoccupied 3*d* electron states is required for a better understanding of the electronic structure and properties of the TM compounds. This information can be easily obtained from 2*p* absorption spectra of TM atoms. The main aim of the present project was (i) to conduct high-resolution, uniformly calibrated measurements of the Cr 2*p* absorption spectra for the series of Cr(II), Cr(III), and Cr(VI) compounds with the different types of chemical bonding and (ii) to analyze them in the context of their relation to the electronic structure and to features of the chemical bonding in these Cr compounds .

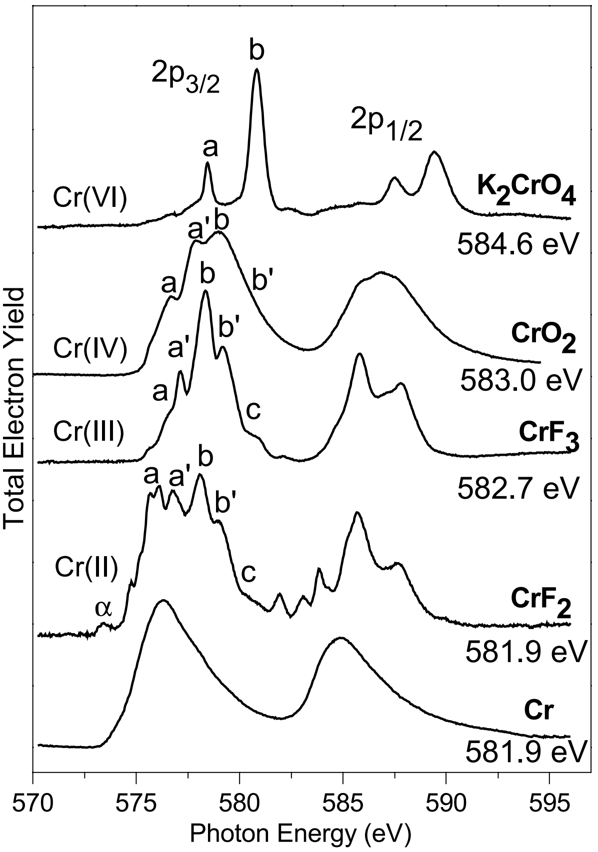

Fig. 1. *Cr 2p NEXAFS spectra of compounds with a different valency of the Cr atom.*

During the single-bunch beamtime at the PM-RD beamline we have measured high-resolution (ΔE ~90 meV) Cr 2*p* absorption spectra of various Cr(II), Cr(III), and Cr(VI) compounds $Cr^{II}F_2$, $Cr^{III}F_3$, $Cr^{III}_2O_3$, $Cr^{III}(acac)_3$, $Cr^{III}(NO_3)_3$, $K_3Cr^{III}(CN)_6$, $Cr^{VI}O_3$, $K_2Cr^{VI}O_4$, $K_2Cr^{VI}_2O_7$, and metallic Cr. The spectrum of $Cr^{IV}O_2$ was taken by us previously [1]. Additionally we have investigated high-resolution (ΔE ~70 meV) N 1s absorption spectra of $K_3Cr(CN)_6$, The NEXAFS spectra of these chromium compounds and metallic Cr were recorded via the total electron yield. The samples of the compounds were prepared by rubbing powders of these materials into the scratched surface of a clean tantalum plate, while the metal sample was a thin (~ 50 nm) polycrystalline film deposited *in situ* with an atomic beam from an evaporation cell heated by an electron beam onto a clean copper plate in a vacuum of 5×10^{-8} mbar. The absorption spectra were normalized to the incident photon flux, which was monitored by detecting the photocurrent from a gold mesh placed at the outlet of the beamline. In order to enable a comparison of the spectral features, the relative intensities of the spectra have been normalized to the same continuum jump at the photon energy of 595 eV. The photon energy in the region of the Cr 2*p* absorption spectra (560 – 610 eV) was calibrated using the known energy position of the first narrow peak in the O 1*s* absorption spectrum of the rutile TiO_2 (531.0 eV [2]) while the first narrow peak in the Ti 2*p* absorption spectra of solid K_2TiF_6 (459.0 eV [3]) was used for the energy calibration of N 1*s* absorption spectra.

As is seen from the Fig.1, the absorption spectra of the compounds, in which the Cr atoms have the octahedral (CrF_2, CrF_3, CrO_2) and tetrahedral (K_2CrO_4) environment by ligand atoms and a different valence (oxidation) state, exhibit considerable distinctions in the shape of absorption structures and their energy positions. These spectral distinctions reflect energy distribution features of empty 3*d*-states conditions as the spectrum is defined by 2*p* → 3*d* transitions. It is evident that a high-energy shift is characteristic of Cr 2*p* spectra in going from the divalent-chromium compound, CrF_2, to hexavalent-chromium one, K_2CrO_4. High-energy shift of Cr 2*p* spectra quantitatively characterized by the energy shift of the center of gravity (CG): Cr(II) – Cr(III) = 0.8 eV; Cr(III) – Cr(IV) = 0.3 eV; Cr(IV) – Cr(VI) = 1.6 eV.

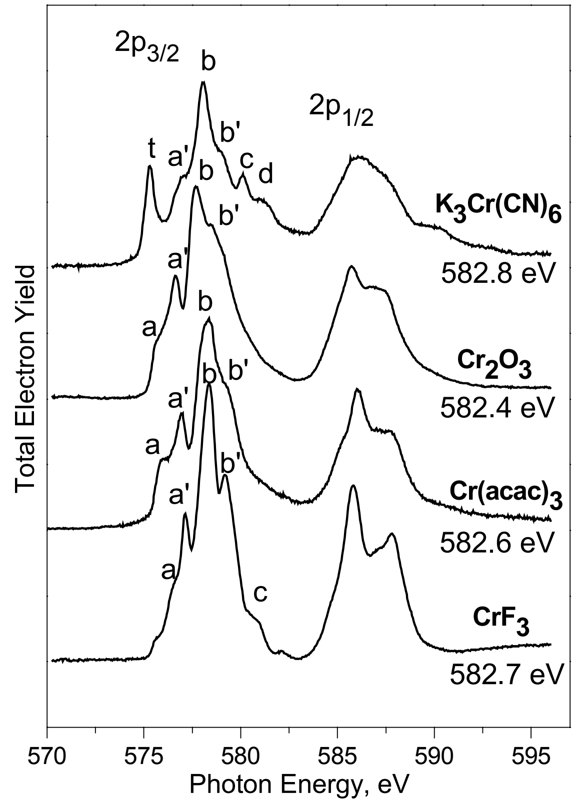

Fig. 2. *Cr 2p absorption spectra of the trivalent cromium atom in compounds. The numbers show energy position of the center of gravity for Cr 2p absorption of each compound.*

The Cr 2*p* absorption spectra of the Cr(III) compounds are shown in Fig. 2. The Cr atoms in these compounds have formally the same chemical state and the octahedral (or nearly octahedral) surroundings by ligand atoms (F, O, or C). As a result, the spectra of these compounds as a whole are very similar, the exception is only provided by that of $K_3Cr(CN)_6$. The most important distinction between the spectra compared is that the absorption structure is shifted to a lower photon energy in going from the most ionic compound, CrF_3 (CG ≈ 582.67 eV), to the less ionic $Cr(acac)_3$ (CG ≈ 582.62 eV) and Cr_2O_3 (CG ≈ 582.44 eV). This low-energy shift of CG reflects a growing screening of the initial and final states of the 2*p* →3*d* absorption transitions by the increasing valence electron charge along the CrF_3 - $Cr(acac)_3$ - Cr_2O_3 series. Thus, only a small chemical effect on these spectra could be detected. As a consequence, the Cr 2*p* excitations should be have the same origin for the three respective compounds and may probably be considered within the frame of various ionic multiplet approaches developed for the 3*d* metal compounds with the strong ionic bonding, such as CrF_3. The valence electron charge may be thought to affect mainly the energy position of this multiplet. Going to the $[Cr(CN)_6]^{2-}$ complex in $K_3Cr(CN)_6$, we observe pronounced changes in absorption structures and a marked high-energy shift of spectrum. This most covalent compound should give a further low-energy shift of the absorption spectrum due to the subsequent increase of the valence electron charge. Thus, the observed shift cannot be associated with the change in the screening of the 2*p*→ 3*d* absorption transition by the valence electrons. The differences between the Cr 2*p* spectra of the most ionic compound, CrF_3, and the covalent $[Cr(CN)_6]^{3-}$ complex are indicative of a decrease of 3*d* electron number on the Cr atom in the complex. This can be explained by the π-back-donation effect in the complex [4,5]. This $3d\pi$-$2p\pi^*$ charge transfer between the 3*d* atom and ligands CN$^-$ with low-lying unfilled antibonding $2p\pi^*$ molecular orbitals is well known to play an essential role in chemical bonding in complexes.

The $[Cr(CN)_6]^{3-}$ spectra aligned in energy at the position of the peak *t* (Fig. 3) can be interpreted using the quasi-molecular approach: the dipole transitions of the core electrons to the empty $2t_{2g}$, $1e_g$, $3t_{2g}$ molecular orbitals (MOs) of the $[Cr(CN)_6]^{3-}$ are allowed. The peak *t* was associated with the core-electron transitions to the low-energy unoccupied electron state $2t_{2g}$. As is seen from the Figure, there is also an energy agreement between other absorption structures for both the spectra. A large splitting (~0.6 eV) for transitions of N 1*s* electrons to unoccupied nonbonding π-MO's of the $[Cr(CN)_6]^{3-}$ complex (A and A') should be also emphasized.

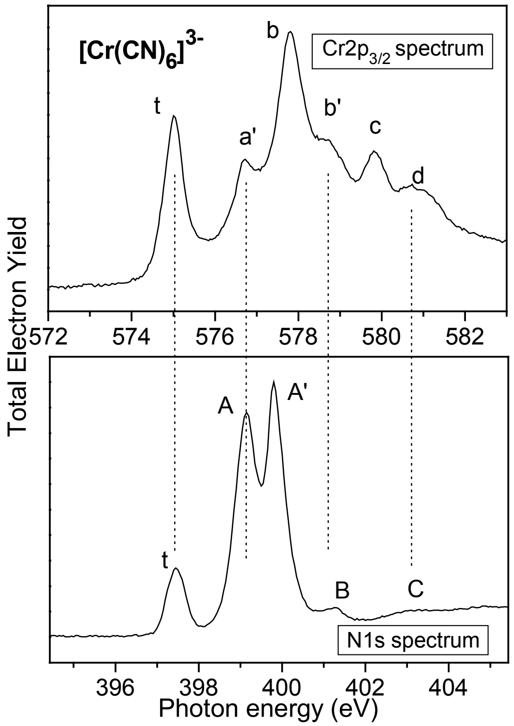

Fig. 3. *Cr2p$_{3/2}$ and N1s absorption spectra of $[Cr(CN)_6]^{2-}$ aligned in energy at the position of the peak t.*

The Cr 2*p* absorption spectra of the Cr(VI) compounds are shown in Fig. 4. The Cr atoms in these compounds have the tetrahedral surroundings by ligand (oxygen) atoms and in consequence spectra of these compounds the similar. Changes in the shape of the Cr 2*p* absorption spectrum, which are observed along the series, K_2CrO_4 – $K_2Cr_2O_7$ – CrO_3, result from the different coupling of tetrahedral CrO_4 groups in the compounds under comparison and hence from a different interaction between them. Actually these groups are quasi-isolated in K_2CrO_4, while they are coupled (i) by the one bridge oxygen atom to form an quasi-isolated atomic group Cr_2O_7 (K_2Cr2O_7) and (ii) by the two oxygen atoms giving rise to an infinite chain of the CrO_4 tetrahedra (CrO_3) [6].

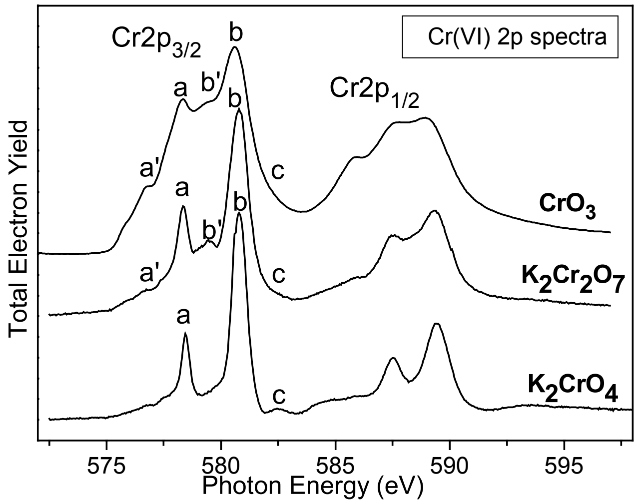

Fig. 4. *Comparison between the Cr(VI) 2p spectra of compounds with a different coupling of the CrO4 groups.*

Acknowledgements.

This work was supported by the bilateral program "Russian-German Laboratory at BESSY II". A.S. Vinogradov gratefully acknowledges the financial support by BESSY. M.A. Nesterov acknowledges the financial support by the Freie Universität Berlin within the Leonhard-Euler fellowship program.

References.

1. Yu.S. Dedkov, A.S. Vinogradov, *et al.*, *Phys. Rev. B* ***72****, 060401(R) (2005).*
2. A.S. Vinogradov, A.Yu. Dukhnyakov, V.M. Ipatov, et al., *Fiz. Tverd. Tela (Leningrad)* ***25****,400 (1982) [Sov. Phys. Solid State* ***25****, 225 (1982)].*
3. A.S. Vinogradov, A.Yu. Dukhnyakov, V.M. Ipatov, et al., *Fiz. Tverd. Tela (Leningrad)* ***24****, 1417 (1982) [Sov. Phys. Solid State* ***24****, 803 (1982)].*
4. A.S. Vinogradov, A.B. Preobrajenski, A. Knop-Gericke, et al., *J. Electron Spectr.Relat. Phen.* ***114-116****, 813 (2001).*
5. F.A. Cotton, G. Wilkinson, Advanced Inorganic Chemistry, 3rd Edition, Wiley, New York, 1972.
6. A.F. Wells, *Structural Inorganic Chemistry, (Clarendon, Oxford, 1984).*

Low-energy electron excitations in complex oxides studied by x-ray Raman spectroscopy

J.-M. Mariot[1], M. Marsi[2], P. Leininger[1], J.-P. Rueff[3], R. Delaunay,[1] J.J. Gallet[1], V. Ilakovac[1]
C. F. Hague[1], M. Sacchi[3], S. Eisebitt[4], W. Felsch[5]
[1]Université Pierre et Marie Curie, Laboratoire de Chimie Physique–Matière et Rayonnement, Paris, France; [2]Université Paris XI Laboratoire de Physique des Solides, Orsay, France; [3] Synchrotron SOLEIL, Saint Aubin, France; [4] BESSY, Berlin, Germany; [5] Georg-August-Universität, Physikalisches Institut, Göttingen, Germany.

(Funded by CNRS Option I and EU-RII3.CT 2004-506008)

Introduction

We have designed and constructed a prototype soft x-ray spectrometer intended for resonant x-ray Raman studies [1]. It will serve as a model for a new instrument to be installed at SOLEIL in 2008. The prototype is necessarily a light–weight mobile instrument compared to the final version but is well suited to refining the design. U41-PGM beamline has proved to be an almost ideal source thanks to an exceptionally high flux over an extensive energy range and a very stable micro-focus.

Our main scientific objective is the study of phase transitions in transition-metal oxides especially across the metal-insulator Mott transition using high-resolution RXRS. Such phase transitions generally involve only small changes in the electronic structure and correspondingly small modifications to low-energy excitations between non-degenarate orbitals with the same symmetry. It means that the experiments must be performed not only under high resolution conditions, but also with good statistics to eliminate spurious differences in the data.

A recognized advantage of the RXRS technique over valence band photoemission experiments, apart from element selectivity, is that the probing depth is much larger thus making it easier to eliminate surface effects and generally means samples can be prepared *ex-situ*.

In 2004 we initiated a study on the electronic structure of the V 3*d* states in V_2O_3 in collaboration with W. Felsch. The phase diagram of V_2O_3 includes high temperature paramagnetic insulating (PI) and metallic (PM) phases and a low temperature antiferromagnetic insulating phase (AFI). Felsch *et al* were able to grow epitaxial thin films on sapphire which mimic the bulk resistivity of monocrystalline materials with the advantage that cycling through the high-to-low temperature phase transition is non-destructive. His team was also able to produce films which correspond to the pressure- or stoichiometry-driven phase properties by varying the preparation conditions. Preliminary results pointed to subtle changes in low-energy excitations at the V L-edges across the metal-AF phase transition. Improvements to the experimental conditions have now allowed us to confirm these findings (see below).

Experiment

The resolving power of the x-ray spectrometer described in Ref. [1] depends critically on the size of the beam focus as it is designed to operate slitlessly. This is to optimize the flux collected from from the sample. To our knowledge these are the first successful attempts to use a soft x-ray grating spectrometer to perform high resolution experiments in a slitless mode. Of course using a slitless spectrometer also makes big demands on the stability of the machine and beam considering that there is no entrance slit to the monochromator on U41 PGM either. The performance of U41 PGM turned out to be excellent. We measured the FWHM of the focal spot to be 13 µm over a ten week interval separating two allocations. The mean beam position was found to be within 2 µm from one injection to the next, which is comparable to the precision limit of the measurement (see Fig. 1). Our setup in any case allows for the accurate realignment of the spectrometer relative to the beam but small drifts in position during measurements would deteriorate the effective resolution.

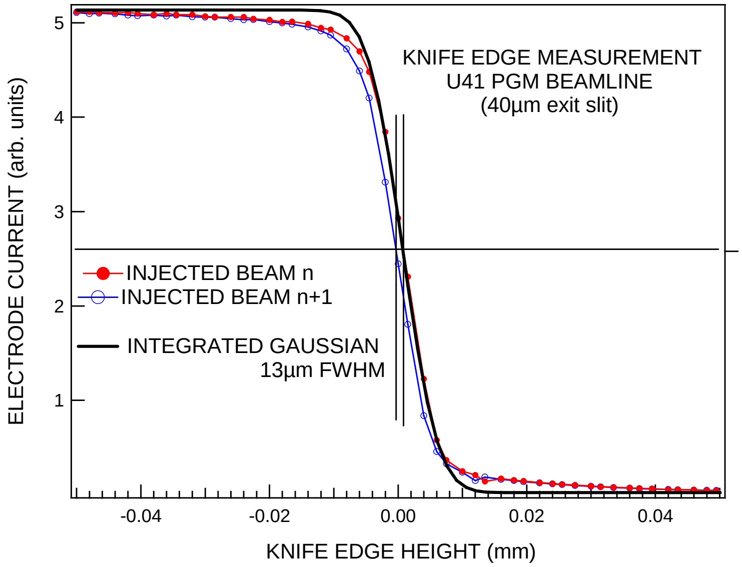

Fig. 1. Assessment of beam size and stability at x-ray spectrometer sample position.

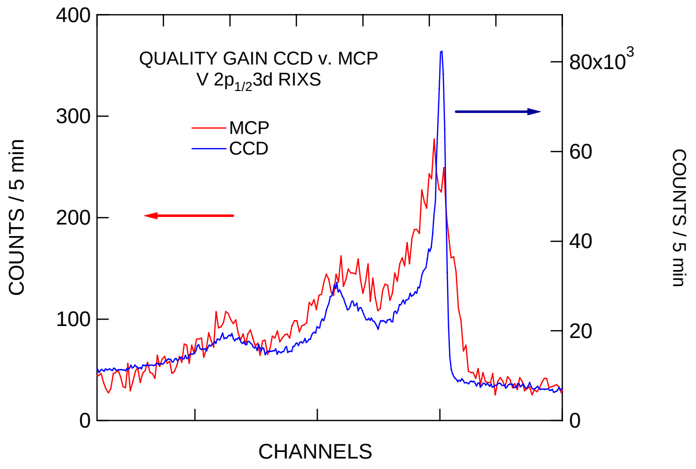

Fig.2 MCP and CCD detector performance compared.

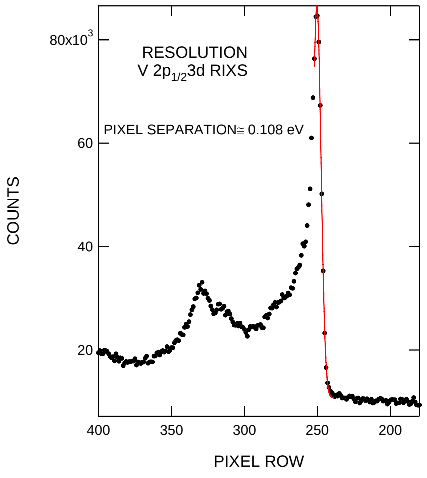

Fig. 3 Resolution at V $2p_{1/2}$ edge

Figure 2 demonstrates the advantages of using a CCD detector over a microchannel plate(MCP) whose channel resolution is of the order of 60 µm. In Figure 3 we show the resolution obtained at the V L_2 edge. The elastic cut-off on the low channel side serves as a measure of the resolution. A gaussian fit yields a FWHM of 0.62 eV i.e. a resolving power of 850. It should be noted that the tailing on the high channel side corresponds to weak energy losses. This is compatible with the design target of 2000 with a beam focus of 5 microns as planned at SOLEIL.

Results and Discussion

In figure 4 we present one set of RXRS data taken at the peak of the V L_3 absorption curve (517.6 eV). It correspond to measurements on two samples one insulating at room temperature and the other metallic. At this energy there is no significant difference between the PI and PM phases, however, there is a marked change in the *dd* excitations identified by arrows at ≈ 2.2 eV and 3.6 eV energy loss across the transition to the AFI phase. Changes in the general shape of the charge transfer peak at -9.8 eV are also observed. Other measurements (not shown) indicate modifications in the *dd* excitations across the PI-PM transition for excitations to the onset of the V L_3 edge. The data will be of help in validating various *ab initio* calculations designed to take into account electron correlation effects (see Ref. 2 for instance). Nevertheless possible excitonic effects due to the core-hole in the intermediate state must also be taken into account and require the development of model calculations. This work is still underway.

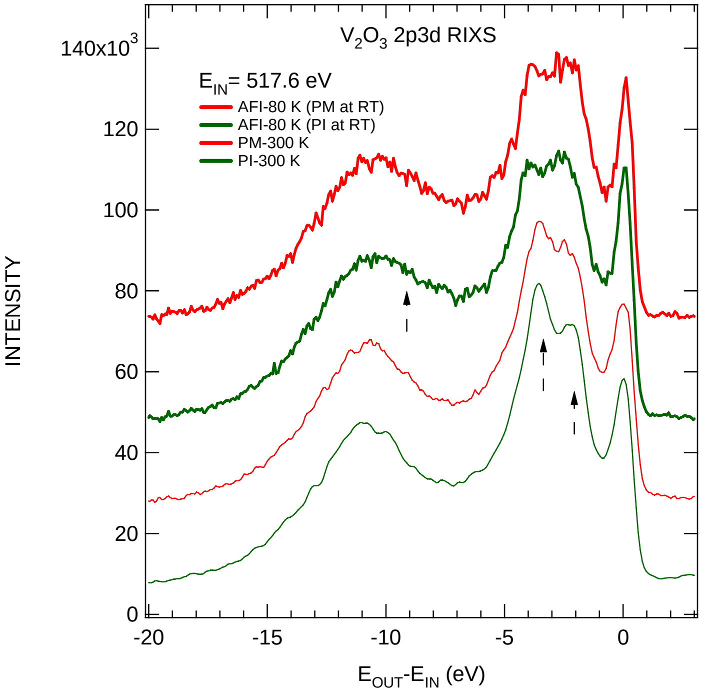

Fig. 4 V 2p3d RXRS in V_2O_3 for excitation to the V L_3 absorption peak.

[1] C. F. Hague, J. H. Underwood,A. Avila, R.Delaunay, H. Ringuenet, M. Marsi, and M. Sacchi, Rev. Sci. Instrum. **76**, 023110 (2005)
[2] G. Keller, K. Held, V. Eyert, D. Vollhardt, and V. I. Anisimov, Phys. Rev. B **70**, 205116 (2004)

Importance of spin fluctuations in 2D Co/Cu/Ni trilayers

C. Sorg, A. Scherz, M. Bernien, N. Ponpandian, K. Baberschke, and H. Wende

Institut für Experimentalphysik, Freie Universität Berlin, Arnimallee 14, D-14195 Berlin, Germany

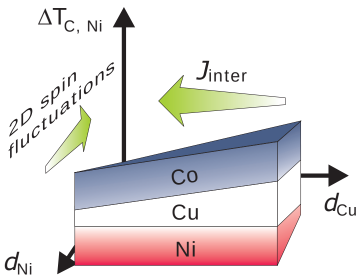

Figure 1: Sketch of a cross wedge Co/Cu/Ni trilayer. $\Delta T_{\mathrm{C,Ni}}$ is determined by (i) the IEC depending on d_{Cu}, and (ii) the thickness d_{Ni}, while d_{Co} is constant [1].

Magnetic multilayers show many magnetic effects that are not present in bulk material. Their relevance for both fundamental research and technological applications due to their magnetic properties is nowadays well accepted. In the present work, two fundamental effects in such multilayers have been studied by X-ray magnetic circular dichroism (XMCD): spin fluctuations and the interlayer exchange coupling (IEC). The main question is what happens when the two are considered simultaneously in the limit of two-dimensional (2D) layers. Co/Cu/Ni trilayers on a Cu(100) single crystal are used as a prototype system. Up to now, numerous investigations of the IEC exist that treat either the dependence on the thickness of one of the ferromagnetic layers (e.g. Ni) or the spacer thickness separately. The oscillatory character of the IEC (ferromagnetic, FM, or antiferromagnetic, AFM, coupling between Ni and Co) as a function of the spacer thickness d_{Cu} is theoretically described [2] and confirmed by experiments [3, 4]. The importance of spin fluctuations as a function of d_{Ni} was demonstrated by Jensen *et al.* [5]. The final goal is to combine the two effects as it is schematically indicated in the three-dimensional plot in Fig. 1. In wedge samples it is possible to scan the thickness of one of the layers while the others are kept constant.

Due to the element specificity of the XMCD technique the magnetic behavior of each ferromagnetic constituent in the trilayers may be revealed individually. Moreover, due to the *in situ* preparation and measurement under UHV conditions the identical Ni film can be investigated both with and without IEC. A Ni film capped with a Cu layer of the desired thickness is prepared and characterized first. Then, the Co film is deposited on top and thereby the IEC with strength J_{inter} is switched on. Now the Ni film can be reinvestigated and the influence of the IEC is revealed. In Fig. 2 two examples of the full XMCD spectra of Co/Cu/Ni trialyers at both the Co and the Ni $L_{2,3}$ edges are plotted. The graph shows that the sign of the Ni XMCD signal depends on the thickness of the Cu spacer layer, thus revealing if the element specific magnetizations of Co and Ni are aligned parallel or antiparallel by the IEC. All details of the measurements and their analysis are included in the original papers Refs. [1,6,7].

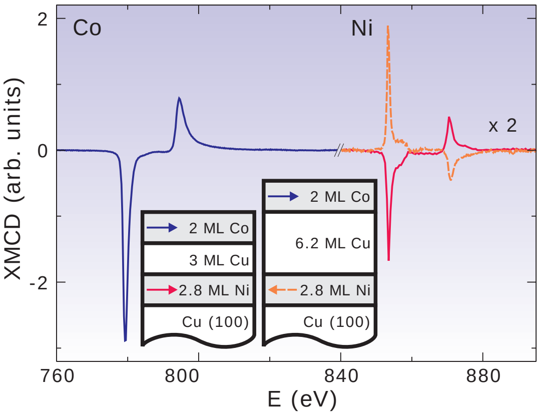

Figure 2: Full XMCD at the Co and the Ni $L_{2,3}$ edges of two trilayer samples. The signal at the L_3 edge of Co is negative in both cases whereas the sign of the Ni XMCD depends on d_{Cu}.

The integrated XMCD signal is a measure of the magnetization of the sample. Thus, the temperature dependence of the XMCD reveals the temperature dependence of the magnetization and thereby the Curie temperature. Four characteristic temperatures are identified: the Curie temperature of the single Ni film $T_{\mathrm{C,Ni}}$, the Curie temperature of the single Co film $T_{\mathrm{C,Co}}$, and the two temperatures at which the individual Ni and Co magnetizations in the trilayer vanish, $T^*_{\mathrm{C,Ni}}$ and $T^*_{\mathrm{C,Co}}$, respectively. The temperature $T^*_{\mathrm{C,Ni}}$ of the Ni film in the trilayer is considerably larger by $\Delta T_{\mathrm{C,Ni}}$ than the Curie temperature of a single Ni film $T_{\mathrm{C,Ni}}$ with the same thickness. Figure 3 shows one example with all the details concerned to characterize the IEC and the critical behavior close to the Curie temperature. The results of the experiments are given by the various symbols: open circles for $M_{\mathrm{Ni}}(T)$ in the Cu/Ni/Cu(100) bilayer before the evaporation of Co, i.e. without IEC, solid circles for $M_{\mathrm{Ni}}(T)$ and solid squares for $M_{\mathrm{Co}}(T)$ after the evaporation of Co on top. The solid and dot-dashed lines are the fitted standard magnetization curve as will be described below. The influence of the IEC is obvious from the experimental data and shows the expected behavior. The Ni magnetization has become larger in a wide temperature range after the Co film was deposited. Even in a temperature range where M_{Ni} was zero within the experimental error before, it has gained considerable magnitude and the expected tail is clearly visible. The relative shift $\Delta T_{\mathrm{C,Ni}}/T_{\mathrm{C,Ni}}$ of the critical temperature is larger than it has ever been observed in bulk magnetism. The shift $\Delta T_{\mathrm{C,Ni}}$ is always toward higher temperature, independent of the relative alignment (FM or AFM) of the individual Ni and Co magnetizations. Their relative orientation is reflected in the sign of J_{inter}, i.e. $J_{\mathrm{inter}} > 0$ for FM and $J_{\mathrm{inter}} < 0$ for AFM coupling. Earlier experiments have shown that $\Delta T_{\mathrm{C,Ni}}$ oscillates as a function of the spacer thickness in the same manner as the IEC does [4,8]. The first interpretations of this behavior have been carried out within a mean field theory (MFT) which turn out to be insufficient [5]. Collective spin excitations have to be taken into account in a more advanced theoretical description. For the present study this has been done within a Green's function theory (GFT). For the details about the calculations, please see Ref. [1].

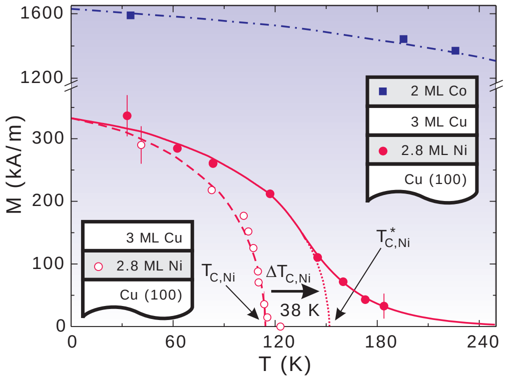

Figure 3: Ni (circles) and Co (squares) magnetizations $M_{\mathrm{Ni}}(T)$ and $M_{\mathrm{Co}}(T)$. The influence of the IEC on the Ni magnetization becomes obvious when comparing $M_{\mathrm{Ni}}(T)$ before (open circles) and after (closed circles) the deposition of the Co film. A standard Ni magnetization curve is fitted to the Ni data points (dashed and dotted lines), yielding $T_{\mathrm{C,Ni}}$ and $T^*_{\mathrm{C,Ni}}$ [1].

For the further analysis the characteristic Ni temperatures of the two cases need to be determined, i.e. $T^*_{\mathrm{C,Ni}}$ for the full trilayer and $T_{\mathrm{C,Ni}}$ for the corresponding Cu/Ni/Cu(100) bilayer system. This is done with the help of a standard magnetization curve which has been obtained from various measurements of 3−5 ML Ni/Cu(100) films [9]. Fitting this standard curve to $M_{\mathrm{Ni}}(T)$ of a Cu/Ni/Cu(100) sample yields $T_{\mathrm{C,Ni}}$ with an accuracy of a few kelvin (dashed line in Fig. 3). Determining $T^*_{\mathrm{C,Ni}}$ of the trilayer is less evident due to the presence of the tail. Therefore, the same standard magnetization curve is fitted to the data points of $M_{\mathrm{Ni}}(T)$ in the trilayer (dotted line in Fig. 3). The point at which the fitted standard curve meets the x-axis is identified with the temperature $T^*_{\mathrm{C,Ni}}$. This $T^*_{\mathrm{C,Ni}}$ is identical to the temperature of the maximum of the susceptibility [5,10].

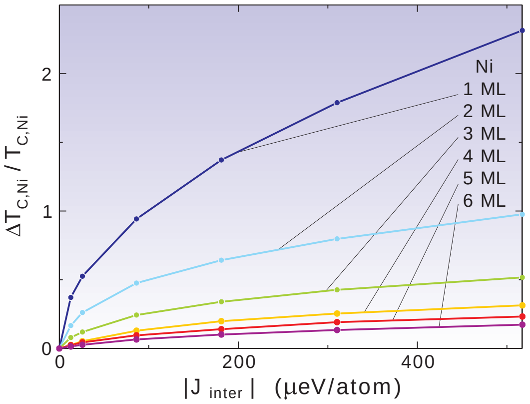

Figure 4: Relative temperature shift $\Delta T_{\mathrm{C,Ni}}/T_{\mathrm{C,Ni}}$ of the Ni magnetization as a function of the strength of the IEC $|J_{\mathrm{inter}}|$ for different d_{Ni} [1].

Before the desired combination of the two known effects $J_{\mathrm{inter}}\,(d_{\mathrm{Cu}})$ and $\Delta T_{\mathrm{C,Ni}}\,(d_{\mathrm{Ni}})$ can be accomplished, it is essential to express $\Delta T_{\mathrm{C,Ni}}/T_{\mathrm{C,Ni}}$ as a function of J_{inter}. In earlier works a linear dependence has been derived in a MFT [4, 8]. However, since MFT does not satisfy the description of the temperature shift $\Delta T_{\mathrm{C,Ni}}$, it is appropriate to find an improved description of $\Delta T_{\mathrm{C,Ni}}\,(J_{\mathrm{inter}})$ within the GFT. For the present study, the relative temperature shift $\Delta T_{\mathrm{C,Ni}}/T_{\mathrm{C,Ni}}$ has been calculated as a function of $|J_{\mathrm{inter}}|$. As Fig. 4 shows the dependence is clearly nonlinear.

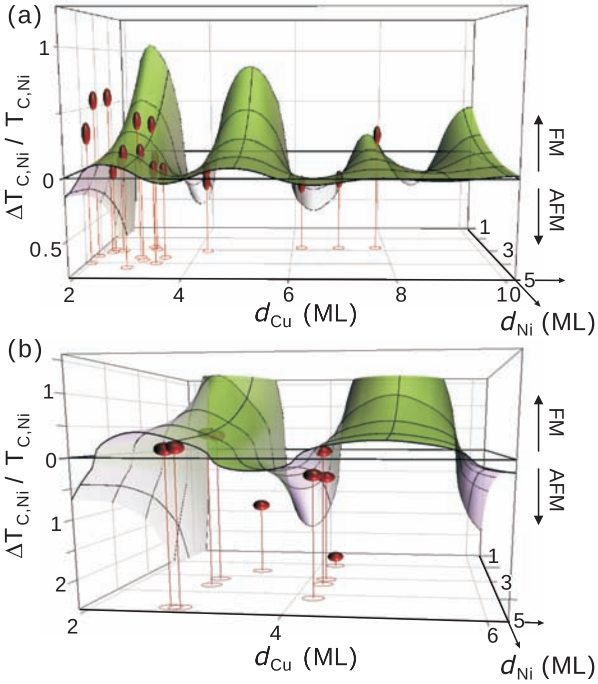

Figure 5: Two-parameter plot of the relative temperature shift $\Delta T_{\mathrm{C,Ni}}/T_{\mathrm{C,Ni}}\,(d_{\mathrm{Ni}}, d_{\mathrm{Cu}})$ for Co/Cu/Ni/Cu(100) trilayers as a function of the Ni film thickness d_{Ni} and the thickness d_{Cu} of the Cu spacer layer with (a) $d_{\mathrm{Co}} = 2$ ML and (b) $d_{\mathrm{Co}} = 3$ ML [1].

The influence of the spin fluctuations, visualized in the relative shift $\Delta T_{\mathrm{C,Ni}}/T_{\mathrm{C,Ni}}$, depends on the one hand on d_{Ni}. On the other hand it depends on the strength of the IEC, i.e. $|J_{\mathrm{inter}}|$. Combining both variables with the help of the relation given in Fig. 4, the 3D plot as anticipated at the beginning can be established. The result is a curved surface of $\Delta T_{\mathrm{C,Ni}}/T_{\mathrm{C,Ni}} = f\,(d_{\mathrm{Ni}}, d_{\mathrm{Cu}})$. Figure 5 shows this final result of the calculation together with the experimental findings. The experimental data are shown as full dots and in the projection to the d_{Ni}–d_{Cu} plane (open circles). The results are sorted according to the thickness of the Co film: $d_{\mathrm{Co}} = 2$ ML in Fig. 5 (a) and $d_{\mathrm{Co}} = 3$ ML in Fig. 5 (b). The zero plane is given by $J_{\mathrm{inter}} = 0$ with a shift $\Delta T_{\mathrm{C,Ni}} = 0$. The illustration has been chosen such that regions with a parallel alignment of the magnetizations of the two FM layers ($J_{\mathrm{inter}} > 0$, above the zero plane) are distinguished from the ones with an antiparallel alignment ($J_{\mathrm{inter}} < 0$, below the zero plane).

In conclusion, fair agreement between the experimental results and the calculations even in the simplified model show the importance of spin fluctuations in the coupled trilayers especially at thin thickness. Furthermore, the desired combination of the two dependencies on d_{Ni} and d_{Cu} and their simultaneous consideration has been accomplished.

This work was supported by the BMBF (05 KS4 KEB/5).

References

[1] A. Scherz, C. Sorg, M. Bernien, *et al.* , Phys. Rev. B **72**, 054447 (2005).

[2] P. Bruno and C. Chappert, Phys. Rev. Lett. **67**, 1602 (1991).

[3] J. Lindner and K. Baberschke, J. Phys.: Condens. Matter **15**, S465 (2003).

[4] A. Ney, A. Scherz, P. Poulopoulos, *et al.* , Phys. Rev. B **65**, 024411 (2002).

[5] P. J. Jensen, K. H. Bennemann, P. Poulopoulos, *et al.* , Phys. Rev. B **60**, R14994 (1999).

[6] H. Wende, C. Sorg, M. Bernien, *et al.* , Phys. Stat. Sol. (b) **243**, 165 (2006).

[7] C. Sorg, A. Scherz, H. Wende, *et al.* , Phys. Scripta **T115**, 638 (2005).

[8] G. Bayreuther, F. Bensch, and V. Kottler, J. Appl. Phys. **79**, 4509 (1996).

[9] P. Poulopoulos and K. Baberschke, Lecture Notes in Physics, Springer **580**, 283 (2001).

[10] U. Bovensiepen, F. Wilhelm, P. Srivastava, *et al.* , Phys. Rev. Lett. **81**, 2368 (1998).

Induced magnetism in O as a surfactant for Fe, Co, and Ni films

C. Sorg[1], N. Ponpandian[1], R. Q. Wu[2], M. Bernien[1], K. Baberschke[1], and H. Wende[1]

[1] *Institut für Experimentalphysik, Freie Universität Berlin, Arnimallee 14, D-14195 Berlin, Germany*
[2] *Department of Physics and Astronomy, University of California, Irvine, California 92697, USA*

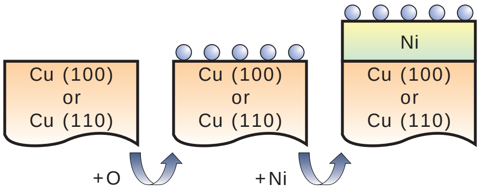

Figure 1: Schematic illustration of the oxygen surfactant assisted growth of Fe, Co, and Ni films on Cu(100).

Surfactant assisted growth of nanoscale structures on surfaces is a well established technique to improve the growth mode of 3*d* ferromagnetic films on single crystalline substrates toward a more layer-by-layer one [1]. Tailoring the growth modes for these ultrathin films is crucial since the magnetic properties are highly sensitive to minimal structural changes: If the nearest neighbor distance varies by 0.03-0.05 Å only, the magnetic anisotropy energy may change by $10^2 - 10^3$. The preparation procedure is schematically presented in Fig. 1 and explained in detail in Refs. [2–4]: At first, atomic oxygen induced is adsorbed onto the clean Cu(100) crystal. Then the Fe, Co, and Ni films are prepared onto the reconstructed surface. All three metals grow more layer-by-layer than without O up to $>$ 15 ML. The O atoms always "float" on top of the ferromagnetic films.

An interesting question is, if the surfactant oxygen affects the magnetic properties of the films. It was demonstrated that the magnetic anisotropy energy of Ni is significantly enhanced using this surfactant, mainly because of a decrease in the magnitude of the surface anisotropy [5–7]. Via the element-specific X-ray magnetic circular dichroism (XMCD) technique we were able to identify an induced moment in the surfactant oxygen [4, 8]. In the present work *ab initio* calculations of the O K edge XMCD were carried out to understand the spectroscopic fine structures from a fundamental point of view.

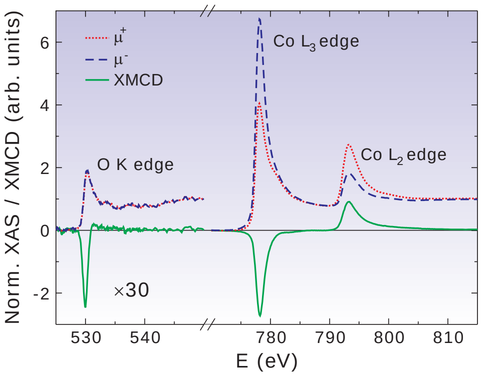

Figure 2: X-ray absorption coefficient and XMCD at the O K edge and Co $L_{2,3}$ edges for the surfactant grown Co film.

X-ray absorption spectroscopy (XAS) and XMCD measurements were carried out at the undulator beamline UE56/2-PGM2 on 3 ML Fe, 4 ML Co, and 15 ML Ni films. The advantage of measurements in the soft X-ray range is that the O K edge as well as the $L_{2,3}$ edges of the 3*d* ferromagnets Fe, Co, and Ni are located in this regime. Both the induced magnetism in the surfactant and the magnetic properties of the ferromagnetic films can be probed in the same experiment as shown in Fig. 2 for the case of Co. A clear XMCD signal at the Co $L_{2,3}$ edges is determined but also a tiny XMCD signal at the O K edge can be revealed. Due to the excellent performance of the beamline this oxygen signal of about 8 % normalized to the small oxygen edge-jump (jump ratio J_r=6 %) can be revealed. The appearance of this signal shows that indeed the Co film induces a magnetic moment in the surfactant oxygen. However, one has to keep in mind, that with XMCD at K edges only the orbital moment μ_L is probed [8]. The sharp structure in the XAS located at 530 eV originates

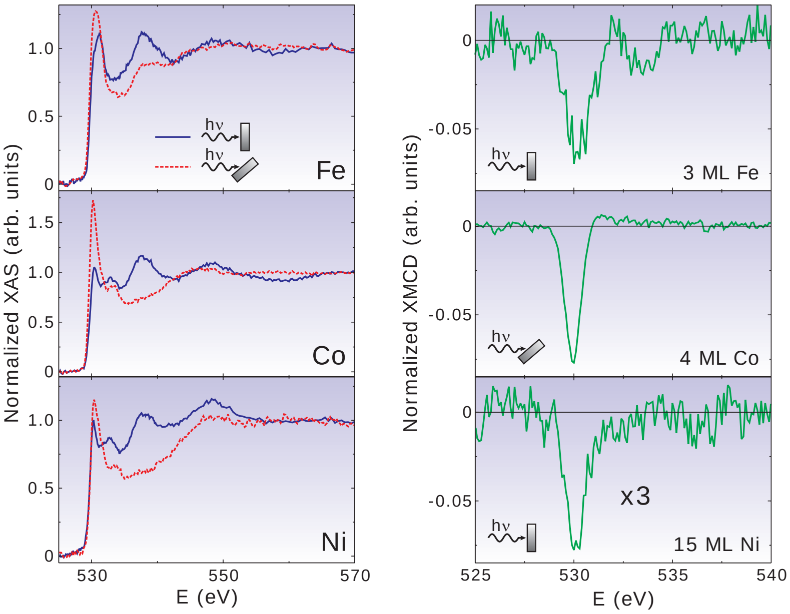

Figure 3: Angular-dependent NEXAFS (left) and XMCD (right) at the O K edge of the $3d$ ferromagnets grown on Cu(100) with oxygen as a surfactant.

from hybridized $2p_z 3d$ states [9]. Since the XMCD is observed exactly at the same position this is a first indication that the $2p_z$ states of the oxygen are magnetically polarized.

For the investigation of systematic trends we carried out these measurements for Fe, Co and Ni films. We start the discussion with the analysis of the angular-dependent NEXAFS spectra presented in Fig. 3 (left). The NEXAFS of Co was recorded with linearly polarized X-rays, the $\vec{E}$-vector aligned perpendicular to the [011] direction. In the case of Ni and Fe the isotropic XAS which is the average of the XAS recorded with circular polarized light of the two helicities is shown. The clear angular dependence of the spectra for all the $3d$ films show that (i) no bulk-like oxide with the $3d$ elements is formed and (ii) the oxygen atoms "float" to the top of the surface. If the oxygen atoms were incorporated into the film, the angular dependence would be negligible because of the high symmetry. In contrast, on the surface the individual oxygen orbitals can be investigated. The spectra show quite similar trends for the three films: A sharp peak located at 530 eV displays the hybridized oxygen $2p_z - 3d$ metal states. Therefore, this peak is prominent at grazing X-ray incidence and decreases at normal X-ray incidence. The second structure at 538 eV originates from transitions to the hybridized O $2p_{xy}$ orbital – $3d$ metal $4sp$ bands. It is strong only in the normal incidence geometry where $\Delta m = \pm 1$. For p_z states $m = 0$ and hence the p_z state does not respond to normal incident light with circular polarization. Therefore, the opposite angular dependence is observed in comparison to the 530 eV structure. The broad peak at 550 eV stems from the scattering of the photoelectron at the nearest neighbor $3d$ metal atoms. Since quite similar spectral features and angular dependencies are determined as seen in Fig. 3 (left) we conclude that the local geometry and the local bonding of the surfactant oxygen atom to the $3d$ metal atoms is alike for the three films.

Turning to the dichroic spectra shown in Fig. 3 (right) we find similar trends: All the XMCD spectra exhibit a sharp dichroic contribution at 530 eV. This negative contribution reveals that the induced orbital moment is aligned parallel to the spin and orbital moments of the ferromagnetic films. Since no XMCD signal is determined at 538 eV we conclude that for all the films the O $2p_z$ are magnetically polarized.

Density functional calculations for O adsorption on the fcc Fe(100), Co(100), and Ni(100) surfaces were conducted using the thin-film full potential linearized augmented plane wave (FLAPW) method [4]. Both the local density approximation (LDA) and the generalized gradient approximation (GGA) were adopted to describe the exchange-correlation interaction. The optimized distances between the oxygen adatom and its nearest Fe, Co, and Ni neighbors are 1.85-1.86 Å from LDA calculations and 1.93 Å from GGA calculations. From the surface extended X-ray absorption fine structure (SEXAFS) at the O K edge of 15 ML Ni grown with O surfactant on Cu(100) we determine a nearest neighbor distance $R_{nn} = (1.85 \pm 0.03)$ Å of the O atoms to the Ni atoms of the topmost layer [4]. Since the LDA results agree with our SEXAFS data very well they are employed for other comparisons henceforth. The experimental determination of the local structure is quite helpful since it turns out that the size of the magnetic moments of the Ni atoms on the surface and also the induced moment in the surfactant oxygen sensitively depend on this distance.

The calculated spin magnetic moments projected into the O muffin-tin sphere ($r = 0.74$ Å) are $0.053\mu_B$, $0.132\mu_B$, and $0.053\mu_B$ in O/Fe(100), O/Co(100), and O/Ni(100), respectively. Their orbital moments are very small, $0.0024\mu_B$, $0.0047\mu_B$, and $0.0021\mu_B$. The O adatoms significantly reduce the magnetization of the surface 3d atoms. Particularly, the spin magnetic moment of the surface Ni atom is only $0.26\mu_B$, much smaller than those of the interior Ni atoms, $0.66 - 0.69\mu_B$. It is important to note that the spin and orbital magnetic moments of both O and surface Fe, Co, and Ni atoms strongly depend on the relaxation of the oxygen atom.

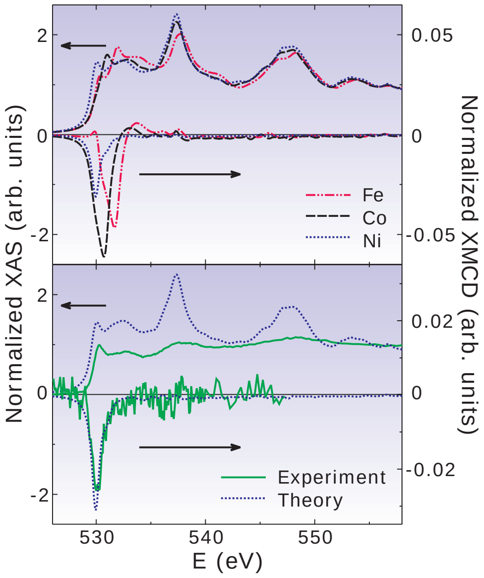

Figure 4: Top: Calculated XAS and XMCD of the O adatom on fcc Fe(100) (dash-2-dotted line), Co(100) (dashed line), and Ni(100) (dotted line) films for the normal incidence geometry. Bottom: Measured (solid line) and calculated (dotted line) XAS and XMCD of the O adatom on the Ni(100) film at normal incidence.

The calculated XAS and XMCD spectra for the normal incidence geometry are presented in Fig. 4, accompanied by the experimental data for O/Ni(100). For more details about the calculations, see Ref. [4]. Intriguingly, all the spectroscopic features, including the peak structures and the XMCD/XAS ratio, are satisfactorily reproduced. Note also that there is no free scaling factor between experiment and theory. This indicates that the model used in calculations represent the atomic arrangements in experimental samples very well. Despite the fact that the spin and orbital magnetic moments of O are small, the XMCD signals are sizable at the threshold for all three systems.

Concluding, the excellent signal-to-noise-ratio for XMCD measurements at the UE56/2-PGM2 allows for a determination of the induced magnetism at 0.5 ML O on surfactant grown Fe, Co, and Ni films. Calculations reproduce the measured spectra quite well and complement the experimental findings by providing, for instance, the magnetic moments.

This work was supported by the BMBF (05 KS4 KEB/5).

References

[1] M. Farle, Surf. Sci. **575**, 1 (2005).

[2] R. Nünthel, T. Gleitsmann, P. Poulopoulos, *et al.* , Surf. Sci. **531**, 53 (2003).

[3] R. Nünthel, J. Lindner, P. Poulopoulos, and K. Baberschke, Surf. Sci. **566-568**, 100 (2004).

[4] C. Sorg, N. Ponpandian, M. Bernien, *et al.* , Phys. Rev. B. **73**, *in print* (2006).

[5] J. Lindner, P. Poulopoulos, R. Nünthel, *et al.* , Surf. Sci. **523**, L65 (2003) .

[6] J. Hong, R. Q. Wu, J. Lindner, *et al.* , Phys. Rev. Lett. **92**, 147202 (2004).

[7] T. Nakagawa, H. Watanabe, and T. Yokoyama, Phys. Rev. B **71**, 235403 (2005).

[8] C. Sorg, N. Ponpandian, A. Scherz, *et al.* , Surf. Sci. **565**, 197 (2004).

[9] F. May, M. Tischer, D. Arvanitis, *et al.* , Phys. Rev. B **53**, 1076 (1996).

Measuring the kernel of time-dependent density functional theory with X-ray absorption spectroscopy of $3d$ transition metals

A. Scherz[1,2], E.K.U. Gross[1], H. Appel[1], C. Sorg[1], K. Baberschke[1], K. Burke[3] and H. Wende[1]

[1] *Institut für Experimentalphysik, Freie Universität Berlin, Arnimallee 14, D-14195 Berlin, Germany*
[2] *SSRL, 2575 Sand Hill Road, Menlo Park, California 94025, USA*
[3] *Department of Chemistry and Chemical Biology, Rutgers University, 610 Taylor Rd, Piscataway, NJ 08854, USA*

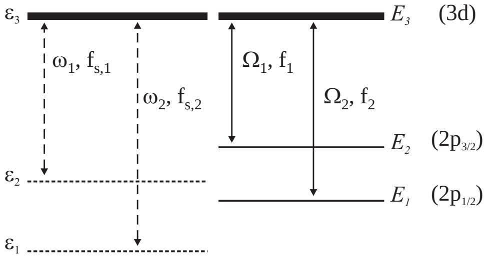

Figure 1: Schematic illustration of the DPA model. The model describes the shifts of the excitation energies (uncorrelated ω_i and correlated Ω_i) and the changes in corresponding oscillator strengths f_i in the presence of an excited core hole [1].

Ground-state density functional theory (DFT) is well-established for atoms, molecules, and solids. But ground-state DFT produces only a one-particle picture of the electronic transitions in matter, neglecting interactions between excitations. The spectroscopic properties of matter in the X-ray regime are substantially governed by dynamical many-body effects involving the creation of a localized core hole [1–6]. While GW calculations and the Bethe-Salpeter equation can be used [4], these are computationally demanding. The simpler and less expensive methodology of TDDFT is now being developed for these effects [5].

We analyze this approach to the X-ray absorption of itinerant systems like the $L_{2,3}$ absorption of $3d$ transition metals (TMs), i.e., exciting a photoelectron from the localized $2p$ core states into the $3d$ band [1]. $L_{2,3}$ X-ray absorption spectra (XAS), especially of early $3d$ TMs, suffer from core-hole correlation effects [2]. Schwitalla and Ebert [3] applied TDDFT linear response theory to calculate the XAS of the $3d$ TMs. Using a local approximation to the frequency-dependent exchange-correlation (XC) kernel, as proposed by Gross and Kohn [7], they qualitatively reproduced the trend of the branching ratios. However, whenever DFT is applied in a new regime, a difficult question arises: Are the existing functional approximations sufficiently accurate in this new regime? And how does one separate XC errors from those due to the practical approximations needed for realistic calculations? The true value of DFT is in constructing one XC approximation that covers many situations, in order to build-in knowledge of the underlying physics.

Our approach here is different, and is based on the philosophy of Ref. [8]. That work examined the TDDFT response when excitations are not strongly coupled to each other. A useful series was developed in the strength of the off-diagonal matrix elements, relative to the frequency shifts induced by diagonal terms. The leading term yields the single-pole approximation [9], which has proven very useful in understanding TDDFT corrections to the one-particle picture. It even yields an immediate estimate of the XC kernel, but only if excitations are well-separated, a criterion rarely realized in practice [8]. However, the same philosophy applies to cases of two levels *strongly* coupled to one another, but weakly coupled to the rest of the spectrum. We call this the three-level or double-pole approximation (DPA), cf. Fig 1. Moreover, the $L_{2,3}$ absorption of $3d$ TMs provides an ideal example of two transitions much closer to each other than the rest of the spectrum. With this in mind, we experimentally measured the branching ratios and level splittings of the $2p_{3/2}(L_3)$ and $2p_{1/2}(L_2)$ core states, and now *deduce* off-diagonal matrix elements of the unknown XC kernel [1]. Since we can also compare with the one-particle Kohn-Sham (KS) spectrum, we can also deduce the diagonal matrix elements. We find that, despite the large deviation of branching ratios from their single-particle values, the off-diagonal matrix elements, a measure of core-hole interaction, are *not* large, and explain why. Thus the DPA to TDDFT explains the observed shifts and oscillator strengths, and also provide benchmarks for future XC kernel approximations. We believe this is the first experimental measurement of a matrix element of the XC kernel of TDDFT.

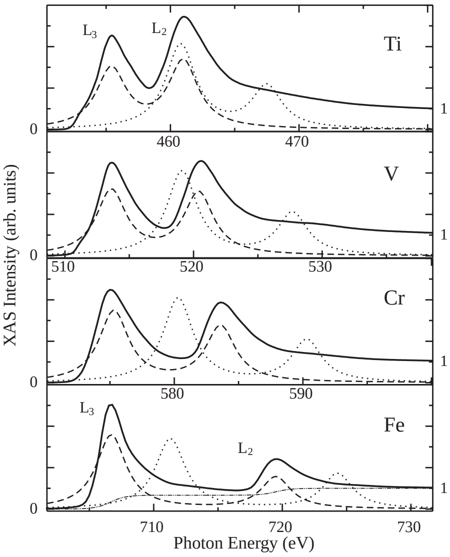

Figure 2: The experimental isotropic absorption spectra (solid line) at the $L_{2,3}$ edges are shown for the early $3d$ TMs Ti, V, and Cr versus Fe. The edge jumps are normalized to unity for direct comparison. The continuum in the experimental spectrum is simulated by a two-step function as shown for Fe (dashed-dotted line). The treatment of the core hole red-shifts the independent particle spectrum (dotted line) and changes the statistical branching ratio in the correlated spectrum (dashed line) as revealed by the DPA model [1].

In the $L_{2,3}$ XAS of the $3d$ TMs, the description of the electron core-hole interaction may be simplified by the assumption that the relativistic spin-orbit coupling (SOC) in the $3d$ band states (~ 0.05 eV) is small compared to that of the core states (several eV) and can be neglected. This means that the oscillator strengths f_j of these levels are all about equal, as their KS orbitals are essentially identical. Since, in this limit, the absorption area is proportional to the oscillator strength, weighted statistically according to the manifold of the $j = 3/2$ and $j = 1/2$ subshells, the branching ratio of the KS system is $B_{\mathrm{KS}} = A_{3/2}/(A_{3/2} + A_{1/2}) \equiv 2/3$, where A_j is the area under the peak of the j-th subshell. Here we replace all dipole-allowed transitions ω_{jk} from a particular absorption edge into the $3d$ band by a single particle transition, as illustrated in Fig. 1. In Fig. 2, we show our experimental isotropic XAS for the $3d$ TM with almost empty $3d$ bands taken from Fe/TM/Fe sandwiches with $\mathrm{TM} = \mathrm{Ti}, \mathrm{V}, \mathrm{Cr}$ and bulk-like Fe. The data were recorded at the UE56-1/PGM beamline at BESSY (for details, see Ref. [10]). The edge jumps are normalized to unity. From these spectra and their absolute energy dependence, the excitation energies $\Omega_{q=1}$ at the L_3 edge and $\Omega_{q=2}$ and the L_2 edge are determined. For the quantitative analysis of the branching ratio B, we very carefully determined the $L_{2,3}$ absorption areas A_j. This determination has the advantage that B becomes independent of the different L_3 and L_2 lifetime broadening and experimental resolution. Note, that the proper experimental intensity is given by the area and not by the height of the resonance. To determine the correct area of the L_3 and L_2 resonances the continuum contribution is removed (e.g. gray line for Fe in Fig. 2). Since the $2p$ SOC decreases towards lower atomic numbers the deconvolution is more complicated for the early $3d$ TMs Ti, V, and Cr because of the strong $L_{2,3}$ overlap. The areas have been fitted using the Fe absorption spectrum as a background simulation underneath the L_2 edge.

In the case of Fe the L_2 absorption is approximately half of the L_3 peak, in agreement with the KS prediction. However, the branching ratios for the other $3d$ elements differ significantly from this. In particular, Ti has an L_2 peak that is even larger than its L_3 absorption. Thus, the experimental branching ratios cannot be interpreted in terms of KS orbitals, suggesting strong electron core-hole interactions. In the language of TDDFT, there must be significant off-diagonal matrix elements in Casida's equations, describing the influence of the electron core-hole interaction on the $L_{2,3}$ XAS. (If only diagonal elements are considered, the eigenvalues are shifted but the eigenvectors are not rotated, and the oscillator strengths retain their KS values [8].)

However, a fully numerical solution of the equations is not needed, as we know there are

Table 1: Excitation energies in eV obtained from KS calculations (ω_i^{KS}) and from experiment (Ω_i), experimental branching ratio B and matrix elements K_{ij} [1]. The experimental error of Ω_i is below 10^{-3}, the one of B in the order of 1 %.

$3d$ TM	ω_1^{KS}	ω_2^{KS}	Ω_1	Ω_2	B	K_{11}	K_{22}	K_{12}
22 Ti	460.8	467.5	455.4	461.0	0.47	-2.57	-3.34	0.54
23 V	519.1	527.7	513.6	520.4	0.51	-2.65	-3.73	0.54
24 Cr	580.3	590.3	575.1	583.6	0.56	-2.55	-3.40	0.47
26 Fe	711.3	724.6	706.7	719.5	0.70	-2.29	-2.55	-0.25

only two dominant transitions, so the electron core-hole interaction can be analyzed within the DPA model. The detailed calculations within the DPA model are given in [1] and the results are presented in Table 1, the corresponding theoretical DPA spectra are shown in Fig. 2. What can we learn from this elementary analysis? Our chief result is that the deviation from the KS branching ratio does *not* imply large off-diagonal matrix elements of K, i.e., large core-hole correlation. In fact, the off-diagonal elements are all about 1 eV or less, compared to diagonal elements of 5-7 eV. Moreover, from Ti-Cr, it is almost constant. The deviation from the KS branching ratio is simply level (or in this case, transition) repulsion, as the two transitions near one another. Thus the shifts are simply interpreted as diagonals of K, while the branching ratios are a sensitive determinant of off-diagonal elements. The success of DPA shows that very little effort beyond a ground-state DFT calculation is needed to compute these spectra in TDDFT. One only needs to integrate a given approximation to the XC kernel for the two diagonal matrix elements, and one off-diagonal.

In summary, we have used TDDFT to understand the XAS of $3d$ transition metals by deriving a double-pole approximation. The main features observed in the experiments can easily be explained by assuming that the spectrum is dominated by two strongly coupled poles via the $2p-3d$ core hole interaction. This shows that, for the beginning of the $3d$ series, the reduced $2p$-SOC is responsible for the strong variation of the branching ratio, not strong interactions between the transitions. Our analysis does not replace a full TDDFT calculation of X-ray absorption spectra. Rather, for the very specific case of spectral regions dominated by two poles it provides, on the one hand, a transparent picture of the changes of spectral weights in particular for the early $3d$ TMs, and on the other, a straight-forward route to testing approximate XC kernels against experimental data.

The work was supported by BMBF (05 KS4 KEB/5), the EXC!TING Research and Training Network of the EU, the NANOQUANTA network of excellence, the US DOE (DE-FG02-01ER45928) and NSF (CHE-0355405).

References

[1] A. Scherz, E.K.U. Gross, H. Appel, C. Sorg, K. Baberschke, H. Wende and K. Burke, Phys. Rev. Lett. **95**, 253006 (2005).

[2] J. Fink et al., Phys. Rev. B **32**, 4899 (1985); J. Zaanen, et al., *ibid.* **32**, 4905 (1985).

[3] J. Schwitalla and H. Ebert, Phys. Rev. Lett. **80**, 4586 (1998).

[4] E.L. Shirley, Phys. Rev. Lett. **80**, 794 (1998).

[5] A.L. Ankudinov, A.I. Nesvizhskii, and J.J. Rehr, Phys. Rev. B **67**, 115120 (2003).

[6] O. Wessely, M.I. Katsnelson, and O. Eriksson, Phys. Rev. Lett. **94**, 167401 (2005).

[7] E.K.U. Gross and W. Kohn, Phys. Rev. Lett. **55**, 2850 (1985).

[8] H. Appel, E.K.U.Gross, and K. Burke, Phys. Rev. Lett. **90**, 043005 (2003).

[9] M. Petersilka, U.J. Gossmann, E.K.U. Gross, Phys. Rev. Lett. **76**, 1212 (1996).

[10] H. Wende, Rep. Prog. Phys. **67**, 2105 (2004).

ARPES study of low dimensional surface states on the Pt(110) surface

M. Minca, E. Dona, S. Penner, V. Brouet*, A. Menzel, and E. Bertel
Institut für Physikalische Chemie, Universität Innsbruck, Innrain 52A, A-6020 Innsbruck (Austria)
**Laboratoire de physique des Solides, Université Paris-Sud, 91405 Orsay (France)*

The photoemission intensity is described by two factors, the hole spectral function $A^h(k,\omega)$ and its modulation by the photoemission process, usually referred to as photoemission matrix element (ME) effects. ME effects might be strong [1] due to e.g. interferences from various atomic sites in the final state [2,3]. Thus, for a satisfactory interpretation of the ARPES spectra it is necessary to distinguish the effects of spectral function and photoemission matrix element. Although calculations in the framework of the one-step model of photoemission (see e.g. [2,3,4]) are able to capture experimentally observed features, the general understanding of ME effects and their dependence on dimensionality, geometry and temperature is still relatively poor.

Recently, we found on clean Pt(110) low dimensional electronic states at the Fermi-energy E_F which show an unusual intensity variation depending on temperature and adsorbates at 21.2eV [5,6]. The intense photoemission peak around 100meV below E_F at the $\overline{X}$ point of the (1x1) surface Brillouin zone is derived from the backfolding of a surface resonance at $\overline{S}$ due to the 1x2 missing row reconstruction. In the following we discuss photoemission intensity changes of this peak which can be induced by adsorbing hydrogen into the so-called β_2-adsorption-state on the Pt(110) surface. The 1x2 overstructure is not affected by hydrogen absorption, whereas the interlayer distance between the outermost missing rows and the second layer is substantially changed from 1.15A to 1.25A [7], the bulk interlayer distance being 1.38A. Since β_2-hydrogen adsorption changes the geometry by increasing the first layer distance by 9%, this model system provides a unique possibility to disentangle different factors determining photoemission intensities.

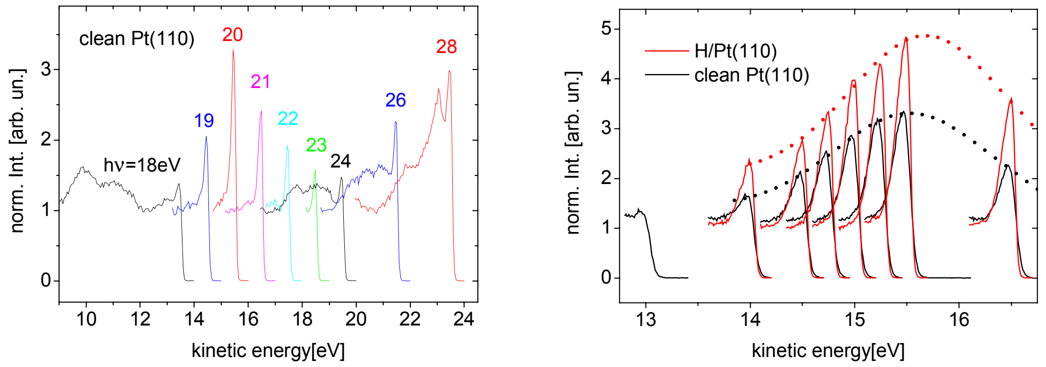

Fig.1: Left: Comparison of EDCs at different photon energies for the clean surface. Right: Zoom into the intensity rise around 20eV photon energy, comparing H/Pt(110) and clean Pt(110). Gaussian envelopes (dotted, black is shifted by -150meV and multiplied by 0.68) are given to guide the eye.

This study was performed at the 10m-NIM beamline using the SURICAT experimental setup. The spectra were taken at the $\overline{X}$-point of the surface Brillouin zone at T=300K (above the hydrogen desorption temperature) for the clean surface and at T=140K for β_2-H/Pt(110). The analyzer resolution (PE=10eV) was 30meV, much better than the natural width of the surface resonance of roughly 100meV. All the spectra have been normalized to the lowest background signal as observed in wide energy range (12eV) spectra (see Fig1, left).

Fig 1 shows a comparison of energy distribution curves (EDCs) at various photon energies for the two different surfaces. Several observations can be made: (a) the position of the peak at E_F does not depend on photon energy and (b) is the same for both surfaces. (c) for all photon energies, the intensity of the peak is smaller for the clean surface. As has been shown before [6,7], this is not due to the difference in the Fermi-distribution at 140K and 300K. (d) the intensity oscillates with photon energy where (e) the behaviour of intensity versus photon energies is very similar for both surfaces.

Observations (c) and (e) show that photoelectron diffraction by the outermost layer cannot be the reason for the influence of hydrogen and the intensity oscillation in general: In the simple diffraction model, the 9% change in geometry between first and second layer should change the kinetic energy for constructive interference for clean and H/Pt(110) in the final state by more than 1.5eV. As shown in Fig.1 (right) by a zoom into the photon energy range from 17.5 to 21eV, this is clearly not observed. Furthermore, the spacing between intensity the maxima (d) at roughly 15, 20, and 30eV (not shown) amounts to a few eV, which in reciprocal space corresponds only to a small fraction of the Brillouin zone in the direction perpendicular to the surface ($k_\perp$).

Observations (a), (d) and (b) corroborate earlier assignments of the peak at E_F [5,6] and hydrogen adsorption sites [7]: Generally, a surface state or a surface resonance should not show any sizeable dispersion (a) with momentum $k_\perp$. Nevertheless, a surface state or resonance extends coherently over a few layers and thus some bulk $k_\perp$ components will dominate in an expansion in bulk Bloch states. Consequently, the remainder (a “propensity rule”) of the $k_\perp$-conservation rule in the bulk is expected to modulate (d) the photoemission intensities upon variation of photon energy. The symmetry of the surface resonance wave function [5,6] and the H adsorption site [7] are consistent with (b) no shift in energy after hydrogen adsorption: The H1s orbital is situated in the short bridge site (symmetry gerade) and cannot interact with the quasi-1D Tamm d-type surface resonance wave function at the $\overline{X}$ -point (ungerade).

On the basis of the present analysis, a simple diffraction model in the final state, such as the assignment of the peak at $\overline{X}$ to a final state umklapp from the $\overline{S}$ point, can be definitely excluded. However, a clear separation of subtle ME effects (see the shift of 150meV suggested by the Gaussian envelopes drawn in Fig1, right) and changes in the initial state effecting $A^h(k,\omega)$ is not possible. This issue will be addressed in a more detailed analysis.

Acknowledgements:

We thank A. Vollmer and G. Reichardt for their excellent support. Financial support by the European Community and the Austrian Science Found (FWF) through contracts R II 3-CT-2004-506008 and S 9004-N02, respectively, is gratefully acknowledged.

References :

[1]. M.C. Asensio, J. Avila, L. Roca, A. Tejeda, G.D. Gu, M. Lindroos, R.S. Markiewicz, and A. Bansil, Phys. Rev. B **67**, 014519 (2003).

[2]. M. Lindroos, S. Sahrakorpi, and A. Bansil, Phys.Rev. B **65**, 054514 (2002).

[3]. R. Matzdorf, R. Panagio, G. Meister, A. Goldmann, Ch. Zubrägel, J. Braun, and G. Borstel, Surf. Sci. **352-354**, 670 (1996).

[4]. R. Eder and H. Winter, Phys. Rev. B **70**, 085413 (2004).

[5]. A. Menzel, Zh. Zhang, M. Minca, Th. Loerting, C. Deisl, E. Bertel, New Journal of Physics **7**, 102 (2005).

[6]. A. Menzel, Zh. Zhang, M. Minca, Th. Loerting, C. Deisl, E. Bertel, J. Phys. Chem. Sol., in press (2005).

[7]. Z. Zhang, M. Minca, C. Deisl, T. Loerting, A. Menzel, E. Bertel, R. Zucca and J. Redinger, Phys. Rev. B **70**, 121401(R) (2004).

Schottky barrier formation and interdiffusion at CdTe/metal interfaces.

B. Späth, J. Fritsche, A. Klein, W. Jaegermann

Cadmium telluride is a promising photovoltaic material for thin-film solar cells. It has a near ideal band gap for photovoltaic conversion efficiency of 1.49eV [1] and a high optical absorption coefficient. The processes used to make all the films, which compose the cell, are quite simple and fast. Small-area CdTe cells with efficiencies of more than 15% have been developed [2, 3].

Ohmic contacts without electrical losses are needed to fully exploit the potentials of CdTe solar cells. Formation of low resistance and stable back contacts has been a research issue for many years[4]. Best contacts are typically obtained with Cu-containing contacts materials. It is generally believed that diffusion of Cu into CdTe leads to an increase of p-type doping of the CdTe substrate, enabling contact formation. In previous studies CdTe/metal contacts have shown significant limitations due to a formation of a Schottky barrier of approx 0.9eV independent of the deposited metal. An important factor for the Schottky barrier formation seems to be a reaction of the metal with the CdTe, the resulting compounds and the formation of elementary Cd.

The formations of CdTe/Cu contacts were investigated with XPS measurements. A stepwise deposition of Cu onto CdTe was carried out at room temperature and 250°C. After every deposition step XPS measurements were made.

The SoLiAS UHV system attached to the TGM7 monochromator offers all the experimental requirements needed. It combines a high-resolution spectrometer and a preparation chamber.

The Te4d-, Cd4d- and valence band spectra for different Cu deposition times at room temperature are shown in Fig. 1. As expected with increasing Cu coverage, the Te4d- and Cd4d- emissions decrease while the structure of the valence band spectra from CdTe changes to the structure of the valence band of Cu. After a deposition time of 4000s seconds no Cd emissions remain in the spectra, but a small Te4d-emission can be seen. After 90s Cu deposition a slight shift of 0.13eV towards higher binding energies can be seen in the Te4d- and Cd4d-emission, due to a shift of the Fermi level in the CdTe substrate. From this follows a Schottky barrier of Φ_B=0.85±0.1eV. After 270s Cu deposition an additional Cd4d-emission is detectable at lower binding energies, due to the appearance of elementary Cd^0. This is the result of a reaction of Cu with CdTe with the formation of Cu_2Te and Cd^0:

$$CdTe + 2Cu = Cu_2Te + Cd.$$

After an annealing step at 400°C the Te4d –emission increase and the structure of the valence band changes but no Cd-emission is detectable. This indicates the formation of Cu_2Te.

In Fig. 2 the Te4d-, Cd4d- and valence band spectra for different Cu deposition times at 250°C are shown. A shift of 0.14eV towards higher binding energies in the Te4d- and Cd4d-emission is detectable after 90s Cu deposition resulting in a Schottky barrier of Φ_B=0.85±0.1eV. Also a decrease of the Te4d- and Cd4d-emission can bee seen but no additional emission of Cd^0 is detectable. Presumably, the Cd^0 diffuses into the CdTe layer or evaporates at this temperature. From the beginning of the deposition of Cu the valence band spectra does not show the structure of elementary Cu but it looks similar to the post heated surface from the first experiment. At 250°C substrate temperature the same Schottky barrier is formed like at room temperature and the Cu reacts with the CdTe: $CdTe + Cu = Cu_2Te + Cd$.

The performed experiments clearly show the interface reaction of CdTe with Cu. The Fermi level at the CdTe/Cu interface is again stabilized at ~ 0.85eV, which is close to the calculated defect level of interstitial Cd.

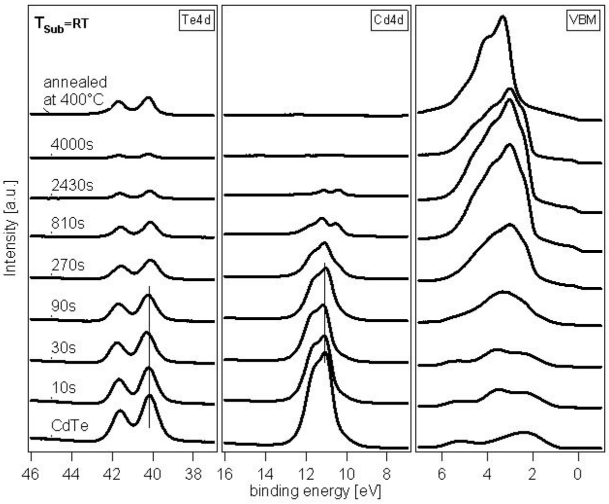

Fig.1: Te4d, Cd4d and valence band spectra from a CdTe surface with increasing Cu coverage at room temperature and an additional post heating.

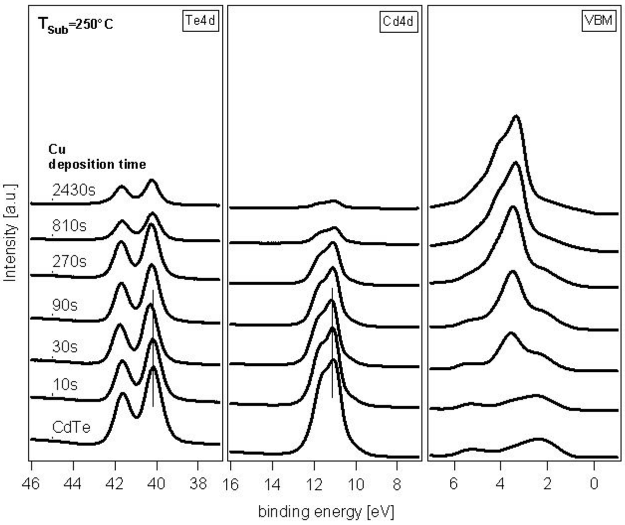

Fig.2: Te4d, Cd4d and valence band spectra from a CdTe surface with increasing Cu coverage at 250°C substrate temperature.

References

1. Fritsche, J., et al., *Band energy diagram of CdTe thin film solar cells.* Thin Solid Films, 2002. **403**: p. 252-257.
2. Britt, J. and C. Ferekides, *Thin-Film CdS/CdTe Solar-Cell with 15.8-Percent Efficiency.* Applied Physics Letters, 1993. **62**(22): p. 2851-2852.
3. Aramoto, T., et al., *16.0% efficient thin-film CdS/CdTe solar cells.* Japanese Journal of Applied Physics Part 1-Regular Papers Short Notes & Review Papers, 1997. **36**(10): p. 6304-6305.
4. Kraft, D., *Präparation und Charakterisierung von Dünnschichtmaterialsystemen für die Rückkontaktbildung bei polykristallinen Dünnschichtsolarzellen,* ed. Dissertation. 2003, Technische Universität Darmstadt.

Spin-conservation upon hybridization: A spin-resolved resonant photoemission study of 1ML Ce/Fe(110)

Yu. S. Dedkov,[1] M. Fonin,[2] S. L. Molodtsov,[1] U. Rüdiger,[2] and C. Laubschat[1]

[1]*Institut für Festkörperphysik, Technische Universität Dresden, 01062 Dresden, Germany*
[2]*Fachbereich Physik, Universität Konstanz, 78457 Konstanz, Germany*

The electronic properties of rare-earth (RE) transition-metal (TM) compounds are strongly dependent on the properties of the RE 4*f* states that maintain their atomic-like character in the solid state and become exchange-coupled via the RKKY-interaction. Hereby, light REs couple usually antiferromagnetically with respect to the TM ions while heavy REs couple ferromagnetically. On the other hand, magnetic ordering may compete with the Kondo-effect that can be described by an electron hopping interaction in the light of the Anderson model and leads to mixed-valent behavior, heavy-fermion properties and in extreme cases even to a breakdown of the Fermi-liquid picture [1,2]. Particularly Ce, the first element of the RE series, is subject of such kind of phenomena. As a function of temperature or pressure, Ce metal undergoes an isostructural phase transition from the paramagnetic γ- to the almost nonmagnetic α-phase that is accompanied by a volume collapse by more than 15%. The latter indicates a decrease of 4*f* occupation caused by increased hybridization of the 4*f* states with the surrounding valence-bands (VB). In CeTM compounds, the 4*f* hybridization is usually strong due to the large VB DOS and the systems behave so-called "α-like". Most direct insight into the electronic structure of these systems is obtained by means of photoemission (PE): In PE spectra, Ce 4*f* hybridization is reflected by a characteristic double-peak structure consisting on a peak at around 2 eV binding-energy (BE) that may be viewed as the $4f^0$ configuration expected from the photoionization of the Ce $4f^1$ ground state, and a spin-orbit split feature at the Fermi energy, E_F, that is a pure hybridization effect and reproduces the $4f^1$ ground state. This phenomenon may quantitatively be described within the "single-impurity" Anderson model using the BE of the unhybridized $4f^0$ state, ε, and a hybridization parameter, Δ, as adjustable parameters [3]. The latter describes the hopping interaction between the 4*f* state and the VB states represented by the non-4*f* derived density of states (DOS) calculated in the light of a LDA band-structure calculation. Introduction of the on-site Coulomb repulsion energy, U_{ff}, allows additionally to describe effects of double-occupation of 4*f* states caused by admixtures of $4f^2$ configurations to the ground and final states.

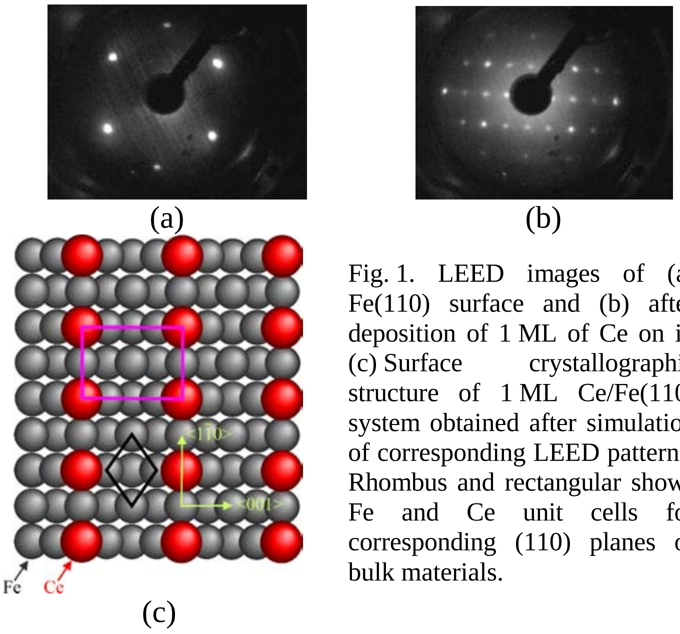

Fig. 1. LEED images of (a) Fe(110) surface and (b) after deposition of 1 ML of Ce on it. (c) Surface crystallographic structure of 1 ML Ce/Fe(110) system obtained after simulation of corresponding LEED patterns. Rhombus and rectangular shows Fe and Ce unit cells for corresponding (110) planes of bulk materials.

No spin-resolved PE study on a ferromagnetically ordered CeTM compound has been reported so far. In the present contribution we report on first results of such a study on Ce/Fe(110). Thin film samples were prepared in-situ by (i) deposition of 5 nm Fe on a W(110) substrate, followed by (ii) thermal annealing in order to achieve an epitaxial Fe layer with (110) orientation, and (iii) deposition of a monolayer Ce. As a result, a sharp LEED-pattern was obtained showing a "$(2\sqrt{2}\times\sqrt{2})$" (in analogy with squared structure) overstructure with respect to Fe(110) that might be explained by an arrangement of Ce and Fe atoms as shown in Fig. 1. Spin-resolved resonant PE experiments at the Ce 4*d*→4*f* absorption threshold were performed using a POIBOS 150 electron-energy analyzer combined with mini-Mott detector for spin-analysis from SPECS and synchrotron radiation from the U 125 undulator beamline of BESSY II. The samples were magnetized by a magnetic coil and PE spectra were taken in remanence.

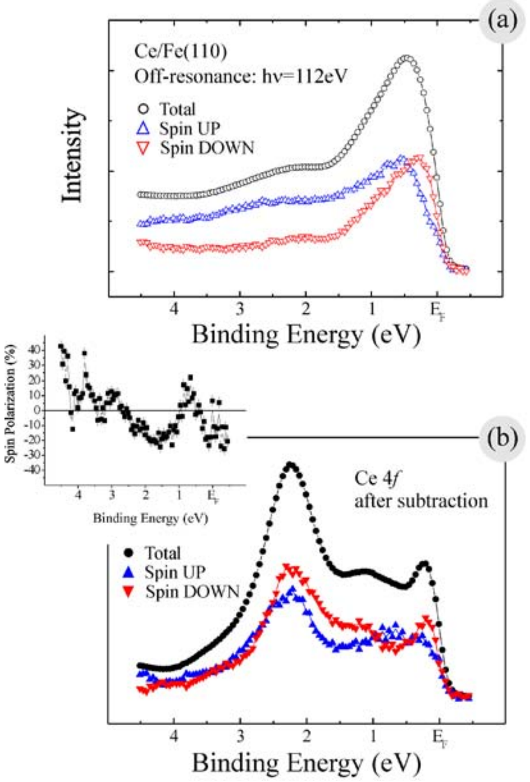

Fig. 2. (a) Spin-resolved off-resonance photo-electron spectra of the Ce/Fe(110) system. (b) Ce 4*f* partial contribution obtained after subtraction and (inset) corresponding spin polarization.

The upper pannel of Fig. 2 shows spin-resolved off-resonant PE spectra taken at 112 eV photon energy that are dominated by emissions from the exchange-split Fe 3*d* bands. As for pure Fe, the majority-spin band (triangle up) is shifted towards higher BE and is almost occupied, while the minority-spin band is shifted towards lower BE and is cut by the Fermi energy in a region of high DOS. The lower panel of Fig. 2 shows respective Ce 4*f* spectra, taken on-resonance at 121 eV photon energy. Residual Fe 3*d* contributions were removed by subtracting the off-resonance spectra, properly normalized with respect to the beam current. The observed asymmetry indicates that the Ce 4*f* states are indeed mainly antiferromagnetically coupled with respect to the Fe spins. Both majority and minority spin components reveal the characteristic double peak structure expected for an "α-like" system, interestingly, however, the relative intensity of the Fermi-level peak with respect to the "$4f^{0}$" feature of the minority spin component is somewhat larger than the one of the majority spin component pointing to an increased hybridization of the minority spin channel. This could be explained by the fact that for the minority spin direction the Fe 3*d* DOS at the Fermi level is higher than the one of the opposite spin direction leading to enhanced hybridization if spin-conservation upon hopping is assumed. In the energy region between the "$4f^{0}$" and "$4f^{1}$" peaks, a third, but weaker feature becomes visible that changes its BE position with spin orientation and reflects probably a Ce 5*d* signal. In order to confirm this assumption layer-resolved band-structure calculations are under way.

We would like to acknowledge help and useful discussions of BESSY staff during experiment.
The work was supported by the BMBF, contract no. 05 KS4OD1/4, and the SFB 463, TP B4.

[1] H. R. Kirchmayr and C. A. Poldy, in *Handbook on the Physics and Chemistry of Rare Earths* ed. K. A. Gschneidner, Jr. and L. Eyring, vol. 2 (North-Holloand, Amsterdam, 1978).
[2] L. Degiorgi, Rev. Mod. Phys. **71**, 687 (1999).
[3] R. Hayn et al., Phys. Rev. B **64**, 115106 (2001).

X-ray Emission Investigation of the O Kα Band in H-RUB-18 and in α-quartz

O.Yu. Khyzhun[a,1], *T. Strunskus*[a] , *H. Gies*[b], *Ch. Wöll*[a]

[a]*Lehrstuhl für Physikalische Chemie I, Ruhr-Universität Bochum, Universitätsstraβe 150, D-44780 Bochum, Germany*
[b]*Lehrstuhl für Kristallographie, Institut für Geologie, Mineralogie und Geophysik, Ruhr-Universität Bochum, Universitätsstraβe 150, D-44780 Bochum, Germany*
[1]*Permanent address: Frantsevych Institute for Problems of Materials Science, National Academy of Sciences of Ukraine, 3 Krzhyzhanivsky street, UA-03142 Kiev, Ukraine*

1. Introduction

Highly crystalline α-quartz and the crystalline layered silicic acid H-RUB-18 were used as reference systems for a ongoing study of microporous and mesoporous silica materials. The possible bonding neighbourhoods of oxygen are similar in all materials, but their quantity varies in the different silicas. Ideally as in α-quartz, oxygen is bonded to 2 silicon atoms. In defects, on the other hand oxygen is bound to one Si atom and one H atom. In H-RUB-18 oxygen is bound to one silicon and one proton in crystalline order. This allows to study the influence of the presence of silanol units (Si-OH) upon the electronic structure in silica materials.

2. Experimental

In the present study the following samples were used:

1) pure α-quartz, α-SiO_2; Dörentrup (Sauerland); space group (SG): $P3_221$; lattice parameters: $a = 4.92$ Å, $c = 5.41$ Å, $\gamma = 120°$;
2) the crystalline layered silicic acid H-RUB-18; SG: $I4_1/amd$; the structure of H-RUB-18 can be represented as a sequence of pseudo tetragonal silicate layers with an intra-layer repeat unit $a = 7.38$ Å and inter-layer distances of $c = 7.44$ Å.[1]

Resonant SXE and near-edge X-ray absorption fine structure (NEXAFS) measurements at the O K edges were carried out using undulator beam-line U41-PGM. The spectra were measured with a high-resolution Rowland-mount grazing-incidence grating X-ray emission spectrometer Scienta XES 300 (Gammadata, Sweden) equipped with a two-dimensional detector. The exit slit of the beam-line during the RSXE measurements was set to 100 μm, yielding a total resolution (combined from synchrotron excitation and spectrometer energy resolution) of approximately 1.1 eV. This value was determined by measuring the full width at half maximum (FWHM) of the elastic peaks in the energy region at the O K edge. The NEXAFS spectra were recorded in the fluorescence yield (FY) mode. No changes in the resonant SXE and NEXAFS spectra were observed as a function of exposure time to the synchrotron radiation. All the measurements were made at room temperature.

3. Results and Discussion

Figure 1 represents the NEXAFS O 1s spectra of α-quartz and H-RUB-18. Energies of photons used in the present work for excitation of the resonant SXE O Kα spectra are marked by arrows above the NEXAFS spectra. It is apparent from Figure 2 that the energy positions of the O K onsets differ slightly for the compounds studied and some minor changes are characteristic for the shapes of the NEXAFS O 1s spectra just above the top of the O K absorption bands positioned at about 539-542 eV.

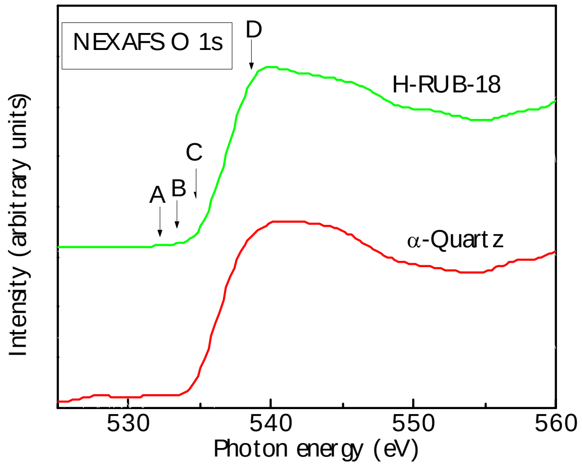

Figure 1. *NEXAFS O 1s spectra of pure α-quartz H-RUB-18; abscissa is the excitation photon energy. Energies of photons employed for excitation of the resonant soft X-ray emission spectra presented in Figure 2 are marked by arrows above the NEXAFS O 1s spectra.*

In Figure 2 we present a series of the resonant SXE O Kα spectra recorded for α-quartz and H-RUB-18 when employing different excitation energies as marked in Figure 1. The O Kα bands excited with the photon energy corresponding to the top of the broad O K absorption bands (point D on the NEXAFS O 1s spectra presented in Figure 1) look quite similar for the two compounds. For the shape of the O Kα band in the two compounds studied, in addition to the main peak "*d*", the presence of a pronounced feature "*b*" and two shoulders, "*a*" and "*c*", is characteristic.

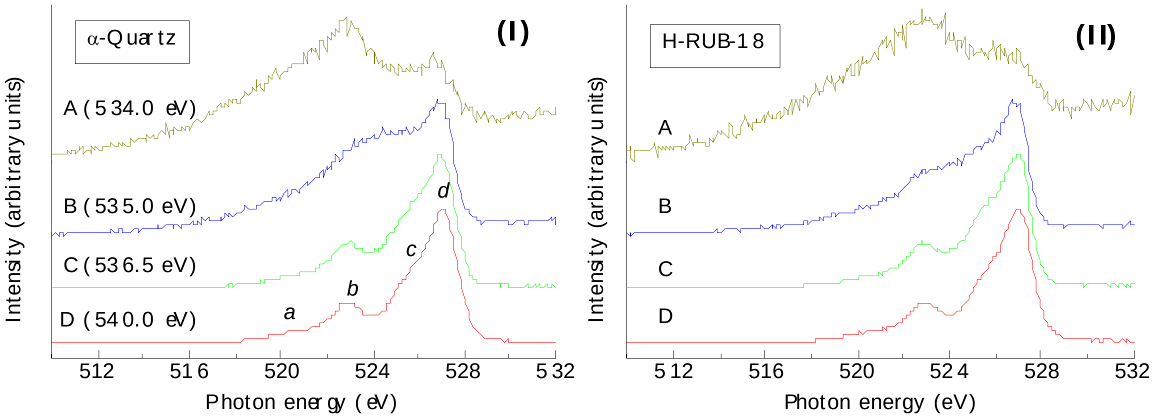

Figure 4*. Resonant soft X-ray emission O Kα bands of (I) α-quartz and (II) H-RUB-18 excited with photon energies indicated by the arrows A–D in the NEXAFS O 1s spectra presented in Figure 1.*

When tuning the excitation energy across the slope of the O K absorption edge just below the O K absorption band, a small increase of the relative intensity of the feature "b" of the O Kα band (with respect to the intensity of its maximum "d") is observed and the valley between the sub-band "b" and the main portion of the O Kα band vanishes (cf. curves D and

C in Figure 2). When tuning the excitation photon energy in the energy region corresponding to the position of the O K onset, the valley vanishes completely. The shape of the resonant SXE O Kα bands excited with the photon energies of 534 eV and 535 eV employed in the present experiments differ significantly.

The similarity of the SXE O Kα spectra excited with the photon energy taken above the O K absorption band (curves D in Figure 2) we can explain by the fact that in all the studied compounds the chemical bonding is determined mainly by the interaction between silicon and oxygen atoms. Surprisingly, the SXE spectra reveal that, the presence of the silanol units in H-RUB-18 does not affect the shape of the SXE O Kα bands that is characteristic for α-quartz. The relative intensities of the fine-structure features of the SXE O Kα bands (as compared to the intensity of the maximum "*d*" of the band) in the above compounds are quite similar if the spectra are excited with photon energies above the top of the O K absorption bands. Currently, ab initio quantum mechanical calculations are in progress in order to help to understand this result.

Changes of the shape of the O Kα bands start to become pronounced when exciting with the photon energies close to the position of the onset of the O K thresholds. The resonant SXE O Kα spectra reveal the appearance of the Raman-like inelastic peak with an energy loss of −11 eV as can be seen from Figures 2. The changes of the SXE O Kα bands when employing photon excitation energies close to the O K onset energy in H-RUB-18 and in α-quartz is explained by superposition of the inelastic peak "*B′*" with the remaining part of the O Kα band. The rather big differences in relative intensities of the inelastic peak and of the resonantly excited SXE O Kα bands in the two materials are not well-understood at present and additional studies are in progress.

4. Conclusions

We have measured NEXAFS O 1s and resonant SXE O Kα spectra for a series of excitation energies at the O K threshold of a crystalline layered silicic acid H-RUB-18 and pure α-quartz. Significant differences were expected for the O Kα spectra for the two compounds since in α-quartz the chemical bonding is determined only by Si–O bonds whereas H-RUB-18 contains a large fraction of silanol groups. Surprisingly, the nonresonant SXE O Kα spectra for the two compounds look very similar and only the resonant spectra (when core electrons are excited by photons to unoccupied states close to the position of the Fermi level) reveal specific changes. The influence of the silanol groups on the shape of the SXE O Kα band in silica materials is not well understood in detail at present and ab initio quantum mechanical calculations are in progress to gain more insight into this matter.

Acknowledgements

The authors thank support by Prof. R. Szargan (University of Leipzig) and the BESSY staff (especially Ch. Jung and M. Mast). Travelling costs for synchrotron measurements provided by BMBF through grant 05 ES3XBA/5 are gratefully acknowledged.

Reference

[1] Borowski, M.; Marler, B.; Gies, H. *Z. Kristallogr.* **2002**, *217*, 233.

The Molecular Orientation of DNA Bases on H-passivated Si(111)(7x7) investigated by means of Near Edge X-ray Absorption Spectroscopy

S. Seifert, G. Gavrila, Y. Suzuki, D.R.T. Zahn
Institut für Physik, Technische Universität Chemnitz, D-09107 Chemnitz, Germany
W. Braun
BESSY GmbH, Albert-Einstein-Str. 15, D-12489 Berlin, Germany

In recent years DNA bases have been discussed as promising candidates for electronic applications, such as (bio-)organic field effect transistors [1] or molecular nano-wires [2]. The strong anisotropy of charge transport within molecular crystals makes the knowledge of the molecular orientation of the DNA bases crucial for any device design. We therefore performed a systematic Near Edge X-ray Absorption Fine Structure (NEXAFS) spectroscopy study of layers of the DNA bases adenine, cytosine and guanine on H-passivated Si(111). The measurements were performed using the Multi User Stage for Angular Resolved Photoemission (MUSTANG) experimental station at the Russian German beam line at BESSY.

Experiment: The substrates were cut from a n-type, highly phosphor doped (resistivity 7.5 Ω/cm) silicon(111) wafer supplied by *SilChem GmbH*. The samples were annealed by direct current (DC) heating under ultra high vacuum (UHV) conditions (base pressure $\leq 3\cdot 10^{-10}$mbar) up to 750°C-800°C. The natural oxide was removed by several DC flushes of 20s duration up to 1100°C-1300°C. The substrates were then cooled down slowly to preserve the (7x7) reconstruction. In order to prevent a reaction of the DNA bases with the substrate, the surface was passivated *in situ* by exposure to (2.0±0.5) Langmuir atomic hydrogen.The dosis was chosen carefully and should be just enough to saturate the dangling bonds of the Si(111)(7x7) without etching the surface. This method of passivation leads to considerably lower surface roughness than achieved by a wet-chemical cleaning and passivation treatment of Si(111).The DNA base layers were deposited by organic molecular beam deposition (OMBD). The nominal layer thickness was monitored by a quartz micro balance.

The (NEXAFS) spectra were recorded in the partial electron yield mode in the region of the secondary electron background (at a kinetic energy of 10eV). The angle of incidence, Θ, between the incident light and the sample surface was varied between of 22°-115°. The measured data were corrected for the photon flux by division of the spectra by the electron yield of the clean H-Si(111)(7x7)

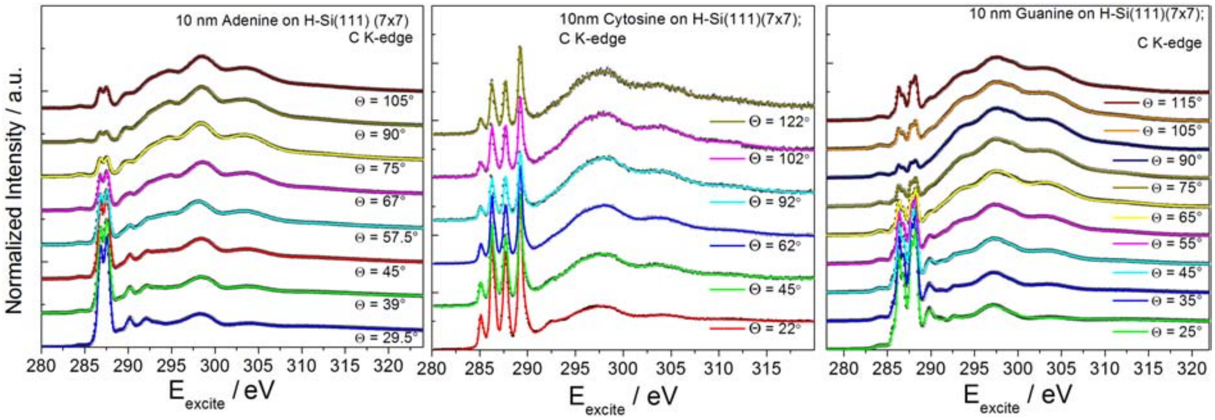

Fig.1: The carbon K-edge NEXAFS spectra of a 10nm adenine (left) cytosine (midle) and guanine (right) on H-Si(111)(7x7) as a function of the angle of incidence, Θ.

sample and the synchrotron ring current, the background was subtracted and the spectra were normalized to the absorption step edge at *320eV*. The angular dependent carbon K-edge NEXAFS spectra of 10nm thick layers of adenine, cytosine and guanine on H-Si(111)(7x7) are shown in Fig.1.

Peak assignment: The prominent features at the low excitation energies correspond to transitions from the carbon 1s core levels into the lowest unoccupied molecular orbitals (LUMO, LUMO+1 ...). The validity of this assignment can be checked by comparison the measured spectra with theoretical calculations employing density functional theory (DFT) for the single DNA base molecules (B3LYP functionals; 6-311G+(d,p) basis sets). For these calculations the commercial software package GAUSSIAN03 [3] was used. The contribution of different excitation sites (i.e. the carbon atoms) are treated separately. In molecules as small as the DNA bases the core hole created at the excitation site has a strong impact on the molecular orbitals and has to be considered in the calculation. This is done by the introduction of an extra charge to the core of the excited atom by replacing it with its Z+1 equivalent (i.e. nitrogen). The DFT calculation is then performed for the positively charged molecule, in order to keep the number of electrons constant. Afterwards, the calculated unoccupied molecular orbitals are decomposed into the contributing atomic orbitals[*]. The contribution of a single carbon atom to the π^*-resonances in the NEXAFS spectrum is mainly contained in the contribution of its antibonding $2p_z$ atomic orbital (were the z-axis is perpendicular to the molecular plane) to the unoccupied molecular orbitals. The excitation energy necessary for a transition into these states is calculated by subtracting the 1s core level binding energy of the particular carbon atom (measured by core level photoemission spectroscopy) from the calculated eigen energies. The contributions of all the carbon atoms within the molecule are averaged and broadened with Voigt functions of 0.3eV FWHM. In Fig.2 the calculated curves are compareed to the measured spectra. For adenine and cytosine, the Z+1 apporoach leads to very good agreement between the simulation and the measurement. The resemblance is not as good in the case of guanine, but still the π^*-nature of the peaks at the lowest excitation energies becomes obvious. The relatively large shift, which had to be introduced, to match the peaks with the highest intensities is due to the fact, that the extra positive charge on the molecule is overestimating the core hole effect on the molecular orbitals.

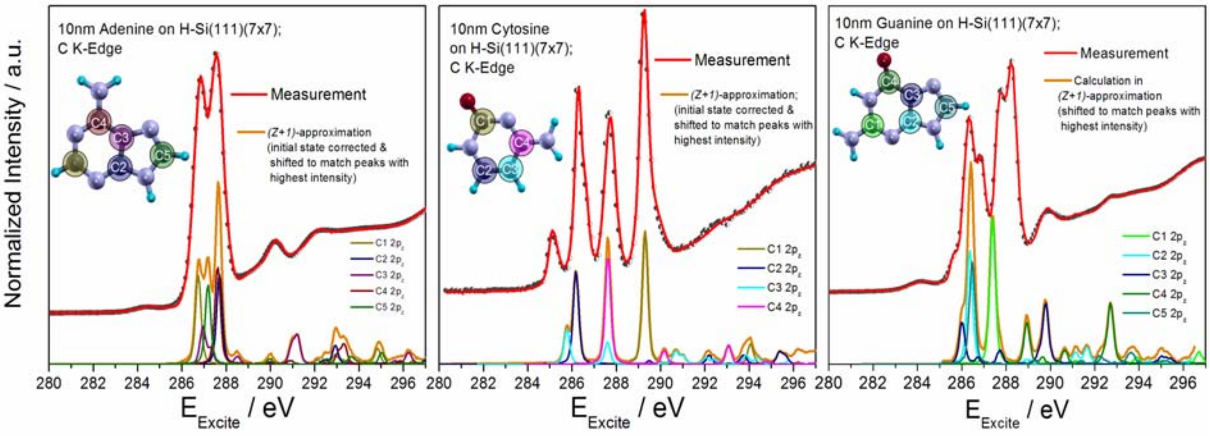

Fig.2: In the Z+1 approximation the DFT calculations are performed after substitution of a carbon (Z=6) atom by a nitrogen (Z=7) atom. The spectra are derived by assuming vertical transition between the atomic 1s and $2p_z$ orbitals. The spectra were shifted by ΔE_C = 4.36eV, ΔE_A = 2.86eV and ΔE_g = 2.54eV towards higher excitation energies.

---

[*] The atomic orbitals were calculated from the Gaussian'03 output, using the AOMix program [5,6], which employs a Mulliken population analysis

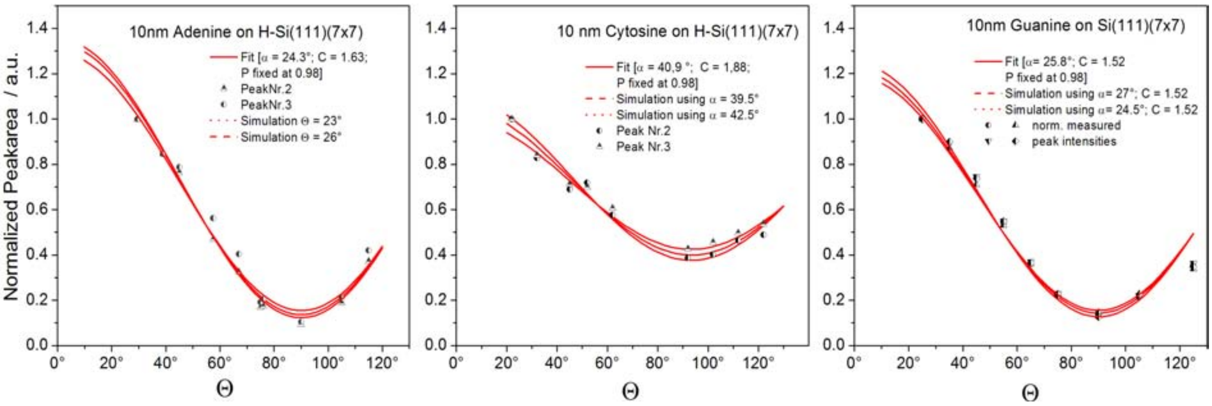

Fig.3: The dependence on the incidence angle (Θ) of selected π*-transition peaks in the NEXAFS spectra of adenine (left), cytosine (middle) and guanine (right). By variation of α and C to optimize the match between measurement and equation (1) the molecular orientation of each DNA base is obtained.

Molecular orientation: For the quantitative analysis of the angular dependence of the NEXAFS spectra at first the π*-transition peaks were fitted using Voigt functions. Because of the spherical symmetry of the initial state (a 1s orbital), the transition dipole moments of these resonances are oriented parallel to the final state, π*-orbitals, which are oriented perpendicular to the molecular plane. In this case, the dependence of the resonance intensity on the angle of incidence, under the condition of threefold (or higher) substrate symmetry is given by [7]

$$I = C\left[P\left(\cos^2\Theta\cos^2\alpha + \frac{1}{2}\sin^2\Theta\sin^2\alpha\right) + \frac{(1-P)}{2}\sin^2\alpha\right] \qquad (1)$$

where P is the degree of polarization and C a normalization factor. Θ is the angle of incidence and α the angle between the transition dipole moments and the surface normal (or the molecular tilt angle). The angle Θ and the polarization factor are known quantities, which only leaves the molecular orientation and the normalization constant C unknown. These parameters can be determined by curve fitting the above equation to the relative intensities of the π*-resonances in the NEXAFS spectra of adenine, cytosine and guanine. The fitted curves are presented in Fig.3. The average molecular tilt angles of the DNA base molecules with respect to the substrate surface are determined to be:

$$\alpha_A = (24° \pm 3°); \quad \alpha_c = (40.5° \pm 1.5°); \quad \alpha_G = (25.8° \pm 1.3°)$$

Acknowledgments: The authors would like to thank the BESSY staff members for their assistance during the beam times (especially Mike Sperling for the technical support). We also acknowledge the financial support granted by the BMBF (FK MUSTANG 05KS40C1/3, FK 05KS1OCA1).

References:

[1] G. Maruccio, *Field effect transistor based on a modified dna base.* Nano Letters **3**, 479 (2003)
[2] D. Porath, A. Bezryadin, S. de Vries, and C. Dekker, *Direct measurement of electrical transport through dna molecules*. Nature **403**, 635 (2000)
[3] Gaussian 03, Revision C02, M. J. Frisch, G. W. Trucks, H. B. Schlegel, G. E. Scuseria, M. A. Robb, J. R. Cheeseman, J. A. Montgomery, Jr., T. Vreven, K. N. Kudin, J. C. Burant, J. M. Millam, S. S. Iyengar, J. Tomasi, V. Barone, B. Mennucci, M. Cossi, G. Scalmani, N. Rega, G. A. Petersson, H. Nakatsuji, M. Hada, M. Ehara, K. Toyota, R. Fukuda, J. Hasegawa, M. Ishida, T. Nakajima, Y. Honda, O. Kitao, H. Nakai, M. Klene, X. Li, J. E. Knox, H. P. Hratchian, J. B. Cross, V. Bakken, C. Adamo, J. Jaramillo, R. Gomperts, R. E. Stratmann, O. Yazyev, A. J. Austin, R. Cammi, C. Pomelli, J. W. Ochterski, P. Y. Ayala, K. Morokuma, G. A. Voth, P. Salvador, J. J. Dannenberg, V. G. Zakrzewski, S. Dapprich, A. D. Daniels, M. C. Strain, O. Farkas, D. K. Malick, A. D. Rabuck, K. Raghavachari, J. B. Foresman, J. V. Ortiz, Q. Cui, A. G. Baboul, S. Clifford, J. Cioslowski, B. B. Stefanov, G. Liu, A. Liashenko, P. Piskorz, I. Komaromi, R. L. Martin, D. J. Fox, T. Keith, M. A. Al-Laham, C. Y. Peng, A. Nanayakkara, M. Challacombe, P. M. W. Gill, B. Johnson, W. Chen, M. W. Wong, C. Gonzalez, and J. A. Pople, Gaussian, Inc., Wallingford CT, 2004.
[5] Gorelsly, S. 'AOMix program, revison 5.92'. http://www.sg-chem.net/
[6] Gorelsly, S. & a.b.p. Lever. J Organomet. Chem. 635, 187 (2001)
[7] J. Stöhr and D. Outka, *Determination of molecular orientations on surfaces form the angular dependence of near-edge x-ray-absorption fine structure spectra.* Phys. Rev B **36**, 7891 (1987)

Molecular Interactions in Organic Ultra Thin films Studied by VUV Spectroscopic Ellipsometry

O. D. Gordan, D. Lehmann, S. Hermann, D. R. T. Zahn
Institut für Physik, TU Chemnitz, 09107 Chemnitz, Germany
S. Silaghi, C. Cobet, N. Esser
ISAS - Institute for Analytical Sciences, D-12489 Berlin
W. Braun
BESSY GmbH, 12489 Berlin, Germany

The ellipsometric studies at BESSY makes it possible to investigate the electronic transitions of organic layers in the Vacuum Ultra Violet (VUV) range. Especially for small molecules, like DNA base molecules which have the HOMO-LUMO transitions at energies higher than 4 eV [1], the access to the VUV range is essential. While the synchrotron radiation extends the range beyond the capabilities of commercial ellipsometers, we proved that the lower wavelength of the light allows the dielectric function of ultra-thin organic films to be investigated on the sub-nanometer scale [2]. Therefore in this work we report the changes in the Vacuum Ultra Violet (VUV) spectra upon increasing thickness for two DNA base molecules: cytosine and guanine. The molecular structure of these two molecules is presented in figure 1.

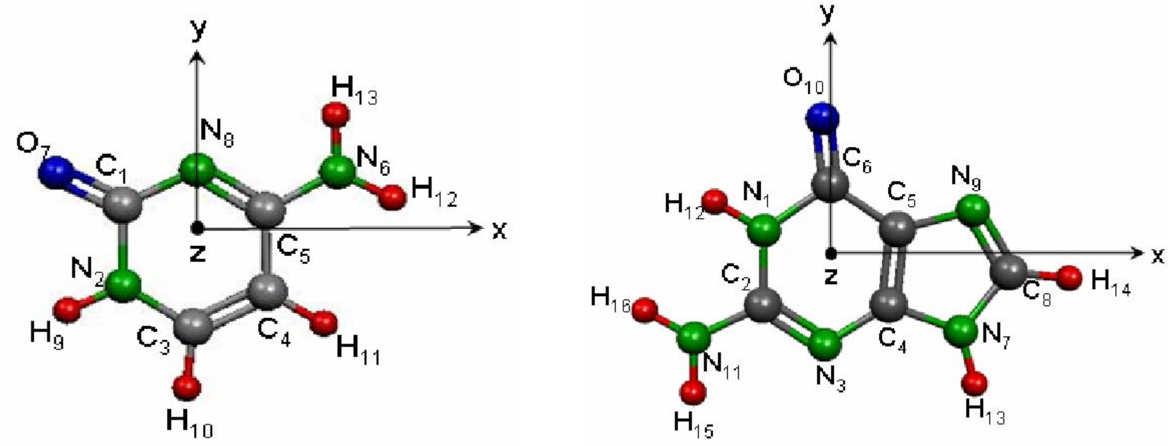

cytosine guanine

Figure 1. Molecular structures of cytosine (left) and guanine (right) projected in the (x, y) plane with z perpendicular on the molecular plane

Vacuum Ultra Violet (VUV) Spectroscopic Ellipsometry (SE) measurements were performed *in situ* for optical characterization of ultra-thin films of cytosine and guanine. The layers were prepared by organic molecular beam deposition (OMBD) on hydrogen passivated silicon H-Si(111). The measurements were performed at BESSY at the 3m-NIM 1A beam line using a rotating-analyser ellipsometer operating in the 4-9.5 eV range with an energy step of 0.025 eV. MgF_2 Rochon prisms were used as polarizers (for details see [3-5]).

Figure 2 shows the imaginary part of the measured effective dielectric function $<\varepsilon_2>$ for H-Si(111) and for a 0.35 nm cytosine layer on H-Si(111). As can be seen in figure 2 clear changes in the ellipsometric data can be observed even for this coverage. While interpreting the ellipsometry data for very thin overlayers on a substrate (less than 10 nm) is rather difficult, the access to the VUV at BESSY makes it possible to achieve a higher separation in the experimental Δ values even for very small changes in the refractive index [6]. In this case the dielectric function of the overlayer can be extracted using a first order approximation [6].

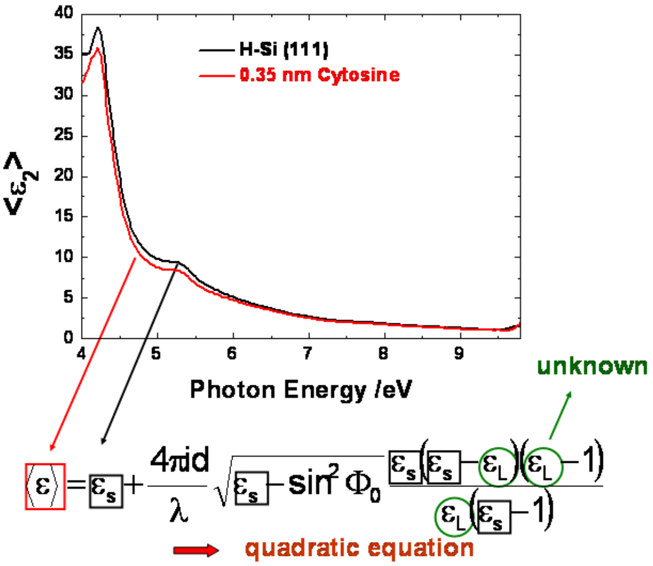

$$\boxed{\langle\varepsilon\rangle} = \boxed{\varepsilon_s} + \frac{4\pi i d}{\lambda}\sqrt{\boxed{\varepsilon_s} - \sin^2\Phi_0}\,\frac{\boxed{\varepsilon_s}\left(\boxed{\varepsilon_s} - \varepsilon_L\right)\left(\varepsilon_L - 1\right)}{\varepsilon_L\left(\boxed{\varepsilon_s} - 1\right)}$$

Figure 2. The measured effective $<\varepsilon_2>$ of the 0.35 cytosine sample compared with the $<\varepsilon_2>$ of the H-Si(111) substrate.

According to Aspnes [6], the measured effective dielectric function $<\varepsilon>$ can be approximated by the formula presented above. As ε_S is the measured dielectric function of the substrate and d is the layer thickness, the quadratic equation can be easily solved to find the dielectric function of the layer ε_L. The solution of the above equation for the 0.35 cytosine layer is presented on the left side of figure 3.

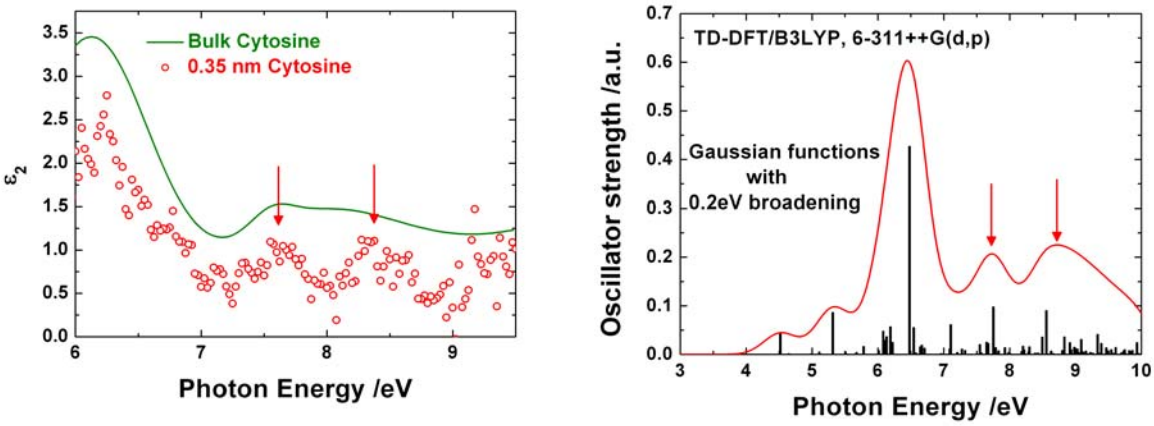

Figure 3. Left - Comparison between the imaginary part of the dielectric functions of the bulk cytosine and 0.35 nm cytosine layer. Right - TD-DFT calculation of the excited states for a single cytosine molecule.

For comparison the imaginary part of the dielectric function of the ultra-thin layer is plotted together with the imaginary part of the dielectric function of bulk cytosine. A detailed description of the experimental conditions and the ellipsometric model used to determine the bulk values can be found in ref. [7, 8]. While in the low energy range (below 7 eV) the dielectric function of the ultra-thin layer has similar shape like the bulk one, in the high energy range a clear splitting at the positions indicated by arrows can be observed. The splitting can be attributed to the reduced intermolecular interactions between the cytosine molecules in the overlayer. This hypothesis is supported by theoretical calculations [8] of the excited states using time dependent density functional theory (TD-DFT). The computation was performed for an isolated molecule using Gaussian software [9]. The convolution of the excited states using Gaussian functions with 0.2 eV broadening is plotted on the right side of figure 3.

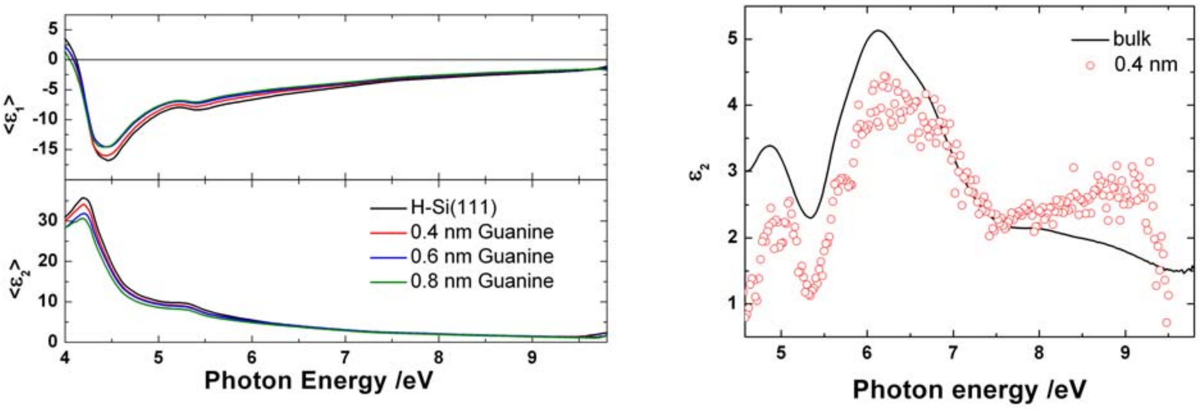

Figure 4. Left – the measured effective dielectric function of H-Si(111) and guanine layers of 0.4, 0.6 and 0.8 nm. Right - Comparison between the dielectric functions of bulk guanine and 0.4 nm guanine layer.

A similar study was performed for guanine layers. The solution of Aspnes formula presented in the right part of figure 4 yields in this case a dielectric function of a 0.4 nm guanine layer very similar to the bulk one. This is probably related to an island growth mode of the guanine.

The authors gratefully acknowledge the BMBF project 05 KS4KTB/3 and BMBF project 05 ES3XBA/5 and the Deutsche Forschungsgemeinschaft, Graduiertenkolleg 829 “Akkumulation von einzelnen Molekülen zu Nanostrukturen“.

[1] S. D. Silaghi, Yu J. Suzuki, O. D. Gordan, C. Himcinschi, G. Salvan, M. Friedrich, T. U. Kampen, D. R. T. Zahn C. Cobet, N. Esser, W. Richter, W. Braun – BESSY Jahresbericht (2003) 209
[2] O.D. Gordan, C. Himcinschi, Yu J. Suzuki, G. Salvan, D. R. T. Zahn, C. Cobet, N. Esser, W. Richter, W. Braun – BESSY Jahresbericht (2004) 170
[3] R. L. Johnson, J. Barth, M. Cardona, D. Fuchs, and A. M. Bradshaw – Rev. Sci. Instrum. 60, 2209, (1989).
[4] J. Barth, R. L. Johnson, and M. Cardona, - Handbook of Optical Constants of Solids II, edited by E. Palik, Academic Press, New York, (1991)
[5] T. Wethkamp, K. Wilmers, N. Esser, W. Richter, O. Ambacher, H. Angerer, G. Jungk, R. L. Johnson, and M. Cardona - Thin Solid Films 313-314, 745, (1998)
[6] D. Aspnes – Spectroscopic Ellipsometry of Solids, Chap 15, Optical Properties of Solids-New Developments, ed B.Seraphin, North Holland 1976
[7] Y. Suzuki, O.D. Gordan, S.D. Silaghi, D.R.T. Zahn, A. Schubert, W.R. Thiel, C. Cobet, N. Esser, W. Braun – Appl. Phys. Lett., 87 (2005) 214101
[8] S. Silaghi- PhD. Thesis, Chemnitz (2005) http://archiv.tu-chemnitz.de/pub/2005/0077/index.html
[9] M. J. Frisch *et al.* - *Gaussian 98*, Version 5.2; Gaussian, Inc.: Pittsburgh, PA, 2001

Electronic Structure of Diluted Magnetic Semiconductor $Zn_{1-x}Co_xO$

M. Fonin,[1] E. Biegger,[1] Yu. S. Dedkov,[2] L. Burova,[3] A. R. Kaul,[3] and U. Rüdiger[1]

[1] *Fachbereich Physik, Universität Konstanz, 78457Konstanz, Germany*
[2] *Institut für Festkörperphysik, Technische Universität Dresden,*
01062 Dresden, Germany
[3] *Department of Chemistry, Moscow State University, Moscow 119899, Russia*

Diluted magnetic semiconductors (DMSs) produced by doping of transition metal ions into nonmagnetic semiconductors which combine charge and spin degrees of freedom in a single material are promising candidates for the next generation spintronic devices [1]. Additionally, wide gap DMSs, among them doped ZnO and SnO_2, combine their electrical conductivity and ferromagnetism with optical transparency, thereby opening up the possibility of new device concepts. Since the prediction by Dietl *et al.* [2] of the Curie temperature (T_C) of Mn-doped ZnO exceeding room temperature (RT), diluted magnetic semiconductors on the basis of ZnO attract strong research interest. However, despite many efforts the experimental situation remains highly controversial. For nominally identical systems reports of high T_C coexist with reports that exclude intrinsic ferromagnetism [3]. Moreover, the origin of the ferromagnetism in doped magnetic ZnO and related DMS materials is still under strong debate [3]. Until now only two studies were performed on the electronic properties of Co-doped ZnO [4,5]. Wi *et al.* [4] performed x-ray absorption (XAS) and photoelectron spectroscopy (PES) on bulk Co-doped ZnO samples prepared by solid-state reaction method which did not exhibit ferromagnetic behavior. XPS and XAS measurements showed that the Co states are divalent (2+) under a tetrahedral symmetry giving clear evidence of properly substituted Co ions into ZnO lattice. On the basis of these findings it was concluded that ferromagnetic properties cannot be produced when Co ions are properly substituted for Zn sites and the origin of the ferromagnetism in Co-doped ZnO should have extrinsic nature [4]. Recently, Kobayashi *et al.* [5] performed a combined PES and XMCD spectroscopic study of ferromagnetic $Zn_{1-x}Co_xO$ films prepared by a pulsed laser deposition technique. XMCD measurements on the $Zn_{1-x}Co_xO$ films showed a multiplet structure characteristic for the Co^{2+} ion tetrahedrally coordinated by oxygen suggesting that ferromagnetism is caused by the substituted Co^{2+} ions at the Zn site in the ZnO lattice and is therefore intrinsic.

In the present study a combined photoelectron spectroscopy (PES) and near edge x-ray absorption fine structure spectroscopy (NEXAFS) of ferromagnetic as well as paramagnetic $Zn_{1-x}Co_xO$ films was performed in order to determine the electronic structure associated with the Co ions in the ZnO host lattice.

PES as well as NEXAFS experiments were carried out at RT at the RGBL-PGM beamline at the BESSY II storage ring. The UHV system located at the Russian-German Laboratory (base pressure of 1×10^{-10} mbar) was equipped with a 127° CLAM4 analyzer. The total energy resolution in the XPS measurements was set to 150 meV. The position of the Fermi energy was determined form the valence-band spectrum of a polycrystalline Au foil in the electrical contact with the sample. All spectra were normalized to the incident photon flux. NEXAFS spectra were collected in the total electron yield mode and normalized to the maximum intensity. The energy resolution in the NEXAFS experiments was set to 100 meV.

High quality 100-200 nm thick $Zn_{1-x}Co_xO$ films with different concentrations of Co (x=0.05;0.1) were prepared by magnetron sputtering on $Al_2O_3(0001)$ substrates. The substrate temperature during the growth was maintained at about 700 K. Two sets of samples were prepared: samples in the first set were deposited in 10^{-3} mbar Ar (samples *S1*) with short postannealing at 700K, samples in the second set were deposited in 10^{-3} mbar Ar/O_2 (1:1) gas mixture with subsequential annealing in O_2 (1bar) at 1000 K (samples *S2*). After introducing

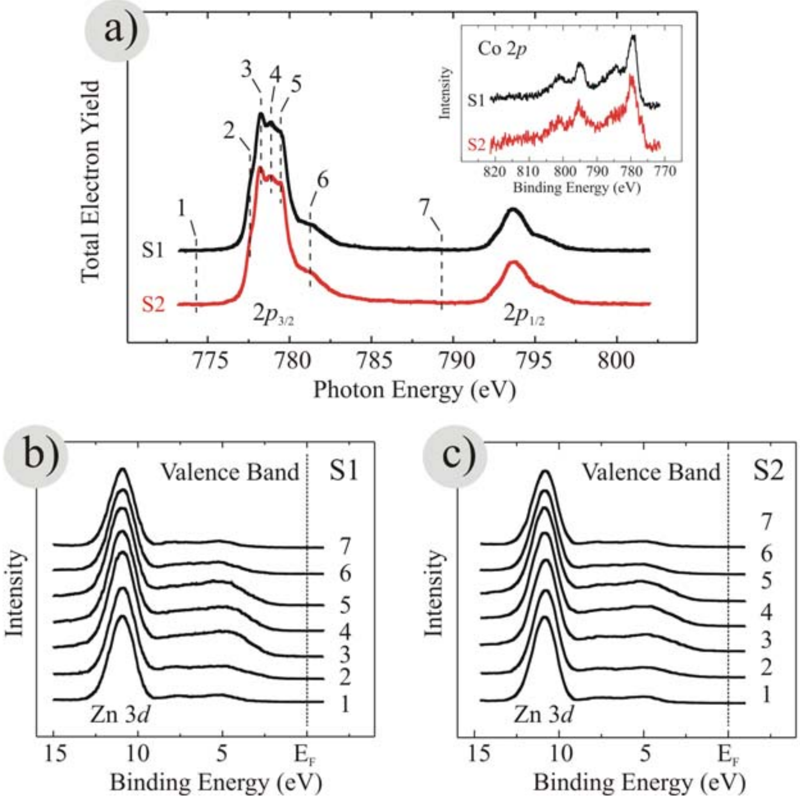

Fig. 1. In (a) experimental Co $L_{2,3}$ NEXAFS spectra of two $Zn_{0.95}Co_{0.05}O$ films (S1 and S2) are presented. Inset shows the corresponding Co 2p core level spectra. (b) Valence band PES spectra of $Zn_{0.95}Co_{0.05}O$ film (S2) obtained at photon energies marked by numbers in the corresponding NEXAFS spectrum .

the samples into the UHV chamber at BESSY II their surface were cleaned by Ar^+ sputtering under grazing angle (E=800 V, p=5×10^{-6} mbar).

X-ray diffraction confirmed that all films crystallized in the wurtzite structure and no impurity or secondary phases were observed. Magnetic properties of the $Zn_{1-x}Co_xO$ films were characterized by means of a Quantum Design superconducting quantum interference device (SQUID) from 0 up to 5 T in the temperature range of 5-300 K. In *S1* samples ferromagnetism with *T*c above the room temperature (RT) was found with magnetic moments of about 0.05-0.1 μ_B/Co at RT increasing to 0.2 μ_B/Co at 5 K. In *S2* samples were paramagnetic at RT and only at temperatures below 50 K a weak ferromagnetic signal was observed.

Fig. 1 (a) compares the Co $L_{2,3}$ NEXAFS spectra of two $Zn_{0.95}Co_{0.05}O$ samples of the *S1* and *S2* sets. The peak positions as well as the line shape [features 2,3,4,5,6 in Fig. 1 (a)] of both Co 2*p* NEXAFS spectra are almost identical and are in good agreement with those measured before for Co-doped ZnO [4,5]. The obtained NEXAFS spectra look similar to that of CoO and are quite different from those of Co metal as well as of Co^{3+} indicating that Co ions in both samples are present in divalent Co^{2+} state. Moreover, calculations on the basis of atomic multiplet theory performed for Co^{2+} ions tetrahedrally coordinated by oxygen was shown to yield the best fit for the presented experemental spectra [5]. Hence, Co ions in both $Zn_{0.95}Co_{0.05}O$ samples are divalent and tetrahedrally coordinated by oxygen ions. Careful analysis of the *S1* and *S2* sample spectra shows that features 5 and 6 in the *S2* spectrum have slightly larger intensities than those of *S1* which may be attributed to better Co incorporation in the sample. The inset in Fig.1 (a) shows the core-level Co 2*p* XPS spectra of both (S1 and S2) $Zn_{0.95}Co_{0.05}O$ samples taken at $h\nu$=1000 eV. The spectra are similar to that of CoO confirming again the presence of Co^{2+} ions in Co-doped ZnO samples. Thus NEXAFS and XPS show that in both samples Co atoms are properly incorporated in the ZnO lattice by substitution of Zn sites.

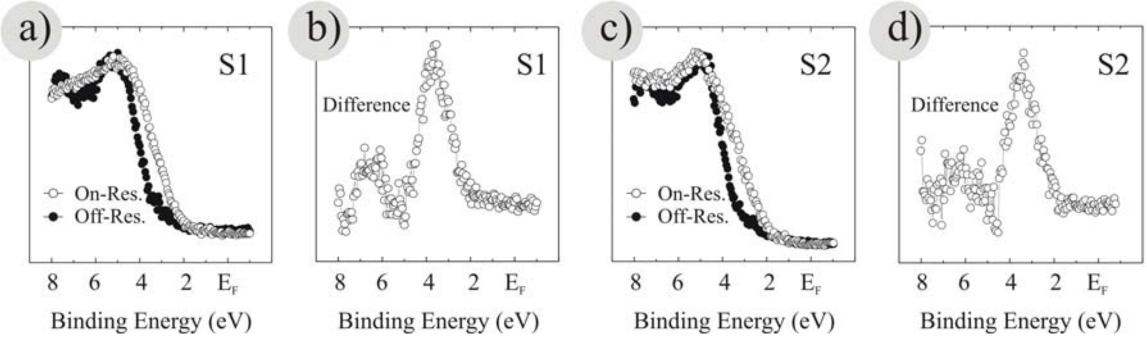

Fig. 2. On-resonance (hν=774 eV) and off-resonance (hν=777 eV) valence band photoemission spectra of $Zn_{0.95}Co_{0.05}O$*: (a) sample S1 and (c) sample S2. Corresponding difference curves showing the Co* 3*d PDOS are presented for both samples in (b) and (d), respectively.*

Fig. 1 (b) and (c) shows representative valence band photoemission spectra of the *S1* and *S2* $Zn_{0.95}Co_{0.05}O$ samples as a function of photon energy including the Co 2*p* – 3*d* core-excitation region. The valence band spectra of $Zn_{0.95}Co_{0.05}O$ are similar to that of ZnO showing a sharp peak at about 11 eV of the binding energy (BE) corresponding to Zn 3*d* states as well as a broad feature between 3 and 8 eV of BE corresponding to O 2*p* band. Almost no photoemission intensity was observed in the E_F region confirming the insulating nature of the $Zn_{0.95}Co_{0.05}O$ films. Thus the charge carrier mediated ferromagnetism based on the RKKY interaction can be ruled out. By substracting the *off*-resonance spectrum from the *on*-resonance one Co 3*d* partial density of states (PDOS) can be obtained. Fig. 2 represents $2p_{3/2} - 3d$ on-resonance (hν=774 eV) and off-resonance (hν=777 eV) valence band photoemission spectra of $Zn_{0.95}Co_{0.05}O$: (a) sample *S1* and (c) sample S2. The corresponding difference spectra for sample *S1* as well as for sample *S2* are shown in (b) and (d), respectively. Here, the intensities of the off-resonance spectra at 7.5 eV were normalized to those of the on-resonance spectra. Both difference curves are almost identical with a sharp peak at about 3.5 eV of BE which is in good agreement with previous studies [4,5]. This results show that in ferromagnetic as well as in paramagnetic Co-doped ZnO samples the Co 3*d* states are located near the top of the valence band.

Concluding, in both ferromagnetic (*S1*) and paramagnetic (*S2*) samples Co ions are divalent (Co^{2+}) and are tetrahedrlally coordinated by oxygen. Ferromagnetism in the *S1* samples is not due to the charge carriers as no photoemission intensity was observed at E_F. The origin of different magnetic behaviors of the samples (*S1* and *S2*) can be due to ZnO lattice distortion or defects as well as variations of local Co concentration leading to Co-rich phases.

This work was supported by SFB 513. The authors (M. F. and E. B.) would like to thank BESSY II for financial support.

1. H. Ohno, Science **281**, 951 (1998).
2. T. Dietl, H. Ohno, F. Matsukura, J. Cibert, and D. Ferrand, Science **287**, 1019 (2000).
3. J. M. D. Coey, M. Venkatesan, and C. B. Fitzgerald, Nature Mater. **4**, 173 (2005).
4. S. C. Wi *et al.*, J. Appl. Phys. **84**, 4233 (2004).
5. M. Kobayashi *et al.*, Phys. Rev. B **72**, 201201(R) (2005).

Electronic structure of organic thin films on metal surface: NTCDA/Ag(111)

Azzedine Bendounan, Frank Forster, Achim Schöll, David Batchelor,
Eberhard Umbach, and Friedrich Reinert

Experimentelle Physik II, Universität Würzburg
Am Hubland, D-97074 Würzburg, Germany

Today many electronic devices contain organic components such as organic light emitting diodes (OLEDs) and organic field electronic transistor (OFETs). Particularly, large conjugated planar aromatic molecules are well suited for such applications, because they present intermolecular π-bonds in which direction the electron mobility is relatively high. On the other hand, the study of the electronic structure of organic/metal interfaces represents a key point to control and improve the properties of these components.

We report here on a new approach to study the bonding in thin organic films deposited on metal surface by a combination of two experimental techniques: resonant photoelectron spectroscopy (R-PES) and near-edge X-ray adsorption fine structure (NEXAFS) spectroscopy using the high-brilliance third-generation synchrotron beamline UES2-PGM at BESSY. We present a method which enables us to identify the origin of different molecular orbitals observed in the valence band measured by PES with respect to the carbon bondings in the molecule. NEXAFS has particularly been used to determine the molecular orientation, i.e., substantial spectroscopic changes are observed depending whether the molecules are oriented parallel or upright to the substrate surface [1]. Photoemission spectroscopy has also been applied to investigate the electronic properties, e.g., the electron-vibron coupling [2,3].

As an ideal model system to explore the possibilities of this method, we have chosen one monolayer of 1,4,5,8-naphthalene tetra-carboxylicacid dianhydride (NTCDA) on Ag(111), since it has already been studied well by NEXAFS and PES. The NTCDA films were evaporated *in situ* by organic molecular beam deposition from a Knudsen cell on clean Ag(111) substrate. The monolayer can easily be obtained by deposition of a thick film followed by a subsequent desorption of the multilayers upon annealing at about 385 K. At this temperature only the first monolayer remains adsorbed on the metal, due to the strong bonding at the interface. This bonding forces the molecules also to adopt a parallel and flat orientation along the Ag(111) substrate [1].

In Fig.1, we present resonant photoemission data on 1 ML NTCDA on Ag(111) measured with *p*-polarized synchrotron light. Panel (a) displays the PES intensity map, where the photon energy was tuned through the Carbon K-edge. This intensity map is dominated by the features between E_B=3.8 eV and 8 eV, which correspond to the d-bands of Ag. In the region with lower binding energy between the Ag d-bands and the Fermi level, two spectroscopic structures are observed. The intensity of these two structures strongly depends on the photon energy as it is clearly observed in the energy distribution curves (EDCs) (panel b). The structure indicated by IV at E_B=2.6 eV represents the highest occupied molecular orbital (HOMO). The second structure indicated by III appears at higher energy E_B=3.5 eV and is assigned as HOMO-1.

A variation of the photon energy induces characterising changes in the photoelectron intensity. As illustrated in panel (c), scans at constant binding energy (constant initial state (CIS) spectra), and the NEXAFS spectrum show the presence of four pronounced resonance features. The resonances marked by (C) and (D) in the CIS spectra were assigned to the excitations of C-1s electrons of the naphthalene core of the molecule to different unoccupied molecular orbitals [3], whereas resonances (A) and (B) are associated mainly to the excitation of the carbon in the anhydride groups [1].

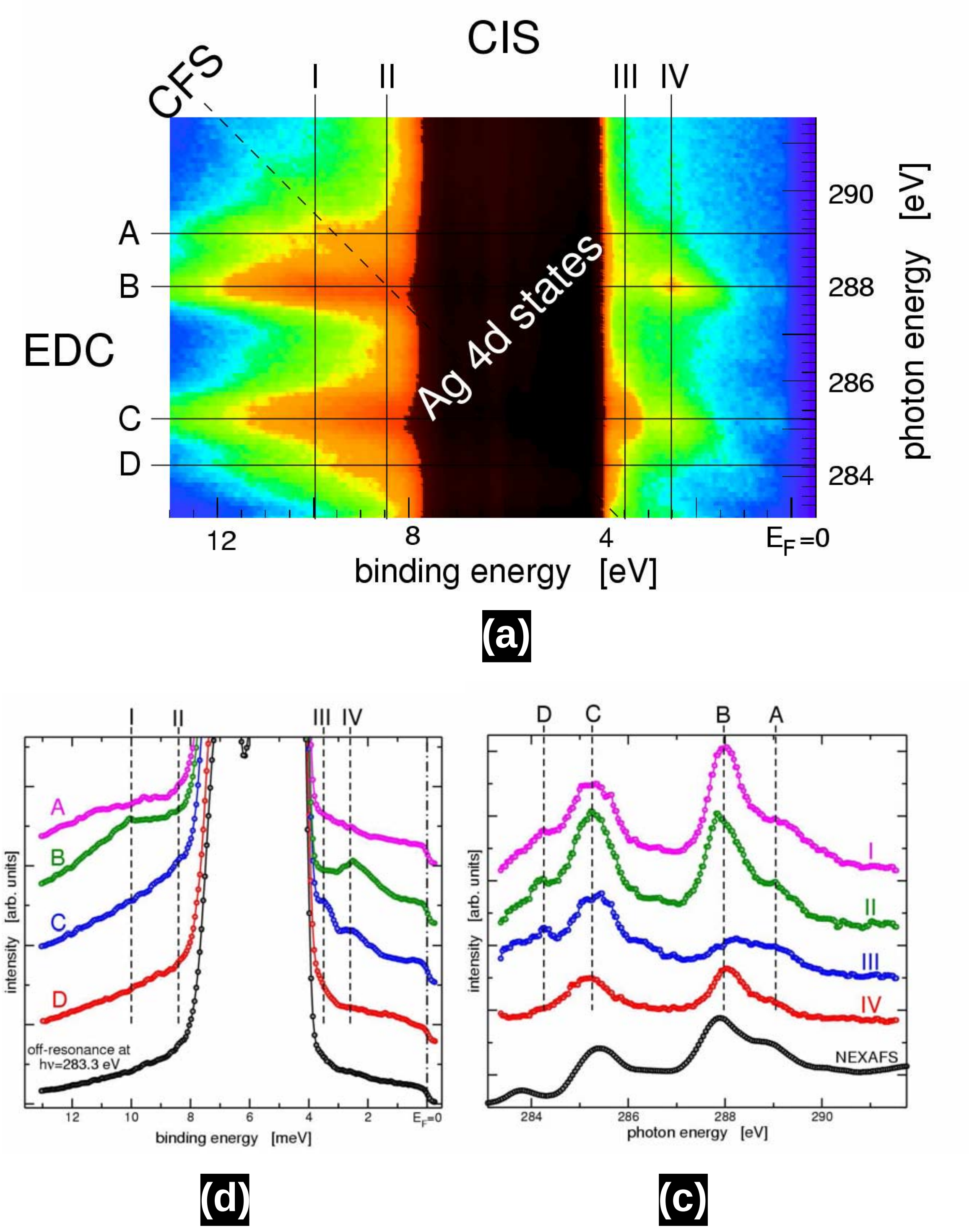

Fig.1: *Resonant photoemission data on 1 ML NTCDA on Ag(111) measured with p-polarized light. Panel (a) gives the photoelectron intensity versus photon energy and binding energy. Panel (b) displays energy distribution curves (EDC) obtained at the photon energy corresponding to on-resonance and off-resonance of the NTCDA molecule. Panel (c) shows constant initial state (CIS) spectra obtained at different binding energy together with a NEXAFS spectrum.*

A comparison of the EDCs with the CIS data, we can assign the molecular orbital peaks observed in the photoemission spectrum to which bonding within the molecule are origin. At a photon energy corresponding to the C1s adsorption resonance of the naphthalene core, the HOMO-1 structure in the EDC spectrum shows high intensity compared to the HOMO. The opposite behaviour is obtained at a photon energy corresponding to the C1s adsorption of the anhydride group. This indicates that the HOMO-1 is due to the carbon bonding of the naphthalene core whereas the HOMO peak seems to be from the carbon bonding of the anhydride group of the molecule. This interpretation is consistent also with the evolution of the spectroscopic structures labelled I and II in Fig. 1, which appear, as the HOMO peak, with high intensity at photon energy corresponding to C1s resonance of the anhydride groups. Additionally, we observe in Fig.1, another structure with binding energy varying linearly with the photon energy. This structure, which has a constant kinetic energy, is described as a constant final state (indicated by CFS in the intensity map of Fig.1).

Acknowledgments:
We would like to thank BESSY staff for the helpful support.

References:

[1]: D. Gador, C. Buchberger, R. Fink, and E. Umbach, Europhys. Lett. **41**, (1998), 231.
[2]: A. Schöll, Y. Zou, D. Hübner, Th. Schmidt, R. Fink, and E. Umbach, BESSY – Highlights (2001), 14-15.
[3]: A. Schöll, Y. Zou, L. Kilian, D. Hübner, D. Gador, C. Jung, S. G. Urquhart, Th. Schmidt, R. Fink, and E. Umbach, Phys. Rev. Lett. 93, (2004), 146406.

Electronic structure of filled and intercalated single wall carbon nanotubes

**T. Pichler[1], H. Shiozawa[1], H. Rauf[1], M. Knupfer[1], M. Kalbac[1], S. Yang[1]
L. Dunsch[1], B. Büchner[1], D. Batchelor[2], and H. Kataura[3]**

[1] *IFW-Dresden, P.O. Box 270116, D-01171 Dresden, Germany*
[2] *Universität Würzburg, BESSY II, Albert-Einstein-Straße 15 D-12489 Berlin, Germany*
[3] *Nanotechnology Research Institute, AIST, Tsukuba 305-8562, Japan*

In the recent years the functionalization of single-wall carbon nanotubes (SWCNTs) via intercalation of atoms and filling of the molecules was in the focus of research on molecular nanostructures since it gives rise to fascinating electronic properties as a consequence of the charge transfer and orbital hybridisation within the quasi-one-dimensional nanospaces. For instance, alkali metal intercalation is a rout for modifying the electronic property of the SWCNTs via electron doping [1,2]. Fullerene-filled SWCNTs, known as peapods, is also being of great interest because of their unique structural and electronic properties [3,4], as well as potential application for the nanoscale devices. Specifically, the endohedral fullerene peapods are though to have a great potential to functionalize single-wall carbon nanotubes in a controlled manner because of a variety of the endohedral species in contrast to empty fullerenes [5]. Especially, high-energy spectroscopy such as x-ray absorption and photoemission has been shown to be a very useful tool to investigate the element- and site-selective electronic structures of the endohedral fullerenes and their peapods since it offers a direct probe of the valency of the encaged metal ions in the endohedrals. Recent photoemission, x-ray absorption and electron energy-loss spectroscopic studies on endohedrals have given great contributions to the understanding of a nature of the endohedrals [6-11].

In this project we have performed high-energy spectroscopy using synchrotron radiation to explore the advanced electronic structures of endohedral fullerenes, as well as functionalized single-wall carbon nanotubes. In-situ functionalization of SWCNTs was carried out via potassium intercalation and filling with the endohedral fullerenes $Dy_3N@C_{80}$(I), a recently synthesized novel trimetal nitride fullerene [12]. The influence of the one-dimensional environment on the electronic structure of encaged endohedrals as well as the impact of the fullerene accommodation on the electronic properties of the carbon nanotubes were investigated in comparison to the electronic structure of the pristine endofullerenes using high-resolution x-ray absorption and photoemission spectroscopy as probe.

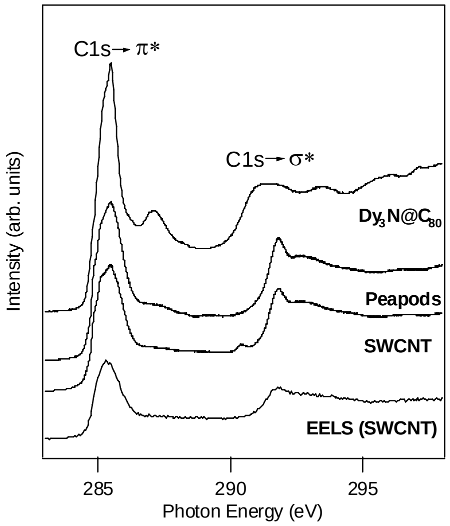

Fig. 1. C1s absorption spectrum of SWCNTs, $Dy_3N@C_{80}$ and the endohedral peapod together with electron energy loss spectrum (EELS) of SWCNTs.

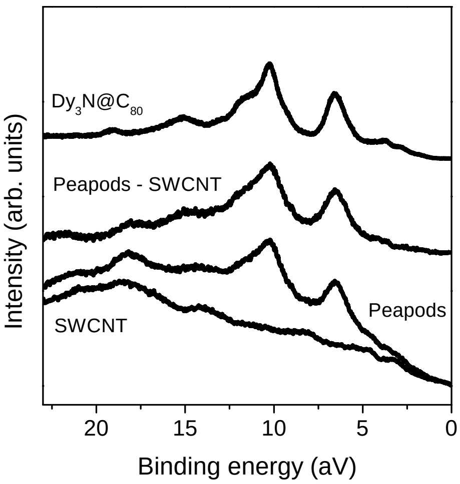

Fig. 2. Photoemission spectra of $Dy_3N@C_{80}$, SWCNTs and their peapods measured at 400 eV photon energy. The difference spectrum between the peapods and $Dy_3N@C_{80}$ is also plotted.

The photoemission experiment was carried out at CRG BUF beamline UE 52 PGM, BESSY II, using a hemispherical photoemission electron energy analyser, SCIENTA SES 200. The x-ray absorption spectrum was obtained by measuring the drain current of the sample. The experimental resolution and Fermi energy were determined from the Fermi edge of a clean Au film. All spectra were recorded with an overall energy resolution better than 50 meV. The base pressure in the experimental setup was kept below 3 x 10^{-10} mbar.

From high-resolution (better than 30 meV) absorption spectroscopy on pristine SWCNTs at C1s excitation edge, we have successfully observed a fine structure in the unoccupied SWCNT desnsity of states. This is complementary to the results of our previous lab based photoemission and electron energy-loss spectroscopic results conducted at the IFW-Dresden [1-3]. In addition, high-energy valence-band photoemission spectroscopy was used to investigate the metal valency of trimetal nitride fullerene $Dy_3N@C_{80}$. The valence-band photoemission spectrum measured at 400 eV photon energy clearly shows the trivalent Dy 4f multiples as main structures and weak divalent Dy multiplets in lower energy side as shown in Fig. 2. The spectral shapes are in good agreement with those observed in x-ray photoemission using Al K_α radiation [11], and points to the intermediate valency of Dy in the fullerene cage. A comparison of the $Dy_3N@C_{80}$ spectrum with atomic calculations estimates the effective valency of Dy ions inside fullerene cage to be 2.9. This value is much bigger than 2.4 of Sc in $Sc_3N@C_{80}$, but slightly smaller than 2.9 of Tm in $Tm_3N@C_{80}$. Considering the Lanthanide contraction from Dy to Tm and the Sc 3d orbitals much delocalised compared to the rare-earth 4f orbitals, we found that the effective metal valency in the endohedrals depends on the size of the metal ions as well as the orbital overlap between the metals and the fullerene cage.

As a next step, $Dy_3N@C_{80}$ was encapsulated in the SWCNT. The filling factor and possible changes of the cluster molecular electronic properties were analysed using x-ray absorption spectroscopy as well as high-energy and resonance photoemission spectroscopy [5]. The C1s absorption spectrum of the endohedral fullerene peapods is similar to that of the SWCNTs. The vHs peaks are observed at the same energies as those of the SWCNTs. As observed in Fig. 2, the high-energy valence-band photoemission spectrum of the endohedral fullerene peapods exhibits prominent structures corresponding to the trivalent Dy 4f multiples in contrast to the broad spectrum of the pristine SWCNT. The Dy 4f spectrum derived by subtracting the SWCNT spectrum from the $Dy_3N@C_{80}$ peapods spectrum also exhibits trivalent Dy 4f character. A more detailed analysis of the Dy valency in the peapods is given by the resonance photoemission study across Dy 4d-4f edge. Figure 3 shows the Dy 4f spectra extracted from the resonance photoemission spectra of the endohedral fullerene peapods and SWCNT. The photon energies of on-resonance (161 eV) and off-resonance (149 eV) were determined from the x-ray absorption spectrum across Dy 4d-4f edge as plotted in the inset of Fig. 3. The x-ray absorption spectrum shows the trivalent Dy multiplets similar to those of Dy metal. The Dy 4f spectrum is very well reproduced with the photoemission multiplets of the trivalent Dy 4f states. The divalent Dy multiples have almost no contribution to the spectrum. This fact demonstrates the Dy valency to be close to 3.0. Compared to the Dy valency of 2.9 in the pristine $Dy_3N@C_{80}$, the fact might indicate the charge transfer from the SWCNT to the

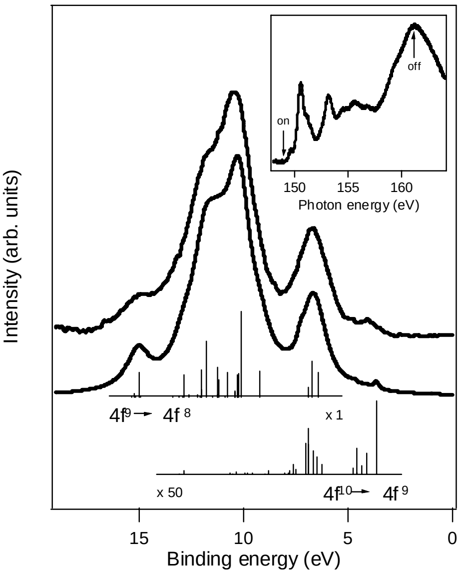

Fig. 3. Dy 4f spectrum (above) and calculated spectrum (below) together with the photoemission multiplets (vertical bars). The inset shows x-ray absorption spectrum of the peapods. The arrows indicate the on-resonance and off resonance photon energies.

endohedral fullerenes within the endohedral fullerene peapod.

To summarize, we demonstrated that a combination of high-resolution photoemission and x-ray absorption across the resonance edges of the composite elements is feasible to analyse the partial electronic structures of the Dy_3N cluster and carbon cages, as well as to estimate the filling factor of the endohedral fullerene peapods. This methodology for determination of the filling ratio and investigation of the partial electronic structures can be applied generally to characterize such molecular nanostructures composed of different molecules and atoms, and to testify the principle of low-dimensional physical properties within such carbon nanostructures.

References

[1] T. Pichler, X. Liu, M. Knupfer, and J. Fink, New Journal of Physics **5**, 156 (2003).

[2] H. Rauf, T. Pichler, M. Knupfer, J. Fink, and H. Kataura, Phys. Rev. Lett. **93**, 096805 (2004).

[3] H. Rauf, H. Shiozawa, T. Pichler, M. Knupfer, B. Büchner, and H. Kataura, Phys. Rev. B **72,** 245411 (2005).

[4] H. Shiozawa, H. Ishii, H. Kihara, N. Sasaki, S. Nakamura, T. Yoshida, Y. Takayama, T. Miyahara, S. Suzuki, Y. Achiba T. Kodama, M. Higashiguchi, X. Y. Chi, M. Nakatake, K. Shimada, H. Namatame, M. Taniguchi, and H. Kataura, Phys. Rev. B **73,** 075406 (2006).

[5] H. Shiozawa, H. Rauf, T. Pichler, M. Knupfer, M. Kalbac, S. Yang, L. Dunsch, B. Büchner, and D. Batchelor, submitted to Phys. Rev. B.

[6] T. Pichler, M. S. Golden, M. Knupfer, J. Fink, U. Kirbach, P. Kuran, and L. Dunsch, Phys. Rev. Lett. **79**, 3026 (1997).

[7] L. Alvarez, T. Pichler, P. Georgi, T. Schwieger, H. Peisert, L. Dunsch, Z. Hu, M. Knupfer, J. Fink, P. Bressler, M. Mast, and M. S. Golden, Phys. Rev. B **66**, 035107 (2002).

[8] T. Pichler, Z. Hu, C. Grazioli, S. Legner, M. Knupfer, M. S. Golden, J. Fink, F. M. F. de Groot, M. R. C. Hunt, P. Rudolf, R. Follath, Ch. Jung, L. Kjeldgaard, P. Br\"uhwiler, M. Inakuma, and H. Shinohara, Phys. Rev. B **62**, 13 196 (2000).

[9] X. Liu, M. Krause, J. Wong, T. Pichler, L. Dunsch, and M. Knupfer, Phys. Rev. B **72**, 085407 (2005).

[10] M. Krause, X. Liu, J. Wong, T. Pichler, M. Knupfer, and L. Dunsch, J. Phys. Chem. A **109**, 7088 (2005).

[11] H. Shiozawa, H. Rauf, T. Pichler, D. Grimm, X. Liu, M. Knupfer, M. Kalbac, S. Yang, L. Dunsch, B. Büchner, and D. Batchelor, Phys. Rev. B **72,** 195409 (2005).

[12] S. Yang and L. Dunsch, J. Phys. Chem. B **109**, 12320 (2005).

Electronic structure of ultrathin MnO films in comparison to MnO bulk samples studied by soft x-ray emission spectroscopy and x-ray absorption spectroscopy

M. Nagel, L. Zhang, H. Peisert, T. Chassé

Institut für Physikalische und Theoretische Chemie, Universität Tübingen,
Auf der Morgenstelle 8, 72076 Tübingen, Germany

Recently it was discussed that ultrathin oxide films on metals may have unique physical-chemical properties due to the mutual interactions between the oxide and the metal such as image potential screening and hybridizational effects [1]. In ultrathin films, the Coulomb interaction U and the anion charge transfer energy Δ may change significantly compared to the corresponding bulk value. Using the MgO/Ag(100) interface as a model system, it was demonstrated that Coulomb and charge-transfer energies in oxide layers deposited on a highly polarizable medium like a metal, are reduced from their bulk values, by as much as 1.8 eV and 2.5 eV, respectively [1]. The properties of non-correlated oxides are mainly determined by electron delocalisation and hybridizational effects. In this report we study the electronic properties of the strongly correlated MnO on Ag(100).

XAS and XES measurements were carried out at the U41 PGM beamline using ROSA endstation equipped with a SCIENTA XES 300 spectrometer and EA10 hemispherical analyser. The absorption was monitored by measuring the total electron yield. The raw data are corrected by the energy-dependent photon flux. Additional XPS reference measurements were performed with a Phoibos 100-MCD 5 analyzer (SPECS GmbH, Germany) and a Mg K_α x-ray source. The MnO thin film was prepared by sputtering and annealing of a 45 Å thick Mn_3O_4 film. The sputtering by argon ions causes a reduction of Mn_3O_4 whereas the subsequent annealing to 400°C produces stoichiometric MnO thin films. The estimated film thickness deduced from photoemission peak intensities was about 6 Å. Additional experiments in the lab applying the same preparation procedure have shown, that the annealing leads to an island formation combined with a relaxed MnO lattice (see also [2]). The island formation was proved by LEED and by XPS signal intensities.

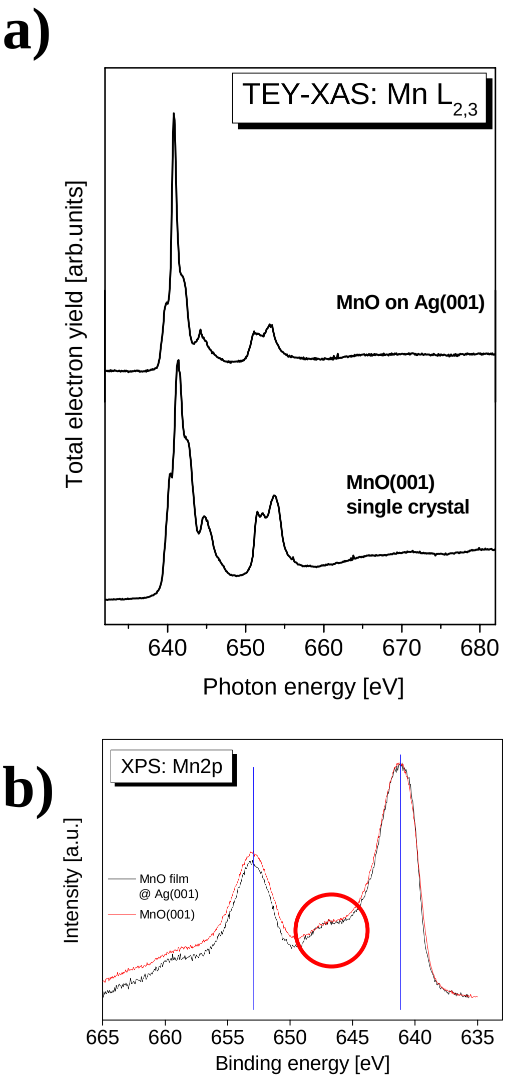

Fig. 1 Characterization of the prepared MnO monolayer: The oxidation state was checked a) by the shape of the XAS spectra and b) by the satellite structures in Mn 2p XPS spectra.

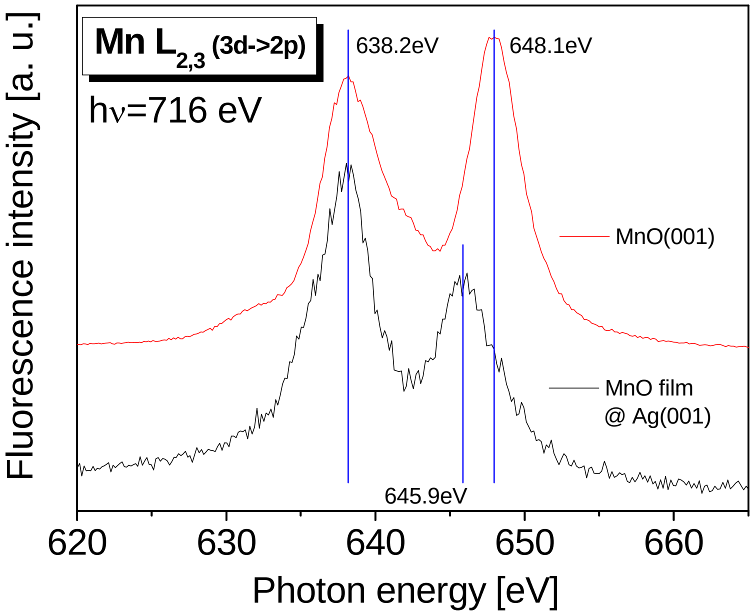

Fig. 2 Comparison of Mn $L_{2,3}$ emission spectra.
black: 6 Å MnO on Ag(001) (film)
red: MnO(001) single crystal (bulk). The different distance of both components is due to interfacial phenomena discussed in the text.

In Figure 1 we show XAS and XPS spectra of the prepared 6 Å MnO film. The Mn 2p absorption spectra are very similar for the single crystal and for the thin film all main features are present in both spectra. XAS is very useful for the identification of Mn species, since spectra for other oxidation states are clearly different [3]. An additional suitable tool for the analysis of the Mn oxidation state is the satellite structure and the spin-orbit coupling of the Mn 2p XPS spectrum. Since satellites are absent for Mn_2O_3 and for Mn_3O_4, the observed features at 645 eV and 650 eV (Fig. 1b) point clearly to MnO in each case. The preparation and characterisation of ordered MnO films is described in detail in Ref. [4].

In Fig. 2 we compare Mn $L_{2,3}$ emission spectra for the thin film and for the bulk (MnO(001) single crystal). The Mn $L_{2,3}$ emission consists of the to main peaks L_3 and L_2 separated by the spin-orbit coupling. According to the dipole selection rules ($\Delta l = \pm 1$ and $\Delta j = 0$ bzw. ± 1), the L_3 peak incorporates two main contributions, namely the transitions $3d_{5/2} \rightarrow 2p_{3/2}$ (higher photon energy) and $3d_{3/2} \rightarrow 2p_{3/2}$ (lower photon energy), whereas the L_2 peak is only the $3d_{3/2} \rightarrow 2p_{1/2}$ transition. In addition, contributions from 4s → 2p can be expected, however the intensity of these transitions is very weak [5].

Beside intensity variations possibly caused by a different ability for self-absorption and fluorescence with increasing film thickness, we observe clearly a change of the energetic position in the spectra, in particular the distance between the main components is decreased significantly by 2.2 eV for the 6 Å MnO film on Ag(001) compared to bulk MnO. In general, different reasons for this observation are possible which will be discussed in turn below:

- The oxidation state of an element changes the size of the spin orbit coupling which affects directly the energy of x-ray emission lines. As discussed above, the composition was checked by XPS and XAS, therefore this explanation can be ruled out.
- An effect of the geometric structure can be expected which affects the position of energetic levels. For instance, for very small particle sizes a splitting of electronic levels may occur. Furthermore, the small shoulder on the low photon energy side of the thin film XES spectrum may suggest the occurrence of two different species. The octahedral ligand symmetry for manganese atoms in MnO is reduced at the surface. Consequently a contribution of such species to the spectrum should be enhanced in ultrathin films. Alternatively an interface strain leading to a tetragonal distortion of the first layers could

explain additional contributions. As drastic changes are not observed in Mn2p XPS or in XAS spectra such explanations seem unlikely.
- The spin-orbit splitting of Mn 2p may be different for the thin film and for the bulk. This can be also ruled out, since no differences were observed in the corresponding XPS spectra.
- The energetic position of the Mn 3d valence states may be different for the thin film and for the bulk. Compared to Mn 2p the measurement of the Mn 3d levels in XPS is more complicated. In the thin film system the corresponding features overlap with the intense substrate Ag 4d features as well as with O 2p contributions from the film itself. Measurements of valence band difference spectra were carried out in the lab but the results were not unambiguous. But changes of this feature may explain the observed results.

In particular at interfaces, the Mn 3d levels can be affected by different mechanisms. First of all, the Mn 3d shell of Mn^{2+} is only half occupied, together with the influence of the oxygen ligands this results in a rich multiplett structure of the spectra. In interface systems the Coulomb interaction U and the anion charge transfer energy Δ may change significantly compared to the corresponding bulk value (see above). Close to the metal surface, the creation of a positive (negative) charge is accompanied effectively by the simultaneous creation of a negative (positive) image charge in the metal, so that the ionisation energy (IE) is reduced and the electron affinity (EA) increased each by the image charge energy (E_{image}), and consequently U is reduced by $2*E_{image}$ [1]. A similar behaviour is expected for Δ, i.e. the charge transfer energy from O2p to a metal cation (Mn 3d). The evaluation of valence band spectra of bulk MnO shows a similar contribution of d^4 and $d^5\underline{L}$ final states [6]. Consequently a change in the charge transfer energy Δ in a thin film on a metal substrate as discussed above should alter the photoemission spectrum of the valence band. The Mn $L_{2,3}$ XES spectrum represents the same final state as the manganese contribution to the valence band XPS. Therefore a change in Δ should be clearly seen in the XES spectrum, too.

In addition, hybridizational effects between orbitals of the substrate and the oxide affect the electronic structure of transition metal oxides at metal surfaces [1]. A hybridisation of O 2p with the Ag4d / Ag 5sp band may affect indirectly the Mn 3d levels.

In summary, we have shown that the properties of correlated oxides can be altered at interfaces to a highly polarizable medium. For valuable discussions and technical assistance we thank R. Szargan, D. Wett, Ch. Jung and W. Neu. The financial support from BESSY is gratefully acknowledged.

[1] **a)** S. Altieri, L. H. Tjeng, G. A. Sawatzky, Thin Solid Films **400** (2001) 9. **b)** S. Altieri L. H. Tjeng, F. C. Voogt, T. Hibma, G. A. Sawatzky,, Phys. Rev. B **59** (1999) R2517.

[2] F. Müller, R. de Masi, D. Reinicke, P. Steiner, S. Hüfner and K. Stöwe, Surf. Sci. 520 (2002) 158.

[3] B. Gilbert, B. H. Frazer, A. Belz, P. G. Conrad, K. H. Nealson, D. Haskel, J. C. Lang, G. Srajer, and G. De Stasio, J. Phys. Chem. A **107** (2003) 2839-2847.

[4] M. Nagel, L. Zhang, H. Peisert, T. Chassé, microchimica acta (submitted).

[5] J.A. Bearden, Rev. Mod. Phys. 39 (1967) 78-124.

[6] F. Parmigiani, L. Sangaletti, J. Electron. Spectrosc. Relat. Phenom. **98–99** (1999) 287–302.

Self-Organized Nanostructure on Si(111): Accumulation Layer on a Step Bunched Surface

K. Skorupska, M. Lublow, M. Kanis, H. Jungblut, H. J. Lewerenz
Division of Solar Energy, Interface Engineering Group, Hahn- Meitner.Institut,
Glienicker Str. 100, 14109 Berlin, Germany

Wet chemical treatments with alkaline solutions are of central importance for miniaturization on the nanometre scale. Despite widespread use of alkaline etching, several aspects of silicon dissolution are still not fully understood. Detailed knowledge of (electro)chemical dissolution steps in combination with a refined control of the (electro)chemical parameters can provide new strategies for directed nanostructuring.

We report here on nanostructure formation and a free standing accumulation layer on n-Si(111) after cathodic polarization in 2M NaOH thus forming a two-dimensional electron gas (2DEG). 2DEGs are of considerable interest for basic research (Quantum Hall effect) and applications, e.g., high electron mobility transistors.

Experiments were done at SoLiAs, the combined chemistry/ultra high vacuum (UHV) analysis system, were synchrotron radiation photoelectron spectroscopy (SRPES) at the U49/2 beamline at Bessy II was performed.

Electrochemical experiments were done in an N_2 atmosphere-purged three-electrode system, directly attached to the UHV apparatus [1] thus protecting samples from ambient air contamination.

Wet chemically H-terminated specimen were inserted via a load lock into the UHV apparatus and then (using the internal sample transport path system) placed in the glass sphere, where electrochemistry was performed, from the machine side. Electrochemical conditioning was done using an electrolyte drop, applied by the capillary with reference electrode. Electrical contact is obtained by lowering the Pt cylinder working electrode towards the electrolyte drop. For fast interruption of the electrochemical processing, this drop was blown off by an N_2 jet; subsequently, samples were rinsed in deionized water, dried in N_2 and transferred into the UHV system for out-gassing and SRPES measurements.

Float Zone n-Si(111) with specific resistivity 5 Ωcm and 0^o nominal miscut served as working electrode, Ag^+ / AgCl was used as references electrode, a Pt cylinder was used as counter electrode. Connections were made to an EG&G 326 potentiostat.

All electrolytes are prepared from ultrapure chemicals, dissolved in deionized water (18 Ωcm), and purged with nitrogen (5.0). The pH of solutions is controlled with a calibrated pH-meter and ultrapure H_2SO_4.

Electrochemical H-termination comprises oxidation in potassium hydrogen phthalate solution under illumination and potentiostatic etching in dilute ammonium fluoride solution of pH=4.0 and pH=4.9 respectively.

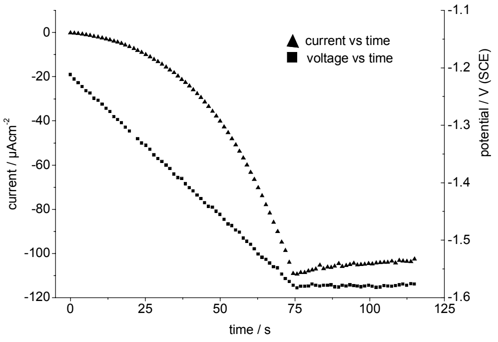

Fig.1 Dark current and applied potential vs. time for n-Si(111) in 2M NaOH. Scan velocity 5mVs^{-1}, open-circuit potential -1.2 V (SCE).

Figure 1 shows electrochemical conditioning in 2M NaOH (experiment was performed in the dark). The potential has been altered from OCP until a current of - 100 µA is obtained; at this stage the potential is held for 40s.

In this specifically designed experiment, the competition between chemical etching and electrochemical reactions, both of them appearing at silicon kink side atoms at Si(111) (1x1):H can be studied. Figure 2 shows the reaction schemes for chemical and electrochemical processes [2]. For the chemical reaction route, two possible sites for hydrolysis can be identified: the Si-Si back bond or the Si-H dangling bond. All reaction paths, however, lead to dissolution of the kink side atom that leaves the Si surface with underlying H-termination. The electrochemical reaction consumes two electrons from the valence band leading, through formation of a radical and hydrogen evolution, to the initial surface state. No silicon atom is dissolved in this process.

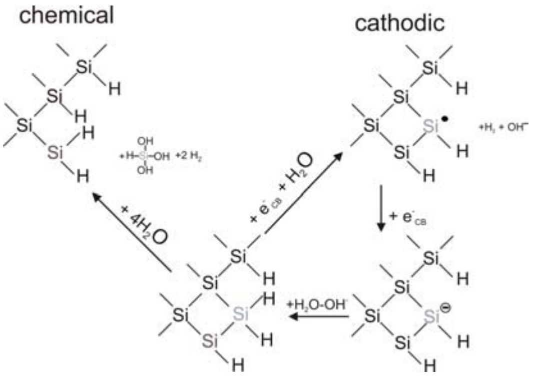

Fig.2 Representation of chemical and cathodic electrochemical reaction paths in alkaline solution in the dark; after refs. [3,4]

SRPES experiments were made for two surface sensitivities for the Si 2p core level (Fig.3): excitation energies of hν=150 eV and hν=585 eV, corresponding to λ_{esc} = 4 and 15 Å escape depth, respectively, were used. For deconvolution, a Shirley-type background has been subtracted and Lorenz- Gaussian lines have been applied. Five components are found: a dominant silicon bulk signal at 99.7 eV and signals shifted by -0.3, 0.2, 0.5 and 0.8 eV with regard to the bulk line. Their intensity decreases with increasing escape depth, but the ratio between them remains unaltered for both photon energies.

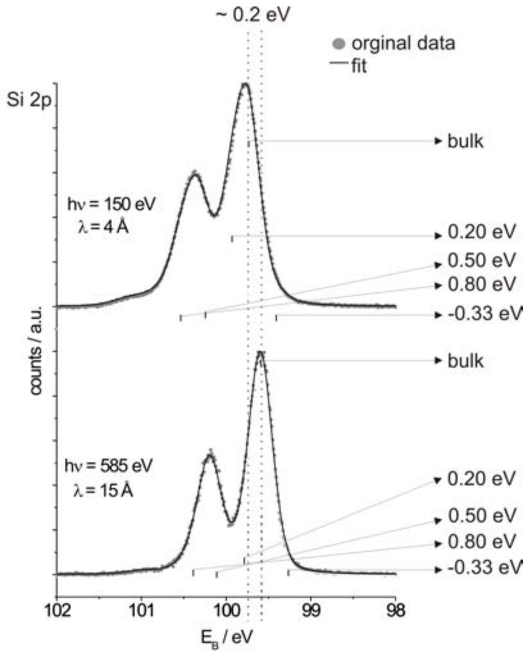

Fig.3 Si 2p lines obtained by SRPES on n-Si(111) for excitation energies of 150 and 585 eV.

The contribution shifted by 0.2 eV is attributed to silicon bonded to one hydrogen atom (≡Si-H) on (1x1):H-terminated Si(111) [5]. Smaller peaks (0.5 and 0.8 eV) are attributed to =Si-H_2 and =Si-H-OH [6,7] respectively.

The presence of silicon atoms bonded to H and to an OH group suggests that in the reaction sequence, a nucleophylic substitution reaction (SN2) takes place where the formation of an activated intermediate is important for chemical etching [2].

Further inspection of the SRPES data reveals a shift of the Si 2p core level of about 0.2 eV towards lower binding energy for higher excitation energy (i.e. lager escape depth). The high surface sensitivity x-ray photoelectron valence band spectrum shows that the energetic position of the valence band w.r.t. the Fermi level is extrapolated to be located at 1.06 eV (data not shown here)[1]. From the band diagram in figure 4 we can learn that an accumulation condition at the surface is responsible for the observed 0.2eV shift in the SRFE spectra. The effective surface electron concentration, n_s=3x10^{18} cm^{-3}, is calculated from the energetic distance of

0.06 eV (~2kT) between Fermi level and conduction band The difference of 0.2 eV in electrostatic potential in the accumulation layer can be calculated according to Thomas-Fermi theory for the two electron escape depths used in our experiment with the calculated surface electron concentration $n_S=10^{18}cm^3$ (data not shown here) [1] showing excellent agreement with the measured SRPES data.

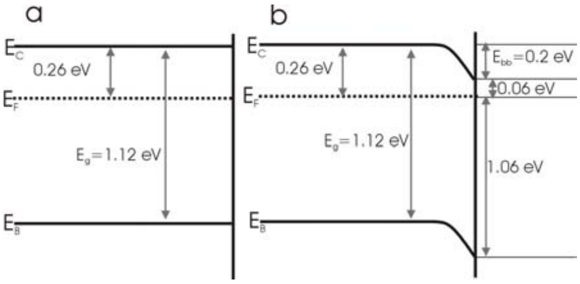

Fig.4 Energy band diagram of n-Si(111) for (a) flat band situation, (b) the electronic surface condition for a step-bunched structure obtained after cathodic polarization in alkaline electrolyte.

For surface nanotopography analysis ex-situ experiments using contact mode atomic force microscope using Si_3N_4 tips were performed. The two images in figure 5 represent a Si(111) H-terminated surface, (top) as starting condition, where atomically flat terraces are visible; their height is a multiple of 3.14 Å which is the height of one BL (bilayer). The bottom part of figure 5 shows the surface after electrochemical experimentation. As can be seen, the Si surface developed step bunching. In the figure, accumulated steps are visible that are about 0.3 µm wide and from 9 to 12 BL high. The phenomenon of step bunching was recently also observed also by others [8] but no indication of a 2DEG was reported.

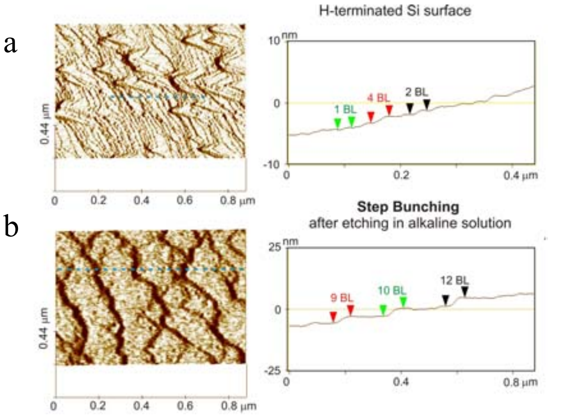

Fig.5 AFM-CM experiment for (a) H-terminated n-Si(111); starting condition and (b) the same surface subjected to electrochemical conditioning as described above.

SRPES data deconvolution showed that almost 30% of surface species are non (111) species. Figure 5 and the dissolution model show that the sample topography is built by the surface of {111} terraces but also by the side walls of bunched steps which are likely made of (100) oriented facets where the non-(111) species are localized.

References:

1. K. Skorupska, M. Lublow, M. Kanis, H. Jungblut, H. J. Lewerenz, Appl. Phys. Lett. **87** (2005) 1.
2. K. Skorupska, M. Lublow, M. Kanis, H. Jungblut, H. J. Lewerenz, Electrochem. Comm. **7** (2005) 1077.
3. P. Allogue, V. Costa-Kieling, H. Gerischer, J. Electrochem. Soc. **140** (1993) 1018.
4. Th. Baum, D.J. Schiffrin, J. Electroanal. Chem. **436** (1997) 239.
5. H. J. Lewerenz, M. Aggour, C. Murrell, J. Jakubowicz, M. Kanis, S. A. Campbell, P.A. Cox, P. Hoffmann, H. Jungblut, D. Schmeißer, J. Electroanal. Chem. **540** (2003) 3.
6. S. R. Sundaram et al., J. App. Phys. **60** (1996) 2530.
7. H. J. Lewerenz, M. Aggour, C. Murrell, M. Kanis, H. Jungblut, J. Jakubowicz, P.A. Cox, S. A. Campbell, P. Hoffmann, D. Schmeißer, J. Electrochem. Soc. **150** (2003) E185.
8. S. P. Garcia, H. Bao, M. Hines, Phys. Rev. Lett. **9** (2004) 166102-1.

A high-resolution NEXAFS investigation of the PEDOT:PSS/pentacene system

M. B. Casu[a], P. Cosseddu[b], D. Batchelor[a], A. Bonfiglio[b], and E. Umbach[a]

[a]Experimentelle Physik II, Universität Würzburg, Am Hubland, D-97074 Würzburg
[b]Dept. of Electrical and Electronic Engineering, University of Cagliari, Piazza d'Armi, I-09123 Cagliari

Organic electronic devices offer an interesting alternative to inorganic semiconductor electronics due to low-cost deposition methods, flexible substrates, and simple packaging [1, 2, 3]. The organic molecules can be vapour deposited under vacuum, spin coated, dip coated or printed on the proper substrate. All these techniques are relevant for low cost electronics. However, the optimisation of the devices requires a strict control of the morphological and electronic properties of the active medium. Thus, studies of the morphology, growth, and structure of organic thin films are the subject of very intense investigations. In addition, the deep knowledge of the substrate/organic interface plays a role of paramount importance also in device applications. A particular class of interfaces is represented by the organic/organic ones. Their knowledge has a strong technological relevance when an organic film, working as active medium in a device, is deposited on a thin film, also organic, working as electrode. Poly(3,4-ethylenedioxythiophene):poly(styrenesulfonate) (PEDOT:PSS) is commonly used as electrode in various organic devices [4], and pentacene is one of the most widely used organic active media due to its physical, chemical and morphological properties. In particular its high mobility and the possibility to grow highly oriented thin films lead to a strong improvement of the device performances [5, 6]. It is easily understandable that the coupling of two such materials, especially toward the realisation of “all plastic” electronics, can be considered an important step in device engineering. In this framework, we improved an organic field effect transistor (OFET) [7], substituting gold with PEDOT/PSS for making the contacts. We have observed a strong improvement of the device performance in the linear part of the I_d-V_d curve. This indicates a lowering of the series resistance effect, one of the most important optimisation parameters at present, since mobilities in organic semiconductors have reached high values. These results demand a better understanding of the interface PEDOT:PSS/pentacene, giving the motivation for the present work.

In this report, we present highly-resolved near-edge x-ray absorption fine structure (NEXAFS) spectroscopy measurements taken on pentacene thin films of different thickness deposited on a spin coated PEDOT:PSS substrate. The main goal of our investigation is focused on the determination of the pentacene molecular orientation. In other words, one of the principal needs is understanding if pentacene can be grown with a certain degree of order also when the substrate is extremely rough and soft like PEDOT:PSS. In addition, the understanding of how the interface PEDOT:PSS/pentacene looks like in terms of morphology is another important aspect.
The measurements were performed at the beamline UE52-PGM at BESSY. This beamline is characterized by a plane grating monochromator. The photon energy ranges from 100 to 1500 eV, with an energy resolving power of $E/\Delta E$= 10500 at 401 eV (c_{ff}=10, 10 μm exit slit). The main chamber (base pressure $2x10^{-10}$ mbar) is equipped with a standard twin anode x-ray source, a SCIENTA SES200 electron energy analyser, and a home-made partial electron yield detector. PEDOT:PSS thin films (~ 50-100 nm) were spin-coated on Si wafers from a commercially available aqueous solution (Baytron P, 1:20). Thin films of pentacene were prepared by organic molecular beam deposition (OMBD) in-situ using strictly controlled evaporation conditions. The deposition (rate: ~3 Å/min) was monitored with a quadrupole mass spectrometer. The nominal thickness was determined by a previously calibrated evaporator and by using the attenuation of the x-ray photoemission (XPS) substrate signal after pentacene deposition on a Ag(111) single crystal. We carried out NEXAFS measurements in the total electron yield (TEY) mode in grazing incidence (60°). In order to investigate the molecular orientation in the films we took advantage of the dependence of the NEXAFS spectra on the polarisation of the incident radiation [8]. Hence, we measured the spectra by using both in plane (p-pol) and out of plane (s-pol) polarised synchrotron radiation, tuning the polarisation by means of the undulator. Finally, the spectra were normalised using the I_0 current and the substrate signal [9]. The energies have been carefully calibrated according to reference 9.

Figure 1 shows the C-K NEXAFS spectra obtained from 84 Å (a), and ~100 ML (b) of pentacene on PEDOT:PSS. The spectra were taken in grazing incidence for p- (black curves) and s- (red curves) polarization. Two main groups of π*-resonances, 1 and 2, dominate the 282-288 eV photon energy range. These features are due to transitions from C1s levels of non-equivalent carbon atoms into the lowest unoccupied molecular orbital (LUMO) and LUMO+1 [10]. It is worth to mention that the energy resolving power of the UE52 beamline gives the opportunity to perform highly-resolved measurements. Thus the spectra exhibit the presence of features that were not resolved in previous works. For example, it is possible to observe the clear presence of two components in feature A (Fig 2), due to contributions from two different carbon sites in the pentacene molecule [10].

The spectral features exhibit a strong polarisation dependence, indicating a high degree of orientational order in the films, and allowing us to determine the molecular orientation from the observed dichroic behaviour [8]. In both cases the molecules adopt an upright standing position of their axis with respect to the substrate. This is clearly seen since the π*-resonances show their strongest intensities for the spectra taken for s-polarisation of the incident radiation (i.e. ***E*** vector parallel to surface). The calculated molecular orientation is 80° for the 84 Å film, while is very close to a perfect upright position for the thicker film. However, from the morphological point of view the two situations are different. While in the case of the 100 ML film the XPS signal from the substrate is not visible, the substrate signal is still clearly visible in the case of the 84 Å. Taking the calculated molecular orientation into account, and assuming that the molecules are standing with their long axis up, 84 Å are equivalent to ~ 5 ML. For this film thickness, the XPS substrate signal should be completely attenuated by the pentacene deposition, when layer-by-layer growth occurred. In our case, the presence of a strong sulphur XPS signal coming from PEDOT: PSS (not shown here) indicates that pentacene follows an island growth mode.

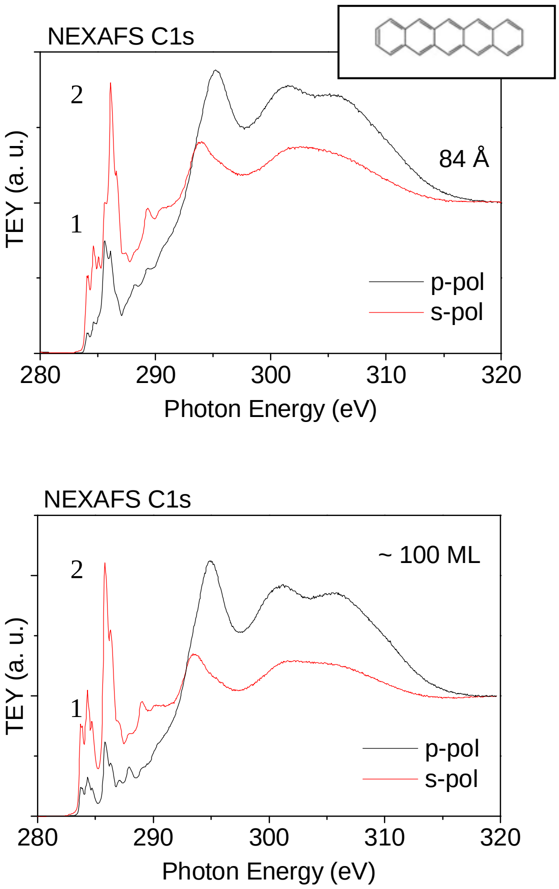

Fig. 1: C1s NEXAFS spectra obtained from 84 Å (a) and 100 ML (b) of pentacene on PEDOT:PSS deposited under different preparation conditions. The spectra were taken in grazing incidence for p- (black curve) and s- (red curve) polarisation.

Comparing the spectra obtained from the two films with different thickness, we can observe a change of the spectral shape and of the ratio of the relative intensities when looking at the two main groups of π*-resonances, 1 and 2. This indicates that pentacene molecules interact with PEDOT:PSS, thus perhaps causing a different short range order and mutual interaction which then changes with thickness.

A point that is still not completely clear regards the possibility that, due to the high PEDOT:PSS roughness, pentacene islands could grow embedded in the matrix formed by PEDOT:PSS at least up to a nominal thickness of around 100 Å. This aspect is important not only for the obvious importance of a basic characterisation of this system, but also because of its technological relevance. As a matter of fact, the device characteristics depend also on the respective charge injection barriers at the interfaces. This can be influenced by the interface morphology in terms of intermixing of the two organic materials. This aspect is still under investigation and requires a careful interpretation of the details characterising the PEDOT:PSS XP spectra as well as the use of complementary techniques like atomic force microscopy to get a picture of the pentacene island distribution.

In summary, our results show that pentacene thin films on PEDOT:PSS are characterised by up-right standing molecules. It worth to point out that the NEXAFS signal is averaged over the area sampled by the incident spot (~50 x 100 μm^2) and that the obtained molecular orientation is an average value. Nevertheless, in the present case, due to the strong dichroic behaviour, the calculated values give a clear indication of the real molecular arrangement in the films and of a high orientational order.

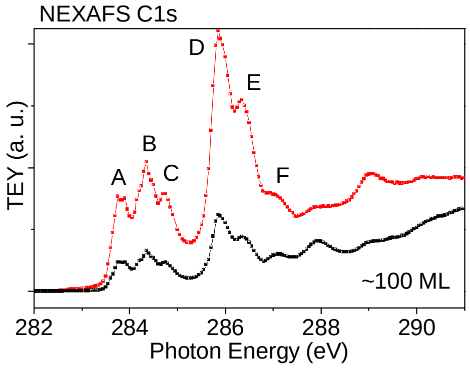

Fig. 2: π*-region enlarged view of the NEXAFS spectra taken for the 100 ML film.

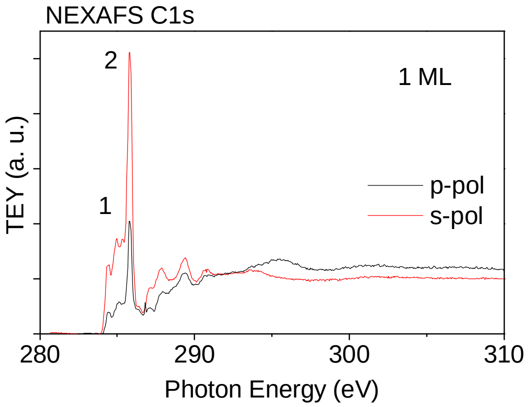

Fig. 3: C1s NEXAFS spectra obtained from a monolayer of pentacene on PEDOT:PSS, taken in grazing incidence for p- (black curve) and s- (red curve) polarisation.

A consequent crucial question is: do the molecules also stand up-right in the first layer? To give an answer we have performed NEXAFS measurements on a pentacene monolayer in order to investigate the molecular orientation of the first pentacene layer when deposited on PEDOT:PSS. The spectra are shown in Fig 3. According to the previous explanation, it is immediately clear that the molecules, also in this case, take a position such that their axis is perpendicular to the substrate. The dichroism is very pronounced indicating once more a high order already at the monolayer level. The calculated molecular orientation is 77°.

This report is only a first step in order to understand the details of the organic/organic PEDOT:PSS/pentacene interface by using synchrotron radiation techniques. Much more experimental and theoretical work needs to be done to answer the demanding open questions.

Acknowledgements

The authors would like to thank the BESSY staff, Dr. Th. Schmidt, Universität Würzburg, and S. Pohl, Fritz-Haber-Institut, Berlin, for the beamline support, Dr. P. Imperia, Hahn-Meitner-Institut, Berlin, for support while measuring at BESSY, and Dr. N. Koch, Humboldt Univestität, Berlin. Financial support by the DFG through the OFET-Schwerpunktprogramm Um 6/8-1 + Um 6/8-2, by the BMBF under contract 05KS4WWC/2, and by the Italian Ministry of Education and Research under the FIRB program is gratefully acknowledged.

References

[1] S. R. Forrest, Nature 428 (2004) 911.
[2] G. Horowitz, J. Mater. Res. 19 (2004) 1946.
[3] J. R. Sheats, J. Mater. Res. 19 (2004) 1974.
[4] M. M. de Kok, M. Buechel, S. I. E. Vulto, P. van de Weijer, E. A. Meulenkamp, S. H. P. M. de Winter, A. J. G. Mank, H. J. M. Vorstenbosch, C. H. L. Weijtens, and V. van Elsbergen, Phys. Stat. Sol. (a) 201 (2004) 1342.
[5] F. Garnier, A. Yassar, R. Hajlaoui, G. Horowitz, F. Dloffre, B. Servet, S. Ries, and P. Alnot, J. Am. Chem. Soc. 115 (1993) 8716.
[6] C. D. Dimitrakopoulos P. R. L. Malefant, Adv. Mater. 14 (2002) 99.
[7] A. Bonfiglio, F. Mameli, and O. Sanna, Appl. Phys. Lett. 82 (2003) 3550.
[8] J. Stöhr and D. A. Outka, Phys. Rev. B 36 (1987) 7891.
[9] A. Schöll, Y. Zou, Th. Schmidt, R. Fink, and E. Umbach, J. Electron. Spectrosc. 129 (2003) 1.
[10] M. Alagia, C. Baldacchini, M. G. Betti, F. Bussolotti, V. Carravetta, U. Ekström, C. Mariani, and S. Stranges, J. Chem. Phys. 122 (2005) 124305.

Conduction band properties of III-nitrides characterized by synchrotron ellipsometry on core level excitations

C. Cobet[1], M. Rakel[1,2], R. Goldhahn[3], and N. Esser[1]

[1] *ISAS- Institute for Analytical Sciences, Department Berlin, Albert-Einstein-Str. 9, D-12489 Berlin*
[2] *Institut für Festkörperphysik, TU Berlin, Hardenbergstr. 36, D-10623 Berlin*
[3] *Inst. f. Physik, Zentrum f. Mikro- und Nanotechnologien, TU Ilmenau, D-98684 Ilmenau*

Group III nitrides such as Ga-, Al- and In-nitride and compounds are a class of semiconductors with one of the highest technological potential today. But in contrast to the recent advances in epitaxial growth and technology, the understanding of fundamental material properties is surprisingly poor. Many questions concerning the electronic band structure are still open. A prominent example is the ongoing discussion about the exact value of the fundamental band gap of InN. A mayor problem for theoretical calculations is the correct treatment of In4d/Ga3d-core electrons, which slightly interact with the nitrogen 2s valence electrons. In GaN this interaction is much weaker than in InN. The s-d-coupling is difficult to handle, because it results also in an additional p-d repulsion effect [2]. This coupling is may be responsible for the very low band gap of InN. The determination of the relative energetic positions between the valence and conduction bands could provide already helpful information [7]. But a complete experimental analysis of electronic transitions (excitations) is mandatory for testing and validating theoretical results. Common methods are either photoemission experiments, which determine e.g. the valence band DOS with respect to the Fermi level, or optical reflection and absorption measurements, which reveal interband electronic transitions in the visible and VUV spectral range.

We use the synchrotron light at BESSY II in order to access the optical properties of GaN and InN in the far VUV spectral range by spectroscopic ellipsometry [4, 11]. This measurement technique is based on the determination of the polarization of light before and after the reflection on the sample surface under a certain angle of incidence. The measured amplitude and phase differences can be translated subsequently into the dielectric function (DF) or the commonly used refractive and absorption coefficient.

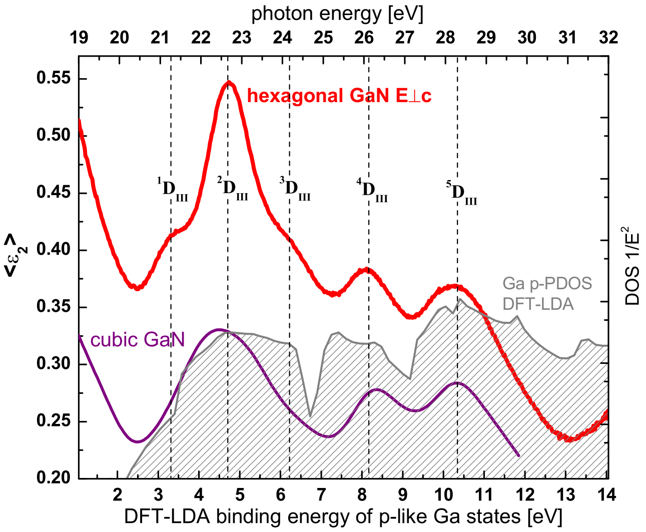

Figure 1: Imaginary part of the measured DF of hexagonal and cubic GaN (solid) in comparison to the calculated PDOS of the p-like empty states around the Ga-atoms (patterned) [10]. The Ga3d transition structures are denoted with $^1D_{III}$ – $^5D_{III}$ according to the notation of Cardona et.al. [3].

Above 18 eV the DF of GaN and InN is dominated by optical transitions between the Ga3d/In4d core states and the p-like unoccupied (conduction) electron bands. Transitions to conduction states with s-character are not allowed due to the dipole selection rules. However, the localized d-states have a sharp binding energy without significant dispersion in the entire Brillouin zone. Thus, these d-levels can be used to explore the site specific density of empty states in a similar manner as known from X-ray absorption on the N1s core level edge [8]. The stable crystal structure of III-nitrides is the hexagonal wurtzite lattice where the hexagonal closed packed III-nitride layers are stacked in an ABAB... sequence. Thus, the electronic and optical properties reveal an extraordinary axis, the c-axis, parallel to the stacking sequence. All other perpendicular directions remain degenerated. The metastable cubic zincblende crystal structure of GaN was successfully stabilized in thin films on appropriate cubic substrates [1]. The electronic as well as optical properties of this cubic material are assumed to be isotropic. However, the integrated density of conduction band states should be almost identical in both crystal structures. This is, in fact, observed in our ellipsometric measurements on a wurtzite and zincblende GaN sample. Figure 1 shows the imaginary part of the DF in the spectral range of Ga3d transitions. The DF is proportional to the number of excited electrons and should directly relate to the partial density of states (PDOS) with dominant p-character in the conduction bands. Both line shapes are almost the same. The lower overall amplitude and the broadening of transition features are related to the lower crystal quality of the cubic sample.

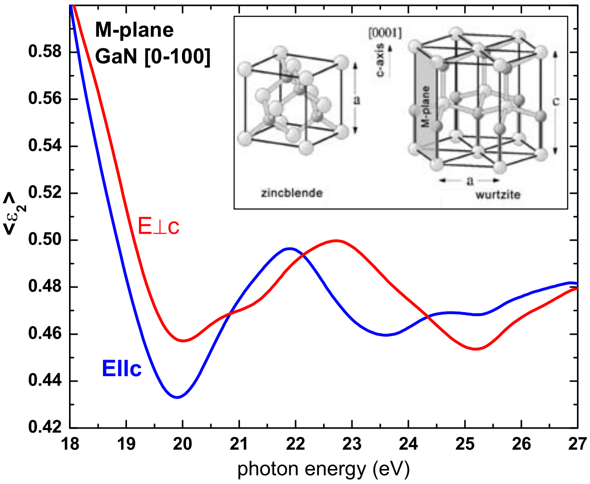

Figure 2: Imaginary part of the ordinary and extraordinary DF of GaN between 18 and 27eV measured on M-plane GaN [1-100].

We compare these measurements in figure 1 also to the calculated PDOS of p-like states on the Ga site (patterned) of cubic GaN. As assumed, the DF is approximately reproduced by the calculated PDOS although excitonic effects as well as k and energy dependent variations of matrix elements could influence the DF. The DF of wurtzite GaN was determined on a c-plane sample, where the c-axis is perpendicularly oriented to the surface. In this orientation we have determined the ordinary DF, which relates to excitations with the electric field vector perpendicular to the c-axis. In order to access also the extraordinary DF we use M-plane GaN [0$\bar{1}$00] sample, where the c-axis lies in the surface plane.

By measuring in the two high symmetry orientations we can determine both dielectric tensor components which are presented in figure 2. According to these measurements we observe a reasonable shift to lower energies and a slightly different line shape of the extraordinary DF while the ordinary component is almost identical to the measurements on the c-plane sample. This shift could be explained by a distortion of the chemical bondings along the c-axis. Polarization effects as well as a charge accumulation at interfaces along the extraordinary crystal axis are already known in III nitrides.

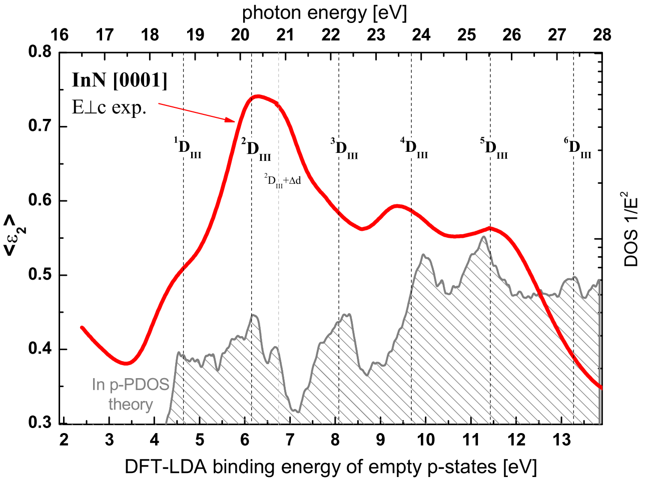

Figure 3: Imaginary part of the measured DF of hexagonal InN (solid) in comparison to the calculated PDOS of the p-like empty states around the In-atoms (patterned) [5]. The In4d transition structures are denoted with $^1D_{III} -^6 D_{III}$. All these valence band characteristic features split up due to a spin orbit splitting of the In4d-states, which is notable e.g. in the $^2D_{III}$ and $^2D_{III} + \Delta d$ structure.

Figure 3 shows a comparison between the imaginary part of the ordinary DF of wurtzite InN and the calculated PDOS of p-like InN conduction band states. Between 16 and 28 eV the DF is again dominated by excitations of In4d core-states. The line shape of the DF and the assumed PDOS are nearly identical to the respective GaN measurements but shifted by about 2 eV to lower energies. This shift correlates to the lower band gap of InN in comparison to GaN. Recent photoemission experiments report a binding energy of the In4d$_{5/2}$ electrons of 17.4±0.1 eV with respect to the valence band maximum [9]. On the other hand, we can determine the onset of In4d transitions to conduction bands at about 18 eV (fig. 3). The comparison of both measurements further support the new results about a InN band gap at 0.68 eV [6].

We gratefully acknowledge the BESSY assistance and the financial support of the BMBF under the contract number 05 KS4KTB/3.

[1] D. J. As, D. Schikora, and K. Lischka. *Phys. Stat. Sol. (c)*, 0(6):1607–1626, 2003.

[2] B. Bouhafs, F. Litimein, Z. Dridi, and P. Ruterana. *Phys. Stat. Sol. (b)*, 236(1):61–81, 2003.

[3] M. Cardona, W. Gudat, E. E. Koch, M. Skibowski, B. Sonntag, and P. Y. Yu. *Phys. Rev. Lett.*, 25(10):659–661, 1970.

[4] N. Esser, M. Rakel, C. Cobet, W. G. Schmidt, W. Braun, and M. Cardona. *phys. stat. sol. (b)*, 242(13):2601–2609, 2005.

[5] F. Fuchs, 2004. Institut für Festkörpertheorie und -optik, Friedrich-Schiller-Universität Jena, Fröbelstieg 1, 07743 Jena, Germany, priv. com.

[6] R. Goldhahn, P. Schley, A. T. Winzer, G. Gobsch, V. Cimalla, O. Ambacher, M. Rakel, C. Cobet, N. Esser, H. Lu, and W. J. Schaff. *phys. stat. sol. (a)*, 203(1):42–49, 2006.

[7] W. R. L. Lambrecht, B. Segall, M. Yoganathan, W. Suttrop, P. Davaty, W. J. Choyke, J. A. Edmond, J. A. Powell, and M. Alouani. *Phys. Rev. B*, 50(15):10722–10726, 1994.

[8] K. Lawniczak-Jablonska, T. Suski, I. Gorczyca, N. E. Christensen, K. E. Attenkofer, R. C. C. Perera, E. M. Gullikson, J. H. Underwood, D. L. Ederer, and Z. Liliental Weber. *Phys. Rev. B*, 61(24):16623– 16632, 2000.

[9] L. F. J. Piper, T. D. Veal, P. H. Jefferson, C. F. McConville, F. Fuchs, J. Furthmüller, F. Bechstedt, Hai Lu, and W. J. Schaff. *Phys. Rev. B*, 72:245319, 2005.

[10] W. G. Schmidt, 2004. Theoretische Physik, Univ. Paderborn, Warburger Str. 100, 33098 Paderborn, Germany, priv. com.

[11] H. G. Tompkins and E. A. Irene. *Handbook of Ellipsometry.* William Andrew Publishing, Norwich, 2005.

Spectroscopy of ordered V_2O_5 and MoO_3 layers on Au(111)

S. Guimond, Y. Romanyshyn, H. Kuhlenbeck, H.-J. Freund
Fritz Haber Institute of the Max Planck Society, Chemical Physics Department
Faradayweg 4-6, 14195 Berlin

This work has been supported by the Deutsche Forschungsgemeinschaft
through its Sonderforschungsbereich 546, 'Transition metal oxide aggregates'

V_2O_5 and MoO_3 are oxidation catalysts which means that they are catalytically active for reactions involving transfer of oxygen. For this reason vanadium oxides as well as molybdenum oxides have been the topic of experimental and theoretical studies. V_2O_5 and MoO_3 can be prepared as small single crystals by chemical transport methods and thanks to their layered structure they can easily be cleaved. However, the fabrication of the crystals is involved and time-consuming, and the handling and cleaving of the small and mechanically sensitive single crystals is not very comfortable. Besides this the crystals are sensitive to beam damage which means that cleavage may be required often which is a problem in view of the small crystal size. These complications may be avoided by the use of thin films. Due to the high oxygen content of the oxides, oxygen pressures are required which are not suitable for UHV systems. Therefore we have used a high pressure cell for the oxidation procedure. Au(111) was chosen as a substrate since gold is insensitive to elevated oxygen pressures. Both types of oxides were prepared by evaporation of a certain amount of the respective metal onto the Au(111) substrate followed by oxidation in the high pressure cell at a pressure of about 50 mbar with the sample held at 400 °C. The vapor pressure of both oxides is rather high already at low temperature so that evaporation during the oxidation process played a role.

LEED patterns are shown in figure 1. The c(4×2) pattern observed after oxidation of 0.5 Å of Mo can not be explained by scattering at regular surfaces of MoO_3. This pattern has also been reported by Biener et al [1]. For V_2O_5 a number of different superstructures is observed at low coverages: a (1.25×3.75) structure, a (1.2×1.2)R30° structure, a structure with an unit cell of 3.6 Å×9 Å, and some intensity due to regular $V_2O_5(001)$. The LEED patterns of the oxide layers obtained after oxidation of a metal layer with a thickness of 5 Å may be explained by assuming that the surface is covered with rotationally disordered $V_2O_5(001)$ and $MoO_3(010)$ crystallites, respectively. The significant background intensity points towards the existence of an appreciable density of defects, which is at least partly due to damage induced by the electron

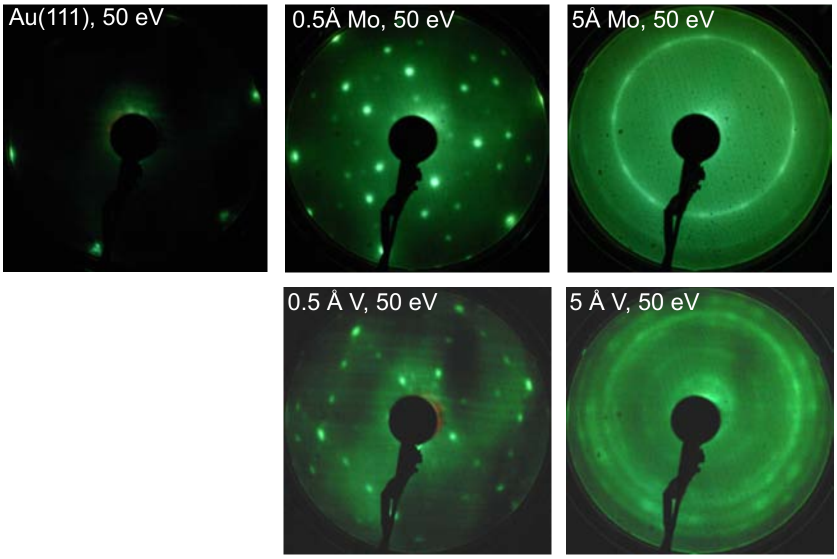

Figure 1: LEED patterns obtained after deposition of different amounts of vanadium and molybdenum onto Au(111) with subsequent oxidation in an atmosphere of 50 mbar of O_2 at 400 °C.

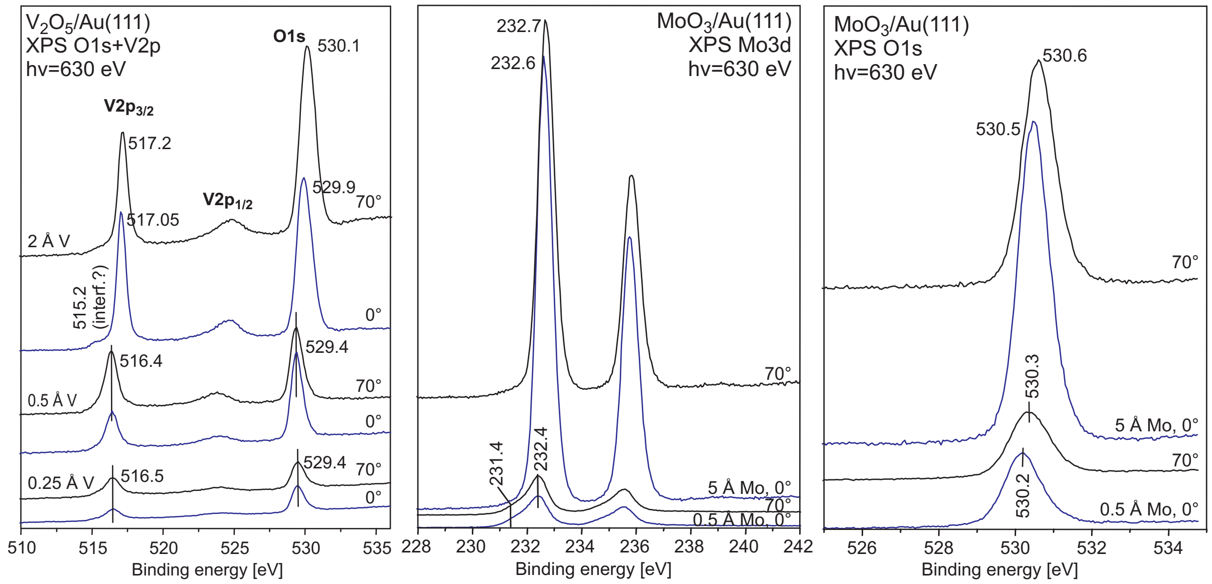

Figure 2: Core level photoelectron spectra of V_2O_5/Au(111) (left) and MoO_3/Au(111) (center and right) as a function of the deposited amount of the respective metal. Detection angles of °0 and °70 with respect to the surface normal were employed.

beam of the LEED optics.

The oxidation state, the homogeneity, and the structure of the oxide layers have been studied with photoelectron spectroscopy of the core levels (figure 2) and the valence band (figure 3), and NEXAFS (figure 4). The V2p and Mo3d binding energies of the thick films correspond well to reported values for V_2O_5 (≈517 eV [2]) and MoO_3 (≈232.7 eV [3]), indicating that the high pressure oxidation indeed leads to the formation of V^{5+} and Mo^{6+} oxides. The peaks do not exhibit obvious fine structure, indicating that homogeneous phases were formed. This is also indicated by the corresponding valence band spectra shown in figure 3: for both oxides the intensity in the gap is negligible for the thick films which indicates that lower oxidation states are not present in noticeable amounts.

The core level binding energies for the thin films are somewhat smaller. This is not necessarily an indication of a lower oxidation state since the XPS final state core holes may be effectively

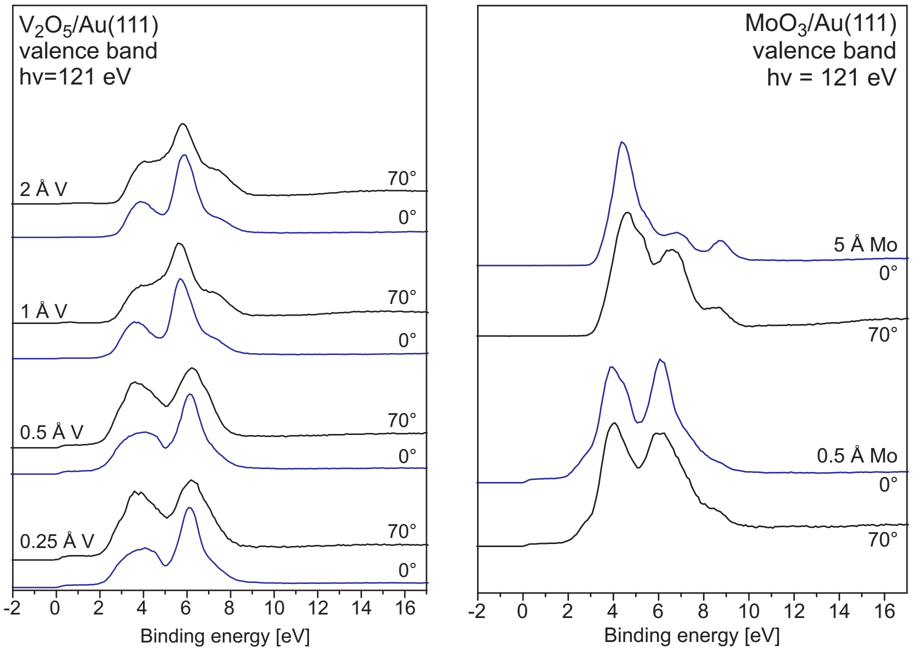

Figure 3: Valence band photoemission spectra of V_2O_5/Au(111) (left) and MoO_3/Au(111) (right) as a function of the deposited amount of the respective metal. Detection angles of °0 and °70 with respect to the surface normal were employed.

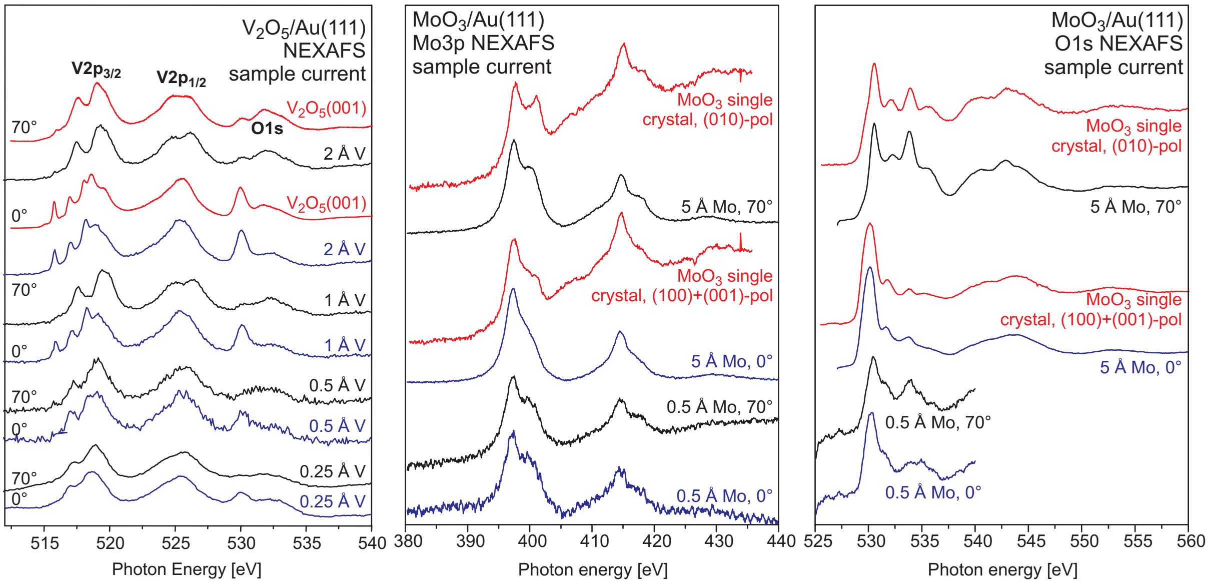

Figure 4: NEXAFS spectra of V_2O_5/Au(111) (left) and MoO_3/Au(111) (center and right) as a function of the deposited amount of the respective metal. Light incidence angles of °0 and °70 with respect to the surface normal were employed. The MoO_3 single crystal data have been taken from reference 3.

screened by Au(111) substrate electrons in the case of the thin layers which would also lead to a reduced binding energy as compared to the thick film case. The observation that the metal levels and oxygen levels are shifted by about the same energy into the same direction may be viewed as an indication that the shift is a final state effect since the O1s binding energies usually depend only weakly on the oxidation state. In the case of Mo3d level of the thin MoO_3 layer a shoulder is observed at lower binding energy. This may be due to different types of molybdenum atoms in the oxide layer or to shake-up processes which may come up due to the increased screening. The observation that the intensity ratio does not depend on the detection angle is somewhat in favor of the second explanation.

Figure 4 exhibits NEXAFS spectra obtained at light incidence angles of 0° and 70° for V_2O_5 and MoO_3 layers with different thicknesses. One point to note is that the Mo3p, V2p and O1s spectra of the thick films depend considerably on the light incidence angle. This demonstrates that the films are ordered as also indicated by the LEED images in figure 1. The thick film data are compared with single crystal spectra in figure 4 showing that the V_2O_5[001] and the MoO_3[010] directions are oriented along the surface normal. As shown by LEED (figure 1), the other directions which are in plane exhibit rotational disorder with some preferential azimuthal orientations. These observations would fit to a film consisting of well ordered crystallites exposing the (001) (V_2O_5) or (010) (MoO_3) surfaces towards the vacuum. The crystallites exhibit different azimuthal orientations, likely due to a weak dependence of the interaction with the Au(111) substrate on the azimuthal orientation.

References

[1] M. M. Biener, J. Biener, R. Schalek, and C. M. Friend, J. Chem. Phys. **121**, 12010 (2004).

[2] J. Mendialdua, R. Casanova, and Y. Barbaux, J. Electron Spectrosc. Relat. Phenom. **71**, 249 (1995).

[3] M. Sing, R. Neudert, H. von Lips, M. S. Golden, M. Knupfer, J. Fink, R. Claessen, J. Mücke, H. Schmitt, S. Hüfner, B. Lommel, W. Aßmus, Ch. Jung, and C. Hellwig, Phys. Rev. B **60**, 8559 (1999).

Surface sensitive X-ray magnetic circular dichroism (XMCD) measurements of Al_2O_3 capped magnetite (Fe_3O_4) for implementation in a magnetic tunnel junction

Marc D. Sacher, Volker Höink, Jan Schmalhorst and Günter Reiss
Thin Films and Nanostructures,Department of Physics,
University of Bielefeld, P.O. Box 100131, 33501 Bielefeld, Germany

Magnetic tunnel junctions (MTJs) consisting of two ferromagnetic electrodes (FM) separated by an ultra-thin insulator (barrier) have a large application potential in magnetoelectronics. The tunneling magnetoresistance amplitude is defined as TMR = $(2P_1P_2) / (1-P_1P_2)$ by Julliere[1] with $P_{1,2}$ the spin polarization of electrode 1 and 2. Half-metallic ferromagnets with only one occupied spin channel at the Fermi energy and thus 100% spin polarization are of greatest interest. There are several materials in current discussion, e.g. Heusler alloys[2] and magnetic oxides[3]. But up to now there is no working MTJ with electrodes showing a spin polarization of 100% at RT. The half metallic magnetic oxide with the highest T_C of 858K is the ferrimagnet magnetite (Fe_3O_4) being a good candidate for future applications in spintronic devices at high temperatures. Although Versluijs measured a magnetoresistance of 85% in a nanocontact between Fe_3O_4 crystals[4], only a few percent TMR have been measured in a plane Fe_3O_4-MTJs up to now[5]. Magnetite grows in the spinell structure, which is a combination of tetrahedral (T_d) and octahedral (O_h) lattices sites. Berdunov showed by STM investigations the large influence of surface defects (unoccupied lattices sites) of magnetite on the spin polarization and thus the TMR value[6]. In a MTJ the same can be assumed for the interface between barrier and Fe_3O_4. Thus the parameters for the creation of the Al_2O_3 barrier by deposition of metallic aluminum and subsequent oxidation must be adjusted carefully. With X-ray magnetic circular dichroism (XMCD) in surface sensitive total electron yield mode it is possible to detect even very small changes in stoichiometry of magnetite. This can be done with respect to the very well understood characteristic peakform in the XMCD asymmetry of magnetite[7]. The excitation of electrons at different lattice sites leads to the characteristic shape of the XMCD spectra at the Fe-$L_{2,3}$ edge. In the spectra measured for a magnetite single crystal the sites related to $Fe^{2+}O_h$: $Fe^{3+}T_d$: $Fe^{3+}O_h$ have a correlation of the peak-height of roughly -2 : 1 : -1,5. Even small changes of the stoichiometry of the Fe_3O_4 result in a significant change of the shape of the spectrum. For additional iron (oxygen) the $Fe^{3+}O_h$ ($Fe^{2+}O_h$) peak is enlarged.

We used the "BESSY Polarimeter" at beamline UE56/2-PGM utilizing 90% right elliptically polarized X-rays at the Fe-$L_{2,3}$-edge. For these measurements the samples were saturated with an alternating field of about 300Oe. The TEY measurements were done in the remanent state. The measurement in the remanent state ensures equal detection efficiencies of the secondary electrons for parallel and antiparallel alignment of the remanent sample magnetization and the photon spin. The angle of incidence of the X-rays was $\theta = 30°$ with respect to the surface.

The investigated layer stack consists of 25nm copper conduction line and about 70nm Fe_3O_4. The magnetite is grown by alternating deposition of a 2nm thick iron layer and subsequent ECR-oxidation (t_{Ox}=200s, U=-25V). The free parameters of this ECR oxidation method are the oxygen-ion dose (controlled with the oxidation time t_{Ox}) and the ion-energy (controlled with the acceleration voltage U). A detailed description of the oxidation method can be found elsewhere[8]. After deposition the Fe-O layer is in-situ annealed to 450°C for one hour to reorganize the iron and oxygen atoms to Fe_3O_4. After cooling down the layer stack is capped with an alumina layer with a thickness of 1,8nm, a typical tunneling barrier in a magnetic tunnel junction. The alumina is also prepared by deposition of metallic aluminum and subsequent oxidation.

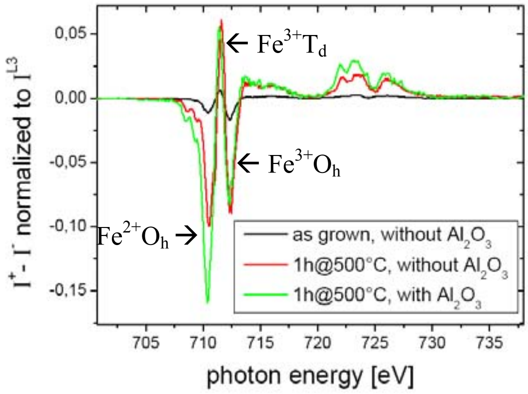

FIG 1: Annealed and as grown sample without capping compared to an Al_2O_3 capped sample. The capping results in a reduction of the magnetite.

We investigated the interface between the magnetite and the barrier with XMCD, with a special focus on the different stoichiometry of the magnetite at this interface. This strongly depends on the oxidation parameters of the Fe-O layer itself, as well as on the interaction with the adjacent alumina layer at the interface. In the case of a not fully oxidized aluminum layer, one expects a reduction of the magnetite layer. For a strong overoxidized alumina layer additional oxygen atoms might diffuse into the magnetite and change the stoichiometry of the Fe_3O_4 to Fe_2O_3.

An XMCD measurement of a not annealed sample (t_{Ox}=200s, U=-25V) without a capping layer is shown in Figure 1 (black line). Because the $Fe^{3+}O_h$ is obviously larger than the $Fe^{2+}O_h$, the surface is slightly overoxidized. Furthermore the magnetic moment is rather small. This overoxidation can be reduced by a loss of oxygen and a reorganization during an annealing to 500°C. The spectrum of the annealed sample shows the expected XMCD curve for magnetite (red line). The preparation parameters of this sample are used for all further investigations of the influence of the adjacent alumina on the magnetite/alumina interface. The influence of a standard alumina tunneling barrier as often used in MTJs[8] on the XMCD signal can also be seen in Fig. 1 (green line). A strong reduction of the magnetite was found due to the deposition of the metallic Al after annealing. The subsequent oxidation of the aluminum layer did not reverse this effect.

In order to build a MTJ with magnetite and alumina, both effects described above were combined. The results of an XMCD measurement made at samples, which were annealed at temperatures ranging from 100°C up to 500°C for one hour *after* the deposition of the Al_2O_3-capping, are shown in Fig. 2. The deposition of the capping layer without a previous annealing step results again in a reduction of the Fe-O, which can be observed as an enlargement of the magnetic moment. For temperatures up to 400°C a further reduction of the Fe-O layer has been observed. Again, this is indicated by change of the relative height of the $Fe^{2+}O_h$ and $Fe^{3+}O_h$ -peaks. For all investigated temperature the reference shape corresponding to magnetite was not found. At 500°C no magnetic signal has been observed. This can be explained by an interdiffusion of the adjacent aluminum and iron atoms. This also has been found in surface sensitive first arrival measurements utilizing Auger electron spectroscopy (AES).

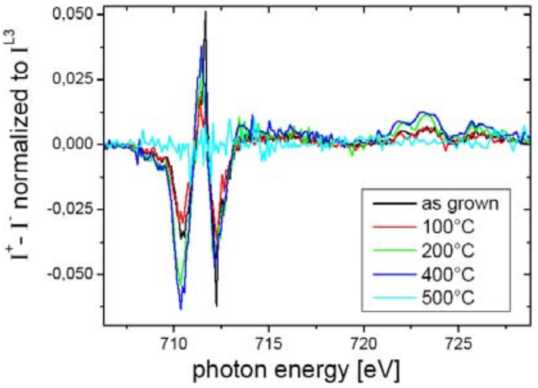

FIG 2: XMCD spectra of as grown and annealed samples. The loss of oxygen can be reduced, but at 500°C the magnetite is destroyed due to interdiffusion of aluminum and iron.

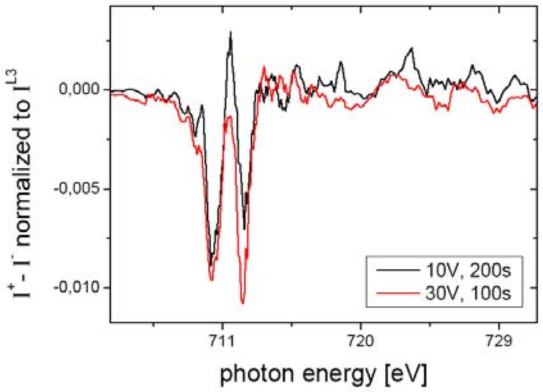

FIG 3: Post-oxidation method leads to a strong amount of additional oxygen at the interface, but the magnetic moment is too small. This could be due to a not ordered Fe-O layer after second oxidation step.

Another possibility how to avoid the loss of oxygen is an additional oxidation after the annealing step (post-oxidation). The idea is to increase the amount of oxygen atoms in the surface layer of the magnetite, the aluminum layer can react with. Fig. 3 shows two XMCD measurements of annealed samples with additional oxidation and Al_2O_3 capping. With increasing ion dose, as well as increasing ion energy the amount of oxygen at the interface is increased. In the case of U=-10V and t_{Ox}=200s the characteristic XMCD shape of the magnetite was found. But the XMCD amplitude is by a factor of 10 smaller than for the uncapped samples. A possible reason is that the post-oxidation implements oxygen, but also destroys the ordering of the magnetite. Maybe a thermally activated reorganization of the Fe_3O_4 at the interface is necessary. This could be done by an additional annealing step at a moderate temperature (below 400°C).

A third approach to get a stoichiometric ordered Fe_3O_4/Al_2O_3 interface is to increase the total amount of oxygen during the deposition/oxidation of the magnetite. This as well as the moderate annealing of post-oxidized samples will be investigated in the near future.

The goal of this project was to investigate the influence of alumina layer on the stoichiometry of the magnetite at the alumina interface with the help of the XMCD asymmetry at the $L_{2,3}$-edge of iron. All systematic measurements hint that the deposition of an adjacent alumina layer results in a loss of oxygen in the magnetite. An extensive and more detailed investigation to avoid this reduction will be done during a future beamtime.

The authors gratefully acknowledge the valuable assistance of Franz Schäfers and Andreas Gaupp prior to and during the beamtime at the BESSY II. The support of BMBF is also acknowledged (grant number: BMBF 05 ES 3XBA/5).

[1] M. Julliere, Phys. Lett. **54A**, 225 (1975)
[2] S. Kaemmerer et.al., J. Appl. Phys. **93**, 7945 (2003)
[3] S. P. Lewis et al., Phys. Rev. B **55**,10253 (1997);
M. Penicaud, J. Magn. Magn. Mater. **103**, 212 (1992)
[4] J. J. Versluijs et al., Phys. Rev. Lett. **87**, 026601 (2001)
[5] X. W. Li et al., Appl. Phys. Lett. **73**, 3282 (1998);
P. J.van der Zaag, J. Magn. Magn. Mater. **211**, 301 (2000)
[6] N. Berdunov, Phys. Rev. Lett. **93**, 057201 (2004)
[7] F. Schedin et. al., J. Appl. Phys. **96**, 1165 (2004);
P. Morall et al., Phys. Rev. B **67**, 214408 (2003)
[8] A. Thomas et. al., J. Vac. Sci. Techn. B **21**, 2120-2122 (2003)

Investigation of the electronic properties of bio-organic/inorganic semiconductor interfaces

S. Seifert, G. Gavrila, D.R.T. Zahn
Institut für Physik, Technische Universität Chemnitz, D-09107 Chemnitz, Germany
W. Braun
BESSY GmbH, Albert-Einstein-Str. 15, D-12489 Berlin, Germany

In recent years the possibility to use DNA bases in electronic devices such as organic field effect transistors[1] has attracted much attention. Also the transport properties of DNA strands (natural as well as artificial, e.g. poly(G)-poly(C) DNA) and whether or not these would be suitable molecular nano wires were subject of scientific discussions and a number of publications [2,3]. There is, however, little experimental work, addressing the electronic structure (i.e. the density of states) of the DNA bases in the condensed phase, which is of utmost importance for transport properties and device performance. Therefore a systematic photoelectron spectroscopy study of thin DNA base films was performed. The experiments were carried out at the Russian German Beam Line at BESSY employing the Multi User Stage for Angular Resolved Photoemission (MUSTANG) experimental station. This system is equipped with a Phoibos150 electron analyzer (SPECS) and consists of two main chambers for analysis and *in situ* sample preparation.

Experimental: The Si(111) substrates (n-type, resistivity 7.5Ω/cm) annealed under ultra high vacuum conditions (base pressure $\leq 3\cdot 10^{-10}$mbar) by direct current heating at 800°C to desorb possible contaminants. Several DC flushes of 20s duration were applied to heat the samples up to 1100°C-1300°C in order to remove the natural oxide. After letting the sample cool down slowly enough to preserve the (7x7) reconstruction, the surface was passivated *in situ* by exposure to (2.0±0.5) Langmuir atomic hydrogen. This dose should be enough to passivate the dangling bonds without etching the surface. The DNA base layers were deposited onto the H-Si(111)(7x7) surface by organic molecular beam deposition (OMBD). The nominal layer thickness was monitored by a quartz microballance. The Valence band photoemission spectra (VB PES) of layers of the DNA bases adenine, cytosine and guanine were recorded for different thicknesses (1nm - 10nm) and with excitation energies of 55eV and 150eV. Exemplary valence band photoemission spectra (VB PES) are presented in Fig.1. The width of the spectra was determined by linear extrapolation of the onset of the VB PES at low binding energies and the cut-off at the vacuum level (i.e. low kinetic

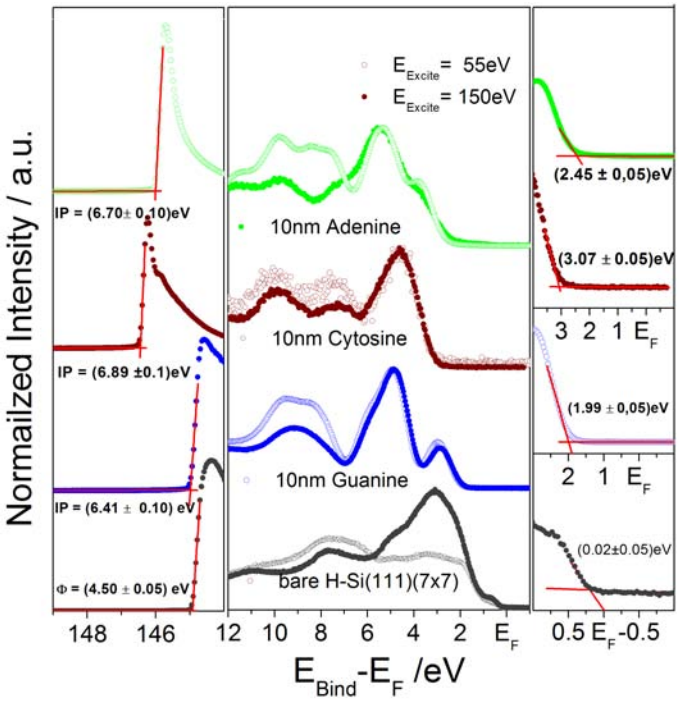

Fig.1: Valence band photoemisssion spectra of 10 nm layers of adenine (green), cytosine (brown) and guanine (blue) taken at E_{excite}=150eV(dots) and E_{excite}=55eV(circles)

energies). The ionization potential (IP) of the DNA base film can be derived by subtraction of the spectral width from the excitation energy. The IPs, determined by this procedure for bulk-like, thick DNA base layers are summarized in Tab.1. The experimentally determined IPs are significantly smaller than the values calculated by Preuss *et al.* for single molecules in [5], using a ∆SFC ansatz. This can be understood qualitatively as the result of the interaction between the molecules in the condensed phase which distributes the effect of the ionization over several molecules so that the individual molecular orbitals are less effected than in the single molecule case. The fact, that the experimental values are much closer to the calculated ground state eigen energies of the highest occupied molecular orbitals (HOMO's) (DFT/B3LYP functionals, 6-311G+(d,p) basis set [6]), suggests a strong interaction of the molecules. This is supported by the DFT/B3LYP calculation of the ionization potential of an infinite stack of guanine molecules published by Prat, Houk and Foote in [7], where they observe a similar shift in calculations including the neighbor interactions with respect to the calculation for single molecules.

DNA base	Experimentally determined IP	IP(∆SCF s.mol.) [2]	HOMO position (DFT/B3LYP; s. mol.)	IP(DFT/B3LYP;inf. stack)[3]
Cytosine	(6.89±0.10)eV	8.66eV	6.67eV	-
Adenine	(6.70±0.10)eV	8.06eV	6.34eV	-
Guanine	(6.41±0.10)eV	7.63eV	6.12eV	6.64eV

Tab 1: The ionization potentials determined from the valence band spectra follow the same trend as the values calculated for single molecules (s.mol.) with DFT/B3LYP(6-311+G(d,p)) and by a DSCF formalism. A better match in the absolute value can be achieved, if neighbor interactions are included, as performed by F. Prat and coworkers [3] for an infinite stack of guanine molecules.

By broadening the eigen energies calculated for single molecules with Gaussian functions, the density of occupied states (DOOS) displayed in Fig.3 is derived. The calculated curves compare very well to the measured VB PES after a shift towards higher binding energies is introduced. The full width at half maximum (FWHM) of the broadening functions is chosen to match the VB PES. It varies from *0.9eV* in the case of the adenine layers to *1.3eV* for cytosine and is considerably larger than the estimated overall experimental resolution of *0.07eV.* The experimentally observed FWHM is considerably larger than that observed in the case of molecules in the gas phase [8]. The broadening due to inelastic electron scattering should be very similar for all three investigated DNA bases and

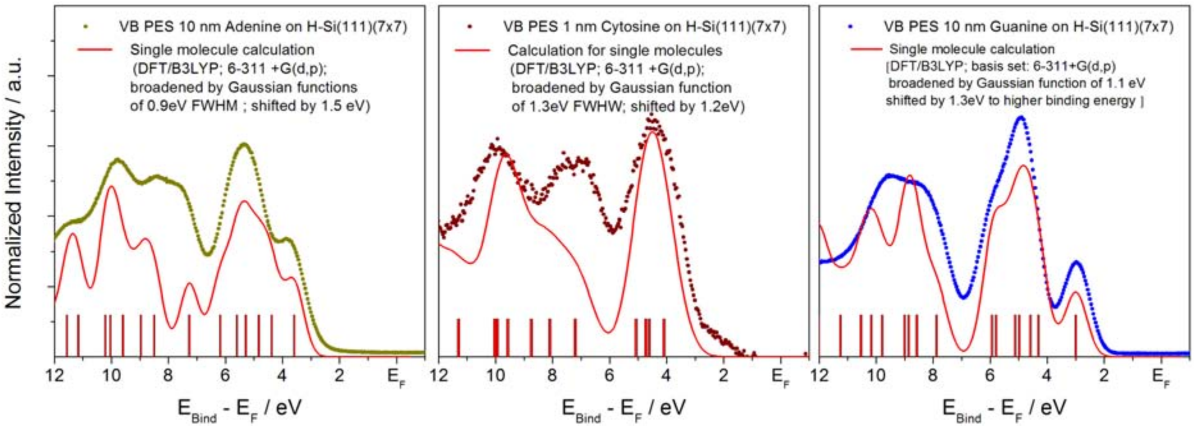

Fig.3: Comparison of the measured VB PES of 10nm thick layers of the DNA base on H-Si(111)(7x7) with the calculated DOOS (DFT/B3LYP; basis set: 6-311+G(d,p)). The molecular ground state eigen energies were broadened by Gaussian functions and shifted towards higher binding energies to fit the experimental data.

therefore one can conclude, that there is an additional, significant contribution to the broadening at least in the cases of cytosine and guanine. A possible broadening mechanism is the overlap of the molecular valence orbitals which could lead to delocalized, Bloch-type orbitals along the stacking direction and band-like behavior or at least to the lifting of the degeneration of the eigen energies of the molecular orbitals of neighboring molecules as proposed by Calzolari, Felice, and Molinari [9]. Since both possibilities would lead to the observed broadening and the spacing between the multiplet lines (0.02eV) described by Calzolari, Felice, and Molinari is smaller than $k_B T$ and well below our experimental resolution, we can not distinguish between the two. Yet an overlap in the valence orbitals that causes either of them, is in very good agreement with the above conclusion of strong molecular interaction.

Acknowledgments: The authors would like to use this opportunity to thank all BESSY staff members for their assistance during beam times (especially Mike Sperling for the technical support). We also acknowledge the financial support granted by the BMBF(FK MUSTANG 05KS40C1/3, FK 05KS1OCA1).

References:

[1] G. Maruccio, Field effect transistor based on a modified dna base. Nano Letters **3**, 479 (2003).

[2] D. Porath, A. Bezryadin, S. de Vries, and C. Dekker, Direct measurement of electrical transport through dna molecules. Nature **403**, 635 (2000)

[3] K.-H. Yoo, D.H. Ha, J.-O. Lee, J.W. Park, Jinhee Kim, J. J. Kim, H.-Y. Lee, T. Kawai, and Han Yong Choi *Electrical Conduction through Poly(dA)-Poly(dT) and Poly(dG)-Poly(dC) DNA Molecules,* Phys. Rev Lett., **Vol. 87**, No. 19, 198102 (2001)

[4] K. Takayanagi, Y. Tanishiro, M. Takahashi and S.Takahashi, *Structural analysis of Si(111)-7×7 by UHV-transmission electron diffraction and microscopy,* J. Vac. Sci. Tech. **A3**, 1502 (1985)

[5] M. Preuss, W. G. Schmidt, K. Seino, J. Furthmüller, and F. Bechstedt, *Ground and excited-state properties of dna base molecules from plane-wave calculations using ultrasoft pseudopotentials.* Journal of Computational Chemistry **25**, 112 (2003)

[6] Gaussian 03, Revision C02, M. J. Frisch, G. W. Trucks, H. B. Schlegel, G. E. Scuseria, M. A. Robb, J. R. Cheeseman, J. A. Montgomery, Jr., T. Vreven, K. N. Kudin, J. C. Burant, J. M. Millam, S. S. Iyengar, J. Tomasi, V. Barone, B. Mennucci, M. Cossi, G. Scalmani, N. Rega, G. A. Petersson, H. Nakatsuji, M. Hada, M. Ehara, K. Toyota, R. Fukuda, J. Hasegawa, M. Ishida, T. Nakajima, Y. Honda, O. Kitao, H. Nakai, M. Klene, X. Li, J. E. Knox, H. P. Hratchian, J. B. Cross, V. Bakken, C. Adamo, J. Jaramillo, R. Gomperts, R. E. Stratmann, O. Yazyev, A. J. Austin, R. Cammi, C. Pomelli, J. W. Ochterski, P. Y. Ayala, K. Morokuma, G. A. Voth, P. Salvador, J. J. Dannenberg, V. G. Zakrzewski, S. Dapprich, A. D. Daniels, M. C. Strain, O. Farkas, D. K. Malick, A. D. Rabuck, K. Raghavachari, J. B. Foresman, J. V. Ortiz, Q. Cui, A. G. Baboul, S. Clifford, J. Cioslowski, B. B. Stefanov, G. Liu, A. Liashenko, P. Piskorz, I. Komaromi, R. L. Martin, D. J. Fox, T. Keith, M. A. Al-Laham, C. Y. Peng, A. Nanayakkara, M. Challacombe, P. M. W. Gill, B. Johnson, W. Chen, M. W. Wong, C. Gonzalez, and J. A. Pople, Gaussian, Inc., Wallingford CT, 2004

[7] F. Prat, K. N. Houk, and C. S. Foote, *Effect of guanine stacking on the oxidation of 8-oxoguanine in b-dna.* J. Am. Chem. Soc. **120**, 845 (1998)

[8] D. Dougherty, E.S. Younathan, R. Voll, S. Abdulnur, S.P.McGlynn, *Photoelectron Spectroscopy of some Biological Molecules,* Journal of Electron Spectroscopy related Phenomena, **13**, 379 (1978)

[9] A. Calzolari, R. Di Felice, and E. Molinari, *G-quartet biomolecular nanowires,* Appl. Phys. Lett., **Vol. 80**, No. 18, 3331 (2002)

Conformational changes in adsorbed molecules

P. M. Schmidt, Th.U. Kampen, J. Hugo Dil, and K. Horn
Department of Molecular Physics, Fritz-Haber-Institut der Max-Planck-Gesellschaft

Stilbene is the monomer buildingblock of phenylenevinylene-type oligomers and polymers. It undergoes an interconversion around the central C=C double bond upon irradiation with UV-light of 250-320nm wavelength[1]. This cis-trans-isomerization of the free molecule follows an in-plane hula-twist mechanism[2] whose pathway can be assumed to work as well in constraint systems as on surfaces – thus assessing a 'molecular switch'.

To investigate the isomerization of stilbene-molecules on surfaces, planar trans-stilbene has been studied on Si(100) surfaces at ~90 K by means of photoemission spectroscopy (PES) and near-edge x-ray adsorption fine structure spectroscopy (NEXAFS).

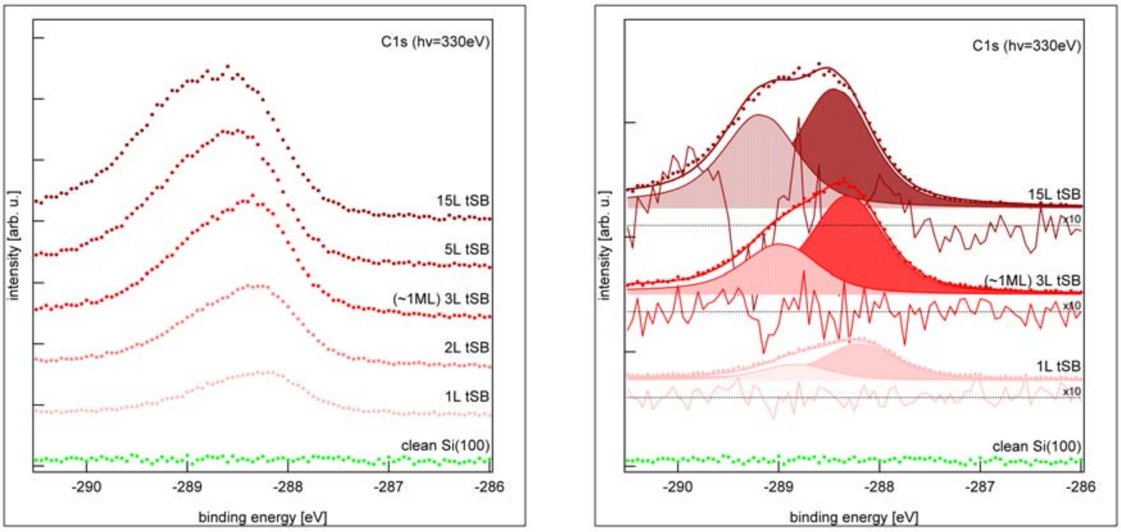

C1s core level spectra of different coverages of cSB on Si(100). The left image shows the data for 1L, 2L, 3L, 5L and 15L coverage while the right image shows the fits of exemplary spectra. The signals can be fitted by two Voigt functions. These two signals can be attributed to the ring atoms (dark red) and the bridge atoms (light-red) of the stilbene-molecules. Development of the intensities of the signals for different coverages show that cSB is bond via the bridge atoms to the Si(100)-surface.

The first layer of trans-stilbene adsorbs in an ordered fashion, with the conjugated π-system of the molecule being parallel to the substrate surface. No dissociation or isomerization takes place during gas phase deposition. This can be shown by comparing valence band spectra with calculated binding energies of molecular orbitals of stilbene[3] and valence band spectra from possible dissociation products (benzene)[4,5]. No energy shifts can be observed in the Si2p core level emission indicating that the interaction of stilbene with the Si surface is only a weak physisorption. The intensity of the contribution from 2nd layer atoms relatively to the bulk contribution is at a maximum for a coverage of about 3L which corresponds to 1ML coverage. In trans-stilbene multilayers the molecules are randomly oriented. C1s core level emission signals with contributions from the different C atoms in stilbene reveal no shift with increasing coverage indicating that the interaction is strongest between the subsrate and the first monolayer. Annealing results in a desorption of the multilayer leaving a monolayer on the surface.

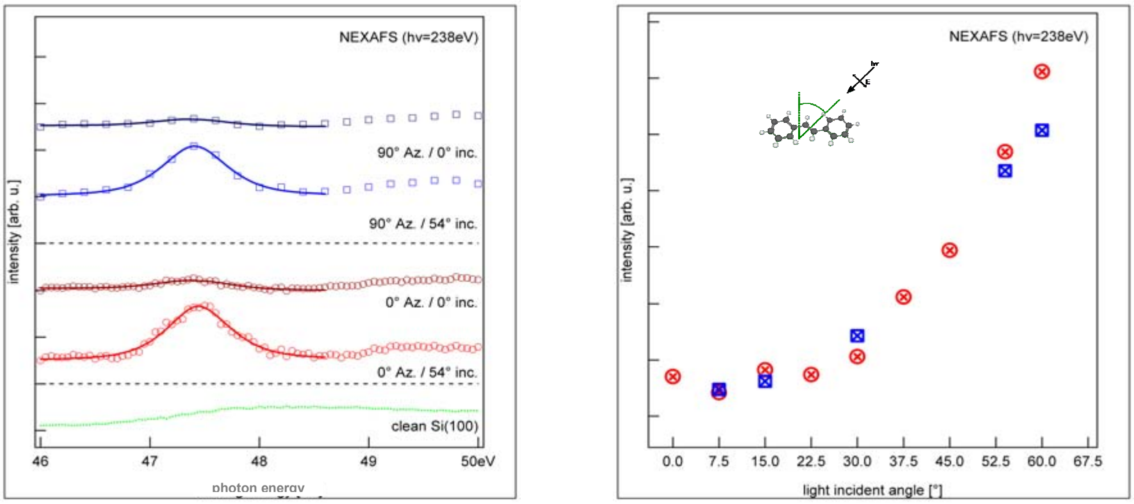

NEXAFS spectra of 3L (~ 1ML) cSB on Si(100) for different sample azimuths. The left image shows exemplarily the spectra for normal incidence (0° inc.) and normal emission (54° inc.), the right image shows the development of the signal intensity over increasing incidence angle. The maximum intensity at grazing incidence angle shows the molecule to be lying flat on the surface.

First comparison of valence band spectra of trans- with cis-stilbene reveal significant differences which will allow identification of both isomers upon laser-2-photon-photoemission studies to be performed for further investigation of the isomerization-process.

[1] Sension, R. J. et al., J. Chem. Phys. 98, 6291 (1993)

[2] Fuß, W. et al., Angew. Chem. Int. Ed. 43, 4178 (2004)

[3] Molina, V. et al., J. Phys. Chem. A 101, 3478 (1997)

[4] Kim, Y. K. et al., Phys. Rev. B 71, 115311 (2005)

[5] Gokhale, S. et al., J. Chem. Phys. 108, 5554 (1998)

Electronic structure of ultrathin NiO(111) films studied by angle-resolved photoemission

A. Gottberg, E. Weschke, A. Helmke, and G. Kaindl
Institut für Experimentalphysik, Freie Universität Berlin, D-14195 Berlin, Germany

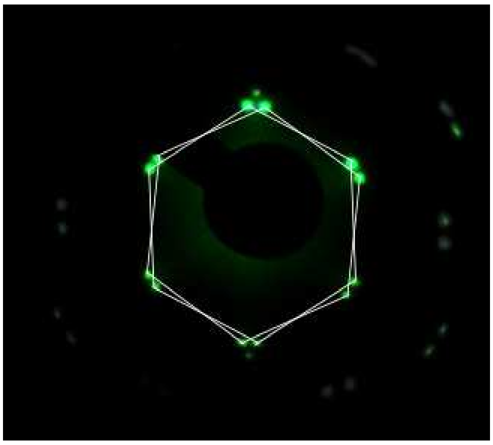

Fig. 1: LEED pattern of a 7 ML-thick Ag(111) film on W(110). The double structure of the hexagonal spots indicates Kurdjumov-Sachs growth geometry.

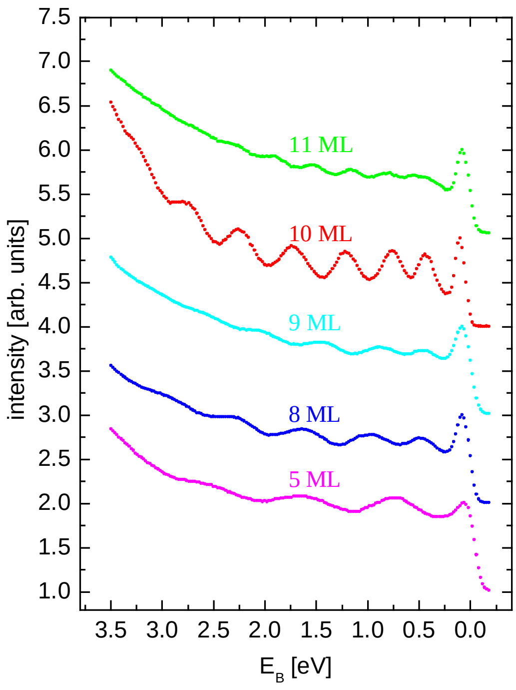

Fig. 2: Angle-resolved photoemission spectra of Ag(111) film on W(110). The spectra were recorded at $h\nu = 41$ eV in normal emission.

NiO is a prototype antiferromagnetic transition-metal oxide, which has regained interest due to its relevance for exchange-bias thin-film systems. While bulk NiO was studied extensively, the properties of thin films, in particular the electronic structure, are not very well explored. Of special importance in this systems is the (111) surface, which is the polar surface of the rocksalt structure and hence attracts substantial scientific interest. From an experimental point of view, essentially nothing is known about its electronic structure due to the difficulties in the preparation of a clean surface.

In this experiment, the valence electronic structure of NiO(111) ultrathin films was studied by angle-resolved photoelectron spectroscopy at beamline U125/2-SGM, using a SES-100 spectrometer. The samples were prepared in the following way: As a first step, a clean Ag(111) film was prepared by epitaxial growth on W(110). Fig. 1 displays a LEED pattern which demonstrates well-ordered growth in Kurdjumov-Sachs geometry [1]. The quality of the Ag films is also reflected in the normal-emission photoemission spectra shown in Fig. 2, which are characterized by pronounced quantum-well states. These Ag(111) films are well suited as substrates for the growth of NiO(111).

Thin films of NiO (111) were prepared by evaporation of Ni in an oxygen atmosphere of $5*10^{-6}$ mbar, with the substrate held at 280°C. The films exhibit hexagonal (1x1) LEED patterns and show pronounced dispersion of d-derived states. Fig. 3 shows corresponding spectra, recorded with a photon energy of hν=100 eV. The figure displays a colour intensity plot as a function of both binding energy and electron emission angle, which directly shows the dispersion of NiO states with the parallel momentum $k_{\|}$ along the $\overline{\Gamma M}$ direction of the surface Brillouin zone. A particularly interesting feature of this electronic structure is the band at the lowest binding energy, which crosses the Fermi energy. This band is originating from Ni 3d states, as verified by photoemission spectra recorded at various photon

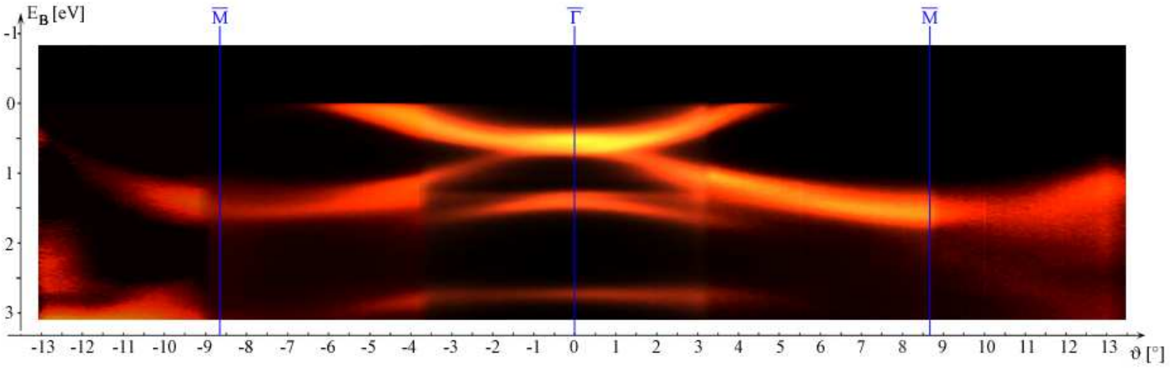

Fig. 3: $k_{\|}$ dispersion of electronic states of a thin NiO(111) film on Ag(111) on W(110). The photoemission spectra were recorded with $h\nu$=100 eV.

energies in normal emission (not shown here). The intensity of the features as a function of hν is shown in Fig. 4. The behavior resembles that of Ni-3d states, with a typical resonance maximum around hν = 63eV, corresponding to the Ni 3p-3d excitation energy [3]. Furthermore, we do not observe any dispersion of the features with perpendicular momentum as expected for the two-dimensional character of electronic states in an ultrathin film.

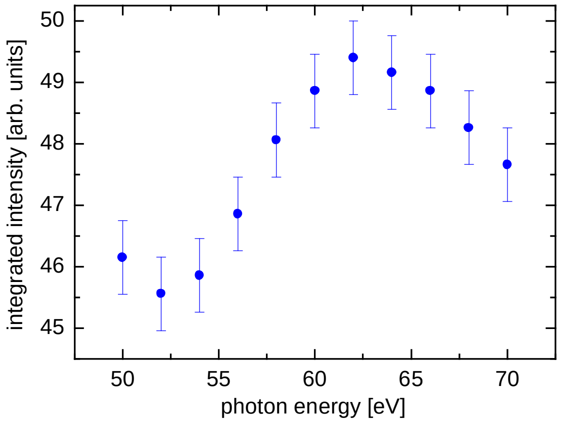

Fig. 4: Photoemission intensity of the electronic states close to the Fermi energy from Fig. 3 as a function of photon energy.

The interesting finding of this study is the existence of a Ni-3d-derived band, that crosses the Fermi energy. This is not expected from the bulk properties of NiO, which is well-known to be a charge-transfer insulator with a large band gap [2]. Obviously, the ultrathin film prepared here exhibits metallic properties, which may be due to the interaction with the Ag substrate or a property of thin NiO itself. At present, there are still open questions concerning the sample preparation to obtain these particular films and concerning the origin of the metallic character. Experiments to clarify the present results as well as on the polar (111) surfaces of other transition metal oxides are in progress.

References:

[1] R. Clauberg *et al.*, Phys. Rev. B **31**, 1754 (1985).
[2] M. L. Hildner *et al.*, Surf. Sci. **388**, 110 (1997).
[3] M. Imada *et al.*, Rev. of Mod. Phys. **70**, 1039 (1998) .

Coupling between spin and orbital order in La$_{0.5}$Sr$_{1.5}$MnO$_4$?

C. F. Chang, M. Buchholz, C. Schüßler-Langeheine, J. Schlappa, M. Benomar, and L. H. Tjeng
II. Physikalisches Institut der Universität zu Köln, Zülpicher Str. 77, 50937 Köln
E. Schierle, G. Kaindl, and E. Weschke
Institut für Experimentalphysik. Freie Universität Berlin, Arnimallee 14, 14195 Berlin

Funded by the DFG through SFB 608, TP C4.

La$_{1-x}$Sr$_{1+x}$MnO$_4$ is the prototypical material for order phenomena in correlated transition-metal oxides because for x = 0.5 charge, spin, and orbital degrees of freedom form an ordered phase. This compound is also the material for which the particular power of resonant soft x-ray diffraction has been predicted first by Castleton and Altarelli calculating the Mn-$L_{2,3}$ spectral shape of the (¼,¼,0) orbital order superstructure peak and showing the high sensitivity of the resonance to the character of this order [1]. The analysis of the experimental resonant diffraction data is however more involved: below the Néel temperature of 119 K the shape of the resonance changes and the intensity of the superstructure peak shows a steep increase for certain photon energies, which was originally explained as a stabilization of the orbital-order by the onset of spin order [2], which means a coupling between spin and orbital degrees of freedom. The interpretation is a present matter of debate: a polarization dependent diffraction experiments indicates rather a cross talk between orbital-order and spin-order intensity due to finite intensity from magnetic ordering at the same momentum transfer as the orbital order peak [3], while a combined theoretical and experimental work indeed suggests a coupling between spin- and orbital degrees of freedom [4].

We used resonant soft x-ray diffraction at the Mn $L_{2,3}$ resonance to study the momentum space around the orbital order peak. The experiments were carried out at the U49/2-PGM2 beamline with the UHV diffractometer built at the Freie Universität Berlin. For the experiment a newly-designed sensitive photon detector was installed to this instrument. A single crystal of La$_{1.5}$Sr$_{0.5}$MnO$_4$ was grown cut and polished with a (115) surface orientation and the (110) and (001) direction in the diffraction plane.

The propagation vectors of the orbital- and spin order point into perpendicular directions with the obital-order superstructure peak at (¼,¼,0) and the spin-order peak at (¼,-¼,½). Because of the tetragonal symmetry of the crystal a twinning of the order pattern should be expected, which would lead to about the same amount of domains with the spin-order peak and domains with the orbital order peak in the diffraction plane.

While we found an intense superstructure peak at (¼,¼,0) for all positions of the sample, we did not find any peak at (¼,¼,½) in contrast to our expectations. What we found at this momentum transfer for some parts of the sample, was a background, which was well defined along the (110) direction but diffuse along the (001) (L) direction. Interestingly this background is almost flat along L and has con-

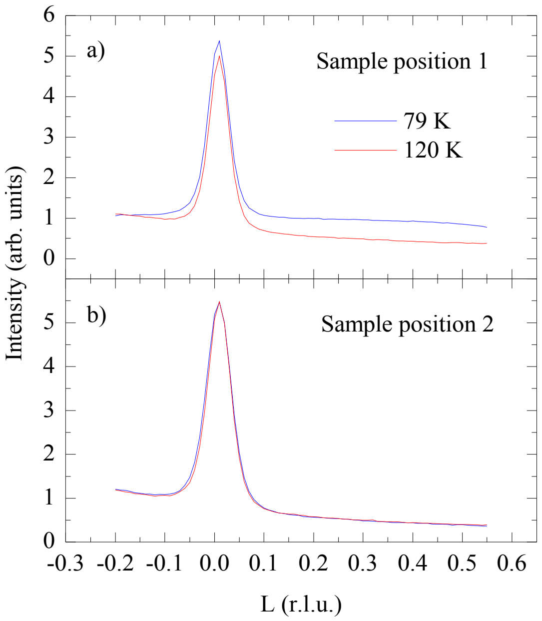

Fig. 1: Scans along the (001) (L) direction through the orbital order peak for two different temperatures below and above the Neél temperature recorded from two different spots on the sample surface.

siderable intensity also at the position of the (¼,¼,0) orbital-order peak [Fig 1a), blue curve]. For other parts of the sample, this background does not exist as can be seen in the blue curve in Fig. 1b), which was recorded from a different spot, and which only shows the slope towards the specular reflectivity at small L-values as all scans do.

By probing the intensity of the diffracted signal as a function of photon energy, we obtain spectroscopic information about its origin [5]. Fig. 2a) contains the spectrum of the diffuse background recorded at L = ½. This spectrum is the fingerprint of the spin-order peak [4] and the same spectrum is found for the whole background up to the onset of the orbital order peak at L = 0.1, which means that despite the missing peak at (¼,¼,½) the background is definitely from magnetic origin. This assignment is further confirmed by the temperature dependence with the background intensity vanishing at the Néel temperature [red curve in Fig. 1a)].

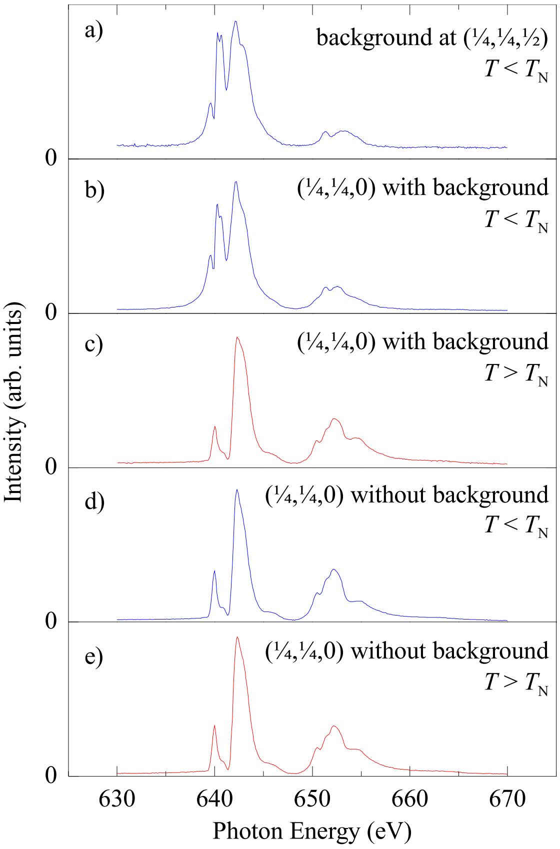

Fig. 2: Spectra recorded at different positions in q-space and for different spots on the sample below and above the Néel temperature.

From this finding it is not surprising that the orbital-order peak appears to gain intensity below the Néel temperature as found in Ref. 2. Because of the different spectral shape of the magnetic and the orbital order spectrum the relative intensity of both contributions is strongly energy dependent as demonstrated in Fig. 2b) and c), where we show spectra taken at the position of the orbital-order peak at a sample spot with particularly high magnetic background. The low temperature spectrum [Fig. 2b)] is a sum of magnetic and orbital-order contributions and the spectral shape hence changes strongly when the sample is heated above the Néel temperature [Fig. 2c)]. This finding explains the peculiar different temperature dependences found for different photon energies [2]. For spectra recorded from sample parts without magnetic background as shown in Fig. 2d) and e) the spectral shape does not change across the Néel temperature. It is therefore plausible that the observed apparent coupling between spin and orbital order is only due to this diffuse magnetic background. Further insight can be expected from experiments using samples with different doping levels, which will affect the orbital orientation [6] and should give additional contrast between spin and orbital contributions.

We gratefully acknowledge the excellent working conditions BESSY, the experimental support from the BESSY staff and from the U49/2-PGM2 team. We further acknowledge helpful discussions with M. Braden and D. Senff.

[1] C. W. M. Castleton and M. Altarelli, Phys. Rev. B 62, 1033 (2003).
[2] S. B. Wilkins et al., Phys. Rev. Lett. 91, 167205 (2003).
[3] U. Staub et al., Phys. Rev. B 71, 214421 (2005).
[4] S. B. Wilkins et al., Phys. Rev. B 71, 245102 (2005).
[5] C. Schüßler-Langeheine et al., Phys. Rev. Lett. 95, 156402 (2005).
[6] D. Senff et al., Phys. Rev. B 71, 24425 (2005).

Electronic structure of Si(100) at high laser intensities

T. Gießel[1], H. Prima-Garcia[1], R. Schmidt[1], R. Weber[1],
M. Weinelt[1,2], W. Widdra[3]
[1]*Max-Born-Institut, Berlin, Germany*, [1,2]*Freie Universität Berlin, Berlin, Germany*
[3]*Martin-Luther-Universität Halle-Wittenberg, Halle (Saale), Germany*

The interest in optically excited dense e-h plasmas in semiconductors, mainly in connection with the investigation of laser-induced phase transitions, initiated several experimental and theoretical studies in recent years [1]. Laser-induced changes of the optical and structural properties were probed applying pump-probe techniques. Conclusions regarding changes of the electronic structure could be drawn from laser-induced changes of the optical and structural properties.

Laser-induced changes of the electronic structure can be probed directly using photoelectron spectroscopy. Moreover, bulk and surface electronic states are in many cases clearly distinguishable allowing for the specific assignment of the laser-induced changes to the surface and bulk, respectively. In this respect Si(100) is a particularly interesting candidate. Due to the technological importance of this system detailed knowledge about its ground state electronic and geometric structure is available [2]. According to both theoretical and experimental studies the surface atoms of the Si(100) surface form asymmetric dimers, which are alternately tilted with respect to the surface plane thereby forming a c(4x2) super structure. The corresponding electronic surface states with an energetic splitting between occupied and unoccupied surface states of $\sim$ 0.8 eV [3] are localized mainly at the upper dimer atoms for the occupied and at the lower dimer atom for the unoccupied states and are therefore referred to as D_{up} and D_{down}, respectively. Using the laser fundamental of 800 nm (1.56 eV) electrons at the surface can be excited into unoccupied states by single photon processes, while electron excitation in the bulk is governed by the absorption of at least two photons, because of the larger direct bulk band gap of around 3.2 eV. Therefore, a higher excitation rate at the Si(100) surface is expected under these conditions.

We have detected laser-induced reversible changes of the electronic structure of Si(100) using time-resolved photoelectron spectroscopy with combined laser and synchrotron radiation (SR). By combining valence band and core level photoelectron spectroscopy we were able to separate surface photovoltage and space-charge effects from transient changes of the electronic structure. Changes of the electronic structure could be assigned specifically to surface and bulk.

For the optical excitation of the sample we used a Ti:sapphire regenerative amplifier system (Coherent, RegA 9050) producing pulses of 70 fs duration at 208,3 kHz repetition rate (pulse energy: 6 μJ at the fundamental wavelength of 800 nm). The laser beam was focused to a diameter of <100 μm in order to access the full intensity range up to the damage threshold (0.18 J/cm^2) of the sample. The excited state of the sample was probed as a function of the delay time between pump and probe by valence band and core level photoelectron spectroscopy using VUV and soft X-ray synchrotron radiation pulses with

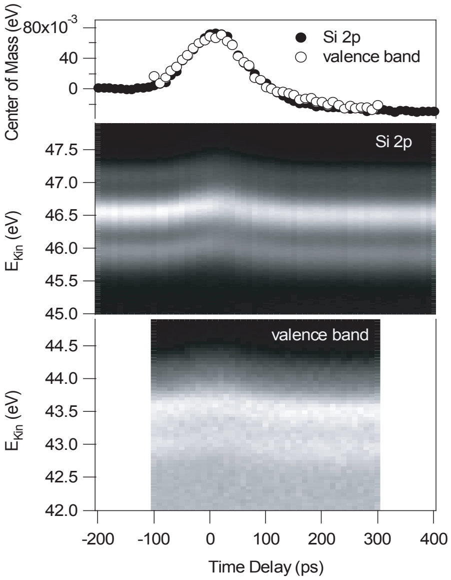

Fig. 1: 2D plots of series of Si(100) valence band spectra (bottom) and of Si 2p spectra (middle) as a function of the time delay between laser and SR. The top panel shows the corresponding center of mass for Si 2p and valence band spectra.

a pulse length of 10 ps. The laser pulses are synchronized (I. Will, MBI) to the 500 MHz BESSY master clock with a jitter < 10 ps, thereby matching the SR pulse length in the low-α mode. Photoelectrons were energy- and angle-selected using a hemispherical electron analyzer with a modified electronics for time-resolved photoelectron detection. Valence band spectra were recorded at an emission angle of 15° and core level spectra at an emission angle of 60°, both with an angular acceptance of $\pm 8°$.

When interpreting photoemission spectra from a semiconductor excited by intense laser pulses surface photovoltage and space-charge effects have to be addressed properly. Laser-induced changes in the spectra due to these effects have to be separated from those caused by changes of the electronic structure itself. Surface photovoltage and space-charge effects at a certain excitation state are characterized by a rigid shift and possibly broadening of the whole spectrum. Hence, these effects can be identified by comparing laser-induced changes in different regions of the photoemission spectrum. Regions with distinct features, which can be used for that purpose, are in the case of Si(100) the Si 2p core level and the valence band region. Figure 1 shows 2D plots of series of Si(100) valence band spectra (bottom) and of Si 2p spectra (middle) as a function of time delay between laser and SR (SR pulse length < 50 ps). The top panel shows the corresponding center of mass for Si 2p and valence band spectra. The change of the center of mass as a function of the time delay for both Si 2p and valence band spectra is mainly induced by a shift of the whole spectrum and is very similar for the two spectral regions. These laser-induced changes are therefore assigned to SPV and/or space-charge effects and can be used within certain limits as independent detectors for the determination of the coincidence time of laser pump and VUV (or soft X-ray) probe pulses.

In order to extract information about changes of the electronic structure from the photoemission spectra a more detailed quantitative analysis is necessary. Figure 2 (left) shows valence band spectra recorded in the BESSY low-α mode (SR pulse length ~10ps) at a laser fluence well below the damage threshold (0.07 J/cm^2) for two different time delays. In a pragmatic approach the data are fitted to a function, which consists of a broadened step function for the bulk states, two gaussian functions for the split occupied D_{up} surface bands and an additional gaussian for the lower branch of the transiently populated unoccupied D_{down} band. The panel on the right shows the result for a whole series of spectra recorded as a function of the time delay between laser and SR. Changes in the edge position of the bulk region are governed by SPV and space-charge effects with an initial

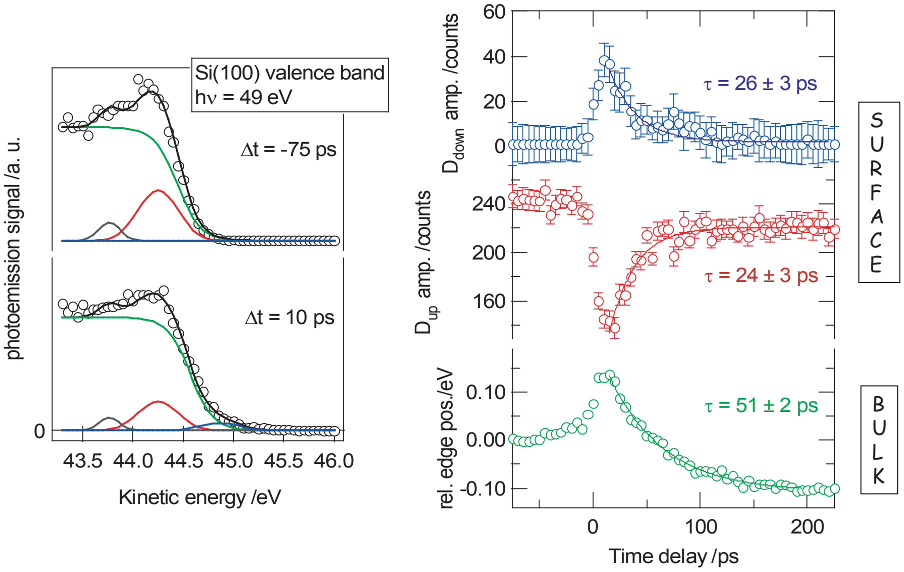

Fig. 2: Left: Valence band spectra recorded in the BESSY low-α mode (SR pulse length $\sim$ 10 ps) at a laser fluence well below the damage threshold (0.07 J/cm^2) for two different time delays. Right: Temporal evolution of the transient population and depopulation of the $\mathrm{D_{down}}$ and $\mathrm{D_{up}}$ surface state, respectively and dynamics of SPV and space-charge relaxation characterized by the change of the valence band edge position.

relaxation time of 51 ps. Depopulation of bulk states is expected to be in the low percentage range and cannot be resolved. The $\mathrm{D_{up}}$ surface bands are depopulated by around 40%. Note, that in the bulk already 10% depopulation leads to a collapse of the band structure and irreversible changes of the sample. The reversibility of the laser-induced changes at the surface at the observed high excitation densities can be understood in terms of a stabilizing effect of the underlying substrate. Relaxation processes at excitation densities above $10^{20}\mathrm{cm}^{-3}$ in the bulk are governed by auger recombination. However, population and depopulation of the $\mathrm{D_{down}}$ and $\mathrm{D_{up}}$ surface state, respectively, show a simple exponential decay. The matching initial decay times of approximately 25 ps for both population and depopulation confirm the assignment of the transient shape changes at the foot of the valence band edge in the spectra to the $\mathrm{D_{down}}$ surface band. The position of the transiently populated $\mathrm{D_{down}}$ band was found 0.65 eV above the $\mathrm{D_{up}}$ surface band in its ground state. This change in the surface band gap by at least 0.15 eV is interpreted in terms of a transient surface band gap renormalization.

References

[1] K. Sokolowski and D. von der Linde, Phys. Rev. B **61**, 2643 (2000).

[2] S.B. Healy, C. Filippi,1 P. Kratzer, E. Penev, and M. Scheffler, Phys. Rev. Lett. **87**, 016105 (2001).

[3] M. Weinelt, M. Kutschera, T. Fauster and M. Rohlfing, Phys. Rev. Lett. **92**, 126801 (2004).

Unravelling the Verwey transition in magnetite via soft X-ray resonant scattering

Y. Su[1], H.F. Li[1], J. Persson[1], W. Schweika[1], D. Schrupp[2], M. Sing[2], R. Claessen[2], A. Nefedov[3], H. Zabel[3], V.A.M. Brabers[4] and Th. Brueckel[1]

[1]Institut fuer Festkoerperforschung, Forschungszentrum Juelich, D-52425 Juelich, Germany
[2]Experimentelle Physik 4, Universitaet Wuerzburg, Am Hubland, D-97074 Wuerzburg, Germany
[3]Institut fuer Experimentalphysik 4, Ruhr-Universitaet Bochum,D-44780 Bochum, Germany
[4]Department of Physics, Eindhoven University of Technology, 5600 MB Eindhoven, The Netherlands

1. Introduction

The nature of the Verwey transition in magnetite (Fe_3O_4) is one of the longest standing puzzles in modern condensed matter physics. In particular, whether and how charge and orbital ordering (CO/OO) take place below the Verwey transition temperature (T_V) at ~ 123 K is still among the central focus of current investigations. Significant (~ 20%) charge ordering was found in a latest high-resolution X-ray and neutron powder diffraction refinement [1]. But such a picture was discarded in a later single-crystal resonant X-ray scattering experiment undertaken at the Fe K-edge [2], where no resonance was observed at the corresponding superstructure wavevector (0, 0, ½) and (0, 0, 1), respectively. The situation was further complicated by two recent LDA+U calculations, where possible orbital ordering of the B-site minority t_{2g} electrons was predicted [3-4]. In fact, a prominent role of multi-orbital electronic correlations with associated Jahn-Teller distortions on the B-sublattice was further demonstrated in a more sophisticated calculation via LDA+DMFT method [5]. Therefore, it seems that the orbital degree of freedom is crucial to the occurrence of the Verwey transition. It should be mentioned that in an alternative approach within a more itinerant-electron picture, Khomskii proposed a new model of CO/OO by using the idea of an interplay of site- and bond-centered ordering, which may explain both the structural data and even the presence of multiferroics in magnetite [6-7]. In view of such a resurgence of the exciting new ideas, it is not surprising to notice that new waves of pursuits are being carried out worldwide to unravel the nature of the Verwey transition, among which soft X-ray resonant scattering stands out due to its tremendous sensitivities to charge and orbital degrees of freedom. In the following part, we will report the first observation of significant resonances of the superstructure reflection (0, 0, ½) at both the O K- and Fe L_{III}-edges on high-quality and stoichiometric single crystals of magnetite. Together with our latest observation of the similar resonance at the Fe K-edge, i.e. in the hard X-ray regime [8], it would become possible now to establish a complete "band topology" of the Verwey transition.

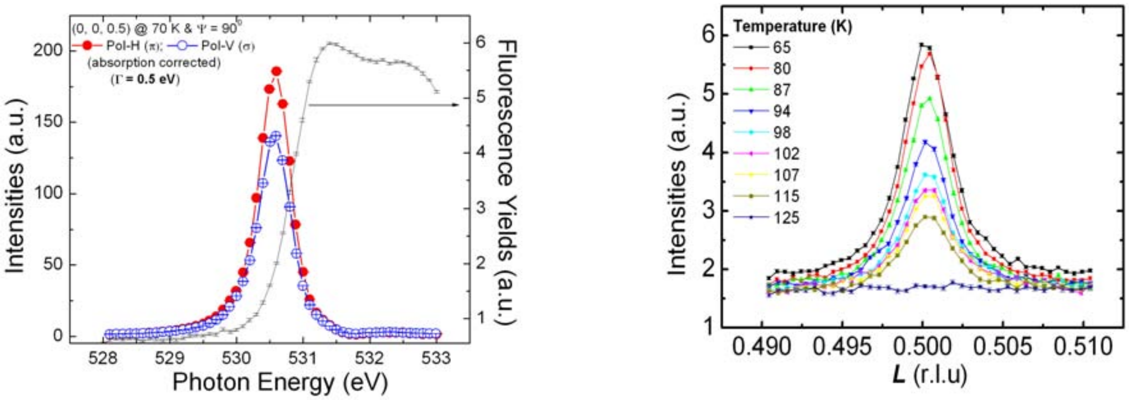

(a) **(b)**

Fig. 1 Resonant scattering from the superstructure refection (0, 0, 1/2)) observed at the oxygen K-edge, (a) energy dependence, (b) temperature dependence of the resonance at 530.5 eV.

2. Results and Discussions

Experiments were undertaken with the two-circle ALICE diffractometer at the beamline of UE56/1-PGM-b. The first major obstacle to work with very high-quality single crystals of magnetite is that even a slight mis-orientation of the sample would easily ruin your experiment due to the extreme sharpness of both the rocking curve (< 0.1°) and longitudinal width (~ 0.001-0.002 Å^{-1}). To overcome this difficulty, a new portable UHV/Low-T goniometer was constructed and successfully tested with the ALICE chamber. This new option finally enabled us to perfectly align all single crystals measured so far. Another obstacle to overcome is the formation of the multiple twins below T_V due to the lowering of the symmetry from cubic. A unique way has been figured out to allow us to as much as possibly have access to the desired twins. As shown in Fig. 1 (a), a tremendous resonance of (0, 0, ½) has been observed in the pre-edge regime of the oxygen K-edge. The width of the energy profile is extremely small at only ~ 0.5 eV, suggesting a rather long lifetime of the core holes and a very narrow bandwidth of the corresponding unoccupied intermediate bands, i.e. possibly a localized band. Away from the resonant energies, (0, 0, ½) is completely undetectable, which is consistent with the hard x-ray observations [2, 8], suggesting that (0, 0, ½) is not resulted from lattice displacements due to the low-T structure phase transition. The temperature dependence of (0, 0, ½), as shown in Fig. 1 (b), clearly indicates its association to the Verwey transition. In a similar way, a giant resonance was also observed near the Fe L_{III}-edge. The temperature dependence of the resonance is shown in Fig. 2. The inverse correlation length along the longitudinal direction of the resonant (0, 0, ½) is estimated at ~ 0.002 Å^{-1}, suggesting a long-range correlation. To summarize, we have finally established an unprecedented picture on the spatial modulation of all relevant bands at the Verwey transition, which would represent a giant step toward a final understanding on the nature of the Verwey transition.

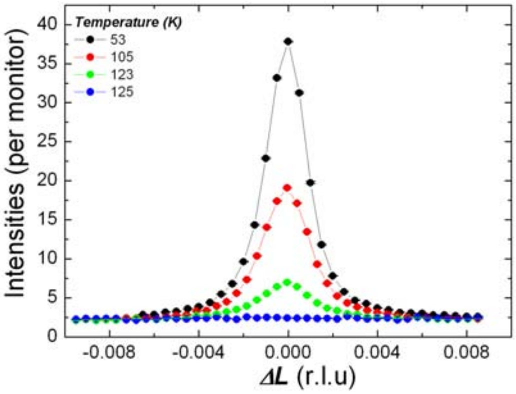

Fig. 2 Temperature dependence of the resonant (0, 0, ½) superstructure reflection near the Fe L_{III}-edge (longitudinal scans were shown)

Acknowledgements

We would like to thank BESSY technical and scientific staffs for providing excellent conditions of the storage ring and the corresponding beamline. This project was also partly funded by the BMBF grant O3ZA6BC2.

References

[1] J.P. Wright, *et al.*, Phys. Rev. Lett. **87**, 266401 (2001)
[2] G. Subías, *et al.*, Phys. Rev. Lett. **93**, 156408 (2004)
[3] H.-T. Jeng, *et al.*, Phys. Rev. Lett. **93**, 156403 (2004)
[4] I. Leonov, *et al.*, Phys. Rev. Lett. **93**, 146404 (2004)
[5] L. Craco, M.S. Ladd and E. Mueller-Hartmann, cond-mat/0511390 (2005)
[6] D.I. Khomskii, *et al.*, Phys. Rev. Lett. **94**, 156402 (2005)
[7] D.I. Khomskii, *et al.*, cond-mat/0601096
[8] Y. Su, *et al.* unpublished

Soft X-ray resonant scattering study of magnetic ordering in $La_{2-2x}Sr_{1+2x}Mn_2O_7$ ($x = 0.5$)

H.F. Li[1], Y. Su[1], T. Chatterji[2], A. Nefedov[3], H. Zabel[3], and Th. Brueckel[1]

[1]*Institut fuer Festkoerperforschung, Forschungszentrum Juelich, 52425 Juelich, Germany*
[2]*Institute Laue-Langevin, BP 156, 38042 Grenoble Cedex 9, France*
[3]*Institut für Experimentalphysik 4, Ruhr Universität Bochum, 44780 Bochum, Germany*

1. Introduction

The physics of highly correlated transition-metal oxides (TMO), including high-T_c cuprates and CMR manganites, is currently attracting enormous attention. In particular, observations of complex ordering phenomena are extremely important for understanding the natures of different intriguing phases, e.g., ferromagnetic insulating (FMI) phase and charge-ordered antiferromagnetic (AF) phase. Like neutron scattering, element-specific resonant soft X-ray scattering also appears to be a powerful probe to magnetic ordering in 3*d* TMO since a very large resonant enhancement can be expected at the corresponding $L_{3/2}$ edges.

The existence of the charge and orbital ordering ($T_{CO/OO}$ ~ 210 K) in the bilayered manganite $La_{2-2x}Sr_{1+2x}Mn_2O_7$ with doping level of $x = 0.5$ was first suggested by the observation of the resistivity anomaly [1] and the associated superstructures were then revealed by the electron diffraction measurements [2]. However, the magnetic phase diagram seems to be complicated, in which the *CE*-type AF phase coexists with the layered AF phase. Wilkins et al [3] for the first time performed resonant X-ray scattering measurements for the $La_{1.05}Sr_{1.95}Mn_2O_7$ and observed extremely large resonant enhancements of the antiferromagnetic (AF) reflection at the L_3 and L_2 edges of Mn. Here we report the results of magnetic resonant exchange scattering experiments on $La_1Sr_2Mn_2O_7$. The experiments were carried out at UE56/1-PGM-b beamline of BESSY-II using the UHV-diffractometer ALICE [4].

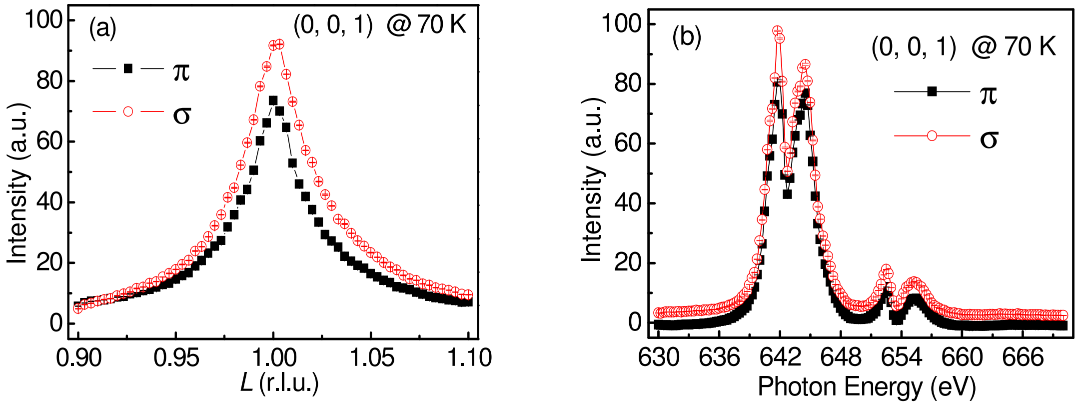

Fig. 1 Resonant magnetic soft X-ray scattering of (001) supperlattice reflection of the $La_1Sr_2Mn_2O_7$ at 70 K. (a) Longitudinal scans at 641.7 eV, (b) the energy dependence of intensity at Mn $L_{2/3}$-edges at the fixed wave vector with σ and π polarizations.

2. Results and Discussions

At 70 K, i.e. well below the magnetic ordering temperature (~210 K), a pronounced resonant enhancement of the AF superstructure reflection (001) was found at the Mn L_3-edge, as shown in Fig. 1(a). Such a resonance is due to an electric dipole transition from the $2p_{3/2}$ to $3d$ levels directly probing the magnetic-exchange split $3d$ bands. The magnetic correlation length along the $\boldsymbol{L}$ direction can be estimated to be less than 100 Å. The energy dependence of the AF (001), as shown in Fig. 1(b), indicates two noticeable peaks showing an extremely large resonant enhancement in the broad region of the L_3-edge. In addition, the magnetic resonant enhancement was also observed in a broad region at the L_2-edge. However, there is no obvious polarization dependence. The temperature dependence of the (001) peak suggests T_N ~ 210 K. Surprisingly, as shown in Fig. 2, a strong resonance of the AF reflection (001) was also observed near the O K-edge with the σ-polarized incident photons. That may indicate the existence of spin-polarized oxygen holes. The origin of the observed O K-edge resonance will clearly be the subject of further investigations.

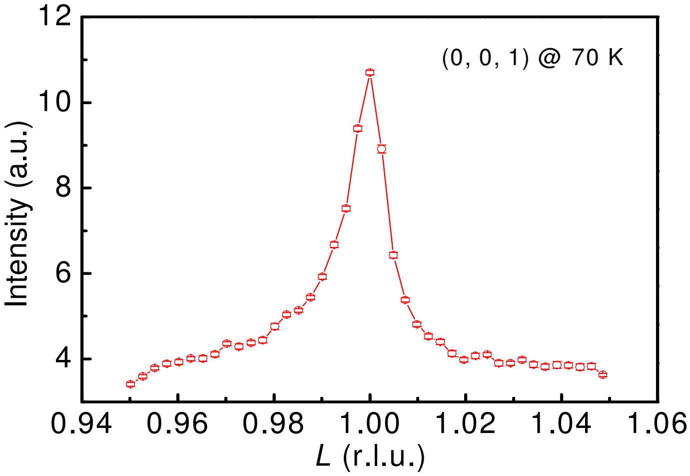

Fig. 2 Longitudinal scan of the superstructure reflection (001) near O K-edge with σ incident polarization

Acknowledgements

We would like to thank BESSY technical and scientific staffs for providing excellent conditions for the storage ring and the corresponding beamline. The project was also partly funded by the BMBF grant O3ZA6BC2.

References

[1] R. Seshadri, C. Martin, M. Hervieu, *et al.*, Chem. Mater. **9** 270 (1997)
[2] J.Q. Li, Y. Matsui, T. Kimura and Y. Tokura, Phys. Rev. B **57**, 3205 (1998)
[3] S.B. Wilkins, P.D. Hatton, *et al.*, Phys. Rev. Lett. **90**, 187201 (2003)
[4] J. Grabis, A. Nefedov and H. Zabel, Rev. Sci. Instr. **75**, 4048 (2003)

Self-assembled monolayers of molecular switches - azobenzene alkanethiols

Roland Schmidt[1], Helena Prima Garcia[1], Tanja Gießel[1],
Ramona Weber[1], Wolfgang Freyer[1], and Martin Weinelt[1,2]

1. Max-Born-Institut, Max-Born-Straße 2 A, 12489 Berlin

2. Freie Universität Berlin, Fachbereich Physik, Arnimallee 14, 14195 Berlin

Alkanethiols are known to form self-assembled monolayers (SAMs), e.g., on gold films. The self-assembly takes about 24 hours in a 10^{-4} molar solution at room temperature. Due to the specific chemical bond between the thiol head-group and the gold surface as well as lateral interactions densely packed self-assembled layers of alkanethiols form ordered layers (*molecular carpet*). The average tilt angle between alkane chain and surface normal amounts to about 35° [1]. This result is rather independent from the alkane chain length $(\mathrm{CH}_2)_n, n = 16, 20, 22$. Therefore, the alkane may be used as a spacer to decouple a functional molecule from the thiol head-group which is in turn used as a linker to the surface. Thus SAMs may be promising candidates for organizing molecular switches at surfaces and may be used as a building block for molecular devices [2].

For this purpose the thiols need to be fuctionalized by an appropriate end-group. We choose azobenzene, i.e. two phenyl rings connected via two double-bonded nitrogen atoms. The azobenzene molecule itself has two isomers, the thermally stable trans- and the metastable cis-form. They can be interchanged by optical excitation with a time constant of the isomerization reaction in the (sub)-ps range [3]. In solution the molecule is successfully used as a photoswitch, e.g., in triggering structural changes of peptides [4]. In our case azobenzene is attached to the alkane chain via a single oxygen bond CF3-azobenzene-O-(CH2)12-SH (Az-12, cf. inset in Fig. 1b). To characterize the molecules prior to adsorption we have measured steady-state absorption in solution. We observe high switching efficiency upon irradiation at around 350 nm (trans → cis) and 440 nm (cis → trans). Furthermore, the trans-form of azobenzene is the stable conformation at 300 K. Adsorbed on the gold surface the potential of these molecules as molecular switches has first been pointed out by Stiller and coworkers [5]. They observed work-function changes upon irradiation which were interpreted as a change of the molecular dipole moment associated with a switch of the molecular conformation.

A first prerequisite for this model to hold is a well oriented azobenzene entity. Therefore, we studied the orientation of the molecules on a gold substrate (200-300 nm Au / 5 nm Ti / Si(100)) by near-edge X-ray absorption spectroscopy (NEXAFS). The data in Fig. 2a and b show the Auger yield at the C1s - and N1s - absorption edges, respectively. To avoid radiation damage samples have been cooled to 100 K and spectra are recorded by scanning the sample through the de-focussed beam [6]. Typically, one sample with a size of 1 cm^2 is used for two to four scans. A load-lock system and sample garage allows us to quickly exchange samples. The spectra have been normalized to the photon flux measuring the transfer characteristics of the beamline by a photodiode.

Overall, the spectra in Fig. 1 show significant variations of the intensity when changing the incidence angle of the incoming X-ray beam. For 90° the polarization of the exciting radiation is parallel to the surface, while the component of the field vector normal to the surface dominates for 20° incidence angle.

An analysis of the C1s → C-H* resonance at $\simeq$ 288 eV (Fig. 1a bottom) gives an average tilt angle of 30° of the pure alkane chain with respect to the surface normal. The spectrum

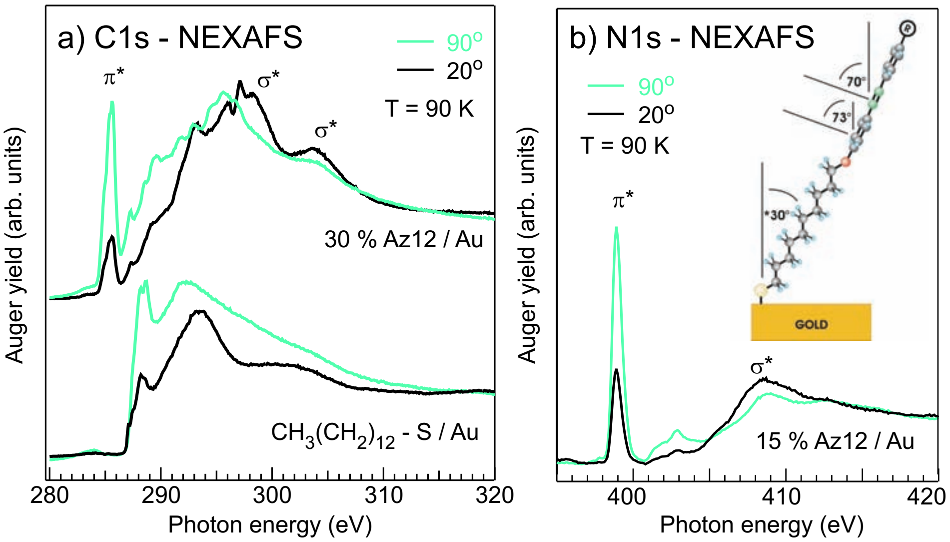

Figure 1: Near edge X-ray absorption spectra for azobenzene - alkanethiols on a 300 nm gold / 5 nm Ti / Si(100) surface. a) C1s edge for 30 % mixture (top) and for a pure alkanethiol layer (0 % mixture, bottom); b) N1s edge for 15 % mixture. The inset shows the average adsorption geometry deduced from the NEXAFS spectra.

recorded for a mixture of 30 % of alkanethiols with azobenzene vs. pure alkanethiols (Fig. 1a top) shows a comparable contrast at around 288 eV. We therefore conclude, that for the mixed layer the average tilt angle is little altered. The latter spectrum is dominated by the $C1s \longrightarrow \pi^*$ transition at a photon energy of $\simeq$ 285 eV. The absorption line shows some structure which unfortunately coincides with a dip in the beamline transmission and needs further experimental clarification. Nevertheless, the C1s $\longrightarrow \pi^*$ transition exhibits a polarization dependence similar to that of the C1s $\longrightarrow$ C-H* resonance. Hence, both the alkane C-H bond and the p_z-orbitals of the phenyl ring are similarly oriented. The analysis gives an tilt angle of about 10° between the phenyl-ring plane and the alkane chain (cf. Fig. 1). This result is corroborated by absorption measurement at the nitrogen edge depicted in Fig. 1b. The N1s $\longrightarrow \pi^*$ resonance at $\simeq$ 399 eV shows a polarization dependence similar to the C1s $\longrightarrow \pi^*$ transition. As expected, the N1s $\longrightarrow \sigma^*$ transition at $\simeq$ 409 eV shows the opposite behavior. Thus both phenyl ring-planes are comparably oriented and the trans conformation is favored at 100 K.

SAMs are well-ordered at 100 K and the molecular orientation of the switch follows the tilt angle of the spacer thiol (see inset of Fig. 1b).

A second prerequisite for a photoswitch to work is that the optical excitation is long lived and not quenched by charge transfer to the substrate. Charge transfer-times can be studied by Resonant Raman Auger [7] applying the so-called core-hole clock method [8]. After, e.g., N1s $\longrightarrow \pi^*$ excitation the N1s core-hole is mainly filled via Auger decay. When the electron is still present in the π^* LUMO (lowest unoccupied molecular orbital) it may either *participate* in the Auger process or may screen the core-hole and thus lead to a *spectator* shift of the decay spectrum. In both cases the kinetic energy of the outgoing electron shifts as the photon energy of the exciting radiation (Resonant Raman Auger). If the electron is in contrast transferred to the substrate or a neighboring molecule before decay of the core-hole takes place we observe a Auger-like spectrum, i.e. with the

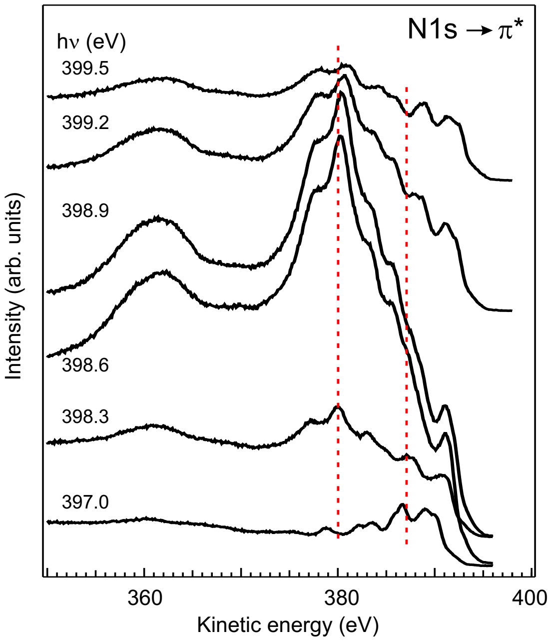

Figure 2: Resonant photoemission spectra for photon energies spanning the N1s → π^* transition. The emission lines shift with the photon energy and are resonantly enhanced.

energetics identical to continuum excitation.

Figure 2 shows Auger Resonant Raman spectra recorded at photon energies spanning the N1s → π^* resonance. The spectrum is clearly dominated by emission lines, which shift linearly with photon energy but resonate reflecting the change of the π^* transition intensity. To estimate the lifetime of the excited electron in the π^* LUMO we compare the intensity of Resonant Raman vs. pure Auger channels. Note that this is of course a rather simplifying approach considering the complex wave-packet dynamics initiated by the resonant transition. We obtain a lifetime of the excited electron of $\geq$ 30 fs at resonance.

We conclude, that the azobenzene switch is significantly decoupled from the gold surface by the alkane chain and optically induced switching should be feasible.

[1] G. Hähner et al., J. Vac. Sci. Technol. A **10**, 2758 (1992).

[2] M. Zharnikov and M. Grunze, J. Vac. Sci. Technol. B **20**, 1793 (2002).

[3] T. Nägele, R. Hoche, W. Zinth, and J. Wachtveitl, Chem. Phys. Lett. **272**, 489 (1997); T. Fujino, S. Y. Arzhantsev, and T. Tahara, J. Phys. Chem. A **105**, 8123 (2001).

[4] H. Satzger et al., Chem. Phys. Lett. **396**, 191 (2004).

[5] B. Stiller et al., Materials Science and Engineering C **8**, 385 (1999).

[6] P. Feulner et al., Phys. Rev. Lett. **93**, 178302 (2004).

[7] O. Karis et al., Phys. Rev. Lett. **76**, 1380 (1996).

[8] W. Wurth, P. Feulner and D. Menzel, Phys. Scr. T41, 213 (1992); O. Björneholm et al., Phys. Rev. Lett. **68**, 1892 (1992).

Electrochemical formation of ultrathin CdS-films on Cu(111): An SXPS study using the SoLiAS Experimental Station at BESSY II

Sascha Hümann, Peter Broekmann and Klaus Wandelt,
Department of Surfaces and Interfaces, Institute of Physical and Theoretical Chemistry, University of Bonn

Ralf Hunger, Thomas Mayer and Wolfram Jaegermann
Surface Science Division, Institute of Materials Science,
Darmstadt University of Technology

Cadmium sulphide (CdS) thin films are widely used in a large number of solid-state device applications such as photoconductive detection, xerography, photovoltaic solar energy conversion and thin-film transistor electronics. In order to prepare these thin films various ways have been used, e.g. spray pyrolysis, dip techniques [1,2] and molecular beam epitaxy [3].

Our work deals with the deposition of ultrathin CdS films using the so-called electrochemical atomic layer epitaxy (ECALE). This method was established by Stickney and co-workers [4] as a low-cost procedure for the production of ultrathin compound semiconductor films of e.g. CdS, CdSe, CdTe and ZnS. This ECALE method is based on the alternating underpotential deposition (upd) of both constituents of the respective film. The deposition of submonolayer or monolayer amounts of a metal on an unlike metal substrate at electrode potentials more anodic than its reversible Nernst potential is well known under the term underpotential deposition (upd). The shift in the deposition potential is caused by an interaction of the adatoms with the substrate which is stronger than the adatom-adatom interaction that is relevant for the bulk deposition.

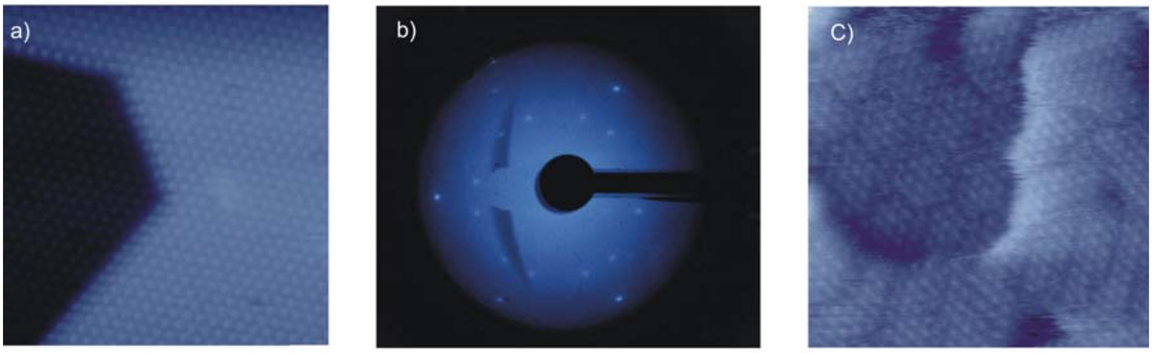

Fig. 1: *a) EC-STM image of the* $\sqrt{7}\times\sqrt{7}R19.1^\circ$ *sulphide layer, 17 nm x 17 nm, E = -375 mV*

b) LEED pattern of the $\sqrt{7}\times\sqrt{7}R19.1^\circ$ *sulphide layer at 116 eV*

c) EC-STM images of Cd upd dislocation network, 17 nm x 17nm, E = -375 mV

Fig. 1a) shows a representative electrochemical scanning tunneling (EC-STM) image of the $\sqrt{7}\times\sqrt{7}R19.1^\circ$ sulphide phase on Cu(111) in 5 mM H_2SO_4 at -375 mV vs. RHE (reversible hydrogen electrode). This phase is highly ordered and nearly defect free with lattice constants of a = b = 0.667 nm [6,7]. After emersion and air-free transfer of this sample into UHV as described below the LEED-pattern shown in Fig. 1b could be detected. It is consistent with the existence of $\sqrt{7}\times\sqrt{7}R19.1^\circ$-S domains on the surface which are rotated by 21.8° with respect to each other, in accordance with the in-situ EC-STM findings. This agreement proves the successful transfer of the electrochemically prepared sulphide layer and its stability in UHV. Underpotential deposition of one monolayer of Cd from a 0.1 mM $CdSO_4$ / 5 mM H_2SO_4 electrolyte at a potential of -375 mV onto the S-precovered Cu(111)-surface leads to an EC-STM image as shown in Fig. 1c. Both, the observed dislocation network being dominated by angles of 60° and the interatomic distance of 0.667 nm imaged within the domains, point to a structural "template" effect from the S-precovered Cu-substrate.

However, it is unclear which atoms are actually imaged within the domains of Fig. 1c. A previous study on the underpotential deposition of Cd onto a chlorine precovered Cu(111) electrode clearly showed an exchange between the preadsorbed Cl- and the postadsorbed Cd-layer leading to a final stacking of Cl/Cd/Cu(111) [8,9,10].

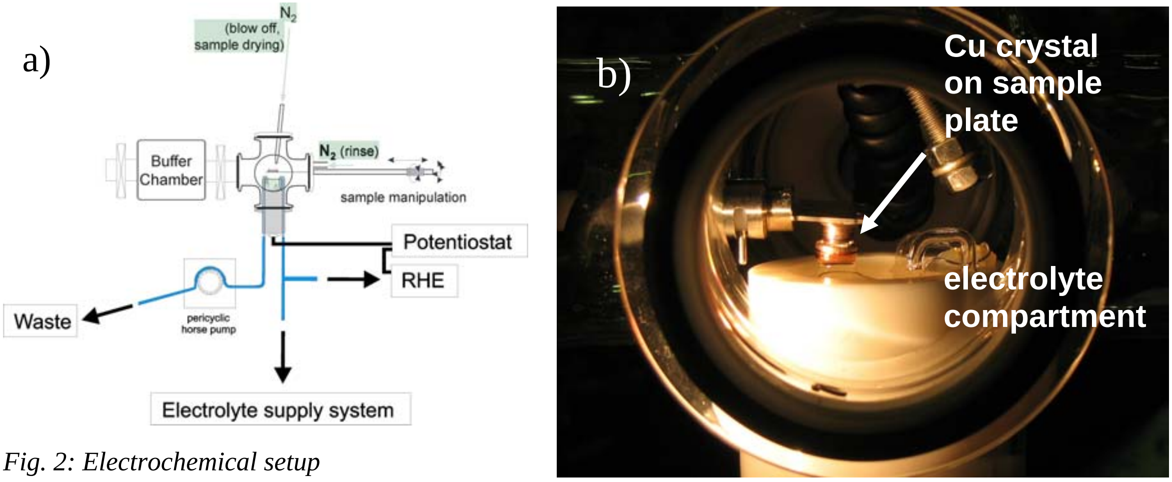

Fig. 2: Electrochemical setup

Thus, in order to answer the question how the domains of the present Cd-S bilayer are terminated we have preformed photoelectron spectroscopy measurements using the SoLiAS experimental station at the U49/2-PGM2 beamline at BESSY II [11]. Photoelectron spectra were recorded with a Phoibos 150 MCD 9 analyzer after each preparation step, using photon energies of 125, 245, 650, and 1040 eV, respectively, thereby varying the information depth of the data. All spectra were recorded in normal emission and are referenced to the Fermi level of a clean, sputtered Cu foil. The electrochemical processing was performed in an Ar purged ambient pressure electrochemistry cell from which a direct air-free transfer of the sample into the UHV chamber was possible (Fig. 2). The electrical contact between the working electrode, i.e. the Cu(111) crystal, and the Pt counter electrode through the electrolyte was established by a "hanging meniscus", while the reference electrode (RHE) was connected via a luggin capillary. After each electrochemical treatment and emersion of the electrode remainders of electrolyte clinging to the surface were blown off with argon before transferring the sample into UHV. In the following we concentrate on the S2p- and Cd3d core level spectra only.

First the clean Cu(111) surface was exposed at -375 mV to pure 5 mM H_2SO_4 solution, the supporting electrolyte in all further experiments. The corresponding S2p spectrum is displayed in Fig. 3a (1). The three observed doublets correspond to the spin-orbit split 2p states of sulphur in the form of some minor sulphide contamination ($S2p_{3/2}$ at 161.7 eV), sulphate ($S2p_{3/2}$ at 168.2 eV) and sulphite ($S2p_{3/2}$ at 166.15 eV), the latter being a reduction product due to irritation damage. The Cu(111) surface was then brought in contact at -375 mV with an electrolyte consiting of a 1:1 mixture of 5 mM H_2SO_4 and 10 mM Na_2S which leads to a stable $\sqrt{7}\times\sqrt{7}R19.1^{\circ}$-sulphide layer (see Fig. 1a and 1b). The corresponding S2p spectrum is shown in Fig. 3a (2) with the $S2p_{3/2}$ component at 161.9 eV. Only very weak sulphate induced intensity can be seen in this spectrum indicating that S^{2-} is bound more strongly than SO_4^{2-} and that only traces of electrolyte may have been transferred. In a third step the sulphide precovered surface was exposed at -375 mV to a mixture of 5 mM H_2SO_4 and 0.1 mM $CdSO_4$ in order to deposit an additional layer of Cd. The corresponding S2p- and Cd3d-spectra are shown in Fig. 3a (3) and Fig. 3b (3), respectively. Note that the S2p-spectrum shows both sulphide ($S2p_{3/2}$ at 161.75 eV) <u>and</u> sulphate ($S2p_{3/2}$ at 168.2 eV) with a minor sulphite component (see above). The binding energies of the spin-orbit split 3d-components of Cd are 405.5 ($d_{5/2}$) and 412.5 ($d_{3/2}$), respectively.

Finally, in order to explain the coexistence of sulphide- and sulphate-species in the presence of Cd on Cu(111) we have deposited a further layer of sulphide (from 5 mM H_2SO_4 and 10 mM Na_2S) onto the surface characterized by the spectra a(3) and b(3) in Fig. 3. After this only the signals of sulphide (161.6 eV) and Cd (405.35 eV) can be seen (Fig. 3a(4) and 3b(4)), the sulphate component has completely vanished.

A careful analysis of both binding energies and intensities of the series of SXPS spectra shown in Fig. 3 leads to the conclusions that sulphide displaces sulphate from the Cu(111) surface, that the first Cd layer resides <u>on</u> the underlying $\sqrt{7}$-sulphide layer, and that it is terminated by sulphate. This sulphate is again displaced by sulphide after exposure to the sulphide containing electrolyte in step 4. These conclusion are visualized by the ball models in Fig. 3c.

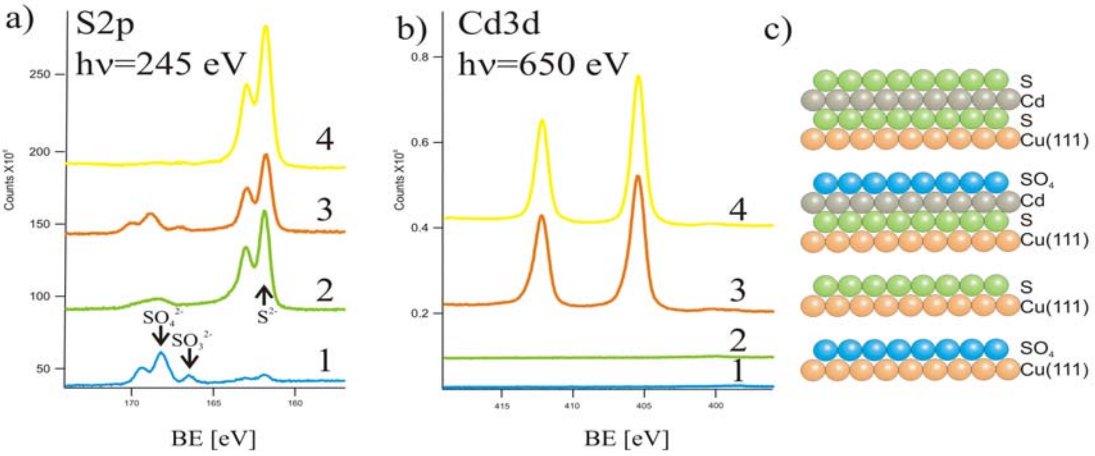

Fig. 3: SXPS spectra of a) S2p (hν = 650 eV) b) Cd3d (hν = 650 eV); c) Ball models for the different layers

References:

[1] M. K. Karanjai and D. Dasgupta, Mater. Lett. **4** (1986) 368

[2] M. K. Karanjai and D. Dasgupta, Thin Solid Films **155** (1987) 309

[3] K. L. Chopra and I. Kaur Thin Film Device Applications 1983 (New York: Plenum)

[4] T.E. Lister, J. L. Stickney, Applied Surface Science **107** (1996) 153-160

[5] S. Hümann, P. Broekmann and K. Wandelt to be published

[6] D. Wang, Q. M. Xu, L. J. Wan, C. Wang and C. L. Bai, Surf. Sci. **499** (2002)159-163

[7] A. Spänig, P. Broekmann and K. Wandelt, Electrochimca Acta **50** (2005) 4289-4296

[8] C. Stuhlmann, Z. Park, C. Bach and K. Wandelt, Electrochimca Acta **44** (1998) 993

[9] J. Hommrich, S. Hümann and K. Wandelt. Faraday Discuss. **121** (2002) 12 9-138

[10] S. Hümann, J. Hommrich and K. Wandelt, Thin Solid Films **428** (2003) 76-82

[11] T. Mayer, M. V. Lebedev, R. Hunger, and W. Jaegermann, Applied Surface Science **252** (2005) 31-42

Probing the Ground State Electronic Structure of a Correlated Electron System by QuantumWell States: Ag/Ni(111)

A. Varykhalov[1], A. M Shikin[2], W. Gudat[1], P. Moras[3], C. Grazioli[3], C. Carbone[3], O. Rader[1]

[1] *BESSY, Albert-Einstein-Str. 15, D-12489, Berlin, Germany*
[2] *St. Petersburg State University, 198904, St. Petersburg, Russia*
[3] *Istituto di Struttura della Materia, Consiglio Nazionale delle Ricerche, I-34012 Trieste, Italy*

The observation of quantized electron states in ultrathin metal films using photoelectron spectroscopy has meanwhile become an experimental routine [1]. Likewise, the theoretical description of the observed discrete electronic states on the base of simple models like the phase accumulation model [2] has considerably matured in recent years. We have recently focused our attention on changes of the quantization conditions given by the electronic structure of the metal substrate comparing the cases where a band gap of appropriate symmetry is present and where quantum well states are degenerate with bulk electronic states of the substrate [3]. The behaviour was described by a phase accumulation treatment extended by the different phase shifts in the gap and the degenerate energy regions. The quantum-well states appear so sensitive to the parameters of the substrate electronic structure that a determination of these parameters through the measurements of quantum well states of the overlayer appears possible.

Recently, this possibility has been demonstrated in an impressive way for Al films on Si(111) where the band dispersion of quantum well states in Al parallel to the film plane is strongly modified by the Si band gap [4]. It was also pointed out in Ref. 4 that in this way properties of the gound state of the substrate are probed.

Ni serves as the test case for metal systems in the present work since its band structure deviates strongly between the ground state as calculated by local density methods and band dispersions derived from angle resolved photoemission experiments on Ni [5]. One of these band parameters is accessible in normal emission from the (111) surface: The bottom of the Λ_1-band is predicted by local density theory at 2.7 eV binding energy whereas photoemission experiments give values between 1.7 and 1.8 eV [5].

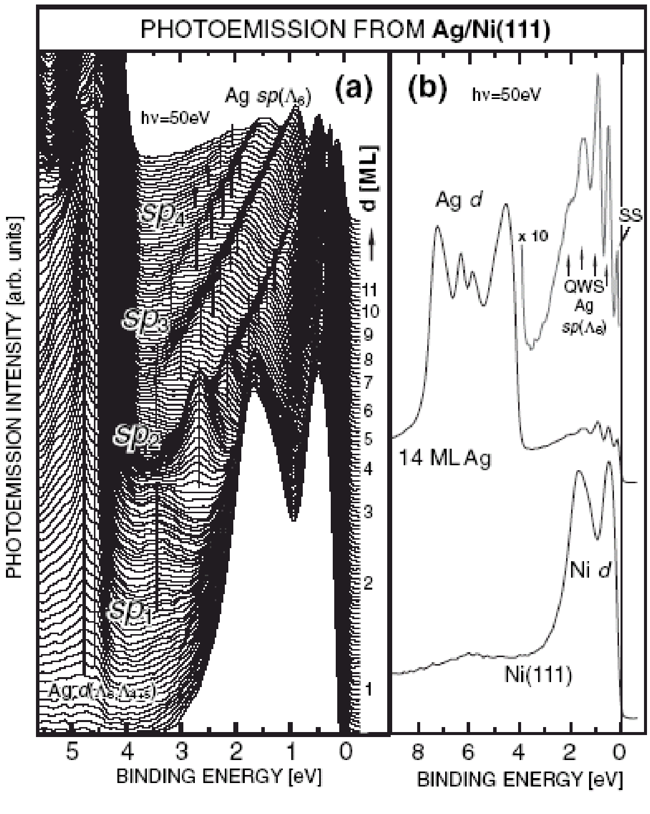

Fig. 1. Photoelectron spectra in normal emission of quantum well states in Ag film on Ni(111). (a) Energy range of Ag d and sp states. (b) Overview spectra of clean Ni(111) and 14 ML Ag.

Fig. 1. shows the behavior of quantum well states with the thickness of the Ag layer. The measured energy positions were introduced into Fig. 2 as circles. Within the phase accumulation model, we have varied the band gap parameters of the Ni substrate, the upper border of which corresponds to the bottom of the Ni Λ_1-band. A fit routine gave the gap parameters in Ni for which the Ag quantum well energies agree best with the experimental data. Fig. 2 shows for example the cases of the gap determined by direct photoemission from Ni (red), the local density gap (green, gap in gray), and the hypothetical case of an absent band gap (magenta). It is seen that the green curve for quantum number 1 ("sp_1") predicts a jump in energy in the region of 2.6 eV which is observed also in experiment. The close agreement is confirmed by the behaviour of states with higher quantum numbers. The behaviour of the sp_1 branch is highlighted in Fig. 3 where the energy difference of quantum well states for consecutive thicknesses (*n* monolayers and *n*+1 monolayers) is plotted.

It is concluded that the band dispersion of Ni in the ground state is (at a scale of ±150 meV) sufficiently described by standard local density theory. This means that the strong deviations observed in direct valence band photoemission of Ni are mainly an effect of the photoemission process [6].

[1] T.-C. Chiang, Surf. Sci. Rep. 39, 181 (2000).
[2] N.V. Smith, N. B. Brookes, Y. Chang, P. D. Johnson, Phys. Rev. B 49, 332 (1994).
[3] A. M. Shikin, O. Rader, G. V. Prudnikova, V. K. Adamchuk, W. Gudat, Phys. Rev. B 65, 075403 (2002).
[4] L. Aballe, C. Rogero, P. Kratzer, S. Gokhale, K. Horn, Phys. Rev. Lett. 87, 156801 (2001).
[5] See, e. g., O. Rader, W. Gudat in Landolt-Börnstein, New Series, Vol. 23C2 (edited by A. Goldmann, Springer, Berlin 1999).
[6] A. Varykhalov, A. M Shikin, W. Gudat, P. Moras, C. Grazioli, C. Carbone, O. Rader, Phys. Rev. Lett. 95, 247601 (2005).

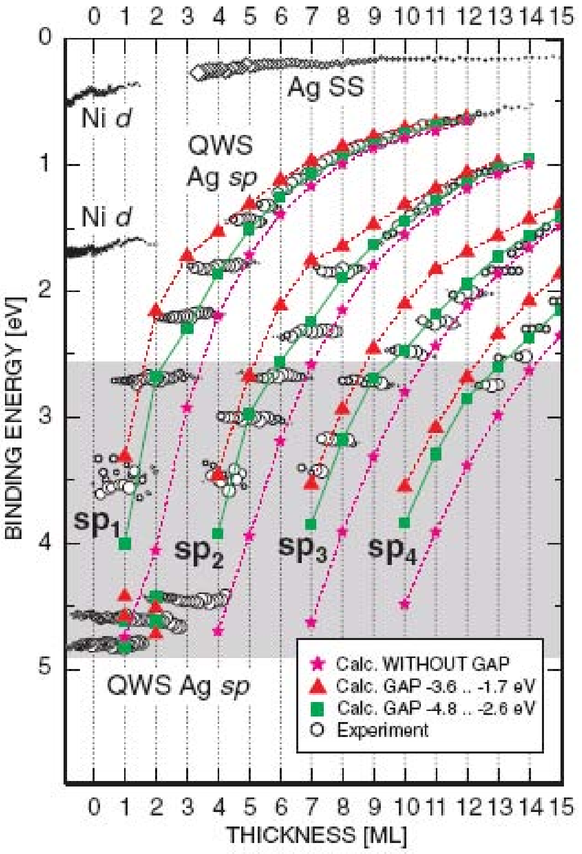

Fig. 2. Thickness dependence of measured quantum well states (black circles) and phase-accumulation-model values for different parameters of the Ni band gap (color).

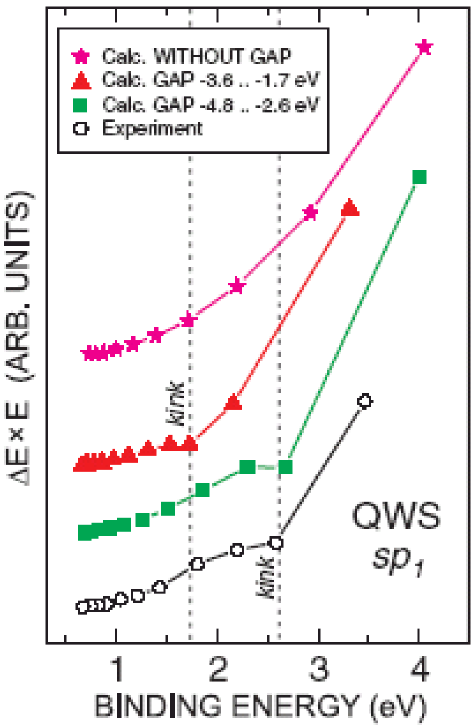

Fig. 3. Plot of the energy difference of consecutive quantum well states for the experiment and three different models. The parameters from local density theory (green) give best agreement.

Valence Band Structure of Intercalated Layered Transition Metal Dichalcogenides

M. Marczynski[1], *M. Helle*[1], *K. Rossnagel*[1], *and L. Kipp*[1]
P. Stojanov[2], *A. Tadich*[2], *E. Huwald*[2], *N. Janke-Gilman*[2], *R. Leckey*[2], *and J. Riley*[2]

[1]*Institut für Experimentelle und Angewandte Physik, Universität Kiel, D-24098 Kiel, Germany.*
[2]*Department of Physics, La Trobe University, Victoria 3086, Australia.*

An interesting and useful property of layered transition metal dichalcogenides (TMDCs) is their ability to intercalate electron donating atoms and molecules between the layers. This can be exploited, for instance, for storing alkali ions as in battery cells as well as for the controlled modification of the host electronic structure [1, 2, 3].

We have investigated the effect of Fe and Rb intercalation on the valence band structure of several TMDCs taking advantage of a second generation toroidal electron spectrometer for fast data acquisition [4] and present here angle-resolved photoemission measurements (ARPES) for VSe_2 / Rb_xVSe_2 taken at the wiggler beamline TGM4 (hν = 30 to 120 eV) and $TiTe_2$ / $Fe_{0.25}TiTe_2$ taken at beamline U125/2-SGM (hν = 50 to 100 eV).

The expectation is that iron/rubidium intercalation leads on the one hand to an electron transfer to the host material and on the other hand to a decoupling of the layers because of their increased separation.

The TMDCs, as well as their iron intercalates, are grown by chemical vapor transport. All of the crystals grow in the $1T$ structure with octahedral coordination of the transition metal. Cleavage in ultrahigh vacuum leads to clean and flat surfaces. Rubidium deposition on VSe_2 is achieved with a carefully outgased SAES Getter source in two steps. The distance to the sample was 3 cm and the evaporation time 10 minutes in both steps at a current of 6 A.

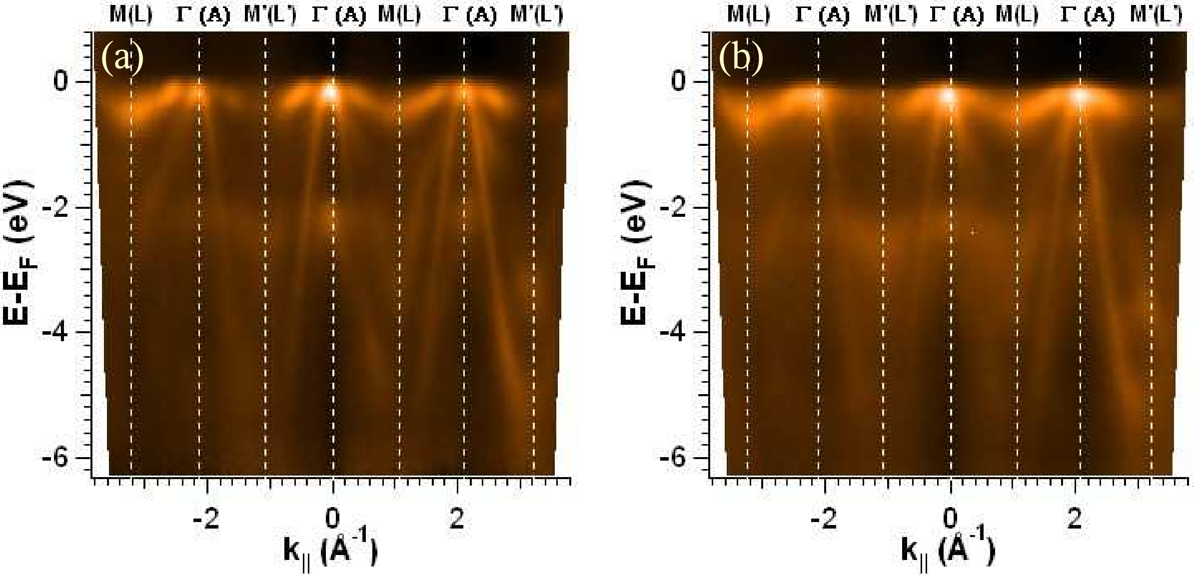

Figure 1: ARPES spectra of VSe_2 taken along the ΓM direction before (a) and after (b) the first adsorption of rubidium at a photon energy of 60 eV. Dashed lines indicate high-symmetry points in the Brillouin zone.

In figure 1(a) we present ARPES spectra of pristine VSe_2. The V 3d$_{z^2}$ band crosses the Fermi energy at almost halfway between Γ and M and is clearly separated from the highest Se 4p bands that touch the Fermi energy at the Γ point. After rubidium adsorption (fig. 1(b)) this separation is hardly resolvable. In terms of the rigid band model we can explain this with an electron transfer that occurs from the adsorbed alkali metal rubidium to the originally half filled V 3d$_{z^2}$ band. This leads to a movement of the Fermi energy crossing towards the Γ point and closer to the Se 3p bands.

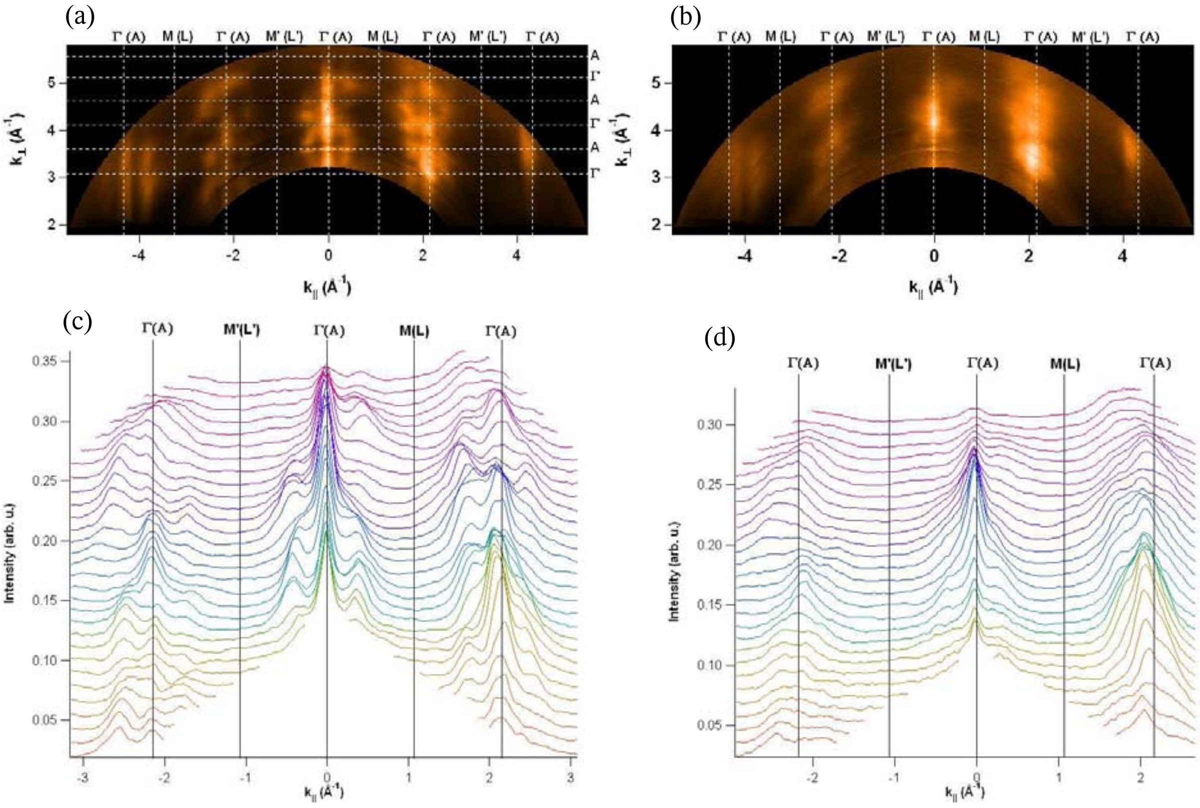

Figure 2: CIS measurements of VSe$_2$ taken along the ΓM direction before (a+c) and after (b+d) the first adsorption of rubidium. (c) and (d) show line profiles extracted from (a) and (b), respectively. Dashed lines indicate high-symmetry points in the Brillouin zone. The parameters of the measurement are: hν = 30 eV ... 120 eV, V$_0$ = 14.7 eV, E$_{initial}$ = E$_{Fermi}$.

To investigate if rubidium atoms intercalate into the van der Waals gaps of VSe$_2$ and thereby decouple the layers we have taken constant initial state (CIS) measurements at the Fermi energy along high-symmetry directions. A layer decoupling would result in a reduction of the band dispersion perpendicular to the layers. Figure 2 shows our results for the ΓM direction. Before rubidium evaporation (fig. 2(a)+(c)) there is a clearly visible dispersion of the V 3d$_{z^2}$ band. (The inner potential V$_0$ of VSe$_2$ could be experimantally determined to be 14.7 eV.) After evaporation (fig. 2(b)+(d)) the band dispersion is reduced, reflecting weaker interlayer interactions.
Furthermore, we present the effects of iron intercalation on the electronic structure of TiTe$_2$ (fig. 3). Again an electron transfer occurs from the iron atoms to the Ti 3d$_{z^2}$ band which leads to larger electron pockets around the M points (see Fermi surface maps in figure 3(a)+(b)). In contrast to rubidium intercalation, no apparent reduction of the band dispersion perpendicular to the layers is observed in our CIS measurements (fig. 3(c)+(d)). This could be due to a stronger interaction between the Fe 3d and Ti 3d states which acts against the decoupling of the layers.

This work was supported by the DFG Forschergruppe 353.

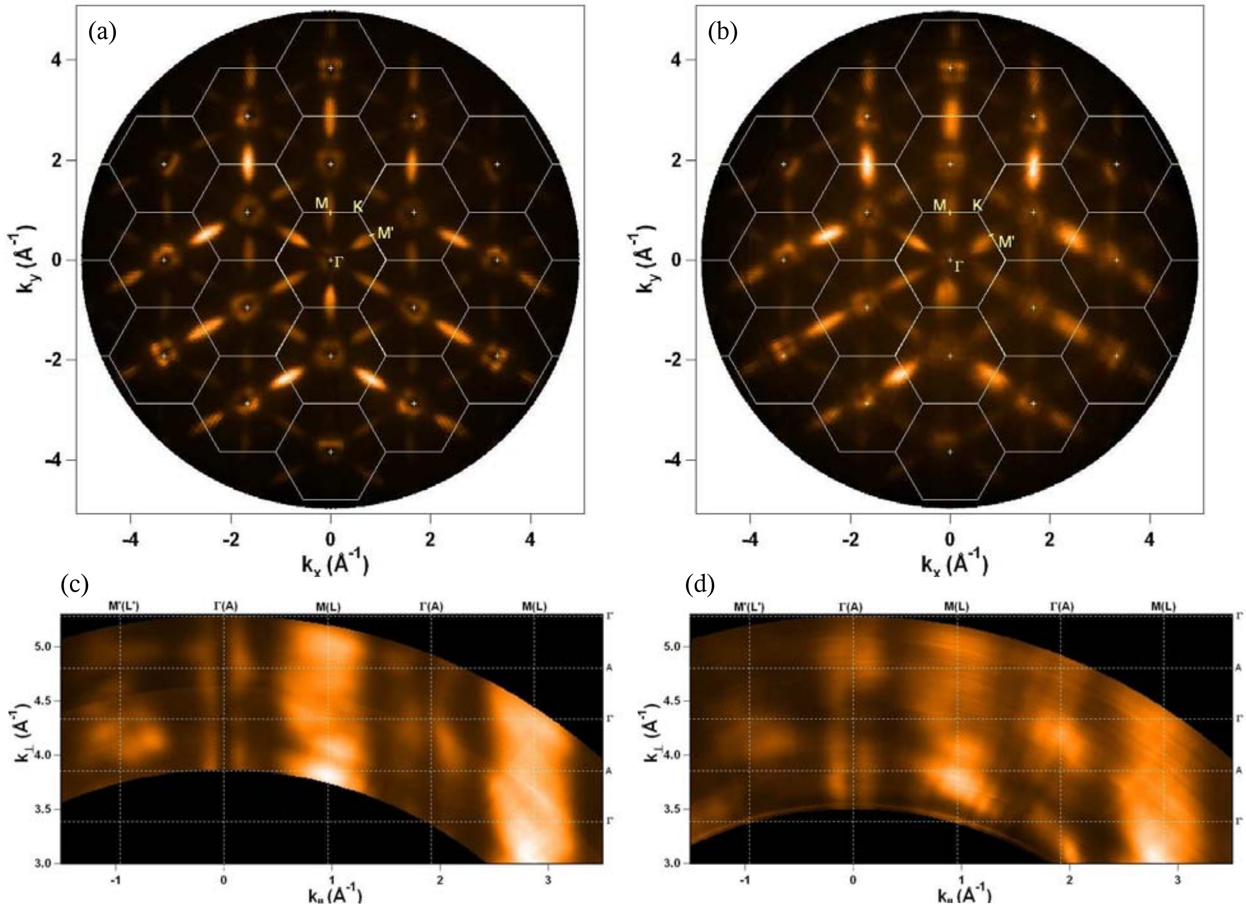

Figure 3: Fermi surface maps of $TiTe_2$ (a) and $Fe_{0.25}TiTe_2$ (b) taken at a photon energy of 100 eV. Yellow lines represent the Brilloin zone boundaries. The CIS measurements of $TiTe_2$ (c) and $Fe_{0.25}TiTe_2$ (d) are taken at photon energies between 50 eV and 100 eV with $E_{initial} = E_{Fermi}$. To calculate the $k_\perp$-values, an inner potential of 12 eV was assumed.

References

[1] H. I. Starnberg, H. E. Brauer, Phys. Rev. B 58, 10031 (1998).

[2] R. Adelung, J. Brandt, K. Rossnagel, O. Seifarth, L. Kipp, M. Skibowski, C. Ramirez, T. Strasser, W. Schattke, Phys. Rev. Lett. 86, 1303 (2001).

[3] K. Rossnagel, E. Rotenberg, H. Koh, N. V. Smith, L. Kipp, Phys. Rev. Lett. 95, 126403 (2005).

[4] A. Tadich, L. Broekman, E. Huwald, R, Leckey, J. Riley, T. Seyller, L. Ley: BESSY Annual Report 2003, p. 515.

The Fermi surface of the single CuO_2-layer of Pb-Bi2201

L. Dudy, B. Müller, B. Ziegler, L. Lasogga, A. Krapf, H. Dwelk, C. Janowitz, and R. Manzke
Humboldt-Universität zu Berlin, Institut für Physik

Among the essential features determining the macroscopic electronic properties of high temperature- superconductors the Fermi surface (FS) topology plays a key role. Over the last years important progress has been made in highly resolved photoemission on various HTc-materials, from which $Bi_{2-y}Pb_ySr_2CaCu_2O_{8+\delta}$ (Pb-Bi2212) is the most commonly studied. For the investigation of the intrinsic features it was found more appropriate to study crystals with partial substitution of Bi by Pb to suppress the $(\approx 1\times 5)$ superstructure in the BiO- planes, which lead otherwise to unwanted diffraction replicas [1].

The situation in the one- CuO_2 layer material $Bi_{2-y}Pb_ySr_{2-x}La_xCuO_{6+\delta}$ (Pb-Bi2201) is not very different from the two-layer material. Here it is also possible to suppress the $(\approx 1\times 5)$ superstructure by partial substitution of Bi by Pb. For the study presented here single crystals of Pb-Bi2201 were grown out of the stoichiometric melt, similar as in [2]. The samples were characterized by energy dispersive x-ray analysis (EDX), susceptibility measurements and LEED. The crystals studied had a typical Pb-content of $y = 0.4$ and a typical La-content of $x = 0.4$ giving *optimally doped* samples with a hole-concentration per CuO_2 - layer of $n_h = 0.15 \pm 0.02$ [3] and a transition temperature T_c=32K. Regarding the LEED-patterns of fig. 1, the high crystal quality is obvious from the sharp spots, and no sign of a superstructure is visible over a sufficient large energy range. In addition, the homogeneity of the samples was controlled by moving the electron beam over the sample surface.

The high-resolution photoemission measurements have been carried out with a Scienta SES-100 analyzer at the U125/2 10m-NIM undulator beamline at BESSY [4]. All data were taken at 22eV photon energy and a sample temperature of 25 K. The overall energy resolution was 18 meV. The angular resolution was below 0.2°. The Fermi level has been determined by measuring the Fermi edge of an evaporated Au film. The normalized photoemission spectra are shown on Fig. 2. The upper inset shows the first Brillouin zone and its orientation relative to the Cu-O bonds of the CuO_2 – layer. The electrical field vector of the synchrotron light was orientated parallel to the line ΓM as indicated by the blue arrow in the Brillouin zone of fig. 2.

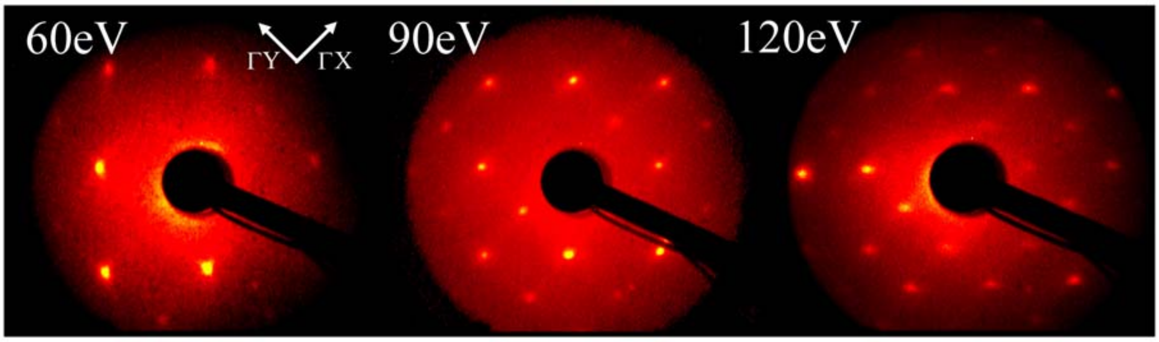

Fig. 1: LEED-patterns of optimally doped $Bi_{2-y}Pb_ySr_{2-x}La_xCuO_{6+\delta}$ with x=0.4 and y=0.4 for electron energies of 60, 90 and 120 eV. The peaks are quite sharp at all energies. No sign of any superstructure is visible

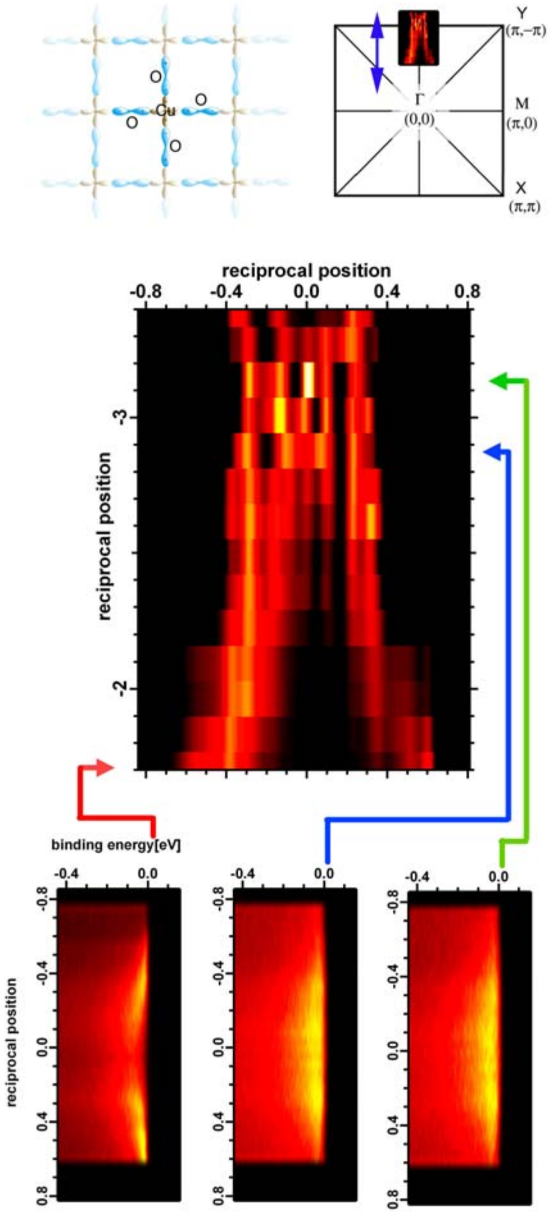

Fig.2: Upper panel: First Brillouin zone and its orientation relative to the Cu-O bonds of the CuO_2 – layer. The direction of the electrical field vector used in the photoemission experiments is indicated by an arrow. **Middle Panel:** The resulting Fermi map computed by integrating the spectra in an energy window of ±10meV around the Fermi-level. For better visualization the density of points along the horizontal line in the Fermi-map were doubled by interpolation with a cubic spline. Typical spectra are shown in the **lower** part of the figure. The colored lines near the spectra point to the position of the integrated spectra in the Fermi map.

The spectra in the lower part of Fig. 2 at different Brillouin zone locations clearly show the typical parabolic-like narrow band near the Fermi level. We computed the Fermi map by integrating the spectra over an energy window of $\pm 10\,meV$ about the Fermi-level. It shall be remarked that this window has the size of the resolution. The resulting Fermi map is shown in fig. 2. An anisotropy in the intensity at different Brillouin zone locations with respect to the symmetry direction ΓM is notable. The momentum distribution curves (MDC) near Γ are less symmetric than near M. Between the main FS other features are visible.

We simulated the FS assuming the main signal of the photoelectrons is disturbed by a *modulated* charge distribution. According to the information gained by LEED, the modulation length in real space should be larger than the typical coherence length of LEED of ~10-30 nm. The intensity of the Fermi surface is then computed by using a intensity function $I_0(k,\omega=0,T)$. This intensity function is weighted by a factor (N_i) and shifted by a reciprocal wave vector k_S. For example for a $(\pi/|k_S|)$x1 like superstructure one gets:

$$\begin{aligned} I(k,\omega=0,T) &= N_0\, I_0(k,\omega=0,T) \\ &+ N_1\, I_0(k+k_S,\omega=0,T) \\ &+ N_2\, I_0(k-k_S,\omega=0,T) \end{aligned}$$

Please note that only the first order shift of k_S is taken into account. Higher orders would result in a ribbon-like structure along the k_S - direction [5]. To simulate the $I_0(k,\omega=0,T)$ we use a simplified approach of [6]. We started with the intensity of the photoemission signal given as the Fermi function times the spectral function (the matrix element was set constant): $I_0(k,\omega,T) \approx f(\omega,T)\cdot A(k,\omega,T)$. The spectral function is due to [6] chosen as

$$A(k,\omega,T) = \frac{1}{\lambda}\frac{\Sigma}{(\omega-\varepsilon(k))^2+\Sigma^2}$$

,

where we set $\lambda^{-1} = 1\,eV$. The imaginary part of the self energy Σ is not only energy dependent but also weakly temperature dependent:

$$\Sigma = \sqrt{(\alpha\omega)^2 + (\beta T)^2} \quad .$$

The energy and temperature dependence is controlled by the constants $\alpha = 1$ and $\beta = 1 meV\,K^{-1}$, respectively. The constants α,β and λ are only correct within an order of magnitude. The dispersion relation is the bare temperature independent tight-binding-like dispersion $\varepsilon(k) = \Delta E - 2t(\cos(k_x) + \cos(k_y)) + 4t'\cos(k_x)\cos(k_y) - 2t''(\cos(2k_x) + \cos(2k_y))$. From a fitting routine the values are $\Delta E = 0.18\,eV; t = 0.17\,eV; t' = 0.015\,eV; t'' = 0.039\,eV$. In Fig. 3 two computed FS's are compared with the measured one. Obviously the experimental FS is asymmetric with respect to ΓM, showing that some superstructure must be superposed. Therefore the FS in the middle is calculated with a 7x1 superstructure with a weight of 40% between the refracted and the main band. For the FS on the right a 7x1 superstructure with weight of 40% and a 1x7 with weight of 20% are included. Note that possible matrix-element effects due to the polarization of the incident light are not taken into account.

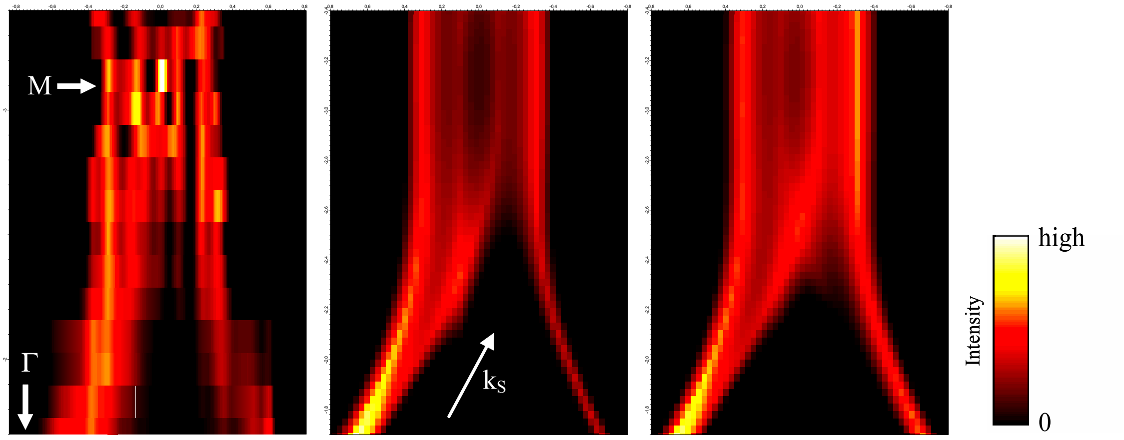

Fig. 3: Measured FS **(left)** compared with **(middle)** the simulated FS with a 7x1 modulation and **(right)** with a 40% weighted 7x1 and a 20% weighted 1x7 modulation.

To conclude: We investigated single crystals of optimally doped Pb-Bi2201. The LEED patterns show no sign of superstructure while the measured Fermi surface is clearly of asymmetric shape. It can be theoretically reproduced by a modulation of about 7x1 or 7x7. Such a modulation can have its origin in the electronic structure *or* the crystal structure. This has to be organized in domains larger than the typical coherence length of LEED.

We would like to thank the staff of BESSY and in particular Dr. G. Reichardt for excellent support during our measurements.

[1] H. Ding *et al.* , Phys. Rev. Lett. 76, 1533 (1996)
[2] I. Matsubara *et al.* , Appl. Phys. Lett. **58**, 409 (1991)
[3] L. Lasogga diploma thesis, Humboldt Univ. (2005) and
M. Schneider doctor thesis, Humboldt Univ. (2005)
[4] G. Reichardt *et al.* , NIM A 467,462 (2001)
[5] M.S. Golden et al., Physica C **341-348**, 2099 (2000)
[6] A.A. Kordyuk *et al.*, Phys. Rev. B **67**, 064504 (2003) and cond-mat/0208418

Cobalt and manganese valence states in complex oxides $La_{0.75}Ca_{0.25}Co_{0.5}Mn_{0.5}O_3$

V. R. Galakhov[1]*, A. S. Shkvarin[1], A. F. Takács[2], M. Raekers[2], M. Prinz[2], M. Neumann[2], A. V. Korolyev[1], G. V. Bazuev[3], O. I. Gyrdasova[3], T. I. Chupakhina[3], D. V. Vyalykh[4], Yu. S. Dedkov[4], and S. L. Molodtsov[4]

[1]*Institute of Metal Physics, Russian Academy of Sciences —*
Ural Division, 620041 Yekaterinburg GSP-170, Russia
[2]*Universität Osnabrück — Fachbereich Physik, D-49069 Osnabrück, Germany*
[3]*Institute of Solid State Chemistry, Russian Academy of Sciences —*
Ural Division, 620041 Yekaterinburg GSP-145, Russia
[4]*Institut für Festkörperphysik, Technische Universität Dresden, D-01062 Dresden, Germany*

Transition-metal perovskites have been known to exhibit varieties of electrical properties, from a large-gap insulator to a metal, and of magnetic properties such as paramagnetism, ferromagnetism, antiferromagnetism, and diamagnetism. $LaMnO_3$ is an antiferromagnetic insulator with high-spin state Mn^{3+} ions ($3d^4$, $S = 2$). When doped with divalent cations, the valence of Mn becomes mixed $3+/4+$.

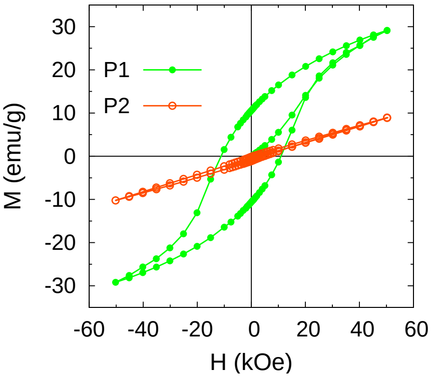

Figure 1: Magnetization hysteresis loops of the phases P1 and P2 of $La_{0.75}Ca_{0.25}Co_{0.5}Mn_{0.5}O_3$ at 2 K.

The mixed-valence $La_{1-x}A_xMnO_3$ compounds undergo a phase transition to a ferromagnetic metallic state and exhibit the colossal magnetoresistance effect near room temperature. Ferromagnetism is also induced in $LaMnO_3$ by the substitution of other transition metal such as Co, Ni, etc., for Mn [1].

Goodenough *et al.* [1] have reported that Mn^{3+}–O–Mn^{3+} superexchange interaction are responsible for ferromagnetism in the series $LaMn_{1-x}Co_xO_3$ and that the trivalent Co ions are present in their low-spin state. On the other hand, X-ray absorption and photoelectron spectral studies [2, 3] have showed that dopant Co in manganese perovskites is divalent, the same as in CoO and the Mn ions are Mn^{3+}–Mn^{4+} mixed valence.

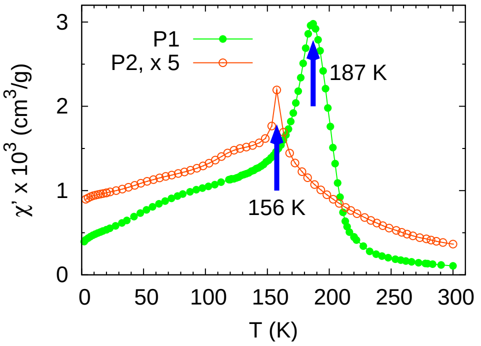

Figure 2: The temperature dependence of real part of the *ac*-susceptibility χ' of the two phases of $La_{0.75}Ca_{0.25}Co_{0.5}Mn_{0.5}O_3$.

It has been shown that two different phases of $La(CoMn)_{0.5}O_3$ can be synthesized in single-phase form and that the spin states of Mn and Co are different in the two different phases [4]. The phase obtained after annealing at 700 °C (P1) undergoes to the ferromagnetic state at the Curie temperature of $T_c \approx 230$ K. The phase synthesized at 1300 °C (P2) has the Curie temperature $T_c \approx 150$ K. Core-level Mn and Co $2p$ X-ray photoelectron spectroscopic studied at room temperature and magnetical measurements indicate that the spin states of Mn and Co are different in these two phases of $La(MnCo)_{0.5}MnO_3$. Mn and Co ions are as in their trivalent states with Co in the low-spin configuration in the P1 phase and as Mn^{4+} and high-spin Co^{2+} in the P2 phase [5, 6].

---

*e-mail: galakhov@ifmlrs.uran.ru

Here we report the first magnetical and X-ray absorption spectroscopy studies of the two phases of $La_{0.75}Ca_{0.25}Co_{0.5}Mn_{0.5}O_3$. The phase $P1$ was prepared by a citrate method at 700 °C. The sample P2 of $La_{0.75}Ca_{0.25}Co_{0.5}Mn_{0.5}O_3$ was synthesized by a ceramic method at 1300 °C. The oxygen content of the samples was determined by means of a thermogravimetric analysis during reduction in hydrogen flow at 900 °C.

Both phases, P1 and P2 show ferromagnetism (see magnetization hysteresis loops $M(H)$ in Fig. 1). The samples P1 and P2 show magnetic transitions at $T_C = 187$ K and 156 K, as one can see in Fig. 2 where the temperature dependence of real part of the *ac*-susceptibility χ' is presented.

At temperatures of 230–300 K, magnetical susceptibility χ follows the Curie-Weiss low $\chi = C/(T - \Theta)$. From the measurements of $\chi(T)$, the following values of effective magnetic moments, p_{eff} have been estimated: 4.67 μ_B and 4.32 μ_B for the phases P1 and P2, respectively. It is not possible to estimate separately valence states of Mn and Co ions in these two phases using these effective magnetic moments only. In order to determine valence states of Mn and Co ions, we have used the method of X-ray absorption spectroscopy.

The Co $2p$ and Mn $2p$ x-ray absorption spectra (XAS) of the $La_{0.75}Ca_{0.25}Mn_{0.5}Co_{0.5}MnO_3$ oxides were carried out at BESSY at the Russian-German Beam Line. The spectra were normalized to the incident current as measured from a gold grid located at the entrance chamber. While P1 and P2 exhibit paramagnetic-to-ferromagnetic transition at T_C, the spectra have been measured at about 100 K (at the temperature lower than T_C) and at about 500 K also (much more than T_C).

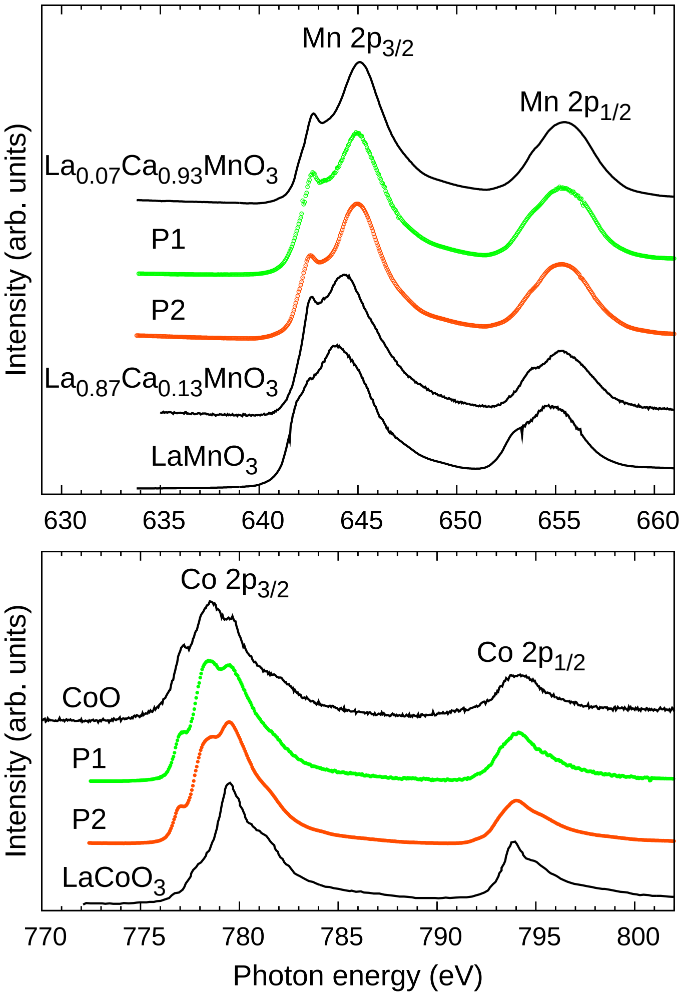

Figure 3: Mn $2p$ and Co $2p$ X-ray absorption spectra of the phases P1 (prepared at 700 °C) and P2 (prepared at 1300 °C) of $La_{0.75}Ca_{0.25}Mn_{0.5}Co_{0.5}MnO_3$. For comparison, Mn $2p$ and Co $2p$ spectra of some manganites, CoO and $LaCoO_3$ are shown. The spectrum of a single crystal of $LaCoO_3$ is reproduced from Ref. [2].

Figure 3 (a) shows the Mn $2p$ X-ray absorption spectra of two phases, P1 and P2, of $La_{0.75}Ca_{0.25}Mn_{0.5}Co_{0.5}MnO_3$ in comparison with spectra of manganites. The maxima of the spectra of the P1 and P2 phases are shifted toward the higher photon energy by ~ 1 eV. This shift arises due to the higher absorption energy of Mn^{4+} ions. Therefore, valence state of manganese ions in the P1 and P2 phases of $La_{0.75}Ca_{0.25}Co_{0.5}Mn_{0.5}O_3$ is closer to 4+ than to 3+.

In figure 3 (b), the Co $2p$ X-ray absorption spectra of the samples P1, P2, CoO, and $LaCoO_3$ are presented. The spectrum of $LaCoO_3$ is reproduced from Ref. [2] and could be served as a reference compound of Co^{3+} ions in the low-spin state. From the comparison of the Co $2p$ spectra of P1 and P2 with those of CoO (Co^{2+} ions) and $LaCoO_3$ (Co^{3+} ions), we have estimated the Co^{2+}/Co^{3+} concentrations as $(0.82 \pm 0.4)/(0.18 \pm 0.4)$ and $(0.64 \pm 0.4)/(0.36 \pm 0.4)$ for the phases P1 and P2, respectively. While the magnetic moment of Co^{3+} in the low-spin state is equal to zero, an increase of the relative Co^{3+} amounts should lead to lowering the effective magnetic moments $p_{\rm eff}$, as it has been found in our measurements of the temperature dependence of the magnetic susceptibility $\chi(T)$.

Figure 4 shows Co $2p_{3/2}$ X-ray absorption spectra of the phases P1 and P2 in ferromagnetic states (measurements at $\sim$ 100 K) and paramagnetic states (measurements at room temperature and at $\sim$ 500 K). One can see that the ferromagnetic-to-paramagnetic transition is accompanied by an increase of the Co^{2+}-ion concentration. On the other hand, an increase of the temperature from 300 K to about 500 K is accompanied by the increase of amount of Co^{2+} ions. For the sample P1, the temperature changes in the Co $2p$ spectra are less pronounced in comparison with those for the sample P2. It means that concentration of Co^{2+} ions in P1 has achieved saturation. Heating does not change Mn $2p$ spectra of the both phases. The observed behavior of the temperature dependence of the Co^{2+}/Co^{3+} concentrations found in the X-ray absorption spectra may be due to the polaron formation in La$_{0.75}$Ca$_{0.25}$Co$_{0.5}$Mn$_{0.5}$O$_3$ and this needs further detailed investigations.

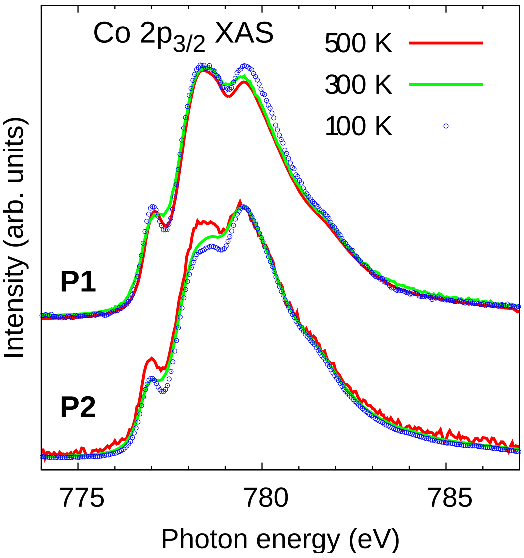

Figure 4: Co $2p_{3/2}$ X-ray absorption spectra of the phases P1 and P2 of La$_{0.75}$Ca$_{0.25}$Co$_{0.5}$Mn$_{0.5}$O$_3$ measured at room temperatures (green lines), heated at about 500 K (red lines) and cooled down to about 100 K (blue symbols).

This work was supported by the Russian Foundation for Basic Research (Grants Nos 04-03-96092-Ural and 05-03-32355), by the grant “Co-operation between the Ural and Sibirian Divisions of the Russian Academy of Sciences”, the Research Council of President of the Russian Federation (Project NSH-4192.2006.2), and by the bilateral Program “Russian-German Laboratory at BESSY”. V. R. G. acknowledges financial support by BESSY. A. F. T. acknowledges financial support by the Ph.D. program of Lower Saxony, Germany.

[1] J. B. Goodenough, A. Wold, R. J. Arnott, and N. Menyuk, Phys. Rev. **124**, 373 (1961).

[2] J.-H. Park, S.-W. Gheon, and C. T. Chen, Phys. Rev. B **55**, 11072 (1997).

[3] M. C. Falub, V. Tsurkan, M. Neumann, I. O. Troyanchuk, V. R. Galakhov, E. Z. Kurmaev, H. H. Weitering, Surface Science **53**, 488 (2003).

[4] P. A. Joy, Y. B. Khollam, and S. K. Date, Phys. Rev. B **62**, 8608 (2000).

[5] V. L. J. Joly, P. A. Joy, S. K. Date, and C. S. Gopinath, J. Phys.: Condens. Matter **13**, 649 (2001).

[6] V. L. J. Joly, Y. B. Khollam, P. A. Joy, C. S. Gopinath, and S. K. Date, J. Phys.: Condens. Matter **13**, 11001 (2001).

Preferential CO oxidation in H_2 (PROX) on Pt/CeO_2 catalyst, high-pressure XPS and in-situ DRIFTS study

D. Teschner[1], E. Vass[1], S. Zafeiratos[1], P. Schnörch[1], M. Hävecker[1], A. Knop-Gericke[1], H. Sauer[1], J. Kröhnert[1], F. Jentoft[1], R. Schlögl[1], O. Pozdnyakova[2], A.Wootsch[2]
[1]Fritz-Haber-Institut der Max-Planck-Gesellschaft, Faradayweg 4-6, D-14195 Berlin
[2]Institute of Isotopes, CRC, HAS, POB 77, Budapest, H-1525, Hungary

Aim of the work and scientific background:

The CO content of hydrogen feed to proton exchange membrane fuel cells (PEMFC) must be kept under 1-100 ppm for their proper operation [1]. This can be achieved by using catalysts able to selectively oxidize CO in the presence of excess hydrogen (PROX). Ceria supported Pt catalysts show remarkable activity in the PROX reaction [2]. In order to gain further insight into the mechanism of the PROX reaction on Pt/CeO_2 catalyst, catalytic tests, high-pressure XPS, in-situ DRIFTS and HRTEM techniques were utilized. In this report we summarize the main results obtained using Pt/CeO_2 catalysts [3]. Some preliminary experiments were also conducted with PtSn and Au/FeO_2 samples (they are also promising candidates for good CO removal performance); however they will be investigated in details during our forthcoming beamtime in March.

Results

Activity pattern of Pt/CeO_2 measured by different techniques (flow reactor, in-situ DRIFT, both at p=atm, and in high-pressure XPS at p=1 mbar) showed similar trends: a maximum selectivity towards CO oxidation at T=360-370 K decreasing with increasing temperature.

Bulk metallic, pronounced adsorbate-induced surface Pt, interface Pt and a small amount of oxidized Pt sites were shown by high-pressure XPS under PROX conditions (Figure 1). The pre-oxidized ceria surface was strongly reduced in pure H_2 but significantly re-oxidized under PROX conditions (i.e. O_2+CO in high excess of hydrogen) at T=358K (Figure 2). The remaining small amount of Ce^{3+} decreased with increasing temperature. HRTEM found well-crystallized CeO_2 particles (8-10 nm) in the case of activated

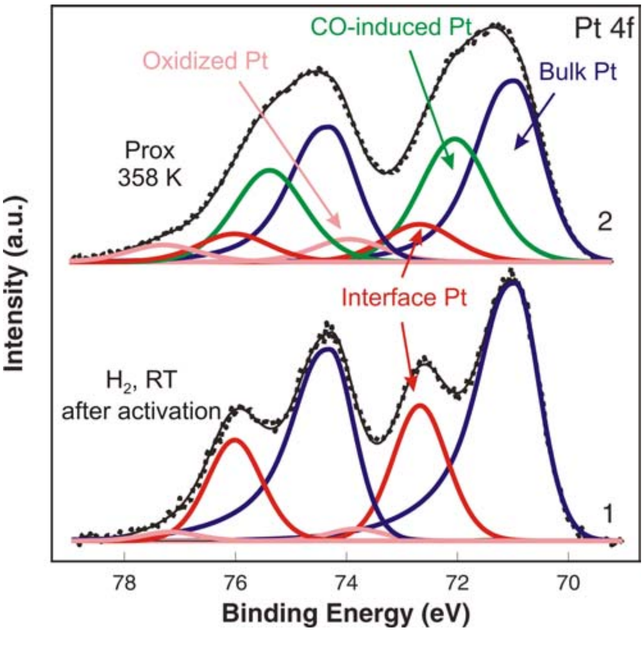

Fig. 1. Pt 4f region of 5% Pt/CeO_2 at different conditions: **1**, in 0.48 mbar H_2 at RT (after O_2 activation at 573 K); **2**, in ~0.5 mbar PROX mixture at 358 K

(pre-oxidized) sample that transformed to an oxygen deficient ceria super-cell structure ($CeO_{1.695}$) after PROX reaction. Metallic Pt particles (2-3 nm) and small (0.5-0.6 nm) Pt clusters were indicated by HRTEM. These findings were in accordance with the variations in relative intensity of the corresponding Pt-CO bands (in-situ DRIFTS). Different types of carbonate and formate species were detected (XPS and DRIFTS). The negative correlation between formate species and CO_2 yield clearly indicates that formates are not intermediates in the PROX reaction. Moreover their accumulation near the metallic particles is suggested at high temperature (T=523 K). Broad, however not resolvable structure in the OH stretching region could be found by DRIFTS in the PROX reaction mixture indicating significant amount of adsorbed water (identified also in XPS) in a hydrogen-bonded structure. Its amount decreased with increasing temperature, with parallel decrease in the selectivity towards CO oxidation. Thus, the presence of adsorbed surface water seems to suppress hydrogen oxidation while CO oxidation still takes place, as the metallic particles are covered by CO (DRIFTS). The direct contribution of surface water in a low-temperature water-gas-shift (LTWGS) type reaction in the PROX mixture is proposed [4] as follows (Figure 1):

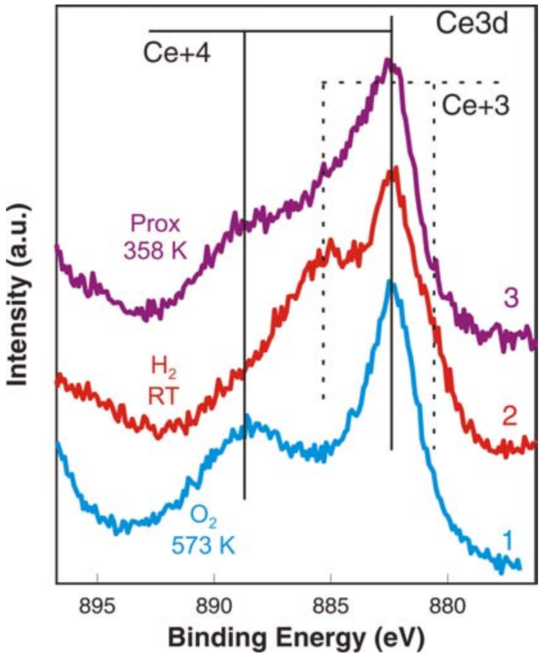

Fig. 8. Part of the Ce 3d region of 5% Pt/CeO_2 at different conditions: **1**, in 0.5 mbar O_2 at 573 K; **2**, in 0.48 mbar H_2 at RT; **3**, in ~0.5 mbar PROX mixture at 358 K

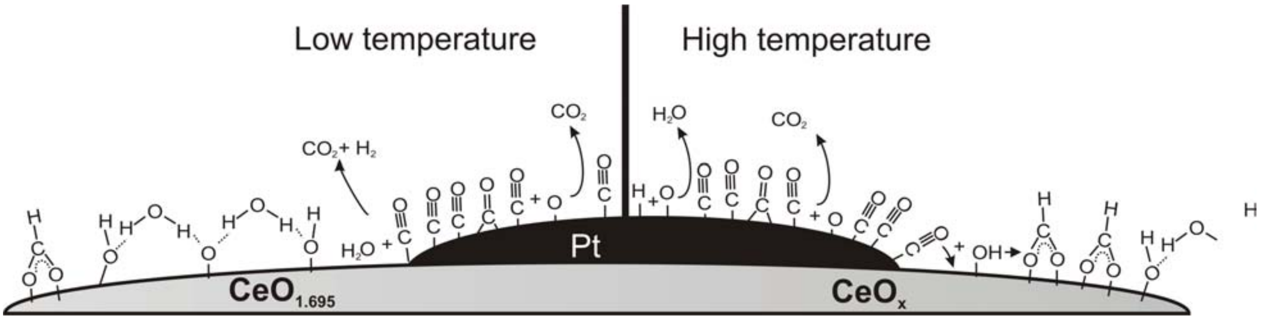

Fig. 1: Proposed model describing the reactions happening on Pt/ceria in the PROX reaction mixture at low and high temperature.

At low temperature, a significant amount of water accumulates on the ceria, via spillover of adsorbed hydrogen atoms from the platinum. This water reacts in LTWGS reaction with linearly bonded CO at the Pt/ceria interface, forming CO_2 and hydrogen. The by-product hydrogen before desorption (or another hydrogen molecule from the gas-phase) regenerates the water structure on the support in the close vicinity of Pt. This adsorbed water, which ensures that CO is linearly bonded to the interface Pt site, might be stabilized by the oxygen-deficient character of ceria ($CeO_{1.695}$). At higher temperature the hydrogen-bonded structure decomposes and water desorbs allowing the liberation of coordinatevely unsaturated (cus) Ce^{n+} sites at the interface. Thus CO can be adsorbed at the interface in a bridged-like manner (both found in DRIFTS and XPS), oxygen coordinating to this cus site. The adsorbed CO can then dissociate or hop to the ceria and react with the first OH group forming formates. The latter species are stable on the ceria at this condition and might block the way of still existing surface water to the Pt particles. The negative correlation of surface formates and CO_2 yield strengthens the proposed model.

To sum up our results point to the beneficial effect of surface water, which suppresses further hydrogen oxidation and can directly participate in a water–gas-shift-like reaction under PROX condition. Whether this mechanism holds for other PROX catalysts will be the topic of our next investigation.

Acknowledgement

The authors thank the BESSY staff for their continual support during the measurements. The work was supported by the Athena Consortium.

References

---

1 A. J. Appleby, F. R. Foulkes, Fuel Cell Handbook, Van Nostrand Reinhold, New York, 1989.

2 A. Wootsch, C. Descorme, D. Duprez, J. Catal. **225** (2004) 259.

3 O. Pozdnyakova, D. Teschner, A.Wootsch, J. Kröhnert, B. Steinhauer, H. Sauer, L. Toth, F. C. Jentoft, A. Knop-Gericke, Z. Paál, R. Schlögl, J. Catal. **237** (2006) 1.

4 O. Pozdnyakova, D. Teschner, A.Wootsch, J. Kröhnert, B. Steinhauer, H. Sauer, L. Toth, F. C. Jentoft, A. Knop-Gericke, Z. Paál, R. Schlögl, J. Catal. **237** (2006) 17.

Selective gas-phase hydrogenation of aliphatic triple and double bond using palladium based catalysts

D. Teschner, E. Vass, S. Zafeiratos, P. Schnörch, E. Kleimenov, M. Hävecker, A. Knop-Gericke, R. Schlögl
Fritz-Haber-Institut der Max-Planck-Gesellschaft, Faradayweg 4-6, D-14195 Berlin

Aim of the work and scientific background:

Heterogeneous catalysis plays an essential role in the field of chemistry and in chemical manufacturing. The complexity of a catalytic process usually requires that chemistry and engineering intimately mix to deliver the desired effect. The research project Athena (Advanced technology in catalytic chemistry and engineering for novel application) is a joint collaboration of Fritz-Haber-Institut and several British and American institutions presenting a multi-disciplinary approach to investigate heterogeneous catalytic reactions. To produce polymer-grade alkene stream the removal of multiple unsaturated hydrocarbons has a crucial importance. This can be done by using catalysts showing high selectivity towards hydrogenating C≡C triple bond instead of C=C double bond. In this study we aimed to understand the governing factors of *selective triple* C≡C hydrogenation (i.e. only hydrogenating to alkene) on palladium by using in-situ X-ray photoelectron spectroscopy. For these purpose single crystals, foils and supported catalysts are used and studied by surface sensitive XPS, *in-situ*, i.e. in the desired manner *during* catalytic experiment.

Results

All catalytic samples (5% Pd/carbon-nanotubes, 3% Pd/Al_2O_3, Pd(111) and Pd foil) showed activity in the hydrogenation of 1-pentyne (~1 mbar). Both, single and total hydrogenation products were formed, however mainly selective hydrogenation to 1-pentene occurred at steady 358 K. This single hydrogenation is related with carbon retention as a special "Pd-C surface phase" builds up in the reaction (Fig.1). The 335.6 eV Pd $3d_{5/2}$ component is surface related (shown by non-destructive depth profiling; Fig. 2); however calculation revealed its

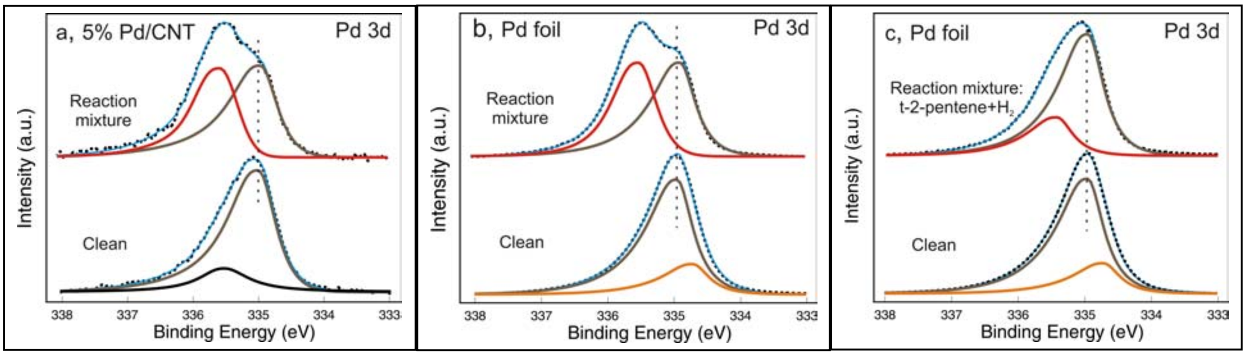

Fig. 1: Pd 3d region of 5%Pd/carbon-nanotube *(a)*, Pd foil *(b)* in the reaction mixture of 0.85 mbar H_2 + ~0.05 mbar 1-pentyne at 358 K. As a comparison Pd 3d of Pd foil in the hydrogenation of t-2-pentene *(c)* is also shown. Incident photon energy, hν = 720 eV.

thickness as 2-3 atomic layers. A direct link between the “Pd-C” component and the 1-pentene yield could be established; therefore the active surface in selective triple bond hydrogenation is a non-metallic Pd phase. Valence band spectra point also to a massive charge redistribution. It is important to mention that in the hydrogenation of trans-2-pentene (Figure 1c) this Pd-C component does not form, only adsorbate induced surface-core-level appeared [1]. This spectroscopic evidence correlates perfectly with recent catalytic work [2] showing that propene formation from propyne occurs only when the catalyst retained a significant amount of carbon on its surface. For propane formation carbon retention was not a prerequisite.

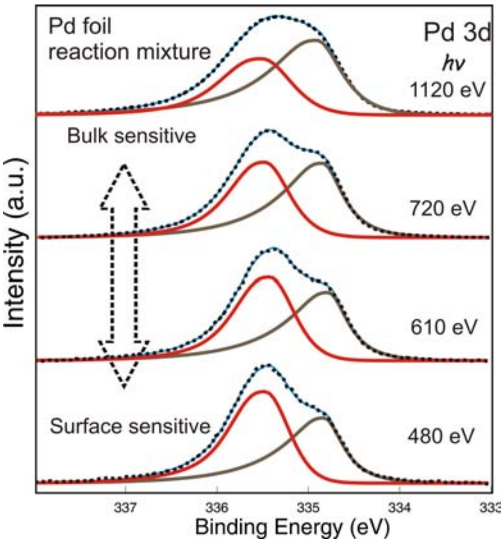

Fig. 2: Pd3d$_{5/2}$ as a function of photon energy (information depth)

HRTEM experiments on used catalysts indicate lattice expansion (i.e. carbon incorporation) which is more pronounced in the surface-near area. Depth-profiling XPS experiment during catalytic run on both palladium and carbon core level reveals maximum carbon content with intermediate information depth (Fig. 3, red line). This clearly indicates that a significant amount of carbon is situated in the near-surface region i.e. in subsurface positions. The remarkable increase of palladium at the most surface sensitive energy suggests that the surface is not fully covered by any type of adsorbates and that the subsurface carbon is located below the 2-3 palladium-atom-thick “Pd-C” layer. By using “switching off” (H_2/C_5) experiments we conclude that the “Pd-C phase” is heterogeneous: a Pd rich layer builds the surface, below of which a Pd-to-C 2-to-1 layer is found. This latter decomposes and forms as pentyne is switched off respectively introduced (Figure 4), emphasizing the dynamics of the system. The switching experiments were performed in depth profiling manner hence carbon depth distribution could be calculated (dashed lines in Figure 3). Although the absence of pentyne in the gas-phase reduces the carbon content, however not on the surface. Carbon was depleted from the subsurface region (note the much less pronounced maximum curve), therefore desorption of pentyne is accompanied not only by a

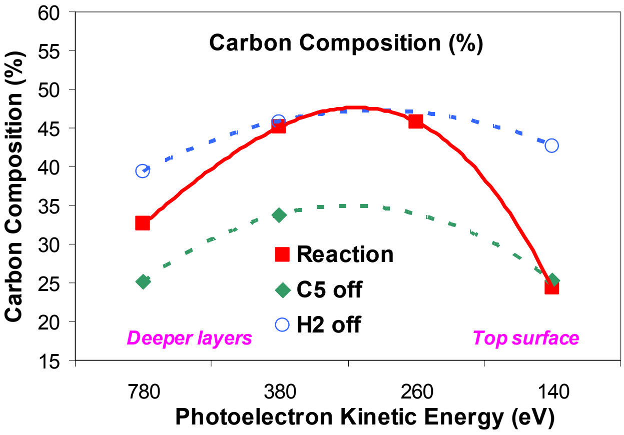

Fig. 3: Carbon distribution as a function of information depth

partial decomposition of “Pd-C” but also by the migration of carbon from subsurface to surface position. Pure pentyne in the feed gas induced desorption of hydrogen and increased the surface coverage of C5. Some subsurface carbon should have moved into deeper layers, as well. The different carbon depth-profiles underline the importance of in-situ surface analysis.

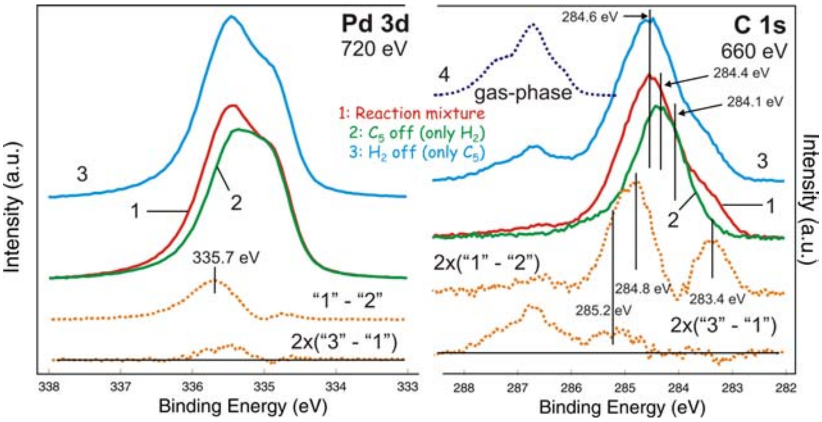

Fig. 4: Pd3d$_{5/2}$ and C1s core levels at three stages. 1: during reaction; 2: pentyne switched off (only H_2); (Spectrum after switching back 1-pentyne is identical to curve 1, not shown.) 3: H_2 switched off (only C_5).

At high temperature (523 K) in the reaction mixture both hydrogen and pentyne desorb and/or decomposes, the double-layer is destroyed, and a blocking surface/subsurface carbon layer builds up inhibiting any further reaction. (Note HRTEM indicated also graphitic carbon after high-T reaction.) The active double-layer can be restored only after regeneration, however by the reaction itself.

Pd-C surface phase was found also when acetylene was hydrogenated, but not during ethylene hydrogenation. The rate of the latter reaction was suppressed roughly by a factor of three if Pd-C like phase was built up from acetylene previously, before switching to ethylene feed. This result give us a new insight why palladium based catalysts are able to handle the job removing multiple unsaturation of hydrocarbons from mainly alkene streams.

Acknowledgement

The authors thank the BESSY staff for their continual support during the measurements. The work was supported by the Athena Consortium.

References

---

1 D. Teschner, A. Pestryakov, E. Kleimenov, M. Hävecker, H. Bluhm, H. Sauer, A. Knop-Gericke, R. Schlögl: J. Catal. **230** (2005) 195.

2 D.R. Kennedy, G. Webb, S.D. Jackson and D. Lennon: Appl. Cat. A **259** (2004) 109.

Single atoms are the most active: Cu-catalyzed carboxylic deprotonation

D. Payer,[1] T. Strunskus,[2] A. Dmitriev,[1] N. Lin,[1] J. V. Barth,[3,4] Ch. Wöll,[2] and K. Kern[1,3]
[1]Max-Planck-Institut für Festkörperforschung, Stuttgart,
[2]Lehrstuhl für Physikalische Chemie I , Ruhr-Universität Bochum
[3]Institut de Physique des Nanostructures, Ecole Polytechnique Fédérale de Lausanne,
[4]Departments of Chemistry and Physics & Astronomy, University of British Columbia

Almost 80 years ago Taylor coined the concept of 'active sites' in heterogeneous catalysis suggesting that adsorbate bond cleavage or formation occurs preferentially at specific arrangements with low-coordinated surface atoms. The identification of such active sites is decisive for the understanding of surface reaction mechanisms, the corresponding rate-limiting steps, and the design of advanced catalysts with improved efficiency or selectivity. Here we demonstrate a new paradigm in this field: the function of highly mobile adsorbed atoms (adatoms) as *dynamic* active sites in surface chemical reactions. In view of the appreciable two-dimensional vapour pressure of many metal catalysts at typical reaction temperatures (>400 K), these findings indicate that mobile adatom deserve general consideration in surface chemical reactions and can bestow dynamic heterogeneity to materials.

Combined scanning tunnelling microscopy and X-ray photoelectron spectroscopy studies reveal that the deprotonation reaction of carboxylic groups of 1,3,5-benzenetricarboxylic acid molecules (trimesic acid, TMA, cf. figure 1A) adsorbed at the Ag(111) surface readily occurs in the presence of a diluted 2-D Cu adatom gas at the surface, while negligible reaction rates occur under similar conditions with Cu in the form of 2-D condensed islands. We demonstrate the function of highly mobile adsorbed atoms (adatoms) as dynamic active sites in surface chemical reactions, as illustrated by scheme 1.

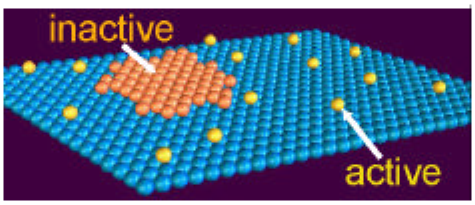

Scheme 1

The hydrogen-bonded open networks can be fabricated by deposition of TMA on a cold substrate (T = 120 K) followed by warming to room temperature, as shown by the STM image in figure 1B. The corresponding model in figure 1C shows how the dimerization of the self-complementary carboxylic groups accounts for the dominating planar honeycomb domains. The XPS data shown in figure 1D prove that the carboxylic groups are protonated.

In order to address the reactivity of coadsorbed Cu, TMA molecules and small concentrations of Cu atoms (0.05 ML) were sequentially deposited on the cold Ag(111) surface (120 K). Under these conditions, the molecules remain protonated at 120K, as evidenced by the corresponding XPS measurements. The chemical activity of the Cu atoms becomes apparent upon increasing the substrate temperature. The spectroscopic data show dramatic changes in the TMA carboxylic groups above 200K. The analysis of the XPS chemical shifts clearly reveals the formation of a tricarboxylate species at 300K, i.e., there is definitely a complete deprotonation of the carboxylic groups which is associated with the presence of Cu adatoms (cf. figure 2A). These findings are substantiated by STM topographic data (reproduced in figure 2B) showing complete inhibition of honeycomb network formation since the underlying H-bond motif is absent. Rather, TMA molecules aggregate in disordered agglomerates containing bright protrusions, which are Cu islands formed in the annealing process. Since carboxylic groups are still present after Cu deposition before the sample warm-up, it is concluded that the deprotonation reaction is not triggered by the impact of Cu in the deposition process, rather it must be mediated by thermal activation and Cu adatoms during warm-up.

In order to clarify whether the boost of chemical reactivity correlates with the highly dispersed Cu adatoms, control experiments were performed, where Cu was offered in a 2-D condensed form by predepositing the same amount of Cu at room-temperature on the clean Ag surface. Subsequently the substrate was cooled down to 120 K and TMA was added. Following warm-up to room temperature, strikingly the formation of perfect honeycomb structures coexisting with the Cu islands was observed, as shown by the STM image in figure 2C. The underlying hydrogen bonding implies that TMA deprotonation does not occur in the presence of pre-grown Cu islands.

The sharp distinction between the two cases demonstrates that the Cu condensation must be associated with a drastically decreased chemical reactivity. Consequently the deprotonation reaction rate depends on the Cu adatom density, and Cu adatoms are the decisive element mediating carboxylic deprotonation, i.e., this mobile species represents the true active site in this surface chemical reaction. Since the two-dimensional vapour pressure of metals is appreciable at typical reaction temperatures (>400 K), the findings indicate that activation by a mobile adatom gas is of general relevance in catalysis and bestows a dynamic heterogeneity to materials.

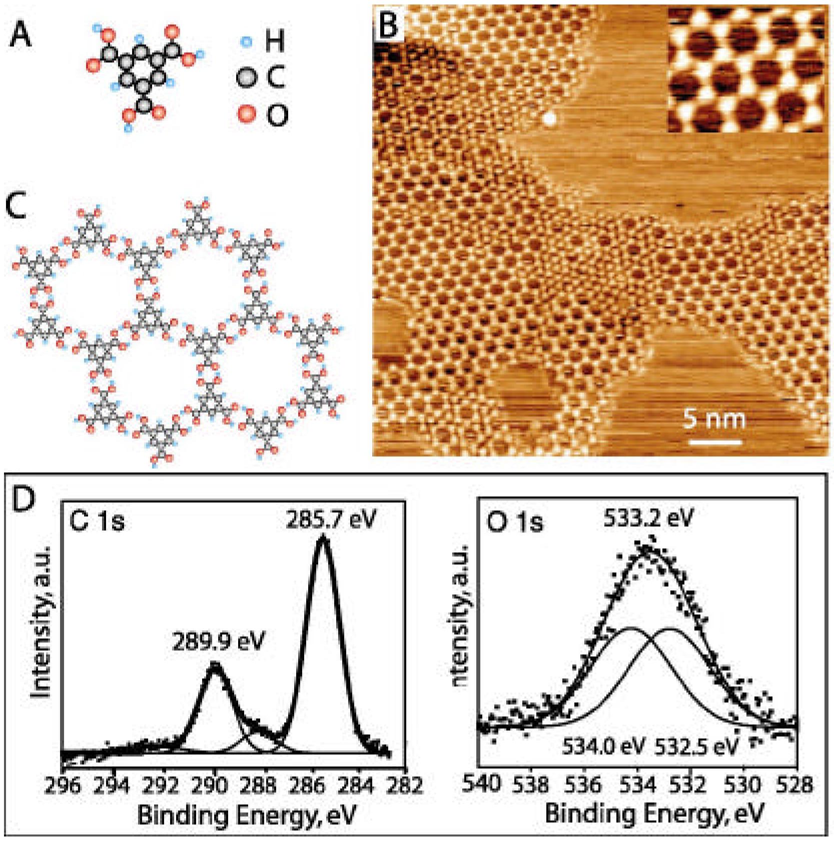

Figure 1. **A** Structural model of the 1,3,5-benzenetricarboxylic acid $C_6H_3(COOH)_3$ (TMA) molecule. **B** Assembly of extended hydrogen-bonded TMA honeycomb networks on Ag(111) following sub-monolayer deposition on the 120 K-cooled substrate and warm-up to room temperature. **C** Model of the hydrogen-bonded nanoporous supramolecular TMA layer with hydrogen-bond mediated dimerization of self-complementary carboxylic groups. **D** XPS data testify the integrity of the organic molecules (photon energy 400 eV for carbon, 670 eV for oxygen spectrum). Indicated are the C 1s position of aromatic ring and carboxylic group, and the convoluted O 1s signal with contributions from carbonyl and hydroxyl groups, respectively.

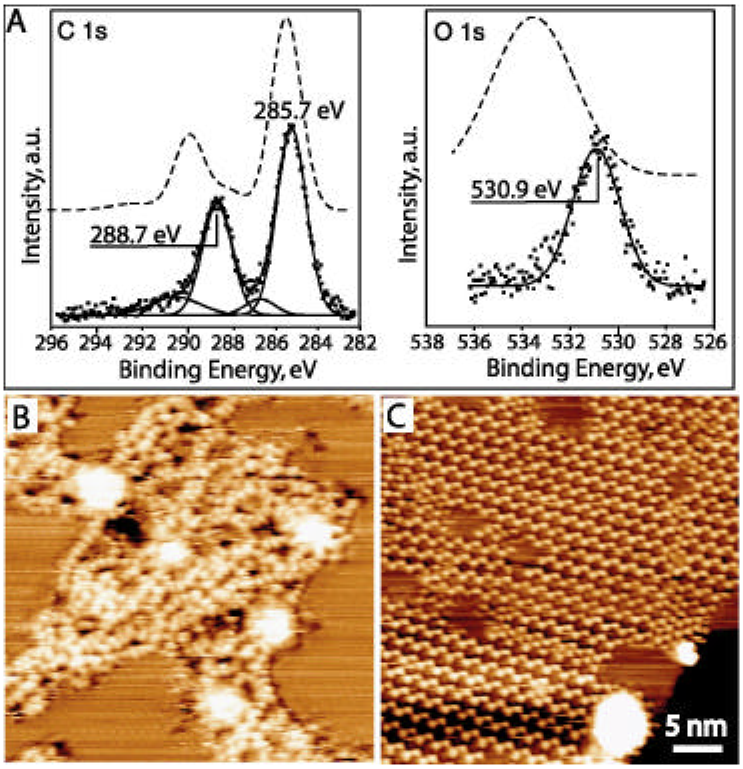

Figure 2. **A** XPS data (solid curves) monitoring the chemical changes occurring in the 300 K warm-up of an intermixed TMA/Cu layer grown at low temperature on Ag(111) (photon energy 400 eV for carbon, 670 eV for oxygen spectrum). For comparison, spectra of the protonated species are shown as dashed curves. The formation of a TMA tricarboxylate species is reflected by the distinct chemical shift of the higher-energy C 1s peak and the characteristic narrowing of the O 1s peak. **B** STM image of irregular TMA agglomerates coexisting with Cu islands when 120 K co-deposited TMA and Cu are annealed to room temperature. **C** In the presence of pre-deposited condensed 2-D Cu islands deprotonation in warm-up is negligible, and regular hydrogen-bonded TMA honeycomb networks evolve.

Local structure determination of a chiral adsorbate: Alanine on Cu(110)

D.I. Sayago[1], M. Polcik[1], G. Nisbet[2], C.L.A. Lamont[2] and D.P. Woodruff[3]
[1] *Fritz-Haber-Institut der MPG, Faradayweg 4-6, D 14195, Berlin, Germany*
[2] *Centre for Applied Catalysis, Department of Chemical and Biological Sciences, University of Huddersfield, Queensgate, Huddersfield, HD1 3DH, UK*
[3] *Physics Department, University of Warwick, Coventry CV4 7AL, UK*

In an earlier study of the adsorption of the simplest (deprotonated) amino acid, glycine(ate), $NH_2CH_2COO^-$, on both Cu(110) and Cu(100) using scanned-energy mode photoelectron diffraction (PhD) [1], we showed that the molecule bonds to the surface through the two carboxylate O atoms and the amino N atom, each of these bonding sites being off-atop. One interesting feature of the (2x3) ordered phase formed on (110) surface is the presence of glide symmetry lines. This may be understood in terms of two different rotational orientations of the amino groups when bonded to the surface. In effect, although glycine in the gas phase is not chiral, when bonded to the surface it becomes chiral, and the (2x3) ordered phase contains equal numbers of the two enantiomers which are mirror images of one another (see fig. 1).

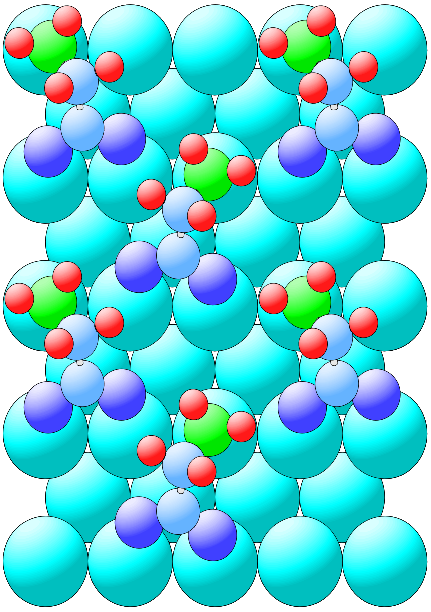

Fig. 1 Plan view of the Cu(110)(2x3) glycinate adsorption phase

Alanine, $NH_2CH_3CHCOOH$, is the simplest truly chiral amino acid and also deprotonates to form alaninate when adsorbed on Cu(110). On this surface it is also found to also adopt a (2x3) phase, even when a single enantiomer is deposited. In this case, it is not possible that the structural phase is heterochiral, as in fig. 1 for glycine, and indeed we have shown through measurements of CDAD [2] (circular dichroism in the angular dependence of photoemission) that the adsorbed species does display the anticipated chirality. The adsorption structure must therefore be homochiral with each (2x3) unit mesh containing two alaninate species which have the same chirality but must have different local adsorption geometries.

Using O 1s and N 1s PhD we have therefore conducted a detailed structure determination of the adsorption geometry of alaninate on Cu(110) in this (2x3) adsorption phase. Analysis of the data clearly shows that the local adsorption geometry is the same as for glycine in that the amino N and carboxylate O atoms are in off-atop sites, with the O atoms significantly further from atop than the N atoms, and with Cu-N and Cu-O bonding distances essentially equivalent to those for glycinate. Obtaining a more precise description of the off-atop offset values without prior constraints is, however, extremely difficult, because there must be at least two different offset values for the N atoms and four different offset values for the O atoms, with two inequivalent alaninate species per surface unit mesh. To gain further information on this aspect we have therefore tested the complete set of structural parameters obtained from a recent density functional theory calculation of the minimum energy structure by Rankin and Sholl [3]. Fig. 2 shows a schematic view of their structure, which also includes small relaxations of the outermost Cu layer atoms both perpendicular and parallel to the surface.

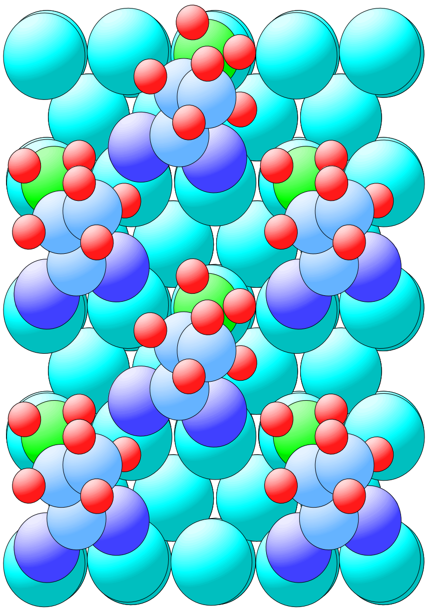

Fig. 2 Plan view of the Cu(110)(2x3) alaninate adsorption phase as determined by the DFT calculations of Rankin and Sholl [3]

We find that this theoretical structure does give a good fit to the experimental PhD spectra, with a slightly lower *R*-factor than the best-fit structure obtained without this final stage of optimisations, *but only if the whole molecular adsorbate layer is displaced towards the surface by approximately 0.10 Å*. Without this shortening of the Cu-O and Cu-N bondlengths, the fit to the data is very poor. Specifically, we find N-Cu and O-Cu bondlength values, averaged over the co-occupied sites, of 2.02 Å and 1.98 Å respectively, with an estimated precision of ±0.03 Å. These bondlengths are shorter than those obtained from DFT by 0.08 Å and 0.10 Å respectively. Such a discrepancy in the bondlengths is surprisingly large; DFT calculations commonly give bondlengths accurate to within ~0.02-0.03 Å.

---

1 J.-H. Kang, R. L. Toomes, M. Polcik, M. Kittel, J.-T Hoeft, V. Efstathiou, D. P. Woodruff and A. M. Bradshaw, J.Chem.Phys. 118 (2003) 6059

2 M. Polcik, F. Allegretti, D.I. Sayago, G. Nisbet , C.L.A. Lamont and D.P. Woodruff, ***Phys. Rev. Lett.*** **92** (2004) 236103

3 R.B. Rankin and D.S. Sholl, Surf. Sci. 574 (2005) L1

The chemisorption bondlength of molecular water on TiO_2(110); a key parameter for theoretical understanding

F. Allegretti[1],S. O'Brien[1], M. Polcik[2], D.I. Sayago[2], D.P. Woodruff[1]

[1]*Physics Department, University of Warwick, Coventry CV4 7AL, UK*
[2] ***Fritz-Haber-Institut der MPG, Faradayweg 4-6, D 14195 Berlin, Germany***

The (110) face of rutile phase TiO_2 is perhaps the most studied of all oxide surfaces as a model system to investigate the range of catalytic applications of this material, of which one of the most interesting is the photochemical production of hydrogen from water, first discovered more than 30 years ago. Most of the very extensive work on the interaction of water with this surface has recently been reviewed [1, 2]. The extent to which H_2O does, and should, dissociate to produce surface hydroxyl species on clean and well-ordered TiO_2(110), remains a subject of controversy, at least between theory and experiment. However, experimentally it is well-established that molecular water can be adsorbed on this surface intact at low temperatures.

Prior to this investigations there has been no quantitative structural information regarding this adsorption, although STM studies have been interpreted in terms of molecular adsorption on the five-fold coordinated (i.e. under-coordinated) Ti atoms at the TiO_2(110)(1x1) surface. This is the site for molecular water adsorption which seems to be implicit in theoretical total energy calculations, although most of these are primarily concerned with whether or not dissociation, to produce surface hydroxyl species, occurs on the perfect surface; most of the earlier studies and some very recent ones predict facile dissociation on the perfect stoichiometric surface, a conclusion inconsistent with experimental results.

Using scanned-energy mode photoelectron diffraction (PhD) [3] in the O 1s emission we have conducted a quantitative determination of the adsorption geometry of molecular water on TiO_2(110) at low temperature [4, 5]. The O 1s signal from the water is clearly resolved from that of the underlying oxide by a large chemical shift, and we found no evidence of dissociation to produce surface hydroxyl species for which there is an intermediate value of the O 1s chemical shift. A defocussed incident synchrotron radiation beam ensured that no radiation damage was seen during the course of the measurements. The structural analysis provides confirmation that the adsorption site is atop the five-fold coordinated surface Ti atoms.

In addition, however, the results provide quantitative data on the adsorption bondlength and the surface relaxation. A key finding is that the $Ti\text{-}O_{water}$ bondlength is 2.21±0.02 Å. This is significantly longer that the strong Ti-O chemisorption bondlengths found to formate (COO-) and hydroxyl (OH) coadsorbates on this surface of 2.08 Å and 2.02 Å respectively [6], reflecting a weaker bond of rather different character for the intact water molecule. This bondlength is also much longer that the Ti-O bonds in bulk TiO_2 (1.94-1.99 Å). However, the measured $Ti\text{-}O_{water}$ bondlength is rather significantly shorter than the value provided by theoretical calculations of this quantity for water adsorbed in this site on TiO_2(110), with published values in the range 2.25-2.41 Å. Unfortunately, despite the many theoretical calculations of this adsorption system, rather few reports of these studies quote values of this adsorption bondlength. Bearing in mind that many of these calculations fail to correctly predict the stability of molecular water to dissociation on this surface it seems likely that the fact that the Ti-O_{water} bondlength is longer than the experimental value is significant. If the calculations fail to correctly describe the interaction of the intact molecule with the surface it may not be too surprising that they also fail to correctly determine the activation barrier to dissociation. Interestingly, of the four published theoretical values for the bondlength, the one closest to experiment (2.25 Å) corresponds to a calculation which does predict that the molecular species is stable on the surface [7]; it would be of interest to know whether similar near-agreement exists for more recent calculations predicting non-dissociative behaviour.

The PhD study also provides some information on the near-surface relaxations of the TiO_2 surface in the presence of the adsorbed water. Most notable is the relaxation of the bondlength the Ti surface atom, bonded to the adsorbed water, makes with the O atom directed below in the surface. This relaxation is found to be essentially identical to that found for the clean TiO_2(110) surface by both experimental and theoretical methods. The absence of a change in this relaxation provides further evidence of the relatively weak Ti-water bonding.

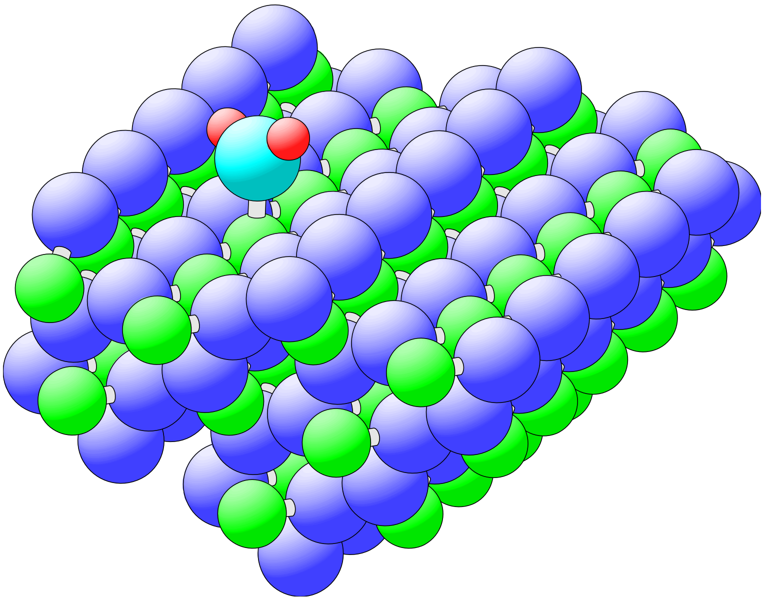

Schematic diagram of the local adsorption site of molecular water on TiO_2(110) as found in this study. The blue spheres represent O atoms, the smaller green sphere represent Ti atoms.

---

1 U. Diebold, Surf. Sci. Rep. 48 (2003) 53

2 M. A. Henderson, Surf. Sci. Rep. 46 (2002) 1

3 D. P. Woodruff, A. M. Bradshaw, Rep. Prog. Phys. 57 (1994) 1029

4 F. Allegretti, S. O'Brien, M. Polcik, D. I. Sayago, D. P. Woodruff, Phys. Rev. Lett, 95 (2005) 226104

5 F. Allegretti, S. O'Brien, M. Polcik, D. I. Sayago, D. P. Woodruff, Surf. Sci. in press

6 D. I. Sayago, M. Polcik, R. Lindsay, J. T. Hoeft, M. Kittel, R. L.Toomes, D. P. Woodruff, J. Phys. Chem. B 108 (2004) 14316

7 E. V. Stefanovich, T. T. Truong, Chem. Phys. Lett. 299 (1999) 623

Dehydrogenation of C4 hydrocarbons using vanadium based catalysts

E.M. Vass, D. Teschner, A. Knop-Gericke, M. Hävecker, S. Zafeiratos,
P. Schnörch, E. Kleimenov, R. Schlögl
Fritz-Haber-Institut der Max-Planck-Gesellschaft, Faradayweg 4-6, D-14195 Berlin

Scientific Background and Aims

Dehydrogenation of n-butane to butene and butadiene is a highly interesting commercial process due to increasing demand for unsaturated hydrocarbons for industrial applications. Many commercial processes for the dehydrogenation of light alkanes use catalysts containing chromia or platinum supported on alumina. The dehydrogenation of alkanes is an endothermic process, which requires high reaction temperatures and low pressures. Unfortunately at higher temperatures light alkanes are produced and coke formation is encouraged causing catalyst deactivation. Oxygen treatment can be used to regenerate the catalyst, hence prolonging the life-time of the catalyst.

This study forms part of the ATHENA project one of the goals of which is to investigate selective gas-phase alkane dehydrogenation. As part of an international collaboration our aim is to utilise the techniques of high pressure *in-situ* XPS and NEXAFS to investigate the electronic structure of the vanadium species under reaction conditions. The techniques are used to gain a better understanding of alumina-supported V_xO_y based catalysts through investigation of their structure-reactivity relationships. In addition, *ex-situ* experiments (typically at 100 mbar pressure) were used to examine the differences in the reaction products and final state catalyst at increased pressure. By performing the experiments in an adjoining reaction chamber, the sample could be transferred under reaction gas atmosphere.

Figure 1. XPS of $V2p_{3/2}$ region during n-butane dehydrogenation (2 mbar).

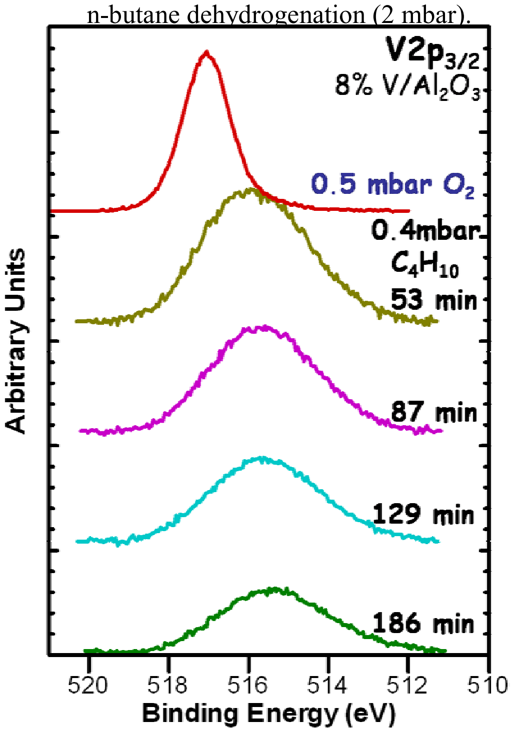

Results and Discussion

The electronic structure of vanadia/alumina catalysts was examined during the dehydrogenation of n-butane. High-pressure measurements were made possible due to a specially designed, differentially pumped, electrostatic lens system. Hence spectra could be measured while the cell pressure was maintained at 2 mbar. The reaction products were detected using a Proton Transfer Reaction Mass Spectrometer (PTRMS). An 8% V/alumina catalyst was examined both *in-* and *ex-situ* for the n-butane dehydrogenation reaction at partial pressures of 0.4 and 100 mbar of butane respectively.

After an initial treatment in oxygen, the 8% V/alumina catalyst contained predominantly V_2O_5 crystallites. This is in agreement with literature, as at vanadium loadings above one monolayer of V on alumina crystalline V_2O_5 is expected to be the major species [1,2,3]. However, immediately after introduction of butane gas NEXAFS (not shown) reveals that the V_2O_5 structure is lost. This effect is confirmed by the XP spectra, which show a reduction of the vanadium species coupled with a decrease in intensity during the reaction (figure 1). The initial reduction may be due to removal of oxygen from the catalyst in the form of oxygenated products. Furan and dihydrofuran/crotanaldehyde) were observed as the catalyst was heated to reaction temperature. After 87 mins there is a further shift in binding energy and a reduction in intensity. The shift to lower binding energy suggests a decrease in the vanadium oxidation state. This correlates with the formation of a surface carbon species, which is the main source of deactivation for dehydrogenation catalysts.

Figure 2. PTRMS reaction profile for 8% V/alumina during n-butane dehydrogenation and area of surface carbon peak from XPS.

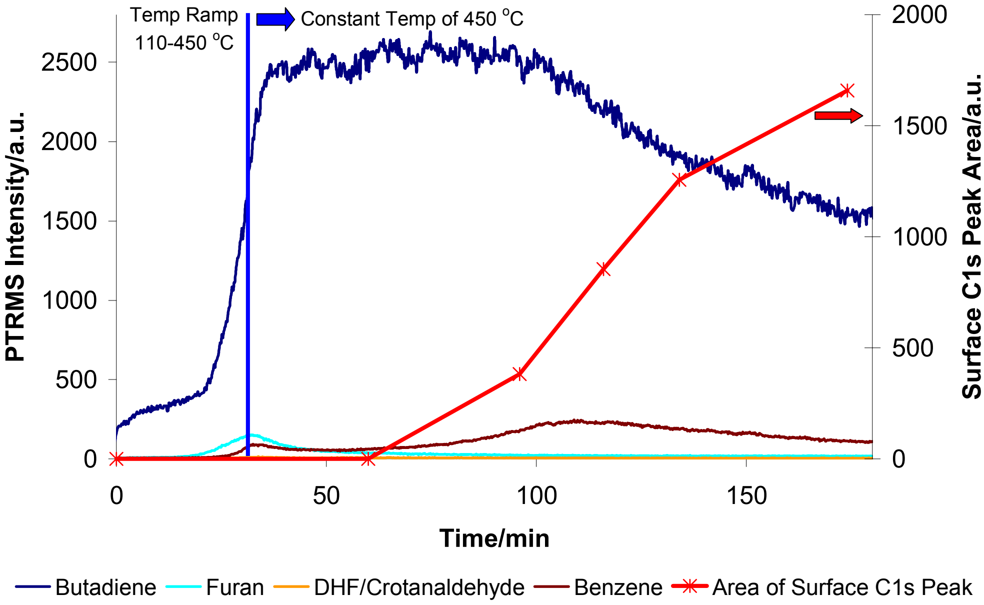

Figure 2 shows the trends of the reaction products: butadiene, furan, DHF/crotonaldehyde and benzene (butene not shown). There is a steep increase in the surface carbon content, which correlates with a maximum in benzene formation and is proportional to the decrease in butadiene formation. The carbon was identified as chain/graphitic carbon.

Therefore investigation of the surface species under reaction conditions has identified two stages. During reaction the vanadium species is reduced to contain a mixture of V^{5+} and V^{4+}. At this point the catalyst is active and shows only slow deactivation. The second step is the deposition of carbon on the surface, which leads to further deactivation. This deactivation is mainly due to carbon laydown, which blocks the active vanadium sites.

Figure 3. NEXAFS VL_3 edge before and after reaction with n-butane (100 mbar).

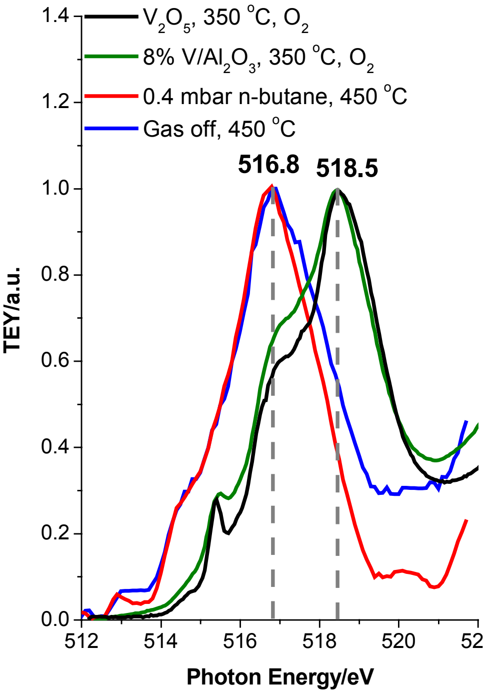

As with the *in-situ* experiment, the *ex-situ* reaction showed formation of oxygenated products during heating in n-butane. Due to the higher partial pressure of n-butane, the catalyst rapidly deactivated over a period of only 30 minutes. A steep decline in activity was detected where benzene production reached a maximum. Hence it is likely that this point coincided with the formation of surface carbon, similarly to the *in-situ* reaction. Once transferred to the measurement cell, NEXAFS (figure 3) showed a great reduction in the vanadium species and XPS indicated high surface carbon content. The total percentage of elemental carbon detected on the catalyst surface was 46 %. The ratio of vanadium to aluminium decreased on comparison of pre- and post-reaction catalysts, suggesting that carbon laydown occurs preferentially on the vanadium.

Acknowledgements

The authors would like to thank the staff of BESSY for their support during the measurements. The funding for this work was provided by the ATHENA Project, which is jointly funded by the EPSRC (UK) and Johnson Matthey Catalysts plc.

References

---

[1] L.J. Burcham, G.T. Deo, X.T.Gao, I.E. Wachs. *Topics in Catalysis* **11**, 85 (2000).

[2] N.R. Shiju, M. Anilkumar, S.P. Mirajkar, C.S. Gopinath, B.S. Rao, C.V. Satyanarayana. *J. Catal.* **230**, 484 (2005).

[3] Z. Wu, H.-S. Kim, P.C. Stair, S.R. Rugmini and S.D. Jackson. *J. Phys. Chem. B* **109**, 2793 (2005).

Catalytically Active States of Ru(0001) Catalyst in CO Oxidation Reaction

R. Blume[1], M. Hävecker[1], S. Zafeiratos[1], D. Teschner[1], E. Kleimenov[1], A. Knop-Gericke[1], R. Schlögl[1], A. Barinov[2], P. Dudin[2], and M. Kiskinova[2*]

[†] *Fritz-Haber-Institut der Max-Planck-Gesellschaft, Faradayweg 4-6, 14195 Berlin, Germany*

[§] *Sincrotrone Trieste, AREA Science Park-Basovizza, Trieste-34012, Italy*

1. Introdiction

The recent XPS microscopy and TDS studies clearly showed that the formation of a rutile RuO_2 phase, starting from an atomically clean Ru(0001) surface, is kinetically hindered at temperatures lower than 500 K and readily occurs at temperatures higher than 550 K[1]. An important finding is that 'surface oxide', which forms by incorporation of O atoms below the top Ru layer and the RuO_2 can coexist in a wide T-pressure range, even when formed in pure O_2 ambient[2]. Undoubtedly, when CO oxidation reaction takes place, the CO will drive the oxidation state away from the equilibrium achieved in O_2 ambient, which implies that the T-p space of coexistence of the two structures may be expanded. The temperature dependence of the actual 'oxidation' state and the complex morphology of the Ru surface evidenced by XPS microscopy have reopen the disputable issue about the active state of Ru catalysts during CO oxidation[3,4,5].

We verified the catalytic activity of the different oxidation states of Ru(0001) catalyst, starting from a metallic Ru surface and following in-situ the temperature evolution of the catalyst surface composition and yield of CO_2 during CO oxidation reaction carried out close to the realistic reaction conditions.

2. Experimental

The experiments were performed in the high pressure XPS station designed and constructed in FHI-MPG, attached to the beamline U49/2-PGM2 at BESSY[6]. The XPS spectra, were measured in-situ using a set-up combining differential pumping and electrostatic focusing of the emitted photoelectrons and simultaneously the CO_2 yield was monitored by a mass spectrometer. The Ru(0001) sample was cleaned before each reaction cycle using the well established procedures of alternating Ar ion bombardment and oxidation-annealing cycles. Photon energies 450 eV and 650 eV were used for monitoring the Ru 3d and O 1s spectra, respectively.

3. Results

The dynamic response of the O 1s and Ru $3d_{5/2}$ core level spectra was used for precise assignment of the catalyst oxidation state in the course of the reaction correlated to the corresponding CO_2 yield. The already available Ru $3d_{5/2}$ and O 1s core level spectroscopy data provided the necessary basis for identification of the adsorption, 'surface oxide' with incorporated oxygen, and stoichiometric RuO_2 states and verifying their actual role in CO oxidation reaction [1,7]. We started from a clean Ru(0001) surface and followed the changes after introducing 0.1 mbar $CO+O_2$ (O_2:CO partial pressure ratio 1) and slowly increasing the temperature. The excess of oxygen with respect to the reaction stoichiometry provided slightly oxidizing conditions ensuring the formation of the different Ru oxidation states.

Fig. 1 (a) shows the CO_2 yield as a function of the reaction temperature. There is a clear sharp onset of the reaction at ~ 420 K, the reaction rate increasing continuously in the temperature range 420-500 K. The selected set of Ru $3d_{5/2}$ and O 1s spectra in Fig. 2, measured at different reaction temperatures, represent the milestones in the evolution of the catalyst

---

[*] M. Kiskinova thanks AvH foundation for the Award to pursue research in FHI-Berlin in 2004-2005.

oxidation state. The first Ru $3d_{5/2}$ and O 1s spectra represent the status of the Ru catalyst after the onset of CO_2 production. The Ru $3d_{5/2}$ spectra of this ‘low temperature’ state require the characteristic components of the ‘surface oxide’, Ru(II)-O_{sub} and Ru(I)-$2O_{ad}O_{sub}$, where Ru(I) and Ru(II) account for emission from the Ru atoms in the 1st and 2nd layer, bonded to oxygen residing on the surface, O_{ad}, and below the surface, O_{sub}[1]. The Ru $3d_{5/2}$ and O 1s spectra undergo negligible lineshape changes in the temperature range 420-480 K despite the gradual increase of the CO_2 yield. They resemble those measured for the ‘surface oxide’ with ~ 2 ML oxygen, but with less oxygen on the surface (the Ru(II)-O_{sub} component at 0.5 eV is dominant). Apparently the adsorbed oxygen is kept low, since it is very effectively consumed by the on-going reaction. The very fast dynamics at the surface is confirmed by the absence of a CO-related feature in the O 1s spectra at binding energy > 531. 0 eV (Fig.2), indicating that the lifetime of the CO on the surface before being reacted is shorter than that of the O species.

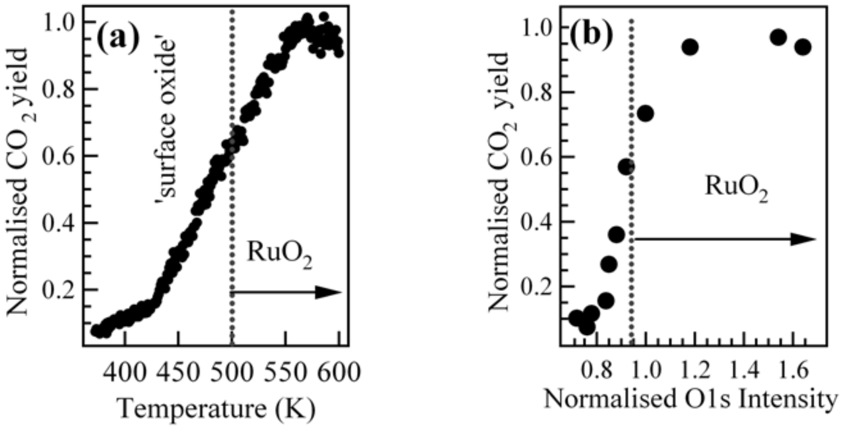

Fig. 1 (a) CO_2 yield as a function of reaction temperature. (b) Plot of the CO_2 yield versus O content at the surface and near surface region. The dashed line in (a) - (c) indicates the onset of the RuO_2 growth.

Natural consequence of the progressive incorporation of oxygen with further increasing the reaction temperature is the nucleation and growth of stoichiometric RuO_2. This is manifested by the significant changes of the Ru $3d_{5/2}$ spectra in Fig. 2 undergone above 500 K, until a ‘steady-state’ composition is reached and maintained in the 550-600 K range, when the ‘oxide’ component is dominant in the Ru $3d_{5/2}$ spectra. Ru_{bulk} component can still be distinguished in the Ru $3d_{5/2}$ spectrum of this ‘steady-state’ as well as the O1s component corresponding to the ‘surface oxide’. This indicates a patchy structure consisting of RuO_2 islands and ‘surface oxide’ areas, as reported in ref. 2, reflecting the kinetic limitations imposed by the presence of CO.

The most striking result is that the growth of the RuO_2 phase above 500 K does not affect the monotonous increase of the CO_2 yield (Fig. 1(a)), suggesting that the nucleation and growth of the oxide phase barely affects the reaction barrier. The plot of the CO_2 yield vs O content in Fig. 1(b) is the best illustration that the high catalytic activity of the Ru catalyst is not exceptionally correlated to the formation of RuO_2 with a well defined surface structure. It clearly shows that the ‘surface oxide’ formed via progressive incorporation of oxygen already exhibits high catalytic activity and there is no significant increase with the formation of stoichiometric RuO_2. Here, it should be noted that since the formation of RuO_2 occurs above 500 K the temperature effect on the reaction rate should be also taken into account when comparing the catalytic activity of the ‘surface oxide’ and RuO_2.

4. Concluding remarks

The present results demonstrate that one cannot draw a clear line between the catalytical activity of the stoichiometric RuO_2 phase and a few layers thick not well-ordered ‘surface oxide’. Our findings are in qualitative agreement with the theoretical predictions[8] that the catalytically active region under realistic dynamic reaction conditions can often lie at the boundary between two structures. Present results also apply well to real Ru catalyst systems which are nano-particles. The 'oxidized' states of these Ru nanoparticles, often described as Ru_xO_y or ultra-thin Ru oxide films covering the metallic core, are comparable to the 'surface oxide' with subsurface oxygen rather than with the well-structured $RuO_2(110)$ surface[9,10].

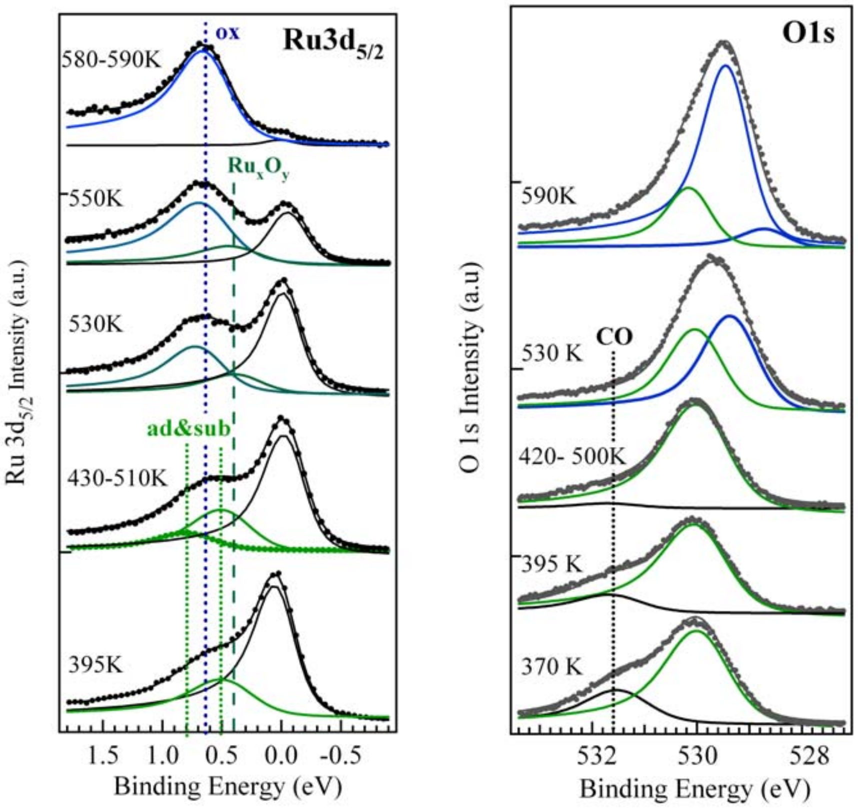

Fig. 2. Ru $3d_{5/2}$ and O 1s spectra illustrating the catalyst composition developed during CO oxidation with increasing of the reaction temperature from 370 to 600 K. dT/dt = 2 K/min. Reaction conditions: $P_{CO} = 0.5x10^{-1}$ mbar, $P_{O2} = 0.5x10^{-1}$ mbar. The Ru(II)-O_{sub} and Ru(I)-$2O_{ad}O_{sub}$ components are labelled as 'ad' and 'sub' in the Ru $3d_{5/2}$, respectively. The component labelled 'Ru_xO_y' correspond to amorphous film which is precursor to growth of the RuO_2 islands, characterised by the component 'ox'[1]. The component used as the zero-energy reference corresponds to metallic bulk Ru at binding energy at 280.1 eV. In the O 1s panel the component at 530.0 corresponds to adsorbed and 'surface oxide' phase, whereas the one at 529.5 eV to oxygen in the RuO_2[1,3]. The position of the O1s component corresponding to CO is indicated as well. It is observed only at temperatures below the real onset of CO_2 production.

References

---

[1] R. Blume, H. Niehus, H. Conrad, A. Böttcher, L. Aballe, L. Gregoriatti, A. Barinov, M. Kiskinova, J. Phys. Chem. B 109 (2005) 14052.

[2] A. Böttcher, U. Starke, H. Conrad, R. Blume, L. Gregoriatti, B. Kaulich, A. Barinov, M. Kiskinova, J. Chem. Phys. 117 (2002) 8104.

[3] H. Over, Y.D. Kim, A.P. Seitsonen, E. Lundgren, M. Schmid, P. Varga, A. Morgante, G. Ertl, Science 287 (2000) 1474.

[4] J. Wang, V.Y. Fan, K. Jacobi, G. Ertl, J. Phys. Chem. B 106 (2002) 3422.

[5] R. Blume, H. Niehus, H. Conrad, A. Böttcher, J. Phys. Chem. 108 (2004) 14332.

[6] H. Bluhm, M. Hävecker, A. Knop-Gericke, E. Kleimenov, R. Schlögl, D. Teschner, V.I. Bukhtiyarov, D.F. Ogletree, M. Salmeron, J. Phys. Chem. B. 108 (2004) 14340.

[7] H. Over, A.P. Seitsonen, E. Lundgren, M. Wiklund, J.N. Andersen, Chem. Phys. Lett. 342 (2001) 467.

[8] K. Reuter, M. Scheffler, Phys. Rev. Lett. 90 (2003) 46103; Phys. Rev. B 60 (2003) 45407.

[9] V. Narkhede, J. Assmann, M. Muhler, Z. Phys. Chem. 219 (2005) 979.

[10] W. Vogel, N. Alonso-Vante, J. Cat., 232 (2005) 395.

Steps make the difference – CO oxidation on Pt(355) and Pt(322) investigated by in-situ high resolution XPS

B. Tränkenschuh, C. Papp, T. Fuhrmann, R. Denecke and H.-P. Steinrück
Lehrstuhl für Physikalische Chemie II, Universität Erlangen-Nürnberg,
Egerlandstr. 3, 91058 Erlangen

The CO oxidation on differently stepped platinum surfaces was studied in-situ using a combination of a supersonic molecular beam and high-resolution x-ray photoelectron spectroscopy (HRXPS). The Pt(355) and Pt(322) surfaces are vicinal surfaces with five atom rows wide (111) terraces. The structural difference of the two surfaces is the orientation of the monatomic steps, being (111) and (100), respectively.

The experiments were performed at beamline U49/2-PGM1, using a transportable apparatus described elsewhere [1]. It combines HRXPS with a supersonic molecular beam for gas dosing at well-defined pressures. In our study, first a layer of atomic oxygen was prepared, and subsequently its reaction with CO was followed by time-dependent XPS at distinct temperatures. O 1s and C 1s spectra were acquired in-situ to distinguish the different species and adsorption sites (O and CO on step and terrace sites) and their surface coverages. The product (CO_2) desorbs at reaction temperature and was detected by a quadrupol mass spectrometer.

Fig. 1 (a) shows O 1s XP spectra of atomic oxygen layers (~0.28 ML) before reaction on both surfaces. One can clearly see that on Pt(322) two different oxygen species are present, whereas on Pt(355) only one peak is detected, although part of the O is adsorbed close to the step edge on both surfaces. In Fig. 1 (b) the C 1s XP spectra of CO saturation coverages on both surfaces are shown, depicting the situation after complete reaction at 260 K. The obvious difference between both surfaces is the amount of CO observed in adsorption sites on the platinum steps. On Pt(322), a smaller CO coverage occupies two step sites, while on Pt(355) only one step site with a higher occupation is observed [2]. By continuously recording such spectra during reaction and merging all quantitative information it is possible to follow the occupation of all these sites on the time scale of seconds. The reactions are carried out at high CO pressures ($1*10^{-6}$ mbar), so that the reaction rate becomes independent of the impinging flux of CO molecules.

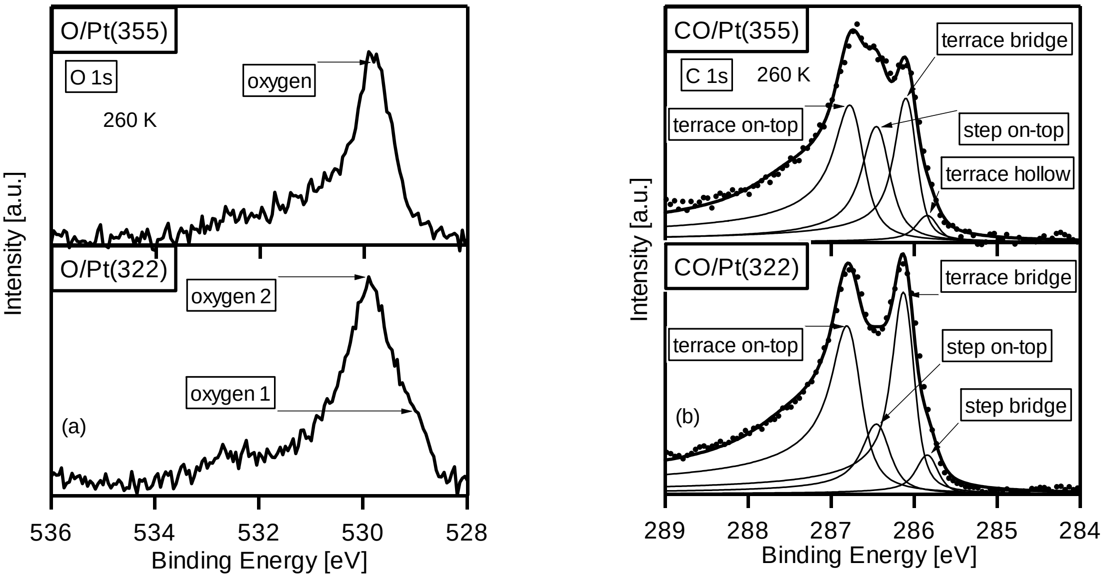

Fig. 1: (a) O 1s XP spectra of the atomic oxygen layers on Pt(355) (upper part) and Pt(322) (lower part). (b) C 1s XP spectra for CO saturation (after reaction at 260 K) on Pt(355) (upper part) and Pt(322) (lower part). Sites labelled "terrace hollow" on Pt(355) are only occupied at high CO coverages (obtained here at CO pressures of $1*10^{-6}$ mbar).

Low temperature (~130 K) co-adsorption experiments of O and CO (data not shown) reveal that on both surfaces oxygen covers the platinum steps, blocking these sites for CO. Therefore, if the occupation of step sites by CO is observed in C 1s spectra during reaction, the oxygen has to be reacted away from the steps. This reaction, indeed, occurs very quickly on both surfaces, as signalled by early CO saturation of step sites. The further reaction path is not that clear because there is a fast exchange of CO adsorbed on step and terrace sites above 200 K, shown by experiments with isotopically marked CO [3].

For both surfaces the CO oxidation was studied at temperatures between 220 and 300 K. Since the reaction rate is independent of CO pressure at the experimental conditions (see above), we are able to evaluate the rate constant only from the oxygen coverage decrease as a function of reaction time.

In Fig. 2 the oxygen coverage is plotted versus reaction time for both surfaces. The decrease of oxygen is faster, i.e., the reaction rate is higher for higher temperatures. Comparing both figures, the reaction occurs faster on Pt(355) (Fig. 2a) than on Pt(322) (Fig. 2b) for all temperatures. Fitting a suitable rate law (assuming surplus CO) to the oxygen decrease, it is possible to determine the activation energy for the reaction of oxygen with CO by an Arrhenius evaluation. In this way, a value of 530 meV was determined by a similar experiment for CO oxidation on Pt(111) [4]. The situation on the stepped surfaces is more complex, with at least two different reaction channels, as suggested by the change of slopes observed in the curves of Fig. 2. While we have hints that the fast channel at the beginning of the experiment is dominated by the reaction at steps, the lower reaction rate observed in the further course of the experiments might not only be attributed to CO oxidation on the (111) terraces. However, the overall reaction rate, just given by the time needed to reduce the O coverage by a certain amount, is on both stepped surfaces significantly higher than on Pt(111). This clearly demonstrates the influence of steps on surface reactivity. A detailed analysis to determine the reaction pathways is in progress.

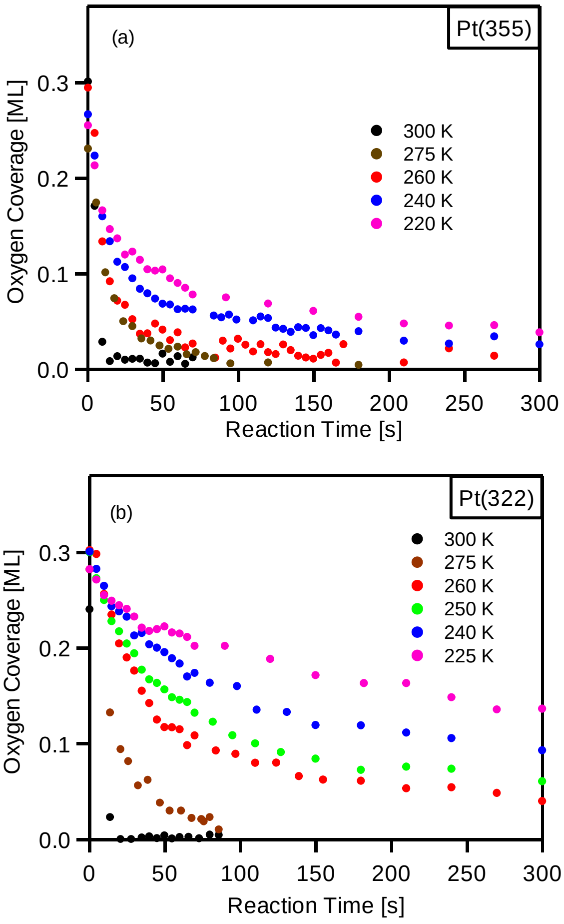

Fig. 2:.Oxygen coverages vs reaction time plotted for different reaction temperatures (a) for Pt(355) and (b) for Pt(322).

Work was supported by DFG (Ste620/4-2).

[1] R. Denecke, M. Kinne, C.M. Whelan, H.-P. Steinrück, Surf. Rev. Lett. 9 (2002) 797.

[2] B. Tränkenschuh, N. Fritsche, T. Fuhrmann, C. Papp, J.F. Zhu, R. Denecke, H.-P. Steinrück, J. Chem. Phys. 124 (2006) (in print).

[3] A. Szabo, M.A. Henderson, J.T. Yates, Jr., J. Chem. Phys. 96 (1992) 6191.

[4] M. Kinne, T. Fuhrmann, J.F. Zhu, C.M. Whelan, R. Denecke, H.-P. Steinrück, J.Chem. Phys. 120 (2004) 7113.

A detailed analysis of the adsorption of benzene on Ni(111) with HR-XPS

C. Papp, B. Tränkenschuh, T. Fuhrmann, R. Denecke and H.-P. Steinrück
Lehrstuhl für Physikalische Chemie II, Universität Erlangen-Nürnberg

Benzene is the prototype of an organic molecule with an aromatic system and, despite its size, it can be described rather simply because of its high symmetry. Aside from fundamental interests, benzene may occur as an intermediate in the nickel-based heterogeneously catalysed petroleum reforming process. Nickel is a particularly relevant substrate, as it plays an important role in various heterogeneously catalysed reactions (*1*).

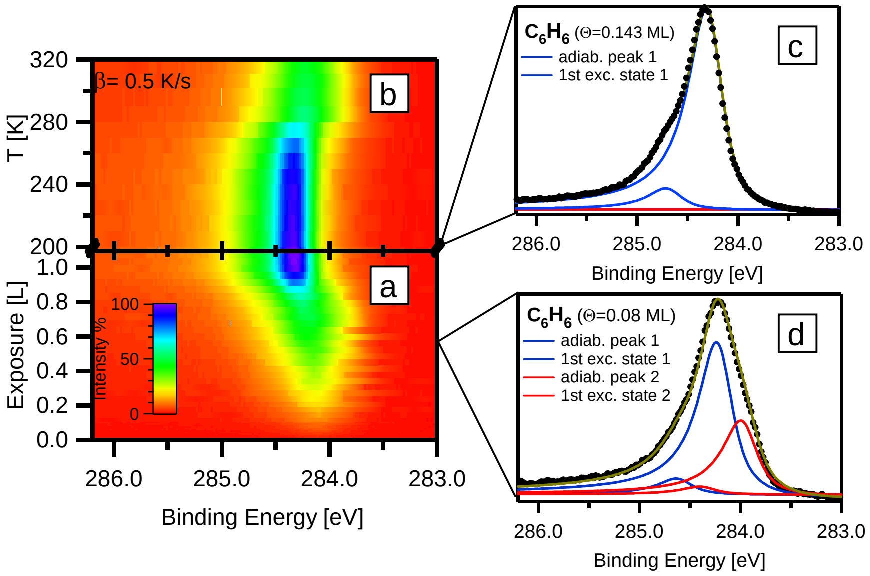

Fig.1: a) Benzene (C_6H_6) adsorption experiment at 200 K; inset: intensity scale. b) TP-XPS experiment, both as colour-coded density plots. c) C 1s spectrum and fit for a saturated layer at 200 K; d) same for a dilute layer.

We recorded C 1s spectra with an excitation energy of 380 eV at beamline U49/2-PGM1 in a time-resolved manner, while adsorbing benzene with a pressure of $2*10^{-9}$ mbar on a Ni(111) crystal. This type of experiment is called “uptake” and is shown in Fig. 1a as a colour-coded density plot. We also performed TP-XPS experiments, shown in Fig. 1b, by heating the sample with a fixed rate while measuring every 10 K. The apparatus used is described in detail elsewhere (*2*).

On the right side of Fig. 1 representative C 1s spectra and their corresponding fits are shown. In Fig. 1c two peaks at 284.3 and at 284.7 eV are needed to model the spectrum for saturation coverage. These are assigned to an adiabatic transition at 284.3 eV and a final state with excitation of the C-H stretching mode at 284.7 eV. This assignment was proven by an isotope exchange experiment with C_6D_6 (data not shown). These two peaks have a constant intensity ratio, called S-factor (*3*), and a constant binding energy difference over the whole coverage range. The C 1s spectra at lower coverages show an additional shoulder at 283.9 eV (Fig. 1d). This shoulder originates also from benzene molecules and is, thus, again fitted with two peaks, with the same parameters as the saturated layer, including binding energy difference, line width and S-factor. The peak areas of the corresponding adiabatic and the first vibrationally excited states are added, as they belong to different carbon components, C1 and C2, within the benzene molecules. In Fig. 2a, we see these carbon components increasing up to a benzene coverage of ~0.09 ML; corrected for photoelectron diffraction effects, a value of 0.10±0.01 ML is obtained from a larger data set. For higher coverages up to saturation of 0.143 ML, the C1-component looses its intensity completely to component C2. The dotted lines show the data for the TP-XPS experiment of Fig. 1b, demonstrating the reversibility within this coverage or temperature range.

The red lines and symbols show a similar experiment with deuterated benzene (C_6D_6), leading to the same result.

In Fig. 2c we show schematic drawings of benzene adsorbed at the sites discussed in this context (*4*). A benzene molecule adsorbed on the hollow site, with C-C bonds along the $[1\bar{1}0]$ direction of the substrate, is depicted on the right hand side. In this geometry, which is reported for saturation coverage (*4*), all six C atoms are equivalent and they are pair wise attached to one Ni atom. Therefore, we only detect one signal in the C 1s spectrum (C2). For benzene adsorbed on bridge sites (see Fig. 2c) with the C-C bonds aligned along the $[2\bar{1}\bar{1}]$ direction of the substrate, we find again pair wise coordinated carbon atoms but also singly coordinated carbon atoms (C1) (*4*). The ratio of the two different carbon components, C1/C2, in the bridge adsorption site is 0.5, which is well matched by the ratio of 0.45 found at coverages up to ~0.09 ML (see Fig. 2b). The ratio C1/C2 for the hollow adsorbed benzene should be zero, as only component C2 is present, and, indeed, a value of zero is found at saturation coverage. At coverages between 0.09 and 0.143 ML the rapidly changing ratio is interpreted as a coverage dependent site change of benzene from bridge to hollow in case of adsorption, and from hollow to bridge in case of a TP-XPS experiment.

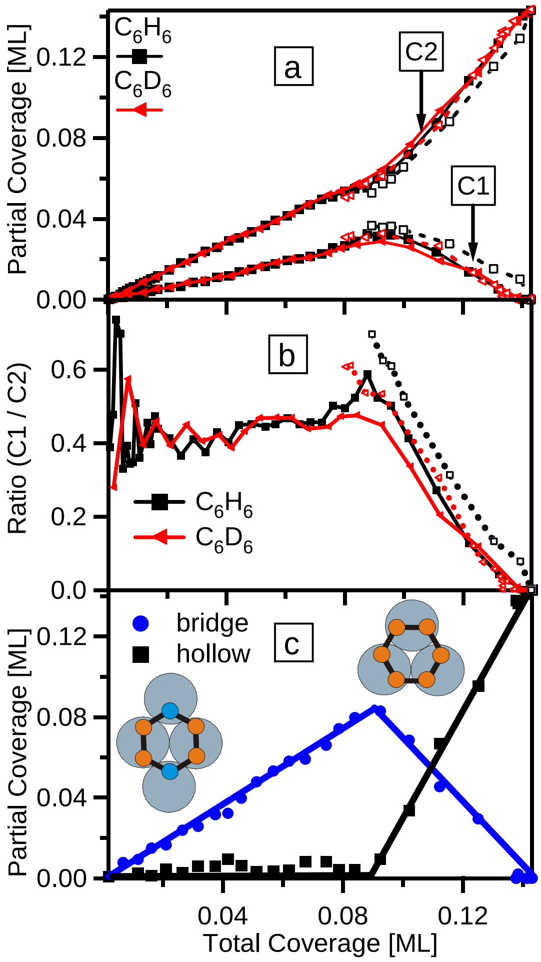

Fig. 2: a) Comparison of adsorption and thermal desorption experiments of C_6H_6 and C_6D_6. b) Ratio of the two components for C_6H_6 and C_6D_6. c) Occupation of adsorption sites during adsorption at 200 K. (Dotted lines mark results of TP-XPS experiments).

In summary, we performed a detailed analysis of the coverage-dependent site preference of benzene on a Ni(111) single crystal surface. Our quasi-continuous measurement of the adsorption of benzene (C_6H_6 and C_6D_6), summarized in Fig. 2c, shows up to a coverage of 0.10±0.01 ML only bridge adsorbed benzene. For higher coverages we find the beginning of a coverage-dependent site change, accompanied by reorientation of the molecules (*5*), resulting in a mixture of hollow and bridge adsorbed benzene. At saturation coverage only hollow adsorbed benzene is found on the surface. Our desorption experiment showed, that this site change is reversible.

This work was supported by the DFG through grant Ste620/4-2.

1. G. A. Somorjai, *Introduction to Surface Chemistry & Catalysis* (Wiley, New York, 1994).
2. R. Denecke, M. Kinne, C. M. Whelan, H.-P. Steinrück, *Surf. Rev. Lett.* **9**, 797-801 (2002).
3. S. J. Osborne *et al.*, *J. Chem. Phys.* **106**, 1661-1668 (1997).
4. O. Schaff *et al.*, *Surf. Sci.* **348**, 89-99 (1996).
5. H.-P. Steinrück, W. Huber, T. Pache, D. Menzel, *Surf. Sci.* **218**, 293-316 (1989).

Combined application of XPS, XANES and mass-spectrometry to *in-situ* study of methanol oxidation over vanadium based catalysts

V.V. Kaichev[1], V.I. Bukhtiyarov[1]

[1]*Boreskov Institute of Catalysis, Lavrentieva prosp., 5, 630090, Novosibirsk, Russia*

D.Yu. Zemlyanov[2,3], S. Belochapkine[2], B.K. Hodnett[2]

[2] *Materials and Surface Science Institute and Physics Department, University of Limerick, Limerick, Ireland*

[3] *Birck Nanotechnology Center, Purdue University, West Lafayette, IN 47907-2057, USA*

E. Kleimenov[4], D. Teschner[4], S. Zafeiratos[4], M. Hävecker[4], A. Knop-Gericke[4], R. Schlögl[4]

[4] *Abteilung Anorganische Chemie, Fritz-Haber-Institut der Max-Planck-Gesellschaft, Faradayweg 4-6, D-14195 Berlin, Germany*

Vanadium-based systems are widely applied as catalysts for selective oxidation of hydrocarbons, alcohols, etc. For example, V-P-O oxide catalysts convert n-butane to maleic anhydride [1], V-Ti-O mixed oxides – beta-picoline to nicotinic acid [3]; V-P-O/TiO_2 catalysts are active in methylpyrazine ammoxidation [2]. Oxidation of methanol to formaldehyde (or to methyl formate) and formaldehyde to formic acid over V_2O_5/TiO_2 catalysts attracts a special attention of researchers due to its practical importance [4-6]. Despite numerous reports, the exact mechanisms of these reactions are not clear yet.

In this report we present the results of *in situ* study of methanol and propane oxidation over V_2O_5/TiO_2 catalysts performed with X-ray photoelectron spectroscopy (XPS) and near edge X-ray absorption fine structure (NEXAFS). Catalytic properties of the catalysts studied were tested simultaneously using mass-spectrometry.

All experiments were performed at beam line U49/2-PGM1 at BESSY. The spectrometer was equipped with a special gas cell which allowed increase in pressure for *in situ* XPS and NEXAFS measurements up to 2 mbar. The gas flows into the experimental cell were regulated using calibrated mass-flow controllers. Before experiments the catalyst powders were pressed to pellets and then mounted on a temperature-controlled heating stage. The sample temperature was measured using a chromel-alumel thermocouple pressed directly at the back of the sample. The overall spectral resolution was 0.1 eV at the Oxygen *K*-edge. All spectra were normalized by the incident photon flux, which was measured using a photodiode with known quantum efficiency. XPS spectra were calibrated against C1s line from adventitious carbon (284.8 eV). To extract the information about chemical states of the elements, the narrow regions of their core level spectra have been measured, original XPS spectra being decomposed on separate components. The latter procedure involved Shirley background subtraction and a curve fitting using Doniach-Sunjic functions.

Vanadia-titania catalysts $20V_2O_5$ – $80TiO_2$ (wt.%) were prepared by spraying titanium dioxide (anatase) suspension in an aqueous vanadyl oxalate solution followed by calcination of the obtained powder in air at 400°C [6]. The specific surface area of the catalyst was equal to 140 m^2/g. In spite of the high content of V_2O_5, X-ray diffraction (XRD) analysis indicates that the catalysts contains only TiO_2 anatase phase. At the same time, transmission electron microscopy (TEM) shows the presence of the V_2O_5 nanocrystals (d = 1-2 nm) located on the surface and inserted between small (3-8 nm) anatase particles, which are joined into aggregates with irregular shape. This sample exhibits high activity in methanol oxidation to formaldehyde and in formaldehyde oxidation to formic acid [6].

This sample was used as an object for our *in situ* experiments which include the step-wise heating of the sample from 50°C to 150°C under near-equimolar CH_3OH/O_2 mixtures at total pressure of ~ 0.1 mbar. MS, XPS and NEXAFS spectra were measured simultaneously at three different temperatures: 50, 90, 110 and 150°C. The corresponding XPS spectra are shown in Fig.1. Before *in situ* experiments were started, the catalyst was activated in 1 mbar of oxygen at 300°C for 30 min directly in the gas cell. This led to full oxidation of vanadia and removal of any carbon-contained impurities. Only sharp single feature at 517.6 eV, which corresponds to V^{5+} ions, is observed in the $V2p_{3/2}$ spectrum (fig.1). Under influence of the CH_3OH/O_2 mixtures, vanadium(V) ions are reduced to V^{4+} state that is identified on

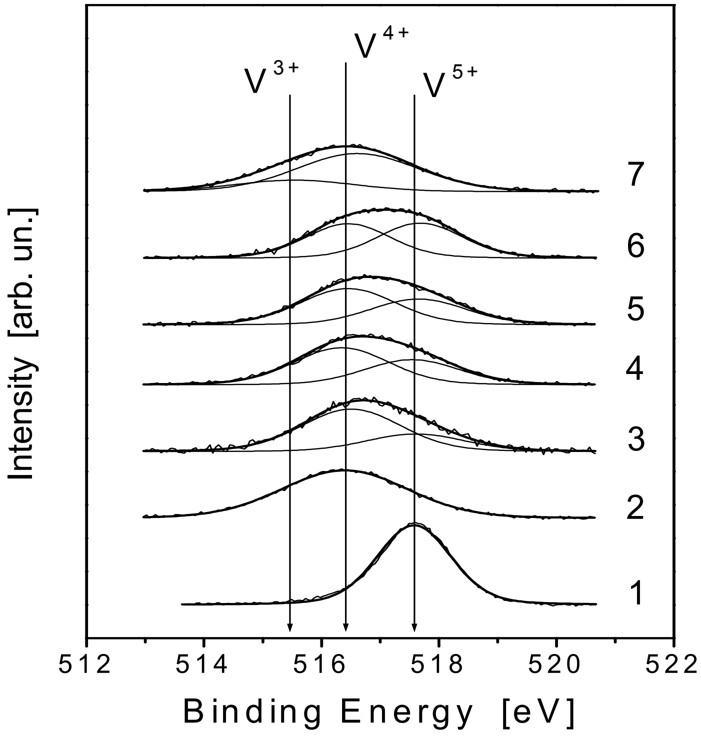

Fig.1. $V2p_{3/2}$ core-level spectra from the V_2O_5/TiO_2 catalyst obtained *in situ*: 1 – under 1 mbar oxygen at 300°C; 2-5 – under near-equimolar CH_3OH/O_2 mixtures at pressure of ~0.1 mbar at temperature 50, 90, 110 and 150°C, respectively; 6 – after switch off methanol flow at 150°C; 7 - similarly after switch off oxygen flow at 150°C.

appearance of wide $V2p_{3/2}$ peak at 516.4 eV. Increasing the temperature led to partial oxidation of vanadium(IV) ions and two features at 516.4 ± 0.1 eV (V^{4+}) and 517.6 ± 0.1 eV (V^{5+}) are observed in the $V2p_{3/2}$ spectra (fig.1). It should be noted, that the fraction of V^{5+} ions are increased constantly with temperature. Significant part of V^{4+} ions are remained on the catalyst surfaces even after removal of methanol form the gas phase. On the other hand, removal of oxygen at 150°C results in further reduction of vanadium and two features at 515.6 and 516.6 eV, which can be attributed with V^{3+} and V^{4+}, respectively, are observed in the $V2p_{3/2}$ spectrum (fig.1). Thus, our data unambiguously show that lattice oxygen of vanadium oxide takes a part in the methanol oxidation via Mars-van Krevelen mechanism, which consists of reduction of the oxide catalyst surface by methanol and subsequent reoxidation by gas phase oxygen. The reduced V^{4+} ions are believed to be the active sites involved in the Mars-van Krevelen redox cycles.

It has been also found that surface composition of the V_2O_5/TiO_2 catalysts is changed as a function of the reaction atmosphere and temperature. At 150°C titanium signal disappears from the surface-sensitive spectra, but it is still detectable in the bulk-sensitive spectra. This result can be explained by the accumulation of carbonaceous species selectively on the low-active titania surface or by the redistribution of the elements so that the titania surface is covered with vanadium. The former concept seems to be more preferable, because recently some author observed agglomeration of the dispersed vanadia during methanol oxidation over V_2O_5/SiO_2 catalysts [7].

Acknowledgement. This work was supported by the European Community - Research Infrastructure Action under the FP6 "Structuring the European Research Area" Programme (through the Integrated Infrastructure Initiative" Integrating Activity on Synchrotron and Free Electron Laser Science - Contract R II 3-CT-2004-506008).V.I.B. and V.V.K. gratefully acknowledge the Max-Planck-Gesselschaft for financial support of the visit to FHI and work at BESSY. We gratefully acknowledge the BESSY staff for the support during beamtime.

References:

1. B.K. Hodnett, Heterogeneous Catalytic Oxidation, Wiley, New York, 2000, Chapter 5.
2. V.M. Bondareva, T.V. Andrushkevich, O.B. Lapina, A.A. Vlasov, L.S. Dovlitova, Reac. Kinet. Catal. Lett. 79 (2003) 165.
3. E.M. Al'kaeva, T.V. Andrushkevich, G.A. Zenkovets, G.N. Kryukova, S.V. Tsybulya, Catal. Today 61 (2000) 249.
4. P. Forzatti, E. Tronconi, A.S. Elmi, G. Busca, Appl. Catal. A 157 (1997) 387.
5. E. Santacesaria, A. Sorrentino, R. Tesser, M. Di Serio, A. Ruggiero, J. Mol. Catal. A 204-205 (2003) 617.
6. G. Popova, T.V. Andrushkevich, I. Zakharov, Yu. Chesalov, Kinet. Catal. 46 (2005) 217.
7. T. Feng, J.M. Vohs, J. Phys. Chem. B 109 (2005) 2120.

The Local Adsorption Geometry of Alanine on the Chiral Cu{531} Surface studied by NEXAFS

M. J. Gladys[1], A. Stevens[1], N. Scott[1], D. Batchelor[2] and G. Held[1]

[1]*University of Cambridge, Department of Chemistry, Lensfield Rd, Cambridge CB2 1EW, UK.*
[2]*BESSY and Universität Würzburg, Experimental-Physik II, Am Hubland, Würzburg, Germany.*

Chiral (enantiomeric) molecules often exhibit drastically different reactivity in living matter. The ‘wrong’ enantiomer of a chiral molecule may have such damaging side effects that any beneficial properties of the ‘right’ enantiomer are completely overshadowed. The importance of producing single enantiomer products cannot be understated and beyond the pharmaceutical sector, chiral modified surfaces have considerable appeal in the production of flavours and fragrances, microelectronics, and magnetic components [Barl03,Coll95]. This report details experiments on the adsorption of the chiral amino acid alanine ($OOC–C^*HNH_2–CH_3$) on chiral copper surfaces that may exhibit enantiospecific selectivity, which can be used in molecular sensors or heterogeneous catalysis. Specifically, synchrotron techniques such as High Resolution XPS and NEXAFS, using variable polarised X-rays provide accurate determination of bonding geometry and the chemical nature of metal-organic interfaces.

It was established that certain single crystal fcc surfaces with high Miller indices are chiral because they contain two inequivalent types of steps constituting a kink site which has no mirror symmetry [Atta01]. The goal of our studies is to find the correct combination of substrate unit cell and organic molecule that will combine to produce stereo-selectivity. We have chosen the Cu{531} surface which contains the smallest chiral unit cell, with only three atoms dividing the step kinks on the surface. This surface incorporates {110} and {311} step kinks and directly correlates with the knowledge gained from the investigations on Cu{110} in which the alanine adsorbs in a three point bonding geometry [Jone06].

The experiments were performed at beamline UE52-PGM (CRG) of BESSY II, which has a spot size of about 100μ x 200μ at the sample. The base pressure of the UHV endstation was $3x10^{-10}$ mbar; all data were recorded at room temperature. XPS data were recorded using a Scienta 200 mm electron energy analyser with pass energies of 20 and 40 eV at a photon energy of 630 eV. The binding energies (BE) were calibrated with corresponding measurements at the Fermi energy for the same photon energy and pass energy. For the NEXAFS experiments the synchrotron beam hit the surface either at normal incidence or at 70˚ off normal incidence, the orientation of the electrical field vector, **E**, within the surface plane was controlled by the undulator settings to be parallel or perpendicular to the [1-21] direction (see Figure 2) as well as angles of 15^o, 45^o and 65^o from parallel (which is now a permanent feature at UE52-PGM). A partial yield detector (PYD) was used with the retarding voltage set to accept electrons in the kinetic energy range up to 50 eV below the lowest photon energy in order to avoid detection of Cu d-band photoelectrons. The raw C, N, and O K-edge NEXAFS data were normalised with respect to the ring current and spectra of the clean sample.

The Cu sample was prepared using standard procedures including electro-polishing, Ar-ion sputtering and oxygen treatment in UHV followed by a final annealing step to 1000 K. R and S-alanine was adsorbed by evaporating a coverage in excess of the amount actually needed at a sample temperature of 300K. After the adsorption was complete the sample was annealed to about 400K to produce the (1x4) ordered structure as determined by LEED. The

LEED pattern of the R-alanine overlayer indicates a lesser degree of order than that observed with S-alanine, for which the data are shown here.

XPS spectra of C1s, O1s and N1s core levels (not shown) were identical for R and S-alanine layers prepared under the same conditions. Narrow O1s and N1s XPS peaks were found at BE 531.3 and 399.5eV, respectively. The absence of a second O 1s peak indicates that both oxygen atoms in the molecule are involved in the bond formation with the substrate and the molecule is in its deprotonated alaninate form. The C 1s spectra show two peaks at BE 288.0 and 285.5eV. According to [Hass98,Barl04,Jone06] we assign the first peak to the OO**C**– carbon atom of the carboxylate group and the second, more intense, peak to the two –**C**HNH$_2$–**C**H$_3$ carbon atoms, which only take part in C-C single bonds. The XP spectra are very similar to data for alanine on Cu{110} [Jone06]. Decomposition of the alanine layer occurs around 470K where an abrupt change in all core levels is observed.

The raw NEXAFS spectra for the Carbon K-edge are shown in Figure 1, for the in-plane **E** orientations listed above. There is a clear polarisation dependence of the π* resonance at 289eV for in-plane angles. The polarisation dependence of the π* resonance for the 70^o NEXAFS data plainly show that the O-C-O triangle is tilted with respect to the surface normal [Stoe92]. The finding that the molecules form bonds with the Cu substrate through three atoms, two O and one N, explains the tilt of the O-C-O group and is in good agreement with results from recent DFT calculations [JoneXX]. Figure 2(a) shows the variation of the π* resonance as the linear polarization is rotated within the surface plane. If only a single adsorption site was occupied the intensity of the resonance should follow a $\cos^2\theta$ relation, θ being the angle between the polarisation vector and the normal of the O-C-O triangle [Stoe92], and the intensity at the minima should be zero. The fact that the intensity does not decrease to zero indicates the existence of multiple molecule orientations on the surface. DFT calculations by [JoneXX] show little difference in the cross sections of the two molecules. It can therefore be assumed that each of the differently oriented molecules will follow a $\cos^2\theta$ relation with a similar pre-factor. Using circular polarised synchrotron radiation as an average over all angles, we are able to normalise the spectra and determine the maximum of the $\cos^2\theta$ dependencies. Assuming two orientations of the molecules, rotated by about 75° with respect to each other, provides an excellent fit to the data, as shown in Figure 2(a). Combining HRXPS, NEXAFS and LEED results, suggests that there is only room for two molecules within the (1x4) unit cell, one binding to a {110} and the other to a {311} step as shown in Figure 2(b). It should be noted that without the newly acquired ability to measure the carbon K-edge at angles between the horizontal and vertical, determination of the exact angles would be impossible.

A comparison of in-plane polarisation dependences of the π* resonance for R and S-alanine show a sizeable deviation. The minimum is at the same angular position, however the intensity variation is larger. This indicates that the orientations of the two types of molecules are different to that of the S-alanine case, which may be the result of slightly different stabilities of the two systems due to different degrees of inter-molecular hydrogen bonding.

This study was supported by the European Commission under the Contract No R II 3-CT-2004-506008 / project BESSY-ID.05.2.090 and the EPSRC. We would like to thank the BESSY staff for their support during the beamtime.

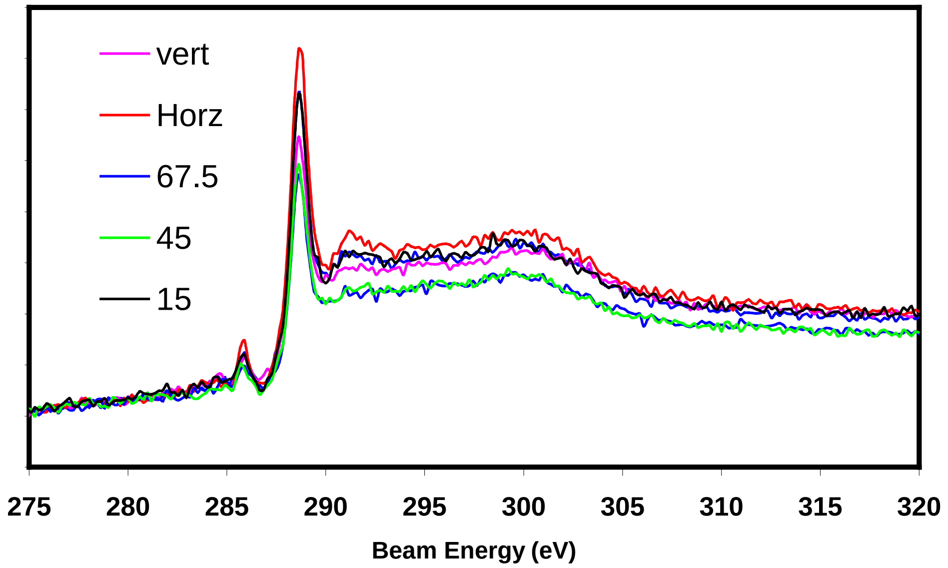

Figure 1: Carbon K-edge spectra for S-Alanine on Cu{531} for in-plane polarisation at different azimuthal angles between and including the horizontal and vertical angles.

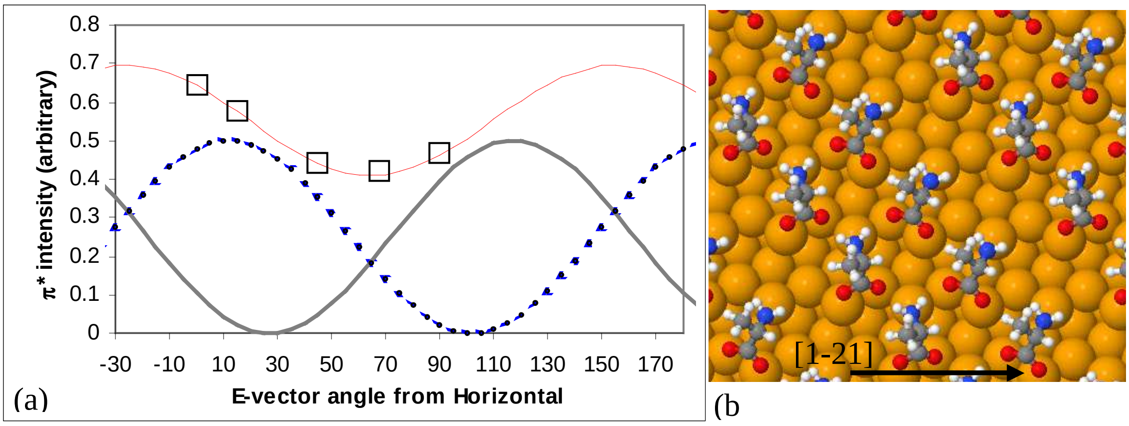

Figure 2: (a) The intensity of the carbon π* resonance for the ordered (1x4) structure of S-Alaninate on Cu{531}. The experimental results (squares) can be fitted by including two molecular orientations (bottom curves) of Alaninate on the surface. (b) The two orientations of the molecule adsorb onto the {110} and {311} steps.

References:

[Atta01] G. Attard, J.Phys. Chem. B, 105, (2001) 3158.
[Barl03] S.M. Barlow and R. Raval. Surface Science Reports 50, (2003) 201.
[Barl05] S. M. Barlow et al. Surf. Sci. 590 (2005) 243.
[Coll95] A. N. Collins, G. N. Sheldrake and J. Crosby (Eds), Chirality in Industry: The Commercial Manufacture and Applications of Optically Active Compounds (John Wiley, 1995).
[Hass98] J. Hasselström et al. Surf. Sci. 407 (1998) 221.
[Jone06] G. Jones, L.B. Jones, F. Thibault-Starzyk, E.A. Seddon, R. Raval, S. J. Jenkins, G. Held, Surf. Sci. (2006) in press.
[JoneXX] G. Jones et al. to be published.
[Stoe92] J. Stöhr 'NEXAFS spectroscopy', Springer, 1992.

A comparative in situ XPS study of PtRuCo catalyst for CH_3OH and CO oxidation using water.

S. Zafeiratos[1], G. Papakonstantinou[2], F. Paloukis[2], A. Knop-Gericke[1],
S.G. Neophytides[2], R. Schlögl[1],
[1]*Fritz-Haber-Institut der MPG, Faradayweg 4-6, D-14195 Berlin (Dahlem), Germany*
[2]*ICEHT-FORTH, GR-26504 Rion, Achaias, Greece*

Grant Number :RII 3 CT-2004-506008

Introduction

Fuel cells using methanol as a fuel are promising future energy technology. Methanol is electro-oxidized in the presence of water at the anode generating CO_2, hydrogen ions and the electrons that travel through the external circuit as the electric output of the fuel cell. The excellent catalytic activity of Pt for methanol oxidation makes this metal electrocatalysts ideal for use as an anode in Direct Methanol fuel cells (DMFCs). However, Pt metal surface is easily poisoned at low temperatures by trace amounts of CO, which exists as a byproduct of methanol electrooxidation. Theoretical and experimental studies have shown that ternary PtRuCo catalyst significantly promotes the methanol oxidation reaction [1]. In this study we investigate the PtRuCo surface for the CH_3OH and CO oxidation in the presence of H_2O.

Experimental

The $Pt_{37.5}Ru_{37.5}Co_{25}$ catalyst was prepared by combustion synthesis and pre-treated in-situ under oxidation (0.5 mbar O_2 at 400°) and reduction (0.5 mbar H_2 at 300°) cycles. XP spectra were recorded at 300° under steady state conditions using depth profiling by variation of the incident photon energy. The overall pressure was 0.5 mbar and the CH_3OH:H_2O and CO:H_2O mixing ratios were 1:2 and 1:10 respectively. Spectra under CO, H_2O, O_2 and H_2 atmospheres were also recorded as a reference. Synchrotron radiation delivered by the undulator U49/2 was used. Changes in the gas phase composition were monitored by on-line mass spectrometry simultaneously to the spectroscopic characterization of the catalyst surface.

Results

On line Mass Spectrometry data for CH_3OH and CO oxidation are given in fig. 1a and b respectively. The activity of the catalyst is demonstrated by the detection of the reaction products (H_2 and CO_2) in the gas phase and the consumption of CH_3OH when the catalyst was heated in the reaction mixture. Blank experiments were performed in order to support the above picture.

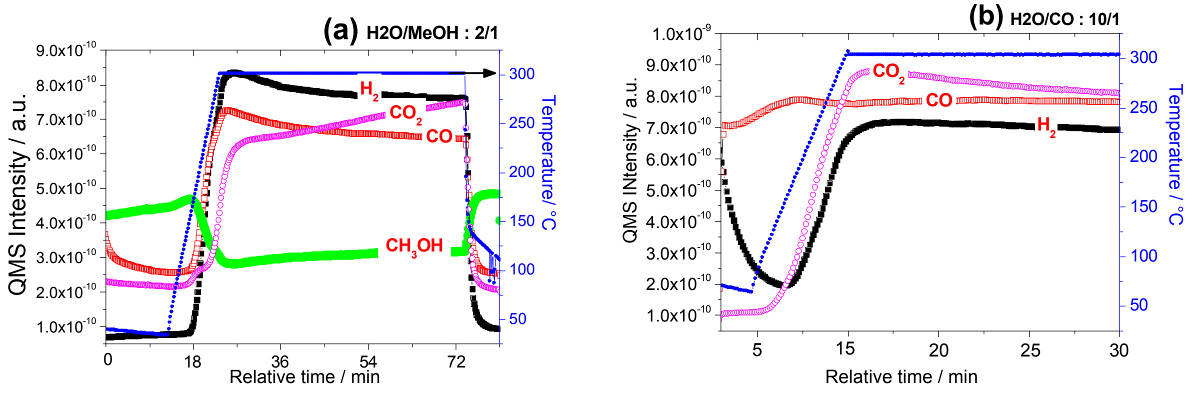

Figure 1. On line Mass Spectrometry data a) Methanol oxidation b) CO oxidation

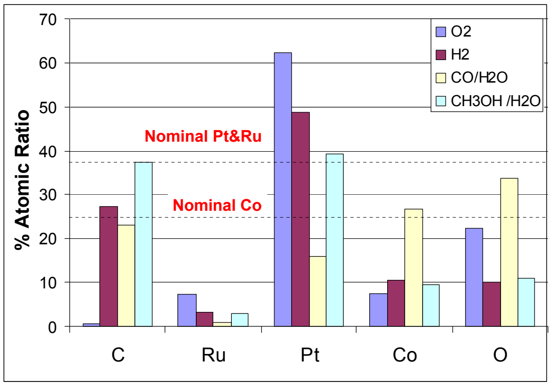

Figure 2. The surface atomic concentration calculated from XPS intensities recorded under various gas atmospheres

Surface segregation, i.e. the enrichment of one element at the surface relative to the bulk, is a ubiquitous phenomenon in metal alloys [2]. In situ XPS gives a unique opportunity to determine the surface composition under various gas atmospheres. In figure 2 the calculated C, Ru, Pt, Co and O atomic concentration at the first 4 atomic layers (electron KE = 180 eV) are presented under various atmospheres. From the results is concluded that Pt segregates on the surface during methanol oxidation, while for CO oxidation the picture changes and cobalt enrichment occurs accompanied with higher O amounts and the decrease of Pt. The chemical state of surface elements is very much depended on the type of the reaction. In figure 3 characteristic C1s&Ru3d$_{5/2}$, Pt 4f, Co 2p$_{3/2}$ and O 1s spectra are presented. In Fig 3a graphitic carbon at 284.4eV dominates C1s region, while a surface located component at 288.1 eV corresponds most probable to adsorbed CO. Ru 3d$_{5/2}$ peak is found at 279.8 eV, very close to the binding energy of metallic Ru. A comparison of Pt 4f peaks for methanol and CO oxidation (fig. 3b) reveals that in the later case a new Pt doublet at 72.5 eV is needed in order to fit the overall spectrum. This peak is primarily surface located and can be attributed to hydroxyl-Pt complexes [3] as supported also from O1s spectra (see below). In fig. 3c, Co 2p$_{3/2}$ spectra under reaction as well as under H_2 and O_2 atmospheres are presented. For methanol oxidation cobalt found completely reduced (778.1 eV), contrary to CO oxidation where it is partially oxidized. O 1s spectra in fig. 3d showed a complex structure, also due to gas phase peaks appear above 534 eV.

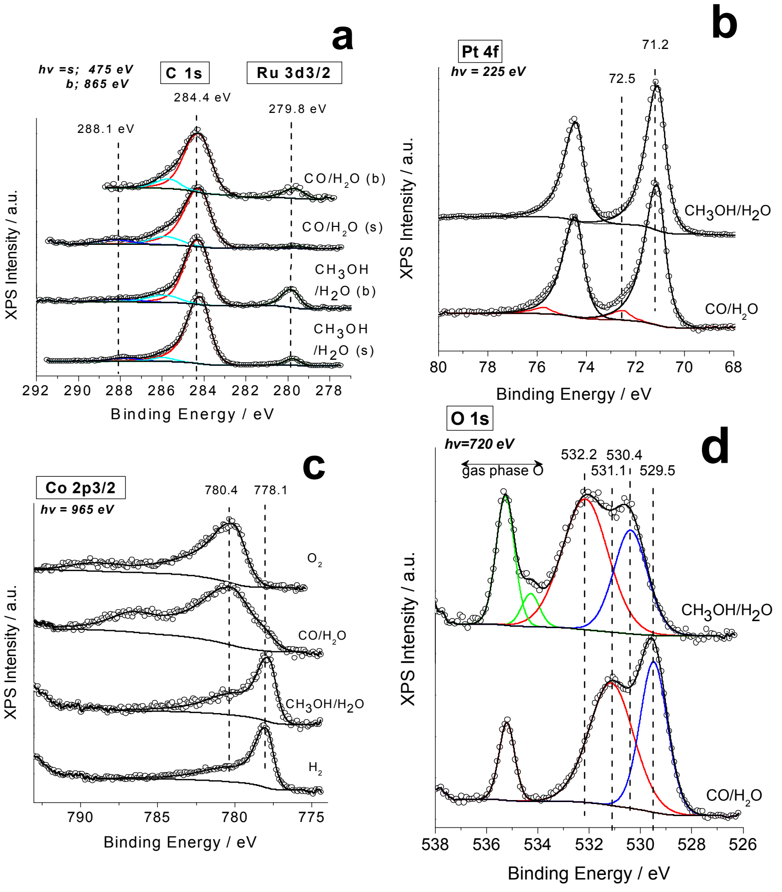

Figure 3. XPS spectra recorded at 300°.

Assignment of the O 1s peak is speculative and should be done taking into account characteristics of the Pt and Co peaks. During CO oxidation non-gas phase peaks are centered at 529.5 and 531.1 eV. Depth analysis showed that the peak at 531.1 eV is mainly surface located testifying for the presence of hydroxyl species on the surface. The bulk component at 529.5 eV is probably related to the oxidized cobalt as showed in fig. 3c. In case of methanol oxidation two broad O1s compounds were found at 530.4 and 532.2 eV. Although definitely assignment of these components is unfeasible, it comes out that different oxygen species are involved in each reaction.

In summary, it was showed that the composition and the chemical state of PtRuCo surface depend on the performed reaction, indicating the dynamic character of the catalyst. It was found that the oxidation state of Co varies, probably acting as a carrier or reservoir of oxidation agents participating in the reaction. This nicely correlates with observations on realistic fuel cells, where PtRuCo found to facilitate CO oxidation at lower potentials compared to Pt and PtRu [1]. The excess of oxidized species on the surface, related with the presence of cobalt, promotes CO oxidation most probable providing OH species on Pt where CO oxidation actually takes place.

References

[1] Strasser P. Fan Q., Devenny M. Weinberg W.H. , Liu P. Norskov J.K., J Phys. Chem B 2003, 107 11013

[2] Markovic, N.M. Ross, P.N. Surf. Sci. Rep. 2002, 45 117

[3] J.E. Drawdy, G.B. Hoflund, S.D. Gardner, E. Yngvadottir, D.R. Schryer, Surf. Interface Anal. 16 (1990) 369.

In-situ XPS study on $(MoV)_5O_{14}$ selective oxidation catalysts

P.Schnörch, E. M. Vass, S. Zaferiatos , D.Teschner, M. Hävecker,

A. Knop-Gericke, R. Schlögl

Department of Inorganic Chemistry, Fritz-Haber Institute of the MPG, Faradayweg 4-6, 14195 Berlin, Germany

Introduction

Catalytic reactions involving partial oxidation belong to the most important processes in the chemical industry [1]. Therefore, Mo based selective oxidation catalysis (propane and propylene to acrylic acid) is one of the main research area in our department. In-situ experiments are necessary to identify the active phase under working conditions. In-situ spectroscopy techniques in the soft X-ray range like X-ray absorption spectroscopy and photoelectron spectroscopy were applied to investigate the electronic structure of the working catalyst surface. In this work we measured two different oxide containing catalysts, (MoVW)Ox and (MoV)Ox which are very good candidates for these reactions.

Results

The experiments were performed at beamline U49/2-PGM1 at the synchrotron source. The in-situ XPS system is a modified standard XPS spectrometer. Three differential pumping stages keep the hemispherical analyzer at high vacuum while the pressure in the sample cell is in the mbar range. The reaction cell is separated from the synchrotron beam line by a 100 nm thick SiNx X-ray window.

The $(Mo_{0.91}V_{0.09})_5O_{14})$ catalyst was prepared by spray-drying technique of a mixed solution of ammonium heptamolybdate (AHM) and vanadyl oxalate. The precursor was treated at 623K in air and 773K in helium.

The $(Mo_{0.68}V_{0.23}W_{0.09})_5O_{14}$ catalyst was prepared also by spray-drying technique of a mixed solution of ammonium heptamolybdate (AHM), ammonium metatungstate (ATM) and vanadyl oxalate. The obtained product was calcined at 623 K for 2h in static air and in flowing He at 12 h at 713 K. [2]

The catalysts were investigated under ~0.5 mbar of propylene-oxygen (1:2) mixtures. We have recorded the Mo3d, O1s/V2p, C1s and valence band regions under reaction conditions. In addition we have performed depth-profiling by varying the excitation photonenergy applied to the same core-level, which leads to a change of the photoelectron kinetic energy, and as a consequence to a change in the information depth.

The catalytic reactivity was measured using PTRMS. Other than CO_2, catalysts $(Mo_{0.91}V_{0.09})_5O_{14})$ and $(Mo_{0.68}V_{0.23}W_{0.09})_5O_{14}$ produced only aldehydes and no acids under these low-P conditions at higher pressure (atmospheric) the catalysts are produced acrylic acid as well. The reason might be a pressure barrier existing between atmosphere and mbar conditions. However further investigations are required to examine the effects of pressure dependence on the reaction.

The mass spectra were recorded simultaneously with the XPS spectra, which allowed us to correlate the XPS results with the catalytic activity of the material.

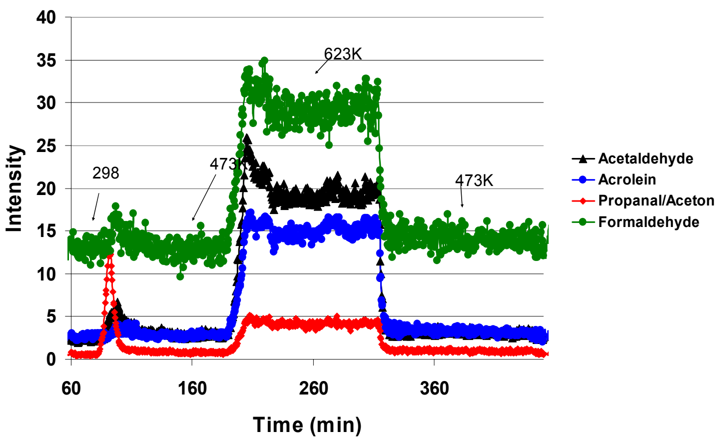

The samples were measured using two different temperature profiles. At 298K – 473K – 623K – 473K, and 298K – 623K – 473K, the heating ramp was in both cases 10K/min. (Fig1.) The catalyst showed different catalytic behavior depending on reaction conditions.

Fig. 1. Catalytic activity under reaction atmosphere

From the XP spectra vanadium enrichment was observed on the catalyst subsurface in both catalysts. (Fig2.)

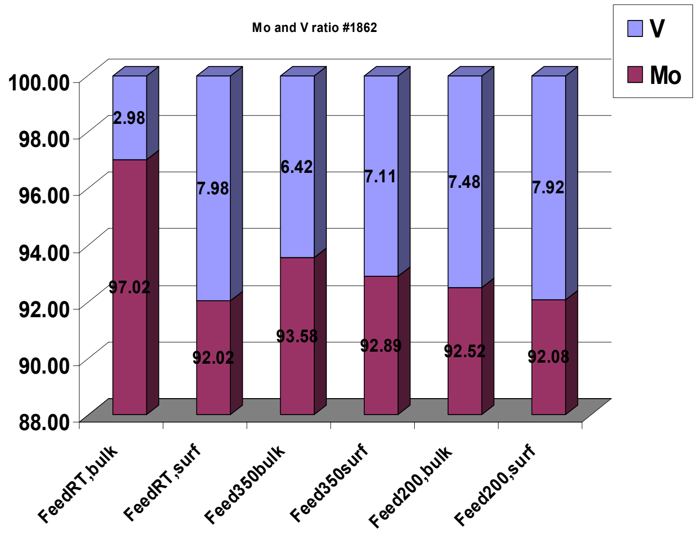

In the case of W containing catalyst the Mo3d oxidation state it was not really changed but the only vanadium and molybdenum containing sample showed different oxidation states in room temperature ,during the reaction the Mo^{5+} state is disappeared and the remaining state is Mo^{6+}. It means the molybdenum completely oxidized under the reaction mixture. (Fig 3. ,Fig 4.)

Fig.2. Molybdenum and Vanadium ratio in “bulk” (~18Å) and surface (~8Å) sensitive mode

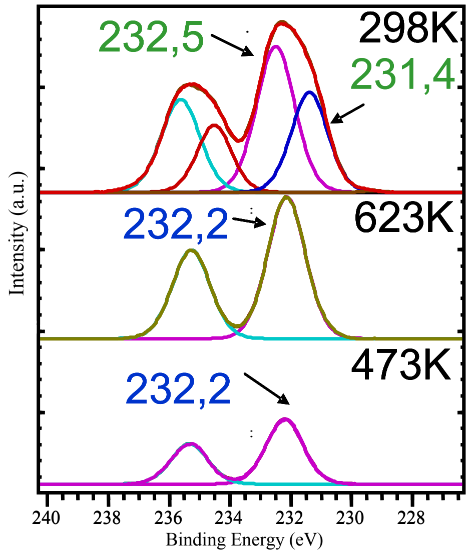

Fig 3. Mo^{5+}statet disappear during the reaction (MoV)Ox

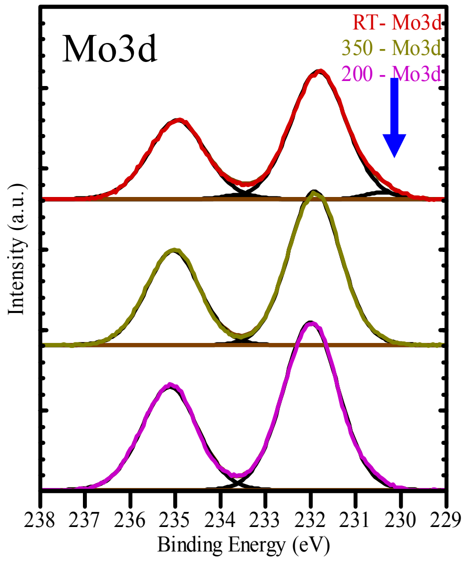

Fig4. Small changes on the oxidation state of the Mo3d core level under the reaction (MoVW)Ox

The V2p core level was more oxidized under the reaction condition. The $V4^{+}$ state increased during catalytic reaction.(Fig5) The initial tungsten oxidation state was 6^{+} and there was no changing under the reaction.

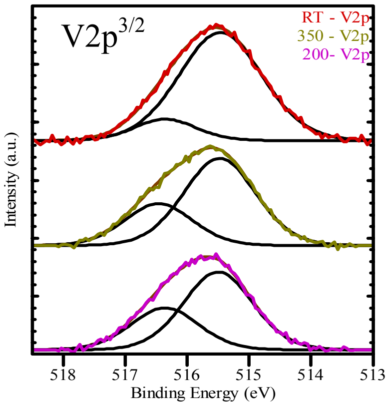

Fig5. V2p spectra at different temperatures

In the future we would like to investigate more precisely the role of the Mo, V oxidations state during the reaction atmosphere because it seems there is no significant changing in the W oxidation states. According to some preliminary investigations the role of the tungsten in the catalysts is to stabilize the structures.

Acknowledgement

The authors thank the Bessy staff for their continual support during the measurements.

References

[1] J. Holmberg, R.K. Grasselli and A. Andersson, *Appl. Catal. A: General* **270** (2004), p. 121

[2] S. Knobl, G. A. Zenkovets, G. N. Kryukova, O. Ovsitser, D. Niemeyer, R. Schlögl, G. Mestl, Journal of Catalysis **215** (2003) 177

.

Remnant XMCD investigation of bimetallic oxalate based magnets: local magnetic contributions to the remnant magnetization

C. Cartier dit Moulin, C. Train
LCIM2, Université Paris 6, 4 place Jussieu, 75252 Paris Cedex 05, FRANCE

We are engaged in the enantioselective synthesis of oxalate-based magnets of general formula $A[M^{II}M^{III}(ox)_3]$ where A is a monocation, M^{II} and M^{III} two transition metal ions and $ox=C_2O_4^{2-}$. Apart from being good candidates to observe magnetochiral dichroism, a new physical effect arising from the synergetic breaking of space and time symmetries, these materials exhibit rich magnetic properties. In particular, depending on the choice of the metal ions, one can obtain coercive magnets [1,2] and magnets exhibiting negative magnetization for $TBA[Fe^{II}Fe^{III}(ox)_3]$ (TBA=tetra(butyl)ammonium).[3]

Up to now, quite all XMCD signals are recorded while applying a high magnetic field in order to saturate the sample and therefore increase the intensity of the XMCD signals. Rare are the XMCD experiments performed with a null or weak magnetic field.

1. On one hand, recording remnant XMCD signals shall allow to precise the respective impact of single ion anisotropy, magneto-structural anisotropy and exchange interaction on the remnant state of these magnets.
2. On another hand, through the XMCD measurements of the respective contribution of Fe^{II} and Fe^{III} in $TBA[Fe^{II}Fe^{III}(ox)_3]$ in a low applied magnetic field (100 G), we want to precise the origin of the negative magnetization observed in this compound at low temperature.

2.Aims of the experiment

2.1 Study of the remnant state in $TBA[Fe^{II}Fe^{III}_{0.77}Cr^{III}_{0.23}(ox)_3]$

We have recently performed XMCD measurements on a two dimensional oxalate based magnet, $[N(C_4H_9)_4][Fe^{II}Fe^{III}_{0.77}Cr^{III}_{0.23}(ox)_3]$, at the Fe and Cr K-edges (Figure 1).[4]

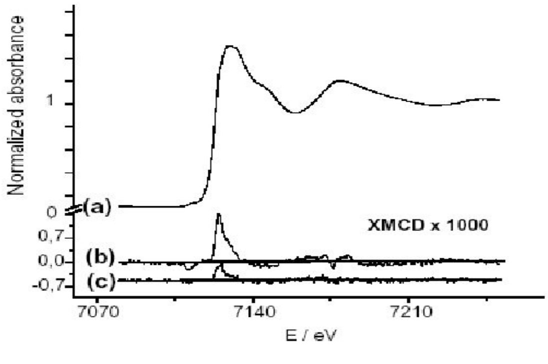

Figure 1: **(a)** Isotropic Fe K-edge XAS spectrum for $\{[N(C_4H_9)_4][Fe^{II}Fe^{III}_{0.77}Cr^{III}_{0.23}(ox)_3]\}$; **(b)** XMCD signals (x1000) measured in H = ±2 T; **(c)** XMCD signals (x1000) measured in zero field after applying H = ±2 T(Ref 4).

This material is a ferrimagnet with a Curie temperature of 36 K. The coercive force at 2K is 1.03 T and the remnant magnetization M_r is 0.25 μ_B. We have evidenced a remnant XMCD signal at H = 0 T at the two edges. The remnant to saturation XMCD signals ratios follow the macroscopic measurements for both ions. We therefore show that the contribution of the local magnetic moments to the total remnant magnetization is the same for Cr(III) and Fe(II) cations despite the higher single-ion anisotropy of the Fe(II) ion. This result is in line with other XMCD investigations on the origin of the hysteretic behavior of single molecule magnets[5] and of extended networks.[6] Measurements at the K-edges do not allow to determine the spin and orbital contributions to the XMCD signal.

2.2 Study of the low field XMCD in TBA[$Fe^{II}Fe^{III}(ox)_3$] *versus* temperature

According to macroscopic magnetic measurements,[3] the magnetization in 100 G goes from positive just below T_c (44 K) to negative below 30 K when the temperature is lowered. This result has been somehow anticipated by the classic theory of ferrimagnets developed by Néel. In this approach, this behavior is strongly related to the higher single-ion anisotropy of the Fe(II) ion compared to Fe(III).

Recording remnant XMCD signal at the Cr and Fe $L_{2,3}$ edges for two compounds, we want to precise the respective impact of single ion anisotropy, magneto-structural anisotropy and exchange interaction on the remnant state of these magnets.

3.Results

Out of two different compounds, we could fully measure one sample at low temperature (1.5K) in a variable magnetic field between 0 Tesla (remnant state) and 5 Tesla. We appreciate the very high quality beam of the beamline necessary to measure the small signal expected in the remnant state. We had not enough beamtime to measure XMCD signals on the second compound and on two reference compounds to calibrate our measurements.

Given the well known fragility of such compounds built with transition metal ions linked with organic ligands, we encountered strong difficulties. Due to the high flux delivered by the beamline, we observed a very rapid radiation damage of the samples. We used quite all the beamtime to try to optimize the recording conditions to reduce as well as possible the radiation damage:

- we check the different ways to reduce the flux with conservation of the circular polarization (the difficulty is the limit of the signal/noise ratio);
- during the series of scans, we changed regularly the position of the sample in the beam, using(and destroying progressively) all the surface of the pellet.

For other molecular compounds as Mn12-acetate (XMCD measurements at BESSY with the same beamline), we used successfully this way to avoid radiation damage and we obtained high quality and reliable XMCD signals.

Despite our efforts, for these iron compounds, the sample radiation damage remains very rapid. After careful analysis of our data, it seems that the results obtained are not reliable and the measured signals traduce only the evolution of the sample.

4. References

(1) Bhattacharjee, A.; Iijima, S.; Mizutani, F. *J. Magn. Magn. Mater.* **1996**, *153*, 235.
(2) Coronado, E.; Galan-Mascaros, J. R.; Gomez-Garcia, C. J.; Martinez-Agudo, J. M. *Adv. Mater. (Weinheim, Fed. Repub. Ger.)* **1999**, *11*, 558.
(3) Mathonière, C.; Nuttall, C. J.; Carling, S. G.; Day, P. *Inorg. Chem.* **1996**, *35*, 1201.
(4) Train, C.; Baudelet, F.; Cartier Dit Moulin, C. *J. Phys. Chem. B.* **2004**, *108*, 12413.
(5) Moroni, R.; Cartier dit Moulin, C.; Champion, G.; Arrio, M. A.; Sainctavit, P.; Verdaguer, M.; Gatteschi, D. *Phys. Rev. B* **2003**, *68*, 064407/1.
(6) Train, C.; Giorgetti, C.; Baudelet, F.; Champion, G.; Cartier dit Moulin, C. *C.R. Chimie* **2003**, *6*, 337.

Effect of molecular conformation on packing density and orientational order of aromatic self-assembled monolayers

A. Shaporenko[1], M. Elbing[2], A. Błaszczyk[2,3], C. von Hänisch[2], M. Mayor [2,4],
and M. Zharnikov[1]

[1]*Angewandte Physikalische Chemie, Universität Heidelberg, Im Neuenheimer Feld 253,*
69120 Heidelberg, Germany

[2]*Forschungszentrum Karlsruhe GmbH, Institute for Nanotechnology, P. O. Box 3640,*
76021 Karlsruhe, Germany

[3]*Faculty of Commodity Science, Al. Niepodległości 10, 60-967 Poznań, Poland*

[4]*University of Basel, Department of Chemistry, St. Johannsring 19, CH-4056 Basel,*
Switzerland

The on-going miniaturization of the silicon-based electronic technology will reach its physical limit in the foreseeable future and hence, alternative concepts that allow further reducing the size of electronic active components are highly desirable. In particular, the concept of molecular electronics that envisages the use of molecular structures to build electronic devices has received considerable scientific as well as popular interest recently. Prototypes of future devices are metal-molecule-metal junctions, in which a single molecule or a molecular assembly is placed between two metal electrodes. In the best case, the molecules should be chemically coupled to the electrodes, e.g., via reaction between organic thiol moieties, attached at both ends of the "device" or "wire" molecule and a metal electrode surface.

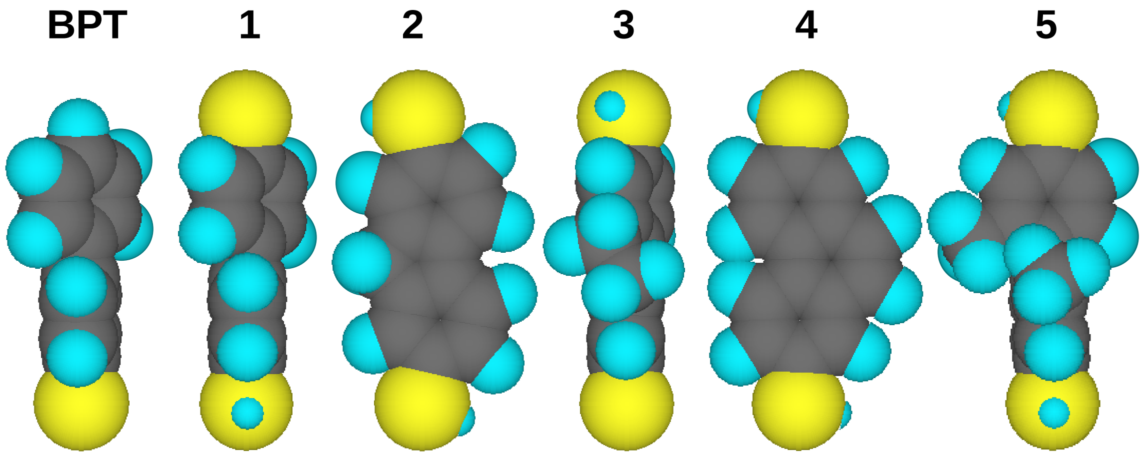

Fig. 1. Biphenyl-derived dithiol molecules with different conformations used for the SAM fabrication. It is generally assumed that the conformation of **BPT** and **1** changes to planar one in the solid state or upon the formation of densely packed SAMs. The conformations of **3** and **5** remain unchanged (torsion angles of 20° and 80°, respectively). **2** and **4** have planar conformation both in the molecular and solid state.

Keeping this general approach in mind, a series of biphenyl-derived dithiol (BDDT) compounds with terminal acetyl-protected sulfur groups and different structural arrangements of both phenyl rings have been synthesized and fully characterized. The different arrangements were achieved by introducing hydrocarbon substituents in the 2 and 2´ positions of the biphenyl backbone as shown in Fig. 1, where the respective molecules marked by **1-5** are shown (without the protection groups), along with the reference system biphenylthiol (BPT). The presented model compounds enable the investigation of the correlation between the intramolecular conformation and other physical properties of interest, like, e.g., molecular assembly or electronic transport properties. As a first step, we studied the ability of these model compounds to form self-assembled monolayers (SAMs) on Au(111) and Ag(111). The deprotection of the target molecules was performed in situ, using either NH_4OH or triethylamine (TEA) deprotection agent. The fabricated films were characterized by

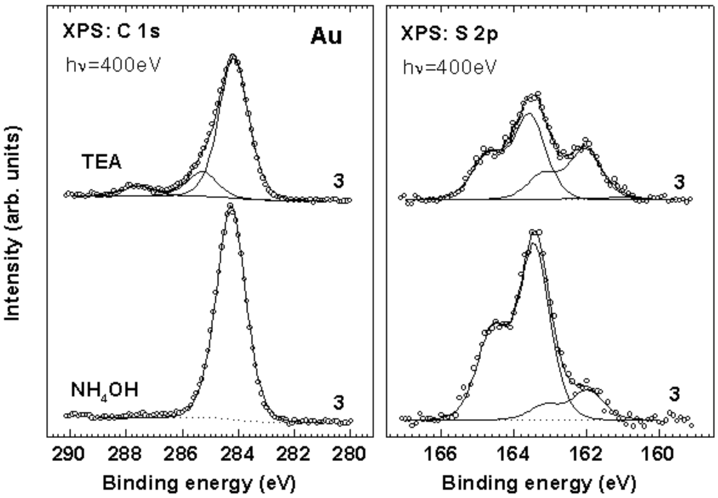

Fig. 2. C 1s (left panel) and S 2p (right panel) HRXPS spectra of **3**/Au prepared using a deprotection by TEA (top curves) and NH_4OH (bottom curves). The spectra are decomposed into the individual contributions.

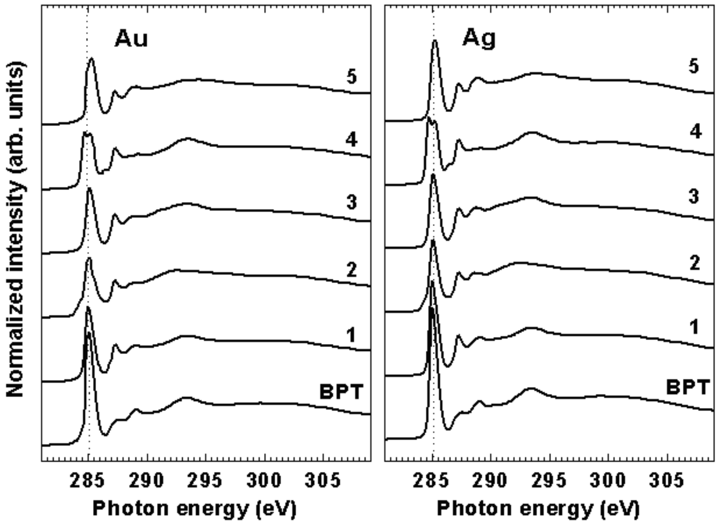

Fig. 3. C K-edge NEXAFS spectra of the TEA-deprotected SAMs **1**-**5** on Au (left panel) and Ag (right panel) acquired at an X-ray incidence angle of 55°.

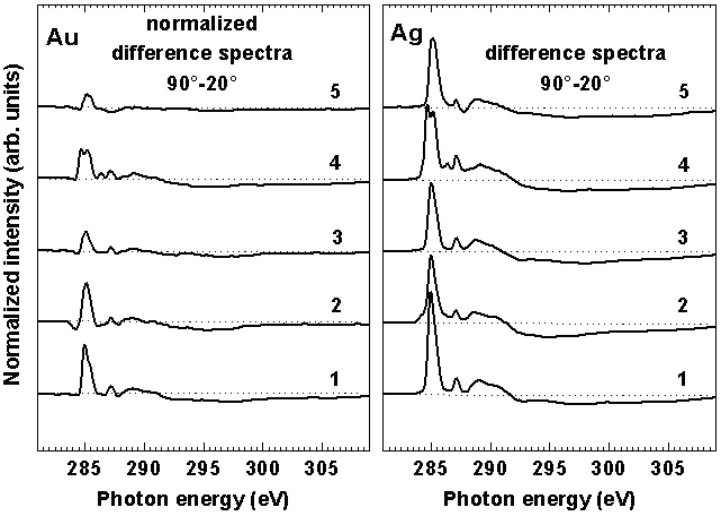

Figure 4. The C K-edge NEXAFS difference (90°-20°) spectra of the TEA-deprotected SAMs **1**-**5** on Au (left panel) and Ag (right panel).

synchrotron-based high-resolution X-ray photoelectron spectroscopy (XPS) and near-edge absorption fine structure (NEXAFS) spectroscopy. Whereas the deprotection by NH_4OH resulted in the formation of multilayer films, the deprotection by TEA allowed the preparation of densely packed BDDT SAMs. This is illustrated by Fig. 2, where the C1s and S2p XPS spectra of the differently deprotected **3**/Au (as an example for **1**-**5**) are presented. Note that in the TEA-deprotected SAMs, not all acetyl protection groups were removed, but 10-20% of the thiol groups at the SAM-ambient interface remained protected (see Fig. 2). The signature of the acetyl group was also seen in the NEXAFS spectra (Fig. 3).

BPDT SAMs are characterized by a noticeably higher orientational order and smaller molecular inclination on Ag than on Au, as shown in Fig. 4, where NEXAFS difference spectra are depicted.

Most important, the introduction of the alkyl bridge between the individual rings of the biphenyl backbone does not lead to noticeable change in the structure and packing density of the BDDT SAMs as far as the molecule had a planar conformation in the respective films. However, the deviation from this conformation, as it e.g. happens in the case of **3** and **5**, results in the deterioration of the film quality and decrease in the packing density and orientational order.

Note that the SAM **1** has the similar properties as SAMs **2** and **4**, which is a proof that **1** has a planar conformation in the SAM.

This work has been supported by BMBF (05KS4VHA/4 and 05 ES3XBA/5).

Magnetic domain structure in bilayers of antiferromagnetic NiMn and ferromagnetic Co

C. Tieg[1], R. M. Abrudan[1,2], M. Bernien[2], W. Kuch[2], J. Kirschner[1]

1 Max-Planck-Institut für Mikrostrukturphysik, Weinberg 2, D-06120 Halle, Germany
2 Freie Universität Berlin, Institut für Experimentalphysik, Arnimalle 14, D-14195 Berlin, Germany

Many modern devices in the field of magnetic data storage and sensing consist of mulilayered magnetic films in which the exchange bias effect between an antiferromagnetic (AFM) and a ferromagnetic (FM) film is exploited in order to tune the switching behaviour of the latter. Despite the enormous technological importance of AFM/FM systems, the fundamentals of the magnetic interaction in such systems are not well understood. Promising candidates to gain a deeper insight are model systems composed of single-crystalline films. In comparison to the widely studied polycrystalline samples, single-crystalline bilayer systems have the advantages of a higher structural and magnetic homogeneity (no grains), in addition to atomically flat interfaces, which greatly reduces the complexity and also simplifies the theoretical description.

We have employed a photoelectron emission microscope (PEEM) in order to study the magnetic domain structure with sub-micrometer resolution in single-crystalline bilayers composed of AFM NiMn and FM Co on Cu(001). The x-ray magnetic circular dichroism (XMCD) at elemental L_3 absorption edges was utilised as a contrast mechanism for magnetic domain imaging. The experiments were performed at the beamline UE56/2-PGM2.

Bulk NiMn exhibits an $L1_0$ phase in the equiatomic concentration range, in which the magnetic moments order in a collinear AFM structure with a Néel temperature of 1070 K. In our experiments, the alloy films were obtained by co-evaporation of Ni and Mn from separate sources with the same deposition rates on Cu(001) held at 300 K. The bilayer structures were prepared as crossed wedges of NiMn and Co, which allows a convenient investigation of thickness dependences.

In Fig. 1 we show the domain structure of the Co layer of an as-grown Co/NiMn/Cu(001) sample. The inset illustrates the sample geometry and the position of the field of view. The thickness of the NiMn layer increases from zero at the bottom to 16 monolayer (ML) at the top of the image. The thickness of the Co wedge with a plateau (7.3 ML) on the right side is indicated at the abscissa. Crystallographic directions and the projection of the direction of the photon beam onto the sample surface ($h\nu$) are indicated at the bottom right. The thick arrows show the magnetisation directions of the domains. The grey level reflects the Co L_3 XMCD asymmetry. Magnetic order in the Co film is absent in the left part of the sample (region with a homogeneous grey level labelled by i)), as concluded from the vanishing XMCD asymmetry. This is due to the thickness dependence of the Curie temperature, which is lower than 300 K in this sample region. The domain structure in the region where the Co film is ferromagnetic exhibits a clear dependence on the thickness of the NiMn layer. Only one single domain with a magnetisation along the [-110] direction can be seen in the sample region where the Co film is in direct contact to the substrate (lower part of the image). Large domains, several μm in size, are present in the region where Co is on top of NiMn thinner than about 8 ML (region ii)). The four different grey levels (black, dark grey, light grey, white) in this part of the image correspond to magnetisation along the four in-plane <110> directions. Above this NiMn thickness, the Co layer is broken up into much smaller domains of irregular shape and size (region iii)). The domain sizes are close to the chosen instrumental resolution, which impedes us to determine exact magnetisation directions. However, as in region ii), four different grey levels are readily recognisable in this region. We ascribe the change of the Co domain structure upon exceeding a NiMn thickness of about 8 ML to the magnetic phase transition in the NiMn layer from para- to antiferromagnetic, similar to the observations in Co/FeMn systems [1]. The small Co domain structure indicates a laterally fluctuating coupling of the FM Co film to the AFM NiMn film, which may stem from a locally varying AFM spin structure due to the presence of terraces and magnetic domains in the AFM.

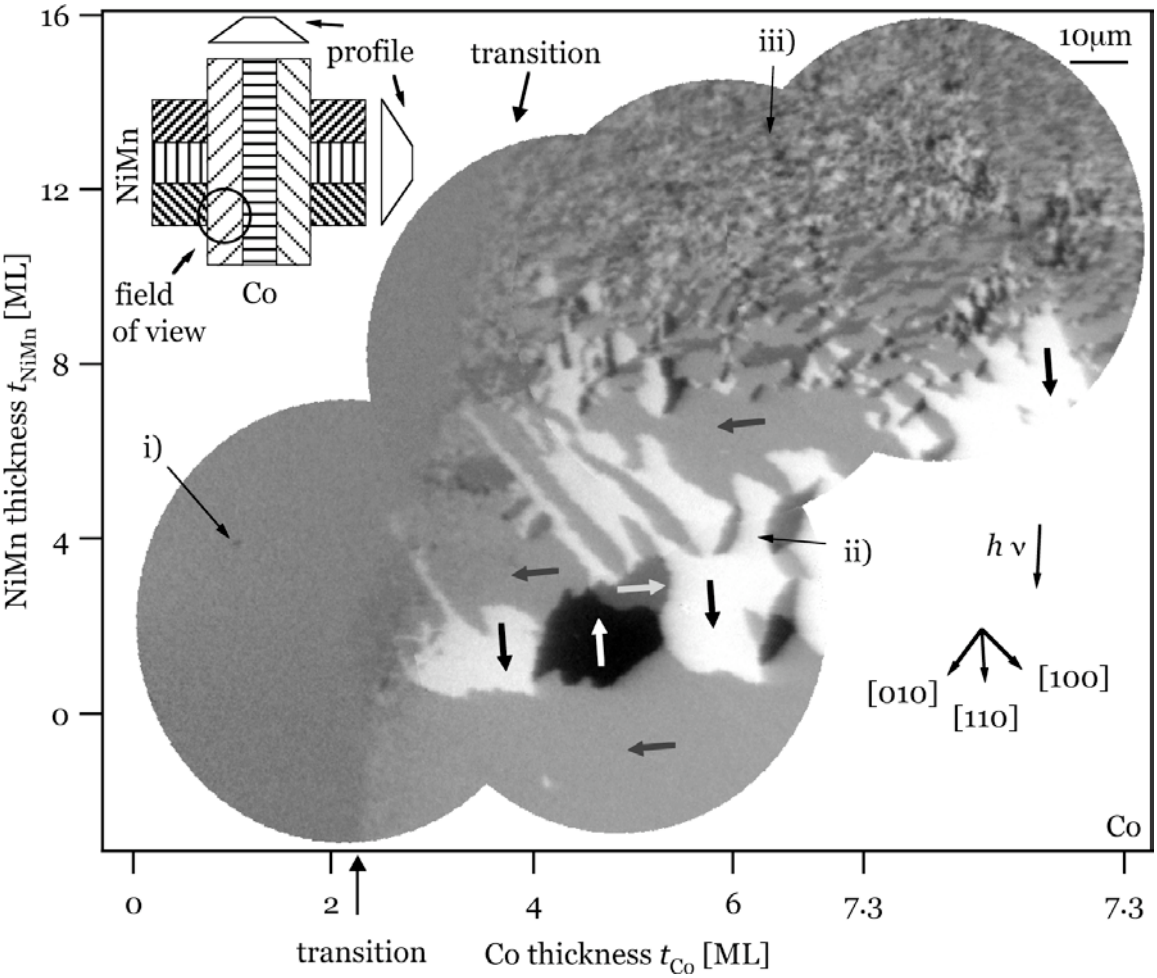

Fig. 1: Magnetic domain structure in an as-grown Co(wedge)/NiMn(wedge)/Cu(001) sample imaged by XMCD-PEEM at the Co L_3 absorption edge at 300 K. The Co is paramagnetic in the left part of the image (region i)). Ferromagnetic order is established above a certain critical film thickness. The magnetic transition line is indicated by arrows. The domain structure in the Co depends on the NiMn film thickness, as can be concluded from the different domain structures (domain sizes) in the lower (region ii)) and upper right (region iii)) part. The change of the Co domain structure at a NiMn thickness of about 8 ML is attributed to the magnetic phase transition in the NiMn film from para- to antiferromagnetic, which results in a locally fluctuating interaction at the Co/NiMn interface. The inset illustrates the sample geometry.

References:

1. W. Kuch, F. Offi, L. I. Chelaru, M. Kotsugi, K. Fukumoto, and J. Kirschner, Phys. Rev. B, **65**, 140408(R) (2002).

Commensurate-to-incommensurate phase transition of sodium ordering in single crystal $Na_{0.48}CoO_2$

E. Dudzik, R. Feyerherm, C. Milne, D. Argyriou, D. A. Tennant
Hahn-Meitner-Institute, 14109 Berlin, Germany

The system Na_xCoO_2 currently arises considerable interest after it has been demonstrated that intercalation of water into samples with $x = 0.35$ leads to superconductivity with a T_C of up to 5K [1]. In order to explain this extraordinary phenomenon, many researchers aim at understanding first the water-free system. In Na_xCoO_2, variation of the Na concentration x allows for a control of the magnetic and electronic degrees of freedom of the quasi two-dimensional triangular CoO_2 sheets, because compositions with $x < 1$ nominally are mixed valence systems $Na_xCo^{3+}{}_xCo^{4+}{}_{1-x}O_2$ where Co^{4+} has a LS $S = 1/2$ configuration. Variation of the Na content has also been shown to result in various types of ordered Na superstructures resulting in the interesting question what constraints the Na ordering may impose on the CoO_2 layer. There are indications, e.g., that $Na_{0.5}CoO_2$ exhibits Co^{3+}/Co^{4+} charge ordering.

The aim of the present x-ray diffraction study was to investigate in detail the temperature dependence of the Na ordering in a single crystal Na_xCoO_2 with an x value close to 0.5 and to look for indications of possible charge-ordering coinciding with the magnetic ordering transitions at 52 and 87 K reported previously [2].

A single crystal Na_xCoO_2 with average composition $x = 0.48$ was grown at HMI, and was studied by x-ray diffraction on the beamline MAGS at the 7 Tesla wiggler in the temperature range 10-550K. A number of weak superstructure reflections were identified and studied as a function of temperature. In order to enhance possible Co^{3+}/Co^{4+} charge ordering effects, resonant scattering at the Co K-edge was involved. Our sample is a piece of a batch used simultaneously for neutron diffraction studies of the magnetic ordering.

The first central result is that there are no indications in our data for any significant structural changes around the magnetic ordering temperatures. In contrast, we unexpectedly found that $Na_{0.48}CoO_2$ exhibits a reversible transition around 225 K from a commensurate superstructure, stable below that temperature, to an incommensurate superstructure existing between 225 and 430 K (see Figure 1). The commensurate phase is consistent with the orthorhombic superstructure reported previously for polycrystalline $Na_{0.5}CoO_2$ [3], related to the original hexagonal cell by $a' = \sqrt{3}a$, $b' = 2a$, $c' = c$, i.e., a doubling of the unit cell along both basal plane axes. The incommensurate phase is a modulation of this orthorhombic cell with a modulation wave vector $\boldsymbol{q} = (0, \delta, 0)'$. The value of δ exhibits a temperature dependent variation between 0.055 and 0.11, showing a broad plateau at the latter value between 260 and 360 K (see Figure 2). Above 430 K, the sodium ordering breaks down.

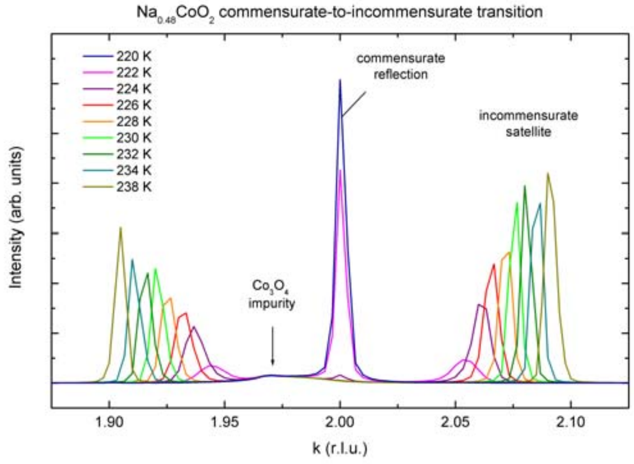

Figure 1: Longitudinal scans along (0k0)' at various temperatures. The (020)' splits off in two satellites around 220 K marking the commensurate-to-incommensurate transition. The broad bump at k = 1.97 stems from the (220) reflection of a highly textured Co_3O_4 impurity.

An incommensurate phase has been observed recently in electron diffraction studies after long irradiation of a $Na_{0.5}CoO_2$ sample and was discussed in terms of a regular arrangement of extra sheets of voids introduced to the Na_xCoO_2 system for $x < 0.5$ [4] (see Figure 3). In this model, the observed plateau value of δ is consistent with $x = 0.47$, in close agreement with $x = 0.48$ measured on our sample by neutron activation analysis. We argue that there are two possible explanations for the in-commensurate-to-commensurate phase transition observed in this phase. Below 225 K, either a phase separation into two volume fractions with $x = 0.5$ and $x<<0.5$ takes place, or the extra sheets of voids loose their regular arrangement and distribute in a random fashion in the commensurate phase. The former model would point to a surprisingly high long-range mobility of Na ions at 225K. The latter model would imply an even more interesting transition from a disordered low-T to an ordered high-T phase, hence a structural analogue to re-entrant spin glass behavior.

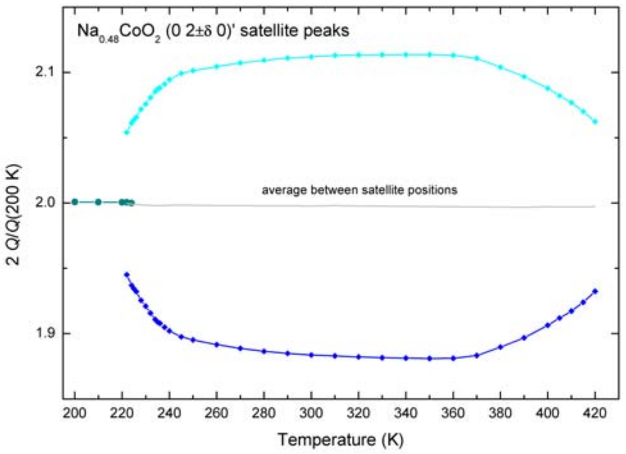

Figure 2: Temperature dependence of the position of the incommensurate satellites (0 2±δ 0)'. The grey line plotted in the center indicates the average between the two satellite positions, reflecting the lattice expansion in that temperature range.

We have also studied several other crystals Na_xCoO_2 with various stoichiometries $x = 0.65$, 0.75, 0.85. Also in these samples, we identified a number of weak superstructure reflections and studied their temperature dependence. So far, however, the results are inconclusive and therefore not reported in more detail here. For a continuation of our studies of these samples we resubmit or previous proposal.

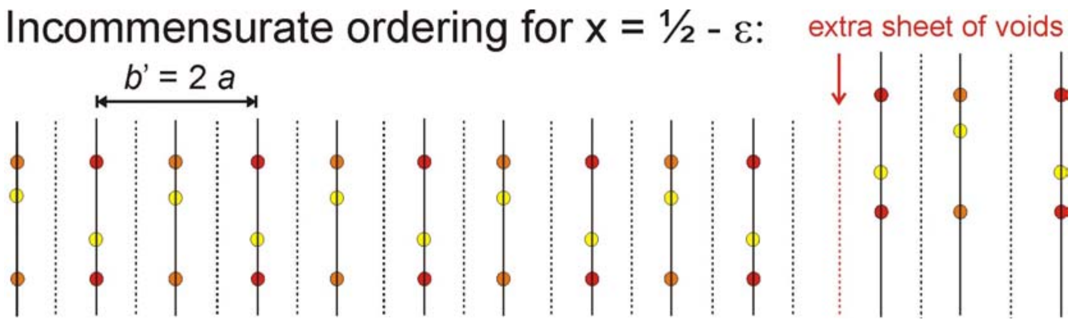

Figure 3: Model for the formation of an incommensurate superstructure by insertion of extra sheets of voids (after [4]). Only a regular arrangement of these extra sheets along the b axis would produce incommensurate Bragg reflections. Red and yellow circles denote Na atoms.

<u>References</u>

[1] K. Takada *et al.*, Nature **422** (2003) 53
[2] P. Mendels *et al.*, PRL **94** (2005) 136403
[3] Q. Huang, *et al.*, J. Phys.: Condens. Matter **16** (2004) 5803
[4] H. W. Zandbergen, *et al.*, PRB **70** (2004) 024101

Incommensurate structural distortion induced by magnetic ordering in $TbMnO_3$ and $DyMnO_3$

E. Dudzik, R. Feyerherm, N. Aliouane, D. Argyriou
Hahn-Meitner-Institute, 14109 Berlin, Germany

The interplay of ferroelectricity and magnetism in rare earth manganites currently arises much interest [1,2]. In orthorhombic $TbMnO_3$ the Mn spins order in an incommensurate magnetic structure below T_{Mn} = 42 K and the corresponding incommensurate magnetic propagation vector q_{Mn} = (0,0.28,0) locks below T_{lock} = 27 K [2]. This lock-in transition is associated with a jump of the electric polarization. The Tb spins also order antiferromagnetically below 7 K with a different q_{Tb} = (0,0.42,0). Similar behaviour is observed for $DyMnO_3$ for which, however, the Dy ordering is unknown yet. Here, $T_{Mn} \sim 40$ K and $T_{\mathrm{lock}} \sim 20$ K. The goal of the present experiments was to study the lattice distortions induced by the incommensurate ordering of the Mn magnetic moments through the magnetic and the successive lock-in transition.

Since the propagation vectors of the magnetic ordering and the lattice distortion are closely related, this experiment aimed at yielding additional information on the magnetic ordering and the lock-in transition.

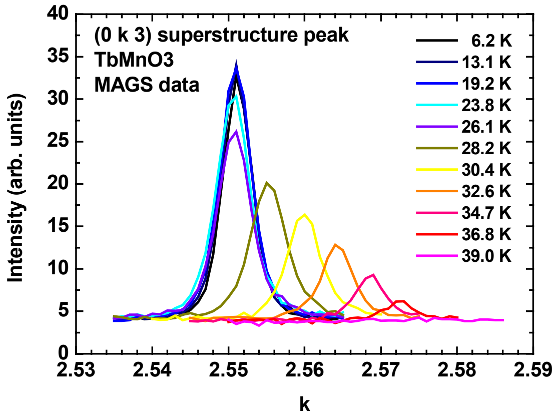

Figure 1: (0, 2+q', 3) superstructure reflection measured at various temperatures.

For $TbMnO_3$, the magnetic transitions have been investigated previously by neutron diffraction [3]. For $DyMnO_3$, no neutron diffraction results are available yet because Dy is a strong neutron absorber, making neutron diffraction experiments difficult. Here, x-ray diffraction provides the only way to determine the propagation vector for the magnetic ordering, both of Mn and Dy.

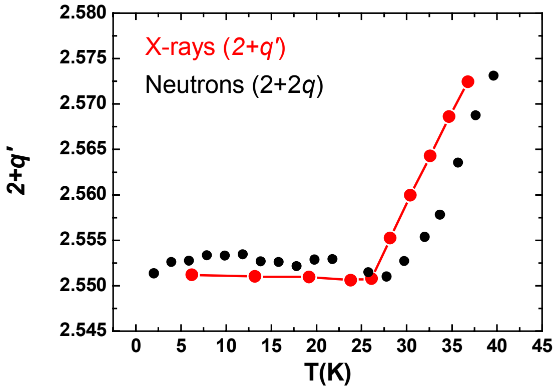

Figure 2: Temperature dependence of the position of the crystallographic and the magnetic superstructure reflections measured by x-ray and neutron diffraction, respectively.

We have performed high-resolution diffraction experiments on single crystals of $TbMnO_3$ and $DyMnO_3$ using the beamline MAGS at x-ray energies between 8 and 14 keV. These crystals were produced and characterized at HMI. The $TbMnO_3$ crystal was a small piece ($0.2 \times 0.3 \times 0.5$ mm^3) of a sample previously used for neutron diffraction experiments at HMI. The $DyMnO_3$ single crystal was plate-shaped ($3 \times 3 \times 0.5$ mm^3). For both crystals we looked for the incommensurate lattice distortion induced by the Mn ordering below T_N = 42 K down to the lowest temperatures achievable with the cryostat at the MAGS beamline (7 K). We observed *crystallo-*

graphic superstructure reflections of type (0 2+*q*' L) with integer L. The intensity of these reflections were less than 10^{-6} of that of the neighbouring (0 2 3) standard reflection, showing that the corresponding superstructure can be hardly studied with a laboratory x-ray instrument or neutron diffraction.

Figure 1 shows the (0 2 + *q*' 3) Bragg reflection observed in $TbMnO_3$ at different temperatures. Our data confirm previously published data by a Japanese group [4] but are of better resolution. Figure 2 shows the temperature dependence of the value of *2+ q'* compared to the corresponding data for the magnetic superstructure measured by neutron diffraction at HMI. We observe the relation *q' = 2 q*, which is expected if the crystallographic distortions at the magnetic ordering are due to exchange striction effects. Our experiments are the first to verify this relation in $TbMnO_3$ by two experiments *on the same crystal*. In addition, we observed that below T_{lock} the *T*-dependence of the intensity of the crystallographic superstructure reflection varies from that of the magnetic order parameter in showing a decrease below about 20 K. We speculate that this decrease is produced by some disorder in the crystallographic distortion induced by the deviation from the commensurate value *q'* = 0.5. The superstructure peaks were not enhanced when measuring at the Mn K-edge, suggesting the distortion is due to the displacement of O rather than Mn atoms.

Similar measurements were carried out on $DyMnO_3$. The crystal was mounted in a suitable way to be able to access large parts of the reciprocal space (0, k, l) plane in Bragg geometry (reflection). Compared to the Laue geometry used for $TbMnO_3$ the scattered intensity was by more than an order of magnitude larger. For $DyMnO_3$, no neutron diffraction results are available yet. Dy is a strong neutron absorber, making neutron diffraction experiment difficult. Therefore, x-ray diffraction provides the only way to determine the propagation vector related to the Mn ordering.

Figure 3 shows the temperature dependence of the position and intensity of the crystallographic superstructure reflection in $DyMnO_3$. We observe an incommensurate value of *q*' = 0.76 below the lock-in transition temperature, consistent with previously reported results [4]. For the first time, however, we observed a pronounced hysteresis of the lock-in transition. Comparison with the results on $TbMnO_3$ suggest that the unusual non-monotonous temperature dependence of the intensity does not directly reflect the behaviour of the magnetic ordering parameter. References

[1] M. Fiebig *et al.*, Nature **419** (2002) 818.
[2] T. Kimura *et al.*, Nature **426** (2003) 55.
[3] R. Kajimoto *et al.*, Phys. Rev. B **70** (2004) 012401.
[4] T. Kimura *et al.*, Phys. Rev. B **68** (2003) 060403.

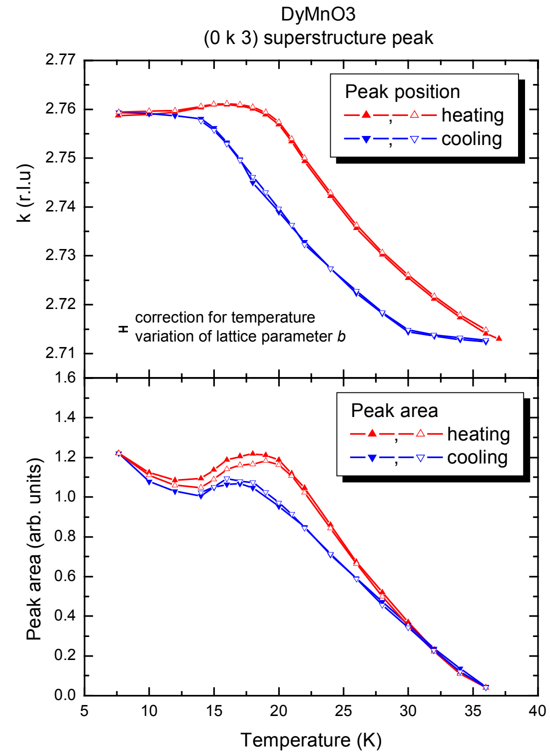

Figure 3: Temperature dependence of the position (upper panel) and intensity (lower panel) of the superstructure reflection in $DyMnO_3$.

Determination of the structural role of Fe as a function of the waste content in a series of stabilized industrial waste glasses.

F. Pinakidou, M. Katsikini, E. C. Paloura[*], P. Kavouras, Th. Kehagias, Ph. Komninou, Th. Karakostas
Aristotle University of Thessaloniki, School of Physics, GR54124 Thessaloniki, Greece.
A. Erko
BESSY GmbH, Albert Einstein Str. 15, 12489 Berlin, Germany.

The solidification and stabilization of toxic industrial waste (lead-oxide-contaminated ash) is a process that allows for its safe disposal. The main advantage of the vitrification process is that it produces a chemically stable material, which can homogeneously incorporate into its matrix numerous toxic elements[1]. The studied samples were produced with an incineration process of Pb- and Fe-rich sludges that produces a highly toxic fly ash, which consists of 47 wt% Fe_2O_3, 42 wt% $PbO{\cdot}PbBr_2$ oxides and 11 wt% other oxides. The Pb-contaminated ash is vitrified via co-melting with the appropriate quantities of vitrifying (SiO_2) and flux (Na_2O) agents at 1400°C, followed by quenching. The studied vitrified products contain various concentrations of fly ash, ranging from 10 % to 60 wt% with a step of 10%, and a SiO_2/Na_2O concentration ratio equal to 2.33. Previously reported XRF maps demonstrated that the samples are homogeneous[2].

The Fe-*K*-EXAFS measurements were conducted at room temperature, using the KMC2 monochromator at BESSY. The fluorescence spectra were recorded with a Si-PIN photodiode, at an angle of incidence θ=85°. The Fourier transforms (FT) of the Fe-*K* edge EXAFS spectra of the vitrified samples are shown in Fig 1(a). As shown in the figure, only the 1st nearest neighbor (nn) shell is resolved, indicating that the samples are amorphous. The Fe-*K* EXAFS spectra of studied glasses were fitted using one shell that consists of oxygen atoms.

Table I. EXAFS analysis results for the waste contaminated glasses; R, N and DW correspond to the interatomic distances, coordination numbers and Debye-Waller factors. The asterisk indicates the parameters that were kept fixed during the analysis.

Sample Name	N (O) (±10%)	R_{Fe-O} (Å)	DW ($x10^{-3}$ Å)
10 ash%	5.2 4.7	1.92 1.91	4.3 3.2
20 ash%	4.6 4.2	1.90 1.89	3.3 2.6
30 ash%	3.8 3.7	1.87 1.88	2.3 2.3
40% ash	5.2 4.7	1.92 1.91	4.3 3.2
50% ash	4.6	1.90	3.3
60% ash	4.2	1.89	2.6

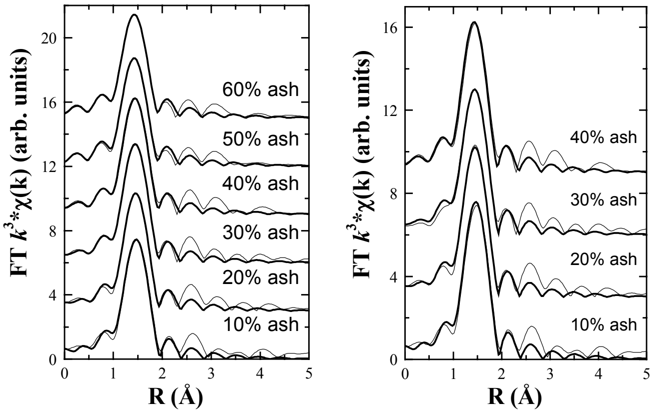

Figure 1: (a) The FTs of the $k^3{\times}\chi(k)$ spectra of the studied glasses. (b) The FTs of the $k^3{\times}\chi(k)$ Fe-*K* edge spectra of the glasses containing 10 to 40wt% ash. The fitting was performed using the mixed model. The raw data and the fitting are shown in thin and thick solid lines, respectively.

The EXAFS analysis results, shown in Table I, disclose that the coordination environment of Fe changes with increasing ash content. More specifically, as the ash content increases from 10 to 60 wt%, the Fe-O bond length (R_1) decreases from 1.92Å to 1.87Å while the coordination number in

---

[*] E. C. Paloura, paloura@auth.gr, tel.:+302310998036, fax: +302310998036

the 1st nn shell (N_1) decreases from 5.2 to 3.7. The simultaneous decrease of R_1 and N_1 indicates that, the ash content increases, the coordination environment of Fe changes gradually from octahedral to tetrahedral. Therefore, it can be proposed that in the samples with low ash content, the majority of the Fe atoms are octahedrally coordinated and thus the dominant role of Fe is that of a modifier[3]. In the intermediate ash concentrations (30-40 wt%) the Fe-O bond length decreases and takes the value 1.89-1.90Å, which is intermediate to the distances corresponding to octahedral and tetrahedral coordination of the Fe atom. Finally, in the high ash concentration limit (50-60 wt%) the measured Fe-O bond length is 1.87Å, a value that corresponds to tetrahedral coordination of Fe.

In order to determine the percentage of FeO_4 and FeO_6 polyhedra in the studied samples we fitted the Fe-*K* EXAFS spectra using an alternative model, the mixed model, according to which X% of the Fe atoms belong to octahedral sites while the rest (100-X)% occupy tetrahedral sites. The fitting of the Fourier transforms (FT) of the EXAFS spectra (k-range 2.8-9.8$Å^{-1}$), using the mixed model, are shown in Fig 1(b). The spectra were fitted in the 1st nn shell and the fitting parameters were the percentages of the Fe tetrahedra and octahedra and the value of the Debye-Waller factor. The fitting was performed simultaneously for all the samples and the distance in the tetrahedral coordination was kept fixed to the value derived from the previous EXAFS analysis (1.88 Å). The iterated distance for the octahedral arrangement was kept the same among all the samples (1.95Å). Analysis using the mixed model (Table II) reveals that in the glass with the lowest ash concentration (10 wt%), 55% of the Fe atoms are octahedrally coordinated in the vitreous matrix, while the rest constitute tetrahedra. As the ash content increases, the percentage of the FeO_4 polyhedra increases, i.e. in the glasses with 20 and 30 wt% ash, the percentage of the octahedrally coordinated Fe is approximately equal to 35%, while it is drastically reduced to 13% when the ash content reaches the value of 40 wt%. In the glasses with ash concentration higher that 50 wt%, the fitting using the mixed model was not possible because the majority of the Fe atoms occupy tetrahedral sites in the glass matrix (i.e. the number of the FeO_6 octahedra is lower than 11 wt%).

Table II. EXAFS analysis results using the mixed model; R_{Fe-O} and DW correspond to the interatomic distances and Debye-Waller factors. The asterisk indicates the parameters that were kept fixed during the analysis.

Sample Name	Percentage of FeO_x (%)	R_{Fe-O} (Å)	DW ($x10^{-3}$ Å)
10 ash%	$FeO_6 = 55 \pm 5$	1.95	3.1
	$FeO_4 = 45$	1.88*	2.3*
20 ash%	$FeO_6 = 35 \pm 4$	1.95*	3.1*
	$FeO_4 = 65$	1.88*	2.3*
30 ash%	$FeO_6 = 38 \pm 6$	1.95*	3.1*
	$FeO_4 = 62$	1.88*	2.3*
40% ash	$FeO_6 = 13 \pm 4$	1.95*	3.1*
	$FeO_4 = 87$	1.88*	2.3*

Given that Fe^{+2} forms only octahedra, the observed changes in the Fe-O distance can only be attributed to a change in the coordination environment of Fe^{3+}, from octahedral to tetrahedral. This change in the coordination environment of Fe^{+3} causes a change in the structural role of Fe^{3+}, which is a glass modifier in the low ash limit (10-20 wt%) and becomes a glass former (along with Si) when the ash content increases to 50-60 wt%, as it is affirmed by the decrease of the number of FeO_6 octahedra. It should be pointed out that while the SiO_2/Na_2O ratio did not vary in the glasses, the Si/O ratio is different. In samples with 10-30 wt% of fly ash the Si/O ratio is larger than the critical value of 0.33 that renders Si the dominant glass former. Therefore, Fe^{+3} is an intermediate. On the other hand, in the samples containing 40, 50 and 60 wt% ash, the Si/O ratio is equal to 0.324, 0.294 and 0.255 respectively and the formation of the vitreous matrix is made possible only due to the glass forming ability of tetrahedrally coordinated Fe^{+3}.

[1] P. Kavouras et al, J. Eur. Ceram. Soc. 23 (2003) 1305.
[2] F. Pinakidou et al, Journal of Non-Cryst. Solids 351 (2005) 2474.
[3] W. Vogel, Glass chemistry 2nd ed., Springer-Verlag, Berlin, 1994, p. 251.

Micro-XRF mapping and micro-EXAFS study of glasses containing Electric Arc Furnace Dust

F. Pinakidou, M. Katsikini, E. C. Paloura[*], P. Kavouras, Th. Kehagias, Ph. Komninou, Th. Karakostas
Aristotle University of Thessaloniki, School of Physics, 54124 Thessaloniki, Greece.
A. Erko
BESSY GmbH, Albert Einstein Str. 15, 12489 Berlin, Germany.

Electric arc furnace dust (EAFD) is one of the largest solid waste streams produced by steel mills. It contains mainly heavy metals and thus is considered as a toxic waste. Recycling of the valuable metals (Fe, Zn and Pb) reduces the disposal problems and results in resource conservation but can recover only a part of the heavy metals from the EAFD. Vitrification, leading to the formation of vitreous or glass-ceramic materials[1], is a promising process to stabilize metallic Zn and Fe and hence permit the safe disposal of the EAF dust[2]. Therefore it is of great importance to study the structural role of both Fe and Zn in vitrified EAFD-rich industrial wastes, since the structural integrity of the glass matrix depends strongly on the type of polyhedra that Fe and Zn form.

The under study samples are vitrified products of EAF dust (which mainly consists of ZnO and ferric oxides ($ZnFe_2O_4$)) that is co-melted with SiO_2, Na_2CO_3 and $CaCO_3$ at 1400°C for 2h, followed by quenching. The under study sample consists of 20% EAFD, 55% SiO_2, 15% CaO and 10% Na_2O and was heat-treated at 20°C above the glass transition temperature (T_g) for residual stress relaxation. Previous work reported on the studied sample disclosed that upon annealing, surface crystallization of wollastonite ($CaSiO_3$) initiates from the edges towards the center. The XRF and μ-XAFS measurements were conducted at the KMC2 beamline using capillary optics that reduce the beam diameter to 5μm. The XRF maps were recorded using excitation photons of 7200 eV. The μ-XAFS spectra were recorded at the Fe-*K* and Zn-*K* edges, using an energy dispersive fluorescence detector, at two spots of the sample surface, one at the edge (position E) and one at the centre (position C).

The XRF spectra shown in Fig.1 were recorded with excitation energy of 9400 eV, i.e. high enough to excite both Fe and Zn. As shown in the spectra, the studied samples contain Fe, Zn, Ca and Mn. The concentration of either Fe or Zn is the same in both the as-casted and heat-treated sample and does not vary across the sample surface.

The XRF map recorded from the annealed sample, shown in Fig.2, reveals that the concentration of either Fe or Zn varies less than 15% across the sample and the formation of Fe and Zn clusters has been avoided. This observation, along with the EXAFS results discussed in the following, indicates that both Fe and Zn have been successfully incorporated into the vitreous matrix.

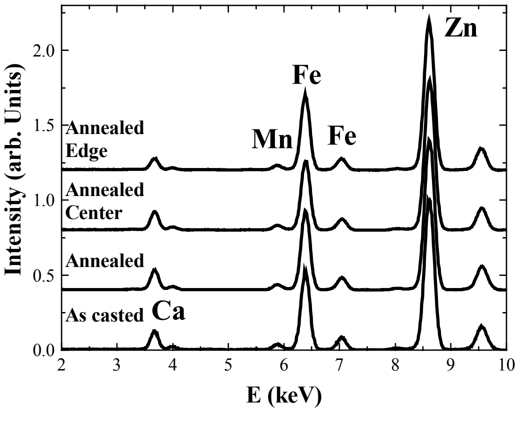

Figure 1: Fluorescence spectra normalized at the Zn Kα peak recorded at the edge and the centre of the annealed sample and at random positions of the as-casted and annealed sample.

In order to investigate possible changes in the local coordination of Fe and Zn, due to local compositional variations or due to differences in the cooling rate between the center and at the edge of the samples, we recorded μ-EXAFS at the Fe-*K* and Zn-*K* edges, from the two spots of

---

[*] E. C. Paloura, paloura@auth.gr, tel.:+302310998036, fax: +302310998036

the sample surface. The Fourier transforms (FTs) of the k^3 - weighted μ-EXAFS spectra recorded at the Fe- and Zn-*K* edges are shown in Fig. 3(a) and (b), respectively. As shown in the figure, the FTs of the studied samples have well-resolved structure up to a distance of about 3.5Å. Therefore, mid-range order exists, possibly in the form of nanocrystallites, around both the Fe and Zn atoms. The EXAFS spectra recorded at the Fe-K-edge were fitted using a mixed model according to which X% of the Fe atoms occupy octahedral sites that belong to the $ZnFe_2O_4$ phase, while (1-X)% form tetrahedra, and participate in the formation of the glass. In both the as-casted and annealed samples, the fitting procedure was performed using four shells: the first nearest neighbor (nn) shell consists of oxygen atoms that are either octahedrally or tetrahedrally coordinated to the Fe atom. The second, third and forth nn shells comprise of Fe, Zn and O atoms, according to the $ZnFe_2O_4$ model. The Zn-*K* EXAFS spectra were fitted in the four nn shells, using the $ZnFe_2O_4$ model: the Zn atom in the 1st nn shell is tetrahedrally coordinated with four oxygen atoms at a distance 2.02Å, while the 2nd, 3rd and 4th shells comprise of Fe, O and Zn atoms, respectively

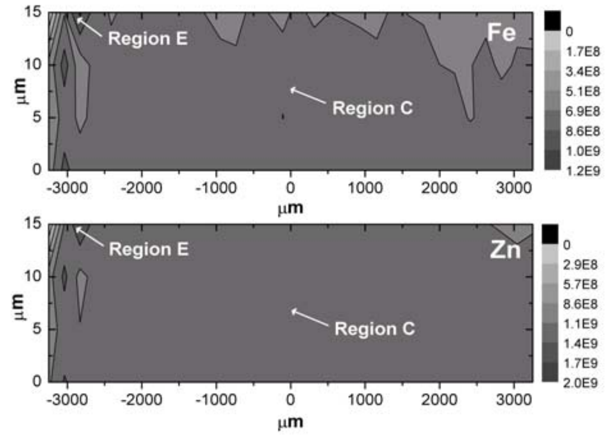

Figure 2: 7500x15μm XRF maps of the annealed sample. The regions depicted as E and C, refer to the positions at the edge and at the centre, respectively.

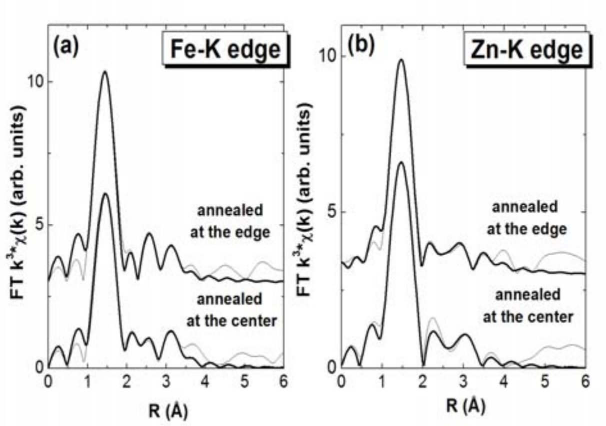

Figure 3: Fourier Transforms of the (a) Fe-K and b) Zn-K edge μ-EXAFS spectra recorded at the edge and the center of the annealed samples. The raw data and the fitting are shown in thin and thick line, respectively.

The analysis of the μ-EXAFS spectra from the annealed sample reveals that the percentage of the Fe atoms that constitute octahedra is, within the error bar, equal at the center and at the edge of the sample. More specifically, 55% of the Fe atoms form octahedra at the edges of the sample, while 65% form octahedra at the center of the sample. The Fe-O bond length in the FeO_6 polyhedron is equal to 1.93Å whilst the respective value in the FeO_4 tetrahedron is 1.86Å. Therefore, the intermediate role of Fe is disclosed: Fe participates in the formation of the vitreous matrix by forming FeO_4 tetrahedra and acts as a glass modifier when bonded in FeO_6 octahedra. Thus, Fe partially occupies octahedral sites that belong to $ZnFe_2O_4$ nanocrystallites, which are not resolved in the XRF maps, due to the limited spatial resolution of the experimental setup. On the other hand, the μ-EXAFS analysis at the Zn-*K* edge reveals no alteration in the bonding environment of the Zn atom. In both regions, the Zn atom participates in the formation of ZnO_4 tetrahedra, i.e. Zn is coordinated with 4 oxygen atoms at a distance 1.94Å and thus acts as a glass former.

---

[1] Sheng, J., 2002, Fuel 81, 253

[2] Pellino M., A. Karamanov, P. Pisciella, S. Criscussi and D. Zonetti, 2002, Waste Management 22, 945.

Resonant x-ray Bragg scattering on a magnetic grating patterned by ion bombardment in a magnetic field

V. Höink, M. D. Sacher, J. Schmalhorst, and G. Reiss
Thin Films and Nanostructures,Department of Physics,
University of Bielefeld, P.O. Box 100131, 33501 Bielefeld, Germany

D. Engel, T. Weis, and A. Ehresmann
Institute of Physics and Center for Interdisciplinary Nanostructure Science and Technology (CINSaT),
Kassel University, Heinrich-Plett-Str.40, D-34132 Kassel, Germany

The exchange bias effect (EB) in antiferromagnet (AFM) / ferromagnet (FM) systems results in a shift of the hysteresis loop of the FM with respect to zero magnetic field [1], caused by the exchange interaction at the interface between both materials (pinning). The EB is usually initiated by field cooling (FC) resulting in a homogenous distribution of the EB orientation within the sample. An alternative method for initializing the EB is the ion bombardment (IB) of the sample in the presence of an external magnetic field H_{IB} [2–5]. Besides the initialization of the EB it is also possible to change of the size and orientation of an existing EB-coupling by IB. Furthermore it is possible to define the area in which the unidirectional anisotropy is manipulated by a local restriction of the area exposed to IB. For small external fields below H_{EB} this local manipulation of the EB-coupling results in a corresponding pattern of the magnetization of the pinned FM. Our measurements show no unintentional change of the topographical microstructure due to the magnetic patterning. This technique opens the opportunity to build a magnetic grating showing a soft x-ray interference pattern based on the x-ray magnetic circular dichroism (XMCD) effect [6]. It will be demonstrated that it is possible to switch the magnetic scattering on and off by an external magnetic field.

The sample used in the present experiment consists of a layer stack with 3 nm $Co_{70}Fe_{30}$ pinned to 15 nm $Mn_{83}Ir_{17}$ with a Cu seed layer and 1.4 nm Al oxide as an oxidation preventing capping layer. A homogenous EB was initialized by FC in an external magnetic field $\mathbf{H}_{FC}$. Ion bombardment induced magnetic patterning (IBMP) with He-ions (10keV, 1×10^{14} ions/cm^2) in an external magnetic field $\mathbf{H}_{IB}$ was performed through a resist mask with 1.6 μm wide lines parallel to $\mathbf{H}_{FC}$ and a periodicity of 5 μm ($\mathbf{H}_{IB} \uparrow\downarrow \mathbf{H}_{FC}$). The test of the magnetic grating was performed with the ALICE experimental setup [7] at beamline UE56/1-PGM-b at BESSY. A circular polarized x-ray beam was directed at the rotatable sample with a variable angle while the detector was fixed at an angle of Θ=20° relative to the incident beam (Fig. 1). The grating was tilted by about 45° relative to the plane of the incident/reflected beam. This made it possible to measure the interference pattern which results from the XMCD effect with a detector in the plane of the incident / reflected beam. The direction of the external magnetic field was oriented parallel to the direction of the incident photon beam. All measurements were done at room temperature.

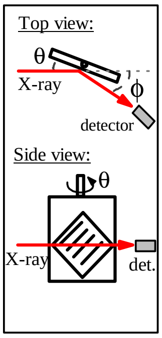

FIG. 1: Experimental setup with angle Θ between sample surface and incident photon beam and angle ϕ between detector and incident photon beam, rotation axis perpendicular to scattering plane;

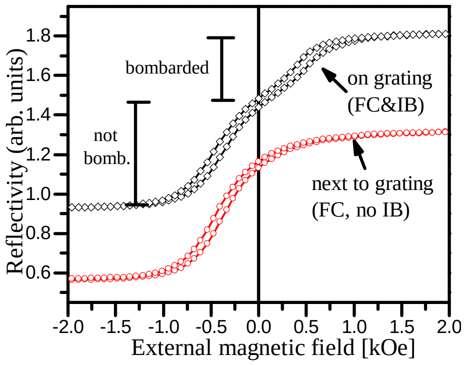

FIG. 2: Hysteresis loops measured on the magnetic grating (black diamonds) and next to the magnetically patterned grating (red circles) on the same sample (Co L_3-edge, Θ= 10°, ϕ=20°, loops shifted on y-axis for better visibility)

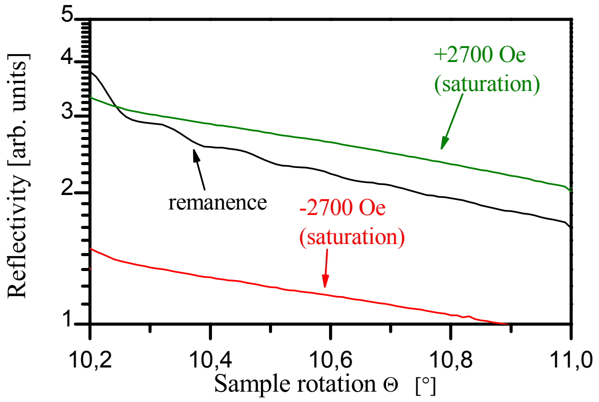

FIG. 3: Sample rotated by angle Θ with the detector fixed to ϕ=20° in saturation in a magnetic field of +2700 Oe (green line) and -2700 Oe (red line) and without an external magnetic field after saturation at -2700 Oe (black line). All measurements were done at the Co L_3-resonance.

As it can be seen in Fig. 2, bombarded areas as well as not bombarded areas contribute to the hysteresis loop measured on the magnetic grating. The change in reflectivity due to the not bombarded area between the lines is approximately twice as high as for the bombarded lines. This corresponds to the fact, that the average distance between the lines is by a factor of about two larger than the width of the bombarded area. The hysteresis loop of the same layer system measured on the only field cooled area aside the magnetically patterned grating can be seen in the lower part of Fig. 2. The shape of the hysteresis loops is rounded in both cases because the measurement is not performed parallel to the easy axis of the pinned $Co_{70}Fe_{30}$-Layer. Magneto optical Kerr effect measurements carried out parallel to the easy axis (not shown) show that the shift of the hysteresis loop due to EB is for all areas much larger than the the coercivity field. Therefore, one can assume an approximately antiparallel orientation of the FM-magnetization in the bombarded and not bombarded areas in remanence. A small deviation of the antiparallel orientation of up to 5° might occur because of a possible small inaccuracy in the alignment of the directions of $\mathbf{H}_{FC}$, $\mathbf{H}_{IB}$ and the lines.

Apart from the charge scattering of the x-rays which is independent of the IB-induced magnetic changes, a resonant magnetic scattering occurs at the $L_{2,3}$-white lines of Co and Fe. When investigated in remanence, the part of the scattered x-rays which is due to resonant magnetic scattering will have a different intensity on areas with a magnetization direction oriented predominantly parallel to the incident beam than on areas with the opposite orientation of the magnetization. Therefore a superposition of an interference pattern like that of a topographic reflective grating which is due to resonant magnetic scattering and the signal obtained by the field independent charge scattering can be expected. Figure 3 shows a Θ-scan measured with a rotating sample and the detector fixed at Θ=20° (Co L_3-resonance). The maximum possible magnetic signal is defined by the difference between the two measurements for the sample saturated in the X-ray propagation direction and opposite to it. The expected oscillation of the reflectivity clearly can be seen at the measurement without an external magnetic field. This oscillation vanishes when a magnetic field of ±2700 Oe, which is sufficient to saturate the ferromagnetic layer (see Fig.2), is applied. This shows that the observed oscillation at the measurement in remanence is due to interference at the magnetic pattern and not related to any topographic structures. Θ-scans have been measured with various magnetic fields in the range between saturation at -2700 Oe and saturation at +2700 Oe (not shown). The angles of the individual maxima are not changed considerably by the magnetic field. The magnitude of the interference pattern of the magnetic grating decreases with increasing magnetic field and vanishes at a magnetic field larger than 675 Oe which is in the range of the external field necessary to saturate the sample (see Fig. 2). This shows that it is possible to build a gradually tuneable magnetic grating by IBMP.

The grating period d can be calculated by applying the grating equation [8] $m\lambda = d \times (sin(\alpha) + sin(\beta))$ (spectral order m, wavelength λ=1.59 nm, angle α between the incident beam and the surface normal, angle β between the scattered x-rays and the surface normal) to the experimental results. The first visible maxima next to the specular peak at 10.02° are located at 9.81° and at 10.32°. The measured distance between adjacent maxima is 0.12° to 0.13°. Therefore, the maximum at 10.32° (9.81°) is of order -3 (2). The maxima of lower orders are hidden by the specular peak. The position of the maxima on the flank of the specular peak can be shifted in the direction of the peak by the superposition of the maxima due to

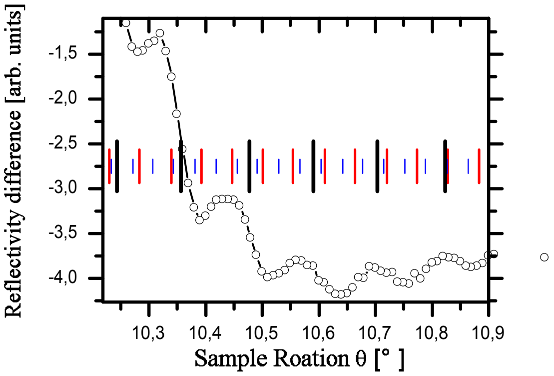

FIG. 4: Θ-scan measured in remanence subtracted by the Θ-scan measured in saturation at +2700 Oe; vertical lines: angle at which a maximum is predicted by the grating equation for a grating with d=1.6 μm (big black lines), d=3.4 μm (medium sized red lines) and d=5 μm (small blue lines)

XMCD and the specular peak itself (compare Fig.4). By taking into account that the bombarded lines were tilted by 45° relative to the horizontal plane defined by the incident beam and the detector and that the measured angles represent the projection of the interference pattern on this plane, values in the range of d=1.58 μm to d=1.92 μm can be calculated. This result does not match with the periodicity of the magnetic grating of $d = 5\mu$m, but it is in the range of the width of the bombarded lines. This is a hint that the Néel wall like boundaries between the bombarded and the not bombarded areas are of a great importance for the interference process. The maxima one would expect from the interference of x-rays scattered at Néel wall like boundaries with a distance of 3.4 μm corresponding to the width of not bombarded areas have a smaller distance. Therefore more maxima of this kind are hidden by the specular peak and only weaker maxima of higher order can contribute to the observed interference pattern. Figure 4 shows the angles at which maxima can be expected according to the grating equation for the used experimental setup and a grating with d=1.6 μm, d=3.4 μm and d=5 μm. To compare this values with the experimental results, the difference between the reflectivity measured at a Θ-scan in remanence and that resulting from a measurement done in saturation at +2700 Oe is printed in the same graph. This emphasizes the interference signal due to magnetic scattering. It can be seen, that interference at a grating with a periodicity of d=5 μm can not explain the observed interference pattern and therefore the observed angular distribution of the reflected x-rays might be connected to the resonant scattering of x-rays at the magnetization of the Néel walls.

We have shown, that it is possible to measure an x-ray interference pattern with a purely magnetic grating patterned by ion bombardment induced magnetic patterning. Regular topographical patterns as an origin of the interference pattern can be ruled out. Scattering at the edges between bombarded and not bombarded areas as an important contribution for the observed interference pattern has been suggested.

The authors thank H. Zabel, A. Nefedov and A. Remhof (Ruhr-Universität Bochum) for the possibility to use the ALICE experimental setup und the valuable assistance during the measurements at the BESSY. The support of the DFG and the BMBF is acknowledged (grant number: BMBF 05 ES 3XBA/5).

---

[1] J.Nogues and I. K.Schuller, Journal of Magnetism and Magnetic Materials **192**, 203 (1999).
[2] C. Chappert, H. Bernas, J. Ferre, V. Kottler, J.-P. Jamet, Y. Chen, E. Cambril, T. Devolder, F. Rousseaux, V. Mathet, et al., Science **280**, 1919 (1998).
[3] J. Fassbender, D. Ravelosona, and Y. Samson, Journal of Physics D: Applied Physics **37**, R179 (2004).
[4] A. Ehresmann, Recent Research Developments in Applied Physics **7 part 2**, 401 (2004).
[5] D. Engel, A. Ehresmann, J. Schmalhorst, M. Sacher, V. Höink, and G. Reiss, Journal of Magnetism and Magnetic Materials **293**, 849 (2005).
[6] J. Stöhr, Journal of Electron Spectroscopy and Related Phenomena **75**, 253 (1995).
[7] J. Grabis, A. Nefedov, and H. Zabel, Review of Scientific Instruments **74**, 4048 (2003).
[8] *X-Ray Data Booklet, second edition* (Center for X-Ray Optics , Advanced Light Source, Berkeley, 2001).

Long-range order in thin epitaxial Fe_3Si films on GaAs(001)

B. Jenichen, V. M. Kaganer, J. Herfort, D. K. Satapathy, H.-P. Schönherr, W. Braun, and K. H. Ploog
Paul-Drude-Institut für Festkörperelektronik, Berlin

Fe_3Si on GaAs is a promising candidate for spintronic applications. It can be grown by molecular-beam epitaxy at GaAs substrate temperatures near 200 °C. The Curie temperature of Fe_3Si is as high as 840 °C. Fe_3Si has the face-centered cubic $D0_3$ structure. This structure can be regarded as four interpenetrating fcc sublattices A, B, C, and D with origins at (0, 0, 0), $(\frac{1}{4}, \frac{1}{4}, \frac{1}{4})$, $(\frac{1}{2}, \frac{1}{2}, \frac{1}{2})$, and $(\frac{3}{4}, \frac{3}{4}, \frac{3}{4})$, respectively. In the ordered Fe_3Si crystal, Fe atoms occupy the three sublattices A, B, and C, while Si atoms fill the sublattice D. Si(D) and Fe(B) are located on opposite corners of the same cube. In as-grown thin epitaxial films of Fe_3Si on GaAs, the lattice mismatch and the long-range order depend on the stoichiometry. Significant changes of the resistivity with film stoichiometry have been observed [J. Herfort *et al.*, J. Vac. Sci. Technol. **22**, 2073 (2004)]. A clear minimum of the resistivity near stoichiometric conditions is found, which had previously been ascribed to reduced alloy scattering. The scattering is smallest for an ordered crystal structure, but the degree of order has not been determined. The aim of the present work is the determination of long-range order in thin Fe_3Si films by grazing incidence x-ray diffraction. In addition, we use the same measurements for a precise determination of the position of the Fe_3Si unit cell with respect to the GaAs substrate. Since the structures of the substrate and the epitaxial layer are different, the relative positions of the unit cells are not known in advance, and an additional phase factor in the polarizability of one layer with respect to the other may appear.

A common origin for all structures is chosen. This is standard in surface diffraction, but it is not taken into account in conventional dynamical diffraction calculations. Figure 1 shows the influence of the relative shift of the crystal lattices on the calculated diffraction curves. We compare a crystal truncation rod (CTR) scan at the 111 reflection calculated for relative positions of the Fe_3Si and GaAs lattices without a lateral shift with the same scan for the case that the Fe_3Si lattice is shifted by one half of the unit cell along the [100] direction in the interfacial plane. The corresponding shift of the layer thickness oscillations in the diffraction curve is obvious. Thus, we have included the relative positions of the layer and the substrate crystal lattices in our calculations to obtain the registry of the layer on the substrate.

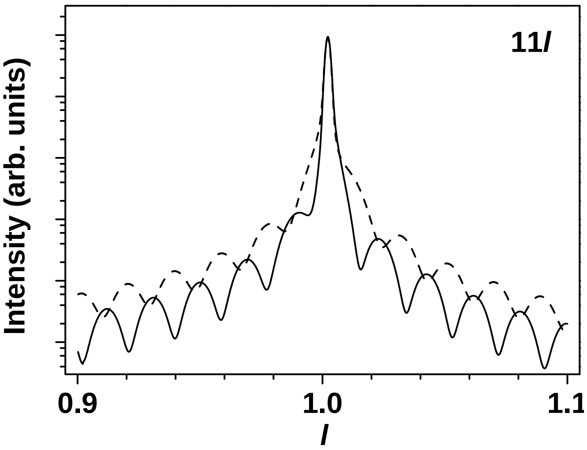

Fig. 1. Calculated CTRs at the 111 reflection from a stoichiometric fully-ordered Fe_3Si layer (30 nm thick) on GaAs(001) for the lattice registry without lateral shift (full line) and for the case of the Fe_3Si structure shifted by 1/2 of the unit cell in the [100] direction (dashed line).

The z-component (normal to the interface) of the shift corresponds to a relaxation at the interface. Three types of reflections are expected for the ordered stoichiometric compound Fe_3Si. Fundamental reflections, which are not influenced by disorder, are given by $h+k+l=4n$, where n is an integer and (hkl) are the Miller indices of the diffracting net planes. There are two distinct types of superlattice reflections sensitive to the disorder, which is described by the two order parameters α and β, defined as the fractions of Si atoms occupying the Fe(B) and Fe(A,C) sites, respectively.

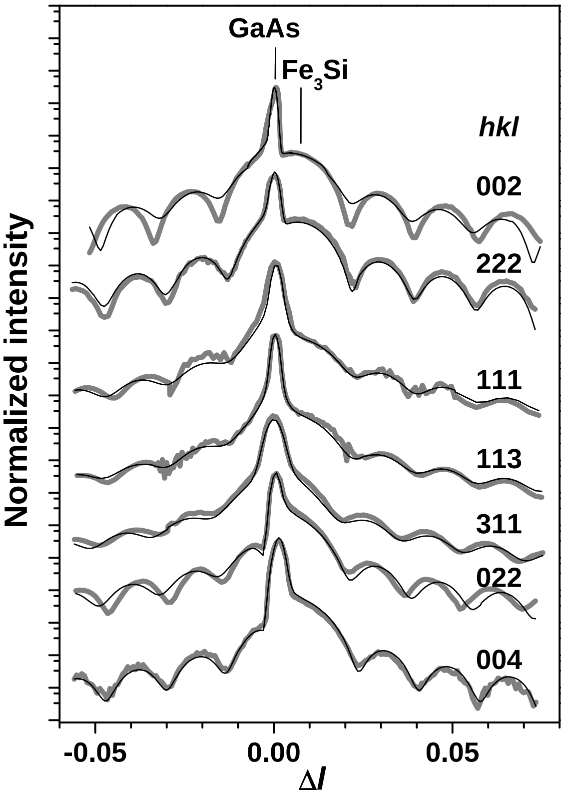

Fig. 2. Measured (gray lines) and fitted (black lines) CTRs on a logarithmic scale near different reciprocal lattice points. The fits of all curves are performed simultaneously with the same set of parameters. The sample is nearly stoichiometric with a slight surplus of Si and exhibits an ordered structure with some disorder due to migration of Si atoms into the Fe(A,C) sublattice. The coordinate L along the CTRs has its origin at the respective GaAs peak.

Reflections with odd h, k, and l are sensitive to both types of disorder. Reflections given by the condition $h+k+l=2n$ (where n is an integer), however, are sensitive to disorder in the Fe(A,C) sublattice alone. In order to obtain α and β, we measure diffraction curves of all three types of reflections and fit them using dynamical diffraction calculations. Figure 2 combines CTR scans performed at different bulk reflections. The width of the GaAs substrate peak is limited by the resolution of the experimental setup. The Fe_3Si layer peak is broadened due to the small layer thickness of 33 nm. Periodic side maxima reveal the high quality of its top and bottom interfaces. The layer peak is fairly close to the substrate peak, indicating that the sample is nearly stoichiometric. Well-pronounced Fe_3Si layer reflections in all these scans with their different sensitivity to disorder indicate a high degree of long-range structural order in the layer.

The long-range order in Fe_3Si epitaxial layers strongly depends on their stoichiometry. In our example the sample contains 25.5% Si, i.e., it is nearly stoichiometric. The resulting order parameters are $\alpha=0$ and $\beta=0.3$ with an accuracy of ± 0.05, i.e., 30% of the Si has left its sublattice exchanging solely with Fe(A,C) atoms. For a clearly nonstoichiometric sample with 16.5% Si, we detected complete disorder ($\alpha=0.25$ and $\beta=0.5$, vanishing Fe_3Si peaks in the superlattice reflections), which resulted in a higher resistivity of the layer. Note that the almost complete long-range order in nearly stoichiometric samples is observed without additional thermal treatment, which is usually required for the preparation of bulk samples.

NEXAFS spectra of polymer-fullerene (C_{60}) composites

A.O. Pozdnyakov[1], M.M. Brzhezinskaya[2], D.A. Zverev[2], E.M. Baitinger[3], A.S. Vinogradov[2], K. Friedrich[4]

[1] *Institute of Problems of Mechanical Engineering, St. Petersburg,199178, Russia*
[2] *V.A. Fock Institute of Physics, St. Petersburg State University, St. Petersburg, 198504 Russia*
[3] *Preussiches Privatinstitut für Technologie zu Berlin, D-13187 Berlin, Germany*
[4] *Institut für Verbundwerkstoffe GmbH, Technisches Universität Kaiserslautern, Kaiserslautern, D-67663, Germany*

Polymer-fullerene composites (PFC) are studied in depth because they exhibit interesting optical, mechanical, biological and other properties [1]. The properties of the composites are strongly dependent on the dispersion state of fullerene molecules inside the matrices. The degree of dispersion can vary over a wide range from molecules to clusters and crystallites. Donor-acceptor properties of polymer matrices and the solvent used for the formation of the composite may determine the degree of dispersion and, as a consequence, the character of thermal desorption of fullerene C_{60} molecules [2]. Below we report on the study of the electronic subsystem of PFCs using the NEXAFS technique.

Polymer matrices with different physical properties have been chosen. One of the polymers, poly(pyromellitic dianhydride-co-4,4'-oxydianiline) (PMDA-ODA), is a typical high temperature rigid chain polymer which has the glass transition temperature (T_g) above 600 K. Polydimethylsiloxane is a flexible chain polymer with low T_g~126 K. Poly(methyl methacrylate) (PMMA) and polystyrene (PS) are amorphous polymers with intermediate T_g~400 K and 378 K, respectively[1]. Polymer-C_{60} suspensions were prepared by co-dissolution of the C_{60} solutions either in toluene (Tol) or in 1-methyl-2-pyrrolidinone (NMP). PS and PMMA were dissolved in Tol. PDMA-ODA is a 15 wt. % NMP solution. The solution of C_{60} in NMP was added to this solution. The C_{60} content in NMP and Tol before mixing with a polymer solution amounted to the equilibrium solubility of C_{60} in these solvents at room temperature (2.9 and 0.89 mg/ml for Tol and NMP, respectively [3]). Details of handling the suspensions and coatings formation can be found elsewhere [2]. Common solutions were pipetted onto the steel foil (12X18H10T) with a roughness of about 1 µm. The mean rated coating thickness of PFC coatings was ~ 5 µm. PMDA and PMDA-ODA-C_{60} coatings were heated up to ~ 320°C in air for imidization.

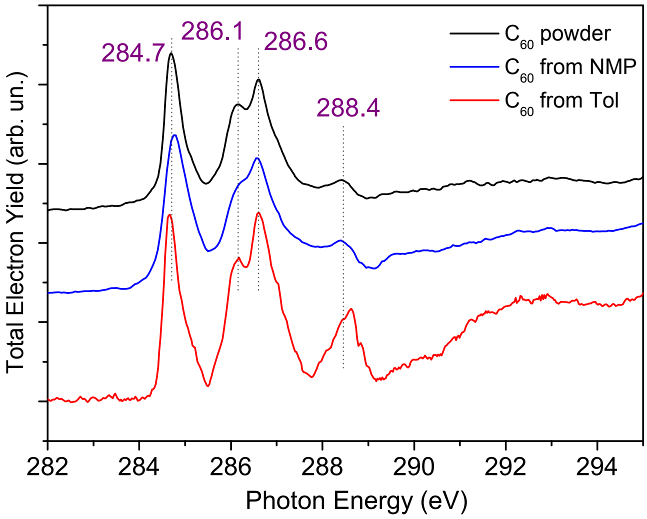

Fig. 1 C1s NEXAFS spectra of C_{60} powder and C_{60} layers deposited from toluene and 1-methyl-2-pyrrolidinone at the surface of stainless steel substrate

All measurements were performed during the single-bunch beam time at the Russian-German beam line at BESSY-П. The NEXAFS spectra of these composites were obtained at room temperature (RT) in the total electron yield mode by detecting a sample current. No noticeable charging effects were observed in the experiments. The photon-energy resolution was set to 0.15 eV at the C1s edge (~285 eV). The absorption spectra were normalized to the incident photon flux, which was monitored by measuring the total electron yield from a clean

---

[1] *The following materials have been used: PMMA Fluka, standard M_w=500000; PS Fluka, 81414, standard Mw=500000; poly(pyromellitic dianhydride-co-4,4'-oxydianiline) amic acid (Aldrich, 575801, ca. 15 wt.% sol. in 1-methyl-2-pyrrolidinone (NMP); fullerene C_{60} (522500, Aldrich, sublimed, 99.9%); toluene (650579, Sigma-Aldrich, Chromasolv plus, for HPLC >99.9%); 1-methyl-2-pyrrolidinone (270458, Aldrich, 99+% HPLC grade).*

gold substrate with the use of a channeltron. The photon energy in the region of the C1s absorption spectra was calibrated using the Ti2p absorption spectrum of K_2TiF_6 (459.0 eV [4]). Lateral resolution of the method is about 300 µm. All spectra were normalized to the intensity of the main absorption band in the spectrum. In this report NEXAFS spectra at the C1s threshold obtained on PMMA-C_{60}, PS-C_{60} and PMDA-ODA-C_{60} composites are briefly compared with the spectrum of neat C_{60} layers. The N1s and O1s absorption spectra (not reported here) were investigated additionally.

Fig 1 shows C 1s NEXAFS spectra for the C_{60} fullerite powder covered over the steel substrate as well as C_{60} films formed at the steel substrate from NMP and Tol solutions. The general similarity in the shape of the NEXAFS spectra shown in Fig 1 is obvious. This is due to the rigidity of the structure of the C_{60} molecule. The energy position of LUMO (284.7 eV), LUMO+1 (286.1 eV), LUMO+2 (286.6 eV), LUMO+3 (288.4 eV) corresponding to the first, second, third and forth unoccupied orbitals (vertical dotted lines) are in a good agreement with literature [5]. Note the differences in the shape of both the LUMO (284.7 eV) and LUMO+1 (286.1 eV) for C_{60} layer deposited from NMP compared with the spectrum of C_{60} layer deposited from Tol and the spectrum taken from C_{60} powder. Additionally, the LUMO+3 is evidently more intense for C_{60} deposited from Tol. These effects may be tentatively explained to result from the donor-acceptor (polar) interaction of NMP and Tol molecules with C_{60} [6]. Similar effects are probably characteristic also of the solutions containing carbon nanotubes since NMP is a good solvent for these objects as well [7].

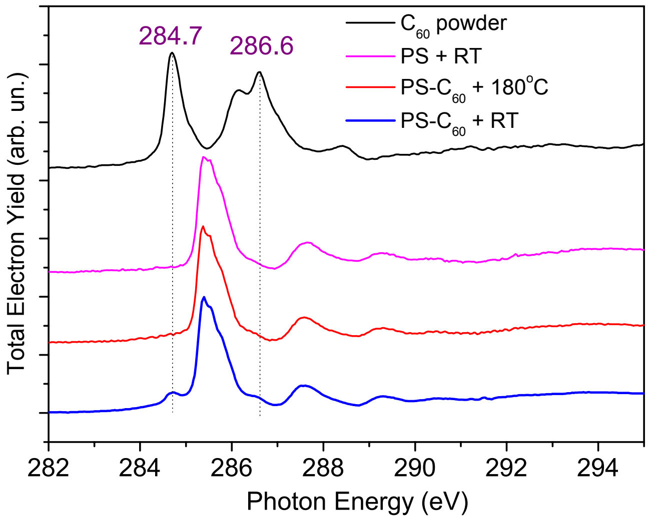

Fig. 2 C1s NEXAFS spectra of PS-C_{60} composite subjected to different heat treatment regimes

Fig 2 presents spectra of the PS-C_{60} composite after heating at different temperatures in air along with the spectra of neat PS and C_{60} powder. The vertical dashed lines indicate the positions of LUMO and LUMO+2 in the spectrum of C_{60} powder. Note that additional contribution of C_{60} in the spectrum of PS-C_{60} composite is seen as clearly discernable shoulders on both sides of the main absorption band of PS spectrum. The decrease and yet disappearance of these shoulders has been observed for the PS-C_{60} composite heated at 180°C.

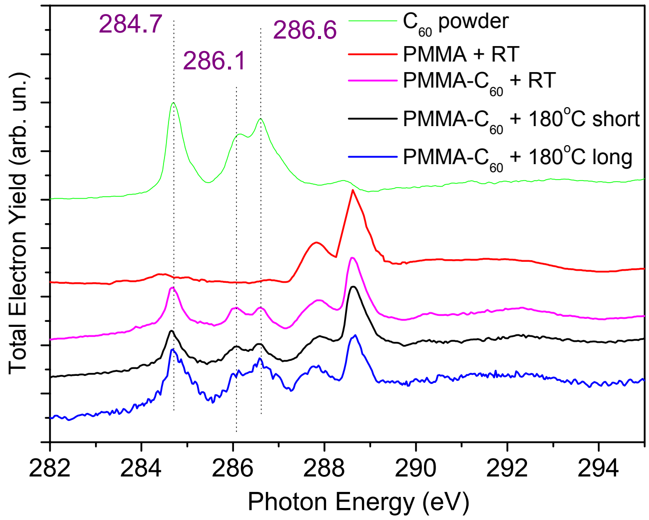

Fig. 3 C1s NEXAFS spectra of PMMA-C_{60} composite subjected to different heat treatment regimes

Fig. 3 shows the spectra of PMMA-C_{60} composite formed at RT and after treatment at about 180°C for different time periods in air. The spectrum of a composite formed at RT indicates the presence of the LUMO, LUMO+1 and LUMO+2 of C_{60}. Notable is the decrease in relative intensity of LUMO+1 upon heating the PFC and the loss of intensity of the peaks characteristic of PMMA matrix on prolonged heating at 180°C. More detailed quantitative data analysis is under way to reveal if this is an effect of thermal degradation of the matrices and/or the indication of its interaction with C_{60}.

Fig. 4 shows the spectra of PMDA-ODA-C_{60} composite along with the spectra of neat PMDA-ODA and C_{60} powder for comparison. No discernable effect of C_{60} on the shape of C1s NEXAFS spectrum is observed. One may speculate that the sedimentation process results in the drop of C_{60}

concentration below the sensitivity threshold of the experimental technique (~2 wt. %). In order to elucidate this effect the experiments on the samples formed from the sediment are needed.

Finally, the results obtained reveal changes in the shape and position of electronic states of C_{60} in different PFCs and solvents. The effect of temperature in redistribution the intensity of these states is observed pointing to the probable changes in the interaction mechanism between polymer matrices and C_{60} upon heating. The results provide good grounds for further studies of the interrelated problems of the nature of C_{60} dispersion states in the polymer matrices and the polymer-fullerene interaction mechanisms.

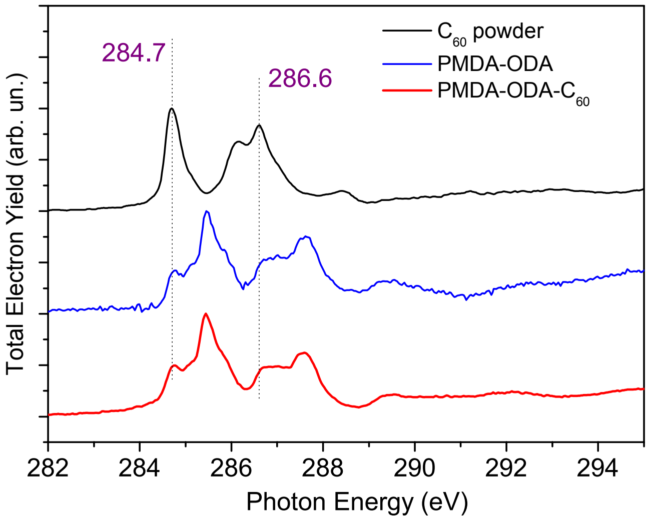

Fig. 4 C1s NEXAFS spectra of PMDA-ODA-C_{60} composite

Acknowledgements

This work was supported by the bilateral Program "Russian-German Laboratory at BESSY". We thank Dr. Yu.S. Dedkov for valuable technical assistance. A.O. Pozdnyakov expresses gratitude to the Alexander von Humboldt Foundation for support of his research stay at IVW, Technical University of Kaiserslautern.

References

1 The physics of fullerene-based and fullerene-related materials, Ed. W. Andreoni, Kluwer Academic Publishers, 2000, 445p.
2 A.O. Pozdnyakov, B.M. Ginzburg, T.A. Maricheva, et. al., Fiz. Tverd. Tela, 2005, 12, 2239-2245 [Phys. Solid State, 2005, 47(12), 2333-2340]
3 V.N. Bezmelnizin, A.V. Eleckii, M.V. Okun, Usp. Phys. Nauk, 1998, 168(11), 1195
4 A.S. Vinogradov, A.Yu. Dukhnyakov, V.M. Ipatov, et al., Fiz. Tverd. Tela, 1982, 24, 1417 [Sov. Phys. Solid State 24, 803 (1982)]
5 J.-H. Guo, P. Glans, P. Skytt, N. Wassdahl, et. al., Phys. Rev., B, 1995, v. 52, № 15, 10681-10684
6 I. Baltog, M. Baibarac, L. Mihut, N. Preda, T. Velula, S. Lefrant, Romanian Reports in Physics, 2005, 57(4), 807-814
7 K. D. Ausman, R. Piner, O. Lourie, and R. S. Ruoff, The Journal of Physical Chemistry B, 2000, 104(38), 8911-8915

2. Cd^{2+}/NH$_3$ treatment-induced formation of a CdSe surface compound on CuGaSe$_2$ thin film solar cell absorbers

M. Bär[1,2], S. Lehmann[1], L. Weinhardt[2,3], M. Rusu[1], A. Grimm[1], I. Kötschau[1], I. Lauermann[1], P. Pistor[1], S. Sokoll[1], Th. Schedel-Niedrig[1], M.C. Lux-Steiner[1,4], C. Heske[2], Ch. Jung[5], and Ch.-H. Fischer[1,4],
(1)Solarenergieforschung (SE 2), Hahn-Meitner-Institut, 14109 Berlin, Germany
(2)Department of Chemistry, University of Nevada, Las Vegas, NV89154, USA
(3)Experimentelle Physik II, Universität Würzburg, 97074 Würzburg, Germany
(4)Freie Universität Berlin, 14195 Berlin, Germany
(5)BESSY GmbH, 12489 Berlin, Germany

CuGaSe$_2$ ("CGSe")-based high-gap thin film solar cells have up to date not reached their potential performance level. To elucidate possible shortcomings of the electronic interface structure, we have studied the initial stage of the interface formation between the CGSe absorber and the CdS buffer layer by use of a simple Cd^{2+}/NH$_3$-treatment [1]. For our investigations, we used CGSe/Mo/soda-lime glass structures. Mo was evaporated onto the glass substrate, followed by the deposition of the CGSe absorber using chemical close-spaced vapor transport (CCSVT) [2] with a [Ga]/[Cu] ratio of approx. 1.16. Each sample was cut into two pieces, one of which was treated in an aqueous solution of 1.5 mM CdSO$_4$ and 1.5 M NH$_3$ for 10 min inside the glovebox of the CISSY apparatus. The other half was used as a reference.

Subsequently, both types of CGSe surfaces were characterized by photoelectron spectroscopy (PES) using synchrotron radiation (BESSY II, beamline UE 41-PGM). For normalization purposes, the excitation intensity was also recorded. A CLAM4 electron spectrometer (Thermo VG Scientific) was used. The electron spectrometer was calibrated using XPS and Auger line positions of different metals (Cu 3p, Au 4f$_{7/2}$, Cu L$_3$VV, and Cu 2p$_{3/2}$). For the synchrotron measurements, the zero point of the energy scale was adjusted for each excitation energy used, such that the Au 4f$_{7/2}$ reference line appears at a binding energy of 84.00 eV.

From the Cd M$_{45}$N$_{45}$N$_{45}$ Auger peak at $E^{Cd\,M_4N_{45}N_{45}}_{Kinetic}$ = (381.6 ± 0.1) eV, CdSe is identified on the surface of the Cd^{2+}/NH$_3$-treated CGSe absorber (literature values $E^{Cd\,M_4N_{45}N_{45}}_{Kinetic}$ (CdSe) between 381.4 and 381.7 eV). In order to investigate whether Cd atoms diffuse into the absorber and thereby occupy vacant cation sites or whether a separate CdSe surface compound is formed, we have varied the spectroscopic information depth by applying different excitation energies (E$_{Phot}$). Since the valence states of Se 3d, Ga 3d, and Cd 4d are energetically close together (binding energy between 11eV and 54 eV) and the escape depth λ?cosφ?and the spectrometer characteristic are almost identical, these signal intensities can be directly compared. Variation of the excitation energy between 1254 eV and 174 eV resulted in a decrease of kinetic energies of the considered photoelectrons from

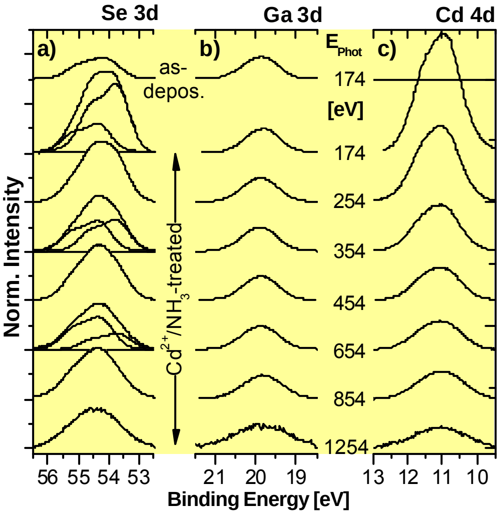

Fig. 1 Se 3d (a), Ga 3d (b), and Cd 4d (c) photoemission lines measured at different excitation energies (E$_{Phot}$). All spectra are presented on the same intensity scale. After removal of a linear background they were normalized by the excitation intensity and the respective photoionization cross sections.

1221 eV to 141 eV and, consequently, also a decrease of their escape depth from approx. 1.2 nm to 0.4 nm (for φ ≈ 45°) [3], i.e., the surface sensitivity is strongly enhanced. Fig.1 shows the Se 3d, Ga 3d, and Cd 4d signals of the treated CGSe sample for such an energy variation, as well as that of the untreated reference for 174 eV. The intensity of the Cd 4d peak increases with decreasing excitation energy. The Se 3d signal of the treated sample stems from both, $CuGaSe_2$ (higher binding energy) and CdSe (lower binding energy). Peak-fitting based on a Voigt function doublet reveals that the CdSe contribution also increases for higher surface sensitivity. Both observations clearly indicate a very thin CdSe layer on the very top of the treated surface.

In Fig. 2a the calculated Cd/Ga- and Cd/Se_{CGSe}-ratios are plotted as a function of excitation energy and escape depth. For the latter, the area of the Cd 4d line was compared with the intensity of the Se 3d contribution of CGSe. Both ratios increase with decreasing photon energy. In Fig. 2b, the ratio of the two contributions to the Se 3d signal (Se_{CdSe}/Se_{CGSe}) are plotted in the same way. Assuming an abrupt CdSe/CGSe interface, the area intensity ratio of Se_{CdSe}/Se_{CGSe} can be calculated to be proportional to the corresponding concentration ratio c_{CdSe}/c_{CGSe} = c, multiplied by $(\exp(d/(\lambda\cdot\cos\varphi))$ - 1). As shown by the fit in Fig. 2b, the escape depth dependence of the Se_{CdSe}/Se_{CGSe} ratio can be described well by this approach. The thickness of the CdSe surface layer is determined to d = (0.7 ± 0.1) nm, corresponding to about one monolayer of CdSe. This is in good agreement with the value determined based on the attenuation of the absorber peaks induced by the CdSe layer, as judged from the Ga and Cu signals [4].

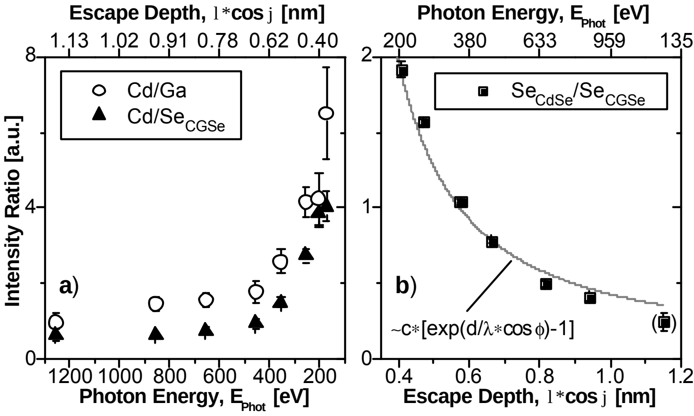

Fig. 2a. Cd/Ga- and Cd/Se_{CGSe}-ratios calculated from the spectra shown in Fig. 1 versus excitation energy (corresponding escape depth at the top).

b. Ratio of the two contributions to the Se 3d line (Se_{CdSe}/Se_{CGSe}) versus escape depth of the respective photoelectrons and fit of the data to determine the thickness of the CdSe surface layer (solid line). At the top, the corresponding excitation energy of the respective spectra in Fig. 1 is given.

In summary, we do not find any experimental evidence for a significant Cd diffusion into the CGSe absorber. We conclude that Cd–Se bonds are formed at the CGSe absorber surface after a Cd^{2+}/NH_3 treatment, which is in close analogy to the previously observed formation of a CdS monolayer at the S-rich CIGSSe absorber surface [5]. This demonstrates the possibility to modify the electronic surface and interface structure by deliberate surface modification treatments and describes the early stages of the CdS/CGSe interface formation by a conventional CdS chemical bath deposition.

References

[1] M. Bär, S. Lehmann, M. Rusu, A. Grimm, I. Kötschau, I. Lauermann, P. Pistor, S. Sokoll, Th. Schedel-Niedrig, M. Ch. Lux-Steiner, Ch.-H. Fischer, L. Weinhardt, C. Heske, Ch. Jung, Appl. Phys. Lett. **86** (2005) 222107

[2] M. Rusu, S. Wiesner, D. Fuertes Marrón, A. Meeder, S. Doka, W. Bohne, S. Lindner, Th. Schedel-Niedrig, CH. Giesen, M. Heuken and M.Ch. Lux-Steiner, Thin Solid Films **451-452** (2004) 556

[3] M.P. Seah, W.A. Dench, Surf. Interf. Anal. **1**, (1979) 2

[4] M. Bär, M. Rusu, S. Lehmann, S. Sokoll, A. Grimm, I.M. Kötschau, I. Lauermann, P. Pistor, L. Weinhardt, O. Fuchs, C. Heske, Ch. Jung, W. Gudat, Th. Schedel-Niedrig, M.Ch. Lux-Steiner, and Ch.-H. Fischer, Proc. 31st IEEE PVSC, Lake Buena Vista, **2005**, p. 307-310

[5] L. Weinhardt, Th. Gleim, O. Fuchs, C. Heske, E. Umbach, M. Bär, H.-J., Muffler, Ch.-H. Fischer, M. Ch. Lux-Steiner, Y. Zubavichus, T. P. Niesen, F. Karg, Appl. Phys. Lett. **82**, (2003) 571

X-ray emission and photoelectron spectroscopy at Cu(In,Ga)(S,Se)$_2$ thin film solar cells in the CISSY endstation

1. XES of a liquid/solid interface through a 100 nm Si_3N_4-window

I. Lauermann$^{(1)}$*, A. Grimm*$^{(1)}$*, M. Bär*$^{(1,2)}$*, S. Lehmann*$^{(1)}$*, Ch. Loreck*$^{(1)}$*, H. Mönig*$^{(1)}$*, S. Sokoll*$^{(1)}$*, M. Ch. Lux-Steiner*$^{(1,3)}$*, C. Heske*$^{(2)}$*, Ch. Jung*$^{(4)}$*, and Ch.-H. Fischer*$^{(1,3)}$
$^{(1)}$*Solarenergieforschung (SE 2), Hahn-Meitner-Institut, 14109 Berlin, Germany*
$^{(2)}$*Department of Chemistry, University of Nevada, Las Vegas, NV89154, USA*
$^{(3)}$*Freie Universität Berlin, 14195 Berlin, Germany*
$^{(4)}$*BESSY GmbH, 12489 Berlin, Germany*

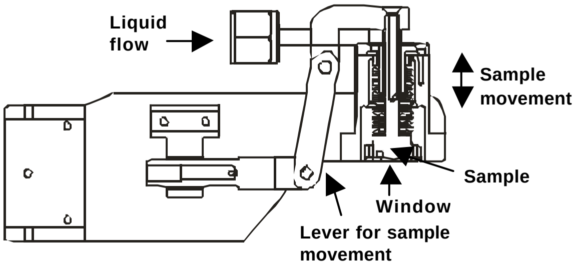

Figure 1: *Cross-section of the flow-through cell, top view (drawing by PINK® GmbH).*

Chalcopyrite ("CIGSSe") thin film solar cells with a typical structure n$^+$-ZnO/i-ZnO/CdS/Cu(In,Ga)(S,Se)$_2$/Mo/glass are promising candidates for future low-cost, high efficiency power conversion devices. Some functional materials in chalcopyrite thin film solar cells, e.g., buffer layers like CdS, are usually deposited wet-chemically. However, the exact mechanisms of material formation, inter-diffusion, and possible chemical changes of the absorber are often unknown. *In-situ* analysis is necessary to answer some of these questions. Therefore, we developed a UHV-compatible flow-through cell for in-situ x-ray emission spectroscopy at liquid/solid or gaseous/solid interfaces. The set-up of the flow-through cell is shown in Figure 1. The sample is mounted on a moveable stub inside the flow-through cell. The variable distance sample-window between 0 and 5 mm allows either XES-measurements (without prohibitive absorption by the liquid) or liquid flow (for continuous chemical reactions), respectively. A crucial part of the cell is the Si_3N_4 window, which is only 100 nm thick (supplied by Silson Ltd, England). Yet is has to withstand a pressure difference of around 1000 mbar between the inside of the flow-cell (which is under ambient pressure) and the UHV in the analysis chamber. For that reason it was chosen to be as small as possible, i.e. the dimensions are 0.5 x 1 mm^2. The front view of the window mounted in the front flange of the flow-through cell is shown in Figure 2.

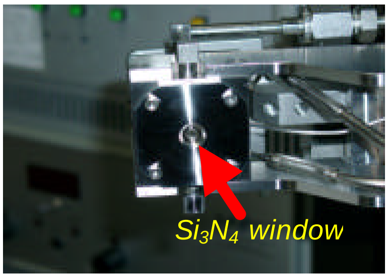

Figure 2: *View of the Si_3N_4 window of the flow-through cell*

The CISSY flow-through cell was tested for UHV-compatibility, and first O K_α XES spectra of liquid water flowing through the cell were acquired in 2004. During the beam time in June 2005, we overcame window rupture problems and monitored Cu $L_{2,3}$, Se $L_{2,3}$, and S $L_{2,3}$ XES spectra from a $Cu(In,Ga)(S,Se)_2$ sample mounted inside the flow-through cell filled with water. To prove that the signal actually originated from the sample and not from contamination of the wet cell window or the solution, we measured spectra with the sample close (distance of > 1 µm) to the window and about 3 mm away from the window, respectively. While the attenuation of x-rays in water in the utilized energy range is sufficiently low to allow the detection of signals from a sample covered by a few µm of water, it is impossible to detect a signal through 3 mm of water. For example, at 1380 eV, the emission energy of the Se L_3 peak, the attenuation length for an incidence angle of 45° is around 4 µm. Furthermore, when the sample is moved away from the window by more than 1 mm, it will be out of the line-of-sight of the spectrometer, which is mounted at an angle of 45° with respect to the wet cell window.

Figure 3 shows Cu $L_{2,3}$ and Se $L_{2,3}$ XES spectra, acquired at a small and at a large sample-window distance, respectively. Clearly no signal is visible at a large distance in the case of Cu. Since only the sample-window distance was changed between the two spectra, this shows that the detected signal actually originated from the sample. In the Se $L_{2,3}$ spectrum recorded at large sample-window distance, a small signal is visible at the Se L_3 emission energy (vertical line). This could be due to traces of a dissolved Se species in the circulating liquid which might have been produced in a photo-(electro)chemical reaction at the illuminated CIGSSe-surface. With this setup it is now possible to examine wet-chemical processes at surfaces *in-situ.*

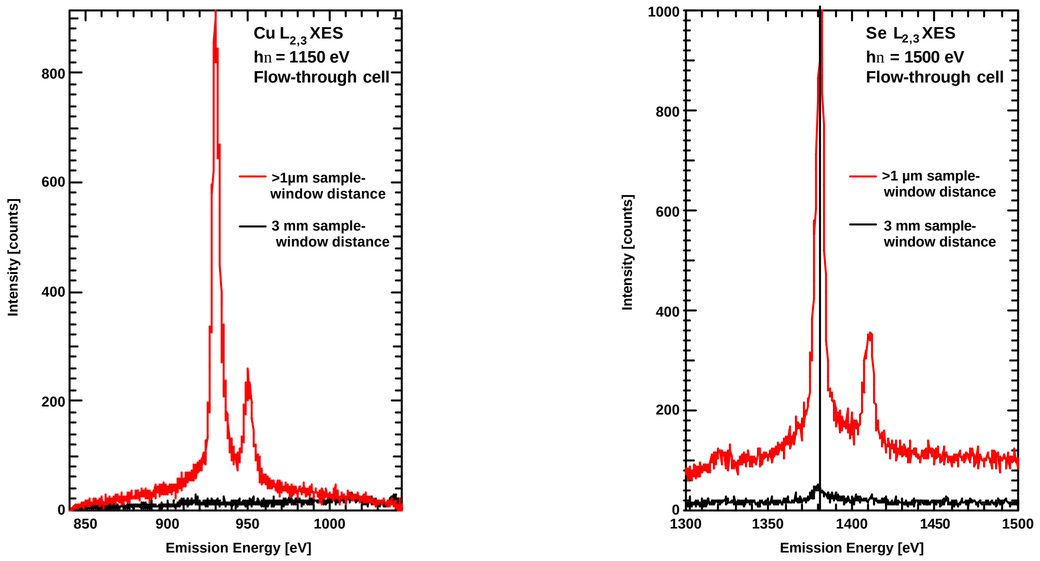

Figure 3: *Cu $L_{2,3}$ XES (left) and Se $L_{2,3}$ XES spectrum (right) of CIGSSe "under water", mounted in the CISSY wet cell. Red: sample is close to the window, black: sample is 3 mm away from the window*

Structural and magnetic properties of $[Co_2MnGe/Al_2O_3]_n$ multilayers

M.Vadalá, K. Westerholt and H. Zabel

Experimental Physik IV, Ruhr-Universität Bochum,
Universitätstrasse 150, 44780 Bochum Germany

From electronic energy band structure calculations the Co_2MnGe Heusler alloy has been predicted to be a half metallic ferromagnet with a 100% spin polarization at the Fermi level. This property is very attractive for application in spin dependent electron transport devices such as giant magnetoresistance (GMR), spintronics devices or for the injection of a spin polarized current into semiconductors. We have grown multilayers of the Heusler phase Co_2MnGe and normal metals like V and Au [1] and found that the formation of non ferromagnetic interlayers at the interfaces is a common feature. It was found before [2] that x-ray resonant magnetic scattering (XRMS) is well suited for the determination of the magnetization profile inside the Heusler layer.

Following these lines, in our present experimental investigations we show the results obtained on $[Co_2MnGe/Al_2O_3]_n$ multilayers. This system is very interesting because magnetic tunnelling junction using the fully spin polarized Heusler phases as electrodes typically possess Al_2O_3 as tunnelling barrier. Since the TMR reacts sensitively on the spin polarization of the first few monolayers of the ferromagnetic electrodes, detailed knowledge of the surface magnetism of very thin Heusler layers at the interfaces with Al_2O_3 is very important. Recent magnetization measurements on $[Co_2MnGe/Al_2O_3]_n$ multilayers indicated that the interface magnetism in this system is similar to that observed for the Heusler/normal metal interfaces before. Thus in this contribution we present results of the determination of the magnetization profile using XRMS technique.

$[Co_2MnGe/Al_2O_3]_n$ Multilayers	P14	P34
$[Co_2MnGe]$ [thickness in Å]	27.3	20.7
$[Al_2O_3]$ [thickness in Å]	41.7	41.7

Table 1: Characteristics of the Heusler multilayers, investigated at the beamline UE56/1-PGM-b BESSY.

In Table 1 the parameters of the samples used for the present study were summarized. The multilayers were deposited on single crystalline Al_2O_3 substrates at room temperature; both samples have 25 bilayers. The experiments have been carried out at the beamline UE56/1-PGM-b, using the diffractometer ALICE [3]. The measurements have been performed with a fixed photon polarization (the right hand circularly polarized radiation) and a reswitching of the magnetization direction by applying a magnetic field. All measurements have been done at room temperature. In Fig.1 -the first row- we show the energy dependence of the scattering intensities measured on the sample P14 (taken at the first three multilayer Bragg peaks positions) after applying the magnetic field of 2000 Oe (blue curves) and the negative field of -2000 Oe (green curves). The corresponding asymmetry (the ratio between their difference and their sum) around the Co $L_{3,2}$ absorption edges is shown in the second row.

One clearly observes a non vanishing asymmetry, which gives evidence that the Co atoms in the multilayer possess a magnetic moment. The precise determination of the magnetization profile

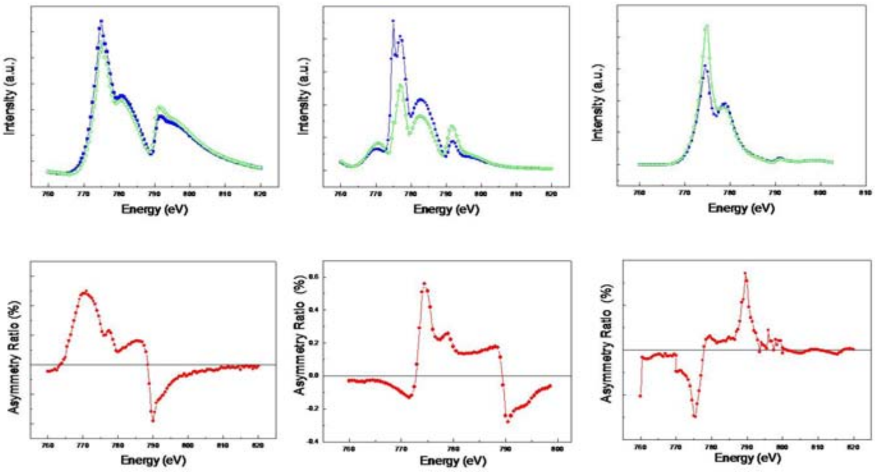

Figure 1: Scattering intensity (the first row) and asymmetry ratio (the second row) taken for the sample P14 at the positions of the first three Bragg peaks around the Co $L_{3,2}$ edges.

needs sophisticated model calculations and requires accurate fitting procedures which are now in progress.

The authors acknowledge the financial support provided through the European Community's Marie Curie actions (Research Training Networks) under the contract MRTN-CT-2003-504462, ULTRA-SMOOTH.

References

[1] U. Geiersbach, A. Bergmann and K. Westerholt, *Thin Solid Films* **425**, 225 (2003)

[2] J. Grabis, A. Bergmann, A. Nefedov, K. Westerholt and H. Zabel, *Phys. Rev. B* **72**, 024438 (2005)

[3] J. Grabis, A. Nefedov and H. Zabel, *Rev. Sci. Instr.* **74**, 4048 (2003)

Surface Crystallinity and High Energy Ion Induced Amorphization of InP

N. Darowski, I. Zizak, G. Schumacher

Hahn-Meitner-Institute Berlin, Glienicker Strasse 100, D-14109 Berlin, Germany

Indium phosphide (InP) is a promising material for various electronic and opto-electronic applications. As InP has no natural oxide additional defects or impurities have to be introduced to create isolating material needed for device production. Because of the low thermal stability of InP the most prominent way to dope or electrically isolate the material is ion implantation with MeV ion beams. For the fabrication of thick or buried layers high-energy ion implantation has to be utilized.

When a swift heavy ion penetrates a solid, it mainly slows down via the electronic energy loss S_e. The energy is first deposited to the electronic system and subsequently transferred into the atomic system via various mechanisms, e.g. electron-phonon-interaction. If the electronic stopping power is sufficiently large thermal spikes can be induced along the straight ion path leading to formation of a latent track.

In pre-damaged InP tracks are observed after irradiation with Xe ions [1].The cores of the tracks are amorphous and track overlap leads to complete amorphization at sufficiently high fluences. At room temperature continuous tracks are generated while at liquid nitrogen temperature the tracks are discontinuous. At low temperatures melting of the tracks is possibly suppressed by the high thermal conductivity which allows for a fast dissipation of heat [2]. Interestingly, Rutherford backscattering spectrometry [3] and cross-section transmission electron microscopy (TEM) analysis [2] of InP irradiated up to 1.4×10^{14}Xe/cm^2 point to a 40 nm thick surface layer which is almost defect-free while at depths larger than 40 nm complete amorphization was observed. X-ray diffraction on InP specimens irradiated with 390 MeV Xe ions confirmed both, a crystalline surface layer [4] and a decreased sensitivity to defect generation in case of low temperature ion irrradiation [5].

The energy loss in a material is ion specific, i.e. different ion species with different energy and charge state lead to different defect structures. As the electronic and nuclear energy loss in InP of 350 MeV Au ions is larger compared to 390 MeV Xe ions enhanced track formation is expected in case of Au irradiation. No pre-damaging should be necessary for the generation of amorphous tracks. Each Au ion impigning to the sample should result in a single track.

In order to investigate the damage production depending on the irradiation conditions pieces of InP(001) samples were irradiated with 350 MeV Au ions up to different fluences $\Phi t = 1 \times 10^{12} \ldots 3 \times 10^{14}$ Au/cm^2 at the cyclotron of the ISL, Hahn-Meitner-Institute Berlin. One series of samples was covered by a $2\,\mu$m thick gold degrader foil to change the charge state of the projectiles without changing the electronic energy loss significantly. A part of the specimen was shadowed from the ion beam during irradiation and served as a reference. To study the bulk and the near surface lattice structure as well as surface and interface roughness different non-destructive x-ray scattering techniques were combined. Symmetrical x-ray diffraction (XRD) at the (002) Bragg reflection yields information about the mean bulk properties of the crystal lattice, whereas x-ray reflectometry (XRR) measurements and grazing incidence x-ray diffraction (GID) at the (220) reflection are sensitive to the surface. As the disadvanteous ratio between incoming and scattered intensity in case of GID demands the utilization of synchrotron radiation the experiments were performed at KMC2 bending magnet beamline with a photon energy of E = 8.0keV. The versatile psi-circle diffractometer was used as it allows for all of the above mentioned scattering techniques without sample re-mounting. To enhance the spatial resolution small slits were used in front of the scintillation detector. All recorded curves were normalized to the intensity of the primary x-ray beam.

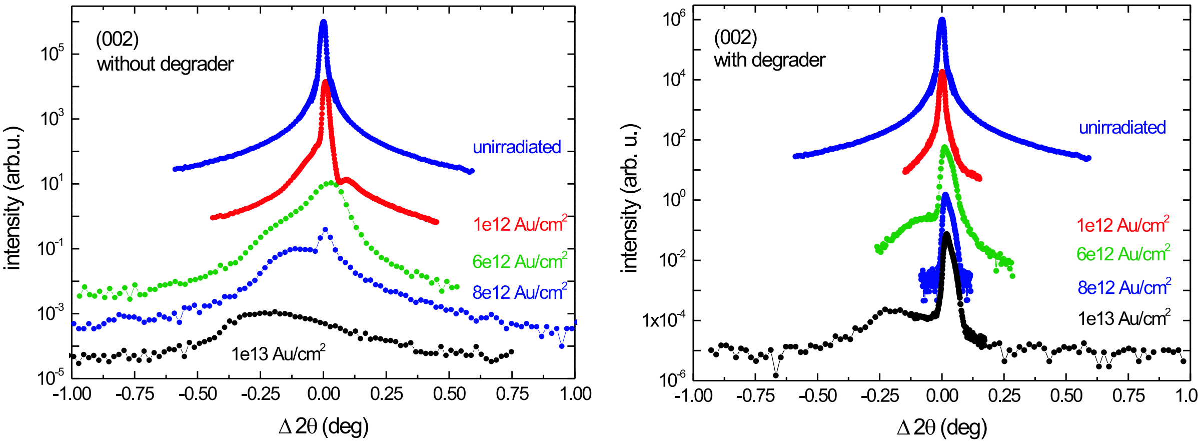

Figure 1 (002) diffraction curves recorded from InP samples irradiated with 350 MeV Au ions directly (left) and with 2 μm Au degrader (right). Consecutive profiles are multiplied by a factor of 10 for better visibility.

Figure 1 shows the diffraction curves recorded at the (002) Bragg reflection. $\Delta 2\theta$ denotes the scattering angle with respect to the Bragg angle of the unirradiated sample. In case of direct irradiation with 350 MeV Au ions (left) a fluence depending Bragg peak intensity decrease, peak broadening and small peak shift to higher 2θ-values is observed. Additionally a scattering contribution at the low 2θ side of the central Bragg peak arised in the diffraction curves, showing a strong asymmetry and broadening with increasing fluence. No Bragg peak could be observed for irradiation with $1 \times 10^{13}\mathrm{Au/cm}^2$, thus a high damage level in the bulk, i.e. amorphization is assumed for this fluence. In case of irradiation with gold degrader (right) a sharp Bragg peak without significant intensity decrease was observed up to $\Phi\mathrm{t} = 1 \times 10^{13}\mathrm{Au/cm}^2$.

The differences between the diffraction curves recorded at samples irradiated directly and with degrader are even more prominent in case of surface sensitve GID geometry shown in figure 2. For direct irradiation (left) a sharp Bragg peak of nearly unchanged width, i.e. a low damage level, was recorded up to a fluence of $\Phi\mathrm{t} = 1 \times 10^{13}\mathrm{Au/cm}^2$. For irradiation with degrader (right) a strong broadening together with an intensity decrease occured for $\Phi\mathrm{t} > 3 \times 10^{12}\mathrm{Au/cm}^2$. No peak at all could be observed for $\Phi\mathrm{t} = 1 \times 10^{13}\mathrm{Au/cm}^2$, indicating a severe damage of the surface near crystal structure.

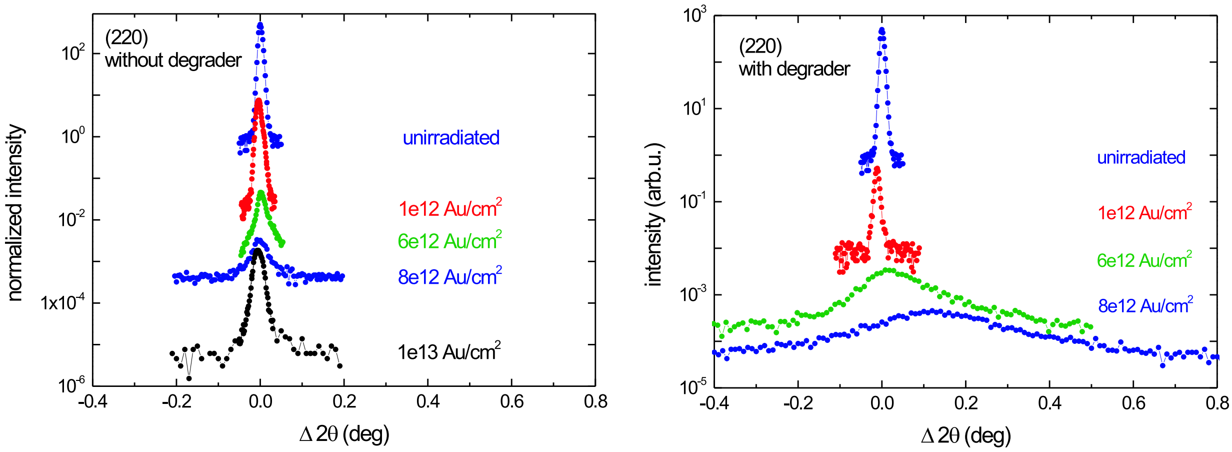

Figure 2 (220) diffraction curves recorded from InP samples irradiated with 350 MeV Au ions directly (left) and with 2 μm Au degrader (right). Consecutive profiles are multiplied by a factor of 10 for better visibility.

These results verify the supposed influence of the charge state of the ion on the damage level after irradiation. A possible explanation is that the projectile has to travel a certain distance in the solid to reach its equilibrium charge state which seems to lead to more effective defect generation. The differences in the diffraction curves recorded for different fluences can be explained by a complicated depth depending strain distribution caused by amorphization along single tracks. As the mass density is larger for amorphous InP compared to single crystalline InP [6,7] the densification in the amorphous tracks introduces stress into the crystalline matrix. The resulting strain and distortion field is depth dependent due to surface relaxation. Obviously there are large differences between the distortion field of a track network where each amorphous track starts at the sample surface (irradiation with degrader) and a track network which is covered with a crystalline layer of a certain thickness (direct irradiation). A simple phenomenological strain model based on this assumption reveals compressed as well as tensily distorted regions in the crystalline matrix between the amorphous tracks. These distorted regions would lead to the observed contributions in the x-ray intensity profiles. An anlysis based on finite element calculation of the fluence depending distortion field of amorphous tracks in a crystalline matrix is planned for the near future to verify this interpretation.

[1] W. Wesch, O. Herre, P.I. Gaiduk, E. Wendler, S. Klaumünzer, P. Meier, *NIM* B **146** (1998) 341.

[2] P.I. Gaiduk, F.F. Komarov, W. Wesch, *NIM* B **164-165** (2000) 377.

[3] O. Herre, W. Wesch, E. Wendler, P.I. Gaiduk, F.F. Komarov, S. Klaumünzer, P. Meier, *Phys. Rev.* B **58** (1998) 4832.

[4] N. Darowski, I. Zizak, G. Schumacher, S. Klaumünzer, E. Wendler, *NIM* B (2003) **209** (2003) 131.

[5] N. Darowski, I. Zizak, G. Schumacher, *Physica B: Condensed Matter* **357** (2005) 118.

[6] C.J. Glover, M.C. Ridgway, K.M. Yu, G.F. Foan, T.W. Lee, Y. Moon, E. Yoon, *Appl. Phys. Lett.* **74** (1999) 1713.

[7] L. Cliche, S. Roorda, R.A. Masut, *Appl. Phys. Lett.* **65** (1994) 1754.

NEXAFS - spectroscopy on freshly prepared and aged plasma-polymerised films

Sufal Swaraj, Umut Oran, Andreas Lippitz, Wolfgang Unger
Bundesanstalt für Materialforschung und –prüfung (BAM), D-12203 Berlin, Germany

NEXAFS spectroscopy has proved to be a powerful tool in the analysis of certain aspects of plasma-polymerised films. Along with XPS (photoelectron spectroscopy) and ToF-SIMS (Time of flight static ion mass spectroscopy) we have employed NEXAFS spectroscopy for the characterisation of plasma polymerised films to obtain information which either XPS and ToF-SIMS are incapable of obtaining or less sensitive to. A dedicated plasma chamber was designed and added to the respective spectrometers. This enabled analysis of freshly prepared samples without exposure to air as well as after exposure to air (aged). In our investigations we have used the organic monomers such as ethyene, allyl alcohol, styrene, allyl amine and acrylic acid to prepare different homopolymers and copolymer films. The aim was to study the correlation of deposition parameters like duty cycle, power, pressure, and monomer (or comonomer) flow rate on the chemical character of the deposited film. In addition to this, the important effect of 'aging' in air of these films was also studied by our unique multi-method approach [1-5]. Here we present some NEXAFS results of the selected case of allyl amine homopolymer films as well as allyl amine/styrene copolymer films.

Plasma deposited allyl amine films:

Figure 1a presents the N K-edge spectra of a single plasma polymerised allyl amine film measured at different intervals of aging time. The main features observed are the π*(C=N) resonance at 398.2 eV, π*(C≡N) resonance at 399.2 eV, σ*(C-N) resonance above 405 eV and a feature A prominent in the aged sample probably due to an amide π* resonance at 400.6 eV. The extent of unsaturation of these films in terms of the presence of C=N and C≡N bonds was observed in terms of the sum of maximum intensity of the π*(C=N) and π*(C≡N) resonances for samples prepared at different deposition parameters. From figure 1b it is clear that the samples prepared at high duty cycles or power show a high degree of unsaturation when measured in-situ. After exposure to air there is a decrease in this unsaturation, and the decrease is high for samples prepared at hard deposition conditions.

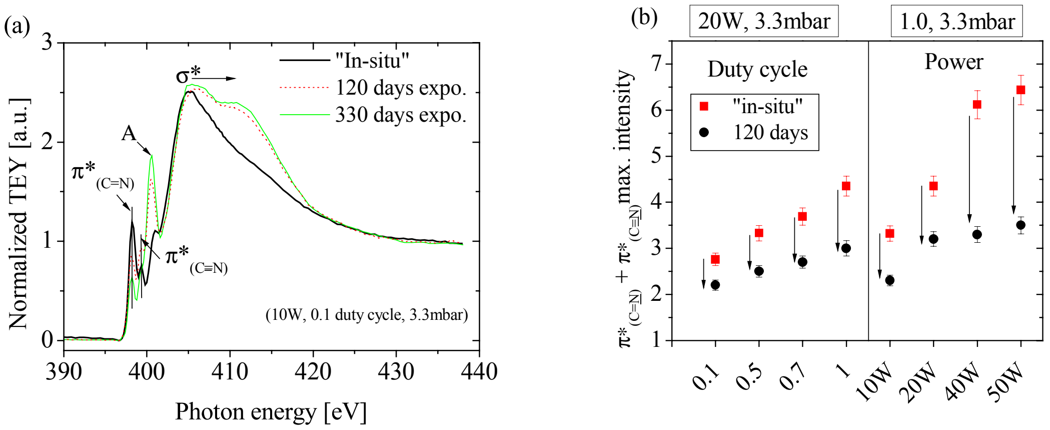

Figure 1: (a) NEXAFS N-K edge spectra of plasma polymerized allyl amine film. (b) Sum of maximum intensity of the π*(C=N) and π*(C≡N) resonances for different plasma polymerised allyl amine films (in-situ and aged) (boxes on top indicate constrained deposition parameters).

From XPS studies an increase in the O/C and a decrease of the N/C atomic ratios was observed due to aging. A loss of nitrogen after absorption of humidity from the ambient air has been discussed in ref. [6] to be due to the reaction

$$\text{R-CH=NH} + H_2O \rightarrow \text{R-CH=O} + NH_3.$$

The concentration of C=N species was high in the case of samples prepared at hard plasma conditions. Consequently N/C decrease was found to be stronger in these cases. The oxygen uptake due to aging originated from an oxidation preocess starting at embedded $C^{\bullet}$ radical sites adjacent to N atoms. In ref. [7] the authors proposed such kind of a reaction:

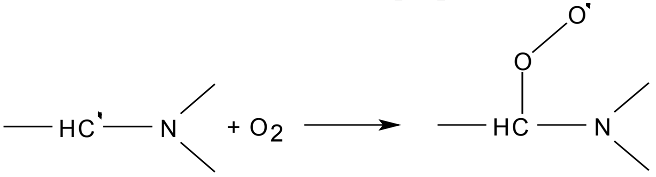

This reaction leads to the formation of amides and similar groups during the aging process. The amides are clearly identifies in the case of the NEXAFS N K-edge spectrum as shown in figure 1a.

Plasma deposited allyl amine/styrene copolymer films:

Figures 2a and 2b present the C K-edge and N K-edge of plasma deposited allyl amine/styrene copolymer measured in-situ, respectively. The area under the resonance $C1s \rightarrow \pi^*_{ring}$ (C K-edge), is found to decrease with the decrease in the partial flow rate (PFR)

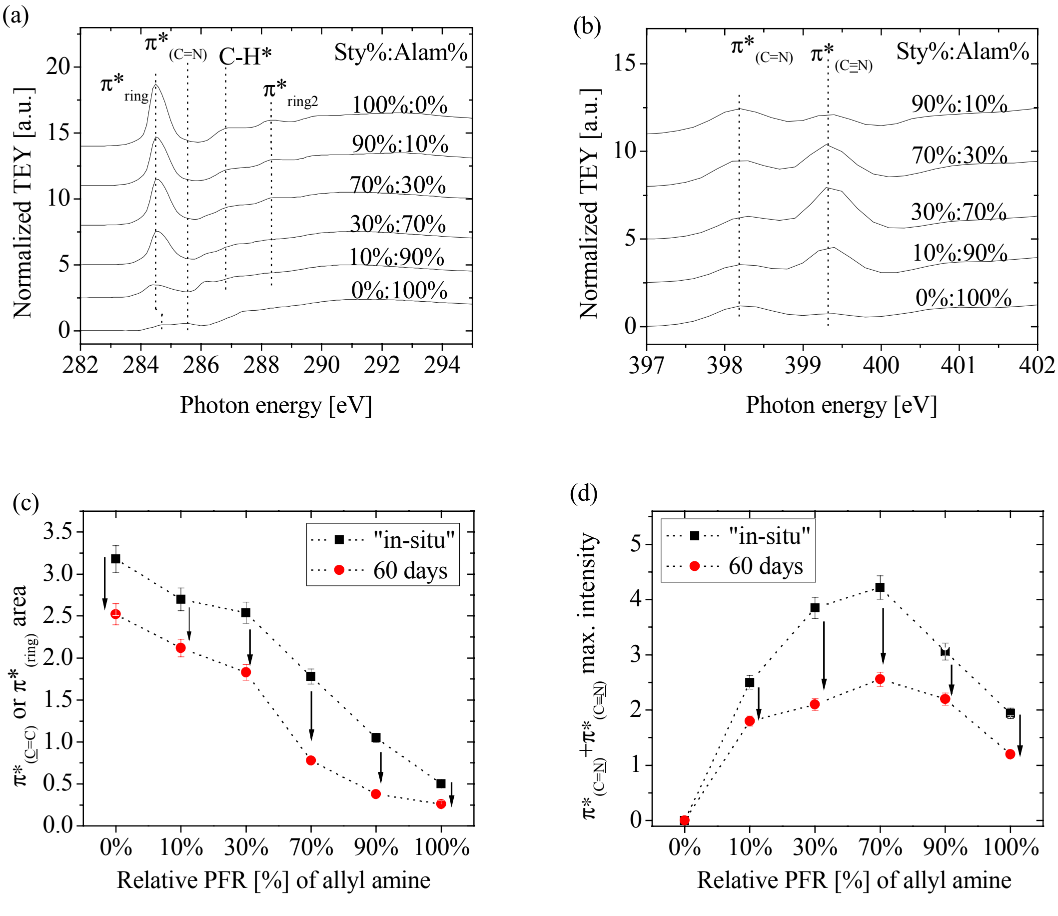

Figure2: (a) NEXAFS C K-edge (b) NEXAFS N K-edge (c) $C1s \rightarrow \pi^*_{ring}/\pi^*_{C=C}$ area (d) sum of $N1s \rightarrow \pi^*_{(C=N)}$ and $N1s \rightarrow \pi^*_{(C\equiv N)}$ resonance maximum intensities for freshly prepared and 60 days aged allyl amine/styrene copolymer films [20W, 0.1, 3.3mbar, 20sccm].

of styrene. This indicates a decrease in the overall unsaturation of the deposited films (Figure 2c). However, in the case of N K-edge the unsaturation (sum of N1s→$\pi^*_{(C=N)}$ and N1s→$\pi^*_{(C\equiv N)}$ resonance maximum intensities) first increased with the increase in the PFR of allyl amine and then decreased (Figure 2d). The increase was observed as long as there was a sufficient styrene concentration in the feed gas (up to 30% PFR) and then found to decrease. Styrene along with a sufficient concentration of allyl amine favors the formation of unsaturated CN bonds such as nitriles and imines. This leads to the increase in unsaturation till the percentage of partial flow rate of allyl amine was 70% as shown in Figure 2d. This increase in the extent of unsaturation does not continue further because there is insufficient styrene to favor the formation of unsaturated CN bonds. This result implies a higher level of unsaturation in the copolymer films as compared to the respective homopolymers. The films when measured after exposure to air were found to lose unsaturation in terms of $\pi^*_{ring}/\pi^*_{C=C}$ bonds, $\pi^*_{(C=N)}$ and $\pi^*_{(C\equiv N)}$ bonds. There is no particular trend found in the loss of unsaturation of the copolymer films.

Summary: NEXAFS can be successfully used along with XPS and ToF-SIMS for the analysis of freshly prepared and aged plasma polymerised organic films. In some cases it has been found that aging is influenced by the deposition parameters. Key intermediate species and end products of auto-oxidation reactions during aging can be successfully identified by NEXAFS.

Acknowledgement: Thanks are due to BESSY staff and other CRG members for the excellent collaboration during commissioning of the HESGM beamline. Special thanks to Matthias Mast (BESSY) and Olaf Schwarzkopf (BESSY) for support during experiments.

References:

1. U. Oran, S. Swaraj, J. F. Friedrich and W. E. S. Unger; Plasma Processes and Polymers, 1, 2004, 123.
2. Swaraj S, Oran U, Lippitz A, Schulze RD, Friedrich JF, Unger WES; Plasma Processes and Polymers, 2 (4): 310-318 MAY 12 2005.
3. Swaraj S, Oran U, Lippitz A, Friedrich JF, Unger WES; Plasma Processes and Polymers, 2: 572-580 2005.
4. Swaraj S, Oran U, Lippitz A, Schulze RD, Friedrich JF, Unger WES; Plasma Processes and Polymers, 1 (2): 134-140 SEP 24 2004.
5. U. Oran, S. Swaraj, J. F. Friedrich and W. E. S. Unger; Plasma Processes and Polymers, 1, 2004, 141.
6. L. J. Gerenser, J. Adhesion Science Technol. Vol. 1 (1987), p. 303.
7. T. R. Gengenbach and H. J. Griesser, J. Polym. Sci.: Part A: Polymer Chemistry, Vol. 37 (1999), p. 2191.

Photoelectron Diffraction on Transition Metal Oxide Ultrathin Films

K.-M. Schindler, M. Huth, A. Chassé, Ch. Langheinrich,
Ch. Hagendorf, Stefan Großer, Steffen Sachert, W. Widdra
FB Physik, Martin-Luther-Universität Halle-Wittenberg, D-06099 Halle, Germany

D. Sayago, E. Kröger
Fritz-Haber-Institut der MPG, Faradayweg 4-6, D-14195 Berlin, Germany

The particular physical properties of transition metal oxides make them promising candidates in applications such as nonvolatile computer memory. Therefore, there is much interest in the growth mode, structure and properties of ultrathin films. This investigation aims at the determination of their structure with photoelectron diffraction (PED) in energy scanned mode. Furthermore, the feasability of PED to study their magnetic structure is investigated. Their elemental composition, reactions and electronic structure is probed with XPS and NEXAFS as necessary.

Ultrathin films of manganese oxides were studied on a Ag(001) substrate. The films were prepared by reactive metal evaporation in an oxygen atmosphere with the substrate heated to 400 K. Former studies have shown that these conditions lead to a mostly layer-by-layer mode with the smallest roughness of the film. The resulting manganese oxide strongly depends on the deposition parameters

Previous investigations have shown that the splitting of the Mn 3s lines is very sensitive to the occupation of the Mn 3d levels. Fig. 1 shows spectra of two preparations. Whereas the splitting of the annealed film is 5.6 eV, it is 6.2 eV for the RT deposited film. The splitting of 6.2 eV is in agreement with published data for MnO, whereas the reduced splitting indicates that annealing to 350 °C results in a different occupation of the Mn 3d levels, i.e. a change of the oxidation state of Mn. Most likely, Mn diffuses into the Ag bulk resulting in a decreased Mn/O ratio. Contrary to claims in the literature, the details of the preparation clearly show that the oxidation state of the film is not controlled by thermodynamics, but kinetics.

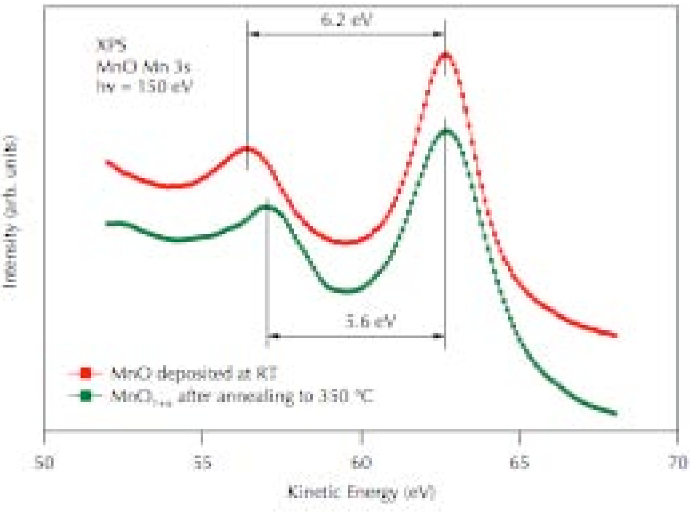

Fig. 1: XPS Mn 3s spectra of Ag(001)/MnO$_x$

Further difference of the two systems become evident in their NEXAFS O K-edge spectra (fig. 2). The spectra of the RT film (bottom) have far less peaks and only a minimal difference between normal and gracing incidence. Both findings indicate higher symmetry in the RT film than in the annealed one. Another significant difference is the shift of 2.6 eV between the low energy resonances of the two films. This difference will be the topic of theoretical multiple scattering calculations. The precise knowledge of the geometrical structure, however, is a major help in such calculations. In order to obtain such information, photoelectron diffraction data were recorded and compared to theoretical calculations.

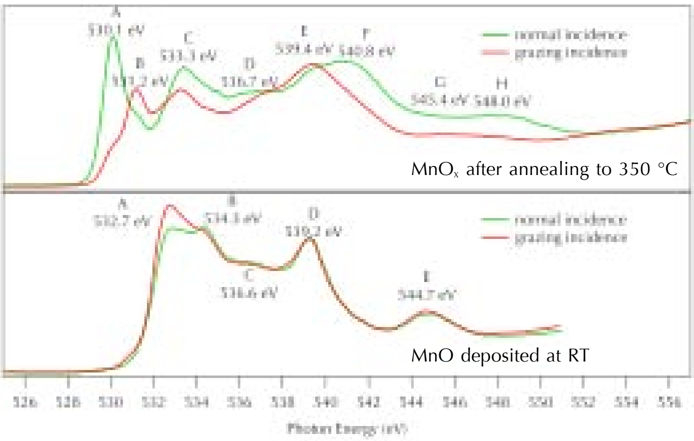

Fig. 2: NEXAFS O K-edge of Ag(100)/MnO_x

The high symmetry in the RT film is confirmed by strong and simply structured PED O 1s intensity modulations in normal emission (fig. 3). The first step towards a complete structure determination are theoretical cluster calculations with one emitter in the top plane of the film. Figure 3 shows the dependence of the intensity modulations on the unit cell lengths. Good agreement is achieved for unit cell lengths ranging from 4.25 Å to 4.45 Å, i.e. larger than the Ag unit cell (4.09 Å), but probably slightly smaller than the MnO unit cell (4.45 Å). However, the magnitude of the experimental modulations were adjusted by a factor of 3 and the experimental modulations vanish for energies above 250 eV contrary to the calculated ones. Both findings could be due to averaging over similar scattering processes, such as modulations from the emitters in deeper layers of the film with different geometric environments.

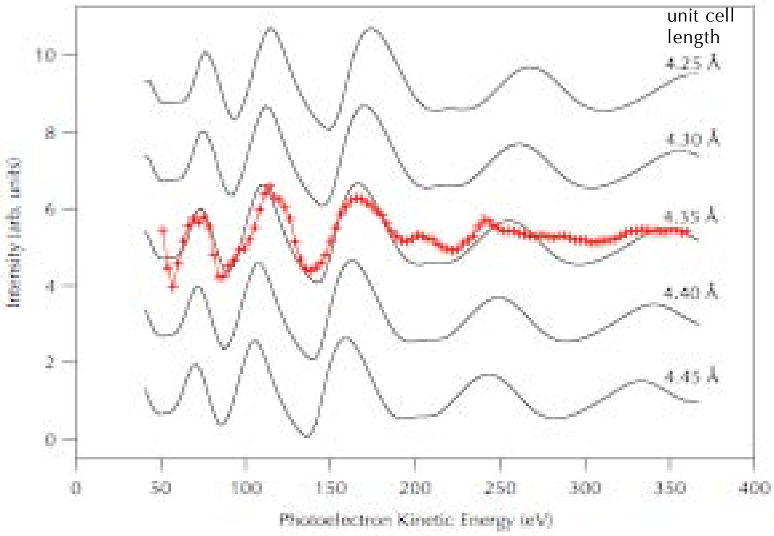

Fig. 3: Experimental and theoretical PED O 1s intensity modulations of Ag(001)/MnO in dependence on the unit cell length.

The success of this preliminary analysis of the PED data gives good reasons to record additional data in off-normal emission directions and perform calculations in order to address further structural questions. This is the route to an increase in precision and reliability of the structure determination.

Determination of the illumination function for coherent x-ray reflectivity experiments at the EDR-beamline at BESSY II

T. Panzner ,G. Gleber and U. Pietsch

Institut für Physik, Universität Potsdam, 14415 Potsdam, Germany
Now: FB7- Physik University of Siegen, 57068 Siegen, Germany

funding source : BMBF 05KS41PC/7

For coherent reflectivity experiments the knowledge about the incident beam intensity distribution at the sample site is one of the important parameters for the correct reconstruction of an unknown height function [1]. Up to now the incident beam function B(x) is approximated by a Gaussian und used in formular (1) for calculating the scattered amplitude:

$$A(q_x)\cdot e^{i\alpha(q_x)} \equiv \frac{1}{2\pi}\int_{-\infty}^{\infty} B(x)\cdot e^{iq_z h(x)}\cdot e^{-iq_x x}dx \qquad (1)$$

This approximation is not correct if a circular pinhole is used in front of the sample to select the coherent part of the incident beam. In this case one has to consider Fresnel diffraction also within the incident beam. In order to quantify the effect we have calculated the intensity distribution at sample position. We used the Lommel-solution-algorithm [2] for a numerical calculation of the Fresnel integrals. The results of the calculations have been compared with measurement taken at the sample position using the set-up shown in figure 1. Here the sample was replaced by the energy-dispersive detector which was scanned through all sample positions illuminated by the incident beam.

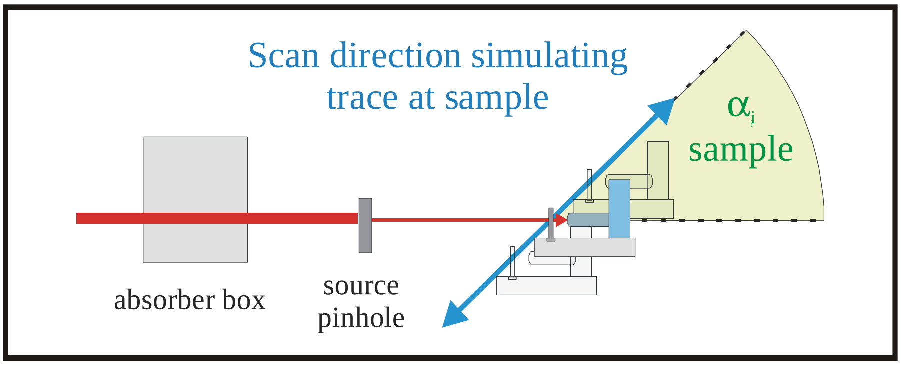

Figure 1: set up for measuring the intensity distribution of the incoming coherent radiation at sample position

The set-up shown in fig.1 is a small modification of our coherent reflectivity set-up reported in 2005 [3]. The results for the measurements and calculation for two different pinhole diameters are shown in figure 2 (part a)).

The good agreement between the measurements and the calculations of the intensity distributions are clearly visible. This confirms our approach for considering the Fresnel diffraction from incident pinhole and that the Lommel algorithm works well. The main advantage of this formalism consists in the fact that it provides amplitudes and phases of the incident beam at various sample positions (figure 2 part b). Therefore one is able to replace the Gaussian illumination function B(x) in equation (1) by the correct illumination function B(x, ϕ) which includes amplitudes and phases.

Using this improved formalism we hope for better results in the reconstruction of surface height profile of samples from coherent x-ray reflectivity measurements.

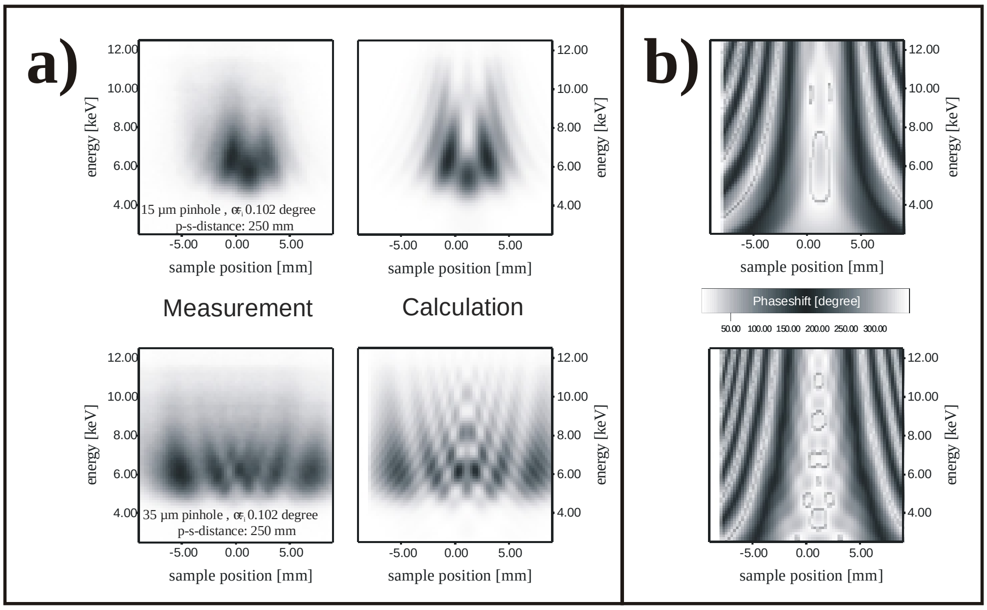

Figure 2: a) measured and calculated intensity distribution at the sample after diffraction at a 15µm and a 35µm pinhole, b) calculated phase distribution at the sample position.

References:

[1] I. Vartanyants et al, PRB Vol 55, 19, 13193
[2] K.D. Mielenz, J. Res. Natl. Inst. Stand. Technol. 103, 497 (1998)
[3] U. Pietsch et all, PHYSICA B 357 (1-2): 45-52 FEB 28 2005

EXAFS study of the effect of aging on the microstructure of $SmCo_3Cu_2$ magnets.

M. Katsikini[(a)], E. C. Paloura[(a)], F. Pinakidou[(a)], A. Gabay[(b)], G. Hadjipanayis[(b)].
[(a)]*School of Physics, Aristotle University of Thessaloniki, 54124 Thessaloniki, GREECE*
[(b)] *University of Delaware, Department of Physics & Astronomy, 223 Sharp Lab, Newark, DE19716, USA*

Samarium - cobalt permanent magnets are important industrial materials used for the construction of travelling wave tubes and DC brushless motors.[1] They are characterized by high coercivity that originates from the Sm-sublattice anisotropy while the Co sublattice yields high Curie temperature. Addition of Cu causes an increase of the coercive field which is further increased after prolonged annealing/aging.[2,3] The scope of this work, is to study the effect of aging on the microstructure of $SmCo_3Cu_2$. Although aging alters the magnetic properties (coercivity and Curie temperature) no differences in the x-ray diffraction spectra (XRD) occur. Therefore, we resorted to EXAFS spectroscopy which can identify aging-induced local distortions.

The $SmCo_3Cu_2$ sample was synthesized from pure components by arc melting on a water-cooled copper hearth under an argon atmosphere.[4] The sample was studied after solution treatment at 1323K and after subsequent aging at 623K for 200 h. The EXAFS measurements were recorded at the KMC-II beamline at the Co and Cu *K* edges in the fluorescence yield mode. The use of the XFlash energy-dispersive detector permits the electronic isolation of the Co K_α and Cu K_α and K_β fluorescence photons that allows elimination of the background due to the preceding absorption edges. The detector was positioned in the horizontal plane at right angle to the beam. The angle of incidence was 80° to the sample surface in order to minimize the self-absorption. The EXAFS spectra were normalized with the I_0 current, i.e. the current recorded using an ionization chamber positioned in front of the sample.

The Fourier Transforms (FT) of the Co and Cu *K* edge χ(k) spectra, that result after subtraction of the atomic background and transformation from the energy space to the k-space, are shown in Fig. 1. In order to obtain information on the bonding environment around the Co and Cu atoms, the spectra were fitted using the FEFF8 package.[5] The proper model for the fitting was constructed according to the XRD characterization which has shown that the sample before and after aging has the $CaCu_5$ (1:5) structure. The 1:5 structure is shown in Fig.2. Both Co and Cu can occupy the M_1 (light pink) or M_2 (dark pink) sites. The atoms that occupy the M_1 site belong to the plane that contains the Sm (red) atoms while the atoms of M_2 are "out-of-Sm-plane". The coordination numbers, the Debye-Waller factors and the nearest neighbour (nn) distances were iterated. The fitting results for both edges (before and after aging) are listed in Table I.

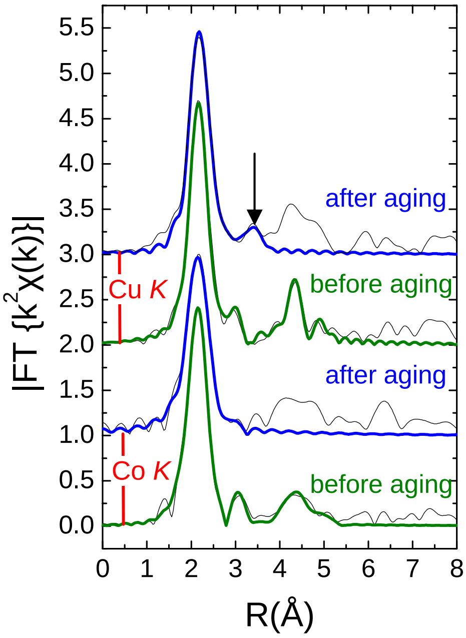

Figure 1: *FTs of the Co and Cu K edge $k^2\chi(k)$ spectra, before and after the aging process. The fitting and the experimental curves are shown in color and black lines, respectively.*

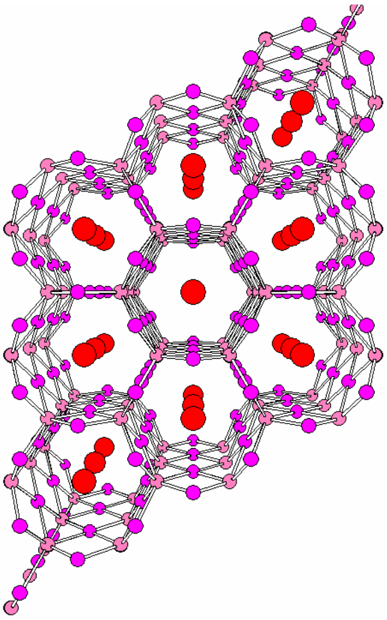

Figure 2*: The $CaCu_5$ (1:5) structure of the SmCoCu magnets. The red sites are occupied by Sm atoms while the pink sites are occupied by Co and Cu atoms.*

Table I: *Fitting results of the spectra recorded at the Co and Cu K edges for the samples before and after aging. R is the nn distance, N is the coordination number and A is the Debye – Waller factor .M-Sm$_1$ and M- Sm$_2$ correspond to the distance of M=Co,Cu (that belong to sites M$_1$ and M$_2$ respectively) to the Sm atoms.*

	Before aging			**After aging**		
Co K edge						
	R (Å)	**A×10^{-3} Å^2**	**N**	**R (Å)**	**A×10^{-3} Å^2**	**N**
Co-Co	2.43	6.9	4.2	2.43	6.9	3.9
Co-Cu	2.48	7.1	2.8	2.48	7.1	2.2
Co-Sm1	2.91	14.4	1.5	2.94	14.4	1.4
Co-Sm2	3.16	7.2	2.0	3.16	7.2	1.0
Cu K edge						
	R (Å)	**A×10^{-3} Å^2**	**N**	**R (Å)**	**A×10^{-3} Å^2**	**N**
Cu-Co	2.48	7.1	4.2	2.48	7.4	2.1
Cu-Cu	2.49	4.9	2.8	2.50	4.6	4.2
Cu-Sm1	2.90	6.4	1.5	2.93	6.6	2.0
Cu-Sm2	3.20	8.7	2.0	3.19	8.7	1.6
Cu-Cu				***3.62***	***3.0***	***1.5***

The Co-Co distance is found smaller that the Co-Cu distance which is smaller than the Cu-Cu distance. The coordination numbers in the as-grown sample correspond to a random distribution of the Co and Cu atoms in the M$_1$ and M$_2$ sites, i.e. the M$_1$ and M$_2$ sites are occupied by 60% Co and 40% Cu atoms, respectively.

Aging does not cause significant alteration in the bonding environment of Co, except from a decrease of the number of Co atoms that occupy the M$_2$ site (decrease of the Co-Sm$_2$ coordination number). In the case of the Cu *K* edge spectra, Cu seems to be preferably coordinated with Cu atoms after aging. Additionally, the number of the Cu atoms that occupy the M$_1$ sites increases at the expense of Cu atoms that occupy the M$_2$ sites. The results suggest that partial ordering takes place after aging, with the Cu atoms preferentially occupying the M$_2$ sites. Analysis using a more sophisticated model that will yield the exact percentage of Cu and Co atoms that occupy the M$_1$ and M$_2$ sites is in progress.

In the FT of the Cu *K* edge spectrum, recorded from the sample subjected to aging, an additional peak at 3.62Å is detected (indicated by an arrow in Fig.1). This distance is not predicted by the model of the 1:5 structure and does not correspond to multiple scattering paths. Using the Fourier Filtering technique, the contribution of that peak was fitted separately. Fitting is almost equally good by using either Cu or Co paths but not Sm. The coordination number, nearest neighbor distance and Debye-Waller factor for this peak are used as fixed values for the fitting of the non-filtered spectra. The Cu-Cu distance of 3.62Å is characteristic of metalic Cu and thus it could be an indication of formation of a “metallic” Cu phase, in the form of very small precipitates, which can not be detected by XRD. The presence of Co atoms in the Cu matrix is not excluded.

In conclusion, Co and Cu *K* edge EXAFS characterization of $SmCo_3Cu_2$ shows that there is no preferential occupation of the *in-the-Sm-plane* and *out-of-Sm-plane* sites by the Co and Cu atoms. Aging at 623K for 200h results to alterations mainly in the bonding environment of Cu. More specifically, Cu preferentially occupies sites in the out-of-Sm plane. At the FT of the Cu *K* edge spectra of the sample after aging, an additional Cu-M (M=Co, Cu) peak at the distance of 3.62Å is detected. That distance is not predicted by the model and it could be attributed to the formation of Cu rich precipitates.

---

[1] *M. F. de Campos F. J. G. Landgraf, R. Machado, D. Rodrigues, S. A., Romero, A. C. Neiva, F. P. Missel, Journal of Alloys and Compounds, **267**, 257 (1998).*

[2] *J. C. Tellez- Blanco, R. Sato Turtelli, R. Grössinger, D. Givord, D. Eckert, A. Handstein, K. –H. Müller, Journal of Magnetism and Magnetic Materials, **238**, 6, (2002).*

[3] *E. Estévez-Rams, J. Fidler, A. Pentón, J. C. Téllez-Blanco, R. S. Turtelli, R. Grössinger, Journal of Alloys and Compounds, **283**, 327 (1999).*

[4] *A. M. Gabay, P. Larson, I. I. Mazin, G. C. Hadjipanayis, J. Phys. D: Appl. Phys. **38,** 337(2005).*

[5] *A. L. Ankudinov, B. Ravel, J. J. Rehr, S. D. Conradson, Phys. Rev. **B58**, 7565 (1998).*

H induced restauration of the Fe moment in Fe/V superlattices

A. Remhof, G. Nowak, A. Nefedov, and H. Zabel

Experimentalphysik IV, Ruhr-Universität Bochum, Universitätstrasse 150, 44780 Bochum Germany

M. Björk, M. Pärnaste and B. Hjörvarsson

Department of Physics, Uppsala University, SE-751 21 Uppsala, Sweden

Due to their unique magnetic and superconducting properties Fe/V multilayers are model systems to investigate interface magnetism [1], interlayer exchange coupling [2] and superconducting spin valves [3]. V metal is paramagnetic and becomes superconducting at low temperatures. However, V it is at the edge of ferromagnetism. The instability of V towards forming magnetic moments leads to complex magnetic interfaces in Fe/V multilayers. In contact with ferromagnetic Fe, V gains a magnetic moment, aligned antiparallel to the Fe moments. At the same time a reduction of the Fe magnetic moment near the Fe/V interface has been observed [4]. Both effects lead to a strong reduction of the total magnetic moment with decreasing thickness of the Fe layers. Samples with thin V show the largest induced V moment of up to 1.1μ_B/atom, while samples with thin Fe layers display the strongest reduction of the Fe moment down to 1.34μ_B/atom. Interface alloying plays an essential role in the formation of the magnetic structure of Fe/V interfaces. An increasing number of Fe (V) nearest neighbors to the V (Fe) atoms clearly enhances the effect [1].

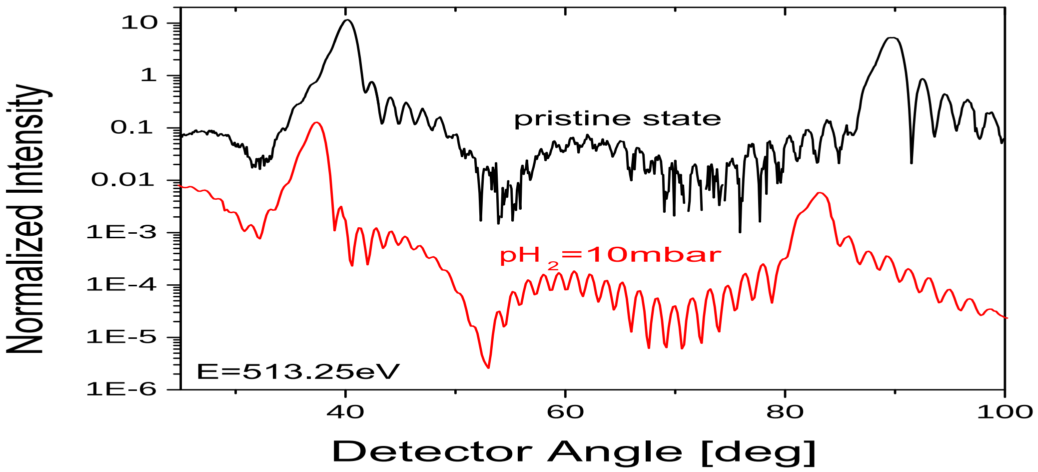

Figure 1: Reflectivity curves of a [Fe(2)/V(16)]×30 superlattice prior (black) and after hydrogen exposure

Exposed to H_2, Pd capped Fe/V superlattices are known to dissolve large amounts of hydrogen. In the loaded state hydrogen atoms fill the interstitial octahedral z sites inside the V bcc unit cell and lattice expansion takes place only in the out-of-plane direction. As the hydrogen solubility in Fe is extremlx low, the amount of hydrogen dissolved into the Fe matrix is negligible.

The presence of hydrogen within the superlattice has drastic effects on the magnetic properties [2, 5]. In particular, upon hydrogen loading the saturation magnetization was found to increase with increasing hydrogen concentration [6]. This could be either due to an increase of the Fe moment or to a decrease of the antiparallel V polarization. In order to check these two possibilities we employed element specific X-ray magnetic resonant scattering (XRMS) to investigate the response of the Fe and the V moments individually. To maximize the expected effect an epitaxial [Fe(2)/V(16)] superlattice with 30 repetition was sputter deposited onto a Mg0 [110] substrate, ensuring a high number of V neighbors of each Fe atom.
The XRMS measurements were carried out using the ALICE diffractometer [7] at the undulator beamline UE56/1-PGM. The sample is fixed to the cold finger of a closed cycle cryostat, placed between two magnetic poles. This set-up covers temperatures between 30 K and 350 K and magnetic fields up to 2.5 kOe. The magnetic field is applied parallel to the scattering plane. Thus using circularly polarized light longitudinal Kerr effect (L-MOKE) geometry can be realized, in which the magnetic moments are both parallel to the scattering plane and to the sample surface. The reflected beam yields magnetic information as it uses the resonant absorption of polarized synchrotron radiation in the vicinity of the L edges of the transition metals. Hydrogen loading was carried out by exposing the sample to a hydrogen pressure of 10 mbar at room temperature for several minutes. As the diffusivity of H in V is very large, we expect the sample to be in a homogeneously loaded state [8]. Subsequently the chamber was evacuated and the sample was cooled down to 30K. Hydrogen gets absorbed rapidly by the sample under these conditions, while hydrogen desorption is rather slow and stops completely at temperatures below 250K.

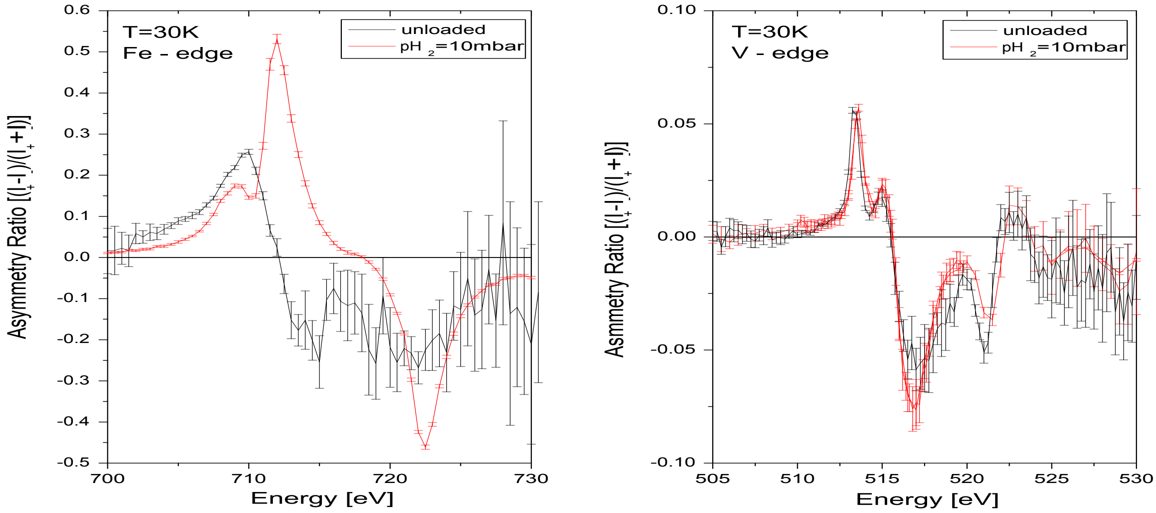

Figure 2: Magnetig asymmetry ratios measured on a [Fe(2)/V(16)]×30 superlattice in the vicinity of the Fe L-edges in reflection at the 2^{nd} superlattice reflection prior (black) and after (red) hydrogen exposure. The spectra on the right panel were recorded on a [Fe(6ML)/V(16ML)]×30 superlattice close to the V L-edges.

The hydrogen uptake can be monitored by the shift of the superlattice peak, as seen in figure 1, indicating the hydrogen induced lattice expansion. At low temperatures the superlattice reflections do not shift in time, proving that there is no hydrogen loss. The comparison between the two reflectivity curves also demonstrate that the hydrogen loading does not affect the structural quality of the sample. The magnetic properties, however, change drastically. Figure 2

displays asymmetry ratios recorded at the 2^{nd} superlattice reflection in the vincity of the Fe and V L-edges prior and after hydrogen exposure.
The data clearly show a strong increase of the Fe moment upon hydrogen loading. We also investigated the response of the magnetic asymmetry of the V in the same sample. No effect could be seen. However, due to the small magnetic moment of the only two ML thick Fe layers, the induced moment in V and consequently the asymmetry ratio is rather small. Therefore we investigated a second sample, containing 6ML of iron. Figure 2 (right) depicts the asymmetry ratio close to the V L-edges at the 2^{nd} superlattice reflection. Again, the presence of hydrogen obviously does not affect the magnetic state of the V. Also this sample shows an increase of the Fe moment upon H loading. Our measurements confirm nicely the theoretical model by Uzdin et al. [9], predicting an increasing Fe moment and a stable V moment in H loaded Fe/V superlattices. In this model the increase of the Fe-V bond at the interface is responsible for the restauration of the Fe moment. The increasing bond-length leads to a narrowing of the 3d band and to an increase of the Fe magnetic moment. The more V neighbors a Fe atom has, the more pronounced is the effect. Therefore, Fe atoms in the close contact with the V atoms, e.g. those with the reduced moment are most sensiively affected by the presence of dissolved hydrogen.

The authors are grateful for technical support by T. Kachel. We would like to thank the DFG for financial support under contract RE 2203-1/1. The soft x-ray work was supported by the BMBF under contracts O3ZA6BC2 and 05 ES3xBA/5.

References

[1] A. Scherz, H. Wende, P. Poulopoulos, J. Lindner, K. Baberschke, P. Blomquist, R. Wäppling, F. Wilhelm, and N. B. Brookes, *Phys. Rev. B* **64,** 180407 (2001).

[2] B. Hjörvarsson, J. A. Dura, P. Isberg, T. U. Watanabe, T. J. Udovic, G. Andersson, and C. F. Majkrzak, *Phys. Rev. Lett.* **79**, 901 (1997).

[3] K. Westerholt, D. Sprungmann, H. Zabel, R. Brucas, B. Hjrvarsson, D. A. Tikhonov, and I. A. Garifullin *Phys. Rev. Lett.* **95**, 097003 (2005).

[4] G. R. Harp, S. S. Parkin, W. L. O Brian, B. P. Tonner, *Phys. Rev. B* **51,** 3293 (1995).

[5] V. Leiner, K. Westerholt, A. M. Blixt, H. Zabel, and B. Hjörvarsson, *Phys. Rev. Lett.* **91**, 037202 (2003)

[6] D. Labergerie, K. Westerholt, H. Zabel and B. Hjrvarsson, *J. Magn. Magnet. Mat.* **225,** 373 (2001).

[7] J. Grabis, A. Nefedov, H. Zabel, *Rev. Sci. Instr.* **75,** 4048 (2003).

[8] A. Remhof, S. J. van der Molen, A. Antosik, A. Dobrowolska, N. J. Koeman, and R. Griessen, *Phys. Rev. B* **66**, (R)020101 (2002).

[9] V. Uzdin, K. Westerholt, H. Zabel, and B. Hjörvarsson, *Phys. Rev. B* **68,** 214407 (2003).

X-ray Standing Wave/EXAFS Measurements with Nano-Resolution

A. Gupta[1], N. Darowski[2], I. Zizak[2], C. Meneghini[3], A. Erko[4], G. Schumaher[2]

[1]UGC-DAE Consortium for Scientific Research, University Campus, Khandwa Road, Indore 4520017, India
[2]Hahn-Meitner-Institute Berlin, Glinicker Str. 100, D-14109 Berlin, Germany
[3]Via della Vasca Navale 84, I-00146 Roma, Italy
[4]BESSY GmbH, Albert-Einstein Str. 15, D-12349 Berlin, Germany

X-rays are highly penetrating radiations, and therefore, any information obtained through x-ray based measurements is averaged over a depth of several microns. However, x-ray based techniques can be made depth selective by generating standing waves inside the nanostructure of interest by making use of the phenomenon of total reflection [1, 2]. X-ray intensity is localized in the anti-nodal regions, the position of which inside the nanostructure can be varied by varying the angle of incidence. Use of such x-ray standing waves in elemental depth profiling, XANES or fluorescence measurements with nanometer depth resolution has been demonstrated for organic [3] and inorganic material systems [4].

For the first time angular dependences of the fluorescence yield from a single organic monolayer on a solid substrate modulated by a standing wave in a total external reflection conditions has been measured experimentally. The scanning by standing wave field of a single organic molecule has been done, the depth positions of particular ions in the molecule structure have been determined [4]. In this experiment a depth resolution on the order of 1-5 nm has been achieved.

Depth selectivity can further be enhanced by making use of wave-guide structures [5, 6]. For the first time at BESSY, depth selective EXAFS studies have been performed. The absorption spectra of Fe and W nano-layers were recorded with in-depth resolution on the order of 1 nm. This method is combining total external reflection standing waveguide mode and EXAFS measurements.

We present the results of depth resolved tungsten XAFS measurements in a Si/W/Si trilayer embedded in a Au waveguide structure.

The graded-crystal monochromator beamline KMC-2 was used to set-up of the in-depth nanoprobe EXAFS system [7]. The x-ray beam in the energy range of 10 keV - 14 keV was monochromatized by the double-graded-crystal monochromator and collimated in both directions using two slit systems and collimating mirror shown in figure 1. The beam size on the sample position was 100 µm horizontal and 700 µm vertical.

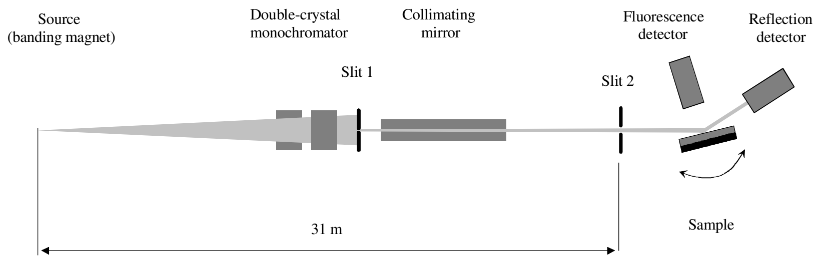

Figure 1. Experimental setup, top view.

The beam divergence was on the order of 20 arc sec obtained by rocking curve measurements of a Si (111) reference crystal. The total flux in the spot was in the range of 10^9 phot/sec/100 mA. Beamline monochromator, stabilized by MOSTAB feedback system for EXAFS measurements, provides RMS intensity variations in the order of 1.7 10^{-3} in entire energy range. PIN photodiode detectors were used for measurements of reflected (diffracted) beam as well as x-ray fluorescence signal from the investigated sample. Energy-dispersive detector RONTEC X-

FLASH was also used to record the fluorescence spectrum of the sample. Control software was used to realize simultaneous energy scan of the monochromator and angular scan of a sample.

The objective has been to study the swift heavy ion induced intermixing in this system. A detailed information about various phases formed as a function of depth can be very valuable in understanding the mechanism of mixing induced as a result of the electronic energy loss incurred by the bombarding ions.

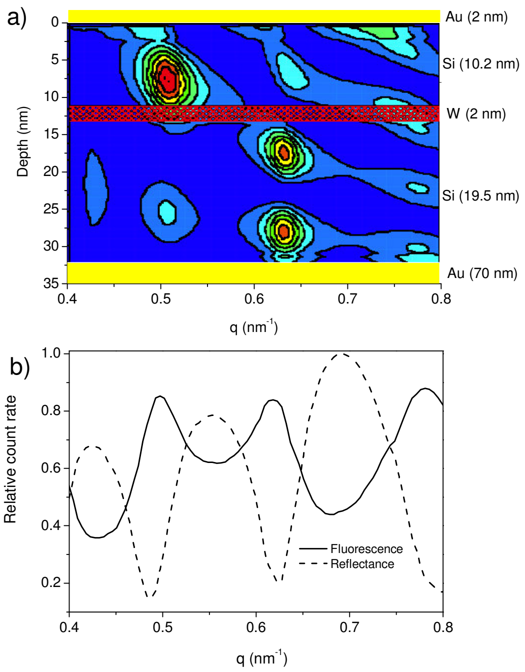

Figure 2. The multilayer sample structure. The contour plot represents the intensity of x-rays as a function of depth and q. The hatched strip marks the position of W (a), normalized intensity curves of reflected radiation and W Lα fluorescence radiation at 10.3 keV incidence energy (b).

The structure of the multilayer is shown in figure 2a and consists of several layers: Si substrate 400μm / Cr 20nm / Au 70nm / Si 19.5nm /W 2nm / Si 10.2nm/Au 2nm. The two layers of Au form the walls of the wave-guide. A Cr buffer layer has been used for improving the adhesion of the film. For the sake of clarity, depth dependence of the x-ray intensity inside the multilayer as a function of q is also shown as a contour plot. The scattering vector q defined as $q = 4\pi \sin\theta/\lambda$, θ being the angle of incidence and λ being the wavelength of x-rays. The sample multilayer has been irradiated with 600MeV Au ions to various fluences in order to induce intermixing of W layer with Si at room temperature.

In figure 2b the corresponding normalized intensity curves of reflected radiation and W Lα fluorescence radiation are shown vs the q values at 10.3 keV incidence energy. XAFS measurements across the L-edge of W were done for various values of q. With varying q, the depth distribution of x-ray intensity inside the multilayer varies, thus providing weighted information from different depths.

A typical W L-edge XAFS data and the corresponding radial distribution function is shown in figure 3.

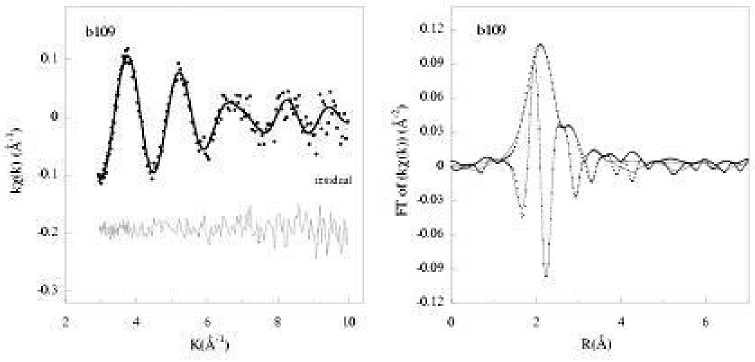

Figure 3. Calculated XAFS function and the corresponding fourier transform of the sample irradiated with 600MeV Au ions to a fluence of 1×10^{13} ions/cm^2

The XAFS data of the pristine as well as irradiated samples was fitted by taking a three-shell structure into account: i) a W-Si shell which is the main contribution to the whole XAFS signal, ii) a W-W shell around 2.7 Å, similar to the W-W nearest neighbors distance in metallic W, and iii) a W-W shell around 3.2 Å which is similar to the W-W second neighbors shell in metallic W. The XAFS data of pristine sample suggests about 60 % of W in metallic environment and 40% in WSi_2. Irradiation provokes the partial dissolution of W in Si giving rise to higher fraction of W-Si correlation. Figure 4 shows the variation of a) fraction of W-Si bonds, $X_{W\text{-}Si}$ and b) W-Si bond length, $R_{W\text{-}Si}$, as a function of the scattering vector q. From figure 4, despite the quite large uncertainty, it is clear that the fraction of W-Si bonds increases with irradiation and seem larger in the deeper region below the W layer. The W-Si distance shows a clear trend as a function of depth and irradiation. At lower irradiation fluences ($2x10^{12}$ ions/cm^2 and $5x10^{12}$ ions/cm^2) the W-Si distance is systematically shorter but it grows as the depth increases. The low $R_{W\text{-}Si}$ value is consistent with W-rich W-Si structures such as W_5Si_3 and W_3Si. In the deeper regions a large W-Si distance is suggestive of a Si rich WSi_2 phase. At higher irradiation fluences ($1x10^{13}$ ions/cm^2 and $2x10^{13}$ ions/cm^2) the structure is dominated by W-Si correlations while the metallic W contributions become weak. The Si content increases as a function of depth. The W-Si distance changes weakly as a function of depth.

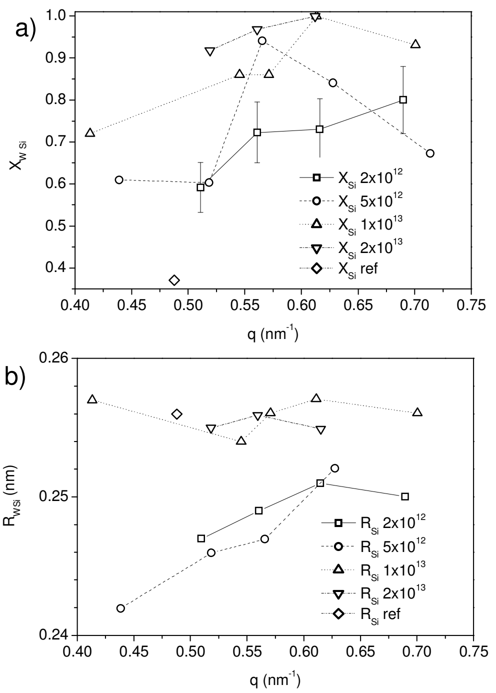

Figure 4. Results of the analysis of XAFS data taken at different values of q. $X_{W\text{-}Si}$ is the fraction of the bonds of type W-Si, while $R_{W\text{-}Si}$ is the corresponding bond length.

The combination of EXAFS and standing wave methods in investigation of the layers placed into an x-ray waveguide provides sub-nanometer in-depth resolution with an extremely high sensitivity to the layer structure. The method was successfully used to structure measurements of the nanometer-thick layers exposed to heavy-ion beam. In the future the EXAFS/XRSW combination can be applied for investigations of different kinds of diffusion processes, as well as interfaces of different materials in layered structures.

References

1. B. N. Dev, A. K. Das, S. Dev, D. W. Schubert, M. Stamm, G. Materlik, Phys.Rev. B 61 (2000) 8462.
2. S. K. Ghose, B. N. Dev, A. Gupta, Phys. Rev. B 64 (2001) 233.
3. A. Gupta, C. Meneghini, A. Saraiya, G. Principi, D. K. Avasthi, Nucl. Instr. Meth. B 212 (2003)458
4. N. N. Novikova, E. A. Yurieva, S. I. Zheludeva, M. V.Kovalchuk, N. D. Stepina, A. L. Tolstikhina, R. V. Gaynutdinov, D. V. Urusova, T.A. Matkovskaya, A. M. Rubtsov, O. D. Lopina, A. Erko and O.V. Konovalov, J. Synchrotron Rad. (2005). 12, 511–516
5. S. I. Zheludeva, M. V.Kovalchuk, N. N. Novikova, et al. Crystallography Reports, 40, (1995), 132-144
6. A. Gupta, C. Meneghini, P. Rajput, G. Principi, to be published
7. A. Erko, I. Packe, W. Gudat, N. Abrosimov, A. Firsov Nuclear Instruments and Methods in Physics Research, A467–468 (2001) 358–361

Effect of Zn and Ni impurities on the renormalization effects in Bi-2212

D. Inosov,[1] V. Zabolotnyy,[1] S. Borisenko,[1] A. Kordyuk,[1,2] J. Fink,[1] J. Geck,[1] A. Koitzsch,[1]
M. Knupfer,[1] B. Büchner,[1] H. Berger,[3] A. Erb,[4] C. T. Lin,[5] B. Keimer,[5] and R. Follath[6]

[1]*Institute for Solid State Research, IFW-Dresden,*
P.O.Box 270116, D-01171 Dresden, Germany
[2]*Institute of Metal Physics of National Academy of Sciences of Ukraine, 03142 Kyiv, Ukraine*
[3]*Institute of Physics of Complex Matter, EPFL, CH-1015 Lausanne, Switzerland*
[4]*Walther-Meißner-Institut, Bayerische Akademie der Wissenschaften,*
Walther-Meißner Strasse 8, 85748 Garching, Germany
[5]*Max-Planck Institut für Festkörperforschung, D-70569 Stuttgart, Germany*
[6]*BESSY GmbH, Albert-Einstein-Strasse 15, 12489 Berlin, Germany*

The anomalies in the single-particle spectral function of a superconductor are commonly believed to be crucial for understanding HTSC. Along the Brillouin zone (BZ) diagonal the renormalization effects are represented by the unusual dispersion, the so called "kink". In the vicinity of $(\pi, 0)$ point of the BZ the renormalization is noticeably stronger and makes itself evident even in the shape of a single spectral line measured for a fixed momentum. It is widely accepted that these anomalies are naturally explained by coupling to a collective mode, while the origin of this mode remains a current controversy between phonons and spin fluctuations.

Some of our recent experiments, which were carried out at the U125/1-PGM beam line with an angle-multiplexing photoemission spectrometer (SCIENTA SES100) at BESSY, showed that substitution of Cu in $Bi_2Sr_2CaCu_2O_{8-\delta}$ with Zn and Ni essentially influences the renormalization anomalies in ARPES spectra both along the nodal and antinodal regions of the BZ. Moreover, the changes in ARPES spectra are consistent with the behaviour of the spin resonance mode as seen by inelastic neutron scattering in YBCO. This provides evidence that it is the magnetic excitations that are responsible for the unusual renormalization features in the quasiparticle excitation spectrum of cuprates.

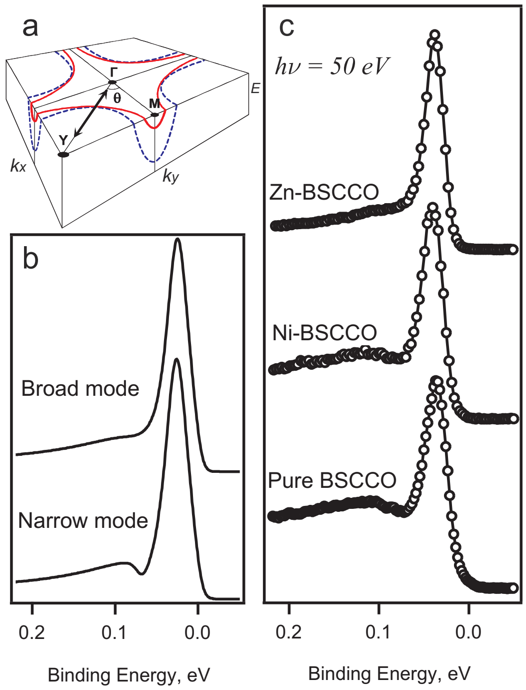

Fig. 1. (a) Cut of a $k\omega$-space at the Fermi level. The top of the cube contains two sheets of the Fermi surface, red solid line corresponds to the dispersion of the antibonding band, blue dashed one – to the bonding band. (b) Model line shape of the $(\pi, 0)$ EDC, when coupled to a narrow (2 meV) and broad (20 meV) collective mode. (c) Experimental EDC's taken at $(\pi, 0)$ point.

In the antinodal region, the "dip" in a single band EDC can be a good indicative of the mode width and energy. Comparing the EDC's, measured at (π, 0) point (Fig. 1), we see differences in the line shapes caused by the impurity substitution: while for the pure sample the spectrum has a pronounced dip, for the Zn substituted sample the dip vanishes, and for the Ni substituted sample its "strength" is intermediate.

In the nodal region, the raw distributions of photoemission intensity as a function of energy and momentum are presented in the Fig. 2(a-c) together with the experimental dispersions. To compare the renormalization effects, one can use the area under the "kink" as shown in Fig. 2(d-f). It is easy to see that renormalization in case of the Zn substituted sample is decreased in comparison to the pure sample. Subtracting a bare particle band dispersion from the experimental dispersion the real part of the self-energy can be obtained, see Fig. 2(g-i).

On Fig. 3 we also show experimental spectra at 20 meV below the FL. These data have been used to determine the exact doping level of each of the samples. Panels (a – c) correspond to the samples under consideration, and for comparison, in the panel (d) we give the identical map for an overdoped sample. Grey scale images below the experimental data represent tight-binding fits to the antibonding sheets of the FS.

Summing up, we have shown that the substitution of Cu atoms in Cu-O plane changes renormalization features in ARPES spectra both in nodal and antinodal parts of the Brillouin zone, which can be well explained by coupling to a magnetic resonance mode. The effect of Zn and Ni substitution on the antinodal ARPES spectra agrees with the influence of these impurities on magnetic resonance mode seen by INS experiments. This provides another strong evidence that the mode, coupling to which causes observed renormalization effects, has rather magnetic than phononic origin.

For details see Zabolotnyy *et al.*, Phys. Rev. Lett. **96**, 037003 (2006).

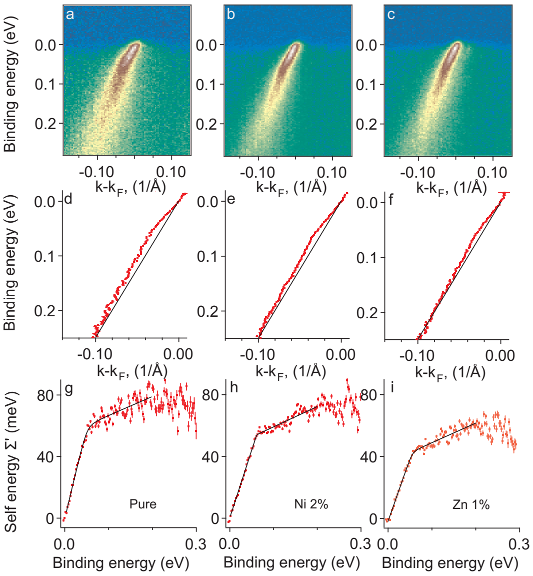

Fig. 2. (a)-(c) Photoemission intensity distributions along the BZ diagonal. (a) Pure BSCCO, (b) Ni substituted and (c) Zn substituted BSCCO. Middle row shows corresponding experimental dispersion. In the last row the real part of the self-energy is displayed.

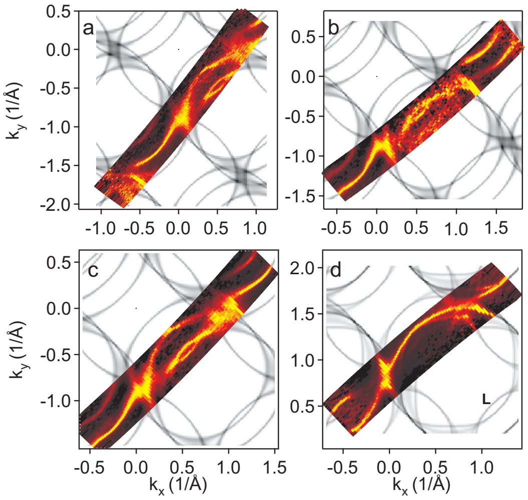

Fig. 3. Cuts of $k\omega$-space made 20 meV below the Fermi level and tight binding fits. (a) Ni substituted sample. (b) Zn substituted sample. (c) Pure BSCCO close to optimal doping. (d) Overdoped BSCCO, $\delta \approx 0.20$.

Investigations of Optically Inhomogeneous Samples by Means of Infrared Spectroscopic Ellipsometry

K. Roodenko[1], M. Gensch[1], H. M. Heise[2], U. Schade[3], N. Esser[1], K. Hinrichs[1]

[1]*ISAS - Institute for Analytical Sciences, Dept. Berlin, Albert-Einstein-Str. 9, 12489 Berlin, Germany.*

[2]*ISAS - Institute for Analytical Sciences, Bunsen-Kirchhoff-Str. 11, D-44139 Dortmund, Germany.*

[3]*Berliner Elektronenspeicherring-Gesellschaft für Synchrotronstrahlung m.b.H. (BESSY), Albert-Einstein Str.15, 12489 Berlin, Germany*

Characterization of organic layers is an indispensable step in development and design of new devices. Fast and reliable methods that could provide information on composition and structure of organic layers are thus of great technological importance. Infrared spectroscopic ellipsometry (IR-SE) has recently been proven to be a suitable technique in this field [1]. Its application in studies of inorganic materials, organic and biological films could be relevant in characterization and development of components of functional hybrid materials, biosensors, microelectronic devices and solar cells. A schematic drawing of the IR-SE principle is sketched in Fig. 1a, showing also a definition of the ellipsometric parameters $\tan\psi$ and Δ through the relations to the complex reflection coefficients r_p and r_s.

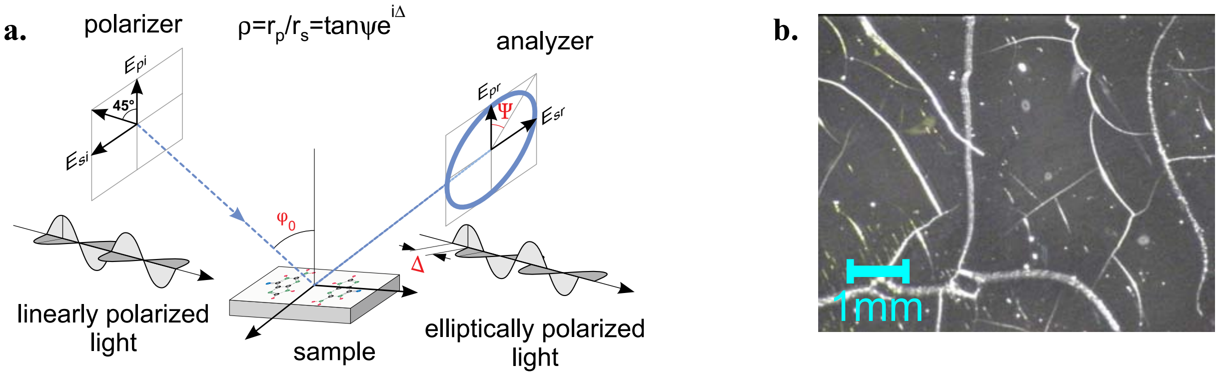

Fig. 1.(a) Schematic drawing of the IR-SE principles. (b) Light microscope photograph of a several micrometer thick bacteriorhodopsin film on gold.

Biological samples are of a particular technological interest, yet characterization of many biological films implies hardships associated with the inhomogeneity of such samples. These samples can exhibit variation of density and thickness on the microscopic scale, influencing the optical properties of a film and thus making interpretation of spectroscopic results very difficult. For example, a light microscope photograph of a several micrometer thick bacteriorhodopsin film on gold is shown on Fig. 1b, from which the discussed problem is obvious. Such films have been investigated within a previous report period [2].

However, some obstacles can be overcome by focusing on smaller areas on the sample, thus reducing inhomogeneity influences. For characterizations performed in the infrared spectral range, this solution is not obvious due to the lack of suitable radiation sources that could offer intense radiation fluxes per limited sample area in a wide infrared spectral range. Synchrotron sources, on the other hand, have a high brilliance, thus enabling a higher photon flux per unit area into a unit solid angle, than the standard laboratory globar sources.

Figs. 2a and 2b show results achieved with the synchrotron-based IR-SE setup on a thick, inhomogeneous, but isotropic polyethylene film. Two different graphs are presented in this figure: the degree of polarization, P_{ph} (Fig. 2a), and the refractive index n (Fig. 2b). For comparison, results obtained with a standard globar source are shown in black. Three regions are marked in the figure: regions A and C are non-transparent due to absorptions resulting from the CH_2 symmetric and antisymmetric stretching vibrations (region A) and from CH_2 bending vibrations (region C). Region B is in general infrared transparent. Weak absorptions in this region are due to combination modes [3].

The degree of polarization, P_{ph}, is in general a measure of the *depolarization* of radiation that reaches the detector, and in the ideal case, it should equal 1. Fig. 2a, however, shows that this is not the case for the investigated systems. The deviation from unity is especially striking in the transparent region B. It occurs for both synchrotron and the globar sources. Depolarization can happen due to scattering in the bulk of the sample, due to lateral inhomogeneities in the refractive index, or due to uneven sample thickness. However, for the globar radiation the deviation from unity is much larger. The lateral inhomogeneities of the sample play a significant role in this case: with globar, for which the irradiated area on the sample was around 50 mm^2, the deviation from unity is much stronger than for the synchrotron, for which the irradiated area is about 1mm^2. This occurs since the inhomogeneities are much more pronounced on larger scales, than on small local ones (see, for example, Fig. 1b)

The simulated refractive index is shown in Fig. 2b (dashed grey line) along with the measured pseudo refractive indices obtained with the globar (black trace) and the synchrotron sources (red trace), respectively. The pseudo refractive indices [1] that were obtained directly from the measured ellipsometric parameters are very sensitive to weak absorptions of combination modes in the transparent region B, due to multiple reflections (Fig. 2c) and inhomogeneities. When the multiple reflections and inhomogeneity of the sample are correctly taken into account, the simulated refractive index, which now gives the material constant, is flat within the presented scaling. The spectrum has been simulated using an incoherent optical model, in which the phase correlations of waves reflected at the backside are neglected [3]. The simulated refractive index better represents the true material properties, since it does not show the characteristic background in the transparent region which is present in the measured spectra.

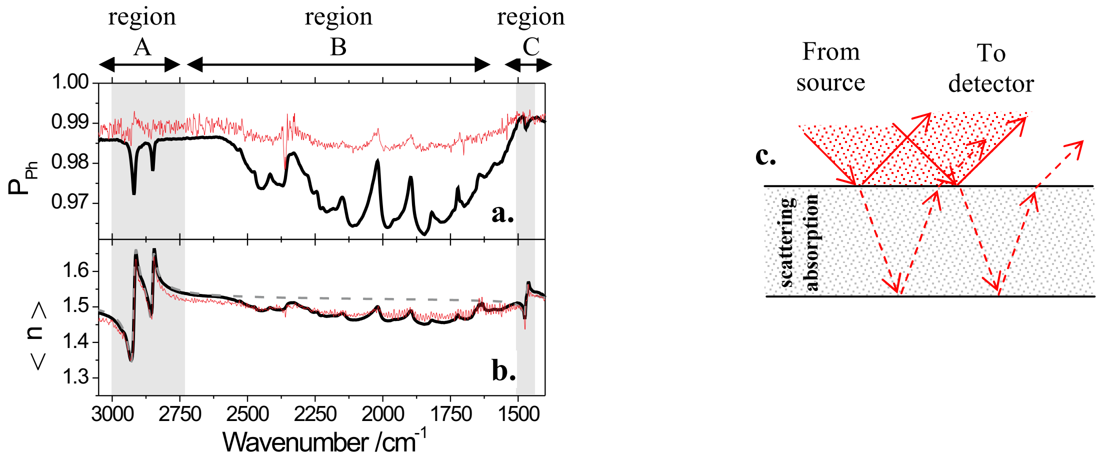

Fig. 2. Degree of phase polarization of a 433 µm thick free-standing polyethylene film (**a**); and refractive index (**b**) measured with the synchrotron (red) and the globar (black) sources, respectively. The simulated refractive index n is shown as dashed grey trace; illustration of the single-reflected and back-reflected radiation (dashed rays) (**c**).

In summary, the infrared beamline IRIS at the BESSY synchrotron facility allowed us to perform one step further towards the understanding of the complicated optical response from inhomogeneous materials. We have shown that the variation of thickness, refractive index and roughness on the micrometer scale can be included in the evaluations and can help in determination of the refractive index of the material [3]. Potentially, ellipsometric spectra of inhomogeneous biological samples can be interpreted quantitatively.

Acknowledgements:

K. Roodenko gratefully acknowledges support from the Minerva foundation. H.M.H. thanks D. A. Batista from LACTEC and P. R. Janissek from the Centro Universitario Positivo (UnicenP), both in Curitiba, Brazil, for the PE-sample preparations. We acknowledge the cooperation on biological samples with J. Heberle from Forschungszentrum Jülich. We thank Dr. A. Röseler for valuable communications and Ms. I. Fischer for technical support. The financial support by the Senatsverwaltung für Wissenschaft, Forschung und Kultur des Landes Berlin and of the Bundesministerium für Bildung und Forschung, as well as by the BMBF grant no. 05 KS4KTB3 and the European Union support through SSA (DASIM, ctr. No. 0005326) are gratefully acknowledged.

References

---

[1] K. Hinrichs, M. Gensch, N. Esser, Appl. Spectrosc. **59**. 272A (2005)

[2] M. Gensch et al., Bessy Annual Report 2003, 512 (2003)

[3] K. Roodenko et al., Infrared Phys. Technol., in press (2006).

Can magnetic flux lines be detected in optimally doped $YBa_2Cu_3O_{7-\delta}$ by magnetic oxygen K-edge spectroscopy?

J. Albrecht, M. Djupmyr and E. Goering
Max-Planck-Institut für Metallforschung, Heisenbergstr. 3, D-70569 Stuttgart, Germany

In the last 20 years cuprate-based high-temperature superconductors have attracted an enormous amount of interest. Nevertheless, all attempts failed so far to explain the origin of the superconductivity completely. It has been shown that not only the superconducting properties are very unusual, also the normal conducting state exhibits a variety of unique properties. In this context, the electronic structure of the high-temperature compound $YBa_2Cu_3O_{7-\delta}$ (YBCO) has been successfully investigated by tunneling spectroscopy inside and outside a flux line. Figure 1 shows the differential conductance of an YBCO crystal at low temperatures, extracted from Ref. [1]. A clear superconducting gap is observable in these conductance measurements, as shown in the lower part of Fig. 1. Positioning the tunneling tip at the center of a flux line, where superconductivity is not existent, it is found that the intensity in the gap region is significantly enhanced. In contrast to conventional BCS superconductors these structures are not flat, a finite density of states is found in this gap region. It is obvious that the understanding of the origin and the symmetry of these “in-gap” states is crucial for a complete description of the mechanisms of high-temperature superconductivity.

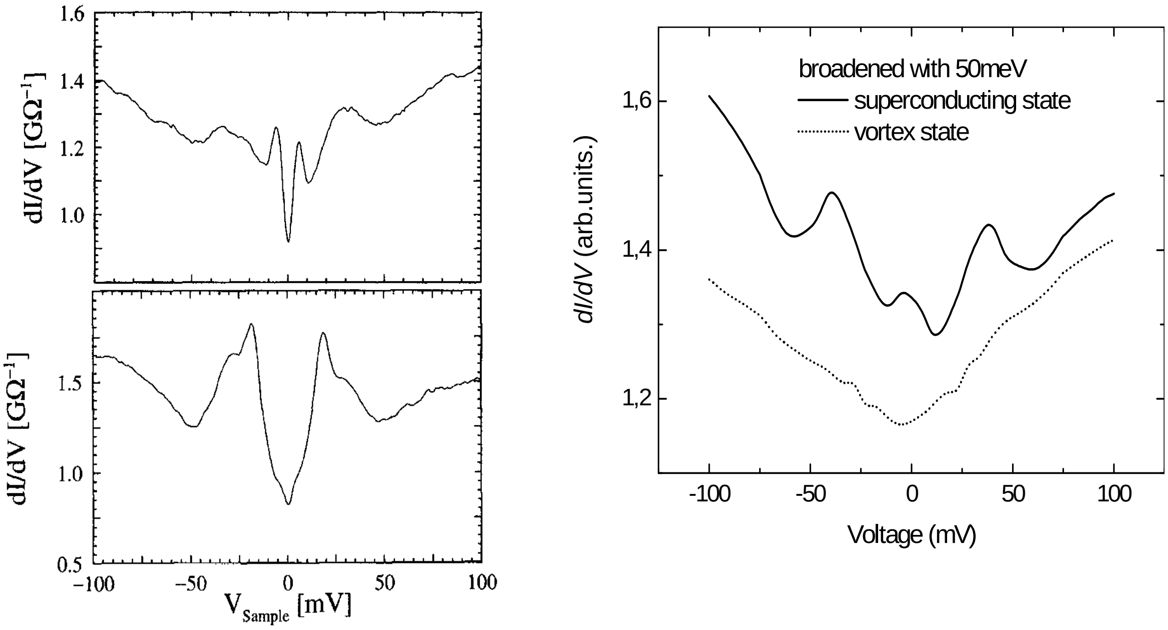

Figure 1: *Left: Differential conductance spectra dI/dV(V) of an YBCO single crystal performed at T = 4.2 K from Ref. [1]. The upper curve shows the spectrum at the center of a vortex core. The lower curve shows the quasiparticle excitation spectrum of the superconducting state. Right: Differential conductance spectra broadened by 50 meV.*

We use high energy resolution x-ray absorption spectroscopy to investigate epitaxially grown thin films of optimally doped YBCO. It is tried to resolve these “in-gap” states at the threshold of the O K edge as a function of external applied magnetic field. For this purpose XMCD-like (X-ray magnetic circular dichroism) spectra between the zero-field cooled nonmagnetic superconducting state and a flux-lattice state at B = 2 T are obtained. The experiment is performed over the temperature range between T = 25 K and T = 90 K to provide the required information about the normal conducting unoccupied density of states of the highly renormalized quasiparticles. Some of these structures should be observable with an energy resolving power better than 15000 at the O K edge [2]. The 50 meV broadened *dI/dV* curves (from the left part of Fig.1) are shown in the right part of Fig. 1. Strong and clear differences between core and superconducting spectra are observable. This is strongly encouraging, that the proposed features are observable at the O K edge. If so, this could at the same time offer a contrast mechanism for magnetic x-ray microscopy of flux lines in superconductors. Note, that an important property of the high-Tc flux lines is their very small diameter, which prevents a direct observation of the flux lines by conventional optical microscopy.

Fig. 2 shows the XAS (X-ray absorption spectrum, black) and the obtained XMCD-like effect (red) of an YBCO film at the oxygen K-edge at a temperature of T = 80 K. The XAS spectrum clearly shows two peaks, the Zhang-Rice singlet (left) and the lower Hubbard band (right). The high intensity of the Zhang-Rice peak indicates the high quality of the superconducting film [3]. The magnetic effect is measured as an average of about 30 spectra, each determined as difference between the x-ray absorption spectrum at zero field and at B = 2 T, respectively. The red curve is scaled by a factor 100 for better visibility.

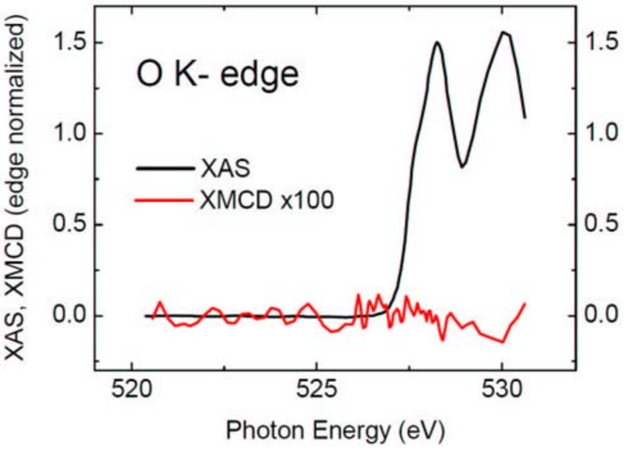

Figure 2: *XAS (black) and XMCD-like (red) spectra of the oxygen K-edge of YBCO at T = 80 K. The red curve is obtained by subtracting the XAS spectra at B = 0 and B = 2 T, respectively, averaging over about 30 experiments and multiplying it by a factor of 100.*

Figure 2 clearly shows that no significant magnetic effect can be seen in the experimental data. We can state that the modification of the absorption signal due to the presence of flux lines is smaller than 0.1 %. Analogue experiments have been performed at different temperatures but no significant signal referring to a magnetic field induced modification of the absorption edge could be obtained. It is worth to say that a time-dependent decay of the absorption spectra intensities has been noticed during the illumination of the superconducting samples. The used high photon intensities could have introduced a significant damage of the superconducting state.

In conclusion, we state that the experimental set-up that has been used in our experiment does not allow the detection of quasiparticle states inside of magnetic flux lines in high-temperature superconductors. Up to now it is not clear if this is in general impossible with magnetic fields of B = 2 T and a resolving power of 15000 or if the incident photon beam at UE49 might be harmful for the superconducting samples.

[1] I. Maggio-Aprile et al., Phys. Rev. Lett **75**, 2754 (1995).
[2] M. Coreno et al., Chem. Phys. Lett. **306**, 269 (1999); A. S. Schlachter et al., J. Phys. B **37**, L103 (2004); E. McGuire, Phys. Rev. **185**, 1 (1969).
[3] M. Merz et al., Phys. Rev. B **55**, 9160 (1997).

Magnetic anisotropy of triangular shaped, hexagonally arranged Co nanostructures

P. Imperia[1], W. Kandulski[2], A. Kosiorek[2], H. Głaczyńska[2], D. Schmitz[1], H. Maletta[1] and M. Giersig[2]
[1]Hahn Meitner Institut, Glienicker Strasse 100, 14109 Berlin, Germany
[2]CAESAR Research Center, Ludwig-Erhard-Allee 2, 53175 Bonn, Germany

The quest for new materials and technical solutions able to match the requirements of modern performances for data storage devices produced in the last few years a large number of studies about the magnetic properties of nanostructured materials. The control of the magnetic properties by means of the shape could be decisive in improving the performances of newly designed devices [1, 2]. The ways devised to induce the shape anisotropy have especially tampered with adjustments of the substrate topology or have deployed the power of electron beam lithography. Here we report on the in plane magnetic anisotropy observed in nanostructured Co thin films prepared by nanosphere lithography [3]. This relatively young technique allows the simple and economical preparation of thin films of magnetic metals laterally structured in a number of different topologies [4].

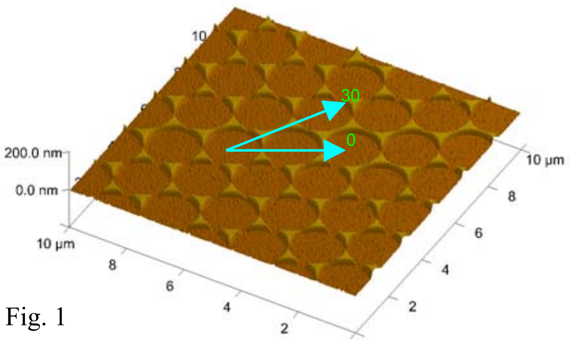

Fig. 1

Polystyrene (PS) latex particles of 1710 nm diameter were deposited from a water surface on the polished surface of a chemically cleaned Si substrate by a methodology related to the preparation of Langmuir-Blodget films [4]. Then, a Co layer of 32 nm thickness was deposited by electron beam evaporation on top of the PS mask in high vacuum (HV) conditions. After the chemical removal of the nanosphere mask the final result is a matrix of polycrystalline triangular elements arranged in a highly ordered hexagonal symmetry. Atomic force microscopy (AFM) has been used to investigate the samples homogeneity and to determine the orientation of the evaporated triangular nanostructures with respect to the substrate (fig. 1). The magnetic properties were studied by means of x-ray magnetic circular dichroism (XMCD) at the beam line UE 46 PGM at BESSY, Berlin. The experimental technique allows to determine separately the orbital and spin moment.

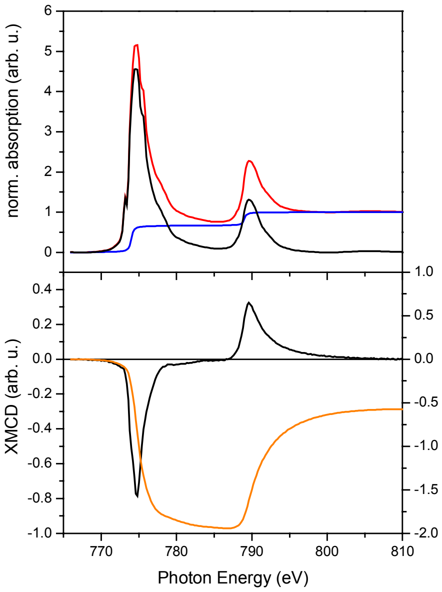

Fig. 2

The relative simplicity of the substrate preparation constitutes the main advantage of the sample preparation technique. However, the necessity to chemically remove the mask *ex situ* produces Co structures covered with a natural thin layer of CoO, thus the X-ray absorption spectra (XAS) show the typical splitting of the Co L_3 edge. A way designed to remove the CoO layer is H^+ ion sputtering. This method has been already successfully used to remove the oxide shell of chemically synthesised Co nanoparticles [5]. The samples were etched for 210 minutes at a relatively low sputtering energy (700 eV, H^+ pressure of 2.4×10^{-5} mbar). The sputtering parameters were carefully adjusted to allow an effective removal of the CoO layer without destroying the

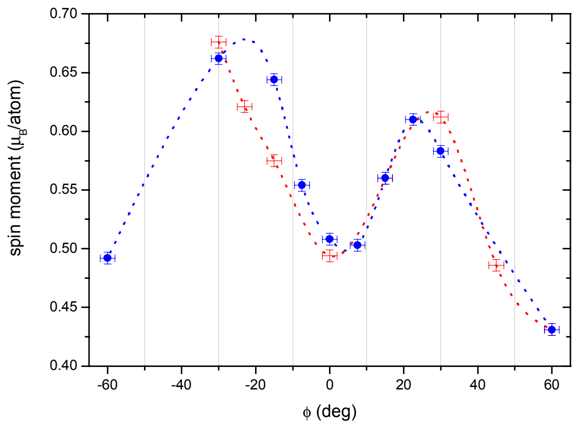

sample's regular pattern. Longer sputtering time at lower energy as well as shorter sputtering time at higher energies destroy partially or completely it. The sputtering energy and the time necessary to remove the CoO layer depend on the sample thickness and on the diameter of the PS lattex spheres. Each combination of Co thickness and triangles lateral dimension has a different sputtering time. Fig. 1 shows a typical AFM picture of our samples, the triangular structures are well defined with a very low density of defects, the shape and dimension of the Co pattern are given by the curvature of the latex spheres. The AFM scan shows that the samples retain their well-ordered geometry after the correct H^+ sputtering procedure. Small debris, resulting from the cleaning action of the H^+ ions and having a diameter between 2 and 10 nm, are present on the Si surface in between the metal triangular structures.

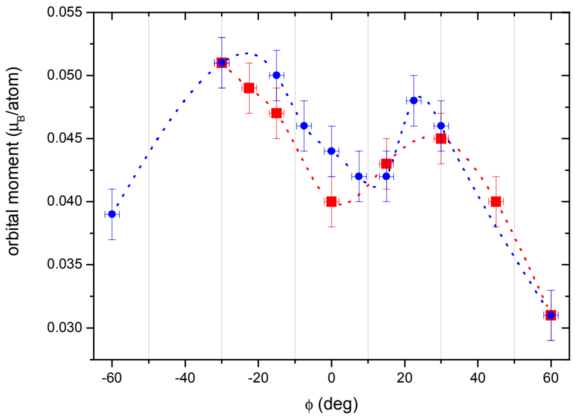

The XMCD measurements were done in remanent magnetisation at room temperature (RT). A pulsed field of 800 Oe was applied alternating its direction planar to the sample surface at each energy scan point. After each scan the sample was rotated around its axis. The arrows imposed on the AFM picture of fig. 1 show the geometry of the experiment. The angle φ defines the direction along the triangle pattern; the angle φ = 0° is the direction along the spherical voids, while φ = 30° defines the direction along the triangles edges. The geometry of the experiment was carefully planned to make sure the position of the centre of the samples remained unaltered after changing the azimuthal angle, the correct position of the sample with respect to the incident synchrotron light beam was checked at each measurement step. The XAS spectra were recorded in total electron yield, collecting the sample drain current. The spectral curves were normalised toward the incident incoming light by means of the last mirror current. The measurements were performed in grazing incidence, the angle of the sample surface with respect the incoming circularly polarised light was θ = 20°. In the data analysis no self absorption effects were taken into account.

The upper panel of fig. 2 shows the typical line shape of the absorption spectra after sputtering. Three lines are drawn: the sum of the positive and negative magnetised spectra (black), the step function representing the $L_{2,3}$ absorption edge jump (blue), and the isotropic spectrum resulting from the subtraction of the previous two (black). During the data analysis the orbital and spin moments, μ_l and μ_s respectively, were calculated assuming the 3d electron occupation number as for bulk hcp Co $\mathbf{n}_{3d}$ = 7.5. The shoulders at the lower and higher energies of the main peak at the Co L_3 edge (fig. 2) reveal that despite the H^+ etching procedure a small amount of oxide is still present. The separation of the metallic and non metallic contributions to the magnetic properties of the Co crystal cannot be easily achieved; the presence of a small amount of CoO on the surface of the samples has an impact on the results obtained by the surface sensitive XAS technique. It leads primarily to a reduced remanent magnetisation of the samples. The calculated values of the orbital and spin moment

are lowered by an unknown factor with respect to a perfectly oxide free surface. The lower panel of fig. 2 shows the dichroic signal as a result of the subtraction of the positive and negative magnetised XAS spectra, the XMCD signal (black line), together with its integral value (red line). Fig. 3 shows the spin moment, μ_s versus the azimuth angle φ, while fig. 4 shows the orbital moment, μ_l. Clearly, the patterned samples have an angular dependency with a period of φ = 60 degrees. Two sets of data are shown in the graph. The black line represents the first run from φ = –30° to φ = 60° while the red line the way back from φ = 60° to φ = -60°. The μ_s and μ_l maxima were both found at azimuth angles of φ = –30 and φ = 30 degrees while the minima at φ = –60, φ = 0 and φ = 60 degrees, respectively. According to the geometry of the experiment this means that the magnetization easy axis lies along the edge to edge direction of the triangle pattern, while the hard magnetization axis lies along the sphere to sphere center direction. The orbital and spin moment variation is about 15% for both values. The maximum value calculated for the spin moment is $\mu_s = 0.68\ \mu_B$/atom while the minimum value is $\mu_s = 0.43\ \mu_B$/atom. The maximum and minimum value for the orbital moment are $\mu_l = 0.051\ \mu_B$/atom and $\mu_l = 0.031\ \mu_B$/atom.
The absolute values of μ_l and μ_s calculated by means of the sum rules are lower with respect to the calculated or measured values of the orbital and spin moments for hcp bulk Co. Several factors play a role in such a result. Probably the applied pulsed field of 800 Oe leads to an incomplete magnetisation of the samples measured in remanence. Static magnetization loops show that the saturation for non H^+ sputtered samples is achieved at about 2 kOe and the cycle becomes reversible at about 800 Oe. However, for samples having their oxidised surface removed the magnetic hysteresis cycles are different and 800 Oe should be enough to nearly fully saturate them. Turning back the angle φ the minima/maxima get shifted of about 10 degrees like if an energetic barrier must be overcome in order to rotate the magnetic ordering of the triangles. Theoretical calculation have been planned to explain such behaviour. The dipolar interaction probably plays a role in the magnetic alignment of the triangular elements and the geometrical arrangement of the patterned elements should play a significant role in the observed anisotropic effect. The sixfold magnetic anisotropy shown by the Co patterned samples is consequence of the pattern shape. The effect probably can be ascribed to configurational anisotropy [6]; a deviation from the uniform magnetization driven by the shape of the pattern. With respect to previous studies on triangular nanostructures in the present case the sixfold anisotropy cannot be ascribed only to the shape of a single triangular element, but is consequence of the symmetry of the whole Co pattern. The variation of the magnetic moment as a function of the azimuthal angle obtained by XMCD was also independently confirmed by the angular dependence of the coercive field obtained from magnetic hysteresis loops using a vibrating sample magnetometre.

We thank S. Rudorff for the technical support during measurements at BESSY, Dr. H. Rossner, Dr. E. Holub-Krappe and Prof. A. Tennant for useful scientific discussion and continuos encouragement.

References

[1] C. Chappert, H. Bernas, J. Ferré, V. Kottler, J.-P. Jamet, Y. Chen, E. Cambril, T. Devolder, F. Rousseaux, V. Mathet, and H. Launois, Science **280**, 1919 (1998).
[2] A. Ney, C. Pampuch, R. Koch , and K. H. Ploog, Nature **425**, 485 (2003).
[3] J. Rybczynski, U. Ebels, and M. Giersig, Colloids Surf. A: Physicochem. Eng. Aspects **219**, 1 (2003).
[4] A. Kosiorek, W. Kandulski, P. Chudzinski, K. Kempa, and M. Giersig, Nano Lett. **4**, 1359 (2004).
[5] P.Imperia, D. Schmitz, H. Maletta, N. Sobal, and M. Giersig, Phys Rev. B **72**, 014448 (2004)
[6] R. P. Cowburn, D. K. Koltsov, A. O. Adeyeye, M. E. Welland, and D. M. Tricker, Phys. Rev. Lett. **83**, 1042 (1999).

Reading magnetism of one layer of Single Molecule Magnets

D. Gatteschi,[1] M. Mannini,[1] R. Sessoli,[1] A. Cornia,[2] L. Zobbi,[2]
C. Cartier dit Moulin,[3] P. Sainctavit,[4] and P. Imperia.[5]

1. INSTM & Department of Chemistry, University of Florence, via della Lastruccia 5, I-50019 Sesto Fiorentino, Italy
2. INSTM & Department of Chemistry, University of Modena and Reggio Emilia, via G. Campi 183, I-41100 Modena, Italy
3. Laboratoire de Chimie Inorganique et Matériaux Moléculaires, Case 42, Université Pierre et Marie Curie, 4, place Jussieu F-75252 Paris cedex 05, France
4. Laboratoire de Minéralogie Cristallographie de Paris, Tour 16-26, Université Pierre et Marie Curie, 4, place Jussieu F-75252 Paris cedex 05, France
5. Hahn-Meitner-Institut Berlin Glienicker Str. 100 D-14109 Berlin, Germany

Nowadays chemists are able to produce molecules having, individually, properties of bulk materials or even capable to execute a function. Thus molecules can constitute the building blocks for the growing little world of nanotechnologies.

Magnetic materials make no exception. Actually since the early nineties of the last century a new kind of molecules has been investigated that individually behaves like a magnet and for this reason they have been called Single Molecule Magnets (SMMs).[1] They show a magnetic hysteresis that, contrarily to traditional materials is not a cooperative effect but rather a feature of the molecule on its own. SMMs are in fact polynuclear metal complexes comprising paramagnetic transition metal centres that, thanks to exchange interactions inside the molecule, originate a high spin ground state. When a large spin in the ground state is associated with a strong easy axis magnetic anisotropy the magnetization freezes at low temperature as its reversal requires the overcome of an energy barrier. Due to their reduced dimensions quantum effects are important and in principle SMMs could be exploitable in quantum devices.[2]

The first and most investigated SMM is a cluster constituted by twelve Mn atoms (called Mn12, Fig.1) organized in an internal tetrahedron of four Mn^{IV} and an external ring of eight Mn^{III} atoms; all Mn atoms are in an octahedral coordination, connected by oxygen atoms creating a sort of mixed valence manganese oxide in which the growth is systematically blocked by an external organic shell (16 carboxylic acids) creating a perfectly monodisperse set of magnetic particles. Each Mn^{IV} owns a magnetic moment antiparallel to those of the Mn^{III} atoms, resulting in a ferrimagnetic structure that determines a ground state characterized by a total spin S=10.

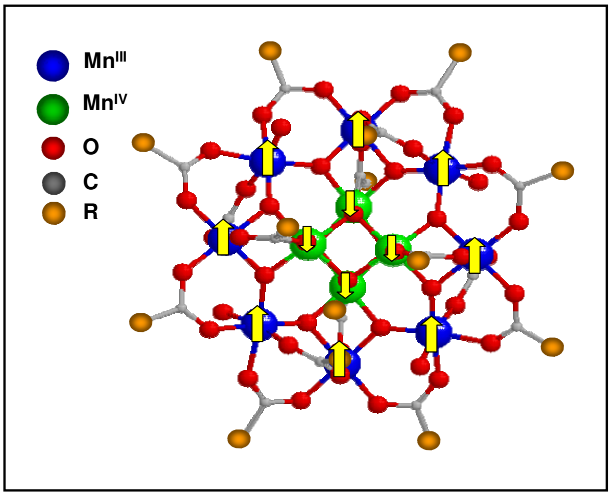

Fig1. Schematic view of the structure of the Mn12 cluster.

The interesting potentiality of this kind of materials resides in the magnetic memory of the individual molecule, but, up to now, single molecule properties have been extrapolated from the those of bulk samples (single crystal, powder, and diluted solution). The simplest strategy to reach individual addressing of the clusters is to organize SMMs on surfaces and use techniques such as Scanning Probe Microscopy (SPM) that indeed have the high spatial resolution required for single–molecule addressing.

Recently different methods of depositing Mn12 derivatives on a surface have been reported.[3] For instance we have suggested some chemical modifications of the original external organic shell to graft the clusters on a gold surface. A crucial step is to evidence that during the deposition procedure the complex molecule still retains its structure and, above all, its peculiar magnetic behaviour. Traditional techniques for magnetic characterization lacks the necessary sensitivity while the x-ray absorption spectroscopy (XAS), through the x-ray magnetic circular dichroism (XMCD) method, has shown to be able to detect the magnetism of a submonolayer of magnetic atoms.[4] Moreover, by recording the magnetic dichroic signal at the manganese $L_{2,3}$ edges in Mn12 clusters, one has immediate access to the magnetic structure of the cluster, because the contribution from Mn^{III} is easily distinguished from that of the antiparallel aligned Mn^{IV} ions, as shown for the simplest derivative of Mn12.[5]

We have used XMCD technique to characterize the bulk properties of Mn12TE = ($[Mn_{12}O_{12}(OOCPhSCH_3)_{16}(H_2O)_4]$), a more complex Mn12 derivative (Fig. 2) that is able to bind gold surfaces through sulphur atoms; XAS and XMCD characterizations, obtained recording signals in total electron yield at 4K and using a field of 4 T evidence the persistence of the characteristic ferrimagnetic spin structure.

When transferring this kind of characterizations to the analysis of a single layer of molecule problems related to photo-reduction can be easily encountered due to the high energy of third generation synchrotron radiations. The necessity of a lower flux appears as counter-intuitive but indeed position and energy stability play a key role in our experiment. For this reason BESSY, and in particular UE 46 PGM beamline, represents the ideal facility for this kind of characterizations. In fact, playing with various parameters we reduced the number of photons by a factor of 500 and an extra factor of 400 concerning the photon density was obtained thanks to the UE46 parallel beam mirror system.

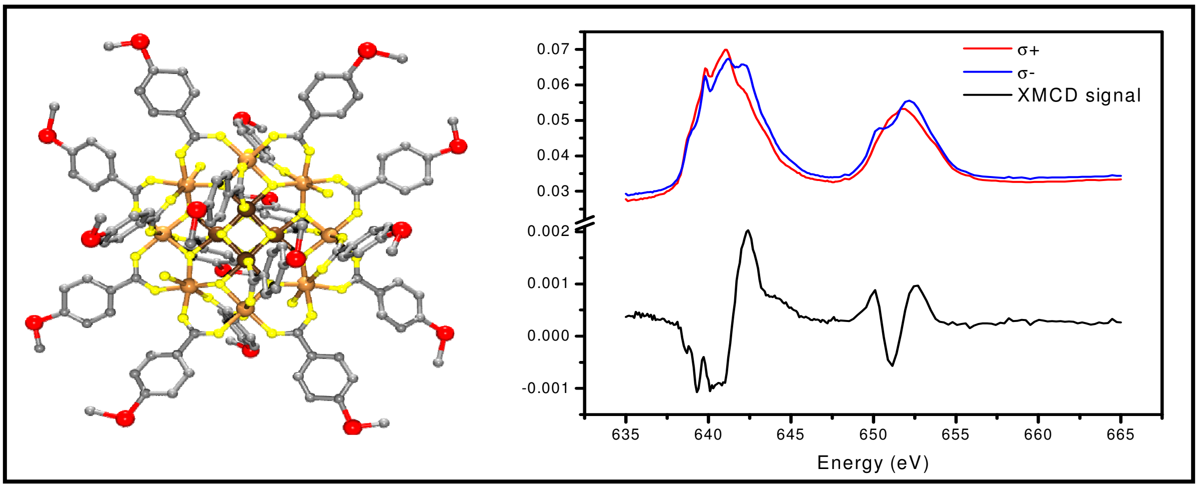

Fig2. Structure of the Mn12TE cluster (*left*) and bulk XAS and XMCD spectra (*right*).

In this way we have been able to characterize samples prepared ex situ starting from a solution o f Mn12TE that is adsorbed on a gold (111) surface. The Mn12TE clusters form a submonolayer in which each molecule is isolated from the others, as shown in Fig. 3, leaving a wide clean gold surface in which each molecule is well identifiable and addressable.[6]

This kind of sample was inserted inside the liquid He cryostat of the XMCD setup and during one day of measurements no evidences of significant photo-reduction have been noticed.

Preliminary results (see Fig. 3) evidence that XAS spectra strongly resemble those of the bulk sample with a slight increase of a signal due to spurious Mn^{II} contributions. Surprisingly the dichroic signal is substantially modified after the deposition on the Au surface.

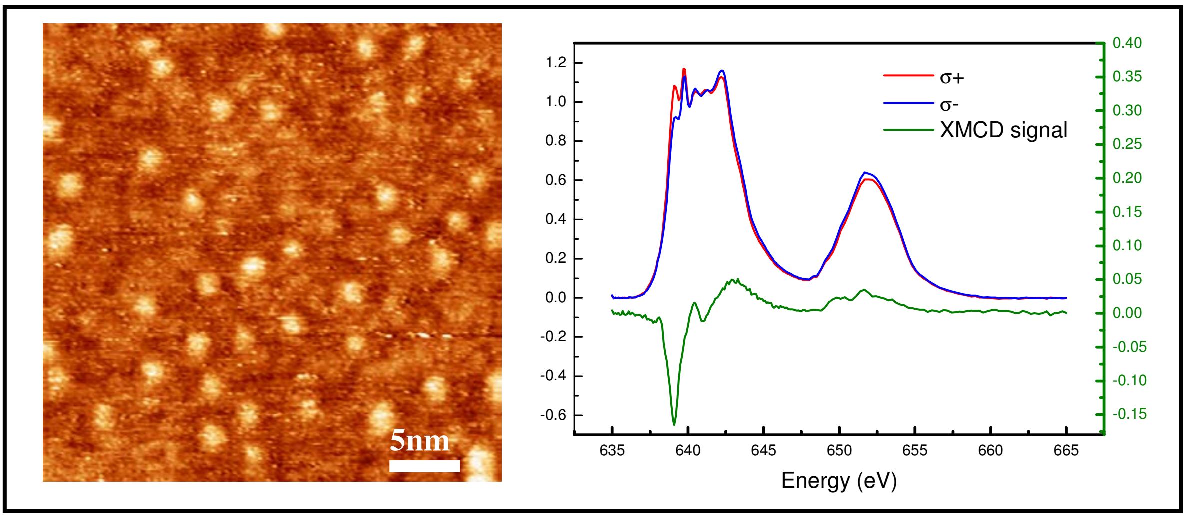

Fig3. Constant–current STM image of Mn12TE assembled on the Au(111) surface (*left*) and XAS and XMCD spectra (*right*) of this submonolayer.

A qualitative analysis, to be confirmed by a series of detail calculations now in progress, suggests that in addition to Mn^{III} and Mn^{IV} also a Mn^{II} component is present. Moreover the typical fingerprint of antiparallel alignment of Mn^{III} and Mn^{IV} is not detected from the monolayer. Interactions with the gold substrate, as well as a reduction during the grafting reaction, might be at the origin of this observation. This intriguing result does not however reduce the interest in this kind of innovative materials but suggests us to continue this investigation by playing on the deposition conditions and by exploiting different substrates.

References

[1] D. Gatteschi, R. Sessoli, J. Villani Molecular Nanomagnets, Oxford University Press, Oxford 2006.

[2] H. Park, J. Park, A. K. L. Lim, E. H. Anderson, A. P. Alivisatos and P. L. McEuen *Nature* **407**, 57 (2000).

[3] A.Cornia, A. C. Faretti, L.Zobbi, A. Caneschi, D. Gatteschi, M. Mannini, R. Sessoli *Structure & Bonding*, (2006) in press.

[4] P. Gambardella, A. Dallmeyer, K. Maiti, M. C. Malagoli, W. Eberhardt, K. Kern, C. Carbone *Nature* **416**, 301 (2002).

[5] R. Moroni, Ch. Cartier dit Moulin, G. Champion, M.-A. Arrio, Ph. Sainctavit, M. Verdaguer, and D. Gatteschi, *Phys. Rev. B* **68**, 064407 (2003).

[6] L. Zobbi, M. Mannini, M. Pacchioni, G. Chastanet , D. Bonacchi, C. Zanardi, R. Biagi, U. Del Pennino, D.Gatteschi, A. Cornia and R. Sessoli *Chem. Comm.* **12**, 1640 (2005).

Acknowledgments

The authors are grateful to the BESSY staff, for support before and during measurement time.
Financial support from the EC through BESSY IA-SFS Access Programme Contract N° R II 33-CT-2004-506008, "Magmanet" NMP3-CT-2005-515767, and "QuEMolNa" MRTN-CT-2003-504880 projects is gratefully acknowledged.

IR - Synchrotron Ellipsometry for the Characterisation of nanostructured organic and biomolecular films: DNA Bases and Polymer Brushes

K. Hinrichs[1], S. D. Silaghi[2], U. Schade[3], K.-J. Eichhorn[4], M. Stamm[4], L. Ionov[4],
D. R. T. Zahn[2], N. Esser[1] and M. Gensch[1]

[1] *Institute for Analytical Sciences- ISAS, Albert-Einstein-Str. 9, D - 12489 Berlin*
[2] Chemnitz University of Technology, Semiconductor Physics*, D- 09107 Chemnitz*
[3] *BESSY GmbH, Albert-Einstein-Str. 15, 12489 Berlin, Germany*
[4] *Leibniz Institute of Polymer Research Dresden e.V., Hohe Str. 6, 01069 Dresden, Germany*

Nanostructured and biomolecular films were characterized by IR ellipsometry [1-4] and complementary methods (VUV ellipsometry, XRD and AFM). For the laterally resolved ellipsometric measurements the recently upgraded IR synchrotron mapping ellipsometer at the IRIS beamline was used and it could be shown that the molecular structure of nanopatterned organic films can be derived from the measurements. Organic films are of technological interest for development of electronic, optical and sensoring devices. For the design of such organic devices it is often important to know the structural and optical properties of organic films and how they are bonded to the substrate. Optical methods are well suited for the contactless and non-invasive characterization. Infrared and VUV optical properties of thin films are correlated to vibrational and electronic excitations, respectively. Therefore the corresponding spectra are well suited for structural analysis, while the application of VIS ellipsometry for this purpose is often limited by the similarity of refractive indices for many organic materials. Ellipsometric results for two thin organic films on silicon, a DNA base and a polymer brush gradient film are discussed in the following.

Guanine film on silicon

In cooperation with Chemnitz University of Technology different films of DNA bases were studied and it could be shown that the average molecular orientation and the anisotropic optical constants can be determined from synchrotron ellipsometric spectra. Fig.1 shows measured and calculated ellipsometric spectra for a 84 nm thick guanine film together with schematic drawings for the molecular orientations used for the calculation. The shape of molecular bands, which are assigned to characteristic molecular vibrations, is characteristic for the average molecular orientation. From simulations within optical models the thickness and the molecular orientations can be derived [1-4]. However, even from the raw data qualitative assertions concerning the molecular orientation can be drawn from the observed spectral line shapes.

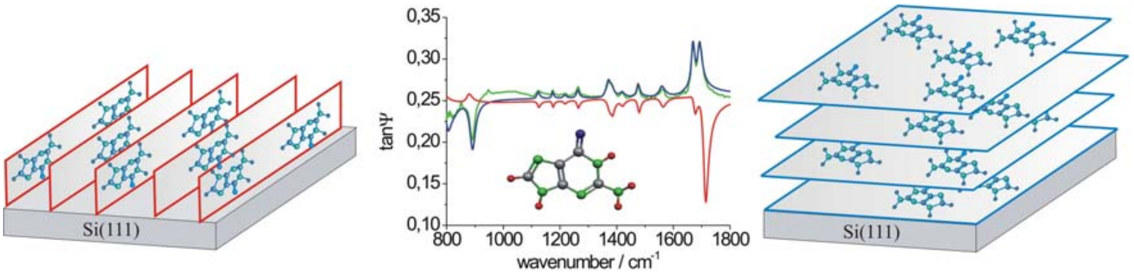

Fig.1: Thin guanine film on silicon: Measured tanΨ spectrum is shown in comparison with calculated spectra for two different molecular orientations. In the shown spectra dip-up features indicate predominant in-plane orientation of the corresponding transition dipole moments, dip-down features indicate substantial out-of plane components. A single tanΨ spectrum was measured within less than 25 s (including the time needed for rotation of polarizers). The structure of the guanine molecule is shown as inset.

Polymer brush film on silicon

During the 2nd semester of 2006 the existing IR ellipsometric set up was modified to allow micro-focus mapping experiments for scanning areas up to 50 x 50 mm. The upgrading of the ellipsometer was successfully tested with the investigation of mixed polymer brush gradient films. These ultra thin stimuli responsive films are studied in collaboration with IPF Dresden with the aim to analyze the dependence of their functionality on the brush composition. As a proof of principle 1D polymer gradient brushes of PS/PBA and PS/P2VP were mapped (see figure 2).

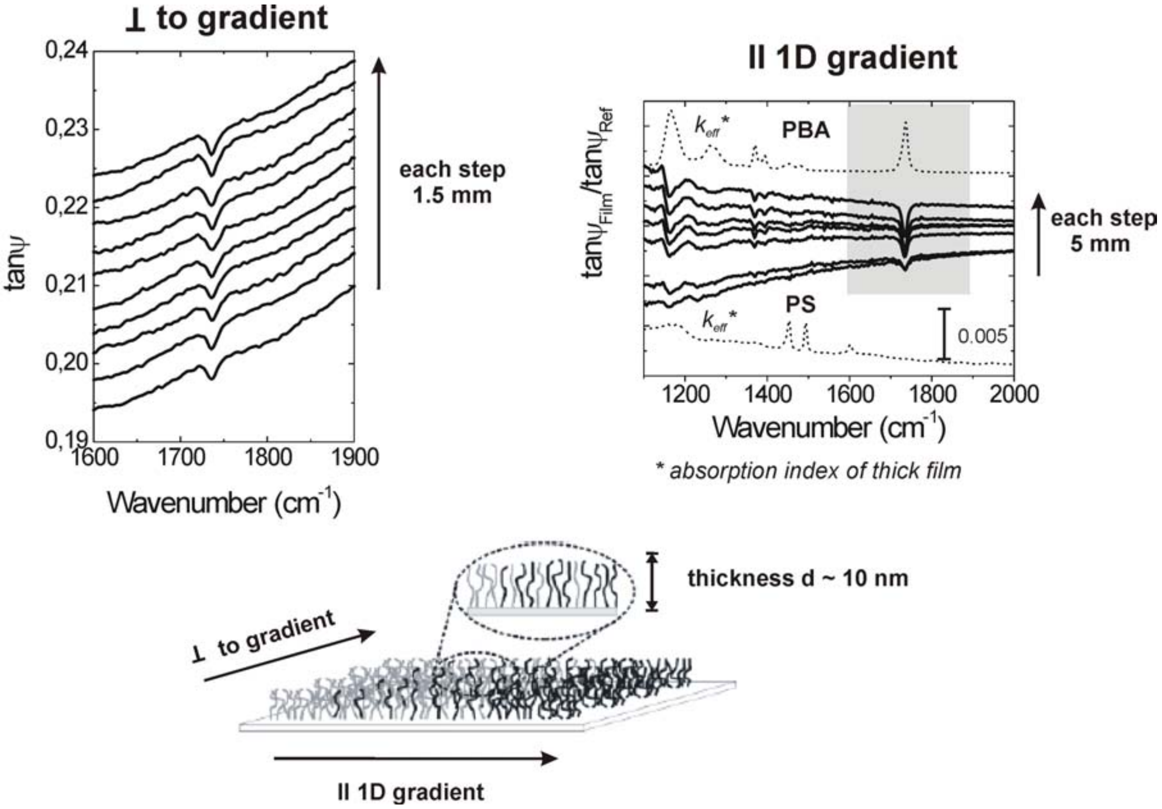

Fig. 2: Schematic of the geometry of a polymer brush gradient film and maps perpendicular to the gradient (top left) and along the gradient (top right) of a PS /PBA brush on silicon. The laterally varying composition of the brushes can easily be followed by the IR ellipsometric parameter tan Ψ.

In conclusion the presented results show that mapping ellipsometric measurements for structural analysis of nanostructured thin organic films are now possible within suitable time scales (a single spot with a size of 400 x 400 μm^2 can be investigated in 25 seconds). Based on these results further mapping experiments for analysis of biodiagnostic arrays and stimuli-responsive polymer brush gradients are scheduled in 2006. For example the binding of biomolecules to a specific linker will be investigated. Support by the EU through SSA DASIM (ctr. Nr. 00055326) and through the EFRE program (ProFIT grant, contract nr. 10125494) is gratefully acknowledged.

[1] K. Hinrichs, M. Gensch, N. Esser, Applied Spectroscopy ***59*** *(2005) 272A*

[2] K. Hinrichs, S. D. Silaghi, C. Cobet, N. Esser and D. R. T. Zahn, phys. stat. sol. b ***242*** *(2005) 2681*

[3] L. Ionov, A. Sidorenko, K.-J. Eichhorn, S. Minko, K. Hinrichs, Langmuir ***21*** *(2005) 8711.*

[4] M. Gensch, E.H. Korte, N. Esser, U. Schade and K. Hinrichs, Infrared Phys. Technol. (2006) in print.

Polarization of oxygen in Co-doped TiO_2

A. Nefedov[1], *N. Akdogan*[1], *R.I. Khaibullin*[2], *L.R. Tagirov*[2,3], *H. Zabel*[1]

[1]*Institut für Experimentalphysik/Festkörperphysik, Ruhr-Universität Bochum, Germany*
[2]*Kazan PhysicalTechnical Institute of RAS, Kazan 420029, Russian Federation*
[3]*Kazan State University, Kazan 420008, Russian Federation*

Diluted magnetic semiconductors (DMSs), in which a portion of atoms of the nonmagnetic semiconductor hosts are replaced by magnetic ions, are key material for spintronics. Recently several oxide-based DMSs (and in particular, the Co-doped TiO_2 system) have been reported to be robust, room temperature ferromagnets. Recently, we have reported room temperature ferromagnetism and in-plane magnetic anisotropy of single-crystalline rutile structures after Co implantation [1]. We concluded that ferromagnetism in this system results from incorporation of Co ions in the TiO_2 lattice, but co-existence with Co nanoclusters could not be excluded. To clarify this situation we studied in a detail magnetic properties of Co-doped (100)-oriented rutile TiO_2 single crystals for different implantation doses. The investigations were made by using x-ray resonant magnetic scattering (XRMS) at room temperature and below. In this contribution, we report on a polarization of oxygen ions in TiO_2 matrix, which can be one of possible origins of ferromagnetism in oxide-based DMSs. The (100)-oriented single-crystalline rutile TiO_2 plates were implanted using by Co^+ ions with the energy of 40 keV and with the current density of 8 mA/cm^2. The implantation dose varied in the range of 0.25-1.50$\cdot 10^{17}$ ions/cm^2. In order to understand nature of magnetism in oxide-based DMSs we carried out XRMS studies at Co and Ti $L_{3,2}$ edges as well as at O K edge. The XRMS experiments were carried out using a UHV-diffractometer ALICE at the undulator beamline UE56/1 of BESSY. For measurements at Co L edges the scattering angle was fixed at position of $2\theta = 8.2°$, but at Ti $L_{3,2}$ and O K edge the scattering angle was fixed at $2\theta = 12°$, which corresponds to the same scattering vector in reciprocal space. Within our sensitivity no magnetic signal was found at Ti edges, however, in addition to a strong magnetic signal on Co L edges a small, but clearly visible magnetic signal was observed at O K edge.The hysteresis curves measured at 30 K at Co L edge

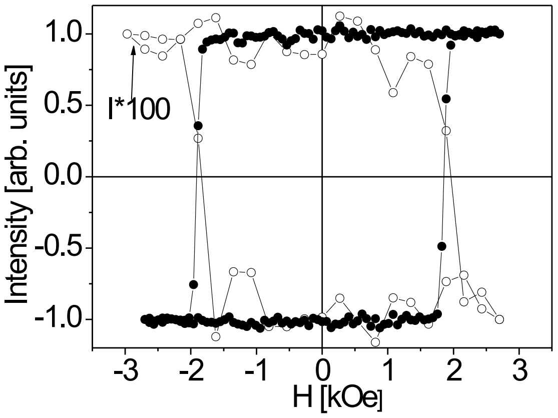

Figure 1: Hysteresis curves measured at Co L (closed symbols) and O K (open symbols) edges at T=30 K.

(E=780 eV) and O *K* edge (E=533 eV) are depicted in Fig. 1 (closed and open symbols, respectively). In the figure it is seen the shape of both hysteresis curve is the same, but with the opposite sign. It means that oxygen atoms neighbouring to Co atoms are polarized antiferromagnetically and ferromagnetic behaviour of Co-doped TiO_2 samples can be explained by exchange mechanism through oxygen atoms.

In order to distinguish ferromagnetic behaviour from superparamagnetism field cooling (FC) and zero field cooling (ZFC) measurements were carried out for sample implanted with the dose of $0.25 \cdot 10^{17}$ ions/cm^2. This sample demonstrates a pure paramagnetic behaviour at room temperature after subtracting diamagnetic contribution from the substrate. In Fig. 2 the XRMS results are presented after cooling down this sample to 4.2 K with a magnetic field H=2700 Oe and without magnetic field. In Fig. 2a) asymmetry ratio data measured in remanent state after FC (closed circles) and ZFC (open circles) are depicted. Both curves are the same within experimental errors and clearly demonstrate the same value of the remanence magnetization. The asymmetry ratio measured after field cooling to T=30 K, i.e. temperature above T_C ($T_C = 12 \pm 3$ K) is depicted by star symbols. In Fig. 1b) the hysteresis curves measured at 4.2 K after FC (closed circles) and ZFC (open circles) are shown.

In a conclusion, magnetic signal at O *K* edge was observed, i.e. after implantation of Co ions into TiO_2 substrates the polarization of oxygen atoms is taken place. We believe that this polarization can be responsible for nature of ferromagnetism in DMSs.

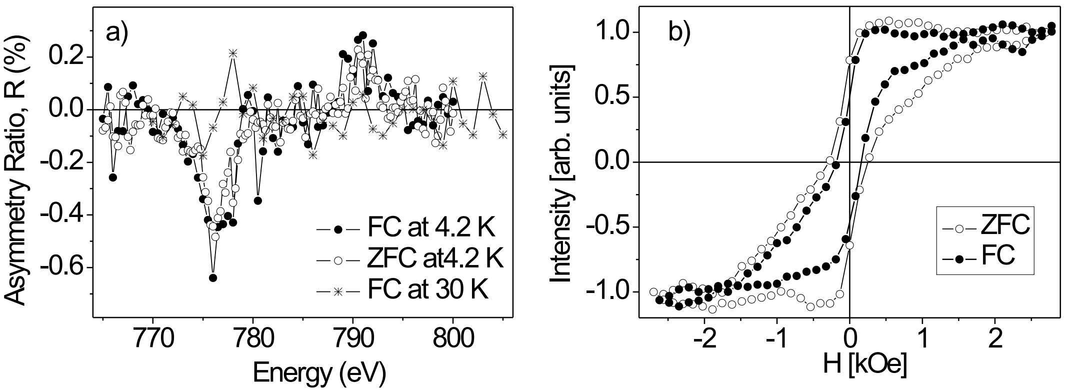

Figure 2: Asymmetry ratio measured after FC (closed circles) and ZFC (open circles) at T=4.2 K. Star symbols corresponds to a data measured after FC to T=30 K. b) Hysteresis curves measured after FC (closed symbols) and ZFC (open symbols) at T=4.2K.

We gratefully acknowledge the BMBF for the financial support through Contracts No. 03ZA6BC2 (ALICE diffractometer) and No. 05ES3XBA/5 (travel to BESSY). N. Akdogan acknowledges a fellowship through the International Max-Planck Research School "SurMat".

References

[1] N. Akdogan et al., *J. Phys.: Condens. Matter.* **17**, L359 (2005).

Energy Dispersive Small Angle X-ray Scattering

Tushar P. Sant[a], Wolfram Leitenberger[b], Tobias Panzner[a], Ullrich Pietsch[a]

[a] Institute of Physics, University of Siegen, D-57068 Siegen, Germany
[b] Institute of Physics, University of Potsdam, D-14469 Potsdam, Germany.

We report on energy dispersive small angle X-ray scattering (EDSAXS) experiments using white synchrotron radiation performed at Energy Dispersive Reflectivity (EDR) beamline at BESSY II. The experimental set-up is shown schematically in Fig.1.

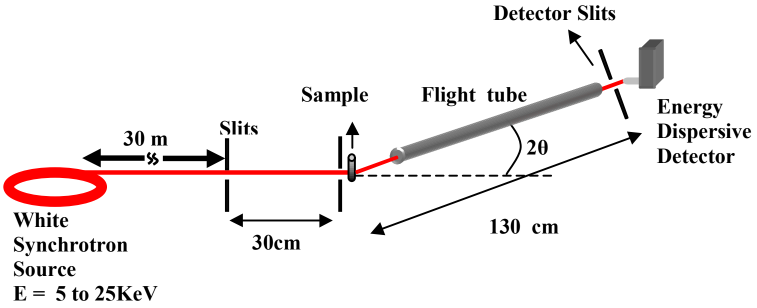

Figure 1 : Schematic sketch of experimental set-up at EDR beamline at BESSY II

Fig. 2 shows the measured spectrum at a fixed scattering angle of 0.18 deg for pure water in a glass capillary tube with 1.5 mm diameter and 100 micron wall thickness. Compared to emission spectrum from the bending magnet the measured spectrum is modified by absorption due to air and sample in low energy range. This spectrum is used as reference standard for further measurements.

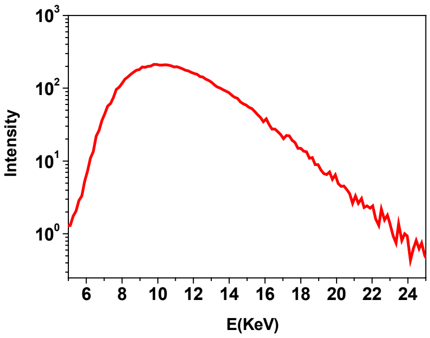

Figure 2 : Measured spectrum of water at fixed scattering angle of 0.18 deg

We measured EDSAXS spectra for Gold nanoparticles with diameters of about 12 nm and 40 nm solved in water. Fig. 3 shows the scattering for Au nanoparticles with 12 nm diameter as a function of energy. The nanoparticle solution was filled in glass capillary of 1.5 mm diameter. The sample to detector distance was 1.3 m. The measurement time for each spectrum is 10 min for emission at 15 mA current from the storage ring. The initial spectrum as seen in Fig. 2 becomes modified by the form factor of the particles to the spectrum shown in Fig.3. We could observe a weak minimum and a subsequent maximum in the scattering profile. To confirm that the origin of both is the form factor of the particle we performed the measurements at different scattering angles 0.42, 0.47, 0.50, 0.52, 0.57 deg. One can clearly observe that the position of the peak maximum (also the minimum) shifts from higher to lower energies as the scattering angle is increased (see arrows). In Fig 4 the SAXS spectra are plotted as a function of scattering vector *q*. These spectra are obtained by normalizing spectra of nanoparticles (Fig. 3) to that of water (Fig. 2) at the corresponding scattering angles. This procedure removes all experimental influences from the data.

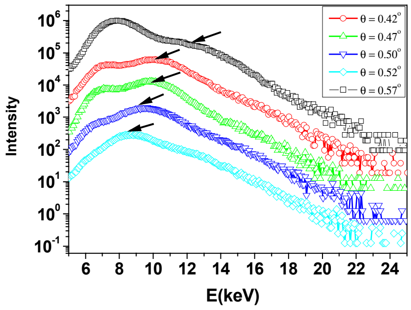

Figure 3 : **Au nanoparticle 12 nm spectra as a function of energy at different scattering angle.**

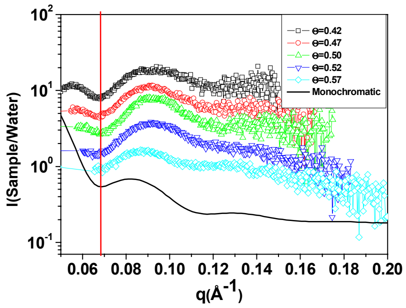

Figure 4 : **Au Nanoparticle 12nm spectra normalised to water spectra as a function of scattering vector *q*.**

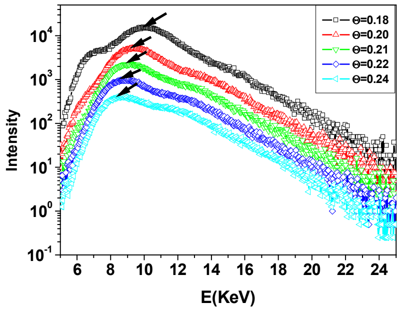

Figure 5 : **Au Nanoparticle 40 nm spectra as a function of energy.**

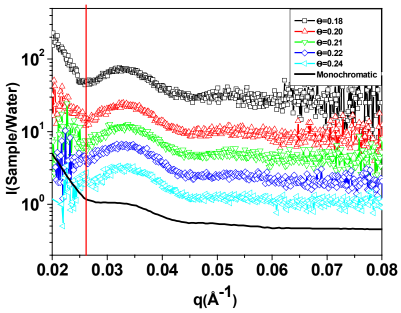

Figure 6 :Au nanoparticle 40 nm spectra as a function of *q*.

The position of the first minimum occurs at $q_{\min}R = 4.5$. For the above sample (see red line in Fig.4) with $q_{\min} = 0.066$ Å^{-1} one obtains R = 6.8 nm. This agrees well with the results of monochromatic SAXS measurement. Fig. 5 shows the scattering from other sample Au nanoparticles with diameter of 40nm. Again the measurements are taken at different scattering angles 0.18, 0.20, 0.21, 0.22, 0.24 degrees. The time for measurement was 3 min for normal emission from storage ring. Fig. 6 is the spectra for Au nanoparticles 40 nm normalized to water spectra as a function of scattering vector q. $q_{\min}$ occurs at 0.026Å^{-1} which gives diameter of nanoparticles as 34 nm. This again agrees with the monochromatic SAXS measurements but is smaller then expected (2R=40nm).

Comparing monochromatic SAXS measurements in home laboratoty with EDSAXS at BESSY we were able to reduce the measurement from 3 hours to 3 minutes. This fact can be useful in systematic investigation of large series of samples which is essential for optimising the synthesis procedure of nanoparticles. Also we can use EDSAXS for studying the processes with slow dynamics. But the specific experimental conditions at BESSY II limit the accessible q range of investigation. This in turn puts the limit for the measurable size of the particles.

References

[1] Yu, K.L., Lee, C.H., Hwang, C.S., Tseng, H.C., Tseng, P.K., Lin, T.L., Chang, S.L., Sheu, R.J., Chen, S.H. (1999) *Rev. Sci. Instrum.* 70, 3233-3238.

[2]Portale, G., Longo, A., D´llario, L., Martinelli, A., Caminiti, R. (2004) *Appl. Phy. Lett.* 85, 4798-4800.

[3] Pietsch, U., Panzner, T., Leitenberger, W. (2003) *Physica B* 357, 45-52.

Relaxation of lattice distortion in Creep-deformed Single Crystal Superalloy SC16 at 1173 K

G. Schumacher[1], N. Darowski[1], I. Zizak[1], H. Klingelhöffer[2], W. Chen[3] and W. Neumann[3]

[1]*Hahn-Meitner-Institut Berlin GmbH*
[2]*Bundesanstalt für Materialforschung und –prüfung*
[3]*Institut für Physik, Humboldt-Universität zu Berlin*

Single crystal superalloys show excellent creep and fatigue properties at high temperatures and are widely used as structure materials in gas turbines. Up to now, few is known about thermal stability of the microstructure in creep-deformed single crystal superalloys. Therefore, we have measured positions and profiles of 001 and 002 reflections in moderately creep-deformed single crystal superalloy SC16 (Ni-16Cr-3Mo-3.5Ti-3.5Al-3.5Ta; in wt %) as a function of time at 1173 K. The initial two-phase microstructure of the alloy consisted of cuboidal γ' precipitates with $L1_2$ structure of Ni_3Al-type which were coherently embedded in the γ fcc solid solution matrix phase. The precipitates had an average edge length of 450 nm and a volume fraction of about 40 % [1].

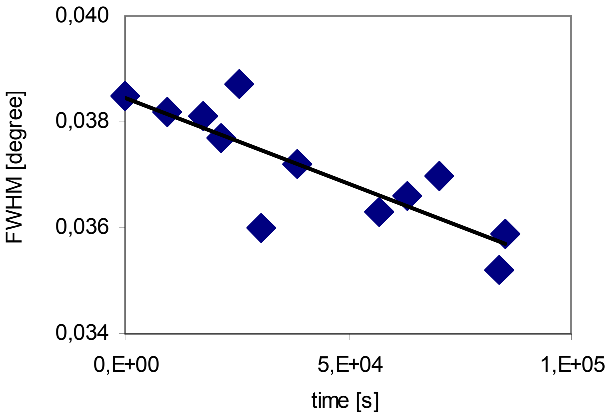

Fig.1 Line width of 001 reflection in creep-deformed SC16 (ε = 0.5%, T = 1223K) as a function of time measured at 1173 K.

Prior to X-ray analysis the specimens were creep deformed at 1223 K and 150 MPa parallel to the [001] direction under tensile load. The maximum creep strain ε was 0.5 %. XRD measurements were carried out using the 6-circle diffractometer at the KMC-2 beamline at BESSY at an X-ray energy of 8 keV. Symmetrical Bragg geometry was used on samples with surface perpendicular to the load axis. Measurements were performed in a high vacuum chamber at 1173 K. The widths and positions of the 001 reflections were determined by fitting Gaussian functions to the data. 001 superlattice reflection provided information on the crystal lattice of the γ' precipitates only, while measurements of 002 profiles contained information on both phases, γ and γ'. The procedure to determine the lattice misfit from the 002 profile is described in previous work [2-4].

Fig. 1 shows the line width of the 001 peak as a function of time measured at 1173 K. Though variation of data is considerable the line width shows a clear trend to lower values with increasing time. The line is a linear least squares fit to the data. With increasing time the position of the 001 reflection shifted to higher values (see Fig. 2) indicating a decrease in lattice spacing within the γ'-precipitates parallel to the [001] direction. The 002 profiles split into two maxima which can be assigned to the lattice parameters of the γ and γ' phase (Fig. 3). From the position of the 001 reflection of γ' phase it can be concluded that the maximum at larger angles is predominantly due to the 002 reflection of the γ'-phase. The maximum at lower angles can therefore be ascribed to the 002 reflection of the γ-matrix phase. After thermal treatment for $8.5 \cdot 10^4$ s the distance between the two maxima has increased. The shift of the 002 γ' peak is consistent with the observed shift in 001 peak position shown in Fig. 2. A more detailed analysis showed that the difference in 002 peak position between γ and γ' phase increased by about 25 % after t = 8.5x10^4 s with respect to the value at t = 0.

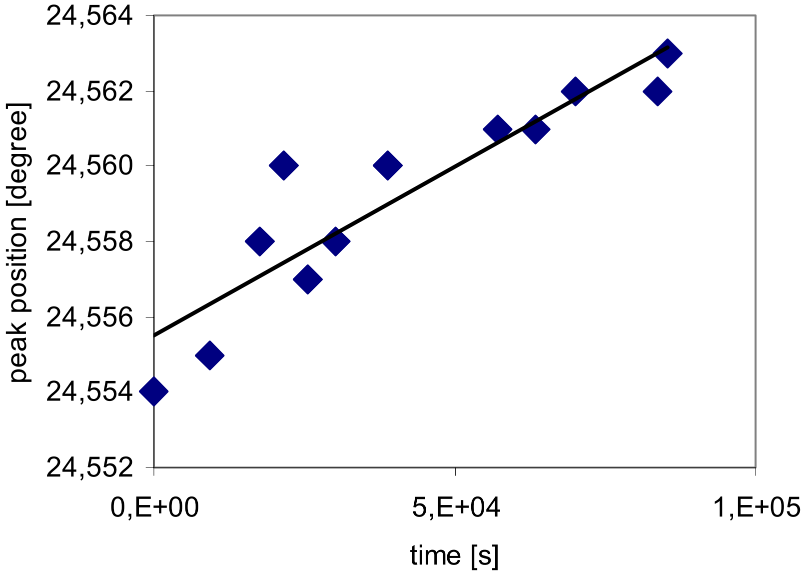

Fig. 2 : Position of 001 reflection in creep-deformed SC16 (ε = 0.5%, T = 1223K) as a function of time measured at 1173 K.

In the present experiment, the temperature was kept constant. The measured decrease in 001 line width and the change in lattice misfit can, therefore, not be ascribed to thermoelastic behavior caused by the different thermal expansion coefficients of the two phases. The observed changes are rather due to relaxation of the deformed state to a different structural state which corresponds the state prior to deformation. Prior to deformation the microstructure is free of dislocations. The arrangement of dislocations after deformation prior to thermal treatment is schematically depicted in Fig. 4. During tensile creep-deformation dislocations have arranged in a way that the half-planes lie within the γ'-precipitates at the interfaces which are aligned perpendicular to the [001] load axis while the half planes lie within the γ matrix phase at the interfaces which are parallel to the load axis [3,4]. This configuration has been shown to change the misfit in the positive direction compared to the non-deformed state

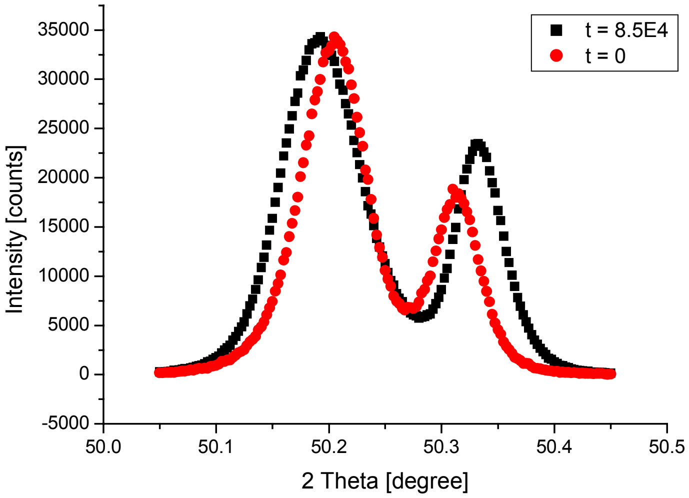

Fig. 3: Profiles of the 002 X-ray reflections measured at 1173 K in SC16 immediately after tensile-creep deformation (t=0, dots) and after heating (t = 8.5 x 10^4 s , squares).

[3,4]. The changes in γ and γ' lattice parameters measured in the present work suggest changes in dislocation substructure during thermal treatment. The dislocations at the γ/γ' interfaces rearrange in a way to approach the configuration prior to deformation. This state has a lattice misfit which is more negative than the one prior to heat treatment.

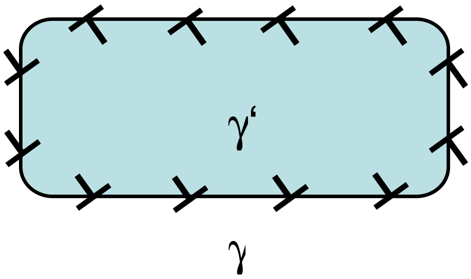

Fig. 4: Schematic illustration of the side view of a γ' raft in creep-deformed superalloy SC16 directly after creep-deformation

Support by the DFG (NE646/5-3 and Schu1254/3-4) is gratefully acknowledged.

References

[1] T. Malow, J. Zhu and R.P. Wahi, Z. Metallkd. 85 (1994) 9.
[2] N. Darowski, I. Zizak, G. Schumacher, H. Klingelhöffer, W. Chen and W. Neumann, J. Phys. D: Appl. Phys. **38** (2005) A200-A203.
[3] W. Chen, N. Darowski, I. Zizak, G. Schumacher, H. Klingelhöffer and W. Neumann Proc. Spring Meeting of the EMRS, May 31 – June 3, 2005, Strasbourg (France), Symposium O "Synchrotron Radiation and Materials Science", Nucl. Instr. Meth. B, in press.
[4] W. Chen, N. Darowski, I. Zizak, G. Schumacher, H. Klingelhöffer, N. Wanderka and W. Neumann, Mat. Sci. Forum **426** (2003) 4555.

Temperature Dependence of Lattice Distortion in Strongly Creep-deformed Single Crystal Superalloy SC16 Measured by Means of X-Ray Diffraction

G. Schumacher[1], N. Darowski[1], I. Zizak[1], H. Klingelhöffer[2], W. Chen[3]
and W. Neumann[3]

[1]*Hahn-Meitner-Institut Berlin GmbH*
[2]*Bundesanstalt für Materialforschung und –prüfung*
[3]*Institut für Physik, Humboldt-Universität zu Berlin*

In previous work we investigated lattice distortion of γ’-precipitates after tensile creep deformation to 0.5 % strain by means of X-ray diffraction (XRD) [1-3]. While creep-straining to 0.5% occurs within stage I of creep-deformation, creep-straining to fracture proceeds over three stages, stage I to stage III characterized by different deformation processes. We studied therefore lattice distortion after severe plastic deformation (15% strain) of single crystal superalloy SC16 and compared the results to those obtained after straining to 0.5%.

The single crystal superalloy SC16 (Ni-16Cr-3Mo-3.5Ti-3.5Al-3.5Ta; in wt %) was used for our study. The initial two-phase microstructure of the alloy consisted of cuboidal γ’ precipitates with $L1_2$ structure and a γ fcc matrix phase. Prior to deformation the precipitates had an average edge length of 450 nm and were coherently embedded in the γ matrix phase. The volume fraction of the γ’ phase was about 40 %.

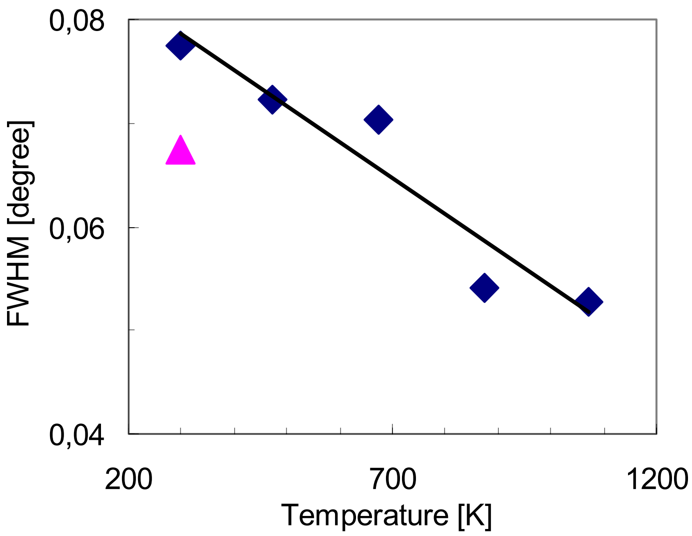

Fig. 1. Line-width (FWHM) as a function of temperature measured on creep-deformed single crystal superalloy SC16.

Specimens were creep-deformed at 1223 K and 150 MPa parallel to the [001] direction under tensile load to maximum creep strain of 15 %. The measurements were performed at various temperatures during heating from room temperature to 1073 K and after cooling back to room temperature.

X-ray diffraction (XRD) measurements were made at X-ray energy of 8 keV. The 6-circle diffractometer at the KMC-2 beamline of BESSY was used for the measurements. The 001 super-lattice reflection and the 002 fundamental reflection were measured in symmetrical Bragg geometry on samples with surface perpendicular and parallel to the load axis, respectively. The measurements made on the 001 reflection provide information on the crystal lattice of the γ’ precipitates only, while measurement of the 002 profiles reflects changes in the crystal lattice of both the precipitate phase and the matrix phase. The widths and positions of the 001 reflections were determined by fitting a Gaussian function to the data. The difference in lattice paramters was deduced from the 002 profiles.

Fig. 1 shows the line width (FWHM) as a function of temperature. The line width decreases as a function of temperature indicating relaxation of micro-strains within the γ'-precipitates. The relative decrease in line width is about 35 %. This relative change is comparable to that measured on the 0.5 % creep deformed specimen [2]. After the heat treatment the specimen was cooled down to room temperature and the line-width was measured again. This value of the line width (indicated by a triangle in Fig. 1) is lower compared to the value measured prior to heat treatment. The measurements performed after 0.5% creep strain did not indicate different values before and after heat treatment and were therefore discussed in terms of thermo-elastic effects [2-3]. The decrease in line width measured in the present work might therefore not exclusively be due to thermo-elastic effects. Inelastic structural relaxation at high temperatures might also affect the line width.

The position of 001 reflection as a function of temperature is shown in Fig. 2. The values of the 001 reflections were used to determine the position of the 002 reflection of the γ' precipitates.

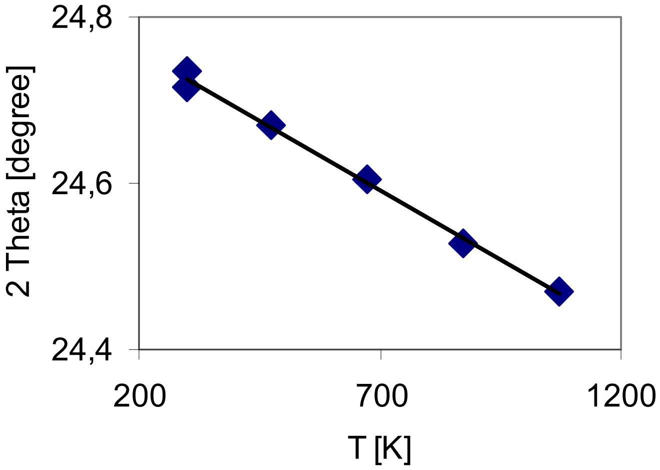

Fig. 2: Position of the 001 reflection as a function of temperature after tensile creep deformation to 15 % strain.

The 002 profiles measured at room temperature and at 1073 K are shown in Fig. 3a and 3b, respectively. The profile shown in Fig. 3a has two separate maxima. The first maximum coincides with the position of the 002 reflection of the γ'-phase calculated by use of the 001 peak position. The maximum at higher angles is, therefore, ascribed to the γ matrix phase indicating a positive lattice misfit $\delta = 2\cdot[a(\gamma')-a(\gamma)]/[a(\gamma')+a(\gamma)]$ at room temperature. A rough estimation of the misfit yields a value at room temperature of about +0.34 %. This value is large compared to the value δ = 0.10 % measured at room temperature on non-deformed specimens [1,4], but it is only slightly larger than the value δ = 0.28 % measured on the specimen creep-deformed to 0.5% strain [1]. The changes in lattice misfit are therefore large in stage I of creep-deformation, while further deformation obviously does not cause comparable changes in lattice parameters. This is a remarkable result, as further deformation to 15 % strain causes further appreciable changes in the γ'-raft morphology. The measured changes in lattice misfit are, therefore, rather ascribed to changes in the arrangement of dislocations at the differently aligned interfaces than to the evolution of γ'-rafts.

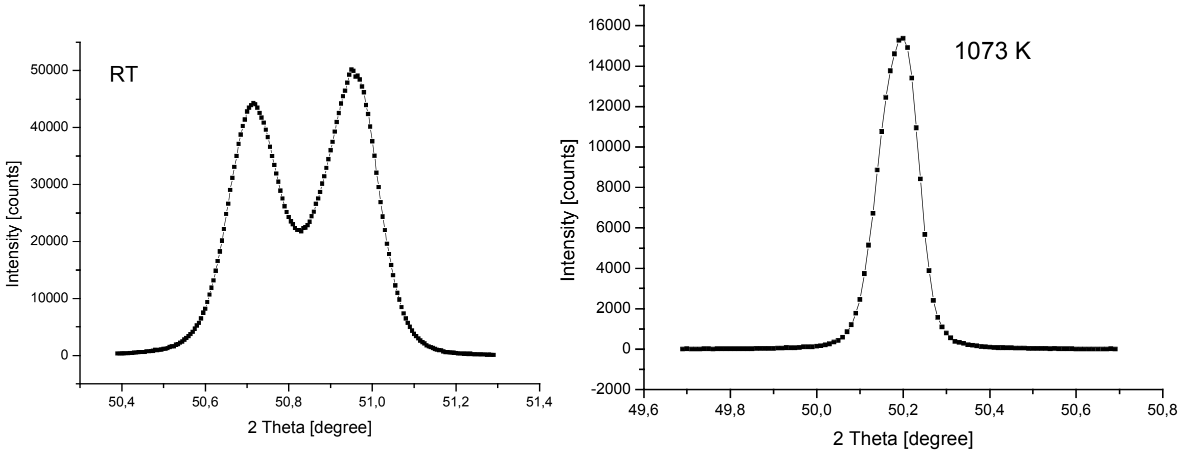

a) b)

Fig. 3: 002 profile measured by means of X-ray diffraction on creep-deformed superalloy SC16 at RT (a) and at 1073 K (b)

At 1073K the 002 profile reveals only one maximum without any pronounced shoulder. This indicates that the lattice misfit at 1073 K is close to zero. Using the date shown in Fig. 2 the position of the 002 peak of the γ' phase is determined to be 2θ = 50.153 °. This position is on the left hand side of the profile maximum of Fig. 3b. The lattice misfit is therefore still slightly positive. The decrease in lattice misfit with increasing temperature indicates a larger thermal expansion coefficient of the γ-phase compared to the γ'-phase in agreement with previous measurements [4,5].

This work was supported by DFG (NE646/5-3 and Schu1254/3-4). Help in specimen preparation by C. Förster (HMI) and H. Kropf (HMI) is gratefully acknowledged.

[1] W. Chen, N. Darowski, I. Zizak, G. Schumacher, H. Klingelhöffer, N. Wanderka and W. Neumann, Mat. Sci. Forum, 426 (2003) 4555.
[2] W. Chen, N. Darowski, I. Zizak, G. Schumacher, H. Klingelhöffer and W. Neumann Proc. Spring Meeting of the EMRS, May 31 – June 3, 2005, Strasbourg (France), Symposium O "Synchrotron Radiation and Materials Science", Nucl. Instr. Meth. B, in press
[3] N. Darowski, I. Zizak, G. Schumacher, H. Klingelhöffer, W. Chen and W. Neumann, J. Phys. D: Appl. Phys. 38 (2005) A200-A203.
[4] G. Bruno, G. Schumacher, H. C. Pinto, C. Schulze, Metallurgical and Materials Transactions A 34 (2003) 193.
[5] G. Schumacher, W. Mieckeley, W. Chen, R.P. Wahi, G. Frohberg and W. Wever, Z. Metallkd. 89 (1998) 661.

Analysis of EXAFS and MEXAFS above the L_3-edge of Fe

H.H. Rossner, D. Schmitz, P. Imperia, H. Maletta, and H.J. Krappe,
Hahn-Meitner-Institut Berlin,
Glienicker Str. 100, D-14109 Berlin, Germany,

and J.J. Rehr,
Department of Physics, University of Washington, Seattle, Washington 98195-1560

Spectra of spin-averaged and spin-polarized extended x-ray absorption fine structure (EXAFS and MEXAFS) data above the L_3-edge of Fe have been measured at temperatures of 180 K and 296 K. The data were taken at the elliptical undulator beamline UE46-PGM using the gap-scan technique in the energy range of 690 eV $\leq$ E $\leq$ 1160 eV. At each energy step the absorption measurements were performed with magnetization vector parallel ($\boldsymbol{\mu}^+$) and anti-parallel ($\boldsymbol{\mu}^-$) to the photon beam direction, resulting in the spin averaged and spin polarised absorption coefficients $\boldsymbol{\mu}$ and $\boldsymbol{\mu}^M$:

$$\boldsymbol{\mu} = \frac{\boldsymbol{\mu}^+ + \boldsymbol{\mu}^-}{2} \qquad , \qquad \boldsymbol{\mu}^M = \boldsymbol{\mu}^+ - \boldsymbol{\mu}^- .$$

For the analysis of the EXAFS data we applied the Bayes-Turchin procedure described in Ref. [1], using the results of the code FEFF8.2 [2] for 97 scattering paths within a cluster radius of 8 Å. The fitting procedure is applied to the measured absorption coefficient $\boldsymbol{\mu}_{\mathrm{exp}}$, which has been normalized to FEFF results. Possible deviations of the atomic like background absorption component $\boldsymbol{\mu}_0$ are taken into account by the introduction of correction functions $\delta\boldsymbol{\mu}_{0,L_s}(k)$ $(s = 1, 2, 3)$, which were determined by cubic splines at fixed support points k_p [1]. For all three edges the same correction function has been used, just scaled with the proper normalization factor of FEFF. The FEFF code further provides the E_0 reference energies for the three L-edges and the k-dependent values for amplitude reduction factor, scattering amplitudes, phases, and the effective mean free path lengths which also include the core hole life times. In addition to these parameters EXAFS Debye-Waller (DW) parameters σ_j^2 are needed for all paths j. The total crystal disorder σ_j^2 for each path was separated into the two components of structural disorder $\sigma_{j,\mathrm{struct}}^2$ and thermal disorder $\sigma_{j,\mathrm{therm}}^2$:

$$\sigma_j^2 = \sigma_{j,\mathrm{struct}}^2 + \sigma_{j,\mathrm{therm}}^2 .$$

It has been assumed that the structural disorder is independent of temperature and proportional to the number of atoms in the path, and that the thermal disorder is related to an ideal bcc-crystal structure. The thermal components $\sigma_{j,\mathrm{therm}}^2$ were calculated for each scattering path starting from the elements of the dynamical matrix that describe the lattice vibrations, and applying the recursion method proposed by Poiarkova and Rehr [3], which has been described in Ref. [4]. Different from Ref. [4], where the elements were determined by spring constants, they are now constructed by Born-von Karman (BvK) parameters taking into account the crystal symmetry. The 13 BvK parameters used for the first five shells around the absorbing atom had been extracted from phonon dispersion relations measured by inelastic neutron scattering [5]. These parameters determined the thermal disorder at both measured temperatures of 180 K and 296 K, assuming that the BvK parameters do not depend on temperature.

For further reduction of the fit parameters we fixed the amplitude reduction factor to 0.9, took the energy differences between the L-edges from the FEFF code, set the third cumulants $C_{3,j}$ for all paths to zero, and calculated the variations of the scattering half path lengths R_j from the variation of the lattice parameter a, assuming an ideal bcc-crystal structure and using the relation

$$\frac{\delta\boldsymbol{\chi}}{\delta a} = \sum_j \frac{\delta\boldsymbol{\chi}}{\delta R_j}\frac{\delta R_j}{\delta a} .$$

The reference energy E_0 for the wave vector k has been fixed to $E_0 = 713.08$ eV. The energy scales of experiment and model have been adjusted such that the centers of the first EXAFS oscillation coincide.

During the fitting procedure we observed significant oscillations of the model function $\boldsymbol{\mu}_{\rm mod}$ above the L_1 edge, which were not present in $\boldsymbol{\mu}_{\rm exp}$. To take into account possible variations of the core-hole life-times for the 2s and 2p electrons corresponding to the L_1 and $L_{2,3}$ edges, we introduced fitting factors f_{λ,L_1} and $f_{\lambda,L_{2,3}}$ for the effective mean free paths lengths

$$\lambda_{L_1}(k) = f_{\lambda,L_1}\lambda_{0,L_1}(k), \qquad \lambda_{L_{2,3}}(k) = f_{\lambda,L_{2,3}}\lambda_{0,L_{2,3}}(k),$$

where $\lambda_{0,L_s}(k)$ were taken from FEFF8.2. The number of equally distributed support points k_p on the considered k range 3.6 Å$^{-1} \leq k \leq 10.6$ Å^{-1} was chosen to be 10. This is the smallest number of points necessary to reach the condition that the minimum of χ^2 with respect to the model parameters is lower than the number of degrees of freedom.

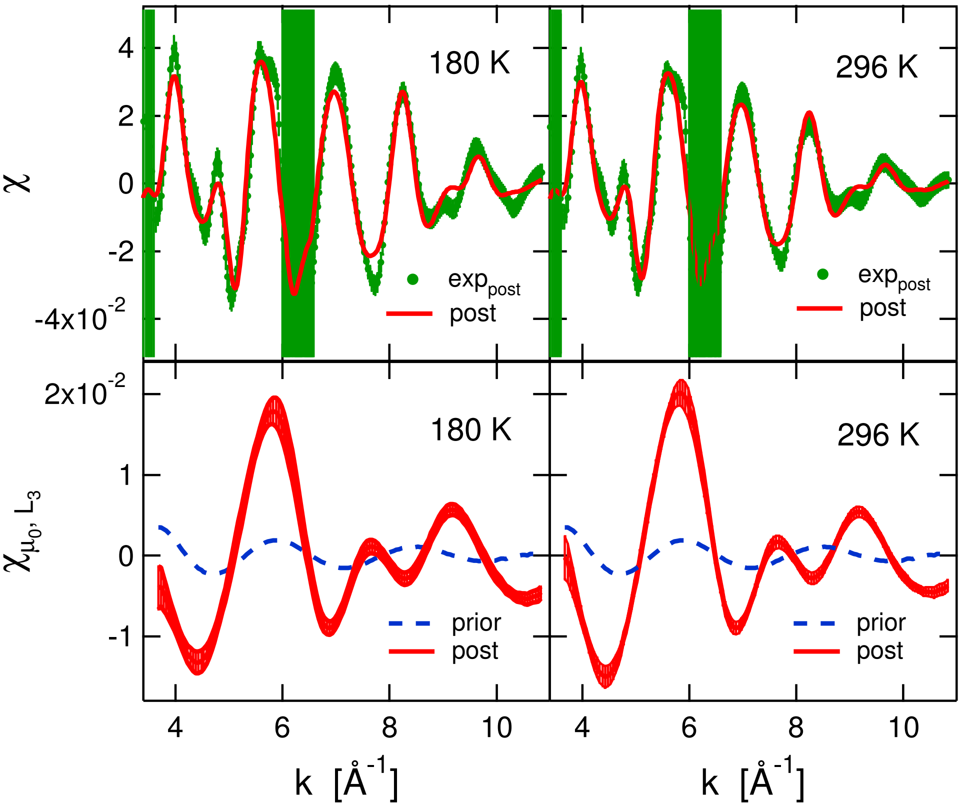

Figure 1: Upper part: Comparison of *a posteriori* experimental EXAFS oscillations (green dots with error bars) and the corresponding *a posteriori* model functions. Lower part: Comparison of *a priori* (blue dashed line) and *a posteriori* (red line with error band) background oscillations.

In a preliminary fitting procedure the correction functions $\delta\boldsymbol{\mu}_0(k_p)$, ($k_p = 1\ldots10$), the factors f_{λ,L_1} and $f_{\lambda,L_{2,3}}$, the structural component $\sigma^2_{\rm struct}$, and the lattice parameter a were determined for both absorption spectra measured at 180 K and 296 K. Assuming that f_{λ,L_1}, $f_{\lambda,L_{2,3}}$, and $\sigma^2_{\rm struct}$ are independent of temperature, the corresponding values of the two temperatures were averaged and kept constant in the final fit. The values used were $S_0^2 = 0.9$, $E_0 = 713.08$ eV, $f_{\lambda,L_1} = 0.49$, $f_{\lambda,L_{2,3}} = 0.81$, $\sigma^2_{\rm struct} = 0.005$ Å^2, resulting in $a = 2.869 \pm 0.003$ Å for both temperatures. The EXAFS and L_3-background oscillations of the experimental data and the corresponding model functions are shown in Fig. 1. The background oscillations were defined by the smoothed L_3 component of the atomic-like background $\overline{\boldsymbol{\mu}_{0,L_3}}$: $\boldsymbol{\chi}_{\boldsymbol{\mu}_0,L_3} = (\boldsymbol{\mu}_{0,L_3} - \overline{\boldsymbol{\mu}_{0,L_3}})/\overline{\boldsymbol{\mu}_{0,L_3}}$. The amplitudes of the background oscillations $\boldsymbol{\chi}_{\boldsymbol{\mu}_0,L_3}$ and of the EXAFS oscillations $\boldsymbol{\chi}$ are of similar size, which underlines the importance of the background determination. We further note that the resulting background correction functions for the two independent measurements at 180 K and 296 K coincide within their error bands and that their enhancement relative to the *a priori* FEFF function has been interpreted as an atomic EXAFS effect [6].

The spin polarized absorption coefficients measured at the two temperatures 180 K and 296 K are shown in Fig. 2. These coefficients are given in $\mathring{A}^2$ due to the normalization of the measured data to FEFF results. Application of a simplified rigid band model picture results in a correlation between the EXAFS

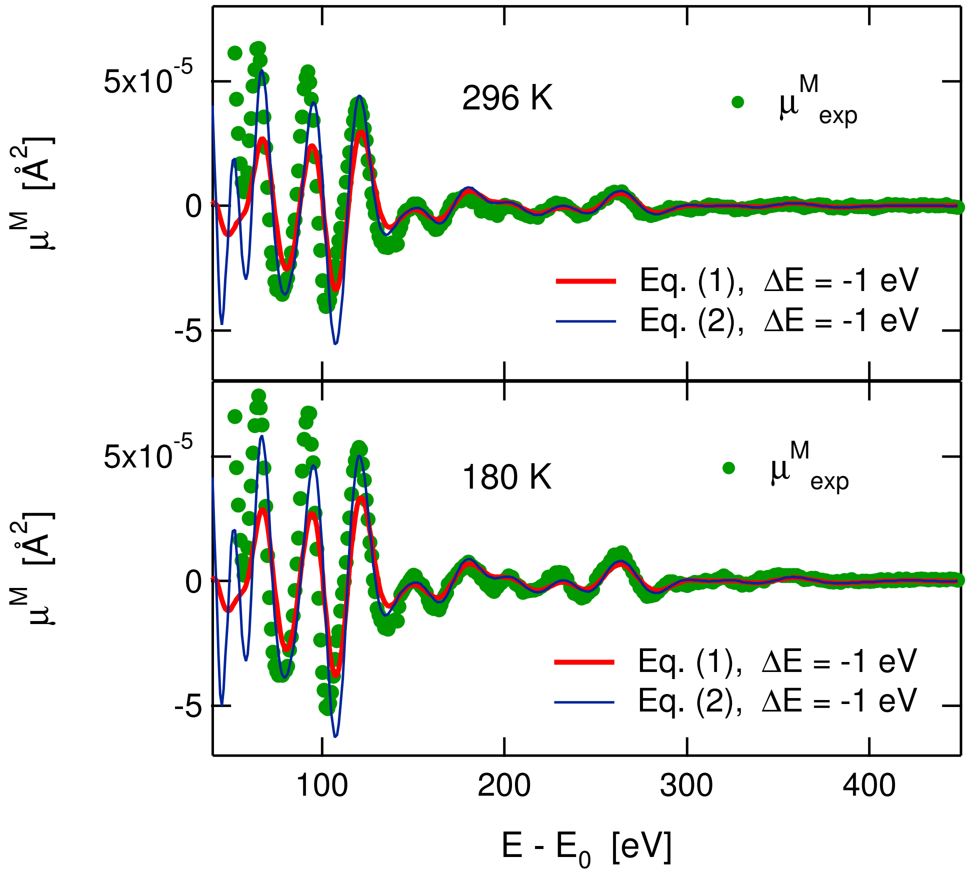

Figure 2: Experimental MEXAFS oscillations $\boldsymbol{\mu}^M$ (green dots) measured at the temperatures of 180 K and 296 K are compared with the approximations of Eq. (1) (red line) and Eq. (2) (blue line).

and magnetic EXAFS (MEXAFS) oscillations:

$$\boldsymbol{\mu}^M_{L_3}(E) + \boldsymbol{\mu}^M_{L_2}(E) \approx \frac{\boldsymbol{\mu}_{0,L_3}(E)}{4}\left[\frac{d\boldsymbol{\chi}_{L_3}(E)}{dE} - \frac{d\boldsymbol{\chi}_{L_2}(E)}{dE}\right]\Delta E, \tag{1}$$

$$\approx E_{\mathrm{SO}}\frac{\boldsymbol{\mu}_{0,L_3}(E)}{4}\left[\frac{d^2\boldsymbol{\chi}_{L_3}(E - E_{\mathrm{SO}}/2)}{dE^2}\right]\Delta E. \tag{2}$$

Whereas this rigid band model picture has been verified above the separated L edges of Gd [6], a phase shift of roughly 180^0 corresponding to a negative exchange correlation potential ΔE is observed for the 3d transition metal Fe. We conclude that either the simple band model picture or the exchange correlation potential have to be modified in this case.

References

[1] H.J. Krappe and H.H. Rossner, Phys. Rev. B **70**, 104102 (2004).

[2] A.L. Ankudinov, B. Ravel, J.J. Rehr, S.D. Conradson, Phys. Rev. B **58**, 7565 (1998), A.L. Ankoudinov, Ph.D. thesis, Univ. of Washington (1996).

[3] A.V. Poiarkova and J.J. Rehr, Phys. Rev. B **59**, 948 (1999).

[4] H.J. Krappe and H.H. Rossner, Phys. Rev. B **66**, 184303 (2002).

[5] V.J. Minkiewicz, G. Shirane, and R. Nathans, Phys. Rev. **162**, 528 (1967).

[6] H. Wende, Rep. Prog. Phys. **52**, 2105 (2004).

Stress distributions in finite structures

Karen Pantleon

Technical University of Denmark, Department of Manufacturing Engineering and Management
IPL Building 204, DK – 2800 Kgs. Lyngby, Denmark

Electrochemical deposition has become the key technology in manufacturing functional thin films with finite structures, e.g. for microsystems and microcomponents. For instance, electroplating through a mask results in free-standing line patterns, which can either directly be used as metallic patterns in micro-systems or act as mould for the specially developed injection moulding process. The two most important materials in this field are i) Cu, which has become the dominating material for interconnects in integrated circuits in microelectronics, and ii) Ni, a promising material to realize movable structures for micro-electro-mechanical (MEMS).

Recently, the influence of the geometry of free-standing line patterns of electrochemically deposited Cu- and Ni-films on their microstructure and crystallographic texture was studied by means of conventional X-ray diffraction [1]. Supplementary to X-ray diffraction averaging over hundreds of lines, finite element modelling (FEM) of the strain distribution within a single line was carried out [2]. FEM calculation indicate fairly inhomogeneous strain distributions; both in depth as well as over the line width. The stress state of line patterns has a dramatic effect on failure of the electrodeposited lines. An experimental verification of the strain (stress) distribution in such line patterns could not be obtained so far. Stress analysis by means of X-ray diffraction using conventional X-ray radiation was found to be unsuitable, because of insufficient diffraction intensities related to the small diffracting volume.

Experiments at the beamline MagS were aimed to check the possibilities for analyzing internal stress in such line patterns using synchrotron radiation.

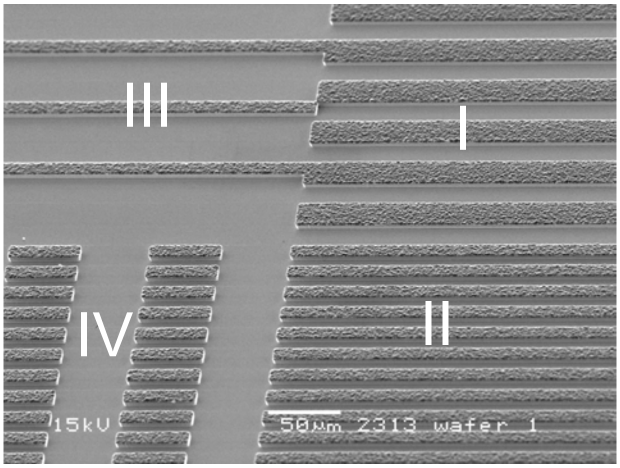

Fig. 1: Electrodeposited line patterns (SEM-image). Individual arrays (I…IV) contain several hundreds of parallel lines.

Synchrotron experiments at the beamline MagS at BESSY were carried out on Ni-line patterns, which have been electrodeposited on a glass wafer. Four different arrays of parallel Ni-lines with varying line width (10 mm, 20 µm), interline distance (10 µm, 20 µm, 50 µm) and line length (50 µm, several millimeters (infinite)) were arranged on one and the same wafer, see Fig. 1. For comparison, it was additionally measured on a non-patterned Ni-film. The diffracted intensity of the 111 lattice plane was recorded as a function of the sample tilt angle ψ. During the experiments the sample was mounted and adjusted by appropriate rotation around the sample normal such that lines were oriented either vertically or horizontally with respect to the primary beam, i.e. stress was determined across (rotation angle φ = 0º) and along (φ = 90º) the lines, respectively. As a result, the dependence of the position 2θ of the diffraction peak, the integrated intensity and the corresponding full-width-half-maximum on $\sin^2\psi$ was obtained. In principle, this should lead to a straightforward calculation of stresses from the measured lattice strain (from changes of the peak position, i.e. the corresponding d-spacing) according to the $\sin^2\psi$-method [3]. However, the obtained 2θ dependence on $\sin^2\psi$ revealed interesting peculiarities, see Fig. 2.

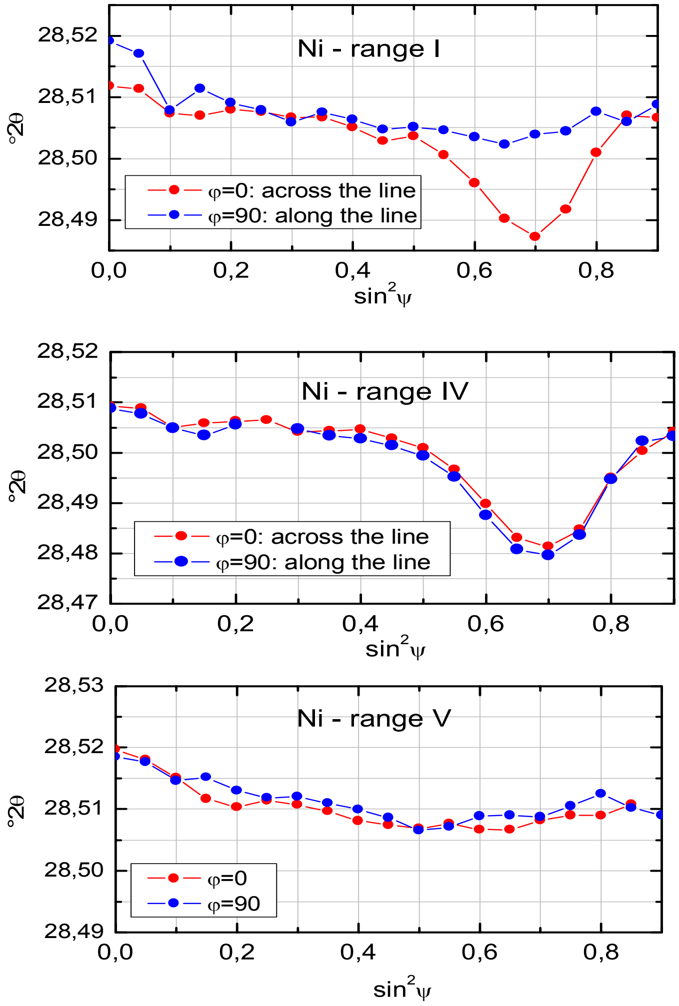

range I:
W = D = 20 µm, L infinite

range IV:
W = D = 10 µm, L = 50 µm

continuous film

Fig. 2: The diffraction angle 2θ in dependence on the sample tilt angle ψ ($\sin^2\psi$) for various line geometries (W – line width, D – interline distance, L – line length) as well as a non-patterned film.

A pronounced non-linearity was observed in the $\sin^2\psi$-plot by a sudden decrease of the measured position of the 111-peak, which becomes lowest at a tilt angle of about 54.5º. The measured intensity distribution as well as previous studies indicate that the Ni-films have a pronounced <100> fibre texture and indeed, the angle between the measured 111 lattice plane and the 200 amounts to 54.7º. It was found that the extent of the non-linearity depends strongly on the pattern geometry and the adjustment of the sample during the measurement, i.e. whether the lines are oriented vertically or horizontally. Comparison to the non-patterned Ni-film indicates that not the texture solely, rather the specific geometry of the various line patterns is responsible for the observed effect. Stress relaxation is expected to be different for the two stress components (across and along the lines) and to depend on the line geometry.

[1] K. Pantleon, M.A.J. Somers, Acta Materialia 52 (2004) 4929-4940.
[2] K. Pantleon, H. M. Jensen, M.A.J. Somers, Mat. Res. Soc. Proc. vol. 812 (2004) F3.20.1-F3.20.6.
[3] Structural and residual stress analysis by nondestructive methods, ed.: V. Hauk, Elsevier Science, The Netherlands 1997.

The excellent support by E. Dudzik and R. Feyerherm (HMI Berlin) during the experiments is gratefully acknowledged.

High-resolution tomography investigations of micro-cracks in hard rocks

K. Thermann[1], B. Kremmin[1], S. Zabler[2], I. Manke[1], J. Tiedemann[1]

[1]TU Berlin, FG Ingenieurgeologie,13355 Berlin
[2]Hahn-Meitner-Institut, 14109 Berlin

To investigate fracture propagation in hard rocks in response to applied loads it is essential to know the existence and orientation of pre-existent microcracks. Because nucleation, growth and interaction of microcracks are considered to be the dominant, controlling mechanisms of macroscopic failure. Nevertheless, grain boundaries, low-aspect ratio cavities or interfaces of two different minerals can also function as stress concentrators and be responsible for crack initiation. In former publications, transparent materials (resin, glass, PMMA) or rock type materials (gypsum, cements, mortar) that simulate brittle failure of rock were investigated to study the different influences and their interaction [2, 3, 4, 5, 6]. Synchrotron tomography at BESSY provides the possibility to investigate microscopic features of natural rock samples.

Two different types of sedimentary rocks were investigated. A Carboniferous greywacke as a clastic sedimentary rock and a Triassic limestone as a chemical sedimentary rock. Whereas limestone is composed mainly of the mineral calcite ($CaCO_3$) a greywacke consists of angular grains of quartz, feldspar, and small rock fragments (e.g. quartzite, slate, various schists, or gneiss) set in a compact, clay-fine matrix. Because of the large sample height of 10 mm three vertical sections were measured. After the reconstruction the sections were merged to a complete tomogram of the sample on which the analysis was finally done. Rock samples loaded to different stress stages were investigated. A noticeable crack initiation was not observed until the loading stage at approximately 90 % of the uniaxial compressive strength of the particular material. In Fig. 1 voids (pores, cavities, cracks) are coloured red whereas high absorbing particles have a yellow colour. In the greywacke tomogram (Fig. 1a) a quartzite healed fracture (yellow) can be seen. The new propagated crack has nearly the same orientation as the healed crack. The high absorbing phase in the limestone sample (Fig. 1c) is pyrite (FeS_2). As a result of limiting resolution these cubic minerals appear spherical in the tomogram. In Fig. 1b) the fracture process zone in front of the crack tip can be seen.

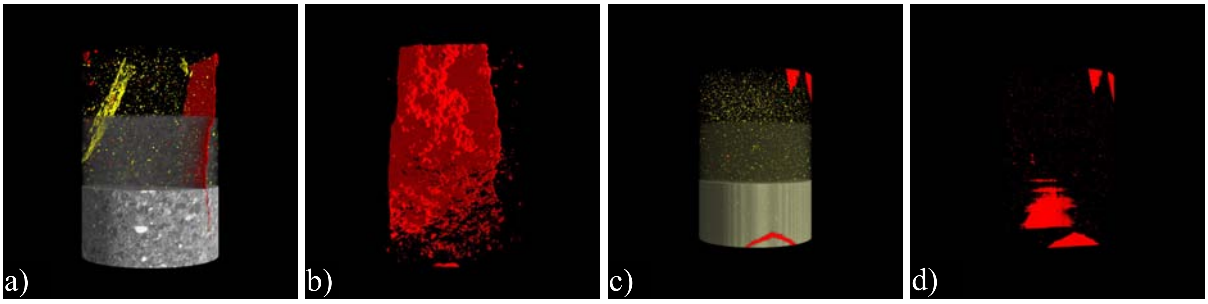

Fig. 1: Different viewing options of the greywacke (a, b) and the limestone sample (c,d)

According to the site of origin microcracks can be subdivided into grain boundary cracks, intragranular cracks and inter- or transgranular cracks but often an unambiguous classification is not possible. Hence, crack type labels also depend to some extent on the resolution of the observation [6]. Concerning crack tip displacement three basic modes exist: mode I - tensile, mode II – in-plane shear and mode III – anti-plane shear [1].

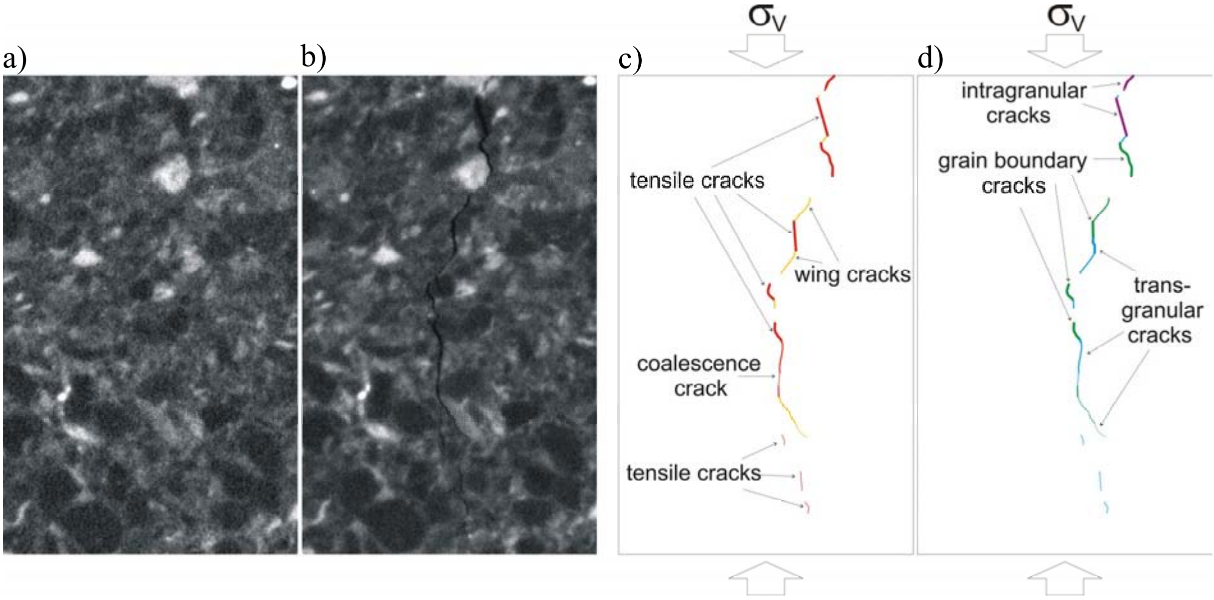

Fig. 2: Section of the unloaded (a) and loaded (b) sample and sketches of the propagated cracks (c and d)

In Figure 2 a section of the unloaded (a) and loaded sample (b) is shown. In Fig. 2c) the cracks were characterized according to their type of mode whereas in Fig. 2d) the location was analyzed. As is shown in Figure 2, first tensile or mode I cracks at grain boundaries are generated. In the upper part of Figure 2b) can be seen that intragranular crack initiation is possible, too. The tensile cracks are oriented sub-parallel to the loading direction. At the tips of these cracks were wing cracks initiated. These wing cracks start at the tips of the pre-existing cracks and propagate in a curvilinear path as the load is increased. According to [2] wing cracks grow in a stable manner since an increase in load is necessary to lengthen the cracks, and align with the direction of the most compressive load. In Figure 2 can also be observed that crack coalescence occurred when cracks (grain boundary, intragranular or transgranular) were sufficiently close to each other.

In a next step the crack in the greywacke sample (Fig. 1b) was precisely analyzed. At first the crack was separated from the sample and the geometrical parameters were determined. A plane was fitted to the crack to investigate the orientation (dip direction, dip angle) of the crack. The distance of each crack voxel to the plane can be calculated and so information about the crack surface roughness can be gained.

Further investigations on a larger number of samples are needed to specify the results and to accomplish a statistical assessment.

References

[1] Atkinson, B.K. (1987) *Fracture mechanics of rock.* Academic Press, London.

[2] Bobet, A. Einstein, H.H. (1998) Fracture coalescence in rock-type materials under uniaxial and biaxial compression. *Int. J. Rock Mech. Min. Sci.* Vol. **35**, No. 7, 863-888.

[3] Dyskin, A.V., Sahouryeh, E., Jewell, R.J., Joer, H., Ustinov, K.B. (2003) Influence of shape and locations of initial 3-D cracks on their growth in uniaxial compression. *Engineering Fracture Mechanics* **70**, 2115-2136.

[3] Hoek, E. Bieniawski, Z.T. (1965) Brittle fracture propagation in rock under compression. *Int. J. Fract. Mech.* **1**, 137-155.

[5] Horii, H., Nemat-Nasser, S. (1985) Compression-induced microcrack growth in brittle solids: axial splitting and shear failure. *Journal of Geophysical Research* Vol. **90**, No. B4, 3105-3125.

[6] Kranz, R.K. (1983) Microcracks in rocks: a review. *Tectonophysics* **100**, 449-480.

[7] Landis, E.N., Nagy, E.N., Keane, D.T. (2003) Microstructure and fracture in three dimensions. *Engineering Fracture Mechanics* **70**, 911-925.

Energy and time resolved coherent X-ray reflectivity of a smooth polymer film

G. Gleber[1], T. Panzner[1], W. Leitenberger[2], A. Pucher[2], U. Pietsch[1]

[1] Institute of Physics, University of Siegen, D-57068 Siegen, Germany
[2] Institute of Physics, University of Potsdam, D-14469 Potsdam, Germany

The aim of the EDR coherence project consists in the use of coherent white radiation provides by a BESSY bending magnet for time correlation spectroscopy. As model system we used a light-sensitive polymer film covered with gold colloids. Under influence of external green light the polymer becomes soft which may induce the colloids to sink into the film. The expected dynamics is slow enough to detect variations of speckle pattern in a time scale of a few seconds. The experimental setup used is shown in fig.1. The coherent part of the radiation is selected by the incident pinhole of 15 µm in diameter. In order to extend the usable spectral range (5 <15 keV) we installed a flight tube between sample and energy-dispersive detector. Unfortunately the experiment was partially successful up to now, only, caused by technical reasons. The first time-correlation we observed was the evolution of a radiation damage at the polymer induced by the intense synchrotron radiation. Furthermore we suffered from some instabilities in speckle positions caused by thermal drift of the sample table, which causes the whole reflected beam to move. The first problem will be solved by installation of a fast shutter. It will reduce the radiation dose at the sample, also. Additionally we plan to optimize the conditions of green laser irradiation to the sample in order to tune the dynamics to the time window accessible by the experiment. The second has to be solved by extracting the thermal drift by means of numerical analysis of data. Nevertheless the first experiment has shown speckle modifications under influence of the external light. Figure 2 shows the spectra

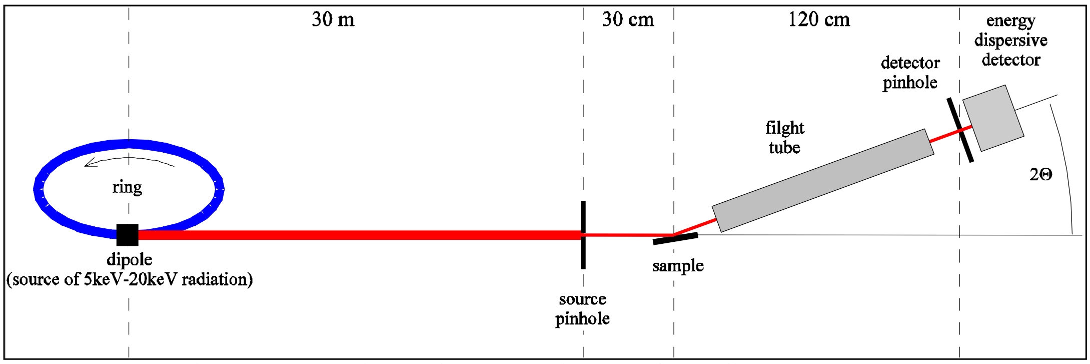

Figure 1: Experimental set up at the EDR beam line at BESSY II

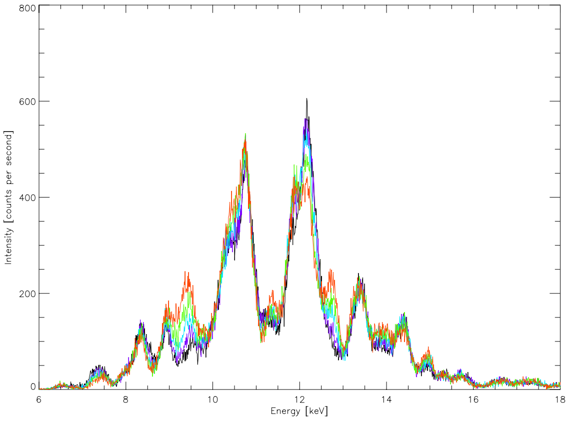

Figure 2: The spectra changes with time: The black line is the first measurement, the red one the last. The change in the spectra is clearly seen, especially at 9keV and 12keV.

taken at an incidence angle of 0.2 deg. The intensity strongly varies as function of energy, indicating the existence of speckles. The various speckle changes as function of time which is the proof for the appearance of a dynamical process induced by the external light. This process must be quantified in future experiments. In case of success white beam correlation spectroscopy could provides the advantage of stable illumination conditions during the whole experiment and the potential for detecting the *q*-dependence of the speckle dynamics from one and the same experiment.

Reference:

[1] T. Panzner, W. Leitenberger, J. Grenzer, U. Pietsch, *J. Phys. D Appl. Phys.*2003, *36*, A93

[2] Dirk O. Riese, Willem L. Vos, Gerard H. Wegdam, Frank J. Poelwijk, *Phys. Rev. E* 2000, *61*, *p*.1676-1680

[3] O. Henneberg, et al., *Z. Kristallogr.* 2004, *219*, 218-223

Study of segregation process in $Ni_{94}Pd_6$ foil using XPS

G. A. Dosovitskiy,[1] L. I. Burova,[1] M. Fonin,[2] Yu. S. Dedkov,[3] U. Rüdiger,[2] A. R. Kaul[4]
[1] *Department of Material Sciences, Lomonosov Moscow State University,*
119899 Moscow, Russia
[2] *Fachbereich Physik, Universität Konstanz, 78457 Konstanz, Germany*
[3] *Institut für Festkörperphysik, Technische Universität Dresden, 01062 Dresden, Germany*
[4] *Chemical Department, Lomonosov Moscow State University, 119899, Moscow, Russia*

The discovery of high temperature superconductivity (HTSC) in 1986 [1] have atttracted sufficient interest to materials possessing HTSC properties, among them $YBa_2Cu_3O_{7-\delta}$. A number of technological applications, such as power cables, motors, transformers, fault current limiters [2] require long current-carrying wires with superconducting properties. Several approaches to produce long superconducting cables[3], and the second generation HTSC cables (coated conductors) [3,4] are of the highest interest at the present moment. A promising way to obtain coated conductors is so-called rolling assisted biaxially textured substrates (RABiTS) technology [5], which is based on the deposition of multilayer structures on biaxially textured tapes of Ni-alloys as substrates. The main point of this concept is translating the texture of a metal tape to a buffer layer and then to an HTSC layer. The Ni-alloy tape should be highly textured with sharp (100) cubic texture in oreder to ensure good quality of HTSC layer. RABiTS technology is very sensitive to the surface quality of the Ni-tape. For example Ni oxidation can significantly influece the texture of the buffer layer. Noble metal, such as Pd, are used as dopants in order to increase the tape stability against oxidation. In the catalytic chemistry Ni-Pd system is widely used. Recently structure and chemical composition of $Ni_{92}Pd_8$ single crystal surface was investigated [6]. In this study intensities of Ni 2*p* an Pd 3*d* peaks were measured by x-ray photoelectron spectroscopy (XPS) as a function of emission angle. These measurements have shown that Pd segregates on the single crystal surface. Pd concentrations of about 28 at.% and 38% were observed on the (111) and the (110) surface, respectively. According to the LEIS data Pd concentration in the surface layerwas even higher (up to 81 at.%). High Pd concentration in the surface layer makes the crystal surface more stable against oxidation in comparisson with the pure Ni surface.

Until now Pd segregation process have been investigated on NiPd single crystals, so it is still unknown how the additional factors such as polycrystallinity and high degree of mechanical deformation may influence the segregation process. The main goal of the present study was to investigate segregation process in Ni-Pd textured polycrystalline samples.

XPS experiments were carried out at room temperature (RT) at the RGBL-PGM beamline at the BESSY II storage ring. The RGBL-PGM dipole beamline provides a tunable source of photons over a 20-1500 eV energy range with a linear polarization of the light. The UHV system located at the Russian-German Laboratory (base pressure of 1×10^{-10} mbar) was equipped with a 127° CLAM4 analyzer. The total energy resolution in the XPS measurements was set to 100 meV. The position of the Fermi energy was determined form the valence-band spectrum of a polycrystalline Au foil in the electrical contact with the sample. Ni-Pd samples were prepared by cold rolling of rods of $Ni_{94}Pd_6$ alloy (60 cycles, ~99% deformation) followed by texturing annealing. The sample $Ni_{94}Pd_6$ was annealed in Ar/H_2 atmosphere at 1100^oC for about 1 hour (texturing annealing) and subsequentally at 600 ^oC for 6 hours (texturing annealing).

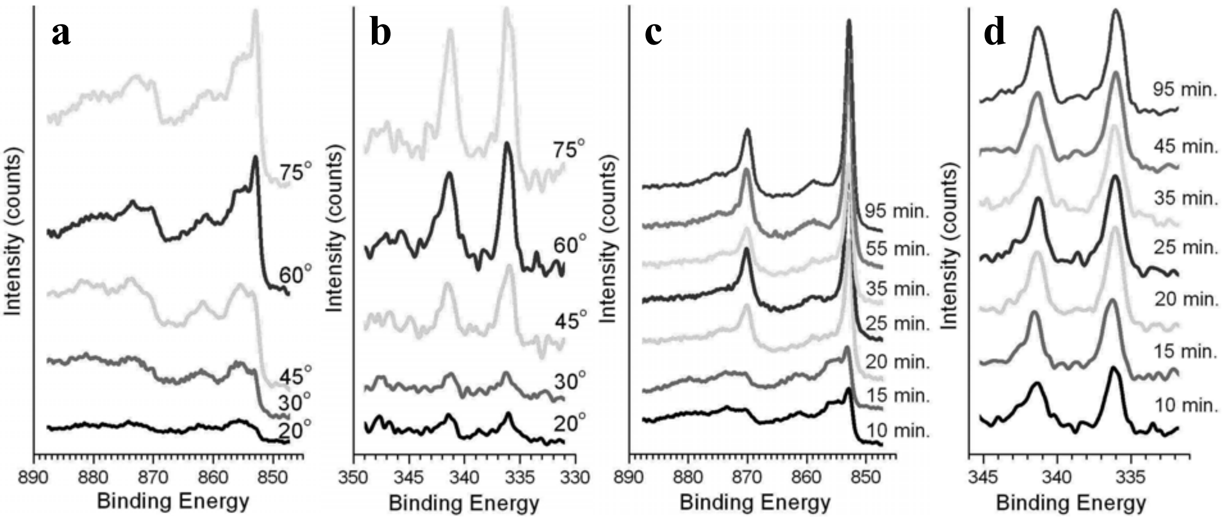

Fig. 1. Photoemission spectra taken on the $Ni_{94}Pd_6$ sample at different photoemission angles: (a) Ni 2p peak,(b) Pd 3d peak, and as a function of sputtering: (c) Ni 2p peak, (d) Pd 3d peak.

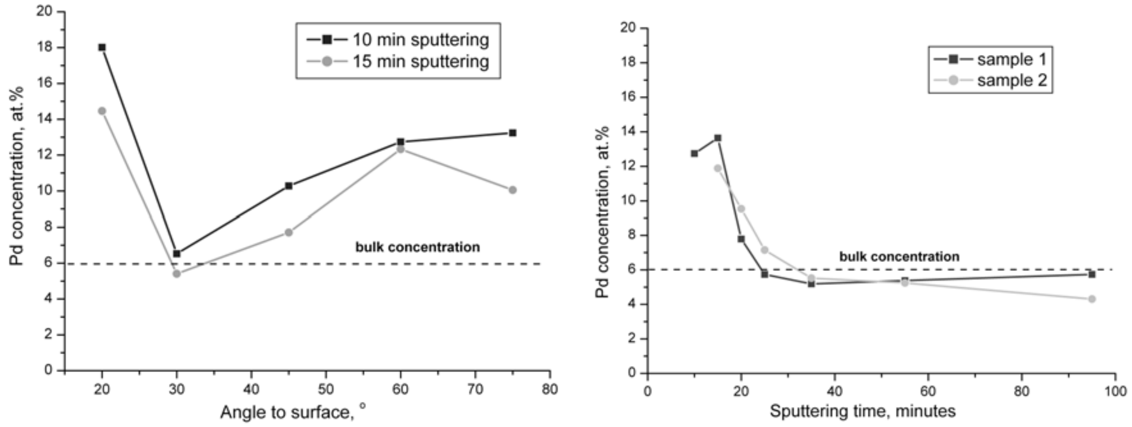

Fig. 2. Pd concentration depth profiles obtained by photoemission intensity analysis of the Ni 2p and Pd 3d peaks: as a function of the photoemission angle (left-hand panel) and as a function of the sputtering time (right-hand panel).

After the introduction into the UHV S, C and O ipurity peaks were found on the sample surface. O and C are common surface impurities, and S is an impurity, which is usually present in Ni. After the Ar^+ sputtering the intensities of impurity peaks decreased significantly.

Ni 2*p* and Pd 3*d* peak intensities depending on electron emission angles were measured to study the concentration in-depth profile [Fig. 1 (a) and (b)]. The series of spectra after differnet Ar^+ sputtering times were taken for the same purpose. Pd concentration was calculated from Ni $2p_{3/2}$ and Pd $3d_{5/2}$ peaks intensities[Fig. 1 (c) and (d)]. Fig. 2 shows Pd concentration depth profiles obtained by photoemission intensity analysis of the Ni 2*p* and Pd 3*d* peaks: as a function of the photoemission angle (left-hand panel) and as a function of the sputtering time (right-hand panel). It could be seen from the concentration depth profiles, that Pd segregates on the Ni surface. Inelastic mean free path calculated from the Tanuma, Powell, and Penn formula in [7] for electrons with energies 140 eV (Ni2p electrons) and 660 eV (Pd3d electrons) are 4,58 Å and 11,35 Å respectively. It means, that information, obtained from angle dependences, refers to 2 atomic layers. It could be supposed, that the data from fig. 2 (a) approves the model of oscillatory distribution of Pd on the surface of Ni-Pd alloy [8].

1. J. G. Bednorz and K. A. Muller, Physica B **64**, 189 (1986).
2. M. Chen, L. Donzel, M. Lakner, W. Paul, J. Eur. Ceram. Soc. **24**, 1815 (2004).
3. L. J. Masur *et al.*, Physica C **392–396**, 989 (2003).
4. T. Watanabe et al., IEEE Transactions on Appl. Superconductivity **13**, 2445 (2003).
5. D. K. Finnemore *et al.*, Physica C **320**, 1 (1999).
6. A. C. Michel et al., Surf. Sci. **416**, 288 (1998).
7. S. Tanuma, C. J. Powell, D. R. Penn, Surf. Interf. Anal. **21**, 165 (1993).
8. G. N. Derry, C. B. McVey, P. J. Rous, Surf. Sci. **326**, 59 (1995).

Computed tomography experiments at BAM*line*

G. Weidemann, J. Goebbels, H. Riesemeier, Th. Wolk, M. Bartscher, U. Hilpert**
Bundesanstalt für Materialforschung und -prüfung (BAM)
Unter den Eichen 87, 12205 Berlin, Germany
* Physikalisch-Technische Bundesanstalt (PTB)
Bundesallee 100, 38116 Braunschweig, Germany

Photo resist negatives of micro gears have been studied to evaluate the geometrical shape. The measurements were performed with 15 keV X-ray energy and voxel sizes of $(3.6\ \mu m)^3$ and $(1.5\ \mu m)^3$. From the resulting 3D voxel data set a surface mesh was extracted and stored in the stereo-lithography file format (‘stl’ – format), which is commonly used for surface representations.
Fig. 1 shows a cross section (3.6 µm voxel size) from the 3D image data set.

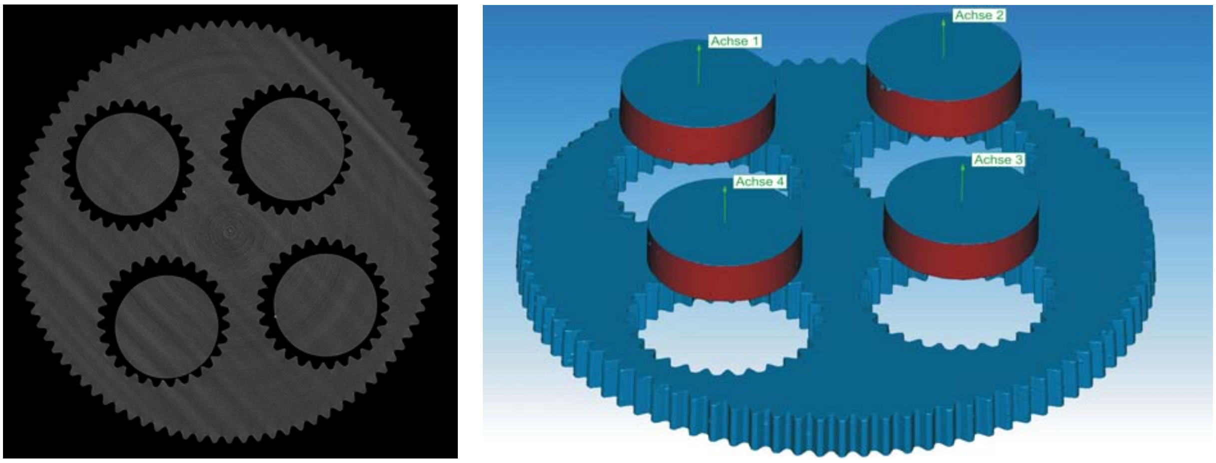

Fig. 1: Cross section (left) of a micro component, outer diameter about 6.5 mm. Conversion of CT data to stl-data format and segmentation of the four cylinders (right).

From the surface mesh data set the four cylinder geometries are segmented. To study the deviation of geometry the cylinder geometries are compared each with each other. As an example fig. 2 shows the deviation of the geometry of cylinder 1 from cylinder 2. The deviations are colour coded. The colour scale extends from –10 µm (dark blue) to +10 µm (dark red). Smaller details of the geometry were studied with improved spatial resolution (voxel size $(1.5\ \mu m)^3$).

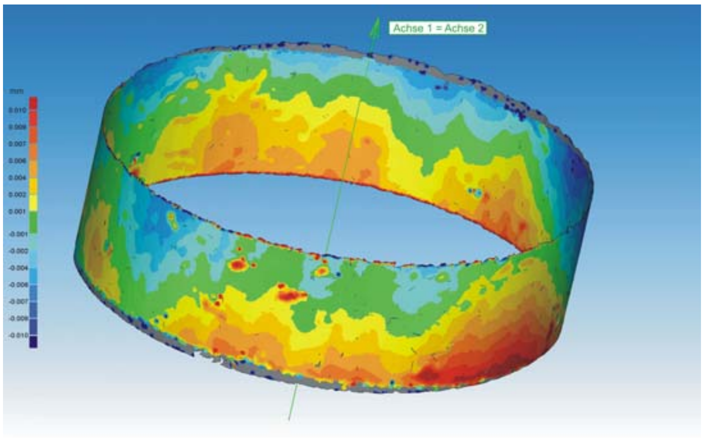

Fig. 2: Evaluation of cylinder geometry; comparison of cylinder 1 with cylinder 2.

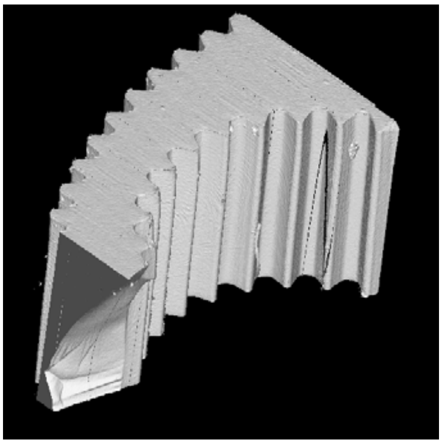

Fig. 3: Iso-surface of a detail with improved spatial resolution

The spatial resolution of the CT set-up was further improved using new scintillators together with other lens optics in cooperation with HMI. Now a voxel size of $(0.6\ \mu m)^3$ is available. As an example fig. 4 shows a spore studied with 9 keV in cooperation with TU Leipzig.

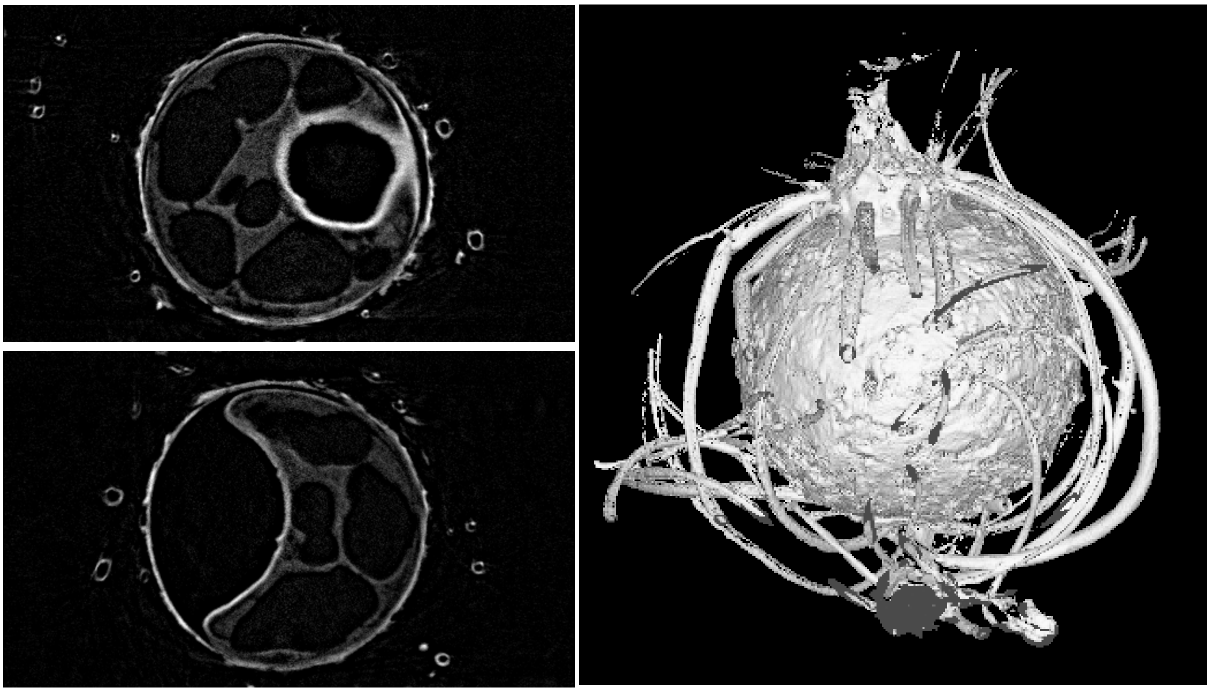

Fig. 4: Two cross sections and an iso-surface visualisation of a spore.

Inorganic contact formation on oriented organic films

S. Berkebile, J. Ivanco, G. Koller, M.G. Ramsey
Institut für Physik, Karl-Franzens-Universität Graz, A-8010 Graz, Austria

HPRI-CT-1999-00028

Oligomers such as sexiphenyl (6P) and sexithiophene (6T) are attracting renewed interest not only as models for their related polymers, but also in their own right as active materials in organic devices such as FETs, LEDs and solar cells. The bonding interaction at the organic-inorganic interface has been shown to be important to the electronic properties via the band alignment [1], and there is much interest regarding molecular geometry in this interfacial region as it is crucial to many aspects of organic devices, from charge injection and transport to thin film growth. The corresponding interface of inorganic on organic, the formation of a top contact, however, remains less explored. Given that the surface free energies of organics are between one to two orders of magnitude lower than for metals it should be all but impossible to form metallic wetting layers on organic films. In earlier work we have shown that Al (a common contact in organic devices) does not wet vertically oriented sexiphenyl. However, when evaporated in oxygen environment (10^{-7} mbar) ultra-thin, conducting wetting layers could be produced [2]. Our goal was to explore the formation of contact layers on organics in a controlled manner for a number of different materials on sexithiophene and sexiphenyl films with known molecular orientations.[3][4]

Here we report an investigation into the formation of ultra-thin metallic films of Ti on pristine 6P(001) and Al on 6P(001) using a layer of LiF as a surfactant. Ti is increasingly used in the semiconductor industry as a contact material; and layers of LiF often proceed the metal evaporation to improve device characteristics, yet it is unclear as to what is occuring at this interface. The 6P(001) orientation is such that the molecular axes are tilted 17° w.r.t. the surface normal of the underlying substrate [3] and organic film thicknesses were chosen such that the underlying substrate is spectroscopically covered (i.e. a closed film was produced). Molecular orientation was observed with NEXAFS prior to and after metal evaporation. The surfaces were prepared in-situ under UHV and investigated in the MUSTANG end station attached to the Russian-German beamline. 6P was evaporated using a home-made triple source Knudsen cell type evaporator. Ti, Al and LiF were evaporated using an Oxford e-beam evaporator. SXPS, UPS and CK-edge Auger yield NEXAFS spectra were obtained using a SPECS Phoibos 150 electron energy analyzer with an overall resolution of <0.1eV.

The incremental deposition of Ti on a 6P(001) substrate was monitored by SXPS and NEXAFS. Figure 1 displays the development of the C1s and Ti2p core levels as a function of

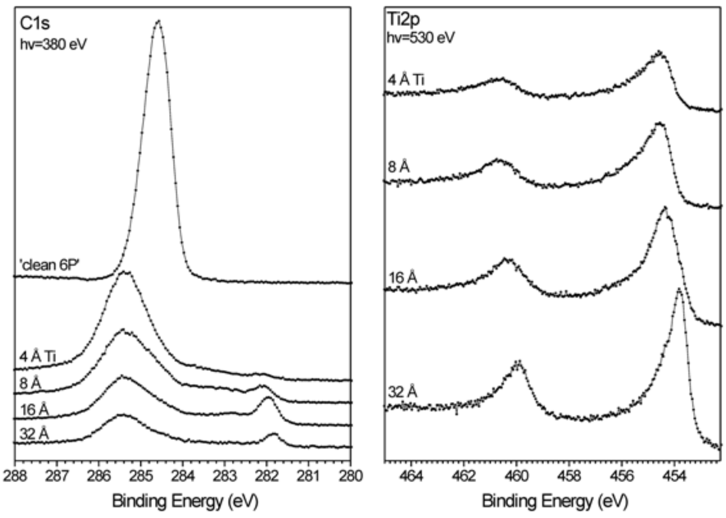

Fig 1: *The development of the C1s and Ti2p core levels as a function of Ti coverage on 6P(001) as observed by SXPS.*

the Ti coverage. The C1s intensity decreases rapidly with increasing Ti coverage. At an initial coverage of 4 Å, it has about half the intensity with a tail at lower BE, indicative of a chemical reaction with the Ti. On increasing coverage, the quanitity of reacted components increases to a coverage of 16 Å of Ti and becomes increasingly one species at 282 eV, suggestive of the formation of TiC. The Ti2p intensity increases and shifts to lower BE with coverage implying a transition from TiC to metallic Ti. At a coverage of 16 Å, the broad Ti2p peak suggests both TiC and metallic Ti are present. This transition to metallic Ti after 32 Å of Ti is also seen in the decrease in intensity of the carbidic peak of the C1s spectrum (282 eV), from which we infer that the TiC remains buried at the interface and is covered by a metallic contact layer, also indicated by the sharp Ti2p peak at the metallic BE. Dramatic changes in the NEXAFS spectra, particularly in the π^* resonances, also indicate a chemical reaction with the 6P film.

The deposition of 2.5 Å of LiF and the subsequent incremental deposition of Al on a 6P(001) substrate was also monitored by SXPS and NEXAFS. In Figure 2, the development of the C1s, Al2p, Li1s and F2s core levels are shown as a function of LiF and Al deposition. After 2.5 Å of LiF is deposited on a 6P film, the C1s peak shifts significantly by 1.1 eV to higher BE, suggesting the Li is diffusing into the film and doping the 6P at the interface. The shoulder remaining at the pristine 6P C1s position hints at deeper layers of undoped 6P. A doping effect is further supported by the appearance of states in the bandgap of the 6P just below the Fermi level (not shown). In addition to this electronic effect, the NEXAFS also suggests a disturbance in molecular orientation which becomes more marked after Al deposition. As Al is deposited on top of the LiF/6P(001), the development of a metallic Al2p peak is steady and gradual. At a small coverage of 3 Å Al, the Al2p peak is at a higher BE than metallic Al and the spin-orbit splitting is unresolved, suggestive of charging in an electrically discontinuos film. As the Al coverage is further increased, the Al2p peak gradually shifts to the metallic position and the spin-orbit splitting becomes more apparent until, at a coverage of 38 Å Al, it is well resolved, indicating that a continuous conductive metallic layer has been formed. This is supported by a concurrent decrease in the intensity of the C1s, Li1s and F2s core levels. We note that a continuous metallic layer could not be achieved if Al was directly evaporated on 6P(001).[2]

Here our studies have shown that LiF, which is often used in device production to improve contacts, acts in two ways: the lithium dopes the 6P causing a large band offset favourable for e-injection and the layer of LiF allows the Al evaporated on this surface to form a continuous layer. Also, Ti evaporated onto 6P(001) forms a TiC capping layer on which a continuous metallic Ti film grows.

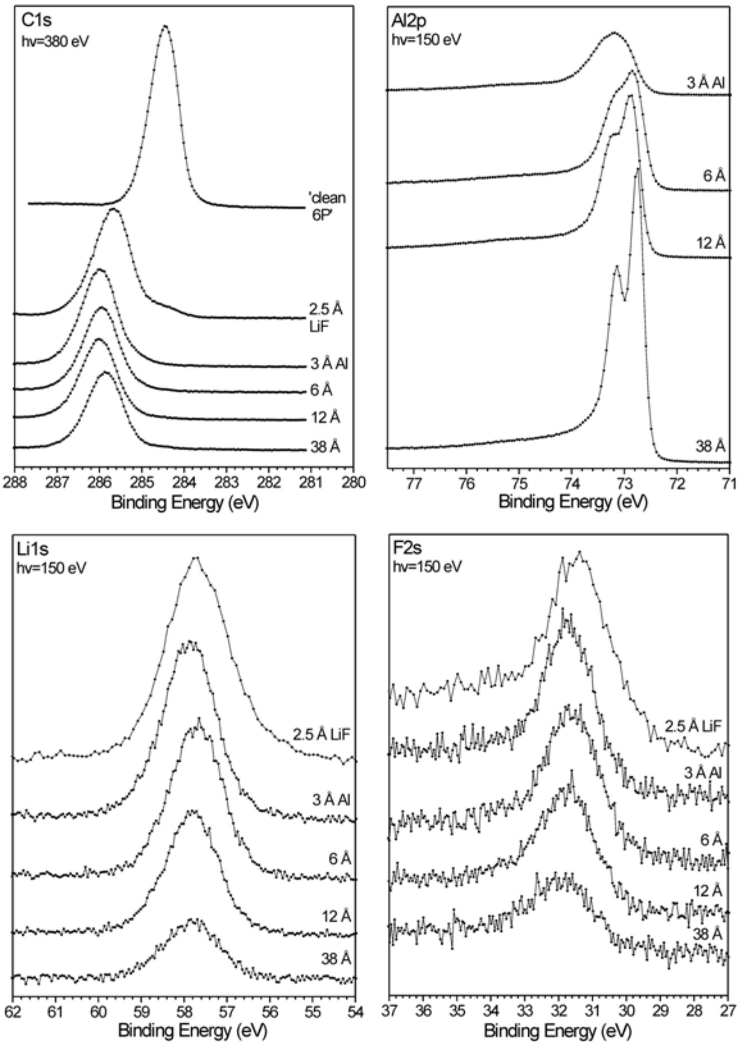

Fig 2: *The development of the C1s, Al2p, Li1s and F2s core levels as a function of LiF and subsequent Al coverage on 6P(001) as observed by SXPS.*

Acknowledgments: This work has been supported by the Austrian Science Foundation (FWF) and the EU via HPRI-CT-1999-00028. The assistance of Mike Sperling with the MUSTANG chamber and the beamline staff at the RG-BL is gratefully acknowledged.

References:

1) G. Koller, R.I.R. Blyth, A. Sadar, F.P. Netzer, M.G. Ramsey, Appl. Phys. Lett. **76** (2000) 927.

2) J. Ivanco, B. Winter, F.P. Netzer, L. Gregoratti, M. Kiskinova, M.G. Ramsey, Appl. Phys. Lett. **85** (2004) 585.

3) G. Koller, S. Berkebile, G. Tzvetkov, M.G. Ramsey, Bessy Report 2003; G. Koller, S. Berkebile, F. Pfuner, M.G. Ramsey, Bessy Report 2004.

4) B. Winter, S. Berkebile, J. Ivanco, G. Koller, F.P. Netzer, M.G. Ramsey, Appl. Phys. Lett. Submitted 2006.

Exotic growth mode in molecular-beam epitaxy of GaMnSb on GaSb

Wolfgang Braun[⋆], **Bernd Jenichen**, **Achim Trampert**, **Dillip Kumar Satapathy**,
Klaus H. Ploog
Paul-Drude-Institut für Festkörperelektronik, Hausvogteiplatz 5-7, D-10117 Berlin, Germany
⋆ email: braun@pdi-berlin.de, phone: +49-(0)30-20377-366, fax: +49-(0)30-20377-366.

To make use of the spin in addition to the charge in future spintronic devices, the preparation of a defined spin state of the charge carriers is required. One option to achieve this is to inject spin-polarized carriers into a semiconductor, an operation that presumably requires the fabrication of a highly perfect interface between a ferromagnetic injector and a semiconductor. MnSb offers the advantage of a much higher Curie temperature (851 K) compared to MnAs (313 K). Just as in the MnAs case, the use of a joint element between film and substrate material offers a convenient way to fabricate heterostructures by MBE. We have therefore studied the deposition of MnSb on GaSb to investigate the interface configuration of this heterostructure.

The results are unexpected and fascinatingly different from the MnAs/GaAs system. MnSb was deposited on a high-quality GaSb(001) buffer layer by opening the Mn shutter under constant Sb flux. The sample temperature was initially 330 °C during MnSb nucleation, and then was increased during the growth to 470 °C. The surface morphology of the resulting structure measured by AFM is shown in Fig. 1. Instead of a continuous film, we observe rectangular patches with strongly rounded corners. These patches usually have a flat upper surface which is either coplanar with the substrate surface or slightly inclined. Some crystals tower above the surface in diferent orientations, exposing hexagonal shapes.

The origin of this peculiar morphology can be clarified by cross-sectional transmission electron microscopy. Images taken from the same sample are shown in Fig. 2. The image reveals homogeneous single crystals of sub-micrometer

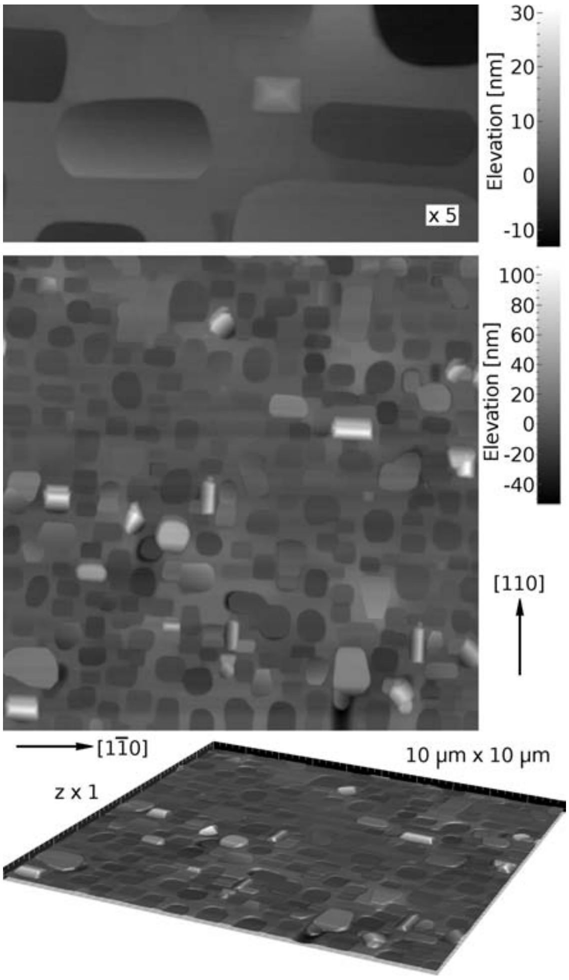

Figure 1: Atomic force microscopy scan revealing the surface morphology of the GaMnSb microcrystals grown into GaSb. Note that the z scale for the 3D rendering is unity, therefore giving an accurate representation of the angles.

size embedded in the surface of the GaSb substrate matrix. Atomic resolution images like the one shown in the top of Fig. 2 allow the analysis of the lattice constants parallel and perpendicular to the surface of both the microcrystals and the substrate matrix. Within the accuracy of such a graphical evaluation, the lattice match perpendicular to the surface is perfect. Laterally, the microcrystal lattice constant perpendicular to the viewing direction is around 5 % smaller than the one of the substrate.

The shape of the buried section is close to hemispherical to minimize the interfacial energy. On the other hand, facets defined by the GaSb (111) planes are also discernible. The difference between the 35.26° the (111) planes make with the surface normal and the 30° of a possible hexagonal microcrystal structure may explain the tilt angles of $\pm 5^\circ$ of some grains as well as the rare atypical orientations in which the a or c axis of the microcrystal is parallel to the GaSb (111) planes. The TEM shows remarkably little strain, within the area sampled by TEM both the microcrystals and the GaSb matrix are free of dislocations.

In situ synchrotron x-ray diffraction performed at the PHARAO beamline during the growth reveals the formation process of the phase-separated embedded microcrystals. Figure 3 shows two $\omega - 2\theta$ in-plane scans around the GaSb $2\,\bar{2}$ peak in reciprocal space along the $[1\,\bar{1}]$ direction of the GaSb substrate. During the nucleation at low growth temperature, the deposited material develops an epitaxial relationship with one of the broad film peaks closely matching the narrow GaSb $2\,\bar{2}$ peak. Additional reflections are present. Upon continuation of the growth at elevated temperatures, the migration process of the deposited material into the substrate matrix becomes evident by the fusion of the substrate and film peaks at $2\,\bar{2}$. The growth at this stage can be performed arbitrarily close to thermodynamic equilibrium, as we have observed the reduction of the deposited material peak when further increasing the substrate temperature during deposition.

The dominant peak at 152.3° (a distance 3.3 % smaller than 2 2 in real space agreeing well with the TEM analysis) does not match a peak

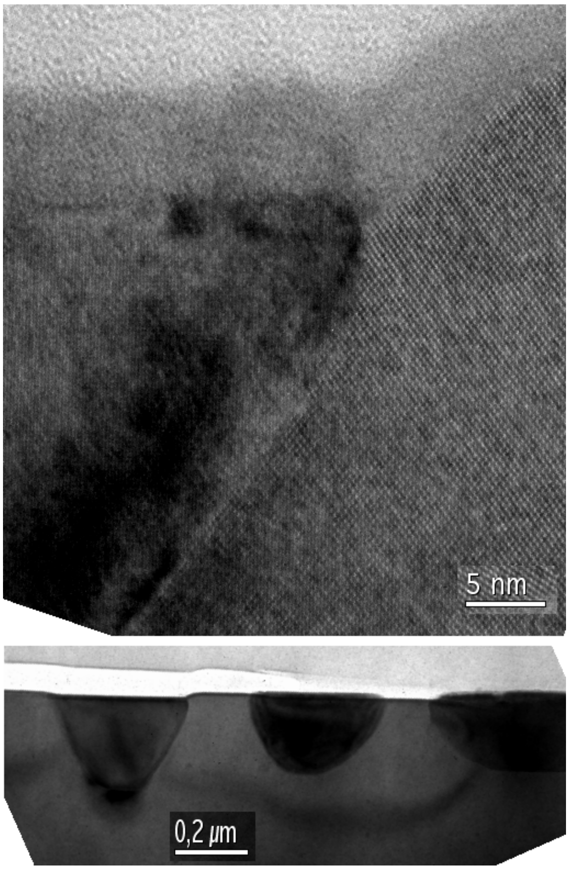

Figure 2: Atomic resolution (top) and overview (bottom) TEM micrographs of the epitaxial microcrystals forming during Mn and Sb codeposition. The microcrystals are homogeneous, single crystal and lattice-matched to GaSb.

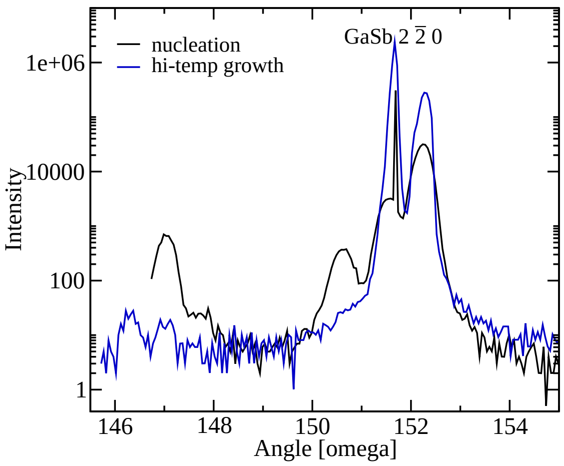

Figure 3: In-situ x-ray diffraction scans along the surface containing reflections from the substrate and the microcrystals. During the nucleation (black curve), an epitaxially oriented structure with additional peaks due to other orientations forms. During growth at elevated temperatures, the substrate and layer peaks merge and other orientations vanish (blue curve).

of MnSb. This suggests that the deposited Mn forms a Ga-Mn-Sb alloy of a composition that minimizes the strain between microcrystals and substrate.

A comparison of $\omega - 2\theta$ scans along the two orthogonal $<2\,2>$ in-plane directions is shown in Fig. 4. It reveals clear differences that cannot be induced by the fourfold symmetry of the substrate matrix. This means that the orientation of the final microcrystals is determined by the initial nucleation on the surface reconstruction that has a twofold symmetry. If the microcrystal orientation were determined by the bulk properties only, no such preference would be expected.

Measurements of the magnetization vs. temperature show strong ferromagnetism of the system even well above room temperature. Between 20 K and 370 K (the measurement range of our magnetometer), the magnetization decreases by a mere 20 %.

Both the microcrystals and the surrounding matrix are highly perfect crystals. To form an alloy, atoms therefore have to migrate into the bulk, unlike the typical MBE growth mode where only surface atoms are considered mobile enough to contribute to the growth. It seems possible that the microcrystals form by migration of Mn along the interface with the GaSb instead of by bulk diffusion through the volume of the microcrystals or the host lattice. Obviously, such a migration could take place along the more stable GaSb(111) planes.

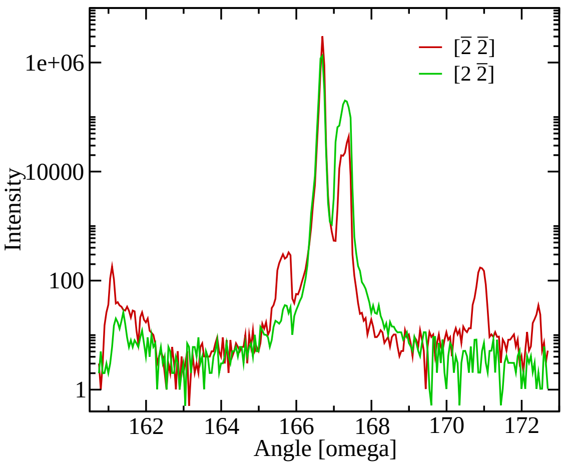

Figure 4: In-plane anisotropy of the microcrystal structure. The different peaks present in the two orthogonal directions indicate a preferential alignment along one of the azimuths.

The exotic growth mode observed here has intriguing and far-reaching implications. Both bulk migration and the growth of highly perfect epitaxial crystals into the substrate are concepts that are not common in MBE. A system that self-adjusts its lattice constant to minimize defects at the interface is ideal for the formation of heterostructure devices. Since one of the materials involved is ferromagnetic and the other is a high mobility semiconductor, the growth mode presented here has a high potential for spintronic device technology. Using the mechnism demonstrated here, it may even be possible to form very high quality epitaxial contacts by mere alloying of prepatterned Mn into GaSb under an Sb flux following a photolithographic process.

Analysis of binding media in cross sections using synchrotron infrared radiation

Oliver Hahn[1], Jens Bartoll[2], Ulrich Schade[3]

[1]Bundesanstalt für Materialforschung und –prüfung (BAM),12200 Berlin
[2]Stiftung Preußische Schlösser und Gärten Berlin-Brandenburg (SPSG), 14414 Potsdam
[3]BESSY GmbH, Albert-Einstein-Straße 15, 12489 Berlin

The present study is the continuation of a project dealing with the analysis of binding media in cross sections. Cross sections are small samples extracted from art objects embedded in a matrix of resin. The characterisation of different organic compounds in different layers of the cross sections is of special interest in conservation science and art history. Usually binding media are identified by infrared spectroscopy in transition mode. For this purpose it is necessary to separate each layer from the other mechanically which is very difficult or often impossible because of the smallness and complexity of the samples.

Usually only microscopic methods are applied to study the inorganic pigment grains within the cross section. Until now there are no satisfying methods for the analysis of organic compounds in cross sections. The method described here presents a direct investigation without any mechanical separation in high local resolution by using infrared spectroscopy in reflection.

The measurements were performed at the synchrotron infrared beamline IRIS. A FTIR spectrometer (Bruker 66/v) and an IR microscope (Thermo Nicolet Continuum and Nexus) were used. Selected samples of typical binding media such as dry oil, resins, and glues were measured in order to collect reference data. In addition, the half of each sample was sputtered with gold. The golden surface was measured for background correction.

The results indicate that it is possible to distinguish different classes of binding media using this method. Two examples are shown in Figures 1a/b and 2a/b. Spectra of gelatine and shellac in original furniture coatings could be detected. They fit well to the spectra of the reference samples. However, the reliable identification of oil coatings causes difficulties (Fig. 3). The specific surface properties of binding media containing oil might influence the process of reflection.

All in all these results indicate that this technique provides a suitable method for organic analyses with high lateral resolution in the field of archaeometry.

Acknowledgements

The authors thank Alexander Firsov for his versatile support.

References

S. Wülfert, Der Blick ins Bild, Lichtmikroskopische Methoden zur Untersuchung von Bildaufbau, Fasern und Pigmenten, Bücherei des Restaurators Bd. 4, U. Schießl (Hrsg.) Ravensburger Buchverlag 1999.

M.R. Derrick, D. Stulik und J.M. Landry, Infrared Spectroscopy in Conservation Science, The Getty Conservation Institute Los Angeles (ed.) 1999.

J. Bartoll, O. Hahn, U. Schade: Analysis of binding media in cross sections using synchrotron infrared radiation, in preparation.

Figures

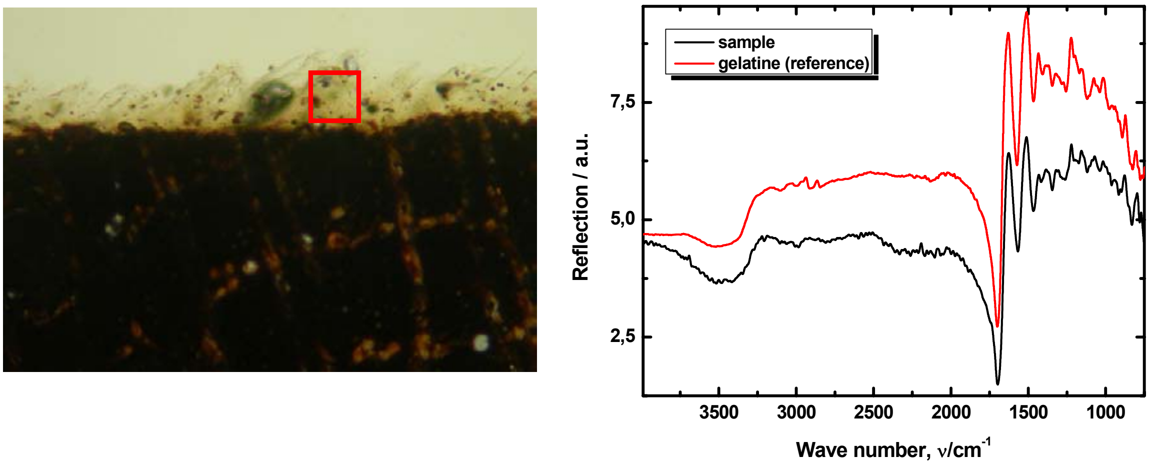

Fig. 1a/b: Cross section / Identification of gelatine in a furniture coating (spot size: 20 µm x 20 µm)

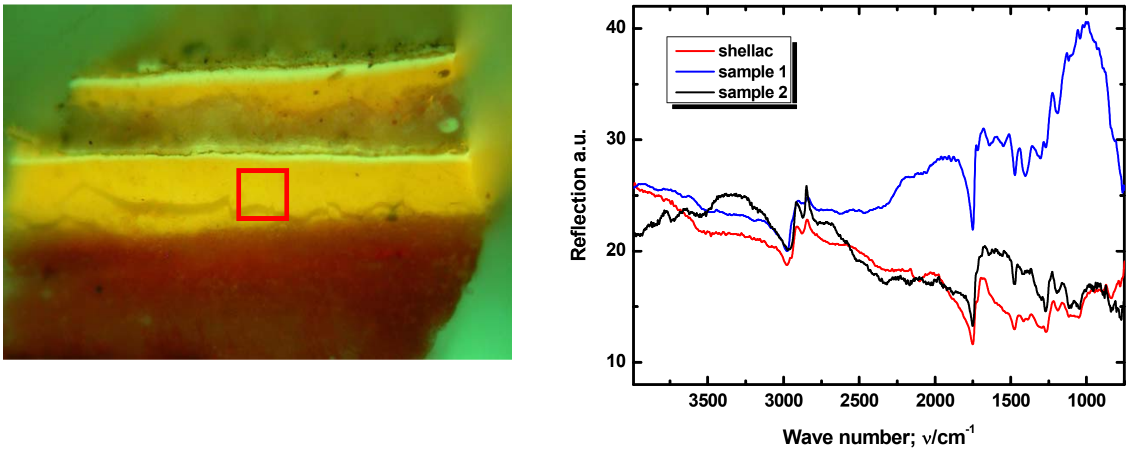

Fig. 2a/b: Cross section / Identification of shellac in furniture coatings (spot size: 20 µm x 20 µm)

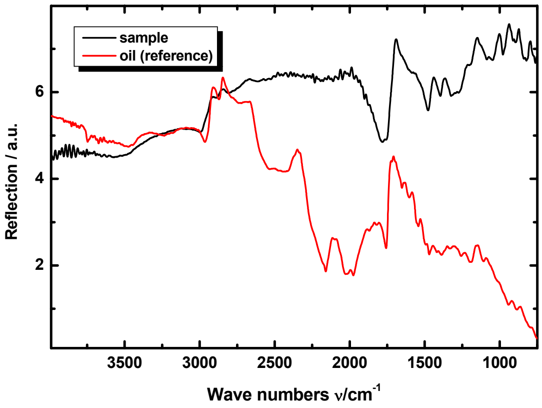

Fig. 3: FTIR-spectra of oil in comparison with an unknown sample (containing probably oil)

Magnetic linear dichroism in the reflectivity of iron and cobalt in the vicinity of the 2p edges

A. Kleibert, P.M. Oppeneer* and J. Bansmann**
Institut für Physik, Universität Rostock, D-18051 Rostock
****Department of Physics, Uppsala University, Box 530, S-75121 Uppsala, Sweden***
*****Abteilung Oberflächenchemie und Katalyse, Universität Ulm, D-89069 Ulm***

Supported by BMBF 05KS4HRA2/4.

During the last decade magnetic soft x-ray spectroscopy techniques have experienced a rapid development. Among the various magneto-optical effects – occurring in absorption, transmission as well as reflection of light by a magnetic sample – particularly the x-ray magnetic circular dichroism (XMCD) in absorption received considerable attention. This is mainly due to the so-called 'sum rules' relating the magnetization dependent absorption of circularly polarized radiation to detailed information on electronic and magnetic ground state properties [1, 2]. In combination with these sum rules, the XMCD allows to study both the spin and the orbital magnetic moments of a material separately in an element-specific manner. Since the magneto-crystalline anisotropy energy (MAE) is connected to the anisotropy of the spin-orbit interaction, XMCD has been used as a valuable tool to investigate the microscopic origin of this fundamental magnetic quantity [3]. Recently, a new 'sum rule' was published connecting the x-ray magnetic linear dichroism (XMLD) directly to the anisotropy of the spin-orbit interaction, thus offering a new opportunity to study the magneto-crystalline anisotropy [4]. Moreover, in contrast to magnetic circular dichroism, the XMLD effect is even in the magnetization and therefore well suited for the study of antiferromagnetic materials.

Since the magneto-optical properties of a magnetic sample (in transmission, absorption, and reflection) are determined by one and the same dielectric tensor, the information that can be obtained from XMCD/XMLD absorption experiments, is also accessible by means of corresponding reflectivity based techniques. Reflectometry-based experiments benefit especially from the large probing depth being solely limited by the penetration depth of the radiation. They are therefore well suited to study capped samples or buried layers in multilayers, respectively. Moreover, measurements of the reflectivity are not disturbed by large external magnetic fields [5, 6]. Recently, we demonstrated the possibility to use the transverse magneto-optical Kerr-effect in the vicinity of the $2p$ core levels of ultrathin Co films as an alternative to XMCD photoabsorption experiments [7, 8]. In this contribution we present recently obtained experimental results concerning the XMLD and its manifestation in corresponding reflectivity measurements. The XMLD effect usually occurs in absorption experiments where the polarization plane is aligned first parallel and then perpendicularly to the magnetization of a sample. In the case of $3d$ transition metals the measurable XMLD effect is quite weak (in the order of 3%), thus making high demands on experimental investigations when quantitative analysis is desired [9].

The experiments have been carried out at the PM3 dipole beamline with the BESSY polarimeter chamber [10]. Sputtered iron and cobalt films with a thickness of about 200 Å have been investigated, both samples were capped with a chromium layer of ∼30 Å. Absorption and reflectivity spectra have been recorded simultaneously by means of total electron yield detection and a photodiode, respectively. An external magnetic field could be applied parallel as well as perpendicularly to the plane of incidence. In the upper panel of figure 1 reflectivity spectra of s-polarized light for both orientations of the magnetization are shown as red (transverse magnetization) and black dashed (longitudinal) lines. The complex shape of the reflectivity spectra is generally determined by interference effects. Note that reversing the magnetization in the transverse or longitudinal direction will not result in any intensity change in this geometry. However, rotating the magnetization from longitudinal to transverse orientation obviously gives rise to a remarkable intensity change, especially in the vicinity of the Fe $2p_{3/2}$ edge (cf. inset in the upper panel). The corresponding asymmetry given by the blue line in the lower panel of figure 1 shows values of up to 40%, and thus is an order of magnitude larger than the XMLD in absorption. Moreover, the observed intensity change depends strongly on the angle of incidence as well as on the polarisation (not shown here). Similar effects have been observed when investigating the cobalt films. The data therefore underline the promising potential of magneto-optical reflectometry when compared to the weak effects in absorption experiments. Moreover, they will probe recent predictions on the shape of XMLD spectra [11]. A detailed, quantitative analysis of the data and an explanation of the magnitude of the observed effects will follow in the near future.

References:

[1] P. Carra et al., Phys. Rev. Lett. **70**, 694 (1993).
[2] B.T. Thole et al., Phys. Rev. Lett. **68**, 1943 (1992).
[3] J. Stöhr, J. Magn. Magn. Mat. **200**, 470 (1999).
[4] G. van der Laan et al., Phys. Rev. Lett. **82**, 640 (1999).
[5] J. B. Kortright et al., Phys. Rev. B **62**, 12216 (2000).
[6] P.M. Oppeneer et al., Phys. Rev. B **67**, 052401 (2003).
[7] A. Kleibert et al., Phys. Rev. B **72**, 144404 (2005).
[8] A. Kleibert, Dissertation, Universität Rostock (2006).
[9] S. S. Dhesi et al., Phys. Rev. Lett. **87**, 067201 (2001).
[10] F. Schäfers et al., Appl. Opt. **38**, 4074 (1999).
[11] J. Kunes et al., Phys. Rev. B **67**, 024431 (2003).

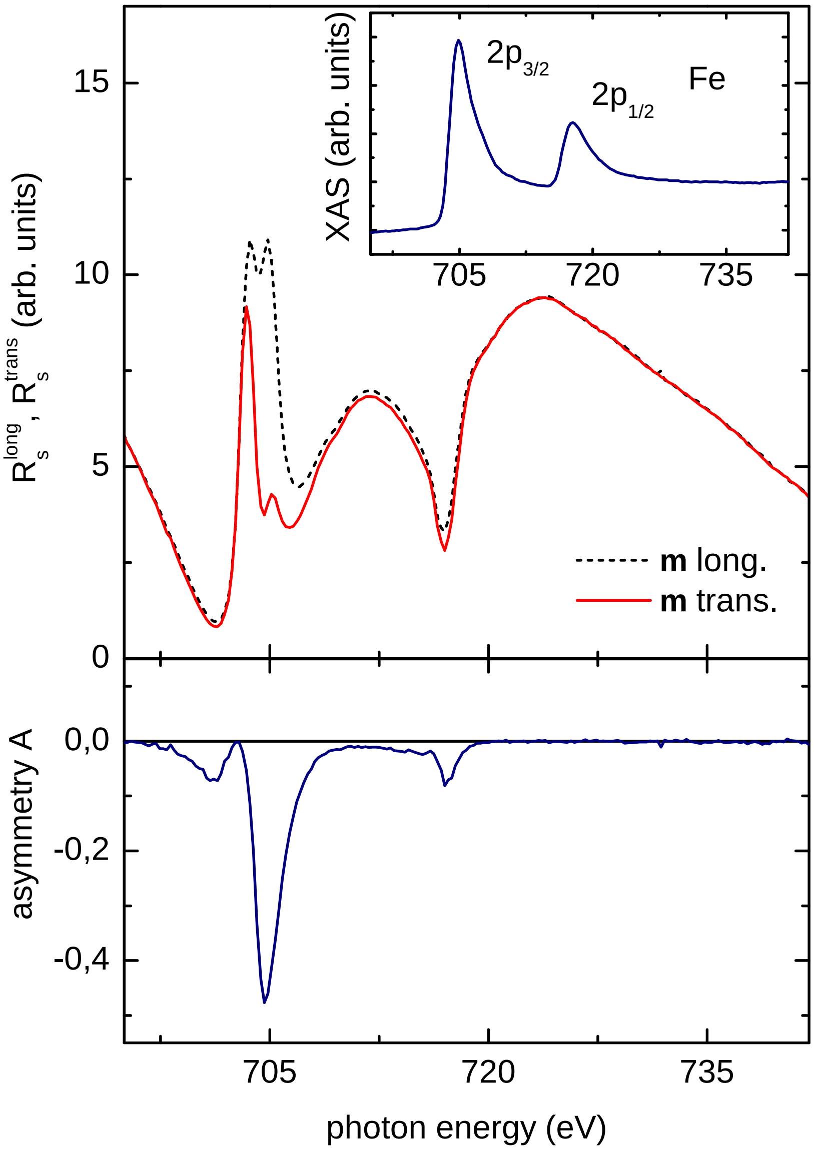

Figure 1: Top: Reflectivity spectra of s-polarized light with longitudinal (black dashed line) and transverse (red line) magnetization. The inset shows the absorption peaks in the vicinity of the $2p$ Fe edges. Bottom: The calculated XMLD asymmetry of the reflectivity spectra shows large values of up to 40%. The angle of incidence was 20° with respect to the surface plane.

High-pressure XPS of transparent conducting oxides: Fermi level position and composition at ITO surfaces

Y. Gassenbauer, R. Schafranek, A. Klein
Darmstadt University of Technology, Institute of Materials Science, D-64287 Darmstadt

S. Zafeiratos, M. Hävecker, A. Knop-Gericke, R. Schlögl
Fritz-Haber Institut, Department of Inorganic Chemistry, D-14195 Berlin

Tin-doped indium oxide (In_2O_3:Sn or ITO) is a degenerately doped semiconductor with a high transparency in the visible optical regime. Its high electron concentration of up to ~ $10^{21}cm^{-3}$ is obtained by substitutional doping with tin. ITO is largely used as a transparent electrode in optoelectronic thin film devices and also as sensor material. For these applications the electric surface potentials (Fermi level and vacuum level) are important. The use of ITO in organic light emitting diodes (OLEDs) combines two apparently excluding properties: The bulk of ITO needs to be as conducting as possible requiring a Fermi level as high as possible with respect to the band edges or the vacuum level. In contrast, the low injection barrier is reached by a Fermi level at the interface to the organic conductor as low as possible. Obviously both features can be combined using ITO. In order to assess the influence of ITO on the stability of OLEDs, the influences which change the ITO surface potentials must be understood. ITO thin films deposited by radio frequency magnetron sputtering exhibit changes of up to ~ 1 eV in XPS binding energies depending on deposition conditions when measured in-situ directly after deposition [1]. The Fermi level in these measurements is found as low as ~ 2.2 eV above the valence band maximum for the most strongly oxidized samples. These large shifts are interpreted in terms of a surface depletion layer and a change of the Fermi level position with respect to the band edges.

At BESSY we have investigated the changes of the ITO surface potentials using high-pressure XPS. The experiments were performed at the U49/2-PGM 2 undulator beamline. The photoelectron spectrometer system uses a differentially pumped lens system. ITO films prepared at 400 °C substrate temperature with pure Ar as sputter gas have been used for the experiments. Samples were heated using light from a laser diode array fed into the vacuum system with a glass fiber and placed ~ 2 mm before the entrance slit of the electron lens system. All spectra were recorded in normal emission. Hydrogen and oxygen gas was dosed via leak valves. For measurements at pressures above 0.1 Pa, the pumping speed was reduced by closing the valve between the measurement chamber and the turbomolecular pump. Residual pumping was thereby maintained through the small entrance slit of lens system. Pressures were measured using a Pfeiffer PKR full range gauge at lower pressures and a Baratron at higher pressures. All spectra were recorded using a photon energy of $h\nu = 600$ eV to avoid changing of the excitation energy because of the importance of energy calibration.

An overview of ITO surface potentials where the ITO was exposed to different gases with changing pressure and substrate temperature is shown in Figure 1. Here the core level and valence band maximum binding energies were determined after a saturation of the shifts was almost reached. Three important features are noticed: i) As expected oxygen leads to a lowering of the Fermi energy in the band gap whereas hydrogen raises the Fermi level and thus reduces the surface. ii) The variation in binding energy for the In 3d core line is significantly lower than variation of the valence band maximum. This phenomenon is explained by a screening of the core holes caused by metallic surface states [2]. iii) At higher temperature the surface seems to be stronger oxidized. This unexpected behavior has been reproducibly observed in different gas environments and for different samples. However, at present we can not give an explanation.

The change of the $In3d_{5/2}$ kinetic energy with time as a response to a sudden raise of the oxygen pressure at a substrate temperature of 400 °C is shown in Figure 2. The changes of kinetic energy correspond to changes of the surface Fermi level position, which is the expected mechanism leading to the sensor response of such materials. A high temporal resolution (~5 seconds / spectra) was possible due to the high intensity of the In 3d core-level. The changes occur much slower than expected for adsorption/desorption equilibria. This suggests that the changes are not caused by changes of surface coverage but rather by changes in the substrate oxygen stoichiometry, leading to changes in doping. As this was not expected, the stoichiometry was not recorded systematically during the beamtime. However, we found evidence for changes in the surface tin concentration with gas atmosphere and temperature. The intensity ratio [Sn]/([Sn]+[In]) is plotted in Fig. 3 in dependence on the surface Fermi level position. The changes in E_F are induced by changes in substrate temperature, gas environment (H_2, O_2) and pressure. For substrate temperatures >300°C there is a clear correlation of the surface tin concentration with the position of the Fermi level. Only for a sample temperature of 250°C the tin concentration deviates from the observed general dependence, which is indicated by the dashed line. This can be explained by a too slow diffusion of Sn. The segregation of tin is most likely driven by changes in the surface potential gradient [2].

High pressure XPS allows a detailed insight into the changes of electronic and chemical surface properties of conducting oxides, which can not be directly assessed otherwise. The results from only 1 week of beamtime already revealed several unexpected dependencies, which have and will significantly improve the understanding of these materials and their applications.

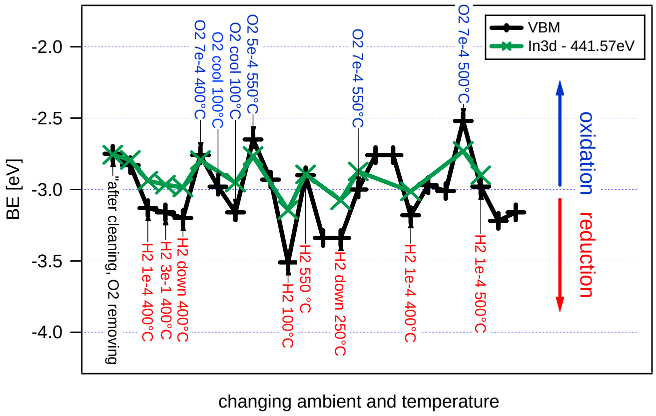

Figure 1: Variation of core level and valence band maximum binding energy with changing temperature and gas exposure.

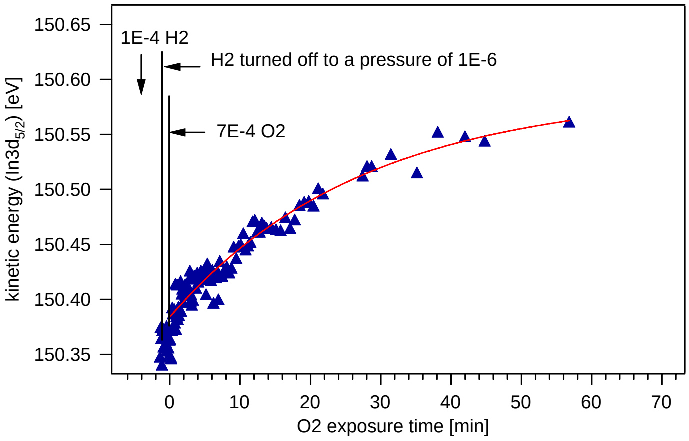

Figure 2: Variation of In3d5/2 kinetik energy with exposure time to pure oxygen ($p(O_2)$ = $7*10^{-4}$ mbar) at a substrate temperaure of 400 °C. Excitation energy hν = 600 eV. The stepwise change of kinetic energy gives a hint on several overlapping processes with different time constants.

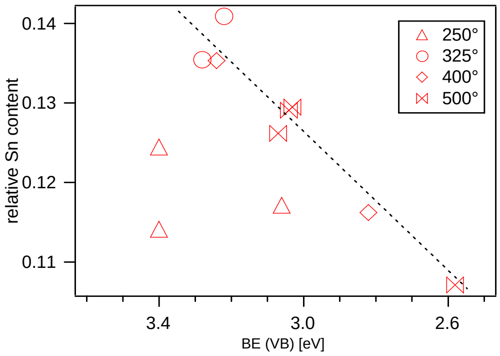

Figure 3: Dependence of relative tin content for different temperatures of Fermi level position. The straight line represents the tin-concentration expected for an equilibrium situation.

[1] Y. Gassenbauer, A. Klein; Solid State Ionics Vol. 173 (2004) pp 141-145
[2] Y. Gassenbauer, R. Schafranek, A. Klein, S. Zafeiratos, M. Hävecker, A. Knop-Gericke, R. Schlögl; Physical Review B, submitted

In situ SXPS and XAS studies of Lithium intercalation and deintercalation in transition metal oxide thin films

Andreas Thißen, David Ensling, Massimiliano Liberatore, Ralf Hunger
and Wolfram Jaegermann

In the last years, the development of thin film rechargeable batteries has attracted a great deal of interest due to their reduced resistivity with respect to bulk materials, and due to the technological perspectives of integration with other thin film devices as rechargeable power supplies for implantable medical devices, CMOS-based integrated circuits, as well as smart IC packages or chips. The transition metal oxides, especially V_2O_5 and $LiCoO_2$, are widely used materials for such technological applications. Fig. 1 (upper row) shows the first discharge of the battery. When discharging the battery, the Li^+-ions are transported through the electrolyte into the cathode material, while the electrons are used in the outer circuit and, while entering the cathode, fill unoccupied states. These changes, together with structural changes, determine the performance of the battery, and are studied in this project. The left picture in the bottom row shows a typical battery design. In principle it is possible to study the properties of the cathode coming from such a setup, but contact with air and moisture has to be avoided. One possible realization of an *in situ* cell connected to the SoLiAS system using liquid electrolyte is shown in the right bottom picture.

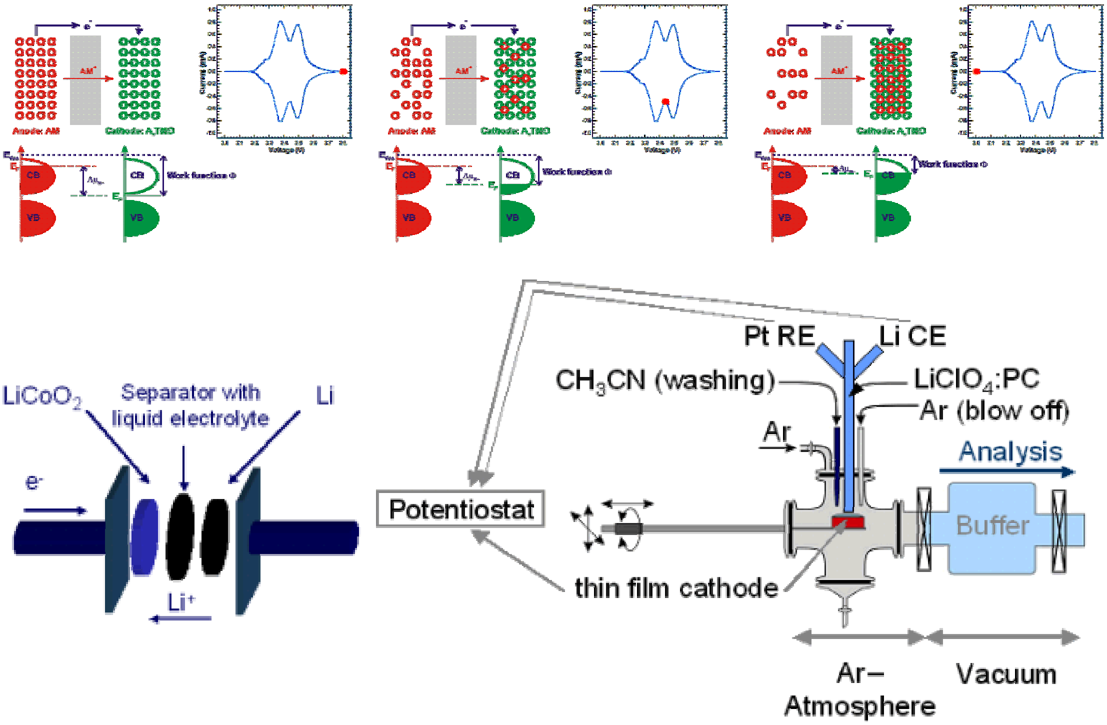

Fig. 1: Upper row: principle of battery operation Bottom row: Standard and in situ battery setup.

As cathode materials thin polycrystalline films of V_2O_5 and $LiCoO_2$ have been deposited onto Cr/glass and Ti foil substrates, respectively, using RF magnetron sputter deposition. As sputter gas mixtures with an Oxygen to Argon ratio of 2:1 and 1:1 have been used, while the substrates were kept at temperature of T=300°C and T=500°C during deposition. The deposition chamber has been directly connected to the SoLiAS setup, so that a sample transfer from deposition to analysis, to the electrochemical cell and back was possible either under UHV conditions or Argon atmosphere, so that contaminations and reaction, especially of the Lithium containing materials has been avoided. Intercalation or deintercalation can therefore be studied by transferring the cathode films to the buffer chamber, venting it with Argon, tranferring in this Argon atmosphere the sample to the electrochemistry cell, mounting the counter and reference electrode, filling the liquid electrolyte (1 molar Lithium perchlorate/propylene carbonate solution) into the electrode, performing a potentiostatic polarization experiment, retracting the counter electrode assembly, washing the sample with acetonitrile and drying in Argon flow. Then the sample returns to the buffer chamber, that is pumped down again to UHV conditions. For this studies SoLiAS was located at the U49/II PGM2 beamline.

Fig. 2 shows SXPS and XAS data of the pristine V_2O_5 film giving an open circuit voltage against Lithium (OCV) of 3.1V, and of three different potentiostatic polarization steps leading to the intercalation phases LiV_2O_5 (polarization voltage 2.5V) and $Li_2V_2O_5$ (polarization voltage 1.7V) and a final deintercalation step leading again to non-intercalated V_2O_5 (polarization voltage 4.0V). Obviously, the Li content rises by lowering the polarization voltage. The intercalated Li atoms transfer their electrons to the host material leading to the formation of V^{4+}-ions (V^{5+} for pristine film). The transferred electron can be found in localized split-off V3d-states in the band gap region at binding energies around 1.5eV. A small amount of Na contamination from the glass electrode can also be detected. After deintercalation of the film most V-ions return to their initial V^{5+} oxidation state. But a significant amount of Lithium stays as Solid-liquid interface (SEI) layer at the surface, mainly formed of Li_2CO_3 and Li_xO_y.

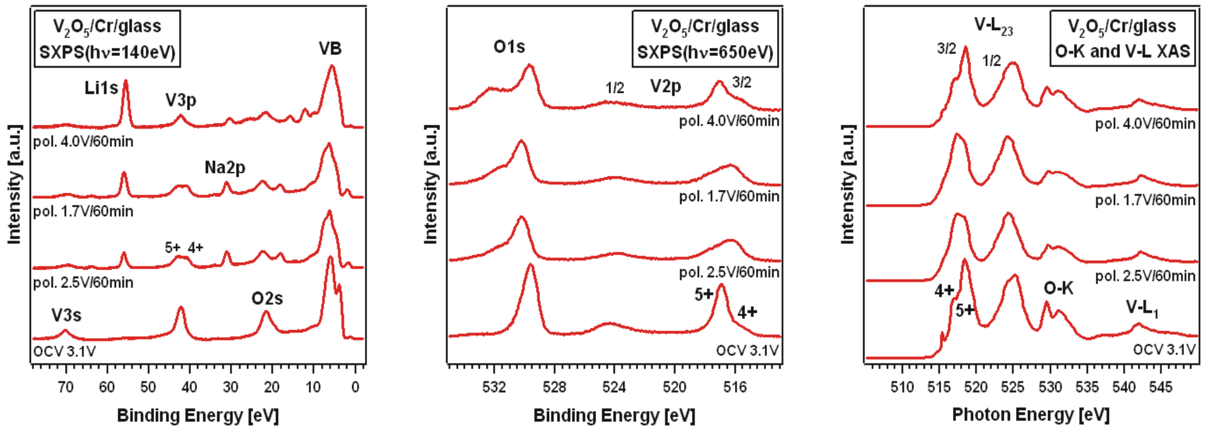

Fig. 2: SXPS (left and middle) and XAS data (right) of electrochemically intercalated/deintercalated $Li_xV_2O_5$.

In Fig. 3 shows SXPS data of the same type of experiments for a $LiCoO_2$ thin film cathode. The difference is, that in this case the completely intercalated host material (completely discharged battery) is the staring point of the experiment with an OCV of 2.6V. The first two polarization steps (3.9V and 4.3V) leads to partial and complete deintercalation, respectively, while the third polarization step (3.0V) leads to the intercalation of the material again. While the deintercalation is obviously working well, accompanied by the oxidation of the Co ions (Co^{3+} to Co^{2+}) and the formation of a $(CO_3)^{2-}$- and peroxo-ion containing SEI layer, obviously the reintercalation is blocked by this layer and the structural collapse of the host material after complete deintercalation. Only a very small amount is reintercalated, while a significant amount reacts with the SEI.

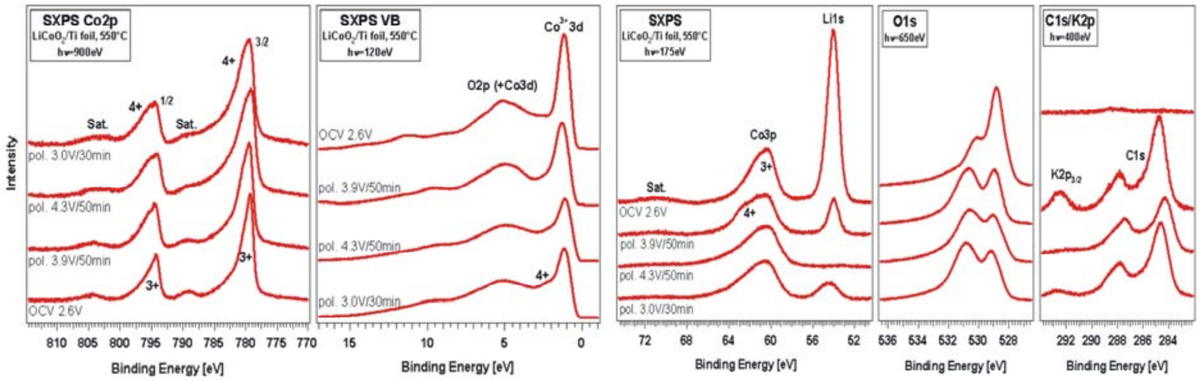

Fig. 3: SXPS data of electrochemically intercalated/deintercalated Li_xCoO_2.

To study the reason for the structural collapse and the poor reintercalation kinetics XAS experiments at the O-K- and Co-L_{23}-edge have been performed (Fig. 4).

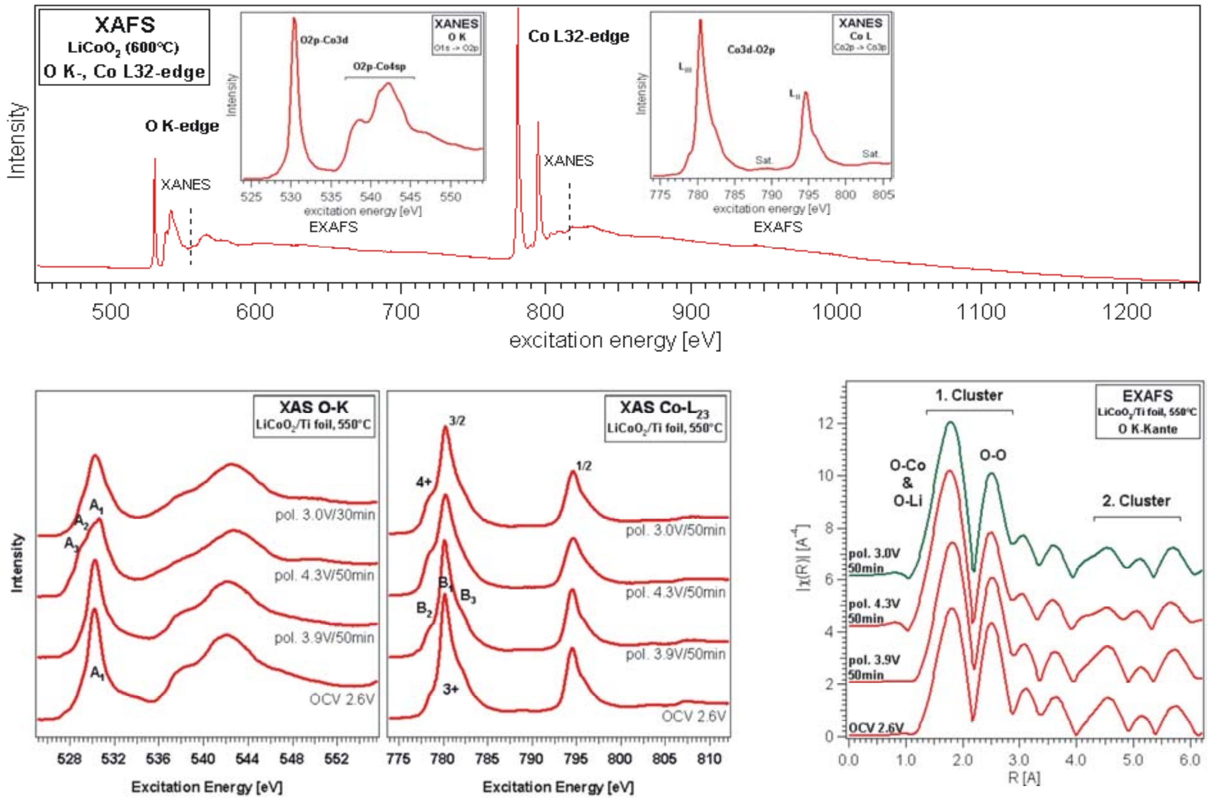

Fig. 4: XAS data of electrochemically intercalated/deintercalated Li_xCoO_2 and radial distribution functions.

By data analysis using FEFF8.0 simulation software the radial atom distribution functions have been derived. When using the O-K-edge absorption, the radial distribution is systematically normalized to the oxygen concentration in the sample. Obviously, the cobalt to oxygen concentration ratio increases with electrochemical deintercalation, clearly indicating the oxygen loss as a reason for materials degradation.

Acknowledgements

We acknowledge the DFG (SFB595/A3 and JA859/12-1), the EU (FP5-RTN INTERCALNET) and the BMBF (05ES3XBA/5) for funding and the collaborating CRG groups of D. Schmeisser (BTU Cottbus) and C. Pettenkofer for help, especially P. Hoffmann for beamline support. Thanks also to the BESSY staff for all kinds of assistance.

The search for uncompensated moment: X-Ray Resonant Magnetic Reflectivity investigation of the NiCoO/Co exchange bias system.

S. Brück[1], U. Grüner[1], Y.J. Tang[2], E. Goering[1], G. Schütz[1] & A.E. Berkowitz[3]

[1]Max-Planck-Institut für Metallforschung, Heisenbergstrasse 1, D-70569 Stuttgart, Germany.
[2]Center for Magnetic Recording Research, University of California at San Diego, 9500 Gilman Dr., La Jolla, CA 92093-0401, USA.
[3]Dept. of Physics and Center for Magnetic Recording Research, University of California at San Diego, 9500 Gilman Dr., La Jolla, CA 92093-0401, USA.

A ferromagnet (FM) in direct contact to an antiferromagnetic (AFM) material can exhibit a shift of its hysteresis loop. This so called exchange bias effect has attracted much attention during the last decade due to its importance for modern magnetic applications like spin-valve and tunnel magneto resistance systems. Although already widely used, the underlying physical mechanisms are still not fully understood. Especially, the question of where the uncompensated moments, which exchange couple to the FM and thus produce the offset field H_E, are located could not yet been answered. Are there only uncompensated moments in the first monolayer as has been proposed already by Meiklejohn and Bean [1] or do AFM domains exist and account for the effect?

The x-ray resonant magnetic reflectivity (XRMR) is, because of its capability to provide magnetic depth profile information, the perfect experimental technique to tackle this problem.

XRMR is a combination of standard reflectivity with x-ray magnetic circular dichroism. By measuring the reflectivity of the sample using circularly polarized light, reflectivity curves are obtained which contain chemical and magnetic depth information.

The sample we investigated consists of 1nm Ru as capping layer followed by 1 nm Co and 50 nm NiCoO as AFM and was grown on a Si (100) wafer. It has been shown that such a system exhibits a well pronounced exchange bias up to temperatures of 400 K [2].

Dichroic reflectivity curves at the $L_{2,3}$ edge of Co and also the $L_{2,3}$ edge of Ni have been measured as well as element selective hysteresis for both elements at UE52-SGM.

Figure 1 shows the resulting hysteresis loop as obtained by measuring the intensity at a fixed angle and varying external field H_{ext} at the resonance energy of the L_3-edge of cobalt.

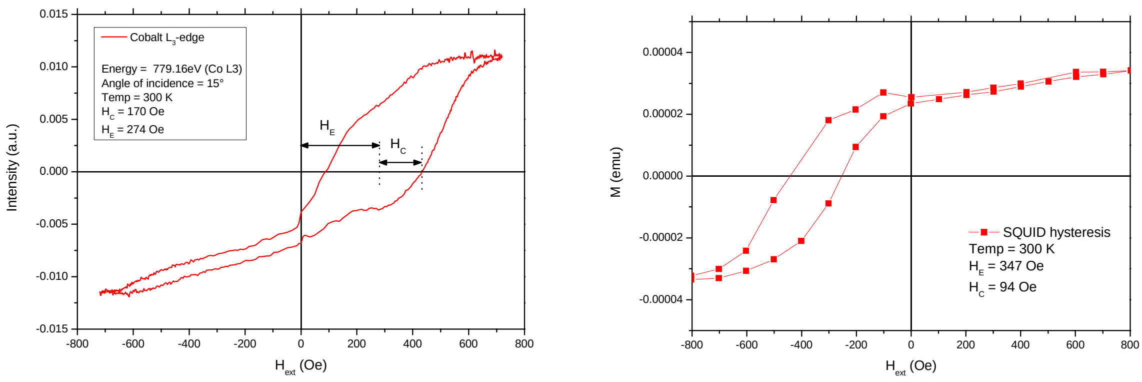

Figure 1: *Left – Room temperature hysteresis measured at the L_3-edge of Cobalt. The angle of incidence is 15° which is the angle of maximal asymmetry. The sample shows an exchange bias of H_E=274 Oe and a coercivity of H_C=170 Oe. Right – Hysteresis curve of the same sample measured with a SQUID magnetometer.*

Plotted in the figure are the relevant parameters H_E, which is found to be 274 Oe, and H_C which is 170 Oe, respectively. The result of a hysteresis measurement at the energy of the nickel L3-edge for the same field range H_{ext} is shown in Figure 2. Although the signal is very small and it is difficult to really determine the saturation magnetization, a clear hysteretic behaviour is observable.

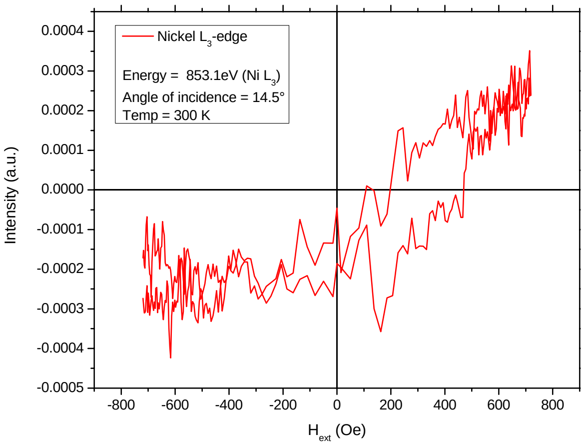

Figure 2: *The room temperature hysteresis as obtained by measuring at the L_3-edge of Ni (853,1 eV) at an angle of incidence of 14.5°.*

The existence of a hysteresis at this energy comes unexpected because, due to the AFM character of the NiCoO, it can only be related to uncompensated nickel atoms, i.e. nickel atoms which are not antiferromagnetically coupled. A second important point is the fact that the hysteresis is shifted related to an exchange coupling present for these uncompensated nickel atoms.

From the reflectivity data it should, in principle, be possible to judge whether and where the magnetic moment in the NiCoO, either for the Ni or for the Co, is located. To obtain the magnetic depth profiles for both elements, reflectivity curves have been measured at the respective resonance energies. The resulting curves for cobalt are shown in figure 2 left while the resulting magnetic asymmetry ratio is shown on the right.

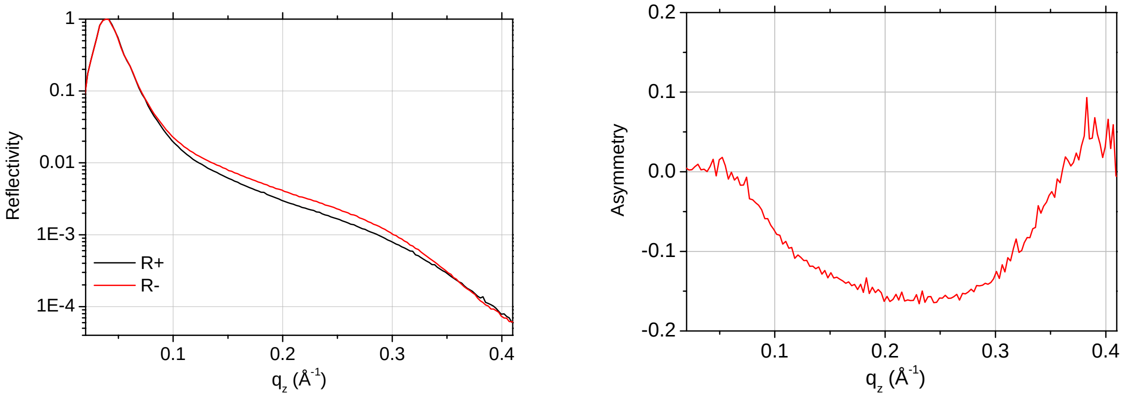

Figure 3: *Left – Dichroic reflectivity curves measured at an energy of 779.2 eV. A clear difference between the two magnetization directions is found between q_z=0.1 and 0.35. Right – Asymmetry ratio as obtained from the left shown reflectivity according to the formulae $(R_+-R_-)/(R_++R_-)$.*

Further analysis will include detailed reflectivity simulations based on the modified Parrat algorithm by J. Geissler [3] which has recently be optimized for the soft x-ray regime [4].

We thank K. Godehusen for the support during our beamtime.

[1] W. H. Meiklejohn & C. P. Bean *Phys. Rev.* **105**, 904 (1957).
[2] A.E. Berkowitz et al. *Phys. Rev. B* **72**, 134428 (2005).
[3] J. Geissler et al. *Phys. Rev. B* **65**, 020405R (2002).
[4] M. Harlander Diploma thesis University of Stuttgart (2006).

Soft X-ray investigations of exchange coupled FM/AM bilayers

V. R. Shah[1], C. Schanzer[2], S. Legl[1], J. Mayer[1], F. Schäfers[3], A. Gaupp[3], S. Valencia[3], P. Böni[1]

[1]Physics Department E21, Technical University of Munich, D-85747 Garching, Germany
[2]Laboratory for Neutron Scattering, ETHZ & PSI, CH-5232 Villigen PSI, Switzerland
[3]BESSY GmbH, Albert-Einstein Strasse 15, D-12489 Berlin, Germany

In the recent years, soft x-ray studies gained lot of momentum on the study of ultrathin magnetic layers exploiting the element sensitivity of x-rays at the absorption edges [1]. Ferromagnet (FM)/Antiferromagnet (AF) layers have posed challenging issues due to their complex nature of interfacial exchange and non-collinear internal magnetic structures leading to a unidirectional anisotropy that give rise to the phenomenon of exchange biasing. Soft x-ray magneto-optic Kerr effect has been applied as a depth and element sensitive probe to extract information on magnetic heterogeneity [2]. Our recent investigations on FM/AF/FM (FM= 20 nm of Fe$_{50}$Co$_{48}$V$_2$ and AF= 5 – 60 nm of NiO) and their bilayer counterparts using bulk and polarized neutron reflectometry revealed interesting AF thickness dependence of magnetization reversal [3]. For a systematic study, we examine the bilayers in detail and in this project we report, the soft x-ray magnetic circular dichroism (XMCD) as well as element specific hysteresis properties of Fe, Co and Ni as a function of the thickness of the AF. We measured dichroism by performing energy scans around the absorption edges of the constituent elements at the positive and negative saturation states of the FM, for a fixed helicity of the incoming elliptically polarized light.

The experiments were performed at the undulator beamline UE56-1-PGM 1b of BESSY using the ultra high vacuum polarimeter chamber [4]. The angle of incidence θ_i was set to 20°, with respect to film surface. For some samples θ_i was varied to 10° and 5° to facilitate more surface sensitivity [2]. Typical energy scans around the Fe, Co and Ni absorption edges for the samples with the AF on top and bottom of the FM are shown in Fig. 1.

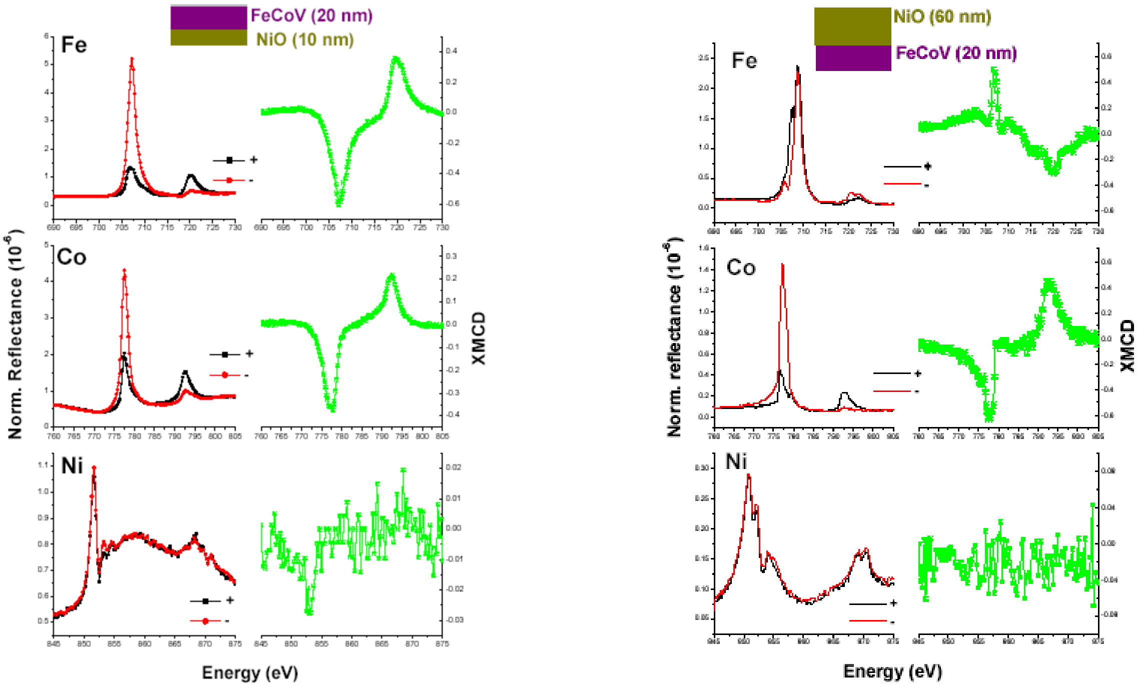

Fig. 1. Energy scans of Fe, Co and Ni absorption edges of the (a) NiO(10 nm)/FeCoV(20 nm) and (b) FeCoV(20 nm)/ NiO(60 nm) bilayers at $\theta_i = 20°$. The respective XMCD (the difference divided by the sum of the reflected intensities at the saturation magnetization states + / - of the FM) is also shown. The peculiar reflectance profile is expected as due to morphological or magnetic heterogeneity within the probing depth.

The XMCD signal decreased gradually with increasing NiO layer thickness when the FM is on top of the AF. The decrease in XMCD might be a consequence of increasing magnetic heterogeneity resolved within the probing depth of the x-rays near the absorption edge. Such a magnetic heterogeneity would be caused e.g. by the fanning of FM magnetization close to the FM/AF interface like in an exchange spring magnet. A comparison of energy scans at θ_i = 5° and 20° is given in Fig. 2 (a). A higher sensitivity for magnetic contrast is observed at θ_i = 5°. The representative hysteresis curves apparently illustrate the depth averaged complex incoherent magnetization reversal process. However, when the NiO under-layer thickness is reduced, the magnetization reversal appears to occur via a coherent rotation process as described below.

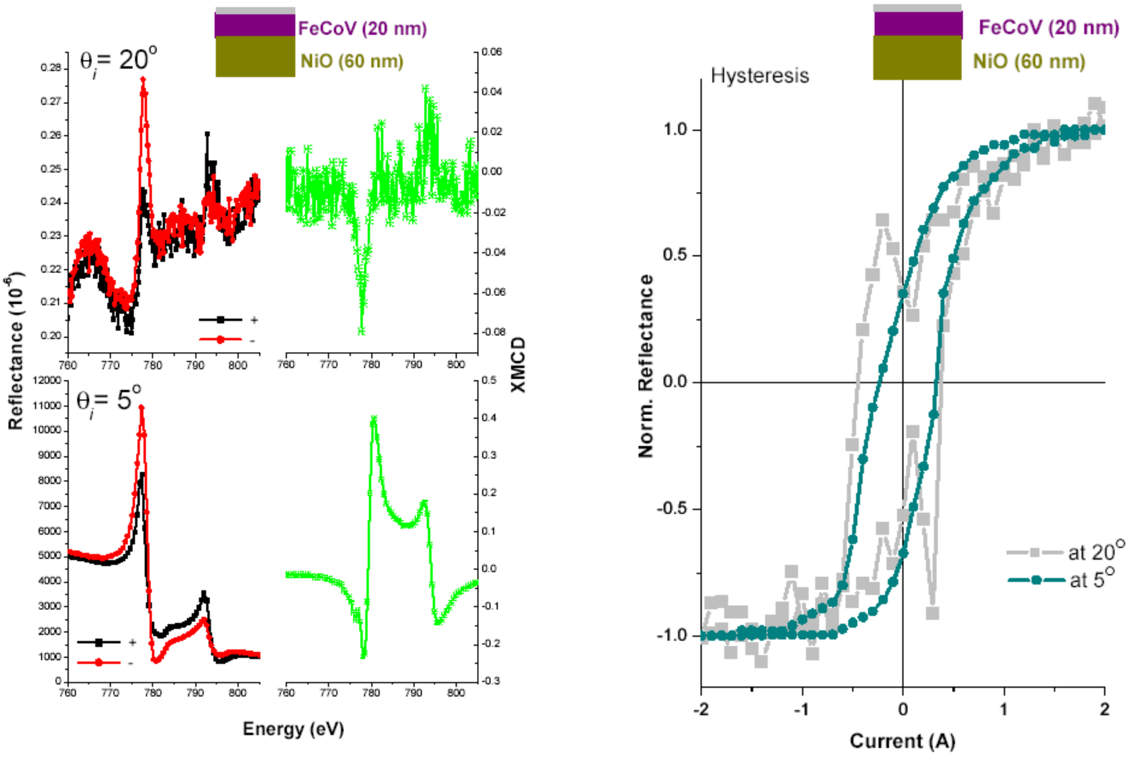

Fig. 2(a) The Energy scans at the Co absorption edge of NiO(60 nm)/FeCoV(20 nm) layer at two incident angles θ_i = 5° and 20° and (b) the representative hysteresis behaviour at these incidence angles.

In all the bilayers, both Fe and Co exhibits ferromagnetic hysteresis loops with nearly identical shapes, indicating a uniformly alloyed Fe and Co in the magnetization process. Fig. 3 depicts the hysteresis behaviour obtained at the Fe, Co and Ni absorption edges of an AF/FM bilayer with a thin NiO bottom layer. A very week ferromagnetic behaviour at the Ni absorption edge is also observed in this bilayer. The origin of FM Ni is unclear at the moment. However, there have been indications for the traces Ni from the antiferromagnet NiO, as expected at the NiO surface due to the oxidation-reduction process happening at the metal/oxide interface [5]. Recent investigations suggest that AF spins rotate with the FM due to strong exchange coupling at the AF/FM interface [6]. This is especially the case when the AF has a weak anisotropy [7]. For the rest of the samples in the present series, the FM behaviour of NiO was too weak to detect. XMCD, element selective magnetization curves and a systematic AF dependence of magnetization reversal in NiO/FeCoV bilayers are in accordance with the recent theoretical models [8,9] of the domain wall formation in the FM and AF.

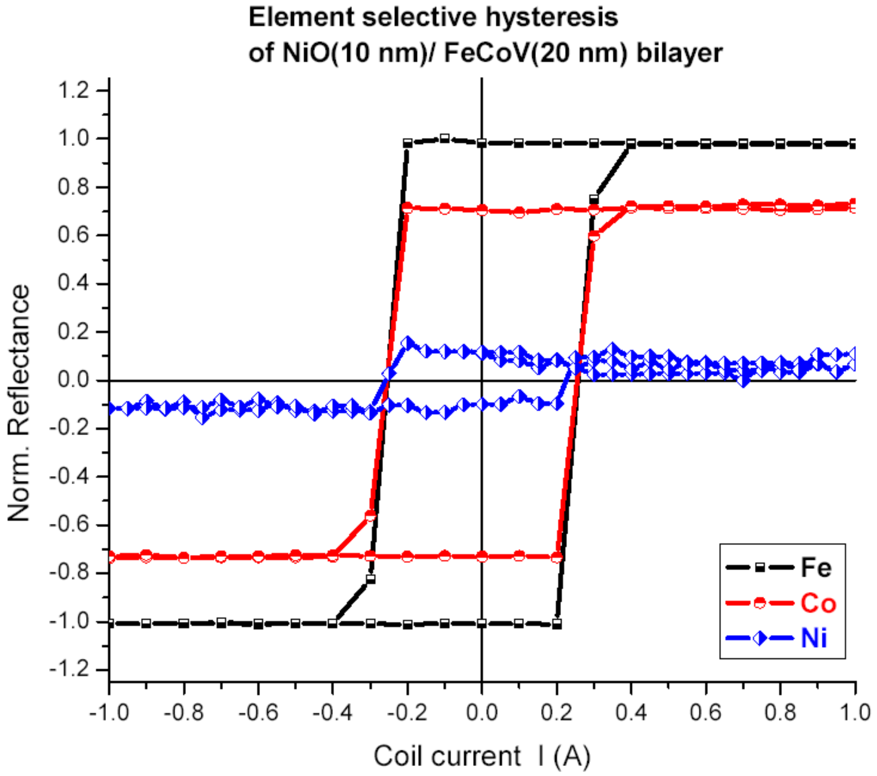

Fig. 3. Element selective magnetic hysteresis of Fe, Co and Ni edges in NiO(10 nm)/FeCoV(20 nm) bilayer. The individual plots are scaled according to their relative intensities of the reflected signal.

The authors thank BMBF support (05 ES3XBA/5) for the experiments at BESSY.

References

1. J. Stöhr, Exploring the microscopic origin of magnetic anisotropies with X-ray magnetic circular dichroism (XMCD) spectroscopy, *J. Magn. Magn. Mater.* **200** (1999) 470.
2. K. S. Lee, S. K. Kim and J. B. Kortright, Atomic scale depth sensitivity of soft x-ray resonant Kerr effect, *Appl. Phys. Lett.* **83** (2003) 3764.
3. V. R. Shah, C. Schanzer, P. Böni and H. B. Braun, Magnetization reversal in FM/AF/FM trilayers: dependence of AF thickness, *J. Magn. Magn. Mater*. **286** (2005) 484.
4. F. Schäfers, H. C. Mertins, A. Gaupp, W. Gudat, M. Mertin, I. Packe, F. Schmolla, S. D. Fonzo, G. Soullie, W. Jark, R. Walker, X. Le Cann, R. Nyholm and M. Eriksson, Soft X-ray Polarimeter with Multilayer Optics: Complete Analysis of the Polarization State of Light, *Appl. Opt.* **38** (1999) 4074.
5. T. J. Regan, H. Ohldag , C. Stamm, F. Nolting, J. Lüning, J. Stöhr and R. L. White, Chemical effects at metal/oxide interfaces studied by x-ray absorption spectroscopy, *Phys. Rev.* **B 64** (2001) 214422.
6. A. Scholl, M. Liberati, E. Arenholz, H. Ohldag and J. Stöhr, Creation of Antiferromagnetic Exchange Spring", *Phys. Rev. Lett*. **92**, 247201 (2004).
7. F. Radu, A. Westphalen, K. Theis-Bröhl and H. Zabel, Quantitative description of the azimuthal dependence of exchange bias effect, *J. Phys.: Condens. Matter* **18** (2006) L29.
8. H. Xi and R. M. White, Antiferromagnetic thickness dependence of exchange biasing, Phys. Rev. **B 61** (2000) 80.

Layer-resolved magnetization of EuTe by resonant magnetic soft x-ray scattering:

E. Schierle,[1] E. Weschke,[1] A. Gottberg, [1] G. Springholz,[2] G. Kaindl[1]
[1]Institut für Experimentalphysik, Freie Universität Berlin, D-14195 Berlin, Germany
[2]Institut für Halbleiter- und Festkörperphysik, Johannes Kepler Universität, A-4040 Linz, Austria

The characterization of magnetic structures in thin films and particularly at interfaces is important for the understanding of nanostructured materials. Resonant magnetic soft x-ray scattering, which involves core-electron excitations into exchange-split unoccupied states, is a particularly sensitive tool for such studies [1]. Here, the method was employed to characterize the temperature-dependent magnetic structure in a thin film of EuTe. The antiferromagnetic semiconductor EuTe crystallizes in the NaCl structure. With a $4f^{7}$ configuration, the Eu^{2+} ions carry S=7/2 and L= 0. Thus, EuTe is a prototype realization of the classical Heisenberg model and has been studied in detail as bulk material, both experimentally and theoretically. Bulk EuTe exhibits antiferromagnetic order along the [111] direction (Fig. 1A) below the ordering temperature of T_N= 9.6 K. In the thin-film samples of the present study, where EuTe is sandwiched between two PbTe layers (Fig. 1B), the ordering temperature is enhanced to T_N=12.8 K due to epitaxial strain [2].

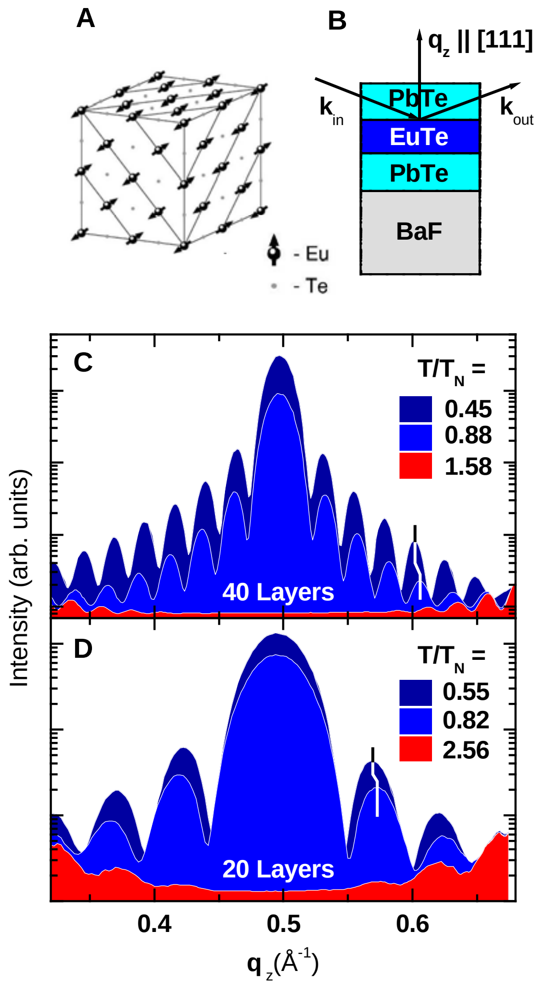

Fig. 1. A: Antiferromagnetic structure of EuTe along [111], B: Sample structure and scattering geometry. C,D: Magnetic x-ray scattering from monocrystalline EuTe films at the M_5 resonance of Eu.

Since soft x-rays are strongly absorbed in air, the scattering experiments require vacuum-compatible diffractometers. The experiments reported here were carried out with a UHV-compatible Θ-2Θ diffractometer designed and set up at the Insitut für Experimentalphysik of the Freie Universität Berlin. The instrument allows to use a liquid-He cryostat with rigid sample mounting, providing a minimum sample temperature of less than 6 K. The data were taken at the UE46/1-PGM1 beamline of the HMI.

EuTe is ideally suited to employ magnetic x-ray scattering at the Eu M_5 resonance, since the photon wavelength matches the magnetic structure in the sense that the magnetic diffraction peak occurs almost exactly at 2Θ = 90°, i.e. at the Brewster angle. With π-polarized incident light charge scattering is therefore strongly suppressed and the magnetic signal can be recorded virtually free of charge background. This is shown in Figs. 1C and D, which display magnetic diffraction patterns recorded from 40 and 20 monolayers (ML) of EuTe at various temperatures. In films of finite thickness, the magnetic Bragg diffraction (blue) is broadened and displays side maxima, so-called Laue oscillations. Above T_N (red), the coherent magnetic contribution has vanished and only the charge scattering remains, which is a very weak background. In the present case, the Laue

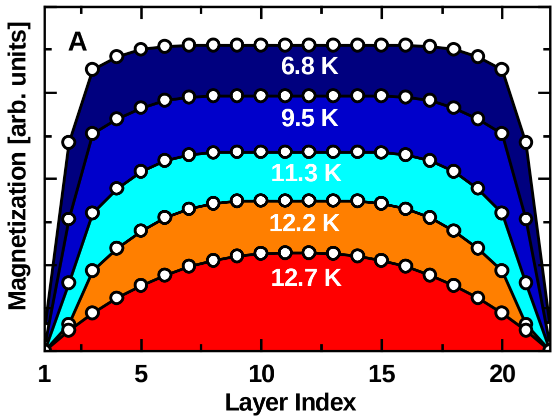

Fig. 2: Temperature-dependent magnetization profiles obtained from the magnetic diffraction peaks of a 20 ML EuTe film.

oscillations are extemely well resolved due to the very high crystalline quality of the films and the high magnetic sensitivity of the method. They can be observed over a substantial range in *k* space. The integrated intensity of the magnetic Bragg peak represents the order parameter in an antiferromagnet and hence decreases with increasing temperature. A closer look at the Laue oscillations in Fig. 1 reveals additional details. As emphasized by the vertical lines, the side maxima move away from the main maximum, indicating that the magnetization does not decrease in a homogeneous way across the film, but that the mean number of magnetic layers also decreases with increasing temperature. To analyze this behavior in more detail, the magnetic diffraction signals were Fourier transformed after background substraction and proper normalization for polarization and absorption effects. In this way, the so-called Patterson functions, i.e. the autocorrelation functions (not shown here) were obtained. These were reproduced by model calculations, using the scattering factors of the individual layers as adjustable parameters, in this way yielding the temperature-dependent magnetization profiles across the films.

As an example, the behavior of the 20-ML thick film is shown in Fig. 2. At low temperatures, the magnetization is constant across the film, with perturbed regions at the interfaces with PbTe. Due to the lack of magnetic neighbours contributing to the exchange energy, the magnetization in the interface region is reduced. This effect is strongest in the outermost two layers, which are characterized by substantial intermixing with PbTe. With increasing temperature, the profiles become rounded, showing that the influence of the interfaces becomes increasingly important for the inner layers. This behavior is reflected in different temperature dependences of the magnetizations of the individual layers (not shown here).

The present results are in very good agreement with early theoretical results [3]. Further quantitative details, such as the amount of intermixing at the interface, can be obtained by a comparison to Monte-Carlo calculations employing a Heisenberg model with realistic exchange parameters, which are presently under way.

The expert support and excellent beamline conditions are gratefully acknowleged.

References:

[1] E. Weschke *et al.*, Phys. Rev. Lett. **93**, 157204 (2004).
[2] G. Springholz and G. Bauer, Appl. Phys. Lett. **19**, 2399 (1993) .
[3] K. Binder and P.C. Hohenberg , Phys. Rev. B **9**, 2194 (1974).

A quantitative look on temperature effects in radiation damage of aliphatic and aromatic self-assembled monolayers.

M. Zharnikov and A. Shaporenko
Angewandte Physikalische Chemie, Universität Heidelberg, Im Neuenheimer Feld 253,
D-69120 Heidelberg
D. Menzel and P. Feulner
Physikdepartment E20, Technische Universität München, James-Franck-Str.,
D-85747 Garching

Self-assembled monolayers (SAMs) are prototypical for thin organic layers on solids with a huge potential for applications in electronics, micromechanics, printing, medicine and biotechnology /1/. Irradiation by electrons and photons is commonly used for materials modification and structuring /2/. We have demonstrated that the sample temperature is an important parameter in beam induced modifications of SAMs /3/. This previous investigation, however, was limited to aliphatic SAMs and only two temperature values, room temperature and 60K. Here we take a more detailed look by including intermediate temperatures and comparing aliphatic (dodecanethiol on gold, C12/Au) as well as aromatic (biphenylthiol on gold, BPT/Au) SAMs. The ex-situ preparation of these layers is described elsewhere /4/. All data were recorded at the U49-II-PGM-1 beamline.

In previous investigations /2,3/ it has been shown that the main irradiation effects by electrons and photons for these samples are loss of material, abstraction of hydrogen with subsequent double bond formation and cross linking, loss of orientation, breaking of the headgroup-substrate bond, and formation of dialkylsulfide species and atomic S. Particularly, the reaction of dialkylsulfide formation, which occurs within the organic film, requires diffusive transport of the entire hydrocarbon chain or at least larger fragments of it /2/. All reactions but the hydrogen abstraction followed by double bond formation were found to be slowed down by cryogenic conditions as compared to room temperature /3/. In order to obtain a more detailed picture of the temperature effect on these processes we first examined the saturation behavior, which, for room temperature, has been investigated by electron irradiation before /2/.

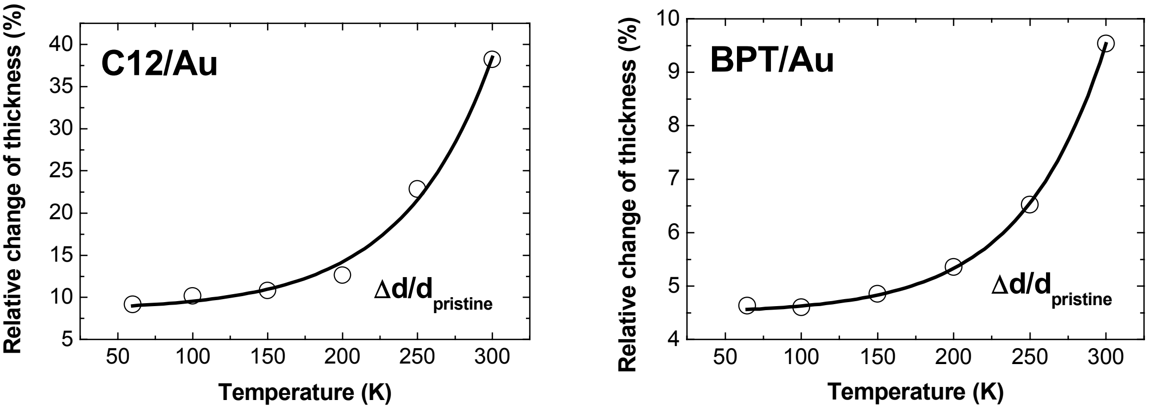

Fig 1: Saturation values for the relative reduction of the layer thickness by extended irradiation with 250 eV photons as a function of the sample temperature, for C12/Au (left) and BPT/Au (right).

We extracted cross section and saturation values for the relative radiation induced material loss from exponential fits of the Au4f photoemission intensity as a function of photon exposure, with the sample temperature as parameter. The radiation induced material loss saturates at lower values for lower temperatures; the maximum amount of desorption is always larger for C12/Au than for BPT/Au (Fig.1). The values obtained for room temperature (40% reduction for C12/Au, and 10% for BPT/Au) are in perfect agreement with values recorded previously by electron irradiation /2/.

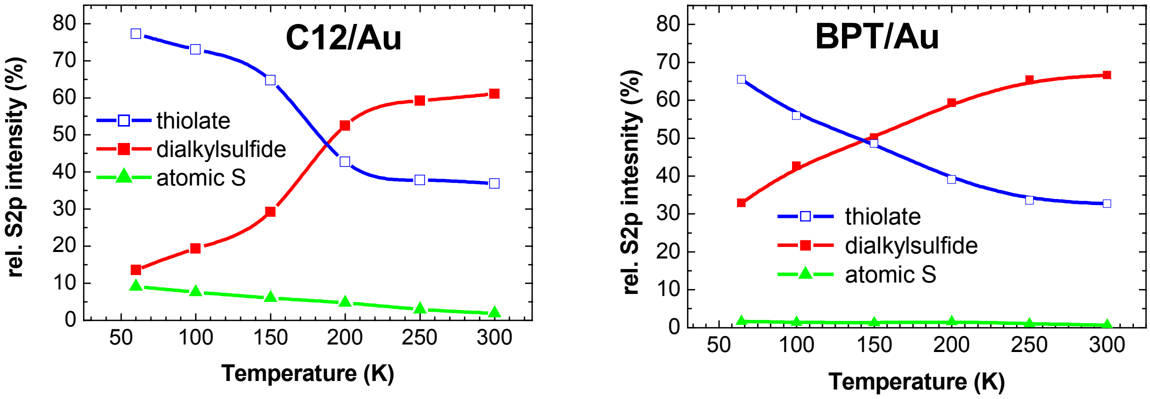

Fig.2: Temperature dependent composition (sulfur-derived species) of C12/Au (left) and BPT/Au SAMs (right) after irradiation with 5x10^{16} photons per cm^2 (hν = 250 eV).

The film temperature affects not only the total amount of material loss, but also the branching of the headgroup's beam damage. After exposure to 5x10^{16} photons of 250 eV, S2p photoemission indicates conversion of the pristine thiolate species into dialkysulfide and atomic S. Dialkysulfide is the main product, mirroring the decaying thiolate curve (Fig.2). The conversion yield depends strongly on the film temperature (Fig.2). It is lower for the aromatic than for the aliphatic SAM for all temperature values. Conversion to atomic S competes with the dialkysulfide reaction and gets important only for low temperatures, where the latter is hindered. For BPT/Au it is negligible (Fig.2).

We finally compare the temperature dependence of the cross sections for material loss on the one hand and dialkylsulfide build-up on the other, which have been extracted from exponential fits of the respective PE peak areas (Fig.3). For both reactions we find practically identical cross section values at cryogenic conditions which increase with sample temperature, by a factor of 5 for C12/Au and by a factor of 3 for BPT/Au at room temperature. These values are almost identical for material loss and dialkylsulfide creation, indicating that the rates of both processes are governed by similar factors.

We explain these findings by the following microscopic scenario: Permanent rupture of the headgroup-substrate bond, which enables diffusion of the primarily excited molecular chain towards the vacuum interface, and the transport of large chain fragments through the film towards desorption are both thermally activated processes. Diffusive movement is necessary for both of these processes and is presumably the major factor affecting their rates. At low (cryogenic) temperatures these processes are hindered and only hydrogen and small fragments are released as shown by previous mass spectrometric measurements /3/. This abstraction of hydrogen inside the film which also shows up by the appearance of double bonds in XAS /2,3/ depends only to a small extent on the film temperature. It creates dangling bonds which, apart from double bond formation, also lead to cross-linking of the SAM molecules, thus immobilizing them in the layer and hindering further beam induced material loss in form of large fragments. This competition of diffusion assisted rapid material loss, which is thermally activated, and the temperature independent cross-linking explains the observed saturation behavior as well as the branching scheme displayed in Fig.2. Obviously, cross-linking is more efficient for the aromatic than for the aliphatic SAMs /2/.

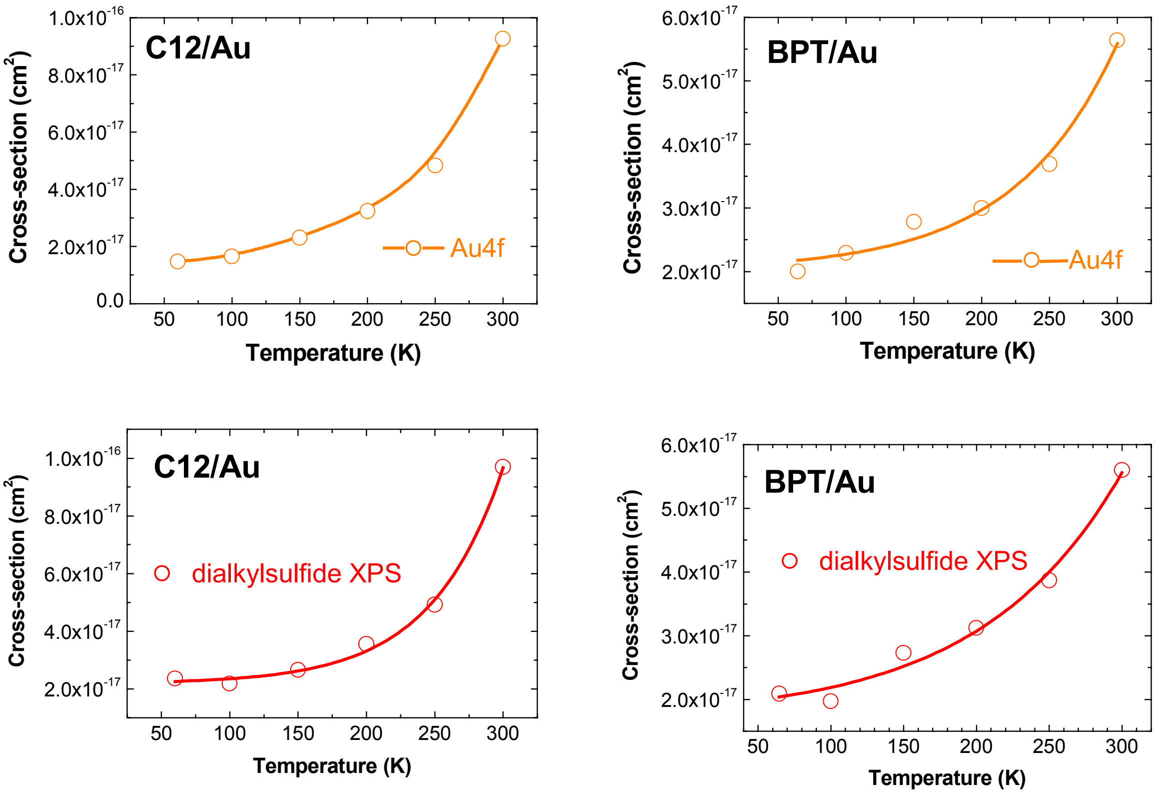

Fig.3: Cross sections as a function of temperature for (top) the increase of substrate Au4f photoemission due to radiation induced material loss of the SAMs, and (bottom) for the build-up of dialkylsulfide products, for C12/Au (left) and BPT/Au (right).

In summary, we find that stabilization of the structure by cryogenic conditions, which is the key idea of cryomicroscopy /5/, is an important point in temperature effects in beam damage in thin organic films as well, although not the only. The fact that temperature can steer electronically induced reactions as shown in Fig.2 is of its own importance. A permanent destruction of the thiolate-metal bond is only possible if the products are sufficiently mobile, otherwise it will recombine.

Acknowledgement: We thank K. Eberle, R. Schneider, M. Glanz, and the staff of BESSY, in particular W. Braun, H. Pfau, and O. Schwarzkopf for help during the experiments and M. Grunze for support of this work. Financial support by the BMBF (05 KS4VHA/4 and 05 ES3XBA/5) is gratefully acknowledged.

1. see, e.g., *Handbook of Nanotechnology*, ed: B. Bushan, Springer, Berlin 2004, chapt. 27.
2. M. Zharnikov and M. Grunze, J. Vac. Sci. Technol. B **20**, 1793 (2002), and references therein.
3. P. Feulner, M. Zharnikov et al., Phys. Rev. Lett. **93**, 178302 (2004).
4. K. Heister et al., Surf. Sci. **529**, 36 (2003); S. Frey et al., Langmuir **17**, 2408 (2001).
5. V. E. Cosslett, J. Microscopy **113**, 113 (1978).

Size Effects in Thermally Cycled Thin Films

E. Eiper[a], K.J. Martinschitz[a], J.W. Gerlach[b], J.M. Lackner[c], I. Zizak[d], N. Darowski[d]
and J. Keckes[a,e]

[a]*Erich Schmid Institute for Materials Science, Austrian Academy of Sciences and Institute of Metal Physics, University of Leoben , Leoben, Austria*
[b]*Leibniz-Institut für Oberflächenmodifizierung (IOM), Leipzig, Germany*
[c]*Joanneum research, Laser Center Leoben, Niklasdorf, Austria*
[d]*Hahn-Meitner-Institute, Berlin, Germany*
[e]*Materials Center Leoben, Leoben, Austria*

Thin metal films and multilayered structures are used for a variety of technologically important application. The structures possess always a certain amount of residual stress which influences their performance and modify important physical parameters. The stress state in thin films can be significantly influenced by external factors – especially by temperature changes during thermal cycling. The cycling results in elastic and plastic deformation in film which can decisively influence the reliability of structures [1].

The yield stress of thin film depends on the grain size and film thickness and is decisive for the performance and lifetime of film. According to the *phenomenological Hall-Petch relationship*, the yield stress increases with the decreasing grain size. Unusually high flow stresses were reported for thin films whereby thin films with the thickness below critical did not even exhibit the plastic flow at very high strains [1]. The exact physical reasons for the mechanical size effects are however not fully understood.

In this work, firstly, we present a methodology for the quantification of absolute magnitude of stress factors and residual stresses in thin films by diffraction. Secondly, temperature cycling is applied to Al thin films deposited on Si(100) and the film strength is determined as a function of the thickness. The experiments were performed at KMC-2 beamline.

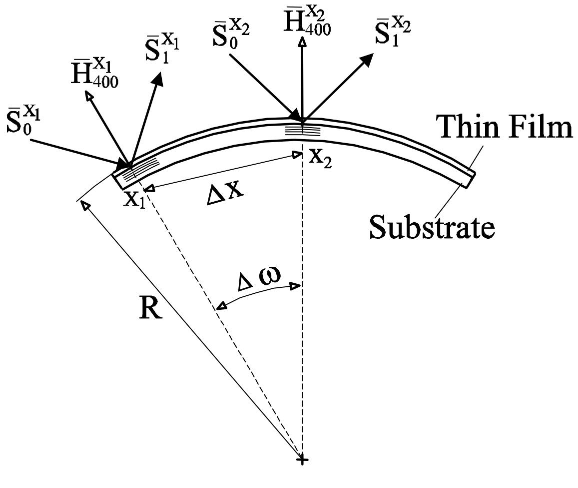

Figure 1 A schematic description of the diffraction setup used for the characterization of the radius of the curvature *R*. The angle between the primary and secondary diffraction vectors $\overline{S}_o^{x_i}$ and $\overline{S}_1^{x_i}$, respectively, was set to the position corresponding to the Si 400 reflection. Then, for each sample position x_i, the sample was rotated around the ω axis and the integral intensity from the 2D detector was collected as a function of the ω angle. For each sample position x_i, the diffraction on Si(400) planes was observed at specific ω_i corresponding to the condition $(\overline{S}_1^{x_i} - \overline{S}_o^{x_i})/\lambda = \overline{H}_{400}^{x_i}$, where $\overline{H}_{400}^{x_i}$ is the diffraction vector. The dependence of ω_i on x_i was used to quantify the substrate curvature and the stress in film.

X-ray diffraction (XRD) is routinely used to determine elastic strains in thin films [2]. To calculate residual stresses, elastic constants of the materials from literature are usually used. In this work elastic strain characterization of the film was combined with the characterization of substrate curvature by measuring substrate symmetrical reflection at different sample positions (Fig. 1). The curvature data were used to determine the magnitude of the stress in the film using the Stoney formula. Combining the experimental stress and strain values, experimental elastic constants and stress factors of the film were determined [3]. This opened the way for the characterization of absolute magnitude of stresses in thin films.

In the second experiment, polycrystalline Al thin films with the thickness in the range 50-2000 nm were thermally cycled using non-ambient diffraction attachments DCS350 (provided by Anton Paar Ltd.) in the temperature range from -100 to 350 °C. XRD was used to characterize lattice spacing of films at different sample tilt angles. The diffraction data were used to calculate residual stresses in the films as a function of film thickness.

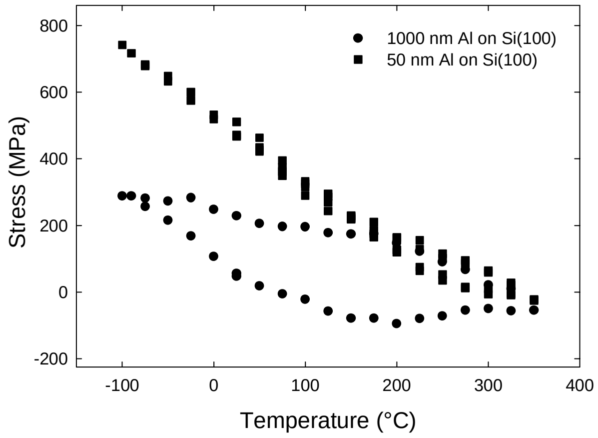

Figure 2 Temperature dependence of residual stressed in Al thin films with different thickness. The dependencies indicate that the 50 nm thick film exhibits very high tensile stresses at -100 °C.

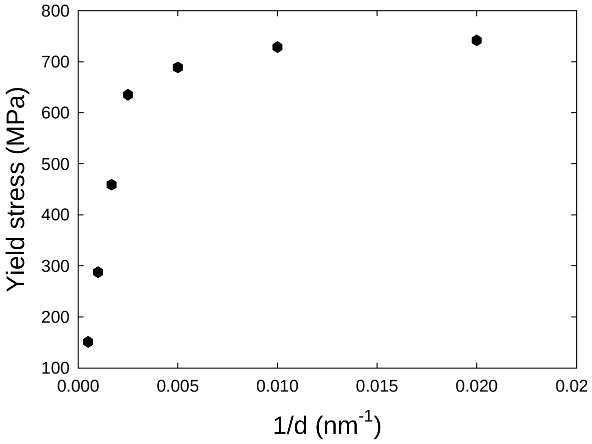

Figure 3 Yield stress in Al thin films on Si(100) as a function of inverse film thickness at -100 °C. The data document that 50 nm film exhibits the maximal tensile strength.

In Fig. 2, exemplary residual stress dependencies for polycrystalline Al thin films with the thickness of 50 and 1000 nm are depicted. The results indicate that, due to the temperature cycling, the residual stress at -100 °C in 1000 nm thick film reached about 300 MPa in tension in contrast to 750 MPa in 50 nm thick film.

Analyzing the stress-temperature dependency of films with different thickness, it was possible to identify the change from elastic to plastic behaviour and determine also the magnitude of the yield stress in Al thin films with different thickness (Fig. 3). The plot of yield stress versus inverse film thickness documents that the thinnest film (50 nm) exhibits the highest magnitude of the stress at -100 °C. For the thinnest film, the plastic limit was thus reached at about 750 MPa. The biaxial strength of Al film deposited on Si(100) is significantly higher than that of bulk (90 MPa). In the future, the analysis of the dislocation formation and movement using in-situ XRD is planned in order to understand deeper the size effects in thin films.

Ackowledgments

We gratefully acknowledge the European Community for a financial support grant through the Contract N° RII 3-CT-2004-506008, project BESSY-BM.05.2.117. A part of this work was supported by by the Austrian NANO Initiative via a grant from the Austrian Science Fund FWF within the project "StressDesign - Development of Fundamentals for Residual Stress Design in Coated Surfaces".

References

[1] W. D. Nix, *Metallurgical Transactions* 20A (1989) 2217.
[2] J. Keckes, *J. Appl. Cryst.* 38 (2005) 311.
[3] E. Eiper, K. J. Martinschitz, J. W. Gerlach, J. M. Lackner, I. Zizak, N. Darowski, J. Keckes, *Zeitschrift für Metallkunde* 96 (2005) 1069.

Texture modification in nano-crystalline materials using swift heavy ions

I. Zizak[1], N. Darowski[1], G. Schumacher[1], S. Klaumünzer[1], W. Assmann[2], J. Gerlach[3]

[1]Hahn-Meitner-Institut, Glienicker Straße 100, D-14109 Berlin,
[2]Sektion Physik der Universität München, Am Coulombwall 1, D-85748 Garching
[3]Leibniz-Institut für Oberflächenmodifizierung, Permoserstr. 15, D-04318 Leipzig

Introduction

Many properties of nano-crystalline materials differ from the properties of materials with larger grains. Among these grain-size dependent properties are the enhancement of specific heat, fast diffusion in nano-crystalline materials, the “inverse Hall-Petch” effect, and many others. The standard Hall-Petch effect describes the changes in elastic properties in polycrystalline materials. Plastic deformation in crystalline materials occurs through the pile-up of dislocations in the crystal. The high mechanical strength of fine-crystalline materials is also considered to be caused by the lack of dislocation source or a difficulty in dislocation multiplication in small grains. However, some nano-crystalline materials (grain size 5-100 nm) obey the inverse Hall-Petch rule, showing the softening when the grains get too small. Since the grains are still too small to allow a pile-up of dislocations, deformation in these materials must be described by another process. The most promising candidate is the process which includes sliding of the grains along the grain boundaries.

In a series of ion irradiation experiments we managed to activate the grain sliding even in materials with grains larger than 30nm. Taking advantage of the nature of the interaction between swift heavy ions and solid we introduced thermal energy directly in grain boundaries, resulting in grain rotation and sliding, which was later verified by measuring the texture of thin layers at the KMC2 beamline at BESSY synchrotron light source.

Experiment

Polycrystalline Ti, Pd, and TiN layers were irradiated with 350 MeV Au ions with different fluences up to $3\text{x}10^{15}$ ions/cm^2. Direction of the ion beam was chosen to be different from the normal incidence to the sample surface to be able to separate the influence of the sample surface and the ion beam.

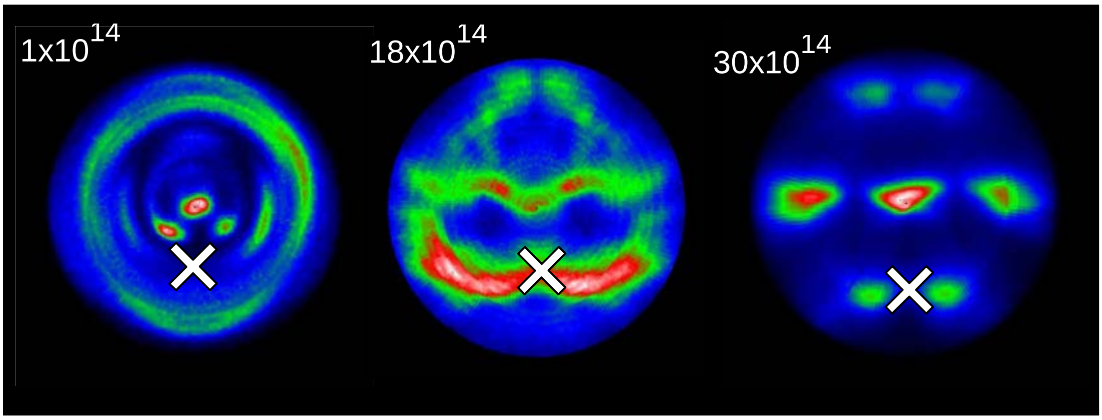

Fig. 1. Combined pole figures of 110 and 101 planes in the nano-crystalline Ti layer in false colour after irradiation with different fluences (colours black for low intensity, than blue, green and red up to white for high intensity). Fluences in ions/cm^2 are shown in corner of corresponding pole figure. White 'x' marks the direction of the incident beam. Concentric rings originating from cylindrical symmetry are very pronounced for $1\text{x}10^{14}$ ions/cm^2. After $18\text{x}10^{14}$ ions/cm^2, the texture rotated about 60° upwards. Although the rings are still observable, the braking of the cylindrical symmetry has already started. After $3\text{x}10^{15}$ ions/cm^2 the texture rotation stopped and a mosaic texture showing the symmetry of the hexagonal lattice is visible. 100 lattice plane is parallel to the surface.

Irradiation was performed at the ISL heavy ion accelerator at Hahn-Meitner-Institute in Berlin. Irradiation of samples with swift heavy ions is a time consuming task. For this reason we performed stepwise irradiation for accumulation of the high fluences together with characterization of the texture of the sample between two subsequent irradiation steps.

Textures were measured at the diffractometer experimental station at the KMC2 bending magnet beamline at BESSY using photon energy of 8 keV. A combination of an area-sensitive wire detector and intense synchrotron beam allowed very fast acquisition of complete orientation distribution in the sample. (see previous BESSY Annual Reports) Additionally, the area detector allowed the determination of the grain size without acquisition of additional data. However, since the grains grow during the irradiation, the resolution of the area detector is sufficient to estimate the grain size only at the beginning stages of the irradiation. A possible trend could be deduced.

Results

We measured the change of the crystalline orientation distribution after the irradiation with swift heavy ions. The further irradiation of already studied samples up to a fluence of $3x10^{15}$ ions/cm^2 revealed some new interesting effects.

In different nano-crystalline materials we observed two distinct changes which showed up with different magnitude in different materials:

i) the texture rotated continuously away from the direction of the ion beam. New finding is that the rotation slows down and stops when the 100 lattice plane becomes parallel to the surface.

ii) the cylindrically symmetric texture, specific for the deposited films, broke into a mosaic texture, improving alignment between the grains.

At the beginning of the irradiation the grain size was estimated to be around 50nm. Already at fluences of $1.8x10^{15}$ ions/cm^2 grains were larger than 100nm and could not be resolved in this experiment.

Discussion

Since the texture in highly irradiated samples rotated almost 90°, we can not explain the rotation through the interaction of the ion beam with the crystalline grains in the sample. However, the grain boundary, which is supposed to be amorphous, is in polycrystalline materials few nanometers thick. If the grains are of the size of 10-100 nm large part of material is located in the grain boundaries, i.e. amorphous.

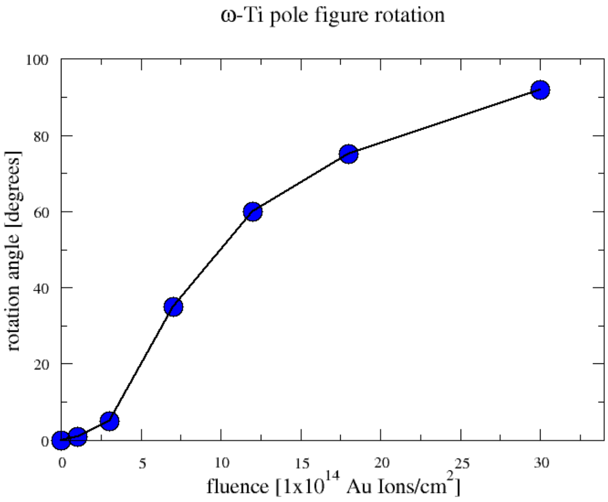

Fig. 2. Dependence of the angle of the grain rotation on the fluence. The newly added point at $3x10^{15}$ ions/cm^2 emphasises the slowing down of the rotation.

There is a well-known effect, referred as ‘ion hammering’, which describes anisotropic elongation of amorphous materials during ion irradiation [2]. Swift heavy ions deposit their energy in solids mainly through electronic interaction. Since the collisions with solid nuclei are unlikely at high energies, ions travel through the solid on a straight path. The energy deposition is concentrated in the volume few nanometer around the ion path. Due to the cylindrical shape of this volume, the material is plastically lengthened in the direction normal to the ion path and shortened in the direction parallel to it. If the amorphous layer fixed on the substrate is bombarded with swift heavy ions from a direction other than normal, elongation is transformed into shearing of the layer away from the direction of incoming ion beam. This effect was not observed in crystalline samples.

To measure the shearing of the nano-crystalline layer, a gold marker was deposited on the surface of the sample. The translation of the marker was measured in situ during the irradiation. A comparison with the mean-field calculation for the shearing in amorphous Ti layer (it is not possible to grow the amorphous Ti layer) showed that the measured nano-crystalline Ti layer shears with 2% of the expected rate for homogeneously amorphous Ti. This indicates that there is 2% amorphous material in the nano-crystalline Ti, which corresponds to the volume contained in 0.5 nm thick grain boundaries for 60nm large grains. This would also, in connection with the measured grain growth, explain the slowdown of rotation due to the growth of grains. However, the mean-filed theory and shearing measurements fail to explain the breaking of the cylindrical symmetry in textures. The change of the symmetry can only be explained by the rotation of grains with respect to their neighbouring grains, which implies the sliding of the grains along boundaries or more complicated creep processes. Grains rotate until they reach a minimum in grain boundary energy, i.e. the grain boundary matches a low-indexed crystalline plane. It is obvious that the sample does not behave like a partially amorphous layer. The grain boundaries themselves rather behave like individual thin amorphous layers. Thus, the shearing occurs between two grains applying a rotational momentum on individual grains as shown in figure 3.

Fig 3. Shearing of the nano-crystalline layer schematically shown as the sum of the grain boundary shearing. Green arrow marks the direction of the impinging ions. Grain boundaries, behaving like thin amorphous layers are sheared in the direction of small red arrows. As the grains are sliding along the boundaries, net elongation of the layer occurs along the direction normal to the ion beam (orange arrows). This dilatation tends to tilt the bottom interface of the layer (red line). However, since the layer is fixed on the substrate, similar like in amorphous layers, the red line must stay horizontal resulting in the rotation of the whole layer together with the grains within. In our texture measurements we observe this rotation.

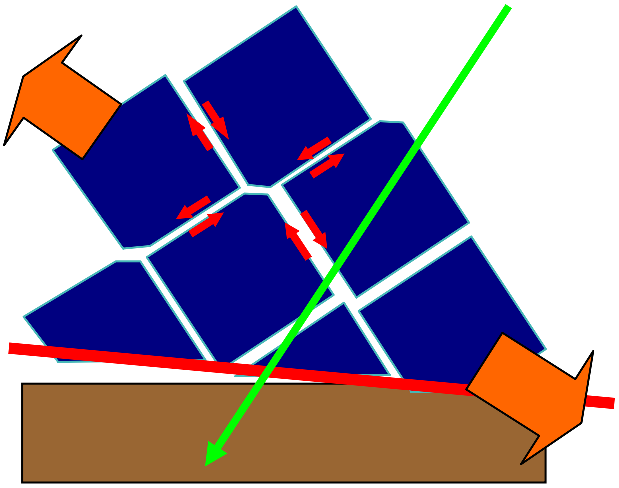

[1] I. Zizak, N. Darowski, G. Schumacher, S. Klaumünzer, W. Asmann, J. Gerlach, Texture Modification in Nano-crystalline Materials Using Swift Heavy Ions, *BESSY Annual Report 2004*

[2] S. Klaumünzer, Plastic flow of amorphous materials induced by swift heavy ions, *Mater. Sci. For.* 97-99, 623-630 (1992)

Element-resolved magnetic properties of epitaxial FeCu alloy films

M. A. Niño[1], J. Camarero[1], N. Mikuszeit[1], R. Miranda[1], J. J. de Miguel[1], R. Abrudan[2,3],
K. Fukumoto[2], W. Kuch[2], S. G. Wang[3], C. Tieg[3], J. Kirschner[3]

1 Departamento de Física de la Materia Condensada and Instituto de Materiales "Nicolás Cabrera", Universidad Autónoma de Madrid, E-28049 Madrid, Spain
2 Freie Universität Berlin, Institut für Experimentalphysik, Arnimallee 14, D-14195 Berlin, Germany
3 Max-Planck Institut für Mikrostrukturphysik, Weinberg 2, D-06120 Halle, Germany

(DAAD D/03/39337)

The magnetic properties of a given material are strongly related to its crystalline structure. Among others, aspects as important as the magnetic moment per atom, the type of magnetic long-range order (ferro- or antiferromagnetic), or the coercive field are extremely sensitive to any modification of the interatomic distances or the chemical environment. Iron-based structures are an example of this subtle interplay between structural and magnetic properties, and have consequently attracted extensive attention. A great variety of properties has been predicted if the structure and lattice parameter of Fe could be changed from their bulk properties [1, 2]. In previous experiments carried out in Madrid, LEED I-V curves measured on Fe$_x$Cu$_{1-x}$ films demonstrated that these alloys exist in the fcc structure for many monolayers and up to x≈70% Fe content on Cu(111) substrates [3].

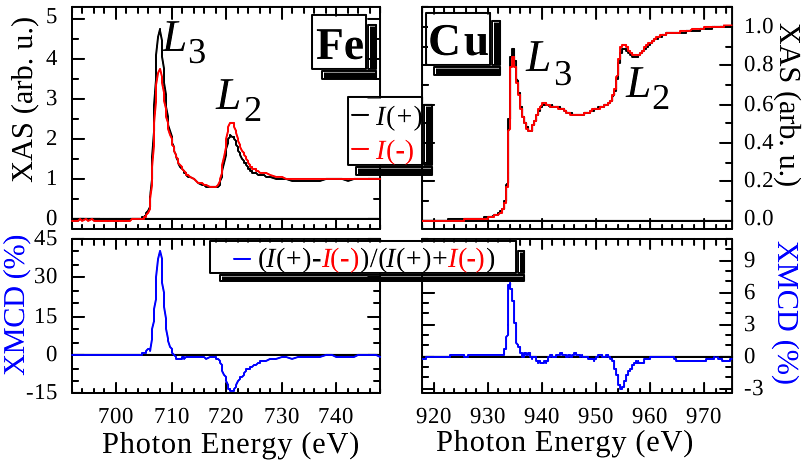

Fig. 1: Absorption (top) and dichroism (bottom) spectra at the Fe-$L_{2,3}$ (left) and Cu-$L_{2,3}$ (right) edges of 37 ML Fe$_{55}$Cu$_{45}$ for parallel (red) and antiparallel (black) alignment of magnetization direction and light helicity.

We performed element-resolved measurements of the magnetic moments in single-crystalline thin films of the artificial alloy Fe$_x$Cu$_{1-x}$ by x-ray magnetic circular dichroism (XMCD) at the Fe and Cu $L_{2,3}$ absorption edges at the UE56/2-PGM2 beamline. The absorption spectra were recorded in total electron yield mode by measuring the drain current of the sample. The artificial alloy films were prepared in-situ at room temperature on a Cu(111) substrate by thermal co-evaporation, while pre-deposited Pb served as a surfactant. The latter reduces the film roughness and, at the same time, prevents the segregation of the two components by reducing the atom mobility on the surface layer [4]. The measurements were performed in remanence. We studied the influence of thickness, concentration, and temperature on the electronic and element-resolved magnetic properties.

Figure 1 shows x-ray absorption spectra (top) for positive and negative helicity (black and red curves, respectively) and the difference, the magnetic dichroism (bottom), at the Fe and Cu $L_{2,3}$ absorption edges of a 37 ML $Fe_{55}Cu_{45}$ film on Cu(111). The induced magnetic moment of the Cu atoms is clearly visible in the difference curve between absorption spectra of opposite helicity. It is aligned parallel to the moment of the Fe atoms, as can be seen from the identical sign of the Fe and Cu dichroism at the L_3 and L_2 edges. The evaluation of the magnetic moments by sum rule analysis reveals an Fe spin moment of about 1.8 μ_B, smaller than that of bulk Fe. The induced moment at the Cu atoms is about 0.1 μ_B, comparable to that found in artificial FeCu alloys on Cu(001) [5].

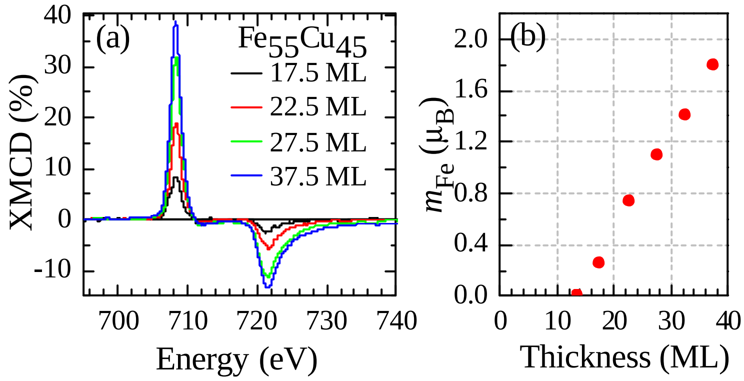

Fig. 2: Room temperature evolution of XMCD spectra (a) and Fe moment (b) with film thickness of an $Fe_{55}Cu_{45}$ alloy.

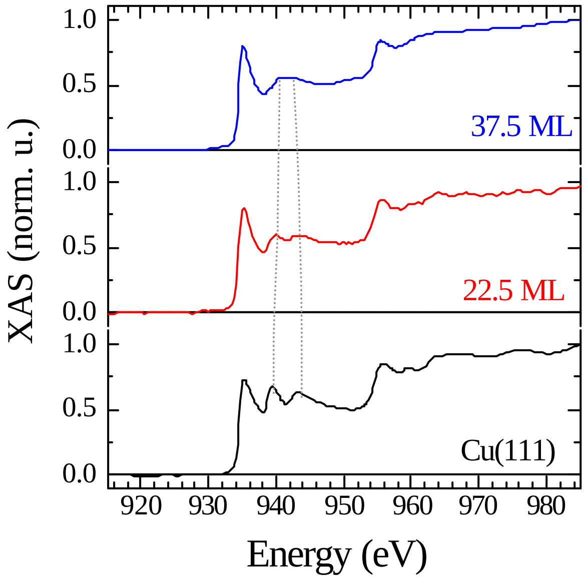

Fig. 3: Cu $L_{3,2}$-XAS spectra of a 37.5 ML (blue line) and a 22.5 ML (red) $Fe_{55}Cu_{45}$ film, averaged over both magnetization directions, and a clean Cu(111) sample (black). Two peaks around 942 eV photon energy (gray dotted lines) indicate an fcc-Cu like structure, whereas one peak indicates a bcc-like structure.

A detailed investigation of the thickness dependence of the element-resolved moments has been performed. For instance, the XMCD spectra at the Fe $L_{3,2}$ edge for $Fe_{55}Cu_{45}$ films shown in Fig. 2 (a) indicate a strong thickness-dependent XMCD effect in these films. A sum-rule analysis of these spectra yields an estimated depth-averaged magnetic moment of the Fe atoms, which increases with film thickness (see Fig.2 (b)). A similar behavior is also found for the value of the induced moment in the Cu atoms (not shown).

The thickness-dependent magnetic moments are probably related to the structural fcc–bcc transformation that takes place with increasing thickness. This transition is clearly observed in the absorption spectra at the Cu edge. Figure 3 compares the XAS spectra at the Cu $L_{3,2}$ edge for two chosen thicknesses of the $Fe_{55}Cu_{45}$ alloy and for the Cu substrate. The structural change in the alloy is reflected in the change of XAS line shape just above the L_3 edge, around 942 eV, where a two-peaked feature converts to a single peak when the thickness of the alloy increases. Moreover, information about the unoccupied electronic states at the Cu sites can also be obtained from absorption measurements. For instance, an enhancement in intensity for the alloy film is observed at the Cu L_3 edge, ~934 eV photon energy. Since the $L_{3,2}$ XAS reflects the Cu unoccupied density of states above the Fermi edge, this can be judged as manifestation of an enhanced number of unoccupied Cu-like states in FeCu with respect to pure Cu metal.

Although a similar general behaviour is found also in FeCu alloys with a lower Fe concentration, there are still important differences. Figure 4 (a) shows the XMCD spectra of an $Fe_{45}Cu_{55}$ alloy film for different thicknesses. In this case, smaller Fe-L_3 XMCD values are found. Therefore, a lower Fe concentration would permit to grow thicker FeCu alloy films which may exhibit a low-spin magnetic phase. This is because the fcc–bcc structural transition is delayed when the concentration of the Fe in the alloy is smaller. Low temperature measurements show that this structural transition could also occur by decreasing the temperature.

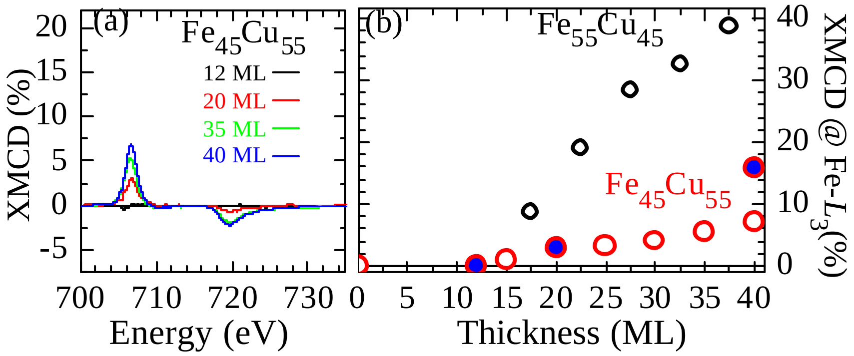

Fig. 4: (a) Evolution of XMCD spectra of an $Fe_{45}Cu_{55}$ film with thickness. (b) Thickness-dependence of the XMCD signal at Fe-L_3 of $Fe_{55}Cu_{45}$ (black circles) and $Fe_{45}Cu_{55}$ (red circles). The circles filled with blue color were extracted from measurements performed at 130 K.

In summary, our results demonstrate that it is possible to tune at will the average magnetic moments of the iron atoms by combining the appropriate thickness and chemical composition of the alloy.

[1] V. L. Moruzzi, P. M. Markus, and J. Kübler, Phys. Rev.B **39,** 6957 (1989).

[2] V. M. García-Suárez, C. M. Newman, C. J. Lambert, J. M. Pruneda, and J. Ferrer, J. Phys.: Condens. Matter **16**, 5453 (2004).

[3] D. Farias, M. A. Niño, J. J. de Miguel, R. Miranda, J. Morse, and G. Bozzolo, Appl. Surf. Sci. **219**, 80 (2003).

[4] J. Camarero, J. Ferrón, V. Cros, L. Gómez, A. L. Vázquez de Parga, J. M. Gallego, J. E. Prieto, J. J. de Miguel, and R. Miranda, Phys. Rev. Lett. **81**, 850 (1998).

[5] W. Kuch, M. Salvietti, X.Gao, M.-T. Lin, M. Klaua, J. Barthel, C. V. Mohan, and J. Kirschner, Phys. Rev. B **58**, 8556 (1998).

Mapping of hydrogen diffusion profiles in orthopyroxene

Roland Stalder
Geowissenschaftliches Zentrum, Göttingen University

Hydrogen is only a minor component in the Earth's mantle. As even small amounts of hydrogen have a strong effect on many physical properties of minerals, the knowledge of the concentration of hydrogen in natural mantle minerals is crucial for understanding many upper mantle processes. Orthopyroxene ($(Mg,Fe)_2Si_2O_6$) as the second most abundant mineral in the Earth's upper mantle incorporates traces of hydrogen and may be regarded as an important host for water in the Earth's upper mantle. However, during ascent to the Earth's surface by volcanic eruptions, the hydrogen content of mantle minerals may be modified and may therefore not reflect the original mantle concentration. The aim of this study is the quantification of hydrogen mobility in orthopyroxene depending on their chemical composition. One important feature is the anisotropic behaviour of hydrogen diffusion, i.e., in natural Fe-bearing samples hydrogen diffusion along the [001]-direction is faster by one order of magnitude than along [010], which may contribute to the observed electrical anisotropy of the asthenosphere inferred from magnetotelluric data.

In this study synchroton IR-spectroscopy has been used to map OH- and OD-concentrations in orthopyroxene crystals exhibiting a diffusion profile due to thermal treatment in atmospheres with different H_2-, H_2O- and D_2O-pressures. During IR-analysis an automatic X-Y-stage moved the sample to the next analysis point. Because of the higher

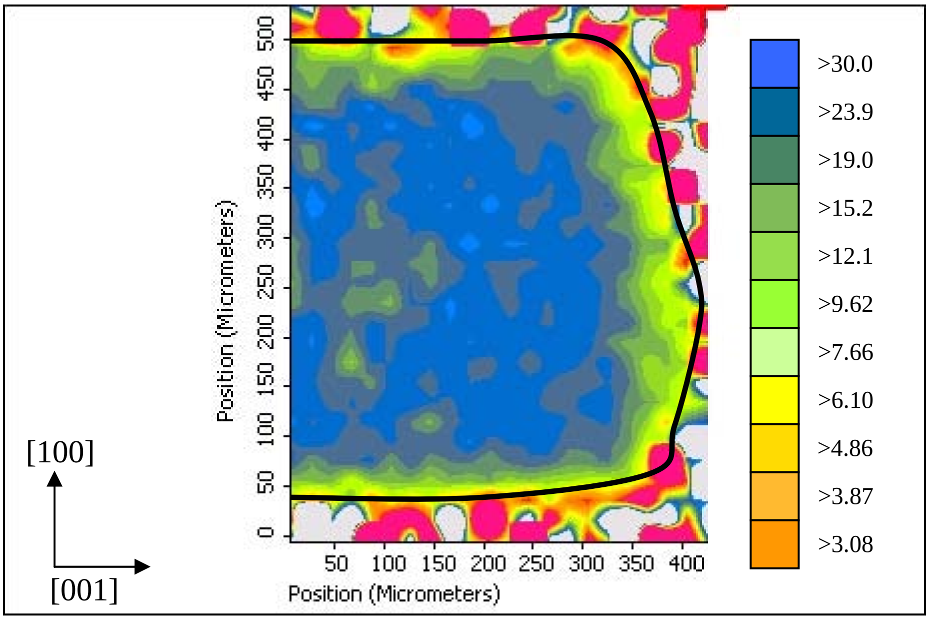

Fig.1 : Map showing the distribution of OH/OD in a Cr-doped enstatite after thermal treatment in H_2 at 1 bar and 800°C. OH/OD-ratios were determined by peak area ratios (spectral range between 3435-3460 cm^{-1} for OH and 2540-2570 cm^{-1} for OD). The solid black line highlights the boarder of the crystal; spectra taken outside or on the edge of the sample lead to random values. Data points were acquired with an increment of 15 or 20 µm, respectively; after data reduction a smoothing function averaging over the 8 nearest neighbour points was performed.

brilliance of the beam, smaller beam diameters (10-20 µm) and shorter counting times (8-32 scans) in comparison to usual IR-spectroscopy could be applied and sufficiently strong absorption signals in the OH- and OD-vibration regions could be generated, enabing mapping of sub-millimeter crystals. All spectra were automatically processed by peak height, peak area, peak height ratio or peak area ratio of two chosen peaks, and encoded as colours (Fig.1).

The major findings of the mapped orthopyroxene crystals are 1) a negative influence of Cr and Al on hydrogen self-diffusion, 2) a less pronounced diffusion anisotropy in Fe-free, Cr (or Al) -bearing crystals compared to natural Fe-, Cr- and Al-bearing orthopyroxenes or pure synthetic enstatite ($Mg_2Si_2O_6$).

Acknowledgements: this project was supported by BMBF (grant 05 ES3XBA5)

Comparaison between synchrotron SRCD experiments

Frank Wien#, Jean-Claude Maurizot*, Simona Miron£ and Matthieu Réfrégiers#
Synchrotron SOLEIL – Fr, * CNRS – Fr, £ Institut Curie – Fr

Support through BESSY EC I3 contract, n° BESSY-BM.05.1.118

1- Objectives

Our primary objective was to follow the structural changes of an analogue of human galactose mutarotase. Our secondary objective was to test the feasability of synchrotron radiation circular dichroism (SCRD) experiments with mixing of DNA and proteins altogether as SRCD is one of few techniques which permits the joint observation of structural changes in proteins and in DNA. All those results will be used for our reflexion on the design of a new SRCD beamline in Europe.

2- Experiments

i. CSA

CSA is a UV circular dichroism standard. It has to be checked regularly.
We verified long and short term baseline stability. Our opinion (FW and MR) is that a medium to short term stability is good and that a long term stability was not reproducible (after several beam fills). For calibrating the protein spectra to a CSA spectrum routinely, we had to measure CSA spectra on a regular basis as internal standard. CSA shall be measured after each beamfill.

ii. Lysozyme and other proteins

Lysozyme in phosphate buffer at a 12 mg/ml solution is shown in blue.
After baseline substraction, the spectrum is very similar to the one of lysozyme taken at Daresbury station 12.1.

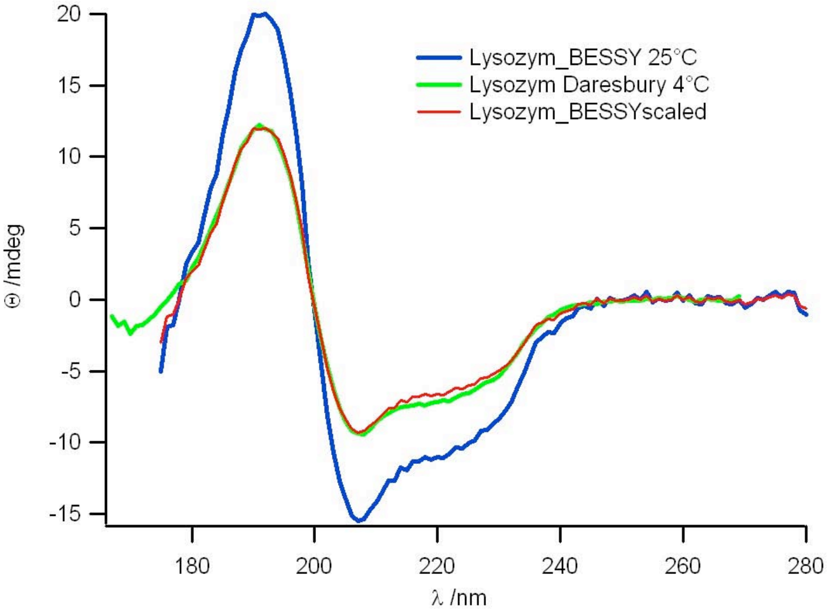

Comparison between BESSY and Daresbury Lysozyms spectra

The same results were obtained with myoglobin and concanavalin A (spectra not shown). Comparison of the spectra with other spectra obtained on different beamlines were very similar (from NSLS, SRS and ISA)

.

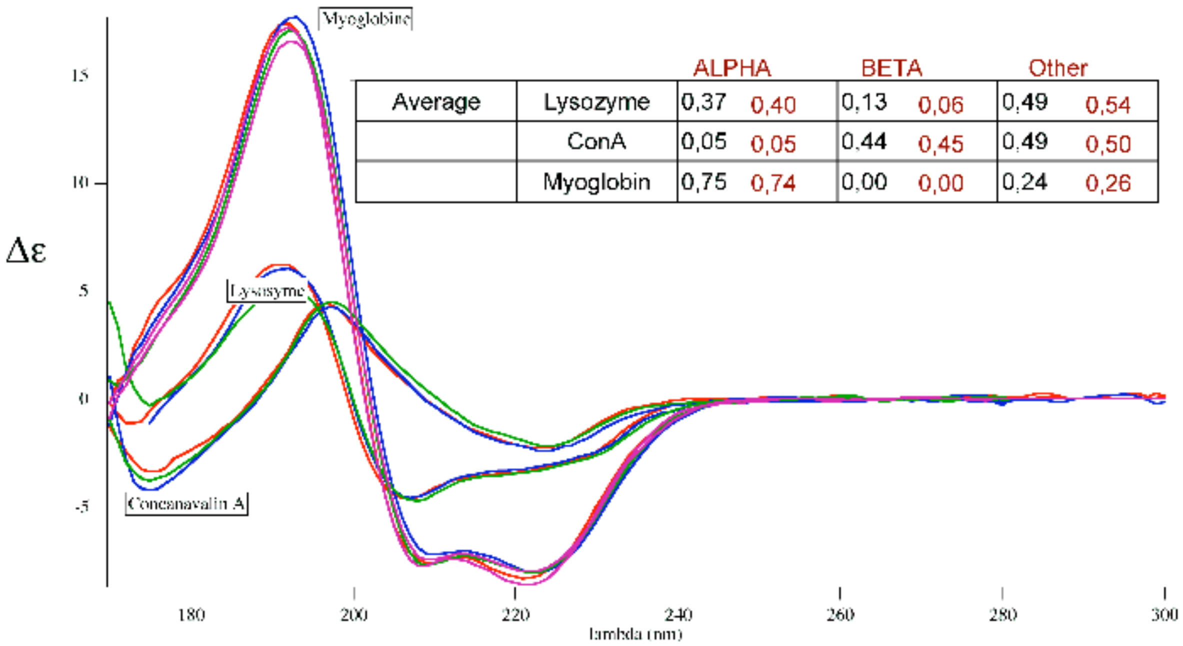

		ALPHA		BETA		Other	
Average	Lysozyme	0,37	0,40	0,13	0,06	0,49	0,54
	ConA	0,05	0,05	0.44	0,45	0.49	0,50
	Myoglobin	0,75	0,74	0,00	0,00	0,24	0,26

Computed structures were very close to protein crystallography prediction (respectively black and red).

iii. DNA

Two oligonucleotides were tested, first, spectra were recorded of nucleotides alone, then it was decided to mix GAA and TTC together, normally we should have a linear combination of both spectra with an intensity decrease due to the dilution (half and half).

After mixing in water 50 % of GAA and 50 % of TTC, the result spectrum is compared to the mean linear combination of the 2 oligonucleotides alone in water. The arithmetic mean and the experimental mean in water are very close, although there do remain some differences, as shown on the difference spectrum, that may come from the fact that the experimental mixture is not really 50 / 50 as was calculated for the arithmetic mixing.
After mixing in NaF, they are no real differences for the oligonucleotides alone. However, differences are more subtle between GA+TC in water and NaF, but they do exist. Notably, man could compare the 190 and the 215 nm peaks.

3- Conclusion

We were able to show that the proteins (Lysozyme, ConcanavalinA, …) spectra collected on 3m-NIM-1 at BESSY are similar if not identical to the spectra collected on other synchrotron stations (Daresbury, UK ; Aarhus, DK ; Brookhaven, USA) after elaborating a joint experimental protocol, opening the possibility to collect data at each synchrotron endstation with quality and reproducibility assurances, in conclusion of this part no matter what the setting, the spectra are equivalents.
We were able to do the first SRCD experiments with oligonucleotides. Our first results encourage us to continue toward the protein-DNA interaction scientific field. SRCD would be a great tool for this field as man can follow structural changes via CD spectrum for DNA and proteins at the same time.

Innershell absorption spectroscopy of proteinogenic amino acids at all relevant absorption edges

Y. Zubavichus,[1,2] A. Shaporenko,[1] M. Grunze,[1] and M. Zharnikov[1]

[1]*Angewandte Physikalische Chemie, Universität Heidelberg, Im Neuenheimer Feld 253,*
69120 Heidelberg, Germany

[2]*Institute of Organoelement Compounds, Russian Academy of Sciences, 28 Vavilova st.,*
119991 Moscow, Russia

NEXAFS (Near-Edge X-ray Absorption Fine Structure) spectroscopy and related synchrotron-based soft X-ray spectroscopic techniques provide powerful tools for the elucidation of the electronic structure of organic substances in a variety of sample environments. One of the current challenges in this field is the application of NEXAFS to bioorganic objects. Such studies are difficult for various reasons, including the complexity of the molecular composition and radiation sensitivity of the target objects. Proteins, the most important class of biopolymers, are composed of amino acids. Thus, a careful spectral characterization of amino acids is a necessary first step in the application of NEXAFS to complex systems of biological significance. Although many NEXAFS studies of amino acids have been performed, no comprehensive spectral libraries have been reported to date. So far, only the C K-edge spectra of the major 20 amino acids have been summarized by Kaznacheyev et al.[1] The spectra were measured in the transmission mode from thin polycrystalline films cast from solutions of the respective amino acids in trifluoroacetic acid onto thin silicon nitride substrates. The samples prepared in this way were shown to contain traces of the solvent and thus a correct analysis of high-lying σ*-resonances appeared difficult. Meanwhile, the N and O K-edge NEXAFS spectra were reported only for a few selected amino acids.

In our study,[2] we present a collection of carefully calibrated low-noise NEXAFS spectra of 22 most common proteinogenic amino acids (i.e., 20 standard gene-encoded amino acids along with cystine and hydroxyl-proline) in the zwitter-ionic form measured at all relevant absorption edges, i.e., at the C, N, and O K-edges using the partial electron yield mode from solvent-free powder films.

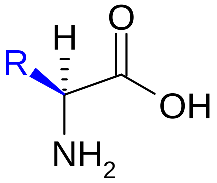

Scheme 1. Molecular formula of an amino acid (as neutral molecule).

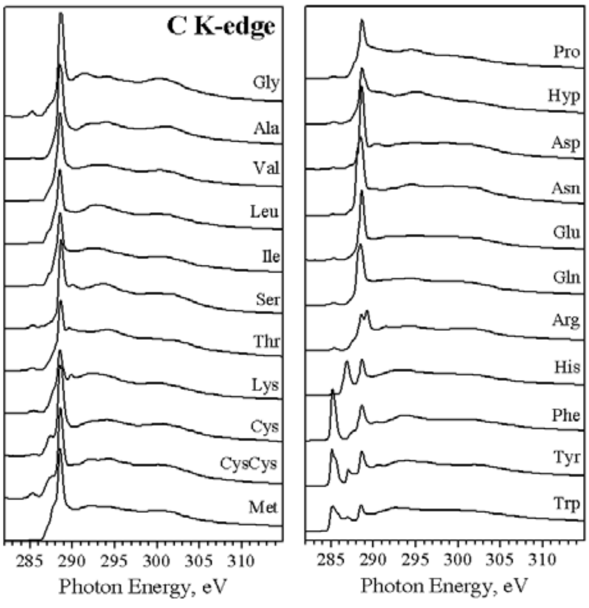

Fig. 1. Experimental C K-edge NEXAFS spectra of the amino acids.

The majority of C K-edge spectra (Fig. 1) are dominated by three features, viz., a narrow resonance at around 288.6 eV attributable to the π*(COO) transition[5] and broader σ*-resonances at ca. 293.0 and 300.0 eV. The former dominantly comprises σ* (C-C) components, whereas the latter corresponds to transitions to σ*-states associated with the carboxylate group. In the case of amino acids with the amide group (i.e., asparagine and glutamine), the major π*-resonance is broadened and shifted to 288.3 eV in agreement with the results reported by Kaznacheyev et al.[1]

Arginine, phenylalanine, tyrosine, histidine, and tryptophan manifest characteristic patterns of narrow π*-transitions. The amino acids containing –OH or –NH_2 substituents in the side chains (i.e., serine, threonine, and lysine) manifest distinct peaks at 289.6-290.0 eV attributable to the σ^*(C-OH/NH_2) transitions. The sulfur-containing amino acids (cysteine, cystine, and methionine) exhibit distinct σ^*(C-S) peaks just below the main π^*(COO) feature at ca. 287.3 eV.

The majority of the N K-edge NEXAFS spectra of the amino acids (Fig. 2) are dominated by a relatively broad σ^*(N-C) peak at 406.2-406.6 eV. In the cases of proline and hydroxyproline, this peak is apparently split into two components at ca. 405.6 and 409.7 eV due to the saturated nitrogen heterocycle. This peak is broadened in the case of phenylalanine and has a diffuse pre-edge structure (400.1-402.8 eV) in the case of lysine, probably due to the additional non-protonated amino group present in this amino acid. Some amino acids show distinct π^*-resonances.

All O K-edge NEXAFS spectra of the amino acids (Fig. 3) are quite similar to each other. They exhibit a dominant π^* peak associated with the carboxylate group at 532.3-532.5eV and the respective σ^*-component at ca. 543.5 eV in agreement with earlier observations. No substantial shifts in the position of the main resonance due to introduction of additional COOH or $CONH_2$ groups is observed although the amino acids containing protonated carboxy groups (i.e., aspartic and glutamic acids) show a minor feature at 534.0 eV, which can be assigned to the transition of the electron from the protonated oxygen atom to the π^* orbital of the carboxy group. The amino acids containing the hydroxy group (serine, threonine, hydroproline, and tyrosine) manifest a broad features at 538.0 (Ser and Thr), 539.0 (Hyp), and 539.4 eV (Tyr), which can be thus attributed to the σ^*(O-C) transitions.

In summary, we have presented and analyzed the C, N, and O K-edge NEXAFS spectra of the 22 most common proteinogenic α-amino acids in the zwitter-ionic form. The respective spectral library is an important step to establish such a powerful technique as NEXAFS spectroscopy to study complex systems of biological significance.

This work has been supported by BMBF (05KS4VHA/4 and 05 ES3XBA/5).

References:

1. K. Kaznacheyev, A. Osanna, C. Jacobsen, O. Plashkevych, O. Vahtras, H. Ågren, V. Carravetta, A. P. Hitchcock, *J. Phys. Chem. A* **106**, 3153 (2002) .
2. Y. Zubavichus, A. Shaporenko, M. Grunze, and M. Zharnikov, J. Phys. Chem. A **109**, 6998 (2005).

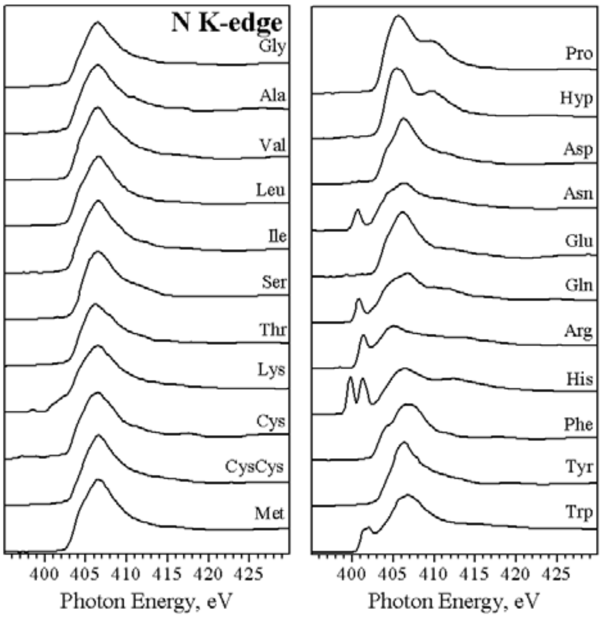

Fig. 2. Experimental N K-edge NEXAFS spectra of the amino acids.

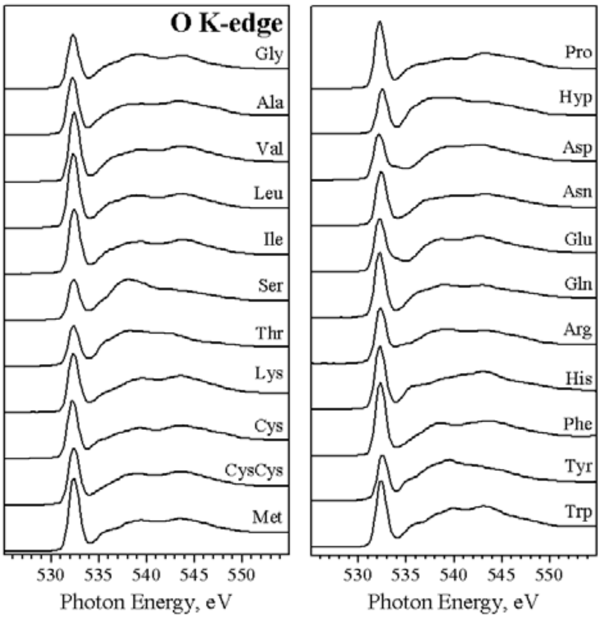

Fig. 3. Experimental O K-edge NEXAFS spectra of the amino acids.

X-ray absorption spectroscopy on biomimetic model complexes - structure and redox behaviour

Paola Loja[a], Peter Liebisch[a], Olga Kirilenko[a], Simone Löscher[a], Ann Magnuson[b], Magnus Anderlund[b], Sascha Ott[c], Michael Haumann[a], Holger Dau[a*]

[a] Freie Universität Berlin, Fachbereich Physik, Arnimallee 14, 14195 Berlin
[b] Uppsala University, Molecular Biomimetics, Villavägen 6, 75236 Uppsala, Sweden
[c] Uppsala University, Department of Organic Chemistry, Box 599, 75124 Uppsala, Sweden
*holger.dau@physik.fu-berlin.de

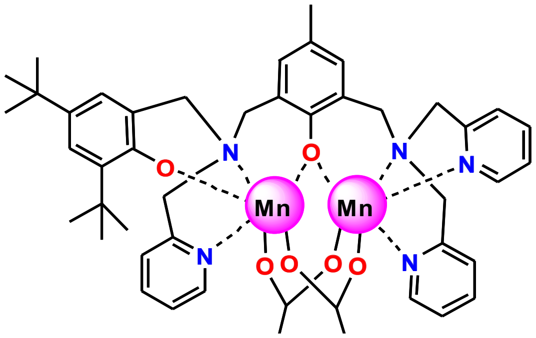

Fig 1: Bi-nuclear manganese complex

During two previous measuring periods we set up a helium cryostat/energy-resolving Ge-detector system designed to perform XAS studies on dilute samples at low temperatures at beamline KMC-1 at BESSY. First measurements on biological protein samples were successfully carried out in July 2005.

During this measuring period several bio-inorganic model compounds were investigated by XANES and EXAFS measurements. These biomimetic compounds are of high interest to elucidate the chemistry underlying oxygenic photosynthesis and biological hydrogen production [1-2]. Three sets of experiments were carried out:

1. The asymmetric binuclear manganese complex shown in Fig. 1 was synthesized and three oxidation states were generated electrochemically in three different solvents: pure acetonitrile (water free), acetonitrile containing 1 % water, and acetonitrile containing 5 % water. Spectra were recorded from all 9 samples up to at least 540 eV above the Mn K-edge. Preliminary EXAFS analysis suggests significant structural changes upon the transition from the Mn(II,III) to the Mn(III,III) state in the presence of water (Figure 2).

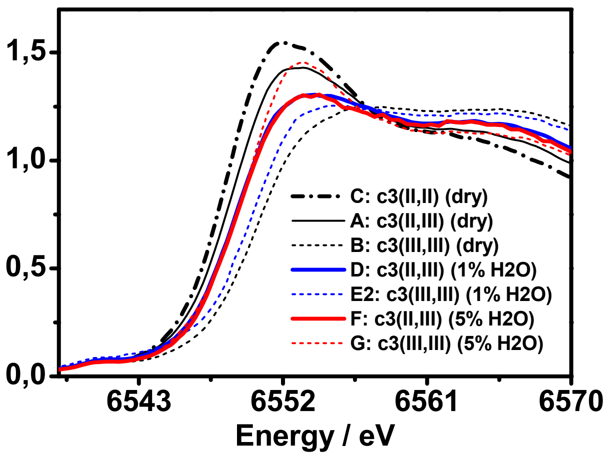

Fig. 2A: XANES spectra at the Mn K-edge of selected samples of the binuclear manganese complex.

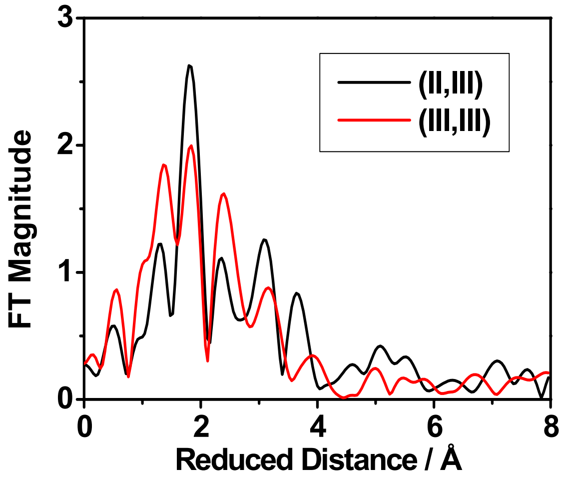

Fig. 2B: Fourier transforms of EXAFS oscillations of samples with 1 % of H_2O (two oxidation states).

2. Temperature dependence studies of EXAFS spectra, aiming at a better understanding of protein dynamics, were performed on a symmetric binuclear Mn complex in solution as well as in its crystalline state. Mn-EXAFS spectra were recorded at 10 different temperatures between 20 K and 300 K. Preliminary data analysis suggests that in the crystalline form only a weak temperature dependence of the Debye-Waller parameter is found. A breakpoint around 200 K in the temperature dependence as previously observed in the manganese complex of oxygenic photosynthesis, which we attribute to protein-specific motions, was not observed. In the dissolved complexes, the situation is less clear.

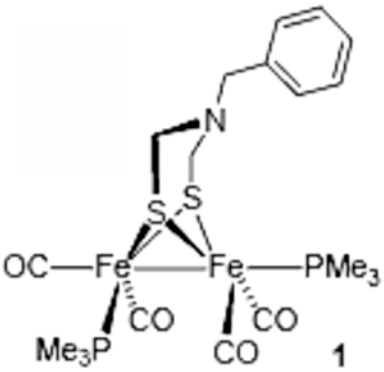

1

Fig. 3: Fe-Fe model complex.

3. EXAFS spectra (10 K) at the Fe K-edge were measured on a crystallized synthetic compound with a [Fe_2(μ-adt)$(CO)_4(PMe_3)_2$] dinuclear iron site (Figure 3). This model mimics certain features of the active site of hydrogen production in iron-iron hydrogenases. In the iron-iron hydrogenase the ligand set of the unusual low-valent di-iron subsite is similar as it contains carbon monoxide and cyanide ligands and a bridging sulfide provided by an azadithiolate-ether. Four different protonation states of the model, which had been characterized previously by FTIR, were investigated by XAFS at the iron K-edge. Quantitative analysis of the spectra is currently underway.

Improvements of the XAS setup: (i) The cryostat/Ge-detector system further was improved before and during this beam time: Small gas leaks in the sample compartment of the cryostat system (filled with He gas at ~200 mBar) were identified and eliminated, thereby reducing problems due to ice formation on the samples after extended measuring periods at 10-20 K. (ii) The detector was tested and operated in a mode suitable for the relatively high fluorescence count rates (10^5 s^{-1} with samples containing ~10 mM metal) achievable at KMC-1. (iii) Further developments are in preparation: Better definition of spot size and incoming X-ray flux using a slit assembly in front of a new I_0-detector system directly at the cryostat entrance; this will provide better definition of the illuminated area on the sample and more precise control of irradiation duration as needed to avoid radiation damage of sensitive biological samples. A new stage for the cryostat system will be constructed to allow for more precise positioning of samples in the X-ray beam.

We consider the November beam time as highly successful. Thanks to the excellent support of the scientists at KMC-1 (F. Schäfers, M. Mertin), in a collaborative approach with Swedish research groups, good-quality EXAFS spectra at the Mn and Fe K-edge could be obtained by us of several sets of biomimetic model compounds. Respective publications are in progress. The promising studies on the temperature dependence of the EXAFS in various samples types (proteins, molecules in crystalline form and in solution, ..) will be continued.

References

[1] A. Magnuson, P. Liebisch, J. Högblom, M. Anderlund, R. Lomoth, W. Meyer-Klaucke, M. Haumann, H. Dau, Bridging-mode changes facilitate successive oxidation steps at about 1 V in two binuclear manganese complexes – implications for photosynthetic water oxidation. J. Bioinorg. Chem., accepted for publication (2006).

[2] S. Ott, M. Kritikos, B. Akermark, L. Sun, R. Lomoth, A biomimetic pathway for hydrogen evolution from a model of the iron hydrogenase active site. Angew. Chem. Int. Ed. 43, 1006-1009 (2004).

Crystal structure of *Yersinia enterocolitica* type III secretion chaperone SycT

Carina R. Büttner[1], Guy R. Cornelis[2], Dirk W. Heinz[1] and Hartmut H. Niemann[1]

[1]Division of Structural Biology, German Research Centre for Biotechnology, D-38124, Braunschweig, Germany. [2]Division of Molecular Microbiology, Biozentrum, University of Basel, CH-4056 Basel, Switzerland

Type III secretion (TTS) systems function as molecular syringes used by many pathogenic gram-negative bacteria to inject effector proteins directly into the host cell cytoplasm. A hollow protein conduit (the needle) is attached to the base spanning the inner and outer bacterial membrane. For translocation, some TTS effectors require cognate chaperones - small, acidic proteins sharing only very limited sequence homology. The exact role of the TTS chaperones in secretion is still under debate.

Yersinia enterocolitica is a food-borne human pathogen causing enteritis. *Y. enterocolitica* cross the intestinal barrier and multiply in lymphatic tissue. Effector proteins injected via the type III secretion pathway exert anti-inflammatory and anti-phagocytic effects, thereby allowing survival in lymphatic tissue. The effector protein YopT is a cysteine protease that contributes to the anti-phagocytic effect by cleaving the membrane anchor of Rho GTPases. The specific chaperone for YopT is called SycT. In order to learn more about the role of chaperones in TTS, we have determined the structure of SycT.

We crystallized C-terminally truncated, Se-Met substituted SycT in two space groups. At BESSY BL14.1 we collected a three-wavelength MAD data set from a crystal in $P6_2$ (top) and a SAD peak data set from a $P2_12_12_1$ crystal (bottom). Finally, we determined the structure by SAD using the $P6_2$ peak data set. The $P2_12_12_1$ structure was solved by molecular replacement.

Data collection statistics

Space group	$P6_2$	$P2_12_12_1$
Unit cell dimesions [Å], [°]	a = b = 92.0, c = 55.4 $\alpha = \beta = 90$, $\gamma = 120$	a = 51.5, b = 63.1, c = 74.4 $\alpha = \beta = \gamma = 90$
Wavelength [Å]	0.97957 (peak)	0.9795 (peak)
Resolution [Å]	79.0 - 1.9 (2.0 - 1.9)	48.1 - 2.0 (2.1 – 2.0)
Mosaicity [°]	0.14	0.25
Completeness [%]	99.5 (96.4)	98.4 (96.4)
Anomalous redundancy	5.8	3.9
Observations	237251	118050
Unique reflections	21134	16331
I/σ [I]	16.6 (5.4)	12.3 (4.6)
R_{meas}	7.2 (39.8)	8.0 (37.3)

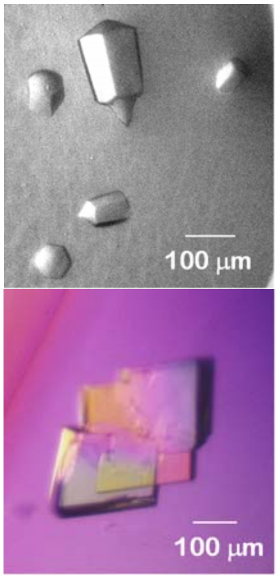

Selenium atoms (green cross in left image) were located with ShelxD. Experimental electron density after solvent flattening with ShelxE is shown in both images. On the right, the initial electron density from ShelxE is superposed with the final refined model.

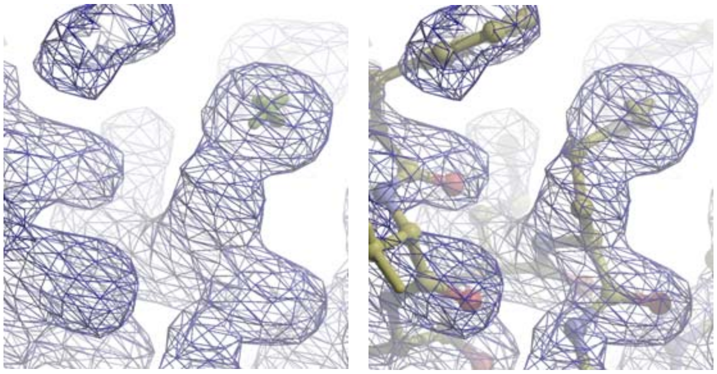

SycT forms a homodimer. In each monomer, two α-helices pack against a six-stranded antiparallel β-sheet. Overall, SycT shares the global fold of other TTS effector chaperones. Two main differences are found: (1) In SycT, loop regions form the dimerization interface, whereas a helix mediates homodimer formation in the other chaperons. (2) While most chaperones have a five stranded β-sheet, SycT has an additional edge strand β0.

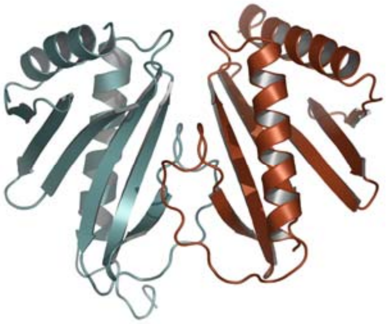

Patches of hydrophobic residues (brown) are found on the surface of SycT. Two of these (patch 1 and 2) are present in other TTS chaperones as well. They are spatially conserved and were shown to be involved in effector binding in other TTS chaperones.

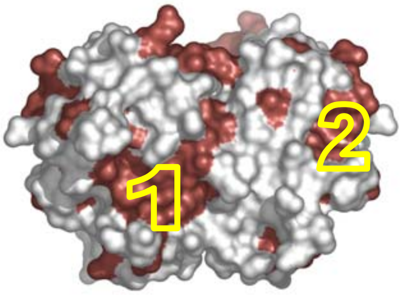

The additional strand β0 in SycT (red ellipse, left) is close to hydrophobic patch 2 and would interfere with effector binding as observed in other chaperones. However, β0 has high B-factors in the hexagonal form (middle) suggesting it may undergo a conformational change upon effector binding. This assumption was confirmed experimentally. In a third crystal form of SycT, we actually observed a β-strand to loop transition for the region forming β0 (right).

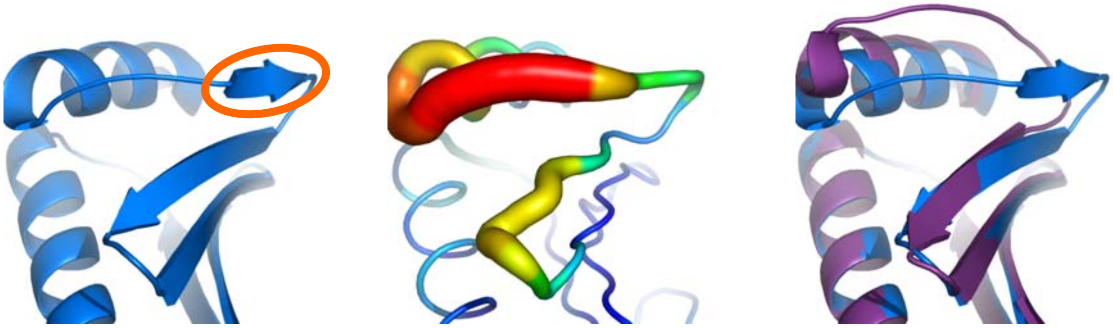

Büttner, C.R.; Cornelis, G.R.; Heinz, D.W.; and Niemann, H.H. (2005) Crystal structure of *Yersinia enterocolitica* type III secretion chaperone SycT. *Protein Sci.*:**14**:1993-2002.

X-ray fluorescence characterization of human nails

E. Mavromati, M. Katsikini, F. Pinakidou, E. C. Paloura
School of Physics, Aristotle University of Thessaloniki, 54124 Thessaloniki, GREECE

X-ray fluorescence (XRF) spectroscopy using Synchrotron Radiation (SR-XRF) provides high sensitivity due to the high flux and the polarized nature of SR as well as the energy tunability. Additionally, the small size of the SR beam allows the two-dimensional XRF mapping for the detection of fluctuations in the concentration of certain elements in inhomogeneous samples. In this report, results of test XRF measurements on human fingernails are presented. Like hair, the nail is a modified type of epidermis that is composed of compact layers of dead cells of epithelium formed by a-keratin. The keratins are a family of fibrous, insoluble, structural proteins, which are rich in cysteine, a sulphur-containing amino acid. Elements essential for the human organism can be found in nails at high (major elements e.g. Mg, Ca) or low (trace elements e.g. Cu, Zn) concentration. The lack or excess of the essential elements is related to illnesses or disorders.

Nail samples from seven female donors with age ranging from 29 to 91 years, are studied by means of SR-XRF. The samples s2 and s6 were used as control samples since they belong to “healthy” donors. The other samples belong to donors with identified health problems. The XRF spectra were recorded at the KMC-II beamline using excitation energies of 9.5, 10.5 and 13keV. The fluorescence photons were detected using the Xflash energy dispersive detector positioned on the horizontal plane at right angle to the beam.

The XRF spectra recorded for three different energies of impinging photons (excitation energy) are shown in Fig. 1. Along with the *K* emission lines of the elements S, Cl, K, Ca, Fe, Cu, Zn and As the lines due to elastic (Rayleigh) and inelastic (Compton) scattering are also present. As shown in Fig. 1, as the excitation energy increases, emission peaks of elements of higher atomic number emerge in the spectra. The Rayleigh peaks appear at energies equal to the excitation energy. In contrast, the energy position of the Compton peak, E, depends on the excitation energy, E_0, and is in agreement with the theoretical value calculated using the formula $\frac{1}{E}=\frac{1}{E_0}+\frac{1-\cos 2\vartheta}{511}$ The scattering angle, 2θ, was equal to 90° in our case.

In order to correct the spectra for the different mass and surface shape effects of the samples, as well as for the different sample-detector distance and photon flux, they were normalized with the total area under the scattering (Rayleigh and Compton) peaks. The Rayleigh peak was fitted with a Gaussian while the Compton peak is asymmetric[1] and was fitted using a Pearson IV function. The use of a Pearson IV function has no physical meaning, but it was used since it fits very well the Compton peak and thus provides accurate value for the area under the peak. The area under the K_α and K_β fluorescence peaks was determined using the WINQXAS program, after proper energy calibration and background subtraction.

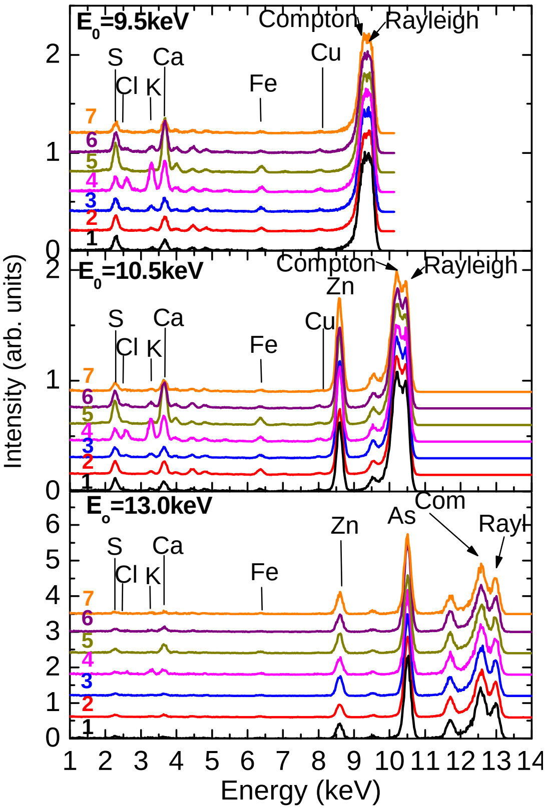

Fig. 1*: XRF spectra recorded at three different excitation energies: 9.5, 10.5 and 13 keV.*

The concentration of the element A in a sample, C_A, is given by $C_A \propto \frac{I_A}{Q_A \omega_A \alpha_A Abs_A}$ where I_A is the area under the corresponding emission peak, Q_A is the absorption cross section of the element, ω_A is the fluorescence yield and α_A is the probability of de-excitation of the atom by a specific line emission from a series of lines (e.g. the line K_α from the *K* series, K_α and K_β). Abs_A is the self-absorption term that can be ignored due to the low concentration of the essential elements in the nail. It is evident that, for a specific emission line of the certain element and for spectra recorded at the same excitation energy, higher area under the peak means higher concentration of the corresponding element. Fig. 2 shows the normalized area under the K_α peak of the K, Cl and Ca for the spectra recorded with excitation energy 10.5keV. The horizontal blue lines correspond to the values in the control samples. The ratio of the concentrations of two different elements in the same sample is $\frac{C_A}{C_B}=\frac{Q_B\cdot\omega_B\cdot\alpha_B}{Q_A\cdot\omega_A\cdot\alpha_A}\frac{I_A}{I_B}$. After substituting the values of Q, ω and α.[2,3,4] from the peak intensity ratios the concentration ratios result. The Zn/Cu ratio for the various samples is shown in Fig. 3

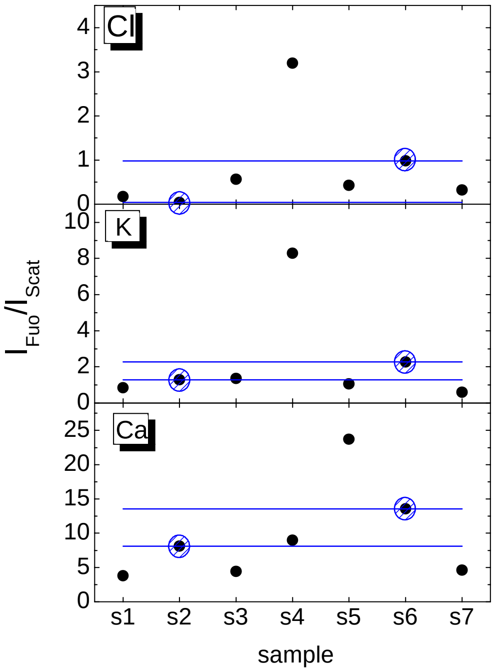

Fig. 2: *Normalized intensities of K_α peaks of Cl, K and Ca at the spectra recorded with excitation energy 10.5keV. The blue lines represent the values of the control samples.*

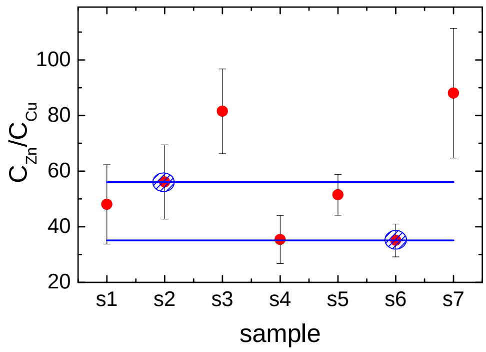

Fig. 3: *Concentration ratio of Zn and Cu The blue lines represent the values of the control samples.*

The concentration of the K and Cl electrolytes was very high in the sample s4 although the Cl over K ratio does not differ from the corresponding value in the healthy donor samples. This is expected since K and Cl are positively correlated in the human organism in the sense that increase of one causes the increase of the other. The high concentration of K in the sample s4 is related to the tremors from which the donor of the s4 sample suffers since hyperkalemia causes disorders in the neuromuscular system.[5] The high Ca concentration in the sample s5 can be attributed to osteomalacia / ostepoporosis, where the bones brittle and Ca is liberated in the blood.[6] Low concentration of Ca has been observed in the samples s1 and s3 due to the cortisone intake which is known to affect the Ca absorption in the organism[7] and s7 due to hyperthyroidism which causes hypocalcemia.[8]

The Zn/Cu ratio is increased in the samples s3 and s8. Cu and Zn are two antagonistic trace elements that are related to the immune system.[9] The Zn/Cu ratio is found equal to ~29 in nails of healthy donors.[10] Increased Zn/Cu ratio shows a hyperactive immune system that is related to the autoimmune diseases from which the donors of samples 3 and 7 suffer (s3: allergic vasculitis, s7: rheumatoid arthritis).

In conclusion, SR-XRF can be used for the detection of lack or excess of essential (major and trace) elements in the human nails, related to illnesses or disorders.

---

[1] *M. Van Gysel, P. Lemberge, P. Van Espen, X-ray Spectrometry,**32**, 139 (2003)*
[2] *B.L. Henke et al, X – ray Interactions. Atomic Data and Nuclear Data Tables, Vol **54**, 181 (1993)*
[3] *M. O. Krause, J. Phys. Chem. Ref. Data **8**, 307 (1979).*
[4] *X – ray Properties of the Elements: xdb.lbl.gov*
[5] www.update4nurses.com/92005.htm
[6] *http://www.postgradmed.com/issues/2004/04_04/inzucchi.htm*
[7] *Canadian Asthma prevention Institute: www.asthmaworld.org/Corticosteroid.htm*
[8] *The Merck manual of medical information: www.merck.com/mmhe/sec12/ch155/ch155b.html*
[9] http://www.health2us.com/zn_cu.htm
[10] *S. Kazi,S. S. Ali, F. Furrukh, T. G. Kazi, H. Kazi, T. G. Kazoo, American Clinical Laboratory, **19**, 8(2000)*

Studies with high resolution synchrotron-tomography of regenerated bone tissue using rapidly resorbable bone substitute materials

A. Rack[1], C. Knabe[2], M. Stiller[2], S. Zabler[3], Ch. Koch[2], G. Weidemann[4],
H. Seligmann[2], H. Riesemeier[4], J. Goebbels[4]

[1]Institute for Synchrotron Radiation, Research Center Karlsruhe (Germany)
[2]Charité Berlin (Germany) – DFG-grant: KN 377/3-1
[3]Technical University Berlin (Germany)
[4]Federal Institute for Materials Research and Testing (Germany)

The current gold standard for bone reconstruction in implant dentistry is the use of autogenous bone grafts. But the concept of guided bone regeneration (GBR, [1]) has become a predictable and well-documented surgical approach using biomaterials (bioactive calcium phosphate ceramics) which qualify as bone substitutes for this kind of application as well [2]. An animal study was performed in which these novel rapidly resorbable bone substitute materials were implanted in sheep. We applied high resolution synchrotron-tomography (S-CT) and subsequent 3d imaging in order to visualise bone formation and degradation of the bone substitute material in a threedimensional manner.

Experiments were caried out at the BAM*line* [3]. Corresponding to the size of the samples a 2048x2048 pixel CCD detector (Princeton Instruments VersArray:2048B) was chosen. The effective pixel size of 7 µm (zoom optics combined with CCD chip's pixel size) leads to a 14x14 mm^2 field of view. As scintillator an approx. 10 µm thick Gadox powder screen was used, the resulting spatial resolution is 20 µm and better. 1500 projections were recorded per 180° scan. The X-ray energy was set to 27 keV with the help of the installed double multilayer monochromator. For the reconstruction in parallel beam geometry PyHST was used to create the volume images [4]. The 3d rendering was done with VolumeGraphics VGStudio*Max* [5].

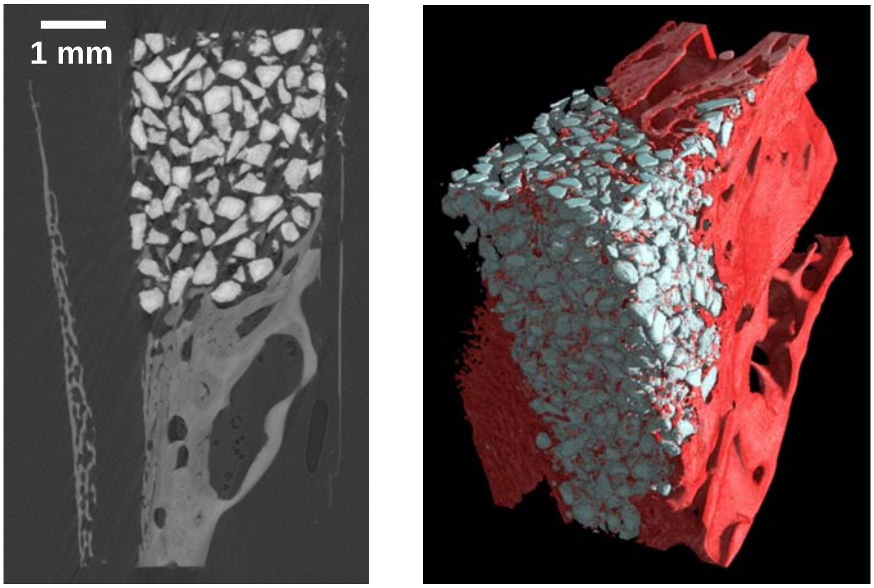

Fig. 1. Tomographic slice of a sheep sinus (light gray) with ceramic particles (white) 3 months after implantation (left) and corresponding 3d image after segmentation (right)

A typical tomographic slice of a sheep bone with ceramic particles three months after implantation is displayed in figure 1 (greyscale). Morphological objects (bones, ceramic particles) were separated by using a threshold hysterisis in combination with a 3d region growing algorithm [6]. Pixelwise multiplication of so created Boolean images with the input image creates noiseless data sets of each material phase which can be rendered in one image, see again figure 1.

A comparison with histologic images as shown in figure 2 allows to distinguish newly formed bone in spongy state from the fully evolved hard bone due to the density contrast in CT vs. chemical contrast in histologic images.

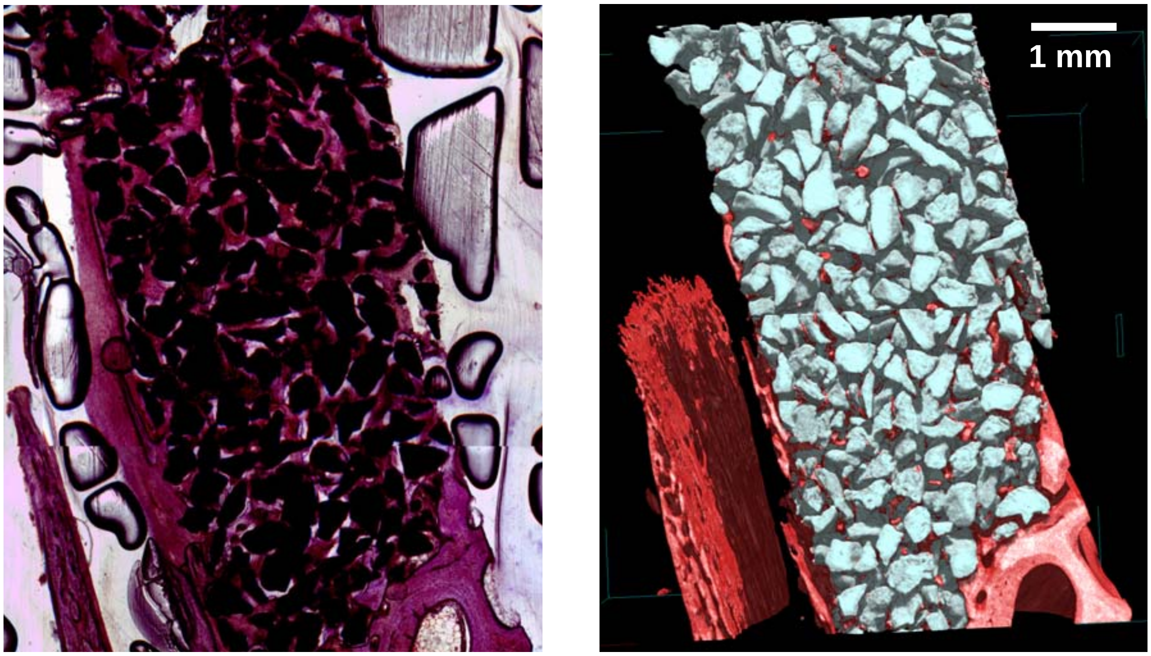

Fig. 2. Histologic image of bone substitute particles in sheep sinus – corresponding to the sample in figure 1 (left) and 3d rendering of a comparable sample section from the 3d data set (right)

References

[1] D. Buser, K. Dula, H. P. Hirt, H. Berthold. Localized ridge augmentation using guided bone regeneration. In: Buser D, Dahlin C, editors. Guided bone regeneration in implant dentistry. Chicago, Quintessenz; 1994.

[2] P. Ducheyne. Bioactive calcium phosphate ceramics and glasses. In: Sedel L, Cabanela M, editors. Hip surgery: New Materials and Developments. London, UK: Martin Dunitz; 1998. p 75-82.

[3] G. Weidemann, J. Goebbels, Th. Wolk and H. Riesemeier. First Computed Tomography Experiments at BAM*line*. BESSY Annual Report 2001, p. 249-250.

[4] A. Mirone. www.esrf.fr/UsersAndScience/Experiments/TBS/SciSoft .

[5] C. Reinhart, C. Poliwoda, T. Günther, W. Roemer, S. Maass, C. Gosch. Modern voxel based data and geometry analysis software tools for industrial CT. Proc. 16th World Conference on Nondestructive Testing (WCNDT2004), Montreal, Canada (2004).

[6] J. Ohser and F. Mücklich. Statistical Analysis of Microstructures, John Wiley & Sons, 2000

Microfluidic Mixers for the Investigation of Protein Folding Using Synchrotron Radiation Circular Dichroism Spectroscopy

A.S. Kane[1,2], D. Hertzog[2], P. Baumgärtel[3], J. Lengefeld[3], D. Horsley[4], R.Seckler[3], O. Bakajin[2], B. Schuler[5]
[1] Department of Electrical & Computer Engineering, University of California, Davis;
[2] BioSecurity and Nanosciences Lab., Lawrence Livermore National Lab., Livermore, CA;
[3] Department of Physical Biochemistry, University of Potsdam, Germany;
[4] Department of Mechanical & Aeronautical Engineering, University of California, Davis;
[5] Department of Biochemistry, University of Zurich, Switzerland

An unresolved question in biophysics is the structure formation of proteins. Synthesised as linear chains of amino acids, proteins are known to acquire their three-dimensional structure spontaneously, but the fundamental mechanisms of this folding process are not understood. However, a protein's structure is essential for its function, making an understanding of protein folding an important prerequisite for interpreting the vast amount of DNA sequence data now available. To investigate the kinetics of protein folding and secondary structure formation with Synchrotron Radiation Circular Dichroism (SRCD) spectroscopy, we have coupled a microfluidic mixing device to the SRCD station at BESSY II (beamline U125/2-NIM). Use of microfluidic mixers with a variety of spectroscopic techniques such as single molecule [1], and ensemble FRET [2], SAX [3], FTIR [4,5] has improved the time resolution and greatly reduced sample consumption over more conventional stopped flow mixing methods. SRCD allows us to use wavelengths below 220 nm where differences between the CD spectra of random coil and the various secondary structure types are most pronounced. Microfluidic mixing allows a fast initiation of the protein folding reaction. By combining this with SRCD, we can clarify an intense debate in the protein folding community as to when, in the process of folding, the secondary structure content forms.

We designed, fabricated and characterized mixing in the microfluidic device prototype (**Fig. 1**). At high concentrations, denaturant prevents proteins from folding, so folding can be initiated through rapid dilution of denaturant. A protein solution with high denaturant concentration is injected into one channel and buffer solution is injected into another channel. These channels meet at a serpentine-shaped region (**Fig. 2**) which performs mixing in the laminar flow regime by virtue of diffusion and chaotic advection [6]. Spectroscopic measurements are performed

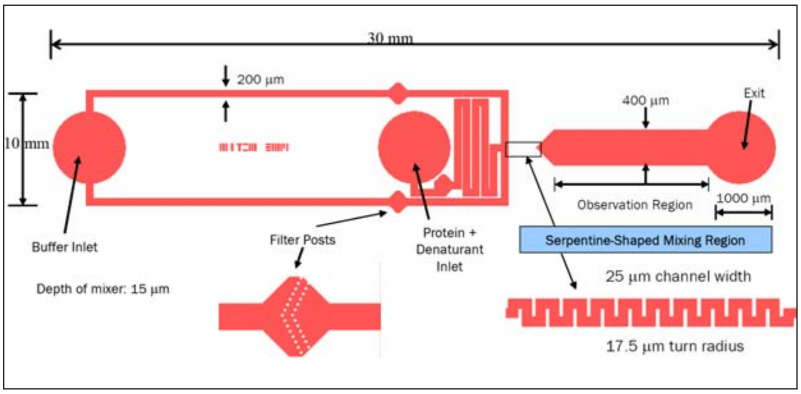

Fig 1: Scheme of the microfluidic mixing device

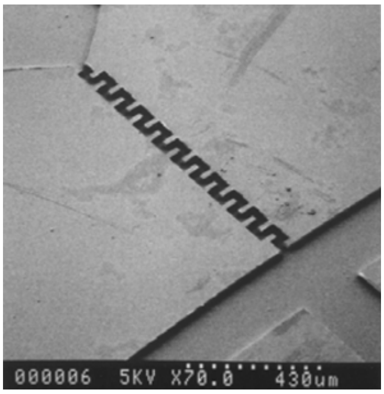

Fig 2: SEM image of serpentine mixing region

downstream in an "observation channel". The mixers are fabricated by DRIE of fused silica substrates with nearly vertical sidewalls. Etching is performed with an STS Advanced Oxide Etcher with a selectivity of approximately 17:1 using an undoped polysilicon mask. Sealing of microfluidic mixers is accomplished by direct fusion wafer bonding to another fused silica substrate. The mixing behavior of the chip was characterised at various flow rates by measuring the fluorescence intensity of fluorescein dye mixed with buffer in the ratio 1:10. To quantify the mixing process, we define a mixing metric, M, based on the standard deviation of the fluorescence intensity, where M=0 represents a completely unmixed state, and M=1 represents a completely mixed state. At progressively higher flow rates, Dean and corner vortices interact to stretch and fold streamlines, thus enhancing mixing. With this device design, the fastest mixing time obtained was 49 µs at a flow rate of 400 µl/min. This indicates that we will be able to observe folding events that occur in 50 µs or more, thus allowing us to observe early processes of protein folding.

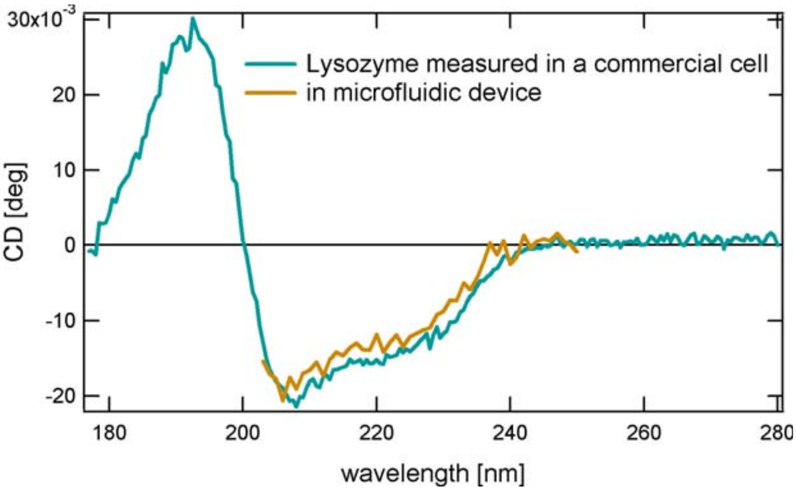

Fig 3: SRCD Data of filtered lysozyme protein solution inside microfluidic device.

Initial tests of the microfabricated mixers at beamline U125/2-NIM equipped with SRCD detection have shown that the mixers are suitable for measurements of protein folding kinetics. By focussing the beam to a diameter of approximately 50 µm, we were able to acquire CD data in the channels of the microfluidic mixing devices. This suggests that the etching process does not alter the surface in way that would reduce the polarization of the CD signal or interfere with the measurement. The SRCD data presented in **Fig. 3** are from of a filtered lysozyme protein solution inside the microfluidic device. Kinetic data will be acquired by focussing the beam at different points along the detection channel, corresponding to different times after mixing. Further SRCD measurements will be performed to analyze the formation of protein secondary structure of lysozyme and other proteins with the denaturant guanidinium hydrochloride. The current microfluidic mixer channel depth (15 µm) will be further optimized in order to achieve the highest mixing metric M for a given flow rate. Introducing a microfluidic mixer for synchrotron-based spectroscopy opens up additional avenues not only for protein folding, but also generally for research in the quantitative biological sciences.

[1] Lipman, E., Schuler, B., Bakajin, O., Eaton, W., Science, 2003, v. 301, pp. 1233-1235.
[2] Hertzog, D., Bakajin, O. et al, Analytical Chemistry 2004, v. 76, pp. 7169-7178.
[3] Pollack, L, Tate, M., Proc. Natl. Acad. Sci. U.S.A., 1999, v. 96, pp. 10115-10117.
[4] Akiyama, S., Takahashi, S., Proc. Natl. Acad. Sci. U.S.A., 2002, v. 99, pp. 1329-1334.
[5] Kaufmann, E., Darnton, N.C., Proc. Natl. Acad Sci. U.S.A.. 2001, v. 98, pp. 6646-6649.
[6] Chamarthy, P, Werely, S., Mixing Characteristics in a Serpentine Microchannel, 2004 ASME International Mechanical Engineering Congress and Exposition, Anaheim, CA.

3D structures of alternatively spliced gene products

Konrad Büssow[1,2], Babu A. Manjasetty[2,3], Christoph Scheich[1,2], Yvette Roske[2], Frank H. Niesen[4], Joachim Behlke[2], Udo Heinemann[2,5]

[1]Max-Planck-Institut für Molekulare Genetik, Ihnestr. 73, 14195 Berlin, Germany.
[2]Protein Structure Factory and Forschungsgruppe Kristallographie, Max-Delbrück-Centrum für Molekulare Medizin, Robert-Rössle-Str. 10, 13092 Berlin, Germany.
[3]Protein Structure Factory, c/o BESSY GmbH, Albert-Einstein-Str. 15, 12489 Berlin, Germany. *Current address:* Case Centre for Proteomics, Case Western Reserve University, Upton, New York 11973, USA
[4]Charité Universitätsmedizin Berlin, Institut für Medizinische Physik & Biophysik, Ziegelstr. 5-9, 10098 Berlin, Germany. *Current address:* Structural Genomics Consortium, University of Oxford, Botnar Research Centre, Oxford, OX3 7LD, United Kingdom
[5]Institut für Chemie und Biochemie, Freie Universität, Takustr. 6, 14195 Berlin, Germany

The Protein Structure Factory (PSF) is a collaborative research project for high-throughput structure analysis of human proteins. The PSF has established X-ray diffraction data collection and structure determination units at the BESSY synchrotron source. These facilities serve not only the PSF, but also many other academic groups and companies.

Structural genomics initiatives like the PSF determine protein structures in a systematic fashion. Especially structures of microbial proteins have been produced at an amazing rate in recent years. Not much is known about the biological function of many of these proteins. What can be learned of a structure of a novel protein? Here we present structures of two human proteins which not only allow insights into the proteins' function, but also allow drawing conclusions on variants produced by alternative splicing. In humans, approximately 30-60% of the genes undergo alternative splicing and, in some cases, splice variants are associated with human diseases.

We have determined the structures of human APEG-1 and PTD012 by X-ray crystallography [1, 2]. Both proteins were selected according to a systematic sequence analysis of human proteins [3]. Alternative splicing had been reported for the APEG-1 and the PTD012 genes. The structure of the small APEG-1 protein allows drawing conclusions on a much larger protein that is produced from the same chromosomal location. The structure of PTD012 reveals a novel fold and an active site with a zinc ion. It suggests that a shorter splice variant cannot fold and has no biological function in the cell.

APEG-1

Human Aortic Preferentially Expressed Protein-1 (APEG-1) is a marker of arterial smooth muscle cells (SMCS) that may play a role in differentiation. In addition to the small APEG-1 transcript, three larger products of the gene have been identified in rodents: in striated muscle, SPEGα and SPEGβ, and in the brain, BPEG [4]. The originally discovered APEG-1 mRNA is transcribed from a different promoter than the SPEGβ mRNA. This promoter is located between two exons of the much larger SPEGβ open reading frame.

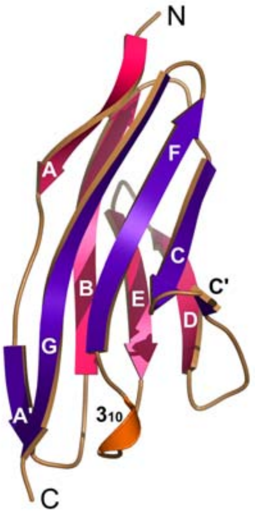

The full length APEG-1 protein, which has 113 amino acids, could not be crystallised. We searched for flexible regions in the sequence of the protein that might prevent its crystallisation. The programs PONDR and DisEMBL predicted that fourteen residues at the amino terminus are not part of the protein's globular, folded structure. A new construct was cloned to produce a shortened protein lacking the amino terminus (ΔAPEG-1). Crystals of this protein were obtained by a semi-automated method [5]. Diffraction data from a single crystal were obtained at the beamline PSF-ID14.2 at BESSY. The structure was determined by molecular replacement to a resolution of 0.96 Å (PDB 1U2H).

The structure adopts a Greek-key β-sandwich fold and belongs to the I (intermediate) set of the immunoglobulin superfamily, as expected from the sequence. It has the best resolution for an immunoglobulin domain structure so far.

In the crystal, APEG-1 forms distinct inter-protein contacts with neighbours. The homodimer with the largest buried surface area utilizes end-to-end packing with the subunits' N-termini pointing in opposite directions. This interaction is stabilised by various salt bridges between amino acids of the carboxyl terminal loops and 3_{10} helix. Interactions that are caused by Coulomb interaction depend on the salt concentration. Therefore, we tested the quaternary structure of APEG-1 at different salt concentrations by analytical ultracentrifugation. Indeed, a pronounced correlation was found. The dissociation constant is increased hundred fold – from 2 µM to 200 µM – when the salt concentration is increased from 0 to 250 mM.

APEG-1 appears not only as an isolated protein, but also becomes part of the large SPEGβ, an alternative product of the APEG-1 gene. The dimerisation of the APEG-1 Ig-like domain could induce antiparallel homodimerisation of SPEGβ. This dimerisation could be stabilized by additional binding sites within SPEGβ.

PTD012

Human PTD012, a protein of 315 amino acids, was selected as a target by the PSF. The ENSEMBL database, a comprehensive index of eukaryotic genomes and gene products, lists one additional splice variant corresponding to a protein of 265 amino acids for PTD012. Nothing had been known about the function of PTD012 and the splice variants.

The protein and its selenomethionine derivative were produced in *Escherichia coli* cells, purified and crystallised according to the standardised procedures of the PSF [5, 6]. The structure of the protein was solved by X-ray structure analysis with SAD-phasing (Single-wavelength anomalous diffraction). Diffraction data were collected at beamline PSF-ID14.2 of BESSY.

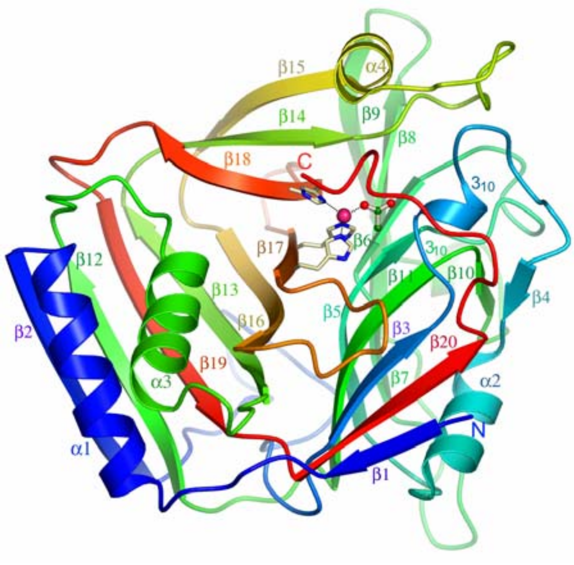

The protein is organized into a four-layer αββα topology (PDB 1XCR). A metal ion residing between the central β-sheets is partially coordinated by three histidine residues. This ion was identified as zinc by fluorescence spectroscopy and X-ray Absorption Near-Edge Structure (XANES) analysis at the zinc Kα line, performed at the BESSY synchrotron source.

Structure-based searches with DALI and VAST did not reveal any homologous structures. PTD012 is a four-layer sandwich, but its topology does not fall under any existing class of this structure type. The order of β-strands, the connectivity and crossovers of the sheets are highly different. Therefore, the structure represents a novel fold.

In the predicted active site, the tetrahedral zinc coordination is completed by an acetate molecule that was most likely recruited from the crystallization buffer. The arrangement of the histidines coordinating the zinc and a glutamate and an arginine nearby is reminiscent of α-carbonic anhydrase and human carboxypeptidase A2. However, we could not find any of these enzymatic activities in PTD012. Consequently, we reasoned that PTD012 is a hydrolytic enzyme with a substrate yet to be identified. Indeed, we could show that PTD012 cleaves *p*-nitrophenyl acetate, a generic substrate of ester hydrolases. This demonstrates that the structure corresponds to a protein with enzymatic activity. The physiological substrates of PTD012 remain to be found.

We have also studied the shorter splice variant of PTD012, lacking 50 amino acids in the center. The shorter variant is expressed strongly in *Escherichia coli* but is completely insoluble. The PTD012 structure suggests that a protein lacking those 50 residues cannot fold and is likely non-functional. This suggests that the protein corresponding to the shorter splice is not stable and may not exist at all in the cell.

Acknowledgements

This work was supported by the German Federal Ministry for Education and Research (BMBF) through the "Leitprojektverbund Proteinstrukturfabrik" and the National Genome Network (NGFN; FZK 01GR0471, 01GR0472), and by the Fonds der Chemischen Industrie.

References

1. Manjasetty BA, Niesen FH, Scheich C, Roske Y, Goetz F, Behlke J, Heinemann U, Büssow K: **X-ray structure of engineered human Aortic Preferentially Expressed Protein-1 (APEG-1)**. *BMC Structural Biology* 2005, **5**:21.
2. Manjasetty BA, Büssow K, Fieber-Erdmann M, Roske Y, Gobom J, Scheich C, Götz F, Niesen FH, Heinemann U: **Crystal structure of Homo sapiens PTD012 reveals a zinc-containing hydrolase fold**. *Protein Sci* 2006, **in press**.
3. Büssow K, Scheich C, Sievert V, Harttig U, Schultz J, Simon B, Bork P, Lehrach H, Heinemann U: **Structural Genomics of human proteins - target selection and generation of a public catalog of expression clones**. *Microbial Cell Factories* 2005, **4**:21.
4. Hsieh CM, Fukumoto S, Layne MD, Maemura K, Charles H, Patel A, Perrella MA, Lee ME: **Striated muscle preferentially expressed genes alpha and beta are two serine/threonine protein kinases derived from the same gene as the aortic preferentially expressed gene-1**. *J Biol Chem* 2000, **275**(47):36966-36973.
5. Mueller U, Nyarsik L, Horn M, Rauth H, Przewieslik T, Saenger W, Lehrach H, Eickhoff H: **Development of a technology for automation and miniaturization of protein crystallization**. *J Biotechnol* 2001, **85**(1):7-14.
6. Büssow K, Quedenau C, Sievert V, Tischer J, Scheich C, Seitz H, Hieke B, Niesen FH, Götz F, Harttig U *et al*: **A catalogue of human cDNA expression clones and its application to structural genomics**. *Genome Biology* 2004, **5**:R71.

Structural Studies of the Human Tethering Complex TRAPP Involved in Vesicular Transport

Daniel Kümmel[1,2], **Andrew P. Turnbull**[1,3], **Jürgen J. Müller**[1], **Yvette Roske**[1,4], **and Udo Heinemann**[1,2]

[1] Max-Delbrück-Center for Molecular Medicine, Berlin, Germany
[2] Chemistry and Biochemistry Institute, Free University, Berlin, Germany
[3] Protein Structure Factory, c/o BESSY GmbH, Berlin, Germany
[4] Protein Structure Factory, Berlin, Germany

Introduction

Living cells are separated from their surrounding by lipid bilayer membranes which fence off the interior of the cell, the cytosol, from the outside world. In addition, the cells of all higher organisms contain specialized compartments which are separated from the cytosol also by lipid membranes. Because of their chemical properties, membranes constitute a barrier for the exchange of substances, allowing the maintenance of distinct environments.

The exchange of proteins and other molecules between different compartments of the cell and the outside world is achieved by vesicular transport: Small membrane vesicles bud at a donor membrane, loading cargo in their interior, and travel through the cell to their target compartment. The recruitment of vesicles to the correct destination compartment is mediated through tethering factors, such as long coiled-coil proteins or tethering complexes, and followed by membrane fusion, catalyzed through the class of SNARE (soluble NSF-attachment protein receptor) proteins (Fig. 1).

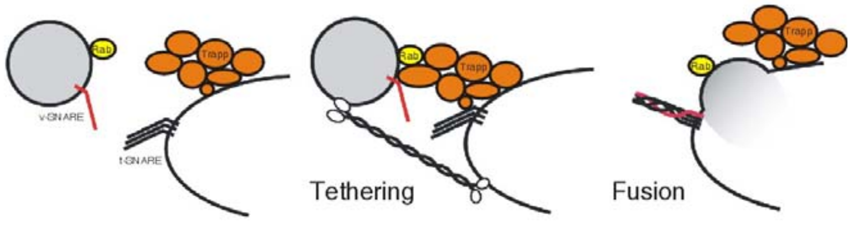

Fig. 1: The cargo delivery of a vesicle to the target compartment requires tethering and membrane fusion (after [1]).

We are interested in the TRAPP (Transport Protein Particle) tethering complex that is involved in the transport of vesicles from the endoplasmic reticulum (ER), where proteins are synthesized, to the Golgi network, where proteins are further processed. TRAPP was shown to interact with ER-derived vesicles and to promote nucleotide exchange of a regulatory protein, the Rab-GTPase Ypt1p. The human TRAPP complex contains at least seven subunits. Our goal is to structurally characterize the different TRAPP subunits and subcomplexes. This information will allow us to gain better understanding of the essential vesicle tethering process. We have so far succeeded in the crystallization and structure determination of two human TRAPP subunits, BET3 [2] and TPC6 [3]. The crystal structures of Sedlin [4] and Bet3 [5] from mouse have been determined by others.

Structure of palmitoylated BET3: Insights into TRAPP complex assembly and membrane localization

The BET3 protein reveals the novel α/β-plait protein fold (Fig. 2A). The secondary structural elements are arranged in a topology constructed by a twisted, antiparallel, four-stranded β-sheet on one side, with helices forming the other side of the structural motif. BET3 forms a dimer around the crystallographic two-fold axis, primarily involving interactions between the helices α1 and α2. The dimeric structure of BET3 adopted in the crystal has been confirmed in solution by analytical ultracentrifugation.

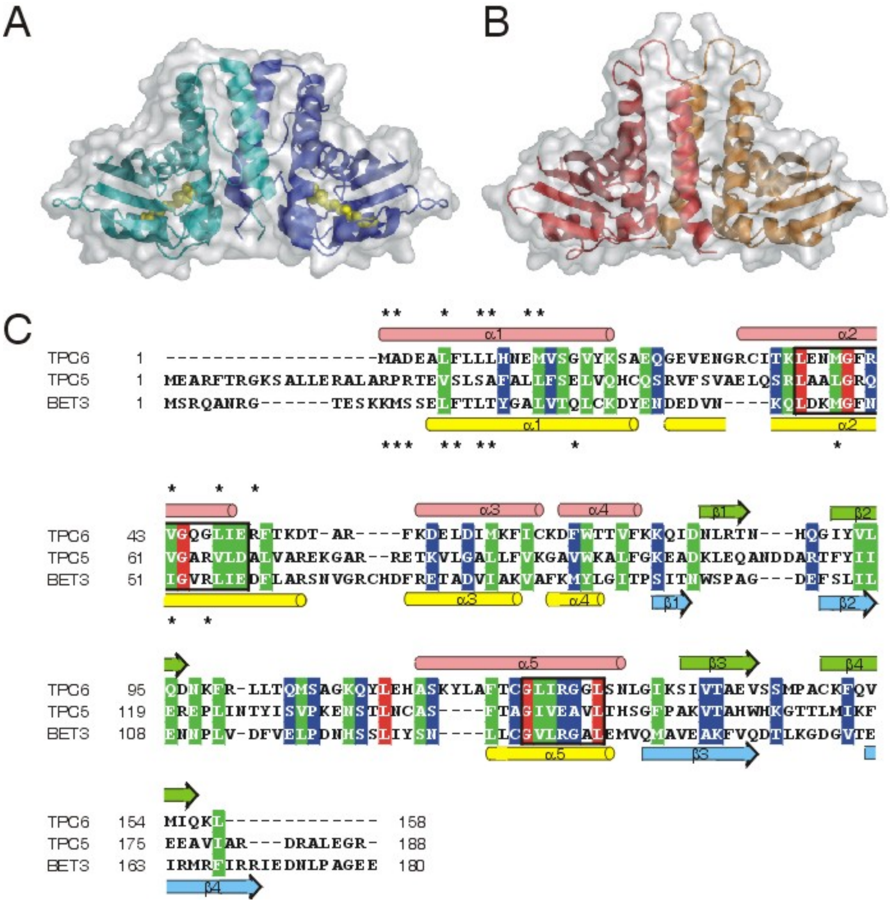

Fig. 2: A Schematic representation of the BET3 dimer with atoms in the palmitoyl moieties represented as yellow spheres. **B** Schematic representation of the TPC6 dimer. **C** Multiple sequence alignment of human TPC6, TPC5 and BET3 with secondary structure elements of TPC6 and BET3. Identical, strongly similar, and weakly similar residues are highlighted in red, green, and blue. Residues of TPC6 and BET3 marked by an asterisk denote amino acids most strongly involved in dimer formation. Sequences corresponding to the BET3 family motif are enclosed in boxes.

A striking feature of the BET3 structure is the presence of a hydrophobic pocket within the core of the α-helical face which is occupied by a palmitate molecule covalently attached to the protein at the fully conserved residue Cys68. Palmitoylation most commonly promotes membrane binding of proteins but has also been shown to modulate protein–protein interactions. Palmitoylation of BET3 was demonstrated *in vivo*, but is not essential for cell viability or membrane localization of BET3 in yeast. Thus the hydrophobic cavity alone might mediate membrane recruitment of BET3 *via* the interaction with an acylated anchoring moiety.

The crystal structure of TPC6 suggests a model for a TRAPP subcomplex with BET3

TPC6 was also found to be dimeric, and the overall structure resembles strikingly that of BET3 (Fig. 2B). In spite of only 17% sequence identity, the superposition of the α-carbon backbones of the monomers of both proteins shows high similarity. Differences in structure are mainly confined to the loop regions, whereas the α/β-plait cores of both proteins show little divergence. Considering the structural similarity between TPC6 and BET3 we suggest that the α/β-plait fold might represent the common fold for all paralogous BET3 family members including a third TRAPP subunit, TPC5. A sequence alignment of the human proteins TPC6, TPC5, and BET3 (Fig. 2C) shows that conserved and similar residues between different family members are predominantly located in the α-helical secondary structure elements. Major variations in length and conservation of the primary structure are only found in loop regions. In addition, the proteins differ in the length and sequence of their N- and C-termini. The highest similarity is found for two motifs ($LX_2\#GX_2\#GX_2LXE$ and $G\#_2XGXL$) that have been previously described [6], and these motifs are located in the interior of the proteins. Taken together these data suggest that TPC5 may adopt a similar fold to that of TPC6 and BET3.

The similarity between BET3 and TPC6 is especially prominent at the dimerization interfaces of the proteins leading to the intriguing possibility of a hetero-dimerization between TPC6 and BET3. Heterodimerization could be demonstrated by *in vitro* and *in vivo* association studies. We therefore suggest a model of BET3-TPC6 heterodimer, representing a putative TRAPP subcomplex (Fig. 3).

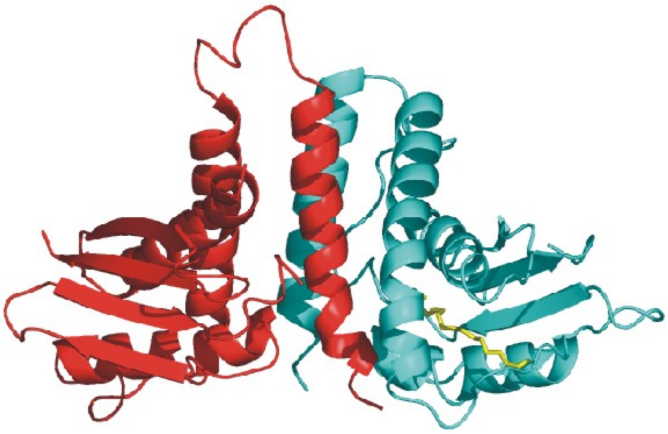

Fig. 3: Model of a TPC6-BET3 heterodimer. The structure of this TRAPP subcomplex is derived from a superposition of the TPC6 (red) and BET3 (cyan) dimers.

References

[1] Whyte JR, Munro S (2002) Vesicle membrane complexes in membrane traffic. *J Cell Sci*, **115**: 2627-2637

[2] Turnbull AP, Kümmel D, Prinz B, Holz C, Schultchen J, Lang C, Niesen FH, Hofmann KP, Delbrück H, Behlke J, Müller EC, Jarosch E, Sommer T, Heinemann U (2005) Structure of palmitoylated BET3: Insights into TRAPP complex assembly and membrane localization. *EMBO J*, **24**: 875-884

[3] Kümmel D, Müller JJ, Roske Y, Misselwitz R, BüssowK, Heinemann U (2005) Structure of the TRAPP-complex subunit TPC6 suggests a model for a TRAPP subcomplex. *EMBO Rep*, **6**: 787-793

[4] Jang SB, Kim YG, Cho YS, Suh PG, Kim KH, Oh BH (2002) Crystal structure of SEDL and its implications for a genetic disease spondyloepiphyseal dysplasia tarda. *J Biol Chem*, **277**: 49863-49869

[5] Kim YG, Sohn EJ, Seo J, Lee KJ, Lee HS, Hwang I, Whiteway M, Sacher M, Oh BH. (2005) Crystal structure of bet3 reveals a novel mechanism for Golgi localization of tethering factor TRAPP. *Nat Struct Mol Biol*, **12**: 38-45

[6] Sacher M, Barrowman J, Schieltz D, Yates JR III, Ferro-Novick S (2000) Identification and characterization of five new subunits of TRAPP. *Eur J Cell Biol* **79**: 71-80

Determination of organic structures in the vicinity of implanted magnesium alloys with synchrotron-based IR-Microspectroscopy

[1]R. Dargel, [1]K. Bechstein, [2]F. Witte, [3]U. Schade, [1]C. Vogt

[1]Institute for Inorganic Chemistry, University of Hannover, Callinstr. 9, 30167 Hannover, Germany,
[2]Department of Orthopaedic Surgery, Hannover Medical School, Anna-von-Borries-Str.1-7, 30625 Hannover, Germany
[3]BESSY GmbH, Albert-Einstein-Str.15, 12489 Berlin, Germany.

Introduction

Biodegradable magnesium-alloys represent a promising new class of implant materials [1]. As they dissolve during the healing process of the fractured bone, surgery to remove the implant is no longer necessary. It is, however, crucial to understand the mechanism of degradation to assess potential health risks. A combination of several analytical methods with high lateral resolution and the ability to analyze the elemental composition as well as the organic structures are required to analyze the influence of the alloy on the surrounding tissue on a micro- and submicrometer scale [2]. Of particular interest is the direct vicinity of the corrosion layer, as possible changes in the distribution and composition of essential components such as proteins, fatty acids and peptides will probably occur in this area. We evaluated the applicability of synchrotron-based infrared reflection microspectroscopy to examine these phenomena on a scale of few micrometers by investigating cross-sections of rabbit-bones after implantation. The brilliance of synchrotron radiation exceeds that of IR sources (like globars) by 2-3 magnitudes, enabling to gain chemical information with the required lateral resolution.

Experimental setup

For the IR-measurements bones of adult New Zealand White rabbits with implants of magnesium alloy LAE442 were harvested 2 and 24 weeks after implantation. Subsequently they were fixated, embedded and cut to prepare cross-sections. All animal experiments were conducted under a governmental approved protocol. To determine the spatial distribution of organic and inorganic compounds distribution mappings and linescans were performed. All measurements were taken in reflection mode, with an aperture of 20 microns and a spectral resolution of $2cm^{-1}$ wavenumbers.

Results

The obtained distribution mappings indicate regions of different chemical composition in the vicinity of the corroding magnesium rod. In fig.1 the metallic implant, the dark corrosion layer and the adjacent bone tissue can be optically distinguished. The white arrow indicates the start and end points of the measured linescan, which had a length of 630 microns. Choosing a stepsize of 10 microns and an aperture of 20 microns we measured 63 points with half overlap.

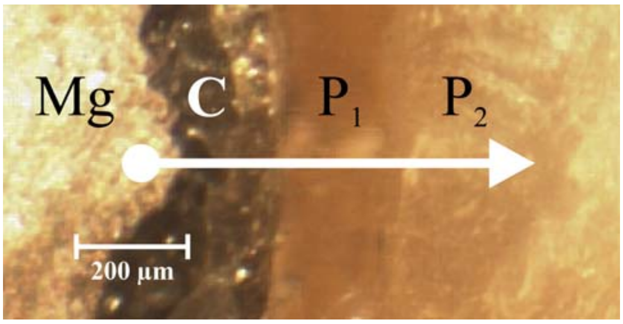

Figure 1. Video image of cross-section of bone with magnesium implant. White arrow displays line mapping region (line length: 630 µm, 10 µm step-size,
Mg: magnesium implant, **C**: corrosion layer, $\mathbf{P_1}$: phase 1, $\mathbf{P_2}$: phase 2).

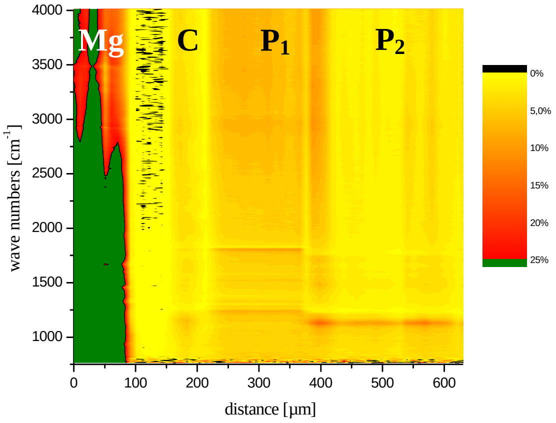

Figure 2. IR-spectra from a line mapping in the vicinity of the magnesium implant surface of a bone cross-section from a New Zealand White rabbit 24 weeks after implantation. **Mg**: magnesium implant, **C**: corrosion layer,
$\mathbf{P_1}$: phase 1, $\mathbf{P_2}$: phase 2.

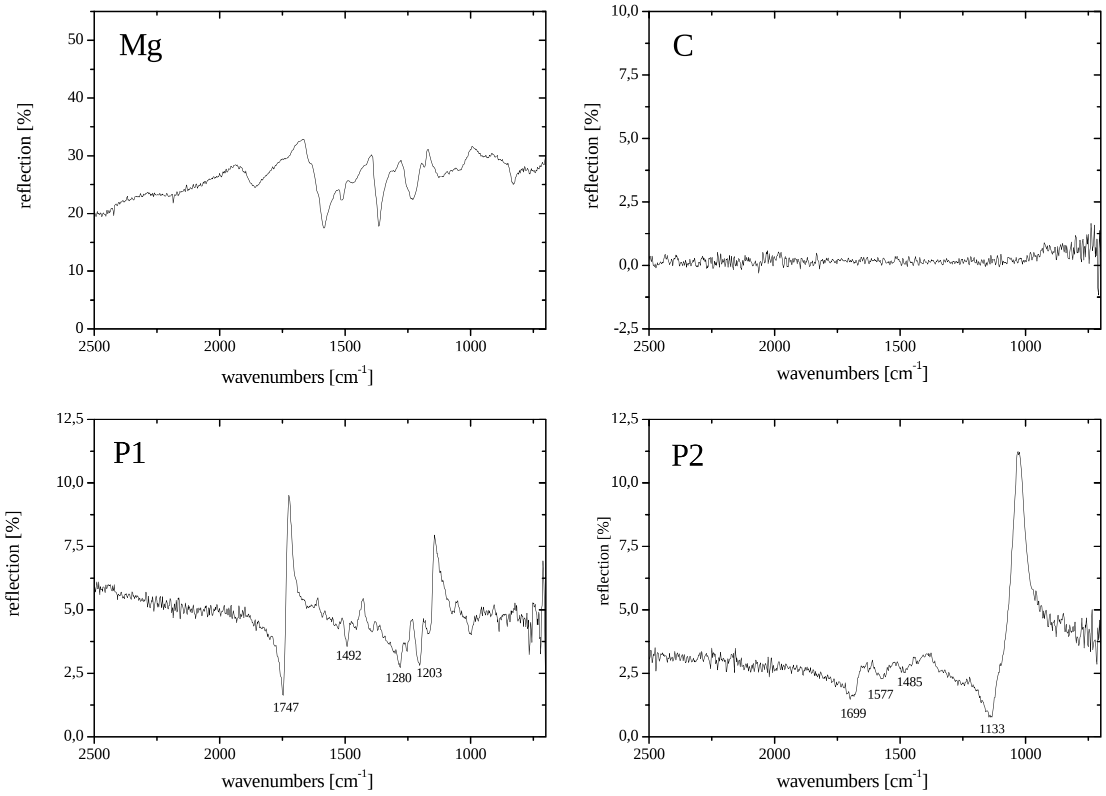

Figure 3: IR-spectra from Mg alloy (A), Corrosion phase (C), Phase 1 (P1) and Phase 2 (P2)

In fig.2 the obtained spectra of an implant after 24 weeks retention are plotted against the scandistance, showing at least three regions of different chemical composition adjoining the magnesium rod (Mg). These regions have not been observed in samples collected after 2 weeks of retention. The area of the alloy implant is indicated by very high reflectivity (green-red coloured). It is followed by totally absorbed intensities caused by the corrosion layer (C). Between the following phases P1 and P2 distinct differences in IR-spectra are observable. These might indicate changes in the mineral structure (phosphate-peak at 1133 in P2, carbonate peak at 1492 cm^{-1}) as well as in the organic composition (Amide-bands between 1699 and 1485 cm^{-1} in P2, missing in P1). This agrees with previous investigations [3].

Discussion

Our results indicate that synchrotron-based infrared microscopy is an appropriate analytical technique to investigate structural changes in tissue due to corrosion processes of degradable implants. Our measurements showed evidence of at least three regions of differing organic composition. To observe time-depending differences of the chemical composition in the vicinity of bone implants we have and will further investigate samples with implants of different retention in bone. These and following results obtained by synchrotron-based IR-Microspectroscopy measurements might contribute to a better understanding of the mechanisms of the degradation process of magnesium implants in-vivo.

References

[1] Witte F et al., Biomaterials **26**, 2005 (17):3557-63.

[2] Vogt C, Witte F., GDCh, **27**, 2005

[3] Miller LM, Carlson SC, Carr GL, Chance MR, Cell Mol Biol, 44 (1), 117-129, 1998

Secondary structural changes in the autoassembly and photoconversion of bacteriophytochromes[†]

Berthold Borucki, Harald Otto*, Sven Seibeck*, Maarten P. Heyn* and Tilman Lamparter*[§]
Freie Universität Berlin, 14195 Berlin, *Physics Department, Arnimallee 14, [§]Institut für
Biologie, Pflanzenphysiologie, Königin-Luise-Strasse 12–16.
[†]This work was supported by the Deutsche Forschungsgemeinschaft, grant Bo 1911/1-1.

Phytochromes are red-light photoreceptors initially found in higher plants but recently also discovered in a variety of bacteria and fungi [1]. The present studies were carried out with the bacteriophytochromes Cph1 from *Synechocystis* and Agp1 from *Agrobacterium tumefaciens*. Their photochromic properties with two almost thermally stable states, P_r and P_{fr}, are very similar to that of plant phytochromes. The autocatalytic assembly of holo-phytochrome from the apoprotein and a bilin chromophore is associated with conformational changes in the chromophoric site that may also induce changes of the secondary structure. Circular dichroism (CD) in the far-UV is a sensitive method to detect these changes and to determine the fractions of secondary structures qualitatively. The experimental set-up at the 3m-NIM monochromator at beamline 12.1B is superior to commercial lab instruments due to the higher intensity in the far-UV.

A substantial increase of the α-helical content in the assembly of Cph1 phytochrome was reported from previous CD measurements [2]. In contrast to these results, our measurements reveal only small differences between the CD spectra of apo- and holoprotein of Cph1 and Agp1, respectively. Large scale changes of secondary structure in the autoassembly as reported in ref [2] could thus be excluded. Figure 1 shows the UV-Vis absorption spectra (A) and the far-UV CD spectra (B) of Agp1 apo- and holo-phytochrome.

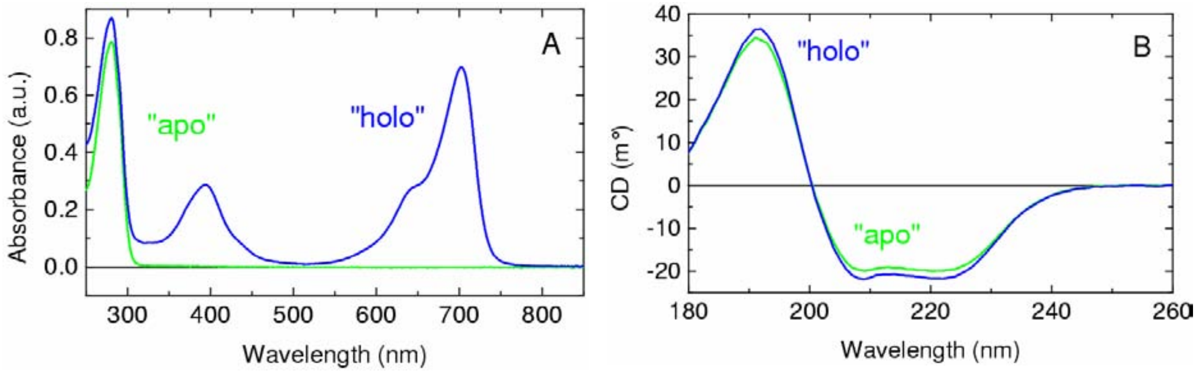

Fig. 1: UV-Vis absorption spectra (A) and far-UV CD spectra (B) of Agp1 apo- and holo-phytochrome.

Direct comparison of the far-UV CD spectra Cph1 and Agp1 shows that the secondary structure of both proteins is not identical (Figure 2). A quantitative analysis using the CDsstr program [3] reveals that the helical content (α-helix + 3/10 helix) in Cph1 is larger than in Agp1 (51% vs 48%), whereas the unordered fraction is smaller in Cph1 (see Table 1).

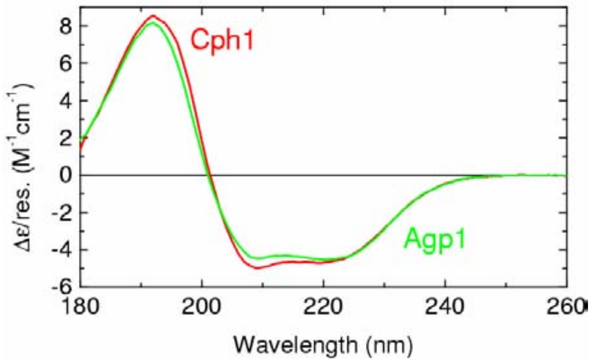

Fig. 2: molar Δε per residue of Cph1 and Agp1

	Cph1	Agp1
α–Helix	41.7 %	39.0 %
3/10 Helix	9.5 %	8.9 %
β–Sheet	7.2 %	8.0 %
poly(Pro)II Struct.	2.7 %	3.4 %
Turns	12.7 %	12.7 %
Unordered	27.3 %	28. 7%

Tab. 1: fractions of secondary structure of Cph1 and Agp1 as determined by the CDsstr program [3]

Light-induced secondary structural changes of very small magnitude could be observed for Cph1 and Agp1 (data not shown). These changes are very similar in both proteins suggesting a uniform mechanism of light-induced receptor activation in bacteriophytochromes. The much larger light-induced changes in plant phytochromes [4,5] were attributed to an amphiphilic a-helix forming motif in the N-terminus that is absent in bacteriophytochromes [2].

[1] Lamparter T. (2004) *FEBS Lett. 573*, 1–5.

[2] Park, C.M., Shim, J.Y., Yang, S.S., Kang, J.G., Kim, J.I., Luka, Z., and Song, P.S. (2000) *Biochemistry 39*, 6349-6356.

[3] Johnson, W.C. (1999) *Proteins 35*, 307-312.

[4] Sommer, D., and Song, P.S. (1990) *Biochemistry 29*, 1943-1948.

[5] Chen, E., Lapko, V.N., Song, P.S., and Kliger, D.S. (1997) *Biochemistry 36*, 4903-4908.

Preliminary crystallographic analysis of the photosensory module of phytochrome Agp1 from the plant pathogen *Agrobacterium tumefaciens*

Patrick Scheerer, Norbert Michael[1], Jung-Hee Park[2], Steffi Noack[1], K. Inomata[3],
Hui-Woog Choe[2,4], Tilman Lamparter[1]* and Norbert Krauß*

Institut für Biochemie - CCM, Charité - Universitätsmedizin Berlin, Monbijoustr.2, D-10117 Berlin, Germany

[1]Institut für Biologie/Pflanzenphysiologie, Freie Universität Berlin, Königin-Luise Str. 12-16, D-14195 Berlin, Germany

[2]Institut für Medizinische Physik und Biophysik - CCM, Charité - Universitätsmedizin Berlin, Ziegelstr. 5-9, D-10117 Berlin, Germany

[3]Division of Material Sciences, Graduate School of Natural Sciences and Technology, Kanazawa University, Kakuma, Kanazawa, Ishikawa 920-1192, Japan

[4] Department of Chemistry, College of Natural Science, Chonbuk National University, 561-756 Chonju, South. Korea

*Grant: by Deutsche Forschungsgemeinschaft (DFG), Sfb498-B2

Phytochromes are photoreceptors which sense light in the red and far-red region by means of a bilin-type chromophore. These photoreceptors were first identified in plants, but later also in bacteria. Typically, the photocycle of phytochromes contains two thermostable forms, so-called Pr and Pfr which absorb light maximally in the red and the far-red spectral region, respectively. The initial events in this two-step photocycle are Z-E and E-Z isomerisations about the double bond located between rings C and D of the open-chain tetrapyrrole chromophore. In plants, phytochromes are known to modulate numerous physiological responses like e.g. seed germination or shade avoidance [1]. Two phytochromes, Agp1 and Agp2, were found by genome sequencing of *Agrobacterium tumefaciens*, a tumour-inducing soil bacterium. The biological functions of these photoreceptors are presently unknown. Both phytochromes, which bind biliverdin as chromophore, were expressed as polyhistidine-tagged proteins in *E.coli* cells [2]. Agp1 is a light-regulated histidine kinase like other bacterial phytochromes. For crystallization purposes, we have focused on the truncated phytochrome Agp1-M15 which lacks the histidine kinase module and contains the complete chromophore module consisting of the PAS-like-domain, the GAF-domain and the PHY-domain. A holo-protein which is fully active in Pr-to-Pfr photoconversion showing the same spectral features as the full-length phytochrome was obtained by assembling Agp1-M15 by either an *in-vitro* or an *in-vivo*-approach with its natural chromophore biliverdin (BV).

Crystals of the adduct BV-Agp1-M15 (Figure 1) are of limited diffraction quality, yielding data sets to a maximum resolution of ca. 6 Å [3]. The crystal quality improved significantly when a synthetic chromophore was used, which due to an additional cyclisation between rings C and D cannot undergo the isomerisations which are necessary to initialize photoconversion of the receptor. Using the adduct of Agp1-M15 with this synthetic “locked” chromophore, the maximal resolution could be improved to 3.4 Å [3].

In order to solve the crystallographic phase problem, we have expressed selenomethionine-labeled protein Agp1-M15 in *E. coli* and crystallized its adduct with the “locked” chromophore. At the Protein Structure Factory beamline BL14.1 of BESSY and Free University Berlin at BESSY we have collected 95 % complete data at the selenium K-edge to 3.4 Å resolution. Like the previously characterized crystal forms of Agp1-M15, the crystals belong to the tetragonal space group I422 with unit cell dimensions a = b =173 Å, c= 81 Å, corresponding to an Agp1-M15 monomer per asymmetric unit. So far even the first step in SAD (single-wavelength anomalous dispersion) phasing which would consist in the determination of the selenium sites was not successful. We are currently optimizing protein expression, - purification and - crystallization conditions in order to grow crystals which diffract to higher resolutions.

Very recently, the crystal structure of another bacterial phytochrome which is closely related to Agp1 has been published at 2.5 Å resolution [4]. The structure provides a detailed insight into the chromophore binding site and an interesting new folding feature of this protein. The protein which was crystallized in this work does not contain the PHY domain which is present in Agp1-M15 and seems to be required to stabilize the Pfr state. Interestingly our first attempts to solve the phase problem by molecular replacement using the structural model of this phytochrome have failed so far, which might indicate major conformational differences between the two proteins.

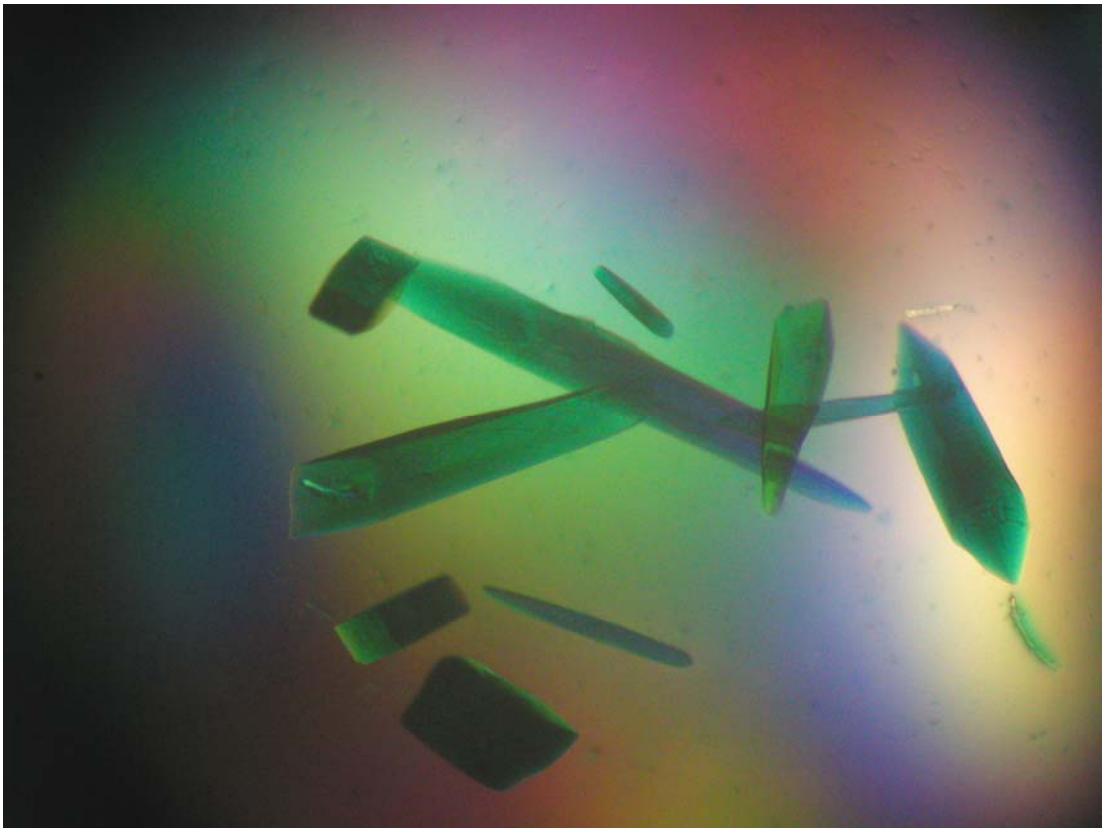

Figure 1: Crystals of BV-Agp1-M15 (size: 500 x 250 x 100 μm^3).

References

[1] H. Smith, Phytochromes and light signal perception by plants - an emerging synthesis, *Nature* **407**, 586-591 (2000)

[2] T. Lamparter, N. Michael, F. Mittmann, and B. Esteban, Phytochrome from *Agrobacterium tumefaciens* has unusual spectral properties and reveals an N-terminal chromophore attachment site, *Proc. Natl. Acad. Sci. U. S. A.* **99**, 11628-11633 (2002)

[3] P. Scheerer, N. Michael, J.H. Park, S. Noack, C. Förster, M.A.S. Hammam, K Inomata, H.-W. Choe, T. Lamparter, and N. Krauß, Crystallization and preliminary X-ray crystallographic analysis of the N-terminal photosensory module of phytochrome Agp1, a biliverdin-binding photoreceptor from *Agrobacterium tumefaciens, J. Struct. Biol.***153**, 97-102 (2006)

[4] J.R. Wagner, J.S. Brunzelle, K.T. Forest, and R.D. Vierstra, A light-sensing knot revealed by the structure of the chromophore-binding domain of phytochrome, *Nature* **438**, 325-331 (2005)

Conjugated bile acid hydrolase is a tetrameric N-terminal thiol hydrolase with specific recognition of its cholyl but not of its tauryl product

Maksim Rossocha[1], Robert Schultz-Heienbrok[1], Holger von Moeller[2], James P. Coleman[2] and Wolfram Saenger[1,#]

[1] *Freie Universität Berlin, Institut für Chemie und Biochemie - Kristallographie, Takustrasse 6, 14195 Berlin, Germany.*

[2] *Department of Microbiology and Immunology, East Carolina University, Greenville, North Carolina 27858.*

[#] *Corresponding author*

Bacterial bile salt hydrolases catalyze the degradation of conjugated bile acids in the mammalian gut. The crystal structures of conjugated bile acid hydrolase (CBAH) from *Clostridium perfringens* as apoenzyme and in complex with taurodeoxycholate that was hydrolyzed to the reaction products taurine and deoxycholate are described here at 2.1 and 1.7 Å resolution, respectively [1]. The crystal structures (Figure 1) reveal close relation-ship between CBAH and penicillin V acylase from *Bacillus sphaericus*. This similarity together with the N-terminal cysteine classifies CBAH as a member of the N-terminal nucleophile (Ntn) hydrolase superfamily. Both crystal structures show an identical homotetrameric organization with dihedral (*D*2 or 222) point group symmetry. The structure analysis of *C. perfringens* CBAH identifies critical residues in catalysis, substrate recognition, and tetramer formation which may serve in further biochemical characterization of bile acid hydrolases.

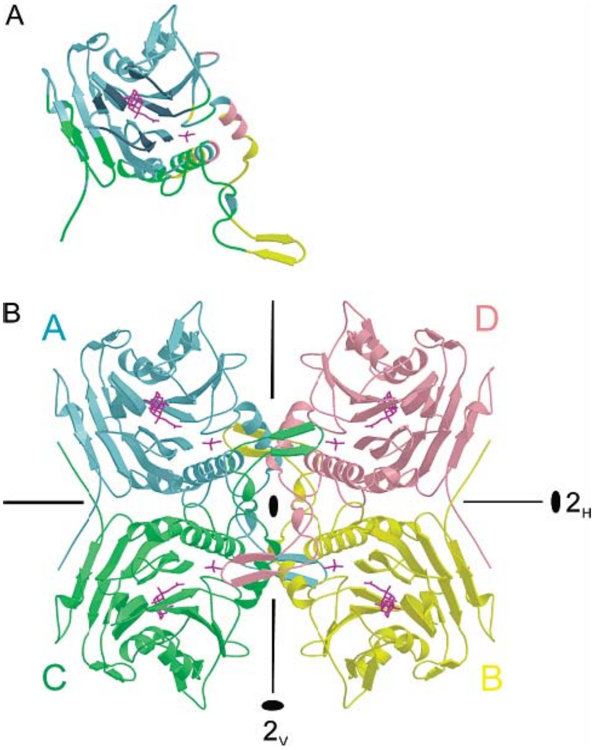

***Figure 1**: Tetramer formation of CBAH.*

Reaction products taurineand deoxycholate are indicated in stick (magenta) presentation.

(A) Ribbon diagram of CBAH monomer. Contact surfaces with other molecules in the tetramer indicated by color-coding as in panel B. The shown monomer has the same orientation as protomer A in panel B.

(B) CBAH homotetramer with monomers colored differently. Twofold rotation axes in the paper plane are marked 2H (horizontal) and 2V (vertical), and the one perpendicular (normal) to the paper plane (2p) is indicated by the black ellipse in the center.

References

1. Rossocha, M., Schultz-Heienbrok, R., von Moeller, H., Coleman, J. P. and Saenger, W. (2005) *Biochemistry* **44**: 5739-5748.

Allele-dependent similarity between viral and self-peptide presentation by HLA-B27 subtypes*

Maria T. Fiorillo[1], Christine Rückert[2], Martin Hülsmeyer[3], Rosa Sorrentino[1], Wolfram Saenger3[,#], Andreas Ziegler[2] and Barbara Uchanska-Ziegler[2,#]

[1] Dipartimento di Biologia Cellulare e dello Sviluppo, Università di Roma "La Sapienza," via dei Sardi 70, 00185 Roma, Italy.
[2] Institut für Immungenetik, Charité-Universitätsmedizin Berlin, Campus Virchow-Klinikum, Humboldt-Universität zu Berlin, Spandauer Damm 130, 14050 Berlin, Germany.
[3] Freie Universität Berlin, Institut für Chemie und Biochemie - Kristallographie, Takustrasse 6, 14195 Berlin, Germany.
[#] Corresponding author

Molecular mimicry is discussed as a possible mechanism that may contribute to the development of autoimmune diseases. It could also be involved in the differential association of the human major histocompatibility subtypes HLA-B*2705 and HLA-B*2709 with ankylosing spondylitis. These two subtypes differ only in residue 116 of the heavy chain (Asp in B*2705 and His in B*2709), but the reason for the differential disease association is not understood. Using X-ray crystallography, we show here that the viral peptide pLMP2 (sequence RRRWRRLTV, derived from latent membrane protein 2 (residues 236–244) of Epstein-Barr virus) is presented by the B*2705 and B*2709 molecules in two drastically deviating conformations. Extensive structural similarity between pLMP2 and the self-peptide pVIPR (sequence RRKWRRWHL, derived from vasoactive intestinal peptide type 1 receptor (residues 400–408)) is observed only when the peptides are presented by B*2705 because of a salt bridge between Arg5 of both peptides and the subtype-specific heavy chain residue Asp116. Combined with functional studies using pLMP2/pVIPR-cross-reactive cytotoxic T cell lines and clones, together with target cells presenting these peptides or a modified peptide analogue, our results reveal that a pathogen-derived peptide can exhibit major histocompatibility complex class I subtype dependent, drastically distinct binding modes. Furthermore, the results demonstrate that molecular mimicry between pLMP2 and pVIPR in the HLA-B27 context is an allele-dependent property.

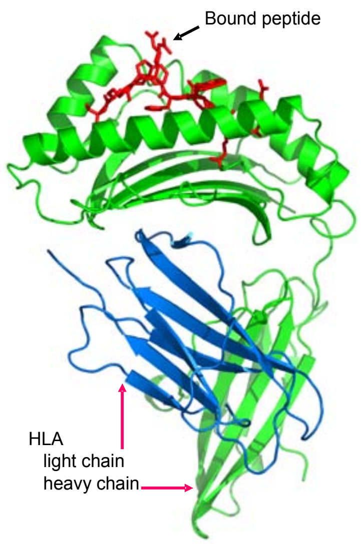

***Figure 1**: Ribbon representation of HLAB* 2705 (light chain in blue, heavy chain in green, pVIPR peptide with amino acid sequence RRKWRRWHL as stick model in red). Because the binding grooves are highly similar, only the backbone of the heavy and light chains of B*2705 is depicted.*

References

1. Fiorillo, M. T., Rückert Ch., Hülsmeyer, M., Sorrentino, R.,Saenger, W., Ziegler, A. and Uchanska-Ziegler, B. (2005) *J Biol Chem* **280**: 2962-2971.

DIAGNOSTICS BEAMLINE FOR THE SRF GUN PROJECT

T. Kamps, V. Dürr, K. Goldammer , D. Krämer, P. Kuske, J. Kuszynski, D. Lipka,
F. Marhauser, T. Quast, D. Richter, BESSY, D-12489 Berlin, Germany
U. Lehnert, P. Michel, J. Teichert, FZ Rossendorf, D-01314 Dresden, Germany
P. Evtushenko, Jefferson Lab, Newport News, VA 23606, USA
I. Will, Max Born Institut, D-12489 Berlin, Germany

Radio-frequency (RF) photoinjectors offer excellent performance characteristics for application at Free Electron Lasers (FEL). Strong RF accelerating fields together with emittance compensating solenoidal fields deliver high bunch charges in the order of 1 nC at low normalized emittances close to 1 mm mrad. Future FEL light sources such as the proposed BESSY FEL [1] operate with superconducting RF (SRF) for electron acceleration to enable continuous wave operation to generate flexible bunch patterns to meet the user demands.

Current photoinjectors work with normal conducting RF in a pulsed mode. Using SRF for the injector as well allows one to fully exploit the benefits of SRF technology. There are however issues with the application of SRF technology at electron gun cavities related to the high gradients and solenoidal fields. The emittance compensation scheme, which makes use of the solenoidal field in normal conducting RF guns cannot be used in a SRF gun without modifications. When superconducting material is placed in direct vicinity of strong magnetic fields, magnetic flux lines might be trapped. In case of a SRF gun this leads to a vast enlargement of the surface resistance, thus beating down the quality factor and impeding operation at the desired accelerating gradients. The SRF gun under development within the framework of this project utilizes a modified TESLA [2]-based design for a three and a half cell gun cavity made of Nb with a RF frequency of 1.3 GHz [3]. The expected axis peak field of the accelerating mode is 50 MV/m. In order to work with high gradients the quality factor has to be in the region of 10^{10}. To avoid degradation of the quality factor due to additional surface resistance the contribution from the solenoid magnetic flux has to be kept below $3.5\ \mu$T [4, 5].

The SRF gun collaboration of BESSY, DESY, FZR and MBI sets out to tackle these issues. The target of the collaboration is to setup a SRF photoinjector [6] together with a diagnostics beamline serving as a test facility. The injector will be able to work in three different operation modes with beam parameters as listed in Tab. 1.

Mode	**ELBE**	**HC**	**BFEL**
Repetition Rate	13 MHz	1 MHz	1 kHz
Bunch Charge	77 pC	1 nC	2.5 nC
Bunch Length	5 ps	20 ps	50 ps
Transverse Emittance	1.5 μm	2.5 μm	3.0 μm

Table 1: Beam parameters of the injector operation modes ELBE, High charge (HC) for neutron experiments and energy recovery linac R&D, and BESSY FEL (BFEL).

The diagnostics beamline enables the measurement of the transverse emittance, energy spread and bunch length beside beam position, mean momentum and charge. A schematic overview of the beamline is shown in Fig. 1. It consists of beam position monitors (BPM), integrated current transformers (ICT), profile monitors based on YAG-screens, an emittance measurement system (EMS), a spectrometer dipole, a Cherenkov radiator, electro-optical sampling system (EOS) and Faraday cups (FCup). In addition the beam can be focused with a quadrupole triplet, guided to the ELBE beamline with a dipole magnet and the beam position will be corrected with steerer coils. In the following diagnostic elements to measure selected beam properties are described in more detail.

For the foreseen operation regimes the emittance of the electron beam will vary between 0.5 mm mrad and 5 mm mrad. The required resolution is $d\epsilon/\epsilon = 0.20$ for all regimes. The beam is in all nominal operation modes space-charge dominated rendering emittance measurement techniques impossible which assume linear beam optics. For this reason a slit-based phase space sampling method (see for example [7]) is considered, where a narrow slit is moved perpendicular across the beam. The slit collimates the beam into emittance dominated beamlets, whose divergence is measured at screen stations following the slit mask. From these data the divergence of the beam in front of the slit mask can be reconstructed. Together with a transverse profile measurement at the slit mask plane the emittance can be calculated. In order to meet the requirements from the various operation modes a single-slit mask with two slits of $100\ \mu$m and $50\ \mu$m width is under construction. The beamlets will be measured with three high resolution viewscreen stations downstream in the diagnostics beamline. The mask itself is made of 1.5 mm thick tungsten, being an optimum between acceptance and background due to Coulomb scattering.

A precise measurement of the bunch length is essential as the transverse emittance is directly linked to the longitudinal charge distributions. The required resolution will be in the order of $d\sigma_z/\sigma_z = 0.10$ which is challenging for the low charge regime with a bunch length of 5 ps. Two systems with overlapping working range are selected. Both

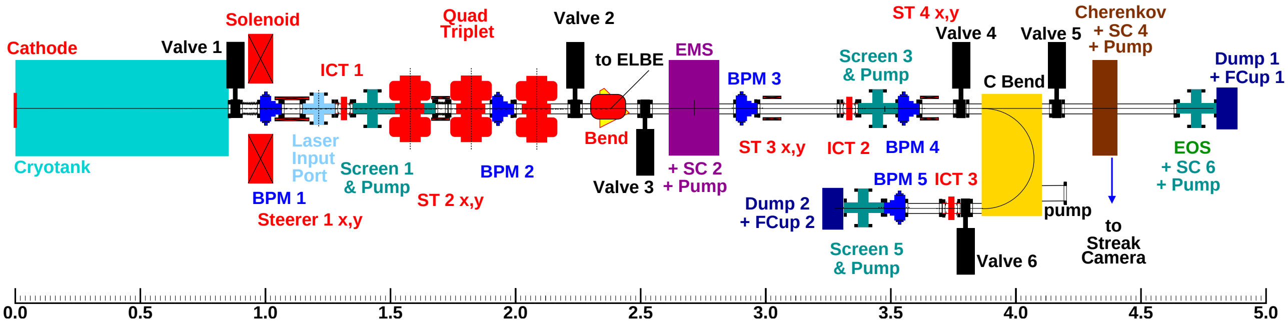

Figure 1: Diagnostics beamline overview including dipole magnet for the transfer to ELBE.

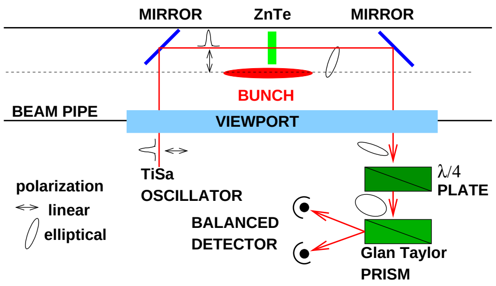

Figure 2: Setup of the bunch length monitor system with Electro-Optical Sampling. The arrows and ellipses indicate the orientation of the polarization when the electron beam moves in the vicinity of the crystal.

methods rely on the conversion of the electron intensity distribution into a corresponding light pulse. One uses the partial conversion of the energy of the electron bunch via Cherenkov radiation into a flux of photons with the same time properties as the electron bunch [8]. These light pulses are then measured with a streak camera which is placed at some distance to the injector.

The second method is based on electro-optical sampling [9] by sampling the birefringence induced by the electro-magnetic field of a relativistic electron bunch in a ZnTe crystal with ultrashort laser pulses. The resolution of this technique is determined by the width of the laser pulse, the relative time jitter between the laser pulse and electron bunch and the dispersion of the field pulse in the optical crystal. Here a laser pulse with 100 fs length and linear polarization produced with a TiSa oscillator is transported to the ZnTe crystal (see Fig. 2).

The energy and energy spread will be measured using a 180^o dipole spectrometer.

The diagnostics beamline currently under construction will play a vital role in the commissioning and successful running of the SRF gun project. Proven and mature technology will be implemented in order to observe beam parameters at a multitude of operation modes. Critical observables will be addressed by two complementary monitor types. The conceptual design phase of the diagnostics beamline runs until mid 2005, after which procurement and construction of parts will begin. Shipment of components from BESSY to FZR will start mid 2006 so beam operation can start end of 2006. The commissioning and beam dynamics studies phase are planned in 2007 after which the injector will be handed over to ELBE.

REFERENCES

[1] The BESSY Soft X-ray Free Electron Laser, TDR BESSY March 2004, eds.: D. Krämer, E. Jaeschke, W. Eberhardt, ISBN 3-9809534-0-8, BESSY, Berlin (2004).

[2] The TESLA Technical Design Report, TESLA TDR, DESY March 2001

[3] D. Janssen et al, Status of the 3 1/2 cell Rossendorf Superconducting RF Gun, Proceedings of the FEL 2004, Trieste, Italy, 2004

[4] The Conceptual Design Report for the TESLA Test Facility (TTF) Linac, Ed. D.A. Edwards

[5] K. Goldammer, Numerical Investigations of Superconducting Multicell Photoinjector RF Gun Cavities, Diploma Thesis, May 2004, TU Berlin

[6] J. Teichert et al, Progress of the Rossendorf SRF Gun Project, THPP034, FEL 2005 proceedings

[7] J. Rosenzweig, G. Travish, Design Considerations for the UCLA PBPL Slit-Based Phase Space Measurment System, UCLA PBPL Note 1994

[8] D. Lipka et al, Measurement of the Longitudinal Phase Space at PITZ, Proceedings of the DIPAC 2003, Mainz, Germany, 2003

[9] D. Oepts et al, Picosecond electronbunch length measurement using an electro-optic sensor, Proceedings of the FEL 1999, Hamburg, Germany, 1999

Determination of magnetization depth profiles of V/Fe/V(110) with X-Ray Resonant Magnetic Reflectometry

D. Schmitz, P. Imperia, H. Maletta, D.A. Tennant
Hahn-Meitner-Institut Berlin, Glienicker Str. 100, 14109 Berlin

U. Grüner, M. Harlander, S. Macke, E. Goering
Max-Planck-Institut für Metallforschung, Heisenbergstr. 3, 70569 Stuttgart

The magnetic part of the x-ray scattering amplitude is resonantly enhanced by orders of magnitude if the photon energy is tuned to an absorption threshold [1]. This has been utilized to determine the element-specific magnetization depth profiles of ultrathin Fe films deposited *in-situ* onto a V(110) single crystal and covered with V. For this purpose X-Ray Magnetic Circular Dichroism (XMCD) measurements in absorption, X-Ray Resonant Magnetic Reflectance (XRMR) measurements and a reflectance simulation program have been combined [2]. The XMCD was measured as a function of photon energy across the $L_{2,3}$ absorption edges at fixed angle of incidence in order to determine the optical constants which were later used to simulate the reflectances. The specular reflectances were measured as a function of the angle of incidence reversing the helicity of the incoming elliptically polarized radiation. For all measurements the samples were magnetized to remanence.

Tuning the photon energy to an absorption threshold has important consequences for the optical constants. They depend on the chemical environment and the magnetic state of the element under consideration, experimental conditions like energy resolution, and especially the magnetic part is resonantly enhanced. Therefore a careful experimental determination of the optical constants has been performed. The imaginary part of the scattering amplitude f_2 and the corresponding magnetic part m_2 were measured in absorption, and the corresponding real parts f_1 and m_1 were determined by Kramers-Kronig transformation. The resulting scattering amplitudes are shown in Fig.1 for Fe (upper row) and V (lower row), respectively.

In order to determine a magnetization depth profile the measured reflectance asymmetry has to be fitted with a simulated reflectance asymmetry. This was performed with a computer program which is based on the Parratt algorithm. The program takes into account the non-magnetic and magnetic contributions to the scattering amplitude and the polarization of the incident radiation. Moreover, it is possible to simulate the magnetization at interfaces by magnetic Gaussian depth profiles. The chemical profile was determined from the non magnetic average reflectance and kept constant during the determination of the magnetic profile.

In Fig.2 the reflectance asymmetries (a, b) and resulting magnetization depth profiles (c, d) of V(5 Å) on Fe(13 Å) on V(110) are shown. The measured asymmetries (black line) were taken with resonant excitation, *i.e.*, with photon energies tuned to the Fe L_3 (704.25 eV, Fig.2a) and V L_3 (511.6 eV, Fig.2b) absorption edge. The grazing incidence angle range was from 0° to 80° which corresponds to a momentum transfer range along the sample surface normal from 0 $Å^{-1}$ to 0.7 $Å^{-1}$ for 704.25 eV and to 0.5 $Å^{-1}$ for 511.6 eV. For each element two simulated asymmetries are shown for comparison: one for a reasonable starting configuration (red line) and one for the best fit (green line).

For Fe a homogeneous magnetization (red line, Fig.2c) results in a simulated asymmetry (red line, Fig.2a) which agrees already quite well with the measured asymmetry, except that the peak at 0.5 $Å^{-1}$ is slightly too high in momentum transfer and too small in intensity. If the Fe magnetization is reduced at both interfaces to V the agreement between measurement and simulation (green line) becomes very good. Please note that the problem of the wrong sign of the simulated asymmetry below 0.05 $Å^{-1}$ as described for Fe in the former annual report [3] has been solved. It was due to a systematic error in the determination of $m_1(Fe)$.

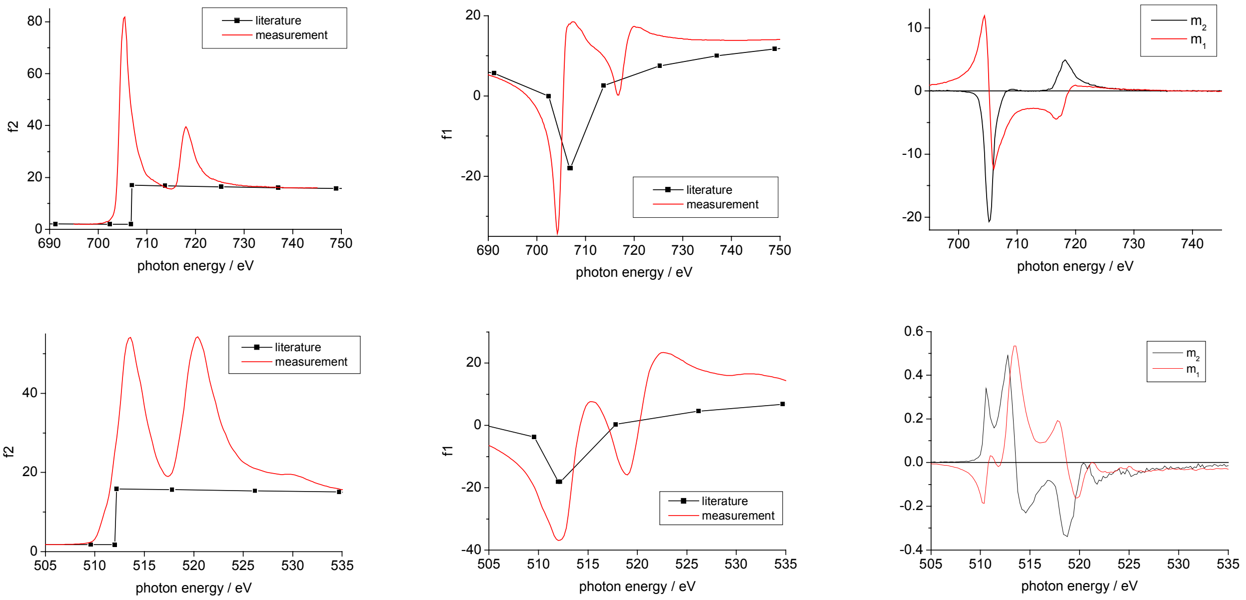

Fig.1: *Scattering amplitudes of Fe (upper row) and V (lower row). The imaginary parts f_2 and m_2 were measured in absorption and with XMCD, and the corresponding real parts f_1 and m_1 were determined by Kramers-Kronig transformation.*

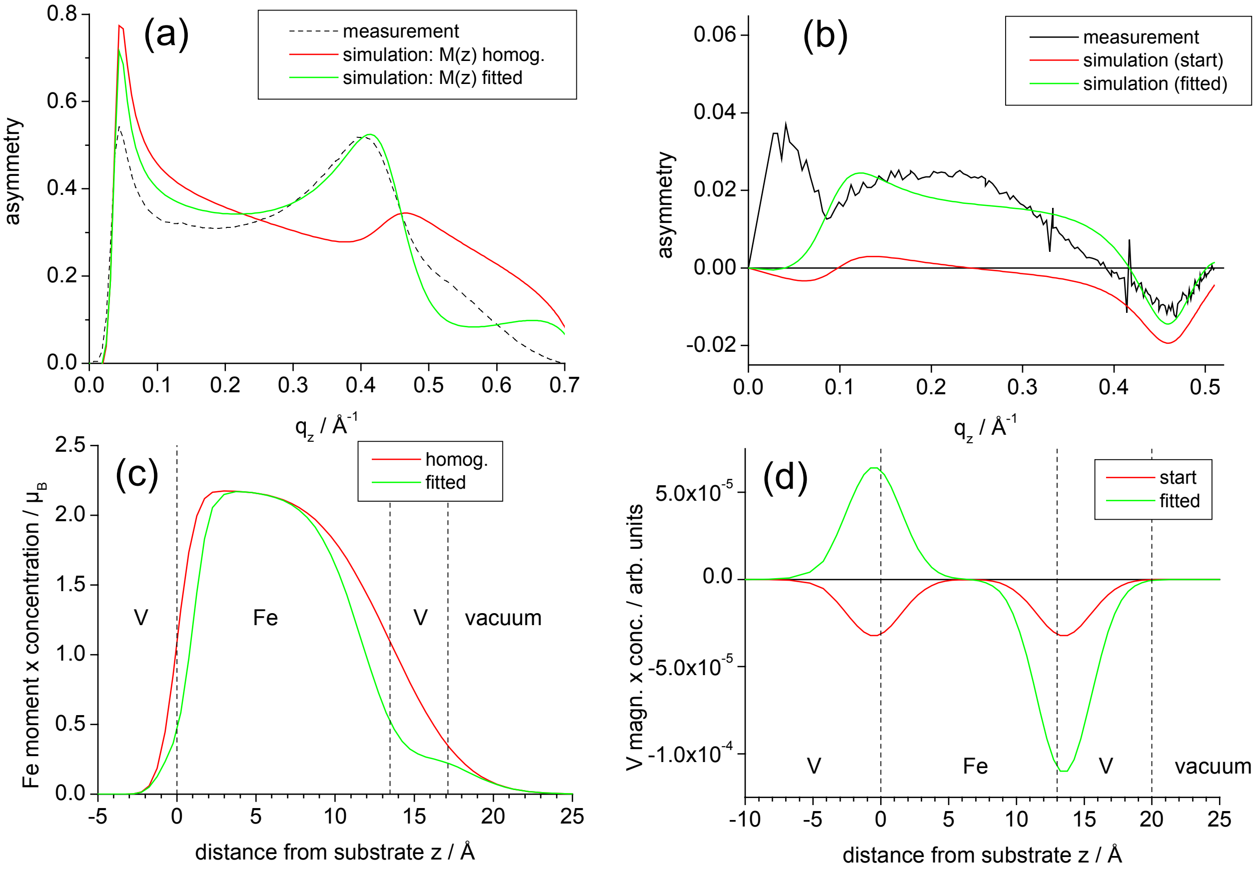

Fig.2: *Reflectance asymmetries (a, b) and magnetization depth profiles (c, d) of Fe (a, c) and V (b, d) in V(5 Å) on Fe(13 Å) on V(110).*

The reduction of the Fe magnetization at the interfaces to V is theoretically expected because of the Fe*3d*-V*3d* hybridization [4] and has been measured with XMCD comparing Fe/V(001) superlattices with different layer thicknesses [5] and Fe/V/Fe(110) trilayers with different deposition temperatures [6]. The fact that our XRMR results are in accordance with these earlier findings clearly proofs that our realization of this new method including the simulation program works.

The reasonable starting configuration for the V magnetization profile is shown as a red line in Fig.2d. There it has been assumed that V at the interface to Fe is ferromagnetic with *antiparallel* coupling to the Fe magnetization and with values for the magnetic part of the optical constants as determined with XMCD (Fig.1). The overall shape of the corresponding simulated asymmetry (red line, Fig.2b) is quite similar to the measured asymmetry, but the relative amplitudes differ. The agreement becomes better (green line) if it is assumed that the V magnetization at the lower interface is *parallel* to the Fe magnetization and that the absolute value of the V magnetization at the upper interface is larger as the one at the lower interface (green line, Fig.2d).

The V asymmetry is more than one order of magnitude smaller than the Fe asymmetry, because the V magnetization is induced only at the interface to Fe. On the one hand the statistical quality of the measured V asymmetry is still good, indicating that the sensitivity of the measurement is sufficient. On the other hand we have not yet found a V magnetization profile for the capped samples which is consistent with both, the measured asymmetries in reflection and in absorption. Therefore the question arises whether our realization of the new method is accurate enough to determine the profile of the tiny V magnetization. Further analysis is under way to answer this question.

We would like to thank S. Rudorff and S. Miemietz for technical support.

[1] M. Blume, J. Appl. Phys. 57, 3615 (1985); D. Gibbs, D.R. Harshman, E.D. Isaacs, D.B. McWhan, D. Mills, C. Vettier, Phys. Rev. Lett. 61, 1241 (1988); E.D. Isaacs, D.B. McWhan, C. Peters, G.E. Ice, D.P. Siddons, J.B. Hastings, C. Vettier, O. Vogt, Phys. Rev. Lett. 62, 1672 (1989)

[2] J. Geissler, E. Goering, M. Justen, F. Weigand, G. Schütz, J. Langer, D. Schmitz, H. Maletta, R. Mattheis, Phys. Rev. B 65, 020405(R) (2001)

[3] D. Schmitz, P. Imperia, H. Maletta, U. Grüner, M. Harlander, S. Macke, E. Goering, BESSY Annual Report, 242 (2004)

[4] J. Izquierdo, R. Robles, A. Vega, M. Talanana, C. Demangeat, Phys. Rev. B 64, 060404 (2001)

[5] A. Scherz, H. Wende, P. Poulopoulos, J. Lindner, K. Baberschke, P. Blomquist, R. Wäppling, F. Wilhelm, N.B. Brooks, Phys. Rev. B, 180407 (2001)

[6] A. Scherz, P. Poulopoulos, R. Nünthel, J. Lindner, H. Wende, F. Wilhelm, K. Baberschke, Phys. Rev. B 68, 140401(R) (2003)

Broadband Multilayer Polarizers for Extreme Ultraviolet Radiation

A.G. Michette, A.K. Powell, S.J. Pfauntsch
King's College London, Department of Physics, Strand, London, WC2R 2LS, UK

Z. Wang , H. Wang, J. Zhu, F. Wang, Z. Gu, L. Chen
Institute of Precision Optical Engineering, Tongji University, Shanghai 200092, China

F. Schäfers
BESSY GmbH, Albert Einstein Straße 15, D-12489 Berlin, Germany

For polarization-sensitive studies accurate evaluation of the polarization state of the radiation is clearly crucial. At EUV and soft x-ray wavelengths this is an increasingly important area for applications such as the study of micro-magnetic structures in magneto-optical materials and the chiral properties of a wide range of, e.g., pharmaceutical materials. In the visible and ultraviolet regions of the spectrum, birefringence and dichroic polarizers are used but in the EUV the closeness of the real part of the refractive index, coupled with high absorption, means that such polarizers are not feasible. Polarizers based on periodic multilayers are effective over very small wavelength ranges and only close to the Brewster angle ($\approx 45°$ for EUV radiation). Ways of overcoming these limitations, such as the double-multilayer polarizer [1] and laterally graded multilayers [2] require complex systems based on translation and/or rotation of the components.

Translation of the polarizer may be eliminated if non-periodic multilayers, designed to work over wide spectral ranges, are used. The best material pairs for multilayers are those that form smooth and compositionally abrupt interfaces with high optical contrast and low absorption. In the wavelength range 12.5–20 nm molybdenum and silicon are suitable materials, providing good optical performance, and the design and performances of three broadband Mo/Si multilayer polarizers, as indicated in table 1, are described in this report.

Table 1. Design parameters and calculated and measured performances of Mo/Si multilayer polarizers for different spectral bandwidths (errors are rms values). The calculations are for grazing angles of 50°.

	No. of bilayers	R_s (%) calc.	R_s (%) meas.	R_p (%) calc.	R_p (%) meas.	P calc.	P meas.
15–17 nm	33	50.0±0.2	36.6±0.7 (36–38)	0.17±0.07	0.24±0.08	0.993	0.987
14–18 nm	31	35.0±0.1	21.1±2.5 (17–25)	0.18±0.14	0.16±0.16	0.990	0.986
13–19 nm	30	30.4±1.2	18.2±3.6 (15-27)	0.24±0.16	0.20±0.16	0.985	0.980

The reflectivity of a multilayer is defined by

$$R = \frac{R_s + R_p}{2} \tag{1}$$

where R_s and R_p are the intensity reflectivities for s- and p-polarized radiation. The quasi-Brewster angles, where R_p is close to zero, are close to 45° for reflective multilayers. The degree of polarization obtained is

$$P = \frac{R_s - R_p}{R_s + R_p}. \tag{2}$$

For low R_p, $P \to 1$ and so in the multilayer design the Merit Function (MF)

$$\mathrm{MF} = \frac{1}{m}\sum_{j=1}^{m}\left[1 - P\left(\lambda_j\right)\right]^2 \tag{3}$$

is minimized; the summation is over a selection of discrete wavelengths in the desired range.

During the recursive optimization, only randomly selected layer thickness changes that decrease MF are retained, leading to an optimized layer thickness distribution that provides minimum in MF. Although this may not correspond to the global minimum, in practice it is usually sufficient to find a sufficiently deep minimum of the merit function that approximately produces the desired reflectivity profile and degree of polarization. At each stage in the optimization the reflectivities are calculated using the Fresnel formulae and tabulated optical constants. Alternative approaches based on simplified analytic formulae lead to structures that give strongly oscillating reflectivities profiles over the design wavelength range. In the designs presented here the initial period distributions were deduced using an analytic method [3], and the MF was then minimized using the standard Levenberg-Marquardt algorithm.

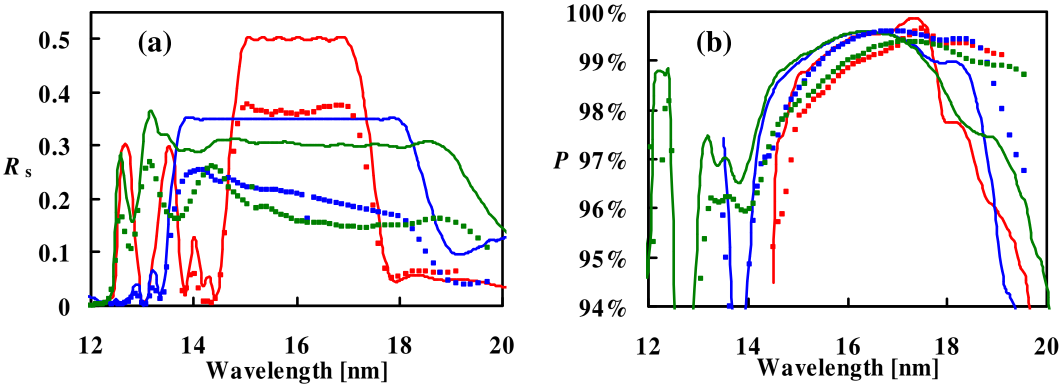

Figure 1. (a) The calculated (curves) and measured (points) s-reflectivities of Mo/Si multilayer polarizers optimized for constant reflectivities over the wavelength ranges 15–17 nm (red), 14–18 nm (blue) and 13–19 nm (green). (b) The calculated and measured polarizations produced by the multilayers.

The calculated s-reflectivities and polarizations are shown in figure 1. The layer thicknesses vary between 1 nm and 7 nm (see the example in figure 2), a range which is feasible to manufacture. The multilayer polarizers were made using a calibrated ultra-high vacuum direct current magnetron sputtering system with targets of Mo (purity 99.95%) and Si (99.999%) in Ar (99.999%). They were deposited on 20×30 mm silicon substrates at room temperature. The deposited multilayers were measured, for quality control, using a Bede D1 small angle X-ray diffractometer.

The polarizers have been measured using the high precision 8-axis polarimeter on the plane grating monochromator beam line UE56/2-PGM-1 at BESSY [4]. The results are summarized, and compared with the design values, in table 1 and figure 1. The measured p-reflectivities are very low in all cases. The measured s-reflectivities are smaller than the calculated values due to interfacial roughness and diffusion.

From the Bragg equation, if a multilayer mirror is designed to reflect over a range of wavelengths at a fixed angle, it will also reflect over a range of angles at a fixed wavelength. This has been demonstrated by

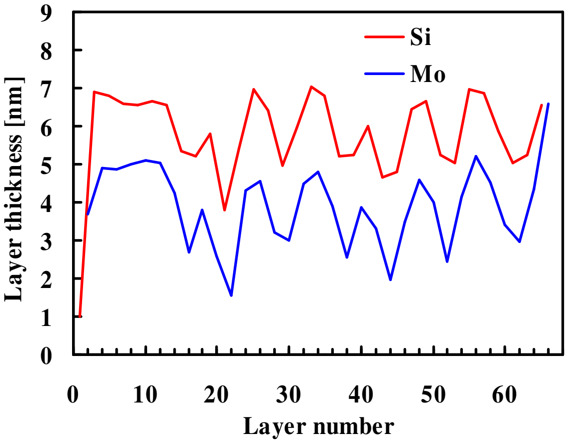

Figure 2. The layer thickness distribution of the 15–17 nm multilayer polarizer. Higher layer numbers are closer to the substrate.

measuring the s-reflectivities and polarizations of the sample designed for the wavelength range 15–17 nm at different angles (figure 3).

The work described above has been accepted for publication in the Journal of Applied Physics [5], and submitted to Optics Express [6].

In addition to the reflecting samples, broadband transmission multilayers have also been designed and made. These were used as analyzers in conjunction with the reflective polarizers during the measurements at UE56/2-PGM-1. The data analysis is not yet complete, but some preliminary results summarised in table 2 indicate that the measured performances are compatible with the calculated ones if an interfacial roughness of about 0.6 nm is assumed.

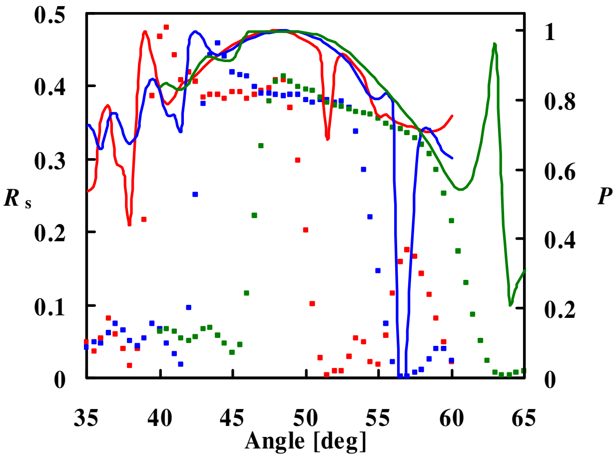

Figure 3. The measured s-reflectivities (points) and polarizations (curves) as functions of incidence angle for the multilayer designed for the wavelength range 15–17 nm. The wavelengths are 14.5 nm (red), 15.5 nm (blue) and 16.5 nm (green).

Table 2. Preliminary results of the polarimetry analysis, based on equation (8) of reference [4]. Δ_1 is the phase shift (p–s) induced by the polarizer, R_p and R_s are the reflectivities of the polarizer, and T_p and T_s are the transmissivities of the analyzer.

	Δ_1	R_p/R_s	T_p/T_s
Design (σ=0.6 nm)	–29.22	0.0112	0.9551
Average fit	–28.00±0.28	0.010±0.032	0.980±0.023

Acknowledgements The authors are indebted to Dr IV Kozhevnikov for useful discussions. This work was supported by the National Natural Science Foundation of China (contract numbers 60378021 and 10435050), by the Royal Society, London (contract number NC/China/16660) and by the European Union through the BESSY-EC-IA-SFS contract (BESSY-ID.05.2.165).

1. M Yanagihara, T Maehara, H Nomura, M Yamamoto, T Namioka, H Kimura 1992 *Rev. Sci. Instrum.* **63** 1516

2. JB Kortright, M Rice, KD Franck 1995 *Rev. Sci. Instrum.* **66** 1567

3. C Morawe, E Ziegler, J-C Peffen, I V Kozhevnikov 2002 *Nucl. Instrum. Methods Phys. Res.* **A493** 189

4. F Schäfers, H-C Mertins, A Gaupp, W Gudat, M Mertin, I Packe, F Schmolla, S Di Fonzo, G Soullié, W Jark, R Walker, X Le Cann, R Nyholm, M Eriksson 1999 *Appl. Opt.* **38** 4074

5. Z Wang , H Wang, J Zhu, F Wang, Z Gu, L Chen, AG Michette, AK Powell, SJ Pfauntsch, and F Schäfers 2005 *J. Appl. Phys.* (in press)

6. Z Wang , H Wang, J Zhu, F Wang, Z Gu, L Chen, AG Michette, AK Powell, SJ Pfauntsch, and F Schäfers 2005 *Optics Express* (submitted)

W/B$_4$C Multilayers for soft X-ray Polarisation Analysis

A. Gaupp, F. Schäfers, St. Braun[1]

BESSY GmbH Berlin
[1]IWS Dresden, Fraunhofer-Institut für Werkstoff- und Strahltechnik

Knowledge of the polarisation state of synchrotron radiation is essential for many experiments. Especially at the 2p absorption edges of the magnetic substances Fe, Co, Ni, (700-900 eV) the degree of polarisation is the normalization factor for the degree of the magnetic effects (e.g. MLD; MCD,…).However, since so far there are no primary optical standards as phase plates available up to 600 eV, above this energy the circular polarisation can only be deduced from a measurement of the linear polarisation assuming complete total polarisation.

In this project new W/B$_4$C-multilayers have been developed and characterised by at-wavelength reflectometry using the reflectometer at the BESSY optics beamline and using the polarimeter /1/ at UE56/1. The multilayers are be used as linear analysers around the Fe and Ni 2p edges, respectively. The working angle is at the Brewster angle at which the polarising power $(R_s-R_p)/(R_s+R_p)$ is maximum. Polarisation measurement is done by azimuthal rotation of the multilayer optic around the light axis. Due to the highly stabilised sputter systems available now such multilayers with individual layer thicknesses of the W and the B$_4$C layers down to 0.4 nm such multilayers are possible to be produced with sufficient interface perfectness and sufficient number of periods to give reasonable reflectivity. Using magnetron sputter deposition operated at low argon pressures ($p \sim 7 \cdot 10^{-4}$ mbar) multilayers with extremely small period thicknesses ($d \sim 1$ nm) and minimized interface widths can be produced /2/.

In contrast to other previously investigated and highly monochromatic multilayers such as Cr/C, Cr/Sc, Ni/V /3,4/ which gain the high performance by expoiting resonance features at the absorption edges of the materials, we choose this material combination since it has excellent growth conditions and can be operated over a large energy range in the soft x-ray spectrum, since it has no resonating absorption edges.

As an example the Fig. 1 shows the results for 3 W/B$_4$C multilayers developed for the Fe 2p edge at 710 eV. The d-spacing was kept at 1.23 nm, while the number of periods varied between 50, 300 and 600 periods.

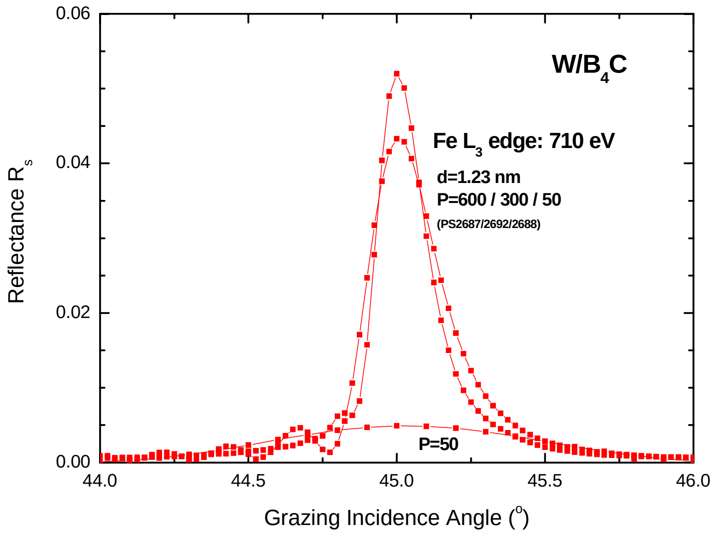

Fig. 1 *Reflectivity of W/B$_4$C multilayers matched to the Fe 2p edge at the Brewster angle. The three multilayers have different numbers of periods.*

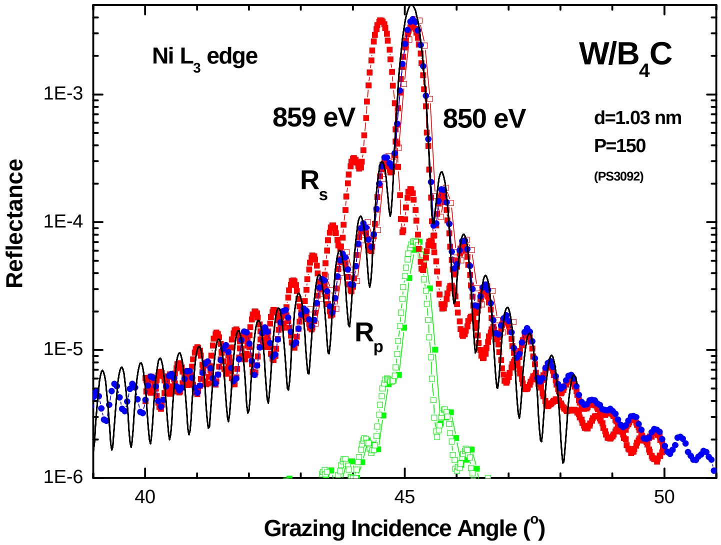

Fig. 2 *Angle dependence of the s- and p-reflectivity for the W/B$_4$C multilayer around the Brewster angle at 850 and 859 eV. Black curve (850 eV only) is a simulation with REFLEC (s=0.3 nm)*

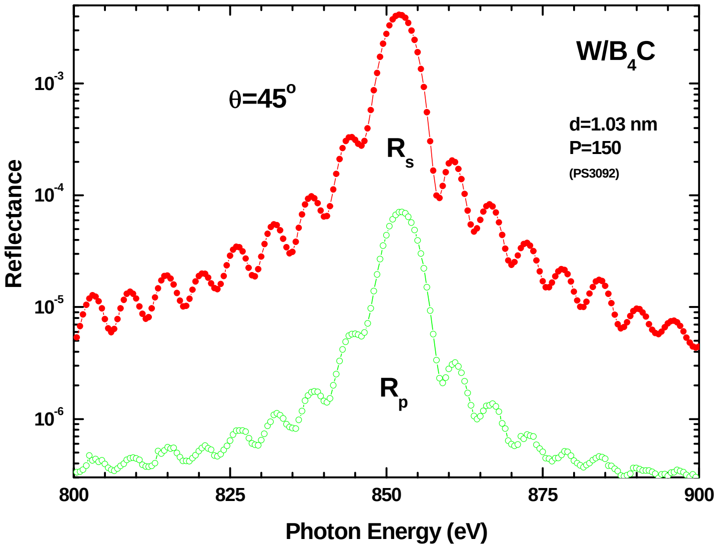

Fig.3 *Energy dependence of the s- and p-reflectivity for the W/B$_4$C multilayer around the Ni-2p edge*

Correspondingly the reflectivity Rs increased from 0.5 %, 4.3 to 5.3 % while the angular resolution reduces to 0.2 degrees. Thus the choice is between broad-band or high reflectivity behaviour /5/.

Fig. 2 and 3 show the reflectivity data for another W/B$_4$C multilayer optimised for operation at the Ni 2p edge around 850 eV. The angular and energy dependence is shown, each time measured for s- and p-polarised light. This multilayer has 150 periods with a period thickness of only 1.03 nm. Despite of the small individual layer thicknesses of not much more than an atom the very well-resolved Kiessig fringes indicate an excellent homogeneity of the total multilayer stack throughout the 300 layers. A simulation with REFLEC-program yields a state-of-the-art interface width (roughness + diffuseness) of σ = 0.3 nm.

The maximum reflectivity is 0.4 % for s-polarisation and 0.07 % for p-polarisation. Thus, the analysing power for linearly polarised light is better than 0.965. With these multilayers an unequivocal determination of polarised light is possible.

References

[1] http://www.bessy.de/user/Beamlines/Optic beamline
http://www.bessy.de/user/Experimental stations/Polarimeter and -/Reflectometer, respectively

[2] S. Braun, H. Mai, ***Multilayers for X-ray optical purposes*** in Metal based thin films for electronics, edited by K. Wetzig and C.M. Schneider, WILEY-VCH, 277-291 (2003)

[3] F. Schäfers, S. Yulin, T. Feigl, N. Kaiser, ***At-Wavelength Metrology on Sc-based Multilayers for the VUV and Water Window,*** SPIE-Proc. Vol. **5188**, 138-145 (2003)

[4] F. Schäfers, ***Multilayers for the EUV/Soft X-ray Range,*** Physica B **283,** 119-124 (2000)

[5] A. Michette et al., this report and Z. Wang, ***Broadband multilayer polarizers for soft X-rays,*** J. Appl. Phys. in press (2006)

Multilayer monochromators for the wavelength-dispersive X-ray fluorescence spectrometry

S. Braun[1*], T. Foltyn[1], M. Menzel[1], A. Leson[1], F. Schäfers[2], M. Mertin[2]

[1] IWS Dresden, Fraunhofer-Institut für Werkstoff- und Strahltechnik, Winterbergstr. 28, 01277 Dresden, Germany
[2] Berliner Elektronenspeicherring-Gesellschaft für Synchrotronstrahlung, Albert-Einstein-Str. 15, 12489 Berlin, Germany
[*] e-mail: stefan.braun@iws.fraunhofer.de, phone: +49.351.258.3432, fax: +49.351.288.3314

For many years X-ray fluorescence analysis (XRFA) has been well-established as a powerful tool for the qualitative as well as the quantitative element analysis. For instance, they are applied in production plants (e.g. cement and pharmaceutical industry), quality assurance (e.g. detection of sulphur in fuel) and environmental techniques (e.g. inspection of wastewater).

In wavelength-dispersive X-ray spectrometers the atoms of an unknown sample are excited by X-rays or electron beams. Subsequently the characteristic spectrum of the sample is analyzed by using Θ-2Θ goniometers, equipped with monochromators which separate the different emission lines (figure 1).

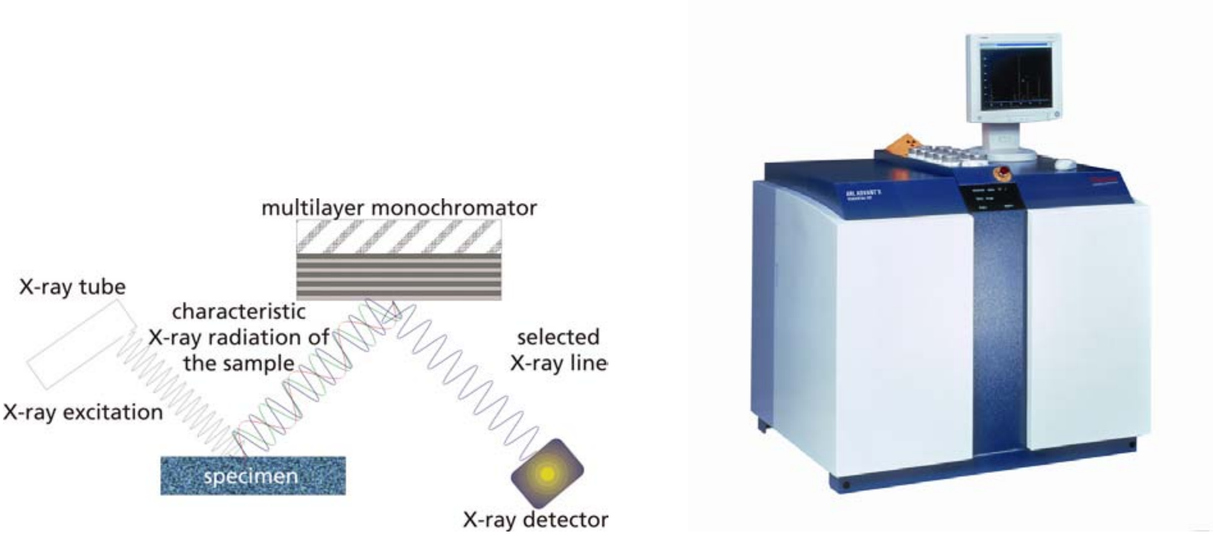

Fig. 1: left hand side: Scheme of the principle of wavelength-dispersive XRFA,
right hand side: Photograph of the system ARL Advant'X. of the Thermo Electron Corporation, where the XRFA principle is realized.

Almost any application requires continuous improvements of the X-ray spectrometers in order to reduce detection limits or to increase the measurement speed. Performance enhancements of the multilayer monochromators can significantly contribute to the overall improvement of the whole system. Main issues concerning the multilayers are high reflectance, low background scattering, high resolving power and long-term stability. In order to fulfil these requirements the following conditions have to be met:

- proper choice of multilayer materials, layer thicknesses and number of periods for particular X-ray wavelengths,
- strict periodicity of the layers in growth direction,
- multilayers with sharp and abrupt interfaces (low diffuseness),
- multilayers with morphological smooth interfaces (low roughness),
- single layers with low absorption and high X-ray optical contrast to each other,
- application of suitable capping layers to avoid oxidation and contamination.

For wavelength dispersive XRFA multilayer monochromators are mainly used for light elements (Be … Ar). The X-ray emission lines of these elements are in the range of 109 eV (11.4 nm) to 2957 eV (0.419 nm). In this soft X-ray region any layer material shows more or less absorption, which abruptly increases above the absorption edges of the material. Therefore it is impossible to find one single multilayer that shows optimal performance for all emission lines. Typical material combinations for different emission lines are shown in table 1.

Table 1: Multilayer systems used for the wavelength-dispersive XRFA.

Chemical element	**K_α emission line** **λ / nm**	**Multilayer materials**
Be	11.43	Mo/Be, Mo/B_4C, La/B_4C
B	6.76	La/B_4C, Mo/B_4C
C	4.48	Cr/C, Ni/C
N	3.16	Cr/Sc
O	2.36	W/Si, Ni/BN
F, Na, Mg, Al, Si	1.83, 1.19, 0.989, 0.834, 0.713	W/Si, W/B_4C, Mo/Si, Mo/B_4C

The constructive interference of X-rays in multilayers and crystals follows BRAGG's law $n \cdot \lambda = 2d \cdot \sin\Theta$ (n … order of the reflection (multilayers) or refraction (crystals), λ … X-ray wavelength, d … multilayer period or lattice distance, Θ … grazing angle). With given values of d and Θ, intensity maxima are observed for the photon wavelength $\lambda_1 = 2d \cdot \sin\Theta$ and for $\lambda_2 = \lambda_1/2 = d \cdot \sin\Theta$ at the same time. Therefore with usual monochromators it is not possible to resolve signals arising from elements with characteristic lines of λ_1 and λ_2. As an example for the overlapping of signals from different elements, the left hand side of figure 2 shows the reflection of sodium (Na) and oxygen (O) emission lines using a standard multilayer monochromator. Because of the fact, that $\lambda_{Na} \sim 0.5 \cdot \lambda_O$, the characteristic radiation of sodium will be detected at the same grazing angle Θ in the second order reflection as the oxygen radiation in the first order reflection.

One of the particular properties of multilayer monochromators is the fact, that in difference to crystals, the layer design can freely be chosen. This offers the opportunity to suppress higher order reflections. The n^{th} reflection order is eliminated by changing the thickness ratio $\Gamma = d_{absorber}/d$ to 1/n. However, for highest possible reflectances and resolving powers, a thickness ratio Γ between 0.2 and 0.3 has to be used. For W/Si multilayers a change of Γ from 0.25 to 0.5 results in a reflectance decrease from 50 % to 36 % and a resolving power reduction from 83 to 53 (figure 2, right hand side). The reason for this behavior is the strong absorption of X-rays within the tungsten layers. With $\Gamma = 0.5$ the tungsten layer thickness is two times higher than in standard high-reflection W/Si multilayers and the penetration depth of X-rays into the multilayer is decreased. Consequently, a lower number of periods contributes to the total reflection and both reflectance and resolving power decrease.

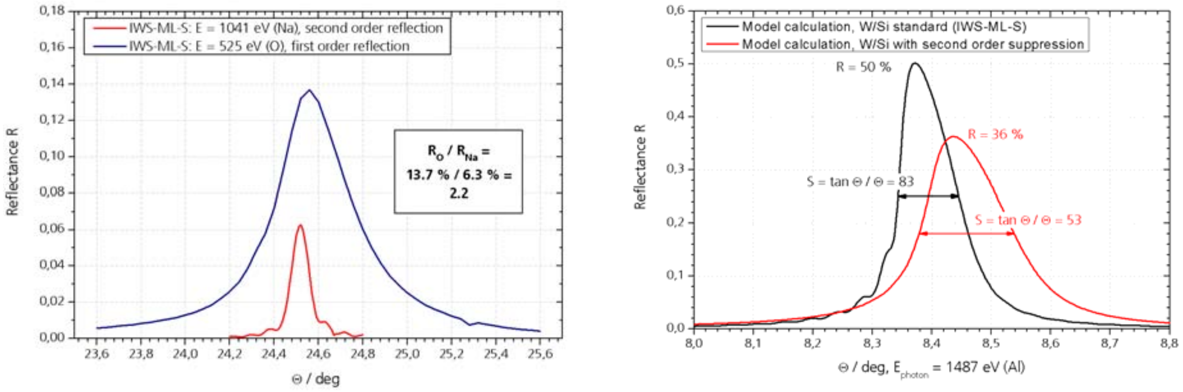

Fig. 2: left hand side: Overlap of the second order reflection of the sodium emission line and the first order reflection of the oxygen emission line for the monochromator type IWS-ML-S
right hand side: Model calculations of the reflection spectra of W/Si multilayers with optimum Γ for the highest possible reflectance and with $\Gamma = 0.5$ for the second order suppression.

A better solution for multilayers with second order suppression is to use layer materials with lower absorption. Model calculations show that the replacement of tungsten by molybdenum results in a significant improvement of reflectance and resolving power. Hence, the replacement had been made, the multilayers have been produced and characterized at BESSY II. In comparison to W/Si multilayers used for the second order suppression a significant improvement of reflectance and resolving power can be obtained with Mo/Si multilayers (figure 3).

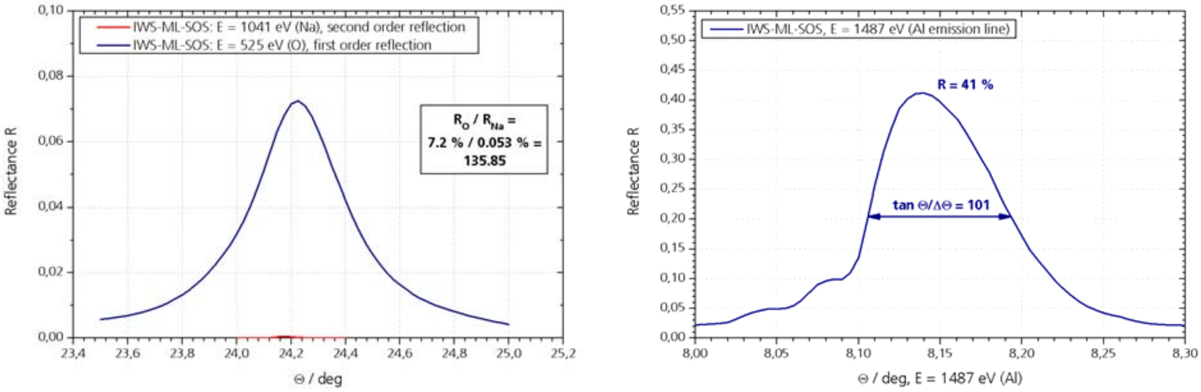

Fig. 3: left hand side: Overlap of the second order reflection of the sodium emission line and the first order reflection of the oxygen emission line for the monochromator type IWS-ML-SOS
right hand side: Reflection spectra of IWS-ML-SOS for the Al emission line. The relative reflectance increase of Mo/Si multilayers is appr. 14 % compared to W/Si (41 % versus 36 %).

Multilayers do not only give the opportunity to design multilayer stacks for the suppression of higher orders. It is also possible to tailor the resolving power of multilayers according to the application needs. By changing the multilayer parameters (materials, period thickness, ratio between absorber and spacer layer thickness, number of periods) a reasonable compromise between the demands for high reflectance and for high resolving power can be found. An overview of the results of recently produced state-of-the-art multilayer monochromators is shown in figure 4.

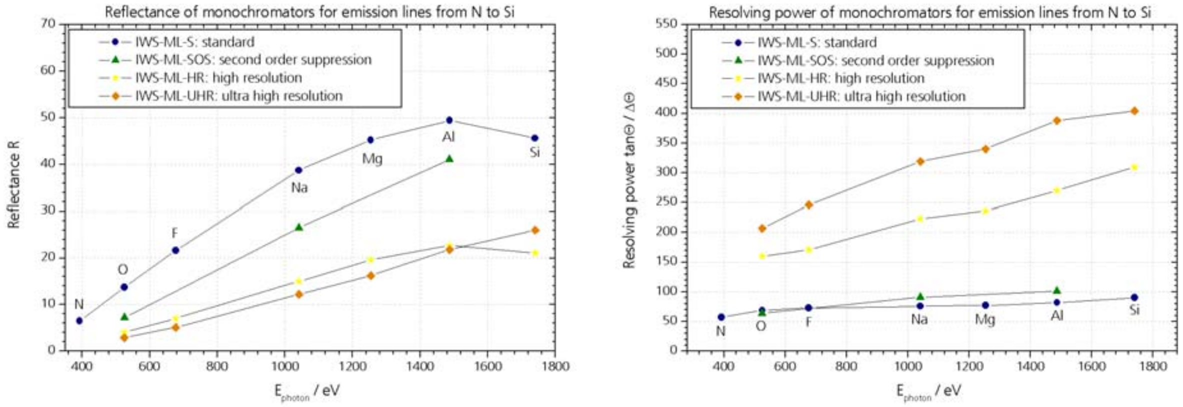

Fig. 4: left hand side: Reflectance of different multilayer monochromator types for XRFA,
right hand side: Resolving power of different multilayer monochromator types for XRFA. Outstanding resolving powers close to 400 for the Al emission line are possible.

Acknowledgments

We would like to thank R. Dietsch (AXO DRESDEN GmbH) and P.-Y. Negro (Thermo Electron Corporation) for many discussions and the fruitful cooperation.

First Soft X-Ray Energy Dispersion at BESSY II: A Pilot Experiment

D.R. Batchelor[1], Th. Schmidt[1], A. Schöll[1], M. Knupfer[4], R. Fink[3], R. Follath[2], C. J. Jung[2], and E. Umbach[1]
[1]Exp.Physik II, Univ. Würzburg, [2] BESSY GmbH, [3] Phys. Chem. II, Univ. Erlangen , [4] IFW Dresden

Near-edge X-Ray absorption fine structure (NEXAFS) is a powerful spectroscopic technique for the investigation of organic molecules, as it provides not just information concerning the molecular orientation but more importantly the electronic structure of the adsorbate, namely the unoccupied density of states. The elucidation of this electronic structure is becoming increasingly available through NEXAFS calculations with codes such as STOBE and GSCF3. However obtaining high resolution data is time consuming, and hence a parallel data acquisition would be advantageous. Energy dispersive NEXAFS is a well known technique in the Hard X-Ray region but not so well known in the Soft X-Ray region [1]. By combining the energy dispersion of a monochromator and the imaging properties of a hemispherical electron analyser the simultaneous detection of electron distribution curves as a function of photon energy is possible.

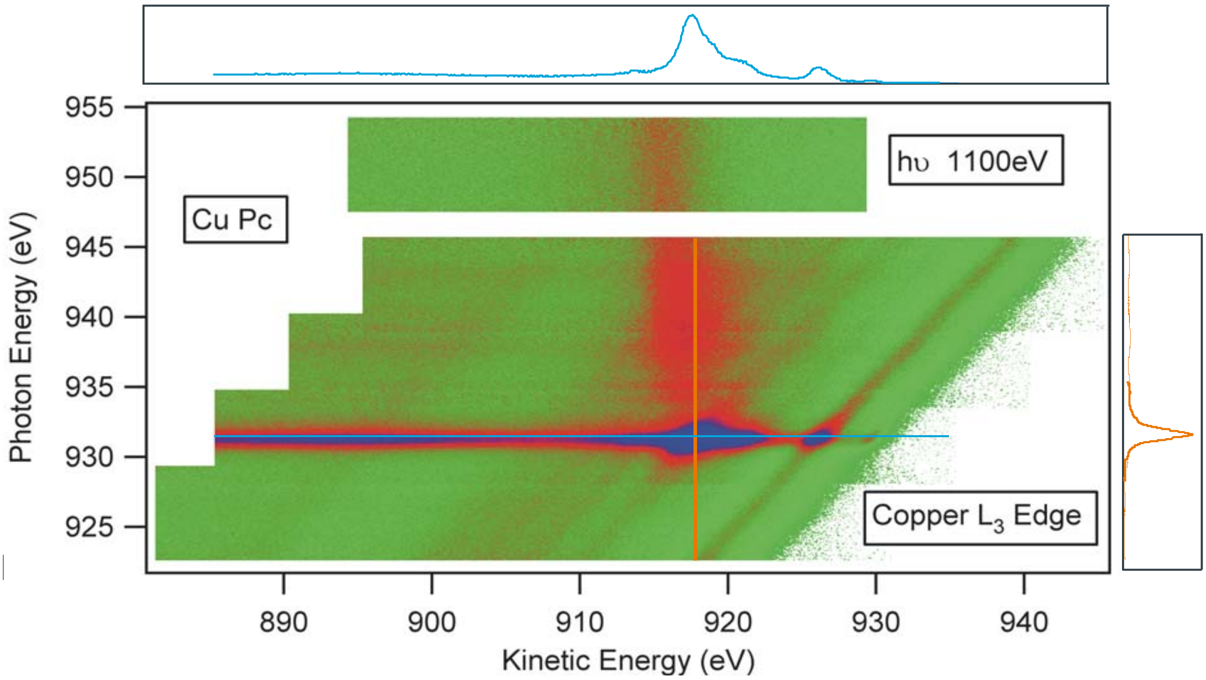

Figure 1. Map of the Cu $L_{2,3}$ resonance of Copper Phthalocyanine with projected NEXAFS and EDC spectra taken from the lines on the map. The Auger spectrum (top) taken at 1100eV is shown as reference.

In the present experiment the photon energy dispersion of the monochromator is projected on to the sample, and the photoelectrons are subsequently imaged in the non-dispersive direction of the analyser. Such an instrument is able to fully exploit the small spot size of state-of-art soft X-Ray monochromators and modern electron energy analysers with 2D imaging detectors. In addition to being able to do energy dispersive NEXAFS it is also possible to look at the resonant Auger and photoemission processes inherent in NEXAFS plus other CFS/CIS techniques, e.g. photoelectron diffraction. The parallel detection enables a large parameter space to be efficiently sampled such that time domain experiments are also possible.

As part of the modification to realise Soft X-Ray dispersion at the UE52-PGM beamline, a new GammaData Scienta R4000 analyser capable of a spatial resolution of ~10 µm has been installed in a horizontal geometry. As stated above the analyser has to image the monochromator dispersion which is normally at the exit slit plane. However, by using a small beam divergence, by operating the monochromator at small C_{ff} values, and by closing the insertion device apertures it is possible to extend the depth of focus (with corresponding loss of flux). This now allows electron distribution curves to be taken as a function of photon energy, the data being collected in the form of pictures, i.e. using both the beamline and analyser dispersion in a true two dimensional sense.

Fig. 1 shows data taken over the Cu $L_{2,3}$ edge of Copper Phthalocyanine. The height of the images (dispersion width) is determined by the analyser slit length and thus by the monochromator exit slit size and analyser magnification. The resonance is simply mapped by stepping the monochromator and analyser energies and taking “pictures”. The individual pictures are normalised to take into account the transmission function of the analyser and the intensity variation over the undulator harmonic. The on-resonance shift of the LMM Auger and the resonant photoemission (i.e. autoionization spectra) of the valence band are easily observable. For high photon energies (~1 keV) the dispersion is large leading to a small number of pictures required to map a resonance. For low energies (~ 100 eV) the photon energy range is much smaller and can be of the order of the width of the resonance itself. However, with suitable normalisation it is possible to map the resonance as shown below in the carbon map for Buckminster fullerene (C_{60}) in Fig. 2.

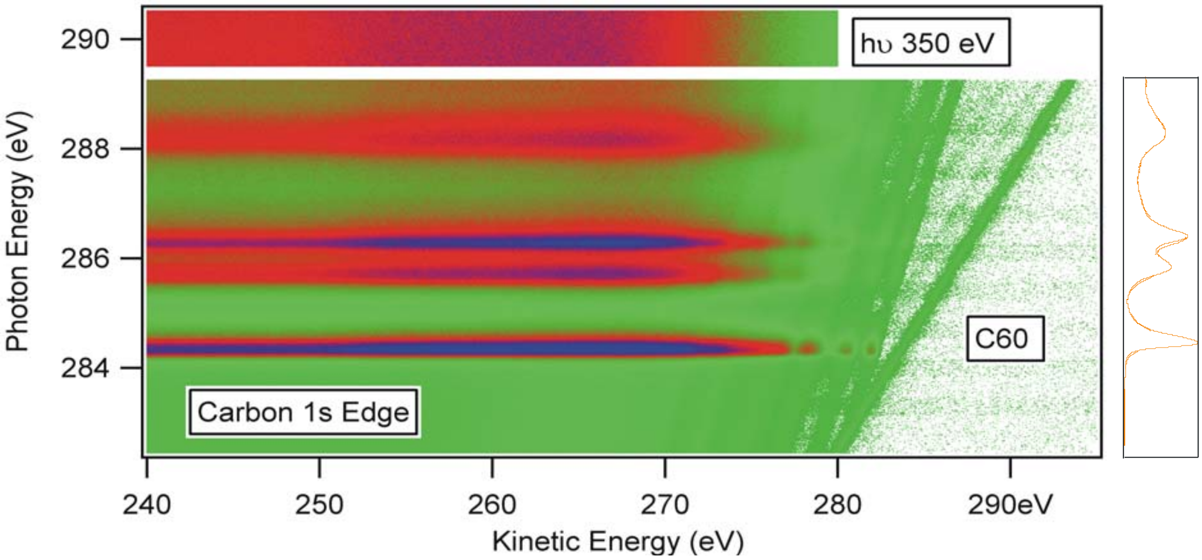

Figure 2. Map of the C 1s resonance of Buckminster Fullerene with the projected NEXAFS. The Auger taken at 350eV is shown as reference

Apart from other changes required to fully realise the dispersive monochromator/ beamline the pilot experiment shows that additional spatial lens modes utilising a lower magnification (~ 5) would increase the available dispersion range, of particular use at low photon energies as for example the C 1s edge.

Acknowledgment: This project is funded by the BMBF (project number 05KS4WWC/2).

References

[1] K. Amemiya, H. Kondoh, T. Yokoyama, and T. Ohta, Journal of Electron Spectroscopy and Related Phenomena 124 (2002) 151–164.

Actinic EUVL mask blank defect inspection by EUV photoelectron microscopy

Jingquan Lin[a], Ulrich Neuhaeusler[a], Jawad Slieh[a], Ulrich Heinzmann[a], Nils Weber[b], Matthias Escher[b], Michael Merkel[b], Andreas Oelsner[c], Dima Valsaitsev[c], Gerd Schoenhense[c] ,
Ulf Kleineberg*[a]
[a]University of Bielefeld, Universitaetsstr. 25, D-33615 Bielefeld, Germany
* (on leave to LMU Munich, Department for Physics, Am Coulombwall 1, D-85748 Garching)
[b]Focus GMBH, Neukirchner Str. 2, D-65510 Hünstetten-Kesselbach, Germany
[c]University of Mainz, Institute of Physics, Staudinger Weg 7, D-55099 Mainz, Germany

INTRODUCTION

Extreme Ultraviolet Lithography (EUVL) is one of the leading next-generation lithography candidates for fabricating integrated circuits with critical dimensions of 45 nm in lateral size and below. EUVL at 13.5 nm wavelength utilizes a reflective mask with patterned absorber ontop of a Mo/Si multilayer-coated mask blank. Defects inside or below the multilayer at the mask blank can either disrupt the layers, reducing the reflectivity, or can generate a conformal multilayer topography inducing a phase error in the reflected electric field. Simulations show that an 80 nm phase defect with a height of 3 nm is considered to be printable [1]. The density of these critical defects must be reduced to the level of 0.005 defects per cm^2 according to International Semiconductor Road Map [2] which equals only a few defects on the whole quality area of a 6 inch mask blank. Therefore, a key challenge for EUV lithography is to develop essentially defect-free multilayer coated reflective mask blanks including adequate defect inspection metrology.

In support of EUVL mask blank development, defect inspection becomes a field of active research [3] [4] [5], as the development of defect free masks is largely dependent on the development of emerging mask blank defect metrology with high sensitivity. In order to ensure a reliable supply of defect-free mask blanks, it is necessary to develop techniques to detect and locate defects on unpatterned mask blanks. Visible or deep ultraviolet laser-based mask inspection tools were initially thought to be suitable for the inspection of EUVL mask blank in terms of their high throughput. However, those tools tend to have limited probing depth into the multilayer, and there is strong indication that non-actinic defect inspection tools may be inadequate for identifying all EUV defects, especially for those deeply buried and with low height [6].

At-wavelength inspection can provide useful information on the direct EUV response of defects and is highly desirable. Here we report on a new at-wavelength EUVL mask blank defect inspection approach, in which EUV PhotoElectron Emission Microscopy (PEEM) is used. In this approach, multilayers on mask blank substrates serve as a standing wave generator to illuminate the mask blank. Due to the small escape depth of photoelectrons of just a few nm in the EUV range, structures buried in a bulk sample normally cannot be accessed by PEEM measurements. However, in multilayer-coated mask blank, the incident wavefield propagates several 100 nm deep into the MoSi-multilayer down to the substrate interface and a standing wave field is formed as a superposition of incoming and outgoing wave. Wavefront distortions caused by defects result in a variation of the phase of the reflected wavefield and can thus be probed with a PEEM at the multilayer surface taking advantage of high photoelectron emission for surface regions being penetrated by standing wave antinodes and low photoelectron emission for wavefront nodes [7]. As a result, an image contrast is generated between the defect region and defect-free region on the multilayer mask blank surface. We will show that this method is very suitable for inspecting buried multilayer phase defects.

EXPERIMENTAL SETUP

A scetch of the EUV-PEEM instrument (Focus GmbH, Germany) is shown in Fig.1.

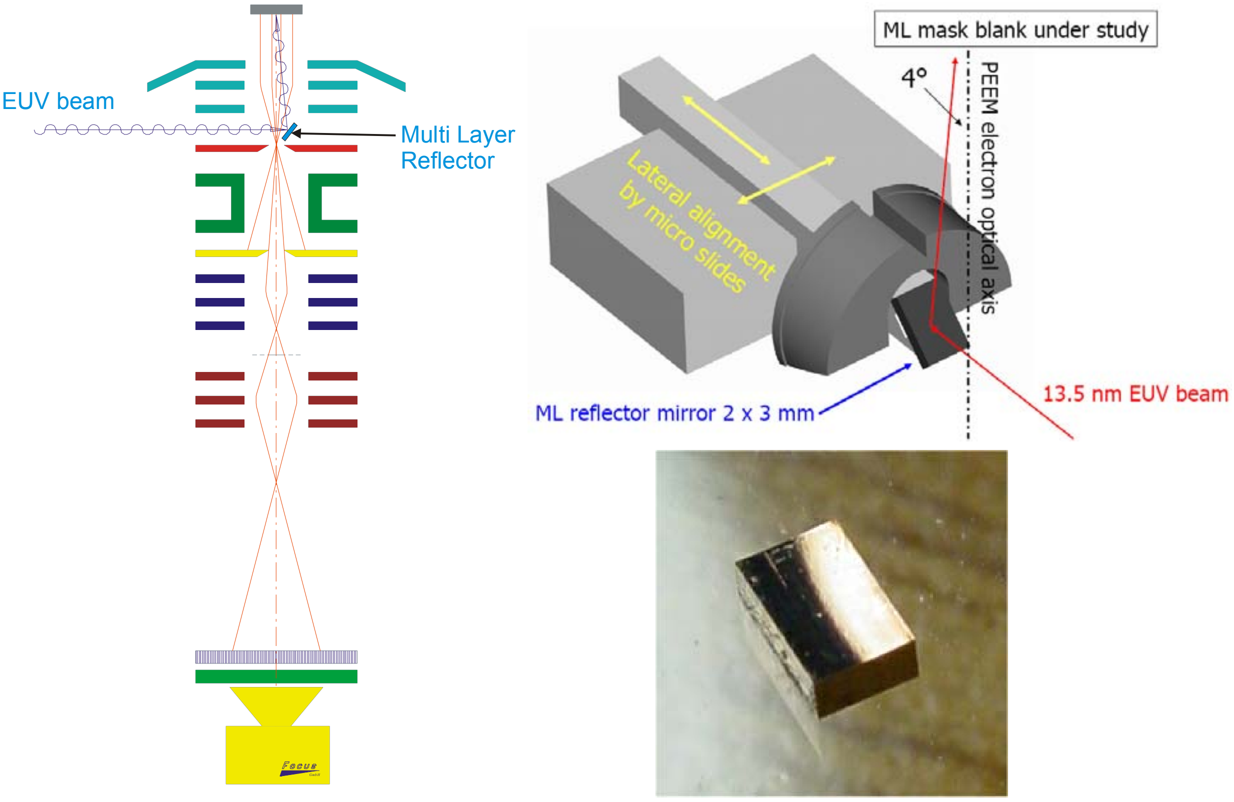

Fig. 1 : Scheme of the EUV PEEM (left) with multilayer-coated toroidal EUV microreflector (right)

The instrument consists of a piezodriven xy sample stage, an imaging electrostatic lens system and an image amplifier and acquisition assembly. Photoelectrons and secondary electrons emitted from the surface of a mask blank sample are projected onto a Micro Channel Plate (MCP) assembly for amplification and finally onto a fluorescent screen. A slow-scan Charge Couple Device (CCD) camera is connected to the fluorescent screen for recording the PEEM image. Compared to a conventional PEEM with a shallow incident angle for illuminating the sample (typ. 70 deg off-normal), the novelty of our PEEM instrumentation is that the mask blank sample is illuminated at near normal incidence with an EUV microreflector placed inside the electronoptical column close to the PEEM diffraction plane as shown in Fig.1.

To produce reliable inspection results, it is highly desirable to realize identical illumination conditions (in terms of wavelength and illumination angle) in the inspection tool as in the EUV lithography stepper later on. Therefore, a 2*3 mm^2 multilayer-coated microreflector was employed to direct the EUV beam at an angle of 4° off normal to illuminate the mask blank, which is similar to the mask illumination in EUV stepper.

In addition, a near normal incidence EUV wave resonantly illuminating near the Bragg wavelength at 13.5 nm wavelength is generating a strong standing wave field at multilayer surface. The field of view (FoV) of the PEEM can be adjusted from 2.3 µm to 1 mm within seconds. The spatial resolution of this instrument has been measured to be 29 nm (edge slope width, following a 16 % - 84 % criterion) using a 248 nm wavelength Hg discharge lamp source in the normal incidence illumination configuration [8]. During our initial experiments with this near normal incident illumination EUV-PEEM, a flat multilayer mirror was used as a microreflector to couple EUV light to illuminate the mask blank sample, and several minutes of acquisition time were required to obtain a clear EUV PEEM image with a field of view of about 100 micron [9]. This unsatisfactory long acquisition time was required due to the 1 mm large EUV focal size on the mask blank sample, which is much larger than the field of view of the PEEM (a typical value of about 100 micron) at high magnification. In order to increase the photon flux density on the sample, improvement was made to replace the flat multilayer mirror by a toroidal multilayer mirror. The toroidal mirror refocuses the EUV beam onto the sample generating a focal spot size matching the FoV of PEEM. By the help of this toroidal micro-reflector, the EUV beam focal size on surface of the sample was reduced to about 100 micron in diameter, and correspondingly the photon flux density was increased by 2 order of magnitude on the sample surface. As a result, with the same magnitude of incident photon flux, the EUV-PEEM image acquisition time was reduced down to sub-second.

The mask blank inspection experiments were carried out at two different undulator beamlines (linear undulator U125) at the 1.7GeV electron storage ring BESSY II in Berlin Germany. The beamline "U125-1/PGM" is equipped with a grazing incident plane grating monochromator, while the beamline U125-1/ML is utilizing a near-normal incidence multilayer monochromator. The wavelength can be tuned by changing the magnetic gap in the undulator and adjusting the monochromator accordingly. The available photon flux at 13.5 nm wavelenght (for both beamlines) in first undulator harmonics is about $2x10^{13}$ photon/s*100 mA*0.1%BW.

RESULTS AND DISCUSSION

Sensitivity to nanosized phase defect is required for a mask blank inspection tool aiming at 45 nm chip feature size and below. In order to check the ability to inspect phase defect on the scale of several tens of nanometers, a mask blank sample with programmed tiny defects of known size and location was prepared. The prepared defects are square and rectangle Titanium nanostructure (bumps) on a silicon substrate ranging in their lateral dimensions between 1 µm and 50 nm. The spacing between two neighbouring defects is about 6 micron in each direction. These lithographic structures with 50 nm height were fabricated by means of electron beam lithography and a lift-off technique. A 50 bilayer Mo/Si multilayer (each pair having a period of 6.8 nm) was deposited by Ion Beam Deposition to cover the structures. Fig.3 displays a PEEM image obtained from only illuminating a small part of the sample. The rectangular shaped defects shown in the bottom row from left to right are 300 x 50 nm^2, 200 x 50 nm^2, 100x50 nm^2 and 50nm x 50 nm^2 (not clearly shown up in this image) respectively. The rectangle shape defects in the rightmost column from up to down are 50x300 nm^2, 50x200 nm^2, 50x100 nm^2 respectively. The defects located in the diagonal line of the array from up-left to bottom-right are square defects with sizes of 300x300 nm^2, 200x200 nm^2 and 100x100 nm^2. The image in Fig.3 shows that defects with lateral sizes down to 50 nm width in both horizontal and vertical directions are clearly observed. The image contrast of these observable defects is between 20% to 30%. The programmed defect with a size of 50 x 50nm^2, which is supposed to be prepared on the substrate, does not clearly show up in this PEEM image. According to the measured 29 nm spatial resolution of our PEEM and the already observed 50 nm size in both horizontal and longitudinal directions, we should be able to observe this 50x50 nm defect in the PEEM image as well. Most probably, the 50nm * 50 nm defect was not fully developed during the lithography and lift-off process. However, there are indications of residuals at the position of the 50 *50 nm^2 programmed defect.

It is very interesting that we observed several random "real" defects with different sizes in the PEEM image of this programmed defect sample. Some of them appear in the PEEM image with a size even smaller than that of the observed programmed defect of 50 x 100 nm. one of the random defects, with a relatively large size in PEEM image, is clearly shown at the bottom of Fig.3. These real defects are quite likely to be the particulates contamination incurred in the process of mask blank sample fabrication or during the handing of the sample since these processes were conducted in a non-cleanroom environment.

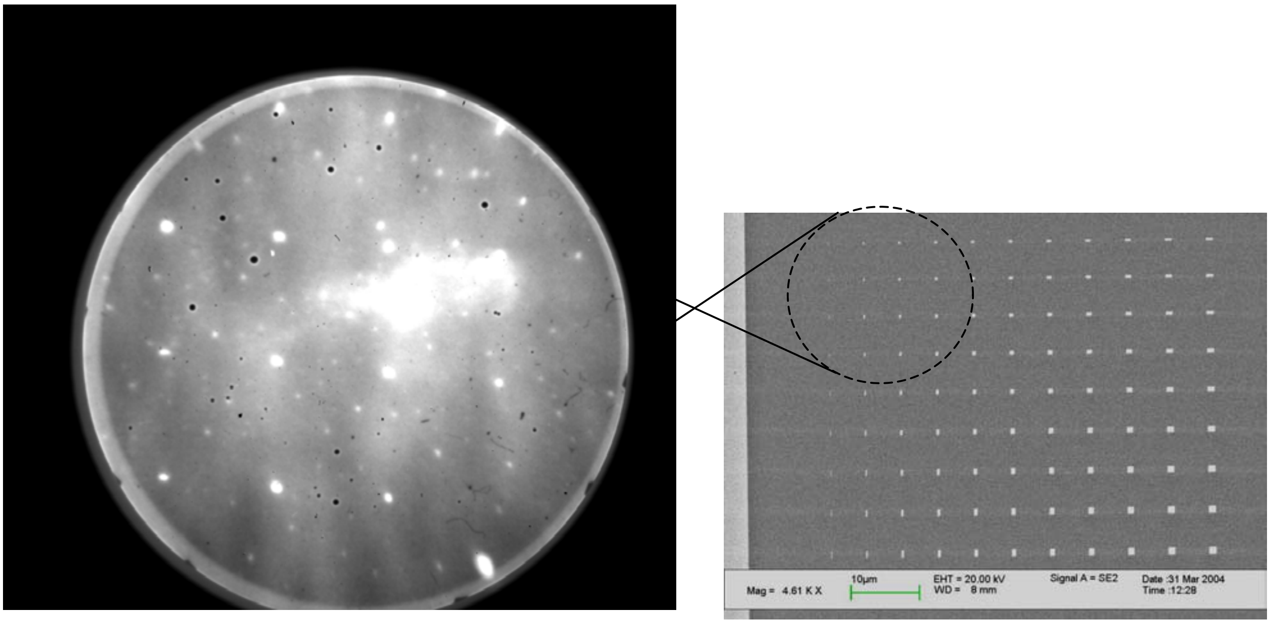

Fig. 3 : EUV-PEEM image (FoV 23 µm) of programmed multilayer phase defect sample (left) and corresponding SEM image of lithographic Ti nanostructures *before Mo/Si multilayer coating* (right)

SUMMARY AND OUTLOOK

We have performed at-wavelength inspection of EUVL mask blank defects by means of a novel near normal incidence standing wave illumination PEEM. This EUV-PEEM with standing wave illumination is especially suitable for the inspection of buried defects inside the multilayer stack due to the phase distortion of the reflective wave in the vicinity of a buried defect. With PEEM as an inspection tool, 50 nm sized defects in programmed defect EUV mask blank samples were detected in a rather large field of view (around 100 micron). Furthermore, by tuning the inspection wavelength, we found that the PEEM image contrast shows a strong wavelength dependence. In this respect, a very interesting observation is that PEEM image contrast at 13.10 nm is reverse to that at 13.55 nm. Moreover, some random defects, which were found in the programmed defect sample study process, show a contrast variation with changing the inspection wavelength, while others do not. By observing the wavelength dependence of the contrast of a defect, we can distinguish a phase defect from underneath multilayer from an amplitude defect at the multilayer surface. This may help to trace the origin of a native defect in a EUVL mask blank and correspondingly take further measures to improve the manufacturing process.

ACKNOWLEDGEMENT

This work is supported by the 6th Framework program of the European Union within the project ‘Exploring new limits to Moore’s law – More Moore’ (sub-project 3: Innovative Technologies for 22 nm node and beyond, work-package 4: Low defect mask blanks).
We are grateful to BESSY II, Berlin, Germany for the technical support and for providing excellent working conditions and would furthermore like to thank Etienne Quesnel from CEA-LETI for providing the line-space phase defect mask blank sample. The AFM characterization of the phase grating by Armin Brechling (Univ Bielefeld) is gratefully acknowledged. The fabrication of the lithographic phase defect structures was supported by M. Brzeska and H. Brueckl (University of Bielefeld).

REFERENCES

[1] P.Naulleau, K.Goldberg, E.Anderson et al. J. Vac. Sci. Technol. B21(4) Jul/Aug, 1286(2003)

[2] Sematech EUVL mask defect road map (2004)

[3] Y. Liu, A. Barty, E. M. Gullikson, J. S. Taylor, J. A. Liddle, O. Wood, Proc SPIE 5751 (2005) 660

[4] K.kinoshita, T.Haga, K.Hanamoto et al. J. Vac. Sci. Technol. B22(1) Jan/Feb, 264(2004)

[5] M.Yi, T.Haga,C.Walton, C.Larson and J.Borkor Jpn. J. Appl. Phys. Vol(41), 4101(2002)

[6] M. Park, M. Yi, P. Mirkarimi et al. J. Vac. Sci. Technol. B20(6) Nov/Dec, 3000(2002)

[7] German patent DE 100 32 979 A1 (2002)

[8]U. Neuhäusler, A. Oelsner, M. Schicketanz, J. Slieh, N. Weber, M. Brzeska, A. Wonisch, T. Westerwalbesloh, H. Brückl, M. Escher, M. Merkel, G. Schönhense, U. Kleineberg, U. Heinzmann, Applied Physics Letters (online 2006)

3D Micro X-ray Fluorescence Spectroscopy on Persian Tiles from the 19th century

Yvonne Höhn[1], Ioanna Mantouvalou[1], Wolfgang Malzer[1], Birgit Kanngießer[1]
Ina Reiche[2], Stefan Röhrs[2], Friederike Voigt[3]

[1] Institut für Atomare Physik und Fachdidaktik, Technische Universität Berlin, Berlin
[2] C2RMF Centre de Recherche et Restauration des Musées de France, Paris
[3] Institut für Asien- und Afrikawissenschaften, Humboldt-Universität zu Berlin, Berlin

Introduction

In the frame of a German French interdisciplinary project Persian tiles from the 19th century of the Qajar period are investigated with the help of non-destructive analytical methods. The Persian tiles, which are conserved in museums in Berlin, Edinburgh, London, and Paris, are analyzed with respect to the material employed, the manufacturing process, and decoration techniques. Up to now only scarce information is available on special 19th century decoration techniques. The main aim is the creation of a broad data basis collected with various analytical methods in order to assign these objects to known manufacturing centers.

An important method for this research program is the 3D micro X-ray fluorescence spectroscopy (3D micro-XRS), with which depth resolved X-ray fluorescence analysis (XRF) and X-ray absorption near edge structure spectroscopy (XANES) is possible. First measurements already showed that the method facilitates investigation on elemental distribution and chemical speciation at the same site in a certain depth. Various XANES-spectra at different sites in the depth around the Cu K-edge were measured to get new insight into the chemical binding of Cu in the transition layer between the glaze and the pigment layer. However, the evaluation of such kind of spectra is not straight forward. XANES-spectra collected in a certain depth are a product of transmission- and fluorescence-XANES spectra, which prevents the application of common evaluation strategies in XANES investigation.

Therefore, a systematic investigation has been carried out on self-prepared standards with varying thickness and varying concentration during this beam time in November 2005. The evaluation of the depth resolved XANES spectra of known standards may help to establish a procedure for analyzing such XANES spectra measured on the Persian tiles and for other applications.

Experimental Set-up

The 3D micro-XRF is realized by a confocal arrangement, which consists of X-ray optics in the excitation as well as in the detection channel. A probing-volume is defined by the overlap of both foci of the X-ray optics. If the sample is moved through this probing-volume, its chemical composition can be non-destructively investigated not only laterally along the surface but also within the sample at the depth of interest [1]. If the excitation energy is varied around an absorption edge, chemical speciation at the same spot in the sample is also possible.

The 3D micro-XRS was built up at the BAMline located at a 7T wavelength shifter at BESSY. To create the probing-volume we used a polycapillary halflens with a focus of about 30 μm (at 18 keV) at a working distance of 16 mm in the excitation channel. In the detection channel a polycapillary conical collimator was adjusted directly on the snout of the Si(Li) detector. The focus of this polycapillary conical collimator has a FWHM of 20 μm (at 10 keV) at a working distance of 1.2 mm. The "standard" micro-XRF measurements were realized by removing the X-ray optic from the detection channel.

The characterization of the confocal arrangement was carried out with the help of a thin Cu-foil which was scanned through the micro-volume. The FWHM of the Cu intensity-curve excited at 9 keV is about 40 μm, which can be regarded as the spatial resolution of the set-up.

Measurements

All measurements were carried out with excitation energy of about 9 keV. From the Ethnological Museum in Berlin two Persian tiles were investigated with 3D micro-XRS (3D micro-XRF and micro-XANES) and with micro-XRF. For validation of the evaluation of the Persian tiles spectra depth scans and XANES measurements at various points in the depth were obtained of self prepared, synthetic glazes. In addition, measurements were carried out on self prepared pigment containing samples: two single layers made out of $CuCO_3$ and Cu_2O, and on double layers with the $CuCO_3$- and the Cu_2O-layers in changing sequential order and with various concentrations of Cu. The last series of measurements was performed on pigment layers with various concentrations of $CuCO_3$ and Cu_2O. The investigation has the intended purpose to obtain a data set of Cu oxide XANES spectra showing varying distortion due to absorption. The comparison with measurements of the Persian tiles will provide a better interpretation. Furthermore, this will be the first step for a absorption correction algorithm of the XANES spectra in the depth. In order to calibrate the confocal setup one reference glass standard was measured, additionally.

As an example, figure 1 shows at the left hand side a depth scan of a $CuCO_3$ layer enriched with Co on a Cu_2O layer. The counts of the net peak areas of the respective elements are plotted in dependence of the relative depth position. The depth scan was carried out with a step width of 10 μm and a live time of 20 s at each point. At the various depths numbered XANES-spectra at the Cu K-edge were measured. These XANES-spectra obtained are shown on the left hand side of figure 1. The energy was varied between 8.95 keV and 9.12 keV with a step width of 2 eV. Live time per energy step was 40 s for points 1 and 2, 50 s for point 3, and 90 s for point 4, respectively.
The change of the XANES-spectra with depth is obvious. The shape of the spectra at depth positions 1 and 2 is quite similar to the one of a $CuCO_3$ single layer. At depth position 3 the spectrum is coming from the transition zone of the $CuCO_3$ and the Cu_2O layer. At depth position 4 the probing volume is completely located in the Cu_2O layer. Nevertheless, the shape of this spectrum does not resemble to the one of a Cu_2O single layer. This is due to the absorption of the exciting and fluorescence radiation from the upper layer. XANES spectra taken at deeper layers may be regarded as product of a transmission and an fluorescence spectrum. The deeper the probing volume from which a XANES spectrum is recorded the more pronounced is this effect. For comparison figure 2 shows Cu K-edge XANES spectra obtained at the surface of a $CuCO_3$ and of a Cu_2O single layer, of a pure Cu foil, and of a Cu containing synthetic glaze, respectively. The shape of the XANES spectrum of the Cu_2O single layer is very different to the one in figure 1. The spectra were taken in the same energy range as for figure 1, but with a lifetime of 20 s per point.

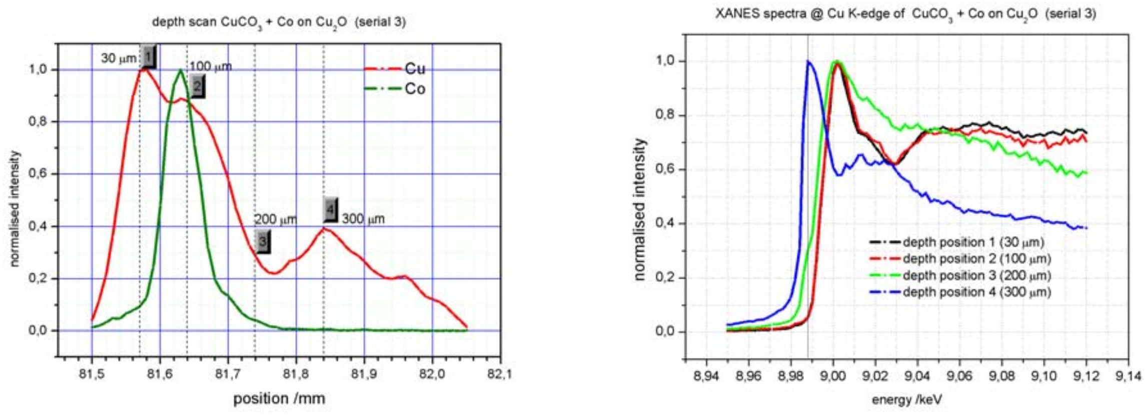

Figure 1: Depth scan of a double layer of $CuCO_3$ on Cu_2O (left hand side). At the depth positions indicated Cu K-edge XANES spectra were measured (right hand side).

The absorption effect for XANES measurements in the depth may be clarified by the measurements carried out at a simple sandwich sample consisting of a 2 μm thick Cu foil as top layer, a 10 μm thick Cu foil as bottom layer, and a 100 μm thick paper layer in between. Figure 3 shows in the upper part the Cu K-edge XANES spectra obtained in the top and in the bottom layer, respectively. The distorted XANES spectrum from the bottom layer could be reproduced as a product of the XANES spectrum obtained in the top layer (fluorescence spectrum) with the transmission function of the Cu top layer. The transmission is calculated using the fluorescence spectrum measured and the Lambert Beer law. The absorbance of the paper layer can be neglected for that energy. The shape of the measured XANES spectrum from the bottom layer can be reproduced by this calculation. However, the fitting of a considerable number of free parameters was necessary, because the calibration has yet not been introduced.

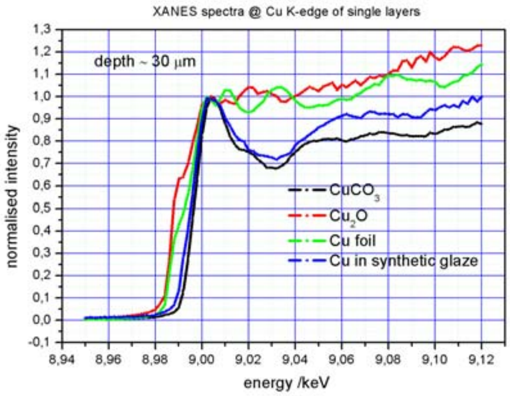

Figure 2: Cu K-edge XANES spectra of various single layers taken in the surface.

Figure 3: Interpretation of depth sensitive XANES

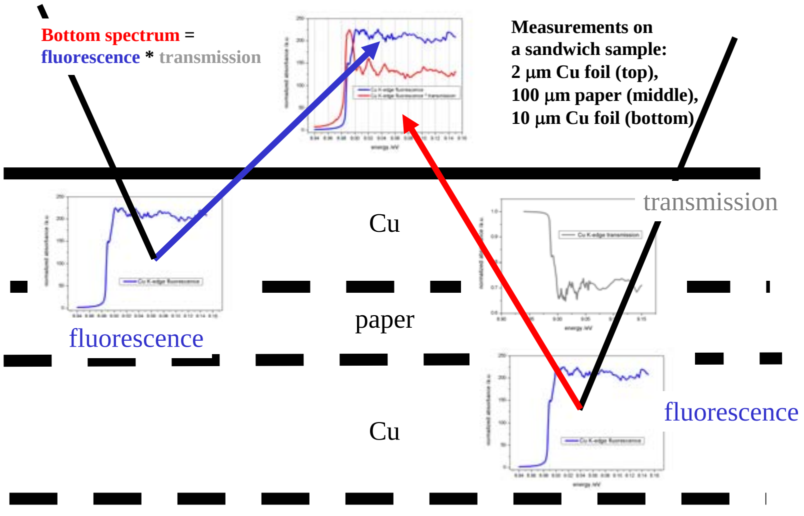

Conclusions

The examples shown above demonstrate the need for a new absorption correction algorithm to evaluate depth sensitive XANES measurements. The complete evaluation of the various XANES spectra obtained from the self-prepared standards and glazes will give an access to the simulation and reconstruction of depth sensitive XANES spectra. Herewith, it will be possible to interpret the spectra obtained from the Persian tiles.

References
[1] B. Kanngießer, W. Malzer, I. Reiche, Nucl. Instr. Meth. B 211/2, 259-264 (2003).
[2] B. Kanngießer, W. Malzer, I. Reiche, BESSY-Highlights 2002 – Scientific Highlights (2003).
[3] F. Voigt, Qadscharische Bildfliesen im Ethnologischen Museum in Berlin, Staatliche Museen zu Berlin Preussischer Kulturbesitz Berlin (2002).

3D Micro X-ray Fluorescence Spectroscopy
Validation of a three-dimensional model of the sensitivity for quantification

Ioanna Mantouvalou, Yvonne Höhn, Wolfgang Malzer, Birgit Kanngießer

Institut für Atomare Physik und Fachdidaktik, Technische Universität Berlin, Berlin

Introduction

3D Micro X-ray fluorescence spectroscopy (3D Micro-XRS) is a new analytical method that enables non-destructive, three dimensionally resolved measurements of elemental distribution and chemical speciation of samples. The method is realized with a confocal setup of two X-ray optics [1]. For the quantitative evaluation of 3D Micro-XRF we developed a model of the spatial distribution of the sensitivity of the probing volume defined by the two X-ray optics [2]. The spatial sensitivity distribution characterizes the confocal setup and can be ascribed to the characteristics of the X-ray optics. It replaces the calibration constant for conventional XRF setups as a position dependent quantity. A theoretical correlation between the confocal setup characterized in such a way and count rates measured has also been developed. Figure 1 illustrates the ellipsoidal shape of the isosurface of the sensitivity of the probing volume. The surface is shown where the sensitivity dropped to half of its maximum. Detector and beam axis are perpendicular to each other. The integral sensitivity $\tilde{\eta}$ for this geometry (equation 1) is expressed by the transmission (T_A, T_D) and the characteristic width of the flux density (σ_A, σ_D) of the X-ray optics and the solid angle (Ω) and the quantum efficiency of the detector (ε) of the detection channel (equation 1). The width of the sensitivity profile σ_y presents the other characteristic parameter for the description of the probing volume, where Ψ is the angle between angle between the normal on the sample surface and the beam axis (equation 2).

$$\tilde{\eta} = \frac{T_A T_D \Omega \varepsilon}{4\pi} \frac{\sigma_D^2}{\sqrt{\sigma_A^2 + \sigma_D^2}} \qquad (1)$$

Equation 1: Integral sensitivity function.

$$\sigma_y = \sqrt{\sigma_A^2 \sin^2 \Psi + \sigma_D^2 \cos^2 \Psi} \qquad (2)$$

Equation 2: Width of the sensitivity profile.

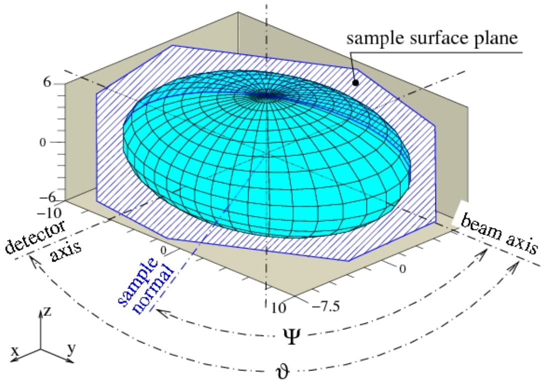

Figure 1: Sketch of the ellipsoidal shape of the isosurface of the sensitivity. The surface marks half of the maximum sensitivity. Detector and beam axis are perpendicular to each other.

With these two characteristic parameters $\tilde{\eta}$ and σ_y an expression can be derived for intensity depth profiles of characteristic fluorescence lines (see equation 3). Such a kind of parameterized model shows various advantages: a fast and straightforward characterizing of the probing volume becomes possible, a selective optimization of the setup is feasible, and it constitutes the foundation of quantification procedures.
With the measurements described below an experimental validation of this model has been carried out. The performance of the model and its use for a calibration procedure is tested.

Experimental Set-up

The 3D micro-XRS was built up at the BAMline located at a 7T wavelength shifter at BESSY. To create the probing-volume we used a polycapillary halflens with a focal width of about 30 μm (at 18 keV) at a working distance of 16 mm in the excitation channel. In the detection channel a polycapillary halflens was adjusted directly on the snout of the Si(Li) detector. The focus of this polycapillary halflens has a FWHM of 20 μm (at 18 keV) at a working distance of 6.8 mm.

For the characterization procedure we used two Breitländer reference glass standards (BRB2, BRA3).

Measurements

All measurements were carried out with excitation energy of 18 keV. The two standards were moved through the probing volume with step widths' of 10 μm, and of 3 μm in the maximum of the intensity profiles. At each step spectra were taken with a life time of 100 s. This series of measurements was carried out for three different angles Ψ (45°, 60.3°, and 32.3°), describing the angle between the normal on the sample surface and the beam axis.

For the three series of measurements depth intensity profiles were obtained for the Kα fluorescence lines of the elements K, Ca, Ti, Cr, Mn, Fe, Co, Ni, Cu, Zn, and Ge, and for the Lα fluorescence lines of the elements Te, Ba, Ta, W, and Pb. Each intensity depth profile was fitted with equation 3 with $\tilde{\eta}$ and σ_y as free parameters. As an example, figure 2 shows the fit of the depth intensity profile of the Ca Kα fluorescence line.

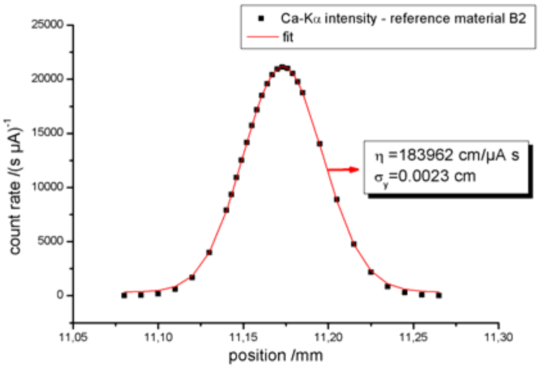

$$\Phi(y)=\frac{\Phi_0\tilde{\eta}\sigma_F\rho_i}{2}e^{\frac{(\mu_{lin}\sigma_y)^2-2\mu_{lin}y}{2}}\times\left[1-erf\left(\frac{\mu_{lin}\sigma_y^2-y}{\sqrt{2}\sigma_y}\right)\right] \qquad (3)$$

Equation 3: Function for the depth intensity profile with $\tilde{\eta}$ and σ_y as the characteristic parameters for the probing volume. All other parameters are constant.

Figure 2: Fit for the depth intensity profile of Ca Kα fluorescence line.

Figure 3 shows the integral sensitivity $\tilde{\eta}$ for elements in reference material B2 (Ca, Te, Ti, Mn, Fe, Co, Ni, Cu, Ta, W, Zn, and Pb) scanned with an angle Ψ of 45°. The integral sensitivities for the various elements have been obtained in the same manner as described for the Ca Kα fluorescence line (see figure 1). The energy dependence of the integral sensitivity is due to the energy dependence of the critical angle for total reflection in the polycapillary optics. Within an uncertainty of around 10 % all the values for Kα fluorescence lines fit well to the fit function derived from the model for the spatial distribution of the sensitivity of the probing volume. In contrast, the values for the Lα fluorescence lines (Te, Ta, W, Pb) exceed partially the uncertainty of 10 %.

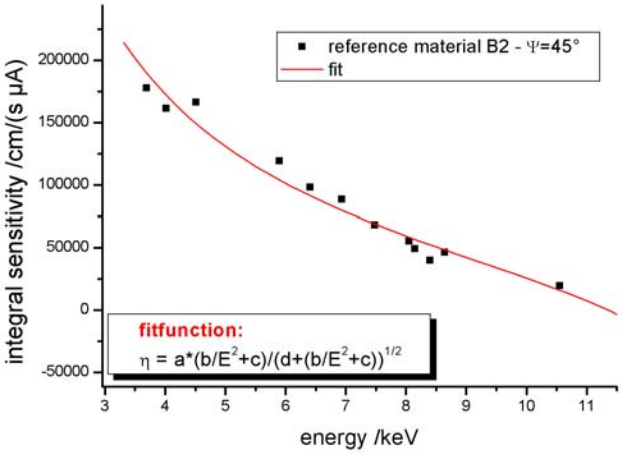

Figure 3: Integral sensitivity $\tilde{\eta}$ for elements in reference material B2 for a scanning angle of 45°

The same holds for the widths' of the sensitivity profile σ_y for the various elements evaluated. Figure 4 shows σ_y for the elements evaluated of the reference material B2 for three different scanning angles (Ψ). Similar satisfying results have been obtained for the second reference material.

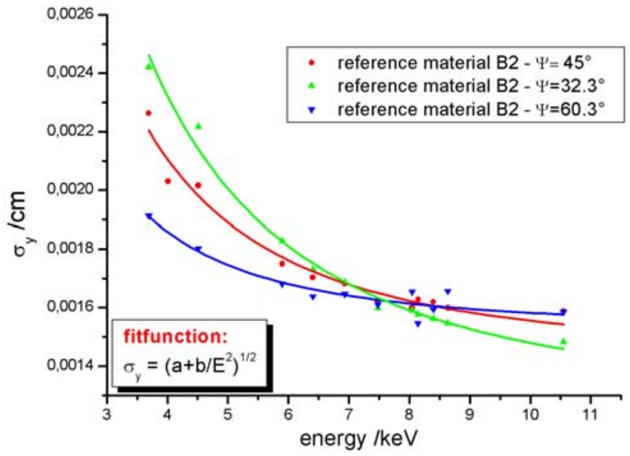

Figure 4: Width of the sensitivity profile σ_y for the elements evaluated of the reference material B2 for three different scanning angles (Ψ).

Conclusions

The evaluation of the measurements carried out on two reference materials corroborates the model developed for the spatial distribution of the sensitivity of the probing volume defined by two X-ray optics. The angular dependence of the width of the sensitivity profile approves the concept of isosurfaces of the three dimensional sensitivity. The energy dependence of the integral sensitivity and the width of the sensitivity profile are modeled adequately. The higher uncertainties for the L fluorescence lines have to be investigated.

Furthermore, the evaluation corroborates the possibility of calibrating the confocal setup with thick multi-element reference material. Thus, a tedious calibration procedure with specific thin reference materials becomes obsolete. Thick multi-element standards to be considered for a calibration procedure should have elemental concentrations in the per mill to per cent region, other wise the calibration becomes too inefficient.

The last step of the validation of our three dimensional sensitivity model will be the comparison of the FWHM of the X-ray optics' foci derived from the model with FWHM determined by measurements. These measurements to determine the FWHM of the foci have still to be carried out.

References

[1] B. Kanngießer, W. Malzer, I. Reiche, Nucl. Instr. Meth. B 211/2, 259-264 (2003).
[2] W. Malzer, B. Kanngießer, Spectrochim. Acta, Part B 60 (2005), 1334-1341.

Time- and layer-resolved magnetization dynamics in magnetic multilayered systems

J. Miguel[1], B. Heitkamp[2], D. Bayer[3], K. Fukumoto[1], L. Heyne[2], N. Höfer[2], J. Sanchez-Barriga[2], M. Bernien[1], H. Dürr[2], W. Kuch[1], M. Aeschlimann[3]

1 Freie Universität Berlin, Institut für Experimentalphysik, Arnimallee 14,
14195 Berlin, Germany
2 BESSY GmbH, Albert-Einstein-Straße 15, 12489 Berlin, Germany
3 University of Kaiserslautern, Department of Physics, 67663 Kaiserslautern, Germany

(BMBF Nr. 05 KS4UK1/4)

A very large amount of the latest ultra-small information recording technology is based on magnetic random access media devices, with the key feature of the non-volatility of the stored information. These devices generally comprise a stack of two thin magnetic layers separated by a non-magnetic spacer. For a fast operation, the magnetization direction of one of the magnetic layers has to be reversed with maximum speed, e.g. by applying a current pulse in an underlying strip line. A fundamental understanding of the processes occurring during the fast magnetization reversal in coupled multilayered magnetic systems is indispensable for achieving optimum operation speed of such devices.

With the aim of studying the magnetization reversal processes of multilayered magnetic microstructures at fast time scales, we have to set up a time- and spatially-resolved experiment using photoelectron emission microscopy (PEEM) with x-ray magnetic circular dichroism (XMCD) as magnetic contrast mechanism [1, 2]. This technique provides both the layer selectivity and the necessary spatial information, with a maximum resolution of about 100 nm. In the time-resolved variant (TR-PEEM), it is thus possible to correlate the transient magnetic domain patterns of the different ferromagnetic layers. Magnetic field pulses are achieved by using fs laser pulses that trigger current pulses in a lithographic strip line by means of a photoconductive switch [3, 4]. The current pulse thus produced travels along a Au strip line creating a magnetic field at the position of the multilayered magnetic microstructure.

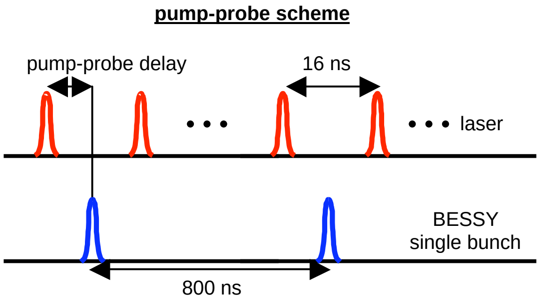

Figure 1. Schematics of the laser pump–synchrotron probe setup.

Magnetization dynamics is detected by a laser pump-, synchrotron probe scheme. The time between two subsequent pulses of the fs laser is set to 16 ns, which are phase-locked to the BESSY single bunch with a period of 800 ns. So every 50th laser pulse acts as pump pulse to trigger the dynamics. Changing the phase between laser and synchrotron allows studying their temporal evolution (Fig. 1). The measurements are carried out in a stroboscopic fashion averaging over millions of pulses at a fixed delay time between laser pulse and the synchrotron x-ray pulse. The time resolution is determined by the x-ray bunch length of approximately 50 ps, and the jitter of the electronics.

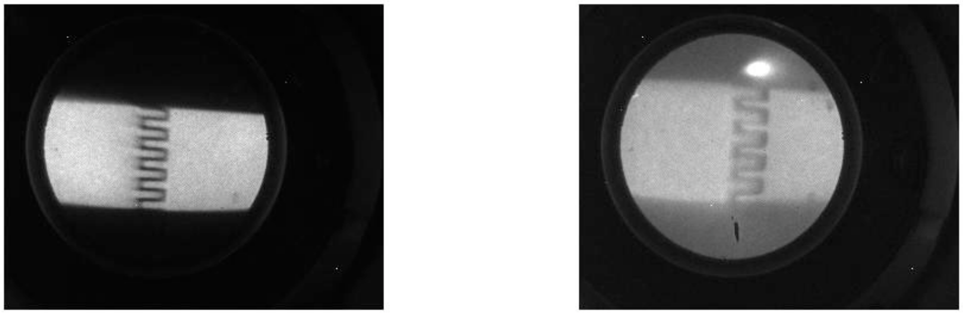

Figure 2. PEEM images of the photoconductive switch (left)
and of the switch together with the laser spot (right).

Coplanar waveguide structures consisting of 20 nm Cr and 100 nm Au on top of a low temperature GaAs substrate were produced by a photolithographic lift-off process in the Nano+Bio Center at the University of Kaiserslautern. The switching area is about 15 µm x 100 µm and consists of 10 fingers (5 µm width, 10 µm length, 5 µm distance). Lithographic laterally microstructured Co/Cu/$Fe_{20}Ni_{80}$ heterostructures were deposited on the Au strip line, which at the sample position is narrowed down to 15 µm.

A PEEM image of the photoconductive switch is shown in Fig. 2. Using a lens inside of the ultrahigh vacuum system, the laser spot could be focused down to a size smaller than ~ 20 µm. Fig. 2 (right) shows the photoconductive switch together with the laser spot (moved out of the photoconductive switch for better visibility), which can be seen by multiphoton photoemission induced by the laserpulse.

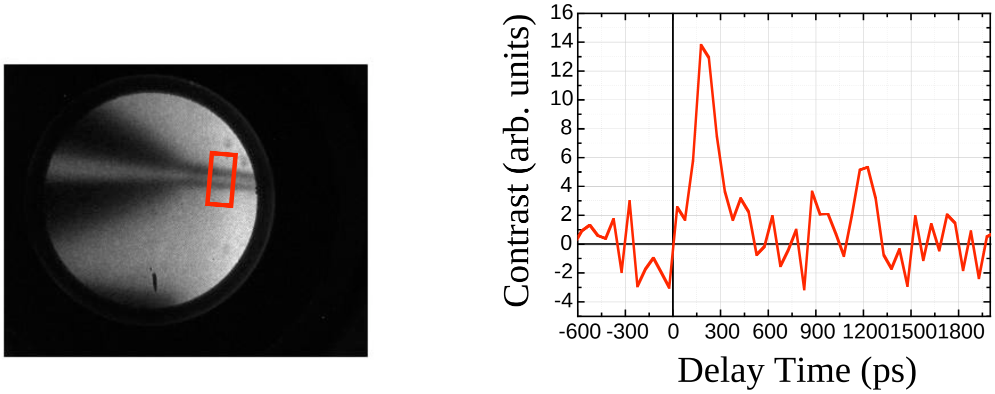

Figure 3. Left: PEEM image of the strip line taken during the laser pulse. Right: temporal evolution of the contrast of the area enclosed by the red rectangle in the left panel, representing the temporal evolution of the magnetic field pulse.

In order to test the synchronization between the BESSY x-ray pulse and the fs laser pulse, we used PEEM images of the strip line taken during the laser pulse as shown in the left panel of Fig. 3. The switch is localized left of the field of view. The current pulse induces a transient image distortion in the PEEM image of the strip line due to its electric and magnetic fields. This can be followed as a change of contrast between the strip line and the ground pads. The temporal evolution of the contrast in the area enclosed by the red rectangle is shown in the right panel. The magnetic pulse is characterized by an initial rise time of 150 ps and a decay time of about 200 ps. Taking into account the dimensions of the strip line and the distance to the FeNi layer, a peak field of 8 Oe at the magnetic microstructure position is calculated. The laser pulse thus creates a magnetic pulse with a rise time of about 150 ps and a total width of 350 ps. With a voltage difference of 50 V, the average current in the strip line is 650 µA.

Different magnetic microstructures were grown onto the strip line, and characterized by XMCD-PEEM. Fig. 4 shows two different magnetic domain patterns in a 10×10 μm^2 $Fe_{20}Ni_{80}$ microstructure on top of the stripline, obtained by subtracting the two PEEM images acquired with left and right circularly polarized x-rays under static conditions.

In the coming experiments we aim at combining these three results in order to study the magnetic response of the soft magnetic layer in a trilayered structure under ultrafast magnetic pulses as a function of the domain configuration of the hard magnetic layer.

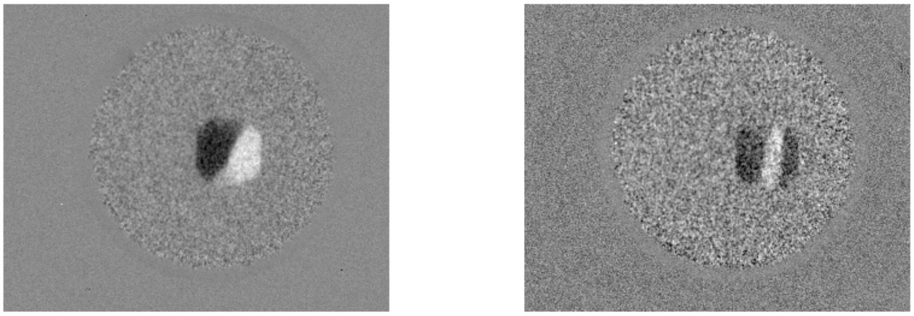

Figure 4. Magnetic domains present in square $Fe_{20}Ni_{80}$ magnetic microstructures grown onto the strip line, as seen by XMCD-PEEM.

References

[1] J. Stöhr, Y. Wu, B. D. Hermsmeier, M. G. Samant, G. R. Harp, S. Koranda, D. Dunham, and B. P. Tonner, Science **259**, 658 (1993).

[2] W. Kuch, Appl. Phys. A **76**, 665 (2003).

[3] D. H. Auston, APL **26**, 101 (1974).

[4] Th. Gerrits, H. A. M. van den Berg, J. Hohlfeld, L. Bär, and Th. Rasing, Nature **418**, 509 (2002).

Characterization of the performance of a shallow blaze angle grating for the 0.4-6 keV range

D. Cocco, A. Bianco
Sincrotrone Trieste ScpA, S.S.14-Km 163.5, 34012, Trieste, Italy
F. Schaefers, M. Mertin, G. Reichardt
BESSY GmbH, Albert-Einstein-Str. 15, D-12489, Berlin, Germany.
B. Nelles, K. F. Heidemann
Carl Zeiss Laser Optics, Carl-Zeiss-Str.22, 73446 Oberkochen, Germany

In these years there has been an increasing interest in developing optical devices able to monochromatize synchrotron radiation in a wide photon energy range, from the soft up to the hard X-ray region, as an alternative to expensive and mechanically complicated instruments such as interchangeable grating/crystal monochromators. The solution chosen for the Twin Mic beamline [1,2] at Elettra, the Italian 3rd generation synchrotron radiation source, is a blazed diffraction grating with a shallow blaze angle of 0.4°, which can be operated at on-blaze condition. This grating will provide monochromatized radiation from 0.4 to 4 keV, which is the desired working range for the twin X-ray microscope served by this beamline. The very shallow blaze angle allows reaching the high energy range where very grazing incidence angles are necessary. The grating has 600 grooves/mm, which is a good compromise to have the requested energy resolving power (of the order of 4000 in most of the range) and to have as much flux as possible, mandatory for the proposed experiments. The grating was manufactured at Carl Zeiss Laser Optics on a silicon substrate of dimensions 100 mm x 20 mm x 30 mm and then coated with a 30 nm thick gold layer. The grating pattern with a groove density of 600 l/mm and a blaze angle of 5.6° was mechanically ruled by the Zeiss ruling engine GTM6, operating under interferometric control, over a gold layer evaporated onto the silicon substrate surface. A blaze angle reduction to 0.4° was obtained by reactive $Ar^+ + O^+$ ion beam etching, a technique [3] which exploits the significant higher $Ar^+ + O^+$ ion beam etching rate of gold in comparison with that of silicon. This effect is used to reduce the blaze angle by transferring the groove pattern from the gold ruling layer into the silicon substrate. In addition to the blaze angle reduction, this technique reduces the micro roughness on the blaze facets: the 0.9 nm rms micro roughness of the mechanically ruled grating decreased to 0.3 nm rms.

To test the performance of this grating, efficiency measurements were carried out at the BESSY bending magnet beamline KMC-1. This beamline is particularly suitable for this kind of measurements because has a double crystal monochromator that can go down to 1.7 keV and can be equipped with a high-precision reflectometer. The grating was mounted in the reflectometer so that the radiation was incident on the center of the ruled area and the groove facets with the 0.4° blaze angle faced the incident beam. The incident beam was approximately 0.5 mm in diameter and a slit of angular width 0.4 mrad covered the photodiode detector. The efficiency of the grating was measured at fixed incident angle, whereas the detector was rotated to scan the various diffraction orders. The measurement was repeated at different incident angles and several photon energies between 1700 and 6000 eV. The measured efficiencies for the zero and first internal order as functions of the incidence angle at different fixed photon energies are shown in figure 1 (top) and summarized in table 1. Figure 1 (bottom) illustrates the same set of data as a function of the incidence photon energy at different fixed incidence angles. The obtained results demonstrate that this grating can work up to 6 keV with still enough efficiency (5% at 6keV and 11% at 1.8 keV). The efficiency in the lower part of the energy range was tested at Elettra, again with very good results (more then 20% at 950 eV and 15% at 600eV).

Photon energy (eV)	Measured efficiency (%)	Incidence angle (°)
1700	11.4	1.2
1800	11.1	1.1
2000	10.1	0.8
2500	6.7	0.8
3000	7.9	0.6
3500	7.6	0.6
4000	7.2	0.6
5000	5.9	0.6
6000	5	0.6

Table 1. Measured maximum efficiency of the blazed grating for the first internal order at different photon energies in the 1.7-6 keV range.

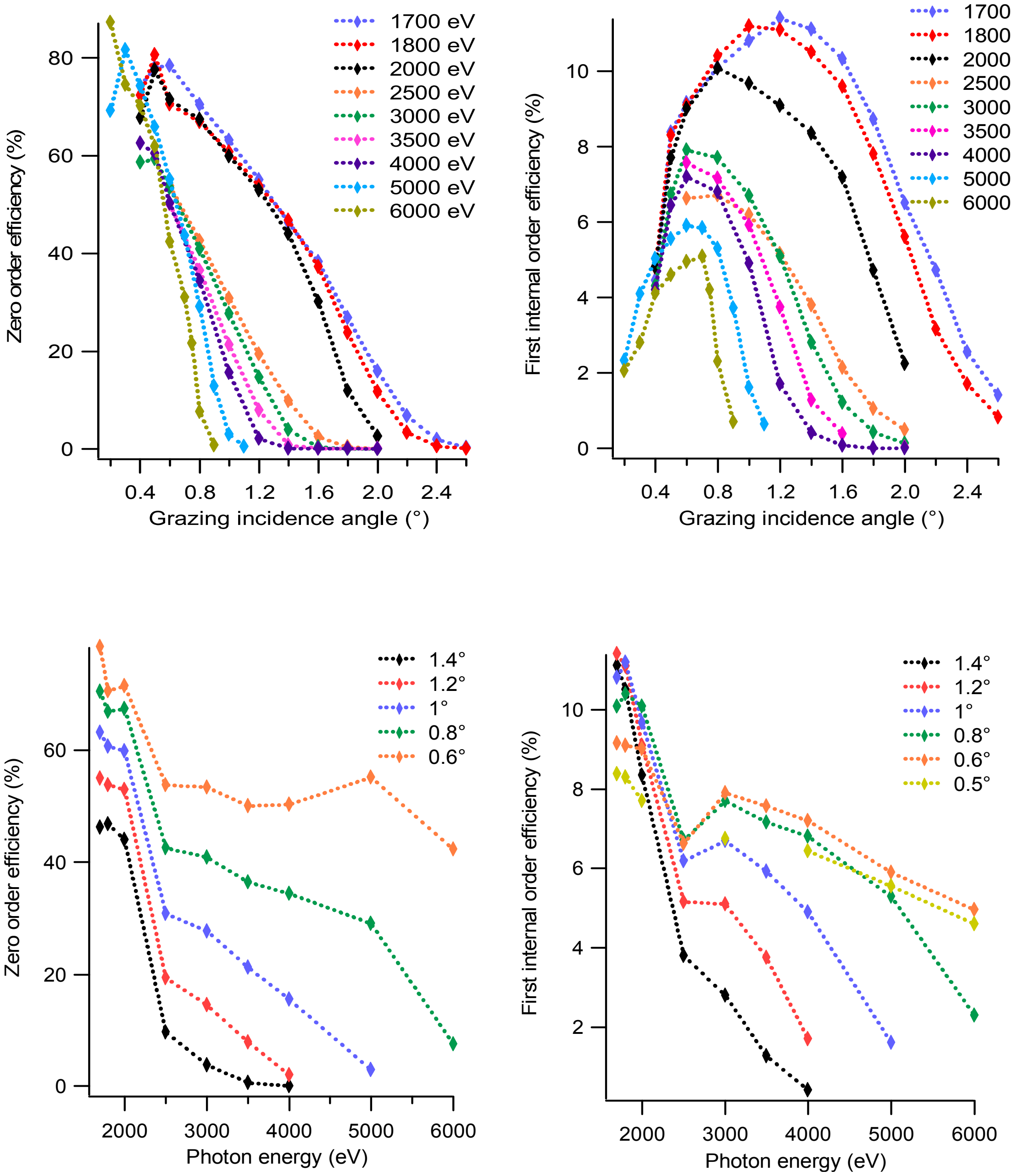

Figure 1. Measured efficiency curves of the blazed grating for the zero order (left) and the first internal order (right) as a function of the incidence angle at different fixed photon energies (top) and as a function of the photon energy at different fixed incidence angles (bottom).

This work was supported through the EC under IA-SFS Contract RII 3-CT-2004-506008.

References

[1] B. Kaulich et al., "TwinMic - A European X-ray spectromicroscopy station", XRM2005 conference (Himeji, Japan), to be published in JPAP.

[2] B. Kaulich, D.Bacescu, D.Cocco, J.Susini, M.Salome', O.Dhez, C.David, T.Weitkamp, E.Di Fabrizio, S.Cabrini, G.Morrison, P.Charalambous, J.Thieme, T.Wilhein, J.Kovac, M.Podnar and M.Kiskinova, "Twinmic: A European twin microscope station combining full-field imaging and scanning microscopy", J.Phys. IV 104, pp.103-107, 2003.

[3] A.Bianco,G.Sostero,B.Nelles,K.F.Heidemann,D.Cocco, "A plane grating with single-layer coating for the sub-nanometer wavelength range", Proc. of SPIE vol. 5918, San Diego, CA, 2005.

A new portable UHV goniometer for soft X-ray resonant scattering

Y. Su, H.F. Li, B. Schmitz, P. Hiller, C.M. Schneider and Th. Brueckel

Institut fuer Festkoerperforschung (IFF), Forschungszentrum Juelich, D-52425 Juelich, Germany

Soft X-ray resonant scattering has been emerging as a powerful method to investigate complex charge, orbital and spin ordering phenomena in strongly correlated electron systems [1-3]. Naturally, there is a surge of demand for beamtime at worldwide synchrotron radiation sources. The construction and then successful operation of the ALICE diffractomter [4] at BESSY-II, one of the most brilliant soft X-ray sources in the world has brought the German community with a unique opportunity in this field. However, most available soft X-ray diffractomters are more-or-less two-circle ones, including ALICE, which means that the possibilities to *in-situ* manipulate the samples, i.e. tilting (χ-circle) and rotating around the surface normal (φ-circle) are severely limited. Therefore, a precise pre-alignment on all samples to be measured even before the starting of the experiment becomes especially crucial. Even such a perfect pre-alignment is possible, any small mis-orientations that often appear up later due to the cooling of the sample or certain intrinsic structure phase transitions may still easily ruin your efforts. To overcome this limitation, a new portable goniometer consisting of two piezo-driven high-precision positioners has been built and successfully tested with the ALICE diffractometer, as shown in Fig. 1. In particular, this goniometer is fully compatible with UHV and various sample environments such as low-temperature and high magnetic field. This new option available to the ALICE diffractometer has dramatically increased the efficiency of measuring single-crystal samples of complex oxides by resonant soft X-ray scattering. In addition, it also becomes possible to measure so-called azimuthal-angle dependence, i.e. the sample rotation around the moment transfer in a scattering process.

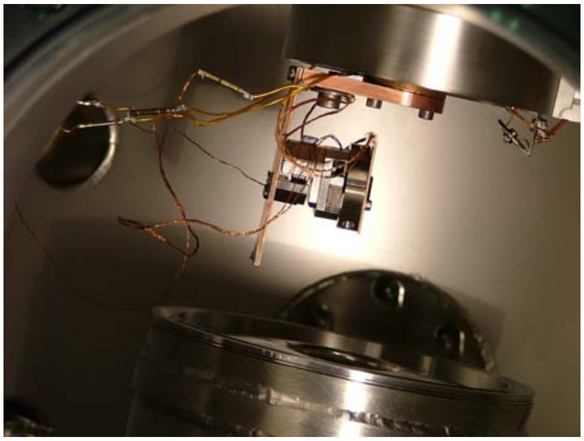

Fig. 1 A new portable UHV/Low-T goniometer in the ALICE chamber

Acknowledgements

We would like to thank Dr. Alexei Nefedov and Prof. Dr. Hartmut Zabel for their cooperation to realize this goniometer in ALICE diffractometer.

References

[1] S.B. Wilkins, *et al.*, Phys. Rev. Lett. **90**, 187201 (2003)
[2] P. Abbamonte, *et al.*, Nature **431**, 1078 (2004)
[3] S.B. Wilkins, *et al.*, Phys. Rev. Lett. **91**, 167205 (2003)
[4] J. Grabis, A. Nefedov and H. Zabel, Rev. Sci. Instr. **74**, 4048 (2003)

Study of organic matter in soils using image stacks taken with the STXM at U41

J. Thieme[1], G. Mitrea[1], S.-C. Gleber[1], P. Guttmann[2], S. Heim[3]

[1]Institut für Röntgenphysik, Georg-August-Universität Göttingen,
Friedrich-Hund-Platz 1, D-37077 Göttingen

[2]Institut für Röntgenphysik, Georg-August-Universität Göttingen,
c/o BESSY GmbH, Albert-Einstein-Str. 15, 12489 Berlin

[3]BESSY GmbH, Albert-Einstein-Str. 15, 12489 Berlin

Introduction

The colloidal size fraction of soils, i.e. the fraction of particles with an equivalent diameter < 2 µm, is an important constituent of soils. The micro structure built up by colloids, the pore system, influences the diffusive mass transport within soils and thus the availability of certain substances for chemical or microbial processes. Due to their very large surface area colloids, are able to adsorb organic and inorganic substances. This adsorption influences the stability of the soil structure. However, some substances may gain additional mobility due to colloid bound transport.

Colloids are surface active particles consisting of organic and/or inorganic material. One important example of interaction is the accumulation of organic matter. This may lead to a formation of larger flocks of colloidal particles. As the size and the structure of these flocks determine the surface available for reactions and thus influences the above mentioned soil parameters, it is important to scrutinize the flocks with spatial as well as with spectral resolution.

A scanning transmission X-ray microscope (STXM) is a tool very well suited for this task as it offers spatial resolution in the sub-100nm regime, which is well within the colloidal range, and it allows a detailed spectral study of the sample at the same time.

Materials and Methods

An otherwise well characterized soil has been used as a sample to prove the spectromicroscopical capabilities of the STXM at the undulator U41. It is a chernozem from a test field close to Göttingen, a soil with a high content of organic matter (organic carbon content = 4.1%) and an alkaline pH (approx. pH = 8.5) [1]. The soil sample has been suspended in water to a 1% dispersion. This leads to a delamination of flocks too thick for examination with X-ray microscopy. A drop of that suspension has been placed on a silicon nitride membrane and left drying. As a result the membrane acts as a carrier foil for small flocks of colloidal particles.

The STXM at undulator U41 has been used for studying these flocks. The instrument has been described in detail elsewhere [2-4]. By tuning the wavelength of the monochromator below and above the K-absorption edge of Carbon, and by subsequently dividing the resulting images, the distribution of that element within the sample can be mapped. In addition, it is possible to use near-edge resonances for XANES studies. As the X-ray energy is raised to match the absorption edge, these resonances, which reflect the chemical bonding state of the element, are reached before a step-like rise in absorption due to the element occurs. By stepwise increasing the energy at the monochromator and by taking an image of the sample at each energy, a stack of images can be obtained providing spectral and spatial information on the sample at the same time. A very good way to analyze these stacks has been developed for a STXM at the NSLS, Brookhaven, USA [5]. This software has been adapted in that the images obtained with the STXM at U41 can be inserted into the programs.

Results

Images of chernozem samples have been taken below and above the K-absorption edge of carbon. In figure 1, a set of images taken at E = 280 eV and E = 305 eV and the carbon map resulting from the division can be seen. Figure 2 shows one image of colloidal particles from a whole stack. Three regions have been marked in green and in red. Integrating the transmission signal I of each region as a function of energy and using the regions marked red as I_0 the spectra adjacent to each image could be obtained as $-\ln(I/I_0)$, which yields the optical density. The top image and spectrum clearly reveal the L_{II}- and L_{III}-absorption features of potassium, a strong indication for clay particles. The spectrum in the middle reveals the organic origin of the particle marked in the adjacent image. The set at the bottom shows the result of the sum of all particles from that flock. The differences in the spectra are a clear proof for the need of spatially resolved data.

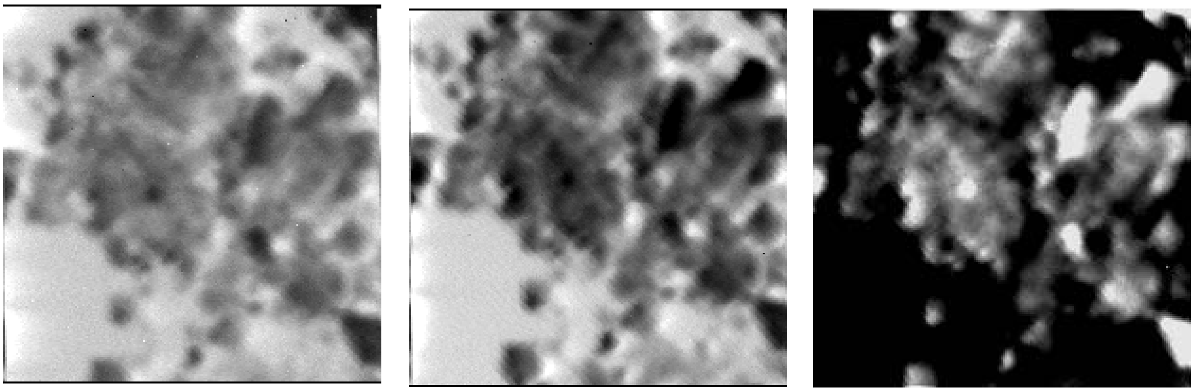

Figure 1: STXM images of colloidal structures within the soil chernozem, taken at E = 280 eV (left) and E = 310 eV (middle), and the carbon map obtained by division of these images. The image size is 10 x 10 μm^2 with 200 x 200 pixel^2, i.e. 50 nm step size. The dwell time per pixel is 20 ms.

Outlook

Improvements can be made on the instrumental side as well as on the analytical side. Due to some mechanical problems with the monochromator the useful step size for increasing the energy is approx. 0.5 eV, limiting the achievable energy resolution. This has to be corrected within the near future. The analysis of the stack data can be refined using principal component analysis and cluster analysis routines [6]. The next step in sample preparation will be to study colloids directly in aqueous media.

Acknowledgements

This work has been funded by BMBF under contract number 05KS4MGB/7 and under contract number 02WU9893/0. We want to thank the staff of BESSY for excellent working conditions.

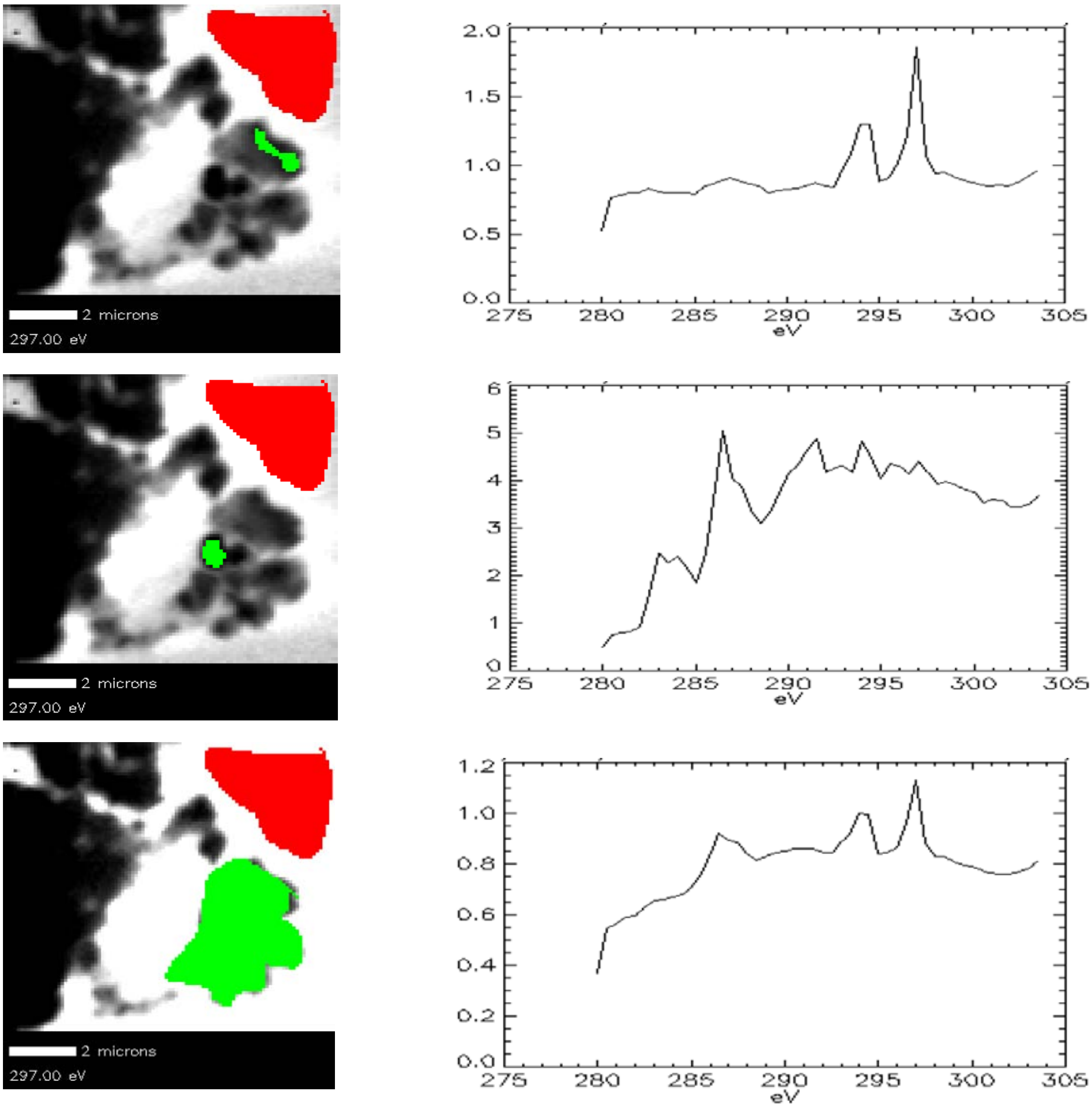

Figure 2: STXM image representing an image stack. The spectra are obtained from the regions marked green. The image size is 10 x 10 μm^2 with 100 x 100 pixel^2, i.e. 100 nm step size. The dwell time per pixel is 10 ms.

References

[1] C. Ahl, H.-G. Frede, S. Gäth, B. Meyer: Böden aus Löss. Mitteilgn. Dtsch. Bodenkundl. Gesellsch. 42 (1985) 359-434.
[2] U. Wiesemann, J. Thieme, P. Guttmann, R. Früke, B. Niemann, D. Rudolph, and G. Schmahl: The New Scanning Transmission X-Ray Microscope at BESSY-II. In: W. Meyer-Ilse, T. Warwick, and D. Attwood, eds., X-Ray Microscopy: Proceedings of the 6th International Conference, AIP Conference Proceedings 507, New York (2000) 430–434.
[3] U. Wiesemann, J. Thieme, P. Guttmann, R. Früke, B. Niemann, D. Rudolph, and G. Schmahl: Construction of a scanning transmission X-ray microscope at the undulator U-41 at BESSY II. In: W. Gudat and P. Zimmermann, eds., Proceedings of the 7th International Conference on Synchrotron Radiation Instrumentation, NIM A 467–568 (2001) 861–863.
[4] U. Wiesemann, J. Thieme, P. Guttmann, R. Früke, S. Rehbein, B. Niemann, D. Rudolph, and G. Schmahl: First results of the new scanning transmission X-ray microscope at BESSY-II. In: J. Susini, D. Joyeux, F. Polack, eds., X-Ray Microscopy 2002, Journal de Physique IV 104 (2003) 95–98.
[5] C. Jacobsen, G. Flynn, S. Wirick, and C. Zimba: Soft x-ray spectroscopy from image sequences with sub-100 nm spatial resolution. Journal of Microscopy 197, no. 2, (2000) 173-184.
[6] M. Lerotic, C. Jacobsen, J.B. Gillow, A.J. Francis, S. Wirick, S. Vogt and J. Maser: Cluster analysis in soft X-ray spectromicroscopy: finding the patterns in complex specimens. Journal of Electron Spectroscopy and Related Phenomena 144-147C (2005) 1137-1143.

HIKE experiment at KMC-1: Progress and Proposed Experiments

P. Bressler[1],F. Schäfers, M. Gorgoi, W. Braun, M. Sperling, M. Mertin, G. Öhrwall[2], S. Svensson[3] and W. Eberhardt

BESSY GmbH Berlin
[1]Present address: European Science Foundation, Strasbourg
[2]Dept.of Physics, Uppsala University,
[3]BESSY and Dept.of Physics, Uppsala University

The HIKE experiment was first set up in September 2004 on the high resolution double crystal monochromator KMC-1 beamline [1]. This beamline operates on a bending magnet. The x-ray energy band pass in the range 1.7-12 keV is selected via Bragg reflection at variable incidence on different crystal planes (e.g.: Si(422)). The HIKE station is equipped with a Gammadata Scienta R-4000 hemispherical electron kinetic energy analyzer specifically modified for high transmission and highest-resolution at kinetic energies up to 10 keV, an analysis chamber and a liquid helium cryostat manipulator (T_{min} [sample] < 25 K), which also can be heated to several hundred °C. The chamber will soon receive a rapid entry load lock, and complete remote control of the apparatus, including automated alignment, is in planning to enable operation in the safety hutches of hard x-ray undulator source beam lines. This year the HIKE station received a position alignment and monitoring system for very precise alignment of analyzer-to-beam, which is necessary for ultimate highest resolution at reasonable intensity.

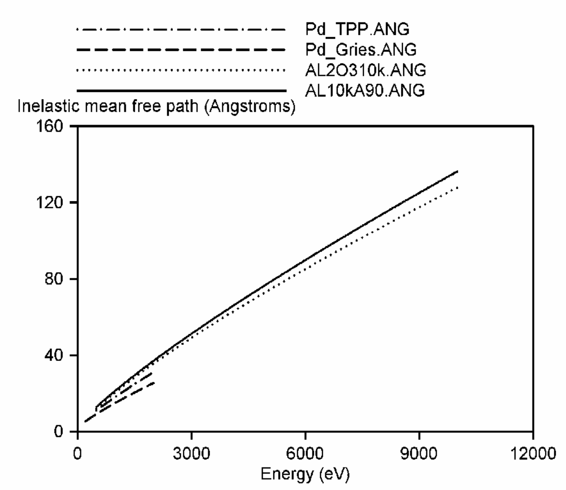

Fig. 1: Calculated IMFPs for Al_2O_3 and Pd using different sources from /2/. TPP: ref. 3, A90 & 10k: ref. 4, Gries: ref. 5. Values for Al_2O_3 E_{kin}: 1440 eV: 27.2 Å, E_{kin}: 4110 eV: 66.8 Å.

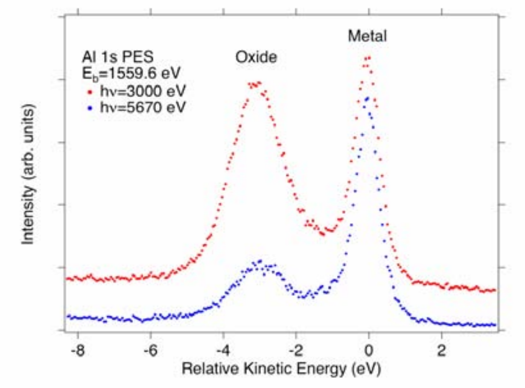

Fig. 2: Depth profiling via different excitation energies: Al 1s photoelectron spectrum at different photon energies. The Al plate is coated by a natural oxide film. Metall/oxide ratio increases with excitation energy. Simple exponential attenuation using IMFPs for 1440 eV and 4110 eV yields an averaged layer thickness of 57 Å aluminium oxide.

During the Autumn 2005 beamtime we tested the new high precision adjustment system. Overall performance was excellent and we recorded novel high quality volume-sensitive photoemission (PE) data. These data have been obtained in standard high vacuum conditions, showing that – once the experimental difficulties with ultra high resolution - high kinetic energy is resolved – one has a very simple yet very efficient technique to study deep lying (buried) interfaces and bulk materials.

By varying the excitation energy, and so, the kinetic energies of the photoelectrons, E_{kin}, originating from distinct initial states the sample information dept is altered: The inelastic mean free paths (IMFPs) increase with kinetic energy roughly proportional to $E^{3/4}$ and can be obtained through predictive formula and tabulated empirial data, e.g.: in [2]. Figure 1 presents a compilation of calculated IMFPs for Al, Al_2O_3 and Pd for energies up to 10 keV where available.

In Figure 2, we show Al 1s photoelectron spectra taken off a standard workshop aluminum plate, which had only been scraped in air before introduction in the HIKE chamber. The Al (metal) related 1s and the chemically shifted oxide (Al_2O_3) 1s peaks are shown. One easily sees the depth profiling effect, as the PE-electrons travel through the oxide layer on the top of the metal. At an excitation photon energy of 5700 eV the influence from the very thick aluminum oxide layer is heavily reduced. We can estimate the thickness of the oxide film, d, by a simple exponential attenuation model for the intensities of the oxide layer and the buried metal (I_{ox} and I_{metal}):

$$I_{ox}^{film}(E) = I_{ox}^{bulk}(E) \times (1 - e^{-d/\lambda(E)});$$

$$I_{metal}^{buried}(E) = I_{metal}^{bulk}(E) \times e^{-d/\lambda(E)}$$

With IMFP values [$\lambda(E_{kin})$] of 27.2 and 66.8 Å for 3000 eV and 5970 eV E_{kin}, repectively, we obtain an oxide layer of 57 Å to model the measured decrease in the oxide related Al 1s emission as the photon energy changes from 3 to 5.97 keV energy. Considering the sample quality and preparation this is in good agreement with literature values of ca. 50 Å for the natural oxide layer.

The double crystal monochromator has its optimal resolution at back scattering conditions. The energy resolution of a crystal monochromator is determined by differentiating the Bragg-equation and is given by $E/\Delta E = \tan(\theta)/\Delta\theta$. Thus at large Bragg-angles i.e. back scattering geometry the resolution is optimal and - for collimated light - approaches crystal limited resolution. Since the KMC-1 is optimised for soft x-rays (minimum energy 1.7 keV) it can be tuned to a maximum Bragg-angle of as much as 82° to access the lowest energy possible for a given crystal. This is 'automatically' connected with a very high resolution, as can be seen in

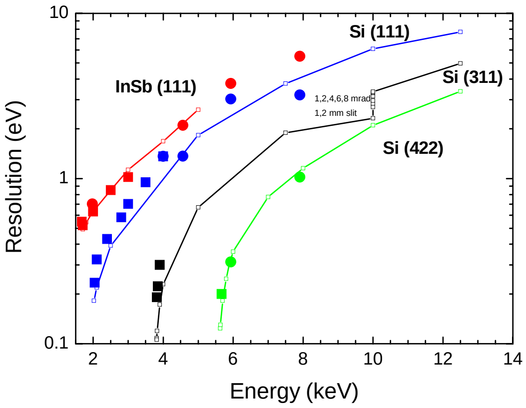

Fig. 3: Resolving power of the KMC-1 double crystal monochromator beamline for the various crystal sets. Experimental data from HIKE (solid squares), experimental data from crystal backscattering photodiode (solid circles) and raytracing calculations (lines and open symbols)

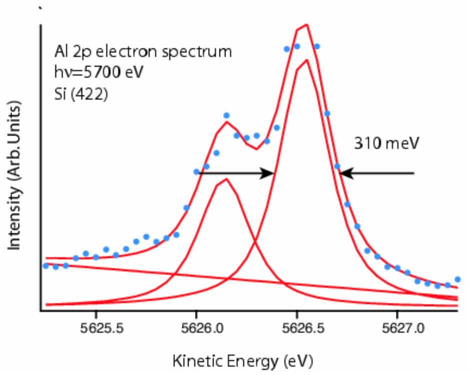

Fig. 4: The high resolution Al 2p core photoelectron spectrum at 5700 eV photon energy. The total FWHM is 310 meV. The contribution from the spectrometer is around 125 meV, which implies that the photon energy resolution is around 280 meV. This gives a monochromator resolving power of over 20.000.

Fig. 3 for the various crystal sets, reaching resolving powers down to 200 meV at 5700 eV. In order to study the resolution properties we used the same low quality aluminum (the advantages with HIKE are best demonstrated by such test samples) and we studied the Al 2p photoelectrons with the monochromators set near to the backscattering onset for the Si 422 reflection, i.e. at photon energies near to 5700 eV. In Fig. 4 we show a result. The total Full Width at Half Maximum (FWHM) of the Al 2p spin orbit component lines in this figure is 310 meV. The Al 2p line is excellent for testing of the resolution, since we know that the inherent width is only a few tenths of a meV [6] and the spin orbit splitting of 450 meV [6] gives a very good internal calibration of the energy scale. From Fig. 4 one can conclude that the monochromator resolving power was over 20 000, in good agreement with the calculated value for this beamline. The resolution can be improved by obtaining spectra nearer to the onset and we will proceed with optimizing this in the future.

As a final result we show in Fig. 5 a recording of a V sample buried under ≈80 Å of Pd. The Pd was put as a cap in order to protect the V sample from oxidation. As can be seen the buried V layer can easily be studied. Again applying the simple exponential attenuation model we receive an IMFP for Ekin = 5485 eV of 44 Å, a value slightly lower than extrapolation of Pd values in figure 1 delivers (ca. 60 Å) but in very good agreement with effective attenuation length estimates (40-50 Å) in [2] and refs therein. Comparison of the expected excitation cross sections, IMFPs and the actual Pd film thickness is consistent.

For the future, as already mentioned we plan to further characterize the resolution properties. We will furthermore perform a series of studies where we will correlate the core level binding energies to the quality of the interface [7]. This can potentially provide a tool to correlate interface roughness to the photoelectron profile of the core level. These studies will be in collaboration with magnetism research groups from the Department of Physics in Uppsala. We also will plan for operation at other beam lines at BESSY.

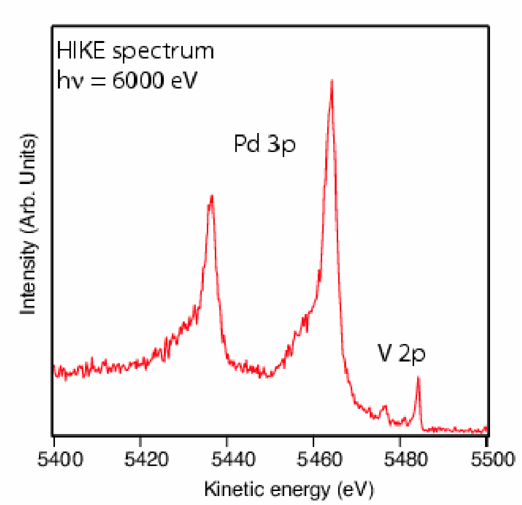

Fig. 5: Vanadium sample under an ≈80 Å thick cap of palladium. The deeply buried vanadium can easily be studied. The photon energy was 6000 eV.

References

[1] http://www.bessy.de/users_info/02.beamlines/linespdf/D_01_1B.pdf

[2] NIST Electron Inelastic-Mean-Free-Path Database, C. J. Powell, A. Jablonski, version 1.1 National Institute of Standards and Technology, Gaithersburg, MD (2000).

[3] S. Tanuma, C. J. Powell and D. R. Penn, Surf. Interface Anal. **21**, 165 (1994).

[4] Al: J. C. Ashley, J. Electron. Spectroscopy **50**, 323 (1990), Al2O3: Akkeman et al. Phys. Stat. Sol. (b), **198**, 769 (1996).

[5] W. H. Gries, Surf. Interface Anal. **24**, 38 (1996).

[6] M. Watanabe, T. Kinoshita, A. Kakizaki and T. Ishii, Journal of the Physical Society of Japan **65**, 1730 (1996)

[7] W. Olovsson et al., Phys. Rev. B **68**, 045411 (2003)

The new Mags-beamline: an instrument for hard x-ray diffraction at Bessy

E. Dudzik, R. Feyerherm, G. Wagener

Hahn-Meitner-Institut/Bessy, Albert-Einstein-Str. 15, 12489 Berlin

The new Hahn-Meitner-Institut beamline Mags has started user operation in spring 2005. The beamline uses a 7 Tesla multipole wiggler to produce high photon fluxes (of the order of 10^{12} photons/s/100 mA) at photon energies between 4 to 30 keV. It has adaptive optics which provide flexible horizontal and vertical focussing and compensate the wiggler heat load. The beamline is intended for single-crystal diffraction for the study of ordering phenomena, but has also been used successfully in various other diffraction experiments in the study of organic superconductors, materials science etc.

Beamline

Figure 1 shows the overall layout of the beamline optics. The beam is vertically collimated by the first mirror at 20.5 m from the source, passes through a fixed-exit double crystal mono-chromator at 23 m, with a sagittal bender on the second crystal for horizontal focussing, and is finally vertically refocussed by a second mirror at 25.5 m from the source. The experiment is situated at 36.5 m from the source. The basic beamline design and specifications were provided by HMI. The beamline (including the control system) was built by the German company Accel.

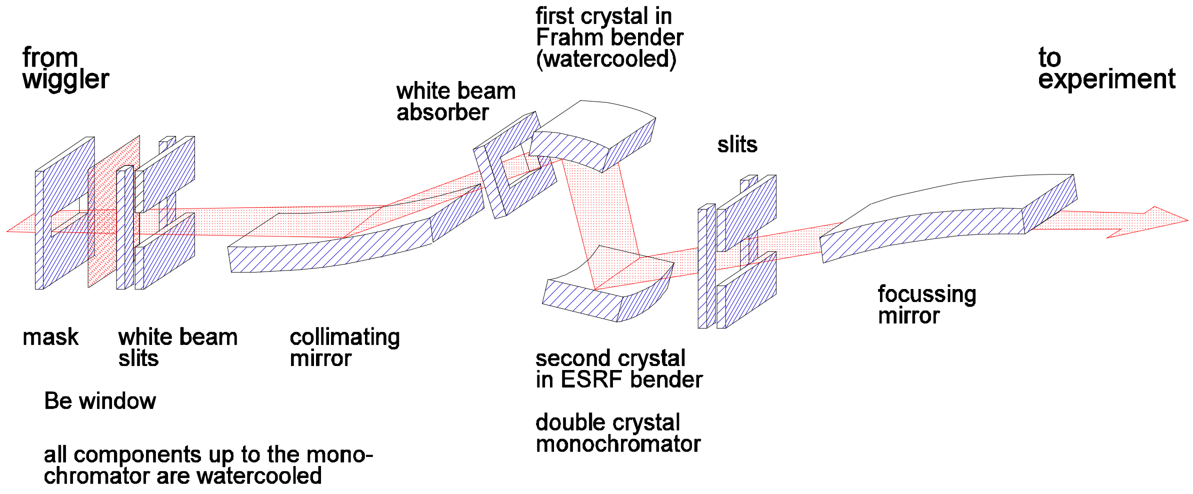

Figure 1

The mirrors were made by Seso in France. The first mirror is designed to withstand the high wiggler heat loads of up to 2 kW. Both mirrors have two tracks, one with Rh as optical coating, the other the Si substrate (polished to 3 Å roughness). The mirror pitch angle is variable between 0 and 5 mrad. The pitch is used, together with the two mirror coatings, to suppress higher order light in the beamline. Both mirrors also have variable bending radii to adapt the focussing to the heat load and the pitch angle. They provide vertical collimation and focussing up to 15 keV photon energy. Above 15 keV the beamline is operated in mirrorless mode. The changeover between mirror mode and mirrorless mode can be made in about 30 minutes.

The fixed-exit double crystal monochromator at 23 m from the source was built by Accel. It uses a pair of Si(111) crystals with an energy resolution of about eV at the Cu K-edge. The first monochromator crystal is designed to withstand heat loads of about 700 W. It is indirectly watercooled and mounted on a crystal bender that counteracts the thermal bump (based on a design by Zaeper et al., Rev. Sci. Instrum. 73 (2002), 994). Figure 2 shows the effect of counterbending on the monochromator rocking curve. The heat load on the first monochromator crystal was 550 W. This broadens the rocking curve to twice the theoretical value (7.8 arcsec at 9 keV). When the bender applies force to the crystal, the thermal bump is gradually removed until the broadening is less than 1.5 x the theoretical value. Further bending causes the rocking curve to deteriorate rapidly.

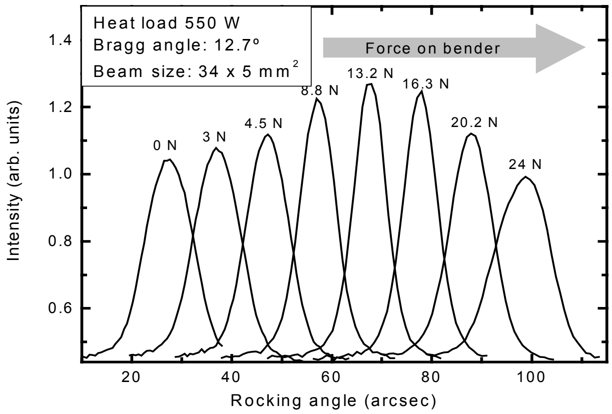

Figure 2

The second monochromator crystal is mounted on an ESRF-type sagittal bender which provides horizontal focussing at all photon energies. Figure 3 shows the various modes of focussing possible with the Mags beamline. The double spots in the horizontal focus are due to the two source spots in the wiggler. A parallel beam can be achieved by collimation with several sets of slits in the beamline. There is a Desy monochromator stabilising system (Mostab) available, but it was found to be unnecessary in practice.

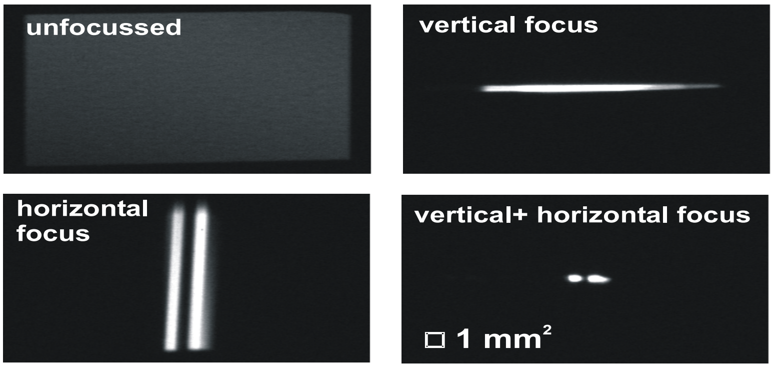

Figure 3

Experiment

The last part of the beamline inside the experimental hutch consists of a series of graded attenuators, and horizontal and vertical slits. A scattering foil with a photodiode can be used as the Io monitor, alternatively an ion chamber is available.

The experimental endstation consists of a six-circle Huber diffractometer (four circles for the sample, two for the detector), with a three-circle polarisation analyser that can also be used as an ordinary analyser. The diffractometer is mounted on a yz-table and can be moved relative to the beam. If no temperature control is required, samples can be mounted either on a standard goniometer head, or on an xyz-table. There are several closed cycle cryostats available: a cryofurnace covers a broad temperature range from approximately 8 to 800 K; a 3-300 K cryostat is available on demand, and a 1.4 K cryostat should become available in the near future.

There are two detectors: an energy-resolving Canberra Ge diode with a multichannel analyser, and an Oxford-Danfysik Cyberstar scintillation detector. Because of its low weight and robustness, the scintillation detector is normally used in conjunction with the analyser.

Both the beamline and the experiment are controlled with the spec software from Certified Scientific software. A large macro library is available for temperature control, special scan modi, rapid powder scans etc., and several special scan modes have been programmed during user experiments.

The Nano-Optic-Measuring Machine NOM at BESSY - further improvement of the measuring accuracy

Heiner Lammert, Frank Siewert, Thomas Zeschke
BESSY GmbH, Albert Einstein Strasse 15, D 12489 Berlin. http.//www.bessy.de/
E-mail: Lammert@Bessy.de

BESSY Annual Report 2005, (30.1.2006)

Introduction

The last year BESSY Annual report presented the results of the cooperative research project "Nanometer-Optikkomponenten" – NOK showing results of the in house developed Nano-Optic-Measuring Machine NOM [1]. Further development details and results have been reported in [2] [3] [4] [5]. The breakthrough in the manufacture and metrology is characterized in a fivefold increase of accuracy of the quality of optical components for Synchrotron Radiation and in a tenfold increase of accuracy of their measurement compared to common deflectometry methods (LTP) [3]. The Main attributes of the BESSY – NOM are at **first**: the measurement accuracy has been improved from 0.1 arcsec rms to less than 0.01 arc sec rms with sub nanometer accuracy, **secondly:** Three dimensional mapping over up to a 1200mm x 300 mm surface, and **thirdly:** the NOM development has a stadium of a measuring machine for science and industry. In the past year the NOM was attached for multifaceted measurements, so that some new results were detected in respect of the accuracy by measuring of ultra precise otpical components. We can show here, that is it possible to get very accurate measuring results by practice of some different measuring strategies.

Reproducibility and the random measuring deviations

The necessary but not sufficient constraints for the uncertainty of the measuring results are the random measuring deviations ("random errors"). Every result may be not more accurate than the sum of the random deviations. Their sources may be electronically, optically or mechanically noises or drifts, and the sum of all this sources results into the reproducibility of a measuring result. Because all this sources are not only dependant on random influences but also on the variation of all this random sources and due to a special measuring problem you may not able to declare one value for the accuracy of the whole measuring machine NOM but for a specific measuring problem and its individual solution. A quasi ideal case to characterize the uncertainty of a measuring result is, that you can see in the sum of variations of all single measuring values (the rms value) of what spread are the random deviations, and with help of the increase of the number of series of measurements you may minimize the random deviations possibly. At least it is a point of great importance for the accuracy of a measuring result, that all different variety of random errors are minimized as possible. The following example "four days – four measurements" demonstrates the achievable reproducibility for measurements at the NOM.

During the course of four successive days the middle trace of a spherical Silicon mirror (R=1280 m) were measured with a scan length of 100 mm by use of the NOM in 10 runs in a particular time of 100 min. The average of this 400- min-4-day-measurement results in an radius of 1280,137 m, and the differences of the 4 separate results from the average is +/- 0.004 arcsec rms or +/-0.06 nm. By measuring of 130 runs (54 measuring hours during this four days) the confidence level (95%) amounts +/- 0.002 arcsec and +/- 0.04 nm. In Fig. 1 the residual slope and height curves are displayed out of phase to detect the high concordance of the measuring results. Small irregularities on the sample surface of about 0.2 nm are traceable details on all of the four measurements.

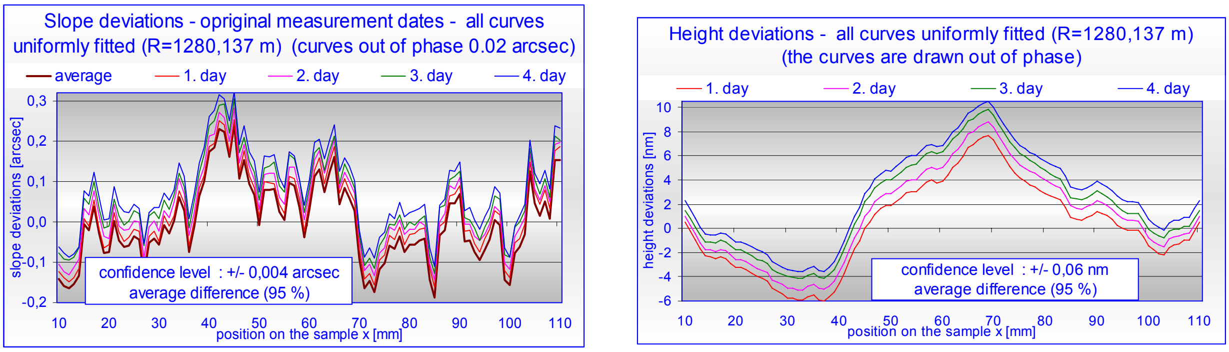

Fig.1 Reproducibility: Four-days-four-measurements on the NOM of 100 mm spherical Si-mirror. Left the slope and right the height differences of the averages are displayed out of phase. The 95%-confidential level of average difference are in this case 0.004 arcsec rms or 0.06 nm rms

The determinate confidence level of less than 0.1 nm or 0.005 arcsec rms permits low measuring uncertainties of the NOM. The excellent reproducibility of 0.1 nm or 0.005 arcsec rms expresses a very low level of the random error budget. This is at least an essential point to identify the systematical part of the error budget.

Determination of systematic measuring deviations and their compensation

Based on the typically very low random measuring deviations it is possible to determine the systematic measuring deviations ("systematic errors") in the range of the random confidence of less than 0.01 arcsec and less than 0.1 nm. Of course all imaginable influences of systematic measuring deviations are eliminated or extreme minimized by the design and construction of the NOM in first and particularly in second order. But the residual systematic influences are widely identifiable and consequently compensable for every measuring procedure with help of different measuring strategies. We define four different groups of measuring strategies to minimize the influences of the systematic measuring deviations: calibration, correction, compensation and control.

Calibration of the NOM

The calibration of the NOM is realized by three different strategies: external, internal and auto calibration. The external calibration is realized by the manufacturer of the c ACT and the LTP, the ACT is indirectly cross checked by the German national standard institution, the Physikalisch Technische Bundesanstalt – PTB in Braunschweig. The internal calibration of the NOM was conducted by use of a precise tilt angle device.
The different angle positions are measured by high accurate length sensors with nm resolution.
The third calibration strategy is the auto calibration using a spherical mirror characterized by low slope deviations of less than 0.1 arcsec rms. This mirror is measured at different angle positions of the NOM sensors ACT or LTP. Fig. 2 shows height results of 13 different measurements at 13 different ACT angle positions. The deviations of this results represent the systematical measuring deviations of the whole optical path system from ACT to the sample and back to the sensor display in every special ACT angle position. The adding in overlapped phase of this different deviations in their special angle positions leads to the device function, see diagram fig. 3. This curve describes the systematical deviations of the beam and sensor system and is directly applicable to compensate the systematical error part by adding onto the measured values. Not included in the correction by auto calibration is the summarized inclined deviation of the slope curve corresponding to the exactly spherical radius. This auto calibration is implemented at the NOM with an accuracy of 0.01 arcsec rms or less than 0.3 nm rms thus the level of the random deviations. In table 1 the detected residual deviations are summarized.

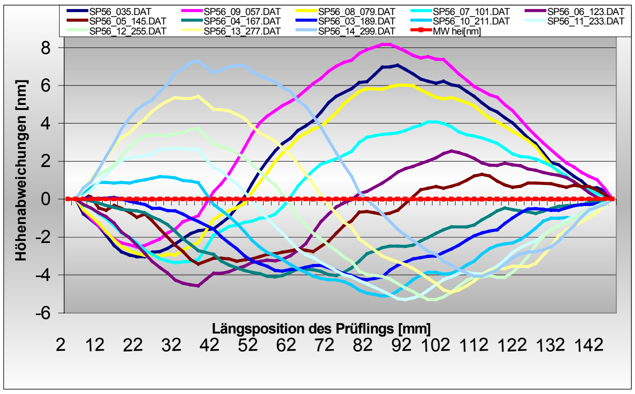

Fig. 2 Auto calibration of the NOM with a spherical mirror (R=46m) in 13 different ACT angle positions. The height deviations of a average radius fit as results from the different systematical deviations of each angle position.

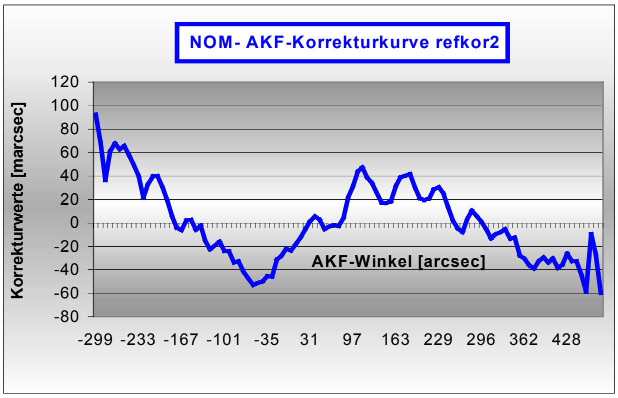

Fig.. 3 Device function as summarized correction curve of all systematical deviations for correction of the measured angle values as result of auto calibration like the height deviations in fig 2 are shown.

Correction of linear drifts

These however very small linear drift effects occurs in a stringent temperature stabilized environment over a long time duration. Due to this the basic measuring strategy at the NOM attends a measuring time for one scan as short as possible and a immediate followed second scan in reverse scan direction with automatically averaging of the bidirectional measuring values. This correction process compensates the first order of the drift effects and minimizes related errors on the measuring result in the most cases to values of less than 1 %.

Compensation of systematic measuring deviations

The compensation of systematic measuring deviations at the NOM is applied by quickly 3-D-measurements with help of the y-carriage positions for the line scan correlation in y direction or by utilization of booth orthogonal AKF-measuring values in one measuring process. In the first case the linearity of the y-carriage may be detected and by compensation take into consideration. The residual deviations result from the random angle deviations of the carriage by its movement. In the second case the roll deviations of the x carriage are important and may be detected and compensated. In both cases the residual measuring deviations as result of the random movement deviations is less than 0.01 arcsec rms.

Control of systematic measuring deviations

The control of systematic measuring deviations represents a main point in the evaluation of the achievable accuracies at highly accurate measurements of optical components at the NOM. The control can be realized by internal or by external comparison of measuring results on identical test samples. The external comparison with other measuring methods or in other labs is in the most cases problematically, due to the problem to find a measurement method or instrument of comparable or higher accuracy. In an external comparison of the NOM with the ESAD-method at the PTB we achieved a concordance of 0.3 nm rms for a line scan measurement on a plane reference [3].

The internal comparison control is a constructive attribute of the NOM, because external comparisons are extensive impossible for the evaluation of the NOM accuracy. That is a main reason, why the design of the NOM is including several internal comparison options, in particular the two different slope measurement sensors LTP and ACT. So there are some different internal confirmations of the high accuracy of the NOM in respect on its systematical measuring deviations. The comparison of the NOM internal LTP- and ACT sensors is detected with about 0.01 arcsec rms or 0.14 nm over 60 mm.

An other NOM internal control comparison results from the 3-D-pofiling [5]. The 3-D-topography is calculated over parallel line scans in two different orthogonal directions of the sample surface. For the control of possible small distortion of this calculated 3-D-result two diagonals of the sample are measured. After a small distortion correction with help of the first diagonal the difference between the second diagonal and the orthogonal line scan is calculated to a 3-D-measuring result is a control possibility of the accuracy of the measuring result. So far with the NOM a concordance of about 0.3 nm rms for 2D-3D-measurements have been achieved. But last results with more definite x-y-positioning over 150 mm of a 2000 mm² plane surface the residual 2D-3D-defferences were 0.1 nm rms. Because the 3D and 2D results were sampled at different scan position on the NOM, with different calculation methods for generating and evaluation of the 3-D- measuring result, the so found 2D-3D-concordance is usable as a highly sensitive criterion for systematical deviations of NOM-measuring related to the systematical deviations.

By realizing an other very descriptive experiment it is shown how small systematical deviations can be detected by comparison of the calculation of a sample bending effect with the measuring result of this bending effect. A plan mirror of 200 mm length shows a minimum of bending because of its own weight, if the marginal supporting point distance is 44.6 mm ("Bessel points") and the central bending is Zero by a overlaid distance of 49 mm. This two cases were measured by the NOM. In the diagrams fig. 4 the differences of this two bending modifications between the calculated and the measured of the 45 nm sag surface are demonstrated. The difference of the calculated and measured curves is less then 0.2 nm rms, a very high accurate proposition for systematical deviations of the NOM in this measuring range.

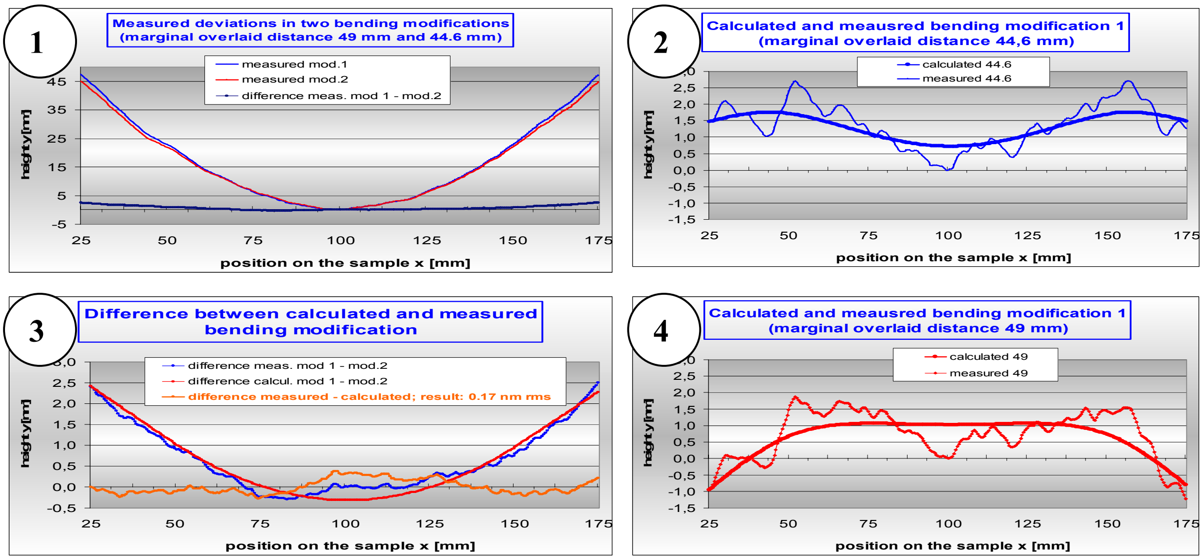

Fig. 4 Comparison of the calculated and NOM-measured bending effect of the two modifications minimum of bending and central bending zero. Diagram 1: Bending of a 200 Si-mirror caused by gravitation by change of the supporting point distance; diagram. 2: Calculated and measured curves of "Bessel"-points (bending = minimum); diagram. 3: 2.7 mm supporting point variation (central bending cero); diagram 4: The difference of calculated (red) and measured (blue) curves are less than 0.2 nm rms (orange).

Summary of accuracy measuring results of the NOM

A Summary of the before demonstrated results and in addition some further high accurate NOM-measuring results are shown in table 1. All this results can be seen as a verification for the accuracy of the NOM. Tab. 1 shows, that all detected residual systematic deviations are near by 0.01 arcsec rms or less than 0.3 nm rms or < 0.01 %. A main improvement of the NOM the compared to other instruments about fivefold lower level of systematical deviations is abstracted in this table. On the other hand tab.1 points at the described factor, that the external comparisons with other LTP`s like with the European SR labs [6, page 41], or with different precision interferometers result to a deviation more than a tenfold compared to the NOM. With this accuracy the NOM enables different applications for the future [8].

Nano-Optic Measuring Machine - NOM - measuring results in respect of the NOM-accuracy					
		method or sample	**measuring results**		
			Slope deviations	Height deviations	Curve radius
			arcsec rms	nm rms	%
random deviations					
reproducibility confidence level (95%)		sph. 1.3 km,140 mm	0.002	**0.04**	0.01
systematic deviations measuring strategies			**detected residual deviations or estimated uncertainty**		
Calibration	external	Möller-Wedel - AKF	0.03		< 0.01
	internal	variable calib.slope	< 0.04		0.007
	auto	sphere 56 m	0.01	0.3	
Correction	internal	linear drift	< 0.01	< 0.1	< 0.01
Compensation	internal	y- carriage	< 0.01		
		roll deviation of x-carriage	< 0.008		
Control	internal comparison	NOM - AKF – LTP spher (6 km) 45 mm	ca. 0.01	0.14	
		2D – 3D 60 mm 2.000 mm²		**0.1** (ca.λ/5,000)	
		plane bending calculation	< 0.02	**< 0.2** (<λ/3000)	
	external comparison	Interferometry plane 300 mm²		ca. < 5 (<λ/100)	0.05
		Round robin, div. LTP internat. 100mm sph.1.3 km,140 mm		2.2 (<λ/200)	
		ESAD ap.size 5 mm plane 130 mm;		0.3 (ca.λ/2000)	
some examples for measuring uncertainties					
plane 100 mm x 20 mm NOK-demonstrator		3 D 2000 mm²	< 0.02	< 0.4 (<λ/1000)	
Plane 500 mm x120 mm NOK-demonstrator		3 D 60,000 mm²	< 0.03	< 1 (<λ/600)	
Ell.Cyl. 210 mm x 20 mm NOK-demonstrator		3 D < 4000mm²	< 0.03	< 0.5	

Tab. 1: Measuring results in consideration of the random and systematical deviations inclusive the comparison with other measuring methods and some NOM-measured optical components demonstrate the accuracy of the NOM.

Conclusion

New measuring results at BESSY demonstrate a very high accuracy of the Nano Optic Measuring Machine NOM and exceeds the up to now detected accuracy. Primarily the demonstrated measuring strategies internal methods of calibration, correction, compensation and control allows to achieve an accuracy of near by 0.01 nm rms or less than 0.3 nm rms (< λ/2,000). Correspondingly a detected reproducibility of 0.002 arcsec rms or 0.04 nm rms (< λ/15,000) have been demonstrated. This measuring accuracy should become to a criterion for evaluation of measuring methods and facilities for ultra precision optical components in future.

References

[1] Heiner Lammert, Tino Noll, Thomas Schlegel, Fred Senf, Frank Siewert, Thomas Zeschke; Accuracy of Optical Components for Synchrotron Radiation. Results of the Cooperative Research Project "Nanometer-Optikkomponenten NOK. BESSY Annual Report 2004, p. 503-505, BESSY: www.bessy.de/

[2] Heiner Lammert, Tino Noll, Thomas Schlegel, Fred Senf, Frank Siewert, Thomas Zeschke, "The Nanometer Optical Component Measuring Machine – NOM – at BESSY", BESSY annual report , Berlin 2002, p. 399-404. www.bessy.de

[3] Heiner Lammert, Tino Noll, Thomas Schlegel, Fred Senf, Frank Siewert, Thomas Zeschke; Breakthrough in the Metrology an Manufacture of Optical Components for Synchrotron Radiation, BESSY Annual Report 2003, p. 530-533, BESSY: www.bessy.de

[4] Frank Siewert, Tino Noll, Thomas Schlegel, Thomas Zeschke and Heiner Lammert, The Nanometer Optical Component Measuring Machine: a new Sub-nm Topography Measuring Device at BESSY; SRI 2003, San Francisco, 2003, Am. Inst.of Physics Conf. proc. Melville, New York 705 (2004), p.847-850

[5] Frank Siewert, Heiner Lammert, Tino Noll, Thomas Schlegel, Thomas Zeschke, Thomas Haensel, Andreas Nickel, Axel Schindler, Bernd Grubert, Carsten Schlewitt; Advanced metrology, an essential support for the surface finishing og high performance x-ray optics. SPIE Conf. San Diego 2005, Proc. of SPIE Vol.5921 (2005), p. 1-11

[6] Heiner Lammert (report author); Nanometer-Optikkomponenten für die Synchrotronstrahlung; Messen und Endbearbeitung bis in der Subnanometer-Bereich unter λ/1000. Final report NOK-NOM, sponsored by BmbF/VDI 13N7929. BESSY Berlin, Dec. 22,.2004, Signatur F05 B 1105, Techn.Informations-Bibliothek TIB der TU Hannover (2004), 70 pages

[7] German Patent No. 103 03 659 B4, Date: July 28, 2005; Method of Optically Measuring and Precision measuring Apparatus for Determining Deviation from the Ideal Shape of Technically Polished Surfaces, Inventors; H. Lammert, T. Noll, F. Siewert, T. Schlegel, T. Zeschke, Jan 23, 2003

[8] Heiner Lammert, Fred Senf, Frank Siewert, Thomas Zeschke; New ways in the ultra precision technology by surface measuring in sub-nanometer accuracy lower than λ/1000 with the Nano Optic Measuring Machine - NOM -. Preprint BESSY, Berlin Nov.21, 2005

THE EARTH'S WATER CYCLE
EXPERIMENTS BEAR EVIDENCE OF POSSIBLE HIGH WATER CONTENTS IN THE EARTH'S MANTLE

M. Koch-Müller, R. Wirth, D. Rhede and S.S. Matsyuk
GeoForschungsZentrum Potsdam, Telegrafenberg, 14473 Potsdam

The presence of water in the Earth's mantle has enormous effects on geodynamical processes of the Earth, because the presence of water may change the physical properties of the minerals such as the melting point, rheological behavior (hydrolytical weakening) and the transformation kinetics. Therefore, experimental, petrological and theoretical studies of the storage capacity of water in the Earth's mantle are in the focus of recent research. Petrological-geochemical investigations evidence that hydrogen can be stored in nominally anhydrous minerals of the Earth's mantle (NAMs) such as pyroxene, garnet and olivine. Hydrogen in these minerals is structurally bound as hydroxyl. Although the amount of water in these minerals is generally very low (up to 0.1 wt % H_2O), on a global scale the water content that can be dissolved in the upper mantel may exceed the amount of water in the hydrosphere. Experimental studies confirm the hydrogen incorporation in nominally anhydrous mantle minerals and show that the incorporation of hydrogen increases with increasing pressure, e.g. depth. Experiments conducted at very high pressures, i.e. at depths in the Earth which are not directly accessible even show that under these conditions extrem water-rich new mineral structures can be synthesized and that they are thermodynamically stable (e.g. Koch-Müller et al., 2005). For example, minerals of the model system of the Earth's mantle MgO-SiO_2 synthesized with water in excess in the pressure range of 10 to 30 Gpa (300 to 900 km depth) and relative low temperature contained up to 20 wt % water. They are called dense hydrous magnesian silicates DHMS. Whether these minerals indeed exist in the Earth, is not known. If yes, they could transport water along subducting slabs very deep into the Earth's mantle. Dehydration of these minerals in hotter regions in the deep Earth could be an explanation for deep earthquakes observed by seismologists in the Earth'mantle.
Thus, for a better understanding of the global water cycle and its effect on processes in the Earth mantle it is essential to investigate both, natural minerals and synthetic, potential minerals of the Earth's mantle.
Here we present a petrological-geochemical study on quantification and location of structrurally bonded OH groups in natural olivine from the kimberlite pipe Udachnaya, Siberia. The minerals were brought to the Earth's surface by eruption from dephts of 75 – 150 km. Incorporation of hydroxyl groups were investigated by Fourier Transform Infrared Spectroscopy (FTIR). In combination with a microscope up to 30 µm small crystalls can be studied. Using synchrotron IR radiation the local resolution can even be higher (8 x 8 µm).

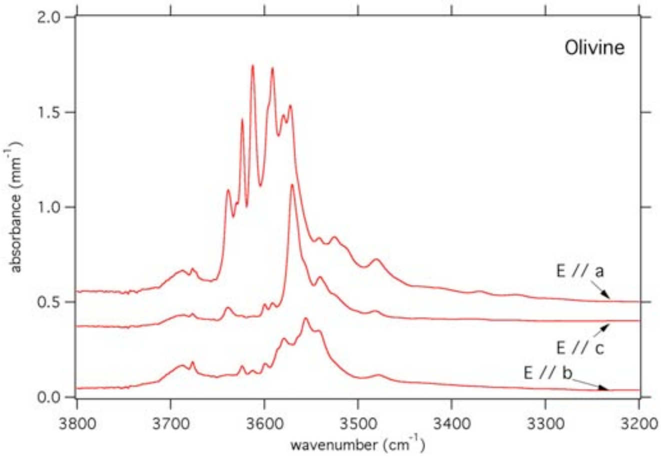

Fig. 1: Polarised infrared spectra of olivine, taken parallel to the crystal axes *a*, *b* und *c*. The bands are assigned to vibrations of structurally bound OH-groups, which are connected with cation vacancies.

Fig. 1 shows representative polarised FTIR spectra with up to 20 strongly pleochroic OH bands. The bands at high energies (3730 – 3670 cm^{-1}) were assigned to inclusion of serpentine, talc and 10-Å phase. Using Transmission Electron Microscopy (TEM) hydrous olivine polymorphs (MgH_2SiO_4)$^{\cdot}$ n(Mg_2SiO_4), were also identified in inclusions. Hydrous olivine and 10 Å-Phase belong to the DHMS phases and evidence high-pressure condition during the formation of the inclusions. The OH bands in the range 3660 – 3200 cm-1 are believed to be intrinsic to the olivine lattice. The corresponding point defects are (i) associated with vacant Si sites ((3607 cm^{-1} E//a, 3597 E // a , 3571 cm^{-1} E//c, 3567 E //c, 3556 E // b),) and (ii) with vacant Mg1 sites (the most of the bands polarized parallel *a*; Fig. 2).

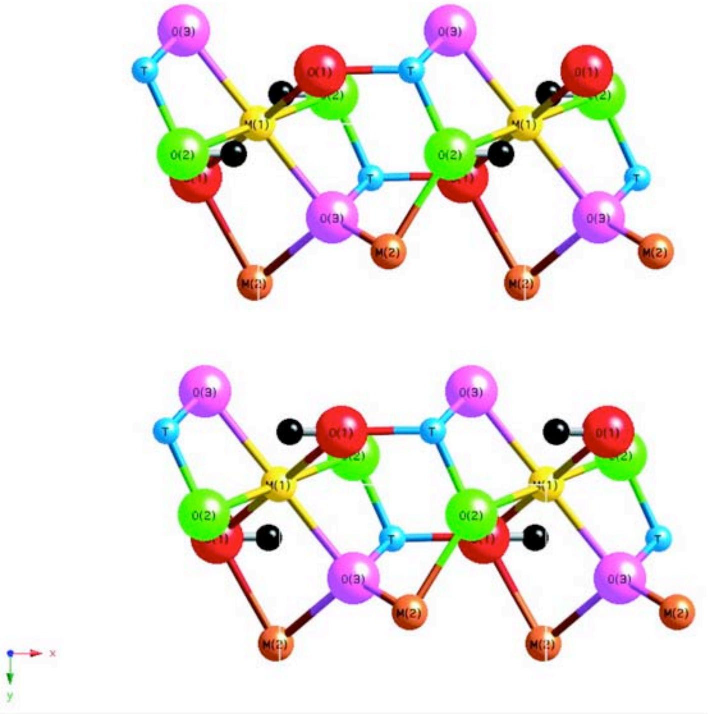

Fig. 2: Part of the olivine structure showing the proposed hydrogens (black balls) associated with vacant M1 sites and bonded to O(2) and to O(1) oxygens.

From the pleochroic behavior of the OH bands associated with the vacant M1 sites we propose that the corresponding hydrogens are bonded to O1 and O2, so that both OH vectors are strongly aligned parallel to *a*. The O2-H groups may be responsibel for the OH bands at higher wavenumbers than those for the O1-H groups. The multiplicity of the corresponding OH bands in the spectra can be explained by different chemical environments and by slightly different distortion of the M1 sites in these high-pressure olivines. The water content was quantified using the Secondary Ionen Mass Spectrometry (SIMS). Compared to olivine from volcanic origin, which incorporate only 1-2 wt ppm H_2O, the kimberlitic high-pressure olivine contain with 400 wt ppm H_2O much more water. Recent experiments show that olivine synthesized at much higher pressure as the kimberlitic samples experienced do incorporate 10 to 20 times more water (Smyth et al., 2005).

References:

Koch-Müller M., Dera P., Fei Y., Hellwig H., Liu Z., van Orman J. and Wirth R. (2005) Polymorphic Phase Transition in Superhydrous Phase B. Phys. Chem. Min., 32, 349 – 361.
Smyth J.R., Nestola F., Frost D.J., Holl C.M. and Bromiley G. (2005) Hydration effects on molar volume and compressibility of olivine, Eos Trans. AGU, 86(52), Fall Meet. Suppl., Abstract MR44A-03.

Residual Stress Depth Scanning of Thin Films by means of White Beam Diffraction

I. A. Denks[1,a], M. Klaus[2,b], Ch. Genzel[3,c]

[1,2,3]Hahn-Meitner-Institut Berlin (c/o BESSY), Bereich Strukturforschung,
Albert-Einstein-Straße 15, D-12489 Berlin, Germany
[a]denks@hmi.de, [b]klaus@hmi.de, [c]genzel@hmi.de

Introduction

The non-destructive assessment of residual stress gradients in the near surface region of some ten to some hundred microns is of great importance in materials science in respect of surface treated materials, thin films or in-situ investigations. However, no method has been proposed yet that delivers a stress distribution in real space with sufficient resolution. The aim of this project is to develop an appropriate non-destructive residual stress analysis (RSA) technique by use of a white synchrotron beam as featured by the EDDI beamline at BESSY [1] in order to enlarge the range of applications and to provide an assessment tool for the currently used Laplace methods.

Principle idea with regard to existing methods

In difference to the currently used “strain scanning” methods, where the slits are fixed in the laboratory system [2,3], the new technique is based on a setup where the slits are coupled to the sample system in such a way that they follow all sample tilts. Hence, the gauge volume depth and orientation stay constant relative to the sample surface for all sample tilts ψ. In other words, within the fixed gauge volume a $\sin^2\psi$ measurement can be carried out. By translation of the sample relative to the slits, depth scanning is realized.

The new technique is proposed to be named “stress scanning” method, a detailed desciption is given in [4]. In respect of the intended application field, a gauge volume height in the range of less than 10 μm is aimed.

Determination and optimization of the volume gauge

The measurement’s accuracy is mainly determined by a well-defined gauge volume in respect of its spatial extension and diffraction peak stability within the volume gauge. For appropriate investigations, a test sample consisting of a thin Au layer of 0.09 μm thickness on a glass substrate is being scanned through the gauge volume. At $2\theta = 6°$, the 111 reflection appears at about 47 keV once the gauge volume touches the sample surface, and disappears when the gauge volume is totally located in the amorphous substrate. Representing the diffraction lines in a 3-D-plot gives a visualization of the gauge volume dimensions (Fig. 1, left).

The line energy position increases linearly of about 50 eV due to a geometrical effect owing an effective sample height variation, when the thin foil is scanned through the volume (Fig. 1, right). The deviation is being considered in later measurements of layers having a smaller dimension than the used volume gauge.

Application to multilayer systems

Apart from the scientific interest in a high resolution real space method, unique application fields exist such as multilayer systems as being used for hard coatings on cutting tools. Such layers often contain alternating sequences of identical layers for stress relaxation reasons.

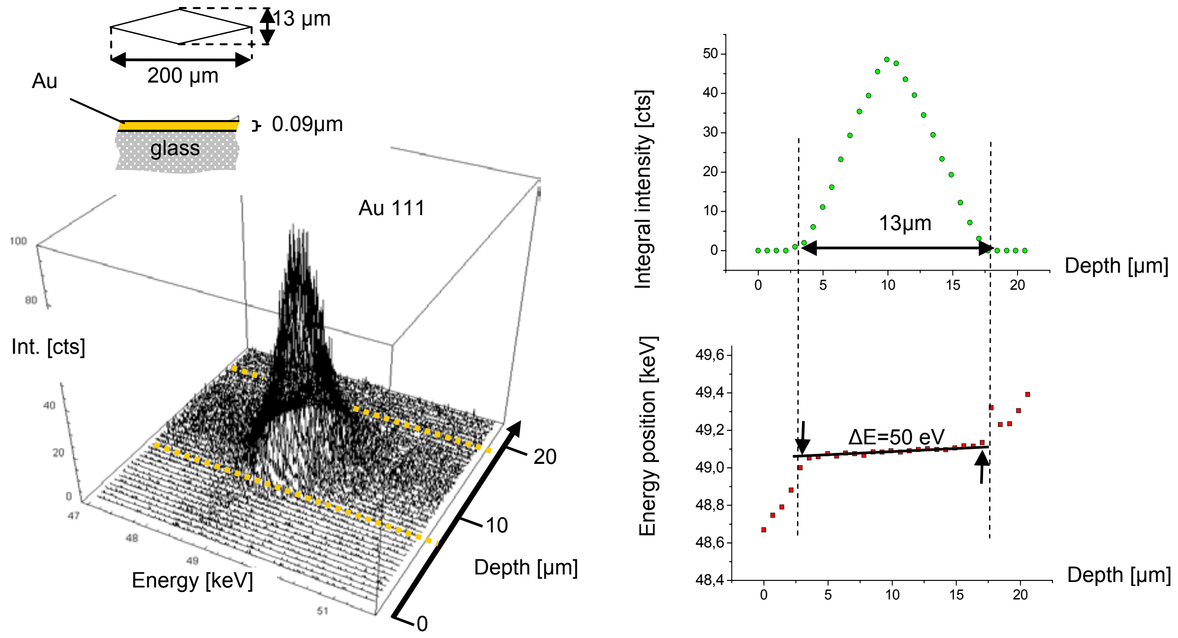

Fig. 1:
Left: Stack plot of the 111 Au diffraction peak obtained from a depth scan covering 30 µm in 0.8 µm steps.
Right: Analysis of the 111 Au diffraction line in terms of integrated intensity and line position shows both, high spatial resolution and a defined energy position.

However, by means of the conventional Laplace methods, the stress state in identical layers can not be investigated separately.
For the scanning experiment a 16 µm multilayer system has been chosen, which contains two TiN layers on top and on the bottom, respectively; the intermediate layers have a total thickness of approx. 9 µm. The gauge volume used is 13 µm in height and 200 µm in width.

The stack plot in Fig. 2 (left) contains all diffraction lines within 30 to 50 keV. Diffraction lines from the substrate can be clearly distinguished from layer ones. Diffraction lines from the respective TiN layers are marked in the figure.

Fig. 2 (right) shows the result of the 220 TiN diffraction line analysis. The gauge volume causes a smearing of the information illustrated by the intensity curve. When the gauge volume is situated right between the two TiN layers, it touches both at the opposite corners and two overlapping diffraction lines appear. Hence, the line width increases and the peak fit procedure delivers unstable values. The peak position was corrected in terms of the geometrical effect and thus - at the centre of the layers - represent the strain ε_{33} owing to the transversal contraction caused by the layer inherent residual stresses. The difference in energy of some 40 eV corresponds to $\varepsilon_{33} \approx 5\cdot10^{-4}$.

Acknowledgement

The authors are indebted to the German Research Foundation (DFG) for financial support of parts of the investigations, Reference number GE 853/2-1 & 2.

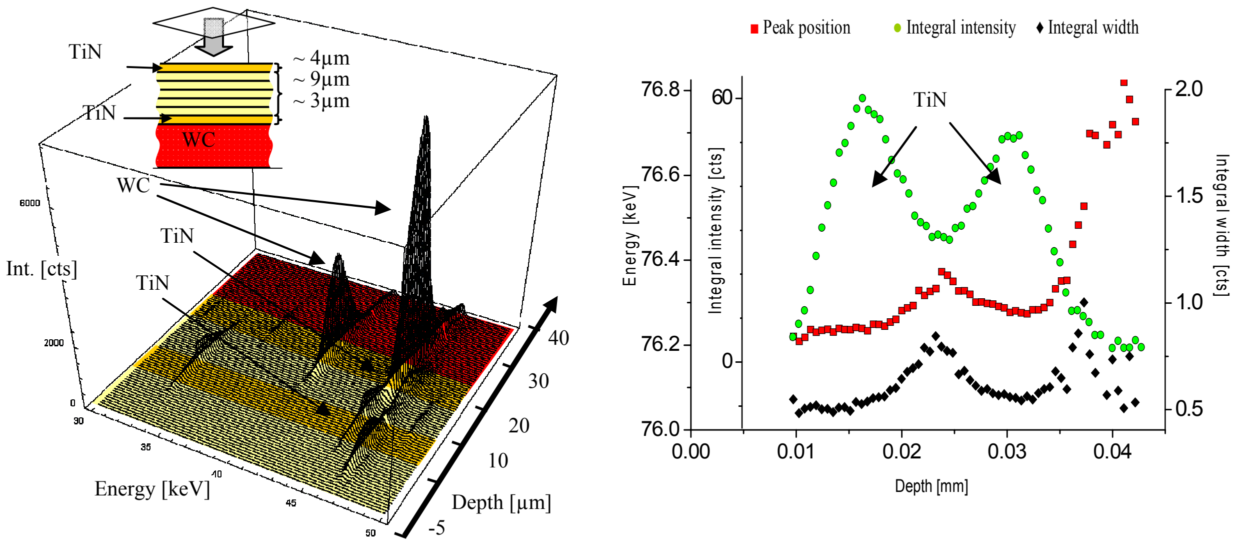

<u>Fig. 2:</u>
<u>Left:</u> Scanning of a multilayer system with two TiN layers. Intensity from 30 to 50 keV plotted vs. the depth illustrates the different information regions regarding multilayer system and substrate. The step in intensity in approx. 10 µm depth is due to the injection.
<u>Right:</u> The analysis of the 220 TiN diffraction line shows that the two neighbouring layers can be clearly distinguished.

References

[1] Ch. Genzel, I.A. Denks, M. Klaus: submitted to the ECRS7, Berlin, 2006

[2] P.J. Withers, P.J. Webster: Strain Vol. 37 (2001), p. 19 - 33

[3] U. Lienert, H.F. Poulsen, R.V. Martins, A. Kvick : Materials Science Forum Vol. 347 – 349 (2000), p. 95 – 100

[4] I.A. Denks, M. Klaus, Ch. Genzel: submitted to the ECRS7, Berlin, 2006

Supercooled High Spin State in Metallo-supramolecular Assemblies

Y. Bodenthin[1], G. Schwarz[2], U. Pietsch[1], D. G. Kurth[2*], H. Möhwald[2]
[1]*University Siegen, FB7 Solid State Physics, D-57068Siegen (Germany)*
[2]*Max Planck Institute of Colloids and Interfaces, D-14424 Potsdam (Germany),*
[*]*National Institute for Materials Science, 1-1 Namiki, Tsukuba, Ibaraki 305-0044 (Japan)*

At Bessy II we investigate the thermodynamic properties of a metallo-supramolecular polyelectrolyte-amphiphile-complexes (PAC), showing an unusually supercooled high-spin phase accompanied by a structural reorganization of the system. Contrary to the previous observation in thin films of PAC, were we find a complete reversible spin transition at room temperature, the spin transition is irreversible in bulk material and shows a shift of spin transition temperature, T_{SC}, towards higher temperatures. The polyelectrolyte-amphiphile-complex (PAC) used here is made by sequential self-assembly of 1,4-bis(2,2´:6´,2´´-terpyridine-4´-yl)benzene, a ditopic bis-terpyridine ligand, Fe^{2+} and dihexadecyl phosphate (DHP) as amphiphilic component.[1] In the solid state, PACs show thermotropic polymorphism and the structure of the system can be described by a lateral arrangement of lamella of MEPE separated by hexagonal closed packed DHP strata (Figure 1).[2]

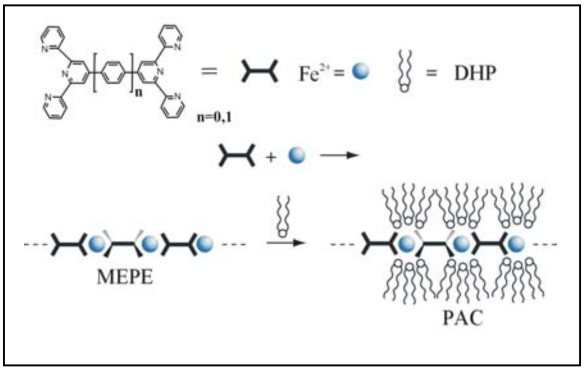

Figure 1: Self-assembly of ditopic bis-terpyridine ligands, iron ions and amphiphiles results in metallo-supramolecular coordination polyelectrolytes (Fe^{2+}-MEPE) and the corresponding polyelectrolyte-amphiphile complexes (PAC).

To explore the origin of the apparently stable high spin fraction we take a detailed look at the structure of PAC at the Energy Dispersive Reflectometer (EDR) at the BESSY II.[3] Small angle x-ray scattering (SAXS) patterns are collected in transmission geometry as a function of temperature using two energy-dispersive Röntec detectors with a resolution of $\Delta E/E=10^{-2}$. To enhance the accessible q range we install the detectors at two different scattering angles of $2\theta=2.79°$ and $2\theta=5.78°$, providing good counting statistics in a q range of 0.1 Å$^{-1} \leq q \leq 0.8$Å^{-1}. This setup provides a time resolution of 60s per spectra and allows determining structural changes as a function of temperature.

Figure 2 summarizes the collected SAXS pattern of PAC of a heating and cooling cycle with 1K/min. The peak at q=0.15 Å^{-1}, which is continuous over the entire temperature range is associated with the K-fluorescence of Fe^{2+} ions at E=6.4 keV. The black bar between 395K and 400K is ascribed to the lack of intensity during the injection process of the electron storage ring. The two signals at q=0.22 Å^{-1} and q= 0.44 Å^{-1} at 303K represent the 1st and 2nd order scattering peak suggesting a stacks-of-layers superstructure with a translational period of d=28.8 Å.[4] At 328K the two scattering peaks shift towards lower q values of q=0.206 Å^{-1} and q=0.41 Å^{-1}, respectively. This is reflecting a widening of the superstructure to d=30.5 Å. At the spin transition temperature of T_{SC}=415K the first order scattering peak becomes broad. This is accompanied by the appearance of a new second peak at q=0.31 Å^{-1}. The appendant second order scattering peak can be found at q=0.62 Å^{-1} reflecting a new structure with a characteristic length of d=20 Å. At T~420 K a broad peak becomes visible reflecting the diffuse scattering associated with the disorder induced during the spin transition. The new structural phase remains stable during cooling down to room temperature. This result verifies the assumption that the spin transition is associated with the formation of a new structure.

In order to clarify the origin of the magnetization we measure X-ray circular dichroism (XMCD) on PAC at the iron L-edge. The measurements are performed at the UE56/1 PGM beam line at BESSY II using the ALICE diffractometer[5]. Because of the high absorption of the thick free-standing films, XMCD measurements in transmission are not successful. Therefore, the X-ray reflectivity of the sample, placed on a silicon wafer, is measured at fixed angle of incidence ($\alpha_i=2°$) using circularly polarized synchrotron radiation and an alternating external field of $B = \pm 0.27$ T. This method offers high accuracy and is an element selective probe of the magnetism in the super-cooled high-spin phase. Figure 3 shows a typical XMCD measurement of PAC. The two distinct minima at 708 eV and 721 eV correspond to the L_3 and L_2 absorption edges of iron. The intensities of the minima differ for both directions of the applied longitudinal filed of B = ±0.27 T. The difference in reflectance is displayed by the asymmetry ratio $A(E) = (I_+ - I_-)/(I_+ + I_-)$. We find an asymmetry of about (0.8 ± 0.2)% for PAC. This asymmetry at the iron L_3 edge at 706 eV is clear evidence that the magnetism is caused by the iron ions.

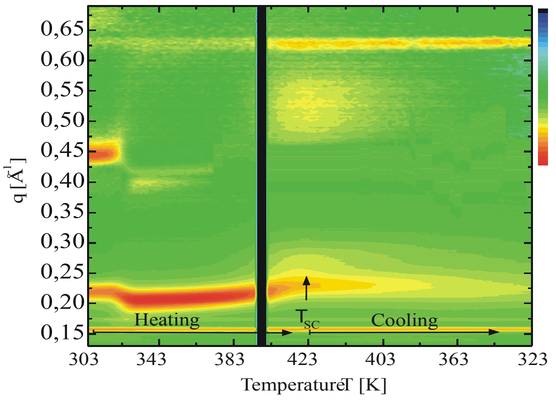

Figure 2: Energy-dispersive SAXS pattern of PAC collected in transmission. The time resolution of 60s per spectra allows determining structural changes as a function of temperature. Clearly, the spin transition at T_{SC}=415 K is connected with the appearance of a new structure, which remains stable during cooling to room temperature.

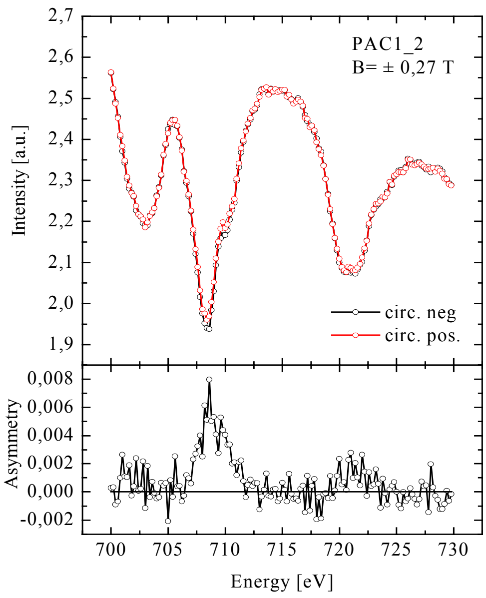

Figure 3: X-ray Magnetic Circular Dichroism (XMCD) measurement at the $L_{3,2}$ edge of iron (top) of a PAC sample with two amphiphiles per metal center. The spectra is recorded in reflection at a fixed angle of incidence (α_i=2°). Bottom: The asymmetry ratio $A(E) = (I_+ - I_-)/(I_+ + I_-)$ between both directions of the applied longitudinal Filed of B = ±0.27 demonstrates the occurrence of molecular magnetism.

This work was supported by Deutsche Forschungsgemeinschaft as part of the priority program 1137 “Molecular Magnetism”.

---

[1] D. G. Kurth, P. Lehmann, M. Schütte, *Proc. Natl. Acad. Sci.* 97 , 5704- 5707,2000

[2] A. Meister, G. Förster, A. F. Thünemann and D.G. Kurth, *CHEMPHYSCHEM* 2003, 4, 1095-1100

[3] U. Pietsch, J. Grenzer, Th. Geue, F. Neissendorfer, G. Brezsesinski, Ch. Symietz, Möhwald, W. Gudat, Nucl. Instrum. Methods 467-468, 1077, 2001

[4] D. G. Kurth, A. Meister, A. F. Thünemann, G. Förster, Langmuir, 2003, 19, 4055

[5] J. Grabis, A. Nefedov, H. Zabel, Rev. Sci. Instr. 74, 4048, 2003

XANES investigation of iron, oxygen, nitrogen and bromine elements in aminoacid derivatives of protoporphyrin IX.

M.S. Walczak[1], K. Lawniczak-Jablonska[1], M. Klepka[1], H. H. Rossner[2], M. Czuba[3], A. Graczyk[3]

[1] *Institute of Physics, Polish Academy of Science, Al. Lotników 32/46, 02-668 Warsaw, Poland*
[2] *Hahn-Meitner-Institut Berlin, Glienicker Straße 100, D-14109 Berlin, Germany*
[3] *Institute of Optoelectronics, Military University of Technology, ul. Stefana Kaliskiego 2, 00-908 Warsaw, Poland*

We investigated compounds which serve as photosensitive drags in photodynamic diagnosis and therapy (PDT) – treatment for malignant diseases employed nowadays in many clinical applications. The ideal photosensitizer should have such specificity to be able selectively load in the malignant tissue and produce reactive oxygen species (ROS) upon illumination with definite wavelength of light. ROS are responsible for cells' destruction and death. At the Laboratory of Biochemistry and Spectroscopy (Military University of Technology) new class of photosensitizes was produced – diaminoacid (alanine - Ala, arginine - Arg, serine - Ser, phenylalanine – Phe) derivatives of protoporphyrin IX. [1, 2] The good ability of these compounds in cancer therapy was confirmed by performed treatment on animals and humans. However, determination of the detail structure and especially position of iron and bromine atom in molecule is needed to put them on officially used cancer drugs list.

Iron and bromine L-edges and oxygen and nitrogen K-edges were acquired at U41 - PGM beamline (BESSY). X-ray energies were selected using grating with 600 l/mm. Spectra were detected by one-element germanium detector and channeltron. The reported spectra for protoporphyrins were collected in fluorescence mode. Several spectra were summed up till a reasonable statistics was achieved. All the spectra were recorded at room temperature and under high vacuum.

The examples of the Fe L_3 and L_2 – edges of protoporphyrins with several amino acid attachments are shown in Fig.1 after background subtraction and normalization to the same value at the L_3 edge intensity.

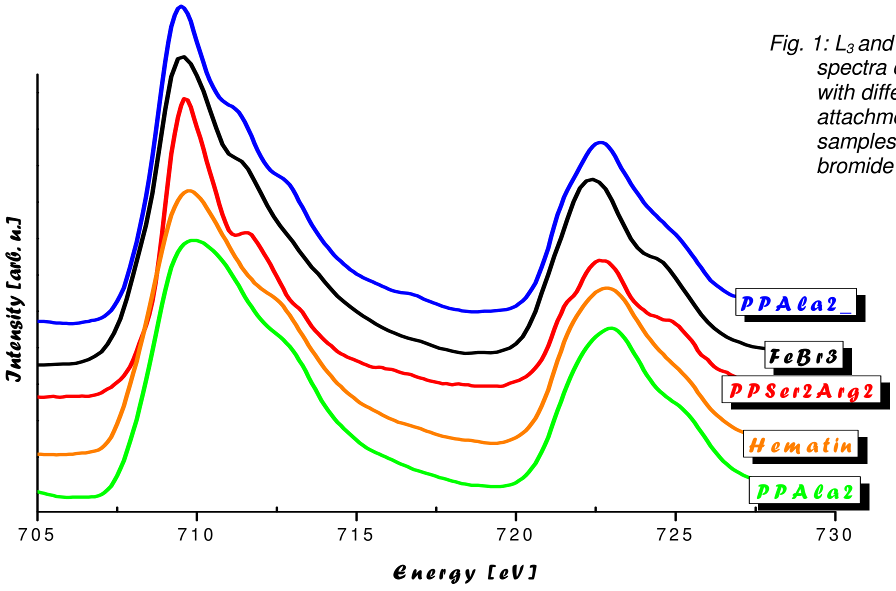

Fig. 1: L_3 and L_2 – edge Fe XANES spectra of protoporphyrins IX with different amino acid attachments and reference samples: hematin and iron (III) bromide

There is clearly visible that spectra differ from each other and can be grouped in three classes:

- PPAla2 (one molecule is built by protoporphyrin and two alanine amino acids): two slightly-separated components at L_3 and L_2 edges are observed, structure is similar to that of hematin
- PPSer2Arg2 (one molecule is built by protoporphyrin, two arginine and two serine amino acids): the second peak at the L_3 edge is more resolved and shifted toward lower energies and the third component on the right slope emerged, structure similar to the $FeBr_3$
- PPAla2_ (one molecule is built by protoporphyrin and two alanine amino acids): three peaks at the L_3 edge , structure is probably the mixture of hematin and $FeBr_3$.

Samples PPAla2 and PPAla2_ have the same nominal composition but the location of Fe ions differs. Judging from the observed shape of the L_3 edge, in the first group most of the Fe atoms have similar surrounding as in protoporphyrin ring (hematin), in second class Fe surrounding is similar to that in $FeBr_3$ and in third class we have a mixture of both.

Bromine L_3 edges are easily detectable in all investigated samples, Fig. 2. We suppose that some of the Br atoms are bonded into iron (III) bromide but surrounding of others is different, because shape of the Br edge varied in each of investigated sample. We considered the possibility of existence $FeBr_2$ but one cannot fit the shape of Br edge by simple weighted sum of both compounds. The location of Br atoms in the molecule need advanced modeling exploring the FEFF8 codes.

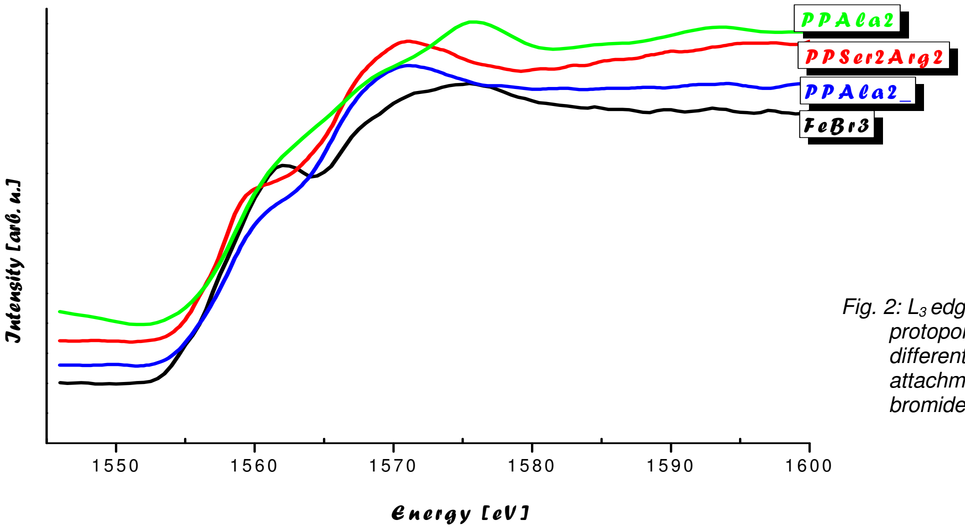

Fig. 2: L_3 edge Br XANES spectra of protoporphyrins IX with different amino acid attachments and iron (III) bromide compound

We have observed also differences in shape of K-edges of oxygen and nitrogen, Fig. 3. The studied photosensitizers had attached different amino acids, each of acid consists of different number of oxygen and nitrogen atoms, therefore the edges have to be different. However, differences in edge shape were observed also for PPAla2 and PPAla2_, samples nominally the same. One of explanations is that these two protoporphyrins have different ratio of attached alanine amino acid or Fe and Br atoms are located in each of them at different places.

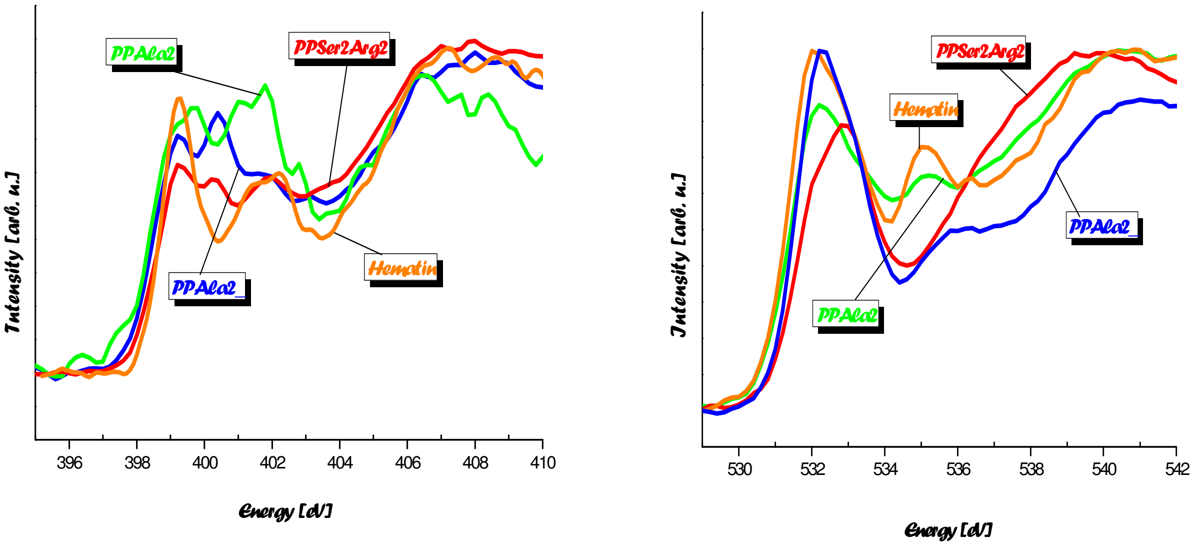

Fig. 3: K edge N (left) and K edge O (right) XANES spectra of protoporphyrins IX with amino acid attachments.

We observed a lot of changes in the measured edges of Fe, Br, O and N. This indicated on different atomic order in these samples. The determination of these differences need consideration of many possible models and simulation of the spectra. This analysis is in progress.

Acknowledgments

This work was partially supported by the State Committee for Scientific Research (Republic of Poland) *(Grant No72/E-67/SPB/5.PR UE/DZ 27/2003-2005)* and by the RII3-CT-2004-506008 and G1MA-CI-2002-4017 (CEPHEUS) of the European Commission.

References

[1] S. Ye, M. Czuba, et al. Optica Applicata, vol. XXXIII, no. 2-3 (2003)
[2] S. Ye, M. Kwasny, M. Czuba, A. Graczyk, Optica Applicata, vol. XXXIII, no. 2-3 (2003)

The oxidation state and phase content of Fe in Norwegian ilmenite estimated using XANES spectra

M. Klepka[1], K. Lawniczak – Jablonska[1], M. Jablonski[2], M.S.Walczak[1], H.H.Rossner[3]

[1] Institute of Physics, Polish Academy of Sciences, Al. Lotnikow 32/46 PL-02668, Warsaw, Poland
[2] Technical Uniwesity, Szczecin, Institute of Chemistry and Environmental Protection, Al. Piastow 42, PL-71065 Szczecin, Poland
[3] Hahn-Meitner-Institut Berlin, Glienicker Str. 100, D-14109 Berlin, Germany

Norwegian ilmenite is a natural mineral used by many companies all over the world as a source of TiO_2 – white pigment. The composition of minerals varies depending on the place where they are collected (e.g. Norway, Australia, India, China). TiO_2 is produced mainly by sulphate method, where reaction of titanium raw material with sulphuric acid is the first step of the process [1, 2]. Knowledge about Fe and Ti, main elements in raw mineral, oxidation state and phase content is very important for proper adjustment of conditions of chemical reactions. Aware of fact that the shape of XANES spectra is a fingerprint of chemical state of elements we have studied the L – edge of Fe from Norwegian ilmenite and reference samples at Bessy U41 PGM station. As reference samples the ilmenite compound ($FeTiO_3$), FeO and hematite (Fe_2O_3) were selected. The samples were powdered and pressed into conductive carbon tape. Spectra were registered in fluorescence mode, using single element Ge detector, at room temperature.

XANES of Fe at L and K – edges in investigated materials are presented in Fig 1 and Fig 2, respectively. The K – edges have been measured in Hasylab at A1 station. Results from analysis of Ti K and L – edges, confirmed that Ti is in the mineral only on Ti $^{+4}$ oxidation state [3].

According to the K and L – edges position Fe oxidation state in Norwegian ilmenite is close to that in ilmenite compound but differ slightly from that in FeO (Fe $^{+2}$). Nevertheless the shape of spectra differs what indicates presence of other compounds. For phase analysis we use the principal component approach and XANDA dactyloscope freeware program [4]. This approach based on the assumption that if the element is bound in several chemical compounds, the spectrum is a weight sum of the spectra of these compounds. The analysis of Fe L – edge gives 89,1 ± 1 % of ilmenite compound and 10,9 ± 1,2 % of hematite (Fig 3). The same analysis was perform for K – edge and results were 87,3 ± 0,3 % of ilmenite compound and 12,7 ± 0,3 % of hematite (Fig 4). No Fe in the phase of FeO oxide was detected. Analysis of both edges provides the same result in the limit of errors.

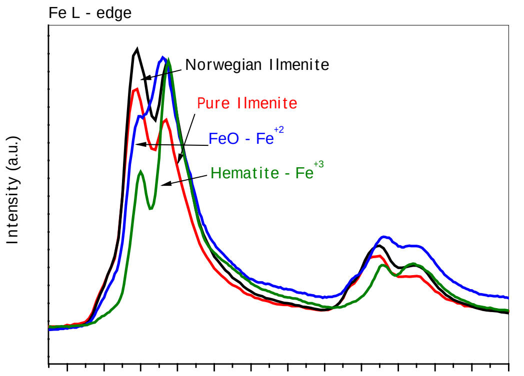

Fig 1.

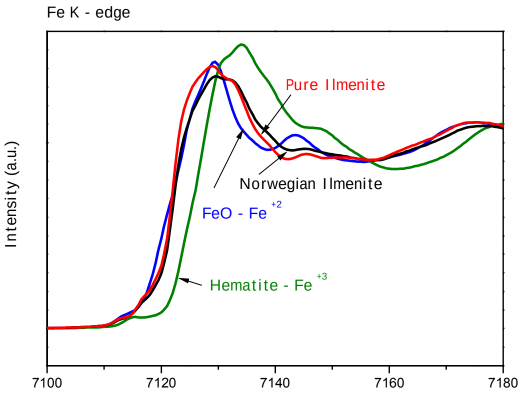

Fig 2.

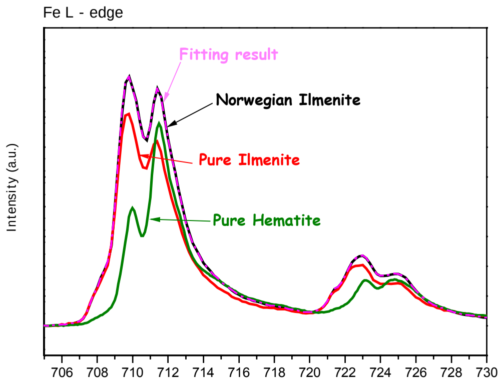

Fig 3.

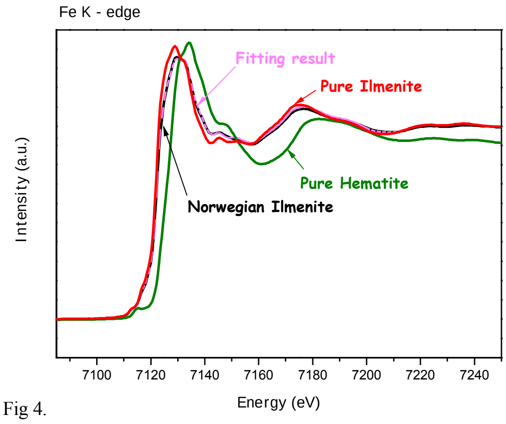

Fig 4.

In the mineral some of the Fe or Ti atoms in $FeTiO_3$ compound can be substituted by other minority elements. The Electron Probe Microanalysis (EPMA) from 270 points gives the following elements content.

Element	Atomic content ± standard deviation in %
O	60 ± 9
Fe	16 ± 7
Ti	15 ± 7
Mg	4 ± 3
Si	3 ± 6
Al	1 ± 3
V	1 ± 1
Ca	0,4 ± 1

The large standard deviation in the estimation of elements content indicates on the non-homogeneity of mineral compositions. Thus in some of the analyzed grains of mineral, either minority elements are present in the form of oxides, either substituted in Ti or Fe position in ilmenite. To check this, it is necessary to measure XANES at the edges of these minority elements and reference oxides, what we plan to perform in the future.

The standard powder x – ray diffraction was also performed to gain quantitative information about phase content in mineral. But due to the fact that substitution of other elements in ilmenite change lattice constant and intensity relation between particular diffraction peaks, it was impossible to get quantitative information. Introducing as a starting point in Rietveld analysis information from XANES measurements, we result in following phase content: 91,8 % of ilmenite compound, 8,2 % hematite and third minority phase enstatite ($MgSiO_3$). The presence of this phase is only one from several considered in Rietveld analysis and should be checked by measurements of XANES.

We would like to continue studies on Australian, Indian and Chinese ilmenite to compare the content of particular phases, which has an impact on the amount and quality of final industrial product. The knowledge of phase content enables to properly adjust thermodynamic of chemical reaction what can result in economic profit.

Acknowledgments

This work was partially supported by the State Committee for Scientific Research (Republic of Poland) *(Grant No72/E-67/SPB/5.PR UE/DZ 27/2003-2005)* and by the RII3-CT-2004-506008 and G1MA-CI-2002-4017 (CEPHEUS) of the European Commission.

References

[1] T. Chernet, Minerals Engineering, 12 (1999) 485
[2] R.G. Teller, et al., J. Solid State Chem., 88(1990), 351-367
[3] M. Klepka, et al, J. Alloys and Compounds, 401 (2005) 281 – 288
[4] K.V. Klementiev, XANES dactyloscope for Windows, freeware: www.desy.de/~klmn/xanda.html

The effect of cryogenic treatment on structural and phase transformations in iron martensite – the role of stresses

Karen Pantleon, Allan Stojko, Marcel A.J. Somers

Technical University of Denmark, Department of Manufacturing Engineering and Management
IPL Building 204, DK – 2800 Kgs. Lyngby, Denmark

The wear performance of tool steels and the associated lifetime can be improved essentially, up to a factor 7, due to cryogenic treatment, i.e. storing the hardened material (after quenching and prior to tempering) at temperatures as low as -196°C. Although the process is very popular in the USA and impressive results show the effectiveness of cryogenic treatment, so far scepticism has prevented its large-scale application in Europe. This scepticism finds its origin in the absence of a scientific explanation for the improvement of the wear performance and the mystification of the subject in literature.

Hardening of steel, i.e. carbon containing iron, consists of heating the materials to a temperature where the fcc crystal structure of iron (austenite) is thermodynamically stable. During cooling to room temperature the austenite phase tries to transform to bcc-iron (ferrite) and iron carbides. The carbon content of austenite in hardenable steel is much higher than the solubility for carbon in ferrite and thus, if cooling proceeds so fast that long-range diffusion of carbon is prevented, the bct martensite phase is formed, which is supersaturated with carbon atoms. Additional tempering is required, in the course of which carbides develop and an optimization of strength and toughness can be achieved. The transformation of austenite and martensite is associated with a volume expansion, which implies the introduction of a state of compressive stress in the not yet transformed (retained) austenite. These compressive stresses can become so high that further transformation of austenite to martensite virtually ceases. A remedy to reduce the content of retained austenite is cooling to a temperature below room temperature. The larger fraction of transformed austenite is expected to influence the magnitude and distribution of internal stresses within the material [1], which finally may explain the beneficial effect of cryogenic treatment.

Various steel samples (AISI 52100 and AISI 1070) have been heat treated differently applying

i) conventional heat treatment, i.e. hardening with subsequent annealing,
ii) deep cooling down to -80ºC after hardening prior to annealing and
iii) cryogenic treatment down to -180ºC after hardening prior to annealing.

Conventional X-ray diffraction carried out on these samples confirmed that the fraction of retained austenite essentially decreases as a result of the sub-zero treatment. Additionally, the fraction of retained austenite becomes lower (and finally becomes zero) with increasing annealing temperature. For stress analysis, conventional X-ray diffraction is not suitable, because the penetration depth in steel is limited to about 10 μm and, at least, for the austenite phase reflections are very weak according to the low volume fraction contributing to diffraction.

Synchrotron measurements at BESSY were aimed to the investigation of internal stresses both in the martensite and the austenite phase as well as to the study of the depth dependence of stresses. The experiments were carried out applying energydispersive synchrotron diffraction at the beamline EDDI, where we actually have been the first users after commissioning of the beamline.

Energydispersive diffraction spectra were collected at a fixed diffraction angle of 2θ = 10°, for which a multitude of reflections was expected in a wide energy range according to Fig. 1.

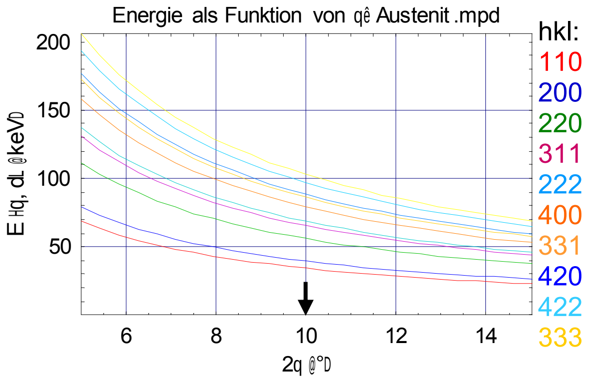

Fig. 1: Relation between the diffraction angle 2θ (2θ = 10° was used) and the position of various reflections hkl on the energy scale for the example of the austenite phase, calculated applying the software package EDDI (Genzel, HMI Berlin).

For the analysis of lattice strain (stress) the samples were tilted applying azimuth angles 0 ≤ ψ ≤ 86° with a step size of Δψ = 2° and stresses were determined for the various diffracting lattice planes according to the $\sin^2\psi$-method [2]. Energy spectra were recorded by means of a Ge-detector for a measurement time of 300 s for each spectrum (results show that even 200 s yields reliable results). For comparison, measurements with conventional X-rays in the angular dispersive mode, i.e. applying standard laboratory equipment, require a measurement time of some hours and only very few reflections can be obtained within the available measurement range.

For data evaluation the software package EDDI (Genzel, HMI Berlin) was used. An absorption correction was applied assuming that all phases behave the same with respect to absorption. Additionally, measured intensities were corrected for background. Peaks were fitted with a Gauss function. Overlapping peaks of different phases as well as splitted peaks due to tetragonal martensite were separated by least square fits of two Gauss functions. The position of reflections on the energy scale was calibrated applying suitable reference samples.

The energy spectrum obtained without tilting the sample (ψ = 0°) was used for phase analysis. As Fig. 2 shows, recorded energy spectra revealed reflections of reasonable intensity in the energy range between 20 keV and 120 keV.

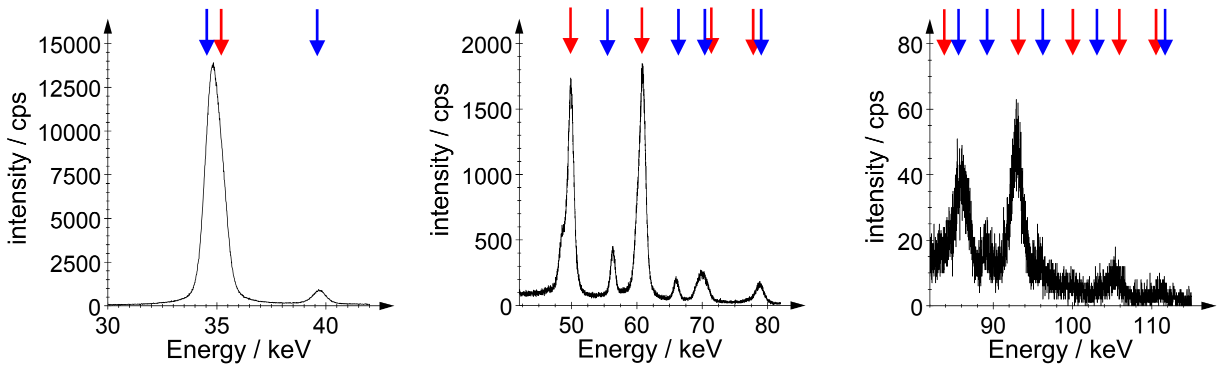

Fig. 2: Example of an energy spectrum as obtained for AISI 1070 after hardening with subsequent annealing at 60°C (conventional heat treatment). Reflections of the martensite and austenite phase (blue) are marked.

Qualitative phase analysis indicates that the presence of various phases strongly depends on i) the type of steel (AISI 1070 or AISI 52100), ii) the type of heat treatment (conventional, with additional deep cooling or with additional cryogenic treatment) and iii) the annealing temperature (between 60°C and 350°C). Martensite/ferrite, retained austenite as well as various carbide phases can be identified. Compared to conventional X-rays, synchrotron radiation yields a clear advantage for identifying carbides with a rather low volume fraction and consequently, very small diffracted intensities.

Since for energy dispersive diffraction a multitude of reflections is recorded simultaneously and each reflection originates from a specific penetration depth [3], stress analysis was carried out for various reflections and by this, as a function of depth ranging from about 6 µm to 73 µm. An example for the depth dependence of internal stresses as obtained both for the martensite and the austenite phase is shown in Fig. 3. It should be emphasized that even for rather small diffracted intensities of retained austenite corresponding to small amounts of not transformed austenite, stress analysis was possible; thus, results clearly indicate the great advantage of measurements with synchrotron radiation.

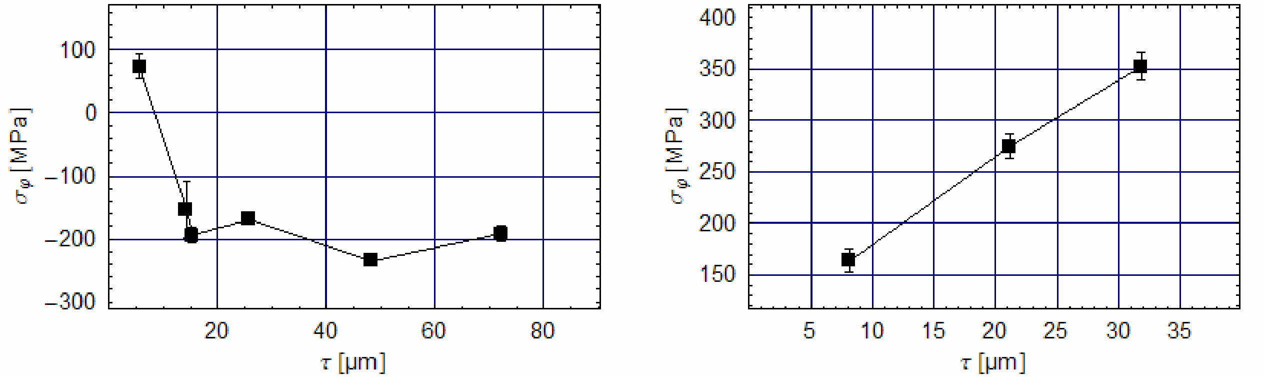

Fig. 3: Example for the depth dependence of internal stresses in the martensite and austenite phase of AISI 1070 after hardening with subsequent annealing at 60°C (conventional heat treatment). Only non-overlapping reflections were considered here.

Results show that both magnitude and depth profile of stresses are affected by an additional treatment of the hardened steel at sub-zero temperatures (deep cooling, cryogenic treatment) prior to annealing. Furthermore, a strong effect of the applied annealing temperature was observed. Results on the depth profile of the phase related stresses, i.e. stresses in martensite, in austenite and also in the various carbides, will be supplemented by neutron diffraction experiments at BENSC covering even larger depths.

[1] A. Stojko, R.B. Frandsen, M.A.J. Somers, Kryogenbehandling – vejen til forståelse, Winter Meeting of the Danish Metallurgical Society (2003), 187-206.

[2] Structural and residual stress analysis by nondestructive methods, ed.: V. Hauk, Elsevier Science, The Netherlands 1997.

[3] Ch. Genzel, C. Stock, W. Reimers, Mater. Sci. Engineering A372 (2004) 28-43.

We wish to thank Ch. Genzel and co-workers (HMI Berlin) for the excellent support and the outstanding interest in our work.

Integer Fe 3d Spin Moments in high quality magnetite single crystals

E. Goering, M. Lafkioti, and G. Schütz
Max-Planck-Institut für Metallforschung, Heisenbergstrasse 3, 70569 Stuttgart, Germany

We performed detailed magnetic absorption spectroscopy of in situ cleaved high quality single crystals of magnetite. The experimental setup was carefully optimized to reduce drift, self absorption, and offset phenomena as far as possible. Our results are in strong contradiction to recently published data. We found nearly vanishing orbital moments, and spin moments quite close to the integer values proposed by theory. This important results supports the half metallic full spin polarized picture of magnetite, and is a key issue to understand the Verwey transition, which is still under discussion.

Fe_3O_4 shows a phase transition, the so called Verwey transition at $T_V \approx 123$K, accompanied by a jump in the electrical conductivity, extensively investigated in the last. Today magnetite has attracted enormous interest, because of the proposed high-spin-polarization and related possible applications[1]. The nature of the conducting electrons and the influence of local electronic correlations are one of the key issues to understand Fe_3O_4 [2].

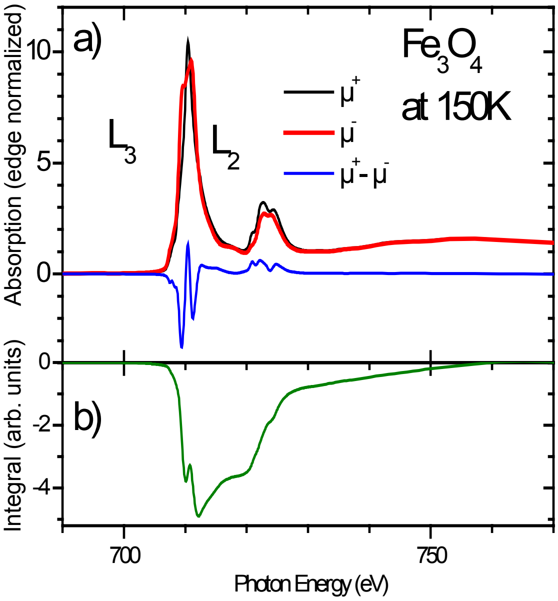

Figure 1: a) X-ray absorption and XMCD spectrum of a fractured single crystal of Fe_3O_4 at 150K and normal incidence geometry. b) Integrated XMCD spectrum used for sum rule analysis.

Fe_3O_4 crystallizes at room temperature in the antiferromagnetic cubic inverse Spinel structure ($Fd\bar{3}m$), formally written as Fe(A) $Fe(B)_2O_4$ [3]. The *A*-type ions are tetrahedrally coordinated and nominally in a Fe^{3+} ($\approx -5\mu_B$) configuration. The *B*-site ions are located on octahedral sites and mixed valent with equally distributed Fe^{3+} ($\approx +5\mu_B$) and Fe^{2+} ($\approx +4\mu_B$) ions. The magnetic moments of the *A* and *B* sites are aligned antiparallel to each other with a resulting magnetization per formula unit $5_B+4_B-5_A = 4\mu_B$, consistent to the experimental result of $4.07\mu_B$ [4]. An observation of an integer spin moment is therefore a clear indication for a *B*-site minority electron conduction mechanism, and its accompanied full spin polarization.

In a recent Letter [5] the spin and orbital Fe 3d magnetic moments of magnetite have been evaluated experimentally by X-ray magnetic circular dichroism (XMCD) and calculated within the LDA+U framework. Non integer spin moments and large unquenched orbital moments of $0.33\mu_B$ have been found per B-site ion, which have been attributed to a strong onsite Coulomb interaction and corresponding 3d correlation effects. In contrast, other reported band structure calculations and LDA+U calculations using the original LDA+U functional found only small orbital moments, and the Fe spin moments were just slightly reduced from the integer value due to hybridization with O [2,6-8].

Our XMCD experiments, discussed below, are consistent to the majority of theoretical predictions [2,6-8], confirming the integer moment description and the full spin polarized model of Fe_3O_4 with an very small integral orbital moment. To clearly point out the quality and validity of our results, we have discussed the experimental procedure and possible experimental error sources, like surface effects, signal drift, self absorption, and offset phenomena in detail elsewhere [9].

All XMCD spectra have been measured in total electron yield mode (TEY) at the BESSY II bending magnet beamline PM3 in an applied magnetic field of 10kOe. All sum rule related values have been corrected for the finite circular polarization of 0.93±0.02. The sample magnetization has been flipped at every data point to compensate even for smallest synchrotron related drift phenomena. In addition, the results have been verified for opposite light helicity. The monochromator energy resolution was set to ≈6000. High quality synthetic single crystalline samples have been prepared by V.A.M. Brabers in an arc-image furnace using the floating zone technique, For details see Ref. [9,10]. The single crystal has been *in situ* cleaved. We have demonstrated that the shown absorption results of the cleaved single crystal used here, exhibit bulk properties of magnetite [10].

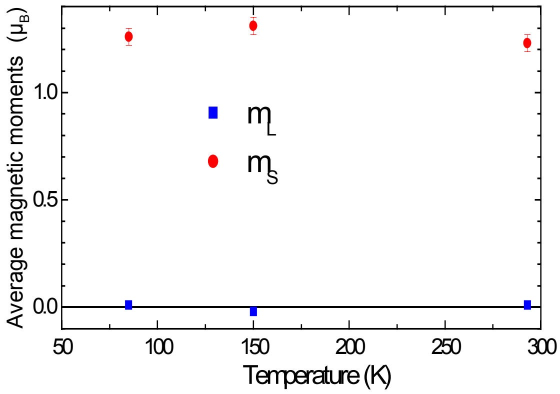

Figure 2:Spin and orbital magnetic moments, determined for a short and extended integration range at different temperatures (see text).

A typical XAS and XMCD spectrum is shown in Fig.1a. The integrated XMCD signal (Fig. 1b) exhibits a non vanishing slope between 730-765eV, which is related to a very small and reproducible XMCD signal above the L_2 edge region.

Sum rules [11,12] have been applied for an extended integration range (718-764.5eV) to take into account the small high energy XMCD signal. N_h/Fe=13.5/3 has been used for the number of 3d holes as in Ref. [5]. The sum rules results are shown in Fig.2. For the orbital moments the estimated error bar is about the symbol height. Only minor temperature dependencies are observable, quite comparable to SQUID related magnetization curves. An important point is the absence of prominent difference between above and below the Verwey transition.

The average orbital moments are -0.001μ_B. The obtained average sum rule related effective spin moment/FU is $3^*(m_s+<T_z>)=3.90\pm0.09\mu_B$ .Our results demonstrate the necessity of high quality wide range XMCD data for Fe_3O_4 to extract correct spin and orbital moment values. The origin of this difference to Ref [5] is most likely not related to the physics of Fe_3O_4, and has been discussed in more detail elsewhere [13]. Saturation effects have been carefully checked (see Ref, [9]).

In conclusion, the shown carefully performed experimental XMCD results are in very good agreement to the majority of theoretical investigations of magnetite. Self absorption and other experimental effects have been neglected as a possible source of significant orbital moment variation. Taking into account an extended XMCD integration range gives a magnetic spin moment, quite close to the expected integer value of 4μ_B, while the orbital moment vanishes. This result clearly supports the full spin polarized picture of magnetite.

We thank M. Fähnle, F. Walz, and H. Kronmüller for fruitful discussions, and the Max-Planck-Society for financial support. Many thanks to V.A.M.Brabers providing the magnetite sample and T. Kachel from BESSY II for support during the beamtime.

References

1. J. M. D. Coey, J. J. Versluijs, and M. Venkatesan, J.Phys.D: Appl.Phys. **35**, 2457 (2002).
2. Ze. Zhang and S. Satpathy, Phys.Rev.B **44**, 13319 (1991).
3. P. W. Anderson, Phys.Rev. **102**, 1008 (1956).
4. P. Weiss and R. Forrer, Ann.Phys. **12**, 279 (1929).
5. D. J. Huang, C. F. Chang, H. T. Jeng, G. Y. Guo, H. J. Lin, W. B. Wu, H. C. Ku, A. Fujimori, Y. Takahashi, and C. T. Chen, Phys.Rev.Lett. **93**, 077204-1 (2004).
6. V. N. Antonov, B. N. Harmon, and A. N. Yaresko, Phys.Rev.B **67**, 024417-1 (2003).
7. M. Penicaud, B. Siberchicot, C. B. Sommers, and J. Kübler, J.Magn.Magn.Mater. **103**, 212 (1992).
8. A. Yanase and K. Siratori, J.Phys.Soc.Jpn. **53**, 312 (1984).
9. E. Goering, S. Gold, M. Lafkioti, and G. Schuetz, Europhys.Lett. **73**, 97 (2006).
10. E. Goering, S. Gold, M. Lafkioti, G. Schütz, and V. A. M. Brabers, Phys.Rev.B **72**, 033112-1 (2005).
11. B. T. Thole, P. Carra, F. Sette, and G. van der Laan, Phys.Rev.Lett. **68**, 1943 (1992).
12. P. Carra, B. T. Thole, M. Altarelli, and X. Wang, Phys.Rev.Lett. **70**, 694 (1993).
13. E. Goering, M. Lafkioti, and S. Gold, Phys.Rev.Lett. **96**, 39701 (2006).
14. B. L. Henke, E. M. Gullikson, and J. C. Davis, At.Data Nucl.Data Tables **54**, 181 (1993).

Resonant x-ray diffraction from defect order in NbO

H. Ott, C. Schüßler-Langeheine, M. W. Haverkort, Z. Hu, A. A. Nugroho, C. F. Chang,
J. Schlappa, and L. H. Tjeng
II. Physikalisches Institut, Universität zu Köln, Zülpicher Str. 77, 50937 Köln.
E. Schierle, G. Kaindl and E. Weschke
Institut für Experimentalphysik, Freie Universität Berlin, Arnimallee 14,14195 Berlin.

During the last beam time, we performed the first resonant x-ray diffraction experiment on defect order and made a start-up in the energy range of the $L_{2,3}$ threshold of the 4d Elements. While spectroscopy techniques, like x-ray absorption spectroscopy (XAS), usually provide integrated information about the electronic structure, and conventional diffraction experiments only the structural information, with resonant x-ray diffraction we combine both methods to make spectroscopy on only the ordered part of the sample [1], i.e. the defect order of NbO.

NbO has a quite unique crystal structure. It may be described as based on the rocksalt structure but with a quarter of both metal and oxygen atoms removed. Both, Nb and O occupies sites of square plane coordination in a three dimensional net, which is a very unusual feature for a transition-metal ion with d^3 configuration. The observation of oxygen in a square planar environment is unusual, too. Defect rocksalt structures are frequently found in early transition-metal oxides, nitrides and carbides [2,3,4], and thus the problem is more general than it appears at first sight.

In an otherwise perfect NaCl structure, the compounds may crystallize with varying amounts of metal and oxygen vacancies, resulting in nonstoichiometric chemical formulas MO_x. These compounds generally exhibit a wide stoichiometry and composition range depending on temperature and pressure and leading to a variety of interesting physical properties.

In the prominent cases of TiO_x and VO_x, x ranges from about 0.7 to 1.3. At a composition $TiO_{0.7}$, the Ti sublattice is almost completely occupied, but about one-quarter of the oxygen sites are vacant, while for $TiO_{1.25}$ the oxygen sublattice is almost filled and about quarter of the titanium sites are vacant. In the stoichiometric case (x=1) there are 15% vacant sites of both the titanium and oxygen sublattice [5,6]. As opposed to TiO_x and VO_x, single phase NbO_x exists only in a very narrow range for x between 0.98 and 1.02 [2].

In some cases, when the number of vacancies is large enough, clustering and/or ordering of the vacancies may occur. However, the strength of the vacancy - vacancy interaction is very different from one compound to another, which leads to different thermodynamic behavior of different oxides [6]. In NbO_x the vacancies are ordered up to the melting temperature in the whole x range and as a single phase [6]. In the case of TiO_x two ordered structures of composition x = 1 and x = 1.25, respectively, appear below 1273 K, while VO_x is always disordered (short-range order cannot be ruled out). These features indicate that the strengths of the interaction between vacancies are very different from one oxide to another: the interaction is strong in NbO_x, plays a major role in TiO_x around 1273 K and is probably weak in VO_x [6].

Why do these oxides have the structure they have? Focusing on the local coordination of the atoms raises more questions than answers. Madelung energy of this defect structure is unfavorable with respect to ideal rocksalt structure [7]. Some theoretical investigations indicate that the loss in Madelung energy is (over)compensated by the presence of numerous metal-metal bonding levels which are present in the NbO defect structure [7,8]. Both metal-metal bonds as well as metal-oxygen π bonds seems to be responsible for stabilizing these defect structures and for the observed properties and differences in this class of materials. But up to now, there is no experimental proof.

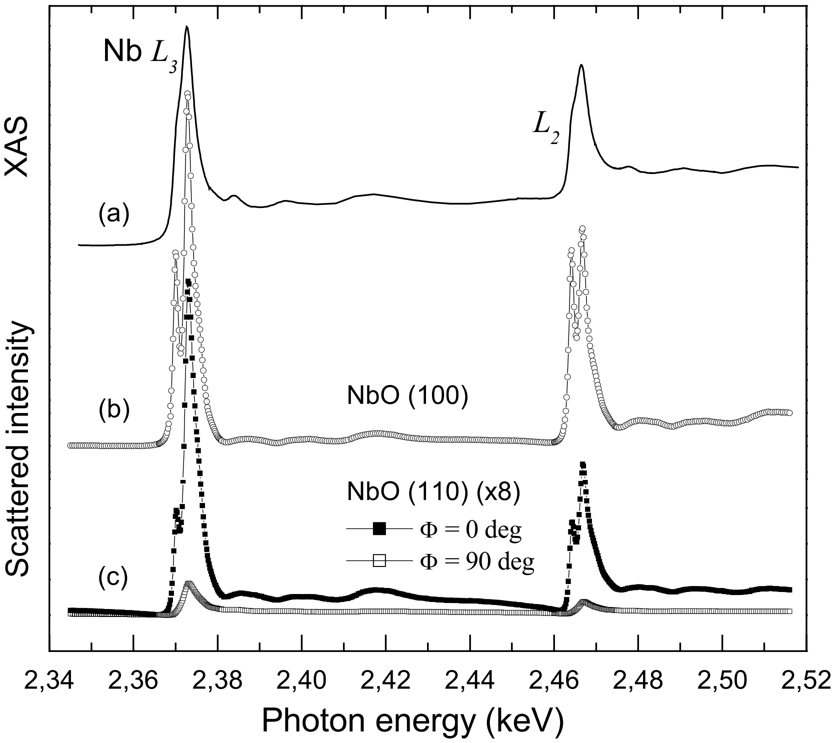

Fig.1: (a) $L_{2,3}$ x-ray absorption spectrum of NbO. (b) Energy dependence of the NbO (100) Bragg peak, representing isotropic scattering. (c) Energy scan of the Nb (110) Bragg peak and its azimuthal dependence.

The tool of resonant x-ray diffraction, i.e. the combination of a diffraction experiment and spectroscopy, provides us the sensitive to the different Nb lattice sites.
The energy dependencies of the Bragg peaks, which can be reached in the photon energy interval of the Nb $L_{2,3}$ threshold ((100) and (110)) are shown in Fig. 1. Diffraction from the (100), shown in Fig 1 (b), represents the isotropic case; it should be entirely describable by the XAS (Fig1 (a)) and its Kamers-Kronig transform, representing the complex scattering factor. Indeed, the (100) does not show a polarization dependence. Information about the different lattice sites and thus complementary information about orbital ordering, orbital occupation and hybridization of and between the Nb ions on different lattice sites caused by the vacancies can be extracted from the energy dependence of the (110), and its dependence on the azimuthal rotation, as shown for 0 and 90 deg in Fig. 1 (c).
Starting with a planar NbO_4 cluster, the calculation of the spectra requires to include the next Nb neighbors to describe the metal-metal bonds, which would not be present in the perfect rocksalt structure and which are assumed by theory to stabilize the defect structure of NbO. The theoretical effort, however, increases rapidly with the number of Nb neighbors and thus requires clever approximations, which is in progress at present.
We acknowledge the BESSY staff for providing us with an extremely stable beam.

[1] C. Schüßler-Langeheine, J. Schlappa, A. Tanaka, Z. Hu, C. F. Chang, E. Schierle, M. Benomar, H. Ott, E. Weschke, G. Kaindl, O. Friedt, G. A. Sawatzky, H.-J. Lin, C. T. Chen, M. Braden, and L. H. Tjeng, *Spectroscopy of Stripe Order in* $La_{1,8}Sr_{0,2}NiO_4$ *Using Resonant Soft X-Ray Diffraction*, Phys. Rev. Lett. 95, 156402 (2005).

[2] Ali M. Okaz and P. H. Keesom, *Specific heat and magnetization of the superconducting monoxides: NbO and TiO*, Phys. Rev. B**12**, 4917 (1975).

[3] E. C. Ethridge, S. C. Erwin and W. E. Pickett, *Metastability of NbN in the ordered NbO phase*, Phys. Rev. B**52**, R8589 (1999).

[4] J. Carrasco, N. Lopez and F. Illas, *First Principles Analysis of the Stability and Diffusion of Oxygen Vacancies in Metal Oxides*, Phys. Rev. Lett. **93**, 225502 (2004).

[5] M. D. Banus, T. B. Reed and A. J. Strauss, *Electrical and magnetic properties of TiO and VO*, Phys. Rev. B**5**, 2775 (1972).

[6] C. Giaconia and R. Tetot, *Defect structure and statistical thermodynamics of the transition metal monoxides* TiO_x, VO_x, *and* NbO_x, J. Phys. Chem. Solids, Vol. **58**, No. 7, pp. 1041-1053 (1997).

[7] Jeremy K. Burdett and Timothy Hughbanks, *NbO and TiO: Structural and Electronic Stability of Structures Derived from Rock Salt*, J. Am. Chem. Soc. **106**, 3101 (1984).

[8] E. Wimmer, K.Schwarz, R. Podloucky, P. Herzig and A. Neckel, *The effect of vacancies on the electronic structure of NbO*, J. Phys. Chem. Solids, Vol. **43**, No. 5, pp. 439-447 (1981).

Novel application of synchrotron IR-radiation in reaction chemistry in aqueous phase

N. Kaun[a], S. Kulka[a], U. Schade[b], J. Frank[c], M. J. Vellekoop[d],M. Harasek[e] and B. Lendl[a]

a Inst. of Chemical Technologies and Analytics, Vienna University of Technology, Getreidemarkt 9-164, 1060 Vienna, Austria
b BESSY, 12489 Berlin, Germany
c Institute of Materials Chemistry, Vienna University of Technology, 1060 Vienna, Austria
d Inst. of Sensor and Actuator Systems, Vienna University of Technology, 1040 Vienna, Austria
e Inst. of Chemical Engineering, Fuel and Environmental Technology, 1060 Vienna, Austria

Funding by EU, R II 3-CT-2004-506008, project BESSY-BM.05.1.103

A micro mixer for (bio)chemical reaction monitoring using mid-infrared synchrotron radiation is introduced for the first time. It is implemented on a chip made of calcium fluoride and SU-8 polymer. The design allows taking advantage of the highly collimated beam of synchrotron radiation at the IR microscope.

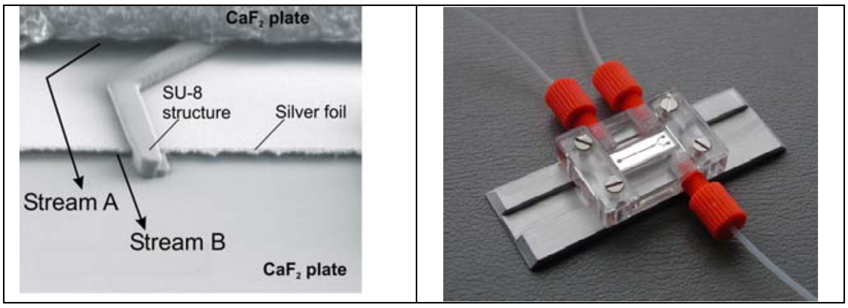

Figure 1 Left, image of the construction of the mixer chip. Right, the mixer chip mounted to the support for connection to the liquids.

Mixing based on diffusion is performed by superimposition of two flow sheets. Due to the small overall dimensions of the channels the short distances can be overcome fast, so the mixing process is finished within the first fiftieth part of the channel. Thereafter the chip acts as an IR-transparent flow-through-cell allowing the observation of the ongoing reaction. The small dimension of the mixing channel assures high time resolution as well as minimum reagent consumption and the ability to measure even in high IR absorbing medium such as water. Time resolved measurements are performed by moving the measuring spots downstream the mixing channel, while employing a constant flow-rate, see Fig. 2. The time resolution achieved is thereby determined by the flow rate, the distance of subsequent measurement points and the focus of the IR beam from the microscope.

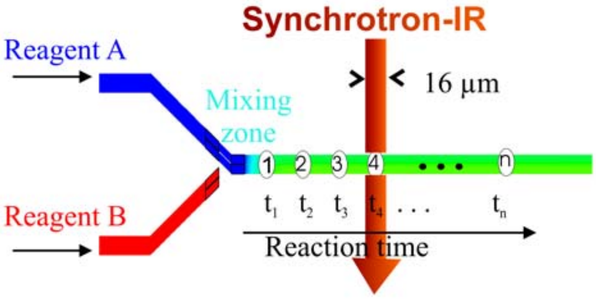

Figure 2. Scheme of the time resolved IR measurements using a continuous flow mixer.

The performance for the ability of reaction monitoring in the continuous flow mode after the mixing was checked by an ester hydrolysis. First pure water and then solutions of methyl monochloroacetate and sodium hydroxide were pumped into the chip at a flow speed of 0.5 µL/min at each channel inlet. Spectra were recorded every 1000 µm with a 20 x 20 µm² spot size. Fig. 3 shows that the characteristic ester bands (νC=O at 1744 cm^{-1}, at 1330 cm^{-1} the CH_3 bending vibrational band and the asymmetric stretching vibration of ester C-O-C at 1218 cm^{-1}) are present at the beginning of the channel and decreasing measuring along the channel towards the outlet, while an increase of the carboxylate band of the forming deprotonated acid (asymmetric and symmetric acetate stretching vibration at 1591 and 1397 cm^{-1}) is recorded. According to the flow speed and the mixer dimensions spacing of the measurement spot at the 1000 µm correspond to a relative time resolution of 90 ms between the spots. The mixing process is considered complete after 250 µm (proven by simulations). Any changes in spectra later at the channel must derive from changes in structure of the molecules inside due to a reaction. Fig. 3 presents clearly that the hydrolysation of methyl monochloroacetate by NaOH and IR spectra can be taken at different states of the reaction, which corroborates the functioning of the experimental set-up employing the Synchrotron IR.

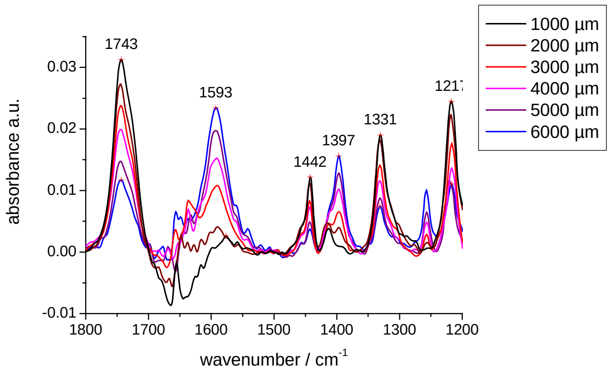

Figure 6. Hydrolysation of methyl monochloroacetate: The IR spectra present the reaction time resolved

In the way the ester hydrolysation was monitored the set-up is also capable of mixing organic substances of biochemical interest: The reaction of the antibiotic vancomycin and the tripeptide Ac_2KAA, resembling an analogue of bacteria cell wall precursor, is known to be of

2nd order kinetics [P. H. Popieniek and R. F. Pratt, *J. Am. Chem. Soc.*, 1991, **113**, 2264]. The binding mechanism processes via a co-operative array of hydrogen bonds and hydrophobic interactions, thus can be followed by IR spectroscopy. Solutions of 20 mM vancomycin and 20 mM Ac_2KAA in D_2O phosphate buffer were injected into the channel and then a set of 50 spectra with 16 x 16 µm sample spot size with a flow of 0.5 µL was recorded (Fig. 4). These settings result in a relative time resolution of 3 ms.

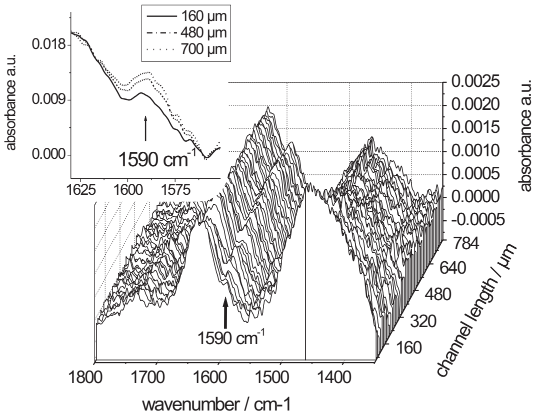

Figure 4 The reaction of Vancomycin and Ac_2KAA time resolved. While the bigger spectrum shows the spectra with a spatial resolution of 16 µm giving a well resolved increase of the band at 1590 cm^{-1}, the small spectrum simplyfies this trend using the average spectra of the first five, the middle five and the last five spectra.

The increase of the band at 1590 cm^{-1}, which is tentatively assigned to the asymmetric carboxylate stretch vibration, can be observed strongly in the first 5 spectra and a continuing increase is also observable at longer reaction times. Counting the time required for diffusion based mixing as obtained from simulations it follows that at the very beginning the observed reaction and mixing overlap. However, as the spectral changes continue after the mixing process has been completed and it is the ongoing reaction solely that is monitored using the developed system. Apart from the observed increase at 1590 cm^{-1} other spectral changes are most likely present in the recorded spectra, which could be attributed to the chemical reaction. However, in order to discuss these in a meaningful way a further improved S/N ratio needs to be obtained. The low optical throughput of our experiment resulting from the strong IR absorption of the sample and the aimed high spatial resolution in the mixing channel drastically reduces the photon flux reaching the detector even using an almost diffraction-limited synchrotron radiation source. It shall be mentioned here that the experiment presented would not have been possible using a standard spectroscopic Globar source. Still, noise in the IR flux typical for IR synchrotron sources and originated by electron beam motion in the storage ring, deteriorates the S/N ratio. However, further future improvements of the S/N ratio of the mixer-IR synchrotron microscopy experiment are planned.

NEXAFS Investigation on the Self-Assembled Monolayer of Biphenyldimethyldithiol formed by the deprotection method.

K. Rajalingam, T. Strunskus, Ch. Wöll

Physikalische Chemie I, Ruhr-Universität Bochum,
Universitätsstr. 150, D-44801 Bochum

Introduction

Self-assembled monolayers (SAMs) are highly ordered molecular assemblies that are formed spontaneously by the adsorption of a surfactant with a specific affinity of its head group to a substrate[1]. The functional group at the end of the molecular chain that is pointing away from the substrate defines the surface properties of the organic film. A good way to obtain a highly ordered SAM with a thiol endgroup is the deprotection of the mono-acetylated derivative, an organothiol with one SH group at one end whereas the other end of the molecule contains a protected S-atom in the form of a thioacetate. After the SAM formation, the thioacetate can then be cleaved under basic conditions, thus yielding a SH-terminated surface. NEXAFS spectroscopy is employed to follow the deacylation process. A highly oriented thiol terminated self-assembled monolayer results from this deprotection strategy.

Experimental

NEXAFS and XPS (X-ray Photoelectron Spectroscopy) measurements were performed in an UHV-system operated at the HE-SGM beamline. The UHV-system consists of a loadlock, a preparation chamber, and an analysis chamber. The base pressure of the analysis chamber of the UHV-system was below 1 x 10^{-10} mbar. It was equipped with a LEED-optics (Vacuum Generators), a quadrapole mass spectrometer (Balzer), an ion sputter gun, an Al/Mg twin anode X-ray source (VG), an energy analyzer (Clam2, VG), and a homemade electron detector based on a double channel plate (Galileo).

Chemicals

The mono acetylated derivative of Biphenyldimethyldithiol (BPDMT) was synthesized using the previously described procedure[2]. Fig. 1 shows the molecular structure of BPDMAc-1 and BPDMT. Ethanol (Merck), Dichloromethane (Merck) and Sodium hydroxide (Backer) were used as received.

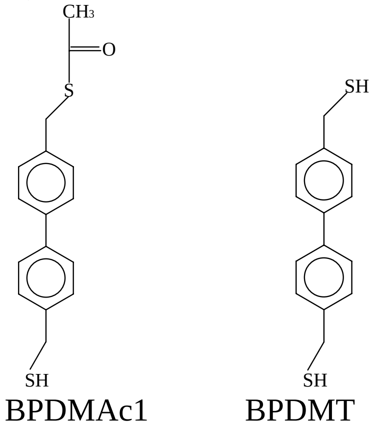

Figure 1 - Molecular structure of BPDMAc-1 and BPDMT

Sample Preparation

(i) Preparation of the Gold Substrates.

For the NEXAFS and XPS measurements, polycrystalline gold substrates were prepared by evaporating 5 nm of titanium (99.8%, Chempur) and subsequently 100 nm of gold (99.995%, Chempur) onto polished silicon wafers (Wacker) in an evaporation chamber operated at a base pressure of 10^{-7} mbar. These substrates were stored in vacuum desiccator until the adsorption experiments were carried out.

(ii) Preparation of the Gold Thiolate Films

Self-assembled monolayer of BPDMAc-1 was prepared by immersing the gold substrates into a 50 μM BPDMAc-1 solution in dichloromethane (DCM) at room temperature (RT). After 4 hrs of immersion, the sample was thoroughly rinsed with the solvent (DCM) and dried in a stream of nitrogen.

(iii)Removal of the Protecting Group in BPDMAc-1 Film

After formation of the organothiolate adlayer, the protecting group can be removed by immersion into NaOH solution. The deprotection scheme is illustrated by the flowchart below.

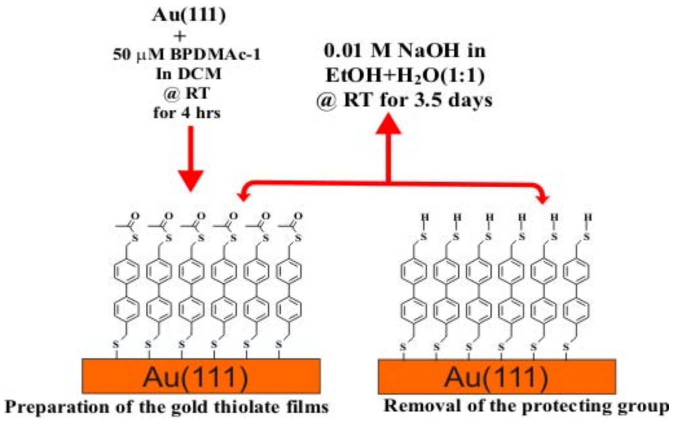

Results and Discussion

In Fig. 2 the NEXAFS spectra recorded at the C 1s line for the samples before and after deprotection are displayed. For the deprotection the following conditions were used. The BPDMAc-1-gold SAM was immersed into a 0.01 M Sodium hydroxide solution in (1:1) ethanol + water mixture for 3 and half days (~ 84 hours) at RT. After removal of the sample from the solution, it was thoroughly rinsed with ethanol and then dried in a stream of nitrogen.

The solid lines correspond to spectra recorded at an incidence angle (angle between the Ē vector of the polarized synchrotron light and the surface normal) of 30°, whereas the dashed lines represent spectra taken at normal incidence of the synchrotron light (angle between the Ē vector of the synchrotron light and the surface normal of 90°). The intensities of the resonances depend on the relative orientation of the corresponding transition dipole moment relative to the polarization direction of the light. The BPDMAc-1 SAM spectrum exhibits strong resonances at 285.2, 287.4, 289.1 and 293.8 eV. The first π^*-resonance located at 285.2 eV is assigned to a transition of the carbon atoms in the benzene ring, the second at 287.4 eV to a transition of the carbonyl carbon of the acylate group. Therefore the deprotection procedure can be followed by the disappearance of the π^*-resonance of the acetate group at 287.4eV.

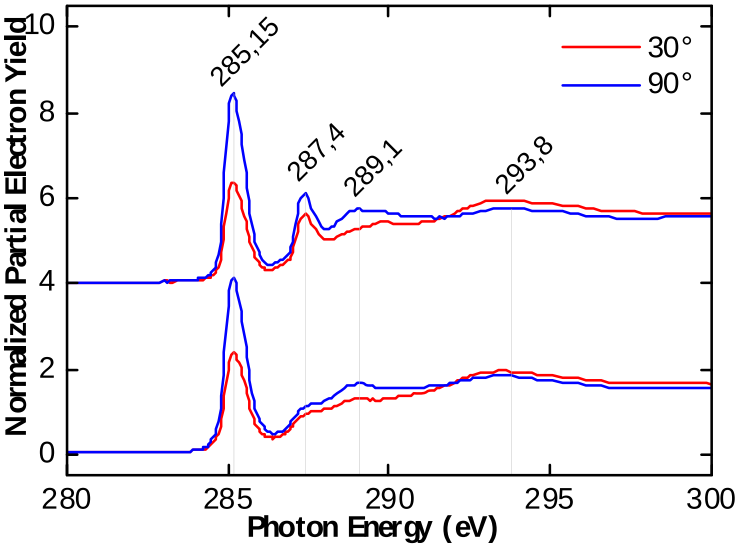

Figure 2 - NEXAFS spectra of BPDMAc1 and the deprotected BPDMT

Both the BPDMAc1 and the deprotected BPDMAc1, i.e., the BPTDMT, show a pronounced and similar dichroism. This suggests that the good orientational order (i.e. an average tilt angle of 75±5° of the molecular backbone relative to the surface) is retained during the deprotection. The deprotection was also followed by infrared reflection absorption spectroscopy further supporting the results obtained here by NEXAFS.

References

[1] F. Schreiber *J. Phys.: Condens. Matter* **16**, R881 (2001).

[2] Niklewski, A.;Azzam, W.; Strunskus, T.; Fischer, R. A.; Wöll, C. *Langmuir* **20**, 8620 (2004).

XANES-PEEM chemical imaging of sub-micron cosmic grains

J. Maul[1], P. Bernhard [1], T. Berg [1], F. Wegelin [1], U. Ott [2], Ch. Sudek [2], H. Spiecker[3], G. Schönhense [1]

[1] Institut für Physik, Staudingerweg 7, Johannes Gutenberg-Universität, D-55099 Mainz,
[2] Max-Planck-Institut für Chemie, Becherweg 27, D-55128 Mainz,
[3] LaVision BioTec GmbH, Meisenstraße 65, D-33607 Bielefeld, Germany

Cosmic grains of pre-solar origin are valuable indicators for stellar processes (see reviews [1,2]). Their mineral compositions provide information about particle growth in circumstellar space, and trace elements included give insight into stellar nucleosynthesis by their unusual isotopic compositions. Such grains are also found in meteorites, and are thus amenable to terrestrial analysis. Facing the small amount of disposable material, common mass spectrometric methods for isotopic analysis have the disadvantage of being destructive.

Here, we demonstrate non-destructive elemental mapping of such cosmic grains by combination of XANES (X-ray Absorption Near Edge Structure) spectroscopy with PEEM (Photo Emission Electron Microscopy) [3], performed at BESSY II beamline UE52 SGM. This novel access enables the detection of elements together with their chemical environment, and thus facilitates the pre-selection of particular mineral phases and of yet unexplored trace contents prior to mass analysis.

Within our study, an acid-resistant fraction from the Murchison meteorite has been investigated. From the chemical separation procedure, the major part of the sample was expected to consist of silicon carbide (SiC). This sample was transferred onto a gold foil with grid pattern which helps to localize individual grains, as recognized from the SEM image of Fig. 1a. The insert of Fig. 1a shows a high resolution SEM micrograph of a single Murchison SiC grain.

In a field of view slightly different to that of Fig. 1a, XANES-PEEM image stacks have been recorded at different photon energies, with a scanning step width of 0.2eV. The image of Fig. 1b has been obtained near the silicon K edge at a fixed photon energy of hν = 1837 eV. The observed brightness already indicates high concentration of silicon. Several marked microareas of two microns in diameter have been chosen for extraction of XANES spectra from the image stacks, which provide additional information about the chemical environment. For example, the XANES spectrum from the selected microarea A clearly presents silicon bound as carbide, as evidenced by comparison with literature [4].

Exploiting a novel unmixing algorithm, the lateral distribution of different binding surroundings has been visualized. This algorithm classifies the lateral grain distribution according to given XANES signatures. In Fig. 2a, the spectral information of oxygen (near O-K edge, microarea B) and of aluminum (near Al-K edge, microarea C) has been used as input. These scans are in accordance with XANES spectra from α-Al_2O_3 (corundum) [5]. From the good lateral correlation of both the aluminum and the oxygen signature in the spectrally unmixed images (Fig. 2b for oxygen and Fig. 2c for aluminum, resp.), we conclude the presence of a corundum fraction within this sample.

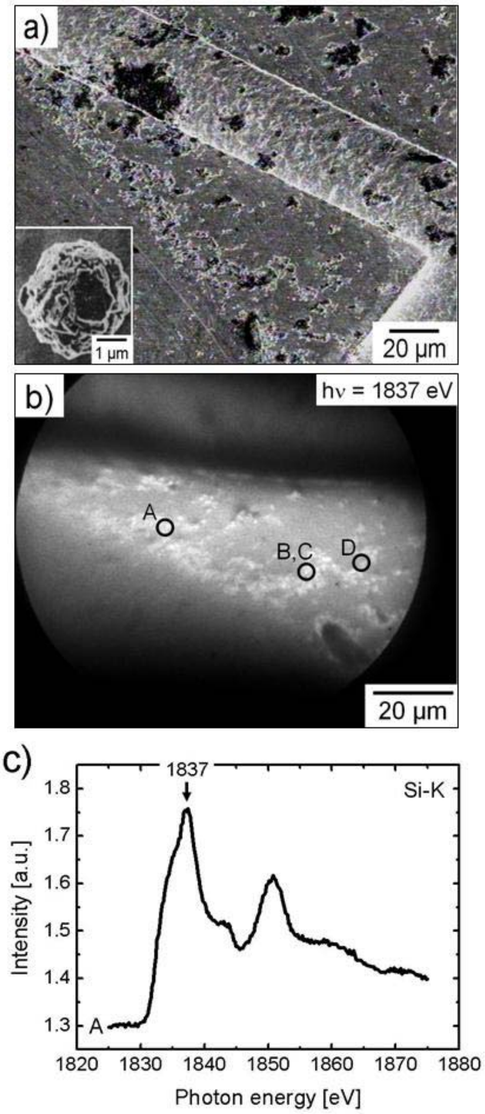

Fig. 1. (a) SEM micrograph of the Murchison meteorite grain sample on a gold grid substrate. (b) XANES-PEEM image of a slightly different field of view recorded at a photon energy of the Si-K edge. (c) Local XANES signature extracted from the selected microarea A.

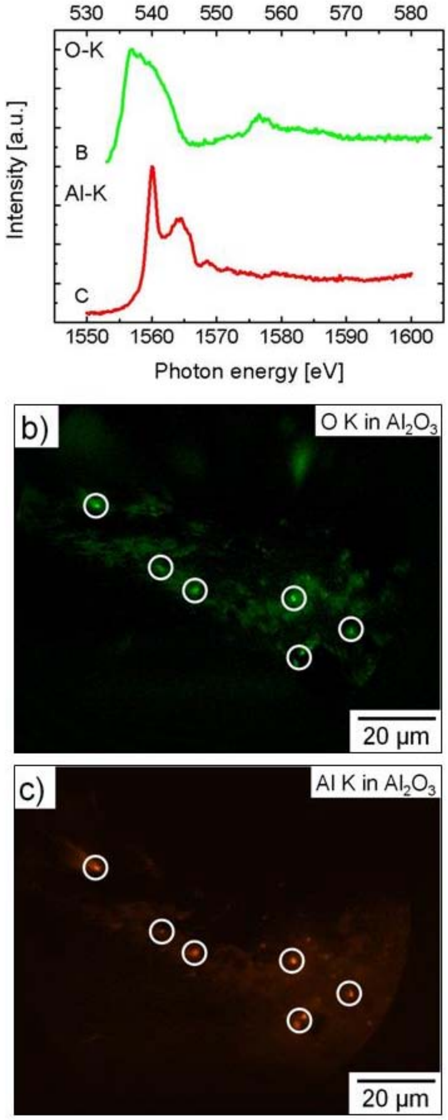

Fig. 2. (a) Local XANES signatures of O-K from microarea B in Fig. 1b, and of Al-K from microarea C in Fig. 1b. These spectra have been used as input for the spectral unmixing algorithm to obtain the “chemically purified” images in (b) and (c) for Al-K and O-K, respectively.

This procedure has been also applied to the XANES spectrum in Fig. 3a, which was recorded from microarea D. It completely covers the oxygen K and the chromium L_2/L_3 edges. The enhancement of the L_3 peak over the L_2 peak, together with the appearance of the oxygen edge in the same scan, indicate oxidized chromium. Fig. 3b shows the corresponding spectrally unmixed XANES-PEEM image from a microarea which contains grains of smallest detectable size. Therefore this domain is further suitable for the determination of the spatial resolution. Since the spectral unmixing algorithm cancels any signature different from the pre-selected one, a good signal to noise ratio is obtained, leading to relatively sharp boundaries. From the line scans over the smallest grains (1-4 in Fig. 3c), diameters of 2.34 µm, 1.37 µm, 0.74 µm and 0.94 µm are obtained using the intensity profile criterion provided by [6].

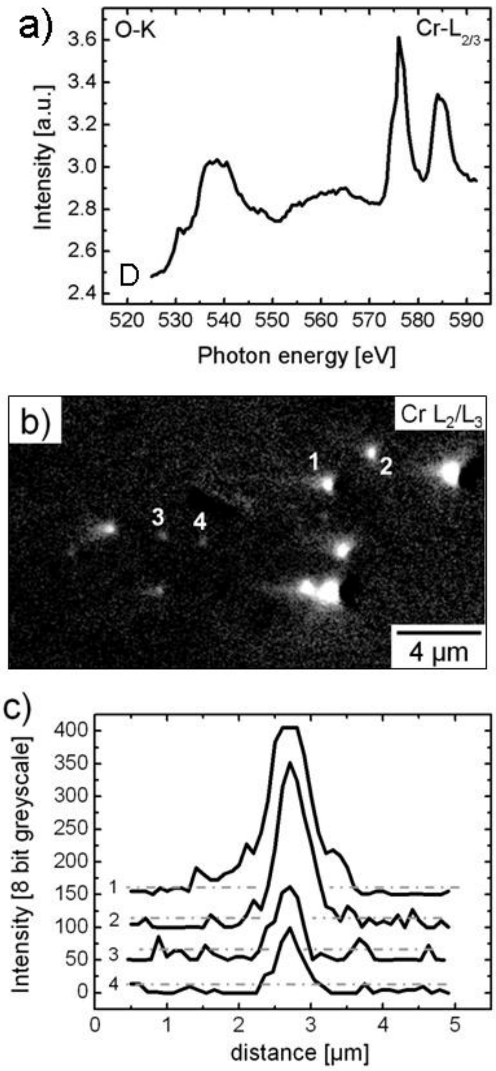

Fig. 3. The XANES spectrum in (a) (from microarea D in Fig. 1b) covering both O-K edge and Cr-$L_{2/3}$ doublet has been used to obtain the spectrally unmixed Cr-$L_{2/3}$ image in (b). Photoelectron intensity distribution across line scans over the smallest grains (1-4) allow for a determination of the spatial resolution (background is indicated by dotted lines).

While imaging XPS (Nano-ESCA, [7]) has been shown to be superior for the detection of trace elements within these grains [8], XANES-PEEM in combination with the spectral unmixing algorithm is unique for a chemical characterization on a lateral scale below one micron. Application of both XANES-PEEM and Nano-ESCA provide unprecedented possibilities for a non-destructive screening also of other fine-grained extraterrestrial materials such as interplanetary dust particles (IDPs) and cometary material recently caught by the NASA Stardust Mission.

References:

[1] U. Ott, Nature **364**, 25 (1993).
[2] U. Ott and P. Hoppe, Sterne und Weltraum **9**, 38 (2005).
[3] Ch. Ziethen et al., J. Electr. Spectr. Rel. Phenom. **107**, 261 (2000).
[4] J. Wong et al., Solid State Commun. **92**, 559_(1994).
[5] S.-D. Mo and W.Y. Ching, Phys. Rev. B **62**, 7901 (2000).
[6] S.A. Nepijko et al., J. Microsc. **202**, 480 (2001).
[7] M. Escher et al., J. Phys.: Cond. Matt. **17**, 1329 (2005).
[8] P. Bernhard et al., Nucl. Instr. Meth. Phys. Res. B, in press (2006); G. Schönhense et al., BESSY Highlights, 34 (2004).

Spatially resolved Sy-XRF measurements of archaeological objects made of a silver and gold

M.-F. Guerra[1], I. Reiche[1], M. Radtke[2], H. Riesemeier[2]

[1]Laboratoire du C2RMF – UMR 171 CNRS, 75001 Paris, France
[2]Bundesanstalt für Materialforschung und –prüfung (BAM), 12205 Berlin, Germany

Introduction

After the successful analysis of silverpoint drawings of different origins [1-3], the interdisciplinary project is enlarged to the study of other archaeological objects made of silver and gold alloys.

Trace element analysis can give precious clues for the determination of manufacture techniques of archaeological objects, their provenance and trading. Trace element analysis of gold and silver objects is very interesting because gold and silver have already been exploited in ancient times by Man to manufacture prestige or common objects. The elements present in gold and silver depend on the geological situation [4]. After metal processing, only a few elements present at the ppm level can be used for instance to fingerprint gold as the platinum group elements (PGE). Indeed, Pt is a good tracer of gold as, it is not lost during gold processing and together with Pd is the most soluble in gold [5].

The investigations of precious and unique objects have to be carried out using non-destructive point analysis. Therefore, few techniques are well-suited for the analysis of archaeological objects. X-ray fluorescence analysis is one of the techniques of choice. However, measurement of Pt in gold is difficult by means of XRF due to the overlap of their X-ray lines. In this project, synchrotron radiation induced XRF (Sy-XRF) is tested for its suitability.

The aims of our Sy-XRF experiments are threefold:

1/ it is attempted to improve the limits of detection (LOD) of trace elements as Pt group elements in gold, by realising measurements using an excitation energy below and above the platinum absorption edge,

2/ two series of archaeological samples of the Wisigothic treasure of Guarrazar (7th–8th century AD), kept at the National Archaeological Museum of Madrid, and from the decoration of the coffins of the Xiongnu tombs (3rd century BC – 2nd century AD) from a Bronze Age site in Mongolia excavated by the French Archaeological Mission are analysed in order to determine the origin of the gold used,

3/ the LODs of minor and trace elements in silver objects are determined in order to evaluate the potential of Sy-XRF to study manufacturing techniques and the provenance of archaeological silver.

Experimental Set-up and Material

For the investigations of gold objects, we used the hard X-ray synchrotron beamline (BAM*line*) operated by the Bundesanstalt für Materialforschung und -prüfung to determine major and minor element contents in different gold and silver objects. An intense monochromatic photon beam of size 0.2x0.2 mm² was obtained with a monochromator system consisting of two silicon (1 1 1) crystals. One of the crystals can be bent to focus the beam in the horizontal direction. The size of the beam was defined by a slit. A 20 mm² Si(Li) detector with nominal resolution of 130 eV at 5.9 keV photon energy was used. In order to take advantage of the polarization of the synchrotron light, the detector was placed at a distance of about 2.5 cm from the samples, perpendicular to the photon beam in the plane of the electron storage ring. This geometry assures a minimum background contribution from the scattered radiation. Measurements were performed at different excitation energies. Platinum traces in a gold reference material (certified NIST fine gold RM 8058 standard containing 40.8 ppm of Pt) were measured at an excitation energy around the Pt L edge and tests at the K edge were also performed. Under the same condition the archaeological gold samples were measured. In addition, we looked for characteristic elements of silver using two different energies: at 35 keV we measured Sn, Sb and Ag and at 22 keV (lower than Ag K absorption edge) elements such as Pb, Au and As. The composition of one silver standard containing trace elements was measured together with 30 samplings from medieval French silver coins.

Spectrum evaluation for determination of LOD at the Au L edge

Several measurements were made on the certified NIST fine gold RM 8058 reference material containing 40.8 ppm of Pt. To determine the Pt concentration of this standard, three measurements were necessary (Fig. 1). At first the fluorescence spectrum of a pure Pt foil was measured with an excitation energy of 11.574 keV (called C), thus above the Pt L_3 edge. The fluorescence spectrum of RM 8058 was also measured using the same energy (called B). At last, the fluorescence spectrum of RM 8058 was measured with an excitation energy of 11.547 keV, (called A), thus below the Pt L_3 edge.

Figure 2 shows a difference between A and B at the location of the Pt L lines. This difference is attributed to the Pt fluorescence signal and the shift of the Raman scattering. The theory of Raman scattering is quite complex and can be found in e.g. [6]. The most important characteristic for this work is that the Raman peak has a fixed energy difference, namely the energy of the L edge, to the excitation peak. To calculate the fraction due to the Raman scattering, a special procedure is necessary. First, we must shift the spectrum A in a way that the scattered peaks are at the same position as in spectrum B. After this shifting, spectrum B can be fitted with the following equation: B=p(0)*A+p(1)*C, where p(0) is a measure of the intensity of the Raman scattering and p(1) gives the factor concerning the Pt content in the foil relative to the pure thick Pt foil measured. Fitting was performed with the Powell routine of IDL (Interactive Data Language). At the end the Pt signal is determined from the spectrum of the Pt foil measured below the Pt L3 absorption edge. For RM 8058 we calculate: p1 = 4.18 x 10-5 which corresponds to 33 µg/g of Pt, where 40.8 µg/g is expected.

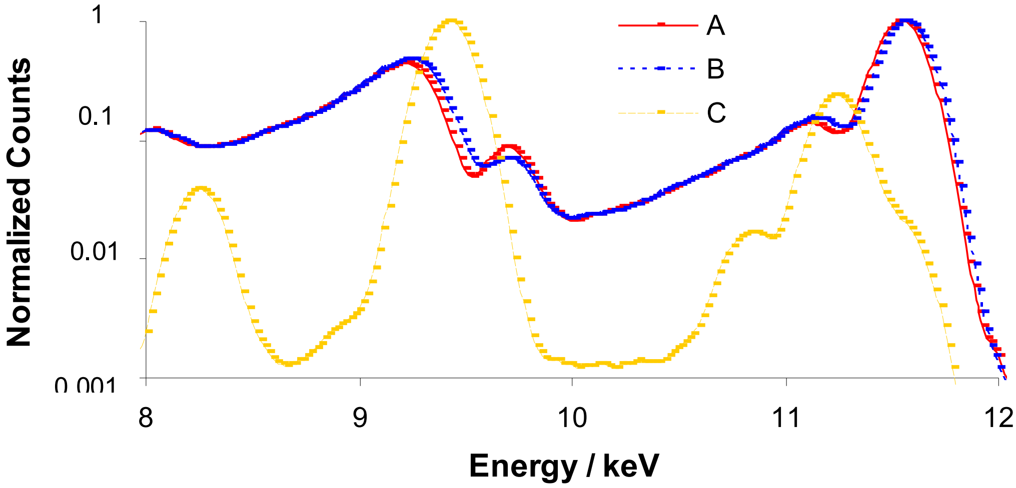

Figure 1. Sy-XRF spectrum A (RM 8058 below Pt L_3 edge), B (RM 8058 above Pt L_3 edge) and C (Pt foil above Pt L3 edge), respectively.

Results and discussion

The LOD for Pt in gold is calculated from the fit of the non-normalized spectra: 20 ppm [4]. The Sy-XRF LOD for Pt is thus some orders of magnitude lower than routine filtered PIXE (1000 ppm) and PIXE-induced XRF (80 ppm). These latter techniques are also non-destructive and usually applied in the field of cultural heritage [5].

As the measurement of Pt in gold at high energy requires very long acquisition times, it was only possible to complete the analysis of the first set of archaeological samples from the Wisigothic treasure of Guarrazar (7th–8th century AD), kept at the National Archaeological Museum of Madrid. Only a part of the Mongolian gold samples could be analysed. Together with the archaeological samples we analysed a small set of gold standards in order to verify our first results concerning the determined LOD for Pt in gold. Furthermore, we approached for the first time the possibilities of Sy-XRF to study ancient objects fabricated with silver alloys. However, beam time was too short to end this series of measurements. The evaluation of the measured spectra of the archaeological gold and silver is still in progress.

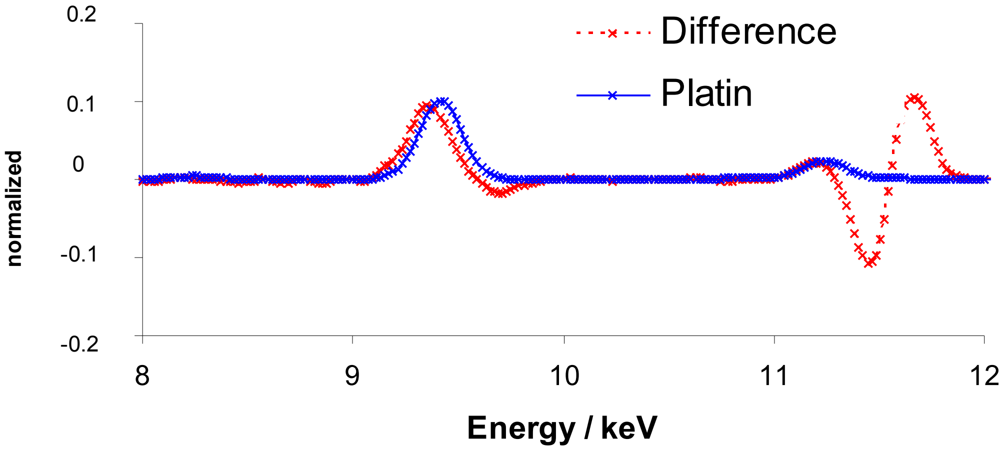

Figure 2. Difference between A and B at the location of the Pt L lines. This difference is attributed to the Pt fluorescence signal and the shift of the Raman scattering.

Conclusions and perspectives

The first measurements showed that Sy-XRF is a very powerful tool to analyse archaeological gold and silver because this techniques allows improving the limit of detection of heavy trace elements as Pt in gold by a factor of several orders of magnitude in comparison to other non-destructive techniques. However, spectrum evaluation is difficult because the thickness of the samples has to be taken into account during the quantification procedure of spectra measured at high energy (around 80 keV). Together with a very long acquisition time and the need of the analysis of a long series of archaeological samples in order to gain representative and validated archaeological results, further measurements are necessary to be able to finally conclude on the origin of gold thanks to the chemical fingerprint based on trace elements. Even if the analysis of silver is simpler, more time is needed to finish the analysis of standards and archaeological samples, before conclusions could be drawn on the LODs of trace elements in silver and on the potential of this technique to get new insights into the origin of ancient silver and manufacturing.

References

[1] I. Reiche, M. Radtke, A Berger, W. Görner, S. Merchel, H. Riesemeier, H. Bevers, Appl. Phys. A, 5 pages in print.

[2] I. Reiche, S. Merchel, M. Radtke, ZfP-Zeitung 95 (2005) 40-45.

[3] T. Ketelsen, I. Reiche, O. Simon, S. Merchel, The Burlington Magazine Vol. CXLVII, #1224 (2005) 170-175.

[4] M.F. Guerra, T. Calligaro, M. Radtke, I. Reiche, H. Riesemeier, NIMB 240 (2005) 505-511.

[5] M.F. Guerra, J. Archaeol. Sci. 31 (9)(2004) 1225-1236.

[6] L. Vincze, K. Janssens, F. Adams, M.L. Rivers, K.W. Jones, Spectrochim. Acta B 50 (2) (1995) 127-147.

Acknowledgements

We thank BESSY for allowing beam time. Support by W. Görner and S. Merchel is gratefully acknowledged. This research project was partially financed by the European BESSY-EC-IA-SFS contract (project n° BESSY-ID.05.2.189).

Projects in Basic Research
(January 2006)

Project leader	Partners / Co-workers	Institute	Project title
Albrecht	Hellwig	Universität Konstanz	Element Specific X-ray Magnetic Circular Dichroism Studies of Antiferromagnetically Coupled Gd/Ni Bilayers
Albrecht	Goering	MPI für Metallforschung	Field dependent spectroscopic investigation of the flux line vortex states in YBa2Cu3O7-□
Amiens	Fauth	Laboratoire de Chimie de Coordination CNRS	Magnetic properties of chemically synthesized bimetallic nanoparticles
Andersen		Aarhus University	Crystal structure of the sarcoplasmic reticulum Ca2+-ATPase in the E2-ATP state
Andersen		Aarhus University	Crystal Structure of the sarcoplasmic reticulum Ca2+-ATPase in the E2-P to E2 transition
Andersen		Aarhus University	Structural basis for toxin mediated translational control of eukaryotic protein synthesis
Andersen		Aarhus University	Structure of complement factor 3
Andersen		Aarhus University	Structure of the bacterial homologue of the yeast tRNA editing enzyme, TadA
Andriyevskyy	Esser	Technical University of Koszalin	Optical reflectance spectra of ferroic crystals in the region 3-30 eV for ordered and disordered phases
Argyriou		HMI	Charge Ordering in Na0.5CoO2 ?
Bansmann		Universität Rostock	Magneto-optische Reflexionsspektroskopie
Bansmann	Meiwes-Broer Getzlaff Maletta	Universität Rostock	Ferromagnetic clusters on surfaces: size-dependent magnetic properties
Barla	Sanchez	IPCMS / GEMME	Electronic structure and magnetic properties of the intermediate valent Kondo insulator SmB6 by x-ray absorption spectroscopy and magnetic circular dichroism.
Barman		Inter-University Consortium for DAEF facilities	Electronic structure of manganese films on aluminium
Barth		IPN EPFL	Bonding and Orientation of di-Phenylalanine Peptide on Cu(110)
Barth		IPN EPFL	Engineering low-dimensional metallosupramolecular systems at metal surfaces
Bartl		Inst. of Medical Physics and Biophysics	Spektroskopische Untersuchungen zur Biologischen Signaltransduktion
Batchelor	Umbach	Uni Würzburg	Comissioning the UFF-CRG eamline and endstation SCIENTA SES200 Analyser
Baumgärtel	Seckler	Universität Potsdam	Einbau einer Stopped Flow Zelle, Probemessungen, Kalibrierung Optimierung der Normierung für quantitative Absorptionsmessungen Undulator: Aufbau und Steuerung, Charakterisierung, Standardmessungen und Projekte

Project leader	Partners / Co-workers	Institute	Project title
Beaurepaire		IPCMS	Dilute Magnetic Semiconductors (Co,Zn)O studied by Magnetic Circular Dichroism
Becker	Viefhaus Lablanquie	Fritz-Haber-Institut der Max-Planck-Gesellschaft	Multi-photoionisation processes studied by electron spectrometry using a magnetic bottle spectrometer.
Benzerara		IMPMC, CNRS-University Paris 6-IPGP	STXM study of experimental calcification in Cyanobacteria
Birch	Schäfers	Linköping University	At-wavelength (13 nm) characterization of interfaces and reflectivity of Mo/Si interface-engineered multilayer mirrors for EUV lithography.
Birkholz	Darowski (HMI)	IHP Microelectronics	Biomolecules on Semiconductors (Semi-Bio I)
Bjoras		Institute for Medical Microbiology	Define the structural biochemistry of base recognition and backbone incision by E.coli endonuclease V.
Bjoras		Institute for Medical Microbiology	Mechanism of endonuclease IV incision next to oxidized bases
Bjoras		Institute for Medical Microbiology	Recognition of abasic sites by the human Cytomegalovirus uracil DNA glycosylase.
Bjoras			Structural characterization of a novel protein from S.pombe involved in coordination of AP-site repair in DNA
Bjoras		Institute for Medical Microbiology	Structural characterization of enzymes for repair of oxidative demethylation of alkylation damage.
Björneholm	Hergenhahn	Uppsala University	High resolution photoelectron spectroscopies of small free clusters
Bleuzen		Laboratoire de Chimie Inorganique CNRS	Crystal Field and photomagnetism in Prussian Blue Analogues.
Bodenthin	Pietsch Nefedov	Uni Potsdam	Super-cooled high spin state in metallo-supramolecular assemblies
Bodenthin	Pietsch	Uni-Potsdam	Determination of coordination spheres of metal centres in thin metallo-supramolecular films
Boeglin	Bansmann	IPCMS-GSI	Magnetic properties of in-situ grown NiO nanostructures on PLD Fe3O4 films.
Boeglin		IPCMS-GSI	Thickness and temperature dependence of FM/AFM magnetic coupling in NiO/Fe/W(110)
Bonanni	Esser	Universität Linz	VUV-ellipsometry: determination of optical constants for the hexagonal GaN:Fe and cubic GaN material systems.
Bonfiglio	Umbach	University of Cagliari	X-ray Spectroscopic Investigations of Organic Devices
Borisenko	Knupfer/Fink	IFW Dresden	Origin of renormalization of low energy electronic states in LSCO high-Tc superconductors
Borucki	Heyn Otto	FU Berlin	Structural Changes in the Photoreceptors Phytochrome and Photoactive Yellow Protein detected with Circular Dichroism

Project leader	Partners / Co-workers	Institute	Project title
Boyen	Ziemann	Universität Ulm	Electronic properties of mass-selected supported gold clusters (<60 atoms)
Boyen	Ziemann	Universität Ulm	Non-interacting L10-ordered FePt Particles: Temperature Dependence of the Magnetic Anisotropy
Boyen	Ziemann	Universität Ulm	Temperature Dependence of the Orbital Magnetism and its Correlation to Exchange Bias in Co/CoO nanoparticles
Braun	Schäfers	IWS Dresden	Reflectance and resolving power of nanometer multilayers with small period thicknesses
Braun (PDI)	Schulz	Paul-Drude-Institut	Analysis of the structure and formation of the substrate-film interface during epitaxy of Pr2O3 on Si(100)
Braun (PDI)	Schulz	Paul-Drude-Institut	In situ synchrotron xray diffraction during molecular beam epitaxy growth (PHARAO)
Bressler		BESSY	Commissioning of the new HIKE endstation on KMC 1 and on 7T MPW (HMI). Tests of Bulk Sensitive Photoemission Spectroscopy on metals with additional beam line optics.
Bressler		LSU-ISIC-BSP	Local structure of complex chemical systems-time-resolved structures of solid state systems
Brückel	Su	Institut fuer Festkoerperforschung (IFF)	Challenging the classic model of ionic charge ordering in mixed-valence 3d transition-metal oxides by soft X-ray resonant scattering
Bucher	Kappler	Institut de Physique et de Chimie des Materiaux de Strasbourg	Onset of magnetic properties upon thermal stripping of organo-bimetallic molecules on surfaces
Bunke	Erko	TU Berlin	Quantitative Untersuchungen zur räumlichen Schwermetallverteilung in biologischen Sorbentien und Charakterisierung der Bindungsstellen der Biomasse sowie der Natur der Metallbindung.
Calvani		Universita' di Roma “La Sapienza” and Coherentia-INFM	Far-Infrared Spectroscopy of High-Tc Superconductors Bi2-xLaxSr2CuO6 and MgB2
Carbone	Rader Gambardella	Consiglio Nazionale delle Ricerche	Photoemission spectroscopy of isolated Fe impurities on metal surfaces
Carbone	Rader Gambardella	Consiglio Nazionale delle Ricerche	XAS-XMCD investigation of surface Kondo systems
Cartier		LCIM2 – CNRS	Remnant XMCD Investigation of Bimetallic Oxalate-based Magnets: Local Magnetic Contributions to the Remnant Magnetisation
Chassé	Lei Zhang	Universität Tübingen	Electronic structure of semiconductor quantum dots and bulk and epitaxial oxides studied by soft x-ray emission spectroscopy
Chassé	Lei Zhang	Universität Tübingen	Orbital mixing-originated fine features in x-ray emission spectroscopy and local partial density of states of sulfides and selenides studied by x-ray emission spectroscopy

Project leader	Partners / Co-workers	Institute	Project title
Cimino		Laboratori Nazionali di Frascati dell'Istituto Nazionale di Fisica Nucleare (LNF-INFN)	A photon conditioning study on the Large Hadron Collider (LHC) beam screen industrial surfaces.
Claessen		Physikalisches Institut der Universität Würzburg	Polarization-dependent x-ray absorption spectroscopy of quasi-one-dimensional electron systems
Cobessi		UPR9050 CNRS	Structural studies of the ion transport in Pseudomonas aeruginosa PAO1
Cocco	Schäfers	Sincrotrone Trieste ScpA	Characterisation of the performance of a shallow blaze angle grating
Cramm	Schneider	Institut für Festkörperforschung	Electronic Structure and Magnetism of Heusler Alloys
Cramm	Schneider	Institut für Festkörperforschung	Magnetism in Ferromagnetically Filled Carbon Nanotubes (continuation of a CRG project)
Dähne		Technische Universität Berlin	Electronic structure of self-organized dysprosium silicide nanowires on Si(001)
Dau		FU Berlin	XAS on metalloenzymes and related model molecules - comparison of the PSII manganese complex with synthetic models
de Groot		Utrecht University	A bi-functional Cr-based catalyst for the ethylene trimerization-polymerization :An in-situ soft X-ray absorption study
Dobbek		Universität Bayreuth	2-hydroxyglutyryl-CoA Dehydratases
Dobbek		Universität Bayreuth	4-Hydroxybutyryl-CoA Dehydratase from Clostridium aminobutyricum
Dobbek		Universität Bayreuth	Molydenum hydroxylases
Dobbek		Universität Bayreuth	Ni-CODH
Dobbek		Universität Bayreuth	Rieske Oxygenases
Domashevskaya		Voronezh State University	XANES study of interaction between transition metals and SiO2 matrix in granular magnetic nanocomposites, between transition metals and porous silicon matrix.
Dowek	Simon	CNRS	Vector Correlation studies and nondipole effects in K-shell photoionisation of simple molecules in gasphase

Project leader	Partners / Co-workers	Institute	Project title
Dürr		BESSY	Exploring the surface magnetisation deficit in (GaMn)As ferromagnetic semiconductors
Eckström		FOI NBC Defence	Acetylcholinesterase inhibited by organophosphorous compounds: Structural and biochemical studies of novel reactivators
Eckström		FOI NBC Defence	The role of acetylcholinesterase peripheral anionic site challenged by structure determnation of Asp74 site directed mutants
Ehresmann		TU Kaiserlautern	Autoionisation der N2(1s-1πg*) und N2(1sσ*) Resonanz in die Zustände N2+ B und C
Ehresmann		TU Kaiserlautern	Höchstaufgelöste Spektroskopie von Zweielektronenresonanzen in Kr
Ehresmann		TU Kaiserlautern	Resonante magnetische Röntgenreflektometrie an FeMn/Co/Cu/Co- und Co/Cu/Co/IrMn- Spinvalves und an NiO/FeNi Bilayern nach deren Modifikation durch He-Ionenbeschuss
Ehresmann	Schmalhorst	Universität Kaiserlautern	Resonante magnetische Röntgenreflektometrie an bis zur Tunnelbarriere aufgebrachten halben magnetischen Tunnelelementen V/ Co2MnSi / AlOx und Pt-Mn / Co-Fe / Ru / Co-Fe-B / AlOx
Eichinger		TU Muenchen	Structure determination of Alpha-1-acid glycoprotein
Eichinger		TU Muenchen	Structure determination of Apolipoprotein D
Eisebitt		BESSY	X-Ray Holographic Imaging of Low-Contrast Objects
Eisebitt	Aziz	BESSY	Soft x-ray spectroscopy in liquid environments: towards an understanding of the electronic structure in active centers of biomolecules
Eisebitt	Stöhr	BESSY	Coherent resonant X-ray scattering from magnetic domain patterns
Elmers	Schneider Schönhense	Universität Mainz	Magnetic circular dichroism of Co2FeSi and Fe3-xVxSi compounds
Erko		BESSY	Bragg-Fresnel Gratings on Multilayer Substrates.
Esser	Gensch	ISAS	VUV - XUV ellipsometry on polymers
Esser	Cobet	ISAS	VUV-XUV-Ellipsometrie: Optische Charakterisierung von kristallinem Zinkoxid
Esser		ISAS	Aufbau eines breitbandigen Synchrotronellipsometers im UV bis EUV-Spektralbereich für grundlagen- und materialwissenschaftliche Fragestellungen an Festkörpern und organischen Materialien
Esser	Esser/Richter/ Braun	ISAS	Chemisch modifizierte Halbleiteroberflächen: Molekülterminierung und Oxidation am Beispiel Si(001) und InN(0001)

Project leader	Partners / Co-workers	Institute	Project title
Farle	Fauth	Universität Duisburg-	Size and composition dependence of induced magnetic moment of Pt in FePt and CoPt colloidal nanoparticles
Farle	Fauth	Universität Duisburg-	Preparation and magnetism of the L10 high anisotropy state in non-agglomerated 3nm FePt colloidal nanoparticles
Farle	Fauth	Universität Duisburg-	Size dependence of magnetovolume instabilities in Fe72Pt28 Invar nanoparticles
Fauth	Schütz	MPI für Metallforschung	Magnetic properties of anisotropic nanoparticle arrays
Fauth	Schütz	MPI für Metallforschung	Size selected Fe clusters on Pt(111)
Fedoseenko		St.-Petersburg State University	Radiation-stimulated destruction of thin fullerite films on Si-oxide surface
Felser	Reller Elmers	Johannes Gutenberg-Universität	Circular dichroism in photoabsorption from ferrimagnetic brownmillerites
Feulner	Menzel	TU-München	Photon induced dynamics by inner shell excitations
Feyerherm		HMI	Interplay of ferroelectricity and magnetism and in REMnO3, RE= Tb, Dy
Feyerherm		HMI	The Ferroelectric Transition in TbMnO3
Ficner		Universität Göttingen	2-Thiouridine Synthetase (MnmA)
Ficner		Universität Göttingen	4-Thiouridine Synthetase (Thil)
Ficner	Dickmanns	Universität Göttingen	human FGE enzyme and one of its paralogues (PFGE)
Fiechter		Hahn-Meitner-Institut Berlin	Investigations of catalytic centres in noble metal free catalysts for direct methanol PEM fuel cells: In-situ EXAFS measuerements of Fe-, Co- catalysts for PEM fuel cells under oxygen reduction conditions
Fiechter		Hahn-Meitner-Institut Berlin	XANES measurements of Fe-, Co-catalysts and In-situ EXAFS measurements of Fe-, Co-catalysts for PEM fuel cells under oxygen reduction conditions
Fink		Universität Erlangen-Nürnberg	Elektronische Struktur von molekularen Nanomagneten
Fink		Universität Erlangen-Nürnberg	Röntgen-Mikroskopie zur Physiologie von Insektenaugen
Frankenberg-Dinkel		Technical University Braunschweig	Probing the active site of Pseudomonas aeruginosa porphobilinogen synthase using synthetic inhibitors
Freund	Kuhlenbeck	Fritz-Haber-Institut der Max-Planck-Gesellschaft	Elektronische Struktur molekularer Schichten auf reinen und modifizierten Oxid-, Karbid- und Nitridsubstraten
Fucini		MPI for Molecular enetics	Crystallography of Ribosome Functional Complexes
Gajhede		Department of Medicinal Chemistry Biostructural Research	Extracellular modules of neural cell adhesion molecules
Gajhede		Department of Medicinal Chemistry Biostructural Research	Structure determination of α-L-arabinofuranosidase from Thermobacillus xylanilyticus by multi-wavelength anomalous diffraction.

Project leader	Partners / Co-workers	Institute	Project title
Galakhov	Neumann	Institute of Metal Physics	Temperature dependent study of Mn 3s photoelectron spectra in manganites
Gallani		IPCMS	2D assemblies of magnetic organic molecules
Gatteschi	Sainctavit	University of Florence	XMCD of Self Assembled Monolayers of functionalized Mn12 clusters on gold surfaces
Genzel	Klauss	HMI c/o BESSY	Depth resolved X-ray residual stress analysis in CVD multi-layer hard coatings on WC-substrates.
Genzel	Denks	HMI c/o BESSY	Energy-dispersive diffraction analysis of non-uniform near surface residual stress fields induced by mechanical surface processing – II. Evaluation of the real space stress profiles □ij(z)
Genzel	Klauss	HMI c/o BESSY	Locally resolved residual stress analysis in individual sublayers of CVD multi-layer systems by means of energy dispersive diffraction
Genzel	Denks	HMI c/o BESSY	Optimization of residual stress analysis in real space, enhancement of applicability on engineering materials
Gießel	Weinelt	Max-Born-Institut	Laserinduzierte Bandstrukturänderungen an Halbleiteroberflächen
Glass-Maujean	Schmoranzer Ehresmann	Université Pierre et Marie Curie	The hydrogen molecule: determination of the transition moments, dissociation and ionization yields of superexcited states
Goering	Schütz	MPI für Metallforschung	Grenzflächenmagnetisierung in Ferromagnet-Supraleiter bzw. Ferromagnet-Antiferromagnet Heterostrukturen
Goering	Schütz	MPI für Metallforschung	Roughness dependent variations of the Co magnetization profiles and the induced Cu magnetization of Co/Cu/Co trilayers.
Goering	Schütz	MPI für Metallforschung	REBaCo2O5.5: Magnetocrystalline anisotropy, high orbital moments and Giant X-ray Natural Circular Dichroism
Golden		Van der Waals-Zeeman Instituut	k-space microscopy of high Tc superconductors
Goldhahn		Technische Universität Ilmenau	Surface preparation of hexagonal InN films
Gonzalez-Doncel	Bruno	CENIM	Study of the micro and macro residual stress relaxation in 6061Al-SiC and 6061Al-Al2O3 composites upon annealing.
Gordeev		Ioffe Physical-Technical Institute	C60F18 as a Photoresist for dry x-ray Nanolithography
Gräber		Universitätsklinikum RWTH Aachen	Investigations of teeth with high resolution µ-tomography
Grunze	Rosenhahn	Universität Heidelberg	Digital in-line holography with synchrotron radiation: Characterization experiments for a 3D-imaging method

Project leader	**Partners / Co-workers**	**Institute**	**Project title**
Grunze	Fratzl	Applied Physical Chemistry	Intracellular Structures
Gudat	Valencia	BESSY	Magneto-Optical Polarization spectroscopy on CMR thin film systems
Güntherodt	Schneider	RWTH Aachen	All-oxide tunnel junctions and influence of the interface on the value of the tunnel magnetoresistance
Hague		Universität Pierre et Marie Curie	Low energy electron excitations in complex oxides studied by X-ray Raman spectroscopy
Hahn	Kanngießer	BAM	Untersuchung organischer Bestandteile von Malschichtsystemen auf Kunstwerken - Bindemittelanalyse an Querschliffen mit hoher Ortsauflösung mittels Synchrotron Infrarotspektroskopie
Hahn	Kanngießer	BAM	Untersuchung von Migrations- und Oxidationsprozessen anorganischer Verbindungen in Tintenfraß-geschädigten Manuskripten
Haibel	Banhart	HMI	Microstructure Investigation on Thixotropic Alloys and Metal-Matris-Copmposites by Synchrotron Computed Tomography
Haibel	Zabler Banhart	HMI	Quantitative Analysis of Thixotropic Aluminium Alloys by Holographic Synchrotron Tomography
Haibel	Kieback	HMI	Synchrotron Tomographic Investigations of Sintering Mechanisms
Hartnig	Manke, Haibel	Zentrum für Sonnenenergie- und Wasserstoff-Forschung (ZSW) Baden-Württemberg	Investigation of fuel cells by means of synchrotron radiography and tomography
Hecker	Gudat, Schäfers	IFW Dresden	Magnetisation reversal in exchange-coupled layer systems
Heinz		German Research Centre of Biotechnology	Change to: Components of the Type III Secretion System of Gram-negative Bacteria
Heinz		German Research Centre of Biotechnology	DNA Complex of the transcipt factor PrfA of Listeria monocytogenes
Heinz		German Research Centre of Biotechnology	Listerial surface proteins
Heinz		German Research Centre of Biotechnology	Modulating the binding affinity of internalin from Listeria monocytogenes for human E-cadherin.
Heinz		German Research Centre of Biotechnology	Structure and function of Yersinia protein kinase, YopO in complex with activating actin
Heinz		German Research Centre of Biotechnology	The first enzymes in tetrapyrrole biosynthesis - structure determination and functional characterization.
Held		University of Cambridge	Characterising chiral surfaces using polarised light –the adsorption of chiral organic molecules on chiral surfaces.

Project leader	Partners / Co-workers	Institute	Project title
Hellwig		Universität Frankfurt	Low-far and far infrared spectroscopc studies on biological molecules using conventional and synchrotron light sources
Hellwig	M. Albrecht / Uni Konstanz	BESSY	Scattering, SPECKLE and Spectro Holography Studies from Perpendicular Magnetic Multilayers on Nanospheres
Hellwig	Fullerton	BESSY	X-ray Resonant Magnetic Scattering and X-ray Magnetic Circular Dichroism from Perpendicular Hard/Soft Bilayer Systems
Hellwig	Eisebitt	BESSY	Magnetic SPECKLE studies of the domain evolution in perpendicular magnetic films during external field reversal
Henricksen		Carlsberg Laboratory	Arabidopsis thaliana acyl-CoA oxidase1 : substrate complexes
Henricksen		Carlsberg Laboratory	Arabidopsis thaliana mitochondrial KAS: ligand complexes
Henricksen		Carlsberg Laboratory	Barley Aldose reductase
Henricksen		Carlsberg Laboratory	E. coli beta-ketoacyl-ACP synthase: C4-C12 fatty acyl complexes
Henricksen		Carlsberg Laboratory	human mitochondrial KAS
Henricksen		Carlsberg Laboratory	Short chain specific acyl-CoA axidase ACX4
Hergenhahn	Bradshaw	MPI for Plasma Physics	Photoelectron-Auger-Electron Coincidence Measurements with high Energy Resolution
Hergenhahn	Bradshaw	MPI for Plasma Physics	Photoionisation of a free cluster beam
Herrero-Albillos		Universidad de Zaragoza-CSIC	XMCD study of the zero-μCo line in RCo2: searching the orbital instability of Co
Hillebrecht	Schneider	FZ Jülich	Exchange coupling at the NiO/magnetite interface
Hillebrecht	Schneider	FZ Jülich	Magnetism of Mn in ordered surface alloys
Hinrichs	Palm	Universität Greifswald	Chemistry and photochemistry of green fluorescent protein (GFP)
Hinrichs		Universität Greifswald	Complexes of TetR with tetracyclines and influence of mutations
Hinrichs	Rappich Schade	ISAS	IR-Ellipsometrie für die Untersuchung der Struktur und der optischen Eigenschaften ultradünner Filme aus Benzolderivaten auf Si
Hinrichs	Rappich Schade	ISAS	IR – ellipsometry on 1D-polymer brushes
Hodnett		University of Limerick	An in situ glancing incidence XRD investigation of the growth of Aluminium trihydroxide on steel.
Hoell	Zizack	Hahn-Meitner-Institut	Commissioning of the new SAXS/ASAXS/GISAXS instrument at the monochromatic 7T-wiggler beam @ BESSY
Horn		Fritz-Haber-Institut der	Low-dimensional metal structures: electronic states, optical and vibronic excitations
Hunger	Jaegermann	TU Darmstadt	Photoelectron spectroscopy of interfaces for silicon/organic hybrid devices
Hunger	Jaegermann	TU Darmstadt	Band mapping of CuInSe2, CuInS2, and CuGaSe2

Project leader	Partners / Co-workers	Institute	Project title
Ionov		Institute of Solid State Physics	Photoemission studies of electronic structure of valence band and core level spectra of Pt based metalloporphyrines
Jaegermann	Mayer	Technische Universität Darmstadt	Characterisation of 2-6 semiconductor/organic pigment interfaces
Jaegermann	Thißen	Technische Universität Darmstadt	Electronic structure of ion conducting oxides
Jaegermann	Mayer	Technische Universität Darmstadt	Elementary Processes in Contact Formation at Semiconductor/Electrolyte Interfaces Exemplified by Dye Sensitised Solar Cells: TiO2-Dye-Solvent Interaction
Jaegermann	Thißen	Technische Universität Darmstadt	Lateral inhomogeneities of semiconductor surfaces and -interfaces
Jaegermann	Fritsche	Technische Universität Darmstadt	Schottky barrier formation and interdiffusion at CdTe and ZnTe/metal interfaces
Jaegermann	Thißen	Technische Universität Darmstadt	High resolution SXPS and XAS studies of the electrochemical Li intercalation into crystalline thin V2O5 films prepared by different deposition techniques
Jones	Woodruff Polcik	University of Nottingham	Carbon-Carbon Bond Formation Followed Using Scanned-Energy Mode Photoelectron Diffraction
Jung		BESSY	Charakterisierung und Justierung des U41-PGM
Kachel		BESSY	MUSTANG- Commissioning
Kamarás		Hungarian Academy of Sciences	Terahertz investigation of carbon nanotubes
Kampen	Horn	Fritz-Haber-Institut	Self-assembly and electronic structure of highly ordered organic thin films
Kanngießer		Technische Universität Berlin	3D Micro X-ray Spectroscopy on Persian Tiles from the 19th century
Kanngießer		Technische Universität Berlin	3D Mikro-Röntgenfluoreszenzanalyse Validierung eines dreidimensionalen Modells der Empfindlichkeit für die Quantifizierung
Kappler		IPCMS	XMCD of a single molecule magnet (SMM)
Keckes	Zizak	Erisch Schmid Institute	Stress Gradients in Thermally Cycled Thin Films
Keckes		Erisch Schmid Institute	Texture and Strain Mapping using Position-Resolved Laue Diffraction
Kera	Schöll Umbach	Chiba University	High-resolution NEXAFS investigation of condensed large organic molecules
Kirschner	Kuch	Max-Planck-Institut für Mikrostrukturphysik	Elementspezifische Abbildung magnetischer Domänen in gekoppelten magnetischen Dünnschichtsystemen
Kiskinova	Schlögl Knop	Sinchrotrone Trieste	Activity of different O-phases on Ru surface in water formation and NO neutralization reactions: in-situ high pressure-XPS study
Kiskinova	Schlögl Knop	Sinchrotrone Trieste	Catalytic activity of different oxidation states of Ru in partial oxidation of methanol and propene: an attempt to bridging the material gap using polycrystalline and powdered catalyst
Klein	Jaegermann	Technische Universität Darmstadt	Interfaces of Polycrystalline Conducting Oxides

Project leader	Partners / Co-workers	Institute	Project title
Kleineberg	Oelsner Weber (Focus)	Universität Bielefeld	At-wavelength defect characterization of EUV mask blanks utilizing a dedicated EUV-PEEM
Knabe		Charité University Medical Center Berlin	Synchrotron-tomography on regenerated bone tissue using rapidly resorbable bone substitute materials applying the Guided Bone Regeneration Technique
Kneipp	Moss (ANKA)	Institut fuer Molekularbiologie und BioInformatik	Investigating molecular aspects of nanoparticle-mediated transfer processes into eukaryotic cells by synchrotron FTIR microspectroscopy
Knop-Gericke	Schlögl	Fritz-Haber-Institut der Max-Planck-Gesellschaft	In situ electron spectroscopy of the partial oxidation of small molecules over supported and unsupported nanostructured vanadia agglomerates
Knop-Gericke	Schlögl	Fritz-Haber-Institut der Max-Planck-Gesellschaft	Propane oxidation to acrylic acid on Mo based model catalysts
Knop-Gericke	Schlögl	Fritz-Haber-Institut der Max-Planck-Gesellschaft	Selective gas-phase hydrogenation of C5 multi-functional molecules using palladium and nickel based catalysts
Knupfer	Aristov	Leibniz-Institut für Festkörper- und Werkstoffforschung	Metallic/insulator properties of doped organic semiconductors
Koch	Vollmer	HU Berlin	Organic Electronic Materials: Gas-Exposure Dependent Electronic Structure
Koch-Müller		Geoforschungszentrum Potsdam	Location and quantification of OH in nominally anhydrous minerals
Köhler		Humbold-Universität zu Berlin	X-ray image magnification by asymmetric Bragg reflection
Kolodziejczyk		Wroclaw University of Technology	Crystallographic studies of juvenile hormone binding protein (JHBP)
Konovalov	Szargan	Uni Leipzig	Optical transitions through the fundamental direct band gap in CuInO2
Konovalov	Szargan	Uni Leipzig	Origin of donor-like intrinsic defects in CuIn5S8 and AgIn5S8
Krauß	Lamparter Tilman	Charite-Universitätsmedizin Berlin	Bacterial Phytochromes
Krauß	Hofmann	Charite-Universitätsmedizin Berlin	Centrin
Krauß	Friedrich	Charite-Universitätsmedizin Berlin	HypF1, a [NiFe]-hydrogenase maturation protein from Ralstonia eutropha
Krauß	Schneider-Mergener Höhne	Charite-Universitätsmedizin Berlin	Structural investigation of heterospecific coiled cell interactions in complexes of GCN4 leucine zipper variants
Krauß	Höhne	Charite-Universitätsmedizin Berlin	structure of triosephosphate isomerase from Tenebrio molitor
Kretlow		Robert-Koch-Institut	Infrared Microspectroscopy of CNS Tissue from Scrapie infected Syrian Hamsters

Project leader	Partners / Co-workers	Institute	Project title
Kuch	Camarero	Freie Universität Berlin	Element-resolved magnetic properties of epitaxial alloy films and multilayers
Kuch	Aeschlimann Dürr	Freie Universität Berlin	Zeit- und lagenaufgelöste Magnetisierungsdynamik in magnetischen Mehrschichtsystemen
Kühbacher	Ohm	HMI	Lokalisation von Proteinablagerungen bei Morbus Alzheimer
Lablanquie	Eland Viefhaus	LCP-MR	Multi-photoionisation processes studied by electron spectrometry using a magnetic bottle spectrometer Part 1 = Spectroscopy of multiply charged cations
Lambert	Woodruff Sayago	Cambridge University	Towards an understanding of chemo-selective catalytic hydrogenation
Lau	Wurth	TU Berlin	X-Ray Absorption Spectroscopy of Small, Size-selected Transition Metal Clusters on Alkali Metal Surfaces
Lau	Tobias	Tu Berlin	Magnetic Properties of Size-selected Implanted Iron Clusters in Graphite
Lawniczak-Jablonska	M. Walcak	Polish Academy of Science	Iron in malarialpigments and diaminoacid derivatives of proroporhyrin IX
Le Normand		IPCMS-GSI	Ferromagnetic alloyed nanoparticles encapsulated in carbon nanotubes
Leach	Baumgärtel Jochims	Observatoire de Paris-Meudon	Photophysics of exobiological molecules
Leitenberger	Pietsch	Uni-Potsdam	Application of X-Ray interferometry for beam characterisation
Leitenberger	Pietsch	Uni-Potsdam	Energy Dispersive Small Angle X-Ray Scattering
Lendl		Institute of Chemical Technologies and Analytics	Novel application of synchrotron IR-radiation in reaction chemistry in aqueous phase
Lewerenz	Jungblut	HMI	Photoelectron spectroscopy on electrochemically grown fluorinated silicon oxides
Ley	Seyler Leckey Riley Rader	Uni Erlangen	Photoelectron spectroscopy on SiC
Ley	Riley, N.Smith	Uni Erlangen	Studies of Fermi surfaces using photoelectron spectroscopy
Loan	Genzel	Un iversity of Limerick	In situ time-resolved diffraction studies of crystallization and dissolution at 250oC and 50 bar pressure
Lux-Steiner		Hahn-Meitner-Institut Berlin GmH	X-ray emission and photoelectron spectroscopy at thin film solar cells based on Cu(In,Ga)(S,Se)2
Maletta	Imperia Andreazza	Hahn-Meitner-Institut Berlin GmH	Spin and orbital magnetization studies of Co/Pt core/shell nanoparticles prepared ex-situ by electron beam evaporation deposition
Maletta	Schmitz Gruyters Winter	Hahn-Meitner-Institut Berlin GmH	Exchange bias and the role of uncompensated Fe spins in epitaxially grown fcc FexMn1-x at the interface to Co
Maletta	Rossner	Hahn-Meitner-Institut Berlin GmH	Investigation of the correlation between EXAFS and MEXAFS at L-edges of 3d-systems.

Project leader	Partners / Co-workers	Institute	Project title
Maletta	Imperia	Hahn-Meitner-Institut Berlin GmH	XMCD studies of magnetic Co structures prepared by nanosphere lithography
Maletta	Rossner	Hahn-Meitner-Institut Berlin GmH	Investigation of the MEXAFS method for thin films
Manescu		Università Politecnica delle Marce	Residual stress and texture analysis in Cu-based alloy reed tongues of medieval and baroque organs
Manzke		Humboldt Universität zu Berlin	Polarisationsabhängige Photoemission an Hochtemperatursupraleitern
Martins		Universität Hamburg	Charge transfer in free metal halides
Marvaud	Holub-Krappe Sainctavit	Université Pierre et Marie Curie	Measurement of the local magnetic moment in polymetallic magnetic systems of the family of molecule magnets
Matthes	Schneider C.	Forschungszentrum Jülich	Spin-resolved photoemission spectroscopy at the Fe/MgO interface probing the influence of the oxygen concentration on the spin polarization
McNulty	Eisebitt	Advanced Photon Source	Quantification of signal to noise and resolution in nano-scale x-ray holography
Menzel	Bertel	Universität Innsbruck	Correlation on the (modified) Pt(110)surface
Meyer		LURE	Strahlender Zerfall von rotatorisch kalten Molekülen im Bereich der Innerschalenanregung
Meyer	Rühl	LIXAM	Symmetry and dissociation dynamics of inner-shell excited molecules
Michette		King's College London	Characterisation of broad-band multilayer soft x-ray and EUV polarisers
Miron		Centre de Biophysique Moléculaire,	Conformational properties of galactose mutarotase from *Escherichia coli* : a synchrotron circular dichroism study
Mitdank	Manzke	Humbold Universität Berlin	Röntgenabsorptionsspektroskopie an einkristallinen Hochtemperatursupraleitern zur Bestimmung der sauerstoffabhängigen Dotierung in den CuO2-Ebenen
Molodtsov	Geibel	TU Dresden	Electron correlation effects in Yb and Eu compounds
Molodtsov	Mertig	Technische Universität Dresden	Metallization of low-dimensional protein templates
Mueller		Universität Würzburg	Binding specificity of BMP type I receptors
Mueller		Universität Würzburg	Structure determination of the ternary ligand-receptor complex of BMP-2 and its receptors BRIA and ActRIIb
Müller	Hillen, Wolfgang	Universität Erlangen-Nürnberg	Allosteric mechanisms of Tet-Repressor action
Müller	Riesemeyer	Bundesanstalt für Materialforschung und -prüfung	Charakterisierung keramischer Grünkörper mit SR-CT; SR-Refraktions-topographie; SR-RFA und SR-µRFA Experimente
Müller	Dahlbaeck, Bjoern	Universität Erlangen-Nürnberg	Crystal structure determination of ApoM

Project leader	Partners / Co-workers	Institute	Project title
Müller	Hammond, Geoffrey	Universität Erlangen-Nürnberg	Crystal structure determination of CBG
Müller	Dahlbaeck, Bjoern	Universität Erlangen-Nürnberg	Mechanism of the activation of Tyro3 by its ligand Gas6
Müller	FU Berlin	PSF c/o BESSY	Three dimensional structure determination of human proteins selected from the Protein Structure Factory target list
Murin		Institute of Chemistry, St.	X-ray absorption and photoemission study of magnetic two-dimensional iron-oxygen nanostructures on the silicon, (Fe-O)n/Si(111).
Neophytides	Knop Schlögl	Institute of Chemical Engineering and High Temperature Chemical Processes,	Pt alloy nanocluster electrocatalysts for enhanced methanol oxidation and CO tolerance in fuel cells
Nordlund	Erlandsen	Department of Biochemistry and Biophysics	Crystal structure determination of substrate and inhibitor complexes of human protein protein phosphatase 2C (PP2C).
Nordlund	Hallberg	Department of Biochemistry and Biophysics	E. coli rRNA methyltransferase YebU
Nordlund		Department of Biochemistry and Biophysics	Human cytosolic deoxyribonucleotidase - dNT-1
Nordlund	Hallberg	Department of Biochemistry and Biophysics	Pseudouridine synthase TruD
Nordlund		Department of Biochemistry and Biophysics	Structural studies of a bifunctional protein catalyzing the second and third step in riboflavin biosynthesis in E. coli.
Nordlund	Eneqvist	Department of Biochemistry and Biophysics	Structural studies of mitochondrial pre-sequence protease (PreP)
Nordlund		Department of Biochemistry and Biophysics	Structural studies of NAD kinase.
Nordlund	Divne	Department of Biochemistry and Biophysics	Studies on pyranose 2-oxidase from Trametes multicolor
Nordlund	Hallberg	Department of Biochemistry and Biophysics	tRNA IPP-transferase, MiaA
Novikova		Institute of Crystallography	Total reflection X-ray fluorescence study of lipid/protein membrane models
Novikova		Institute of Crystallography	Total reflection X-ray fluorescence study of lipid/protein membrane models
Ohresser		LURE-ORSAY	Spectroscopic and magnetic study of exchange coupled Co/Fe2O3 (0001) interfaces
Ott	Weschke Tjeng	Universität zu Köln	Resonant soft x-ray diffraction from defect order in transition-metal oxides
Paloura		Aristotle University of Thessaloniki	Study of vitrified industrial wastes by µ-XRF and µ-XAFS
Paloura		Aristotle University of Thessaloniki	Study on glasses containing industrial waste by µ-XRF and µ-XAFS

Project leader	Partners / Co-workers	Institute	Project title
Pantleon	Feyerherm	Technical University of Denmark	Stress distribution in finite structures
Pantleon	Feyerherm	Technical University of Denmark	The effect of cryogenic treatment on structural and phase transformations in iron martensite the role of stresses
Panzner	Pietsch	Universität Potsdam	Korrelationsspektroskopie mit weißer Synchrotronstrahlung
Peisert	Chassé Knupfer	Uni Tübingen	Ladungsverteilung an Grenzflächen organischer Halbleitern
Pernicka		TU Bergakademie Freiberg	Analysis of archeological gold objects by SyXRF
Pettenkofer		Hahn-Meitner-Institut Berlin GmH	Angle resolved photoemission spectroscopy on epitaxial CuInS2 surfaces
Pettenkofer		Hahn-Meitner-Institut Berlin GmH	In situ investigation of the aluminum-induced layer exchange (ALILE) in amorphous silicon using PEEM
Pettenkofer		Hahn-Meitner-Institut Berlin GmH	Angle resolved photoemission spectroscopy on homoepitaxial ZnO surfaces
Piancastelli	Horn	Uppsala University	Surfaceinduced chirality in molecules adsorbed on silicon surfaces
Pichler	Shiozawa	IFW-Dresden	Electronic structure of filled and intercalated single wall carbon nanotubes
Pietsch	Bodenthin	Universität Potsdam	Development and testing of small angle X-ray scattering with white X-rays
Pietsch	Bodenthin	Universität Potsdam	Spin coupling processes in thin metallo-supramolecular films
Polcik	Hooker	Fritz-Haber-Institut der	Photoelectron diffraction of adsorbed atoms, molecules and thin films
Powis	Hergenhahn	University of Nottingham	Circular Dichroism in the Photoionization of Free Chiral Molecules
Presmanes	Holob-Krappe	Universite Paul Sabatier	Cation redistribution in thin films of zinc ferrites.
Püttner	Becker	Freie Universität Berlin	Angular- and channel resolved photoionization of double-excitation states in Helium
Püttner	Yanisha	Freie Universität Berlin	Initial steps of PbTe and GeTe surface oxidation
Püttner	Zimmrmann Martins	Freie Universität Berlin	Fragmentation of small organic molecules subsequent to core excitations
Pyzalla		TU Wien	Determination of phases and internal stresses in intermetallic buried layers of Fe/Al-joints
Raabe	Al-Sawalmih	MPI für Eisenforschung	Synchrotron X-ray structure and texture analysis of chitin-bio-nanocomposites
Rader		BESSY	Electronic states responsible for chain formation in Gd/W(110)
Rader	Riley/Leckey/ Janke-Gilman Seyller	BESSY	Studies of magnetic order and moment using photoelectron spectroscopy
Rader	Riley/Leckey/ Seyller	BESSY	Studies of the Fermi surface of bcc Fe and Cr from two to three dimensions
Rader		BESSY	Probing the ground state of strongly correlated delta-Mn through quantum well states

Project leader	Partners / Co-workers	Institute	Project title
Rader		BESSY	Orbital symmetry determination of the states responsible for ferromagnetism in Ga1-xMnxAs
Ramsey		KF-Universität Graz	Inorganic contact formation on oriented organic films
Reichardt		BESSY	Investigation and optimisation of the focus properties at U125/2-10m-NIM
Reichardt		BESSY	Linearity and absolute accuracy of angular encoders probed with Hydrogen absorption spectra
Reiche		C2RMF-UMR 171 CNRS	Spatially resolved XRF measurements of silver point drawings by the Holbein family and Rembrandt as well as archaeological objects made of a silver gold alloy
Reif	Fälber	Forschungsinstitut für Molekulare Pharmakologie	High resolution crystal structure of SH3
Reif	Khare	Forschungsinstitut für Molekulare Pharmakologie	pi3k-SH3
Remhof		Ruhr-Universität Bochum	XMCD and XRMS studies from low dimensional magnetic systems
Riesemeyer	Müller	Bundesanstalt für Materialforschung und -prüfung	Charakterisierung keramischer Grünkörper mit SR-CT; SR-Refraktions-topographie; SR-RFA und SR-µRFA Experimente
Rüdiger	Kaul	Universität Konstanz	X-ray Absorption and Resonant Photoemission Spectroscopy of the Diluted Magnetic Semiconductors MnxGe1-x and CoxGe1-x
Rudolph	Dierks, Thomas	Microbiology and Genetics Department	Atomic resolution structure of the formylglycine generating enzyme
Rudolph	Klostermeier (Uni Bayreuth)	Microbiology and Genetics Department	Structural studies of small GTPases and their effectors involved in protein transport
Rudolph	Klostermeier, Dagmar	Microbiology and Genetics Department	Structural studies on RNA helicases
Rudolph	Feussner, Ivo	Microbiology and Genetics Department	Structure of a novel fatty acid double isomerase
Rühl	Graf	Universität Würzburg	Elektronische Eigenschaften von freien, massenselektierten Nanopartikeln im Berreich der Innerschalenanregung
Rühl	Flesch	Universität Würzburg	Zerfall von mehrfach geladenen Clustern nach orts- und elementspezifischer Anregung
Rühl	Graf	Universität Würzburg	Struktur und Dynamik von strukturierten II/VI-Halbleiter-Nanopartikeln
Rühl	Flesch	Universität Würzburg	Größenabhängige Veränderung der Rumpfniveau-Absorption von Clustern aromatischer Moleküle
Sacher	Reiss	Universität Bielefeld	Surface sensitive X-ray absorption spectroscopy (XAS) and X-ray magnetic circular dichroism (XMCD) measurments of Al2O3 apped magnetite Fe3O4 for implementation in a magnetic tunnel junction.

Project leader	Partners / Co-workers	Institute	Project title
Saenger		Freie Universität Berlin	Crystallographic studies of Delta protein in complex with substrates ATP and/or DNA
Saenger	Athina (Max-Vollmer-Inst.)	Freie Universität Berlin	Crystallographic studies of Photosystem II and single subunits
Saenger	Kulikowski Institute for Biochemistry and Biophysiks (IBB PAN)	Freie Universität Berlin	Design of novel inhibitors of HCV RNA helicase
Saenger	Reutter (Charite, Molekular-biologie)	Freie Universität Berlin	Human N-Acetyl-Glucosaminkinase
Saenger	Sandhoff Kekulé-Institut für Organische Chemie, Bonn	Freie Universität Berlin	Human SA-Proteins and Sphingolipid Methabolism
Saenger		Freie Universität Berlin	MTH177 and NAC
Saenger		Freie Universität Berlin	Omega-repressor:DNA-complexes
Saenger	Uchanska-Ziegler	Freie Universität Berlin	Peptide Presentation by Differentially Disease-Associated HLA-B27 Subtypes
Saenger	Reutter (Charite, Molekular-biologie)	Freie Universität Berlin	Structural investigations of humanCD26 in complex with fragments of HIV tat-protein
Saenger		Freie Universität Berlin	Structure and Function of the Antitoxin (epsilon) / Toxin (zeta) post segragational killing system
Saenger	Sandhoff Kekulé-Institut für Organische Chemie, Bonn	Freie Universität Berlin	Structure and Mechanism of human beta-Hexosaminidase B
Saenger	Bardowski	Freie Universität Berlin	Structure of regulatory DNA-binding CcpA Protein
Saenger	Sandhoff	Freie Universität Berlin	Structure of ceramidase
Saenger	Stork	Freie Universität Berlin	Structure of DNA-Methylase MS.ssI in complex with DNA and cofactor adomet
Sänger		Freie Universität Berlin	Joint Berlin Structural Biology Initative at BESSY
Sayago	Kröger	Fritz-Haber-Institut der	Photoelectron diffraction of adsorbed atoms, molecules and thin films
Sayago	Knop Schlögl	Fritz-Haber-Institut der	The structure of active surface oxygen species on silver catalysts for ethylene epoxidation: a test of 'high pressure' photoelectron diffraction

Project leader	Partners / Co-workers	Institute	Project title
Schade		BESSY	Synchrotron infrared microspectroscopic investigation on carbonaceous chondritic meteorites
Schäfers		BESSY	KMC-1 Commissioning
Scharnweber		Technische Universität Dresden	Microtomography (µCT) for quantitative evaluation of the bone formation in the interface to an implantat and surrounding the implantat by stimulation of vascularization
Scheidig	Szedlacsek, Stefan	Structural Biology	Comparative structural analysis of the wild type phosphatase domain of Protein Tyrosine Phosphatase BL and its inactive mutant encountered in colorectal cancer
Scheidig	Friedrich, Cornelius G.	Structural Biology	Structural investigation of the sulfate thiol hydrolase protein SoxB from Paracoccus pantotrophus
Scheurer		IPCMS-GSI	Temperature dependent magnetic anisotropy of self-organized nanoclusters
Schindler	Woodruff Polcik	Martin-Luther Universität Halle-Wittenberg	Photoelectron Diffraction on Transition Metal Oxide Ultrathin Films
Schmalhorst		Universität Bielefeld	Non-destructive depth profiling based on X-ray photoelectron spectroscopy (XPS) and X-ray magnetic circular dichroism (XMCD) studies of Co-Fe-B / AlOx and Co-Fe / AlOx interfaces of magnetic tunnel junctions
Schmeißer		Brandenburgische Technische Universität Cottbus	Photoelektronenspektroskopische Untersuchungen an Pr – O – N - Schich-ten: Dielektrika für 4H-SiC Oberflächen
Schmeißer		Brandenburgische Technische Universität Cottbus	Resonant Photoemission (resPES) at the O1s edge of CuO and NiO in a com-bined angle integrated PES and TEY-XAS study.
Schmeißer		Brandenburgische Technische Universität Cottbus	Spektroskopische und mikroskopische Charakterisierung von Grenzflächen in OFET-Schichtfolgen: Rauhigkeit, Reaktivität und Potential-Verteilung
Schmeißer		Brandenburgische Technische Universität Cottbus	Photoelektronen-spektroskopische Untersuchungen zur Pr-O-N-Schichten: Dielektrika für 4H-SiC Oberflächen
Schneider	Genzel	HMI	Analysis of residual stress gradients within thin bent metal sheets in order to validate finite-element calculations of the bending process
Schneider	Guttmann	BESSY	Hochauflösende Tomographie und Sproktroskopie mit dem Röntgenmikroskop am Undulator U41 bei BESSY II
Schneider	Guttmann	BESSY	Röntgenmikroskopie mit einem PGM/Kondensoroptik-System am UE46-PGM
Schneider		FZ Jülich	Vectorial analysis of incoherent magnetization rotation processes
Schoenes		TU Braunschweig	VUV-Ellipsometrie an Seltenen-Erd-Hydriden, UN und optisch anisotropen UPtGe-Einkristallen bei Photonenenergien größer 10eV
Schomburg	Brüx, Christian	Universität zu Köln	structurdetermination of beta-xylosidase from Geobacillus stearothermophilus T-6

Project leader	Partners / Co-workers	Institute	Project title
Schomburg	Schoepe, Jan	Universität zu Köln	The Shikimate Dehydrogenases from Corynebacterium glutamicum
Schönhense	Schneider	Johannes-Gutenberg-Universität Mainz	Untersuchung neuer magnetischer Materialien mit hoher Orts-, E-nergie- und Zeitauflösung
Schubert	Banhart (HMI)	TU Berlin	Nutzung der Änderung funktioneller Eigenschaften von Biopolymeren für die Formgebung keramischer Bauteile
Schubert	Schade	Universität Leipzig	Terahertz-domain generalizes ellipsometer set-up
Schuler		Universität Zürich	Elementary processes of protein folding and collapse using microfluidic mixing
Schuler		Universität Zürich	Struckturelle Charakterisierung von Amyloiden Proteinkollaps und Sekundärstrukturbildung
Schulz	Kloer, Daniel	Institut für Organische Chemie und Biochemie	Apocarotenoid cleaving oxygenase ACO
Schulz	Mosbacher, Tanja	Institut für Organische Chemie und Biochemie	Benzaldehyde ammonia lysate (BAL)
Schulz	Schleberger, Christian	Institut für Organische Chemie und Biochemie	C2 toxin, component II (C2II)
Schulz	Zocher, Georg	Institut für Organische Chemie und Biochemie	CysM - substrate complexes and protein engineering
Schulz	Kloer, Daniel	Institut für Organische Chemie und Biochemie	Ethylbenzene dehydrogenase EBDH
Schulz	Grüninger, Dirk	Institut für Organische Chemie und Biochemie	Rhamnulose-1-phosphate aldolase (RhuA) mutants
Schulz	Ritter, Holger	Institut für Organische Chemie und Biochemie	Tyrosine aminomutase (TAM)
Schulz	Mittler, Michael	Institut für Organische Chemie und Biochemie	UrdGT2
Schulz	Treiber, Nora	Institut für Organische Chemie und Biochemie	Urocanate hydratase (urocanase), engineered
Schumacher		Hahn-Meitner Institut	Temperature dependence of FWHM of y´phase in non-deformed single crystal superalloys
Schüßler-Langeheine	Tjeng Weschke	Universität Köln	Resonant soft x-ray scattering from transition-metal compounds
Schwarz	Fischer, Katrin	Biozentrum der TU Braunschweig	Crystal structure of Arabidopsis nitrate reductase catalytic domain as well as the holo-enzyme
Schwarz		Biozentrum der TU Braunschweig	Structural analysis of holo-gephyrin and gephyrin splice variants
Schwarz	Fischer, Katrin	Biozentrum der TU Braunschweig	Structural analysis of plant molybdopterin synthase (Cnx6/7)
Schwarz		Biozentrum der TU Braunschweig	Structural basis of eukaryotic Mo insertion into molybdopterin by Cnx1

Project leader	Partners / Co-workers	Institute	Project title
Schwell	Baumgärtel	Laboratoire Interuniversitaire des Systèmes Atmospheriques (LISA)	VUV absorption spectroscopy of planetary molecules at low temperatures
Schwentner		Freie Universität Berlin	Spectroscopy and photochemical reactions af halogens and rare gases
Seckler	Baumgärtel	Universität Potsdam	Circular dichroism spectroscopy (CD) on proteins, Protein secondary structure and folding mechanisms
Senf		BESSY	Characterisation and development of optical components
Senf		BESSY	Commissioning of UE56/2-PGM-1 after replacement of optical components and test measurements of weak CD signals in the chopped mode
Senf		BESSY	Efficiency measurements on high-energy optimised diffraction gratings
Sessoli	Winpenny	University of Florence	XMCD of a new Single Molecule Magnet with high spin and coercitivity
Sheldrick	Söling, Hans-Dieter	Universität Göttingen	Crystal Structures of mutants and complexes of wind, a PDI-related protein
Sheldrick	Zerth, Kornelius	Universität Göttingen	Structure determination of PphA, a bacterial Phosphataseα
Sheldrick	Diederichsen, Ulf	Universität Göttingen	Structure of polyalanyl PNAS and chemical deviratives
Sheldrick	Diederichsen, Ulf	Universität Göttingen	Structures of complexes between Echinanycin and DNAs
Shikin	Rader	St.Petersburg State University	Separation of initial and final state superlattice effects for surface states and resonances on vicinal Cu(111) and their modification by the step decoration and surface alloying process.
Siegbahn	Knop Schlögl	Uppsala University	oSolvation of Biocompatible Coatings
Sluchinskaya	Lebedev	Moscow State University,	EXAFS studies of local atomic potential for Ge off-center atoms on PbTe and SnTe.
Smalås	Nannan Yang	University of Tromsø	Isocitrate dehydrogenase (IDH)
Smalås	Ronny Helland	University of Tromsø	Structure studies of DNase from shrimp
Smalås	Ronny Helland	University of Tromsø	Structure studies of proteins involved in copper homeostasis
Smalås	Vibeke Os	University of Tromsø	Structure study of RAC GTPases from Arabidopsis thaliana
Smalås	Arnt Raae	University of Tromsø	Structure study of spectrin
Smith	Ley	Advanced Light Source.	Momentum-resolved electronic structure of transition metal dichalcogenides with tuned dimensionality.
Stalder		Geowissenschaftliches Zentrum der Universität Göttingen	Hydrogen Diffusion in Orthopyroxene
Starke		FU Berlin	Rashba Effect at Interfaces
Steinrück	Denecke	Universität Erlangen-Nürnberg	Höchstaufgelöste Photoelektronenspektroskopie mit Synchrotronstrahlung zur in situ Untersuchung von Oberflächenreaktionen

Project leader	Partners / Co-workers	Institute	Project title
Sträter		Universität Leipzig	RdpA and SdpA
Sträter		Universität Leipzig	AP endonuclease from the archaeon Methanothermobacter thermoautotrophicus (ExoMt)
Sträter		Universität Leipzig	DNA-binding protein Sac7e from the archeon Sulfolobus acidocalcidarius
Sträter		Universität Leipzig	DNase from archaeon Archeoglobus fulgidus (ExoAf)
Sträter	Küttner, Bartholomeus	Universität Leipzig	Hexokinase-1 from the yeast Kluyveromyces lactis (KlHxk1)
Sträter	Marek, Sascha	Universität Leipzig	Pichia Pfk
Sträter	Krauße, Jörn	Universität Leipzig	RdpA and SdpA
Strempfer		Max-Planck-Institut für Festkörperforschung	Resonant scattering from ferrites
Stubbs		Martin-Luther-Universität Halle-Wittenberg	Crystal structure of the promiscuous natural product class I O-Methyltransferase from Mesembryanthemum crystallinum
Stubbs		Martin-Luther-Universität Halle-Wittenberg	Dipeptidylpeptidase IV - ligand complexes
Stubbs		Martin-Luther-Universität Halle-Wittenberg	Tungsten binding protein TupA
Süllow		TU Braunschweig	Interplay between structural properties and electronic ground states in organic superconductors
Szargan		Universität Leipzig	Electronic structure of photochromic compounds
Teschner	Knop Schlögl	Fritz-Haber-Institut der MPG	Preferential oxidation of CO over supported and alloy catalysts in H2-rich gas for fuel cell applications
Thirup		University of Aarhus	Structural studies of the Vps10p domain of human Sortilin
Thirup	Brodersen, Ditlev	University of Aarhus	Structure of the deadenylation machinery from S. pombe
Thomas	Vidal Erko	Université Paul Cézanne	Glancing Incidence X-ray fluorescence Analysis (GIXA) on a multilayered structures.
Tiedemann	Haibel	Technische Universität Berlin	High-resolution tomography investigations of micro-cracks in granite
Troyanov	Sidorov, Lev	Humbold Universität	Structural Chemistry of Fullerenes and their Derivatives
Umbach	Schöll Umbach	Universität Würzburg	High-resolution x-ray absorption experiments on large organic molecules in the gasphase
Umbach	Schmidt, Th.	Universität Würzburg	Höchstaufgelöste Elektronenspektroskopie mit dem fehlerkorrigierten SMART-Spektromikroskop
Umbach		Universität Würzburg	Organic semiconductors: Analysis of growth modes and electronic structure by multi-technique x-ray investigations
Unger		Bundesanstalt für Materialforschung und -prüfung (BAM)	NEXAFS an Plasmapolymerschichten unter Ausschluss von Luftexposition bzw. definierter Alterung in Luft

Project leader	Partners / Co-workers	Institute	Project title
Unger		Bundesanstalt für Materialforschung und -prüfung (BAM)	Untersuchung ultra dünner, im Plasma abgeschiedener radikalhaltiger Polymerfilme mit der Röntgenabsorptionsspektroskopie (NEXAFS)
Valencia	Gudat	BESSY	Fluorescence K-edge spectroscopy on La2/3Ca1/3MnO3 thin films at the KMC-2 beamline
Valloppilly	Staub (SLS,PSI)	Technische Universität München	Element specific magnetization reversal of FM/AF/FM trilayers by magnetic x-ray reflectivity
Van der Oost		Wageningen University	Sugar dehydrogenases of hyperthermophiles
Van der Oost		Wageningen University	Surface Layer Protein from Pyrococcus furiosus
Varykhalov	Rader Gudat	BESSY	Low-dimensional magnetism of nanoscaled clusters of 3d transition metals: Co and Ni on Au facets
Viart	C. Meny, A. Barla, JP Kappler	IPCMS	Introducing a hard ferrimagnet as a pinning layer in magnetoresistive devices : study of CoFe2O4 by Magnetic Circular Dichroism
Vinogradov	Sokolov	St. Petersburg State University	High-resolution x-ray absorption study of chemical bonding effects in chromium compounds
Vinogradov	Szargan	St. Petersburg State University	Resonant soft X-ray emission study of half-metallic ferromagnetic CrO2 (100) films at the Cr 2p and O 1s edges
Vogt		Univerität Hannover	Spatially resolved analysis of organic compounds within marine biomineralisations products
Wandelt	Broeckmann	Universität Bonn	Template controlled formation of semiconducting CdS-films on Cu(hkl) substrates- an electrochemical approach
Weigelt		Karolinska Institute	Structural Genomics on Human Proteins
Weinelt	Gießel	MBI	NEFAXS Spektroskopie und Autoionisation an photochromen Schaltermolekülen adsorbiert auf Gold Oberflächen
Weinelt	Gießel	MBI	Laserinduzierte Diffusion und Desorption von Adsorbaten nachgewiesen mit hochauflösender Rumpfniveauspektroskopie
Weinelt	Gießel	MBI	Rumpfniveauspektroskopie an photochromen Schaltermolekülen - funktionalisierte Azobenzolderivate an Oberflächen
Wende	Baberschke	FU Berlin	Local Spin-fluctuations close to the Curie temperature
Wende	Baberschke	FU Berlin	Oxygen polarization and magnetic surface anisotropy of surfactant-grown ultrathin 3d ferromagnets
Wernet	Eisebitt	BESSY	X-ray Absorption Spectroscopy of Liquids – Solute-Solvent Interactions, Hydrogen Bonds and Water
Weschke		Institut für Experimentalphysik	Electronic structure of thin monoxide films of 3d transition metals

Project leader	Partners / Co-workers	Institute	Project title
Weschke		Freie Universität Berlin	Resonant magnetic soft x-ray scattering from exchange spring magnets
Weschke		Freie Universität Berlin	Magnetic correlation in Co/Pt nanodot arrays
Wilmanns	Tucker	EMBL Hamburg Outstation	Nucleotide binding for Rv0902c from Mycobacterium Tuberculosis
Wilmanns	Nissen	EMBL Hamburg Outstation	POU4PORE
Wilmanns	Weiss	EMBL Hamburg Outstation	Protein from Mycobacterium tuberculosis
Wilmanns	Tucker	EMBL Hamburg Outstation	Structurae of RV0844c from Mycobacterium tuberculosis
Wilmanns	Kursula, Petri	EMBL Hamburg Outstation	Structural analysis of the activation of human DRP-1 kinase, a death-associated protein kinase
Wilmanns	Groves	EMBL Hamburg Outstation	Structural Genomics of Proteins from Mycobacteria Tuberculosis
Wilmanns	Kursula, Petri	EMBL Hamburg Outstation	Structural genomics of yeast SH3 domains
Wilmanns	Kursula, Inari	EMBL Hamburg Outstation	Structural studies on histone deacetylase 6
Wilmanns	Kuper	EMBL Hamburg Outstation	Structural studies on TrkB and TrkC receptor tyrosine kinases
Wilmanns	Kursula, Petri	EMBL Hamburg Outstation	Structure of the human pro-apoptotic protein kinase ZIP
Wilmanns	Müller	EMBL Hamburg Outstation	Titin kinase
Wilmanns	Kuper	EMBL Hamburg Outstation	Towards the Ig-like domains of the titin I-band
Wilmanns	Pinotsis	EMBL Hamburg Outstation	Towards the structure of the domains 12-13 of the muscle protein M

Project leader	Partners / Co-workers	Institute	Project title
Wilmanns	Weiss	EMBL Hamburg Outstation	Use of longer wavelengths in protein crystallography
Winkler	Kirschner	MPI für Mikrostrukturphysik	Two electron photoemission from surfaces
Winter		Max-Born-Institut für Nichtlineare Optik und Kurzzeitspektroskopie	Photoelectron spectroscopy at liquid surfaces
Wöll	Strunskus	Ruhr-Universität Bochum, NL 5	Charakterisierung von organischen Halbleiterschichten mittels Röntgenabsorptionsspektroskopie
Wöll	Strunskus	Ruhr-Universität Bochum, NL 5	Untersuchung von ausgewählten Katalysatorproben und Zeolithen mittels Röntgenemissionsspektroskopie (XES)
Woodruff	FHI	University of Warwick	Scanned-energy mode photoelectron diffraction at BESSY II
Wurth		Universität Hamburg	Magnetic properties of chemically prepared CoPt3 nano crystals
Wurth	Föhlisch	Universität Hamburg	Interfaces of semiconductor systems studied by resonant inelastic X-ray scattering and NEXAFS: Molecular adsorption on Si-surfaces, Interfaces of III-V semiconductor nanoclusters
Wurth		Universität Hamburg	Magnetic properties of small, size-selected, deposited transition metal clusters
Yashina	Püttner	Moscow State University	Reactions on the PbX(X = S,Se,Te) (001) surfaces involved in H2S detection mechanism
Zabel	Bergmann	Ruhr Universität Bochum	Element-specific characterization of the interface magnetism in [Co2MnGe/Al2O3]n multilayers by x-ray resonant magnetic scattering
Zabel	Nefedov	Ruhr Universität Bochum	XMCD and XRMS studies of ZnO-based diluted magnetic semiconductors
Zabel	Kravtsov	Ruhr Universität Bochum	Induced magnetic moments in Cr/V multilayers
Zahn	Molodtsov	Technische Universität Chemnitz	Bio-organic molecules on silicon: electronic structure and molecular orientation
Zahn		Technische Universität Chemnitz	VUV-XUX Spectroscopy Ellipsometry Investigations of Organic Untra Thin Films
Zeimer		Ferdinand-Braun-Institut für Höchstfrequenztechnik	X-ray analysis of heat sink mounted disk laser devices
Zemlyanov	Knop Schlögl	University of Limerick	XPS and NEXAFS characterization of active phases of vanadium-based heterogeneous catalysts for selective oxidation of paraffins
Zharnikov	Grunze	Universität Heidelberg	Röntgenspektroskopie an organischen Grenzflächen und Biomaterialien in Kontakt mit Lösungen
Zimina		BESSY	Electronic structure if Si nanoccrystals in SiO2 Matrices

Project leader	Partners / Co-workers	Institute	Project title
Zimmermann		Technische Universität Berlin	Angular distribution of Cs 3d photoelectrons testing spin-orbit activated interchannel coupling
Zimmermann	Meyer	Technische Universität Berlin	Correlation Effects in the Photoionization of Laser-excited Atoms
Zimmermann		Technische Universität Berlin	Photoelektronen- und Photoionenspektroskopie an zwei- und dreiatomigen Molekülen
Zizak		Hahn-Meitner-Institut Berlin GmH	Texture modification in nanocrystalline materials using swift heavy ions
Zizak		Hahn-Meitner-Institut Berlin GmbH	Texture modifications inTi by swift heavy ions

List of Publications

Allegretti, F., O'Brien, S., Polcik, M., Sayago, D. I., and Woodruff, D. P.: "Adsorption bond length for H2O on TiO2(110): A key parameter for theoretical understanding." *Physical Review Letters*, **95**(22): 226104 (2005).

Allegretti, F., Polcik, M., Sayago, D. I., Demirors, F., O'Brien, S., Nisbet, G., Lamont, C. L. A., and Woodruff, D. P.: "Can circular dichroism in core-level photoemission provide a spectral fingerprint of adsorbed chiral molecules?" *New Journal of Physics*, **7**: 109 (2005).

Andriyevskyy, B., Ciepluch-Trojanek, W., Romanyuk, M., and Patryn, A.: "Band structure and optical properties of diglycine nitrate crystal." *Physica B: Physics of Condensed Matter*, **364**(1-4): 78-84 (2005).

Andriyevskyy, B., Kapustianyk, V., Ciepluch-Trojanek, W., and Batiuk, A.: "Band structure and optical electron spectra of (TrMA)CoCl3*2H2O crystal." *Physica B: Physics of Condensed Matter*, **367**(1-4): 216-222 (2005).

Bansmann, J., Baker, S. H., Binns, C., Blackman, J. A., Bucher, J. P., Dorantes-Davila, J., Dupuis, V., Favre, L., Kechrakos, D., Kleibert, A., Meiwes-Broer, K. H., Pastor, G. M., Perez, A., Toulemonde, O., Trohidou, K. N., Tuaillon, J., and Xie, Y.: "Magnetic and structural properties of isolated and assembled clusters." *Surface Science Reports*, **56**(6-7): 189-275 (2005).

Bansmann, J., Getzlaff, M., Kleibert, A., Bulut, F., Gebhardt, R. K., and Meiwes-Broer, K. H.: "Mass-filtered cobalt clusters in contact with epitaxially ordered metal surfaces." *Applied Physics a-Materials Science & Processing*, **82**(1): 73-79 (2006).

Bansmann, J., and Kleibert, A.: "Magnetism of mass-filtered nanoparticles on ferromagnetic supports." *Applied Physics a-Materials Science & Processing*, **80**(5): 957-964 (2005).

Bär, M., Bloeck, U., Muffler, H.-J., Lux-Steiner, M. C., Fischer, C.-H., Giersig, M., Niesen, T. P., and Karg, F.: "Cd2+ N H3 -treatment of Cu (In,Ga) (S,Se)2: Impact on the properties of ZnO layers deposited by the ion layer gas reaction method." *Journal of Applied Physics*, **97**(1): 014905-1-014905-8 (2005).

Bär, M., Lehmann, S., Rusu, M., Grimm, A., Kötschau, I., Lauermann, I., Pistor, P., Sokoll, S., Schedel-Niedrig, T., Lux-Steiner, M. C., Fischer, C.-H., Weinhardt, L., Heske, C., and Jung, C.: "Cd2+ N H3 treatment-induced formation of a CdSe surface layer on CuGa Se2 thin-film solar cell absorbers." *Applied Physics Letters*, **86**(22): 1-3 (2005).

Bär, M., Rusu, M., Lehmann, S., Sokoll, S., Grimm, A., Kötschau, I. M., Lauermann, I., Pistor, P., Weinhardt, L., Fuchs, O., Heske, C., Jung, C., Gudat, W., Schedel-Niedrig, T., Lux-Steiner, M. C., and Fischer, C.-H.: "Cd2+/NH3-treatment of high-gap CuGaSe2 thin film solar cell absorbers." *Conference Record of the IEEE Photovoltaic Specialists Conference*: 307-310 (2005).

Barth, S., Joshi, S., Marburger, S., Ulrich, V., Lindblad, A., Ohrwall, G., Bjorneholm, O., and Hergenhahn, U.: "Observation of resonant interatomic Coulombic decay in Ne clusters." *Journal of Chemical Physics*, **122**(24): 241102 (2005).

Beernink, G., Strunskus, T., Witte, G., and Wöll, C.: "The importance of dewetting in organic molecular beam deposition: pentacene on gold." *Appl. Phys. Lett.*, **85**(3): 398-400 (2004).

Bereznev, S., Konovalov, I., Opik, A., and Kois, J.: "Hybrid CuInS2/polypyrrole and CuInS2/poly(3,4-ethylenedioxythiophene) photovoltaic structures." *Synthetic Metals*, **152**(1-3): 81-84 (2005).

Bereznev, S., Konovalov, I., Opik, A., Kois, J., and Mellikov, E.: "Hybrid copper-indium disulfide/polypyrrole photovoltaic structures prepared by electrodeposition." *Solar Energy Materials and Solar Cells*, **87**(1-4): 197-206 (2005).

Biermann, S., Dallmeyer, A., Carbone, C., Eberhardt, W., Pampuch, C., Rader, O., Katsnelson, M. I., and Lichtenstein, A. I.: "Observation of Hubbard bands in gamma-manganese." *Jetp Letters*, **80**(9): 612-615 (2005).

Binns, C., Trohidou, K. N., Bansmann, J., Baker, S. H., Blackman, J. A., Bucher, J. P., Kechrakos, D., Kleibert, A., Louch, S., Meiwes-Broer, K. H., Pastor, G. M., Perez, A., and Xie, Y.: "The behaviour of nanostructured magnetic materials produced by depositing gas-phase nanoparticles." *Journal of Physics D-Applied Physics*, **38**(22): R357-R379 (2005).

Biswas, I., Peisert, H., Schwieger, T., Dini, D., Hanack, M., Knupfer, M., Schmidt, T., and Chasse, T.: "Tetra-t-butyl magnesium phthalocyanine on gold: Electronic structure and molecular orientation." *Journal of Chemical Physics*, **122**(6): 064710 (2005).

Bluhm, H., Havecker, M., Knop-Gericke, A., Kleimenov, E., Schlogl, R., Teschner, D., Bukhtiyarov, V. I., Ogletree, D. F., and Salmeron, M.: "Methanol oxidation on a copper catalyst investigated using in situ X-ray photoelectron spectroscopy." *Journal of Physical Chemistry B*, **108**(38): 14340-14347 (2004).

Bodenthin, Y., Pietsch, U., Grenzer, J., Geue, T., Mohwald, H., and Kurth, D. G.: "Structure and temperature behavior of metallo-supramolecular assemblies." *Journal of Physical Chemistry B*, **109**(26): 12795-12799 (2005).

Bodenthin, Y., Pietsch, U., Mohwald, H., and Kruth, D. G.: "Inducing spin crossover in metallo-supramolecular polyelectrolytes through an amphiphilic phase transition." *Journal of the American Chemical Society*, **127**(9): 3110-3114 (2005).

Borgna, A., Anderson, B. G., Saib, A. M., Bluhm, H., Havecker, M., Knop-Gericke, A., Kuiper, A. E. T., Tamminga, Y., and Niemantsverdriet, J. W.: "Pt-CO/SiO2 bimetallic planar model catalysts for selective hydrogenation of crotonaldehyde." *Journal of Physical Chemistry B*, **108**(46): 17905-17914 (2004).

Bradeanu, I. L., Flesch, R., Meyer, M., Jochims, H.-W., and Rühl, E.: "Radiative relaxation in 2p-excited argon clusters: Evidence for the interatomic Coulombic decay mechanism." *European Physical Journal D*, **36**(2): 173-178 (2005).

Bron, M., Teschner, D., Knop-Gericke, A., Scheybal, A., Steinhauer, B., Havecker, M., Fodisch, R., Honicke, D., Schlogl, R., and Claus, P.: "In situ-XAS and catalytic study of acrolein hydrogenation over silver catalyst: Control of intramolecular selectivity by the pressure." *Catalysis Communications*, **6**(5): 371-374 (2005).

Bron, M., Teschner, D., Knop-Gericke, A., Steinhauer, B., Scheybal, A., Havecker, M., Wang, D., Fodisch, R., Honicke, D., Wootsch, A., Schlogl, R., and Claus, P.: "Bridging the pressure and materials gap: in-depth characterisation and reaction studies of silver-catalysed acrolein hydrogenation." *Journal of Catalysis*, **234**(1): 37-47 (2005).

Buchheim, C., Goldhahn, R., Rakel, M., Cobet, C., Esser, N., Rossow, U., Fuhrmann, D., and Hangleiter, A.: "Dielectric function and critical points of the band structure for AlGaN alloys." *Physica Status Solidi B-Basic Solid State Physics*, **242**(13): 2610-2616 (2005).

Buermann, L., Krumrey, M., Haney, M., and Schmid, E.: "Is there reliable experimental evidence for different dicentric yields in human lymphocytes produced by mammography X-rays free-in-air and within a phantom?" *Radiation and Environmental Biophysics*, **44**(1): 17-22 (2005).

Buttner, C. R., Cornelis, G. R., Heinz, D. W., and Niemann, H. H.: "Crystal structure of Yersinia enterocolitica type III secretion chaperone SycT." *Protein Sci*, **14**(8): 1993-2002 (2005).

Cooke, S. A., Krumrey, C., and Gerry, M. C. L.: "Pure rotational spectra of LuF and LuCl." *Physical Chemistry Chemical Physics*, **7**(13): 2570-2578 (2005).

Darowski, N., Zizak, I., and Schumacher, G.: "Surface and bulk structural changes in InP single crystals induced by 350 Mev Au ion irradiation." *Physica B: Condensed Matter*, **357**(1-2 SPEC. ISS.): 118-121 (2005).

Darowski, N., Zizak, I., Schumacher, G., Klingelhöffer, H., Chen, W., and Neumann, W.: "Temperature dependence of x-ray intensity profile FWHM of the gamma ' phase in the creep-deformed single crystal superalloy SC16." *Journal of Physics D: Applied Physics*, **38**(10 A): A200-A203 (2005).

de Groot, F. M. F., Glatzel, P., Bergmann, U., van Aken, P. A., Barrea, R. A., Klemme, S., Havecker, M., Knop-Gericke, A., Heijboer, W. M., and Weckhuysen, B. M.: "1s2p resonant inelastic X-ray scattering of iron oxides." *Journal of Physical Chemistry B*, **109**(44): 20751-20762 (2005).

Demekhin, P. V., Petrov, I. D., Lagutin, B. M., Sukhorukov, V. L., Vollweiler, F., Klumpp, S., Ehresmann, A., Schartner, K.-H., and Schmoranzer, H.: "Interaction between resonances through autoionization continua near the 4s-threshold in KrII." *Journal of Physics B: Atomic, Molecular and Optical Physics*, **38**(17): 3129-3145 (2005).

Denecke, R.: "Surface chemistry studied by in situ X-ray photoelectron spectroscopy." *Applied Physics a-Materials Science & Processing*, **80**(5): 977-986 (2005).

Denecke, R., and Mårtensson, N.: "Adsorbate induced surface core level shift." Landolt-Börnstein, New series III/42A4 "Physics of Covered Solid Surfaces I. Adsorbed Layers on Surfaces": 388-421.

Denker, A., Hahn, O., Merchel, S., Radtke, M., Kanngießer, B., Malzer, W., Röhrs, S., Reiche, I., and Stege, H.: "X-ray analysis for works of art and cultural assets." *Nachrichten aus der Chemie*, **53**(2): 118-123 (2005).

Ehresmann, A., Junk, D., Engel, D., Paetzold, A., and Röll, K.: "On the origin of ion bombardment induced exchange bias modifications in polycrystalline layers." *Journal of Physics D: Applied Physics*, **38**(6): 801-806 (2005).

Ehresmann, A., Werner, L., Klumpp, S., Lucht, S., Schmoranzer, H., Mickat, S., Schill, R., Schartner, K.-H., Demekhin, P. V., Lemeshko, M. P., and Sukhorukov, V. L.: "Studying the N+ 2(C2? + u ? X2?+ g) fluorescence excited via the 1s-1?* resonance." *Journal of Physics B: Atomic, Molecular and Optical Physics*, **39**(2): 283-304 (2006).

Eiper, E., Martinschitz, K. J., Gerlach, J. W., Lackner, J. M., Zizak, I., Darowski, N., and Keckes, J.: "X-ray elastic constants determined by the combination of sin2 Psi and substrate-curvature methods." *Zeitschrift fuer Metallkunde/Materials Research and Advanced Techniques*, **96**(9): 1069-1073 (2005).

Eisebitt, S., Lörgen, M., Eberhardt, W., Lüning, J., and Stöhr, J.: "Lensless X-ray imaging of magnetic materials: basic considerations." *Applied Physics a-Materials Science & Processing*, **80**(5): 921-927 (2005).

El-Gezawy, H., Rettig, W., Danel, A., and Jonusauskas, G.: "Probing the photochemical mechanism in photoactive yellow protein." *Journal of Physical Chemistry B*, **109**(39): 18699-18705 (2005).

El-Gezawy, H., Rettig, W., and Lapouyade, R.: "Model studies of spectral and photophysical characteristics of donor-acceptor-polyenes: dimethylamino-cyano-diphenylbutadiene." *Chemical Physics Letters*, **401**(1-3): 140-148 (2005).

Engel, D., Ehresmann, A., Schmalhorst, J., Sacher, M., Höink, V., and Reiss, G.: "Initialization of unidirectional anisotropy in a ferromagnet- antiferromagnet bilayer by keV-He ion bombardment." *Journal of Magnetism and Magnetic Materials*, **293**(3): 849-853 (2005).

Ensling, D., Thißen, A., Gassenbauer, Y., Klein, A., and Jaegermann, W.: "In-situ preparation and analysis of functional oxides." *Advanced Engineering Materials*, **7**(10): 945-949 (2005).

Escher, M., Weber, N., Merkel, M., Kromker, B., Funnemann, D., Schmidt, S., Reinert, F., Forster, F., Hufner, S., Bernhard, P., Ziethen, D., Elmers, H. J., and Schonhense, G.: "NanoESCA: Imaging UPS and XPS with high energy resolution." *Journal of Electron Spectroscopy and Related Phenomena*, **144**: 1179-1182 (2005).

Esser, N., Rakel, M., Cobet, C., Schmidt, W. G., Braun, W., and Cardona, M.: "VUV-ellipsometry on GaN: Probing conduction band properties by core level excitations." *Physica Status Solidi B-Basic Solid State Physics*, **242**(13): 2601-2609 (2005).

Fahnle, M., Albrecht, J., Eimuller, T., Fischer, P., Goering, E., Steiauf, D., and Schutz, G.: "On the imaging of the flux-line lattice of a type-II superconductor by soft X-ray absorption microscopy." *Journal of Synchrotron Radiation*, **12**: 251-253 (2005).

Fauth, K., Goering, E., Schutz, G., and Kuhn, L. T.: "Probing composition and interfacial interaction in oxide passivated core-shell iron nanoparticles by combining x-ray absorption and magnetic circular dichroism." *Journal of Applied Physics*, **96**(1): 399-403 (2004).

Fecher, G. H., Kandpal, H. C., Wurmehl, S., Morais, J., Lin, H. J., Elmers, H. J., Schonhense, G., and Felser, C.: "Design of magnetic materials: the electronic structure of the ordered, doped Heusler compound Co2Cr1-xFexAl." *Journal of Physics-Condensed Matter*, **17**(46): 7237-7252 (2005).

Feulner, P., Ecker, M., Jakob, P., Romberg, R., Weimar, R., Menzel, D., Fohlisch, A., Wurth, W., Yang, S. H., Fadley, C. S., Larciprete, R., Lizzit, S., Kostov, K. L., and Tyuliev, G.: "Search for a local effect in multiatom resonant core excitation in a surface species: Photoemission and photon-stimulated desorption from N-2,on Ni(111)." *Physical Review B*, **71**(12): 125409 (2005).

Feulner, P., Niedermayer, T., Eberle, K., Schneider, R., Menzel, D., Baumer, A., Schmich, E., Shaporenko, A., Tai, Y., and Zharnikov, M.: "Strong temperature dependence of irradiation effects in organic layers." *Surface Science*, **593**(1-3): 252-255 (2005).

Föhlisch, A., Feulner, P., Hennies, F., Fink, A., Menzel, D., Sanchez-Portal, D., Echenique, P. M., and Wurth, W.: "Direct observation of electron dynamics in the attosecond domain." *Nature*, **436**(7049): 373-376 (2005).

Friedrich, S., Fliegauf, R., Frank, M., Veldkamp, M., Labov, S., Beckhoff, B., and Ulm, G.: "The spectral response of superconducting tunnel junction X-ray detectors." *Nuclear Instruments and Methods in Physics Research, Section A: Accelerators, Spectrometers, Detectors and Associated Equipment*, **551**(1): 35-45 (2005).

Fuhrmann, T.: "Elektronenspektroskopische Untersuchungen zur aktivierten Adsorption und thermischen Entwicklung von einfachen Kohlenwasserstoffen auf Platin- und Nickel-Einkristalloberflächen," (2005).

Fuhrmann, T., Kinne, M., Trankenschuh, B., Papp, C., Zhu, J. F., Denecke, R., and Steinruck, H. P.: "Activated adsorption of methane on Pt(111) - an in situ XPS study." *New Journal of Physics*, **7**: 107 (2005).

Fukumoto, K., Kuch, W., Vogel, J., Camarero, J., Pizzini, S., Offi, F., Pennec, Y., Bonfim, M., Fontaine, A., and Kirschner, J.: "Mobility of domain wall motion in the permalloy layer of a spin-valve-like Fe20Ni80/Cu/Co trilayer." *Journal of Magnetism and Magnetic Materials*, **293**(3): 863-871 (2005).

Gao, X., Xu, H., Wee, A. T. S., Kuch, W., Tieg, C., and Wang, S.: "Magnetic circular dichroism study of Fe/Co/Cu(001) using electron yield x-ray absorption spectroscopy with different probe depths." *Journal of Applied Physics*, **97**(10): 103527 (2005).

Gavrila, G. N., Mendez, H., Kampen, T. U., Zahn, D. R. T., Vyalikh, D. V., and Braun, W.: "Energy band dispersion in well ordered N,N '-dimethyl-3,4,9,10-perylenetetracarboxylic diimide films." *Applied Physics Letters*, **85**(20): 4657-4659 (2004).

Gensch, M.: "Infrared Ellipsometry for the investigation of interfacial layers and thin organic films on silicon," ISAS and TU Berlin (2005).

Gensch, M., Roodenko, K., Hinrichs, K., Hunger, R., Guell, A. G., Merson, A., Schade, U., Shapira, Y., Dittrich, T., Rappich, J., and Esser, N.: "Molecule-solid interfaces studied with infrared ellipsometry: Ultrathin nitrobenzene films." *Journal of Vacuum Science & Technology B*, **23**(4): 1838-1842 (2005).

Getzlaff, M., Bansmann, J., Bulut, F., Gebhardt, R. K., Kleibert, A., and Meiwes-Broer, K. H.: "Structure, composition and magnetic properties of size-selected FeCo alloy clusters on surfaces." *Applied Physics a-Materials Science & Processing*, **82**(1): 95-101 (2006).

Girol, S., Strunskus, T., and Wöll, C.: "The reactivity of ZnO-surface towards maleic anhydride." *J. Phys. Chem. B*, **108**(36): 13736-13745 (2004).

Goering, E.: "X-ray magnetic circular dichroism sum rule correction for the light transition metals." *Philosophical Magazine*, **85**(25): 2895-2911 (2005).

Goering, E., Gold, S., and Bayer, A.: "Ground-State-Moment-Analysis: A quantitative tool for X-ray magnetic circular dichroism analysis for 3d transition metals." *Applied Physics a-Materials Science & Processing*, **78**(6): 855-865 (2004).

Goering, E., Gold, S., Lafkioti, M., and Schutz, G.: "Vanishing Fe 3d orbital moments in single-crystalline magnetite." *Europhysics Letters*, **73**(1): 97-103 (2006).

Goering, E., Gold, S., Lafkioti, M., Schutz, G., and Brabers, V. A. M.: "Oxygen K-edge shift at the Verwey transition of magnetite." *Physical Review B*, **72**(3): 033112 (2005).

Goering, E., Lafkioti, M., and Gold, S.: "Comment on "Spin and orbital magnetic moments of Fe3O4"." *Physical Review Letters*, **96**(3): 039701 (2006).

Gold, S., Goering, E., Konig, C., Rudiger, U., Guntherodt, G., and Schutz, G.: "Temperature dependence of the magnetocrystalline anisotropy energy and projected microscopic magnetic moments in epitaxial CrO2 films." *Physical Review B*, **71**(22): 220404 (2005).

Goldhahn, R., Schley, P., Winzer, A. T., Gobsch, G., Cimalla, V., Ambacher, O., Rakel, M., Cobet, C., Esser, N., Lu, H., and Schaff, W. J.: "Detailed analysis of the dielectric function for wurtzite InN and In-rich InAlN alloys." *Physica Status Solidi a-Applications and Materials Science*, **203**(1): 42-49 (2006).

Goldhahn, R., Winzer, A. T., Cimalla, V., Ambacher, O., Cobet, C., Richter, W., Esser, N., Furthmuller, J., Bechstedt, F., Lu, H., and Schaff, W. J.: "Anisotropy of the dielectric function for wurtzite InN." *Superlattices and Microstructures*, **36**(4-6): 591-597 (2004).

Gonzalez, C., Benito, I., Ortega, J., Jurczyszyn, L., Blanco, J. M., Peerez, R., Flores, F., Kampen, T. U., Zahn, D. R. T., and Braun, W.: "Selenium passivation of GaAs(001): a combined experimental and theoretical study." *Journal of Physics-Condensed Matter*, **16**(13): 2187-2206 (2004).

Gorgoi, M., Gavrila, G., Zahn, D. R. T., Michaelis, W., Schlettwein, D., and Braun, W.: "Orientation of Perfluorinated Phthalocyanines: from Ultra-low Coverages on Hydrogen Passivated Silicon to Thick Layers." *BESSY Jahresbericht*, **45**: 165 (2004).

Gottwald, A., Richter, M., Ulm, G., and Schühle, U.: "Stability of vacuum-ultraviolet radiometric transfer standards: Electron cyclotron resonance versus hollow cathode source." *Review of Scientific Instruments*, **76**(2): 023101-1-023101-6 (2005).

Grabis, J.: "Element-specific x-ray circular magnetic dichroism of Co2MnGe Heusler thin films." *Physical Review B*, **72**: 024437 (2005).

Grabis, J.: "Element-specific characterization of the interface magnetism in Co2MnGe/Au n multilayers by x-ray resonant magnetic scattering." *Physical Review B*, **72**: 024438 (2005).

Gridelet, E., Dehareng, A., Locht, R., Lorquet, A. J., Lorquet, J. C., and Leyh, B.: "Ground and excited state dissociation dynamics of ionized 1,1-difluoroethene." *Journal of Physical Chemistry A*, **109**(37): 8225-8235 (2005).

Guerra, M. F., Calligaro, T., Radtke, M., Reiche, I., and Riesemeier, H.: "Fingerprinting ancient gold by measuring Pt with spatially resolved high energy Sy-XRF." *Nuclear Instruments and Methods in Physics Research, Section B: Beam Interactions with Materials and Atoms*, **240**(1-2): 505-511 (2005).

Hague, C. F., Underwood, J. H., Avila, A., Delaunay, R., Ringuenet, H., Marsi, M., and Sacchi, M.: "Plane-grating flat-field soft x-ray spectrometer." *Review of Scientific Instruments*, **76**(2): 023110 (2005).

Hahn, O., Malzer, W., Kanngiesser, B., and Beckhoff, B.: "Characterization of iron-gall inks in historical manuscripts and music compositions using x-ray fluorescence spectrometry." *X-Ray Spectrometry*, **33**(4): 234-239 (2004).

Hänel, K., Söhnchen, S., Lukas, S., Beernink, G., Birkner, A., Strunskus, T., Witte, G., and Wöll, C.: "Organic molecular- beam deposition of perylene on Cu(110): Results from near-edge x-ray absorption spectroscopy, x-ray photoelectron spectroscopy, and atomic force microscopy." *J. Mat. Research*, **19**(7): 2049-2056 (2004).

Harding, C. J., Mikajlo, E., Powis, I., Barth, S., Joshi, S., Ulrich, V., and Hergenhahn, U.: "Circular dichroism in the angle-resolved C 1s photoemission spectra of gas-phase carvone enantiomers." *Journal of Chemical Physics*, **123**(23): 1-10 (2005).

Hatsui, T., Setoyama, H., Kosugi, N., Wassermann, B., Bradeanu, I. L., and Rühl, E.: "Photoionization of small krypton clusters in the Kr 3d regime: Evidence for site-specific photoemission." *Journal of Chemical Physics*, **123**(15): 1-6 (2005).

Havecker, M., Knop-Gericke, A., Bluhm, H., Kleimenov, E., Mayer, R. W., Fait, M., and Schlogl, R.: "Dynamic surface behaviour of VPO catalysts under reactive and non-reactive gas compositions: an in situ XAS study." *Applied Surface Science*, **230**(1-4): 272-282 (2004).

Held, G., Jones, L. B., Seddon, E. A., and King, D. A.: "Effect of oxygen adsorption on the chiral Pt{531} surface." *Journal of Physical Chemistry B*, **109**(13): 6159-6163 (2005).

Held, G., and Steinrück, H. P.: "Cyclic hydrocarbons." Landolt-Börnstein, New series III/42A4 "Physics of Covered Solid Surfaces I. Adsorbed Layers on Surfaces": 300-369.

Hennies, F., Polyutov, S., Minkov, I., Pietzsch, A., Nagasono, M., Gel'Mukhanov, F., Triguero, L., Piancastelli, M.-N., Wurth, W., Agren, H., and Föhlisch, A.: "Nonadiabatic effects in resonant inelastic X-ray scattering." *Physical Review Letters*, **95**(16): 163002 (2005).

Hergenhahn, U.: "Photoionization of Molecules and Clusters at a Third Generation Synchrotron Radiation Source," Freie Universität Berlin (2005).

Himcinschi, C., Gordan, O., Salvan, G., Müller, F., Zahn, D. R. T., Cobet, C., Esser, N., and Braun, W.: "Stability of tris(8-hydroxyquinoline)-aluminum(III) films investigated by vacuum ultraviolet spectroscopic ellipsometry." *Applied Physics Letters*, **86**(11): 111907 (2005).

Hinrichs, K., Gensch, M., and Esser, N.: "Analysis of organic films and interfacial layers by infrared spectroscopic ellipsometry." *Applied Spectroscopy*, **59**(11): 272a-282a (2005).

Hinrichs, K., Silaghi, S. D., Cobet, C., Esser, N., and Zahn, D. R. T.: "Ellipsometry from infrared to vacuum ultraviolet: Structural properties of thin anisotropic guanine films on silicon." *Physica Status Solidi B-Basic Solid State Physics*, **242**(13): 2681-2687 (2005).

Hirsch, T., Zharnikov, M., Shaporenko, A., Stahl, J., Weiss, D., Wolfbeis, O. S., and Mirsky, V. M.: "Size-controlled electrochemical synthesis of metal nanoparticles on monomolecular templates." *Angewandte Chemie - International Edition*, **44**(41): 6775-6778 (2005).

Höink, V., Sacher, M. D., Schmalhorst, J., Reiss, G., Engel, D., Junk, D., and Ehresmann, A.: "Postannealing of magnetic tunnel junctions with ion-bombardment-modified exchange bias." *Applied Physics Letters*, **86**(15): 152102 (2005).

Holland, D. M. P., Potts, A. W., Trofimov, A. B., Breidbach, J., Schirmer, J., Feifel, R., Richter, T., Godehusen, K., Martins, M., Tutay, A., Yalcinkaya, M., Al-Hada, M., Eriksson, S., and Karlsson, L.: "An experimental and theoretical study of the valence shell photoelectron spectrum of tetrafluoromethane." *Chemical Physics*, **308**(1-2): 43-57 (2005).

Hunger, R., Schulmeyer, T., Klein, A., Jaegermann, W., Lebedev, M. V., Sakurai, K., and Niki, S.: "SXPS investigation of the Cd partial electrolyte treatment of CuInSe 2 absorbers." *Thin Solid Films*, **480-481**: 218-223 (2005).

Jakob, G., Casper, F., Beaumont, V., Falk, S., Auth, N., Elmers, H. J., Felser, C., and Adrian, H.: "Thin epitaxial films of the Heusler compound Co2Cr0.6Fe0.4Al." *Journal of Magnetism and Magnetic Materials*, **290**: 1104-1107 (2005).

Jensen, P. J., Sorg, C., Scherz, A., Bernien, M., Baberschke, K., Wende, H., Won, C., Wu, Y. Z., Kurahashi, N., Zhao, H. W., Qiu, Z. Q., Scholl, A., and Doran, A.: "Comment on "magnetic phase transition in Co/Cu/Ni/Cu(100) and Co/Fe/Ni/Cu(100)"." *Physical Review Letters*, **94**(3): 039703 (2005).

Jiang, Y. H., Puttner, R., Hentges, R., Viefhaus, J., Poygin, M., Cacho, C., Becker, U., Rost, J. M., and Kaindl, G.: "Partial photoionization cross sections of doubly excited helium below the ionization thresholds I-8 and I-9." *Journal of Physics B-Atomic Molecular and Optical Physics*, **39**(1): L9-L16 (2006).

Jorgensen, R., Merrill, A. R., Yates, S. P., Marquez, V. E., Schwan, A. L., Boesen, T., and Andersen, G. R.: "Exotoxin A-eEF2 complex structure indicates ADP ribosylation by ribosome mimicry." *Nature*, **436**(7053): 979-984 (2005).

Käfer, D., Witte, G., Cyganik, P., Terfort, A., and Wöll, C.: "A Comprehensive Study of Self-Assembled Monolayers of Anthracenethiol on Gold: Solvent Effects, Structure and Stability." *J. Am. Chem. Soc.*, **128**: 1723-1732 (2006).

Kanngießer, B., Hahn, O., Wilke, M., Nekat, B., Malzer, W., and Erko, A.: "Investigation of oxidation and migration processes of inorganic compounds in ink-corroded manuscripts." *Spectrochimica Acta Part B-Atomic Spectroscopy*, **59**(10-11): 1511-1516 (2004).

Kanngießer, B., Malzer, W., Rodriguez, A. F., and Reiche, I.: "Three-dimensional micro-XRF investigations of paint layers with a tabletop setup." *Spectrochimica Acta - Part B Atomic Spectroscopy*, **60**(1): 41-47 (2005).

Khyzhun, O. Y., Strunskus, T., Grünert, W., and Wöll, C.: "Valence band electronic structure of V2O5 as determined by resonant soft X-ray emission spectroscopy." *J. Electr. Spectrosc.*, **149**: 45-50 (2005).

Kleibert, A., Senz, V., Bansmann, J., and Oppeneer, P. M.: "Thickness dependence and magnetocrystalline anisotropy of the x-ray transverse magneto-optical Kerr effect at the Co 2p edges of ultrathin Co films on W(110)." *Physical Review B*, **72**(14): 144404 (2005).

Kleimenov, E., Bluhm, H., Havecker, M., Knop-Gericke, A., Pestryakov, A., Teschner, D., Lopez-Sanchez, J. A., Bartley, J. K., Hutchings, G. J., and Schlogl, R.: "XPS investigations of VPO catalysts under reaction conditions." *Surface Science*, **575**(1-2): 181-188 (2005).

Kolbe, M., Beckhoff, B., Krumrey, M., and Ulm, G.: "Comparison of reference-free X-ray fluorescence analysis and X-ray reflectometry for thickness determination in the nanometer range." *Applied Surface Science*, **252**(1 SPEC. ISS.): 49-52 (2005).

Kolbe, M., Beckhoff, B., Krumrey, M., and Ulm, G.: "Thickness determination for Cu and Ni nanolayers: Comparison of completely reference-free fundamental parameter-based X-ray fluorescence analysis and X-ray reflectometry." *Spectrochimica Acta - Part B Atomic Spectroscopy*, **60**(4): 505-510 (2005).

Koller, G., Berkebile, S., Krenn, J. R., Tzvetkov, G., Hlawacek, G., Lengyel, O., Netzer, F. P., Teichert, C., Resel, R., and Ramsey, M. G.: "Oriented sexiphenyl single crystal nanoneedles on TiO2 (110)." *Advanced Materials*, **16**(23-24): 2159-+ (2004).

Konovalov, I., Makhova, L., Hesse, R., and Szargan, R.: "Intermixing, band alignment and charge transport in AgIn5S8/CuI heterojunctions." *Thin Solid Films*, **493**(1-2): 282-287 (2005).

Krasyuk, A., Wegelin, F., Nepijko, S. A., Elmers, H. J., Schonhense, G., Bolte, M., and Schneider, C. M.: "Self-trapping of magnetic oscillation modes in Landau flux-closure structures." *Physical Review Letters*, **95**(20): 207201 (2005).

Kuepper, K., Falub, M. C., Prince, K. C., Galakhov, V. R., Troyanchuk, I. O., Chiuzbaian, S. G., Matteucci, M., Wett, D., Szargan, R., Ovechkina, N. A., Mukovskii, Y. M., and Neumann, M.: *Journal of Physical Chemistry B*, **109**(19): 9354-9361 (2005).

Kuhn, L. T., Bojesen, A., Timmermann, L., Fauth, K., Goering, E., Johnson, E., Nielsen, M. M., and Morup, S.: "Core-shell iron-iron oxide nanoparticles: magnetic properties and interactions." *Journal of Magnetism and Magnetic Materials*, **272-76**: 1485-1486 (2004).

Lagutin, B. M., Sukhorukov, V. L., Petrov, I. D., Demekhin, P. V., Schartner, K.-H., Ehresmann, A., and Schmoranzer, H.: "Interference shake-up effects in the resonant Auger decay of krypton." *Journal of Electron Spectroscopy and Related Phenomena*, **144-147**: 79-82 (2005).

Lau, J. T., Achleitner, A., Ehrke, H.-U., Langenbuch, U., Reif, M., and Wurth, W.: "Ultrahigh vacuum cluster deposition source for spectroscopy with synchrotron radiation." *Review of Scientific Instruments*, **76**(6): 1-8 (2005).

Lawaczeck, R., Arkadiev, V., Diekmann, F., and Krumrey, M.: "Monochromatic x-rays in digital mammography." *Investigative Radiology*, **40**(1): 33-39 (2005).

Lee, M. J. G., Gensch, M., Shkrebtii, A. I., Herrmann, T., Richter, W., Esser, N., and Hofmann, P.: "Surface states and resonances on Al(110): Ultraviolet photoemission spectroscopy and ab initio calculations." *Physical Review B*, **72**(8): 085408 (2005).

Lenz, K., Kosubek, E., Baberschke, K., Wende, H., Herfort, J., Schönherr, H.-P., and Ploog, K. H.: "Magnetic properties of Fe3SiGaAs(001) hybrid structures." *Physical Review B - Condensed Matter and Materials Physics*, **72**(14): 144411 (2005).

Lin, N., Payer, D., Dmitriev, A., Strunskus, T., Wöll, C., Barth, J. V., and Kern, K.: "Two-dimensional adatom gas bestowing dynamic heterogeneity on surfaces." *Angew. Chemie, Intern. Ed.*, **44**: 1488-1491 (2005).

Locht, R., Leyh, B., Dehareng, D., Jochims, H. W., and Baumgartel, H.: "The vacuum UV photoabsorption spectrum of methyl bromide (CH3Br) and its perdeuterated isotopomer CD3Br: a vibrational analysis." *Chemical Physics*, **317**(1): 87-102 (2005).

Locht, R., Leyh, B., Jochims, H. W., and Baumgartel, H.: "The vacuum UV photoabsorption spectrum of methyl bromide (CH3Br) and its perdeuterated isotopomer CD3Br: a Rydberg series analysis." *Chemical Physics*, **317**(1): 73-86 (2005).

Lohmann, B., Langer, B., Snell, G., Kleiman, U., Canton, S., Martins, M., Becker, U., and Berrah, N.: "Configuration-interaction-induced dynamic spin polarization of the Ar-*(2p(1/2,3/2)(-1)4s(1/2))(J=1) resonant Auger decay." *Physical Review A*, **71**(3): 020701 (2005).

Lohmann, B., Langer, B., Snell, G., Kleiman, U., Canton, S., Martins, M., Becker, U., and Berrah, N.: "Erratum: Configuration-interaction-induced dynamic spin polarization of the Ar*(2p1/2,3/2 -14s1/2)J=1 resonant Auger decay." *Physical Review A - Atomic, Molecular, and Optical Physics*, **71**(3): 039907 (2005).

Makhova, L., Szargan, R., and Konovalov, I.: "Investigation of the growth process and properties of CuIn5S8 and AgIn5S8 spinel thin films." *Thin Solid Films*, **472**(1-2): 157-163 (2005).

Malzer, W., and Kanngießer, B.: "A model for the confocal volume of 3D micro X-ray fluorescence spectrometer." *Spectrochimica Acta Part B-Atomic Spectroscopy*, **60**(9-10): 1334-1341 (2005).

McCord, J., Schäfer, R., Theis-Bröhl, K., Zabel, H., Schmalhorst, J., Höink, V., Brückl, H., Weis, T., Engel, D., and Ehresmann, A.: "Domain propagation in He-ion-bombarded magnetic wires with opposite exchange bias." *Journal of Applied Physics*, **97**(10): 1-3 (2005).

Meyer, R., Lahav, D., Schalow, T., Laurin, M., Brandt, B., Schauermann, S., Guimond, S., Klüner, T., Kuhlenbeck, H., Libuda, J., Shaikhutdinov, S., and Freund, H.-J.: "CO adsorption and thermal stability of Pd deposited on a thin FeO(1 1 1) film." *Surface Science*, **586**(1-3): 174-182 (2005).

Mickat, S., Schartner, K.-H., Kammer, S., Schill, R., Werner, L., Klumpp, S., Ehresmann, A., Schmoranzer, H., and Sukhorukov, V. L.: "Absolute cross sections and branching ratios for the radiative decay of doubly excited helium determined by photon-induced fluorescence spectroscopy." *Journal of Physics B: Atomic, Molecular and Optical Physics*, **38**(15): 2613-2628 (2005).

Mikhlin, Y., and Tomashevich, Y.: "Pristine and reacted surfaces of pyrrhotite and arsenopyrite as studied by X-ray absorption near-edge structure spectroscopy." *Physics and Chemistry of Minerals*, **32**(1): 19-27 (2005).

Mikhlin, Y., Tomashevich, Y., Tauson, V., Vyalikh, D., Molodtsov, S., and Szargan, R.: "A comparative X-ray absorption near-edge structure study of bornite, Cu5FeS4, and chalcopyrite, CuFeS2." *Journal of Electron Spectroscopy and Related Phenomena*, **142**(1): 83-88 (2005).

Morales, F., de Groot, F. M. F., Glatzel, P., Kleimenov, E., Bluhm, H., Havecker, M., Knop-Gericke, A., and Weckhuysen, B. M.: "In situ x-ray absorption of Co/Mn/TiO2 catalysts for Fischer-Tropsch synthesis." *Journal of Physical Chemistry B*, **108**(41): 16201-16207 (2004).

Müller, R., Scholze, F., Klein, R., Plöger, S., and Ulm, G.: "Linearity tests of silicon photodiodes for EUV radiation." *Journal of Alloys and Compounds*, **401**(1-2): 104-107 (2005).

Murali, S., Kharlanov, V., Rettig, W., Tolmachev, A. I., and Kropachev, A. V.: "The tetrafluoro analogue of DMABN: Anomalous fluorescence and mechanistic considerations." *Journal of Physical Chemistry A*, **109**(29): 6420-6429 (2005).

Murali, S., and Rettig, W.: "Meta-positioning effect in sterically hindered N-phenyl-pyrroles: A photophysical study." *Chemical Physics Letters*, **412**(1-3): 135-140 (2005).

Neeb, D., Krasyuk, A., Oelsner, A., Nepijko, S. A., Elmers, H. J., Kuksov, A., Schneider, C. M., and Schonhense, G.: "Sub-nanosecond resolution x-ray magnetic circular dichroism photoemission electron microscopy of magnetization processes in a permalloy ring." *Journal of Physics-Condensed Matter*, **17**(16): S1381-S1395 (2005).

Nefedov, A.: "X-ray resonant magnetic scattering on Fe/Cr superlattices." *Superlattice and Microstructures*, **37**: 99-106 (2005).

Nefedov, A.: "X-ray resonant magnetic scattering on noncollinearly coupled Fe/Cr superlattices." *Physica B*, **357**: 22-26 (2005).

Niklewski, A., Strunskus, T., Witte, G., and Wöll, C.: "Metal-organic chemical vapor deposition (MOCVD) of palladium: spectroscopic study of cyclopentadienyl-allyl-palladium deposition on a palladiumsubstrate." *Chem. Mater.*, **17**: 861-868 (2005).

Oran, U.: "Surface characterization of plasma chemically deposited polymer films by Time of flight static secondary ion mass spectroscopy," Freie University Berlin (2005).

Peisert, H., Biswas, I., Zhang, L., Knupfer, M., Hanack, M., Dini, D., Cook, M. J., Chambrier, I., Schmidt, T., Batchelor, D., and Chasse, T.: "Orientation of substituted phthalocyanines on polycrystalline gold: distinguishing between the first layers and thin films." *Chemical Physics Letters*, **403**(1-3): 1-6 (2005).

Petrov, I. D., Demekhin, P. V., Lagutin, B. M., Sukhorukov, V. L., Kammer, S., Mickat, S., Schartner, K.-H., Ehresmann, A., Klumpp, S., Werner, L., and Schmoranzer, H.: "Strongly perturbed Rydberg series originating from KrII 4p45s ionic states." *Journal of Electron Spectroscopy and Related Phenomena*, **144-147**: 35-38 (2005).

Pozdnyakova, O., Teschner, D., Wootsch, A., Kröhnert, J., Steinhauer, B., Sauer, H., Toth, L., Jentoft, F. C., Knop-Gericke, A., Paal, Z., and Schlogl, R.: "Preferential CO oxidation in hydrogen (PROX) on ceria-supported catalysts, part I: Oxidation state and surface species on Pt/CeO2 under reaction conditions." *Journal of Catalysis*, **237**(1): 1-16 (2006).

Pozdnyakova, O., Teschner, D., Wootsch, A., Kröhnert, J., Steinhauer, B., Sauer, H., Toth, L., Jentoft, F. C., Knop-Gericke, A., Paal, Z., and Schlogl, R.: "Preferential CO oxidation in hydrogen (PROX) on ceria-supported catalysts, part I: Oxidation states and surface species on Pd/CeO2 under reaction conditions, suggested reaction mechanism." *Journal of Catalysis*, **237**(1): 17-28 (2006).

Priest, A. N., Bansmann, P. M., Kaul, M. G., Stork, A., and Adam, G.: "Magnetic resonance imaging of the coronary vessel wall at 3 T using an obliquely oriented reinversion slab with adiabatic pulses." *Magnetic Resonance in Medicine*, **54**(5): 1115-1122 (2005).

Rack, A.: "Charakterisierung komplexer Materialsysteme mittels Synchrotron-Tomography und 3D-Bildanalyse," (2006).

Rader, O., Fauth, K., Gould, C., Ruster, C., Schott, G. M., Schmidt, G., Brunner, K., Molenkamp, L. W., Schutz, G., Kronast, F., Durr, H. A., Eberhardt, W., and Gudat, W.: "Identification of extrinsic Mn contributions in Ga1-xMnxAs by field-dependent magnetic circular X-ray dichroism." *Journal of Electron Spectroscopy and Related Phenomena*, **144**: 789-792 (2005).

Rader, O., Lezaic, M., Blugel, S., Fujimori, A., Kimura, A., Kamakura, N., Kakizaki, A., Miyanishi, S., and Akinaga, H.: "Spin-polarized surface state of MnSb(0001)." *New Journal of Physics*, **7**: 111 (2005).

Reichardt, J., Bär, M., Grimm, A., Kötschau, I., Lauermann, I., Sokoll, S., Lux-Steiner, M. C., Fischer, C.-H., Heske, C., Weinhardt, L., Fuchs, O., Jung, C., Gudat, W., Niesen, T. P., and Karg, F.: "Inducing and monitoring photoelectrochemical reactions at surfaces and buried interfaces in Cu (In,Ga) (S,Se)2 thin-film solar cells." *Applied Physics Letters*, **86**(17): 1-3 (2005).

Reif, M., Glaser, L., Martins, M., and Wurth, W.: "Size-dependent properties of small deposited chromium clusters by x-ray absorption spectroscopy." *Physical Review B - Condensed Matter and Materials Physics*, **72**(15): 155405 (2005).

Reinkoster, A., Korica, S., Langer, B., Prumper, G., Rolles, D., Viefhaus, J., Cvejanovic, S., and Becker, U.: "Photoelectron and photoion study of the valence photoionization of C-60." *Journal of Electron Spectroscopy and Related Phenomena*, **144**: 151-153 (2005).

Remhof, A., Bircan, C., Westphalen, A., Grabis, J., Nefedov, A., and Zabel, H.: "Shining light on magnetic microstructures." *Superlattices and Microstructures*, **37**(5): 353-363 (2005).

Riesemeier, H., Ecker, K., Gorner, W., Muller, B. R., Radtke, M., and Krumrey, M.: "Layout and first XRF applications of the BAMline at BESSY II." *X-Ray Spectrometry*, **34**(2): 160-163 (2005).

Rolles, D., Braune, M., Cvejanovic, S., Gessner, O., Hentges, R., Korica, S., Langer, B., Lischke, T., Prumper, G., Reinkoster, A., Viefhaus, J., Zimmermann, B. R., McKoy, V., and Becker, U.: "Isotope-induced partial localization of core electrons in the homonuclear molecule N-2." *Nature*, **437**(7059): 711-715 (2005).

Rudel, A., Hergenhahn, U., Maier, K., Rennie, E. E., Kugeler, O., Viefhaus, J., Lin, P., Lucchese, R. R., and Bradshaw, A. M.: "Exchange interaction effects in NO core-level photoionization cross-sections." *New Journal of Physics*, **7**: 189 (2005).

Rudolph, R., Pettenkofer, C., Bostwick, A. A., Adams, J. A., Ohuchi, F., Olmstead, M. A., Jaeckel, B., Klein, A., and Jaegermann, W.: "Electronic structure of the Si(1 1 1):GaSe van der Waals-like surface termination." *New Journal of Physics*, **7** (2005).

Sayago, D. I., Polcik, M., Nisbet, G., Lamont, C. L. A., and Woodruff, D. P.: "Local structure determination of a chiral adsorbate: Alanine on Cu(110)." *Surface Science*, **590**(1): 76-87 (2005).

Schalow, T., Laurin, M., Brandt, B., Schauermann, S., Guimond, S., Kuhlenbeck, H., Starr, D. E., Shaikhutdinov, S. K., Libuda, J., and Freund, H.-J.: "Oxygen storage at the metal/oxide interface of catalyst nanoparticles." *Angewandte Chemie - International Edition*, **44**(46): 7601-7605 (2005).

Schartner, K.-H., Schill, R. H., Hasselkamp, D., Mickat, S., Kammer, S., Werner, L., Klumpp, S., Ehresmann, A., Schmoranzer, H., Lagutin, B. M., and Sukhorukov, V. L.: "Partial wave analysis of interfering Kr 3d95p resonant Raman Auger transitions based on measurements of alignment and orientation parameters within the natural line width." *Journal of Physics B: Atomic, Molecular and Optical Physics*, **38**(22): 4155-4170 (2005).

Scherz, A., Gross, E. K. U., Appel, H., Sorg, C., Baberschke, K., Wende, H., and Burke, K.: "Measuring the kernel of time-dependent density functional theory with X-ray absorption spectroscopy of 3d transition metals." *Physical Review Letters*, **95**(25): 253006 (2005).

Schmidt, S., Weber, N., Elmers, H. J., Forster, F., Reinert, F., Hufner, S., Escher, M., Merkel, M., Kromker, B., and Funnemann, D.: "Quantitative microscopy of magnetic domains in Fe(100) by core-level x-ray photoelectron spectroscopy." *Physical Review B*, **72**(6): 064429 (2005).

Schöck, J.: "CO-Adsorption auf Ag-bedecktem Pt(355)," (2005).

Schoenes, J.: "Optical properties of YHx (0 <= x <= 2.1) thin films." *Journal of Alloys and Compounds*, **404-406**: 453-456 (2005).

Scholze, F., Laubis, C., Buchholz, C., Fischer, A., Plöger, S., Scholz, F., Wagner, H., and Ulm, G.: "Status of EUV reflectometry at PTB." *Progress in Biomedical Optics and Imaging - Proceedings of SPIE*, **5751**(II): 749-758 (2005).

Schulmeyer, T., Hunger, R., Fritsche, R., Jäckel, B., Jaegermann, W., Klein, A., Kniese, R., and Powalla, M.: "Interfaces of chalcogenide solar cells: A study of the composition at the Cu(In,Ga)Se2/CdS contact." *Thin Solid Films*, **480-481**: 110-117 (2005).

Schumann, F. O., Kirschner, J., and Berakdar, J.: "Mapping out electron-electron interactions at surfaces." *Physical Review Letters*, **95**(11): 041404 (2005).

Schüßler-Langeheine, C., Schlappa, J., Hu, Z., Chang, C. F., Benomar, M., Ott, H., Friedt, O., Braden, M., Tjeng, L. H., Tanaka, A., Schierle, E., Weschke, E., Kaindl, G., Sawatzky, G. A., Lin, H.-J., and Chen, C. T.: "Spectroscopy of stripe order in La1.8Sr0.2NiO4 using resonant soft X-ray diffraction." *Physical Review Letters*, **95**(15): 156402 (2005).

Senoner, M., Wirth, T., Unger, W. E. S., Escher, M., Weber, N., Funnemann, D., and Krömker, B.: "Testing of Lateral resolution in the nanometer range using the BAM-L002- certified Reference Material: Application of T0F-SIMS and NanoESCA instruments." *Journal of Surface Analysis*, **12**: 78-82 (2005).

Shaporenko, A., Cyganik, P., Buck, M., Terfort, A., and Zharnikov, M.: "Self-assembled monolayers of aromatic selenolates on noble metal substrates." *Journal of Physical Chemistry B*, **109**(28): 13630-13638 (2005).

Shaporenko, A., Cyganik, P., Buck, M., Ulman, A., and Zharnikov, M.: "Self-assembled monolayers of semifluorinated alkaneselenolates on noble metal substrates." *Langmuir*, **21**(18): 8204-8213 (2005).

Shaporenko, A., Heister, K., Ulman, A., Grunze, M., and Zharnikov, M.: "The effect of halogen substitution in self-assembled monolayers of 4-mercaptobiphenyls on noble metal substrates." *Journal of Physical Chemistry B*, **109**(9): 4096-4103 (2005).

Shaporenko, A., Ulman, A., Terfort, A., and Zharnikov, M.: "Self-assembled monolayers of alkaneselenolates on (111) gold and silver." *Journal of Physical Chemistry B*, **109**(9): 3898-3906 (2005).

Shikin, A. M., Varykhalov, A., Adamchuk, V., Ionov, A., Bozko, S. N., Gudat, W., and Rader, O.: "Quantum-well states and lateral superlattice effect in Ag and Au stripes on stepped W(145)." *Journal of Electron Spectroscopy and Related Phenomena*, **144**: 341-343 (2005).

Shikin, A. M., Varykhalov, A., Gorovikov, S. A., Prudnikova, G. V., Adamchuk, V. K., Rieder, K. H., Gudat, W., and Rader, O.: "Photoemission from surface-localized structures on vicinal surfaces: Initial- or final-state superlattice effect?" *Journal of Electron Spectroscopy and Related Phenomena*, **144**: 625-628 (2005).

Shiozawa, H., Rauf, H., Pichler, T., Grimm, D., Liu, X., Knupfer, M., Kalbac, M., Yang, S., Dunsch, L., Büchner, B., and Batchelor, D.: "Electronic structure of the trimetal nitride fullerene Dy3N@C80." *Physical Review B - Condensed Matter and Materials Physics*, **72**(19): 195409 (2005).

Shiraishi, M., Swaraj, S., Takenobu, T., Iwasa, Y., Ata, M., and Unger, W. E. S.: "Spectroscopic characterization of single-walled carbon nanotubes carrier-doped by encapsulation of TCNQ." *Physical Review B*, **71**(12): 125419 (2005).

Sikora, M., Kapusta, C., Zajac, D., Tokarz, W., Oates, C. J., Borowiec, M., Rybicki, D., Goering, E., Fischer, P., Schultz, G., De Teresa, J. M., and Ibarra, M. R.: "X-MCD magnetometry of CMR perovskites La0.67-yREyCa0.33MnO3." *Journal of Magnetism and Magnetic Materials*, **272-76**: 2148-2150 (2004).

Silaghi, S. D., Friedrich, M., Cobet, C., Esser, N., Braun, W., and Zahn, D. R. T.: "Dielectric functions of DNA base films from near-infrared to ultra-violet." *Physica Status Solidi B-Basic Solid State Physics*, **242**(15): 3047-3052 (2005).

Silaghi, S. D., Friedrich, M., Scholz, R., Kampen, T. U., Cobet, C., Esser, N., Richter, W., Braun, W., and Zahn, D. R. T.: "Vacuum ultraviolet spectroscopic ellipsometry investigations of guanine layers on H-passivated Si(111) surfaces." *Thin Solid Films*, **455-56**: 505-508 (2004).

Skorupska, K., Lublow, M., Kanis, M., Jungblut, H., and Lewerenz, H. J.: "Electrochemical preparation of a stable accumulation layer on Si: A synchrotron radiation photoelectron spectroscopy study." *Applied Physics Letters*, **87**(26): 262101 (2005).

Skorupska, K., Lublow, M., Kanis, M., Jungblut, H., and Lewerenz, H. J.: "On the surface chemistry of silicon under reducing conditions: An SRPES investigation." *Electrochemistry Communications*, **7**(10): 1077-1081 (2005).

Starr, D. E., Mendes, F. M. T., Middeke, J., Blum, R.-P., Niehus, H., Lahav, D., Guimond, S., Uhl, A., Kluener, T., Schmal, M., Kuhlenbeck, H., Shaikhutdinov, S., and Freund, H.-J.: "Preparation and characterization of well-ordered, thin niobia films on a metal substrate." *Surface Science*, **599**(1-3): 14-26 (2005).

Stepanow, S., Strunskus, T., Lingenfelder, M., Dmitriev, A., Spillmann, H., Lin, N., Barth, J. V., Wöll, C., and Kern, K.: "Deprotonation-driven phase transformations in terephthalic acid self-assembly on Cu(100)." *JOURNAL OF PHYSICAL CHEMISTRY B*, **108**(50): 19392-19397 (2004).

Strunskus, T., Fuchs, O., Weinhardt, L., Heske, C., Guraya, M., Muhler, M., Staemmler, V., and Wöll, C.: "The valence electronic structure of zinc oxide powders as determined by X-ray emission spectroscopy: Variation of electronic structure with particle size." *J. Electr. Spectrosc.Rel. Phenom.*, **134**: 183-189 (2004).

Suzuki, Y., Gordan, O. D., Silaghi, S. D., Zahn, D. R. T., Schubert, A., Thiel, W. R., Cobet, C., Esser, N., and Braun, W.: "Strong changes in the dielectric functions of cytosine upon molecular modification." *Applied Physics Letters*, **87**(21): 214101 (2005).

Swaraj, S.: "Surface characterization of plasma chemically deposited polymer films by X- ray photoelectron spectroscopy and Near edge X-ray absorption fine structure," Freie University Berlin (2005).

Swaraj, S., Oran, U., Lippitz, A., Friedrich, J. F., and Unger, W. E. S.: "Study of influence of external plasma parameters on plasma polymerised films prepared from organic molecules (acrylic acid, allyl alcohol, allyl amine) using XPS and NEXAFS." *Surface & Coatings Technology*, **200**(1-4): 494-497 (2005).

Swaraj, S., Oran, U., Lippitz, A., Friedrich, J. F., and Unger, W. E. S.: "Surface analysis of plasma-deposited polymer films, 6 - Analysis of plasma deposited allyl alcohol films before and after aging in air." *Plasma Processes and Polymers*, **2**(7): 572-580 (2005).

Swaraj, S., Oran, U., Lippitz, A., Schulze, R. D., Friedrich, J. F., and Unger, W. E. S.: "Surface analysis of plasma-deposited polymer films, 4(a) - In situ characterization of plasma-deposited ethylene films by XPS and NEXAFS." *Plasma Processes and Polymers*, **2**(4): 310-318 (2005).

Tai, Y., Shaporenko, A., Grunze, M., and Zharnikov, M.: "Effect of irradiation dose in making an insulator from a self-assembled monolayer." *Journal of Physical Chemistry B*, **109**(41): 19411-19415 (2005).

Tai, Y., Shaporenko, A., Noda, H., Grunze, M., and Zharnikov, M.: "Fabrication of stable metal films on the surface of self-assembled monolayers." *Advanced Materials*, **17**(14): 1745-1749 (2005).

Teschner, D., Pestryakov, A., Kleimenov, E., Havecker, M., Bluhm, H., Sauer, H., Knop-Gericke, A., and Schlogl, R.: "High-pressure X-ray photoelectron spectroscopy of palladium model hydrogenation catalysts. Part 1: Effect of gas ambient and temperature." *Journal of Catalysis*, **230**(1): 186-194 (2005).

Teschner, D., Pestryakov, A., Kleimenov, E., Havecker, M., Bluhm, H., Sauer, H., Knop-Gericke, A., and Schlogl, R.: "High-pressure X-ray photoelectron spectroscopy of palladium model hydrogenation catalysts. Part 2: Hydrogenation of trans-2-pentene on palladium." *Journal of Catalysis*, **230**(1): 195-203 (2005).

Turnbull, A. P., Kümmel, D., Prinz, B., Holz, C., Schultchen, J., Lang, C., Niesen, F. H., Hofmann, K.-P., Delbrück, H., Behlke, J., Müller, E.-C., Jarosch, E., Sommer, T., and Heinemann, U.: "Structure of palmitoylated BET3: Insights into TRAPP complex assembly and membrane localization." *EMBO Journal*, **24**(5): 875-884 (2005).

Unveren, E., Kemnitz, E., Lippitz, A., and Unger, W. E. S.: "Surface characterization of chromia for chlorine/fluorine exchange reactions." *Journal of Physical Chemistry B*, **109**(5): 1903-1913 (2005).

van Loyen, L., Bottger, T., Schadlich, S., Braun, S., Foltyn, T., Leson, A., Scholze, F., and Mullender, S.: "Laboratory LPP EUV reflectorneter working with non-polarized radiation." *Applied Surface Science*, **252**(1): 57-60 (2005).

Varykhalov, A., Rader, O., and Gudat, W.: "Structure and quantum-size effects in a surface carbide: W(110)/C-R(15 X 3)." *Physical Review B*, **72**(11): 115440 (2005).

Varykhalov, A., Shikin, A. M., Gudat, W., Moras, P., Grazioli, C., Carbone, C., and Rader, O.: "Probing the ground state electronic structure of a correlated electron system by quantum well states: Ag/Ni(111)." *Physical Review Letters*, **95**(24): 247601 (2005).

Viefhaus, J., Braune, M., Korica, S., Reinkoster, A., Rolles, D., and Becker, U.: "Auger cascades versus direct double Auger: relaxation processes following photoionization of the Kr 3d and Xe 4d, 3d inner shells." *Journal of Physics B-Atomic Molecular and Optical Physics*, **38**(21): 3885-3903 (2005).

Viefhaus, J., Grum-Grzhimailo, A. N., Kabachnik, N. M., and Becker, U.: "Electron-electron coincidence study of double Auger processes in atoms." *Journal of Electron Spectroscopy and Related Phenomena*, **141**(2-3): 121-126 (2004).

Vogel, J., Kuch, W., Camarero, J., Fukumoto, K., Pennec, Y., Pizzini, S., Bonfim, M., Petroff, F., Fontaine, A., and Kirschner, J.: "Interplay between magnetic anisotropy and interlayer coupling in nanosecond magnetization reversal of spin-valve trilayers." *Physical Review B*, **71**(6): 060404(R) (2005).

Vogel, J., Kuch, W., Hertel, R., Camarero, J., Fukumoto, K., Romanens, F., Pizzini, S., Bonfim, M., Petroff, F., Fontaine, A., and Kirschner, J.: "Influence of domain wall interactions on nanosecond switching in magnetic tunnel junctions." *Physical Review B*, **72**(22): 220402(R) (2005).

Wang, J., Kuch, W., Chelaru, L. I., Offi, F., and Kotsugi, M.: "Influence of exchange bias coupling on the single-crystalline FeMn ultrathin film." *Applied Physics Letters*, **86**(12): 122504 (2005).

Wang, W. H., Przybylski, M., Kuch, W., Chelaru, L. I., Wang, J., Lu, Y. F., Barthel, J., and Kirschner, J.: "Spin polarization of single-crystalline Co2MnSi films grown by PLD on GaAs(001)." *Journal of Magnetism and Magnetic Materials*, **286**: 336-339 (2005).

Wang, W. H., Przybylski, M., Kuch, W., Chelaru, L. I., Wang, J., Lu, Y. F., Barthel, J., Meyerheim, H. L., and Kirschner, J.: "Magnetic properties and spin polarization of Co2MnSi Heusler alloy thin films epitaxially grown on GaAs(001)." *Physical Review B*, **71**(14): 144416 (2005).

Weschke, E., Ott, H., Schierle, E., Schüß, C., Vyalikh, D. V., Kaindl, G., Leiner, V., Ay, M., Schmitte, T., Zabel, H., and Jensen, P. J.: "Finite-size effect on magnetic ordering temperatures in long-period antiferromagnets: Holmium thin films." *Physical Review Letters*, **93**(15): 157204 (2004).

Weschke, E., Ott, H., Schierle, E., Schussler-Langeheine, C., Kaindl, G., Leiner, V., and Zabel, H.: "Resonant magnetic X-ray scattering at the lanthanide M-5 edges." *Physica B-Condensed Matter*, **357**(1-2): 16-21 (2005).

Winkler, M., Griesche, J., Konovalov, I., Penndorf, J., Wienke, J., and Tober, O.: "CISCuT - solar cells and modules on the basis of CuInS2 on Cu-tape." *Solar Energy*, **77**(6): 705-716 (2004).

Wurz, R., Meeder, A., Fuertes Marron, D., Schedel-Niedrig, T., Knop-Gericke, A., and Lips, K.: "Native oxidation of CuGaSe2 crystals and thin films studied by electron paramagnetic resonance and photoelectron spectroscopy." *Physical Review B*, **70**(20): 205321 (2004).

Wurz, R., Rusu, M., Schedel-Niedrig, T., Lux-Steiner, M. C., Bluhm, H., Havecker, M., Kleimenov, E., Knop-Gericke, A., and Schlogl, R.: "In situ X-ray photoelectron spectroscopy study of the oxidation of CuGaSe2." *Surface Science*, **580**(1-3): 80-94 (2005).

Zahn, D. R. T., Salvan, G., Gavrila, G., and Paez, B. A.: "Chemistry and Morphological Properties of Metal Interfaces to Organic Semiconductors." *Solid State Physiks*, **45**: 313 (2005).

Zahn, D. R. T., Silaghi, S. D., Cobet, C., Friedrich, M., and Esser, N.: "Spectroscopic ellipsometry and reflectance anisotropy spectroscopy of biomolecular layers on silicon surfaces." *Physica Status Solidi B-Basic Solid State Physics*, **242**(13): 2671-2680 (2005).

Zhang, L., Konovalov, I., Wett, D., Schulze, D., Szargan, R., Nagel, M., and Chasse, T.: "Local partial densities of states in CuInS2 upper valence band determined by soft-x-ray emission spectrostopy: Evidence for In 5p contribution." *Journal of Applied Physics*, **98**(1): 013704 (2005).

Zhang, L., Peisert, H., Biswas, I., Knupfer, M., Batchelor, D., and Chasse, T.: "Growth of zinc phthalocyanine onto ZnS film investigated by synchrotron radiation-excited X-ray photoelectron and near-edge absorption spectroscopy." *Surface Science*, **596**(1-3): 98-107 (2005).

Zharnikov, M., Shaporenko, A., Paul, A., Gölzhauser, A., and Scholl, A.: "X-ray absorption spectromicroscopy studies for the development of lithography with a monomolecular resist." *Journal of Physical Chemistry B*, **109**(11): 5168-5174 (2005).

Zubavichus, Y., Shaporenko, A., Grunze, M., and Zharnikov, M.: "Innershell absorption spectroscopy of amino acids at all relevant absorption edges." *Journal of Physical Chemistry A*, **109**(32): 6998-7000 (2005).

Zubavichus, Y., Zharnikov, M., Yang, Y., Fuchs, O., Heske, C., Umbach, E., Tzvetkov, G., Netzer, F. P., and Grunze, M.: "Surface chemistry of ultrathin films of histidine on gold as probed by high-resolution synchrotron photoemission." *Journal of Physical Chemistry B*, **109**(2): 884-891 (2005).

Authors Index

(click on page number to open selected page)

Keyword Index
(click on page number to open selected page)